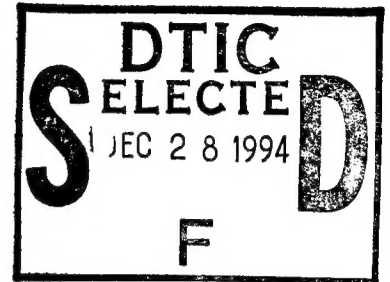


Appendix to
"Passive Spatial Beam Control"

Final Report
DAAB07-88-6-F-405



Report Number
NV-95-C01

CREOL

This document has been approved
for public release and sale; its
distribution is unlimited.

Eric W. VanStryland

September 29, 1994

19941212 067

DTIC QUALITY INSPECTED 1

Appendix to
"Passive Spatial Beam Control"

Final Report
DAAB07-88-6-F-405

Report Number
NV-95-C01

CREOL

Eric W. VanStryland

September 29, 1994

Accession For	
NTIS CRA&I	<input checked="checked" type="checkbox"/>
DTIC TAB	<input type="checkbox"/>
Unannounced	<input type="checkbox"/>
Justification	
By	
Signature/	
Date	
Initials	
A-1	

Eclipsing Z-scan measurement of $\lambda/10^4$ wave-front distortion

T. Xia, D. J. Hagan, M. Sheik-Bahae, and E. W. Van Stryland

Center for Research in Electro-Optics and Lasers and Department of Physics, University of Central Florida,
Orlando, Florida 32816

Received August 13, 1993

We introduce a simple modification to the Z-scan technique that results in a sensitivity enhancement that permits measurement of nonlinearly induced wave-front distortion of $\approx \lambda/10^4$. This sensitivity was achieved with 10-Hz repetition-rate pulsed laser sources. Sensitivity to nonlinear absorption is also enhanced by a factor of ≈ 3 . This method permits characterization of nonlinear thin films without the need for waveguiding.

Since the introduction of the Z scan,¹ a sensitive single-beam technique for measuring nonlinear refraction (NLR), several variations have been introduced to enhance the technique. These include measurements in the presence of nonlinear absorption² (NLA), the two-color Z scan for the study of nondegenerate nonlinearities,^{3,4} the time-resolved Z scan,^{4,5} and measurements of the anisotropy of NLR.⁶ Most of these experiments have been performed with low-repetition-rate (≈ 10 -Hz) picosecond or nanosecond laser systems. Even with these low data-acquisition rates, the technique has demonstrated a sensitivity to wave-front distortion of $\lambda/300$ for a signal-to-noise ratio (S/N) of unity. It has been shown theoretically that a threefold enhancement of the Z scan's sensitivity to NLR can be achieved by the use of a lens between the sample and the aperture,⁷ but this has yet to be realized experimentally. Recently it was demonstrated that the use of a top-hat beam profile in the Z scan results in an increase in sensitivity to NLR of ≈ 2.5 .⁸ Here we introduce a simple variation of the Z-scan technique that provides greater than an order-of-magnitude enhancement of the S/N. This modification involves replacing the far-field aperture used in the standard Z scan with an obscuration disk that blocks most of the beam. The resulting pattern of light that passes around the edge of the disk, shown in the inset of Fig. 1, appears as a thin halo of light, reminiscent of a solar eclipse; hence this technique is named the eclipsing Z scan (EZ scan). This modification of the Z scan, accompanied by methods to compensate for fluctuations of the beam spatial profile, results in a sensitivity to induced wave-front distortion of $\approx \lambda/10^4$ with a S/N of unity from a 10-Hz repetition-rate pulsed laser. Significantly higher sensitivities should be possible for more stable or higher-repetition-rate laser systems.

The EZ-scan experimental setup is shown in Fig. 1, where the aperture of the Z scan has been replaced by an opaque disk in the far field. As with the Z scan, a thin nonlinear sample is scanned along the Z axis of a focused Gaussian beam. In the case of a self-focusing nonlinearity ($n_2 > 0$, where $n = n_0 + n_2 I$), the sample will behave as a positive lens near the focus. Thus, for the sample positioned prior to focus, the far-field beam divergence is increased, and more

light will pass by the disk in the far field. Note that this is exactly opposite the decreased transmittance of the aperture for a Z scan. With the sample positioned after the focal plane, the effect of the sample is to collimate the beam, and the disk blocks more of the light. Consequently, in the EZ scan a self-focusing medium results in an increase in transmittance (peak), followed by a decrease (valley) as the sample is scanned from in front of to behind the focus. For self-defocusing media, the positions of the valley and peak are reversed.

For a thin sample⁹ this behavior can be modeled by the separated equations for irradiance, I , and induced phase shift, $\Delta\phi$: $dI/dz' = -\alpha I$ and $d\Delta\phi/dz' = kn_2 I(z')$, where α is the linear absorption coefficient, $k = 2\pi/\lambda$, and λ is the wavelength in vacuum. z' is the depth within the sample, as distinct from Z , the sample position with respect to the beam waist. In our modeling we assume the incident beam to be Gaussian. The integrated phase shift for a sample of length L follows the radial variation of the

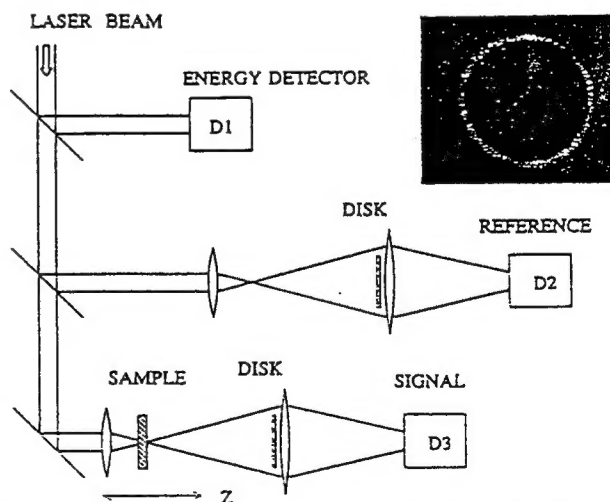


Fig. 1. Experimental arrangement for the EZ scan. D1 is the input energy monitor, and D3 measures the energy transmitted through the sample and past the disk. D2 monitors the energy transmitted through the reference arm, which is identical to the signal arm with no sample. The measured quantity is the ratio $D3/D2$. Inset: CCD image of a picosecond ND:YAG laser beam after it passes a 99% obscuration disk.

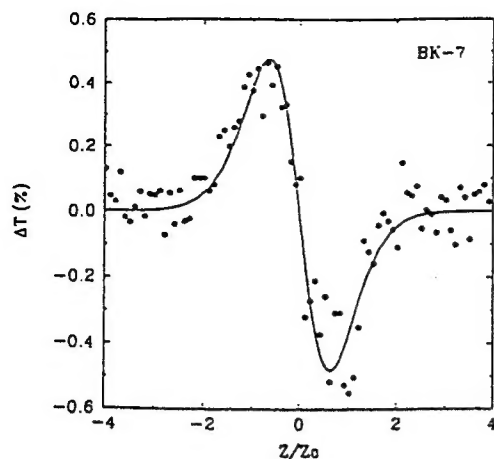


Fig. 2. EZ scan of a 1.5-mm-thick BK-7 sample performed with a frequency-doubled picosecond Nd:YAG laser. The solid curve is a fit to the data, indicating a peak wave-front distortion of $\lambda/2200$ with a S/N of approximately 5.

incident irradiance, $I \propto |E|^2$, for each sample position Z . Hence $\Delta\phi(r, Z, t) = \Delta\Phi_0(t)|E(r, Z, t)/E(0, 0, t)|^2$, where $\Delta\Phi_0(t) = \Delta\phi(0, 0, t) = kn_2 I(0, 0, t)L_{\text{eff}}$ is the on-axis phase shift at focus and $L_{\text{eff}} = [1 - \exp(-\alpha L)]/\alpha$. The electric field inside the medium at the exit surface is given by $E'(r, Z, t) = E(r, Z, t)\exp[-\alpha L/2 + i\Delta\phi(r, Z, t)]$, and the irradiance distribution at the plane of the disk (or aperture) can be found through a diffraction calculation or by the Gaussian decomposition method of Weaire *et al.*⁹

Figure 2 shows an EZ scan of a 1.5-mm-thick sample of BK-7 glass in which the normalized transmittance change, ΔT , is plotted as a function of Z . The laser source is a hybridly mode-locked and Q-switched frequency-doubled Nd:YAG laser emitting single 28-ps (FWHM) pulses at 532 nm with the input energy purposely reduced to less than 50 nJ to show the system noise. The beam was focused to a spot size of 14 μm (half-width at $1/e^2$ intensity), resulting in a peak irradiance of 0.52 GW/cm². Small beam-shape or beam-pointing fluctuations cause significant noise in the signal as measured by the ratio of energies detected by D3 and D1 (see Fig. 1). This led to the introduction of the reference arm shown in Fig. 1 (first proposed by Ma *et al.* for the Z scan⁴), which propagates a portion of the beam along an identical optical path except without a sample. By taking the ratio of energies D3 and D2, we can increase the S/N by a factor of 3–5. In our system, with the 100-shot average per data point shown in Fig. 2, the rms noise can be reduced to $\pm 0.1\%$ with this method. The solid curve fitted to the data in Fig. 2 gives $\Delta\Phi_0 = 2\pi/2200$ for S/N = 5. Thus with a S/N of unity we can resolve $\Delta\Phi_0 < 2\pi/10^4$, corresponding to a physical displacement of the wave front of $< \lambda/10^4$ or 0.05 nm. Using the same system with the reference arm, but performing a Z scan, we find that the sensitivity is limited to $\approx \lambda/700$. The increased sensitivity of the EZ scan is due to the larger fractional change in irradiance in the wings of the beam that are detected in an EZ scan compared with that near the center, as detected in a Z scan. We

conservatively define $S/N = \Delta T_{\text{pv}}/4\sigma$, where ΔT_{pv} is the difference between normalized peak and valley transmittances,¹ and σ is the standard deviation of the data in the absence of a nonlinearity.

For the Z scan,¹ ΔT_{pv} is almost linearly related to the light-induced phase shift at the focus, $\Delta\Phi_0$,

$$\Delta T_{\text{pv}} \approx 0.406(1 - S)^{0.25}|\Delta\Phi_0|, \quad (1)$$

where S is the aperture transmittance. This relationship holds to within $\pm 3\%$ for phase shifts $\Delta\Phi_0 < \pi$. With equal disk and aperture sizes, the corresponding absolute changes in transmitted power or energy are equal and opposite. However, the fractional transmittance changes may differ greatly for aperture and disk since much less light is transmitted with the disk for S near unity. In Fig. 3 we show the calculated ΔT_{pv} versus the disk radius and versus the aperture radius a for the EZ scan and the Z scan, respectively, for $\Delta\Phi_0 = 0.1$. The fraction of light blocked by the disk is simply S , the aperture transmittance in a Z scan, which is $S = 1 - \exp(-2a^2/w_a^2)$, where w_a is the beam radius at the disk plane in the linear regime.^{1,2} We see from Fig. 3 that for large enhancement to be obtained, S must be within a few percent of unity. In practice this limits the maximum sensitivity enhancement as the energy reaching the detector becomes too small to detect. For our system $S = 0.99$, as used in the inset in Fig. 1, gave good enhancement while still giving sufficient energy for easy detection. Note that for $S = 0.5$, corresponding to $a = w_a\sqrt{2 \ln 2}$, the sensitivities of the Z scan and EZ scan are identical, as expected.

For a large disk, $0.995 > S > 0.98$ (the useful range for this technique), and a small nonlinear phase shift $\Delta\Phi_0 \leq 0.2$, we find a similar empirical linear relationship between ΔT_{pv} and $\Delta\Phi_0$ for the EZ scan:

$$\Delta T_{\text{pv}} \approx 0.68(1 - S)^{-0.44}|\Delta\Phi_0|, \quad (2)$$

which is accurate to within $\pm 3\%$. For the above range of S the spacing between the peak and valley,

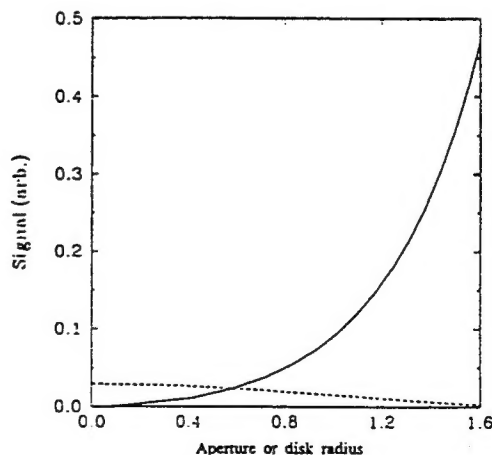


Fig. 3. Calculated ΔT_{pv} for an EZ scan (solid curve) and a Z scan (dashed curve) versus the normalized aperture or disk radius, respectively, for a peak on-axis phase shift of $|\Delta\Phi_0| = 0.1$.

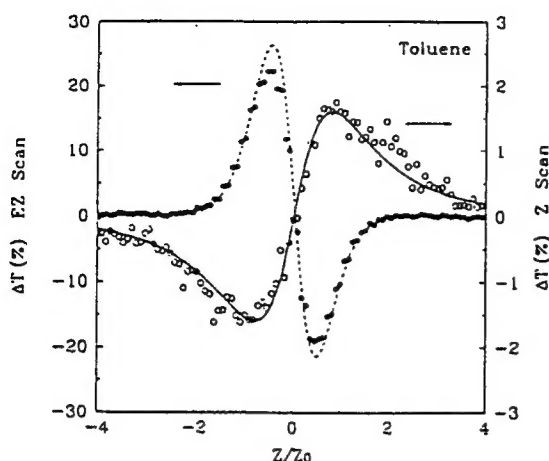


Fig. 4. Experimental comparison of an EZ scan (filled circles) and a Z scan (open circles) of toluene under identical conditions. Note that the Z-scan data are plotted on a 10× expanded scale for clarity. The laser source is a frequency-doubled nanosecond Nd:YAG laser. The solid and dashed curves are the result of calculations with a common $\Delta\Phi_0$ obtained from a best fit to the Z scan only.

ΔZ_{pv} , is empirically found to be given by $\Delta Z_{pv} = 0.9Z_0 - 1.0Z_0$ which grows to the Z-scan value of $\approx 1.7Z_0$ as $S \rightarrow 0$. As described in Ref. 1, the linearity of relations (1) and (2) allows for simple analysis of pulsed laser experiments, as we may simply integrate over the laser pulse shape to get the normalized energy transmittance change. Thus, for pulsed sources, $\Delta\Phi_0$ in relation (2) should be replaced by its time-averaged value.^{1,2}

Figure 4 shows an EZ scan and a Z scan performed under identical conditions on a 1-mm-thick cuvette filled with toluene. Note that the vertical scale for the Z scan has been expanded by a factor of 10 for clarity. Both scans were performed with the second harmonic of a single-longitudinal-mode Q-switched Nd:YAG laser operating in the TEM₀₀ mode. The $\lambda = 0.532$ nm, 4.7-ns (FWHM) pulse was focused to a beam radius of 22 μm (half-width at $1/e^2$ intensity). In each case the incident energy was 62 μJ , corresponding to a peak irradiance at the beam waist of 1.68 GW/cm². The EZ scan used a disk of $S = 0.99$, while for the Z scan an aperture of $S = 0.40$ was used. The solid and dashed curves are fits performed with the thin sample approximation, in each case using the same $\Delta\Phi_0$ as determined from the Z scan. Experimentally, we observe a factor-of-13 increase in sensitivity for the EZ scan, compared with a predicted improvement of 15. This difference may be due to deviations from a perfect Gaussian beam profile or slight misalignment of the disk. Errors that are due to deviations from $S = 0.99$ are small, as the estimated error in $(1 - S)$ is $< \pm 5\%$, which from relation (2) results in an error for $\Delta\Phi_0$ of $\approx \pm 2\%$.

As with the Z scan, one may also study samples exhibiting both NLR and NLA by performing successive EZ scans with and without the disk. Removing the disk gives an open-aperture Z scan that is sensitive only to nonlinear losses.² Interestingly, the presence of a far-field obscuration disk also results

in an increase in sensitivity to NLA. For example, in the case of reverse saturable absorption or two-photon absorption the center portion of the beam is more strongly absorbed than the wings, thereby spatially broadening the beam as it leaves the sample. Propagation transforms this near-field broadening into far-field narrowing, causing more of the beam to be blocked by the disk and enhancing the fractional change in transmittance seen by the detector. For similar reasons, an obscuration disk also enhances the effect of saturable absorption.

In summary, we have demonstrated that the EZ scan, in combination with beam fluctuation compensation, provides a highly sensitive method for measuring small nonlinearly induced phase shifts, while retaining the ability to discriminate between NLR and NLA, and for determining the sign of each of these effects. The method is particularly relevant to the current problem of determining nonresonant nonlinearities in thin films without the need for waveguide coupling. For films of thickness $d = \lambda$, a sensitivity to wave-front distortion of $\lambda/10^4$ corresponds to a sensitivity to index changes of $\Delta n \approx 10^{-4}$.

As we observed from Fig. 4, the enhancement in sensitivity comes at the expense of a reduction in accuracy caused, we believe, by deviations from a Gaussian irradiance distribution. We therefore recommend use of this technique with a known reference to calibrate the system (for our system, without such calibration, the absolute accuracy was within 18%). The Z scan is still the method of choice unless the S/N is a problem.

We gratefully acknowledge the support of the National Science Foundation (grant ECS 9120590), the Defense Advanced Research Projects Agency, and the Night Vision and Electro-Optics Directorate. In addition we thank F. Senesi, A. A. Said, Z. Wang, and C. Wamsley for help in data acquisition. D. J. Hagan and E. W. Van Stryland are also with the Department of Electrical and Computer Engineering, University of Central Florida.

References

1. M. Sheik-Bahae, A. A. Said, and E. W. Van Stryland, *Opt. Lett.* **14**, 955 (1989).
2. M. Sheik-Bahae, A. A. Said, T. H. Wei, D. J. Hagan, and E. W. Van Stryland, *IEEE J. Quantum Electron.* **26**, 760 (1990).
3. M. Sheik-Bahae, J. Wang, R. DeSalvo, D. J. Hagan, and E. W. Van Stryland, *Opt. Lett.* **17**, 258 (1992).
4. H. Ma, A. S. Gomez, and C. B. de Araújo, *Appl. Phys. Lett.* **59**, 2666 (1991).
5. J. Wang, M. Sheik-Bahae, A. A. Said, D. J. Hagan, and E. W. Van Stryland, *Proc. Soc. Photo-Opt. Instrum. Eng.* **1692**, 63 (1992).
6. R. DeSalvo, M. Sheik-Bahae, A. A. Said, D. J. Hagan, and E. W. Van Stryland, *Opt. Lett.* **18**, 194 (1993).
7. J. A. Hermann and P. B. Chapple, *J. Mod. Opt.* **38**, 1035 (1991).
8. W. Zhao and P. Palffy-Muhoray, *Appl. Phys. Lett.* **63**, 1613 (1993).
9. D. Weaire, B. S. Wherrett, D. A. B. Miller, and S. D. Smith, *Opt. Lett.* **4**, 331 (1979).

Time-resolved Z-scan measurements of optical nonlinearities

J. Wang, M. Sheik-Bahae, A. A. Said, D. J. Hagan, and E. W. Van Stryland

Center for Research in Electro-Optics and Lasers, University of Central Florida, Orlando, Florida 32816

Received September 17, 1993; revised manuscript received January 28, 1994

We introduce a temporal delay in one beam of the two-color Z-scan apparatus, which measures nondegenerate nonlinear absorption and nondegenerate nonlinear refraction. This technique allows us to time resolve separately the sign and the magnitude of the nonlinear absorption and refraction at frequency ω_p that are due to the presence of a strong excitation at frequency ω_e . For example, in semiconductors we specifically measure the bound electronic, nondegenerate nonlinear refraction and nondegenerate two-photon absorption, as well as the two-photon-generated free-carrier refraction and absorption as functions of time. We demonstrate this technique on ZnSe, ZnS, and CS₂, using picosecond pulses at 1.06 and 0.532 μm .

1. INTRODUCTION

Interpretations of measurements of optical nonlinearities of materials are often complicated by the presence or the competition of two or more nonlinear mechanisms. In many cases the experimental technique cannot distinguish between these different nonlinearities. For example, the degenerate four-wave mixing (DFWM) signal for a cubic nonlinearity is proportional to $|\chi^{(3)}|^2$, where $\chi^{(3)}$ is the third-order susceptibility.¹ Index changes $\{\text{Re}[\chi^{(3)}]\}$ and losses $\{\text{Im}[\chi^{(3)}]\}$ both contribute to the DFWM signal; therefore they are indistinguishable in DFWM experiments. A further complication can arise from contributions of ultrafast and cumulative nonlinearities. For example, in semiconductors we have observed the simultaneous presence of the bound electronic optical Kerr effect (ultrafast n_2) and two-photon absorption (2PA), along with free-carrier absorption and refraction, which are cumulative for decay times longer than the pulse width.^{2,3} In this paper we present a technique for unraveling the various contributions to the nonlinear response of a material. We demonstrate this technique, which is a time-resolved two-color Z scan,^{4,5} for separating the nonlinearities occurring in ZnSe, ZnS, and CS₂ when these materials are irradiated by picosecond pulses at 1.06 and 0.532 μm .

The two-color Z scan^{4,5} measures the nondegenerate nonlinear response of a material at the probe frequency ω_p that is due to the presence of an excitation beam at frequency ω_e . This method is capable of separating the refractive and the absorptive nonlinear contributions but cannot distinguish between ultrafast and cumulative nonlinearities. The introduction of a temporal delay into the two-color Z-scan apparatus permits separation of the nonlinearities having a different temporal response.

We first describe the experimental arrangement and its calibration. An example of time-resolved data for CS₂ displaying only nonlinear refraction is given, followed by results on ZnSe and ZnS. The semiconductor data give values for the nondegenerate Kerr effect $n_2(\omega_p; \omega_e)$, in-

cluding the sign and the magnitude, the nondegenerate 2PA coefficient $\beta(\omega_p; \omega_e)$, and the free-carrier refractive coefficient $\sigma_r(\omega_p)$ and absorptive cross section $\sigma_a(\omega_p)$.

2. EXPERIMENTAL ARRANGEMENT

The experimental arrangement, shown in Fig. 1, is an extension of the Z-scan arrangement of Refs. 6 and 7. The extracted 43-ps (FWHM) pulse from a Q-switched and mode-locked Nd:YAG laser ($\lambda = 1.06 \mu\text{m}$) is separated into two beams by a variable beam splitter that controls the irradiance ratio between them. One of the beams passes through a variable time-delay stage while the second goes through a second-harmonic-generating crystal to produce 0.532- μm light. The polarization of the beams is separately controlled by half-wave plates. The two beams are recombined by a dichroic beam splitter and are focused with a nearly achromatic lens of focal length $f = 15 \text{ cm}$ onto the sample. A second dichroic beam splitter then separates the two beams for detection after passing through apertures of transmittance S .

In this time-resolved two-color Z-scan experimental setup, the sample position Z , with respect to the probe-beam waist and the time delay t_d between the excitation and the probe beams, is independently varied according to the experiment, as described below. The measured quantity is the normalized transmittance as a function of Z (Z scan) or as a function of t_d (temporal scan). Analogous to the usual single-wavelength Z scan, an open-aperture ($S = 1$, i.e., no aperture) Z scan at a fixed delay is sensitive only to the induced changes in absorption, whereas a closed-aperture (i.e., partially closed aperture) Z scan displays the induced refractive changes as well. We use an aperture of $S = 0.4$ for all closed-aperture data given in this paper. In the absence of nonlinear absorption, the change in transmittance between the peak (transmittance maximum) and the valley (transmittance minimum) in a closed-aperture Z scan, defined as ΔT_{pv} , is linearly proportional to the induced phase distortion,

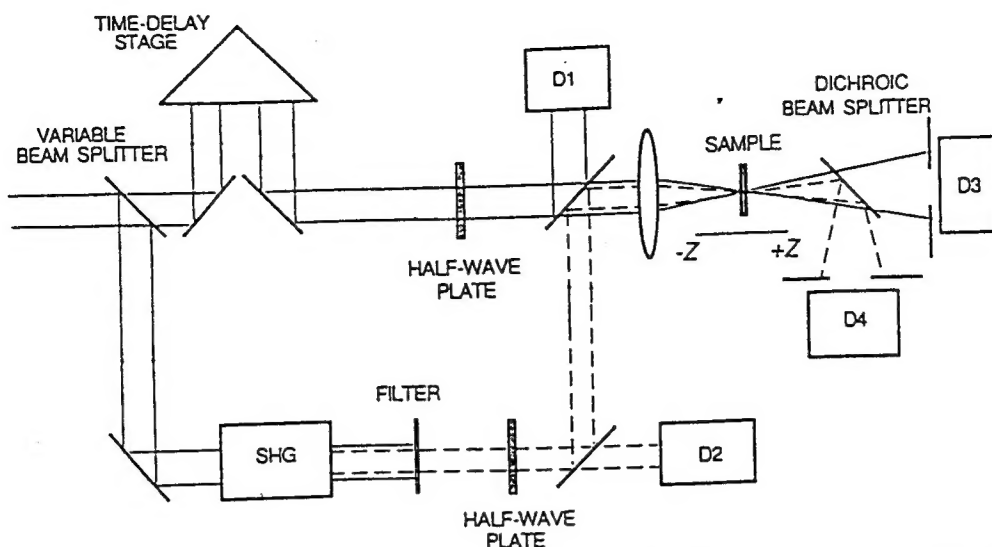


Fig. 1. Time-resolved excite-probe two-color Z-scan experimental apparatus. D1–D4, detectors. SHG, second-harmonic-generating crystal.

which in turn is proportional to the nondegenerate nonlinear refractive index. When nonlinear absorption is also present, as discussed in Ref. 7, the division of closed-aperture data by open-aperture data again gives the nonlinear refraction, as long as the nonlinear absorption is not too large (the same criterion as is discussed in Ref. 7 is valid here). We refer to the results of this division as a divided Z scan. If we measure the transmittance as a function of time delay for a fixed sample position, we can separately determine the dynamics of the nonlinear absorption (open aperture) and refraction (closed aperture). If the time-delay stage is fixed at long time delays such that there is no overlap between probe and excitation, the Z scan is sensitive only to long-lived nonlinearities, which in semiconductors provides an independent measurement of free-carrier absorption and refraction, separated from the bound electronic nonlinearities.

To determine the temporal response of the nonlinear absorption and refraction, we use the following procedure: Zero temporal delay is first determined in the manner discussed toward the end of this section. We then place the sample at the minimum transmittance position of an open-aperture Z scan (i.e., at the position of the waist). The temporal delay is then scanned to measure the normalized transmittance as a function of time delay t_d . We refer to this open-aperture transmittance as $T_{op}(t_d)$, and it gives the nonlinear absorption as a function of time. Measurement of the nonlinear refraction is somewhat more complicated but is based on the linear relation between ΔT_{pv} and the phase distortion.

For materials showing no degenerate or nondegenerate nonlinear absorption, a closed-aperture Z scan at a fixed time delay is used to determine the transmittance peak and valley Z positions. With the sample fixed at the position of the peak, we scan the time-delay stage. This procedure is repeated with the sample placed at the Z position of the valley. The difference between these two sets of data is $\Delta T_{pv}(t_d)$, which is directly proportional to the nonlinear-induced phase change. For the time delay fixed at $t_d = 0$, this phase change is proportional to the nondegenerate nonlinear refractive

index $n_2(\omega_p; \omega_e)$. If both nonlinear absorption and nondegenerate nonlinear refraction are present, both open- and closed-aperture temporal scans must be performed at the position of the peak and the valley for the divided Z scan. The temporal-scan results are then divided to obtain $\Delta T_{pv}(t_d)$ (one can perform these scans simultaneously by using a beam splitter in the transmitted probe beam and the two detectors, one without and one with an aperture). As long as the nondegenerate nonlinear absorption remains small, $n_2(\omega_p; \omega_e)$ remains proportional to ΔT_{pv} .⁷ In general any two frequencies can be used as long as the beams can be spatially and temporally overlapped. This technique can also be used for two beams having the same wavelength; however, the experiment becomes more difficult because of coherent interactions, which require interferometric stability for interpretation. However, the use of counterpropagating beams would permit separation of the beams but would add complexity to temporal-delay measurements.

In the experiments presented here, we can use either the fundamental (1.06- μm) or the second-harmonic (0.532- μm) beam as the excitation. We absolutely calibrate the pulse widths and the beam waists of the two Gaussian beams. This necessitates performing spatial beam scans and temporal autocorrelations of both the fundamental and the second-harmonic beams, as well as determining the longitudinal separation between the two beam waists caused by residual chromatic aberration of the focusing lens. By performing single-wavelength closed-aperture Z scans at 1.06 and 0.532 μm on a 1-mm cell containing CS_2 , we determined that the beam waists were separated by 1.5 mm because of chromatic aberration in the lens. Such aberration is easily accounted for in the numerical fitting routine described in Section 4. Additionally, as the separation between the peak and the valley of the transmittance (ΔZ_{pv}) for a third-order response is ≈ 1.7 times the Rayleigh range, this measurement confirmed that the spot sizes at focus (half-width at $1/e^2$ maximum in irradiance) were 27 and 20 μm for the 1.06- and the 0.532- μm beams, respectively. Using autocorrelation measurements, we determined the pulse

widths (FWHM) to be 43 and 31 ps at 1.06 and 0.532 μm , respectively. The estimated uncertainty in the spot-size and the pulse-width measurements are $\pm 5\%$. The incident and the transmitted pulse energies are detected by integrating silicon photodiodes. A spike filter at the appropriate wavelength is placed in front of each detector. Each data point is an average of 10 shots, taken with the aid of an automated data-acquisition system. While the Z-scan data are acquired, the pulse width and energy are also monitored, and acceptance windows of $\pm 5\%$ are set for both pulse width and input energy to increase the signal-to-noise ratio.⁸ The absolute irradiances at the sample for each beam can then be calculated given the energy as calibrated by a pyroelectric energy meter.

A limitation of this method is the range of temporal delays that can be scanned while the position of focus and the waist size of the delayed beam are kept constant. We maximized this range by minimizing the divergence of the laser beams before the focusing lens. We used a measured input beam divergence of 3.4×10^{-4} rad, and we calculate for our geometry (≈ 2 m from the waist) that a 1-ns time delay changes the waist size by $\approx 4\%$ at 1.06 μm . This delay also results in a displacement of the focus that is negligible ($< 1\%$ of f).

For the two-color experiment, maintaining the spatial overlap around focus is crucial. A 6-arcsec angle between the two beams as they enter the focusing lens would give a 10% offset of the spatial overlap of the two beams at focus ($\Delta x = 2 \mu\text{m}$ for a beam waist of 20 μm). Prior to inserting the focusing lens, we propagate the two beams for ≈ 4 m and ensure their spatial overlap by maximizing the transmittances through apertures. A similar procedure is repeated near the focus once the focusing lens is inserted. Finally, we achieve a fine adjustment of the spatial overlap at focus by maximizing the change in transmittance of the probe, using a nonlinear absorber. The change in the probe transmittance is maximized when the two Gaussian beams are overlapped (i.e., their on-axis points are coincident). The nonlinear absorber used in this technique may be a nondegenerate two-photon absorber, an excited-state absorber, or a saturable absorber; however, because the 2PA process is nearly instantaneous, it requires temporal overlap of the laser pulses as well. Therefore an excited-state or a saturable absorbing medium with a long recovery time is easier to use initially.

After ensuring spatial overlap, it is necessary to determine the position of zero time delay between the excitation and the probe beams. Performing a closed-aperture time scan on CS_2 with the sample stage positioned near the Z-scan peak, we obtain the data shown in Fig. 2. This procedure gives the temporal cross-correlation function between the two beams, provided that the transmittance through the aperture varies linearly with the excitation irradiance. This result is valid as long as ΔT_p is linearly dependent on the excitation, i.e., for transmittance changes to as much as $\approx 20\%$ when the sample is placed at the peak or the valley.⁷ Returning to Fig. 2, we find that the width of 53 ps (FWHM) for this curve agrees with a calculation of the cross correlation for the pulses of FWHM 43 and 31 ps at 1.06 and 0.532 μm , respectively, as measured by the individual second-order autocorrelation functions. Hence we have shown that

the two-color Z scan can be used as a cross correlator to measure pulse widths, provided that one of the pulse widths is known or, as in the case of harmonic or parametric processes, that a fixed relationship between the two pulses exist. Like any nonlinear correlation technique, the temporal resolution of this technique is limited by the response time of the nonlinearity. For UV pulses for which second-harmonic-generating crystals are not available, this method may prove useful.

3. THEORY

A. Semiconductor Nonlinearities

In the picosecond regime optical nonlinearities in semiconductors under nonresonant excitation (i.e., in the transparency regime) are generally a combination of bound electronic and free-carrier effects. Bound electronic nonlinearities arising from an anharmonic response of the valence electrons are ultrafast, with a typical response time being of the order of an optical cycle. This process can be regarded as instantaneous when laser pulses containing many optical cycles are used. We characterize this response with $\chi^{(3)}$. In the transparency regime free-carrier nonlinearities rely on multiphoton carrier generation and appear as higher-order phenomena. In particular, free-carrier refraction and absorption that are due to charge carriers generated by 2PA can be characterized as an effective $\chi^{(5)}$ process.³ Most importantly, free-carrier effects are further distinguishable from the bound electronic effect because of their long recovery time determined by the free-carrier lifetime.⁹ A time-resolved study of these processes can therefore identify and characterize the various contributions.

We define the total change of refractive index (Δn) and absorption coefficient ($\Delta \alpha$) as the sum of the bound electronic (subscript b) and free-carrier (subscript f) contributions:

$$\Delta n(\omega_p; \omega_e) = \Delta n_b + \Delta n_f, \quad (1a)$$

$$\Delta \alpha(\omega_p; \omega_e) = \Delta \alpha_b + \Delta \alpha_f. \quad (1b)$$

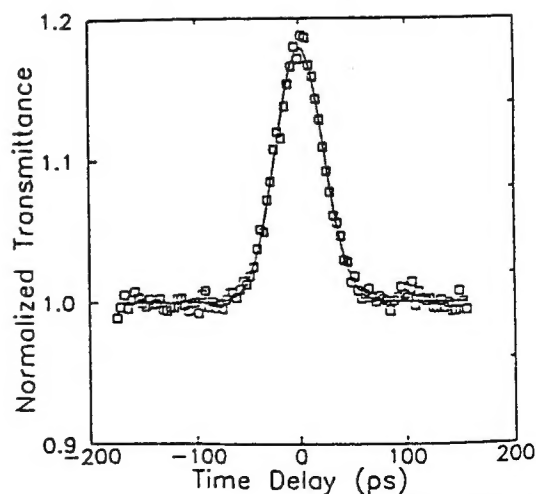


Fig. 2. Time-resolved two-color Z scan of CS_2 obtained with $\lambda = 1.06 \mu\text{m}$ as the excitation and $\lambda = 0.532 \mu\text{m}$ as the probe. This procedure gives the cross correlation of these two pulses and determines the zero-time-delay position.

The quantities for describing the bound electronic effect are the nonlinear refractive index $n_2(\omega_p; \omega_e)$ and the 2PA coefficient $\beta(\omega_p; \omega_e)$ measured at probe frequency ω_p that are due to the presence of the excitation beam at frequency ω_e . We define these coefficients as

$$\Delta n_b(\omega_p; \omega_e) = 2n_2(\omega_p; \omega_e)I_e, \quad (2a)$$

$$\Delta \alpha_b(\omega_p; \omega_e) = 2\beta(\omega_p; \omega_e)I_e, \quad (2b)$$

where I_e is the irradiance of the excitation beam. The factor of 2 comes from weak-wave retardation.^{5,10} The coefficients n_2 and β are related through Kramers-Kronig dispersion relations by virtue of the principle of causality.¹¹⁻¹⁴ Recently the Kramers-Kronig relations were employed to calculate the dispersion and the band-gap scaling of n_2 in solids from the calculated nonlinear absorption spectrum (including 2PA) by use of a simple two-parabolic-band model.¹² The degenerate n_2 and β measured with single-beam Z scans strongly support this theory. Because the nonlinear Kramers-Kronig relation generally relates the nondegenerate nonlinear absorption with the nondegenerate nonlinear refraction, the two-color Z scan provides a direct comparison with this theory.⁵

The induced free-carrier refraction and absorption naturally depend on the density of photogenerated carriers (ΔN) produced by 2PA when it is energetically allowed. For most cases in which the probe photon energy is far enough from the band edge (i.e., the index change is small enough), it is sufficient to assume a linear dependence on ΔN , giving^{9,15-17}

$$\Delta n_f(\omega_p; \omega_e) = \sigma_r(\omega_p)\Delta N(t), \quad (3a)$$

$$\Delta \alpha_f(\omega_p; \omega_e) = \sigma_a(\omega_p)\Delta N(t), \quad (3b)$$

where the time dependence of ΔN is explicitly shown. Here σ_r (in cubic centimeters) denotes the change of refractive index per unit carrier density, whereas σ_a (in square centimeters) is known as the free-carrier absorption cross section. In these experiments the probe is weak compared with the excitation beam, so we consider degenerate 2PA of the excitation beam as the only source of carrier generation. Thus the carrier-generation rate is given by

$$\frac{d\Delta N}{dt} = \frac{\beta(\omega_e; \omega_e)}{2\hbar\omega_e} I_e^2 - \frac{\Delta N}{\tau_r}, \quad (4)$$

where τ_r is the carrier lifetime. Here we assume a quasi-equilibrium condition in which the 2PA-generated carriers in the conduction band have thermalized with the lattice. For the pulse widths used in our experiments this is a valid assumption because electron-phonon scattering ensures the quasi-equilibrium condition within 1–2 ps.¹⁸ The mechanism for free-carrier refraction is a combination of plasma and band-filling effects^{2,15-17} with a lifetime τ_r typically of the order of nanoseconds.⁹ On the other hand, free-carrier absorption in most semiconductors originates from heavy-hole to light-hole intervalence band absorption and is usually weak unless it is probed at longer wavelengths, i.e., in the mid or the far IR.¹⁹

B. Propagation

By invoking the slowly varying envelope approximation and the thin-sample approximation,²⁰ we can reduce the Maxwell equations to obtain separate equations governing the amplitude ($|E_p|$) and the phase (ϕ_p) of the probe beam:

$$2 \frac{\partial |E_p|}{\partial z'} + \alpha_p |E_p| = -2\beta(\omega_p; \omega_e) |E_p| I_e - \sigma_a(\omega_p) \Delta N |E_p|, \quad (5a)$$

$$\frac{\partial \phi_p}{\partial z'} = \frac{\omega_p}{c} 2n_2(\omega_p; \omega_e) I_e + \sigma_r(\omega_p) \Delta N. \quad (5b)$$

The depletion of the excitation beam is given by

$$\frac{\partial I_e}{\partial z'} + \alpha_e I_e = -\beta(\omega_e; \omega_e) I_e^2, \quad (6)$$

where α_p and α_e are the linear absorption coefficients of the probe and the excitation beams, respectively. For a given sample position Z , the incident slowly varying field amplitude E_p and I_e (at $z' = 0$) are taken to have the well-known Gaussian beam functional dependence radially as well as temporally²¹:

$$E_p(z' = 0) = E_{0p} \frac{w_{0p}}{w_p} \exp \left[-\frac{r^2}{w_p^2} \left(1 + \frac{iZ}{Z_{0p}} \right) - \frac{t^2}{2\tau_p^2} \right] \times \exp \left[-i \tan^{-1} \left(\frac{Z}{Z_{0p}} \right) \right], \quad (7)$$

$$I_e(z' = 0) = I_{0e} \frac{w_{0e}^2}{w_e^2} \exp \left[-\frac{2r^2}{w_e^2} - \frac{(t - t_d)^2}{\tau_e^2} \right], \quad (8)$$

where $w_p^2 = w_{0p}^2 [1 + (Z^2/Z_{0p}^2)]$ and $w_e^2 = w_{0e}^2 \{1 + (Z + Z_e)^2/Z_{0e}^2\}$ define the probe- and the excitation-beam radii (half-width at $1/e^2$ maximum in irradiance), respectively, with Z_e accounting for the axial shift of the two foci that are due to the chromatic aberration of the focusing lens. The nonradial-dependent phase shift in Eq. (7) is unimportant in these experiments and is henceforth ignored. $Z_{0j} = \pi w_{0j}^2/\lambda_j$, where ($j = p, e$), are the Rayleigh ranges, and τ_p and τ_e denote the half-width at $1/e$ pulse widths (in irradiance) of probe and excitation beams, respectively.

A simultaneous solution to Eqs. (4)–(6) that uses the initial condition imposed by Eqs. (7) and (8) gives the radial (r dependence) and the temporal variations of $|E_p|$, ϕ_p , and I_e after propagation through the sample of thickness L for a fixed sample position Z . Once the amplitude and the phase of the probe are determined at the exit surface of the sample, we can obtain the probe beam's profile at the aperture plane (E_a) by applying the Huygen-Fresnel principle through a Hankel transformation of E_p evaluated at $z' = L$.²² This yields

$$E_a(r, t, Z) = \frac{2\pi}{i\lambda_p(d-Z)} \exp \left[\frac{i\pi r^2}{\lambda_p(d-Z)} \right] \times \int_0^\infty r' dr' E_p(r', t, Z, z' = L) \times \exp \left[\frac{i\pi r r'}{\lambda_p(d-Z)} \right] J_0 \left[\frac{2\pi r r'}{\lambda_p(d-Z)} \right], \quad (9)$$

where d is the distance between the position of the focal point of the excitation beam and the aperture plane and J_0 is the Bessel function of zeroth order. The normalized transmittance is given by

$$T(t_d, Z) = \frac{\int_{-\infty}^{\infty} dt \int_0^{r_a} r dr |E_a|^2}{\int_{-\infty}^{\infty} dt \int_0^{r_a} r dr |E_a(I_e = 0)|^2}, \quad (10)$$

where r_a is the aperture radius that for an open-aperture Z scan is infinite. It is more convenient to specify the aperture transmittance $S = 1 - \exp(-2r_a^2/w_a^2)$, where w_a is the beam radius at the aperture in the linear regime. Under certain conditions Eqs. (4)–(10) can be solved analytically, but in general a numerical solution is required.²³ In the analysis of time-resolved data, the quantities ΔT_{pv} and T_{op} , as a function of the time delay t_d , are calculated with Eq. (10):

$$\Delta T_{pv}(t_d) = \pm \left[\frac{T(t_d, Z_p)}{T_{op}(t_d, Z_p)} - \frac{T(t_d, Z_v)}{T_{op}(t_d, Z_v)} \right] \quad \text{for } S < 1,$$

$$T_{op}(t_d) = T(t_d, 0) \quad \text{with } S = 1, \quad (11)$$

where Z_p and Z_v are the positions of peak and valley of the Z scan, respectively. The sign of ΔT_{pv} is given by the sign of $Z_p - Z_v$.

As discussed in Section 4, the spatial separation between peak and valley, ΔT_{pv} , depends on the order of the nonlinearity equaling $\approx 1.7z_0$ for a third-order response and $\approx 1.2z_0$ for a fifth-order nonlinearity. Thus, in performing a temporal scan, one can optimize the signal for a third- or a fifth-order nonlinearity, although the difference in signal is only approximately 20%. This must be accounted for in interpreting the results of a temporal scan when both types of nonlinearity are present.

4. RESULTS AND DISCUSSION

The semiconductor samples used in our experiments are zinc blende polycrystalline slabs of ZnSe and Cleartran ZnS. ZnSe has a band-gap energy of $E_g = 2.6$ eV,²⁴ $n_0 = 2.5$ at $\lambda = 1$ μm , and $n_0 = 2.7$ at $\lambda = 0.5$ μm . The sample thickness is 2.7 mm. The ZnS sample has a thickness of 1 mm, $E_g = 3.7$ eV,²⁴ $n_0 = 2.3$ at 1 μm , and $n_0 = 2.4$ at 0.5 μm . In the following discussion, ω refers to 1.06- μm light and 2ω to 0.532- μm light. Table 1 summarizes the results described below.

A. Excitation at 1.06 μm

In both ZnSe and ZnS, degenerate 2PA with $\lambda_p = 1.06$ μm is energetically forbidden (i.e., $2\hbar\omega < E_g$). Therefore, with the strong excitation beam at 1.06 μm , the free-carrier density (ΔN) remains small, and the induced Δn and $\Delta\alpha$ are dominated by ultrafast bound electronic effects. However, in experiments on both polycrystalline ZnSe and ZnS, scattered second-harmonic light at 532 nm could be seen. Hence care was taken to ensure that second-order effects²⁵ did not influence our results. In ZnSe the probe at $\lambda_p = 532$ nm experiences a nondegenerate 2PA because $\hbar\omega + 2\hbar\omega = 3.5$ eV exceeds the band-gap energy of ZnSe. The open-aperture and closed-aperture Z-scan data at zero temporal delay, obtained with an excitation irradiance (I_e) of 0.7 GW/cm², are shown in Fig. 3. Measurements were made for two cases of parallel-polarized (xx) and crossed-polarized (xy) excitation and probe beams. From the calculations, the best fits give $\beta^{xx}2(\omega; \omega) = 15 \pm 3$ cm/GW, $\beta^{xx}(2\omega; \omega/\beta^{xy}(2\omega; \omega)) = 1.7 \pm 0.4$, $n_2^{xx}(2\omega; \omega) = -(5.1 \pm 1.0) \times 10^{-14}$ cm²/W, and $n_2^{xx}(2\omega; \omega)/n_2^{xy}(2\omega; \omega) = 2.0 \pm 0.5$ (see Table 1). All the results in Table 1 refer to parallel polarization unless specifically noted with the superscript xy . The observed polarization dichroism has been attributed to the interference between contributions to $\chi^{(3)}$ from the heavy-hole and the light-hole valence bands.²⁶

For ZnS with $\hbar\omega + 2\hbar\omega < E_g$, nondegenerate 2PA is not permitted, and the measured nonlinearities are purely refractive (degenerate 2PA for the probe at 532 nm is weak). Figure 4 shows the

Table 1. Nondegenerate Nonlinear Parameters Extracted from the Time-Resolved Two-Color Z-Scan Data*

Parameter	Material	
	ZnSe	ZnS
$\beta(1.06; 1.06)$	0	0
$\beta(0.532; 0.532)$	5.8 ± 1 cm/GW	3.4 ± 0.7 cm/GW
$\beta(0.532; 1.06)$	15 ± 3 cm/GW	0
$\beta(1.06; 0.532)$	4.6 ± 1 cm/GW	0
$\beta^{xy}(1.06; 0.532)$	8.6 ± 2 cm/GW	0
$n_2(1.06; 1.06)$	$(2.9 \pm 0.3) \times 10^{-14}$ cm ² /W	$(6.3 \pm 1.4) \times 10^{-15}$ cm ² /W
$n_2(0.532; 0.532)$	$(-6.8 \pm 1.4) \times 10^{-14}$ cm ² /W	Not measured
$n_2(0.532; 1.06)$	$(-5.1 \pm 0.5) \times 10^{-15}$ cm ² /W	$(1.7 \pm 0.4) \times 10^{-14}$ cm ² /W
$n_2^{xy}(0.532; 1.06)$	$(-2.6 \pm 0.3) \times 10^{-14}$ cm ² /W	Not measured
$n_2(1.06; 0.532)$	$(-9 \pm 5) \times 10^{-15}$ cm ² /W	$< 1.5 \times 10^{-14}$ cm ² /W
$\sigma_a(1.06)$	$(4.4 \pm 1.3) \times 10^{-18}$ cm ²	$(7 \pm 2) \times 10^{-18}$ cm ²
$\sigma_r(1.06)$	$(-6.1 \pm 1.5) \times 10^{-22}$ cm ³	$(5.2 \pm 1.1) \times 10^{-22}$ cm ³
τ	≈ 1 ns	$\tau_a = 0.6$ ns; $\tau_r = 0.8$ ns

* β , 2PA coefficient; n_2 bound electronic nonlinear refractive index; σ_a , free-carrier absorptive cross section; σ_r , free-carrier refractive coefficient.

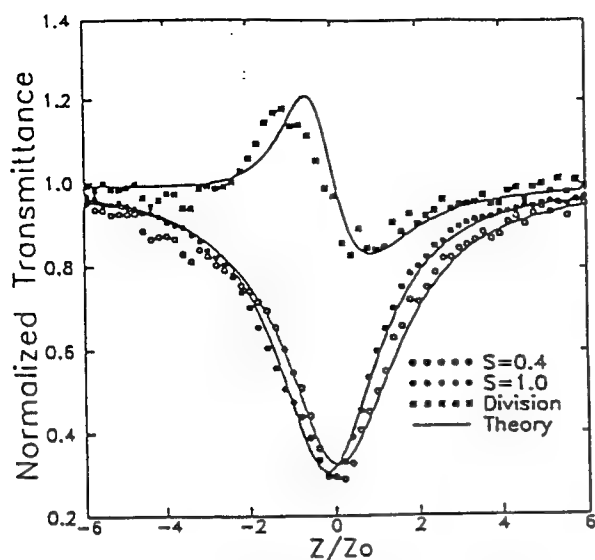


Fig. 3. Open-aperture data (filled circles) and closed-aperture data (open circles) for ZnSe obtained with perpendicularly polarized beams at zero time delay (excitation at $1.06 \mu\text{m}$ and probe at $0.532 \mu\text{m}$). The squares show the division of the two data sets, and the curves represent theoretical fits.

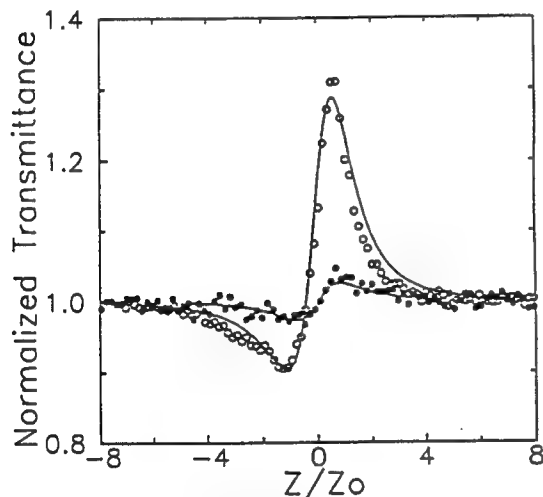


Fig. 4. Closed-aperture degenerate Z-scan data (filled circles) and closed-aperture nondegenerate data (open circles) obtained with excitation at $1.06 \mu\text{m}$ and probe at $0.532 \mu\text{m}$ for ZnS obtained with parallel-polarized beams at zero time delay. The curves represent theoretical fits.

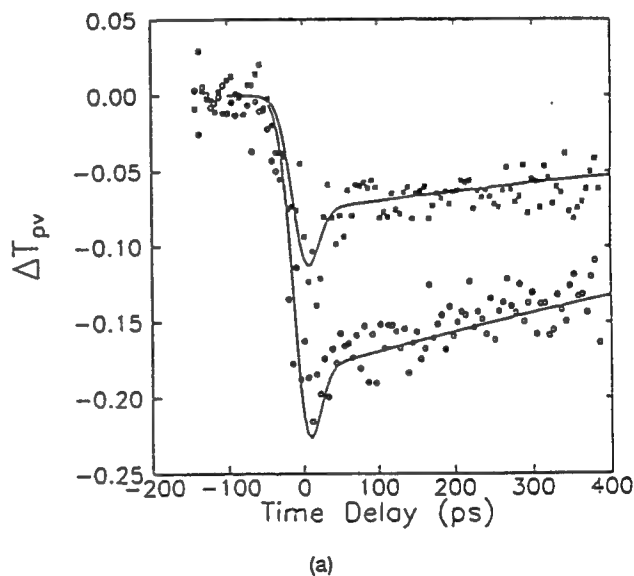
closed-aperture Z-scan signal compared with the single-wavelength Z scan at $1.06 \mu\text{m}$ measured at $I_e = 8.5 \text{ GW/cm}^2$. The best fit to these data gives a ratio of $n_2(2\omega; \omega)/n_2(\omega; \omega) \approx 1.9 \pm 0.2$ for parallel-polarized beams, with $n_2(\omega; \omega) = (7.6 \pm 1.5) \times 10^{-15} \text{ cm}^2/\text{W}$. This large ratio is due to a two-photon resonant enhancement of $n_2(\omega; \omega)$.²⁷ The theoretical analysis regarding the observed dispersion of the nondegenerate n_2 is given in Ref. 12. There is only an ultrafast response at this excitation wavelength, at which 2PA is not permitted.

B. Excitation at $0.532 \mu\text{m}$

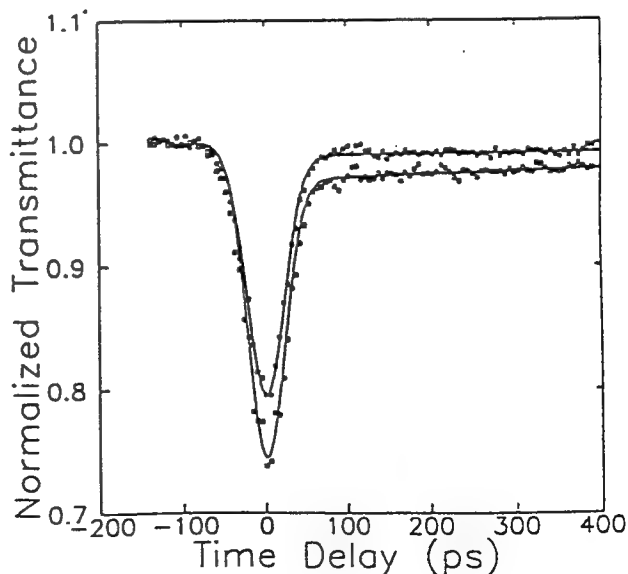
With excitation at $0.532 \mu\text{m}$ during probing at $1.06 \mu\text{m}$, degenerate 2PA of the pump beam is present in both ZnSe and ZnS. We employ this arrangement primarily

to study the induced free-carrier nonlinearities. By performing a temporal scan in the two-color Z-scan experiment, we can differentiate the free-carrier nonlinearities from the bound electronic effects. We use the method discussed in Section 2 to separate absorptive and refractive nonlinearities.

For ZnSe, $\Delta T_{pv}(t_d)$ and the maximum open-aperture transmittance change $\Delta T_{op}(t_d)$ are measured for several different input irradiances. As mentioned above, the signal can be optimized for either the third- or the fifth-order response. Here (as was done for the data given in Fig. 5), we optimized the signal for the fifth-order response of the carrier nonlinearities by first performing a Z scan at a long delay (i.e., $t_d \gg t_p$) to find the position of peak and valley. This means that the fast-response



(a)



(b)

Fig. 5. (a) Nonlinear refraction as determined by $\Delta T_{pv}(t_d)$ and (b) nonlinear absorption from the normalized transmittance $T_{op}(t_d)$ as a function of probe-beam time delay t_d for ZnSe measured at $I_e = 1.2 \text{ GW/cm}^2$ (open symbols) and $I_e = 0.7 \text{ GW/cm}^2$ (filled squares). $\tau_r = 1 \text{ ns}$. The curves are fits to the data obtained with the values given in Table 1.

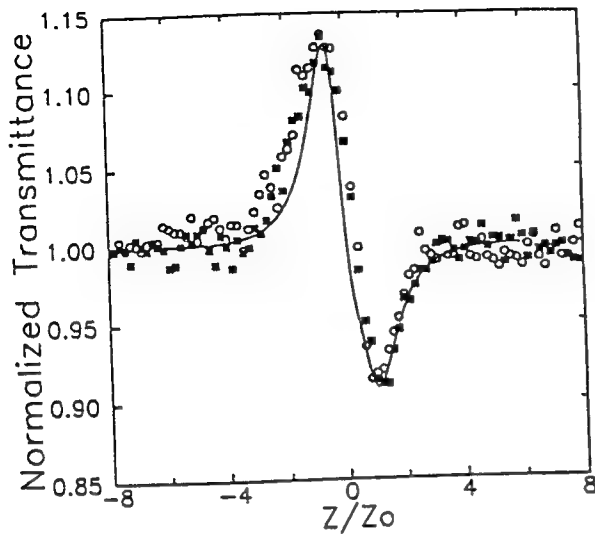


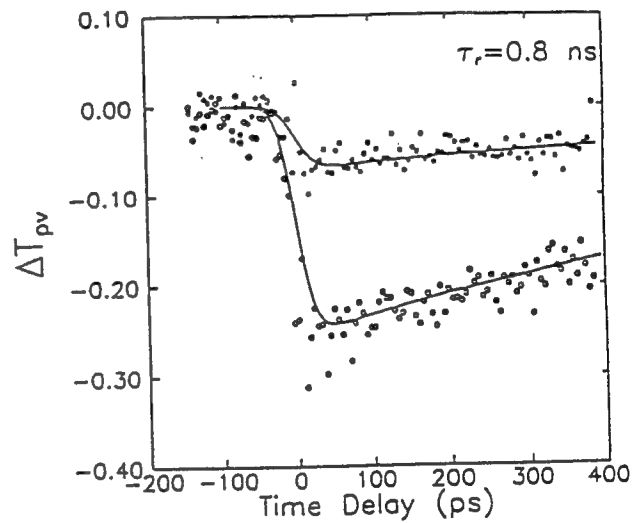
Fig. 6. Nondegenerate divided Z scans on ZnSe at time delays of 100 ps (circles) and 200 ps (squares) obtained with $0.53 \mu\text{m}$ as the excitation source and $1.06 \mu\text{m}$ as the probe. The curve shows the theoretical fit for the free-carrier refraction (and absorption).

signal near zero delay (third-order response) is not optimized, and the signal from this nonlinearity is reduced. The $\approx 20\%$ reduction in this signal is easily calculated from Eq. (10). The fits to the data discussed below take these effects into account. At relatively low irradiance, $\Delta T_{pv}(t_d)$ [Fig. 5(a)] consists of a peak near zero delay and a slow-decaying tail at longer delays, which lasts much longer than the laser pulse. The peak is due to nondegenerate bound electronic nonlinear refraction, as is evidenced by the fast response (i.e., the width is consistent with the width for CS_2 , as is shown in Fig. 2).¹² This nonlinear refraction is determined to be negative from the relative positions of the peak and the valley. The slow-decaying tail comes from free-carrier refraction (also defocusing), at which the carriers are produced by degenerate 2PA of the excitation beam. As the irradiance increases, the relative value of the peak diminishes with respect to the long free-carrier tail. This occurs because the bound electronic effect is a third-order nonlinearity, whereas the two-photon-generated free-carrier nonlinearities result in an effective fifth-order nonlinearity.^{2,3} Fitting the data shown in Fig. 5(a), we obtain $n_2^{xx}(\omega; 2\omega) = (9 \pm 5) \times 10^{-15} \text{ cm}^2/\text{W}$, $\sigma_r(\omega) = 5.4 \pm 1.5 \times 10^{-22} \text{ cm}^2$, and a carrier decay time of $\tau_r = 1 \text{ ns}$. The errors on n_2 are large as the nonlinearity is dominated by free-carrier refractive effects, and such a large difference between $n_2^{xx}(\omega; 2\omega)$ and $n_2^{xx}(2\omega; \omega) = -(5.1 \pm 1.0) \times 10^{-4} \text{ cm}^2/\text{W}$ is not expected from a two-parabolic-band model, which predicts values within $\approx 10\%$ of each other.¹²

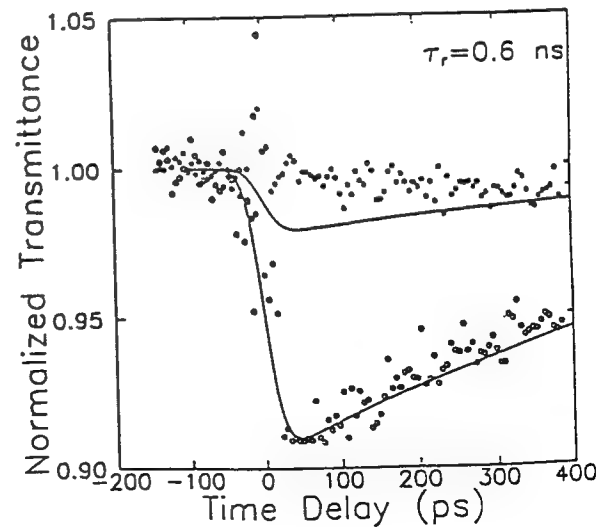
Figure 5(b) shows $T_{op}(t_d)$ for ZnSe, giving the time-resolved nondegenerate nonlinear absorption. At zero delay the nondegenerate 2PA dominates, and at longer time delays we see a small contribution from 2PA-generated free-carrier absorption. As stated above, the free-carrier refraction and absorption are proportional to the density of free carriers, which slowly decays with the recombination time τ_r of the carriers. The fit that is shown uses $\beta = 4.6 \pm 1.1 \text{ cm/GW}$ and $\sigma_a = (4.4 \pm 1.3) \times 10^{-1} \text{ cm}^2$.

Fixing the delay of the probe relative to the excitation beam so that the two pulses have no temporal overlap and performing a two-color Z scan, we see only free-carrier refraction and absorption. Experimental data, depicting the ratio of the closed-aperture to the open-aperture Z scans for ZnSe at 100 and 200-ps time delay (with $I_e = 1.5 \text{ GW/cm}^2$), are shown in Fig. 6. Because a delay time of 200 ps is considerably less than τ_r , the number of free carriers is the same within 10% at the two delays. The free-carrier refraction, $\sigma_r(\omega) = 6 \pm 1.5 \times 10^{-22} \text{ cm}^2$, and absorption, $\sigma_a(\omega) = 4.4 \pm 1.3 \times 10^{-18} \text{ cm}^2$, from these Z scans are consistent with those obtained from the time-delay experiment to within 10%.

The data for ΔT_{pv} for ZnS, as shown in Fig. 7(a), display no fast-response signal near zero delay. This result indicates that the phase change produced by the free car-



(a)



(b)

Fig. 7. (a) Nonlinear refraction as determined by ΔT_{pv} and (b) nonlinear absorption from the normalized transmittance T_{op} as a function of probe-beam time delay t_d for ZnS measured at $I_e = 0.7 \text{ GW/cm}^2$ (filled circles) and $I_e = 1.45 \text{ GW/cm}^2$ (open circles). The curves are fits to the data obtained with the values given in Table 1.

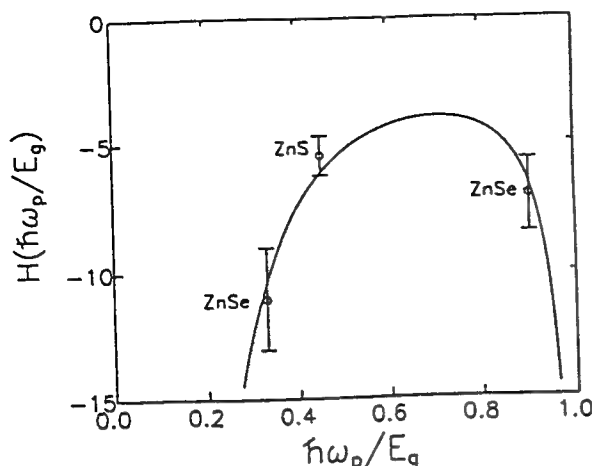


Fig. 8. Free-carrier nonlinear refraction as a function of probe-beam photon energy ($\hbar\omega_p/E_g$) for ZnS at 0.532 μm and for ZnSe at 1.06 and 0.532 μm .

riers is much larger than that produced by the bound electrons. In addition, based on the theory,¹² we expect the nondegenerate n_2 to be positive, partially negating the self-defocusing from the carriers. However, the free-carrier nonlinearities totally dominate the phase change at high irradiance, resulting in a good fit for ZnS by use of only carrier effects. The nonlinear absorption for ZnS, shown in Fig. 7(b), is dominated by free-carrier absorption because there is no nondegenerate 2PA. Note that, for both irradiances, at zero delay there is a narrow spike of unknown origin. We speculate that this result may be caused by transient beam coupling or by a cascading of second-order nonlinearities.²⁵

We find that, from the higher irradiance data shown in Fig. 7 for ZnS, $\sigma_a(\omega) = 8 \pm 2 \times 10^{-18} \text{ cm}^2$ and $\sigma_r(\omega) = -5 \pm 1 \times 10^{-22} \text{ cm}^3$ (curves in Fig. 7). These two experiments give slightly different values for the carrier recombination time ($\tau_r = 0.6 \text{ ns}$ for free-carrier absorption and $\tau_r = 0.8 \text{ ns}$ for free-carrier refraction measurements). This small difference may be explained by the different relative contributions of free electrons and holes to refraction and absorption and by possible differences in electron- and hole-trapping rates.

C. Dispersion of Free-Carrier Nonlinearities

There exist numerous theoretical models dealing with the effects of an electron-hole plasma on the complex dielectric constant.¹⁵⁻¹⁷ We find that the simplest model,^{9,15,16} which incorporates two parabolic bands, sufficiently explains the magnitude and the dispersion of the observed free-carrier effects.³ In this simple model the change of refractive index for wavelengths below the band edge (i.e., for probe photon energy $\hbar\omega_p < E_g$) that is due to an injection of an electron-hole density ΔN is given by^{9,16}

$$\Delta n(\omega_p) = \frac{2\pi e^2 \Delta N}{m_{e-h}} \left(-\frac{1}{\omega_p^2} - \frac{1}{\omega_g^2 - \omega_p^2} \right), \quad (12)$$

where m_{e-h} is the electron-hole reduced effective mass and $\omega_g = E_g/\hbar$. The first term in Eq. (12) describes the Drude plasma contribution, and the second term

represents the band-filling contribution to the refractive-index change. A more general expression can be obtained by elimination of the effective mass with the results of $k \cdot p$ theory²⁸:

$$\frac{m_{e-h}}{m_0} \approx \frac{E_g}{E_p}, \quad (13)$$

where only the heavy-hole valence band is taken into account. Here $E_p = 21 \text{ eV}$ is the Kane energy and is nearly material independent for most semiconductors.²⁸ This allows us to write Eq. (12) as

$$\Delta n(\omega_p) = A \frac{E_p}{n_0 E_g^3} H\left(\frac{\hbar\omega_p}{E_g}\right) \Delta N, \quad (14)$$

where $H(x) = [x^2(x^2 - 1)]^{-1}$ is the free-carrier dispersion function and $A = 2\pi\hbar^2 e^2/m_0 = 3.4 \times 10^{-22} \text{ cm}^3 \text{ eV}^2$. The advantage of Eq. (14) is that it provides a simple E_g scaling as well as a dispersion function that is only a function of $\hbar\omega_p/E_g$. This is analogous to the useful expressions derived for the bound electronic nonlinearities in semiconductors.^{11,27} Under the quasi-equilibrium condition, the free-carrier effects are independent of the means of generation, and thus Δn has no explicit dependence on the excitation photon energy $\hbar\omega_e$.

A best fit to our experimental data for ZnSe and ZnS is obtained with $A \approx 2.3 \times 10^{-22} \text{ cm}^3 \text{ eV}^2$. We plot the dispersion function $H(\hbar\omega_p/E_g)$ and the experimental results in Fig. 8. The good agreement between our results and this simple model may exist in part because the carrier densities reached are relatively low, $\Delta N < 10^{18} \text{ cm}^{-3}$, and in part because we probe relatively far below the gap. At high carrier densities and at photon energies near the gap, many-body effects and excitons may become important.¹⁷

5. CONCLUSION

We have introduced a time delay for one of the beams in a two-color Z-scan apparatus to allow the temporal dependence of the nonlinear absorption and the nonlinear refraction to be separately measured. We have demonstrated the utility of this technique by monitoring the several nonlinearities that occur in semiconductors on a picosecond time scale. Whereas these nonlinearities normally require that several different types of experiments be performed to separate their similar effects, this new technique (temporally resolved two-color Z scan) permits their separation by itself. In particular, we have separately measured the nondegenerate two-photon absorption, bound electronic n_2 , free-carrier absorption, and free-carrier refraction in ZnSe and have performed similar experiments on ZnS, for which nondegenerate two-photon absorption is not energetically permitted, and on CS_2 , which shows only nonlinear refraction. The numerous parameters extracted from these data (see Table 1) have been compared with simple band-theory models that have been presented elsewhere. One can also extend this technique to obtain the temporal dependence of different nonlinear tensor components by changing the relative polarization of the excitation and the probe beams.

It may be of use to contrast this technique with DFWM at this point. Temporally resolved DFWM uses three interacting beams at the same wavelength to produce a

fourth beam whose energy can be measured as a function of the time delay of any one of the three beams, with the other two being fixed at zero delay. The absolute accuracy of determining a nonlinear coefficient with DFWM is expected to be considerably less than with the technique discussed in this paper because in DFWM three, as opposed to two, beams must be both accurately characterized (i.e., beam shape, pulse width, and energy) and overlapped spatially and temporally. In addition, the results of the DFWM experiment for third-order nonlinearities are proportional to $|\chi^{(3)}|^2$ such that absorptive and refractive contributions are mixed. However, temporal information and symmetry properties of the degenerate susceptibilities can be measured. On the other hand, decay is often governed by diffusion between fringes, which can be much faster than diffusion across the entire beam. As stated above, measuring degenerate nonlinearities with the time-resolved Z scan presents other difficulties. Therefore this new technique should be considered complementary to other experimental methods, such as DFWM, for determining the origins of optical nonlinearities of materials.

ACKNOWLEDGMENTS

We gratefully acknowledge the support of the National Science Foundation (grant ECS 9120590), the Defense Advanced Research Projects Agency, and the Night Vision and Electro-Optics Directorate.

REFERENCES

1. J. J. Wynne, "Optical third-order mixing in GaAs, Ge, Si, and InAs," *Phys. Rev.* **178**, 1295 (1969); see also P. Roussignol, D. Ricard, and C. Flytzanis, "Nonlinear optical properties of commercial semiconductor doped glasses," *Appl. Phys. A* **44**, 285 (1987).
2. E. Canto-Said, D. J. Hagan, J. Young, and E. W. Van Stryland, "Degenerate four wave mixing measurements of higher order nonlinearities in semiconductors," *IEEE J. Quantum Electron.* **27**, 2274 (1991).
3. A. A. Said, M. Sheik-Bahae, D. J. Hagan, T. H. Wei, J. Wang, J. Young, and E. W. Van Stryland, "Determination of bound-electronic and free-carrier nonlinearities in ZnSe, GaAs, CdTe, and ZnTe," *J. Opt. Soc. Am. B* **9**, 405 (1992).
4. H. Ma, A. S. L. Gomes, and C. B. de Araujo, "Measurement of nondegenerate optical nonlinearity using a two-color single beam method," *Appl. Phys. Lett.* **59**, 2666 (1991).
5. J. Sheik-Bahae, J. Wang, R. DeSalvo, D. J. Hagan, and E. W. Van Stryland, "Measurement of nondegenerate nonlinearities using a two-color Z scan," *Opt. Lett.* **17**, 260 (1992).
6. M. Sheik-Bahae, A. A. Said, and E. W. Van Stryland, "High-sensitivity, single-beam n_2 measurements," *Opt. Lett.* **14**, 955 (1989).
7. M. Sheik-Bahae, A. A. Said, T. H. Wei, D. J. Hagan, and E. W. Van Stryland, "Sensitive measurement of optical nonlinearities using a single beam," *IEEE J. Quantum Electron.* **26**, 760 (1990).
8. E. W. Van Stryland, H. Vanherzeele, M. A. Woodall, M. J. Soileau, A. L. Smirl, S. Guha, and T. F. Boggess, "Two-photon absorption, nonlinear refraction, and optical limiting in semiconductors," *Opt. Eng.* **24**, 613 (1985).
9. D. H. Auston, S. McAfee, C. V. Shank, E. P. Ippen, and O. Teschke, "Picosecond spectroscopy of the semiconductors," *Solid-State Electron.* **21**, 147 (1978).
10. E. W. Van Stryland, A. L. Smirl, T. F. Boggess, M. J. Soileau, B. S. Wherrett, and F. Hopf, "Weak-wave retardation and phase-conjugate self-defocusing in Si," in *Picosecond Phenomena III*, K. B. Eisenthal, R. M. Hochstrasser, W. Kaiser, and A. Laubereau, eds. (Springer-Verlag, New York, 1982), p. 368.
11. M. Sheik-Bahae, D. J. Hagan, and E. W. Van Stryland, "Dispersion and band-gap scaling of the electronic Kerr effect in solids associated with two-photon absorption," *Phys. Rev. Lett.* **65**, 96 (1989).
12. M. Sheik-Bahae, D. C. Hutchings, D. J. Hagan, and E. W. Van Stryland, "Dispersion of bound electronic nonlinear refraction in solid," *IEEE J. Quantum Electron.* **27**, 1296 (1991).
13. D. C. Hutchings, M. Sheik-Bahae, D. J. Hagan, and E. W. Van Stryland, "Kramers-Kronig relations in nonlinear optics," *Opt. Quantum Electron.* **24**, 1 (1992).
14. F. Bassani and S. Scandolo, "Dispersion relations and sum rules in nonlinear optics," *Phys. Rev. B* **44**, 8446 (1991).
15. D. A. B. Miller, C. T. Seaton, M. E. Prise, and S. D. Smith, "Band-gap-resonant nonlinear refraction in III-V semiconductors," *Phys. Rev. Lett.* **47**, 197 (1981).
16. A. G. Aronov, D. E. Pikus, and D. Sh. Shekhter, "Quantum theory of free-electron dielectric constant in semiconductors," *Sov. Phys. Solid State* **10**, 645 (1968).
17. L. Banyai and S. W. Koch, "A simple theory for the effects of the plasma screening on the optical spectra of highly excited semiconductors," *Z. Phys. B* **63**, 283 (1986).
18. R. Luzzi and A. R. Vasconcellos, "Relaxation processes in nonequilibrium semiconductor plasma," in *Semiconductors Probed by Ultrafast Laser Spectroscopy*, R. R. Alfano, ed. (Academic, New York, 1984), Vol. 1.
19. J. I. Pankove, *Optical Processes in Semiconductors* (Prentice-Hall, Englewood Cliffs, N.J., 1971).
20. S. A. Akmanov, R. V. Khokhlov, and A. P. Sukhorukov, "Self-focusing, self-defocusing, and self-modulation of laser beams," in *Laser Handbook*, F. T. Arecchi and E. O. Schultz-Dubois, eds. (North-Holland, Amsterdam, 1972), Vol. 2, p. 1151.
21. H. A. Haus, *Waves and Fields in Optoelectronics* (Prentice-Hall, Englewood Cliffs, N.J., 1984).
22. J. D. Gaskin, *Linear Systems, Fourier Transforms, and Optics* (Wiley, New York, 1978).
23. J. Wang, "The dispersion and symmetry of optical nonlinearities in semiconductors," Ph.D. dissertation (University of Central Florida, Orlando, Florida, 1993).
24. B. Ray, *II-VI Compounds* (Pergamon, Edinburgh, 1969), Chap. 6.
25. R. J. DeSalvo, D. J. Hagan, M. Sheik-Bahae, G. Stegeman, E. W. Van Stryland, and H. Vanherzeele, "Self-focusing and self-defocusing by cascaded second-order effects in KTP," *Opt. Lett.* **17**, 28 (1992).
26. M. Sheik-Bahae, J. Wang, E. J. Canto-Said, R. DeSalvo, D. J. Hagan, and E. W. Van Stryland, "Two-photon coherence and symmetry of $\chi^{(3)}$ in semiconductors," in *Quantum Electronics and Laser Science Conference*, Vol. 12 of 1993 OSA Technical Digest Series (Optical Society of America, Washington, D.C.), paper QTK26.
27. M. Sheik-Bahae, J. Wang, and E. W. Van Stryland, "Nondegenerate optical Kerr effect in semiconductors," *IEEE J. Quantum Electron.* (to be published).
28. E. O. Kane, "Band structure of indium antimonide," *J. Chem. Phys.* **1**, 249 (1957).

Nondegenerate Optical Kerr Effect in Semiconductors

Mansoor Sheik-Bahae, J. Wang, and E. W. Van Stryland

Abstract—We calculate the nondegenerate bound electronic nonlinear refractive index $n_2(\omega_1; \omega_2)$ (i.e., an index change at frequency ω_1 due to the presence of a beam at frequency ω_2) in semiconductors. We calculate this nonlinearity and its dispersion using a Kramers–Kronig transformation on the calculated nondegenerate nonlinear absorption spectrum due to two-photon absorption, electronic Raman and optical Stark effects. The calculated n_2 values and their dispersion are compared to new experimental values for ZnSe and ZnS obtained using a 2-color Z-scan.

I. INTRODUCTION

LIGHT-INDUCED changes in the optical properties of semiconductors have several applications including all optical switching [1]. The ultrafast optical Kerr effect (bound-electronic nonlinear refraction), leading to self-phase modulation and self-lensing of laser beams in solids, has been studied extensively [2]–[4]. Recently, we presented a simple yet comprehensive theory for this nonlinear refractive index n_2 in semiconductors [5], [6]. The theory used a Kramers–Kronig (KK) transformation to derive n_2 from our calculated nonlinear absorption spectrum. The key features of this theory were the band-gap scaling and the dispersion of n_2 which showed excellent agreement with a large number of experimental data for the degenerate case. Here, we derive a more general expression that gives the nondegenerate optical Kerr effect, namely, the change of refractive index at a frequency ω_1 due to the presence of a strong excitation beam at frequency ω_2 . We define the nondegenerate coefficient n_2 as well as the nondegenerate nonlinear absorption coefficient α_2 by

$$\Delta n(\omega_1; \omega_2) = 2n_2(\omega_1; \omega_2)I_{\omega_2} \quad (1a)$$

and

$$\Delta \alpha(\omega_1; \omega_2) = 2\alpha_2(\omega_1; \omega_2)I_{\omega_2} \quad (1b)$$

where Δn and $\Delta \alpha$ are the changes in refractive index and absorption coefficient respectively, and I_{ω_2} is the irradiance of the excitation beam at frequency ω_2 . The factor of two in these expressions arises from the interference between the pump and the probe beams. In a self-modulation (single-beam) process this factor is unity [7]. The nondegenerate

nonlinear coefficients n_2 and α_2 are related to the real and imaginary components of the third order optical susceptibility $\chi^{(3)}(\omega_1, \omega_2, -\omega_2)$, respectively. We showed that the physical mechanisms responsible for the induced change of absorption ($\Delta \alpha$) originated from three processes: two-photon absorption (2PA), electronic Raman, and optical Stark effect [5]. In the following section, we briefly review the formalism leading to an expression for the degenerate n_2 and then present the extension of this theory to the nondegenerate case. In Section III, we present experimental results for ZnSe and ZnS obtained using a 2-color Z-scan [7]. In Section IV, possible effects of the electron-hole Coulomb interaction are considered using a simple Elliott-type envelope function. This simple approximation can qualitatively explain the two-photon and one-photon resonant enhancement of n_2 observed in semiconductors.

II. THEORY

The nonlinear Kramers–Kronig relations relate n_2 and α_2 through the dispersion integral [4], [5], [8]

$$n_2(\omega_1; \omega_2) = \frac{2}{\pi} \int_0^\infty \frac{\alpha_2(\omega'; \omega_2)}{\omega'^2 - \omega_1^2} d\omega'. \quad (2)$$

In [5], $\Delta \alpha(\omega'; \omega_2)$ was calculated using a two-parabolic band (TPB) model. In this model a “dressed state” approach is adopted where the wave functions for the initial (valence) and the final (conduction) bands are given as follows:

$$\Psi_j(\mathbf{k}, \mathbf{r}, t) = u_j(\mathbf{k}, \mathbf{r}) \exp \left[i\mathbf{k} \cdot \mathbf{r} - \frac{i}{\hbar} \int_0^t E_j(\tau) d\tau \right] \quad (3)$$

where j refers to either conduction (c) or valence (v) band and \mathbf{k} is the lattice wavevector. The functions u_j are the usual (unperturbed) Bloch wavefunctions that have the same periodicity as the lattice. The effects of the optical fields are to alter the energy of the electrons and holes in the final and initial states, respectively. This is written as

$$E_v(\tau) = E_{v0} + \Delta E_{vv}(\tau) + \Delta E_{vc} \quad (4a)$$

$$E_c(\tau) = E_{c0} + \Delta E_{cc}(\tau) + \Delta E_{cv} \quad (4b)$$

where E_{j0} is the unperturbed band energy. $\Delta E_{jj}(\tau)$ and ΔE_{cv} are the linear (LSE) and quadratic (QSE) optical Stark shifts of the energy bands due to the interaction Hamiltonian as follows:

$$H_{\text{int}} = \frac{e}{m_0 c} \mathbf{p} \cdot [\mathbf{A}_{01} \cos(\omega_1 t) + \mathbf{A}_{02} \cos(\omega_2 t)] \quad (5)$$

where \mathbf{p} is the momentum operator. \mathbf{A}_{01} and \mathbf{A}_{02} are the vector potentials of the interacting optical fields. The resultant

Manuscript received January 29, 1993; revised April 5, 1993. This work was supported in part by the National Science Foundation under grant ECS-9120590 and by the U.S. Defense Advanced Research Projects Agency/Center for Night Vision and Electro-Optics.

The authors are with the Center for Research in Electro-Optics and Lasers, University of Central Florida, Orlando, FL 32816.

IEEE Log Number 9215249.

TABLE I
THE VARIOUS CONTRIBUTIONS TO THE NONLINEAR ABSORPTION SPECTRAL FUNCTION $F_2(x_1; x_2)$

Contribution	$F_2(x_1; x_2)$
2-Photon Absorption	$\frac{(x_1 + x_2 - 1)^{3/2}}{2^7 x_1 x_2^2} \left(\frac{1}{x_1} + \frac{1}{x_2} \right)^2$ for $x_1 + x_2 > 1$
Raman	$\frac{(x_1 - x_2 - 1)^{3/2}}{2^7 x_1 x_2^2} \left(\frac{1}{x_1} - \frac{1}{x_2} \right)^2$ for $x_1 - x_2 > 1$
Linear Stark	$-\frac{(x_1 - 1)^{3/2}}{2^6 x_1 x_2^2} \frac{1}{x_2^2}$ for $x_1 > 1$
Quadratic Stark	$-\frac{1}{2^{10} x_1 x_2^2 (x_1 - 1)^{1/2}} \left(\frac{1}{x_1 - x_2} + \frac{1}{x_1 + x_2} - \frac{2(x_1 - 1)}{(x_1 - x_2)^2} - \frac{2(x_1 - 1)}{(x_1 + x_2)^2} \right)$ for $x_1 > 1$

interband absorption change, as calculated using first-order perturbation theory, is given by [5]:

$$\alpha_2(\omega_1; \omega_2) = K \frac{\sqrt{E_p}}{n_{01} n_{02} E_g^3} F_2(x_1; x_2) \quad (6)$$

where K is a constant, E_g (eV) is the band-gap energy, and $x_1 = \hbar\omega_1/E_g$, $x_2 = \hbar\omega_2/E_g$ and n_{0j} ($j = 1, 2$) are the linear refractive indices at ω_1 and ω_2 , respectively. The dimensionless spectral function F_2 , is defined in Table I. The Kane energy E_p (≈ 21 eV) is related to the Kane momentum parameter P by $E_p = 2P^2/m\hbar^2$, and is nearly material independent for most semiconductors [9]. In the TPB approximation, this parameter is related to the electron (or hole) effective mass $m_c (= m_v)$ through

$$m_c/m_0 \simeq E_g/E_p. \quad (7)$$

The constant K was determined from the average degenerate 2PA coefficient of several semiconductors to be $\approx 3100 \text{ cmGW}^{-1} \text{ eV}^{5/2}$, but varied by up to $\approx 30\%$ from one material to the next [9]. A value for K of ≈ 4000 gives a better value for ZnSe and ZnS as compared to the calculated value of $1940 \text{ cmGW}^{-1} \text{ eV}^{5/2}$ from the TPB model [5]. This factor of ≈ 2 in underestimating the absolute value of β may be simply understood by realizing that the transition can initiate from two valence bands (heavy- and light-hole bands) rather than one as modeled here. More rigorously, a Kane 4-band model has been shown to give a closer absolute agreement for several zinc-blend semiconductors [10].

The dimensionless spectral function F_2 , shown in Table I, contains contributions from 2PA when $\hbar\omega_1 + \hbar\omega_2 > E_g$, the stimulated Raman effect when $\hbar\omega_1 - \hbar\omega_2 > E_g$ and optical Stark effect when $\hbar\omega_1 > E_g$ [5]. The nondegenerate 2PA coefficient $\beta(\omega_1; \omega_2)$ is defined as equal to α_2 when $\hbar\omega_1 + \hbar\omega_2 > E_g$ (i.e., contains only the 2PA portion of F_2). Note also that there are four terms associated with the quadratic optical Stark effect in Table I. The first two terms represent the repulsion of the bands which reduces the density of states in the vicinity of $k = 0$. The last two terms, on the other hand, arise from the conservation of total number of states and would lead to an increase in density of states

at $k > 0$ (i.e., removing states near $k = 0$ adds states at larger k). These terms, which contribute less than 10% to the degenerate $n_2(\omega)$ for $\hbar\omega_1/E_g < 0.95$, were ignored in [5] but are included here for the nondegenerate $n_2(\omega_1; \omega_2)$. As $\hbar\omega/E_g \rightarrow 1$, the contribution to n_2 from the QSE is reduced significantly if these two terms are included.

It must be emphasized that we consider here only below resonance excitation ($\hbar\omega_2 < E_g$). For $\hbar\omega_2 > E_g$, in addition to the expressions given in Table I, a term accounting for the stimulated Raman gain of the probe beam when $\hbar\omega_2 - \hbar\omega_1 > E_g$ must be included. In practice, however, above band-gap resonance excitation leads to well known carrier effects (e.g., band-filling) that mask the bound electronic contributions. Above band-gap ultrafast bound-electronic nonlinearities have, nevertheless, been observed in semiconductor laser amplifiers when operating near the transparency point where changes in carrier populations are negligible [11]. Theoretical analysis of active semiconductors has been presented elsewhere [12].

In calculating $\Delta\alpha(\omega_1; \omega_2)$, it has been assumed that the two interacting beams have the same linear polarization. In general, one may assume that the two optical fields have arbitrary polarizations. For instance, consider two linearly polarized light beams with a fixed relative angle ϕ between their polarizations. If we assume that the valence band couples isotropically to all the k states in the conduction band, we obtain a polarization dependent prefactor

$$K(\phi) = K(1 - \frac{2}{3} \sin^2 \phi). \quad (8)$$

The primary assumption leading to this symmetry property is that the electron quasimomentum $\hbar k$ is parallel in k space to the interband momentum matrix element p_{cv} [5]. From Kane's $k \cdot p$ theory, this is characteristic of the transitions that initiate from the light-hole valence band [13]. The p_{cv} associated with the heavy-hole to conduction band transition, on the other hand, is effectively perpendicular to k , leading to a more complex polarization dependence that varies with wavelength and is different for each mechanism [14]. In this paper, however, we focus our attention on the dispersion of the nondegenerate n_2 , and the details of the symmetry properties

TABLE II

THE NONDEGENERATE DISPERSION FUNCTION $G_2(x_1; x_2)$ OF (10) FOR THE ELECTRONIC KERR COEFFICIENT n_2 , CALCULATED BY A KK TRANSFORMATION OF F_2 (TABLE I). THE IR DIVERGENT TERMS ASSOCIATED WITH EACH CONTRIBUTION HAVE BEEN REMOVED. NOTE THAT THE TERMS INVOLVING $(\dots)^{3/2}$ ARE ZERO WHEN THE ARGUMENT (\dots) IS NEGATIVE. THE LAST TERM DUE TO THE DEGENERATE QSE IS THE LIMIT OF THE NONDEGENERATE $G_2^{QSE}(x_1; x_2)$ AS $x_1 \rightarrow x_2$.

Contribution	$G_2(x_1; x_2)$
2-Photon Absorption Raman	$H(x_1, x_2) + H(-x_1, x_2)$ $H(x_1, -x_2) + H(-x_1, -x_2)$ where $H(x_1, x_2) = \frac{1}{2^6 x_1^4 x_2^4} \left[\frac{5}{16} x_2^3 x_1^2 + \frac{9}{8} x_1^2 x_2^2 - \frac{9}{4} x_1^2 x_2 - \frac{3}{4} x_2^3 \right. \\ + \frac{1}{2} (x_1^2 + x_2^2) [1 - (1 - x_2)^{3/2}] + \frac{1}{2} (x_1 + x_2)^2 [(1 - x_1 - x_2)^{3/2} - (1 - x_1)^{3/2}] \\ - \frac{3}{16} x_1^2 x_2^2 [(1 - x_1)^{-1/2} + (1 - x_2)^{-1/2}] + \frac{3}{2} x_1^2 x_2 (1 - x_2)^{1/2} \\ \left. + \frac{3}{4} x_2 (x_1 + x_2)^2 (1 - x_1)^{1/2} - \frac{3}{8} x_2^3 x_1 (1 - x_1)^{-1/2} - \frac{1}{32} x_1^2 x_2^3 (1 - x_1)^{-3/2} \right]$
Quadratic Stark $x_1 \neq x_2$	$\frac{1}{2^9 x_1^2 x_2^2} \left[-\frac{1}{2} - \frac{4}{x_1^2} + \frac{4}{x_2^2} - \frac{x_2^2 [(1 - x_1)^{-1/2} - (1 + x_1)^{-1/2}]}{x_1^2 - x_2^2} \right. \\ + \frac{2x_1^2(3x_2^2 - x_1^2)}{x_2^2(x_1^2 - x_2^2)^2} [(1 - x_2)^{1/2} + (1 + x_2)^{1/2}] \\ \left. - \frac{2x_2^2(3x_1^2 - x_2^2)}{x_1^2(x_1^2 - x_2^2)^2} [(1 - x_1)^{1/2} + (1 + x_1)^{1/2}] \right]$
$x_1 = x_2$	$\frac{1}{2^9 x_1^4} \left[\frac{3}{4} \frac{(1 - x_1)^{-1/2} - (1 + x_1)^{-1/2}}{x_1} - \frac{(1 - x_1)^{-3/2} + (1 + x_1)^{-3/2}}{8} - \frac{1}{2} \right]$

associated with a more general two-valence band system will be discussed in future

With $\alpha_2(\omega_1; \omega_2)$ known, we can obtain the refractive contribution $n_2(\omega_1; \omega_2)$ by applying the KK transformation ((2)). This yields

$$n_2(\omega_1; \omega_2) = \frac{\hbar c K}{2 E_g^4 n_{01} n_{02}} G_2(x_1; x_2). \quad (9)$$

In [5], the interference factor of two, as appears in (1a), was ignored in calculating the n_2 coefficient. In correction, the value of $K \simeq 6000$ gives a better fit to the degenerate n_2 data for semiconductors, although variations of a factor of $\simeq 2$ from one material to another occur. This difference of K values may be attributed to too simplistic a band structure employed in our model and/or electron-hole Coulomb interactions (excitons). The possible effects of excitons are discussed in Section IV.

Equation (9) is identical to the expression obtained for the degenerate n_2 [5] except the dispersion function G_2 now has a general nondegenerate form determined by the KK integral

$$G_2(x_1; x_2) = \frac{2}{\pi} \int_0^\infty \frac{F_2(\xi; x_2)}{\xi^2 - x_1^2} d\xi. \quad (10)$$

It was noted in [5] that as a result of using $\mathbf{A} \cdot \mathbf{p}$ perturbation theory, the calculated dispersion function G_2 diverges as $x_2 \rightarrow 0$ ($\omega_2 \rightarrow 0$). Using a power series expansion we identify the divergent terms of each individual contribution and

find that the QSE term diverges as x_2^{-2} while the remaining contributions have divergent terms that vary as x_2^{-1} , x_2^{-2} , x_2^{-3} , and x_2^{-4} . Upon summing these contributions, however, all divergences cancel except for the x_2^{-2} term. In fact, the contribution of the linear Stark effect (third term in Table I) is only to cancel the x_2^{-4} divergent terms of the 2PA and Raman contributions. Due to their unphysical consequences, it has been a common practice to subtract the remaining divergent terms [15]. This process of divergence removal can be considered as effectively enforcing a sum rule for the two-band system. We obtain an analytical expression for G_2 by evaluating the KK integral of (10). The individual long wavelength divergent terms for each contribution are removed separately and the final result is given in Table II. In summing the 2PA and Raman contributions, all the odd terms in x_2 , arising from the individual divergences, cancel. In this paper, we refer to G_2 as the sum of the three divergence-free functions given in Table II ($G_2 = G_2^{2PA} + G_2^{RAM} + G_2^{QSE}$). Knowledge of the individual contribution from each one of the three mechanisms becomes important when considering the polarization dependence of n_2 or in polarization dependent four wave mixing [14].

Fig. 1 depicts the dispersion function G_2 as a function of $x_1 = \hbar\omega_1/E_g$ for various excitation photon energies $x_2 = \hbar\omega_2/E_g$. By examining the terms in Table II, we can determine their relative contributions to n_2 in different spectral

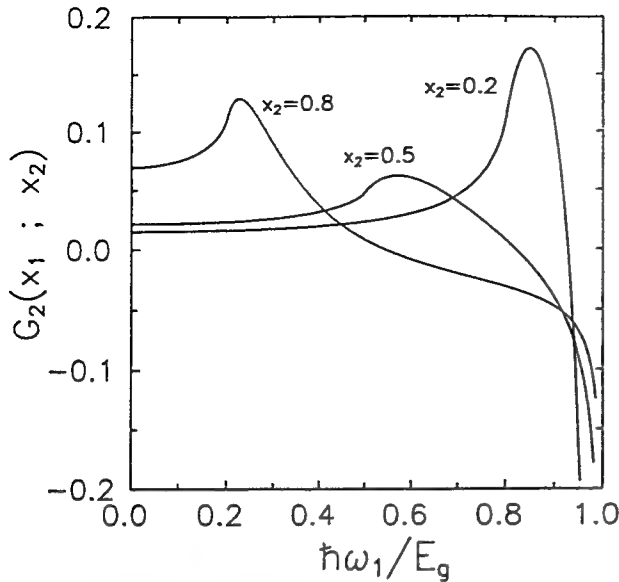


Fig. 1. The nondegenerate dispersion function $G_2(x_1; x_2)$ as a function of probe photon energy (x_1), calculated for various pump photon energies (x_2).

regimes. A general trend is evident in all the curves: n_2 is nondispersive in the infrared regime ($\hbar\omega_1 \ll E_g - \hbar\omega_2$) where 2PA and Raman terms contribute equally, it reaches a two-photon resonance at $\hbar\omega_1 + \hbar\omega_2 \simeq E_g$ where it has its peak positive value, and above this two-photon resonance n_2 becomes anomalously dispersive and ultimately turns negative due mainly to 2PA and the optical Stark effect as $\hbar\omega_1$ approaches E_g .

III. EXPERIMENTS

We use the 2-color Z -scan [7], [16] to measure the nondegenerate n_2 in ZnSe and ZnS. A Q -switched and modelocked Nd:YAG laser is used to generate single $t_p \simeq 83$ ps (FWHM) pulses at $\lambda = 1.06 \mu\text{m}$ as the excitation beam. Simultaneously, the second-harmonic of the same laser at $\lambda = 532$ nm serves as the weak probe ($t_p \simeq 58$ ps). Using this arrangement, we measure $n_2(2\omega; \omega)$ and $\beta(2\omega; \omega)$. At these wavelengths, the choice of the above materials is appropriate for examining the various dispersion regimes of n_2 as predicted by the theory. An important parameter in the experiment is the sum of the photon energies: $\hbar\omega_1 + \hbar\omega_2 \simeq 3.5$ eV. Since ZnSe has $E_g \simeq 2.6$ eV [17], it is a nondegenerate two-photon absorber at these wavelengths. ZnS, on the other hand, with $E_g \simeq 3.6$ eV [17] exhibits no nondegenerate 2PA. According to this theory however, it should exhibit a two-photon resonance enhanced positive n_2 . The degenerate n_2 and 2PA coefficient (β) of ZnSe and ZnS have been studied in the past [5], [9], [16]. The measurements show good agreement with the degenerate limit of the TPB theory [5]. Table III summarizes the earlier results along with the new nondegenerate measurements.

To illustrate the dispersive behavior of the measured n_2 and compare it with this theory, we consider the functions $G_2(2x; x)$ and $F_2^{2PA}(2x; x)$ (2PA contribution in Table I) where $x = \hbar\omega/E_g$ and ω corresponds to the fundamental of

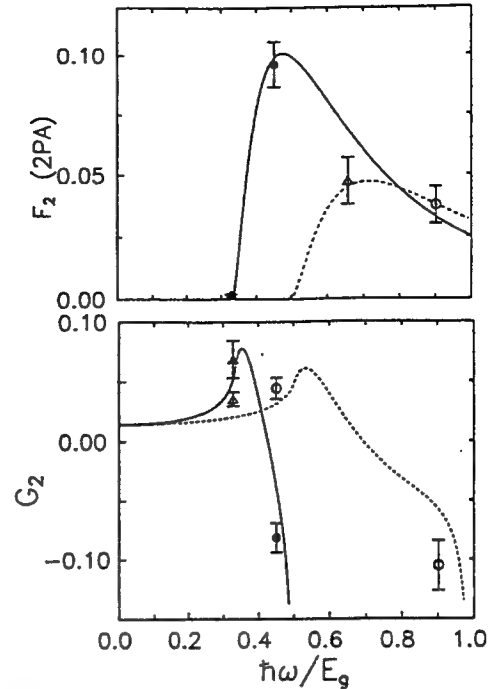


Fig. 2. (a) The measured degenerate $\beta(2\omega; 2\omega)$ (open symbols) and nondegenerate $\beta(2\omega; \omega)$ (solid symbols) for ZnSe (circles) and ZnS (triangles) using laser pulses at frequency ω ($\lambda = 1064$ nm) and 2ω ($\lambda = 532$ nm). The data are scaled according to (6) to compare with the calculated $F_2(2x; x)$ (solid line) and $F_2(x; x)$ (dashed line) functions. (b) The corresponding measured n_2 values, scaled according to (9), to compare with the calculated $G_2(2x; x)$ (solid line) and $G_2(x; x)$ (dashed line) functions.

TABLE III
THE MEASURED 2PA COEFFICIENTS $\beta(2\omega; \omega)$, $\beta(2\omega; 2\omega)$ AND OPTICAL KERR COEFFICIENTS $n_2(2\omega; \omega)$, $n_2(2\omega; 2\omega)$ FOR POLYCRYSTALLINE ZnSe AND ZnS SAMPLES USING A TWO-COLOR Z -SCAN TECHNIQUE. HERE, ω CORRESPONDS TO A WAVELENGTH OF $1.064 \mu\text{m}$. THE UNITS FOR n_2 AND β ARE $[10^{-14} \text{ cm}^2/\text{W}]$ AND $[10^{-9} \text{ cm}/\text{W}]$, RESPECTIVELY. THE DEGENERATE DATA FOR ZnSe ARE FROM [16].

Linear Index	Energy Gap	Degenerate				Nondegenerate	
		0.532 μm	1.06 μm	0.532 μm	1.06 μm	(0.532 μm , 1.06 μm)	
n_0	E_g (eV)	n_2	β	n_2	β	n_2	β
ZnSe	2.7 (0.532 μm)	2.6	-6.8	5.8	2.9	0	-5.1
	2.5 (1.06 μm)						15.3
ZnS	2.4 (0.532 μm)	3.6	N.A.	3.4	0.76	0	1.5
	2.3 (1.06 μm)						<0.073

the Nd:YAG laser frequency. Figure 2 depicts these functions along with the degenerate versions $G_2(x; x)$ and $F_2^{2PA}(x; x)$. The measured data are scaled by the predicted band-gap dependence of E_g^{-3} for β and E_g^{-4} for n_2 , where $K = 4000$ was used. The enhancement of the nondegenerate β in ZnSe is seen to agree with the TPB model. Though good qualitative agreement between experiment and theory is seen, the theory underestimates n_2 by a factor of $\simeq 1.5$ when β is quantitatively correct. In other words, as mentioned earlier, degenerate and nondegenerate n_2 values can be fairly predicted by the theory provided that we use $K \simeq 6000$ in (9) for n_2 . A discrepancy of $\simeq 1.5$ is not surprising for such

a simple theory, and it may be attributed to a more complex band structure than considered here and/or the neglect of the electron-hole Coulomb interaction. A simple treatment of the latter interaction based on the Elliott-Loudon approach, given in Section IV, can partially resolve this discrepancy.

For ZnSe, with ω corresponding to the fundamental wavelength of the Nd:YAG laser, $n_2(2\omega; \omega)$ is negative and resonantly enhanced due primarily to the effects of 2PA. As seen in Fig. 2(b), the degenerate n_2 of ZnSe at 532 nm is also negative while at 1.06 μm the dominant contribution of the 2PA resonance results in a positive n_2 [5], [17]. ZnS, on the other hand, has a positive and 2PA resonantly enhanced nondegenerate n_2 at these wavelengths as predicted by the theory.

IV. THE EFFECT OF EXCITONS

It might be expected that the electron-hole Coulomb interaction could lead to an enhancement of the 2PA coefficient near the $\hbar\omega_1 + \hbar\omega_2 = E_g$ resonance. The TPB theory (without including this interaction) appears to underestimate the experimental degenerate 2PA coefficients when $2\hbar\omega/E_g$ is above but very near unity [9]. Analogous to the case of single photon (linear) absorption, 2PA excitonic enhancement should reflect the increase in the density of states near the band-edge ($k \simeq 0$ region) where $\hbar\omega_1 + \hbar\omega_2 = E_g$. Additionally, this increased density of states will enhance the Raman and particularly the optical Stark contributions near the fundamental absorption edge. Various approaches have been taken previously to include this interaction in the perturbation theory of 2PA [18]. While a rigorous treatment can result in cumbersome calculations, approximate enhancement functions have been suggested as an alternative [19], [20]. In particular, Loudon [20] used an envelope function approach similar to that given by Elliott [21] for the interband one-photon absorption. For the continuum of excitons, this envelope function is given by the following [21]:

$$|U(\eta)|^2 = \frac{\pi\eta \exp(\pi\eta)}{\sinh(\pi\eta)} \quad (11)$$

where $\eta^2 = E_b/(\hbar\omega - E_g)$ with E_b denoting the excitonic binding energy. In Loudon's approach the energy denominator of η is replaced by the two-photon energy term $\hbar\omega_1 + \hbar\omega_2 - E_g$ in the nondegenerate case. In the "dressed state" framework, this can be interpreted as neglecting the excitonic effect on the energy shifts (4) but accounting for it in the transition rate between the "dressed states." Therefore, in generalizing this approximation, we multiply the function $F_2(x_1; x_2)$, in Table I, by the continuum exciton envelope function $|U(\eta)|^2$ where η is now given by

$$\eta^2 = \frac{E}{x_1 \pm x_2 - 1}. \quad (12)$$

Here $E_r = E_b/E_g$, and the \pm sign in the denominator corresponds to 2PA(+) and Raman (-), while for the optical Stark effect the denominator in (12) becomes only $x_1 - 1$ (i.e., $x_2 = 0$). Thus, $|U(\eta)|$ directly gives the enhancement of α_2 which has maxima when the denominator of (12) becomes small (i.e., where $x_2 + x_1 = 1$ at the 2PA edge, and when x_1 approaches 1 for the optical Stark effect).

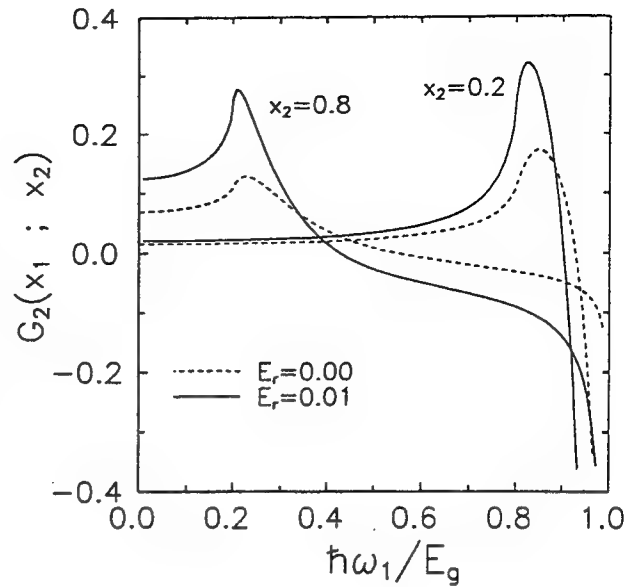


Fig. 3. The excitonic enhanced nondegenerate G_2 function (solid lines) compared to that of Fig. 1 (dashed lines). A typical value of $E_r = 0.01$ was used in the calculation.

In the TPB model and within the effective mass approximation as indicated by (7), $E_r = R/2E_p\epsilon_s^2$ where ϵ_s is the static dielectric constant and $R = 13.6$ eV is the Rydberg energy. Using $E_p \simeq 21$ eV, this gives $E_r \simeq 0.33/\epsilon_s^2$. For most semiconductors ϵ_s ranges from 5 to 10 leading to $E_r \simeq 0.013$ to 0.003. ZnSe and ZnS, for instance, have an E_r of 0.008 and 0.010, respectively [9].

Once the exciton-enhanced nonlinear absorption α_2 is determined, the refractive component can be obtained using the KK integral. This integral and its infrared divergent term can be numerically evaluated. In Fig. 3, the calculated result for the nondegenerate $n_2(\omega_1; \omega_2)$ using a typical value of $E_r \simeq 0.01$ is compared to the case $E_r = 0$ (i.e., no exciton enhancement). As expected, the enhancement is most visible near the one and two-photon transition resonances. The most drastic change is seen near the band-edge ($\hbar\omega_1 \simeq E_g$) where the contribution of the QSE becomes large. This is more clearly examined in Fig. 4 where the effects of excitons on each of the three contributions are plotted individually.¹ It is seen that the QSE contribution has the largest enhancement near the band-edge resonance.

Using $E_r = 0.008$, as shown in Figs. 5(a) and 5(b), we compare the excitonic enhanced F_2 and G_2 functions with the data of Fig. 2. Now using $K = 2600$ for both β and n_2 , excellent agreement between theory and experiment is achieved. Additionally, this value for K is closer to the calculated value of $\simeq 1940$ [5]. Moreover, the predicted band-edge resonant ($\hbar\omega_1/E_g \simeq 1$) enhancement is now in agreement with experiments, as the theory, without the excitonic effect, underestimated n_2 for AlGaAs [22] and CdS [5] at wavelengths near the band.

¹ The nonenhanced G_2 in our Fig. 4 (dotted line) is the corrected version of Fig. 4 in [5], in which the long-wavelength divergences of the individual contributions were removed incorrectly, thus suppressing the bandgap resonance of the electronic Raman effect.

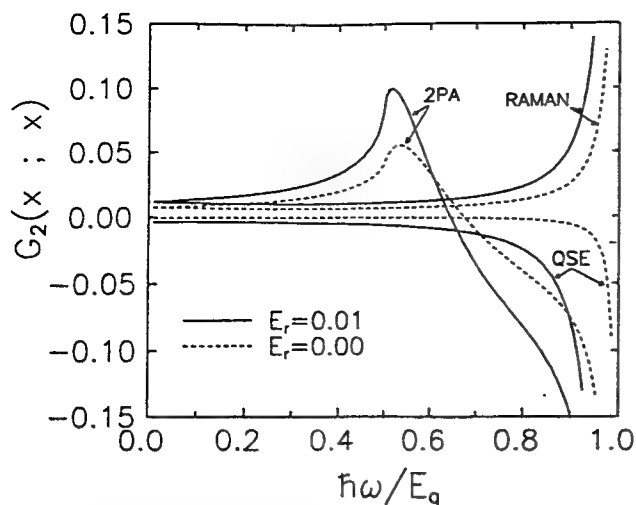


Fig. 4. The effect of excitonic enhancement on the various contributing mechanisms to the degenerate $G_2(x_1; x_1)$ compared to the nonenhanced G_2 as given by Table II.

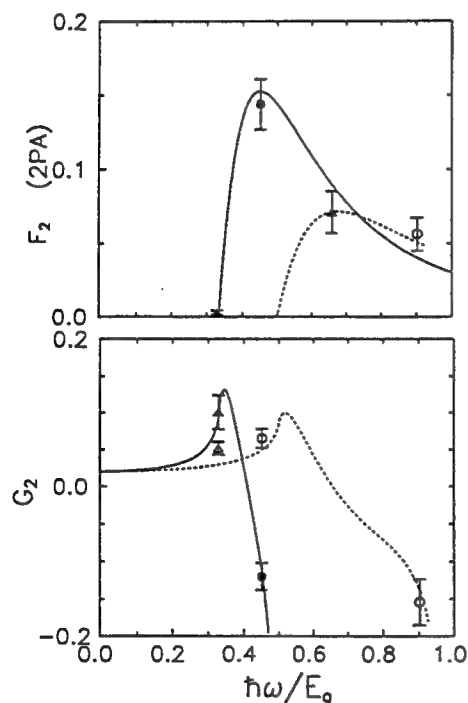


Fig. 5. Data for both (a) and (b) are the same as in Fig. 2 but scaled with $K = 2600$. The lines in (a) and (b) are the F_2 and G_2 functions calculated using the excitonic enhancement with $E_r = 0.008$.

V. CONCLUSION

The nondegenerate 2PA coefficient $\beta(\omega_1; \omega_2)$ and optical Kerr index $n_2(\omega_1; \omega_2)$ were calculated using a *dressed-state* two-parabolic band model. Closed-form analytical expressions were derived giving the variation of these coefficients with bandgap energy, linear index, and photon energy. The experimental results for ZnSe and ZnS show good agreement with this theory for ω_2 and ω_1 , the fundamental and second harmonic of the Nd:YAG laser, respectively. Finally, the possi-

ble effect of electron-hole Coulomb interaction is considered using an Elliott-type envelope function. This approximation leads to an enhancement of n_2 , which is largest near the two-photon and one-photon resonances.

ACKNOWLEDGMENT

The authors thank D. C. Hutchings and D. J. Hagan for useful discussions and A. A. Said for taking some of the data.

REFERENCES

- [1] G. I. Stegeman and E. M. Wright, "All optical waveguide switching," *Opt. and Quantum Electron.*, vol. 22, pp. 95-122, 1990.
- [2] R. Adair, L. L. Chase, and S. A. Payne, "Nonlinear refractive-index measurements of glasses using three wave frequency mixing," *J. Opt. Soc. Am. B*, vol. 4, pp. 875-881, 1987.
- [3] S. A. Akhmanov, R. V. Khokhlov, and A. P. Sukhorokov, "Self-focusing and diffraction of light in a nonlinear medium," *Sov. Phys. Usp.*, vol. 10, p. 609, 1968.
- [4] C. Flytzanis, *Quantum Electronics*, Vol. I, H. Rabin and C. L. Tang, Eds., New York: Academic, 1975, p. 9.
- [5] M. Sheik-Bahae, D. C. Hutchings, D. J. Hagan, and E. W. Van Stryland, "Dispersion of bound electronic nonlinear refraction in solids," *IEEE J. Quantum Electron.*, vol. 27, pp. 1296-1309, 1991.
- [6] M. Sheik-Bahae, D. J. Hagan, and E. W. Van Stryland, "Dispersion and band-gap scaling of the electronic Kerr effects in solids associated with two-photon absorption," *Phys. Rev. Lett.*, vol. 65, pp. 96-99, 1990.
- [7] M. Sheik-Bahae, J. Wang, J. R. DeSalvo, D. J. Hagan, and E. W. Van Stryland, "Measurement of nondegenerate nonlinearities using a two-color Z scan," *Opt. Lett.*, vol. 17, pp. 258-260, 1992.
- [8] D. C. Hutchings, M. Sheik-Bahae, D. J. Hagan, E. W. Van Stryland, "Kramers-Kronig relations in nonlinear optics," *Opt. Quantum Electron.*, vol. 24, pp. 1-30, 1992.
- [9] E. W. Van Stryland, H. Vanherzeele, M. A. Woodall, *et al.*, "Two photon absorption, nonlinear refraction, and optical limiting," *Opt. Eng.*, vol. 24, pp. 613-623, 1985.
- [10] D. C. Hutchings and E. W. Van Stryland, "Nondegenerate two-photon absorption in zinc blende semiconductors," *J. Opt. Soc. Am.*, vol. B-B9, pp. 2065-2074, 1992.
- [11] C. T. Hultgren and E. P. Ippen, "Ultrafast refractive index dynamics in AlGaAs diode laser amplifier," *Appl. Phys. Lett.*, vol. 59, pp. 635-657, 1991.
- [12] M. Sheik-Bahae and E. W. Van Stryland, "Ultrafast nonlinear refraction in semiconductor laser amplifier," *Ultrafast Phenomena VIII*. New York: Springer-Verlag, 1992.
- [13] E. O. Kane, "Band structure of indium antimonide," *J. Chem. Phys. Solids*, vol. 1, pp. 249-261, 1957.
- [14] M. Sheik-Bahae, J. Wang, E. J. Canto-Said, R. DeSalvo, D. J. Hagan, and E. W. Van Stryland, "Two-photon coherence and symmetry of $\chi^{(3)}$ in semiconductors," Paper QTK26, presented at the Digest of Quantum Electronics and Laser Science (QELS) Conference, Baltimore, MD, May 1993.
- [15] D. J. Moss, E. Ghahramani, J. E. Sipe, and H. M. van Driel, "Band-structure calculation of dispersion and anisotropy in $\chi^{(3)}$ for third-harmonic generation in Si, Ge, and GaAs," *Phys. Rev. B*, vol. 41, pp. 1542-1560, 1990.
- [16] M. Sheik-Bahae, A. A. Said, T. H. Wei, D. J. Hagan, and E. W. Van Stryland, "Sensitive measurement of optical nonlinearities using a single beam," *IEEE J. Quantum Electron.*, vol. 26, pp. 760-769, 1990.
- [17] J. I. Pankove, *Optical Processes in Semiconductors*. Englewood Cliffs, NJ: Prentice-Hall, 1971.
- [18] G. D. Mahan, "Theory of two-photon spectroscopy in solids," *Phys. Rev.*, vol. 170, pp. 825-838, 1968.
- [19] C. C. Lee and H. Y. Fan, "Two-photon absorption with exciton effect for degenerate bands," *Phys. Rev.*, vol. B9, pp. 3502-3516, 1974.
- [20] R. Loudon, "Theory of non-linear optical processes in semiconductors and insulators," *Proc. Phys. Soc.*, vol. 80, pp. 952-961, 1962.
- [21] R. J. Elliott, "Intensity of optical absorption by excitons," *Phys. Rev.*, vol. 108, pp. 1384-1389, 1957.
- [22] M. J. LaGasse, K. K. Anderson, C. A. Wang, H. A. Haus, and J. G. Fujimoto, "Femtosecond measurements of the nonresonant nonlinear index in AlGaAs," *Appl. Phys. Lett.*, vol. 56, pp. 417-419, 1990.



Mansoor Sheik-Bahae was born in Esfahan, Iran, in 1956. He received B.S. and M.S. degrees in electrical engineering from Catholic University of America, Washington, DC, in 1980 and 1982, respectively, and the Ph.D. degree in electro-physics from the State University of New York (SUNY) at Buffalo, NY, in 1987. He then joined the Center for Research and Education in Optics and Lasers (CREOL) at the University of Central Florida, Orlando, where he is now an associate research professor in the area of nonlinear optics and ultrafast

phenomena. His research activities in the past include the invention of the Z-scan technique and the development of a simple theory for predicting ultrafast bound-electronic nonlinearities in solids. His present research interests include experimental and theoretical studies of nonlinear optical processes in glasses, bulk semiconductors, and semiconductor diode lasers. He has also been involved in the development and characterization of femtosecond solid-state and picosecond CO₂ laser systems.

J. Wang, photograph and biography not available at the time of publication.

E. W. Van Stryland, photograph and biography not available at the time of publication.



CHARACTERIZATION OF NONLINEAR OPTICAL ABSORPTION AND REFRACTION

E. W. Van Stryland, M. Sheik-Bahae, A. A. Said and D. J. Hagan

Center for Research in Electro-Optics and Lasers, University of Central Florida,
Orlando, FL 32826, U.S.A.

We discuss the characterization of nonlinear optical processes that give rise to changes in the absorption coefficient and refractive index. We primarily concentrate on methods for determining the dominant nonlinearities present in condensed matter and the responsible physical mechanisms. In extensive studies of a wide variety of material, we have found that there is seldom a single nonlinear process occurring. Often several processes occur simultaneously, sometimes in unison, sometimes competing. It is necessary to experimentally distinguish and separate these processes in order to understand and model the interaction. There are a variety of methods and techniques for determining the nonlinear optical response, each with its own weaknesses and advantages. In general, it is advisable to use as many complementary techniques as possible over a broad spectral range in order to unambiguously determine the active nonlinearities. Here we concentrate on the use of nonlinear transmittance, Z-scan and degenerate four-wave mixing experiments as applied to polycrystalline and single crystal semiconductors and dielectric materials.

1. Introduction

Numerous techniques are known for measurements of nonlinear refraction (NLR) and nonlinear absorption (NLA) in condensed matter. As the names imply, NLR describes optically induced changes in the refractive index of a material, while optically induced changes in absorption are categorized as NLA. Nonlinear interferometry [1,2], degenerate four-wave mixing (DFWM) [3], nearly-degenerate three-wave mixing [4], ellipse rotation [5], beam distortion,[6,7] beam deflection [8], and third-harmonic generation [9], are among the techniques frequently reported for direct or indirect determination of NLR. Z-scan is a single beam technique for measuring the sign and magnitude of NLR indices and NLA coefficients [10,11], which offers simplicity as well as high

Nonlinear absorption and refraction always coexist (although with different spectral properties) as they result from the same physical mechanisms. They are connected via dispersion relations similar to the usual Kramers-Kronig relations that connect linear absorption to the linear index (or, equivalently, relate the real and imaginary parts of the linear susceptibility).[18-21] The physical processes that give rise to NLA and the accompanying NLR include "ultrafast" bound electronic processes and "excited state" processes, where the response times are dictated by the characteristic formation and decay times of the optically induced excited states. Ultrafast processes include multiphoton absorption [12,19], stimulated Raman scattering [22] and AC-Stark effects [19,20]. Excited-state nonlinearities can be caused by a variety of physical processes including absorption saturation [22], excited-state absorption in atoms and molecules [23] or free-carrier absorption in solids [24,25], photochemical changes [26], as well as defect and color center formation [27]. The above processes can lead to increased transmittance with increasing irradiance (eg. saturation, Stark effect) or decreased transmittance (eg. multiphoton absorption, excited-state absorption). The key to distinguishing these processes is to pay particular attention to the temporal response. One way of achieving this is the use of pulsewidths much shorter than the decay times of the excited states. As we shall show, in this regime, the excited-state nonlinearities are fluence (ie. energy per unit area) dependent, while the ultrafast effects remain irradiance dependent.

It is important to note early in this paper the importance of accurately measuring the laser mode and pulse parameters. For example, two-photon absorption (2PA) is irradiance dependent. Thus, given the pulse energy, we need to know both the beam area (i.e. spatial beam profile) and the temporal pulse width (i.e. temporal shape) in order to determine the irradiance. Any errors in the measurement of irradiance translate to errors in the determination of the 2PA coefficient, β . Similar comments apply to other nonlinearities. Figure 1 shows a plot of β (cm/GW), on a semilogarithmic scale, as a function of year published in the literature for GaAs. It has been established that these large differences are not due to differences in the materials, but are due to experimental problems and interpretation errors. Clearly, there are a great number of pitfalls for experimenters in NLO.

II.1 Nonlinear absorption:

We will primarily limit our discussion to the increasing loss from two-photon absorption (2PA) and photogenerated excited-state absorption (ESA). The losses from 2PA occur in solids when the photon energy, $\hbar\omega$, is larger than one-half the band-gap energy, E_g . The equation describing 2PA (a third-order response) of a beam of irradiance I as a function of depth z in a material is;

$$\frac{dI}{dz} = -(\alpha_0 + \beta I)I, \quad (1)$$

where β is the 2PA coefficient, and the equation includes residual linear absorption of coefficient α_0 . This linear absorption in solids for $\hbar\omega < E_g$ can come from defects, impurities or band tailing and can often be ignored in good quality materials.

to some time t' in the pulse, substituting for N in Eq. 2 and then integrating over all times t' (i.e. $-\infty$ to ∞) we find the fluence F varies with z as

$$\frac{dF}{dz} = - \left[\alpha_0 + \frac{\alpha_0 \sigma}{2\hbar\omega} F \right] F. \quad (4)$$

Notice that this equation is exactly analogous to Eq. 1 describing 2PA loss with the fluence replacing the irradiance and $\alpha_0 \sigma / 2\hbar\omega$ replacing β . Therefore, since in most experiments the pulse energy is detected, FCA initiated by linear absorption and 2PA, will give nearly identical results for loss as a function of input energy (microscopically ESA can be considered as the limit of 2PA with a resonant intermediate state). The difference between Eqs. 1 and 4 when determining the transmitted energy is in the temporal integral over the pulse for 2PA. For FCA, this integral has already been performed. In other words, in order to determine which of these nonlinearities is present, the temporal dependence must be measured in some way.

If the carriers are produced via a 2PA process (β in Eq. 1) rather than by linear absorption (α_0 in Eq. 1), the resulting equations are considerably different, and cannot be solved analytically. Including 2PA, Eq. 2 becomes,

$$\frac{dI}{dz} = -(\alpha_0 + \beta I + \sigma N) I, \quad (5)$$

which must now be combined with the 2PA carrier generation rate,

$$\frac{dN}{dt} = \frac{\beta I^2}{2\hbar\omega}. \quad (6)$$

The factor of 2 indicates that the energy of two photons is needed to create the carrier pairs. Again we make the simplifying assumption that carriers do not diffuse or decay during the pulse. In semiconductors, this assumption is normally valid with picosecond pulses. In Eq. 5, α_0 is again included only as a residual linear absorption from defects or impurities, and it is assumed that free carriers are not produced in the process.

It is interesting to look at the order of the nonlinear response for the three cases given above. The first two, 2PA and linearly generated FCA, both appear as third-order responses. However, in one case, 2PA, the nonlinearity is proportional to $\text{Im}\{\chi^{(3)}\}$, while for the linear absorption generated FCA the nonlinearity is due to the cascaded process $\text{Im}\{\chi^{(1)}\}:\text{Im}\{\chi^{(1)}\}$ (i.e. two linear absorption processes), where the first $\chi^{(1)}$ is associated with the ground state absorption and the second with FCA. Here $\chi^{(j)}$ refers to the j th order electric susceptibility. Without knowledge of the temporal dependence of the process, FCA and 2PA are indistinguishable.

For the third case, 2PA generated FCA, the nonlinear response appears fifth order, a cascaded $\text{Im}\{\chi^{(3)}\}:\text{Im}\{\chi^{(1)}\}$ (i.e. 2PA followed by FCA). However, the overall nonlinear transmission as given by Eq. 5 has both the third-order response of 2PA (second term) and the fifth-order cascaded

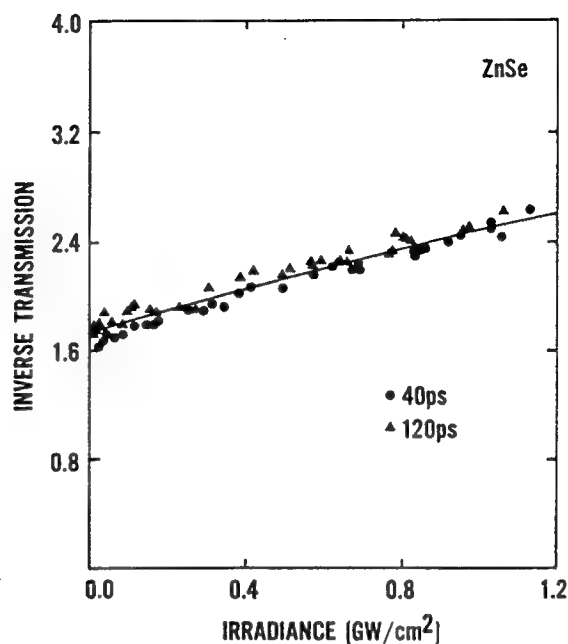


Figure 2. Inverse transmittance for ZnSe as a function of the external incident irradiance using input pulsewidths of 40 psec and 120 psec (FWHM).

where now T is defined as the ratio of output to input fluence. Again, including an integral over the spatial distribution only gives a small deviation from the straight line prediction of Eq. 10 whose slope, in conjunction with the intercept, now determines σ . In experiments to determine T , it is usually the pulse transmitted energy, \bar{E} , that is monitored, meaning that the spatial and temporal integrals for 2PA, or the spatial integral for linearly generated FCA, must be performed. Thus, for a single experiment of $T = E(L)/E(0)$ versus the input energy, these very different nonlinear processes are indistinguishable. Only if the temporal dependence of the transmittance were directly monitored could these two processes be distinguished.

This is a very important distinction between a direct $\chi^{(3)}$ response and a sequential, cascaded $\chi^{(1)}:\chi^{(1)}$ response. In general, many processes can have a third-order response but may not be strictly described by a $\chi^{(3)}$ susceptibility. Thermal nonlinearities, excited-state nonlinearities, electrostrictive nonlinearities, etc. are examples, and this statement is valid for absorptive ($\text{Im } \chi^{(3)}$) and refractive ($\text{Re } \chi^{(3)}$) responses. For example, a thermal nonlinearity is normally described by a $\chi^{(1)}:\chi^{(1)}$ response. The sample first linearly absorbs the light which changes its temperature ($\text{Im } \chi^{(1)}$). This temperature change, in turn, changes the linear absorption ($\text{Im } \chi^{(1)}$) or changes the linear refractive index ($\text{Re } \chi^{(1)}$). This latter effect is referred to as thermal lensing or thermal blooming as it is often a defocusing effect. The turn-on time for thermal effects depends upon the mechanism for the induced changes in $\chi^{(1)}$. For example, lattice heating induces a change in bandgap that, in time,

For the case where free carriers are generated from single photon absorption processes (see Eq. 3),

$$\Delta n(t) = n_2 I(t) + \frac{\alpha_0 \sigma_r}{\hbar \omega} \int_{-\infty}^t I(t') dt' . \quad (13)$$

The bound electronic response follows the temporal dependence of the pulse input while the FCR builds up in time through the pulse. For the case where the carriers are created solely by 2PA (see Eq. 6) Eq. 12 becomes,

$$\Delta n(t) = n_2 I(t) + \frac{\beta \sigma_r}{2 \hbar \omega} \int_{-\infty}^t I^2(t') dt' . \quad (14)$$

Usually, especially when using picosecond or shorter pulses, the phase distortion is not time resolved and only the temporally averaged value is measured. Assuming the nonlinear refraction accumulates throughout the pulse without decay, it can be shown that the temporally averaged index change is simply one half $\Delta n_{FC}(t=\infty)$ or it equals $\Delta n_{FC}(t=0)$ for a symmetric pulse in time.[11] Here, Δn_{FC} refers to the second term in Eq. 13 or 14. The contribution from the bound electronic n_2 (first term in Eq. 14) gives an index change Δn_{n_2} , averaged over a Gaussian temporal pulse, of $1/\sqrt{2}$ times the peak value. Thus, the temporally averaged index change is,

$$\langle \Delta n \rangle = \frac{1}{\sqrt{2}} n_2 I(t=0) + \frac{1}{2} \Delta n_{FC}(t=0) . \quad (15)$$

Integrating Eq. 11 over the sample length to obtain the total phase distortion $\Delta \phi(r, t)$, we define $\langle \Delta \phi \rangle$ as the temporally averaged phase distortion as determined from Eq. 15. We then define $\Delta \Phi$ as $\Delta \phi$ evaluated at the beam center ($r=0$), with similar definitions for the temporally averaged quantities, eg. $\langle \Delta \Phi \rangle$ is the on-axis temporally averaged phase distortion.

$\Delta \phi$ can also be a periodic function of the spatial coordinates x (or y) due to the interference of two or more coherent beams as in, for example, DFWM (discussed in section III.2). Beam propagation and diffraction are discussed in the next section along with experimental techniques.

III. Experimental Techniques

In a single article it would be impractical to satisfactorily describe the many experimental techniques to measure NLA and NLR, so we choose to give just three examples. We describe direct transmission measurements, Z-scan and temporally-resolved DFWM. We discuss the complementary information that these methods give. This choice only reflects the fact that the authors are most familiar with these techniques. In addition this article does not discuss methods that measure nonlinearities in fibers or waveguides; however, these three methods can measure nonlinearities of the constituent materials in bulk or thin film form. In general it is best to use as many complementary experimental techniques as possible to determine the nonlinear optical response of a given material.

traversing the sample. Figure 3 shows a transverse scan through the center of an initially Gaussian spatial profile beam (30 ps FWHM pulse at 532 nm, $Z_0=178$ cm) after transmission through the ZnSe and then propagating 55 cm to the vidicon (near field). The beam breakup into two peaks is characteristic of a self-defocusing (negative induced lens) nonlinearity in the near field. This effect can become very strong at high irradiance and is enhanced for longer pulsewidths (having more energy) by free-carrier refraction. While a detector placed after the sample collects all the beam at low inputs, the detector can miss some of the light at high inputs. Again these effects result in an overestimation of β (see Fig. 1).

While FCA can be negligible for picosecond pulses (see discussion in section II.1), the refraction arising from these free carriers, FCR is not.[12] As shown in Fig. 3, ZnSe displays strong self defocusing even for picosecond pulses. As discussed in section III.2, this defocusing is a combination of bound-electronic and free-carrier refraction as described by Eq. 14 (and 15). The solid line in Fig. 3 shows results of a computer calculation using parameters obtained from Z-scans (see section III.2). The field at the exit surface of the sample is determined by $E \propto \sqrt{I} e^{i\phi}$, and as described in Ref. [25], this field is propagated to the vidicon detector to give the results of Fig. 3. We discuss this further in the next section.

III.2 Z-SCAN

Z-scan measures both the nonlinear loss and phase distortion imposed on a Gaussian beam.[10,11] For measuring NLR this technique exploits the spatial narrowing and broadening of Gaussian beams in the far field which are due to self-focusing or self-defocusing caused by the nonlinear interaction of the beam with the material. A schematic of the experimental setup is given in Fig. 4. A Gaussian beam is focused onto the sample and then collected through an aperture in the far field by the transmission detector (D_2). Keeping the input energy constant, the sample is translated along the beam propagation direction through the focal plane, and the transmittance (D_2/D_1) is measured as a function of this sample position Z with respect to the focal plane (Z should not be confused with z , the depth within the sample). In the case of a material with a negative nonlinear refractive index, the self-defocusing will cause beam narrowing in the far field when the sample is before focus (negative Z) and beam broadening when the sample is after focus (positive Z). An increase in transmittance followed by a decrease in transmittance (peak-valley) for increasing Z denotes negative nonlinear refraction, while a valley-peak configuration implies positive nonlinearity. In Ref. [11] we give a detailed description and analysis of the Z-scan technique. Within the thin sample approximation [16,17], it is found that the change in the index of refraction (Δn) is given by a linear relation between the on-axis temporally averaged phase distortion at focus ($\Delta\Phi_0$) (where the subscript on Φ refers to the sample positioned at the beam waist, i.e. at focus) and the difference between the maximum and minimum values of the normalized aperture transmittance, ΔT_{pv} . This relation for an aperture size that gives 40% linear transmittance is given by:[11]

$$\langle \Delta\Phi_0 \rangle \approx 2.8 \Delta T_{pv} \quad (16)$$

Examining Fig. 4 for a purely refractive case, if the aperture is removed i.e. if all the transmitted

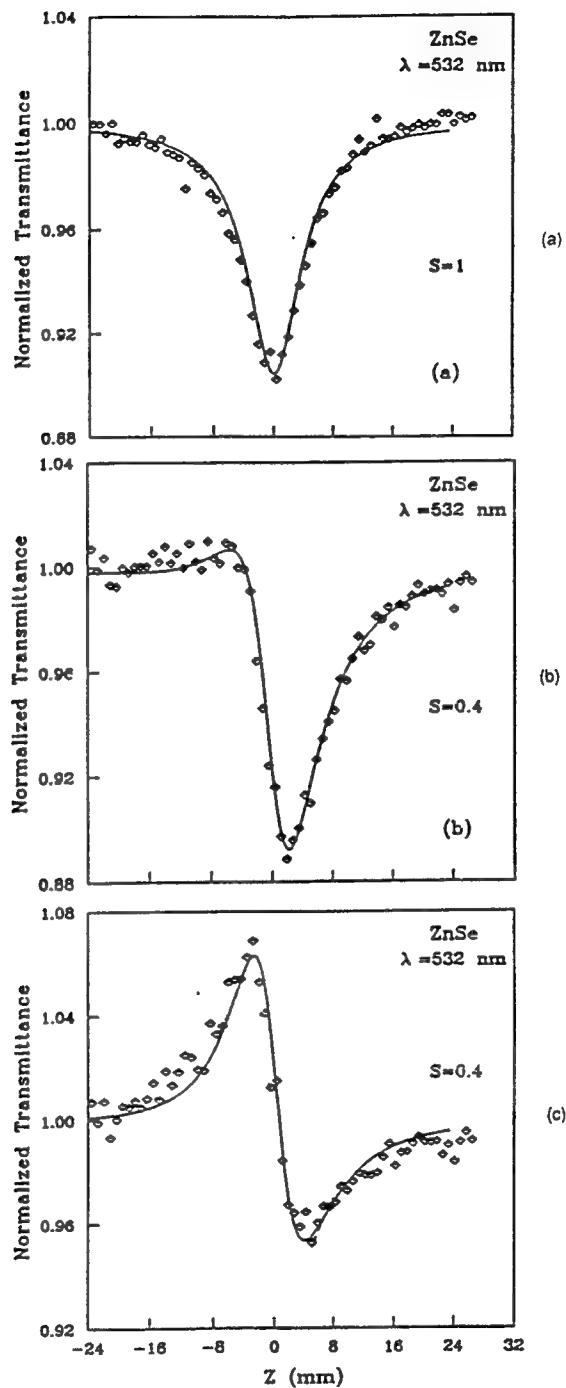


Figure 5. Normalized Z-scan transmittance of ZnSe measured using picosecond pulses at $\lambda=532$ nm with $I_0=0.21$ GW/cm². (a) Open aperture data and fit (solid line) (b) 40% aperture data and fit (solid line) and (c) The result of the division of the Z-scans of (a) and (b).

We also measured n_2 in ZnSe at $1.06 \mu\text{m}$ where 2PA is not present. Using 40 ps pulses (FWHM) from a Nd:YAG laser focused to $w_0 \approx 40 \mu\text{m}$, we obtained $n_2 = +2.9 \times 10^{-14} \text{ cm}^2/\text{W}$ ($+1.7 \times 10^{-11} \text{ esu}$). In Fig. 8 we plot closed aperture Z-scans obtained in ZnSe at $1.06 \mu\text{m}$ and at $0.53 \mu\text{m}$ showing the change in sign of n_2 . In this figure, the nonlinear absorption has been divided out of the $0.53 \mu\text{m}$ data. This observed dispersion in n_2 and change in sign is consistent with the recent theory of Refs. [19-21] and shows the necessity of measuring the nonlinearity at more than a single wavelength.

In addition to separately measuring NLA and NLR, Z-scan can be used to determine the anisotropy of these responses (eg. the different responses to linear and circular polarized light). This is

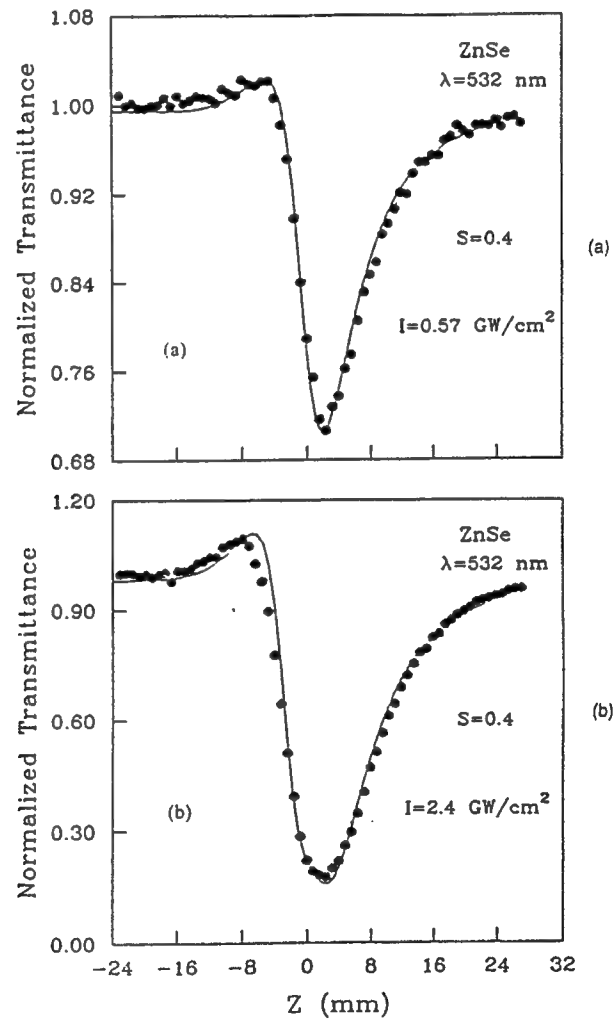


Figure 6. Closed aperture Z-scan data ($S=0.4$) and theoretical fit (solid lines) of the ZnSe sample taken at irradiance levels of $I_0=0.57 \text{ GW/cm}^2$ (a) and $I_0=2.4 \text{ GW/cm}^2$ (b) where free-carrier refraction is large.

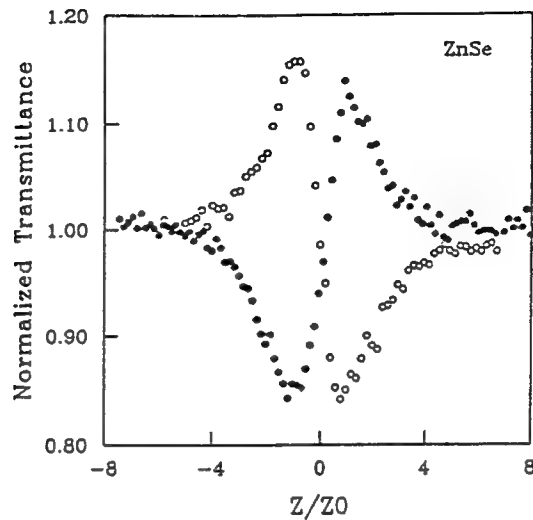


Figure 8. Closed aperture ($S=0.4$) Z-scan experimental data (filled circles) of ZnSe at $1.06 \mu\text{m}$ and 532 nm (open circles) in units of $Z_0 = \pi w_0^2 / \lambda$. This figure clearly shows the dispersion in n_2 as it changes sign from positive at $1.06 \mu\text{m}$ to negative at 532 nm .

amplitude gratings formed that can diffract a pump beam; one between E_i and E_p , and the other between E_b and E_p . The grating spacing is determined by the angle θ which is usually made to be small (a few degrees). In this case, one of the gratings has a spacing larger than λ ($\approx \lambda/\theta n$) while the other has a spacing of $\approx \lambda/n$. Calculating the direction of the beam diffracted off either of these gratings shows that this field, E_c (the conjugate wave), retraces the path of E_p (i.e. the sample retroreflects the beam). This retroreflection is the basis for phase conjugation and phase-conjugate

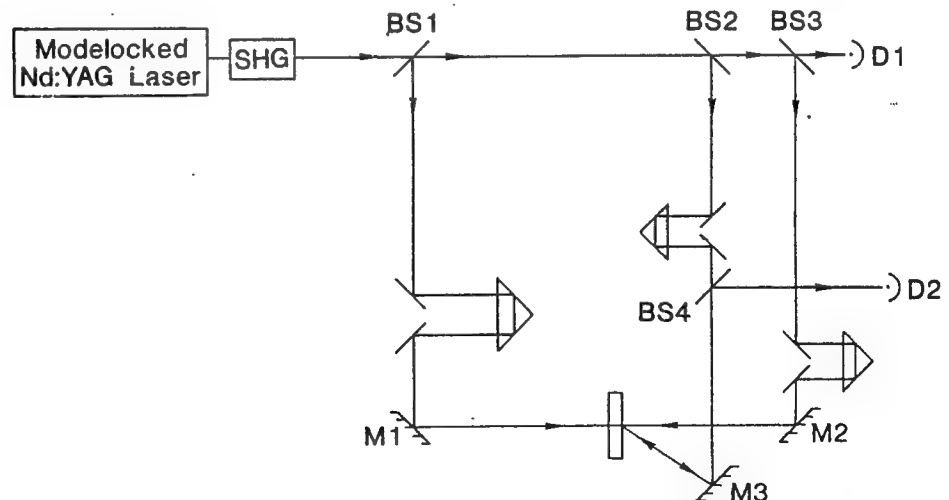


Figure 9. Schematic of experimental DFWM apparatus. D_1 is the input pulse energy monitor, while D_2 monitors the phase-conjugate signal pulse energy.

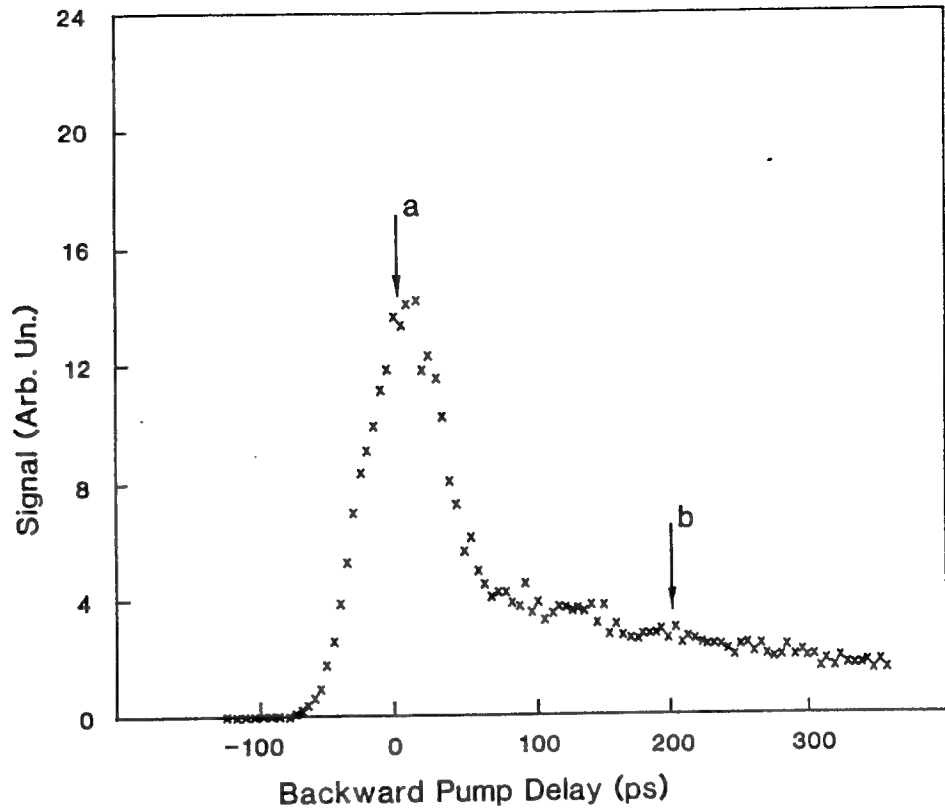


Figure 10. A plot of the phase-conjugate signal versus backward pump delay with the backward pump polarized perpendicular to the other two waves.

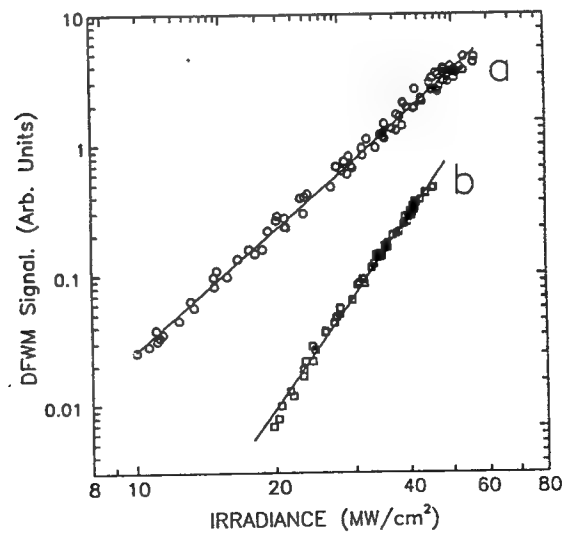


Figure 11. Log-log plots of the phase conjugate signal versus the total input irradiance ($I_t + I_b + I_p$) as all three beams were varied together, for (a) zero delay and (b) 240 ps delay. The solid lines are best-fits to the data giving power dependencies of $I^{3.1 \pm 0.2}$ and $I^{5.0 \pm 0.2}$, respectively.

experimental data to obtain the experimental functions;

$$F^e(\hbar\omega/E_g) = \frac{1}{K\sqrt{E_p}} n_0^2 E_g^3 \beta^e \quad (21)$$

and

$$G^e(\hbar\omega/E_g) = \frac{1}{K'\sqrt{E_p}} n_0 E_g^4 n_2^e \quad (22)$$

where β^e and n_2^e are experimental values of β and n_2 and K and K' are proportionality constants. Here E_p is the Kane energy as discussed in Ref. [12, 19, 39] and is nearly material independent with a value near 21 eV. Figures 12 and 13 plot these scaled data versus photon $\hbar\omega/E_g$, along with the predicted dependence from a two-parabolic band model using a value of $K=3100$ in units such that E_p and E_g are in eV and β is in cm/GW.[18-20] The value of $K'=0.94 \times 10^8$ is determined from the Kramers-Kronig integral of the nonlinear absorption spectrum using the above value for K . [19] The data shown in Fig. 12 come primarily from direct transmittance measurements.[12] The data in Fig. 13 for semiconductors come from Z-scan measurements [19] and for dielectrics come from Z-scan [19] and nearly degenerate three-wave mixing [40]. Several materials have now been measured by both techniques and the agreement for n_2 is excellent. As seen in Fig. 12 the experimental 2PA appears nearly step-function like, turning on at approximately $E_g/2$. Figure 13 shows a small, positive, nearly dispersionless n_2 for $\hbar\omega/E_g$ much less than E_g , reaching a peak near $E_g/2$, where 2PA

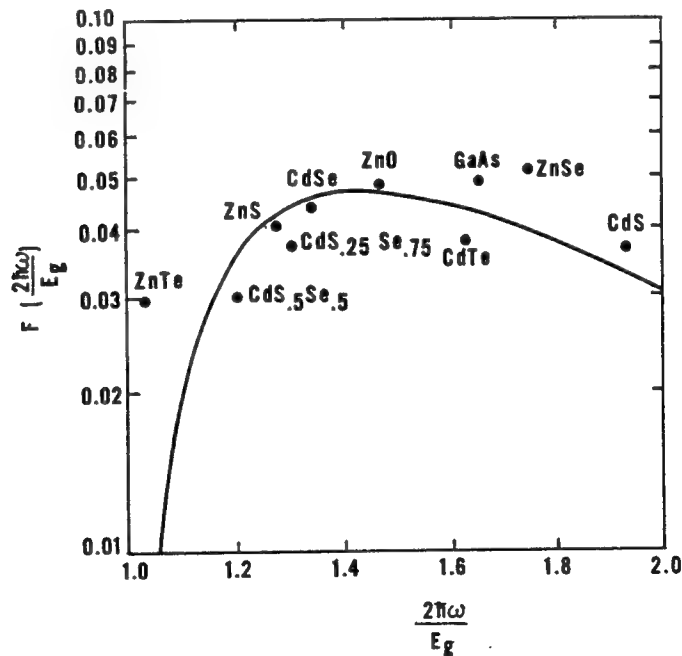


Figure 12. The solid line is the two-parabolic band prediction for the function F plotted as a function of $2\hbar\omega/E_g$ using $K=3100$ in Eq. 21. The data are scaled according to Eq. 21 are from Ref. [12, 62]. Figure reproduced from Ref. [62].

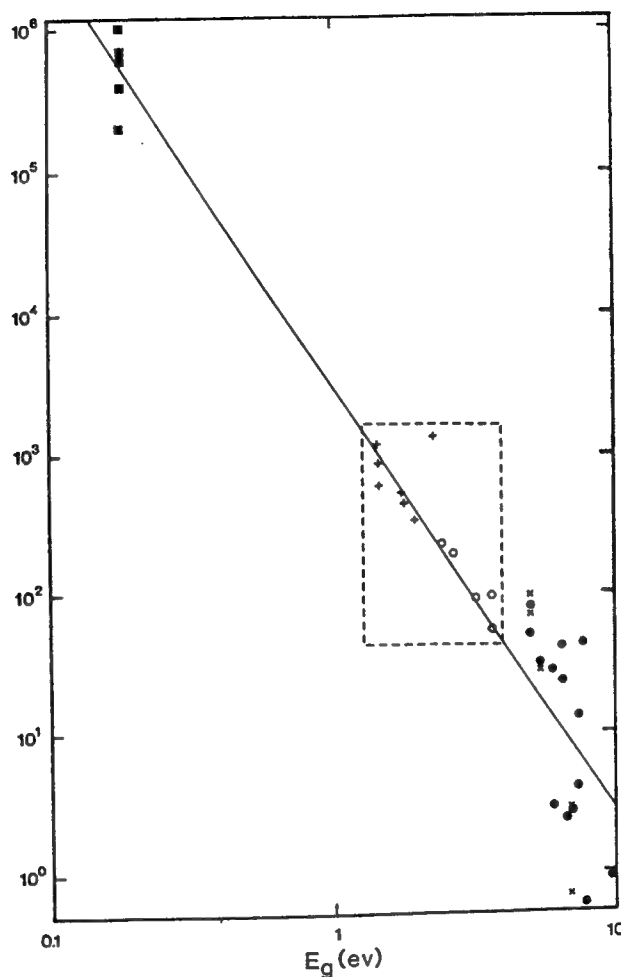


Figure 14. A log-log plot of the scaled 2PA coefficient β as a function of the bandgap energy E_g (in eV). The data are scaled from Eq. 21 as $\beta \cdot n^2 / \sqrt{E_g} F$. The straight line is a fit to the data within the dashed box from Ref. [62] for a line of fixed slope -3. The data to the right of the box are taken from Ref. [59] using the third (X's) and fourth (closed circles) harmonics of 1.06 μm picosecond pulses. The data to the left of the box (closed squares) are taken from Ref. [60] using 10 μm nanosecond pulses, which carefully accounted for free-carrier absorption. Figure reproduced from Ref. [64].

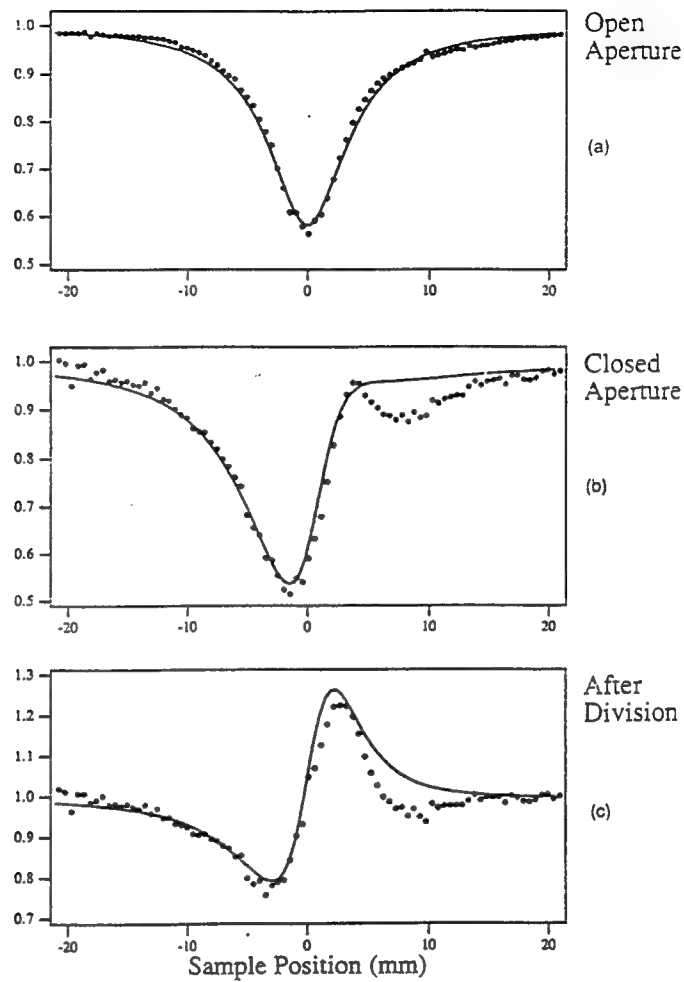
BaF₂ 266nm Z-Scans

Figure 16. Normalized Z-scan transmittance of BaF₂ measured using picosecond pulses at $\lambda=266$ nm with $I_0=72$ GW/cm². (a) Open aperture data and fit (solid line) (b) 40% aperture data and fit (solid line) and (c) The result of the division of the Z-scans of (a) and (b).

shorter wavelengths. We find for BaF₂ at 266 nm, with the light propagating in the [100] direction and the field parallel to [010], $\beta \approx 0.06$ cm/GW, and $n_2 \approx +3.1 \times 10^{-16}$ cm²/W ($+1.1 \times 10^{-13}$ esu) while the anisotropy in this material is large (eg. 30% change in n_2 with orientation). While a thorough study at this wavelength has not been performed, we expect the free-carrier effects at this irradiance and wavelength are small. This is due to both the small magnitude of β and the smaller expected free-carrier cross sections at short wavelengths.

In order to extract the data needed to plot Figures 12, 13, 14 and 15, a clear understanding of the nonlinearities involved was necessary. In the final analysis these figures reveal relatively simple

- [3] R.K. Jain and M.B. Klein, "Degenerate Four-Wave Mixing in Semiconductors", pp. 307-415, in *Optical Phase Conjugation*, ed. R. A. Fisher, Academic Press, N.Y. 1983.
- [4] R. Adair, L. L. Chase, and S. A. Payne, "Nonlinear refractive index measurement of glasses using three-wave frequency mixing", *J. Opt. Soc. Am. B*, **4**, 875 (1987).
- [5] A. Owyong, "Ellipse rotations studies in laser host materials", *IEEE J. Quantum Electron.*, QE-9, 1064 (1973).
- [6] W. E. Williams, M. J. Soileau, and E. W. Van Stryland, "Optical Switching and n_2 Measurements in CS_2 ", *Opt. Commun.*, **50**, 256 (1984).
- [7] W. E. Williams, M. J. Soileau, and E. W. Van Stryland, "Simple direct measurement of n_2 ", in *Proc. 15th Annu. Symp. Opt. Materials for High Power Lasers*, Boulder, CO, 1983.
- [8] M. Bertolotti, A. Ferrari, C. Sibilia, G. Suber, D. Apostol and P. Jani, "Photothermal Deflection Technique for Measuring Thermal Nonlinearities in Glasses", *Appl. Phys.*, **27**, 1811 (1988).
- [9] F. Kajzar and J. Messier, "Cubic Effects in Polydiacetylene Solutions and Thin Films", in *Nonlinear Optical Properties of Organic Molecules and Crystals*, eds. D.S. Chemla and J. Zyss, Vol. 2, pp. 51-83, Academic Press, Orlando, 1987.
- [10] M. Sheik-Bahae, A. A. Said, and E. W. Van Stryland, "High sensitivity, single beam n_2 measurement", *Opt. Lett.*, **14**, 955-957 (1989).
- [11] M. Sheik-Bahae, A. A. Said, T. H. Wei, D. J. Hagan, and E. W. Van Stryland, "Sensitive measurement of optical nonlinearities using a single beam", *IEEE J. Quantum Electron.*, QE-26, 760-769 (1990).
- [12] E. W. Van Stryland, H. Vanherzeele, M. A. Woodall, M. J. Soileau, A. L. Smirl, S. Guha, and T. F. Boggess, "Two photon absorption, nonlinear refraction, and optical limiting in semiconductors", *Opt. Eng.*, **24**, 613 (1985).
- [13] M. Bass, E.W. Van Stryland, and A.F. Stewart, "Laser Calorimetric Measurement of Two-Photon Absorption", *Appl. Phys. Lett.* **34**, 142 (1979).
- [14] Y. Bae, J.J. Song, and Y.B. Kim, "Photoacoustic Study of Two-Photon Absorption in Hexagonal ZnS ", *J. Appl. Phys.*, **53**, 615 (1982). also see, E.W. Van Stryland, and M.A. Woodall, "Photoacoustic Measurement of Nonlinear Absorption in Solids," in *Laser Induced Damage in Optical Materials*, NBS Special Publication 620, 50 (1980).
- [15] for example see; *Picosecond Phenomena*, eds. C.V. Shank, E.P. Ippen, and S.L. Shapiro, Springer Verlag, 1978.

- [29] B.S. Wherrett and N.A. Higgins, "Theory of Nonlinear Refraction Near the Band Edge of a Semiconductor", *Proc. R. Soc. Lond. A* 379, 67 (1982).
- [30] R. DeSalvo, M. Sheik-Bahae, A.A. Said, D.J. Hagan and E.W. Van Stryland, "Z-scan Measurements of the Anisotropy of Nonlinear Absorption and Refraction in Crystals", *Opt. Lett.* 18, 194-196 (1993).
- [31] J. Wang, M. Sheik-Bahae, A.A. Said, D.J. Hagan, and E.W. Van Stryland, "Time-Resolved Z-Scan Measurements of Optical Nonlinearities", *JOSA B*, xx (1993).
- [32] J. R. Salcedo, A. E. Siegman, D. D. Dlott and M. D. Fayer, "Dynamics of Energy Transport in Molecular Crystals: The Picosecond Transient Grating Method", *Phys. Rev. Lett.* 41, 131 (1978).
- [33] H. J. Eichler, P. Gunter, and D. W. Pohl, "Laser-Induced Dynamic Gratings", *Springer Series in Optical Sciences*, 50, eds. J. M. Enoch, D. L. MacAdam, A. L. Schawlow, K. Shimoda and T. Tamir (Springer-Verlag, 1988).
- [34] *Optical Phase Conjugation*, ed. R. A. Fisher, Academic Press, N.Y. 1983.
- [35] E. Canto-Said, D. J. Hagan, J. Young, and E. W. Van Stryland, "Degenerate Four-Wave Mixing Measurements of High Order Nonlinearities in Semiconductors", *IEEE J. Quantum Electron.* 27, 2274 (1991).
- [36] A. G. Aronov, D. E. Pikus, and D. Sh. Shekhter, "Quantum theory of free-electron dielectric constant in semiconductors", *Sov. Phys.-Solid State*, 10, 645 (1968).
- [37] D. H. Auston, S. McAfee, C. V. Shank, E. P. Ippen, and O. Teschke, "Picosecond spectroscopy of semiconductors", *Solid State Electron.* 21, 147-150 (1978).
- [38] B. S. Wherrett, A. C. Walker, and F. A. P. Tooley, "Nonlinear refraction for CW optical bistability", in *Optical Nonlinearities and Instabilities in Semiconductors*, H. Haug ed. (Academic Press, 1988), 239-272.
- [39] B.S. Wherrett, "Scaling Rules for Multiphoton Interband Absorption in Semiconductors", *J. Opt. Soc. Amer. B* 1, 67 (1984).
- [40] R. Adair, L.L. Chase and Stephen A. Payne, "Nonlinear Refractive Index of Optical Crystals", *Phys. Rev. B* 39, 3377-3350 (1987).
- [41] Basov, N. G., Grasyuk, A. Z., Efimov, V. F., Zubarev, I. G. Katulin, V. A. and Popov, J. M., "Semiconductor Lasers Using Optical Pumping", *J. Phys. Soc. Jpn. Suppl.*, 21, 276, (1966).
- [42] Ralston, J. M. and Chang, R. K., "Optical Limiting in Semiconductors", *Appl. Phys. Lett.*, 15,

- [56] Ma Hai-Ming, "Self-transitions of picosecond light pulses in GaAs", in Chinese, Chinese Journal of Phys., 38, 153 (1989).
- [57] A.A. Bugaev, T.Yu. Dunaeva and V.A. Lukoshkin, "Influence of Nonlinear Refraction, Absorption by Free Carriers, and Multiple Reflection on the Determination of the Two-Photon Absorption Coefficient of GaAs", Sov. Phys. Solid State 31, 2031-2034 (1990).
- [58] J.S. Aitchison, M.K. Oliver, E. Kapon, E. Colas and P.W.E. Smith, "Role of Two-Photon Absorption in Ultrafast Semiconductor Optical Switching Devices", Appl. Phys. Lett. 56, 1305-1307 (1990).
- [59] P. Liu, W.L. Smith, H. Lotem, J.H. Bechtel, and N. Bloembergen, "Absolute Two-Photon Absorption Coefficients at 355 and 266 nm", Phys. Rev. B 17, 4620 (1978).
- [60] J. Dempsey, J. Smith, G.D. Holah, and A. Miller, "Nonlinear Absorption and Pulse-Shaping in InSb", Opt. Commun. 26, 265 (1978); A.M. Johnson, C.R. Pidgeon, and J. Dempsey, "Frequency Dependence of Two-Photon Absorption in InSb and HgCdTe", Phys. Rev. B 22, 825 (1980); C.R. Pidgeon, B.S. Wherrett, A.M. Johnson, J. Dempsey, and A. Miller, "Two-Photon Absorption in Zinc-Blende Semiconductors", Phys. Rev. Lett. 42, 785 (1979).
- [61] I.N. Ross, W.T. Toner, C.J. Hooker, J.R.M. Barr, and I. Coffey, "Nonlinear Properties of Silica and Air for Picosecond Ultraviolet Pulses", J. Modern Opt. 37, 555-573 (1990).
- [62] Eric W. Van Stryland, M.A. Woodall, H. Vanherzeele, and M.J. Soileau, "Energy Band-Gap Dependence of Two-Photon Absorption", Opt. Lett. 10, 490 (1985).
- [63] M.J. LaGasse, K.K. Anderson, C.A. Wang, H.A. Haus, and J.G. Fujimoto, "Femtosecond Measurements of the Nonresonant Nonlinear Index of in AlGaAs", Appl. Phys. Lett. 56, 417-419 (1990).
- [64] E.W. Van Stryland, Y.Y. Wu, D.J. Hagan, M.J. Soileau, and Kamjou Mansour, "Optical Limiting with Semiconductors", J. Opt. Soc. Am. B 5, 1980-1989 (1988).



Ali A. Said was born in Lebanon in 1959. He received the B.S. degree in physics and mathematics from Southeastern Oklahoma State University in 1982, and the M.S. and PhD. degrees from the University of North Texas in 1984 and 1991, respectively. His research for the PhD. degree was conducted at the Center for Research and Education in Optics and Lasers (CREOL) at the University of Central Florida.

He is currently a research scientist at CREOL and his current research activities include measurement of optical nonlinearities in semiconductors, dielectrics, and organic liquids and thin films, and the application of nonlinear refraction and absorption to optical limiting.

Dr. Said is a member of the Optical Society of America, and the Society of Photo-optical Instrumentation Engineers.



David J. Hagan

Dr. Hagan was born in Edinburgh, Scotland in 1959. He received the degrees of BSc and PhD in physics from Heriot-Watt University, Edinburgh, in 1985, where he worked on infrared nonlinear optical phase conjugation and optical bistability. He joined the faculty at CREOL in 1987 after two years at North Texas State University where he performed research on self-protecting optical limiters. Dr. Hagan's primary research interest is in characterization of nonlinear optical materials, including bulk inorganics, organic solutions, and microstructures. He is a member of IEEE and the Optical Society of America.

HIGH DYNAMIC RANGE PASSIVE OPTICAL LIMITERS (Invited Paper)

D. J. HAGAN*, T. XIA, A. A. SAID, T. H. WEI[†] and E. W. VAN STRYLAND*
*Center for Research in Electro-Optics and Lasers, University of Central Florida,
Orlando, FL 32816, USA*

Received 12 April 1993

We present results of optical limiting experiments designed to study optical geometries for increasing the dynamic range over which limiters function without incurring optical damage. Specifically, we investigate a tandem geometry with two passive nonlinear elements, one placed in the focal plane of a lens and the second placed "upstream" of the focal position to protect the material at focus from damage. To provide a proof-of-principle demonstration of this geometry, simple limiters consisting of combinations of reverse saturable absorber dyes and a carbon black suspension in thin cells were tested. Our results show that a substantial increase in device performance can be achieved by use of a tandem limiter geometry. Simple modelling predicts that the dynamic range of a separate-element tandem limiter is given by the product of the dynamic ranges of the individual component limiting elements, in agreement with our experimental results.

1. Introduction

An optical limiter is a device that can be integrated into an optical imaging system in order to protect sensitive components, such as detectors in the focal plane, from temporary or irreversible optical damage. For pulsed sources it is usually fluence (energy/unit area), rather than total integrated energy, that determines whether or not a device damages. Therefore, the purpose of the limiter is to keep the fluence below some specified value at all points in the focal plane. Similarly, for cw sources, it is usually the irradiance, rather than the total power that is the important parameter. The device must also exhibit high linear transmittance under normal imaging conditions. An ideal optical limiter response is shown in Fig. 1.

Passive optical limiting has been demonstrated by using optical nonlinearities that result in self-action of optical beams. These include self-focusing¹ or defocusing,² nonlinear absorption (NLA)³ and nonlinear scattering.⁴ In the case of a purely absorptive nonlinearity, it is the total *energy* that is limited, while a purely refractive nonlinearity spreads the beam in the focal plane, so that the *fluence* is limited. In many cases, both effects occur in the nonlinear material.

*Also with the departments of Physics and Electrical and Computer Engineering.

[†]Present address: Liquid Crystal Institute, Kent State University, Kent OH 44242-0001, USA

successful for 30 psec laser pulses, producing a DR of $\sim 10^4$ in a monolithic ZnSe limiter at an input wavelength of 532 nm. The performance of this device is shown in Fig. 2, which plots the normalized far-field fluence transmission as a function of input energy. This was measured by placing a small aperture on axis in front of the transmission detector. The overall low energy transmittance of this device was 12 %, with parasitic linear absorption and scattering being the primary loss mechanisms in this 30 mm long device. The transmission is reduced by more than three orders of magnitude over the range of input energies for which the device was tested. With these picosecond pulses, the device was never observed to damage. However, with nanosecond pulses, the DR is severely reduced by bulk optical damage, possibly caused by thermal nonlinearities.⁶ Such self-protecting geometries can be used for other materials, such as carbon-black liquid suspensions (CBS) or reverse-saturable absorber (RSA) dyes.

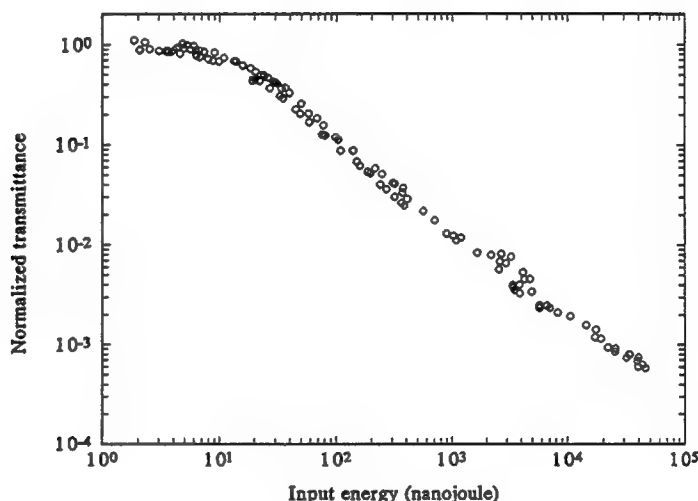


Fig. 2. Normalized fluence transmission of a monolithic ZnSe limiter for 30 psec, 532 nm input pulses. The fluence is measured by placing an aperture on axis in front of the transmission detector. The transmittance is normalized to the low energy aperture transmittance.

A similar, but more versatile implementation of self-protecting devices is to place two or more limiting elements in tandem in the optical path. Such a geometry is schematically shown in Fig. 3, where element 1, the 'primary limiter', is placed at or near focus, while element 2, the 'protector' is placed in front of the primary at a region of lower irradiance. The basic concept is that the primary limiter provides a low limiting threshold while the protector prevents optical damage to the primary limiter. The damage energy threshold of the system is thus determined by the damage threshold of the protector, which occurs at much higher input energies than damage to the unprotected primary. This is because it is positioned far from

transmission of this device are self-focusing, along with absorption and scattering associated with the resulting laser-induced breakdown plasma. The response time has been shown to be $\simeq 2$ psec in the visible.¹⁰ Even larger nonlinearities were found at $10\text{ }\mu\text{m}$ when CO_2 laser pulses were used,¹¹ which demonstrated the potential for extremely broad band operation. However, the critical power, ($\simeq 8\text{ kW}$ in the visible), is often too high for many applications. Large refractive nonlinearities (several orders of magnitude higher than that of CS_2) have been found in liquid crystals;¹² but they are obtained at the expense of speed (response times are usually nanoseconds or longer). Atomic vapors have also been used to build optical limiters. Bjorkholm *et al.*¹³ built a device that uses self-focusing in Na vapor that is due to near-resonant excitation at a wavelength of 590 nm. Some of the largest nonlinearities exhibited to date are in semiconductors.¹⁴ Unfortunately, from the standpoint of optical limiting, these extremely large nonlinearities are associated with near band-gap resonance and are maximized in a region of relatively high linear absorption. In addition, solids undergo irreversible optical damage. Even so, effective limiting has been demonstrated in semiconductors using other mechanisms. In 1969 Geusic *et al.*¹⁵ reported limiting behavior in Si that was attributed to stepwise nonlinear absorption with $1.06\text{ }\mu\text{m}$ radiation. Later, Boggess *et al.*¹⁶ demonstrated fluence limiting in Si that was due to a combination of nonlinear absorption with a refractive contribution induced by the photoexcitation of free carriers. Power-limiting experiments were conducted by Ralston and Chang¹⁷ in a series of semiconductors such as CdS, GaAs, and CdSe. This was the first report to our knowledge of the use of two-photon absorption (2PA) for optical limiting. Boggess *et al.*¹⁸ were the first to use the combined effects of 2PA and carrier defocusing to obtain optical limiting. The geometry used was to focus picosecond $1.06\text{ }\mu\text{m}$ pulses onto the surface of a thin sample of GaAs, refocus the beam, and monitor the transmission through an aperture. Since the damage-prone surfaces are subjected to the maximum fluence of the input pulses, the range over which these devices function without incurring damage is low. More recently, two-step absorption processes in GaP have been used to produce low threshold limiters.¹⁹ In 1989,^{5,6} we demonstrated that if samples of optical thickness much greater than the Rayleigh range are used, the large nonlinearities of the semiconductor can actually be used to self-protect the limiting device from damage.

2.2. Two-Photon Absorbing Semiconductors

For photon energies in the range $E_g/2 \leq \hbar\omega < E_g$, where E_g is the band-gap energy, semiconductors exhibit large two-photon absorption (2PA) while maintaining high linear transmittance.³ Additionally, carriers excited by 2PA impose a negative contribution to the refractive index, resulting in self defocusing. This is in addition to the bound electronic nonlinear refraction, given by $n = n_0 + n_2 I$, which is highly dispersive in the region of 2PA. The quantity n_2 can change sign depending on the wavelength, so that this effect can result either in self focusing or defocusing.

Thermal diffusion in ZnSe has a much longer relaxation time than free-carrier lifetimes (≈ 1 nsec).²⁴ Hence, for nanosecond or longer pulses, carrier nonlinearities may become dominated by thermal nonlinearities. This is opposite to the case of picosecond pulses. This problem may be overcome by the use of materials with negative thermo-optic coefficients.

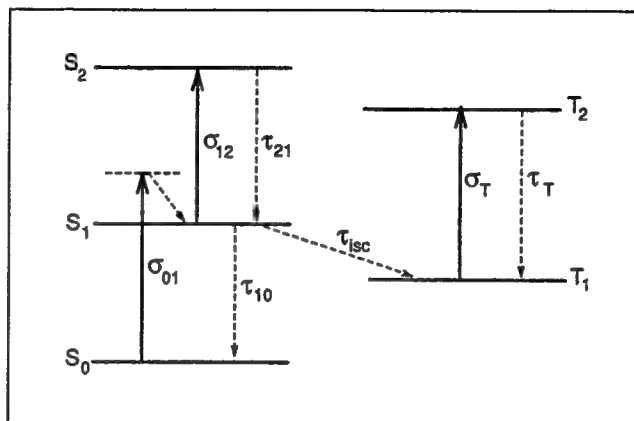


Fig. 4. Level structure for nonlinear behavior of phthalocyanines. Solid arrows indicate absorption processes, dashed arrows indicate decay paths.

2.3. Reverse-Saturable Absorber Dyes

Studies of the nonlinear properties of a number of phthalocyanine and naphthalocyanine derivatives in solution,²⁵ have shown these materials to be suitable for limiting applications. The dominant nonlinearities are excited-state absorption and refraction, (ESA and ESR). The generic level structure for these molecules is shown in Fig. 4. This five-level structure shows the possibility of both excited singlet and triplet absorption. Typically, absorption corresponding to excitation from the ground state to the S_1 band is peaked at wavelengths around 700 nm. The initial absorption at the second harmonic of the Nd:YAG laser, $\lambda = 532$ nm, is low because the excitation is high into the S_1 vibrational manifold. Fast relaxation to the bottom of this band allows ESA for ($S_1 \rightarrow S_2$) to become resonant with the 532 nm input light. The degree of limiting therefore depends upon the ratio of the excited to ground state cross sections at 532 nm. For longer pulses, intersystem crossing leads to triplet-triplet ESA. Hence, these molecules have the attractive property that they are able to respond on both fast and slow timescales. Typical values of the intersystem crossing time τ_{isc} are in the range of a few nanoseconds, so that for our pulsewidths, we can ignore intersystem crossing. Measurements of the nonlinear refraction in these materials have shown that this is dominated by refractive changes due to the occupation of excited states.²⁵ However, nonlinear absorption is usually

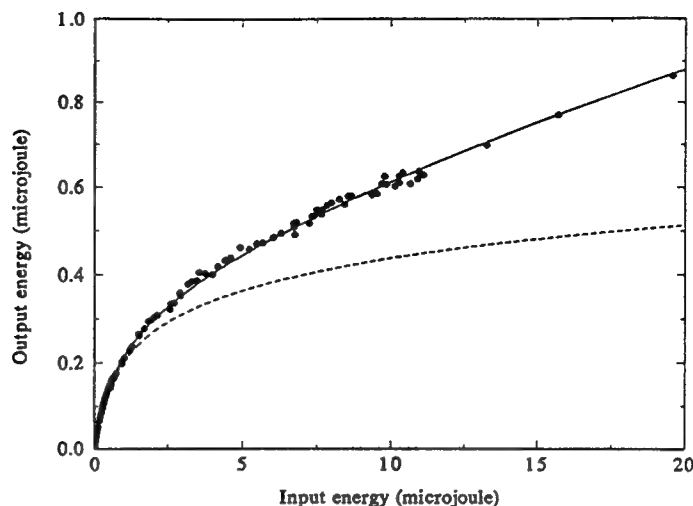


Fig. 5. Limiting response of SiNc solution in 1-mm thick quartz cell. Solid line is fit to data with $\sigma_{12} = 1.65 \times 10^{-17} \text{ cm}^2$, $F_s = 4.5 \text{ J/cm}^2$. The dashed line is for the same σ_{12} , in the absence of saturation.

than N , reducing the maximum obtainable optical density. Additionally, damage may occur before this high fluence limit is reached.

In Fig. 5, we show the input-output energy response for a solution of silicon naphthalocyanine (SiNc) in toluene held in a 1 mm-thick quartz cell, with 4.6 nsec (FWHM) pulses at 532 nm from a single longitudinal mode Nd:YAG laser at a 2 Hz repetition rate. The beam was focused to $8 \mu\text{m}$ ($\text{HW1/e}^2\text{M}$) at the center of the sample. The linear transmittance of the cell was measured to be 59%. Damage to the front surface of the cell occurred for incident energies above $20 \mu\text{J}$. The solid line is a fit to the data using Eq. (6), but including a phenomenological saturation of the $S_0 \rightarrow S_1$ transition, by setting $\alpha = \alpha_0/(1 + F/F_s)$. The best fit was obtained for $\sigma_{12} = 1.65 \times 10^{-17} \text{ cm}^2$ and $F_s = 4.5 \text{ J/cm}^2$. The value for σ_{12} is smaller than the value previously measured using psec pulses of $\sigma_{12} = 3.9 \times 10^{-17}$.²⁵ This is because in the present experiment the assumption that the pulsewidth (4.6 ns) is much less than the excited state decay time (3.1 ns) is not valid, and also because the sample thickness is larger than the confocal beam parameter so that the effective fluence is smaller than F_0 . Hence, our value of σ_{12} is an effective cross section for this experiment only. Nevertheless, the fit is good for all fluences up to damage. The dashed curve shows the predicted output using the same σ_{12} , but without saturation. From this, we see that the overall effect of saturation is to increase the transmitted energy by about a factor of two over the unsaturated case. In Fig. 6, we show the same data and fits plotted as transmittance versus input energy. From this data we conclude that for these pulsewidths it is not necessary to perform a lengthy numerical solution of the rate equations to obtain a satisfactory model for the limiting behavior of these dyes.

quartz cuvette filled with a solution of SiNc. A schematic of this tandem limiter is shown in Fig. 7.

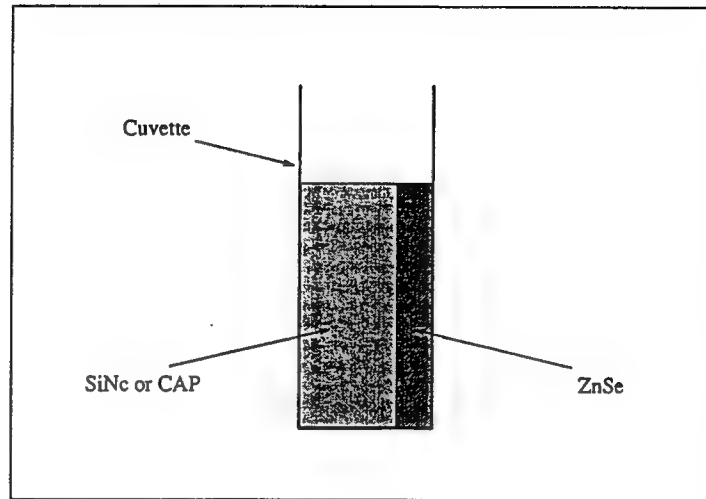


Fig. 7. Adjacent element SiNc/ZnSe limiter.

The limiting in SiNc is dominated by RSA as described in Sec. 2. With the ZnSe sample situated at the rear of the cell, it behaves as the primary limiter, while the solution acts as the protecting element. To optimize the focusing geometry, a *Z*-scan²⁷ was performed at low irradiance to find the position with respect to focus that yields a minimum transmittance. We find that the damage threshold is determined by the front surface of the quartz cell. The thickness of the device protects the first quartz surface from damage since it is many times z_0 away from the beam waist, where $z_0 = \pi w_0^2 / \lambda$ is the confocal beam parameter and w_0 the beam radius at the waist ($\text{HW1/e}^2\text{M}$). The overall effect is a significant increase in the dynamic range of the device.

Experiments show less than a factor of two increase of the limiting threshold between ZnSe and the hybrid limiter. The important observation was that no damage was observed on ZnSe in the hybrid device up to the maximum tested input energy of $80 \mu\text{J}$, while the damage threshold of unprotected ZnSe at 532 nm was measured to be $2 \mu\text{J}$. This shows an increase in the dynamic range of more than a factor of 25. The device has an overall linear transmittance of 40 percent, but does not have antireflection coatings. We also performed comparison experiments with a limiter consisting of chloro-aluminum phthalocyanine (CAP) and ZnSe as the individual elements. The results for both devices are presented in Table 1, along with measured limiting thresholds for CAP and SiNc without the ZnSe. From this table it is clear that the hybrid limiter gives a larger dynamic range than limiters made of the individual elements. In each case, the effect of placing the ZnSe in the cell is to reduce the limiting threshold below that of the dye alone, while maintaining

4.2. FOM for a Tandem Limiter

Now we consider a tandem limiter as shown in Fig. 3, where for simplicity we assume that both elements only exhibit nonlinear absorption. If we further assume they are identical, the limiting fluence, F_L , is the same for both elements, as is the damage fluence, F_D , although the corresponding energies may be vastly different. We position the primary limiter at focus, and the protecting element some distance before the focus such that the peak fluence incident on the primary limiter is kept below F_D . If the effective beam area at focus is given by $\pi w_0^2/2$ and at the protector is $\pi w_1^2/2$, then our requirement is $F_{\max} \cdot w_1^2 \leq F_D \cdot w_0^2$ or simply $E_{\max}(\text{protector}) \leq E_D(\text{primary})$. Therefore, the maximum energy transmitted by the protector must be less than the damage energy of the primary. Assuming that the protector does not significantly change the maximum energy transmitted by the primary limiter, and the damage energy of the entire device is determined by damage to the protector, then the FOM for the tandem limiter is:

$$FOM(\text{tandem}) = \frac{E_D(\text{protector})}{E_{\max}(\text{primary})} \cdot T_L^2. \quad (9)$$

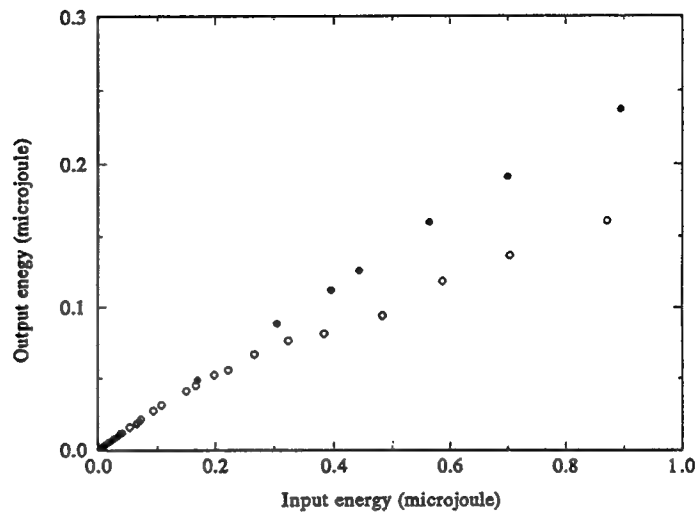
Note the factor of T_L^2 due to the two elements, since each has a linear transmittance of T_L . Now applying Eq. (7) to the protector, $E_D(\text{protector}) = E_{\max}(\text{protector}) \cdot DR/T_L$, so that by setting $E_{\max}(\text{protector}) \simeq E_D(\text{primary})$, we obtain $E_D(\text{protector}) = E_D(\text{primary}) \cdot DR/T_L$. We then obtain from Eq. (9),

$$FOM(\text{tandem}) = \frac{DR}{T_L} \frac{E_D(\text{primary})}{E_{\max}(\text{primary})} \cdot T_L^2 = (DR)^2. \quad (10)$$

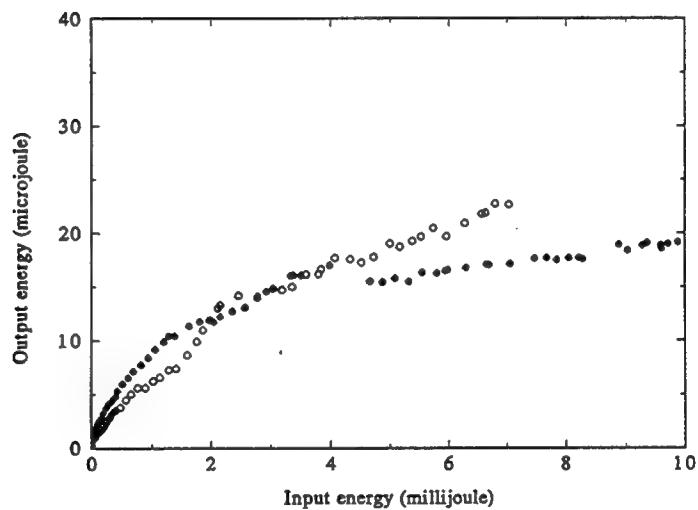
For two identical elements, each of dynamic range DR , the effect of cascading produces a new FOM of $(DR)^2$. Similarly, use of 3 elements can produce a FOM of $(DR)^3$, etc. One problem is that the linear transmission for n elements in tandem is $(T_L)^n$, which may easily become unacceptably small. Extension of the above arguments to a tandem limiter with two nonidentical nonlinear absorbing elements with dynamic ranges $DR(1)$ and $DR(2)$, we find that the overall FOM is just given by the product $DR(1) \cdot DR(2)$. For N nonidentical elements, the FOM is simply the product of the individual DRs, i.e. $FOM = DR(1) \cdot DR(2) \cdot DR(3) \cdots DR(N)$.

4.3. Experimental Results on Tandem Limiters

We performed experiments on two separate element tandem limiter systems, one a combination of CBS and SiNc elements, and the other consisting of two SiNc elements. In both cases, a focusing geometry similar to that shown in Fig. 3. was used. The focusing lens had a focal length of 10 cm and the spot size at the beam waist was measured to be $\simeq 8 \mu\text{m}$ ($\text{HW1/e}^2\text{M}$), which is approximately two times the diffraction limited spot size. The total transmitted energy was monitored on a large-area Si photodiode via an $f/10$ optical system. The laser source was a



(a)



(b)

Fig. 8. Limiting response of SiNc/CBS tandem limiters. Curve (a) shows low energy behavior, (b) shows high energy response. Solid circles: CBS as primary limiter, SiNc as protector. Open circles: SiNc as primary, CBS as protector.

the overall linear transmittance is 21 %, smaller than that of the SiNc/CBS limiter. In Fig. 11, we show the same data in the form of transmittance as a function of input energy. From this curve, we can easily estimate the dynamic range by use of Eq. (8b).

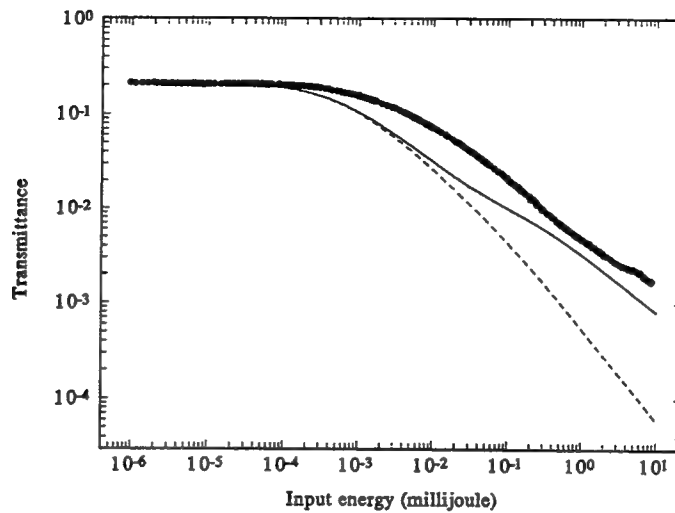


Fig. 11. Transmittance vs. input energy for SiNc/SiNc tandem limiter.

limiter elements were those obtained for the single element. As the beam was not diffraction limited, there was insufficient information to model the propagation accurately. To calculate the input fluence distribution at each element, we simply assume that the beam remains Gaussian, with the same spot sizes as measured in the absence of a nonlinearity. Nevertheless, this simple model can predict the limiting response to within a factor of two over an input energy range of seven orders of magnitude, as shown in the logarithmic plot of Fig. 11. The dashed curve shows the predicted output using the same excited state cross-section, but in the absence of saturation. Comparison of the solid and dashed curves shows that saturation has a major effect on the performance of the SiNc/SiNc tandem limiter.

5. Conclusions

We have designed an optical geometry to extend the dynamic range of single element optical limiters without severely degrading the limiting threshold. The purpose of this study was to provide a proof-of-principle demonstration of the tandem limiter geometry, rather than to produce a fully optimized device. Although these devices have not been optimized, the preliminary results show considerable potential for improving limiter performance. The reason for using thin cells for these initial experiments was to allow simple modelling and optimization. Future studies will build upon these results by employing other geometries. One method for increasing the dynamic range is to make the thickness of the primary limiter much greater than the Rayleigh range. However, this requires a more sophisticated model of the nonlinear propagation equations. We recently succeeded in developing a nonlinear beam propagation code for this purpose and are in the process of performing such

12. D. V. G. L. N. Rao and S. Jayaraman, *Appl. Phys. Lett.* **23**, 539 (1973).
13. J. E. Bjorkholm, P. W. Smith, W. J. Tomlinson and A. E. Kaplan, *Opt. Lett.* **6**, 345 (1981).
14. D. A. B. Miller, C. T. Seaton, M. E. Prise and S. D. Smith, *Phys. Rev. Lett.* **47**, 197 (1981).
15. J. E. Geusic, S. Singh, D. W. Tipping and T. C. Rich, *Phys. Rev. Lett.* **19**, 1126 (1969).
16. T. F. Boggess, S. C. Moss, I. W. Boyd and A. L. Smirl, *Opt. Lett.* **9**, 291 (1984).
17. J. M. Ralston and K. R. Chang, *Appl. Phys. Lett.* **15**, 164 (1969).
18. T. F. Boggess, A. L. Smirl, S. C. Moss, I. W. Boyd and E. W. Van Stryland, *IEEE J. Quantum Electron.* **QE-21**, 488 (1985).
19. S. J. Rychnovsky, G. R. Allen, C. H. Venzke, A. L. Smirl and T. F. Boggess, *Proc. SPIE* **1692**, 191 (1992).
20. M. Sheik-Bahae, D. C. Hutchings, D. J. Hagan and E. W. Van Stryland, *IEEE J. Quantum Electron.* **QE-27**, 1296 (1991).
21. A. A. Said, M. Sheik-Bahae, D. J. Hagan, T. H. Wei, J. Wang, J. Young and E. W. Van Stryland, *J. Opt. Soc. Am.* **B9**, 405 (1992).
22. J. H. Bechtel and W. L. Smith, *Phys. Rev.* **B13**, 3515 (1976).
23. J. Wang, *Ph.D Dissertation*, Univ. of Central Florida (1993).
24. E. J. Canto-Said, D. J. Hagan, J. Young and E. W. Van Stryland, *IEEE J. Quantum Electron.* **QE-27**, 2274 (1991).
25. T. H. Wei, D. J. Hagan, M. J. Sence, E. W. Van Stryland, J. W. Perry and D. R. Coulter, *Appl. Phys.* **B54**, 46 (1992).
26. A. A. Said, H. Wei, J. R. DeSalvo, Z. Wang, M. Sheik-Bahae, D. J. Hagan and E. W. Van Stryland, *Proc. SPIE* **1692**, 37 (1992).
27. M. Sheik-Bahae, A. A. Said, T. H. Wei, D. J. Hagan and E. W. Van Stryland, *IEEE J. Quantum Electron.* **QE-26**, 760 (1990).

Characterization of Nonlinear Absorption and Refraction in Advanced Materials

E.W. Van Stryland, M. Sheik-bahae, A.A. Said, and D.J. Hagan

CREOL

Center for Research in Electro Optics and Lasers

University of Central Florida, Orlando, FL 32826

We discuss the characterization of nonlinear optical processes in materials associated with loss and index changes using the Z-scan. The primary problem addressed is, given a new material, how do you determine the dominant nonlinearities present and their physical mechanisms. In particular, in extensive studies of a wide variety of materials we have found that there is seldom a single nonlinear process occurring. Often several processes occur simultaneously sometimes in unison, sometimes competing. Distinguishing and separating these processes is important for understanding and modeling the interaction. There are a variety of methods and techniques for determining the nonlinear optical response, each with its own weaknesses and advantages. In general it is advisable to use as many complementary techniques as possible and vary as many experimental parameters as possible in order to unambiguously determine the active nonlinearities. Here we show as examples the two cases of semiconductors and reverse saturable absorbing dyes. We concentrate on the use of the Z-scan in determining the responses, but utilize knowledge from other experiments to help in the interpretation.

I. Introduction

Numerous techniques are known for measurements of nonlinear refraction (NLR) and nonlinear absorption (NLA) in materials. Nonlinear interferometry [1], [2], degenerate four-wave mixing (DFWM) [3], nearly-degenerate three-wave mixing [4], ellipse rotation [5], beam distortion, [6,7] beam deflection [8], and third-harmonic generation [9] are among the techniques (direct or indirect) frequently reported for determining NLR. We have recently developed a single beam technique for measuring the sign and magnitude of NLR indices called Z-scan [10,11], which offers simplicity as well as high sensitivity. Techniques for measuring NLA include transmittance [12], calorimetry [13], photoacoustic [14], pulse-probe [15], and now Z-scan [11].

Given all these methods it is rare that any single experiment will determine the complete physics behind the nonlinear response of a given material. The most important point to be made in this paper is that a single measurement of the nonlinear response of a material, at a single wavelength, for a single pulsewidth gives very little information on the material, and in general should not be used to judge whether a material has a large nonlinearity or to compare one material to another. We will elaborate on this point by using two examples, a semiconductor and a reverse saturable-absorbing dye. Here we demonstrate the importance of the pulsewidth dependence of the nonlinear response. Similar comments can be given for, for example, the wavelength dependence. We first describe the Z-scan experiment and then present results for zinc selenide (ZnSe) and the organic dye chloro-aluminum-phthalocyanine (CAP) in solution with methanol. We then discuss the necessity for using different pulsewidths.

II. Z-SCAN

The Z-scan exploits the spatial narrowing and broadening of Gaussian beams in the far field which are due to self-focusing or self-defocusing caused by the nonlinear interaction of the beam with the material. A schematic of the experimental setup is given in Fig. 1. A Gaussian beam is focused onto the sample and then collected through an aperture in the far field by the transmission detector (D_2). Keeping the input energy constant, the sample is translated along the beam propagation direction through the focal plane, and the transmittance (D_2/D_1) is measured as a function of this sample position Z with respect to the focal plane. In the case of a material with a negative nonlinear refractive index, the self-defocusing will cause beam narrowing in the far field when the sample is before focus (negative Z) and beam broadening when the sample

is after focus (positive Z). An increase in transmittance followed by a decrease in transmittance (peak-valley) for increasing Z denotes a negative nonlinear refraction, while a valley-peak configuration implies a positive nonlinearity. In Ref. [11], we give a detailed description and analysis of the Z-scan technique. If the sample length is less than the confocal beam parameter and if the phase changes in the field caused by the nonlinear interaction are not transformed into amplitude changes within the sample then the sample is considered thin (external self-action).[16,17] For such "thin" samples it is found that the change in the index of refraction (Δn) is given from the linear relation between the on-axis phase distortion at focus ($\Delta\Phi_0$) and the difference between the maximum and minimum values of the normalized aperture transmittance (ΔT_{p-v}). This relation for an aperture size that gives 40% linear transmittance is given by:

$$\Delta\Phi_0 = 2.8\Delta T_{p-v}. \quad (1)$$

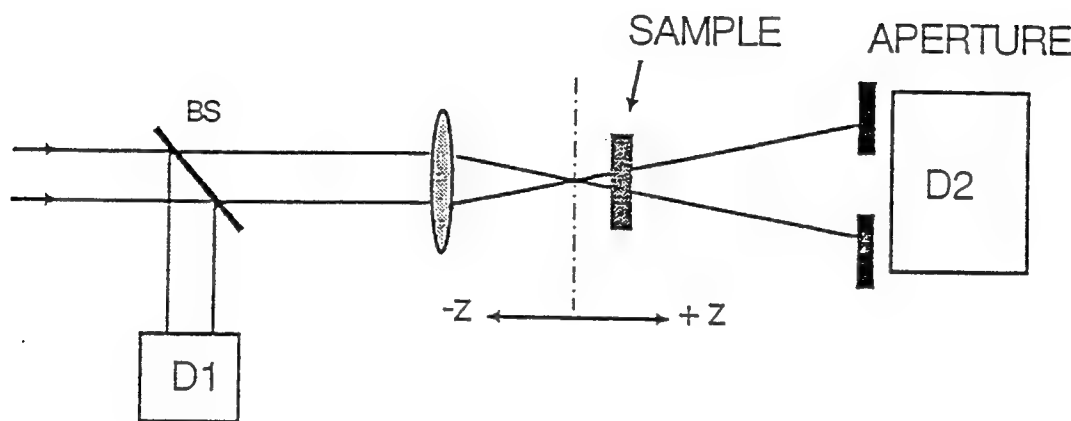


Fig. 1. The Z-scan experimental setup. D_2/D_1 is measured as a function of the sample position z .

Examining Fig. 1 for a purely refractive case, if the aperture is removed i.e. if all the transmitted light from the sample is collected by D_2 , there will be no change in the transmittance at different sample positions. However, if the sample exhibits nonlinear absorption in addition to nonlinear refraction, the measurement will detect the change in the transmittance which is maximized at $Z=0$. This type of measurement, to which we refer as an open aperture Z-scan, yields the nonlinear absorption parameters of the material. When the aperture is in place, the measurement (closed aperture Z-scan) is sensitive to both nonlinear absorption and nonlinear refraction. Dividing the closed aperture data by the open aperture data yields a Z-scan signal which is due to nonlinear refraction which can be determined using Eq. 1 as long as the nonlinear absorption is not too strong. Figure 2 shows an example of this procedure for ZnSe where picosecond 532 nm pulses were used. The limitations of this simple approach and when a more exact analysis is needed are described in detail in Ref. [11].

Considering a thin sample and using the slowly varying envelope approximation, we can separate the wave equation into an equation for the phase, $d\Phi/dz$, and an equation for the irradiance, dI/dz , where z denotes the depth within the sample (as opposed to the sample position Z). Here is where we need to model the nonlinear response of the material. In practice the experiment and analysis go hand in hand and are refined as more data is obtained.

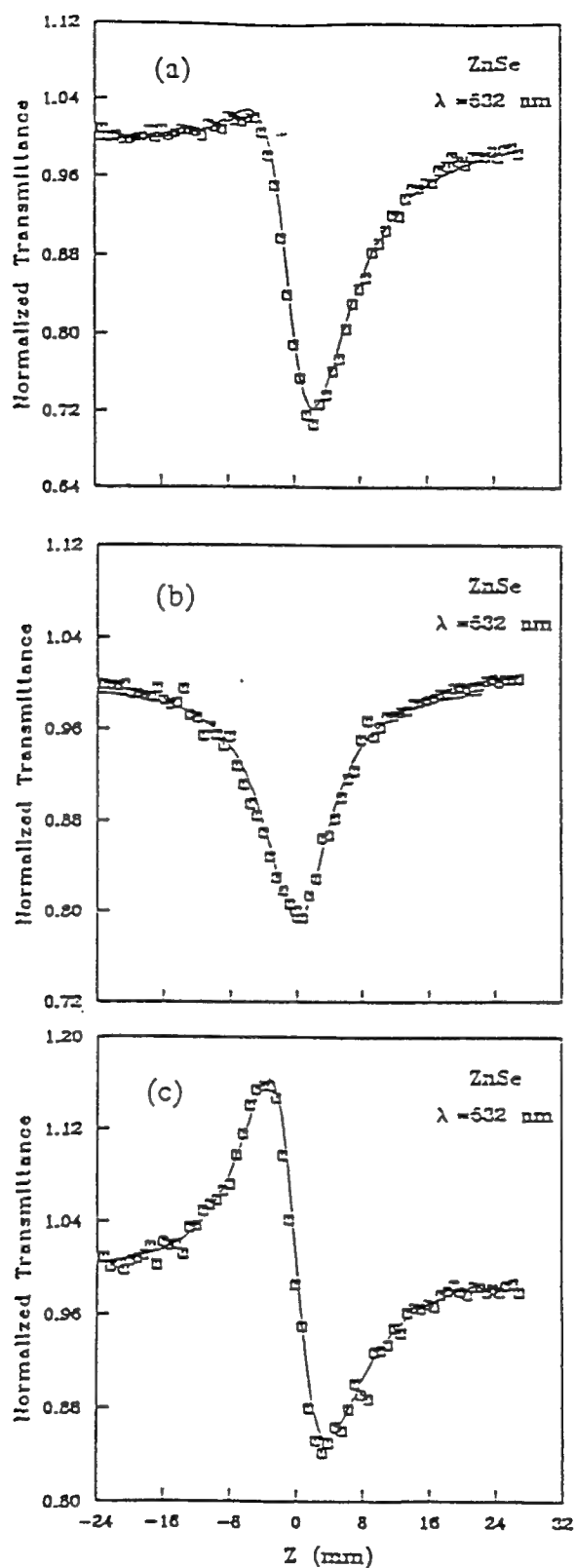


Fig. 2. Normalized Z-scan transmittance of ZnSe measured using picosecond pulses at $\lambda=532$ nm with $I_0=0.57$ GW/cm². (a) Open aperture data and fit (solid line) using 5.8 cm/GW (b) 40% aperture data fitted with $\beta=5.8$ cm/GW, $n_2=-6.2 \times 10^{-5}$ cm²/GW (-4.0×10^{-11} esu) and $\sigma_r \lambda / 2\pi = -8.0 \times 10^{-22}$ cm³. (c) The result of the division of the Z-scans of (a) and (b).

Often the best place to start on a new material of unknown nonlinear response is to look for NLA since measurements of NLR will depend on the strength of the NLA. The open aperture Z-scan, or measuring the change in transmittance as a function of irradiance, I , are relatively straightforward experiments as long as care is taken to collect all the light transmitted by the sample and the detectors used have uniform response (i.e. if the light is spread over a larger or smaller surface area the detector response is unchanged). We have seen problems with several detectors especially in the UV. After the NLA is determined the nonlinear refraction can be determined.

III. Modeling of Nonlinear Loss

We discuss two types of nonlinear absorption, two-photon absorption (2PA) and excited state absorption (ESA). For ESA the incident photon energy is resonant or nearly resonant with an intermediate state such that linear absorption is present and real transitions occur. For 2PA there is no intermediate level to give linear absorption such that the intermediate transition is termed virtual. Any residual linear absorption is not involved in the nonlinear response (eg. are caused by impurities). Both nonlinearities appear as third order responses. However, in one case (2PA) the nonlinearity is proportional to $\text{Im}\{\chi^{(3)}\}$, while for ESA the nonlinearity is due to the cascaded nonlinearity $\text{Im}\{\chi^{(1)}\}:\text{Im}\{\chi^{(1)}\}$ (i.e. two sequential linear absorption processes). Here $\chi^{(j)}$ refers to the j th order electric susceptibility. In the $\chi^{(1)}:\chi^{(1)}$ process the first $\chi^{(1)}$ is associated with the ground state absorption and the second with the ESA.

Equations describing these third order responses for nonlinear absorption are;

for 2PA, including residual linear absorption of coefficient α

$$\frac{dI}{dz} = -(\alpha + \beta I)I, \quad (2)$$

and for ESA

$$\frac{dI}{dz} = -(\alpha + \sigma N)I, \quad (3)$$

where β is the 2PA coefficient, σ is the ESA cross section, and N denotes the density of excited states produced by linear absorption so that

$$\frac{dN}{dt} = \frac{\alpha I}{\hbar\omega}. \quad (4)$$

Here $\hbar\omega$ is the incident photon energy. The irradiance is a function of the transverse spatial coordinate, r , and time t as well as the sample position Z (note the distinction between Z and the depth in the sample z). By integrating Eq. 4 up to some time t' in the pulse, plugging this integral into Eq. 3 and then integrating Eq. 3 over all times t' (i.e. $-\infty$ to ∞) gives

$$\frac{dF}{dz} = -\left[\alpha + \frac{\alpha\sigma}{2\hbar\omega}F\right]F, \quad (5)$$

where $F=F(r)$ is the fluence (i.e. energy per unit area). Notice that this equation is exactly analogous to Eq. 2 describing 2PA loss with the fluence replacing the irradiance and $\alpha\sigma/2\hbar\omega$ replacing β . Therefore, since in most experiments the pulse energy is detected, 2PA and ESA will give nearly identical results for loss as a function of input energy or for a pulsed Z-scan where the transmitted energy is detected. The only difference is in the temporal integral over the pulse for 2PA since for ESA this integral has already been performed. In other

words, in order to determine which of these nonlinearities is present, the temporal dependence must be measured in some way.

The solution to Eq. 5 for ESA at the exit surface of the sample is

$$F(L, r) = \frac{F(0, r)e^{-\alpha L}}{1 + p(r)} \quad (6)$$

where $p(r) = (\alpha\sigma/2\hbar\omega)F(0, r)L_{\text{eff}}$, and $L_{\text{eff}} = (1 - e^{-\alpha L})/\alpha$ with L the sample length. Integrating over an assumed Gaussian spatial distribution of on-axis fluence F_0 , gives the normalized change in transmittance ΔT of;

$$\Delta T = \frac{T}{T_{\text{lin}}} - 1 = \frac{\ln(1 + p_0)}{p_0} - 1 \approx -\frac{p_0}{2} = -\frac{\alpha\sigma F_0 L_{\text{eff}}}{4\hbar\omega}, \quad (7)$$

where T is the transmittance, and T_{lin} the linear transmittance. The last equality defines $p_0 = p(0)$ and the approximation is valid for small p_0 (i.e. for small ΔT). All energy, fluence and irradiance levels are quoted as incident in the sample (i.e. after surface reflections are taken into account). For a Z-scan, F_0 is a function of the position of the sample with respect to the beam waist, Z .

The calculation of ΔT for 2PA is complicated by the necessity to perform the time integral. The irradiance at the exit surface of the sample is obtained from Eq. 2 as,

$$I(L, r, t) = \frac{I(0, r, t)e^{-\alpha L}}{1 + q(r, t)} \quad (8)$$

where $q(r, t) = \beta I(0, r, t)L_{\text{eff}}$ (directly analogous to p in Eq. 6 with the substitutions previously mentioned). Integrating over space and time yields

$$\Delta T = \frac{1}{\sqrt{\pi q_0}} \int_{-\infty}^{\infty} \ln[1 + q_0 e^{-\tau^2}] d\tau - 1 \approx \frac{q_0}{2\sqrt{2}}, \quad (9)$$

where $q_0 = \beta I_0 L_{\text{eff}}$ (I_0 the peak-on-axis irradiance) is the analogue of p_0 in Eq. 7. The approximation is valid for small nonlinear absorption as in the approximation in Eq. 7. The extra factor of $1/\sqrt{2}$ comes directly from the temporal integral.

The question now becomes how to differentiate between these two very different nonlinearities. They both have nearly identical dependences on pulse energy.

The key to differentiating between these two processes is how they depend on time, and hence, the input pulsewidth. Pulses having the same energy but differing pulsewidths will have differing irradiances and therefore, for 2PA show a different ΔT . On the other hand, for ESA pulses having the same energy but differing pulsewidths will have the same fluence and therefore show the same ΔT . Thus, we can differentiate between these processes without having to completely temporally resolve the transmittance changes (of course temporally resolving the transmittance changes as in a pulse-probe experiment will also determine which mechanism dominates).

The next section experimentally demonstrates how the dominant loss mechanism is readily determined by observing the pulsewidth dependence of the nonlinear absorption.

IV. Experimental determination of dominant nonlinear loss mechanism

Figure 3 shows experimental results using two different pulsewidths for ZnSe and for CAP. In Fig. 3a the inverse transmittance of ZnSe is plotted as a function of the input irradiance. Since the horizontal axis is irradiance and not energy the fact that the different pulsewidths give the same change in transmittance shows that 2PA is dominant. A Z-scan is shown for CAP in Fig. 3b for two pulsewidths where the energy, and thus the fluence, was held fixed. In this case the overlap of these data sets indicates that ESA dominates. If instead we had plotted inverse transmittance for CAP as a function of input fluence (rather than the irradiance I as for ZnSe), Fig. 3b would look the same as Fig. 3a.

So far we have neglected the fact that excited carriers generated in the 2PA process in ZnSe could then linearly absorb (i.e. free carrier absorption). It has been shown [18, 19] that this process may be ignored for irradiances below a critical irradiance I_{cr} , where $I_{cr} \approx 2\sqrt{2}\hbar\omega/\sigma\tau$. Here τ is the laser pulsewidth.

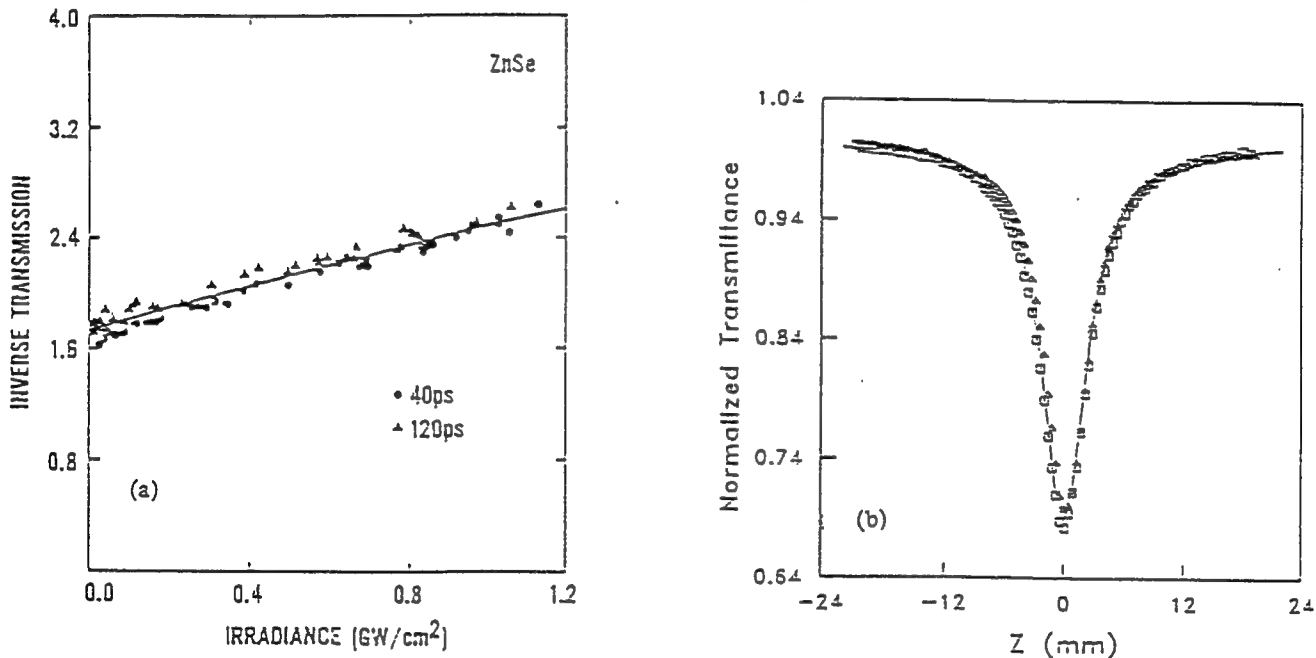


Fig. 3. a) Inverse transmittance for ZnSe using input pulsewidths of 40 psec and 120 psec (FWHM). b) Open aperture Z-scans for 29 ps (squares) and 61 ps (triangles) pulsewidths (FWHM) at an incident energy of $1.16 \mu\text{J}$ in CAP.

Therefore, Eq. 2 does not include free-carrier absorption. We verified that free-carrier absorption was negligible in our experiments by measuring the same 2PA coefficient at several irradiance levels. If nanosecond pulses had been used, however, free-carrier absorption would be large. Thus, great care must be taken in both experiment and analysis. While free-carrier absorption from carriers is negligible for picosecond pulses, the refraction arising from these free carriers is not.[20] This is discussed in the next section. Once the separation of the loss mechanisms is complete the nonlinear refraction can be measured and modeled.

III. Modeling of Nonlinear Refraction

The induced phase distortion, $\Delta\phi$, imposed on a beam by nonlinear refraction is related to the index change,

Δn , by

$$\frac{d\Delta\phi}{dz} = \frac{\Delta n 2\pi}{\lambda} \quad (10)$$

where λ is the wavelength in free space. The refractive index can change from a bound electronic n_2 or it can change from the redistribution of population among levels. In solids this redistribution generates free carriers and the refraction is called free-carrier refraction. In molecules we call this excited-state refraction (ESR)[21] We will henceforth refer to both as ESR.

Defining $\sigma_r 2\pi/\lambda$ as the change in index of refraction per unit of photoexcitation density, N , Δn in Eq. 1 is written as;

$$\Delta n = n_2 I + \frac{\lambda}{2\pi} \sigma_r N. \quad (11)$$

Here σ_r is the excited-state refractive cross section (often the $2\pi/\lambda$ is dropped in the definition of the index change). Here N for semiconductors is the free-carrier density while for dyes it is the excited-state number density. The nonlinear index, n_2 , due to the bound electrons is related to the nonlinear index $n_2(\text{esu})$ through $n_2(\text{esu}) = (cn_2/40\pi) n_2(\text{m}^2/\text{W})$, with c the speed of light in m/sec.

Chloro-Aluminum Phthalocyanine (CAP):

For the case where ESR from single photon absorption processes dominates the refraction in Eq. 10, Eq. 4 shows that Δn is determined by the temporal integral of the irradiance, that is,

$$\frac{d\Delta\phi(Z, t)}{dz} = \frac{\alpha \sigma_r}{\hbar \omega} \int_{-\infty}^t I(Z, \tau) d\tau. \quad (12)$$

Under the condition that the nonlinear refraction accumulates throughout the pulse without decay (i.e. the pulse is much shorter than any excited state decay times), it can be shown that the temporally averaged phase distortion is simply one half $\Delta\phi(t=\infty)$ or it equals $\Delta\phi(t=0)$ at the pulse maximum in time.[11] Therefore, looking at the on-axis phase distortion,

$$\frac{d\Delta\phi(Z, 0)}{dz} = \frac{\alpha \sigma_r}{2\hbar \omega} F_0. \quad (13)$$

Integrating Eq. 13 to find the temporally averaged on-axis phase distortion at focus $\Delta\Phi_0 = \Delta\phi(0, 0)$ we obtain

$$\begin{aligned} \Delta\Phi_0 &= \frac{\sigma_r}{\sigma} \ln[1+p_0] \\ &\simeq \frac{\sigma_r}{\sigma} p_0 \\ &\simeq \frac{\alpha}{2\hbar c} \sigma_r F_0 L_{\text{eff}} \end{aligned} \quad (14)$$

where c is the speed of light and the approximation is valid for small overall loss. This phase distortion can now be determined experimentally from ΔT_{p-v} in Eq. 1.

Zinc Selenide (ZnSe):

For semiconductors the refraction from 2PA generated carriers can become important, and Eq. 4 for dN/dt needs to be changed to include this generation rate. If N is generated primarily by 2PA,

$$\frac{dN}{dt} = \frac{\beta I^2}{2\hbar\omega} \quad (15)$$

We have neglected the loss of N due to recombination or diffusion because these processes occur on time scales longer than the picosecond pulses we use in the experiments. Again, if nanosecond pulses are used the equations and interpretation can be considerably more complex. From Eq. 15 the cumulative nonlinearity (second term in Eq. 11) is proportional to a temporal integral of I^2 for 2PA, resulting in an effective fifth order nonlinearity.[22] In the 2PA case this is a sequential $\text{Im}[\chi^{(3)}]$ (i.e. 2PA) followed by $\text{Re}[\chi^{(1)}]$ process (i.e. linear index change from the carriers or excited states). The existence of two different order nonlinearities having different decay times was observed in semiconductors by Canto-Said *et. al* [23] using picosecond DFWM. The third order effect showed a fast response and is due to a combination of 2PA and bound electronic refraction while the fifth order effect (carrier refraction) showed a slow decay. The DFWM technique cannot by itself identify the nature (refractive or absorptive) nor the sign of these nonlinearities; however, it does give information on the temporal response. Also, examining the two terms in Eq. 11, it is clear that the electronic Kerr effect ($n_2 I$) will be dominant at low irradiance levels (third order effect) while ESR ($\sigma_r N$) will dominate at high input levels (fifth order effect from 2PA generated carriers). This can allow separation of the effects even without temporally resolving the response as in picosecond DFWM experiments.[22]

The phase change experienced by the beam is given by integrating Eq. 10 using Eqs. 8, 11 and 15, to give,[12]

$$\Delta\phi(r, t, Z) = \frac{kn_2}{\beta} \ln[1 + q(r, t, Z)] + \frac{\sigma_r}{2\hbar\omega\beta} \int_{-\infty}^t dt' H(r'), \quad (16)$$

where

$$H(r, t, Z) = \alpha_0 \ln[1 + q(r, t, Z)] - \frac{q(r, t, Z)}{L_{\text{eff}}} \left[1 - \frac{e^{-\alpha_0 L}}{1 + q(r, t, Z)} \right].$$

The second term (including H) corresponds to carrier refraction, while the first term describes the bound electronic refraction. Temporal averaging of the fast nonlinearity has been shown in Ref. [10] to result in a Z-scan signal ΔT_{p-v} of $1/\sqrt{2}$ of the peak phase distortion while the cumulative nonlinearity is divided by a factor of 2. This results in an on-axis temporally averaged phase distortion as seen by a Z-scan of

$$\Delta\Phi_0 = \frac{kn_2}{\sqrt{2}\beta} \ln[1 + q_0] + \frac{\sigma_r}{4\hbar\omega\beta} \int_{-\infty}^{\infty} dt' H(0, t', 0). \quad (17)$$

Evaluation of this integral allows Eq. 1 to be used. Alternatively, the field at the exit surface of the sample is completely determined by Eqs. 8 and 16 for semiconductors (i.e. $E \propto \sqrt{I} e^{i\Delta\phi}$). As described in Ref. [22] this field can be propagated to the aperture and integrated numerically to find both n_2 and σ_r from fitting Z-scans at various irradiance levels.

Using Eq. 1, we empirically find that the following simple procedure gives a quick estimate of n_2 as well as σ_r (n_2 is given quite accurately but σ_r can be overestimated by as much as $\approx 37\%$ when compared with the complete numerical fitting).[22] As before, a closed aperture Z-scan and an open aperture Z-scan are performed at the same input irradiance and the closed aperture data is divided by the open aperture data. From the resultant curve ΔT_{p-v} is determined and this value is divided by $0.36 k L_{\text{eff}} I_0 / \sqrt{2}$ (the 0.36 is

determined by the 40% transmitting aperture). Here α in L_{eff} is taken as $\alpha = \alpha_0 + \beta I_0$. This procedure is performed at different irradiances and the results of these calculations plotted as a function of I_0 . If there were no higher order nonlinearities this procedure would give a horizontal line with vertical intercept n_2 . Thus, with free-carrier refraction present, the curve is approximately a plot of $\Delta n/I_0$ versus I_0 which is a straight line with an intercept of n_2 and a slope of $kC\sigma_f$ where C is given by,

$$C \approx 0.23 \frac{\beta t_0}{\hbar \omega}, \quad (22)$$

for small losses. How the constant C is determined is described in Ref. [22].

In what follows we compare the experimental results to theory for ZnSe and CAP.

III. EXPERIMENTAL RESULTS

Results for ZnSe

With 27 picosecond (FWHM) pulses at 532 nm from a frequency doubled Nd:YAG laser we performed Z-scans at different input energies on a 2.7 mm thick polycrystalline sample of chemical-vapor deposition grown ZnSe which has an energy gap of 2.67 eV.[24] The beam was focused to a radius of $w_0 \approx 25 \mu\text{m}$. First, an open aperture Z-scan was performed. In Fig. 4(a) we plot the experimental data. In addition we show a numerically calculated Z-scan using $\beta = 5.8 \text{ cm/GW}$ in Eq. 9 using $\alpha_0 = 0.3 \text{ cm}^{-1}$. This value for β is within 5% of the value reported in Ref. [12] of 5.5 cm/GW measured using nonlinear transmittance. The fitting uncertainties for this measurement and for the measurements listed below were $\pm 10\%$ but the overall experimental uncertainty is $\pm 20\%$ arising mainly from uncertainties in the irradiance calibration. With the 40% aperture another Z-scan was performed at the same irradiance (Fig. 4b). In this case the measurement is sensitive to both nonlinear refraction and nonlinear absorption. Experiments on ZnSe were conducted at irradiance levels from 0.21 GW/cm^2 to 2.4 GW/cm^2 . All of the experimental irradiances reported here are within the sample (i.e. Fresnel reflections taken into account). At the lowest irradiance we expect the change in the index of refraction to be mostly due to the third order anharmonic motion of the bound electrons.[11] In all, ten Z-scans were performed (5 "open" aperture and 5 "closed"). Closed aperture Z-scans at an input irradiance of $I_0 = 0.57 \text{ GW/cm}^2$ and $I_0 = 2.4 \text{ GW/cm}^2$ are shown in Fig. 5a and 5b respectively.

Applying the method described in section IV to ZnSe at 532 nm we obtain $n_2 = -6.4 \times 10^{-14} \text{ cm}^2/\text{W}$ ($-4.1 \times 10^{-11} \text{ esu}$) and $\sigma_f \lambda / 2\pi = -1.1 \times 10^{-21} \text{ cm}^3$. These values were extracted from Fig. 6 which shows the plot of $\Delta n/I_0$ versus irradiance. The intercept gives n_2 while the slope determines σ_f .

With $\beta = 5.8 \text{ cm/GW}$ we also performed a complete numerical fit. Using an iterative approach to best fit all the data, we found a better fit with $n_2 = -6.2 \times 10^{-5} \text{ cm}^2/\text{GW}$ ($-4.0 \times 10^{-11} \text{ esu}$), and $\sigma_f \lambda / 2\pi = -0.8 \times 10^{-21} \text{ cm}^3$. The fits to the data shown in Fig. 5(a) and 5(b) are shown in these figures as the solid lines. The agreement between experiment and theory is remarkable given that the change in transmittance between peak and valley ranges from approximately 10% at the lowest input irradiance to 90% in Fig. 5(b). The absolute errors on the measurement of σ_f of $\pm 25\%$ are only slightly larger than those for β and n_2 even though the nonlinearity is of higher order. This is in part due to the fact that the calculation of σ_f depends on the products βI_0 and $n_2 I_0$ which we know more accurately than β or n_2 separately. Note also that the approximate method for extracting σ_f described in section IV overestimates σ_f by $\approx 37\%$.

We also measured n_2 in ZnSe at $1.06 \mu\text{m}$ where 2PA is not present. Using 40 ps pulses (FWHM) from a Nd:YAG laser focused to $w_0 \approx 40 \mu\text{m}$ spot size, we obtained $n_2 = +(2.9 \pm 0.5) \times 10^{-14} \text{ cm}^2/\text{W}$ ($+(1.7 \pm 0.3) \times 10^{-11} \text{ esu}$). In Fig. 7 we plot closed aperture Z-scans obtained in ZnSe at $1.06 \mu\text{m}$ and at $0.53 \mu\text{m}$ showing the change in sign of n_2 . In this figure, the nonlinear absorption has been divided out of the $0.53 \mu\text{m}$ data. This observed dispersion in n_2 and change in sign is consistent with the recent theory of Refs. [25,26].

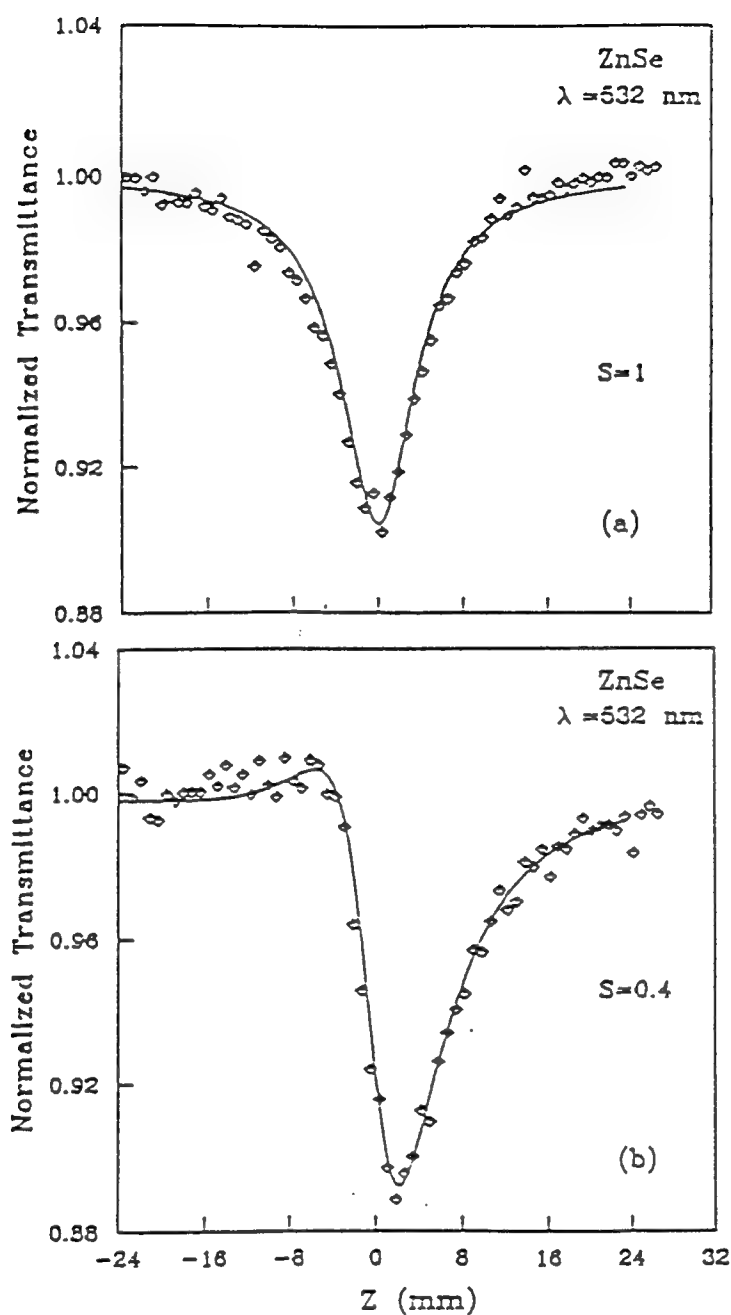


Fig. 4. Normalized Z-scan data of a 2.7 mm ZnSe sample measured with 27 ps (FWHM) pulses and $\lambda=532$ nm at low irradiance ($I_0=0.21$ GW/cm²). The solid lines are the theoretical fits. (a) Open aperture data was fit with $\beta=5.8$ cm/GW. (b) 40% aperture data was fit with $\beta=5.8$ cm/GW and $n_2=-6.2 \times 10^{-5}$ cm²/GW (-4.0×10^{-11} esu), and $\sigma_r \lambda / 2\pi = -0.8 \times 10^{-21}$ cm³.

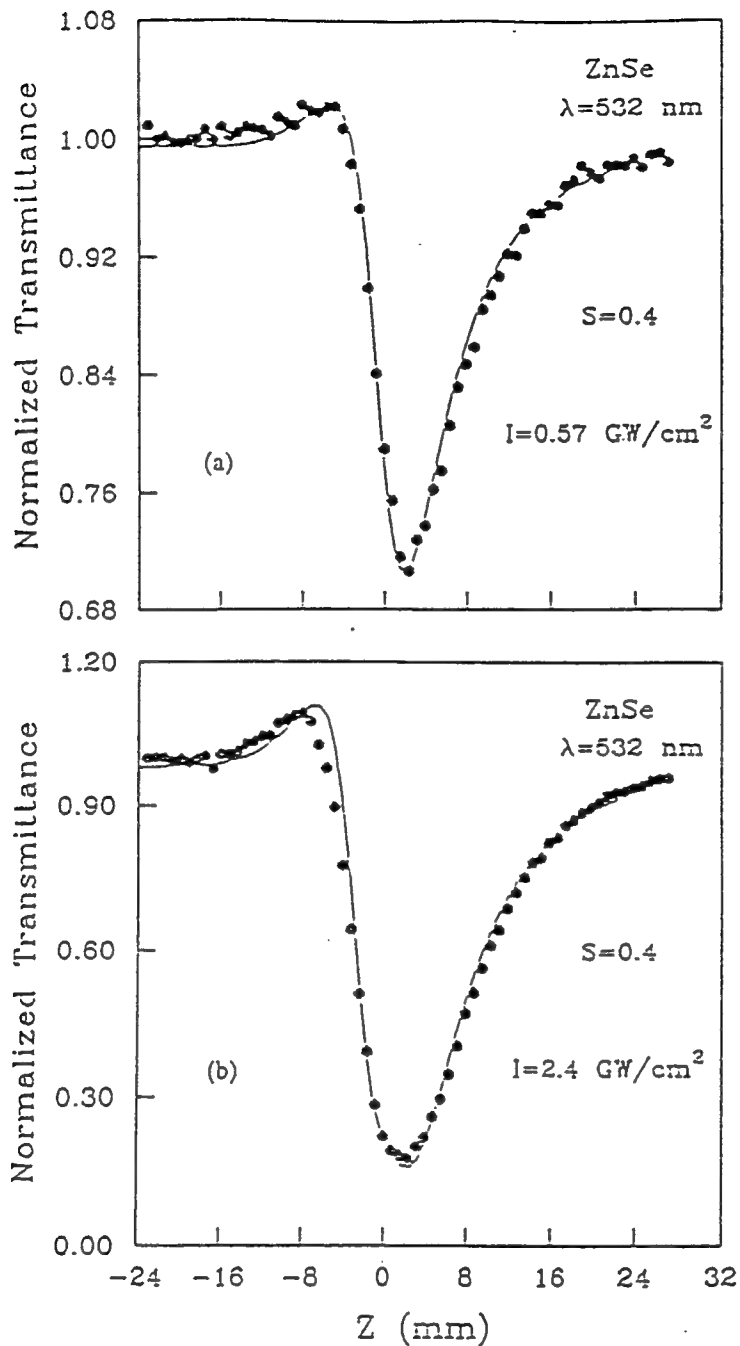


Fig. 5. Closed aperture Z-scan data ($S=0.4$) and theoretical fit (solid lines) of the ZnSe sample taken at irradiance levels of $I_0=0.57$ GW/cm² (a) and $I_0=2.4$ GW/cm² (b) where free-carrier refraction is significant. The data in (a) and (b) were fit with $\beta=5.8$ cm/GW, $n_2=-6.2 \times 10^{-14}$ cm²/GW (-4.0×10^{-11} esu) and $\sigma_r \lambda / 2\pi = -0.8 \times 10^{-21}$ cm².

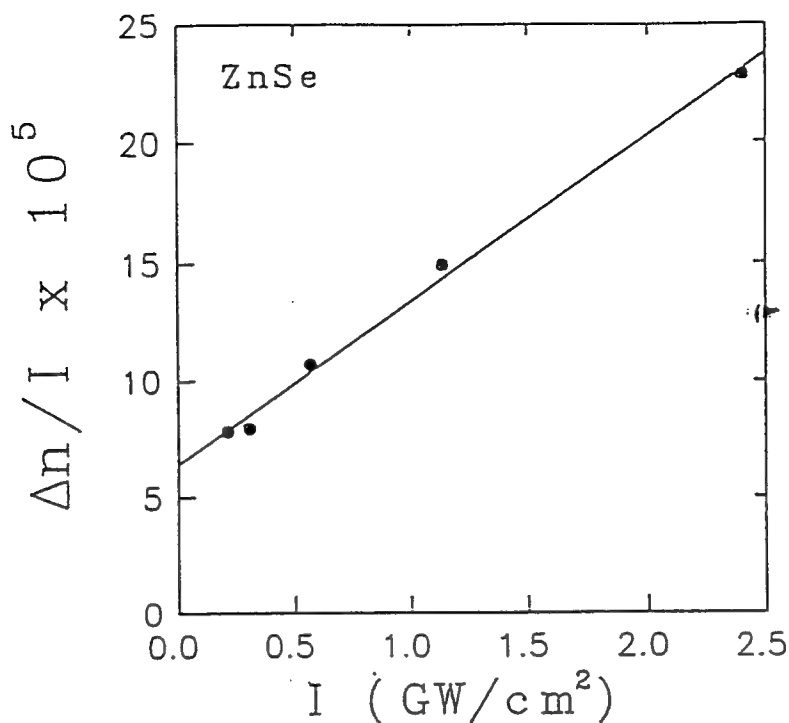


Fig. 6. $\Delta n/I_0$ directly derived from ΔT_{p-v} plotted as a function of I_0 for ZnSe. The intercept of the best fit straight line to the data yields $\gamma = -6.4 \times 10^{-14} \text{ cm}^2/\text{W}$ and the slope gives $\sigma_r = -1.1 \times 10^{-21} \text{ cm}^3$.

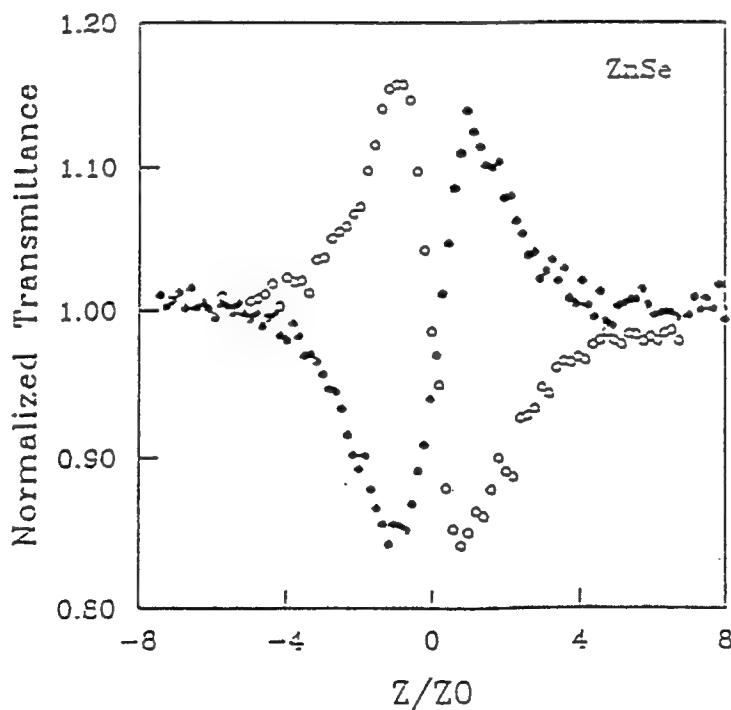


Fig. 7. Closed aperture ($S=0.4$) Z-scan experimental data (filled circles) of ZnSe at $1.06 \mu\text{m}$ and 532 nm (open circles) in units of $z_0 = \pi w_0^2/\lambda$. This figure clearly shows the dispersion in n_2 as it changes sign from positive at $1.06 \mu\text{m}$ to negative at 532 nm .

wide scan

Van Strubbe 12

Results for CAP

For all of our Z-scan measurements on CAP, the beam is focused to a waist of radius $w_0 = 19 \mu\text{m}$ ($\text{HW1/e}^2\text{M}$) and the sample path length is 1 mm. We performed Z-scan experiments on CAP at a concentration of 1.3×10^{-3} moles per liter. The linear transmittance of 84% gives a linear absorption coefficient of $\alpha = 1.8 \pm 0.1 \text{ cm}^{-1}$, which corresponds to an extinction coefficient of $580 \pm 40 \text{ liters cm}^{-1} \text{ mole}^{-1}$. Here the extinction coefficient is defined as, $\epsilon = -\log_{10} T / CL = 10^{-3} \sigma N_A / \ln(10)$, where C is the concentration in moles per liter. We also give the relation for an absorption cross section σ in cm^2 where N_A is Avogadro's number.

Going back to Fig. 3b, we show open aperture Z-scans on a CAP solution at 532 nm for two different pulsewidths of 29 ps and 61 ps (FWHM) using the same input energy of $1.16 \mu\text{J}$ and hence, the same on axis fluence at focus of $F_0(Z=0) = 205 \text{ mJ/cm}^2$. Clearly the nonlinear transmittance for fixed fluence is independent of pulsewidth and hence we conclude that the mechanism is dominated by ESA.

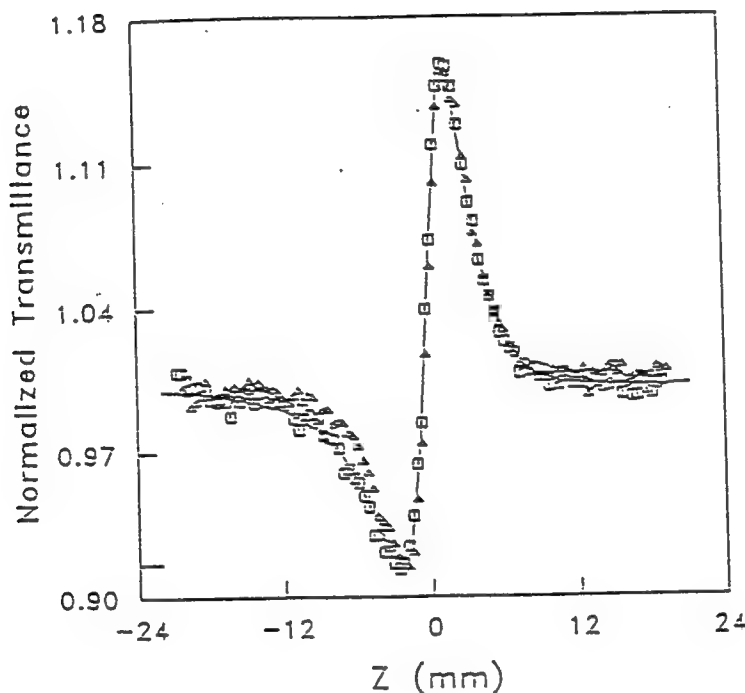


Fig. 8. The results of the division of the closed aperture Z-scan data by the open aperture Z-scan data of Fig. 3b for 29 ps (squares) and 61 ps (triangles) pulsewidths (FWHM) at an incident energy of $1.16 \mu\text{J}$ in CAP.

The solid lines in Fig. 3b are the results of numerically fitting the data to Eq. 6 by integrating over space. Here F_0 is a function of Z . This numerical fit, or simply using ΔT of Eq. 7, gives a value for σ of $\approx 2.3 \times 10^{-17} \text{ cm}^2$ ($\epsilon = 6,020 \text{ liters cm}^{-1} \text{ mole}^{-1}$). Measurements show that σ is the same for concentrations of 5.5×10^{-4} moles per liter and 1.3×10^{-3} moles per liter. We obtain the same values for σ in CAP at input fluences from $0.4 \mu\text{J}$ to $3.6 \mu\text{J}$. Absolute errors in the σ values of $\pm 13\%$ were determined from an estimated 7% error in the concentration, 5% fitting error and a 10% possible error in the fluence calculation.

In order to determine the nonlinear refractive coefficients of these dyes, we performed closed aperture Z-scans on CAP for 29 ps and 61 ps (FWHM) pulsewidths. Figure 8 shows the results of dividing these Z-scans by the open-aperture scans of Fig. 3b taken under identical conditions. Clearly we see that the index change for the

different pulsewidths is positive and identical for the same fluence. This nonlinear refraction is therefore fluence dependent and associated with the real excitation of the singlet state. To determine the contribution of the solvent, Z-scans were performed on the pure methanol solvent. This yielded an n_2 for methanol of $7.0 \times 10^{-16} \text{ cm}^2/\text{W}$ (2.5×10^{-13}) esu. As expected, no nonlinear absorption was seen in the pure solvent.

The overlap of the Z-scans at different pulsewidths and the independence of our measurements on concentration indicate that the nonlinear refractive contribution of the solvent is negligible. This is consistent with the small value of n_2 measured for methanol. Numerically fitting the data including the nonlinear response of the solvent yields $\sigma_r = 1.8 \times 10^{-17} \text{ cm}^2$ for CAP. We obtain the same values of σ_r over the input fluence ranges quoted for the determination of σ . Measurements at concentrations of $\approx 5.5 \times 10^{-4}$ moles/liter and $\approx 1.3 \times 10^{-3}$ moles/liter in CAP also showed the same σ_r .

IV. CONCLUSION

The examples given here demonstrate the importance of measuring materials nonlinearities at different pulsewidths. Had we looked with only a single pulsewidth, we could equally well have fit the data for CAP of Figs. 3b and 10 with β or n_2 values rather than excited state nonlinear coefficients. For example for a pulsewidth of 29 psec for CAP this would give an $n_2 = 1.3 \times 10^{-14} \text{ cm}^2/\text{GW}$ (4.6×10^{-12} esu). However, we would obtain a larger n_2 using 61 psec. Such an "effective" n_2 for CAP would correspond to a third order hyperpolarizability of 4.5×10^{-31} esu. The β or n_2 description is only globally valid if the absorption or index change is dependent on the instantaneous irradiance and hence responds on an ultrafast timescale. The most common example of this is 2PA and the bound electronic Kerr effect as are operable in ZnSe. However, if it is due to the population of excited states, it is much more useful to quote the excited state absorptive or refractive coefficients. Hence what we are observing in CAP is not a true $\chi^{(3)}$ effect but is a sequential $\chi^{(1)}:\chi^{(1)}$ process, where $\chi^{(j)}$ refers to the j th order electric susceptibility. Here, the first $\chi^{(1)}$ is associated with the ground state absorption, and the second with the resulting excited state absorption ($\text{Im}(\chi^{(1)})$) or refraction ($\text{Re}(\chi^{(1)})$).

In ZnSe we have measured these ultrafast nonlinearities associated with the third-order susceptibility $\chi^{(3)}$ as well as excited-state refraction for the 2PA generated free carriers of strength $\sigma_r \lambda / 2\pi$ (the refractive index change per two-photon generated carrier pair density). The nonlinear absorption was due to 2PA and the refraction was due to a combination of n_2 and σ_r . These two nonlinear refractive mechanisms were separated by determining the irradiance dependence.

The Z-scan measurements on ZnSe and a number of other semiconductors and dielectric materials allowed us to determine scaling rules for both the 2PA coefficient β and the optical Kerr coefficient n_2 . From comparisons of our results with theory, we have concluded that β and n_2 can be predicted within factors of two from simple two-band models.[25-28] In addition the free-carrier refraction is explained well by band-filling models.[29-32]

VII. Acknowledgement

We gratefully acknowledge the support of the National Science Foundation grant ECS#9120590, the Defense Advanced Research Projects Agency, the Center for Night Vision and Electro-Optics, and the Florida High Technology and Industry Council. In addition we thank T. Wei, and J. Wang for taking portions of the data. We thank Joe Perry of the Jet Propulsion Laboratory for supplying us with CAP and for many informative conversations. We also express our gratitude to Dr. Joy Arthur of White Sands who was invaluable at getting us interested in looking at reverse saturable absorbing materials.

REFERENCES:

- [1] M. J. Weber, D. Milam, and W. L. Smith, "Nonlinear refractive index of glasses and crystals," *Opt. Eng.* 17, 463 (1978).
- [2] M. J. Moran, C. Y. She, and R. L. Carman, "Interferometric measurements of nonlinear refractive-index coefficient relative to CS_2 in laser-system-related materials," *IEEE J. Quantum Electron.* QE-11, 259 (1975).
- [3] S. R. Friberg and P. W. Smith, "Nonlinear optical glasses for ultrafast optical switches," *IEEE J. Quantum Electron.* QE-23, 2089 (1987).
- [4] R. Adair, L. L. Chase, and S. A. Payne, "Nonlinear refractive index measurement of glasses using three-wave frequency mixing," *J. Opt. Soc. Am. B*, 4, 875 (1987).
- [5] A. Owyong, "Ellipse rotations studies in laser host materials," *IEEE J. Quantum Electron.* QE-9, 1064 (1973).
- [6] W. E. Williams, M. J. Soileau, and E. W. Van Stryland, *Opt. Commun.*, 50 256 (1984).
- [7] W. E. Williams, M. J. Soileau, and E. W. Van Stryland, "Simple direct measurement of n_2 ", in *Proc. 15th Annu. Symp. Opt. Materials for High Power Lasers*, Boulder, CO, 1983.
- [8] M. Bertolotti, A. Ferrari, C. Sibilia, G. Suber, D. Apostol and P. Jani, "Photothermal Deflection Technique for Measuring Thermal Nonlinearities in Glasses", *Appl. Phys.*, 27, 1811 (1988).
- [9] G. R. Meredith, B. Buchalter, and C. Hanzlick, *J. Chemical Phys.* 78, 1533 (1983).
- [10] M. Sheik-Bahae, A. A. Said, and E. W. Van Stryland, "High sensitivity, single beam n_2 measurement," *Opt. Lett.*, 14, 955-957 (1989).
- [11] M. Sheik-Bahae, A. A. Said, T. H. Wei, D. J. Hagan, and E. W. Van Stryland, "Sensitive measurement of optical nonlinearities using a single beam," *IEEE J. Quantum Electron.* QE-26, 760-769 (1990).
- [12] E. W. Van Stryland, H. Vanherzeele, M. A. Woodall, M. J. Soileau, A. L. Smirl, S. Guha, and T. F. Boggess, "Two photon absorption, nonlinear refraction, and optical limiting in semiconductors", *Opt. Eng.* 24, 613 (1985).
- [13] M. Bass, E.W. Van Stryland, and A.F. Stewart, "Laser Calorimetric Measurement of Two-Photon Absorption," *Appl. Phys. Lett.* 34, 142 (1979).
- [14] Y. Bae, J.J. Song, and Y.B. Kim, "Photoacoustic Study of Two-Photon Absorption in Hexagonal ZnS ", *J. Appl. Phys.*, 53, 615 (1982). also see, E.W. Van Stryland, and M.A. Woodall, "Photoacoustic Measurement of Nonlinear Absorption in Solids," in *Laser Induced Damage in Optical Materials*, NBS Special Publication 620, 50 (1980).
- [15] for example see; *Picosecond Phenomena*, eds. C.V. Shank, E.P. Ippen, and S.L. Shapiro, Springer Verlag, 1978.
- [16] A. E. Kaplan, "External Self-Focusing of Light by a Nonlinear Lens", *Radiophys. Quantum Electron.* 12, 692 (1969).
- [17] S. A. Akhmanov, R. V. Khokhlov, and A. P. Sukhorukov, "Self-focusing, self-defocusing, and self-modulation of laser beams," in *Laser Handbook*, F. T. Arecchi and E. O. Shultz-Dubois, eds. (North-Holland,

Van Stryland

Amsterdam, 1972), vol. 2 1151-1228.

- [18] J. H. Bechtel, and W. L. Smith, "Two-photon absorption in semiconductors with picosecond pulses," *Phys. Rev. B* 13, 3515 (1976).
- [19] E. W. Van Stryland, M. A. Woodall, H. Vanherzeele, and M. J. Soileau, Energy band-gap dependence of two-photon absorption," *Opt. Lett.* 10, 490 (1985).
- [20] T. F. Boggess, A. L. Smirl, S. C. Moss, I. W. Boyd, and E. W. Van Stryland, "Optical limiting in GaAs," *IEEE J. Quantum Electron.* QE-21, 488 (1985).
- [21] T. H. Wei, D. J. Hagan, E. W. Van Stryland, J. W. Perry, and D. R. Coulter, "Direct measurements of nonlinear absorption and refraction in solutions of phthalocyanines," *Appl. Phys. B* 54, 46 (1992).
- [22] A. A. Said, M. Sheik-Bahae, T. H. Wei, J. Wang, J. Young, and E. W. Van Stryland, "Determination of bound-electronic and free-carrier nonlinearities in ZnSe, GaAs, CdTe, and ZnTe," *J. Opt. Soc. Am. B*, 9, 405 (1992).
- [23] E. Canto-Said, D. J. Hagan, J. Young, and E. W. Van Stryland, "Degenerate four-wave mixing measurements of high order nonlinearities in semiconductors", *IEEE J. Quantum Electron.* 27, 2274 (1991).
- [24] The ZnSe sample was obtained from Heriot Watt University, Edinburgh, U.K.
- [25] M. Sheik-Bahae, D. J. Hagan, and E. W. Van Stryland, "Dispersion and band-gap scaling of the electronic Kerr effect in solids associated with two-photon absorption," *Phys. Rev. Lett.* 65 96-99 (1990).
- [26] M. Sheik-Bahae, D. Hutchings, D. J. Hagan, and E. W. Van Stryland, "Dispersion of bound electronic nonlinear refraction in solids," *IEEE J. Quantum Electron.* 27, 1296 (1991).
- [27] M. Weiler, "Nonparabolicity and exciton effects in two photon absorption in zinc-blende semiconductors", *Solid State Commun.* 39, 937 (1981).
- [28] B. S. Wherrett, "Scaling rules for multiphotoninterband absorption in semiconductors", *J. Opt. Soc. Am. B* 1, 67 (1984).
- [29] D. A. B. Miller, C. T. Seaton, M. E. Prise, and S. D. Smith, "Band-gap-resonant nonlinear refraction in III-V semiconductors," *Phys. Rev. Lett.* 47 197-200 (1981).
- [30] A. G. Aronov, D. E. Pikus, and D. Sh. Shekhter, "Quantum theory of free-electron dielectric constant in semiconductors", *Sov. Phys.-Solid State*, 10, 645 (1968).
- [31] D. H. Auston, S. McAfee, C. V. Shank, E. P. Ippen, and O. Teschke, "Picosecond spectroscopy of semiconductors," *Solid State Electron.* 21 147-150 (1978).
- [32] B. S. Wherrett, A. C. Walker, and F. A. P. Tooley, "Nonlinear refraction for CW optical bistability," in *Optical Nonlinearities and Instabilities in Semiconductors*, H. Haug ed. (Academic Press, 1988), 239-272.

Van Stryland

NONLINEAR OPTICAL MATERIALS AT 10 μm : FROM PICOSECONDS TO NANOSECONDS

August, 1993

M.P. Hasselbeck[†], A.A. Said, M. Sheik-Bahae, and E.W. Van Stryland
Center for Research in Electro-Optics and Lasers (CREOL)
University of Central Florida, Orlando, FL 32826

ABSTRACT

The nonlinear optical properties of CS_2 , InSb, InAs, Ge and ZnSe have been studied using CO_2 laser pulses in the 10 μm wavelength region. The nonlinearities associated with CS_2 and InSb are particularly strong, making these materials useful in optical power limiting applications that involve nanosecond and microsecond laser pulses. Liquid CS_2 displays thermally induced nonlinear refraction, while two and three photon absorption have been observed with the semiconductor InSb at different temperatures. In semiconductors such as Ge, ZnSe and InAs, having bandgap energy greater than three times the infrared photon energy, avalanche ionization of carriers is primarily responsible for the observed nonlinear behavior. Because the onset of the avalanche process is an abrupt function of laser irradiance, this effect is most conveniently studied with picosecond pulses. In addition, Z-scan measurements with picosecond pulses reveal nonlinear refraction due to bound electrons in these semiconductors.

I. INTRODUCTION

The characterization of the nonlinear optical properties of materials in the infrared region around 10 μm is important not only because it broadens our knowledge of their fundamental physics and damage limitations, but also for applications such as laser beam modulation, optical isolation, and recently, to protect easily damaged infrared sensor elements from pulsed CO_2 laser beams. We have applied the Z-scan technique, developed at CREOL [1] [2], to probe the nonlinear optical behavior of CS_2 , InSb, InAs, Ge and ZnSe at 10.6 μm .

Briefly, Z-scan uses a single Gaussian beam to measure the transmittance of a nonlinear medium through a finite aperture in the far field, as illustrated in Fig. 1. By translating a nonlinear refractive sample along the optic axis (z direction) through the focus of a lens, a peak and valley in the detected signal will be obtained. By analyzing the transmission as a function of position, we can determine the magnitude and sign of the nonlinear refraction. Repeating the Z-scan with the aperture wide open causes the peak and valley associated with nonlinear refraction to disappear. However, it can reveal the presence of nonlinear absorption. We quantify aperture transmission with the parameter S, and denote these two measurements as closed-aperture ($S < 1$) and open-aperture ($S = 1$) Z-scans.

Laser induced changes to the index of refraction (Δn) of a material that are associated with χ^3 processes are conveniently described by the coefficients γ (mks) and n_2 (esu), defined by the relationships:

$$\Delta n = \gamma I = \frac{1}{2} n_2 |E|^2$$

where I is the irradiance of the laser beam (mks) with peak electric field E (cgs). Much of the discussion in this paper is concerned with higher order effects in semiconductors, whereby the nonlinear process generates carriers which then refract and/or absorb the incident laser beam. The Z-scan will resolve such nonlinear behavior, but interpretation of the data becomes more complicated. Although it usually involves higher order effects, we will focus on the optical power limiting application because of its relevance for infrared sensor protection.

Many infrared sensor applications have wide field-of-view requirements, and it is commonly assumed that a protection scheme utilizing nonlinear refraction requires a limiting aperture in front of the detector, thus limiting the field-of-view. Although in principle, the lensing caused by nonlinear refraction allows all the incident energy to strike the focal plane of the detector, the footprint of the focused beam will be changed. The redistribution of energy

has the effect of reducing fluence (energy/area). Since it is fluence, not energy, that determines a detector's damage threshold, nonlinear refraction can be exploited successfully to protect sensors from damage.

II. CS₂

Liquid CS₂ is a well known nonlinear optical medium at wavelengths spanning the visible to 10 μm in the infrared, and its nonlinear coefficients have become a standard to which nonlinear properties of other materials are often referenced. In general, CS₂ displays a strong optical Kerr effect leading to $n_2 \sim 1.3 \times 10^{-11}$ esu, which is essentially independent of wavelength. However, in the proper focusing and imaging geometry, thermal lensing can be realized, suggesting interesting optical power limiting possibilities.

Using 300 ns TEA laser pulses, we have obtained the limiting behavior shown in Fig. 2 by employing thermal lensing [3]. This limiter works in conjunction with an aperture placed in front of the detector in the far field. Only by proper positioning of the beam focus in a "thick" cell of CS₂ will the desired limiting operation take place. By thick, we mean a cell length much longer than the depth of focus. The proper position is found by locating the transmission minimum with a closed aperture Z-scan. A closed aperture Z-scan ($S = 0.5$), obtained with a 2.4 cm cell of CS₂ is shown in Fig. 3. If the focus is placed instead at the point of transmission maximum, the device reverses operation and enhances, rather than limits, transmission at high irradiance.

The thermal nature of the lensing was confirmed by increasing the linear absorption of CS₂. This was accomplished by dissolving sulfur impurities in the liquid to increase the absorption coefficient from $\alpha = 0.22 \text{ cm}^{-1}$ to $\alpha \approx 2 \text{ cm}^{-1}$. As depicted in Fig. 2, dramatic improvement of limiting performance was obtained, and is attributed to the increased deposition of heat in the focal volume. Bearing this in mind, we note that design of a thermal lensing device will depend on linear absorption, density, specific heat, and thermo-optic coefficient of the medium, as well as the laser pulse length and focused spot size.

Thermal lensing in CS₂ is not limited to pulsed lasers. We have also performed experiments with cw CO₂ lasers which show limiting at less than 0.3 W input [4].

With 130 picosecond CO₂ laser pulses, we have been able to detect nonlinear refraction due to the reorientational Kerr effect. Thermal lensing is too slow to be a factor on the picosecond timescale of this measurement. A closed aperture Z-scan is shown in Fig. 4. By fitting this data with the solid line shown in the figure, we obtain $n_2 = 1.5 \times 10^{-11}$ esu, in excellent agreement with previous measurements by other techniques at 10.6 μm and other wavelengths.

III. InSb

Since its discovery in 1968 [5], two photon absorption of CO₂ laser light in InSb has been the subject of extensive study and characterization. The strength and efficiency of both nonlinear refraction and nonlinear absorption derived from two photon absorption has led to many applications including power limiting, pulse shaping, beam deflection, and optical switching. Although the two photon absorption process is broadband, insensitive to temperature, requires no external control or biasing, and is accessible to a wide range of laser pulsewidths, it is only recently that InSb has been embraced by the sensor protection community as an attractive alternative to heated vanadium dioxide, gas plasma shutters, and active electro-optical switching techniques. Several years ago, we demonstrated the utility of InSb as a CO₂ laser power limiter [6].

Two photon absorption has been observed in InSb at temperatures from 77°K to 300°K, over the entire CO₂ laser spectrum with pulses ranging from several microseconds to tens of picoseconds. The immediate applicability of this material as an infrared sensor protection device is illustrated in Figs. 5 and 6. The curves clearly depict energy clamping action obtained with a 1 mm sample at room temperature with 300 ns and 60 ps pulses, respectively. In these measurements, the clamping effect is enhanced by imaging only the central, high irradiance portion of the beam profile by placing an aperture in front of the detector. The same effect would take place if InSb was used to protect a two dimensional detector array, since the high energy portion of the beam striking a pixel would be minimized.

Depending on the optical layout, a system can be sensitive to nonlinear refraction, nonlinear absorption, or both. In Z-scan experiments, restricting transmission in the far field with an aperture will reveal nonlinear refraction and absorption, while removing the aperture shows only nonlinear absorption. In a power limiting arrangement that produced the data of Figs. 5 and 6, an aperture is placed behind an InSb device and in front of the detector in the far field. Electron-hole pairs are generated in InSb at sufficiently high irradiance, causing self-defocusing of a Gaussian laser beam that spreads a portion of the spatial profile outside the aperture. At higher irradiance, the generated carrier

density will cause significant absorption of the incident beam. The effect of self defocusing is easily discernible in the picosecond data of Fig. 6. When the aperture is present, the onset of clamping occurs at 20–25 nJ. With an open aperture, clamping starts at ~ 100 nJ. The clipping aperture geometry displays the effect of nonlinear refraction at lower input energy, until nonlinear absorption dominates at higher input levels.

Free carriers generated by two photon absorption dominate the nonlinear absorption for nanosecond pulses in the 8–12 μm spectral region. Two photon absorption does remove a small number of photons from the laser beam, but this effect is negligible compared to the absorption caused by direct transition of excited holes from the heavy to light hole band. Therefore, the nonlinear absorption is actually a two step process: 1) two photon absorption of the 10 μm light creates a high density of electron-hole pairs, followed by 2) strong absorption of the remaining 10 μm light by the excited holes. This appears as an effective fifth order nonlinearity.

We should also mention that motion of electrons in a non-parabolic conduction band causes nonlinear refraction in InSb [7]. This effect is small compared to the nonlinear optical properties caused by two photon absorption however, and great effort must be expended to isolate non-parabolicity from two photon absorption in experiments. It is not relevant for power limiting.

Although InSb exhibits strong nonlinear absorption at room temperature, the background carrier density leads to unacceptable linear losses in most infrared sensor applications. An option is to make the InSb wafer extremely thin (~ 100 μm), but this compromises the structural integrity of the device and limits the dynamic range in a focusing geometry. A tandem arrangement may make the use of thin wafers possible.

A better option, in applications that permit it, is to use a thick InSb device cooled to $T < 200^\circ\text{K}$ at an intermediate focus in the sensor optical train. In this temperature regime, the background carrier density will be reduced by ~ 100 compared to room temperature, resulting in small linear transmission loss in samples as thick as 1 cm. Lowest linear loss will be obtained with samples that are slightly n-doped, to reduce the background hole concentration. Although the two photon absorption coefficient will be reduced at lower temperatures, this will be offset to some extent by an increase of the excited carrier lifetime. More important, a thick element takes advantage of the "self-protecting" nature of limiters that are longer than the Rayleigh length of the focused infrared beam. Thick, monolithic optical power limiters were first demonstrated by our group some time ago [8]. We have shown such limiters increase dynamic range by many orders of magnitude compared to thin devices [9],[10]. A systematic study of InSb limiters as a function of doping, length, temperature, as well as laser wavelength and pulse duration, needs to be done to provide the key design parameters for an infrared sensor protection device.

Because of band bending, both two photon absorption and intervalence band hole absorption will occur in InSb throughout the 8–12 μm wavelength region. For $T < 100^\circ\text{K}$ however, the long wavelength two photon absorption edge will increase to ~ 11 μm . For sensor protection use, this is probably not an issue because it is difficult to make efficient lasers at these long wavelengths.

At temperatures below ~ 100°K, there is no significant increase of the linear transmission of InSb in the 8–12 μm spectral region. This is because free carrier absorption dominates at these wavelengths, and the free carrier concentration is set by material purity, not the intrinsic carrier density at low temperatures. The purest InSb available has an impurity concentration of ~ 10^{14} cm^{-3} , and these shallow impurity levels are completely ionized even at temperatures as low as 2°K.

When InSb is cooled to $T < 50^\circ\text{K}$, the bandgap increases to $E_g \approx 0.24 \text{ eV}$, making the material inaccessible to two photon transitions by 10.6 μm laser light. Consequently, nonlinear absorption is substantially weakened when sample temperature is reduced from 77°K ($E_g \approx 0.228 \text{ eV}$) to $\leq 20^\circ\text{K}$. For CO_2 laser excitation pulses ranging in duration from 1 ns to 90 ns, the irradiance at which nonlinear absorption occurs increases from ~ 100 kW/cm^2 at 77°K to $> 1 \text{ MW/cm}^2$ at ~ 10°K [11]–[14]. This could have important implications for space-based sensor protection applications where the ambient temperature can be this low.

The nonlinear absorption observed in InSb at $T \leq 20^\circ\text{K}$ has been attributed to laser-driven impact ionization of valence band electrons into the conduction band, and a number of modeling efforts have been reported [13], [15]–[18]. All of these calculations however, fail to predict the correct pulsewidth scaling of the nonlinear absorption threshold, particularly for picosecond experiments [19].

We believe that three photon absorption provides an alternative explanation of the low temperature nonlinear absorption. The data of Dempsey et al [12], obtained with 100 ns pulses, provides detailed spatial and temporal information for the incident and transmitted pulse shapes, permitting evaluation of three photon absorption in InSb at 10°K. The three photon absorption carrier generation process is described by:

$$\frac{\partial \Delta N}{\partial t} = \frac{K_3 I^3}{3 \hbar \omega}$$

where ΔN is the induced carrier density, K_3 is the three photon absorption coefficient, and I is the laser irradiance at frequency ω . Absorption of the laser light is attributed entirely to inter-valence band transitions due to the generated holes. We neglect free carrier absorption saturation in InSb, although its existence has been postulated [20]. Direct bandgap carrier recombination is negligible on this timescale ($\sim 10^{-8}$ sec) at this temperature, and the excited carrier density ($\sim 10^{16} \text{ cm}^{-3}$) precludes Auger recombination. To obtain the transmitted pulse, the nonlinear absorption was spatially and temporally integrated using a numerical procedure with K_3 as the only fitting parameter. This analysis generated a value of $K_3 = 0.003 \text{ cm}^3/\text{MW}^2$.

Schwartz et al [19] have made low temperature (20°K) transmission measurements with InSb using picosecond 10.6 μm pulses. At a fixed irradiance of 30 MW/cm^2 , the pulse duration was increased in steps of 4, 12, 22, 38 and 54 ps – causing increasing nonlinear absorption. This data cannot be reconciled with any proposed avalanche theory, but our three photon absorption analysis produces $K_3 = 4.7 \pm 0.3 \times 10^{-3} \text{ cm}^3/\text{MW}^2$, consistent with the value found above.

Wherret [21] has presented a calculation for estimating the magnitude of K_3 . Although this calculation is designed primarily to ascertain the relative scaling of multiphoton absorption coefficients in different materials, a simple formula is given in his paper that permits direct evaluation of K_3 . This formula yields $K_3 = 4.2 \times 10^{-3} \text{ cm}^3/\text{MW}^2$ for InSb at $T \leq 20^\circ\text{K}$, in remarkably good agreement with the numbers deduced from the experiments in Refs. [12] and [19].

A consistent description of the nonlinear absorption, in experiments with pulse durations varying by over three orders of magnitude, tends to favor three photon absorption over avalanche ionization as the relevant carrier generation process in InSb at low temperature. Furthermore, the scaling relationship of Ref. [21], suggests that there may be a non-negligible component of three photon absorption at higher temperatures, where two photon absorption is allowed. Because of the importance of InSb as an infrared sensor protection material, this problem requires more experimental and theoretical study.

IV. InAs

We have performed a Z-scan analysis of an uncoated, 1 mm thick sample of n-InAs using 80 ps pulses. The results of an open aperture Z-scan measurement are shown in Fig. 7. At an incident intensity of 1.1 GW/cm^2 , a large nonlinear absorption is present, masking any possibility of observing weak nonlinear refraction in a closed aperture Z-scan. Reduction of the irradiance by a factor of 10 caused the nonlinear absorption to disappear, but no nonlinear refraction was detected.

With a bandgap of $E_g = 0.36 \text{ eV}$ at room temperature, InAs is not likely to display two or three photon absorption when excited by 10.6 μm laser light. Unless there is more than 9 meV of band tailing, a four photon absorption process would be needed to directly excite carriers across the bandgap. We believe that a more plausible explanation of our Z-scan data is that avalanche ionization of valence band electrons into the conduction band occurs. This "inverse Auger" process takes place when conduction band electrons are heated by the intense infrared fields and then collide with valence band electrons. If valence band electrons acquire energy greater than the bandgap in a collision, they can be scattered into the conduction band, thereby creating a new electron-hole pair in the material.

To model the avalanche process, we use the approach first proposed by Yablonovitch and Bloembergen to describe laser induced breakdown in solids [22]–[24]. Although our experiments did not cause catastrophic damage, this model allows us to estimate the generated carrier concentration due to avalanche ionization at intensities below the damage threshold.

We need to determine the ionization rate (η) governing the build up of the carrier concentration (N) in the avalanche equation:

$$N = N_0 \exp(\eta t_p)$$

where N_0 is the initial electron concentration and t_p is the laser pulsewidth. In general, η is a very sensitive function of electric field. Bauer and Kuchar [25] have measured the ionization rate for InAs using dc fields, and their results are reproduced in Fig. 8.

As pointed out by James [16], we need only consider electron avalanche, since hole avalanche is a much less efficient process under infrared excitation. To apply this data at infrared frequencies, the laser electric field is scaled by the electron momentum relaxation time (τ):

$$E_{dc} = \frac{E_{ac}}{\sqrt{1 + (\omega\tau)^2}}$$

where ω is the laser frequency (1.77×10^{14} rad/sec) and E_{ac} is calculated from the laser intensity inside the material. Strictly speaking, this is an approximate relationship that is valid provided τ is independent of carrier energy. This should be true for InAs in the avalanche regime because there is negligible intervalley scattering. The momentum relaxation time can be obtained from the field dependent drift velocity. The Monte Carlo study of Curby and Ferry [26] yields a value of $\tau = 0.38 \pm 0.07$ ps for fields around 1 kV/cm, in agreement with experiments at 77°K [25].

In our Z-scan experiment, we observed the transmission decrease by about a factor of 20 at an incident irradiance of ~ 1.1 GW/cm² for 80 ps pulses. This irradiance corresponds to a laser field of $E_{ac} \sim 400$ kV/cm when corrected for Fresnel reflection at the surface of the sample. Using $\tau = 0.38$ ps, we estimate an rms field of 5.9 kV/cm. From Fig. 8, we read an ionization rate of $\eta = 8 \times 10^9$ sec⁻¹. Note that no experimental data is available for this value of electric field. Therefore, we have made a linear extrapolation of the data using a least-squares fit into the high field regime. In the avalanche theory of Baraff [27], it was proposed that such a high field extrapolation requires $\log \eta$ to be plotted against $1/E^2$. However, a detailed Monte Carlo calculation [26] revealed that a linear relationship between $\log \eta$ and $1/E$ is more appropriate, and that is how we have scaled the data in Fig. 8.

Our n-doped InAs sample was specified with $N_0 = 5 \times 10^{16}$ cm⁻³. The combined electron (N) and hole (P) absorption cross section at $\lambda = 10.6$ μ m is $\sigma = 6 \times 10^{-16}$ cm² [13]. It has been proposed that the dominant hole absorption cross section will saturate at 5.1 MW/cm² in InAs [28]. However, since no experimental evidence for this effect has been produced to date, we will neglect absorption saturation. Evaluating the ionization equation, we find $N_{induced} = 9.5 \times 10^{16}$ cm⁻³ corresponding to $\Delta N = \Delta P = 4.5 \times 10^{16}$ cm⁻³. Assuming uniform illumination of our 1 mm thick sample, we calculate a change of transmission by a factor of $\Delta T = 0.067$, or a decrease in signal by a factor of $1/\Delta T = 15$. This compares well with the experimental value of 20.

As a simple check on the validity of the analysis, the calculation was repeated at an incident irradiance of 110 MW/cm², where no induced absorption was observed. This irradiance is a factor of 10 below the level where strong nonlinear absorption was obtained. At this irradiance, we calculate $E_{dc} = 1.8$ kV/cm. From Fig. 8, the ionization rate is found to be smaller than the previous case by over two orders of magnitude, resulting in a negligible increase of the carrier concentration, consistent with the experimental observations.

Jamison and Nurmikko [13] have observed nonlinear absorption in n-InAs ($N_0 = 2.3 \times 10^{16}$ cm⁻³) with 1 ns CO₂ laser pulses at 30 MW/cm². It is not stated whether their sample is AR coated or if the incident irradiance has been corrected for Fresnel reflection, so we will assume the stated incident irradiance is inside the material. Scaling the laser field as before, we get $E_{dc} = 1.2$ kV/cm. Using Fig. 8, we find $\eta = 1.1 \times 10^8$ sec⁻¹. For a 1 ns pulse, we compute an excess carrier concentration of $\Delta N = \Delta P = 3 \times 10^{15}$ cm⁻³. This gives $\Delta\alpha = 1.8$ cm⁻¹, in excellent agreement with their observed value of $\Delta\alpha \sim 2$ cm⁻¹. Although the laser pulses used in their experiment are more than 10 times longer than in the Z-scan measurements, the simple theory correctly predicts the nonlinear absorption.

To conclude this section, we would like to compare our avalanche analysis with the perturbation calculations of R.B. James [16], in which the ionization rate is computed as a function of CO₂ laser irradiance. For the 1 ns experiments, James obtains $\eta = 10^8$ sec⁻¹ at an irradiance of about 60 MW/cm², in reasonable agreement with the 30 MW/cm² threshold found in Ref. [13]. As shown above, the needed ionization rate for the 80 ps Z-scan experiment reported here is close to 10^{10} sec⁻¹. The theory of James indicates that the required rate will be produced at an irradiance of only 75 MW/cm², which is a factor of 15 below our experimental threshold of 1.1 GW/cm².

We believe that the dc scaling model for avalanche ionization more accurately predicts the experimental results because it is based on an empirical curve – namely the dc ionization rate data. Only the electron momentum relaxation time (τ) is needed to scale the dc avalanche ionization to optical frequencies.

V. Ge

Germanium is a well characterized and widely used infrared material. With an indirect bandgap of 0.67 eV, it is no surprise that multi-photon absorption has not been observed at CO₂ laser wavelengths. Other nonlinear optical properties are present however. Absorption saturation of p-type Ge at 10 μ m has received much theoretical and experimental study, and several comprehensive reviews have been published [28]–[30]. Such saturable absorbers have been used for mode-locking high pressure CO₂ lasers, as external cavity pulse compressors, and for optical isolation between high power amplifier stages. In this paper, we will focus on the nonlinear behavior of n-Ge when excited by high power CO₂ laser pulses.

Using the Z-scan technique, we have been able to deduce both nonlinear refraction and absorption in n-type Ge with our picosecond CO₂ laser. Open and closed aperture Z-scan measurements of an AR coated 3 mm thick sample are presented in Figs. 9 and 10. To resolve nonlinear refraction, we kept the irradiance at ~ 0.8 GW/cm² to prevent avalanche induced absorption from dominating the signal. The closed aperture data was fit with $n_2 = 2.7 \pm 1.1 \times 10^{-10}$ esu or $\gamma = 2.8 \pm 1.1 \times 10^{-13}$ GW/cm² (MKS). The same value of n_2 was extracted from a closed aperture Z-scan at a slightly higher intensity of 1.1 GW/cm². The measured value of n_2 compares favorably with the value of $n_2 = 2.3 \times 10^{-10}$ esu deduced by Watkins et al [31] with an ellipse rotation technique. Wynne and Boyd [32] measured $n_2 = 9.2 \times 10^{-10}$ esu in a four wave mixing experiment, which is about three times larger than our value.

The nonlinear refraction in Ge is caused by the anharmonic motion of bound electrons. Our measured value of $n_2 = 2.7 \pm 1.1 \times 10^{-10}$ esu is in good agreement with the calculation of Sheik-Bahae et al [33] who obtained $n_2 = 4.4 \times 10^{-10}$ esu. Previous theoretical efforts to compute n_2 yield values ranging from 2.3×10^{-10} to 4.7×10^{-10} esu [29], that are in general agreement with our measurement. This agreement must be interpreted with some caution however. The relationship between n_2 and χ^3 , the most often quoted coefficient, depends on the definition of the nonlinear polarization, and the definition used is sometimes not given.

The open aperture Z-scan with 60 ps pulses displays an abrupt decrease of transmission at an irradiance of 1.5 GW/cm². Recall that below 0.8 GW/cm², the nonlinear absorption is negligible. As with InAs, we believe this abrupt irradiance dependence of nonlinear absorption is the signature of laser-induced avalanche ionization of electron-hole pairs.

We have found the avalanche process difficult to model in Ge using the dc scaling arguments presented in the previous section for InAs. The electron and hole drift velocities are known to saturate as the electric field is increased into the avalanche regime. Therefore, we cannot make a reliable estimate of the momentum relaxation time τ to allow calculation of the rms (dc) field.

James and Smith [28] and later James [16] have treated CO₂ laser-induced avalanche ionization in Ge. Since both the hole and electron absorption cross section are irradiance dependent, the avalanche threshold was defined as the point at which the electron density doubles. For 60 ps pulses, this requires $\eta = 10^{10}$ sec⁻¹. From the results in Ref [16], this ionization rate occurs at ~ 300 MW/cm², which is a factor of five below the measured irradiance of 1.5 GW/cm². This should be considered reasonable agreement in view of the uncertainties associated with free carrier absorption and the experimental calibration. The calculation also predicts negligible carrier generation when the threshold irradiance is reduced by a factor of two, in agreement with the trend observed in our experiment.

VI. ZnSe

Like Ge, ZnSe is a well known and often used window material in the infrared. To our knowledge, no non-thermal, nonlinear refraction has been observed with ZnSe at $\lambda = 10$ μ m unless picosecond pulses are used. We have made open aperture Z-scan measurements with ZnSe using 80 ps pulses, the results of which are depicted in Fig. 11. The data indicates an abrupt onset of high density carrier generation at an intensity of ~ 7 GW/cm², which we again attribute to avalanche ionization. The avalanche irradiance is much higher than observed with the Ge and InAs samples, and is qualitatively consistent with our physical picture of the avalanche process induced by CO₂ laser pulses. Because the bandgap of ZnSe is wider ($E_g = 23$ h ν at 10.6 μ m) than the other semiconductors tested, the

quiescent carrier distribution must be excited to much higher energies to initiate the impact ionization process, necessitating stronger infrared fields.

An interesting effect occurs when the peak irradiance is increased slightly to $\sim 9 \text{ GW/cm}^2$. The transmission was observed to increase, producing a "kink" in the Z-scan data at the irradiance maximum. This feature can be clearly seen in Fig. 11. Complete recovery of low intensity linear transmission assures that no damage has occurred. Since the avalanche process is highly nonlinear, we cannot reconcile this behavior with saturation of homogeneous or inhomogeneously broadened absorption. Because it is a comparatively weak function of intensity, absorption saturation by itself cannot reverse the aggregate attenuation caused by the rapid build-up of free carriers in the avalanche ionization. Therefore, we speculate that the free carrier absorption cross section becomes drastically reduced (unlike a standard saturable absorber) at sufficiently high carrier temperatures.

We are still studying the free carrier absorption process in ZnSe. Unlike InAs, InSb and Ge, there is not a strong intervalence band transition in ZnSe in the mid-infrared. There are probably components of free carrier absorption due to both the conduction and valence band carriers, and our data forces us to consider the possibility that the absorption cross section may be intensity dependent. Furthermore, the initial carrier concentration in ZnSe is very low ($< 10^5 \text{ cm}^{-3}$), so the ionization rate scaling arguments used to analyze the other semiconductors must be applied here with caution. ZnSe may behave more as alkali-halide dielectrics at CO_2 laser wavelengths, where crystal inhomogeneities and defects have been directly linked to the high field damage process [34]. Clearly this problem requires further study, and at present we cannot determine the generated carrier density as a result of avalanche ionization in ZnSe.

When the irradiance is lowered to $\sim 5 \text{ GW/cm}^2$, the avalanche induced absorption causes $\sim 10\%$ modulation in a closed aperture Z-scan ($S = 0.4$). Since nonlinear refraction was not observable at this irradiance, we can place an upper limit on $n_2 < 5 \times 10^{-11} \text{ esu}$ or $\gamma < 8 \times 10^{-14} \text{ cm}^2/\text{W}$ for $\lambda = 10.6 \text{ }\mu\text{m}$.

VII. CONCLUSION

We have described a variety of measurements that have been made with CS_2 , InSb, InAs, Ge and ZnSe using CO_2 laser pulses. In addition to enhancing our knowledge of the fundamental physics of laser-material interactions in the infrared, we have a good understanding of the potential and limitations of these materials in certain applications.

We have shown that n-Ge, ZnSe, and InAs display an avalanche carrier generation mechanism that has an abrupt irradiance dependence. Although more subtle nonlinear effects are evident in these materials, the avalanche process will define the maximum energy density that can be withstood without damage. The abrupt nature of laser-induced avalanche makes these semiconductors poor choices for use as optical power limiters with nanosecond laser pulses.

In contrast, InSb possesses a strong two photon absorption carrier generation mechanism that is of great utility in sensor protection scenarios. The onset of limiting can be as low as $\sim 100 \text{ kW/cm}^2$ for laser pulses of duration $\sim 1 \text{ }\mu\text{s}$. Two photon absorption generates an electron-hole plasma that manifests in both nonlinear refraction and absorption depending on the optical geometry. These nonlinearities are fairly insensitive to temperature, and excellent performance can be obtained at 77°K , which makes InSb compatible with cooled detector focal planes. The linear absorption of InSb is very low at cryogenic temperatures, which gives the sensor engineer the option of inserting a thick ($\sim 1 \text{ cm}$) slab at or near a focal plane. Thick pieces of InSb, with length greater than the depth of focus, will have low clamping power, high dynamic range (ratio of damage threshold to clamping level), while maintaining low insertion loss.

The laser-induced thermal lensing in liquid CS_2 can also be exploited for optical power limiting. Using the Z-scan to locate the optimum position of focus in a 2.4 cm CS_2 cell, we have built a power limiter that is effective against nanosecond CO_2 laser pulses, as well as cw sources. A good understanding of the thermal nature of laser-induced lensing gives the designer flexibility to accommodate different pulselengths in various optical trains.

† Supported by a Hughes Aircraft Company doctoral fellowship

REFERENCES

- [1] M. Sheik-Bahae, A.A. Said, and E.W. Van Stryland, "High sensitivity single beam n_2 measurement," *Opt. Lett.*, 14, 955-957 (1989)

- [2] M. Sheik-Bahae, A.A. Said, T.H. Wei, D.J. Hagan, and E.W. Van Stryland, "Sensitive measurement of optical nonlinearities using a single beam," *IEEE JQE*, **26**, 760-769 (1990)
- [3] M. Sheik-Bahae, A.A. Said, D.J. Hagan, M.J. Soileau and E.W. Van Stryland, "Nonlinear refraction and limiting in thick media," *Opt. Engr.*, **30**, 1228-1235 (1991)
- [4] M.J. Soileau, S. Guha, E.W. Van Stryland, "Passive optical limiters," in *Proceedings of the Southwest Conference on Optics*, Proc. SPIE 540, 2-8 (1985)
- [5] A.F. Gibson, M.J. Kent and M.F. Kimmitt, "Photoconductivity in indium antimonide at 10.6 μm wavelength," *J. Phys. D*, **1**, 149-154 (1968)
- [6] D.J. Hagan, E.W. Van Stryland, Y.Y. Wu, T.H. Wei, M. Sheik-Bahae, A.A. Said, K. Mansour, J. Young and M.J. Soileau, "Passive, broadband, high dynamic range semiconductor limiters," in *Materials for Optical Switches, Isolators, and Limiters*, Proc. SPIE 1105, 103-113 (1989)
- [7] S.Y. Auyang and P.A. Wolff, "Free carrier induced third order optical nonlinearities in semiconductors," *JOSA B*, **6**, 595-605 (1989)
- [8] D. Hagan, E.W. Van Stryland, M.J. Soileau and Y.Y. Wu, "Semiconductor optical limiters with wide dynamic range," *JOSA A*, **3**, P105 (1986).
- [9] D. Hagan, E.W. Van Stryland, M.J. Soileau and Y.Y. Wu, "Self-protecting semiconductor optical limiters," *Opt. Lett.*, **13**, 315-317 (1988).
- [10] E.W. Van Stryland, Y.Y. Wu, D.J. Hagan, M.J. Soileau and K. Mansour "Optical limiting with semiconductors," *JOSA B*, **5**, 1980-1988 (1988).
- [11] H. Fossum, W. Chen and B. Ancker-Johnson, "Excess carriers in InSb with a carbon dioxide laser," *Phys. Rev. B*, **8**, 2857-2868 (1973)
- [12] J. Dempsey, J. Smith, G. Holah and A. Miller, "Nonlinear absorption and pulse shaping in InSb," *Opt. Commun.*, **26**, 265-268 (1978)
- [13] S.A. Jamison and A.V. Nurmikko, "Avalanche formation and high intensity infrared transmission limit in InAs, InSb and HgCdTe," *Phys. Rev. B*, **19**, 5185-5193 (1979)
- [14] J. Figueira, C. Cantrell, J. Rink and P. Forman, "Time resolved pump depletion in n-InSb Raman spin-flip laser," *Appl. Phys. Lett.*, **28**, 398-400 (1976)
- [15] T. Nee, C. Cantrell, J. Scott and M. Scully, "Nonlinear optical properties of InSb: Hot electron effects," *Phys. Rev. B*, **17**, 3936-3945 (1978)
- [16] R.B. James, "Carrier multiplication in semiconductors induced by the absorption of high-intensity CO₂ laser light," *J. Appl. Phys.*, **54**, 3220-3235 (1983)
- [17] T. Grave, E. Scholl and H. Wurz, "Optically induced avalanche in InSb," *J. Phys. C*, **16**, 1693-1711 (1983)
- [18] M.P. Hasselbeck, "CO₂ laser driven avalanche ionization in InSb at liquid He temperatures," in *Ultrafast Laser Probe Phenomena in Bulk and Microstructure Semiconductors III*, R. Alfano, ed., Proc. SPIE 1282, 182-193 (1990)
- [19] B. Schwartz, P.M. Fauchet and A.V. Nurmikko, "Nonlinear transmission of picosecond 10.6 μm pulses in InSb," *Opt. Lett.*, **5**, 371-373 (1980)
- [20] R.B. James and Y.-C. Chang, "Absorption saturation of heavy to light hole transitions in p-type InSb," *Phys. Rev. B*, **38**, 9778-9789 (1988)
- [21] B.S. Wherret, "Scaling rules for multiphoton interband absorption in semiconductors," *JOSA B*, **1**, 67-72 (1984)

- [22] E. Yablonovitch and N. Bloembergen, "Avalanche ionization and the limiting diameter of filaments induced by light pulses in transparent media," *Phys. Rev. Lett.*, **29**, 907-910 (1972)
- [23] N. Bloembergen, "Laser induced electric breakdown in solids," *IEEE J. Quant. Elec.*, **10**, 375-386 (1974).
- [24] W.L. Smith, "Laser induced breakdown in optical materials," *Opt. Eng.*, **17**, 489-503 (1978)
- [25] G. Bauer and F. Kuchar, "Impact ionization in heavily doped n-InAs and n-InSb," *Phys.Stat. Sol.*, **13**, 169-177 (1972)
- [26] R.C. Curby and D.K. Ferry, "Impact ionization in narrow gap semiconductors," *Phys. Stat. Sol.*, **319**, 319-328 (1973)
- [27] G.A. Baraff, "Distribution functions and ionization rates for hot electrons in semiconductors," *Phys. Rev.*, **128**, 2507 (1962)
- [28] R.B. James and D.L. Smith, "Theory of nonlinear optical absorption associated with free carriers in semiconductors," *IEEE J. Quant. Elec.*, **18**, 1841-1864 (1982)
- [29] R.K. Jain and M.B. Klein, "Degenerate Four Wave Mixing in Semiconductors," in *Optical Phase Conjugation*, R.A. Fisher, ed., 307-415, Academic Press, Orlando, FL (1983)
- [30] A. Miller, D.A.B. Miller and S.D. Smith, "Dynamic non-linear optical processes in semiconductors," *Adv. Physics*, **30**, 697-800 (1981)
- [31] D. Watkins, D. Phipps and S. Thomas, "Determination of the third order nonlinear optical coefficients of germanium through ellipse rotation," *Opt. Lett.*, **5**, 169-171 (1980)
- [32] J. Wynne and G. Boyd, "Study of optical difference mixing in Ge and Si using a CO₂ laser," *Appl. Phys. Lett.*, **12**, 191-193 (1968)
- [33] M. Sheik-Bahae, D.C. Hutchings, D.J. Hagan and E.W. Van Stryland, "Dispersion of bound electronic nonlinear refraction in solids," *IEEE JQE*, **27**, 1296-1309 (1991)
- [34] M.J. Soileau, W.E. Williams, N. Mansour and E.W. Van Stryland, "Laser-induced damage and the role of self-focusing," *Opt. Engr.*, **28**, 1133-1144 (1989)

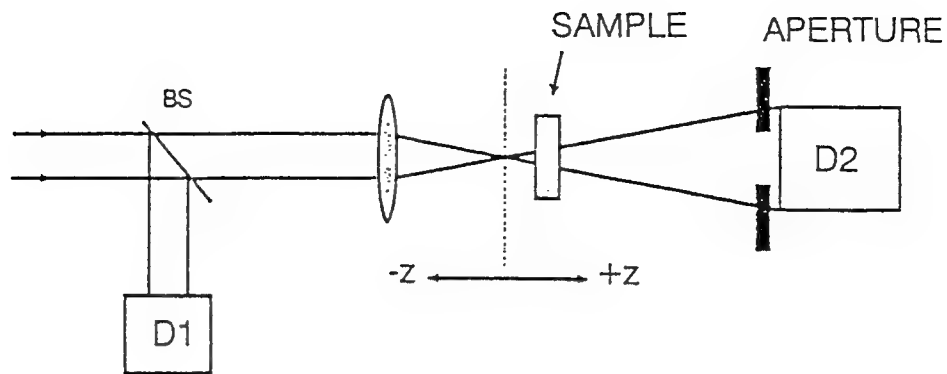


Fig.1. The Z-scan experiment in the closed aperture ($S < 1$) arrangement. The signal on detector D2 is monitored as the nonlinear sample is translated through the focus of a lens. Detector D1 normalizes shot-to-shot variations of the laser beam.

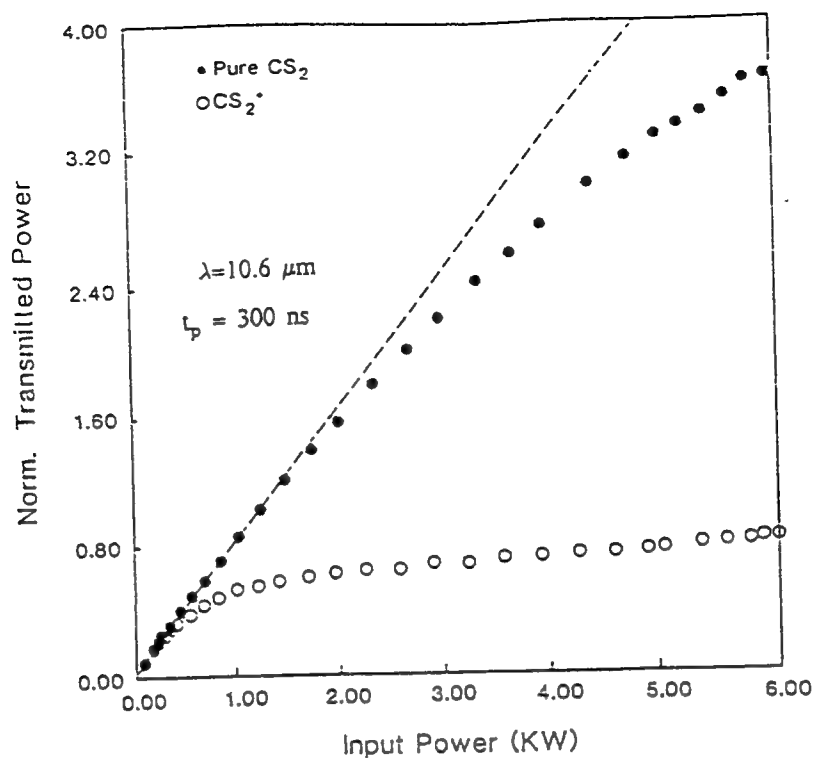


Fig.2. Fluence limiting obtained with pure ($\alpha = 0.22 \text{ cm}^{-1}$) and modified ($\alpha = 2 \text{ cm}^{-1}$) CS_2 . Enhanced absorption dramatically lowers the clamping power.

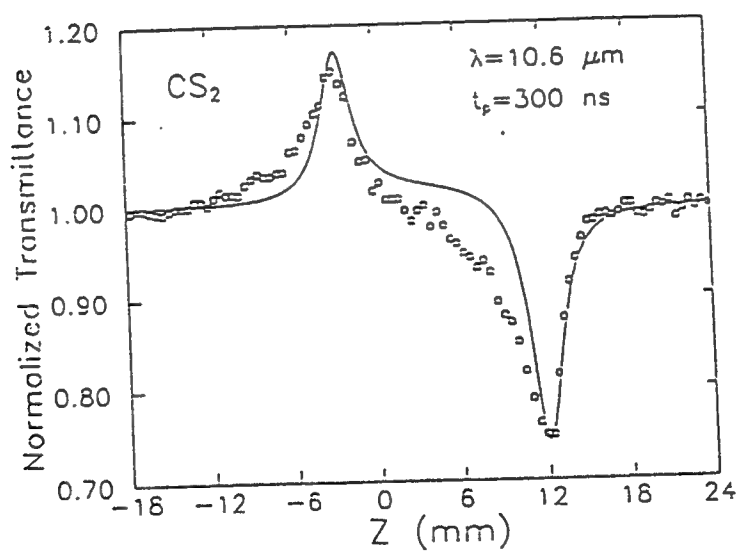


Fig. 3. Characterization of CS_2 using a closed aperture ($S = 0.5$) Z-scan. For optical limiting, the sample is located at the point of transmission minimum.

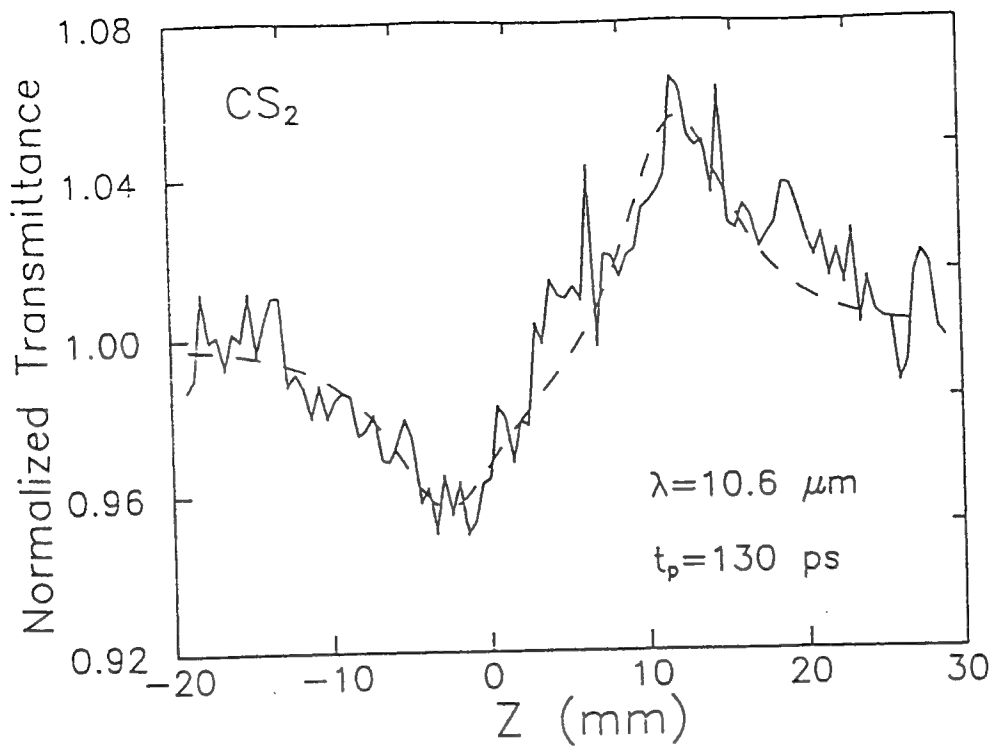


Fig. 4. Closed aperture Z-scan of CS_2 using ps pulses reveals nonlinear refraction due to the Kerr effect.

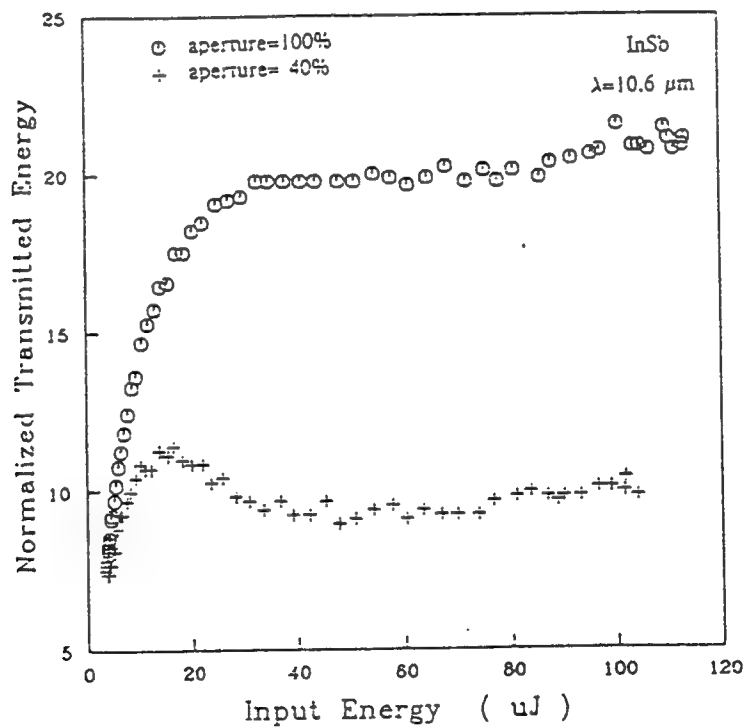


Fig. 5. A 1 mm InSb limiter at 300°K demonstrated with TEA CO_2 laser pulses. A beam clipping aperture illustrates the effect of power re-distribution in the far field. This effect can be used to reduce the fluence (energy/area) on a detector pixel.

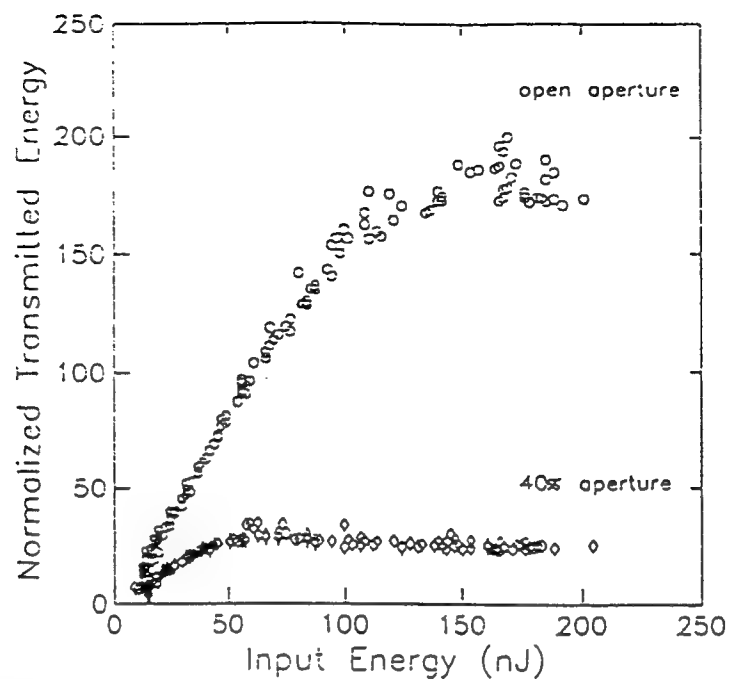


Fig. 6. Power limiting with a 1 mm InSb wafer at 300°K using 60 ps pulses. The upper data set was obtained without an aperture ($S = 1$) and the lower data was found with an aperture set for $S = 0.4$ in the far field in front of the detector.

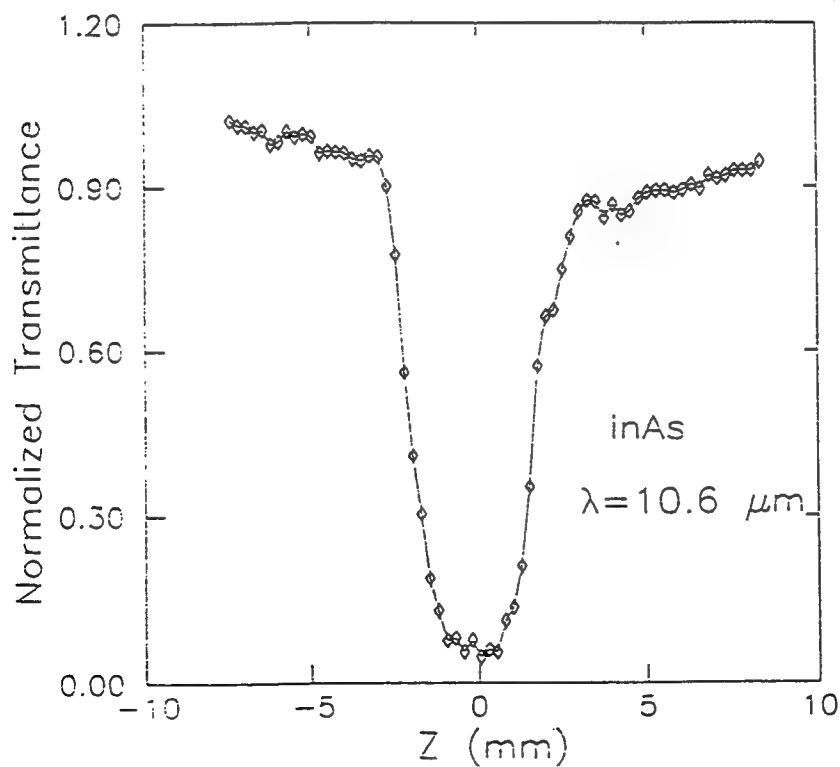


Fig. 7. Z-scan with InAs at room temperature using 80 ps pulses focused to 1.1 GW/cm^2 . The induced absorption is due to laser-driven avalanche ionization.

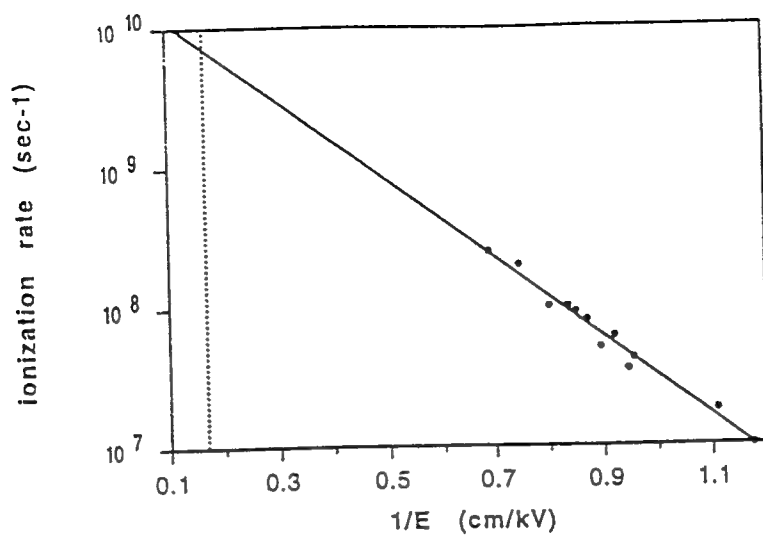


Fig. 8. Measured electron ionization rate in InAs at 300°K obtained by Bauer and Kuchar [25]. A least-squares fit to the data (solid line) permits extrapolation of the ionization rate to the field encountered in the Z-scan measurement (dotted line).

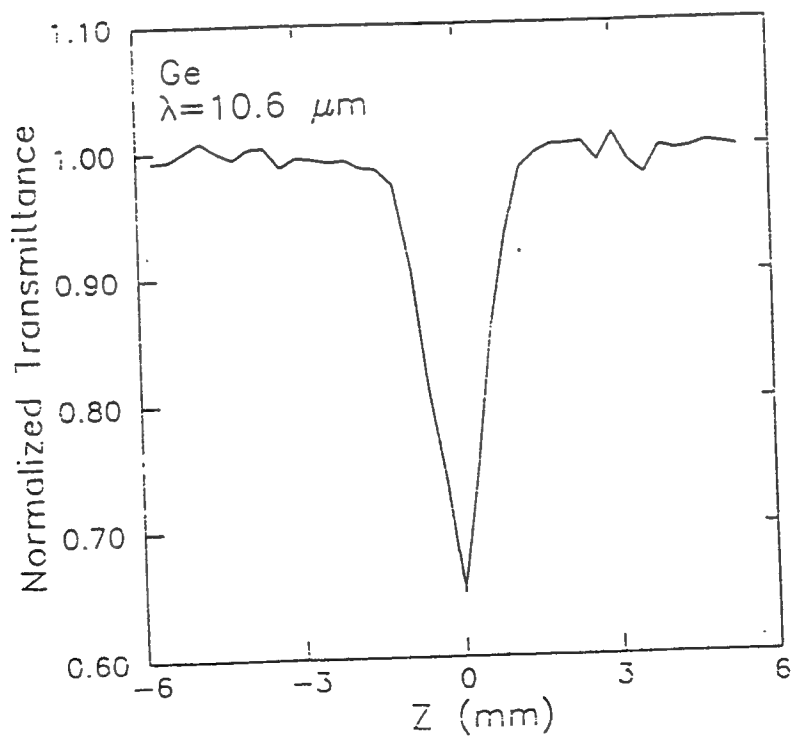


Fig. 9. An open aperture Z-scan of Ge made with 60 ps pulses at 1.5 GW/cm², revealing absorption due to avalanche ionization.

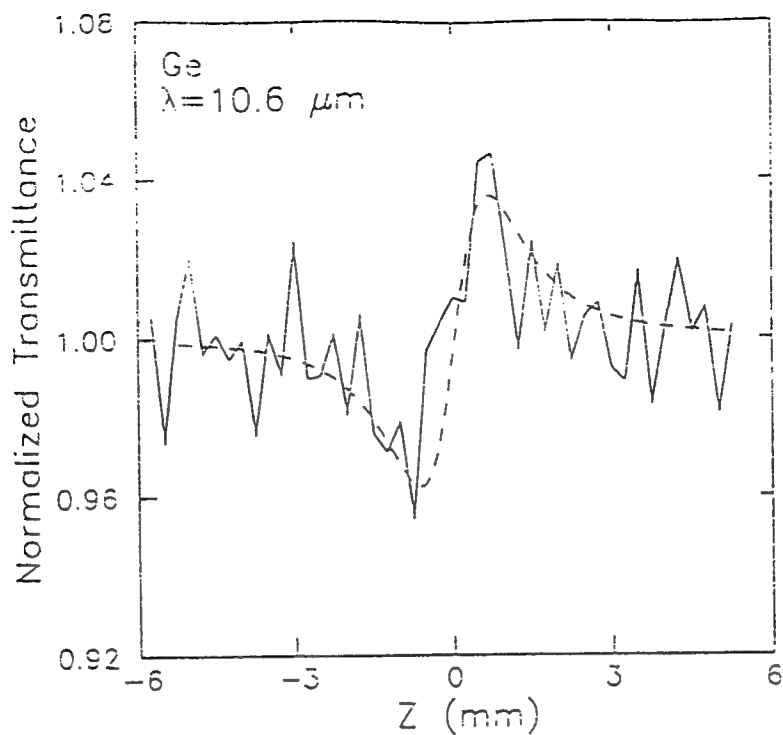


Fig. 10. Closed aperture Z-scan of Ge with 60 ps pulses. The irradiance is reduced to 0.8 GW/cm^2 to eliminate absorption due to avalanche ionization. The peak and valley modulation allow us to deduce a nonlinear index coefficient of $n_2 = 2.7 \times 10^{-10} \text{ esu}$.

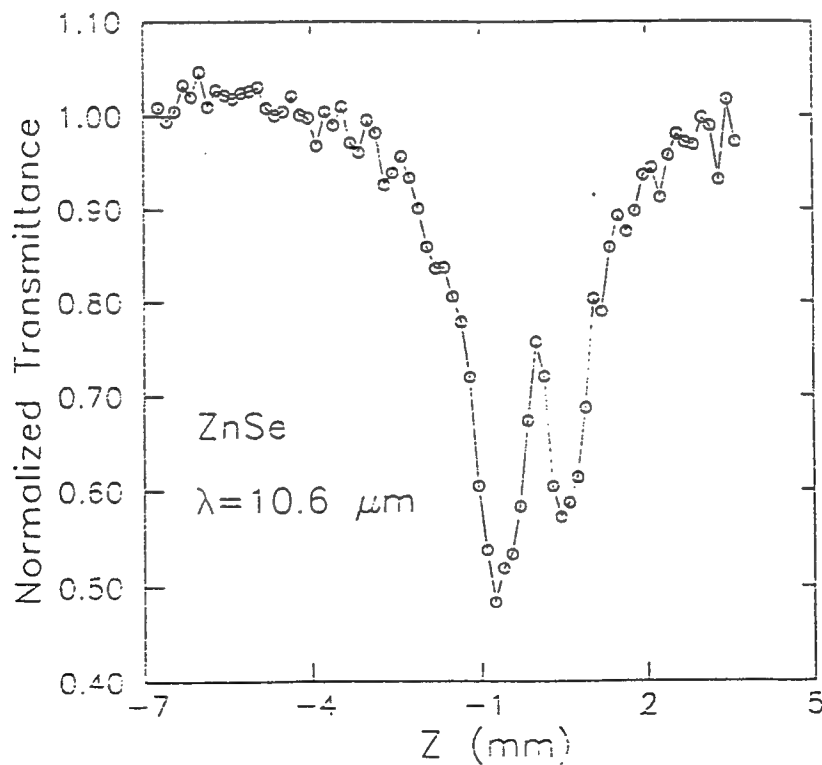


Fig. 11. A Z-scan of ZnSe using 80 ps pulses at an irradiance of 9 GW/cm^2 . Notice the "kink", indicating enhancement of transmission at the position of maximum irradiance.

Laser-induced acoustic phonon gratings in semiconductor thin films

J. Wang, D. C. Hutchings,^{a)} A. Miller,^{b)} and E. W. Van Stryland^{b)}

Center for Research in Electro-optics and Lasers, University of Central Florida, Orlando, Florida 32826

K. R. Welford, I. T. Muirhead,^{c)} and K. L. Lewis

Defense Research Agency, Great Malvern, Worcs. WR14 3PS, United Kingdom

(Received 10 August 1992; accepted for publication 19 January 1993)

Laser induced ultrasonic standing waves are observed in molecular beam deposited ZnSe thin films using the transient grating technique. This observation is attributed to a very short trapping time for single photon absorption in the band tail. The period of the standing wave is used to determine the acoustic phonon velocity in the ZnSe thin film which indicates that it is longitudinal acoustic phonons which are excited.

I. INTRODUCTION

Laser induced ultrasonic waves¹⁻³ have been observed and studied in liquids,⁴ molecular solids,^{1,2} and superconducting thin films⁵ using the transient grating method. The technique uses two time-coincident laser pulses to create an optical interference pattern in the medium. Energy is then transferred to the material by optical absorption or Brillouin scattering, which results in the launching of counter-propagating ultrasonic waves with a wavelength matching that of the original grating. This leads to a standing wave pattern whose oscillations can be probed with an additional time delayed probe pulse. By varying the grating spacing, (by changing the angle between the incident pulses) the acoustic frequency can be continuously tuned. This technique is also referred to as laser-induced phonon spectroscopy (LIPS)³ as it provides a probe of the phonon dispersion.

Coherent acoustic phonon gratings are not observed in bulk semiconductors under normal conditions because optically excited excess carriers usually have (a) relatively long recombination times and (b) high mobilities allowing them to diffuse significant distances before recombining. Either of these effects will inhibit the creation of oscillating ultrasonic standing waves. Acoustic phonons are created in semiconductors from the energy dissipated in nonradiative carrier recombination. In order to produce the necessary coherence of the phonons which will result in an oscillating standing wave (a) carrier diffusion must be restricted to avoid washing out of the grating, and (b) the energy transfer to the lattice must occur on a time scale shorter than the phonon period. When both of these conditions are satisfied a modulating diffracted signal should be observed by the transient grating technique due to the beating of counter-propagating acoustic waves.

In this article we describe the optical generation and detection of acoustic phonon modes in a semiconductor using the transient grating method. The appropriate conditions are created by employing a film of ZnSe microcrys-

tallites with sizes much less than the grating period. Molecular beam deposited (MBD) films of thickness sufficient to allow efficient diffraction of picosecond pulses are used to time resolve the dynamics of the phonon grating. This provides a noncontact method of determining the acoustic phonon velocities.

II. BACKGROUND

The transient grating method is a technique frequently used for measuring and determining the dynamics of optical nonlinearities. Basically, a grating is formed by interfering two coherent light beams on a sample.⁶ This can be accomplished with the two beams incident on the same or opposite sides of the sample. The grating may even be derived from one beam if there is some back reflection within or external to the sample. The optical nonlinearity in the sample results in a corresponding grating modulation in either or both the refractive index and absorption coefficient. This grating in the optical constants can cause the diffraction of a light beam which can be a separate beam or one of those that write the grating (self-diffraction). The amount of diffracted light depends on the grating amplitude and so is a direct measure of the magnitude of the optical nonlinearity (although it gives no information regarding the sign of the nonlinearity). Diffraction from refractive gratings is more commonly observed as efficiencies are typically higher than for absorptive gratings.

In the three beam configuration, if the beam that reads the grating is time delayed, this technique becomes a powerful method for observing the dynamics of optical nonlinearities. For example, by measuring the decay of a carrier induced grating in semiconductors, information can be obtained about carrier diffusion and recombination.⁷

One of the applications of the transient grating technique is laser-induced phonon spectroscopy.³ Here, the optical energy in the grating is transferred into coherent phonons (usually longitudinal) whose wavelength matches that of the optical grating. The mechanism by which these coherent phonons are generated generally depends on whether the sample is optically absorbing or transparent at the laser wavelength. If the sample is absorbing (into vibrational or electronic states) and there is a rapid radia-

^{a)}Present address: Dept. of Electronics and Electrical Engineering, Univ. of Glasgow, Glasgow G12 8QQ, U.K.

^{b)}Also with the Departments of Physics and Electrical Engineering, Univ. of Central Florida, FL.

^{c)}Present address: OCLI, Dunfermline, KY11 5JE, Scotland.

tionless relaxation, there will be local heating at the grating maxima. Thermal expansion then causes the net movement of atoms or molecules away from the interference maxima towards the minima thus setting up the counterpropagating ultrasonic waves. The alternative mechanism for non-absorbing media is that optical energy can be coupled directly into coherent phonons by stimulated Brillouin scattering. Here a photon from one of the writing beams is scattered to create an acoustic phonon and a lower energy photon in the other beam (though still within the spectral bandwidth of the picosecond pulse). The same process also occurs for the other writing beam with the phonon having the opposite wave vector to the first and thus setting up counterpropagating ultrasonic waves. Experimentally, these two mechanisms can be differentiated by the time response with the thermal mechanism giving one diffraction maximum per acoustic cycle and the stimulated Brillouin mechanism giving two diffraction maxima per cycle.³ It should be noted though that in both cases the diffraction signal will be at a minimum at the instant the grating is written and then increase as the material is displaced and strain is induced.

Coherent phonon oscillations have also been optically detected using the excite-probe method with femtosecond pulses in GaAs,⁸ single crystals of Sb, Bi, Te and Ti_2O_3 ,⁹ and thin-film $\text{YBa}_2\text{Cu}_3\text{O}_{6+x}$,¹⁰ where the excite pulse acts as an impulse and the probe detects the "ringing" of the lattice. This technique generally excites optical phonon modes, hence the requirement that the optical pulses be less than a phonon period means that optical pulses typically have to be less than 100 fs in duration.

Absorption of light of wavelengths close to the band edge in semiconductors can lead to a change in the optical properties usually through free-carrier or thermal effects. The excitation of electrons from valence to conduction band can change the optical properties, e.g., by inhibiting further transitions or phenomena associated with the change in conductivity (e.g., photorefractive effect, self-electro-optic effect devices). For wavelengths longer than the fundamental absorption edge in semiconductors, free-carrier effects normally give rise to a reduction in the refractive index. Thermal expansion leads to an increasing band gap with temperature whereas changing the phonon population leads to a decreasing band gap with temperature.¹¹ In most semiconductors it is the latter of these effects which dominates and the band gap decreases with increasing temperature giving an increase in the refractive index.

III. EXPERIMENT

The samples used in this experiment are ZnSe thin films of thickness 5 μm grown by molecular beam deposition on glass substrates.¹² This method was developed for the growth of high quality, high density optical coatings.

Films were grown in a Vacuum Generators load-locked ultrahigh vacuum system fitted with Knudsen sources and *in situ* surface diagnostics. The zinc selenide source was ultrahigh purity polycrystalline ZnSe which had previously been prepared by chemical vapor deposition

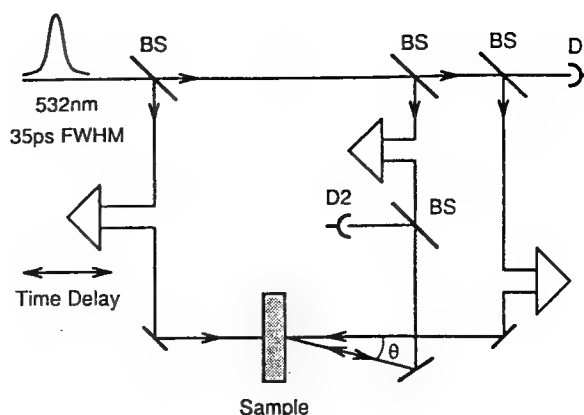


FIG. 1. Standard backward degenerate-four-wave-mixing setup. The forward pump and probe pulses are time coincident on the sample and create a grating which is probed by a variably time delayed backward pump pulse.

from a mixture of zinc vapor and hydrogen selenide. The source material was contained within a high purity graphite crucible which was carefully outgassed following baking of the entire deposition chamber at 180 °C. The deposition process allows the deposition of films with a high degree of perfection. Thick films could be produced which do not delaminate from the substrate and which have a high degree of optical stability as a consequence of lack of open porosity. Interference filters grown by this technique have been used in optical bistability experiments and show higher stability than those produced by more conventional techniques.¹³

MBD ZnSe films on glass substrates show extremely low photoluminescence efficiencies indicating that the primary relaxation of the carriers occurs through traps. This implies a very short relaxation time for the carriers. Time resolved photoluminescence studies in this type of material confirm this with no photoluminescence being visible on a time resolution of 10 ps.¹⁴

Three samples were used in the present experiment. These were grown at substrate temperatures of 20, 100, and 300 °C. Cross-sectional transmission electron micrographs indicate a dense columnar polycrystalline structure with the columns growing perpendicular to the surface and having a length equal to the film thickness. Higher substrate temperatures produce larger microcrystalline diameters. Crystallite diameters measured for MBD ZnSe on GaAs are ~25 nm for room temperature growth and ~100 nm for a growth temperature of 190 °C.¹² Similar measurements for MBD ZnSe on glass are unavailable due to the inability to cleave the sample but microcrystalline diameters are not anticipated to be much larger than those grown on GaAs.

The experimental geometry is the standard backward degenerate-four-wave-mixing geometry as shown in Fig. 1. The input pulses are at a wavelength of $\lambda = 0.532 \mu\text{m}$ produced by frequency doubling a Q-switched mode-locked Nd:YAG laser (Quantel model YG401C) with a single pulse switched out at a repetition rate 10 Hz. The pulse width, which was deduced from an autocorrelation of the

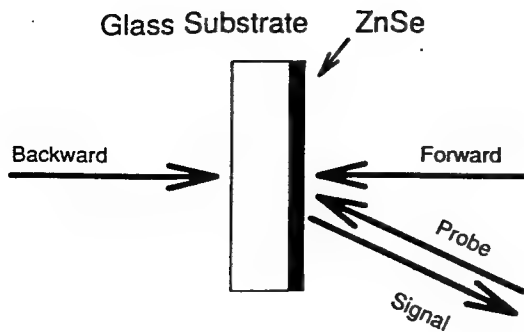


FIG. 2. Sample geometry. The time coincident forward pump and probe pulse writes a transverse grating in the ZnSe film which is read by the time delayed backward pump incident through the substrate.

fundamental pulses, was 35 ps full width at half-maximum (FWHM). The spatial profile of the pulses consisted of a single transverse mode of Gaussian form. In this experimental setup, the 0.532 μm pulses are split into three separate pulses; forward pump, backward pump, and probe. All three pulses pass through separate delay stages which can be adjusted to ensure the forward pump and probe are temporally coincident and all three pulses are spatially coincident at the sample. The backward pump and forward pump are counterpropagating with approximately the same energy. The probe enters the sample at an angle with respect to the forward pump, with 5% of the backward pump energy (Fig. 2). The beam radii ($1/e^2$ irradiance) at the sample position are 0.73 mm for the backward pump, 0.61 mm for the forward pump, and 0.43 mm for the probe. Typical energies for the backward pump pulses were around 150 μJ (corresponding to a peak irradiance of 0.47 GW/cm^2). The two time-coincident laser pulses (forward pump and probe) are crossed inside the sample to setup an optical interference pattern with grating period

$$\Lambda = \frac{\lambda}{2n \sin(\theta/2)}, \quad (1)$$

where n is the linear refractive index of the material and θ the angle between forward pump and probe beams inside the material. By altering the angle between the forward pump and probe beams, the grating spacing can be adjusted. If some nonlinear mechanism exists in the material whereby intense light causes a change in the optical properties of the material, the backward pump will experience diffraction into the counterpropagating direction of the probe beam. The dependence of the diffracted signal strength on delay allows a measurement of the decay of the grating modulation.

Each data point is an average of ten shots, taken automatically by computer. While taking the data, the pulse width and amplitude are also monitored and windows of $\pm 5\%$ have been set for both pulse width and energy in order to increase the signal to noise level. The signals are detected by integrating silicon photodiodes with a peak sample and hold circuitry. A calcite polarizer and half-wave plate were used to adjust the total input energy.

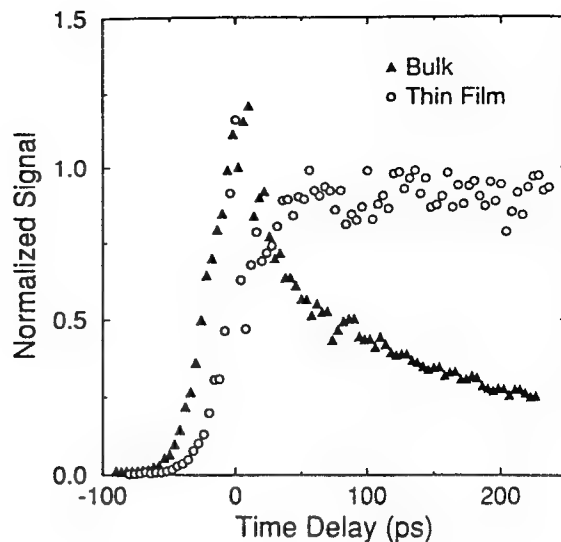


FIG. 3. Comparison of the diffracted signal as a function of time delay (up to 200 ps) for bulk polycrystalline and MBD thin film ZnSe.

IV. RESULTS

Figure 3 shows a comparison of the time response of the diffracted signal obtained from a MBD thin film ZnSe sample to that obtained in bulk polycrystalline ZnSe using the same experimental setup. The diffracted signal from bulk ZnSe shows a peak at zero delay which is the auto-correlation of the laser pulse attributed to the combined effects of the instantaneous bound electronic nonlinear refraction n_2^{15} and two photon absorption. This is followed by an exponentially decaying tail arising from the refractive index change associated with bandfilling by free carriers generated by two-photon absorption.¹⁶ The decay time of the tail is set by a combination of recombination and ambipolar diffusion of the free carriers washing out the grating.

In contrast, the diffracted signal from the thin film of ZnSe is basically an integration of the input pulse and shows no signs of decay on comparable time scales (< 200 ps). There is some evidence of a coherence spike at zero delay which is due to self-diffraction of the backward pump from the grating produced by this pulse and the probe pulse. This may arise from the free electronic contribution to the nonlinearity but needs further investigation.

The lack of an observed decay on these time scales is consistent with a thermal grating. The absorption tail at the band edge is quite extensive in the thin film MBD ZnSe¹³ and a substantial density of free carriers can be generated by single photon absorption at 532 nm. These carriers become trapped on time scales on the order of or less than the pulse width as indicated by photoluminescence studies.

The grating modulation is generated along the thin film and so if carrier diffusion were to wash out the grating, it would need to be in a direction perpendicular to the crystallite columns. Using a diffusion coefficient of 4.5 cm^2/s for ZnSe¹⁶ gives a time scale of around a picosecond for the carriers to reach a 25 nm microcrystallite boundary.

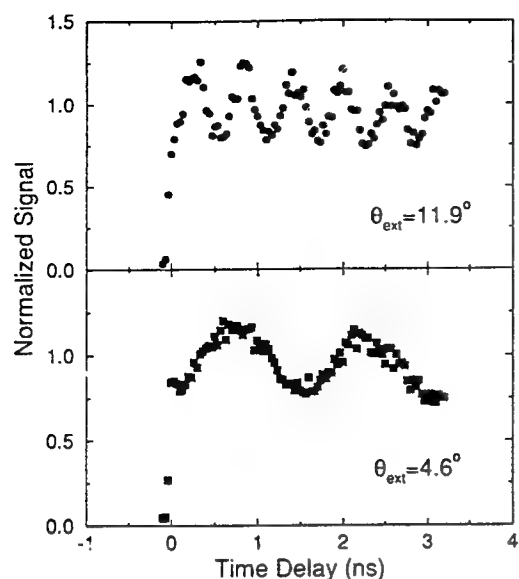


FIG. 4. Diffraction signal as a function of time delay (up to 3 ns) in MBD thin film ZnSe for two different external angles between the forward pump and probe beams as indicated. Changing the external angle results in a variation in the grating spacing and so varies the wave vector of the excited phonon mode.

The crystallite column diameters are much smaller than the grating spacings employed. The trapping of the carriers in defects at these boundaries is consistent with experimental observation. The excess energy of the electrons is all deposited as heat to produce a thermal grating.

The diffracted signal from the thin film MBD ZnSe on longer time scales is shown in Fig. 4 for two different grating spacings using the sample grown at 300 °C. These signals show an oscillating signal superimposed on a background which may show some signs of a slow decay. The period of the oscillation is 1.65 ns for an external input angle of 4.6° (corresponding to a grating spacing of $\Lambda = 6.6 \mu\text{m}$) and 0.60 ns for an external input angle of 11.9° ($\Lambda = 2.6 \mu\text{m}$). The ratio of the magnitude of the oscillation to the background signal seems to be independent of angle. Similar data is obtained for samples corresponding to different growth temperatures Fig. 5 indicating there is no dependence on the microcrystalline diameter (at least in the limit where the diameter is much smaller than the grating spacing).

The oscillating diffraction signal results from an ultrasonic standing wave which is set up in the film (laser induced phonon grating).³ The transfer of energy to the lattice is spatially inhomogeneous, matching the original sinusoidal optical interference pattern. Thus the atoms will be more energetic at the grating peaks causing a net movement of the atoms from the grating peaks to the troughs. This movement results in the initiation of two counter-propagating sound waves which can also be described in terms of a standing wave.¹ This standing wave has exactly the same spatial separation as the original light grating from the interference of the forward pump and probe beams. The fact that the coherence of this ultrasonic standing wave is so evident indicates that energy is transferred

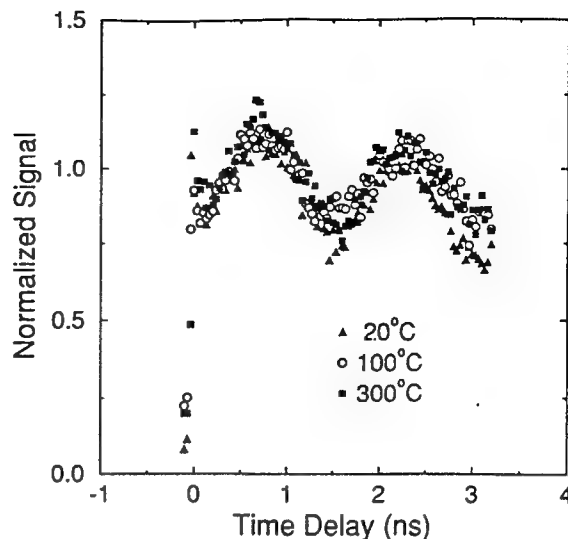


FIG. 5. Diffraction signal as a function of time delay for three different MBD thin film ZnSe samples grown at the different substrate temperatures indicated. The signal shows no dependence on the growth conditions.

from the excited carriers to the lattice on very short time scales (certainly much shorter than the oscillation period).

The period of the oscillation can be used to determine the speed of sound along the ZnSe thin film given that the grating spacing is known. For the 4.6° external angle measurement this gives the speed of sound as $v = 4000 \text{ m/s}$ and for the 11.9° external angle measurement, $v = 4300 \text{ m/s}$. These results are summarized in Table I. These measurements are in agreement with tabulated values for longitudinal acoustic phonon velocities in bulk ZnSe which lie in the range 4000–4600 m/s.¹⁷ This is to be contrasted with the reported observation of coherent longitudinal optical phonons in GaAs using a femtosecond excite-probe technique.⁸

The slowly decaying background signal is due to diffraction from a refractive grating associated with the thermal grating. This can be considered as an incoherent phonon effect. Most semiconductors have a positive $\partial n / \partial T$ at frequencies in the vicinity of the band edge including bulk and thin film ZnSe,¹³ hence the grating consists of an increase in refractive index. The energy for the temperature rise is also obtained from the release of energy from the optically excited carriers. The time evolution of the carrier density N and temperature rise ΔT is described using the coupled partial differential equations

TABLE I. Summary of the data on the two different grating spacings examined. For the external angles indicated, the grating spacing was calculated from Eq. (1), the period is from the observed oscillation in the time-delayed diffracted signal from which the speed of sound is inferred.

θ_{ext}	Λ	Period	Acoustic velocity
4.6°	6.6 μm	1.65 ns	4000 m/s
11.9°	2.6 μm	0.60 ns	4300 m/s

$$\frac{\partial N}{\partial t} = -\frac{N}{\tau_r}, \quad (2)$$

$$\frac{\partial(\Delta T)}{\partial t} = \frac{1}{\rho c} \left[\kappa \nabla^2(\Delta T) + \frac{E_r N}{\tau_r} \right], \quad (3)$$

with the initial conditions $\Delta T(t=0)=0$ and $N(t=0)=N_0 \sin^2(\pi x/\Lambda)$. The solution of this is

$$\Delta T = T_0(1 - e^{-t/\tau_r}) + T_0 \frac{(e^{-t/\tau_r} - e^{-t/\tau_{td}})}{(1 - \tau_r/\tau_{td})} \cos\left(\frac{2\pi x}{\Lambda}\right), \quad (4)$$

where the thermal time constant τ_{td} is given by

$$\tau_{td} = \frac{\rho c \Lambda^2}{4\pi^2 \kappa}, \quad (5)$$

and we define $T_0 = 2E_r N_0 / \rho c$. The recombination of the carriers occurs with a time constant τ_r and releases a quantity of energy E_r per carrier to the lattice. ρ , c , and κ are the density, specific heat capacity, and thermal conductivity, respectively, which for bulk polycrystalline ZnSe at room temperature are tabulated as $\rho = 5.27 \text{ g/cm}^3$, $c = 0.081 \text{ cal/(g } ^\circ\text{C)}$, and $\kappa = 0.043 \text{ cal/(cm s } ^\circ\text{C)}$.¹⁸

The observed decay of the background signal will depend on the recombination of the trapped carriers and thermal diffusion washing out the grating. It can be seen in Fig. 4 that the relative contribution to the diffraction efficiency from the ultrasonic standing wave does not depend on the grating spacing. Since the thermal diffusion time constant τ_{td} is proportional to the square of the grating spacing [Eq. (5)], and the temperature modulation of the grating is proportional to (and so the diffraction efficiency is dependent on) the quantity $(1 - \tau_r/\tau_{td})^{-1}$ [Eq. (4)], it can be concluded that $\tau_{td} \gg \tau_r$ and the observed decay of the thermal grating is completely dominated by thermal diffusion. Hence, Eq. (4) can be simplified to

$$\Delta T = T_0 \left[(1 - e^{-t/\tau_r}) + e^{-t/\tau_{td}} \cos\left(\frac{2\pi x}{\Lambda}\right) \right]. \quad (6)$$

Using the above constants for bulk ZnSe gives thermal time constants τ_{td} of 120 and 17 ns for our two grating spacings using Eq. (5), which is consistent with the experimental observations although the limited delay times prevent an accurate estimation of these time constants. This simplified analysis is for a bulk material (of infinite extent) with no net heat diffusion in the beam propagation direction. Obviously this is not quite the case for a thin film on a glass substrate. However, as the ZnSe thermal conductivity is much larger than for the glass, and the film thickness is of the same order as the grating spacing, it will be the direct transverse route along the film that dominates the decay of the thermal grating rather than any route for the heat diffusion through the glass substrate. Hence, this simplified model is reasonable.

It can be seen from Fig. 4 that the oscillating and background components of the diffraction signal combine together in such a fashion that the overall diffraction efficiency shows an initial increase. It has already been noted that the background (thermal) component is associated

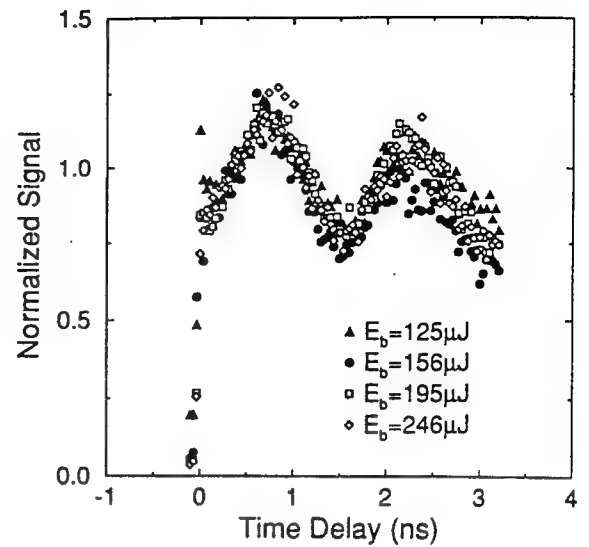


FIG. 6. Diffraction signal as a function of time delay for four different optical energy levels as shown. The optical power level is varied before the beam splitters and so is equally varied in all three beams. The signal is normalized by dividing by the cube of the relative optical input energy. As the normalized signal is identical in all four cases it can be concluded that no saturation of the nonlinearity is evident at these pulse energies.

with a refractive index increase. The observed form of the signal could arise with the oscillating component initially at a minimum and also giving an increase in refractive index. This can be attributed to the atoms being initially equidistant but as they move due to thermal expansion (thereby launching the standing longitudinal acoustic wave), the resulting larger spacing at the grating maximum gives a refractive index increase (and smaller spacing at the minimum gives a decreased refractive index). It should be noted though that the same form of signal could arise if the oscillating component has opposite sign but is initially at a maximum.

To check if the nonlinearity shows any saturation effects (i.e., shows the same power dependence as a third order nonlinearity), the input energy was varied. Figure 6 shows the normalized diffraction signal against the delay time of the backward pump. The normalization process involves dividing the diffraction efficiency by the input energy cubed since the input energy is adjusted before the beam splitters which maintain a constant energy ratio between the three beams. As the normalized signals are identical, it can be concluded that both the coherent acoustic phonon process and the background thermal grating show the same power dependence as a third order nonlinearity with no indication of saturation. Hence, over these optical energy ranges the refractive index change is directly proportional to the optical energy. This implies that the carrier density generated is proportional to the optical energy, the transfer of energy from carriers to acoustic phonons is density independent and shows no saturation of the traps, and the resulting temperature rise is small enough to give a linear dependence of the refractive index on temperature.

V. CONCLUSIONS

Transient grating measurements were performed on high quality MBD ZnSe films on glass substrates. Using 35 ps pulses at near band gap resonance no evidence of free-carrier induced optical nonlinearities were observed. This is attributable to fast trapping of the photogenerated carriers at the boundaries of the microcrystallites. This process results in a rapid transfer of energy into the lattice such that a coherent ultrasonic standing wave is produced. While the same phenomena has been observed in various media, it is rare for it to be observed in semiconductors since ambipolar carrier diffusion usually washes out the excitation grating before the energy is transferred to the lattice.

This LIPS technique provides a noncontact means of determining the acoustic phonon dispersion. At present only the acoustic velocity has been determined for the thin film ZnSe but similar measurements using longer time scales and shorter grating spacings may allow a more detailed determination of the acoustic phonon dispersion curve.

It is interesting to speculate whether the same technique could be applied to other semiconductors. Certainly thermo-optic coefficients in the vicinity of the band edge of most semiconductors are of comparable magnitude. It would be necessary to prevent the diffusion of energy before it is transferred to the lattice. This should be possible by introducing a higher density of impurities or defects to reduce the free-carrier relaxation time. This reduction in relaxation time has been demonstrated by ion-bombardment¹⁹ and by low temperature molecular beam epitaxial growth.²⁰ It also may be possible to use quantum well material in a geometry where the wells are parallel to the grating. Another approach may be to highly excite the carriers given that electrons and holes thermalize with the lattice on a time scale typically of a few picoseconds and this excess energy could result in a LIPS signal superimposed on the usual carrier induced diffraction signal. How-

ever, as the carriers would be excited well into the band, absorption coefficients would be high necessitating the use of thin film samples.

ACKNOWLEDGMENTS

We acknowledge the Defense Advance Research Projects Agency for support of this research and the collaboration between CREOL and DRA (Malvern). We thank D. J. Hagan for valuable discussions.

- ¹K. A. Nelson, D. R. Lutz, M. D. Fayer, and L. Madison, *Phys. Rev. B* **24**, 3261 (1981).
- ²K. A. Nelson, R. Casalegno, R. J. Dwayne Miller, and M. D. Fayer, *J. Chem. Phys.* **77**, 1144 (1982).
- ³M. D. Fayer, *IEEE J. Quantum Electron.* **QE-22**, 1437 (1986).
- ⁴G. Eyring and M. D. Fayer, *J. Chem. Phys.* **81**, 4314 (1984).
- ⁵C. D. Marshall, I. M. Fishman, and M. D. Fayer, *Phys. Rev. B* **43**, 2696 (1991).
- ⁶H. J. Eichler, *Opt. Acta* **24**, 631 (1977).
- ⁷H. J. Eichler and F. Massmann, *J. Appl. Phys.* **53**, 3237 (1982).
- ⁸G. C. Cho, W. Kütt, and H. Kurz, *Phys. Rev. Lett.* **65**, 764 (1990).
- ⁹T. K. Cheng, J. Vidal, H. J. Zeiger, G. Dresselhaus, M. S. Dresselhaus, and E. P. Ippen, *Appl. Phys. Lett.* **59**, 1923 (1991).
- ¹⁰J. M. Chwalek, C. Uher, J. F. Whitaker, and G. A. M. J. A. Agostinelli, *Appl. Phys. Lett.* **58**, 980 (1991).
- ¹¹Y. Tsay, B. Bendow, and S. S. Mitra, *Phys. Rev. B* **8**, 2688 (1973).
- ¹²K. L. Lewis, I. T. Muirhead, A. M. Pitt, A. G. Cullis, N. G. Chew, A. Miller, and T. J. Wyatt-Davies, *Appl. Opt.* **28**, 2785 (1989).
- ¹³Y. T. Chow, B. S. Wherrett, E. Van Stryland, B. T. McGuckin, D. Hutchings, J. G. H. Mathew, A. Miller, and K. Lewis, *J. Opt. Soc. Am. B* **3**, 1535 (1986).
- ¹⁴G. S. Buller (private communication).
- ¹⁵M. Sheik-Bahae, D. C. Hutchings, D. J. Hagan, and E. W. Van Stryland, *IEEE J. Quantum Electron.* **QE-27**, 1296 (1991).
- ¹⁶E. J. Canto-Said, D. J. Hagan, J. Young, and E. W. Van Stryland, *IEEE J. Quantum Electron.* **QE-27**, 2274 (1991).
- ¹⁷Landolt-Börstein, *Numerical Data and Functional Relationships in Science and Technology* (Springer, Berlin, 1982), Vols. 17a and 17b of Group III.
- ¹⁸S. Musikan, *Optical Materials: An Introduction to Selection and Application* (Marcel Dekker, New York, 1985).
- ¹⁹Y. Silberberg, P. W. Smith, D. A. B. Miller, B. Tell, A. C. Gossard, and W. Wiegmann, *Appl. Phys. Lett.* **46**, 701 (1985).
- ²⁰W. H. Knox, G. E. Doran, M. Asom, G. Livescu, R. Leibenguth, and S. N. G. Chu, *Appl. Phys. Lett.* **59**, 1491 (1991).

SPIE Vol. 2114
444-468, 1993SPIE
proceedings

Characterization of nonlinear optical materials

E.W. Van Stryland*, M. Sheik-Bahae, A.A. Said, D.J. Hagan* and M.J. Soileau*

CREOL

Center for Research and Education in Optics and Lasers
University of Central Florida, Orlando, FL 32816

ABSTRACT

We discuss the characterization of nonlinear optical processes that give rise to changes in the absorption coefficient and refractive index. We primarily concentrate on methods for determining the dominant nonlinearities present in condensed matter and the responsible physical mechanisms. In extensive studies of a wide variety of materials we have found that there is seldom a single nonlinear process occurring. Often several processes occur simultaneously, sometimes in unison, sometimes competing. It is necessary to experimentally distinguish and separate these processes in order to understand and model the interaction. There are a variety of methods and techniques for determining the nonlinear optical response, each with its own weaknesses and advantages. In general, it is advisable to use as many complementary techniques as possible over a broad spectral range in order to unambiguously determine the active nonlinearities. Here we concentrate on the use of nonlinear transmittance, Z-scan and degenerate four-wave mixing experiments as applied to polycrystalline and single crystal semiconductors and dielectric materials.

* also with the Departments of Physics and Electrical and Computer Engineering

I. INTRODUCTION

Numerous techniques are known for measurements of nonlinear refraction (NLR) and nonlinear absorption (NLA) in condensed matter. As the names imply, NLR describes optically induced changes in the refractive index of a material, while optically induced changes in absorption are categorized as NLA. Nonlinear interferometry [1,2], degenerate four-wave mixing (DFWM) [3], nearly-degenerate three-wave mixing [4], ellipse rotation [5], beam distortion, [6,7] beam deflection [8], and third-harmonic generation [9], are among the techniques frequently reported for direct or indirect determination of NLR. Z-scan is a single beam technique for measuring the sign and magnitude of NLR indices and NLA coefficients [10,11], which offers simplicity as well as high sensitivity. Other techniques for measuring NLA include transmittance [12], calorimetry [13], photoacoustic [14], and excite-probe [15] methods.

Despite the wide range of available methods, it is rare that any single experiment will completely determine the physical processes behind the nonlinear response of a given material. The most important point to be made in this paper is that a single measurement of the nonlinear response of a material, at a single wavelength, and a single pulsewidth may give very little information on the material. In general such a measurement should not be used to judge the device performance of a material or to compare one material to another. We will elaborate on this point by using data for semiconductors (eg. ZnSe) and dielectric materials (eg. BaF₂). The importance of the pulsewidth and wavelength dependence of the nonlinear response will be demonstrated through these examples. We begin with a background description of the consequences of NLA and NLR in section II. Section III is divided into three subsections covering the experimental techniques of transmittance, Z-scan and DFWM. Each subsection gives a description of the experimental technique and experimental results along with the physical interpretation for the example materials. Section IV describes the importance of determining and understanding the frequency dependence of the nonlinearities and section V contains brief conclusions.

II. BACKGROUND

Nonlinear absorption directly affects the amplitude of the propagating electric field while NLR directly affects the phase. However, during propagation, phase changes propagate to give spatial (and temporal) amplitude changes. This can be seen as the coupling of phase and amplitude in the differential equation describing this propagation (i.e. the wave equation). A great simplification results by making the "thin sample approximation". In this approximation we can separate the wave equation into an equation for the phase ϕ , and an equation for the irradiance, I , as a function of the depth z within the sample. We write the electric field as $E = A\sqrt{I/n} \text{Re}[e^{i\phi} e^{i(kz-\omega t)}]$ where k is the wave number and A is a material independent constant of proportionality. The thin sample approximation allows us to separate phase and amplitude propagation within the nonlinear material by assuming that the sample is thin compared to any changes in the laser beam irradiance distribution due to linear and nonlinear propagation effects. That is, the sample is thin compared to the depth of focus of the beam (i.e. the diffraction length), and compared to distances in which a nonlinearly induced phase distortion can propagate to give amplitude distortion.[16] By choosing the sample thickness and focusing geometry correctly this approximation can be satisfied. If this assumption is not valid the full wave equation must be solved numerically including both spatial and temporal beam characteristics. This often requires a supercomputer. Throughout this paper, we assume the thin sample approximation to be valid. Experimentally the requirement is that the sample thickness L is less than the diffraction length, $Z_0 = \pi w_0^2/\lambda$ where w_0 is the half-width at the e^{-2} of maximum (HW1/ e^2M) of the irradiance distribution and λ is the wavelength in air. In addition, irradiances must be used that give integrated phase shifts less than approximately 2π . This situation is also known as "external self-action".[16,17]

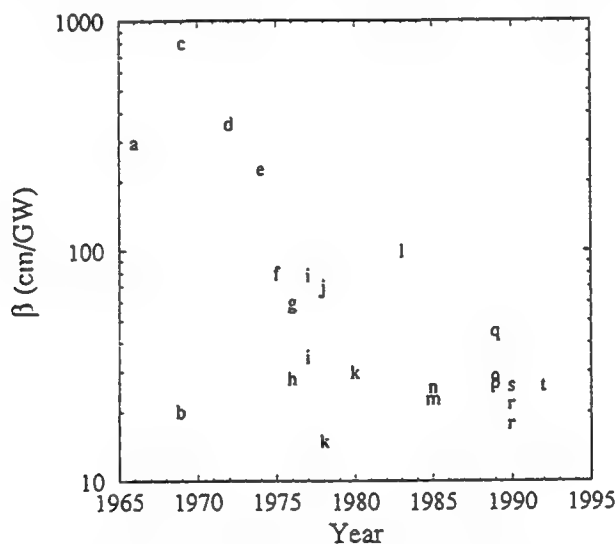


Figure 1. The two-photon absorption coefficient β as a function of year published for GaAs: a [41]; b [42]; c [43]; d [44]; e [45]; f [46]; g [47]; h [48]; i [49]; j [50]; k [51]; l [52]; m [12]; n [53]; o [54]; p [55]; q [56]; r [57]; s [58]; t [25].

Nonlinear absorption and refraction always coexist (although with different spectral properties) as they result from the same physical mechanisms. They are connected via dispersion relations similar to the usual Kramers-Kronig relations that connect linear absorption to the linear index (or, equivalently, relate the real and imaginary parts of the linear susceptibility).[18-21] The physical processes that give rise to NLA and the accompanying NLR include "ultrafast" bound electronic processes and "excited state" processes, where the response times are dictated by the characteristic formation and decay times of the optically induced excited states. Ultrafast processes include multiphoton absorption [12, 19], stimulated Raman scattering [22] and AC-Stark effects [19, 20]. Excited-state nonlinearities can be caused by a variety of physical processes including absorption saturation [22], excited-state absorption in atoms and molecules [23] or free-carrier absorption in

solids [24,25], photochemical changes [26], as well as defect and color center formation [27]. The above processes can lead to increased transmittance with increasing irradiance (eg. saturation, Stark effect) or decreased transmittance (eg. multiphoton absorption, excited-state absorption). The key to distinguishing these processes is to pay particular attention to the temporal response. One way of achieving this is the use of pulsewidths much shorter than the decay times of the excited states. As we shall show, in this regime, the excited-state nonlinearities are fluence (ie. energy per unit area) dependent, while the ultrafast effects remain irradiance dependent.

It is important to note early in this paper the importance of accurately measuring the laser mode and pulse parameters. For example, two-photon absorption (2PA) is irradiance dependent. Thus, given the pulse energy, we need to know both the beam area (i.e. spatial beam profile) and the temporal pulse width (i.e. temporal shape) in order to determine the irradiance. Any errors in the measurement of irradiance translate to errors in the determination of the 2PA coefficient, β . Similar comments apply to other nonlinearities. Figure 1 shows a plot of $\beta(\text{cm/GW})$, on a semilogarithmic scale, as a function of year published in the literature for GaAs. It has been established that these large differences are not due to differences in the materials, but are due to experimental problems and interpretation errors. Clearly, there are a great number of pitfalls for experimenters in NLO.

II.1 Nonlinear absorption:

We will primarily limit our discussion to the increasing loss from two-photon absorption (2PA) and photogenerated excited-state absorption (ESA). The losses from 2PA occur in solids when the photon energy, $\hbar\omega$, is larger than one-half the band-gap energy, E_g . The equation describing 2PA (a third-order response) of a beam of irradiance I as a function of depth z in a material is;

$$\frac{dI}{dz} = -(\alpha_0 + \beta I)I, \quad (1)$$

where β is the 2PA coefficient, and the equation includes residual linear absorption of coefficient α_0 . This linear absorption in solids for $\hbar\omega < E_g$ can come from defects, impurities or band tailing and can often be ignored in good quality materials.

Once absorption has taken place, electrons are excited across the energy gap and are available to subsequently absorb linearly. In semiconductors this linear absorption process is known as free-carrier absorption (FCA) and also includes intraband absorption of holes between light and heavy hole bands. In atoms or molecules this process is referred to as ESA. For pulses longer than a few picoseconds (determined by electron-phonon scattering rates) how the carriers were originally excited is irrelevant to the subsequent FCA. However, the equations governing the transmitted irradiance, and the order of the nonlinear response, are intimately tied to the carrier generation process. If linear absorption (α_0) creates the carriers (as, for example, in a thin indirect-gap material [24], doped semiconductor, or organic [23]) the equation governing I (ignoring 2PA) becomes,

$$\frac{dI}{dz} = -(\alpha_0 + \sigma N)I, \quad (2)$$

where σ is the FCA cross section, and N denotes the density of excited carriers produced by linear absorption. The rate of carrier production is given by

$$\frac{dN}{dt} = \frac{\alpha_0 I}{\hbar\omega}. \quad (3)$$

Here $\hbar\omega$ is the incident photon energy used to produce an electron-hole pair. We have ignored all decay and diffusion processes that can reduce the carrier density in writing Eq. 3. In general these processes must be included which can greatly complicate the determination of nonlinear parameters, however, if pulses are short compared to the recombination and diffusion times (eg. picosecond pulses), this assumption is valid. An analogous pair of equations is valid for excited-state absorption in atomic or molecular systems where N is then the density of excited states. By integrating Eq. 3 up to some time t' in the pulse, substituting for N in Eq. 2 and then integrating over all times t' (i.e. $-\infty$ to ∞) we find the fluence F varies with z as

$$\frac{dF}{dz} = -\left[\alpha_0 + \frac{\alpha_0\sigma}{2\hbar\omega}F\right]F. \quad (4)$$

Notice that this equation is exactly analogous to Eq. 1 describing 2PA loss with the fluence replacing the irradiance and $\alpha_0\sigma/2\hbar\omega$ replacing β . Therefore, since in most experiments the pulse energy is detected, FCA initiated by linear absorption and 2PA, will give nearly identical results for loss as a function of input energy (microscopically ESA can be considered as the limit of 2PA with a resonant intermediate state). The difference between Eqs. 1 and 4 when determining the transmitted energy is in the temporal integral over the pulse for 2PA. For FCA, this integral has already been performed. In other words, in order to determine which of these nonlinearities is present, the temporal dependence must be measured in some way.

If the carriers are produced via a 2PA process (β in Eq. 1) rather than by linear absorption (α_0 in Eq. 1), the resulting equations are considerably different, and cannot be solved analytically. Including 2PA, Eq. 2 becomes,

$$\frac{dI}{dz} = -(\alpha_0 + \beta I + \sigma N)I, \quad (5)$$

which must now be combined with the 2PA carrier generation rate,

$$\frac{dN}{dt} = \frac{\beta I^2}{2\hbar\omega}. \quad (6)$$

The factor of 2 indicates that the energy of two photons is needed to create the carrier pairs. Again we make the simplifying assumption that carriers do not diffuse or decay during the pulse. In semiconductors, this assumption is normally valid with picosecond pulses. In Eq. 5, α_0 is again included only as a residual linear absorption from defects or impurities, and it is assumed that free carriers are not produced in the process.

It is interesting to look at the order of the nonlinear response for the three cases given above. The first two, 2PA and linearly generated FCA, both appear as third-order responses. However, in one case, 2PA, the nonlinearity is proportional to $\text{Im}(\chi^{(3)})$, while for the linear absorption generated FCA the nonlinearity is due to the cascaded process $\text{Im}(\chi^{(1)}):\text{Im}(\chi^{(1)})$ (i.e. two linear absorption processes), where the first $\chi^{(1)}$ is associated with the ground state absorption and the second with FCA. Here $\chi^{(j)}$ refers to the j th order electric susceptibility. Without knowledge of the temporal dependence of the process, FCA and 2PA are indistinguishable.

For the third case, 2PA generated FCA, the nonlinear response appears fifth order, a cascaded $\text{Im}(\chi^{(3)}):\text{Im}(\chi^{(1)})$ (i.e. 2PA followed by FCA). However, the overall nonlinear transmission as given by Eq. 5 has both the third-order response of 2PA (second term) and the fifth-order cascaded response (third term). This can give quite complicated transmission curves as a function of input energy or irradiance. We find similar ambiguities in the interpretation of nonlinear refraction experiments as seen in section II.2 (also see *Results for ZnSe* in section III.2). If pulses having the same peak irradiance but different temporal widths are incident on a material obeying Eqs. 5 and 6, the longer pulses, having more energy, will create more

carriers. Thus, the longer pulse will induce more FCA, assuming slow carrier decay times, and suffer more loss. This is a useful method to determine if such processes are present.

The FCA resulting from 2PA generated carriers can be shown [12,28] to be small compared to the direct 2PA process for irradiances below a critical irradiance, $I_{cr} \approx 2\sqrt{2}\hbar\omega/\sigma\tau$, where τ is the laser pulsewidth. This is one of several reasons why short pulses are valuable for measuring β without the influence of other nonlinear phenomena. In addition the NLR from these carriers is also reduced for shorter pulses.

The solution to Eq. 1 for 2PA at the exit surface of the sample is

$$I(L, r, t) = \frac{I(0, r, t)e^{-\alpha_0 L}}{1 + q(r, t)} \quad (7)$$

where $q(r, t) = \beta I(0, r, t)L_{eff}$, and $L_{eff} = (1 - e^{-\alpha_0 L})/\alpha_0$. Here, we have explicitly shown the possible time (t) and transverse spatial (r) dependences of the irradiance. Assuming continuous, spatially homogeneous beams, Eq. 7 can be written in terms of the transmittance, here given by the ratio of irradiances, $T = I(L)/I(0)$, as

$$\frac{1}{T} = e^{\alpha_0 L} (1 + \beta I(0)L_{eff}), \quad (8)$$

where Fresnel reflections are ignored. This simple expression has led to the historical method of measuring the transmittance as a function of input irradiance $I(0)$, and plotting T^{-1} versus $I(0)$. [12,28] The result is a straight line, the slope of which determines β , and the intercept gives α_0 . There is only a small deviation from this straight line dependence when integrals over the spatial and temporal profiles are included (see Fig. 2).

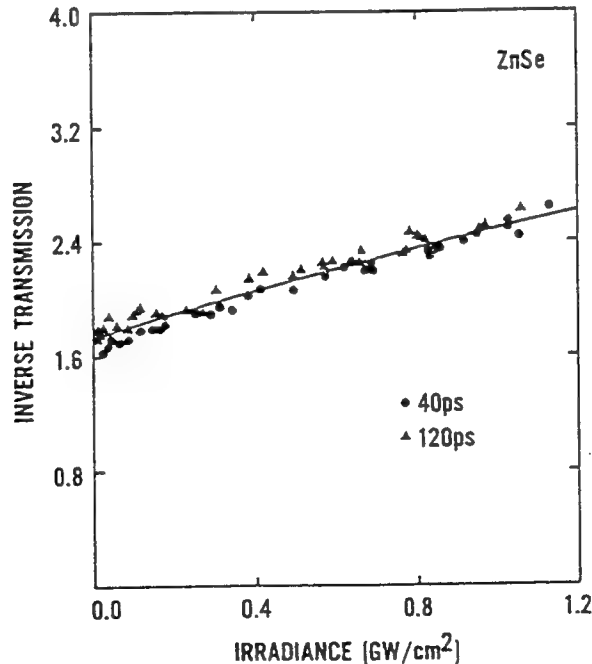


Figure 2. Inverse transmittance for ZnSe as a function of the external incident irradiance using input pulsewidths of 40 psec and 120 psec (FWHM).

Analogous to the case of 2PA, the solution of Eq. 4 for linear absorption generated FCA is

$$F(L, r) = \frac{F(0, r)e^{-\alpha_0 L}}{1 + p(r)} \quad (9)$$

where $p(r) = (\alpha_0 \sigma / 2\hbar\omega) F(0, r) L_{\text{eff}}$. Equation 9 for FCA gives a result similar to Eq. 8 for 2PA but is a function of the input fluence, $F(0)$. That is, assuming a spatially uniform beam,

$$\frac{1}{T} = e^{\alpha_0 L} \left[1 + \frac{\alpha_0 \sigma}{2\hbar\omega} F(0) L_{\text{eff}} \right], \quad (10)$$

where now T is defined as the ratio of output to input fluence. Again, including an integral over the spatial distribution only gives a small deviation from the straight line prediction of Eq. 10 whose slope, in conjunction with the intercept, now determines σ . In experiments to determine T , it is usually the pulse transmitted energy, E , that is monitored, meaning that the spatial and temporal integrals for 2PA, or the spatial integral for linearly generated FCA, must be performed. Thus, for a single experiment of $T = E(L)/E(0)$ versus the input energy, these very different nonlinear processes are indistinguishable. Only if the temporal dependence of the transmittance were directly monitored could these two processes be distinguished.

This is a very important distinction between a direct $\chi^{(3)}$ response and a sequential, cascaded $\chi^{(1)}:\chi^{(1)}$ response. In general, many processes can have a third-order response but may not be strictly described by a $\chi^{(3)}$ susceptibility. Thermal nonlinearities, excited-state nonlinearities, electrostrictive nonlinearities, etc. are examples, and this statement is valid for absorptive ($\text{Im } \chi^{(3)}$) and refractive ($\text{Re } \chi^{(3)}$) responses. For example, a thermal nonlinearity is normally described by a $\chi^{(1)}:\chi^{(1)}$ response. The sample first linearly absorbs the light which changes its temperature ($\text{Im } \chi^{(1)}$). This temperature change, in turn, changes the linear absorption ($\text{Im } \chi^{(1)}$) or changes the linear refractive index ($\text{Re } \chi^{(1)}$). This latter effect is referred to as thermal lensing or thermal blooming as it is often a defocusing effect. The turn-on time for thermal effects depends upon the mechanism for the induced changes in $\chi^{(1)}$. For example, lattice heating induces a change in bandgap that, in time, alters the spectrum of $\text{Re}\{\chi^{(1)}\}$ and $\text{Im}\{\chi^{(1)}\}$. The turn-on time for this is dictated by the rate at which heat is given to the lattice, a combination of electron phonon inelastic scattering rates and nonradiative recombination rates. If the index is changed by thermal expansion of the medium, which is usually the dominant process in liquids, the turn-on time is given by the transit time of an acoustic wave across the beam. In both cases the decay time is dictated by thermal diffusion. The determination of the underlying physics describing the nonlinear response is the major point to be made in this paper.

Section III demonstrates how the dominant loss mechanism is experimentally determined by observing the pulsewidth dependence of the nonlinear absorption. Such experiments are also useful for determining NLR mechanisms as discussed below.

II.2 Nonlinear Refraction:

As discussed in section II, NLR always accompanies NLA and results from the same physical mechanisms. Just as 2PA is a physical process that can be described in terms of $\text{Im}\{\chi^{(3)}\}$, there is a corresponding $\text{Re}\{\chi^{(3)}\}$ that describes ultrafast nonlinear refraction. The same is true for cascaded processes.

The induced phase distortion imposed on a laser beam by NLR is related to the index change, Δn , by

$$\frac{d\phi}{dz} = \frac{\Delta n 2\pi}{\lambda}. \quad (11)$$

The refractive index can be changed from the same large variety of mechanisms that can change the absorption. We, for example, discussed thermal effects in the previous section. Here we discuss the bound-electronic nonlinear refraction characterized by n_2 and excited-state or free-carrier refraction (ESR or FCR).

We restrict the use of n_2 here to only the ultrafast electronic response. FCR has its analogue in atomic and molecular systems where the NLR comes from the redistribution of population among levels. For example, in a two-level system, the absorption saturates which by causality [20] changes the refractive index. In solids this redistribution generates free carriers which block further transitions (Drude band blocking) and the refractive index is changed (i.e. FCR).[25,29]

Defining $\sigma_r 2\pi/\lambda$ as the change in index of refraction per unit of photoexcitation density, N , Δn in Eq. 11 is written as;

$$\Delta n = n_2 I + \frac{\lambda}{2\pi} \sigma_r N. \quad (12)$$

Here σ_r is the FCR cross section (often the $2\pi/\lambda$ is dropped in the definition of the index change), and n_2 is in units of m^2/W . The nonlinear index, n_2 , due to bound electrons can also be expressed in Gaussian units as $\Delta n = n_2 |E|^2/2$, where n_2 is in units of $(\text{cm/statvolt})^2$, or esu. $n_2(\text{MKS})$ is related to $n_2(\text{esu})$ through $n_2(\text{esu}) = (c n_0 / 40\pi) n_2(\text{MKS})$, with c the speed of light in m/sec.

For the case where free carriers are generated from single photon absorption processes (see Eq. 3),

$$\Delta n(t) = n_2 I(t) + \frac{\alpha_0 \sigma_r}{\hbar \omega} \int_{-\infty}^t I(t') dt'. \quad (13)$$

The bound electronic response follows the temporal dependence of the pulse input while the FCR builds up in time through the pulse. For the case where the carriers are created solely by 2PA (see Eq. 6) Eq. 12 becomes,

$$\Delta n(t) = n_2 I(t) + \frac{\beta \sigma_r}{2\hbar \omega} \int_{-\infty}^t I^2(t') dt'. \quad (14)$$

Usually, especially when using picosecond or shorter pulses, the phase distortion is not time resolved and only the temporally averaged value is measured. Assuming the nonlinear refraction accumulates throughout the pulse without decay, it can be shown that the temporally averaged index change is simply one half $\Delta n_{\text{FC}}(t=\infty)$ or it equals $\Delta n_{\text{FC}}(t=0)$ for a symmetric pulse in time.[11] Here, Δn_{FC} refers to the second term in Eq. 13 or 14. The contribution from the bound electronic n_2 (first term in Eq. 14) gives an index change Δn_{n_2} , averaged over a Gaussian temporal pulse, of $1/\sqrt{2}$ times the peak value. Thus, the temporally averaged index change is,

$$\langle \Delta n \rangle = \frac{1}{\sqrt{2}} n_2 I(t=0) + \frac{1}{2} \Delta n_{\text{FC}}(t=0). \quad (15)$$

Integrating Eq. 11 over the sample length to obtain the total phase distortion $\Delta \phi(r, t)$, we define $\langle \Delta \phi \rangle$ as the temporally averaged phase distortion as determined from Eq. 15. We then define $\Delta \Phi$ as $\Delta \phi$ evaluated at the beam center ($r=0$), with similar definitions for the temporally averaged quantities, eg. $\langle \Delta \Phi \rangle$ is the on-axis temporally averaged phase distortion.

$\Delta \phi$ can also be a periodic function of the spatial coordinates x (or y) due to the interference of two or more coherent beams as in, for example, DFWM (discussed in section III.2). Beam propagation and diffraction are discussed in the next section along with experimental techniques.

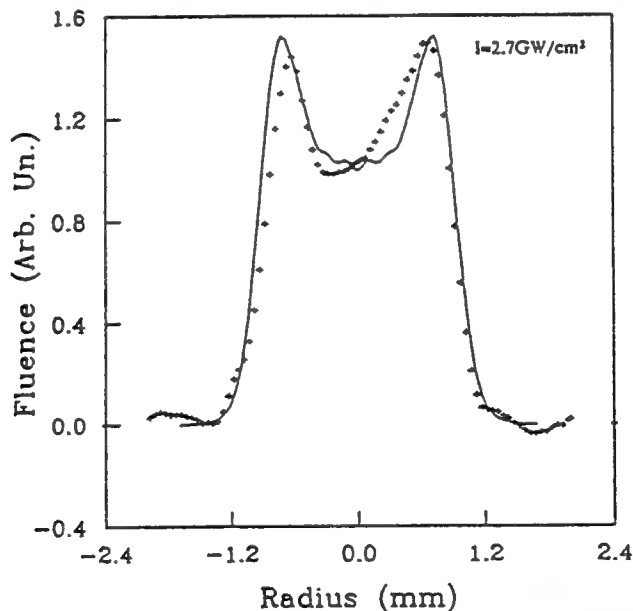
III. EXPERIMENTAL TECHNIQUES

In a single article it would be impractical to satisfactorily describe the many experimental techniques to measure NLA and NLR, so we choose to give just three examples. We describe direct transmission measurements, Z-scan and temporally-resolved DFWM. We discuss the complementary information that these methods give. This choice only reflects the fact that the authors are most familiar with these techniques. In addition this article does not discuss methods that measure nonlinearities in fibers or waveguides; however, these three methods can measure nonlinearities of the constituent materials in bulk or thin film form. In general it is best to use as many complementary experimental techniques as possible to determine the nonlinear optical response of a given material.

III.1 Nonlinear Transmittance

Perhaps the simplest method to measure NLA is to monitor the energy transmitted by a sample as a function of the input energy. We choose energy since normally the irradiance needed to give significant absorption is $\approx 10^7$ W/cm² or higher and short pulses (difficult to time resolve) are extremely valuable to reduce competing nonlinearities.

Figure 2 shows experimental results for the inverse transmittance of a 2.7 mm thick chemical-vapor deposition grown (polycrystalline) sample of ZnSe (linear index $n=2.7$) plotted as a function of the external input irradiance using two different picosecond pulsewidths at 532 nm. ZnSe has an energy gap of $E_g \approx 2.6$ eV and, therefore, displays 2PA at 532 nm.[25] Since the horizontal axis is irradiance and not energy the fact that the different pulsewidths give the same change in transmittance shows that Eq. 1 for 2PA is consistent with the measurement.



- Figure 3. Spatial beam profile (+'s) through the center of an originally Gaussian profile beam after transmission through a 2.7 mm thick CVD grown ZnSe sample and ≈ 55 cm free space propagation to a vidicon detector. The input irradiance is 2.7 GW/cm². The solid line is a theoretical calculation using values for the nonlinear coefficients as determined by Z-scan measurements as discussed in the text.

Many of the discrepancies between values for β shown in Fig. 1 come from the use of nanosecond rather than picosecond pulses. Longer pulses can make competing nonlinear absorption processes such as 2PA induced FCA dominant (see Eq. 5), leading to larger losses than from 2PA alone. Not accounting for such effects results in overestimation of β , sometimes by orders of magnitude. An additional problem in transmission

experiments is the seemingly simple task of collecting all the transmitted beam. Due to the NLR that accompanies 2PA the beam can rapidly spread after traversing the sample. Figure 3 shows a transverse scan through the center of an initially Gaussian spatial profile beam (30 ps FWHM pulse at 532 nm, $Z_0=178$ cm) after transmission through the ZnSe and then propagating 55 cm to the vidicon (near field). The beam breakup into two peaks is characteristic of a self-defocusing (negative induced lens) nonlinearity in the near field. This effect can become very strong at high irradiance and is enhanced for longer pulsewidths (having more energy) by free-carrier refraction. While a detector placed after the sample collects all the beam at low inputs, the detector can miss some of the light at high inputs. Again these effects result in an overestimation of β (see Fig. 1).

While FCA can be negligible for picosecond pulses (see discussion in section II.1), the refraction arising from these free carriers, FCR is not.[12] As shown in Fig. 3, ZnSe displays strong self defocusing even for picosecond pulses. As discussed in section III.2, this defocusing is a combination of bound-electronic and free-carrier refraction as described by Eq. 14 (and 15). The solid line in Fig. 3 shows results of a computer calculation using parameters obtained from Z-scans (see section III.2). The field at the exit surface of the sample is determined by $E \propto \sqrt{I} e^{i\phi}$, and as described in Ref. [25], this field is propagated to the vidicon detector to give the results of Fig. 3. We discuss this further in the next section.

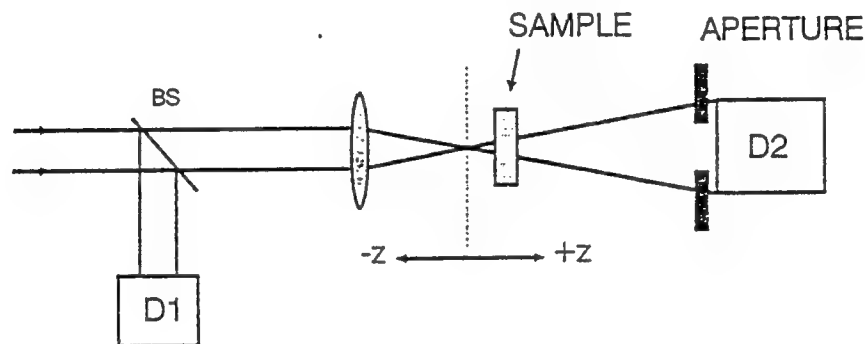


Figure 4. The Z-scan experimental setup. D_2/D_1 is measured as a function of the sample position z .

III.2 Z-SCAN

Z-scan measures both the nonlinear loss and phase distortion imposed on a Gaussian beam.[10,11] For measuring NLR this technique exploits the spatial narrowing and broadening of Gaussian beams in the far field which are due to self-focusing or self-defocusing caused by the nonlinear interaction of the beam with the material. A schematic of the experimental setup is given in Fig. 4. A Gaussian beam is focused onto the sample and then collected through an aperture in the far field by the transmission detector (D_2). Keeping the input energy constant, the sample is translated along the beam propagation direction through the focal plane, and the transmittance (D_2/D_1) is measured as a function of this sample position Z with respect to the focal plane (Z should not be confused with z , the depth within the sample). In the case of a material with a negative nonlinear refractive index, the self-defocusing will cause beam narrowing in the far field when the sample is before focus (negative Z) and beam broadening when the sample is after focus (positive Z). An increase in transmittance followed by a decrease in transmittance (peak-valley) for increasing Z denotes negative nonlinear refraction, while a valley-peak configuration implies positive nonlinearity. In Ref. [11] we give a detailed description and analysis of the Z-scan technique. Within the thin sample approximation [16,17], it is found that the change in the index of refraction (Δn) is given by a linear relation between the on-axis temporally averaged phase distortion at focus ($\langle \Delta \Phi_0 \rangle$) (where the subscript on Φ refers to the sample positioned at the beam waist, i.e. at focus) and the difference between the maximum and minimum values of the normalized aperture transmittance, ΔT_{pv} . This relation for an aperture size that gives 40% linear transmittance is given by:[11]

$$\langle \Delta \Phi_0 \rangle \approx 2.8 \Delta T_{pv} . \quad (16)$$

Examining Fig. 4 for a purely refractive case, if the aperture is removed i.e. if all the transmitted light from the sample is collected by D_2 , there will be no change in the transmittance at different sample positions. However, if the sample exhibits nonlinear absorption, the measurement will detect the nonlinear loss which is maximized at $Z=0$. This type of measurement, to which we refer as an "open aperture" Z-scan, yields the nonlinear absorption parameters of the material. When the aperture is in place, the measurement (closed aperture Z-scan) is sensitive to both nonlinear absorption and nonlinear refraction. Dividing the closed aperture data by the open aperture data yields a Z-scan curve due only to nonlinear refraction which can be determined using Eq. 16 as long as the nonlinear absorption is not too strong. Figure 5 shows an example of this procedure for ZnSe where picosecond 532 nm pulses were used. Figure 5(a) and 5(b) show open aperture and closed aperture results respectively, while Fig. 5(c) shows the results of the division of 5(b) by 5(a). The solid lines are fits as discussed later under "results for ZnSe". The limitations of this simple approach and when a more exact analysis is needed are described in detail in Ref. [11].

The open aperture Z-scan, or measuring the change in transmittance as a function of irradiance, I , is a relatively straightforward experiment as long as care is taken to collect all the light transmitted by the sample and the detectors used have uniform response (i.e. if the light is spread over a larger or smaller surface area the detector response is unchanged).

As a final comment, we note that the Z-scan curve can serve as a calibration on the input fluence. The distance in Z between the peak and valley for a Gaussian beam and a third-order nonlinearity is given by $\Delta Z_{pv} \approx 1.7 Z_0$. Thus, a Z-scan gives the beam size. This is a very convenient method to use if the nonlinear response is understood. On the other hand, once the system is calibrated, the Z-scan shape also contains information concerning the order of the nonlinearity. For example, a fifth-order response has a narrower Z-scan curve with $\Delta Z_{pv} \approx 1.2 Z_0$ [11]

The following experiments on the semiconductor ZnSe illustrate the complexity of the nonlinear interactions even for picosecond pulses, and the difficulties in unraveling the different nonlinear processes.

Results for ZnSe

With 27 picosecond (FWHM) pulses at 532 nm from a frequency doubled Nd:YAG laser we performed Z-scans at different input energies on the 2.7 mm thick polycrystalline ZnSe sample. The beam was focused to give $w_0 \approx 25 \mu\text{m}$. First, an open aperture Z-scan was performed. In Fig. 5(a) we plot the experimental data. In addition we show a numerically calculated Z-scan using $\beta = 5.8 \text{ cm/GW}$ and $\alpha_0 = 0.3 \text{ cm}^{-1}$ in Eq. 7 including spatial and temporal integrals. The Z (as opposed to the depth z) dependence is introduced in the irradiance I in Eq. 7 by the standard Gaussian beam propagation equation,

$$I(Z) = \frac{I(0)}{1 + (Z/Z_0)^2} \quad (17)$$

giving a Lorentzian shaped curve for loss versus Z .

With a 40% linearly transmitting aperture a closed aperture Z-scan was performed at the same irradiance (Fig. 5b). In this case the measurement is sensitive to both NLR and NLA. Experiments on ZnSe were conducted at peak irradiance levels from $I_0 = 0.21 \text{ GW/cm}^2$ to 2.4 GW/cm^2 . The experimental irradiances are within the sample (i.e. Fresnel reflections taken into account).

In all, ten Z-scans were performed (5 "open" aperture and 5 "closed"). Closed aperture Z-scans at a peak input irradiance of 0.57 GW/cm^2 and 2.4 GW/cm^2 are shown in Fig. 6a and 6b respectively. Open aperture Z-scans show a third-order response and a strictly irradiance dependent loss as confirmed by using different

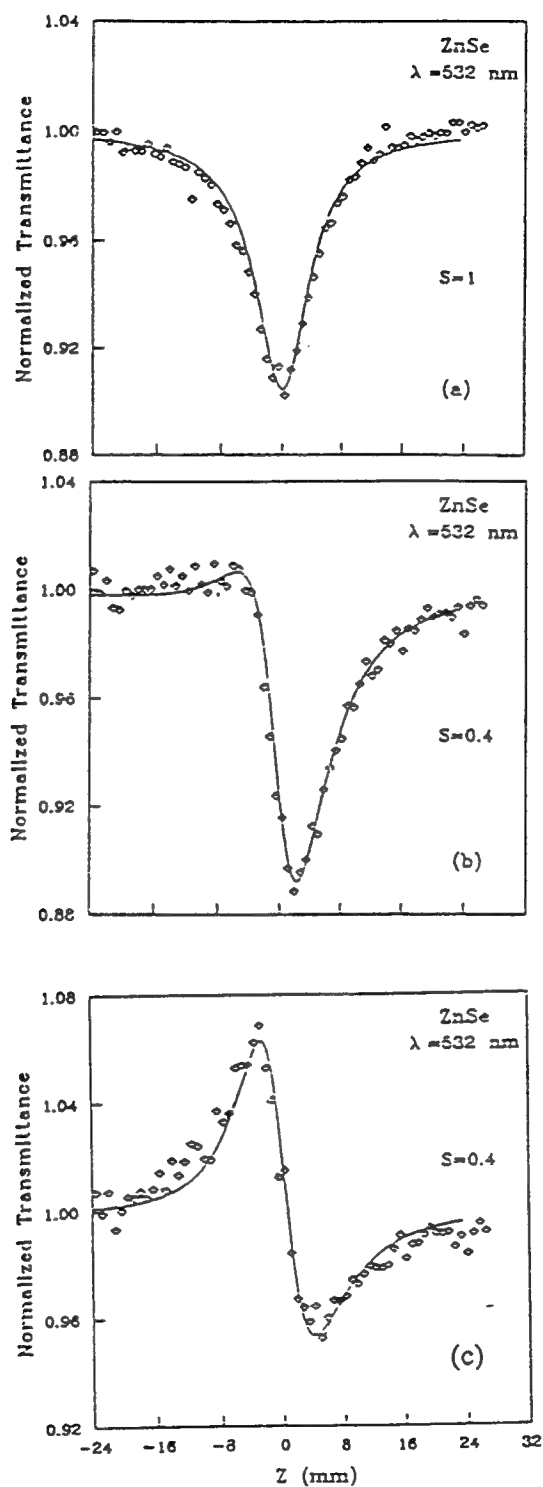


Figure 5. Normalized Z-scan transmittance of ZnSe measured using picosecond pulses at $\lambda=532$ nm with $I_0=0.21$ GW/cm². (a) Open aperture data and fit (solid line) (b) 40% aperture data and fit (solid line) and (c) The result of the division of the Z-scans of (a) and (b).

pulsewidths (see Fig. 2). This confirms that 2PA is the dominant nonlinear loss mechanism and a value of $\beta \approx 5.8 \text{ cm/GW}$ is obtained as shown by the fit to the data of Fig. 5a.

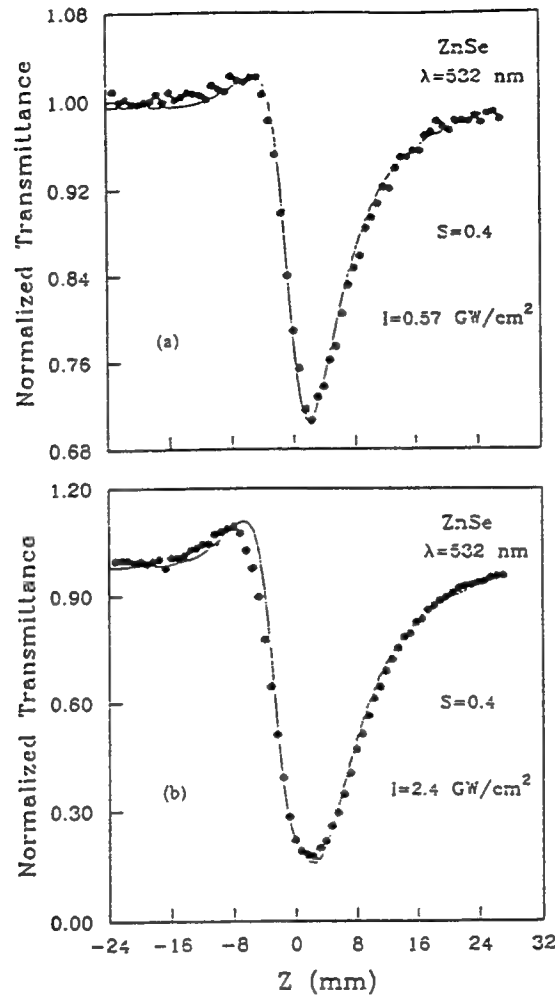


Figure 6. Closed aperture Z-scan data ($S=0.4$) and theoretical fit (solid lines) of the ZnSe sample taken at irradiance levels of $I_0=0.57 \text{ GW/cm}^2$ (a) and $I_0=2.4 \text{ GW/cm}^2$ (b) where free-carrier refraction is large.

Using the 40% aperture Z-scan and dividing out the nonlinear absorption, we calculate Δn from the phase shift data (i.e. using Eqs. 11 and 16).[25] Plotted in Fig. 7 is $\Delta n/I_0$ versus the peak input irradiance I_0 . If this graph showed a horizontal straight line we could interpret this as a third-order response, and since we are using picosecond pulses in a spectral range where there is little linear absorption, we could conclude that it is most likely due to the third-order anharmonic motion of the bound electrons (i.e. n_2).[11,25] Performing Z-scans at different pulsewidths, with pulses shorter than carrier decay rates, could confirm this conclusion by showing a strict irradiance dependence rather than a fluence dependence as would be indicative of linearly generated FCR. The negative slope of the line in Fig. 7 indicates a higher order self-defocusing. Since the graph shows a linear dependence we conclude a fifth order response consistent with 2PA generated FCR. The intercept of this line gives a fitted value of $n_2 \approx -6.4 \times 10^{-14} \text{ cm}^2/\text{W}$ ($-4.1 \times 10^{-11} \text{ esu}$) and the slope gives $\sigma_r 2\pi/\lambda \approx -1.1 \times 10^{-21} \text{ cm}^3$. The details of how this simple method is used to estimate these numbers is given in Ref. [25].

With $\beta \approx 5.8 \text{ cm/GW}$ we also performed a complete numerical fit to the Z-scans. Using an iterative approach to best fit all the data, we found a better fit with $n_2 \approx -6.2 \times 10^{-14} \text{ cm}^2/\text{W}$ ($-4.0 \times 10^{-11} \text{ esu}$), and

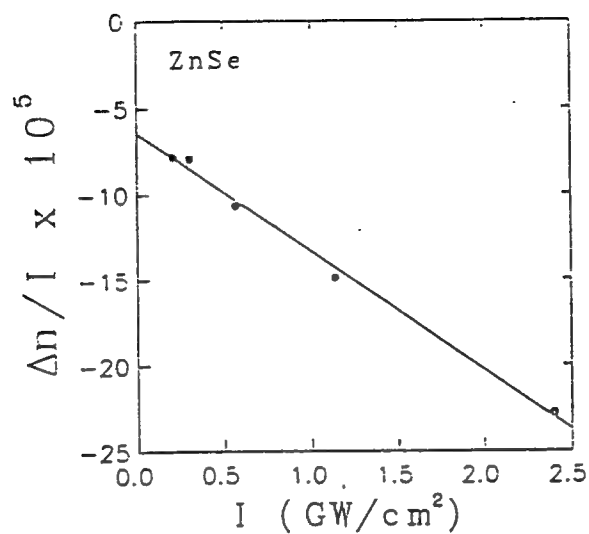


Figure 7. $\Delta n/I_0$ directly derived from ΔT_{pv} plotted as a function of I_0 for ZnSe.

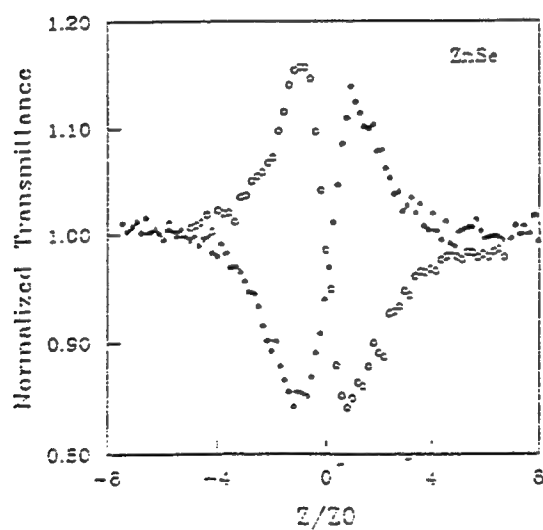


Figure 8. Closed aperture ($S=0.4$) Z-scan experimental data (filled circles) of ZnSe at $1.06 \mu\text{m}$ and 532 nm (open circles) in units of $Z_0 = \pi w_0^2 / \lambda$. This figure clearly shows the dispersion in n_2 as it changes sign from positive at $1.06 \mu\text{m}$ to negative at 532 nm .

$\sigma_r \lambda / 2\pi \approx -0.8 \times 10^{-21} \text{ cm}^3$ ($\sigma_r \approx -9 \times 10^{-17} \text{ cm}^2$). The solid lines shown in Fig. 5 are the fits to the data. These numbers were also used to give the theoretical curve of the beam profile shown in Fig. 3.

We also measured n_2 in ZnSe at $1.06 \mu\text{m}$ where 2PA is not present. Using 40 ps pulses (FWHM) from a Nd:YAG laser focused to $w_0 \approx 40 \mu\text{m}$, we obtained $n_2 = +2.9 \times 10^{-14} \text{ cm}^2/\text{W}$ ($+1.7 \times 10^{-11} \text{ esu}$). In Fig. 8 we plot closed aperture Z-scans obtained in ZnSe at $1.06 \mu\text{m}$ and at $0.53 \mu\text{m}$ showing the change in sign of n_2 . In this figure, the nonlinear absorption has been divided out of the $0.53 \mu\text{m}$ data. This observed dispersion in n_2 and change in sign is consistent with the recent theory of Refs. [19-21] and shows the necessity of measuring the nonlinearity at more than a single wavelength.

In addition to separately measuring NLA and NLR, Z-scan can be used to determine the anisotropy of these responses (eg. the different responses to linear and circular polarized light). This is particularly important for single crystal materials. We recently applied these methods to single crystals of GaAs, BaF_2 and KTP to determine various $\chi^{(3)}$ tensor elements.[30]

One of the difficulties in the interpretation of the Z-scan data is the absence of temporal information. Recently we introduced a temporally resolved, 2-color Z-scan that can separately give the temporal evolution of the NLA and NLR.[31] Next, however, we describe the use of picosecond DFWM to time resolve the nonlinear response.

III.2 Degenerate Four-Wave Mixing

In the experiments described here, the standard "backward" DFWM geometry is used.[3,32,33] A schematic of the experimental geometry using single 43 ps (FWHM) $1.064 \mu\text{m}$ pulses, or 30 ps (FWHM) $0.532 \mu\text{m}$ pulses is shown in Fig. 9. The single pulse input is divided into three pulses which, after passing through variable time delays, are incident on the sample. The three pulses can be independently adjusted in amplitude and polarization using half-wave plate and polarizer combinations. Two strong beams, forward (E_f) and backward (E_b) pumps, of approximately equal irradiance are incident on the sample from counterpropagating directions. A weaker beam, the probe (E_p), is incident on the sample at an angle θ with respect to E_f .

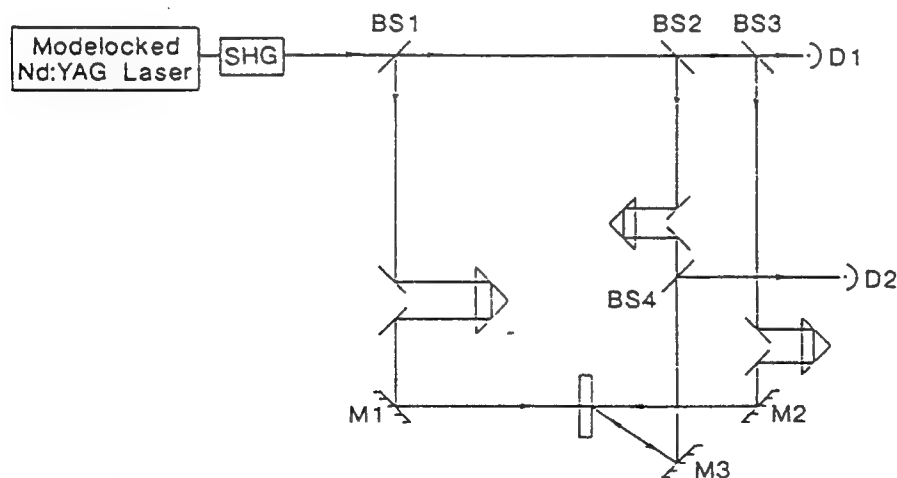


Figure 9. Schematic of experimental DFWM apparatus. D_1 is the input pulse energy monitor, while D_2 monitors the phase-conjugate signal pulse energy.

The physical operation of this technique involves scattering of one of the strong pump pulses off the grating produced by the interference of the probe with the other pump through the nonlinear modulation of the refractive index and/or absorption coefficient. The grating is only formed by a *nonlinear* interaction of the

light with the material. While this is a somewhat simplified physical interpretation (eg. it doesn't describe two-photon coherence effects [3]), it suffices for most experiments. Thus, assuming all beams are linearly polarized parallel to each other, there are two amplitude gratings formed that can diffract a pump beam; one between E_i and E_p , and the other between E_b and E_p . The grating spacing is determined by the angle θ which is usually made to be small (a few degrees). In this case, one of the gratings has a spacing larger than λ ($\approx \lambda/\theta n$) while the other has a spacing of $\approx \lambda/n$. Calculating the direction of the beam diffracted off either of these gratings shows that this field, E_c (the conjugate wave), retraces the path of E_p (i.e. the sample retroreflects the beam). This retroreflection is the basis for phase conjugation and phase-conjugate mirrors.[34] If the beams that write the grating are not polarized parallel, there is a polarization grating formed in the material that can diffract light if the effective nonlinear susceptibility tensor has nonzero off diagonal elements (i.e. polarized light can induce an anisotropy).[34,35] The different DFWM signals obtained using different polarization combinations are useful for determining the various tensor components of the nonlinear electric susceptibility (eg. $\chi^{(3)}$).

Given the above physical interpretation, any spatial modulation of the optical properties of the material, index or amplitude grating, will give rise to E_c . Herein lies the major difficulty with this method in characterizing nonlinear material coefficients. Both NLA and NLR give rise to a similar measured response, thus making it difficult to determine the origin of the nonlinearity. However, by temporally delaying one beam with respect to the others, the lifetimes of the various gratings can be determined which is helpful in determining mechanisms (this is similar to the information obtained by performing pulsewidth dependent studies in transmission or using Z-scan). In what follows we show how DFWM can be used to characterize nonlinearities using ZnSe at an input wavelength of 532 nm as an example.

DFWM in ZnSe

The DFWM signal in ZnSe is monitored as a function of input energy and pulse delay for different combinations of the polarization of the three input beams. Figure 10 shows a plot of the DFWM signal versus the temporal delay τ_b of E_b , with E_b polarized perpendicular to both E_i and E_p ($\theta=13^\circ$, $I_b \approx 34$ MW/cm² and $I_i \approx 22$ MW/cm²). This polarization combination results in an interference between E_i and E_p so that E_b is diffracted into E_c off either amplitude or phase gratings induced by this interference. In addition there can be polarization gratings which can also diffract light into E_c . In this arrangement (Fig. 10) no signal is observed for E_b incident prior to the other two beams, the grating rapidly forms reaching a maximum near zero time delay and then decays. Clearly, two very distinct nonlinearities are evident from Figure 10. Near zero delay, a large rapidly decaying signal is seen, while at longer delays, we observe a more slowly decaying signal. To better understand the two nonlinear regimes, irradiance dependence experiments were performed at different delays. Figure 11 shows a log-log plot of the DFWM signal versus the total input irradiance, (all three input beams were varied simultaneously) at two different delay times. The line in Fig. 10 labeled (a) shows the irradiance dependence at zero delay which follows a power dependence of $I^{3.1 \pm 0.2}$, indicative of a third-order nonlinearity. This could be explained by either 2PA, n_2 , or linearly generated FCR. FCA was ruled out by the results of Fig. 2 as our irradiance is less than I_{cr} . However, as seen in Fig. 10, this third-order response, with a peak near $\tau=0$, lasts for only a time of the order of the pulsewidth. If FCR were responsible, the grating would last as long as the carriers remained excited and did not diffuse to wash out the grating. For many semiconductors, with carrier lifetimes $\geq 10^{-9}$ s and grating spacings of the order of micrometers, diffusion dominates the grating decay. By performing experiments for different values of θ (i.e. different grating spacings), the fast component of response is unchanged. The decay of this fast component is too fast to attribute to decay of the carrier grating. The line in Fig. 11 labeled (b) shows the dependence at a delay of 240 ps, where E_b is no longer temporally coincident with the other two beams, giving a power dependence of $I^{5.0 \pm 0.2}$. The fifth order dependence of the DFWM signal on the input beams is consistent with 2PA generated FCR as discussed previously. Studies in other two-photon absorbing semiconductors, such as CdTe at 1.06 μ m, reveal the same basic behavior, i.e. a fast third-order signal followed by a slowly decaying fifth-order signal. The results obtained from the DFWM experiments help to confirm the Z-scan results. Thus, the rapidly responding signal near zero delay in Fig. 10 is due to a combination of 2PA and n_2 .

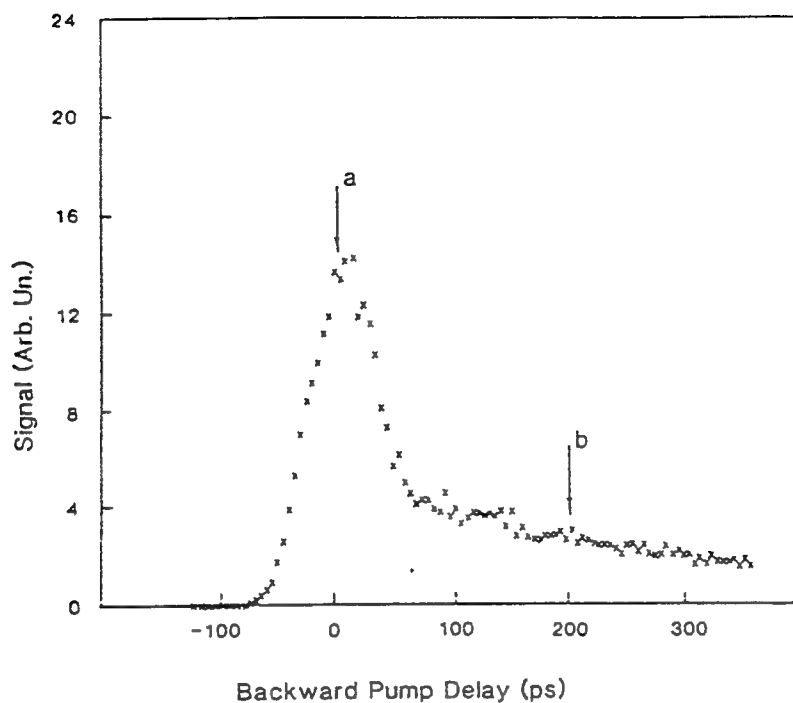


Figure 10. A plot of the phase-conjugate signal versus backward pump delay with the backward pump polarized perpendicular to the other two waves.

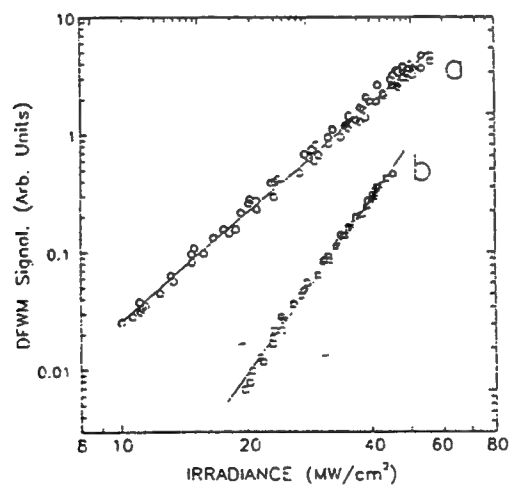


Figure 11. Log-log plots of the phase conjugate signal versus the total input irradiance ($I_r + I_b + I_p$) as all three beams were varied together, for (a) zero delay and (b) 240 ps delay. The solid lines are best-fits to the data giving power dependencies of $I^{3.1 \pm 0.2}$ and $I^{5.0 \pm 0.2}$, respectively.

$(|\chi^{(3)}|^2 = [\text{Im } \chi^{(3)}]^2 + [\text{Re } \chi^{(3)}]^2)$, while the slowly decaying signal is due to FCR (the real part of an effective fifth order nonlinearity). [25, 35]

IV. FREQUENCY DEPENDENCE

Having performed picosecond experiments on a number of different materials using transmission and/or Z-scan and/or DFWM we have observed many similarities. If the photon energy is less than one half E_g , the bound electronic nonlinear refraction dominates the nonlinear response and $n_2 > 0$ (if very high irradiance is used we have occasionally observed 3-photon absorption when energetically allowed prior to damage). Above one half E_g , the nonlinear response is complicated by both 2PA and 2PA generated FCR. At very high irradiance the associated FCA can also become significant prior to damage. In addition we find that n_2 becomes negative for photon energies above approximately $3/4 E_g$. Figure 8 shows this sign change for ZnSe.

To determine the spectrum of 2PA and the dispersion of n_2 , it would be best to perform the above series of experiments as a function of $\hbar\omega$. This is often extremely difficult since the range of frequencies needed can be extremely large (i.e. the transparency range) and tuneable sources with the required irradiance, pulsewidth and beam quality are not typically available. However, using some very simple scaling rules some remarkable relations can be observed. Wherrett [39] has shown that the third-order nonlinear susceptibility $\chi^{(3)}$ in inorganic solids should scale as

$$\chi^{(3)} \simeq \frac{1}{E_g^4} f(\hbar\omega/E_g), \quad (18)$$

where the complex function f depends only on the ratio $\hbar\omega/E_g$ (i.e. upon which states are optically coupled). The nonlinear coefficients β and n_2 are related to $\chi^{(3)}$ by;

$$\begin{aligned} \beta(\hbar\omega/E_g) &\propto \frac{\hbar\omega}{n_0} \text{Im}(\chi^{(3)}) \propto \frac{1}{n_0^2 E_g^3} \frac{\hbar\omega}{E_g} \text{Im}(f(\hbar\omega/E_g)) \\ &\propto \frac{1}{n_0^2 E_g^3} F(\hbar\omega/E_g) \end{aligned} \quad (19)$$

and

$$n_2(\hbar\omega/E_g) \propto \text{Re}(\chi^{(3)}) \propto \frac{1}{n_0 E_g^4} G(\hbar\omega/E_g) \quad (20)$$

where the defined functions F and G are band structure dependent. Thus, F gives the 2PA spectrum and G gives the dispersion of n_2 . One method to test the above scaling relations is to scale the experimental data to obtain the experimental functions;

$$F^e(\hbar\omega/E_g) = \frac{1}{K\sqrt{E_p}} n_0^2 E_g^3 \beta^e \quad (21)$$

and

$$G^e(\hbar\omega/E_g) = \frac{1}{K'\sqrt{E_p}} n_0 E_g^4 n_2^e \quad (22)$$

where β^e and n_2^e are experimental values of β and n_2 and K and K' are proportionality constants. Here E_p is the Kane energy as discussed in Ref. [12, 19, 39] and is nearly material independent with a value near 21 eV.

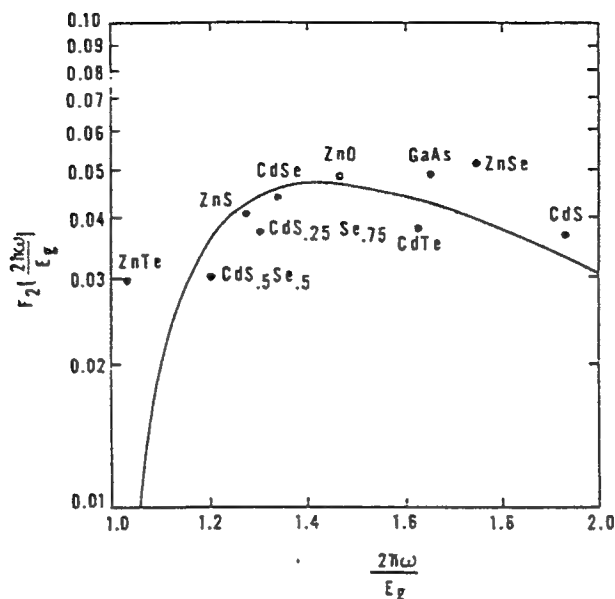


Figure 12. The solid line is the two-parabolic band prediction for the function F plotted as a function of $2\hbar\omega/E_g$ using $K=3100$ in Eq. 21. The data are scaled according to Eq. 21 are from Ref. [12,63]. Figure reproduced from Ref. [63].

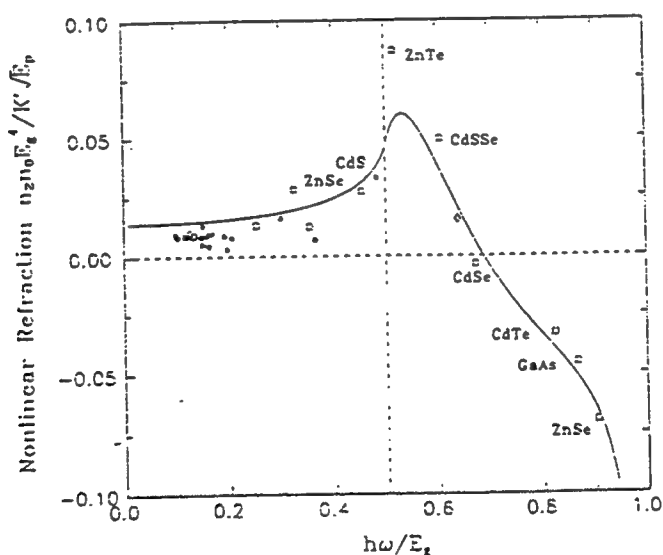


Figure 13. A plot of n_2 data scaled according to Eq. 22. The circles are measurements in [61], the diamond is from [62], and the squares are our Z-scan measurements [19]. We have labeled the semiconductor data. The solid line is the function $G(\hbar\omega/E_g)$ derived here for a two band model of a semiconductor using the 2PA data for the fit to the constant K' .

Figures 12 and 13 plot these scaled data versus photon $\hbar\omega/E_g$, along with the predicted dependence from a two-parabolic band model using a value of $K=3100$ in units such that E_p and E_g are in eV and β is in cm/GW.[18-20] The value of $K'=0.94 \times 10^8$ is determined from the Kramers-Kronig integral of the nonlinear absorption spectrum using the above value for K . [19] The data shown in Fig. 12 come primarily from direct transmittance measurements.[12] The data in Fig. 13 for semiconductors come from Z-scan measurements [19] and for dielectrics come from Z-scan [19] and nearly degenerate three-wave mixing [40]. Several materials have now been measured by both techniques and the agreement for n_2 is excellent. As seen in Fig. 12 the experimental 2PA appears nearly step-function like, turning on at approximately $E_g/2$. Figure 13 shows a small, positive, nearly dispersionless n_2 for $\hbar\omega/E_g$ much less than E_g , reaching a peak near $E_g/2$, where 2PA turns on, and then decreases, reaching negative values as $\hbar\omega$ approaches the band edge. This curve is reminiscent of the behavior of the linear index in a solid which has its peak value at the band edge, where linear absorption turns on, and then rapidly turning down toward smaller values as $\hbar\omega$ increases. Just as the linear index n is related to the linear absorption through Kramers-Kronig relations, so the nonlinear index is related to the nonlinear absorption. These nonlinear Kramers-Kronig relations are discussed in more detail in Refs. [18-21].

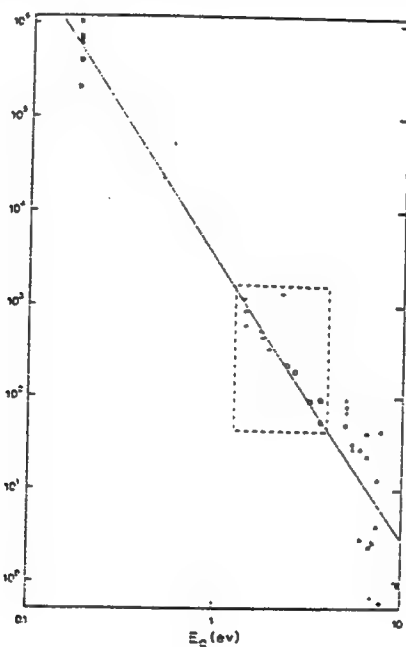


Figure 14. A log-log plot of the scaled 2PA coefficient β as a function of the bandgap energy E_g (in eV). The data are scaled from Eq. 21 as $\beta \cdot n^2 / \sqrt{E_p} F$. The straight line is a fit to the data within the dashed box from Ref. [63] for a line of fixed slope -3. The data to the right of the box are taken from Ref. [59] using the third (X's) and fourth (closed circles) harmonics of 1.06 μm picosecond pulses. The data to the left of the box (closed squares) are taken from Ref. [60] using 10 μm nanosecond pulses, which carefully accounted for free-carrier absorption. Figure reproduced from Ref. [65].

We find that the general trends in the data displayed in Figs. 12 and 13 are well described using the simplest possible band structure, i.e. two-parabolic bands. The solid line in Fig. 12 comes from a calculation of the transition rate for 2PA using such a band structure. Performing a Kramers-Kronig transformation on the nonlinear absorption calculated using this band structure gives the solid line of Fig. 13. While there are deviations from these curves of up to factors of 3, in general there is surprisingly good agreement considering the range of materials and differences in band-gap energies (from 0.2 to 10 eV). Using the calculated spectral responses, we can compare the range of values of β and n_2 for the different materials studied by replotting the scaled data on a log-log plot versus E_g as in Figs. 14 and 15 (i.e. dividing out the respective

theoretical frequency dependences of the nonlinearities). This shows the E_g^{-3} dependence of 2PA in Fig. 14 and the E_g^{-4} dependence of n_2 in Fig. 15, revealing more than four orders-of-magnitude change in n_2 .

After having separated the contributions of "fast" (i.e. β and n_2) and "slow" (i.e. σ_r) we can compare theoretical results for the free-carrier nonlinear refraction with experiment. As long as the photogenerated carriers thermalize extremely rapidly with the lattice, σ and σ_r are independent of their generation mechanism. The so-called Drude band-blocking theory of the frequency dependence of these carrier nonlinearities appears to describe experiments reasonably accurately under a variety of conditions such that the spectral dependences are known.[36-38] Reference 25 gives a detailed comparison of different theories with experiments on semiconductors.

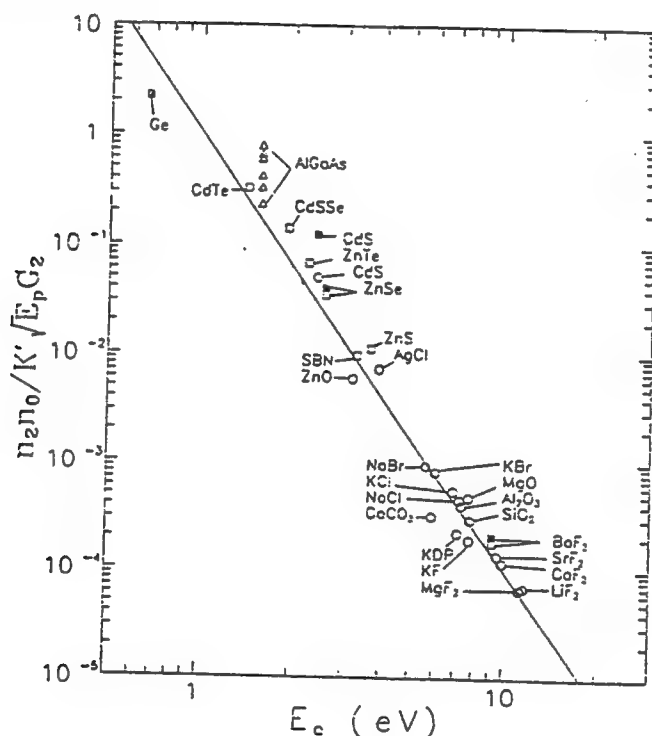


Figure 15. A log-log plot of scaled n_2 data as a function of E_g . The data are scaled from Eq. 22 as $n_2 n_0 / K' \sqrt{E_g} G$. The data (circles) are taken from Ref. [61] using nearly degenerate three-wave mixing, (squares) are Z-scan measurements from Ref. [19] (solid squares at $0.532 \mu\text{m}$ open squares at $1.06 \mu\text{m}$ and half shaded square at $10.6 \mu\text{m}$), and the AlGaAs data (triangles) are taken from Ref. [64]. These data are now scaled by the dispersion function G . The solid straight line has a slope of -4 .

V. CONCLUSION

While we have only explicitly shown data for ZnSe, data obtained for other materials looks remarkably similar. For example, Fig. 16 shows Z-scan data for BaF_2 at an input wavelength of 266 nm where the material is a two-photon absorber ($E_g \approx 9.2 \text{ eV}$). This figure is to be compared with Fig. 5 for ZnSe. The deviation of the fit for negative Z is due to a linear background (i.e. independent of I) caused by surface curvature. Such background effects become more pronounced at shorter wavelengths. We find for BaF_2 at 266 nm , with the light propagating in the $[100]$ direction and the field parallel to $[010]$, $\beta \approx 0.06 \text{ cm/GW}$, and $n_2 \approx +3.1 \times 10^{-16} \text{ cm}^2/\text{W}$ ($+1.1 \times 10^{-13} \text{ esu}$) while the anisotropy in this material is large (eg. 30% change in n_2 with orientation). While a thorough study at this wavelength has not been performed, we expect the free-carrier effects at this irradiance and wavelength are small. This is due to both the small magnitude of β and the smaller expected free-carrier cross sections at short wavelengths.

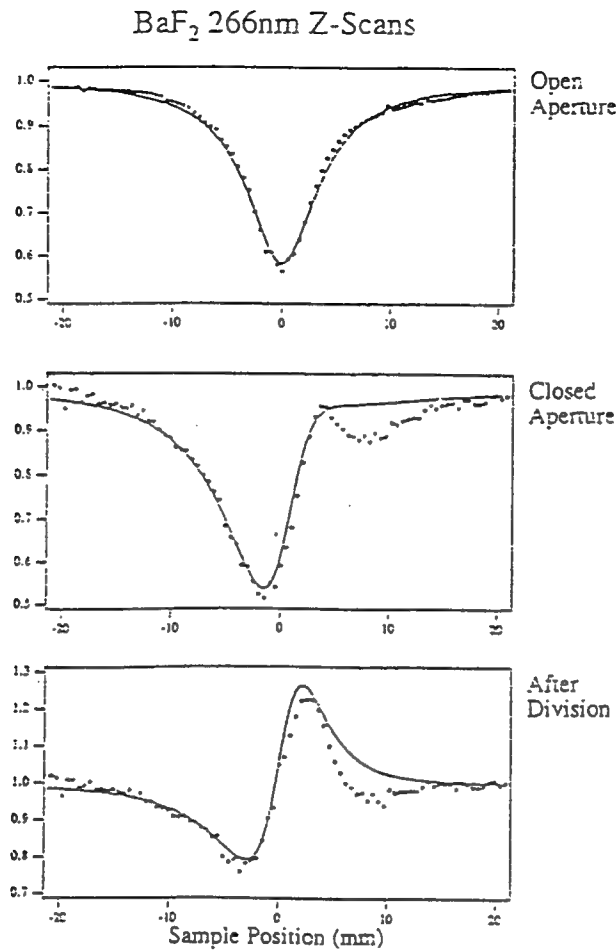


Figure 16. Normalized Z-scan transmittance of BaF₂ measured using picosecond pulses at $\lambda=266$ nm with $I_0=72$ GW/cm². (a) Open aperture data and fit (solid line) (b) 40% aperture data and fit (solid line) and (c) The result of the division of the Z-scans of (a) and (b).

In order to extract the data needed to plot Figures 12, 13, 14 and 15, a clear understanding of the nonlinearities involved was necessary. In the final analysis these figures reveal relatively simple trends and scaling rules. We have found that a simple 2-parabolic band model for semiconductors describes semiconductor data well and even appears to work for wide-gap dielectric materials.

The examples given here demonstrate the importance of measuring materials nonlinearities using different techniques and/or as functions of several parameters including pulsewidth and wavelength. For example had we only measured nonlinear refraction in ZnSe at one pulsewidth we could not have determined whether the response was due to a bound electronic n_2 or to linearly generated free-carrier refraction. Additionally, the nonlinear refraction in ZnSe coming from the two-photon absorption generated carriers, depending on the irradiance range of the experiment, could be mistaken for a larger third-order response (i.e. the fifth-order response may not be recognized without analyzing data over an extended range of irradiance levels). In turn, when analyzing data from different materials in an attempt to discover scaling rules, trends could easily be masked if the nonlinearities were not properly separated.

The wavelength dependence is not only of importance to determine nonlinear mechanisms, but it can be crucial in determining whether a material is promising for a given application. As seen in Fig. 13, n_2 has a zero near $3/4 E_g$. If a measurement were made near this wavelength, the material could be labeled useless for applications involving large n_2 's independent of how large the peak n_2 is (see Fig. 13). While the wavelength dependence of the nonlinearities in these inorganic materials as shown in Figs. 12 and 13 is relatively simple, molecular (organic) crystals can be expected to have considerably more structure, for example several wavelength separated 2PA peaks. It is hoped that the knowledge gained in understanding the nonlinear response of inorganic materials will be helpful in unraveling the response of organics.

VII. ACKNOWLEDGEMENT

We gratefully acknowledge the support of the National Science Foundation grant ECS#9120590, the Defense Advanced Research Projects Agency, and the Night Vision and Electro-Optics Directorate. The work presented in this paper represents many years of effort involving many former and current students as well as post-doctoral fellows. We thank all those involved and acknowledge their contributions through the various referenced publications. We explicitly thank Edesly J. Canto-Said, J. Richard DeSalvo, David C. Hutchings, Hermann Vanherzeele, Tai H. Wei, Milton A. Woodall, and Yuen-Yen Wu for their many contributions.

VIII. REFERENCES

- [1] M. J. Weber, D. Milam, and W. L. Smith, "Nonlinear refractive index of glasses and crystals", *Opt. Eng.*, 17, 463 (1978).
- [2] M. J. Moran, C. Y. She, and R. L. Carman, "Interferometric measurements of nonlinear refractive-index coefficient relative to CS_2 in laser-system-related materials", *IEEE J. Quantum Electron.*, QE-11, 259 (1975).
- [3] R.K. Jain and M.B. Klein, "Degenerate Four-Wave Mixing in Semiconductors", pp. 307-415, in *Optical Phase Conjugation*, ed. R. A. Fisher, Academic Press, N.Y. 1983.
- [4] R. Adair, L. L. Chase, and S. A. Payne, "Nonlinear refractive index measurement of glasses using three-wave frequency mixing", *J. Opt. Soc. Am. B*, 4, 875 (1987).
- [5] A. Owyong, "Ellipse rotations studies in laser host materials", *IEEE J. Quantum Electron.*, QE-9, 1064 (1973).
- [6] W. E. Williams, M. J. Soileau, and E. W. Van Stryland, "Optical Switching and n_2 Measurements in CS_2 ", *Opt. Commun.*, 50, 256 (1984).
- [7] W. E. Williams, M. J. Soileau, and E. W. Van Stryland, "Simple direct measurement of n_2 ", in *Proc. 15th Annu. Symp. Opt. Materials for High Power Lasers*, Boulder, CO, 1983.
- [8] M. Bertolotti, A. Ferrari, C. Sibilila, G. Suber, D. Apostol and P. Jani, "Photothermal Deflection Technique for Measuring Thermal Nonlinearities in Glasses", *Appl. Phys.*, 27, 1811 (1988).
- [9] F. Kajzar and J. Messier, "Cubic Effects in Polydiacetylene Solutions and Thin Films", in *Nonlinear Optical Properties of Organic Molecules and Crystals*, eds. D.S. Chemla and J. Zyss, Vol. 2, pp. 51-83, Academic Press, Orlando, 1987.
- [10] M. Sheik-Bahae, A. A. Said, and E. W. Van Stryland, "High sensitivity, single beam n_2 measurement", *Opt. Lett.*, 14, 955-957 (1989).
- [11] M. Sheik-Bahae, A. A. Said, T. H. Wei, D. J. Hagan, and E. W. Van Stryland, "Sensitive measurement of optical nonlinearities using a single beam", *IEEE J. Quantum Electron.*, QE-26, 760-769 (1990).
- [12] E. W. Van Stryland, H. Vanherzeele, M. A. Woodall, M. J. Soileau, A. L. Smirl, S. Guha, and T. F. Boggess, "Two photon absorption, nonlinear refraction, and optical limiting in semiconductors", *Opt. Eng.*, 24, 613 (1985).
- [13] M. Bass, E.W. Van Stryland, and A.F. Stewart, "Laser Calorimetric Measurement of Two-Photon Absorption", *Appl. Phys. Lett.* 34, 142 (1979).
- [14] Y. Bae, J.J. Song, and Y.B. Kim, "Photoacoustic Study of Two-Photon Absorption in Hexagonal ZnS", *J. Appl. Phys.*, 53, 615 (1982). also see, E.W. Van Stryland, and M.A. Woodall, "Photoacoustic Measurement of Nonlinear Absorption in Solids," in *Laser Induced Damage in Optical Materials*, NBS Special Publication 620, 50 (1980).

- [15] for example see; *Picosecond Phenomena*, eds. C.V. Shank, E.P. Ippen, and S.L. Shapiro, Springer Verlag, 1978.
- [16] A. E. Kaplan, "External Self-Focusing of Light by a Nonlinear Lens", *Radiophys. Quantum Electron.*, 12, 692 (1969).
- [17] S. A. Akhmanov, R. V. Khokhlov, and A. P. Sukhorukov, "Self-Focusing, Self-Defocusing, and Self-Modulation of Laser Beams," in *Laser Handbook*, F. T. Arecchi and E. O. Shultz-Dubois, eds. (North-Holland, Amsterdam, 1972), vol. 2 1151-1228.
- [18] M. Sheik-Bahae, D. J. Hagan, and E. W. Van Stryland, "Dispersion and Band-Gap Scaling of the Electronic Kerr Effect in Solids Associated with Two-Photon Absorption", *Phys. Rev. Lett.*, 65 96-99 (1990).
- [19] M. Sheik-Bahae, D. Hutchings, D. J. Hagan, and E. W. Van Stryland, "Dispersion of Bound Electronic Nonlinear Refraction in Solids", *IEEE J. Quantum Electron.*, 27, 1296 (1991).
- [20] D.C. Hutchings, M. Sheik-Bahae, D.J. Hagan, and E.W. Van Stryland, "Kramers-Kronig Relations in Nonlinear Optics", *Optical and Quantum Electronics*, 24, 1-30 (1992).
- [21] F. Bassani and S. Scandolo, "Dispersion Relations in Nonlinear Optics", *Phys. Rev. B* 44, 8446-8453 (1991).
- [22] see for example, Y.R. Shen, *The Principles of Nonlinear Optics*, John Wiley and Sons, New York, 1984.
- [23] T. H. Wei, D. J. Hagan, E. W. Van Stryland, J. W. Perry, and D. R. Coulter, "Direct Measurements of Nonlinear Absorption and Refraction in Solutions of Phthalocyanines", *Appl. Phys. B* 54, 46 (1992).
- [24] T.F. Boggess, S.C. Moss, I.W. Boyd, and A.L. Smirl, "Nonlinear Optical Energy Regulation by Nonlinear Refraction and Absorption in Silicon", *Opt. Lett.* 9, 291-293, (1984).
- [25] A. A. Said, M. Sheik-Bahae, D.J. Hagan, T. H. Wei, J. Wang, J. Young, and E. W. Van Stryland, "Determination of Bound-Electronic and Free-Carrier Nonlinearities in ZnSe, GaAs, CdTe, and ZnTe", *J. Opt. Soc. Am. B*, 9, 405 (1992).
- [26] see for example, Kosar, in *Light-Sensitive Systems*, J. Wiley and Sons, Inc., N.Y., 1965. also see, D.R. Bosomworth and H.J. Gerritsen, "Thick Holograms in Photochromic Materials", *Appl. Opt.* 7, 95 (1968).
- [27] Nastaran Mansour, Kamjou Mansour, E.W. Van Stryland, and M.J. Soileau, "Diffusion of Color Centers Generated by Two-Photon-Absorption at 532nm in Cubic Zirconia", *Journal of Applied Physics* 67, 1475-1477 (1989).
- [28] J. H. Bechtel, and W. L. Smith, "Two-photon absorption in semiconductors with picosecond pulses", *Phys. Rev. B* 13, 3515 (1976).
- [29] B.S. Wherrett and N.A. Higgins, "Theory of Nonlinear Refraction Near the Band Edge of a Semiconductor", *Proc. R. Soc. Lond. A* 379, 67 (1982).
- [30] R. DeSalvo, M. Sheik-Bahae, A.A. Said, D.J. Hagan and E.W. Van Stryland, "Z-scan Measurements of the Anisotropy of Nonlinear Absorption and Refraction in Crystals", *Opt. Lett.* 18, 194-196 (1993).
- [31] J. Wang, M. Sheik-Bahae, A.A. Said, D.J. Hagan, and E.W. Van Stryland, "Time-Resolved Z-Scan Measurements of Optical Nonlinearities", *JOSA B*, xx (1993).
- [32] J. R. Salcedo, A. E. Siegman, D. D. Dlott and M. D. Fayer, "Dynamics of Energy Transport in Molecular Crystals: The Picosecond Transient Grating Method", *Phys. Rev. Lett.* 41, 131 (1978).
- [33] H. J. Eichler, P. Gunter, and D. W. Pohl, "Laser-Induced Dynamic Gratings", *Springer Series in Optical Sciences*, 50, eds. J. M. Enoch, D. L. MacAdam, A. L. Schawlow, K. Shimoda and T. Tamir (Springer-Verlag, 1988).
- [34] *Optical Phase Conjugation*, ed. R. A. Fisher, Academic Press, N.Y. 1983.
- [35] E. Canto-Said, D. J. Hagan, J. Young, and E. W. Van Stryland, "Degenerate Four-Wave Mixing Measurements of High Order Nonlinearities in Semiconductors", *IEEE J. Quantum Electron.* 27, 2274 (1991).
- [36] A. G. Aronov, D. E. Pikus, and D. Sh. Shekhter, "Quantum theory of free-electron dielectric constant in semiconductors", *Sov. Phys.-Solid State*, 10, 645 (1968).
- [37] D. H. Auston, S. McAfee, C. V. Shank, E. P. Ippen, and O. Teschke, "Picosecond spectroscopy of semiconductors", *Solid State Electron.* 21, 147-150 (1978).
- [38] B. S. Wherrett, A. C. Walker, and F. A. P. Tooley, "Nonlinear refraction for CW optical bistability", in *Optical Nonlinearities and Instabilities in Semiconductors*, H. Haug ed. (Academic Press, 1988), 239-272.
- [39] B.S. Wherrett, "Scaling Rules for Multiphoton Interband Absorption in Semiconductors", *J. Opt. Soc.*

Amer. B 1, 67 (1984).

- [40] R. Adair, L.L. Chase and Stephen A. Payne, "Nonlinear Refractive Index of Optical Crystals", Phys. Rev. B-39, 3377-3350 (1987).
- [41] Basov, N. G., Grasyuk, A. Z., Efimov, V. F., Zubarev, I. G. Katulin, V. A. and Popov, J. M., "Semiconductor Lasers Using Optical Pumping", J. Phys. Soc. Jpn. Suppl., 21, 276, (1966).
- [42] Ralston, J. M. and Chang, R. K., "Optical Limiting in Semiconductors", Appl. Phys. Lett., 15, 164, (1969); also see, same authors "Nd: Laser Induced Absorption in Semiconductors and Aqueous PrCl_3 and NdCl_3 ", Opt-Electron, 1, 182, (1969).
- [43] Arsen'ev, V. V., Dneprovskii, V. S. Klyshko, D. N., and Penin, A. N., "Nonlinear Absorption and Limitation of Light Intensity in Semiconductors", Sov. Phys. JETP, 29, 413, (1969).
- [44] Lee, C. C. and Fan, H. Y., "Two Photon Absorption and Photoconductivity in GaAs and InP", Appl. Phys. Lett., 20, 18, (1972).
- [45] Lee, C. C. and Fan, H. Y., "Two-Photon Absorption with Exciton Effect for Degenerate Valence Bands", Phys. Rev. B, 9, 3502, (1974).
- [46] Bepko, S. J., "Anisotropy of Two-Photon Absorption in GaAs and CdTe", Phys. Rev. B 12, 669, (1975).
- [47] Dneprovskii, V. S. and Ok, S. M., "Role of Absorption by Nonequilibrium Carriers in Determination of Two-Photon Absorption Coefficient of CdSe and GaAs Crystals", Sov. J. Quantum Electron., 6, 298, (1976).
- [48] Bechtel, J. H. and Smith, W. L., "Two-Photon Absorption in Semiconductors with Picosecond Laser Pulses", Phys. Rev. B, 13, 3515, (1976).
- [49] Zubarev, I. G., Mironov, A. B., and Mikhailov, S. I., "Influence of Deep Impurity Levels on Nonlinear Absorption of Light GaAs", Sov. Phys. Semicond., 11, 239, (1977).
- [50] Saissy, A., Azema, A., Botineau, J., and Gires, F., "Absolute Measurement of the 1.06 μm Two-Photon Absorption Coefficient in GaAs", Appl. Phys., 15, 99, (1978).
- [51] Bosacchi, B., Bessey, J. S., and Jain, F. C., "Two-Photon Absorption of Neodymium Laser Radiation in Gallium Arsenide", J. Appl. Phys., 49, 4609, (1978).
- [52] R.A. Bendorius, and E.K. Maldutis, "Nonlinear Absorption of Laser Radiation in InP and GaAs", Sov. Physics-Collection, 23, 69-72 (1983).
- [53] T.F. Boggess, A.L. Smirl, S.C. Moss, I.A. Boyd and E.W. Van Stryland, "Optical Limiting in GaAs", IEEE J. Quant. Electron., QE-21, 488-494 (1985).
- [54] A. Penzkofer, and A.A. Bugayev, "Two-Photon Absorption and Emission Dynamics of Bulk GaAs", Optical and Quantum Electronics 21, 283-306 (1989).
- [55] G.C. Valley, T.F. Boggess, J. Dubard and A.L. Smirl, "Picosecond Pump-Probe Technique to Measure Deep-Level, Free-Carrier, and Two-Photon Cross Sections in GaAs", J. Appl. Phys. 66, 2407-2413 (1989).
- [56] Ma Hai-Ming, "Self-transitions of picosecond light pulses in GaAs", in Chinese, Chinese Journal of Phys., 38, 153 (1989).
- [57] A.A. Bugaev, T.Yu. Dunaeva and V.A. Lukoshkin, "Influence of Nonlinear Refraction, Absorption by Free Carriers, and Multiple Reflection on the Determination of the Two-Photon Absorption Coefficient of GaAs", Sov. Phys. Solid State 31, 2031-2034 (1990).
- [58] J.S. Aitchison, M.K. Oliver, E. Kapon, E. Colas and P.W.E. Smith, "Role of Two-Photon Absorption in Ultrafast Semiconductor Optical Switching Devices", Appl. Phys. Lett. 56, 1305-1307 (1990).
- [59] P. Liu, W.L. Smith, H. Lotem, J.H. Bechtel, and N. Bloembergen, "Absolute Two-Photon Absorption Coefficients at 355 and 266 nm", Phys. Rev. B 17, 4620 (1978).
- [60] J. Dempsey, J. Smith, G.D. Holah, and A. Miller, "Nonlinear Absorption and Pulse-Shaping in InSb", Opt. Commun. 26, 265 (1978); A.M. Johnson, C.R. Pidgeon, and J. Dempsey, "Frequency Dependence of Two-Photon Absorption in InSb and HgCdTe", Phys. Rev. B 22, 825 (1980); C.R. Pidgeon, B.S. Wherrett, A.M. Johnson, J. Dempsey, and A. Miller, "Two-Photon Absorption in Zinc-Blende Semiconductors", Phys. Rev. Lett. 42, 785 (1979).
- [61] R. Adair, L.L. Chase and S.A. Payne, "Nonlinear Refractive Index of Optical Crystals", Phys. Rev. B 39, 3337-3349 (1989).
- [62] I.N. Ross, W.T. Toner, C.J. Hooker, J.R.M. Barr, and I. Coffey, "Nonlinear Properties of Silica and Air for Picosecond Ultraviolet Pulses", J. Modern Opt. 37, 555-573 (1990).

- [63] Eric W. Van Stryland, M.A. Woodall, H. Vanherzeele, and M.J. Soileau, "Energy Band-Gap Dependence of Two-Photon Absorption", Opt. Lett. 10, 490 (1985).
- [64] M.J. LaGasse, K.K. Anderson, C.A. Wang, H.A. Haus, and J.G. Fujimoto, "Femtosecond Measurements of the Nonresonant Nonlinear Index of in AlGaAs", Appl. Phys. Lett. 56, 417-419 (1990).
- [65] E.W. Van Stryland, Y.Y. Wu, D.J. Hagan, M.J. Soileau, and Kamjou Mansour, "Optical Limiting with Semiconductors", J. Opt. Soc. Am. B 5, 1980-1989 (1988).

Nondegenerate two-photon absorption in zinc blende semiconductors

D. C. Hutchings* and E. W. Van Stryland

Center for Research in Electro-Optics and Lasers, University of Central Florida, Orlando, Florida 32826

Received April 10, 1992; revised manuscript received June 16, 1992

An algorithm is presented for the calculation of the nondegenerate two-photon absorption coefficient by using second-order perturbation theory and a Kane band-structure model, including the effects of nonparabolicity and nonzone-center wave functions. The polarization dependence is included by correctly accounting for the symmetry of the electronic wave functions. A comparison is made with degenerate two-photon absorption data in various zinc blende semiconductors, and excellent agreement is found without the use of fitting parameters. Comparisons are also made with nondegenerate two-photon absorption spectra measured in ZnSe and ZnS by using a picosecond continuum and with some polarization-dependent measurements obtained by a two-color Z-scan measurement.

INTRODUCTION

Degenerate (self-action) two-photon absorption (2PA) in a zinc blende semiconductor was previously described and characterized; see, e.g., Refs. 1–3. However, there has been recent interest in the nondegenerate 2PA whereby one light field induces absorption in a second light field, resulting in the loss of one photon from each field. Here we use the term nondegenerate to indicate the effect of one light beam on a different (usually in wavelength or polarization) light beam (cross action), as opposed to self-action effects, which are the effects of light beams on themselves and which we term degenerate. This interest is due partly to recent measurements of nondegenerate nonlinear absorption in semiconductors^{4,5} but also to the fact that the nondegenerate absorption can be used to determine the nonresonant nonlinear refractive index n_2 by means of a nonlinear Kramers–Kronig relation.^{6,7}

A calculation for degenerate 2PA that uses a two-parabolic-band model for a semiconductor is presented in Refs. 7 and 8. This two-parabolic-band model provides the proper scaling of 2PA with material parameters and gives a frequency dependence matching that of experimental data. However, the absolute value of the predicted values is consistently low by approximately a factor of 2 over a wide range of direct-gap semiconductors and some dielectrics.³ This factor can be accounted for by using the present band structure, which is more realistic near the center of the Brillouin zone. In particular, the degeneracy of the valence bands and the band nonparabolicity are correctly accounted for. By this improvement in the band-structure model, one can accurately predict 2PA without the use of fitting parameters.

Another reason for using a more comprehensive band-structure model is that the simple two-band model does not, by itself, give any polarization dependence. This is because the two-parabolic-band model does not provide a direction for the momentum matrix element (although most calculations assume a momentum matrix element parallel to the electronic \mathbf{k} vector). The Kane band structure used here automatically provides a direction and a

magnitude for the momentum matrix element, permitting the determination of nondegenerate 2PA for arbitrary polarization orientations between the two light inputs. However, as the Kane band structure for zinc blende (cubic) semiconductors is isotropic, there will be no polarization dependence with respect to the crystal orientation.

THEORY OF DEGENERATE TWO-PHOTON ABSORPTION

There have been two basic approaches to the calculation of degenerate 2PA coefficients in a crystalline solid. First, second-order perturbation theory can be used to calculate the transition rate from valence to conduction band (resulting from the absorption of two photons). Second, first-order perturbation theory can be used with electronic wave functions that have been dressed to include the acceleration of the electrons as a result of the ac light field. The latter approach was developed by Keldysh⁹ and is often termed tunneling theory.

Second-Order Perturbative Approach

Fermi's golden rule (derived from second-order time-dependent perturbation theory) provides the form of the two-photon transition rate:

$$W_2 = \frac{2\pi}{\hbar} \sum_{\mathbf{v}\mathbf{c}} \left| \sum_i \frac{\langle \psi_{\mathbf{c}} | \hat{H}_{\text{opt}} | \psi_i \rangle \langle \psi_i | \hat{H}_{\text{opt}} | \psi_{\mathbf{v}} \rangle}{E_{i\mathbf{v}}(\mathbf{k}) - \hbar\omega} \right|^2 \delta(E_{\mathbf{c}\mathbf{v}}(\mathbf{k}) - 2\hbar\omega), \quad (1)$$

where $\hat{H}_{\text{opt}} = (e/mc)\mathbf{A} \cdot \hat{\mathbf{p}}$ is the optical interaction Hamiltonian applicable to solids, $\psi_{\mathbf{c}}(\psi_{\mathbf{v}})$ is the Bloch wave function for the conduction (valence) band, and $E_{\mathbf{c}\mathbf{v}}(\mathbf{k})$ is the energy difference between the bands. The sum is over all possible intermediate states i and over all possible transitions starting from a filled state and ending at an empty state (usually valence to conduction band for an intrinsic semiconductor), i.e., a sum over bands and the electronic wave vector \mathbf{k} . The subtlety in this calculation is in de-

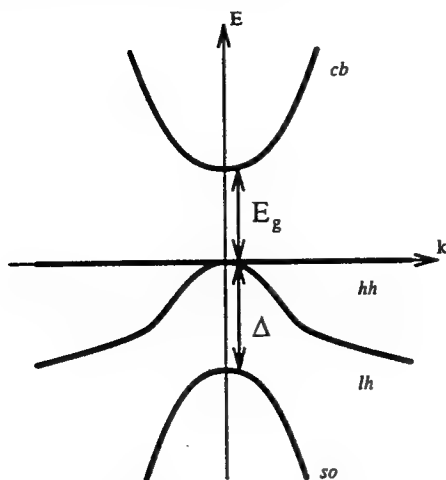


Fig. 1. Band structure for a zinc blende semiconductor near the center of the Brillouin zone as given by Kane.¹² Only the set of four doubly degenerate (in spin) bands are considered: conduction band (cb), heavy-hole band (hh), light-hole band (lh), and split-off band (so).

ciding what model to choose for the band structure and over what bands the summations will be performed.

The simplest model for a semiconductor consists of a single parabolic conduction band and a single parabolic valence band in which the intermediate states are also these bands.^{8,10} Hence the summation will involve an interband (allowed) and an intraband (forbidden) matrix element. This calculation gives a two-photon absorption coefficient of the form

$$\beta(\omega) = K_{pb} \frac{\sqrt{E_p}}{n_0^2(\omega) E_g^3} F_2 \left(\frac{\hbar\omega}{E_g} \right),$$

$$F_2 = \frac{(2x - 1)^{3/2}}{(2x)^5}, \quad (2)$$

where E_p is related to the interband momentum matrix element and for the two-parabolic-band model is defined $E_p = 2|\mathbf{p}_{vc}|^2/m_0$ (E_p is approximately 21 eV for most semiconductors),¹¹ n_0 is the linear refractive index, and E_g is the band gap. K_{pb} is a material independent constant, which the two-band theory gives as⁷

$$K_{pb} = \frac{2^9 \pi}{5} \frac{e^4}{\sqrt{m_0 c^2}} = 1940 \text{ cm/GW (eV)}^{5/2}. \quad (3)$$

Equation (3) gives the correct material scaling ($n_0^{-2} E_g^{-3}$) over a large range of semiconductors and wide-gap optical materials³; however, 2PA coefficient predictions are consistently low. This difference has been compensated for by fitting the constant K_{pb} to the experimental data, which gives a value for the constant of $K_{pb} = 3100$ in the same units as above.³

One of the deficiencies of the above model is that it does not correctly account for the valence band degeneracy. Zinc blende semiconductors usually have a valence band maximum at the center of the Brillouin zone. This maximum consists of three bands: a heavy-hole band and a light-hole band (degenerate at $k = 0$) with a spin-orbit split-off band separated by the spin-orbit interaction energy Δ (Fig. 1). For direct gap materials (conduction band minimum also at zone center) the theory of Kane^{11,12} provides a good description of the bands and the Bloch

wave functions around zone center, which is sufficient for many of the band-edge optical properties.

Lee and Fan¹³ used the Kane band structure with parabolic bands to determine 2PA coefficients (they also discussed excitonic effects). Two-photon transitions still consist of an allowed and a forbidden transition from a valence to a conduction band, but now possible forbidden transitions consist of intervalence band transitions as well as the self-transitions that exist for the two-band model. This calculation (neglecting the split-off band, i.e., $\Delta \gg E_g$, and without excitonic contributions) results in a 2PA coefficient that is a factor of 2.7 greater than that obtained from the two-parabolic-band model but with identical frequency and material dependencies. This form of calculation was extended by Pidgeon *et al.*,¹⁴ who included nonparabolicity, and by Weiler,² who correctly accounted for nonzone-center wave functions with nonparabolicity, which results in a significant reduction in the expected 2PA coefficient. The latter calculation gives a predicted 2PA coefficient that agrees well with (reliable) experimental data for a wide range of semiconductors and optical solids.^{3,15}

Tunneling Approach

Keldysh's tunneling theory involves the use of dressed electronic wave functions, which include the effect of an ac electric field and first-order perturbation theory. It not only provides 2PA coefficients but can be used for any multiphoton process. Jones and Reiss applied this method to a two-parabolic-band model of a semiconductor, using an S-matrix approach, for circularly polarized light,¹⁶ and Brandi and de Araújo made a similar application for linearly polarized light.¹⁷ Provided that the same band-structure assumptions are used in both cases, exactly the same result as that predicted by second-order perturbation theory is obtained for 2PA. This is not surprising since the dressed-electron-states approach is equivalent to a self-transition (intraband) in the second-order perturbation theory approach. However, the tunneling theory cannot easily be applied to the Kane band structure, as the tunneling approach has problems dealing with multiple valence band degeneracies and so cannot correctly account for intervalence band transitions. Care needs to be taken when one is using tunneling theory for multiphoton absorption in general, as this theory often does not account for the dominant contributions. For example, in three-photon absorption the dominant term arises from a threefold interband transition,⁸ whereas tunneling theory accounts only for terms corresponding to one interband and two intraband transitions, which are usually much less significant.

To conclude this preliminary discussion on degenerate 2PA theory, a simple two-parabolic-band model of a semiconductor (that uses either the second-order perturbative or the tunneling approach) provides the material scaling and general frequency dependence but usually underestimates β by approximately a factor of 2 (this difference has been compensated for by fitting to measured data). Including other factors, such as correct valence band degeneracies, nonparabolicity, and correct electronic wave functions away from zone center, in the calculation provides an accurate prediction of the degenerate β without the use of fitting parameters.

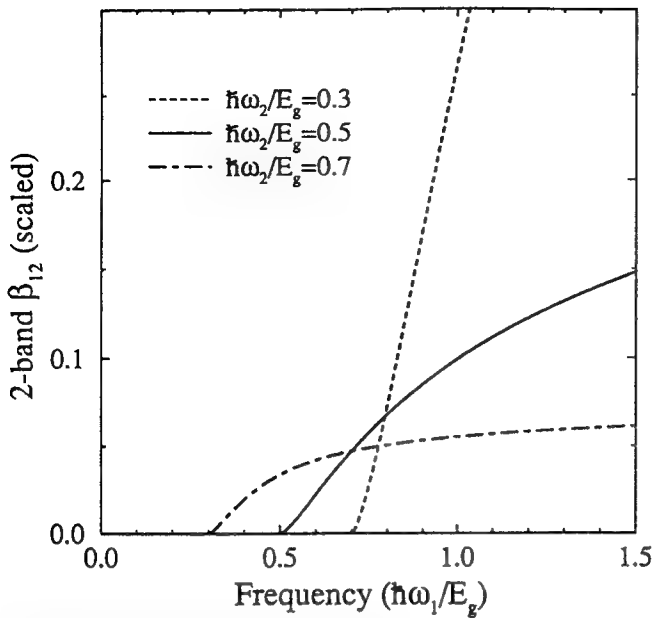


Fig. 2. Theoretical frequency dependence of the nondegenerate 2PA for three different pump frequencies, $\hbar\omega_2 = 0.3, 0.5, 0.7$ for a two-parabolic-band model.

THEORY OF NONDEGENERATE TWO-PHOTON ABSORPTION

In the presence of 2PA alone (i.e., with no linear absorption), the absorption of two spatially and temporally overlapping light beams is described with the following coupled set of equations showing both degenerate (β_{ii}) and nondegenerate (β_{ij}) terms:

$$\begin{aligned} \frac{\partial I_1}{\partial z} &= -\beta_{11}I_1^2 - 2\beta_{12}I_1I_2, \\ \frac{\partial I_2}{\partial z} &= -\beta_{22}I_2^2 - 2\beta_{21}I_1I_2. \end{aligned} \quad (4)$$

The factor of 2 in the nondegenerate term is sometimes referred to as weak-wave retardation,¹⁸ and this definition ensures that the nondegenerate coefficient approaches the degenerate one as the parameters of the I_2 beam approach that of I_1 , i.e., $\beta_{12} \rightarrow \beta_{11}$ as $\omega_2 \rightarrow \omega_1$.

Two-Parabolic-Band Model

The nondegenerate 2PA coefficient can be determined by using two parabolic bands and an S -matrix (tunneling) approach⁷ or second-order perturbation theory to give

$$\beta_{12} = K_{pb} \frac{\sqrt{E_p}}{n_0(\omega_1)n_0(\omega_2)E_g^3} F_2^{nd} \left(\frac{\hbar\omega_1}{E_g}, \frac{\hbar\omega_2}{E_g} \right), \quad (5)$$

where the spectral function F_2^{nd} is defined as

$$F_2^{nd}(x_1; x_2) = \frac{(x_1 + x_2 - 1)^{3/2}}{2^7 x_1 x_2^2} \left(\frac{1}{x_1} + \frac{1}{x_2} \right)^2, \quad (6)$$

provided $x_1 + x_2 > 1$, and is zero otherwise. For the two-parabolic-band model we define the parameter $E_p = 2|\mathbf{p}_{vc}|^2/m_0$. The functional form of F_2^{nd} is shown in Fig. 2.

Kane Band-Structure Model

In a manner similar to our treatment of the degenerate case, we now use a more realistic band structure for the

determination of the relevant optical transitions close to the center of the Brillouin zone. The model used in the following calculation was developed by Kane^{11,12} and is based on $\mathbf{k} \cdot \mathbf{p}$ theory with spin-orbit interaction for three-valence bands plus one conduction band. The basis functions are denoted $S \uparrow$ and $S \downarrow$ for the two spin states for the unperturbed conduction band with spherical symmetry and $X \uparrow, X \downarrow, Y \uparrow, Y \downarrow, Z \uparrow$, and $Z \downarrow$ with p -like symmetry for the unperturbed valence bands. The resulting band structure is shown in Fig. 1 and consists of a conduction band (cb), heavy-hole (hh) and light-hole (lh) valence bands degenerate at $k = 0$, and a split-off (so) valence band removed by an energy Δ at $k = 0$. On diagonalization, the band energies can be obtained from

$$E' = 0,$$

$$E'(E' - E_g)(E' + \Delta) - (kP)^2(E' + 2\Delta/3) = 0, \quad (7)$$

where $E' = E - (\hbar^2/2m_0)k^2$ is the electron energy with the free-electron mass taken into account and P is the Kane parameter defined from the momentum matrix element:

$$P = -\frac{i\hbar}{m_0} \langle S | p_x | X \rangle = -\frac{i\hbar}{m_0} \langle S | p_y | Y \rangle = -\frac{i\hbar}{m_0} \langle S | p_z | Z \rangle. \quad (8)$$

The first of Eqs. (7) gives the heavy-hole energies, which are zero (plus the free-electron mass contribution) because there is no coupling with other bands, and the cubic equation provides the energies for the conduction, light-hole valence, and split-off valence bands. This diagonalization is such that the total angular momentum (sum of orbital plus spin) $\mathbf{J} = \mathbf{L} + \boldsymbol{\sigma}$ and its z projection J_z are also diagonal in the new basis. The conduction band ($L = 0, \sigma = 1/2$) has the two (degenerate) spin states of $J = 1/2$, with $J_z = \pm 1/2$. The valence bands ($L = 1, \sigma = 1/2$) have the possible values of $J = 3/2, J_z = \pm(3/2)$ for the heavy-hole band, or $J = 3/2, J_z = \pm(1/2)$ for the light-hole band, and of $J = 1/2, J_z = \pm(1/2)$ for the split-off band. The diagonalization also gives the electronic wave functions

$$\begin{aligned} \phi_{ia} &= a_i(iS \downarrow) + b_i[(X - iY) \uparrow / \sqrt{2}] + c_i(Z \downarrow), \\ \phi_{i\beta} &= a_i(iS \uparrow) + b_i[-(X + iY) \downarrow / \sqrt{2}] + c_i(Z \uparrow), \\ \phi_{hha} &= [(X + iY) \uparrow / \sqrt{2}], \\ \phi_{hh\beta} &= [(X - iY) \downarrow / \sqrt{2}], \end{aligned} \quad (9)$$

where α and β denote the two (degenerate) spin states and the coefficients for the conduction, light-hole, and split-off bands are determined from the energies

$$\begin{aligned} a_i &= kP(E_i' + 2\Delta/3)/N, \\ b_i &= (\sqrt{2}\Delta/3)(E_i' - E_g)/N, \\ c_i &= (E_i' - E_g)(E_i' + 2\Delta/3)/N, \end{aligned} \quad (10)$$

where $N = (a_i^2 + b_i^2 + c_i^2)^{1/2}$ is a normalizing factor.

The transition rate for nondegenerate 2PA can be determined by using second-order perturbation theory¹³:

$$\begin{aligned} W_2^{nd} &= \frac{2\pi}{\hbar} \sum_{vc} \left| \sum_i \left[\frac{\langle c | \hat{H}_2 | i \rangle \langle i | \hat{H}_1 | v \rangle}{E_{iv}(\mathbf{k}) - \hbar\omega_1} + \frac{\langle c | \hat{H}_1 | i \rangle \langle i | \hat{H}_2 | v \rangle}{E_{iv}(\mathbf{k}) - \hbar\omega_2} \right] \right|^2 \\ &\quad \times \delta[E_{cv}(\mathbf{k}) - \hbar\omega_1 - \hbar\omega_2], \end{aligned} \quad (11)$$

Table 1. z Components of the Scaled Momentum Matrix Element $M_{ij} = \langle i | p_z | j \rangle \hbar / m_0 P$ as a Function of the Electronic k Vector in Polar Coordinates^a

Spin States	$c \alpha$	hh α	lh α	so α
$c \alpha$	$2a_c c_s \cos \theta$	0	$(a_c c_l + a_l c_c) \cos \theta$	$(a_c c_s + a_s c_c) \cos \theta$
$c \beta$	0	$-\frac{a_c}{\sqrt{2}} \sin \theta$	$-\frac{(a_c b_l - a_l b_c)}{\sqrt{2}} \sin \theta$	$-\frac{(a_c b_s - a_s b_c)}{\sqrt{2}} \sin \theta$
hh α	0	0	0	0
hh β	$-\frac{a_c}{\sqrt{2}} \sin \theta$	0	$-\frac{a_l}{\sqrt{2}} \sin \theta$	$-\frac{a_s}{\sqrt{2}} \sin \theta$
lh α	$(a_c c_l + a_l c_c) \cos \theta$	0	$2a_l c_l \cos \theta$	$(a_l c_s + a_s c_l) \cos \theta$
lh β	$\frac{(a_c b_l - a_l b_c)}{\sqrt{2}} \sin \theta$	$-\frac{a_l}{\sqrt{2}} \sin \theta$	0	$-\frac{(a_l b_s - a_s b_l)}{\sqrt{2}} \sin \theta$
so α	$(a_c c_s + a_s c_c) \cos \theta$	0	$(a_l c_s + a_s c_l) \cos \theta$	$2a_s c_s \cos \theta$
so β	$\frac{(a_c b_s - a_s b_c)}{\sqrt{2}} \sin \theta$	$-\frac{a_s}{\sqrt{2}} \sin \theta$	$\frac{(a_l b_s - a_s b_l)}{\sqrt{2}} \sin \theta$	0

^aThe labels α and β refer to the two (degenerate) spin states in each band [conduction (c), heavy-hole (hh), light-hole (lh), and split-off (so)]. The coefficients a_i , b_i , and c_i are the Kane coefficients determined from Eqs. (10). Only transitions from α spin states are shown here, but to get transitions from the β spin states the relations $M_{i\beta, j\beta} = M_{i\alpha, j\alpha}$ and $M_{i\alpha, j\beta} = M_{j\beta, i\alpha}$ can be used.

where the interaction Hamiltonians are given by

$$\hat{H}_j = \frac{e}{m_0 c} \mathbf{A}_j \cdot \hat{\mathbf{p}},$$

$$= \frac{e}{im_0 \omega_j} \left[\frac{2\pi I_j}{n_0(\omega_j) c} \right]^{1/2} \hat{\mathbf{a}}_j \cdot \hat{\mathbf{p}}. \quad (12)$$

Here $\hat{\mathbf{a}}_j$ is the unit vector in the direction of polarization of the j th optical beam, which has frequency ω_j and an irradiance I_j .

In order to determine this transition rate, one must obtain the momentum matrix element among the various bands described by the Kane theory. Table 1 shows the z component of the scaled momentum matrix element taken among the various sets of bands, which we define as

$$M_{ij}^{(n)}(\mathbf{k}) = \frac{\hbar}{m_0 P} \hat{\mathbf{a}}_n \cdot \langle j, \mathbf{k} | \hat{\mathbf{p}} | i, \mathbf{k} \rangle. \quad (13)$$

Only the matrix elements from the α spin states are shown, but those from the β spin states can easily be obtained by using the facts that

$$M_{i\beta, j\beta} = M_{i\alpha, j\alpha},$$

$$M_{i\alpha, j\beta} = M_{j\beta, i\alpha}^*. \quad (14)$$

Lee and Fan¹³ show a similar table for the particular case of parabolic bands and zone-center wave functions. Here the \mathbf{k} vector is given in polar coordinates (k, θ, ϕ), and the (a, b, c) coefficients are the k -dependent wave function coefficients described in Eqs. (10). For parallel optical polarizations we can take both polarizations to be in the z direction. For arbitrary polarizations we can use the z component for one beam and determine the other matrix element for the appropriate orientation. In examples below we consider cross-polarized beams, so the x component (or the y component) of the momentum matrix element is also required, which we show in Table 2 (using the same formalism as above). Whereas the z component is independent of the ϕ component of the electronic wave vector \mathbf{k} , it can be seen the same is not true for the x component.

Using the expression for the nondegenerate two-photon transition rate given in Eq. (11), we obtain the following expression for the 2PA coefficient:

$$\beta_{12}(\omega_1; \omega_2) = \left(\frac{e^2}{\hbar c} \right)^2 \frac{\hbar P}{2n_0(\omega_1)n_0(\omega_2)E_g^3} f_2 \left(\frac{\hbar\omega_1}{E_g}; \frac{\hbar\omega_2}{E_g} \right),$$

$$= K \frac{\sqrt{E_p}}{n_0(\omega_1)n_0(\omega_2)E_g^3} f_2 \left(\frac{\hbar\omega_1}{E_g}; \frac{\hbar\omega_2}{E_g} \right), \quad (15)$$

where the dimensionless spectral function f_2 is defined as

$$f_2(x_1; x_2) = \frac{1}{x_1 x_2^2} \sum_{vc} \int_0^{2\pi} d\phi \int_0^\pi \sin \theta d\theta \int_0^\infty \left(\frac{kP}{E_g} \right)^2 \frac{d(kP)}{E_g}$$

$$\times \left| \sum_i \left[\frac{M_{ci}^{(2)} M_{iv}^{(1)}}{E_{iv}(k)/E_g - x_1} + \frac{M_{ci}^{(1)} M_{iv}^{(2)}}{E_{iv}(k)/E_g - x_2} \right] \right|^2$$

$$\times \delta \left[\frac{E_{cv}(k)}{E_g} - x_1 - x_2 \right]. \quad (16)$$

The material dependent constant K is given by

$$K = \left(\frac{e^2}{\hbar c} \right)^2 \frac{\hbar^2}{2\sqrt{2}m_0}, \quad (17)$$

which has the value of 2.2 cm/GW (eV)^{5/2} (allowing E_p and E_g to be given in electron volts), and E_p is related to the Kane parameter P by $E_p = 2m_0 P^2 / \hbar^2$.

In the Kane band-structure case, there is a dependence on the ratio of the split-off energy to the band gap, Δ/E_g , which is contained within the dimensionless spectral function f_2 (the parameter P also appears, but only for scaling the integral), which obviously does not appear in the two-parabolic-band model. The summations involved are over all valence to conduction band routes via all possible intermediate states (which are themselves the various valence and conduction bands described in this band-structure model). In this calculation only the bands described above are used, i.e., one conduction and three valence bands, each doubly degenerate in spin. Higher band contributions are neglected. With the matrix elements described above for the Kane model, there are 46

Table 2. x Components of the Scaled Momentum Matrix Element $M_{ij} = \langle i|p_x|j\rangle\hbar/m_0P$ as a Function of the Electronic k Vector in Polar Coordinates^a

Spin States	$c\ \alpha$	$hh\ \alpha$	$lh\ \alpha$	$so\ \alpha$
$c\ \alpha$	$2a_c c_c \sin \theta \cos \phi$	0	$\frac{(a_c c_l + a_l c_c) \sin \theta \cos \phi}{\sqrt{2}}$	$\frac{(a_c c_s + a_s c_c) \sin \theta \cos \phi}{\sqrt{2}}$
$c\ \beta$	0	$\frac{a_c}{\sqrt{2}} (\cos \theta \cos \phi - i \sin \phi)$	$\frac{(a_c b_l - a_l b_c) (\cos \theta \cos \phi + i \sin \phi)}{\sqrt{2}}$	$\frac{(a_c b_s - a_s b_c) (\cos \theta \cos \phi + i \sin \phi)}{\sqrt{2}}$
$hh\ \alpha$	0	0	0	0
$hh\ \beta$	$\frac{a_c}{\sqrt{2}} (\cos \theta \cos \phi - i \sin \phi)$	0	$\frac{a_l}{\sqrt{2}} (\cos \theta \cos \phi - i \sin \phi)$	$\frac{a_s}{\sqrt{2}} (\cos \theta \cos \phi - i \sin \phi)$
$lh\ \alpha$	$\frac{(a_c c_l + a_l c_c) \sin \theta \cos \phi}{\sqrt{2}}$	0	$2a_l c_l \sin \theta \cos \phi$	$\frac{(a_l c_s + a_s c_l) \sin \theta \cos \phi}{\sqrt{2}}$
$lh\ \beta$	$-\frac{(a_c b_l - a_l b_c) (\cos \theta \cos \phi + i \sin \phi)}{\sqrt{2}}$	$\frac{a_l}{\sqrt{2}} (\cos \theta \cos \phi - i \sin \phi)$	0	$\frac{(a_l b_s - a_s b_l) (\cos \theta \cos \phi + i \sin \phi)}{\sqrt{2}}$
$so\ \alpha$	$\frac{(a_c c_s + a_s c_c) \sin \theta \cos \phi}{\sqrt{2}}$	0	$\frac{(a_l c_s + a_s c_l) \sin \theta \cos \phi}{\sqrt{2}}$	$2a_s c_s \sin \theta \cos \phi$
$so\ \beta$	$-\frac{(a_c b_s - a_s b_c) (\cos \theta \cos \phi + i \sin \phi)}{\sqrt{2}}$	$\frac{a_s}{\sqrt{2}} (\cos \theta \cos \phi - i \sin \phi)$	$-\frac{(a_l b_s - a_s b_l) (\cos \theta \cos \phi + i \sin \phi)}{\sqrt{2}}$	0

^aAgain only transitions from α spin states are shown, and the relations $M_{\alpha,\beta} = M_{\alpha,\beta}$ and $M_{\alpha,\beta} = M_{\beta,\alpha}$ should be used for the transitions from the β spin states. Abbreviations are defined as for Table 1.

contributing transitions from valence to conduction band, compared with 4 for the two-parabolic-band model (which can be further reduced to one calculation, as all 4 transitions occur at the same magnitude of the \mathbf{k} vector). In both the two-parabolic-band and the Kane band models, these transitions consist of an allowed term (valence to conduction band) and a forbidden term, i.e., not allowed at $k = 0$ (self-valence, self-conduction, or intervalence band).

The algorithm for computing the nondegenerate 2PA is as follows. First, for the given optical frequencies ω_1 and ω_2 , the magnitude of k at which this optical transition occurs is determined. This involves calculating the root of the argument of the Dirac delta function in Eq. (16) [which in turn involves computing the roots of Eqs. (7)]. Second, the wave functions for these states are determined by computing the (a, b, c) coefficients [Eqs. (10)]. Third, the appropriate scaled momentum matrix elements $M_{ij}^{(n)}$ (k dependent) are determined (Tables 1 and 2). Fourth, the summation is performed over all valid intermediate states, and the integrals are computed over the angular coordinates of the \mathbf{k} wave vector (θ, ϕ) .

RESULTS

Indium Antimonide

To check the above algorithm, we first make a comparison with established theories for degenerate 2PA in narrow-gap semiconductors, citing InSb as an example. Weiler² gives an analytic expression for the degenerate spectral function f_2 that includes nonparabolicity and nonzone-center wave functions in the limit of a large split-off energy, $\Delta \gg kP, E_g$, which is applicable to narrow-gap semiconductors:

$$f_2^{np}(x) = \frac{8\pi(2x-1)^{3/2}}{3x^3} \times \left[\frac{4(3x)^{1/2}}{(3x-1)^2} + \left(3x + \frac{3}{2}\right)^{3/2} \frac{(9x^4 + 10x^2 + 6)}{90x^5} \right]. \quad (18)$$

Weiler also gives the correct form of the frequency dependence, using parabolic bands and zone-center wave functions (also in the limit $\Delta \gg kP, E_g$), which was calculated by Lee and Fan¹³:

$$f_2^{pb}(x) = \frac{8\pi(2x-1)^{3/2}}{\sqrt{6}x^5} \left(4 + \frac{29\sqrt{2}}{12} \right). \quad (19)$$

The material scaling of both of these models is exactly the same as that given above in Eq. (15). These forms are plotted in Fig. 3 for InSb at room temperature ($E_g = 0.175$ eV; $E_p = 21.3$ eV; $\Delta = 0.85$ eV), along with the results of the numerical model presented here. It can be seen that the omission of nonparabolicity and nonzone-center wave functions leads to a considerable overestimation of 2PA, except close to the 2PA edge, although the overall shape is qualitatively similar to that in the nonparabolic case. This is a result of the decrease of the interband momentum matrix element with increasing k as the $\mathbf{k} \cdot \mathbf{p}$ perturbation causes more mixing of the s - and p -like wave functions. We find that our calculation gives a result close to that of Weiler's nonparabolic calculation, with only

a small deviation at higher photon energies. This deviation is due principally to there being a term proportional to E_g/Δ in the effective mass as a result of the interaction of the split-off band, which is neglected in Weiler's expression. In the same plot we show some experimental data taken with a CO₂ laser at 10.6 and 9.6 μm .¹⁹⁻²² The spread in the experimental data makes the frequency dependence impossible to confirm, but the results given here seem to confirm that, for 2PA in InSb, nonparabolicity and nonzone-center wave functions have a marked effect on the overall magnitude of the 2PA but that the frequency dependence is not greatly changed, as was stated in Ref. 2.

Degenerate Two-Photon Absorption at 1.06 and 0.53 μm

Reference 3 gives a range of degenerate 2PA measurements in semiconductors at a wavelength of 1.06 μm and its second harmonic, 0.53 μm . The results for the semiconductors with a zinc blende structure are shown in Table 3 along with the predicted values from the present theory. The uncertainty in the measured values was given as $\pm 40\%$. For CdTe, GaAs, ZnS, and ZnSe, excel-

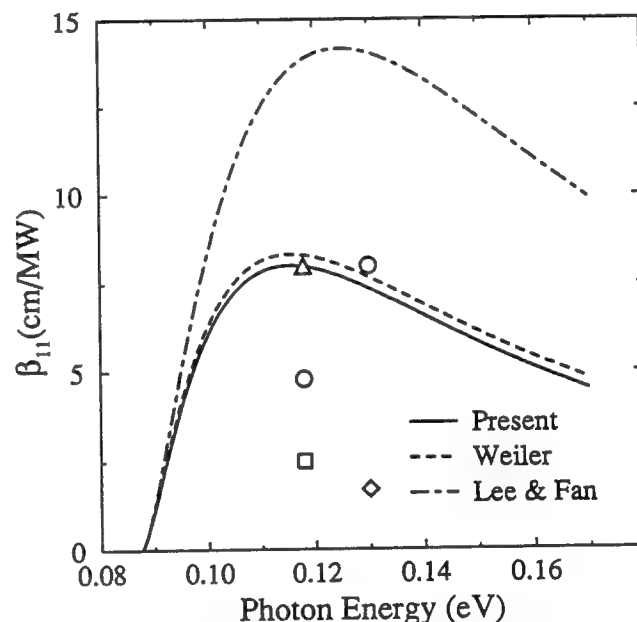


Fig. 3. Frequency dependence of the degenerate 2PA in InSb. Included for comparison are various experimentally determined values at 10.6 and 9.6 μm : Δ , Ref. 19; \circ , Ref. 20; \square , Ref. 21; \diamond , Ref. 22.

Table 3. Degenerate 2PA in a Variety of Zinc Blende Semiconductors

Material	Wavelength (μm)	β (cm/GW)		
		Ref. 3	Ref. 23	Theoretical ^a
ZnSe	0.532	5.5	5.8	5.0
ZnS	0.532	2.0-3.5	—	3.0
GaAs	1.064	23	26	22
CdTe	1.064	15-22	26	18
ZnTe	1.064	4.5	4.2	1.2

^aThe theoretical values were determined by using the algorithm presented here, which includes band nonparabolicity, the contribution from the split-off band, and the use of nonzone-center wave functions.

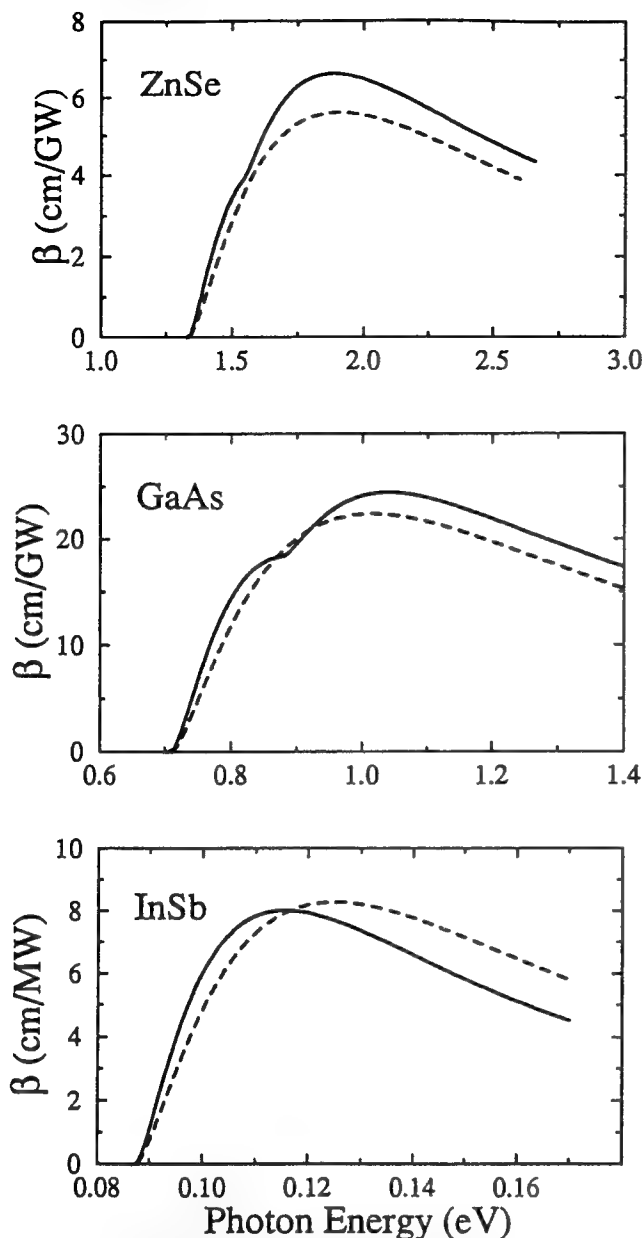


Fig. 4. Comparison of the present calculation (solid curves) with the fitted two-parabolic-band result (dashed curves), i.e., setting $K_{pb} = 3100 \text{ cm/GW (eV)}^{3/2}$, for the degenerate 2PA in InSb, GaAs, and ZnSe.

lent agreement is obtained, especially considering that there are no fitting parameters whatsoever in the present treatment. However, the 2PA in ZnTe at $1.06 \mu\text{m}$ is considerably underestimated. It should be noted, however, that this measurement lies close to the 2PA edge. It has been suggested that this discrepancy is due to excitonic enhancement since the difference corresponds to only a few times the exciton binding energy.³ Other possible explanations are that there may be some degree of band tailing or that allowed-transitions via higher bands become relatively more important close to the 2PA edge.

One of the surprising features of the simpler two-parabolic-band model is that, when it is scaled (i.e., $K_{pb} = 3100$), it provides a remarkably good prediction for the degenerate 2PA over a wide range of materials and frequencies.³ To confirm this fact we compare the results of this model with our present theory in Fig. 4 for

InSb, GaAs, and ZnSe. It can be seen that in all three examples the two curves lie fairly close together over the whole frequency range shown here (certainly well within typical experimental errors for these types of measurement). Note, however, that as the band gap increases, the two-parabolic-band result increasingly underestimates β as the split-off band plays a greater role.

Zinc Selenide

One of the semiconductors in which we make a comparison between theory and experiment for the nondegenerate 2PA spectra is ZnSe. In this material the band gap and split-off energies are of comparable magnitudes ($E_g = 2.67 \text{ eV}$, $E_p = 24.2 \text{ eV}$, $\Delta = 0.42 \text{ eV}$), fulfilling neither of Weiler's analytic expressions for the degenerate 2PA that were calculated for $\Delta \gg E_g$ and $\Delta \ll E_g$. That this is so is demonstrated in Fig. 5, which is a plot of the degenerate 2PA coefficient against frequency and from which it can be seen that the exact numerical calculation performed here (solid curve) agrees with Weiler's nonparabolic expression for $\Delta \gg E_g$ (short-dashed curve) close to the 2PA edge but asymptotically approaches the expression for $\Delta \ll E_g$ at higher frequencies. The point of inflection near 1.5 eV in the present calculation occurs because the photon energies have reached the threshold of split-off to conduction band transitions. The data denoted by the circles are two measurements at $0.532 \mu\text{m}$,^{3,23} which show excellent agreement with the present calculation. Also shown in Fig. 5 is the polarization dependence of the frequency-degenerate 2PA. The solid curve discussed above also gives the nondegenerate 2PA in the limit of identical frequencies and parallel polarizations. The long- and short-dashed curve shows the same quantity, but now

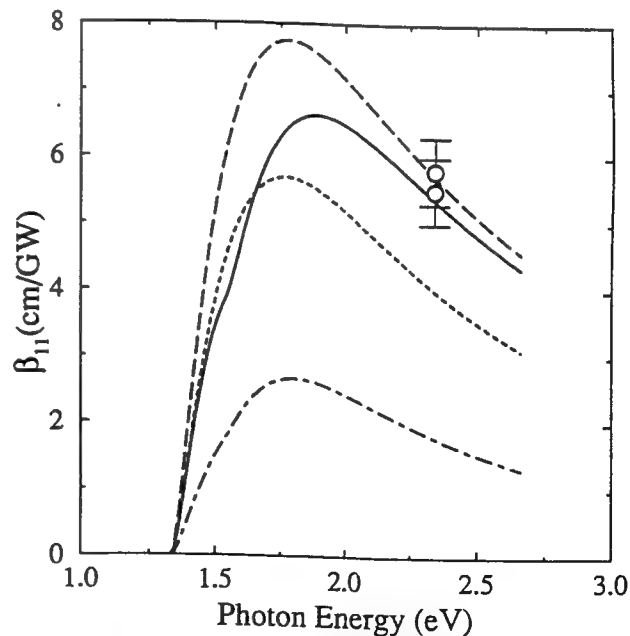


Fig. 5. Frequency dependence of the degenerate 2PA in ZnSe. The solid curve shows the present calculation; the short-dashed curve and the long-dashed curve show Weiler's nonparabolic expressions in the limits $\Delta \gg E_g$ and $\Delta \ll E_g$, respectively. The dotted-dashed curve shows nondegenerate 2PA where the two wavelengths are identical but the optical polarizations are perpendicular. Also included are some data points with appropriate error bars taken from Refs. 3 and 23.

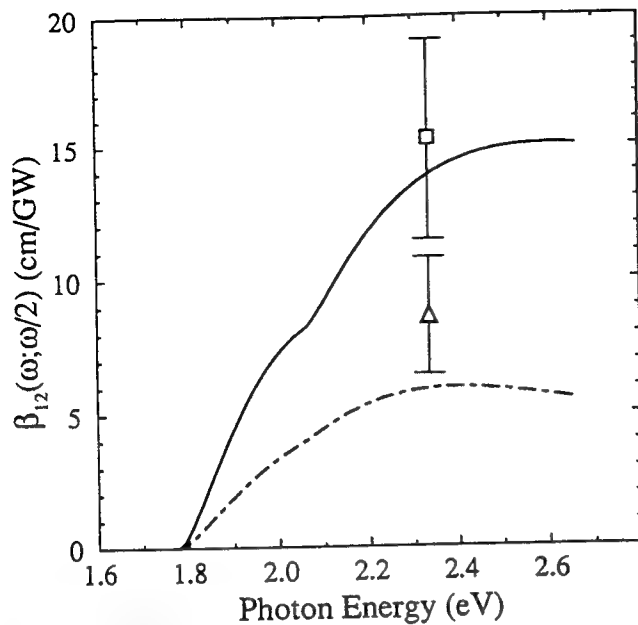


Fig. 6. Nondegenerate 2PA in ZnSe at the second-harmonic frequency that is due to the presence of light at the fundamental frequency. The solid curve corresponds to parallel optical polarizations; the dashed curve, to perpendicular. Two data points are shown, measured at $0.532 \mu\text{m}$ because of the presence of a beam at $1.064 \mu\text{m}$, by the two color Z-scan technique.⁵ The square corresponds to parallel polarizations, and the triangle to perpendicular.

the optical polarizations of the two beams are perpendicular. It can be seen that in the perpendicular case the 2PA coefficient is approximately a factor of 2–3 less than in the parallel case over all frequencies beneath the band edge, $\hbar\omega < E_g$. For ZnSe at a wavelength of 705 nm this theory gives a ratio of 2.4 between the two polarization cases, which agrees fairly well with an experimental measurement of 2.²⁴ Note that the threshold for the split-off transitions is much less obvious in the perpendicular case. This result is a consequence of the direction of the matrix elements involving the split-off band resulting in a reduction in the angular (Euler's) integral for these transitions. It should be noted, though, that one must take care when considering nondegenerate optical effects that arise from two beams of identical frequency, as coherence must play a significant role. The nondegenerate 2PA values given in Fig. 5 should be considered only as the limit obtained, as the two (different) frequencies tend to the same value.

One method of obtaining a nondegenerate 2PA measurement is to frequency double a portion of a pump beam and use it as a probe beam. However, it should be noted that this method can be used only to obtain nondegenerate measurements along a particular line in the (ω_1, ω_2) plane, as the two frequencies used must have a fixed relation between them (i.e., $\omega_1 = 2\omega_2$). Figure 6 shows the nondegenerate 2PA in ZnSe at the second harmonic that is due to the presence of the fundamental within the material, i.e., $\beta(\omega; \omega/2)$. Once again a solid curve is used to denote parallel optical polarizations; and a long-and-short-dashed curve, perpendicular. Again the point of inflection where split-off transitions become allowed is readily seen in the parallel case. The data shown here are nondegenerate 2PA coefficients measured at $0.532 \mu\text{m}$ that are

due to the influence of a strong $1.064\text{-}\mu\text{m}$ pump beam measured by the two-color Z-scan technique.⁵

A recent paper⁴ reported the measurement of nondegenerate 2PA in several wide-gap semiconductors by using a pump at 705 nm and a picosecond continuum pulse as a probe. This directly gives the form of nonlinear absorption applicable to the determination of the nonlinear refractive index n_2 by the nonlinear Kramers–Kronig

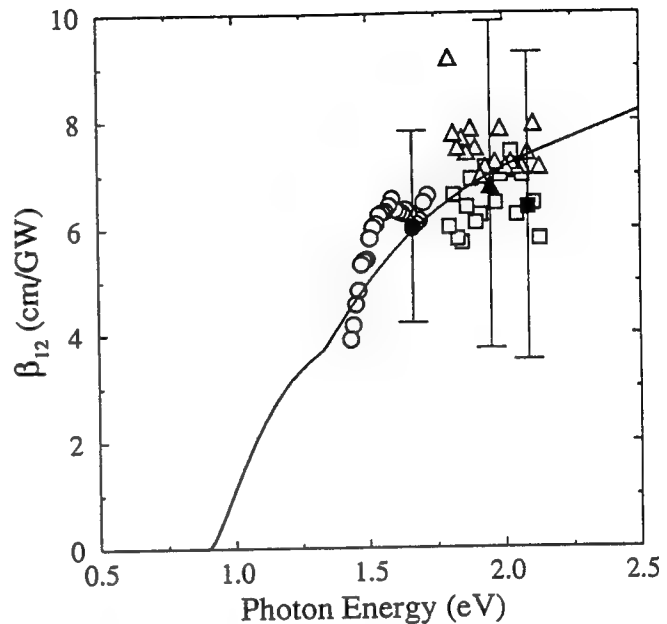


Fig. 7. Nondegenerate 2PA in ZnSe as a function of probe frequency for a fixed pump frequency at $0.705 \mu\text{m}$ (parallel polarizations). The data are from Ref. 4. The circles correspond to a high irradiance, $I_2 = 8 \text{ GW/cm}^2$ (errors $\pm 30\%$), and the squares and triangles to a lower irradiance measurement, $I_2 = 0.7 \text{ GW/cm}^2$ (errors $\pm 45\%$).

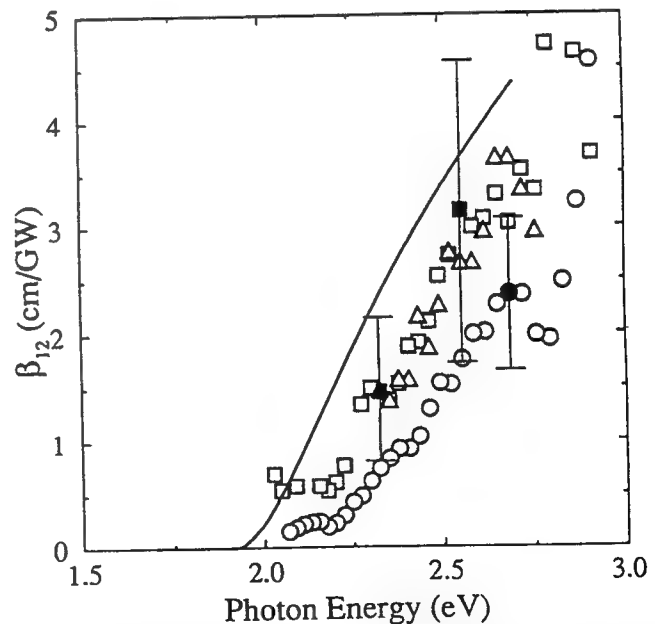


Fig. 8. Nondegenerate 2PA in ZnS as a function of probe frequency for a fixed pump frequency at $0.705 \mu\text{m}$ (parallel polarizations). The data are from Ref. 4. The circles correspond to a high irradiance, $I_2 = 8 \text{ GW/cm}^2$ (errors $\pm 30\%$), the squares to a medium irradiance, $I_2 = 1.8 \text{ GW/cm}^2$ (errors $\pm 45\%$), and the triangles to a lower irradiance $I_2 = 0.7 \text{ GW/cm}^2$ (errors $\pm 45\%$).

relation.⁶ Figure 7 shows the results for ZnSe along with the results of the corresponding theoretical calculation. The circles correspond to a pump irradiance of ≈ 8 GW/cm² and have an estimated error of $\pm 30\%$. The triangles and the squares correspond to a lower irradiance level (≈ 0.7 GW/cm²) and have an estimated error of $\pm 45\%$. The sizes of these errors make it difficult to infer any details of the nonlinear absorption spectrum, but the magnitude is in complete agreement with the present calculation.

Zinc Sulfide

Reference 4 also presents data for ZnS, which is also a zinc blende semiconductor, but in this case the spin-orbit interaction is small, and the split-off energy is much smaller than the band gap ($E_g = 3.54$ eV, $E_p = 20.4$ eV, $\Delta = 0.064$ eV). In the case of ZnS, the picosecond continuum provided the nondegenerate 2PA around the 2PA edge (i.e., $\hbar\omega_1 + \hbar\omega_2 \sim E_g$), as shown in Fig. 8. Here the circles correspond to an irradiance level of ≈ 8 GW/cm² with an estimated error of $\pm 30\%$, the squares to ≈ 8 GW/cm² ($\pm 45\%$), and the triangles to ≈ 0.7 GW/cm² ($\pm 45\%$). Once again, the solid curve is the calculated 2PA and shows excellent agreement with the wavelength dependence and magnitude, considering that the calculation is absolute. Note that in this case because of the small split-off energy Δ the point of inflection corresponding to the threshold of split-off transitions is no longer obvious.

CONCLUSIONS

We have presented an algorithm for the determination of 2PA in zinc blende semiconductors. The calculation uses the band structure described by Kane,^{11,12} consisting of a conduction band and three valence bands (heavy-hole, light-hole, and split-off) and includes the effects of nonparabolicity and nonzone-center wave functions. The 2PA coefficient is determined from the transition rate, which is calculated by using second-order perturbation theory (Fermi's golden rule).

The motivation for this study is threefold. First, while a simple two-parabolic-band model gives the correct material scaling and spectral dependence, the results of that model have to be scaled to fit reliable experimental data (replacing the material independent constant $K_{pb} = 1940$ with the best-fit value of 3100 for a range of semiconductors³). We have shown that this fit provides a good approximation to the fuller band-structure calculation for the degenerate 2PA. However, it is desirable to use a band-structure model that does not require any fitting parameters. The Kane band structure with nonparabolicity and nonzone-center wave functions² seems to satisfy this requirement. Second, in order to account for the optical polarization dependence, one must know the direction as well as the magnitude of the momentum matrix element. The simpler two-band model does not provide this, but the polarization dependence is an integral part of the Kane band-structure model. Third, the nondegenerate 2PA is one of the contributions that can be used to determine the nonlinear refractive index n_2 by a nonlinear Kramers-Kronig transformation⁶ (the other methods being Raman transitions and the ac Stark effect). This determination has already been made by using a two-parabolic-band

model,¹⁷ but again it must be scaled by approximately a factor of 2 to fit the available data. This present research provides the groundwork for a nonlinear Kramers-Kronig calculation of n_2 for the Kane band structure that we hope will not require the use of any fitting parameters.

It is found that the results of the calculation that uses the algorithm presented here agrees well with available degenerate as well as nondegenerate 2PA data in various zinc blende semiconductors (with the exception of degenerate 2PA in ZnTe at $1.06 \mu\text{m}$). Previous publications claim that excitonic effects are important even well above the 2PA edge.^{2,13} We find that in most of our examples good predictions are obtained without the inclusion of such effects. It is shown in Ref. 25 that the coulombic enhancement for linear absorption vanishes at higher photon energies such that $\hbar\omega - E_g \gg E_b$, where E_b is the exciton binding energy (Rydberg). We would expect the same to be true for nonlinear absorption. The examples given here almost all occur well away from photon energies where coulombic enhancement is relevant (again an exception being 2PA in ZnTe). Also, impurities and defects in the semiconductors will lead to screening of the coulombic potential and band tailing, which will reduce the bound exciton resonant absorption and the unbound contribution that gives rise to the aforementioned enhancement of the 2PA. We conclude that the enhancement reported in Ref. 13 must be considered an upper limit of 2PA.

Another effect that is neglected in the present calculation is any contribution from other bands. This contribution has a twofold effect. First, the calculated band structure will be different when other bands are allowed to mix with the set of four bands used in the band-edge optical properties (conduction plus three valence). For example, these contributions are necessary if one wishes to obtain a heavy-hole effective mass different from that of free electrons. In particular, away from zone center, the calculated shape of the conduction band is quite different from that of the Kane model. So, for instance in ZnSe, significant deviations from the Kane model should occur near 1 eV above the band edge²⁶ (corresponding to degenerate 2PA 0.5 eV above the 2PA edge). It is quite remarkable that our model (and to a certain extent the two-parabolic-band model) works so well at these higher photon energies. Second, there are possible two-photon transitions for which the additional bands can be used as the intermediate state. However, these transitions should be significant only close to the 2PA edge (as these are allowed-allowed transitions, compared to the allowed-forbidden transitions considered in this paper) and for transitions high into the conduction band (where the energy difference denominators for transitions via a higher band are not so large). For the intermediate photon energies examined here, these extra transitions should be negligible.

We have calculated only the 2PA contribution to the nondegenerate nonlinear absorption, using transition rates that correspond to loss of energy to the material. Loss or even gain from energy transfer between beams (four-wave mixing) is ignored. This is as it should be for 2PA coefficients; however, one must exercise great care in performing experiments in order to separate clearly the loss contributions of 2PA and energy transfer.

ACKNOWLEDGMENTS

The authors thank A. Miller, B. S. Wherrett, M. Sheik-Bahae, and D. J. Hagan for useful discussions; J. Bolger, A. K. Kar, J. R. DeSalvo, and D. J. Hagan for making their data available before publication; and J. Wang for providing additional experimental data used in comparisons here. We gratefully acknowledge the support of the Defense Advanced Research Projects Agency/Center for Night Vision and Electro-Optics and the Florida High Technology and Industry Council.

E. W. Van Stryland is also with the Departments of Physics and Electrical Engineering, University of Central Florida.

*Present address, Department of Electronics and Electrical Engineering, University of Glasgow, Glasgow G12 8QQ, UK.

REFERENCES

1. V. Nathan, A. H. Guenther, and S. S. Mitra, "Review of multiphoton absorption in crystalline solids," *J. Opt. Soc. Am. B* **2**, 294-316 (1985).
2. M. H. Weiler, "Nonparabolicity and exciton effects in two-photon absorption in zincblende semiconductors," *Solid State Commun.* **39**, 937-940 (1981).
3. E. W. Van Stryland, H. Vanherzeele, M. A. Woodall, M. J. Soileau, A. L. Smirl, S. Guha, and T. F. Boggess, "Two photon absorption, nonlinear refraction, and optical limiting in semiconductors," *Opt. Eng.* **24**, 613-623 (1985).
4. J. Bolger, A. K. Kar, B. S. Wherrett, R. DeSalvo, D. C. Hutchings, and D. J. Hagan, "Nondegenerate two-photon absorption spectra of ZnSe, ZnS and ZnO," *Opt. Commun.* (to be published).
5. M. Sheik-Bahae, J. Wang, J. R. DeSalvo, D. J. Hagan, and E. W. Van Stryland, "Measurement of nondegenerate nonlinearities using a 2-color Z-scan," *Opt. Lett.* **17**, 258-260 (1992).
6. D. C. Hutchings, M. Sheik-Bahae, D. J. Hagan, and E. W. Van Stryland, "Kramers-Kronig relations in nonlinear optics," *Opt. Quantum Electron.* **24**, 1-30 (1992), tutorial review.
7. M. Sheik-Bahae, D. C. Hutchings, D. J. Hagan, and E. W. Van Stryland, "Dispersion of bound electronic nonlinear refraction in solids," *IEEE J. Quantum Electron.* **27**, 1296-1309 (1991).
8. B. S. Wherrett, "Scaling rules for multiphoton interband absorption in semiconductors," *J. Opt. Soc. Am. B* **1**, 67-72 (1984).
9. L. V. Keldysh, "Ionization in the field of a strong electromagnetic wave," *Sov. Phys. JETP* **20**, 1307-1314 (1965).
10. N. G. Basov, A. Z. Grasyuk, I. G. Zubarev, V. A. Katulin, and O. N. Krokhin, "Semiconductor quantum generator with two-photon optical excitation," *Sov. Phys. JETP* **23**, 366-371 (1966).
11. E. O. Kane, "Band structure of narrow gap semiconductors," in *Lecture Notes in Physics: Narrow Gap Semiconductors Physics and Applications*, W. Zawadzki, ed. (Springer-Verlag, New York, 1980), Vol. 133, pp. 13-31.
12. E. O. Kane, "Band structure of indium antimonide," *J. Phys. Chem. Solids* **1**, 249-261 (1957).
13. C. C. Lee and H. Y. Fan, "Two-photon absorption with exciton effect for degenerate bands," *Phys. Rev. B* **9**, 3502-3516 (1974).
14. C. R. Pidgeon, B. S. Wherrett, A. M. Johnston, J. Dempsey, and A. Miller, "Two-photon absorption in zinc-blende semiconductors," *Phys. Rev. Lett.* **42**, 1785-1788 (1979).
15. J. H. Bechtel and W. L. Smith, "Two-photon absorption in semiconductors with picosecond laser pulses," *Phys. Rev. B* **13**, 3515-3522 (1976).
16. H. D. Jones and H. R. Reiss, "Intense-field effects in solids," *Phys. Rev. B* **16**, 2466-2473 (1977).
17. H. S. Brandi and C. B. de Araújo, "Multiphoton absorption coefficients in solids: a universal curve," *J. Phys. C* **16**, 5929-5936 (1983).
18. E. W. Van Stryland, A. L. Smirl, T. F. Boggess, M. J. Soileau, B. S. Wherrett, and F. A. Hopf, "Weak-wave retardation and phase-conjugate self-defocusing in Si," in *Picosecond Phenomena III*, Vol. 23 of Chemical Physics, K. B. Eisenthal, R. M. Hochstrasser, W. Kaiser, and A. Laubereau, eds. (Springer-Verlag, Berlin, 1982), pp. 368-371.
19. A. Miller, A. Johnson, J. Dempsey, J. Smith, C. R. Pidgeon, and G. D. Holah, "Two photon absorption in InSb and Hg_{1-x}Cd_xTe," *J. Phys. C* **12**, 4839-4849 (1979).
20. A. M. Johnson, C. R. Pidgeon, and J. Dempsey, "Frequency dependence of two-photon absorption in InSb and HgCdTe," *Phys. Rev. B* **22**, 825-831 (1980).
21. M. Sheik-Bahae, P. Mukherjee, and H. S. Kwok, "Two-photon and three-photon absorption coefficients in InSb," *J. Opt. Soc. Am. B* **3**, 379-385 (1986).
22. M. Sheik-Bahae, T. Rossi, and H. S. Kwok, "Frequency dependence of the two-photon absorption coefficient in InSb: tunneling effects," *J. Opt. Soc. Am. B* **4**, 1964-1969 (1987).
23. A. A. Said, M. Sheik-Bahae, D. J. Hagan, T. H. Wei, J. Wang, J. Young, and E. W. Van Stryland, "Determination of bound and free-carrier nonlinearities in ZnSe, GaAs, CdTe and ZnTe," *J. Opt. Soc. Am. B* **9**, 405-414 (1992).
24. J. Bolger, Department of Physics, Heriot-Watt University, Riccarton, Edinburgh EH14 4AS, UK (personal communication).
25. R. J. Elliott, "Intensity of optical absorption by excitons," *Phys. Rev.* **6**, 1384-1389 (1957).
26. K.-H. Hellwege, ed., *Landolt-Börnstein Numerical Data and Functional Relationships in Science and Technology* (Springer-Verlag, Berlin, 1982), Vols. 17a, 17b, Group III.

EXCITE-PROBE TWO-COLOR Z-SCAN

*J. Wang, M. Sheik-Bahae, A.A. Said, D.J. Hagan, and
E.W. Van Stryland*

CREOL

Center for Research in Electro-Optics and Lasers
University of Central Florida, Orlando, FL 32816

ABSTRACT

Using an excite-probe two-color Z-scan technique, we investigate the dynamics of optical nonlinearities in semiconductors with picosecond pulses at 1.06 and 0.532 μm . We use the technique to obtain a direct time-resolved measurement of the nondegenerate nonlinear refraction in polycrystalline ZnSe and show how it can resolve the bound electronic and free carrier components.

2. INTRODUCTION

Time-resolved excite-probe techniques such as four-wave mixing [1] and nonlinear interferometry [2] have been used in the past for studying the dynamics of optical nonlinearities. Here, we show that the simple Z-scan technique [1] can be extended to obtain such dynamics in a nondegenerate excite-probe geometry. In this scheme, we obtain information regarding the sign, magnitude, lifetimes and dispersion of both absorptive and refractive components of optical nonlinearities. Such information is of practical interest in the optimization of self-protecting optical limiting devices.[3] In the case of semiconductor limiters, thermal self focusing is believed to initiate bulk damage to the sample for pulsewidths in excess of the carrier recombination or diffusion times. Furthermore, a detailed measurement of the nondegenerate bound electronic nonlinear refractive index (n_2) and the two-photon absorption (2PA) coefficient (β) in semiconductors would give a better insight into the physics of nonlinearities in these materials. Experimental results on a semiconductor will be compared with the predictions of a two-parabolic-band (TPB) theory which uses a nonlinear Kramers-Krönig transformation in relating the absorptive (β) and refractive (n_2) components of the third order optical susceptibility.[4,5] Nondegenerate 2PA in ZnSe and cross-phase modulation in ZnS and ZnSe are measured and the results are shown to be in good agreement with this simple theory.

3. EXPERIMENTS

The experimental arrangement is as shown in Fig.1. This is an extension of the simple arrangement of Ref.[5] where there was no time-delay capability. The arrangement requires two copropagating beams at different frequencies, for example one at $\lambda=1.06 \mu\text{m}$ generated by a modelocked Nd:YAG laser, and the other at $\lambda=0.532 \mu\text{m}$ by second harmonic generation in a KDP crystal. After time delaying one of the beams, the two beams are recombined and focused with a nearly achromatic lens and the far-field transmittance of both beams (through apertures) can simultaneously be measured using a dichroic beamsplitter. In this geometry, we are able to selectively attenuate each of the two beams independently, thus making it possible to use either the fundamental as the strong pump and the second harmonic as the weak probe or vice-versa. Independent control of the polarization state of each beam is also available. Analogous to the usual single-wavelength Z-scan with a 100% transmitting aperture, the measurement is only sensitive to the induced changes in absorption, while a partially closed aperture Z-scan displays the induced refractive changes as well.

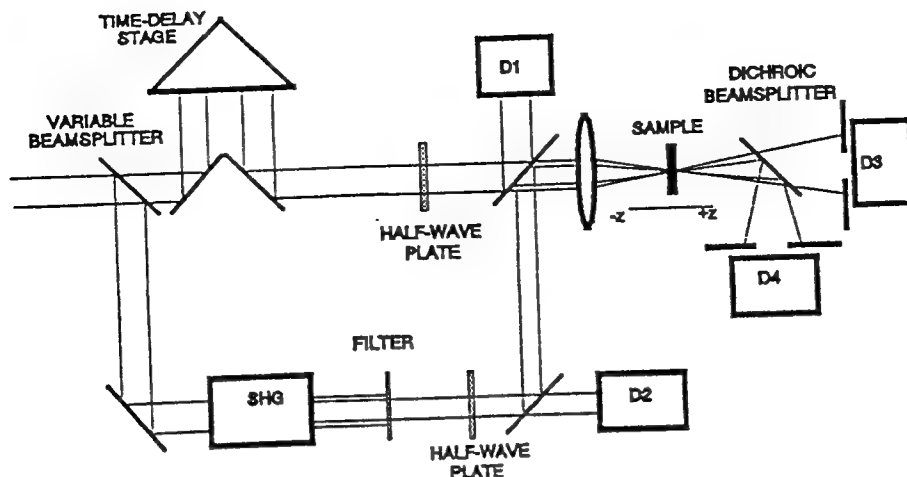


Figure 1. Two-Color time-delay Z-scan experimental setup. $D3/D1$ gives the transmittance of the fundamental beam while $D4/D2$ measures the transmittance of the second harmonic.

The two-color Z-scan for ZnS, measured at zero time delay between the excitation beam at $\lambda=1.06 \mu\text{m}$ and the probe beam at $\lambda=0.532 \mu\text{m}$ is shown in Fig.2. Also shown is the degenerate Z-scan at $\lambda=1.06 \mu\text{m}$. The peak-valley configuration of the Z-scans is indicative of the positive sign of n_2 in both degenerate and nondegenerate cases. Aside from a factor of two enhancement due to cross-phase modulation, we observe a two-photon resonance enhancement of the nondegenerate n_2 in ZnS. This enhancement is in excellent agreement with the TPB calculations. In ZnSe, on the other hand, nondegenerate 2PA is energetically allowed and the two-color Z-scan measurement gives a negative nondegenerate n_2 , also in good agreement with the TPB theory. A comparison of the degenerate and nondegenerate n_2 values for ZnSe and ZnS with that predicted by the theory is given in Fig.3.

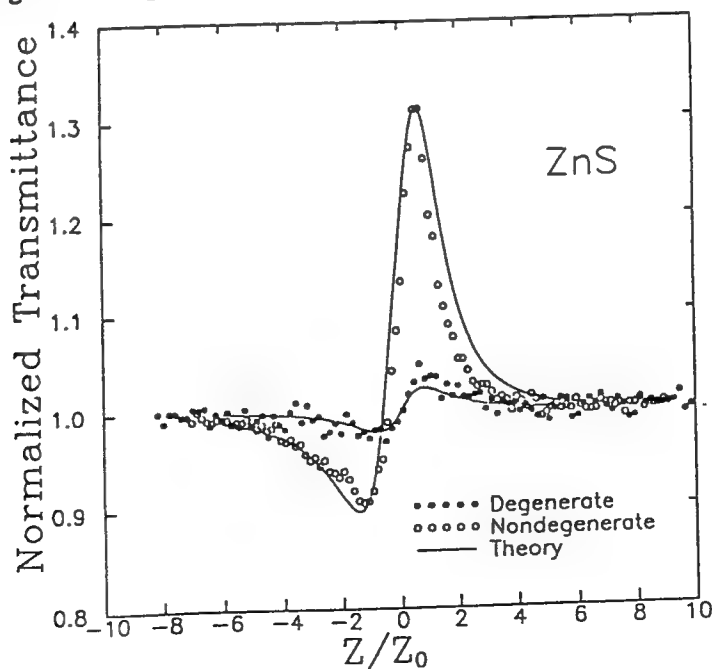


Figure 2. Two color Z-scan for ZnS.

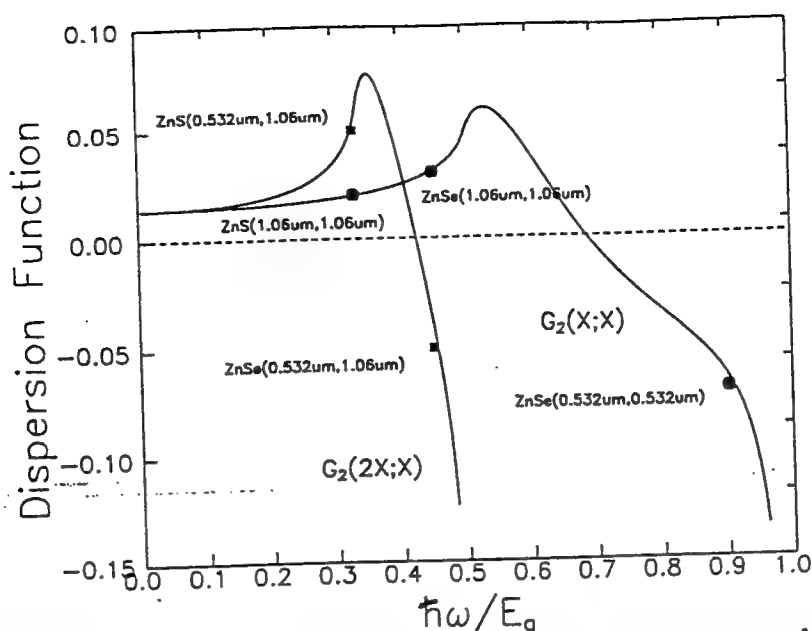


Figure 3. Experimental n_2 data (with bandgap and index dependance scaled out) plotted versus photon energy. The solid lines are dispersion curves calculated from the TPB model.

The response times of the bound electronic nonlinearities are of the order of one optical cycle and, hence, would appear as instantaneous with picosecond pulses. In the presence of 2PA excitation, however, the effect of photogenerated carriers is long lived and can be studied at longer delays where there is little temporal overlap between excitation and probe beams. Note this is possible only if degenerate 2PA is allowed for the excitation beam. Fig. 4 shows the time resolved normalized peak-valley transmittance change ΔT_{p-v} which is a direct measure of the nonlinearly induced phase shift in ZnSe when pumped at $\lambda=0.532 \mu\text{m}$ and probed using the $\lambda=1.06 \mu\text{m}$ beam. This shows the dominance of the ultrafast bound electronic Kerr effect at small delays, while the long-lived and cumulative free carrier refraction (band-filling) is seen at longer delays. The results of our measurements of both nondegenerate 2PA and n_2 are summarized in Table 1.

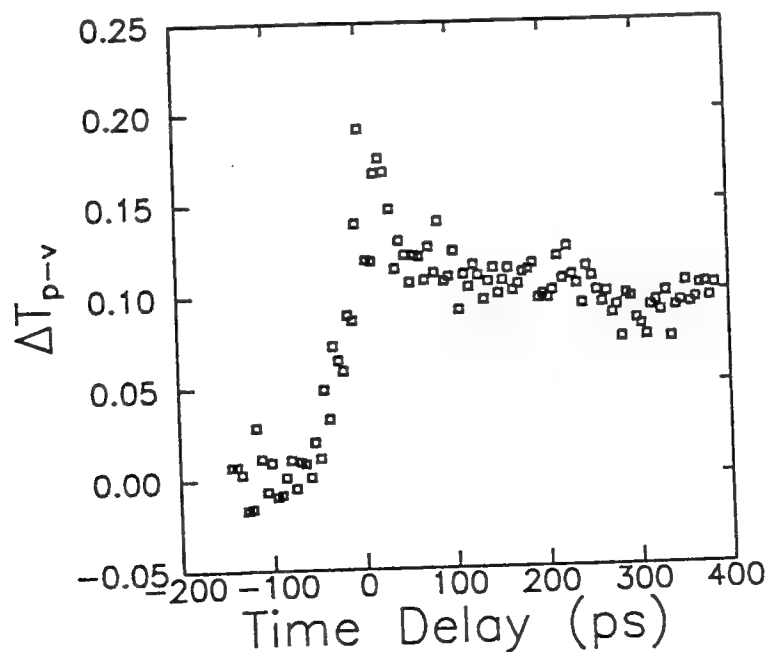


Figure 4. Picosecond time-resolved normalized peak-valley transmittance change for ZnSe with the pump at 532 nm and the probe at 1.06 μm .

COMPARISON BETWEEN EXPERIMENTAL DATA AND THEORY

	Form	Linear index n_0	Energy gap $E_g(\text{eV})$	$n_2(0.532\mu\text{m}, 1.06\mu\text{m})$ ($\times 10^{-12}$ esu)		$\beta_{12}(0.532\mu\text{m}, 1.06\mu\text{m})$ (cm/GW)	
				Exp.	Pred.	Exp.	Pred.
ZnSe	poly-	2.7 (0.532 μm) 2.48 (1.06 μm)	2.58	-34.1	-28.3	15.27	24.4
ZnS	poly-	2.4 (both)	3.54	8.45	9.5	0.073	0

Table 1.

4. CONCLUSIONS

We have reported an excite-probe two-color Z-scan technique for measuring nondegenerate optical nonlinearities. The time delay scheme in this technique allows us to investigate the dynamics of these nonlinearities.

5. ACKNOWLEDGEMENTS

This work was supported by DARPA/CNVEO and the Florida High Technology and Industry Council.

6. REFERENCES

- [1] E.J. Canto-Said, D.J. Hagan, J. Young and E.W. Van Stryland, IEEE J. Quantum Electron. QE-27, 2274 (1991)
- [2] M.J. Moran, C. She and R.L. Carman, IEEE J. Quantum Electron. QE-11, 259 (1975)
- [3] M. Sheik-Bahae, A.A. Said, T.H. Wei, D.J. Hagan, E.W. Van Stryland, IEEE J. Quantum Electron. QE-26, 760(1990).
- [4] M. Sheik-Bahae, D.C. Hutchings, D.J. Hagan, E.W. Van Stryland, IEEE J. Quantum Electron. QE-27, 1296(1991).
- [5] M. Sheik-Bahae, J. Wang, R. DeSalvo, D.J. Hagan, E.W. Van Stryland, Opt. Lett. 17, 258 (1992)

Self-Protecting Optical Limiters
Using Cascading Geometries

A.A. Said, T.H. Wei, R. De Salvo, Z. Wang, M. Sheik-Bahae,
D.J. Hagan, and E.W. Van Stryland

CREOL
Center for Research in Electro-Optics and Lasers
University of Central Florida, Orlando, FL 32816

and

J. W. Perry

Jet Propulsion Laboratory
California Institute of Technology
Pasadena, 91109

ABSTRACT

An increase in the dynamic range of an optical limiting device is achieved by using two different nonlinear elements cascaded within a single limiting device. A comparison between the results of optical limiting experiments for a single nonlinear element limiter and a two element limiter shows a significant increase in the damage threshold of the latter with only a small increase of the limiting threshold.

2. INTRODUCTION

A material possessing large nonlinear refraction and/or nonlinear absorption can be used as a passive optical limiter. Optical limiting with such media has been demonstrated and analyzed.[1-5] Figure 1. shows a typical limiting geometry. The nonlinear element is placed near the waist of a Gaussian beam and the on-axis transmittance is monitored through an aperture in the far field.

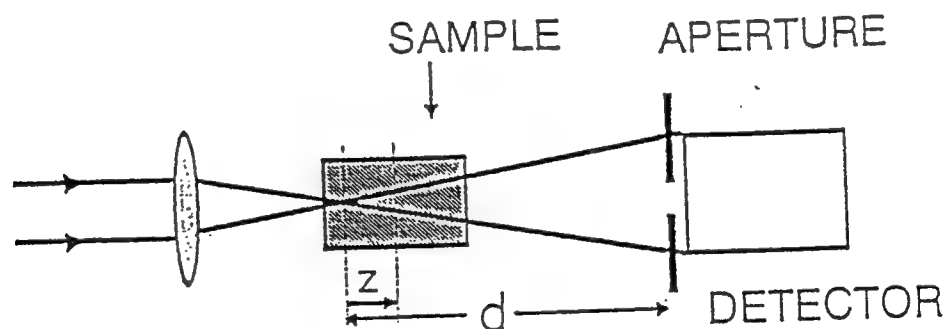


Fig.1. Typical limiting geometry where the transmitted beam is monitored through an aperture in the far field ($d \gg z_0$).

The nonlinear element is placed close to or at focus to increase the incident fluence or irradiance and thus reduce the limiting threshold of the device. However, this same proximity to focus also reduces the damage threshold of the device and therefore, its dynamic range. The dynamic range of a limiting device is defined as the ratio of its damage threshold to its limiting threshold. One way of increasing the dynamic range is by using a "thick" medium with a self-defocusing effect as was demonstrated by Van Stryland *et al* [1] where a monolithic optical power limiting device (MONOPOL) was used. In thick media, a self-focusing effect leads to beam narrowing inside the material causing optical breakdown of the material. Using the Z-scan method, we showed in a previous paper that in thick optical limiters with self-defocusing, the best limiting results "for the far field" are achieved by focusing near the first surface. [6] This however reduces the damage threshold since the surface of the material is more prone to damage than the bulk.

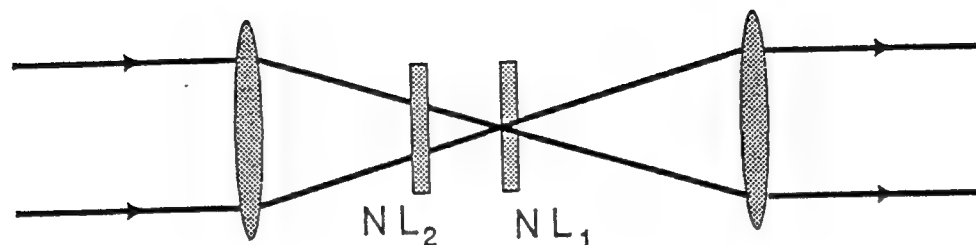


Fig.2. The cascaded optical limiting device. NL1 determines the limiting threshold and NL2 determines the dynamic range.

In this paper we place a second nonlinear element in front of focus which acts as a protector of the first nonlinear element. The second nonlinear element acts as a nonlinear attenuator which turns on at high input energies and whose strength increases with energy. Therefore, it protects the first nonlinear element from damage at high input energies. This scheme is shown in figure 2 where NL1 gives the limiting threshold and NL2 determines the damage threshold. Two different cascaded geometries are used. In one a hybrid limiter is devised where the first element NL1 is immersed in the second element NL2 which is a liquid.

In section 3 we show the formalism and experimental results of the hybrid limiter. In section 4 we discuss the second case where NL1 and NL2 are physically separated by a distance D . Both theoretical and experimental results are presented. A conclusion is given in section 5.

3. HYBRID LIMITER

The hybrid limiter consists of a solution with nonlinear optical properties in which is immersed a solid possessing nonlinear refraction and nonlinear absorption. This tandem limiter is shown in figure 3. In our experiments performed with 30 picosecond pulses (FWHM) at 532 nm, the solid is a 2.7 mm thick ZnSe sample immersed in a 1 cm cell filled with a solution of metallo-phthalocyanine or naphthalocyanine. Nonlinear refraction and nonlinear absorption in ZnSe were completely analyzed and understood in the picosecond regime.[7-9] The optical limiting properties of ZnSe were also studied.[1] In fact, one of the MONOPOL devices by Van Stryland *et al*. [1] was made of ZnSe.

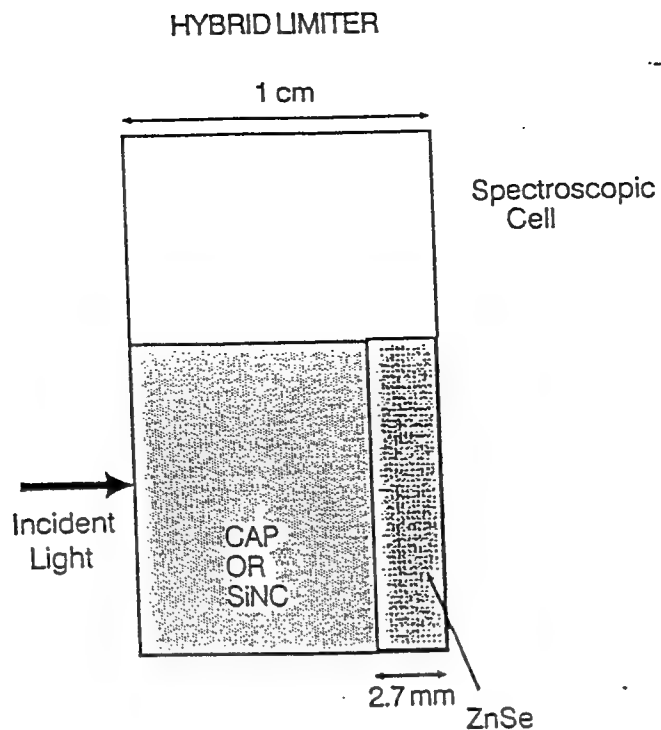


Fig.3. The hybrid limiter where ZnSe is immersed in a solution of CAP or SiNC.

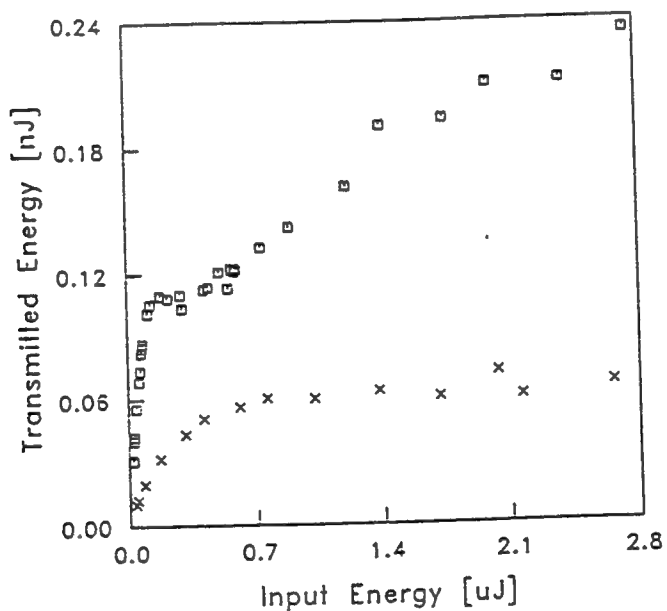


Fig.4. Comparison between the limiting results for ZnSe (squares) and the hybrid limiter (x) of ZnSe. Only a slight increase in the limiting threshold is obtained.

The solution was either chloro-aluminum phthalocyanine in methanol (CAP) or a silicon-naphthalocyanine derivative in toluene (SiNC). Studies of nonlinear refraction and absorption in these materials using 532 nm pulses have shown that they are good limiters in the nanosecond regime.[10,11] These studies indicated lower limiting powers in the nanosecond regime but lower limiting energies in the picosecond regime. This was attributed to the excited state absorption using a five-level model.[10]

The nonlinear effects in CAP and SiNC are dominated by nonlinear absorption.[11] With the ZnSe sample situated at the rear surface of the cell, the solution acts as a nonlinear attenuator whose strength increases with increasing energy. The limiting threshold is still dominated by ZnSe as long as the concentration of SiNC in the solvent is not too high. This means that the limiting threshold, usually at low input energies, might be increased by a small amount while the damage threshold of ZnSe, at high input energies, will increase by a larger amount. The overall effect is a significant increase in the dynamic range of the device. First a Z-scan on the hybrid limiter was performed to find the optimum position of the device with respect to focus. Then the device was placed at a position where the Z-scan signal yields a minimum transmittance.[6] The thickness of the device (1 cm) protects the first surface from damage since it will be many z_0 's away from the beam waist, where $z_0 = \pi w_0^2 / \lambda$ is the confocal beam parameter and w_0 and λ are the beam waist (HW1/eM) and wavelength respectively.

In figure 4 we show a comparison of the experimental limiting results of ZnSe, and a 1 cm cell of the hybrid limiter of SiNC and ZnSe. This device has a 40 percent linear transmission. The curves show less than a factor of two increase in the limiting threshold between ZnSe and the hybrid limiter. However, no damage was observed on ZnSe in the hybrid device up to an input energy of 80 μ J. The damage threshold of ZnSe at 532 nm was measured to be 2 μ J using 30 ps pulses. This shows an increase in the dynamic range of more than a factor of 25. We also performed comparison experiments with the hybrid limiter consisting of CAP and ZnSe with the individual elements. The results of this study and that of ZnSe in SiNC are presented in table 1. From this table it is clear that the hybrid limiter gives a larger dynamic range than the limiters made of any of the individual elements.

	Limiting Threshold	Damage Threshold	Dynamic Range
ZnSe	0.15 μ J	2 μ J	13
CAP/ZnSe (CAP)	0.8 μ J 1.6 μ J	50 μ J	63
SiNC/ZnSe (SiNC)	0.25 μ J 0.45 μ J	>80 μ J	>320

Table 1. Limiting and damage thresholds for ZnSe and hybrid limiters.

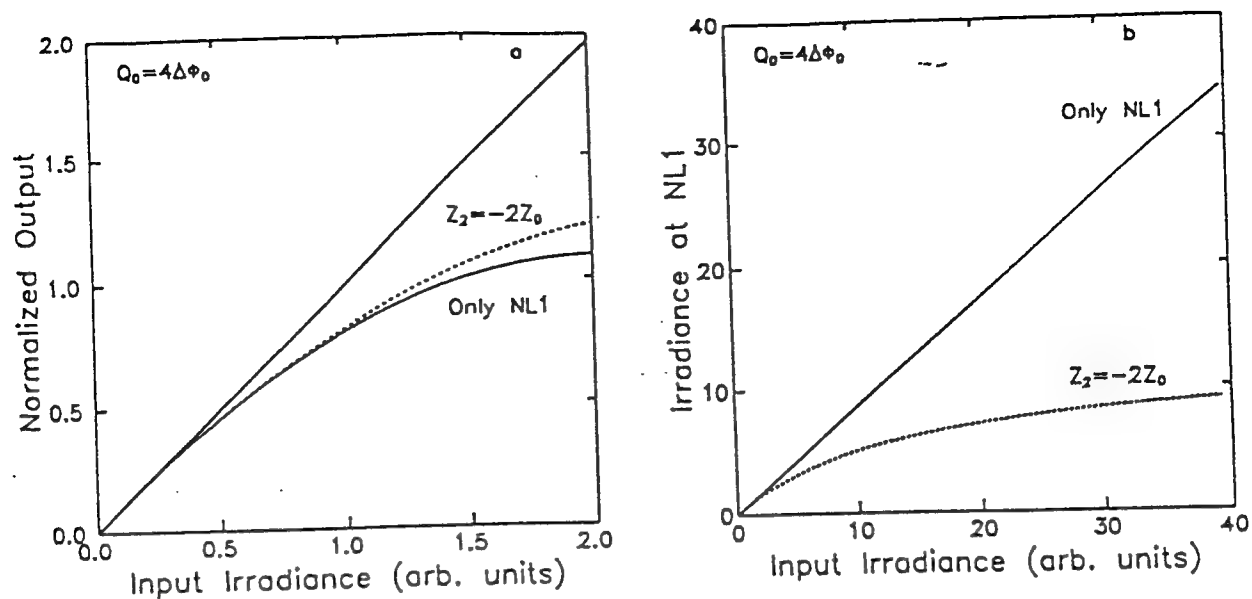


Fig.5. (a) Comparison of the calculated limiting threshold of a single element limiter and a cascaded limiter, and (b) the irradiance incident on NL1 for both cases.

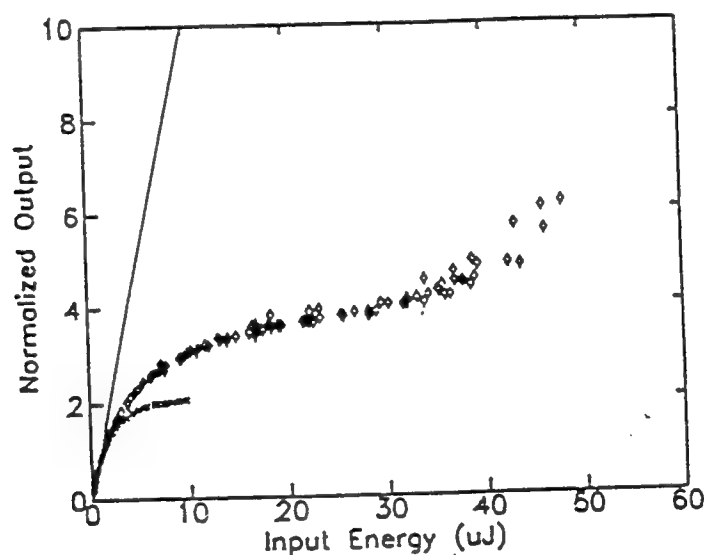


Fig.6. Experimental limiting results for a single element limiter (x) and a cascaded device (diamonds). NL1 is a modified solution of acetone and NL2 is SiNC. The damage threshold was increased from 17 μJ to more than 50 μJ .

4. CASCADED LIMITER

In the geometry of figure 2, two separate nonlinear elements NL1 and NL2 form the limiting device with each element possessing nonlinear refraction or nonlinear absorption or both. NL1 is placed at a distance z_1 from the beam waist and NL2 is at a distance z_2 from focus where $D = z_1 - z_2$ is the separation between the two elements. We performed computer simulations and limiting experiments for the case where NL1 has a nonlinear refractive effect and NL2 has a nonlinear absorptive effect. The irradiance at the exit surface of NL2 is given by

$$I_2 = \frac{I(z_2)}{1 + Q(z_2)} \quad (1)$$

where $Q(z_2) = \beta I(z_2) L_{\text{eff}}$ for two-photon absorption (2PA) and $I(z_2) = I_0 [1 + (z_2/z_0)^2]$ is the input irradiance at NL2. β is the 2PA coefficient and I_0 is the on-axis input irradiance at focus. L_{eff} is the effective interaction length for a material with linear absorption and it is given by

$$L_{\text{eff}} = \frac{1 - e^{-\alpha L}}{\alpha} \quad (2)$$

where L is the medium length and α its linear absorption coefficient. Assuming that the Gaussian beam maintains its Gaussian shape after exiting NL2, we follow the treatment of reference [12] to find the on-axis transmittance in the far field. Given the nonlinearity of NL2, we can determine the input irradiance or fluence on NL1. In figure 5(a) we show the calculated limiting results for NL1 alone and for the cascaded device with NL1 and NL2 both present. In this case $Q_0 = 4\Delta\Phi_0$ where $\Delta\Phi_0$ is the on-axis induced phase shift by NL1 at the focus and $z_2 = -2z_0$. Q_0 and $\Delta\Phi_0$ are given respectively by

$$Q_0 = \beta I_0 L_{\text{eff}} \quad (3)$$

and

$$\Delta\Phi_0 = k\gamma I_0 l_{\text{eff}} \quad (4)$$

Here l_{eff} is the effective length of NL1, $k=2\pi/\lambda$ is the wave vector and γ is the nonlinear index of refraction defined as $n = n_0 + \gamma I$. The calculated results show almost no change in the limiting threshold. On the other hand, figure 5(b) shows that the incident irradiance on NL1 decreases significantly when NL2 is added. This translates to a significant increase in the damage threshold of the device and thus its dynamic range. For example, consider the case where NL1 has a damage threshold of 10 arb. units. This threshold is reached at an input irradiance of ≈ 10 arb units in the absence of NL2. With NL2 in place, this damage threshold is not reached with input irradiance of up to 40 arb. units. The experimental analogue of this case is presented in figure 6. In this case NL1 is a 1 mm thick cell of an acetone solution with impurities added to it in order to increase its linear absorption in the visible. This modified acetone solution exhibits large thermal defocusing when irradiated with nanosecond pulses (≈ 40 ns FWHM) at 532 nm. NL2 is a 2 mm thick cell filled with a solution of SiNC. The linear transmission of this cascaded device is 60 percent. The beam was focused to a radius of $\approx 6 \mu\text{m}$ (HW1/eM) and the distance between NL1 and NL2 was 5.5 mm. In this specific case we were able to increase the damage threshold of the acetone cell from 17 μJ to more than 50 μJ with a very small increase in the limiting threshold.

5. CONCLUSION

We have demonstrated a cascaded geometry where two nonlinear elements are combined in a limiting

device. We showed that by optimizing the geometry, the dynamic range of the limiting device can be significantly increased. For example in the hybrid limiter, we showed more than a factor of 40 increase in the damage threshold and a factor of 25 increase in the dynamic range.

6. ACKNOWLEDGEMENTS

The authors wish to acknowledge the support of DARPA/CNVEO and the Florida High Technology and Industry Council.

7. REFERENCES

1. E.W. Van Stryland, Y.Y. Wu, D.J. Hagan, M.J. Soileau, and K. Mansour, "Optical limiting with semiconductors," J. Opt. Soc. Am., 5, 1980-1989 (1988).
2. R.C.C. Leite, S.P. Porto, and T.C. Damen, "The thermal lens effect as a power-limiting device," Appl. Phys. Lett., 10, 100-101 (1967).
3. J.H. Hermann, "Simple model for a passive optical power limiter," Optica Acta, 32, 541-547 (1985).
4. W.E. Williams, M.J. Soileau, and E.W. Van Stryland, "Optical switching and n_2 measurements in CS_2 ," Opt. Commun. 50, 256-260 (1984).
5. J.M. Ralston and K.R. Chang, "Optical limiting in semiconductors," Appl. Phys. Lett., 15, 164 (1969).
6. M. Sheik-Bahae, A.A. Said, D.J. Hagan, M.J. Soileau, and E.W. Van Stryland, "Nonlinear refraction and optical limiting in thick media," Opt. Eng., 30, 1228-1235 (1991).
7. A.A. Said, M. Sheik-Bahae, D.J. Hagan, E.J. Canto-Said, Y.Y. Wu, J. Young, T.H. Wei, and E.W. Van Stryland, "Nonlinearities in semiconductors for optical limiting," SPIE Proc. 1307, 294-301 (1990).
8. E. Canto-Said, D.J. Hagan, J. Young, and E.W. Van Stryland, "Degenerate four-wave mixing measurements of high order nonlinearities in semiconductors," IEEE J. Quantum Electron. 27, 2274 (1991).
9. A.A. Said, M. Sheik-Bahae, D.J. Hagan, T.H. Wei, J. Wang, J. Young, and E.W. Van Stryland, "Determination of bound-electronic and free-carrier nonlinearities in ZnSe, GaAs, CdTe, and ZnTe," J. Opt. Soc. Am. B, 9, 405-414 (1992).
10. D.R. Coulter, V.M. Miskowski, J.W. Perry, T.H. Wei, E.W. Van Stryland, and D.J. Hagan, "Optical limiting in solutions of metallo-phthalocyanines and naphthalocyanines," SPIE Proc. 1105, 42-51 (1989).
11. T.H. Wei, D.J. Hagan, M.J. Sence, E.W. Van Stryland, J.W. Perry, and D.R. Coulter, "Direct measurements of nonlinear absorption and refraction in solutions of Phthalocyanines", Appl Phys. B, 54, 46-51 (1992).
12. M. Sheik-Bahae, A.A. Said, T.H. Wei, D.J. Hagan, and E.W. Van Stryland, "Sensitive measurement of optical nonlinearities using a single beam," IEEE J. Quantum Electron. 26, 760-769 (1990).

Said et al.

Nonlinear optical properties of carbon-black suspensions (ink)

Kamjou Mansour*

Center for Research in Electro-Optics and Lasers, University of Central Florida, Orlando, Florida 32816

M. J. Soileau and E. W. Van Stryland

*Center for Research in Electro-Optics and Lasers and Department of Physics and Electrical Engineering,
University of Central Florida, Orlando, Florida 32816*

Received August 6, 1991; revised manuscript received March 2, 1992

We performed a series of experiments on suspensions of carbon particles in liquids (ink) and carbon particles deposited on glass to determine the mechanisms for the observed optical-limiting behavior. Both materials show reduced transmittance for increasing fluence (energy per unit area). We found that nonlinear scattering dominates the transmissive losses and that the limiting is fluence dependent, so that limiters based on black ink are effective for nanosecond pulses but not for picosecond pulses. Additionally, the nonlinear scattering and the limiting behavior cease after repeated irradiation. For the liquid, flowing eliminates this effect. All the data obtained are consistent with a model of direct heating of the microscopic-sized carbon particles by linear absorption with subsequent optical breakdown initiated by thermally ionized carriers. A simple calculation gives temperatures higher than the sublimation temperature at the onset of limiting. Emission spectra measurements show singly ionized carbon emission lines with a hot blackbody background emission consistent with temperatures of ≈ 4000 K. A rapid expansion of the microscopic plasmas generated by the breakdown will effectively scatter further input light. Indeed, in time-resolved experiments the trailing portion of the pulse is most heavily scattered. The time-resolved transmittance of a weak cw probe beam also follows the temporal dependence of the singly ionized carbon emission ($\approx 10^2$ ns). We directly monitored the expansion of the scattering centers by angularly resolving the scattered light for different input fluences and fitting to Mie scattering theory. Since the carbon is black and the microplasmas are initiated by linear absorption, the limiting is extremely broadband. Within the context of this model we discuss the limitations and optimization of ink-based optical limiters.

1. INTRODUCTION

There is considerable interest in the application of the nonlinear optical properties of materials for optical limiting. The ideal optical limiter would have high linear transmittance for low-input-energy laser pulses and low transmittance for input energies above a user-specified value so that the output would become clamped. In addition, this ideal limiter would have rapid response (picoseconds for some applications), broadband response (e.g., the visible spectrum), and a large dynamic range. Here dynamic range is defined as the ratio of the input energy at which the device no longer clamps the output or at which the device itself is irreversibly damaged to the input energy at which the output first becomes clamped. Figure 1 shows the input-output characteristics of such an ideal limiter. Figure 2 shows the input-output characteristics of a 1-cm-thick glass cuvette filled with a carbon-black suspension (CBS), a suspension of carbon-black particles in a mixture of water and ethylene glycol (i.e., diluted black drawing ink) along with a similar curve for an identical cell filled with carbon disulfide, CS_2 .^{1,2} In our experiments we filtered the suspension through a $0.25\text{-}\mu\text{m}$ filter, and the largest agglomerates seen after drying and measuring with an electron microscope were $0.21\text{ }\mu\text{m}$, with an individual particle size of ≈ 35 nm. Later we will see that scattering measurements gave an average size of

$\approx 0.14\text{ }\mu\text{m}$. For these measurements the input pulses were focused, 20-nsec (FWHM), $1.06\text{-}\mu\text{m}$, linearly polarized pulses from a Q-switched Nd:YAG laser run at a repetition rate of 1 Hz. The power needed to initiate limiting in a CBS of ≈ 100 W (energy $\approx 1\text{ }\mu\text{J}$) is compared with kilowatts for CS_2 . This low threshold for limiting makes CBS's interesting for a variety of applications.

In this paper we report a comprehensive series of experiments aimed at determining the basic physical mechanisms responsible for the nonlinear response observed in Fig. 2. Our conclusion from the results of these experiments is that the tiny suspended carbon particles are rapidly heated by strong linear absorption, giving rise to thermionic emission, which in the presence of the strong electric field leads to avalanche ionization. The resulting microplasmas then rapidly expand into the surrounding liquid and strongly scatter the incident light for the duration of the existence of the plasma ($\approx 10^2$ ns). Subsequently, at incident energies well above the threshold for obtaining a clamped output, the heating leads to bubble formation and further scattering that lasts for microseconds. These conclusions imply that the limiting is broadband and depends on fluence (energy per unit area) rather than on irradiance, both of which agree with our observations. In addition, since the carbon particles are ionized (and vaporized) during the process, the suspension must be replenished after each laser exposure, again

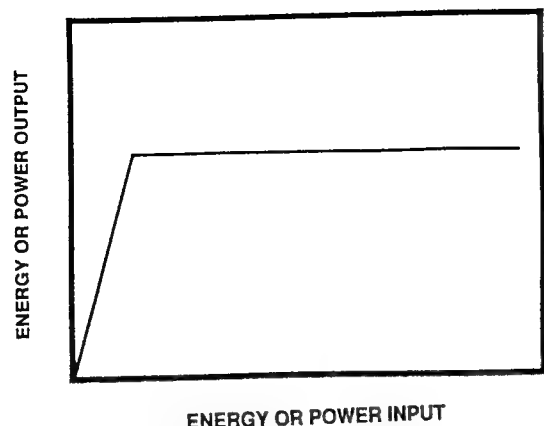


Fig. 1. Power or energy output of an ideal passive optical limiter as a function of the input peak power or energy.

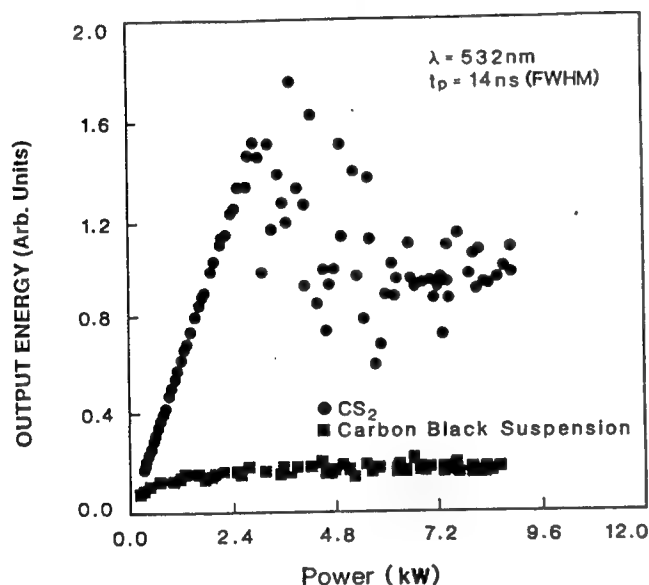


Fig. 2. Energy output for CS₂ and CBS as a function of input peak power for 14-ns (FWHM), 532-nm pulses focused to $\omega_0 \approx 3.5 \mu\text{m}$ for input powers of 1 to 12 kW.

as observed. The experiments leading to these conclusions and the organization of this paper are briefly outlined below.

In Section 2 we first describe optical limiting experiments on the CBS and on a sample of carbon particles deposited upon glass (CBG) performed at 1.06 and $0.53 \mu\text{m}$ with both nanosecond and picosecond input pulses. In Section 3 we describe three methods for monitoring the contribution of nonlinear refraction to limiting, all of which showed negative results. In Section 4 we describe the results of an experiment in which we simultaneously monitored transmittance, absorbance, and the fraction of side-scattered light in CBS, and we also describe a similar experiment in CBG in which we measured transmittance and scattering. Time-resolved transmittance measurements using both a single beam and a pulse-probe technique are discussed in Section 5. In Section 6 we show results of emission-spectra measurements, and we time resolve them. The results of these measurements suggest that microplasmas that scatter the incident light are being formed. Growth of these plasmas in size must be the explanation for the observed limiting,

since the carbon particles already block some of the transmission by their high linear absorption. In Section 6, therefore, we compare the results of measurements of the angular distribution of the side-scattered light for different fluences with results obtained with theory. This comparison confirms growth of the scattering centers as fluence increases. Finally, in Section 8 we look at limiting geometries for which the sample thickness is large compared with the depth of focus of the input beam (thick-sample geometry), and we show why what is fundamentally a fluence-dependent nonlinearity manifests itself as an energy dependence in this thick-sample geometry.

2. OPTICAL LIMITING

Using a nanosecond Q-switched Nd:YAG laser and a mode-locked picosecond Nd:YAG at 1064 and 532 nm, we examined optical limiting in a CBS and CBG as a function of carbon-black microparticle concentration, input polarization, repetition rate, and beam radius. For 14-ns, 532-nm linearly or circularly polarized laser pulses incident upon a 1-cm-thick sample of CBS with 70% linear transmission at 532 nm, we found that the onset of limiting begins for incident peak powers of the order of 100 W for a tight-focusing limiting geometry, as shown in Fig. 3. However, the output is approximately clamped (i.e., the slope of output versus input becomes small) for incident powers $\geq 160 \text{ W}$. This value (the limiting threshold) is that input power (energy, fluence, or irradiance) at which the linear response line, in a plot of output versus input, intersects the line passing through the "clamped" output. This limiting threshold is approximately 1/24 that for CS₂ ($\approx 3.8 \text{ kW}$) if the same focusing geometry is used. The reorientational nonlinearity in CS₂ is known to lead to a power-dependent limiting.³ The lower limiting threshold in CS₂ for 14-ns laser pulses compared with that for single 42-ps pulses ($\approx 8 \text{ kW}$) possibly results from electrostrictive self-focusing that occurs for the longer pulses with a tight-focusing geometry.⁴ Identical focusing geometries were

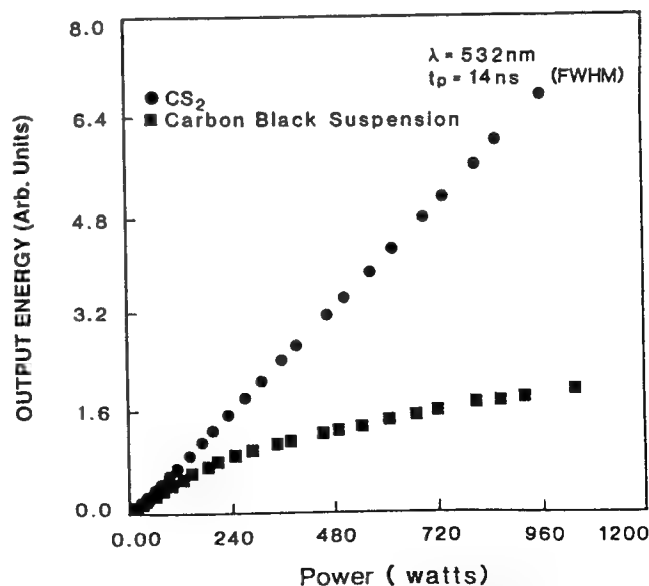


Fig. 3. Energy output for CS₂ and CBS as a function of input peak power for 14-ns (FWHM), 532-nm pulses focused to $\omega_0 \approx 3.5 \mu\text{m}$ for input powers of 1 to 1000 W.

Table 1. Limiting Thresholds for CBS and CS₂ in a Tight-Focusing Geometry

Material	λ (nm)	w_0 (μm)	t_p (ns)	Power (kW)	Energy (μJ)	Fluence (J/cm^2)
CS ₂	532	3.5	14	3.8	57	300
CS ₂	532	3.5	0.042	8	0.36	1.9
CS ₂	1064	5.1	20	13.5	290	710
CBS	532	3.5	14	0.16	2.4	12
CBS	532	3.5	0.042	30	1.3	6.8
CBS	1064	5.1	20	0.40	8.5	21

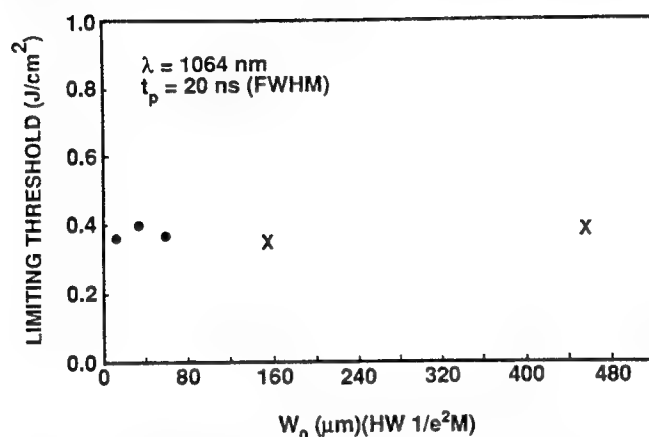


Fig. 4. Limiting threshold fluence as a function of beam radius for 20-ns (FWHM), 1064-nm laser pulses. Circles represent the measured value for a 100- μm -thick flowing jet of CBS with 70% linear transmittance, and \times 's are for a 1-cm-thick sample of CBS with a 70% linear transmittance at 1064 nm (the thin-sample criterion is satisfied).

used in experiments with both the nanosecond and picosecond laser sources. The calculated spot size at focus at 532 nm was $w_0 \approx 3.5 \mu\text{m}$ (half-width at $1/e^2$ maximum in irradiance). Best-form lenses were used for focusing the laser beam in all experiments reported in this paper. We found that for 20-ns, 1064-nm laser pulses focused to $w_0 \approx 5.1 \mu\text{m}$, a CBS limits the output for an incident power of $\approx 400 \text{ W}$, which is approximately $1/34$ that of the threshold for CS₂ at this wavelength. These results clearly indicate that a CBS is a promising material for optical limiting applications, such as optical sensor protection. However, for single 42-ps, 532-nm laser pulses the limiting occurs for incident peak powers of the order of $\approx 30 \text{ kW}$ at 532 nm if a tight-focusing geometry similar to that used for the nanosecond laser pulse experiment is used. This limiting threshold is nearly four times that for CS₂ ($\approx 8 \text{ kW}$). These results are summarized in Table 1. We conclude that limiting works well in a CBS for long pulses ($\geq 10 \text{ ns}$) but is less effective for short (picosecond) pulses. We found that for tight-focusing geometries the limiting depends on input energy, whereas for a collimated beam geometry the limiting depends on fluence (J/cm^2). The energies (and fluences) for limiting in a CBS for nanosecond and picosecond pulses are equal to within better than a factor of 2, as may be seen from Table 1. The small difference (picosecond pulses limit at a slightly lower energy) could be due to small geometry differences and self-focusing in the solvent at the high irradiance used for picosecond pulses.

In Section 8 we discuss the reasons for energy-dependent rather than fluence-dependent limiting for

thick (tight-focusing) versus thin limiters. For thin limiters (i.e., those in which the beams are well collimated within the length of the sample) we used focal beam radii of 14–454 μm with nanosecond laser pulses incident upon a 100- μm -thick jet of flowing CBS (as in a dye laser) to measure the limiting threshold. The results shown in Fig. 4, along with the picosecond measurements discussed above, demonstrate that the limiting is fluence dependent. These measurements show that the onset of limiting (for collimated beams) occurs at $\approx 200 \text{ mJ}/\text{cm}^2$ for 532-nm, 14-ns (FWHM) pulses (not shown) and at $\approx 380 \text{ mJ}/\text{cm}^2$ for 1064-nm, 20-ns (FWHM) pulses, independent of spot size. Thus optical nonlinearities leading to limiting in a CBS depend on the temporally integrated irradiance (i.e., fluence).

We found that the onset of limiting is independent of the concentration of carbon-black particles. However, samples with a higher concentration of carbon-black particles and, in turn, lower transmittance for low-input-light levels block the output light more effectively at higher incident fluences than do samples with a low concentration of carbon particles. As we discuss below, the attenuation of the output light is dominated by scattering from microplasmas initiated at the positions of the carbon particles. Therefore we should observe more microplasma scattering centers and stronger attenuation for the more highly concentrated samples.

The optical nonlinearities in the solvent make a negligible contribution to the limiting processes in the CBS for nanosecond inputs. However, because of the presence of highly absorbing carbon-black microparticles in the CBS, heat diffusion to the surrounding liquid could lead to thermal nonlinearities in the solvent. We investigated the effects of such nonlinearities and found that the nonlinear index change was $\leq 3 \times 10^{-6}$ (see Section 3). This nonlinear index change is too small to have any significant effect on the limiting threshold for a CBS. In addition, we studied the optical-limiting response of CBG. Here, there is no liquid to heat, and we can ignore the thermal nonlinearities of the host medium. We found the optical limiting threshold for CBG to be $\approx 800 \text{ W}$ peak power for 20-ns, 1064-nm laser pulses, as shown in Fig. 5. This limiting

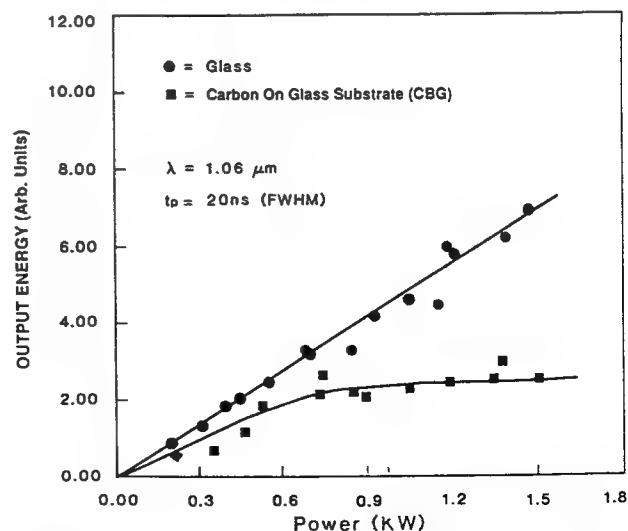


Fig. 5. Energy output for CBG and glass substrate as a function of input peak power for 20-ns (FWHM), 1064-nm pulses focused to $w_0 \approx 8 \mu\text{m}$. The solid lines are guides for the eye.

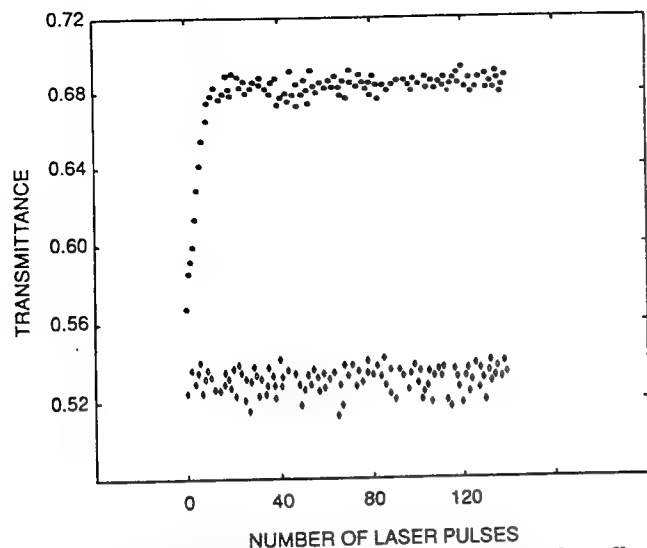


Fig. 6. Transmittance of flowing (open diamonds) and nonflowing (filled circles) CBS as a function of the number of pulses at a repetition rate of 10 Hz with a beam radius of $330\text{ }\mu\text{m}$ and input energy of 2.8 mJ for 20-ns (FWHM), 1064-nm laser pulses. The maximum transmittance of $\approx 70\%$ is from the finite aperture of the detector in this experiment.

threshold is only twice that of the CBS. This factor-of-2 difference may result from the different particle sizes in these samples. Whereas CBS has an average particle size of $\approx 0.14\text{ }\mu\text{m}$, the toner particles used for CBG have an average size of $\approx 5\text{ }\mu\text{m}$. Thus for the same input fluence the temperature rise is smaller in the larger particles, and this leads to a higher threshold.⁴

We observed that for a pulse repetition frequency $\geq 2\text{ Hz}$ the limiting effect diminished after a few laser firings. This is illustrated in Fig. 6 for a 10-Hz pulse repetition frequency. The magnitude of this effect depends on the beam radius and input energy. In addition, for CBG, if we did not translate the sample after each laser firing for inputs above the limiting threshold, limiting ceased for subsequent pulses. Examination of the glass slide showed that the particles were removed from the surface after irradiation. Flowing the liquid at a rate sufficient to replenish the CBS between laser firings removes the apparent dependence on pulse repetition frequency.

To understand the optical nonlinearities leading to the observed nonlinear transmittance, we investigated nonlinear refraction (self-focusing or defocusing), nonlinear absorption, nonlinear scattering, and combinations of these mechanisms.

3. NONLINEAR REFRACTION

The contribution of nonlinear refraction in a CBS was studied by using three different techniques: beam distortion,^{4,5} measurement of the transmitted on-axis irradiance,^{6,7} and the Z-scan method.⁸ These techniques allowed us to investigate the contributions of phase distortion from a thermo-optic effect, electrostriction, or any other nonlinear refractive mechanism. Using the beam-distortion measurement, we monitored the far-field spatial transmitted beam profiles of the TEM₀₀ Gaussian input pulses at 532 and 1064 nm from a Nd:YAG Q-switched laser as a function of incident irradiance. The

beam-distortion measurements indicate that the contribution of nonlinear refraction to optical limiting is small. We estimated the upper limit of the nonlinear refractive index n_2 to be $\approx 4.6 \times 10^{-12}$ esu at 532 nm. This value was calculated with the assumption that the maximum phase distortion was $< 0.3\lambda$ (the sensitivity limit of this technique) for both wavelengths, even at inputs 20 times the optical limiting threshold in a CBS. By using the more sensitive Z-scan technique with wave-front distortion sensitivity $\approx \lambda/25$ for our laser system, we found that the estimated value of n_2 for CBS was $\approx 8 \pm 5 \times 10^{-12}$ esu at 532 nm. The positive sign eliminates the possibility of thermal defocusing. If we compare the n_2 of CBS with that of the solvent calculated by Marburger's equation⁹ for catastrophic self-focusing, we find that the values agree to within the range of error; thus the measured n_2 value is that of the solvent. This clearly indicates that for intensities for which limiting is observed in CBS, the contribution of nonlinear refraction is negligible. This point also was confirmed by the on-axis transmittance measurement, in which we measured the limiting threshold for CBS with or without an aperture in front of the transmission detector and observed no change in limiting threshold. Note that these measurements also indicate that the small-angle forward scattering is always smaller than the transmitted beam.

4. SIMULTANEOUS MEASUREMENT OF TRANSMITTANCE, ABSORPTANCE, AND SCATTERING

Figure 7 shows the experimental setup used for the simultaneous measurement of absorptance (A), the fraction of side-scattered light (S), and the transmittance (T) in a CBS for nanosecond laser pulses at 532 and 1064 nm. This experiment was performed with a well-collimated beam within the length of the sample. The absorptance signal was obtained by placing a piezoelectric transducer at the bottom of the CBS-filled cell. The gated signal voltage from this transducer (with a peak-and-hold circuit) is directly proportional to the absorbed energy.¹⁰ Figure 8 shows the results of these measurements as a function of incident fluence at $1.06\text{ }\mu\text{m}$. Data taken at $532\text{ }\mu\text{m}$ show qualitatively identical results. The data shown are for inputs near the threshold for limiting, so that only a small change in transmittance is seen. The transmittance data are absolutely calibrated, whereas the absorptance and scattering fraction are arbitrarily scaled (i.e., $A + S + T \neq 1$ in this figure). The deviation from a horizontal straight line indicates nonlinear behavior for all three signals.

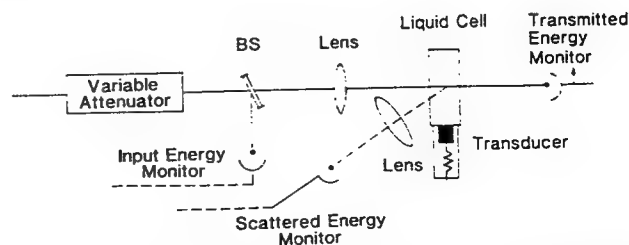


Fig. 7. Schematic diagram for simultaneous measurements of transmittance, absorptance, and the fraction of side-scattered light. BS, beam splitter.

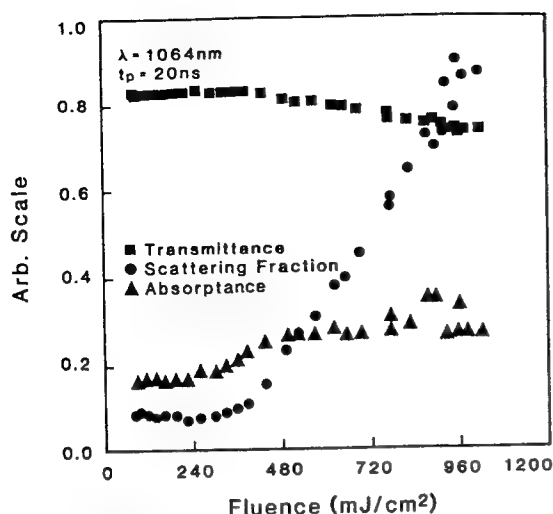


Fig. 8. Transmittance, absorptance, and scattering fraction as a function of incident fluence for 1064-nm, 20-ns (FWHM) pulses focused to $w_0 = 156 \mu\text{m}$ for incident fluences of 0.08 to 1 J/cm^2 .

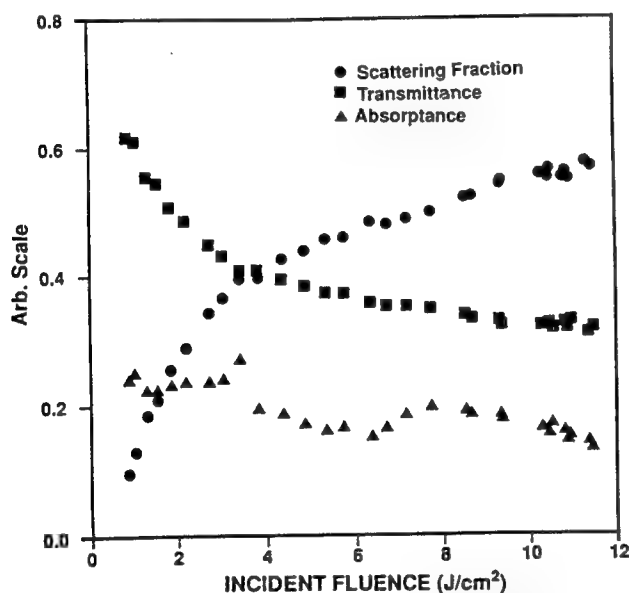


Fig. 9. Transmittance, absorptance, and scattering fraction as a function of incident fluence for 1064-nm, 20-ns (FWHM) pulses focused to $w_0 = 156 \mu\text{m}$ for incident fluences of 1 to 12 J/cm^2 .

We found that for fluences above the onset of a change of transmittance (i.e., $\approx 200 \text{ mJ/cm}^2$ for 14 ns, 532 nm and 380 mJ/cm^2 for 20 ns, 1064 nm), there is a strong increase in the fraction of side-scattered light as well as an increase in the absorptance. The absorptance levels fall off for higher fluences. In addition, we found that the trend of increased side-scattered fraction continues for input fluences even 50 times the threshold, as is shown in Fig. 9. These data indicate that for relatively low fluence levels the material changes from a linear absorber to a nonlinear scatterer.

The strong nonlinear scattering is illustrated best in Fig. 10, which is a photograph of the 532-nm side-scattered light at low [Fig. 10(a)] and high [Fig. 10(b)] fluences. Note that at the high fluence level the input never reaches the back of the cell. That light from plasma emission is overwhelmed by side-scattered laser light was quantitatively verified in experiments on the angular scattering profile; these are discussed in Section 7. Only at $1.06 \mu\text{m}$

could we see the plasma emission in a darkened room after our eyes had adapted to the darkness.

We repeated the measurement of transmittance T and side-scattered fraction S for CBG at $1.06 \mu\text{m}$ and found that, as the transmittance decreased for fluences $\geq 1 \text{ J/cm}^2$, the side-scattered fraction rapidly increased, as for a CBS, again indicating similar mechanisms for the two materials, independent of surroundings. We were unable to perform the photoacoustic experiment to monitor the absorption because the sample had to be moved after each irradiation, changing the photoacoustic signal in an unpredictable fashion.

5. TIME-RESOLVED TRANSMISSION

We performed time-resolved transmission measurements for the 14-ns, 532-nm laser pulses in a CBS. For fluences below the onset of limiting, the material behaves linearly, and the shapes of input and output pulses are the same, as is shown in Fig. 11. However, for fluences above limiting, we observed that a transmittance cutoff occurs within the duration of the pulse and that latter portions of the pulse are strongly attenuated. This is shown in Fig. 11(b), for which the input reference was attenuated by a factor of 10 with respect to the transmitted pulse, which now appears shifted toward early times because of the truncation. These results are reminiscent of those of laser-induced breakdown experiments.^{11,12} The results of this experiment and those described in the previous sections indicate that the physical mechanisms leading to the truncation of

$\lambda = 532 \text{ nm}$
 $t_p = 14 \text{ ns}$

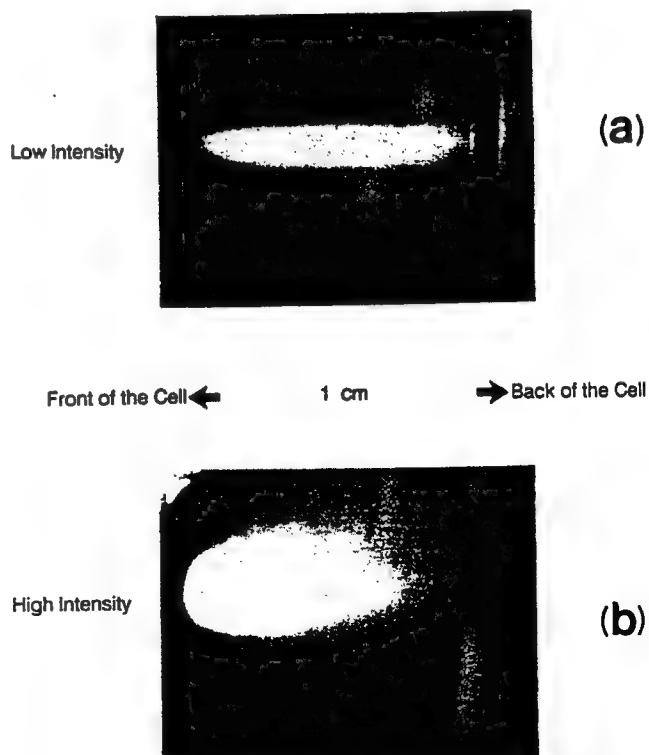


Fig. 10. Photographs of side-scattered 532-nm light from a 1-cm cuvette of CBS for (a) low and (b) high incident intensities (fluences).

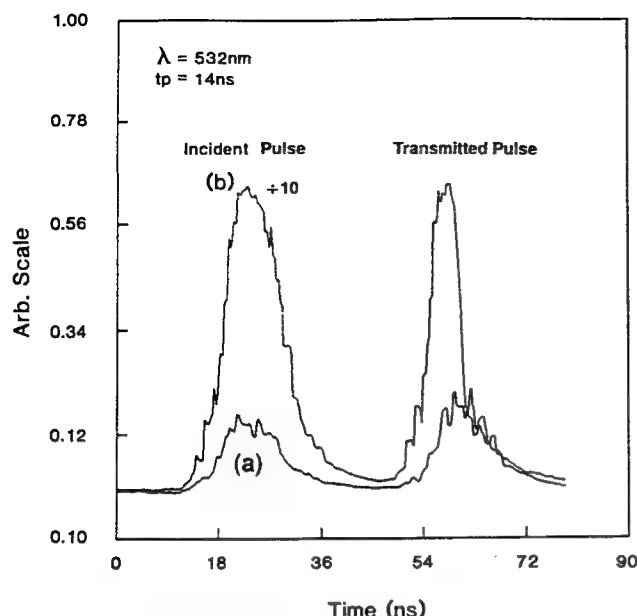


Fig. 11. Temporal profiles of the incident and transmitted 532-nm, 14-ns (FWHM) laser pulses. (a) Incident and transmitted pulses for fluences of $\approx 100 \text{ mJ/cm}^2$ (below threshold). (b) Incident (attenuated by a factor of 10) and transmitted pulses for a fluence of $\approx 1.1 \text{ J/cm}^2$ (above threshold). The spot size was $w_0 \approx 250 \text{ }\mu\text{m}$.

the pulse and subsequent absorption and scattering of the final portion of the pulse may result from the formation and rapid expansion of microplasmas, as occurs in laser-induced breakdown. Before truncation, carbon-black particles linearly absorb the leading edge of the pulse efficiently. The carbon particles are rapidly heated, and the carbon vaporizes and ionizes to form a rapidly expanding microplasma that strongly scatters and absorbs the latter part of the pulse. If microplasmas are formed, we should be able to monitor their emission spectrum and time resolve both their emission and the induced transmittance changes. Such experiments are described in Section 6.

6. EMISSION SPECTRUM AND TEMPORAL DEPENDENCE

We examined the microplasma formation by using spectrally and temporally resolved fluorescence measurements. We monitored the side emission spectrum with a monochromator-fast-photomultiplier system connected to a computer-controlled digitizing oscilloscope. The laser pulses at $1.06 \text{ }\mu\text{m}$ were focused into the CBS or onto the CBG, and the side-scattered light was collected onto the entrance slit of the 0.25-m monochromator. The samples were repetitively irradiated at a fixed fluence (the CBG sample was moved after each firing), and the wavelength was scanned. Figure 12 shows spectral data for CBG. Superimposed upon the data is a blackbody spectrum at 4250 K, which is higher than the sublimation temperature of carbon ($\approx 3850 \text{ K}$). Singly ionized carbon emission wavelengths that coincide with emission peaks in the observed spectra are shown. Data for the CBS show qualitatively similar results, except that the frequency range over which data could be taken was significantly reduced by self-absorption and scattering within the CBS.

The temporal dependence at specific wavelengths was

monitored by using the same monochromator-fast-photomultiplier combination. Monitoring the emitted light at $\approx 800 \text{ nm}$, which coincides with a singly ionized carbon emission peak, resulted in the data of Fig. 13 for CBG. Whereas the decay does not fit a single exponential, the emission decays to $1/e$ of its initial value in $\approx 10^2 \text{ ns}$. This decay time is consistent with previous measurements for the lifetime of ionized carbon.^{13,14}

This $\approx 10^2$ -ns decay time is also consistent with the results of excitation and probe measurements in which we monitored the change in the transmittance of a cw He-Ne beam as a function of the incident fluence of a 20-ns, 1064-nm excitation pulse. From this measurement, shown in Fig. 14, we found that for the CBS the He-Ne transmission recovers to 50% of the attenuation within $\approx 100 \text{ ns}$, which is comparable with the emission time of ionized carbon. Figure 15 shows similar results for CBG. However, for CBG at longer times the transmittance actually increases above the original level. This again indicates that the carbon is ionized and vaporized so that it no longer efficiently absorbs or scatters the incoming light. This is not seen in the CBS, since the material is thick and only a small fraction of the carbon is vaporized with a single laser firing. At the very highest fluence levels in the CBS the transmittance does not fully recover to the original level. This may be attributed to another high-

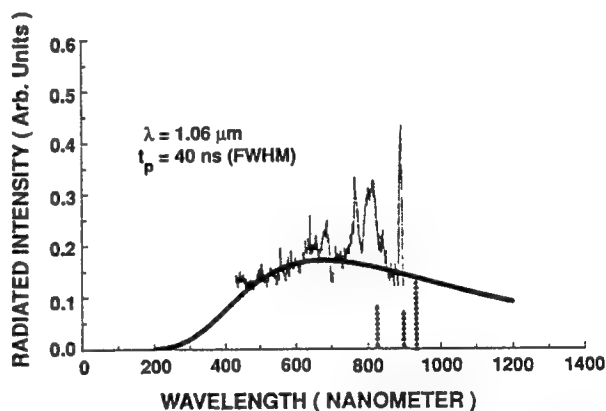


Fig. 12. Spectral emission from carbon particles irradiated by 40-ns, $1.064\text{-}\mu\text{m}$ laser pulses. The triangles show tabulated wavelengths for singly ionized emission lines. The thick solid curve shows the calculated emission for a blackbody source at 4250 K.

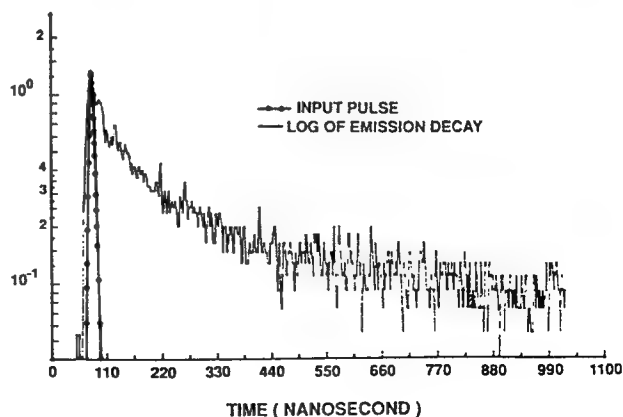


Fig. 13. Semilogarithmic plot of the emission signal at 800 nm as a function of time.

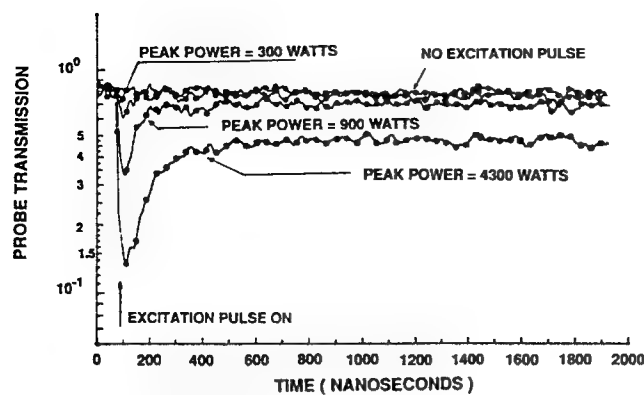


Fig. 14. Semilogarithmic plot of the He-Ne probe-beam transmittance as a function of time for different input powers for 20-ns (FWHM), 1.064- μm excitation pulses for a sample of a CBS with 70% linear transmittance. The dots highlight the digitized curves at specific time intervals.

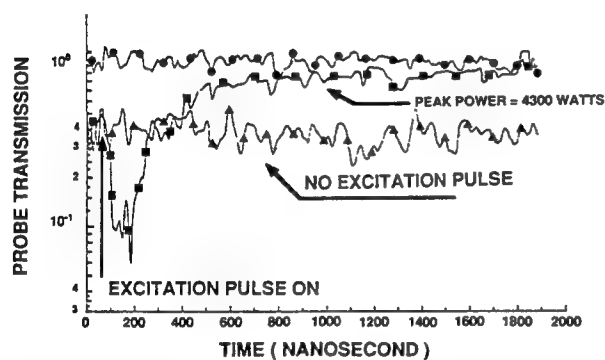


Fig. 15. Semilogarithmic plot of the He-Ne probe-beam transmittance as a function of time for a 4.2-kW, 20-ns (FWHM), 1.064- μm laser pulse for a sample of CBG with 28% linear transmission at 632.8 nm. The dots, triangles, and squares highlight the digitized curves at specific time intervals.

input limiting mechanism, such as vapor formation (i.e., cavitation and bubble formation), which can scatter light for microseconds.¹⁵ Indeed, at high inputs bubbles can be seen in the cell and have been reported by other researchers.¹⁶

The fact that we see the transmittance of CBG almost completely recover to the uncoated glass slide transmittance within ≈ 600 ns implies that the carbon particles are removed or destroyed within this time. To be removed the particle velocities would need to be near the speed of sound if we assume velocities perpendicular to the beam. We conclude that the carbon particles are destroyed (vaporized or atomized) in the limiting process. The result is smaller particles (or atoms) much smaller than the wavelength λ , so that they no longer scatter or absorb the light efficiently. This conclusion is consistent with the limiting behavior discussed in Section 2.

7. ANGULAR SCATTERING PROFILE

To study the nonlinear scattering process in this material, we measured the intensity of the scattered light as a function of angle from 20° to 160° , using a 100- μm -thick flowing jet of CBS with nanosecond 532- and 1064-nm laser pulses. Spike filters that transmit only the laser frequency were placed in front of the detectors, as in the

other transmittance and scattering experiments. The results of these measurements indicate an increase in the scattered light in the forward direction for fluences for which limiting was observed. The normalized scattered radiation pattern for 1064-nm light is shown in Figs. 16 and 17 for fluences near and four times as high as the limiting threshold, respectively. From these results we determined the average size and the index of refraction of the scattering centers by numerically fitting the experimental results with Mie scattering theory. The best theoretical fits to the experimental results are shown as

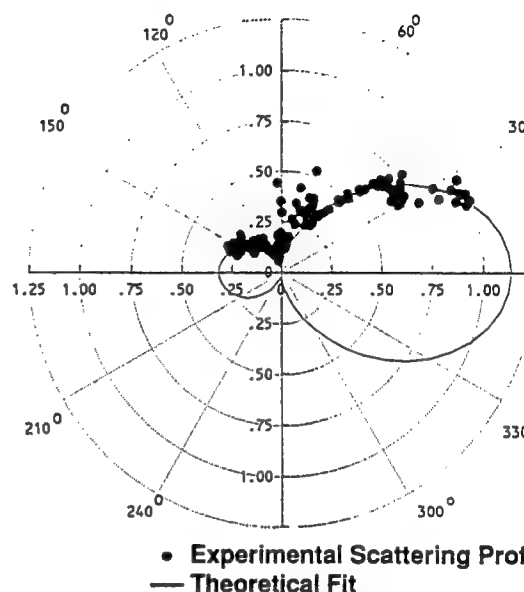


Fig. 16. Polar plot of the fraction of scattered light (arbitrarily scaled) for a CBS for an incident fluence of $\approx 550 \text{ mJ/cm}^2$ for 20-ns (FWHM), 1064-nm linearly polarized light parallel to the plane of observation. The spot size was $w_0 \approx 96 \mu\text{m}$. The theoretical fit is based on Mie scattering theory.

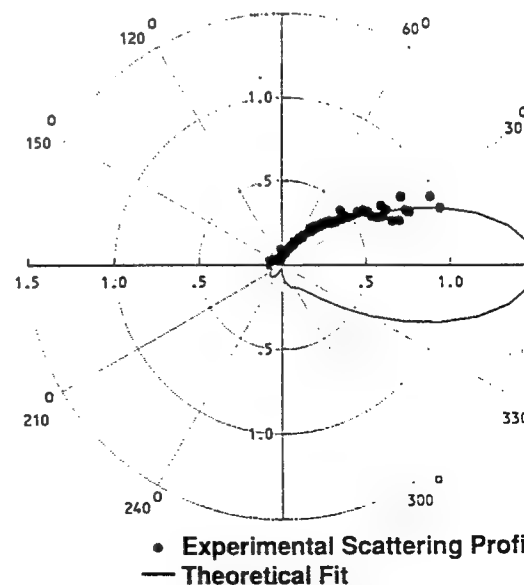


Fig. 17. Polar plot of the fraction of scattered light (arbitrarily scaled) for a CBS for an incident fluence of $\approx 1.5 \text{ J/cm}^2$ for 20-ns (FWHM), $w_0 \approx 96\text{-}\mu\text{m}$, 1064-nm linearly polarized light parallel to the plane of observation. The theoretical fit is based on Mie scattering theory.

solid lines in Figs. 16 and 17. We found that the average radius of the carbon particles at low input energies is of the order of $0.14 \mu\text{m}$ with a complex index of refraction $m = 2.16 - 0.77i$ and that the average size of the induced scattering centers (at high input energies) is of the order of $0.40 \mu\text{m}$ with a complex index of refraction $m = 1.96 - 0.11i$. These results not only indicate that the induced scattering centers are larger by a factor of ≈ 3 than the initial particles but also reveal that the optical properties of these centers are different from those of the initial particles. Similar results were observed at 532 nm. Clearly, this measurement integrates the scattering over the entire pulse width during the time the scattering centers are growing. Presumably the average size at the end of the pulse is considerably larger than that measured in these experiments. We attribute the production of the induced scattering centers to the formation and rapid expansion (within the pulse width) of microplasmas initiated by rapid heating and subsequent thermoionization of the carbon particles. The increase in size but decrease in the imaginary part of m (i.e., decrease in absorption) can explain the observed small increase in overall absorptance but large increase in scattering. In particular, the absorption of the particles decreases significantly (i.e., by a factor of ≈ 7). Thus the area increases by approximately 3^2 , whereas the loss decreases by ≈ 7 , which is consistent with the observed small increase in absorption.

8. THICK-SAMPLE LIMITING

The experiments described in previous sections that show the fluence dependence of the limiting in CBS were performed with thin-sample geometry, for which the depth of focus of the input beam is larger than the sample thickness. This ensures that the beam is collimated in the sample. We found that the fundamental fluence dependence of limiting in a CBS (or CBG) manifests itself quite differently if the focusing geometry is changed so that the sample is much thicker than the beam depth of focus (i.e., thick-sample or tight-focus geometry). This is expected for a fluence-dependent nonlinearity, as is described below. It is analogous to the irradiance-dependent two-photon absorption (2PA) that appears as a power dependence in tight-focusing geometries.

In this experiment the input beam at 532 nm was focused into the CBS sample with a linear transmittance of 60% by using one of three lenses with focal lengths of 51, 25.5, and 10 mm. The depth of focus for all three lenses is much less than the cell thickness of 1 cm. The spot size at the input lens position was $w_0 \approx 0.207 \text{ cm}$ half-width at $1/e^2$ maximum at $0.53 \mu\text{m}$. The input (and output) energy was monitored by a 1-cm-aperture, uniform-response p-i-n photodiode to collect all of the transmitted beam for each of the input lenses. The output energy versus input energy was recorded for one input lens focal length, and then the input lens was changed. This was repeated for all three input lens focal lengths.

Figure 18 shows the data plotted as transmittance (output divided by input) versus input energy. The downward slope shows the limiting behavior. We know that all the

light was collected because the linear transmittance (output energy divided by input energy for low input energy) is independent of the lens used and is approximately equal to the linear transmittance of the 1-cm-thick cell of $T \approx 0.6$. The important point to be made from these data is that the curves for all three lenses are nearly the same. There is a deviation of the data for the most tightly focused lens (10-mm focal length) at high input energies for which the limiting becomes less efficient (not shown), but this deviation is much smaller than that expected for a fluence-dependent nonlinearity.

The following argument shows how a fluence-dependent nonlinearity (or an irradiance-dependent nonlinearity, such as 2PA) can behave as an energy-dependent (or power-dependent in the case of 2PA) nonlinearity for a thick-sample geometry.

The depth of focus z_0 of a lens is given by

$$z_0 = \frac{\pi w_0^2}{\lambda}, \quad (1)$$

where w_0 is the beam radius at the focus of the lens (half-width at $1/e^2$ maximum). The area of the beam is given by

$$A = \frac{\pi w_0^2}{2}. \quad (2)$$

If the nonlinear interaction is fluence dependent, the transmission change will, to some approximation, be proportional to the product of the fluence and the effective interaction length L_{eff} . For a short cell L_{eff} is the sample thickness, and the nonlinear change in transmittance is fluence dependent. However, for the thick cell, the interaction length can be given approximately by z_0 . Thus the change in transmittance (ΔT) is

$$\Delta T \propto F z_0 = \frac{\text{Energy}}{A} z_0 = \text{Energy} \frac{2}{\pi w_0^2} \frac{\pi w_0^2}{\lambda} = \text{Energy} \frac{2}{\lambda}. \quad (3)$$

So now the nonlinear change in transmittance appears to be energy dependent and is independent of the beam size

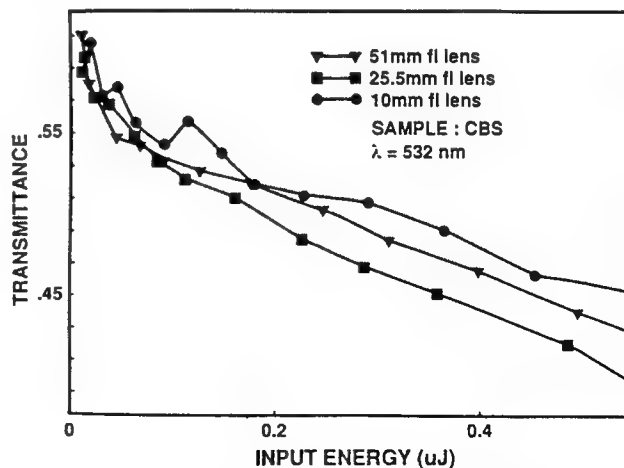


Fig. 18. Plot of transmittance of a 1-cm-thick sample of CBS with $\approx 60\%$ linear transmittance at 532 nm as a function of input energy for a thick limiter for 5-ns (FWHM) laser pulses for input lenses with focal lengths of 51, 25.5, and 10 mm.

at focus. That is, ΔT is independent of both the focal length of the input lens and its f -number, and this is what our experimental results show. In addition to these focal considerations, the effects of lens aberrations may also be contributing since we are using short-focal-length lenses and small f -numbers.¹⁷ However, we cannot easily determine how large such aberration effects are.

This result may be clearer in the case of 2PA, for which the nonlinear equations are well defined and the irradiance change dI with depth in the sample dz is

$$\frac{dI}{I} = -\beta I dz, \quad (4)$$

where β is the 2PA coefficient. This means that the change in transmittance is approximately

$$\Delta T = \frac{\Delta I}{I} = -\beta I L_{\text{eff}}, \quad (5)$$

where L_{eff} is the effective interaction length. For a thick cell the inverse area dependence of the irradiance cancels the area dependence of $L_{\text{eff}} \approx z_0$, which leaves ΔT power dependent.

Our conclusion from these data is that extremely tight focusing is not helpful in lowering the threshold and may indeed be detrimental to the performance. However, focusing is necessary for obtaining sufficient fluence to ionize the carbon particles in CBS. A compromise between these requirements is needed.

9. CONCLUSION

We conclude that the dominant nonlinearity leading to limiting in both carbon black suspension and carbon deposited on glass is nonlinear scattering and that the mechanism for this nonlinearity is rapid heating of carbon particles and their subsequent vaporization and ionization, which lead to the formation of rapidly expanding microplasmas.

We can estimate the temperature rise of the carbon particles at the limiting threshold if we are given the laser-beam parameters and the optical properties of carbon black. Ackerman and Toon¹⁸ give the complex index of refraction of carbon black as $m = 1.96 - 0.66i$, which gives an absorption coefficient of $\alpha \approx 3 \times 10^4 \text{ cm}^{-1}$. These values are consistent with our measurements of the Mie-scattered light. Donnet and Voet¹⁹ show that absorption with the different types (sizes, etc.) of carbon particles varies by factors of no more than 2 to 3 and scales linearly with concentration. It is also observed that the optical properties of a carbon-black dispersion in a liquid behave similarly to those of the powder form. This is true since the powder form generally has a void volume of over 90%, so that it may be considered a dispersion in air. This, in turn, implies that the absorption that must be used to calculate a temperature rise for carbon without voids is an order of magnitude larger than the reported value. If we use this higher value of $\alpha \approx 3 \times 10^5 \text{ cm}^{-1}$ and assume single carbon particles of diameter $\approx 0.14 \mu\text{m}$, we estimate a temperature increase of approximately 10^4C with 12-nsec, 20-MW/cm² pulses. This is consistent with the temperature experimentally estimated from emission measurements.

The dominant role of nonlinear scattering in this process was shown by simultaneous measurements of transmittance, absorptance, and the fraction of side-scattered light. In addition, nonlinear refraction was shown to be insignificant, and the absorptance changed only by a factor of 2, a change far too small to explain the observed limiting. Measurements on CBG confirmed the role of scattering, independent of the surrounding liquid. How scattering could increase the loss over that from the already highly absorbing carbon-black particles is explained by the growth in size and change of index of refraction of the scattering centers. The angular dependence of the side-scattered-light fit to Mie theory demonstrated this growth. The observed volumetric expansion of the plasma is necessary because the volume percent of carbon is small and the carbon particles are already highly absorbing. In addition, the index changes observed in these experiments are not consistent with either shock waves or bubble formation.

The nature of the scattering centers as ionized particles was confirmed from line emission spectra and time-resolved fluorescence measurements, which were consistent with previous measurements of plasma production with carbon targets.²⁰ The time-resolved transmittance measurements also showed that the limiting lasted only for the lifetime of the microplasma, which is again consistent with the microplasma scattering model. The role of bubble formation at the onset of limiting was investigated by performing experiments on samples of CBG. The similarity of the results obtained for these samples and those for the liquid suspensions shows that bubbles are not important at or near threshold. However, well above threshold the heat vaporizes both the carbon and the liquid, so that bubbles are formed. These appear on longer time scales, as reported in Ref. 16, and can cause problems for high-energy or high-repetition-rate limiting applications. The disappearance of the limiting effect after multiple-pulse irradiation of a single site (before the liquid can be replenished) also confirms that the carbon particles are destroyed, i.e., in this case they are ionized and vaporized, or atomized, so that they no longer effectively scatter light.

The fluence dependence was confirmed by focal-spot-size-dependence measurements with collimated beams and by pulse-width-dependence measurements with nanosecond and picosecond irradiation. However, we showed that for a tight-focusing geometry for which the depth of focus is shorter than the sample thickness, the fluence dependence is masked, and the response becomes energy dependent (i.e., independent of focusing). This is an important consideration in optical-limiting applications.

The process involved in a CBS is commonly referred to as laser-induced damage, and we have prepared a material with a low damage threshold. Our understanding of the limiting mechanisms also tells us that we will not be able to lower the limiting threshold significantly (i.e., by $10\times$) or increase the bandwidth. The reasons are that the carbon is black and therefore broadband and highly absorbing. To lower the threshold we must either increase the absorptance (we cannot do this to any significant degree) or lower the ionization threshold (flooding the suspension with ionization radiation may do this). At

the moment, a carbon-black suspension is one of the most effective optical-limiting materials available for nanosecond laser pulses.

ACKNOWLEDGMENTS

We gratefully acknowledge support from the Defense Advanced Research Projects Agency, Center for Night Vision and Electro-Optics, and the Florida High Technology and Industrial Council. We thank Ken McEwan, Royal Signals and Radar Establishment (UK), and A. Miller for useful discussions.

*Present address, Jet Propulsion Laboratory, California Institute of Technology, Mail Stop 67-201, 4800 Oak Grove Drive, Pasadena, California 91109.

REFERENCES

1. K. Mansour, E. W. Van Stryland, and M. J. Soileau, *Proc. Soc. Photo-Opt. Instrum. Eng.* **1105**, 91 (1989).
2. K. Mansour, E. W. Van Stryland, and M. J. Soileau, *Proc. Soc. Photo-Opt. Instrum. Eng.* **1307**, 350 (1990).
3. W. E. Williams, M. J. Soileau, and E. W. Van Stryland, *Opt. Commun.* **50**, 256 (1984).
4. K. Mansour, Ph.D. dissertation (University of North Texas, Denton, Tex., 1990).
5. M. J. Soileau, W. E. Williams, and E. W. Van Stryland, *IEEE J. Quantum Electron.* **QE-19**, 731 (1983).
6. K. C. Jungling and O. L. Gaddy, *IEEE J. Quantum Electron.* **QE-7**, 97 (1973).
7. T. B. Boggess, Jr., A. L. Smirl, S. C. Moss, I. W. Boyd, and E. W. Van Stryland, *IEEE J. Quantum Electron.* **QE-21**, 488 (1985).
8. M. Sheik-Bahae, A. A. Said, T. H. Wie, D. J. Hagen, and E. W. Van Stryland, *IEEE J. Quantum Electron.* **26**, 760 (1990).
9. J. H. Marburger, *Progress in Quantum Electronics* (Pergamon, London, 1977), pp. 35-110.
10. C. N. K. Patel and A. C. Tam, *Rev. Modern Phys.* **53**, 517 (1981).
11. Y. P. Raizer, *Sov. Phys. Usp.* **8**, 650 (1966); also see F. Docchio and C. Sacchi, *Invest. Ophthalmol. Vis. Sci.* **29**, 437 (1986).
12. R. G. Meyerand, Jr., and A. F. Haught, *Phys. Rev. Lett.* **13**, 7 (1964); also see F. Docchio, P. Regondi, M. R. C. Capon, and J. Mellerio, *Appl. Opt.* **27**, 3669 (1988).
13. C. D. David, Jr., *J. Appl. Lett.* **11**, 394 (1967).
14. J. F. Ready, *Effects of High-Power Laser Radiation* (Academic Press, New York, 1971).
15. A. Vogel, W. Lauterborn, and R. Timm, *J. Fluid Mech.* **206**, 299 (1989).
16. K. M. Nashold, R. A. Brown, D. P. Walter, and R. C. Honey, *Proc. Soc. Photo-Opt. Instrum. Eng.* **1105**, 78 (1989).
17. C. G. Morgan, *Rep. Progr. Phys.* **38**, 621 (1976).
18. T. P. Ackerman and O. B. Toon, *Appl. Opt.* **20**, 3661 (1981).
19. J. B. Donnet and A. Voet, *Carbon Black Physics, Chemistry and Elastomer Reinforcement* (Dekker, New York, 1976).
20. C. D. David, Jr., *J. Appl. Phys.* **40**, 3674 (1969).

Z-scan measurements of the anisotropy of nonlinear refraction and absorption in crystals

R. DeSalvo, M. Sheik-Bahae, A. A. Said, D. J. Hagan, and E. W. Van Stryland

Center for Research in Electro-Optics and Lasers, University of Central Florida, Orlando, Florida 32816

Received September 21, 1992

We introduce a method for measuring the anisotropy of nonlinear absorption and nonlinear refraction in crystals by incorporating a wave plate into the Z-scan apparatus. We demonstrate this method by measuring the polarization dependence of the nonlinear refractive index or two-photon absorption coefficient in BaF₂, KTP, and GaAs at wavelengths of 532 and 1064 nm.

The techniques most often used to determine components of the third-order susceptibility, $\chi^{(3)}$, include degenerate four-wave mixing,¹ nearly degenerate three- and four-wave mixing,² ellipse rotation,³ optical third-harmonic generation,⁴ photoacoustics,⁵ beam-distortion methods,⁶⁻⁸ and nonlinear transmission.⁹ Some of these have been adapted to measure the anisotropy of $\chi^{(3)}$.^{2,5,6,9} We introduce a method based on the Z-scan^{8,10} to determine the polarization dependence of nonlinear refraction and nonlinear absorption in crystals. We demonstrate this technique to measure anisotropy of the ultrafast bound electronic nonlinear refractive index n_2 and the two-photon absorption (2PA) coefficient β . Measurements of the anisotropy can also give information about the band structure of the material.¹¹ Sheik-Bahae *et al.*⁸ describe the Z scan in detail, where the transmittance of a sample is measured through an aperture in the far field as a function of the sample's position relative to the beam waist. If only nonlinear refraction is present, a transmittance curve, with a maximum (peak) and a minimum (valley), antisymmetric around the position of the beam waist is obtained. The peak-to-valley change in transmittance, ΔT_{pv} , is approximately proportional to the on-axis nonlinear phase shift $\Delta\Phi_0$.⁸ It is shown that $\Delta T_{pv} = p|\Delta\Phi_0| = pk|\Delta n|L$, where k is the propagation vector and L is the length of the sample. The constant p depends on the size of the aperture in the far field and equals 0.36 for an aperture allowing 40% linear transmittance. Placing the sample at the Z position corresponding to the peak, a half-wave plate situated in front of the sample is rotated, and the transmittance through the aperture is measured as a function of the incident linear polarization direction. This is repeated with the sample positioned at the valley. By subtracting these two sets of data, we obtain ΔT_{pv} as a function of incident electric-field polarization, from which we can infer the polarization dependence of n_2 . Here we define n_2 by the change in refractive index, $\Delta n = n_2 I$.

When the aperture is removed and all the transmitted energy is collected, the experiment is sensitive only to changes in transmittance due to the presence of nonlinear absorption. When the sample is placed

at the beam waist, the loss is maximized, and rotation of the wave plate shows the anisotropy of this loss. To normalize the transmittance change and eliminate other small polarization-dependent losses, a second measurement is performed, with the sample placed far from the waist such that the nonlinear loss is negligible. Subtraction of these data from the data with the sample at the waist gives the normalized transmittance change through the sample, and hence the 2PA coefficient β can be calculated from a spatial and temporal integration of the equation

$$\frac{\partial I(r, z', t)}{\partial z'} = -\alpha I(r, z', t) - \beta I(r, z', t)^2, \quad (1)$$

where z' is the depth in the sample and α is the residual linear absorption coefficient.¹² Measurement of the anisotropy of n_2 in the presence of nonlinear absorption requires a more complicated procedure.⁸

Following Ref. 13, given an input field $E(t) = E_0 \cos(\omega t)$, the amplitude of the third-order polarization at ω is given by

$$P^{(3)}(\omega) = \frac{3\epsilon_0}{4} \chi_{\text{eff}}^{(3)}(\theta) E_0^3, \quad (2)$$

where ϵ_0 is the dielectric permittivity and $\chi_{\text{eff}}^{(3)}$ is the effective third-order susceptibility whose functional form depends on the symmetry and orientation of the crystal. The intensity-dependent refractive index n_2 and the 2PA coefficient β are related to the real and imaginary parts of $\chi^{(3)}$ by⁸

$$n_2 \text{ (m}^2/\text{W)} = \frac{3}{4\epsilon_0 c n_0^2} \text{Re } \chi^{(3)}(\omega; -\omega, \omega, \omega) \quad (3)$$

and

$$\beta \text{ (m/W)} = \frac{3\omega}{2\epsilon_0 c^2 n_0^2} \text{Im } \chi^{(3)}(\omega; -\omega, \omega, \omega), \quad (4)$$

where n_0 is the linear refractive index and c is the speed of light in a vacuum. We use mks units throughout, and the conventions used here follow those of Ref. 14. The conversion to esu is $n_2^{\text{esu}} = (cn_0/40\pi)n_2^{\text{mks}}$, where $\Delta n = n_2^{\text{esu}} E_0^2/2$.

The Q-switched mode-locked Nd:YAG laser used for these experiments produced single 30-ps (FWHM)

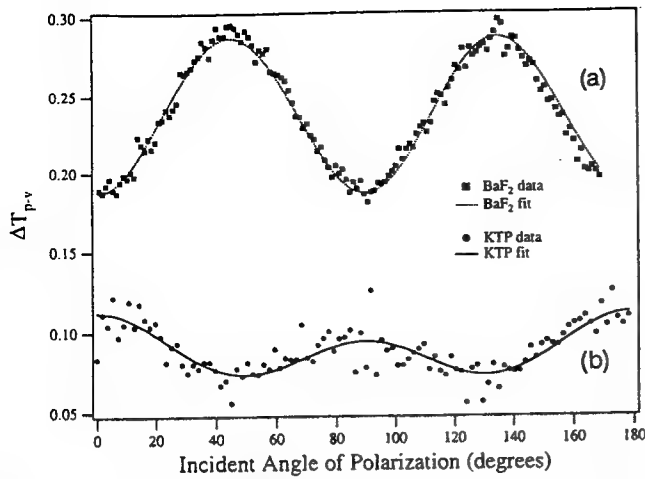


Fig. 1. Curve (a), 532-nm 40% aperture transmittance trace as a function of incident electric-field polarization in BaF₂. Curve (b), 1064-nm trace in KTP to measure the polarization dependence of n_2 .

TEM₀₀-mode pulses that could be frequency doubled to obtain 21-ps 532-nm pulses. When using 1064-nm pulses, we focused the beam to a measured spot size of 37 μm (half-width at $1/e^2$ maximum) with a best-form lens, whereas at 532 nm, the beam waist was 24 μm .

Looking first at BaF₂, which has a cubic lattice belonging to the point group $m\bar{3}m$, we define the electric-field polarization direction θ relative to the [100] crystallographic axis and propagate \mathbf{k} parallel to the [001] crystallographic axis. Figure 1, curve (a), shows data of the aperture transmittance versus polarization orientation of n_2 at 532 nm with an irradiance of 61 GW/cm² for a 0.5-cm-thick sample of BaF₂. The electric-field polarization in the crystallographic xy plane is given by $\mathbf{E} = E_0(\cos \theta \hat{x} + \sin \theta \hat{y})$. Because we consider degenerate frequencies, intrinsic permutation symmetry leaves three independent $\chi^{(3)}$ tensor components given by $\chi_{xxxx}^{(3)}$, $\chi_{xyyx}^{(3)}$, and $\chi_{xyxy}^{(3)}$. Note that this is true for both real and imaginary parts of $\chi^{(3)}$. For this specific geometry, the effective third-order susceptibility from Eq. (2) is

$$\chi_{\text{eff}}^{(3)}(\theta) = \chi_{xxxx}^{(3)}[1 + 2\sigma(\sin^4 \theta - \sin^2 \theta)], \quad (5)$$

where we define a coefficient of anisotropy σ as

$$\sigma = \frac{\chi_{xxxx}^{(3)} - [\chi_{xyxy}^{(3)} + 2\chi_{xyyx}^{(3)}]}{\chi_{xxxx}^{(3)}}. \quad (6)$$

If the material is isotropic, i.e., $\chi_{xxxx}^{(3)} = \chi_{xyxy}^{(3)} + 2\chi_{xyyx}^{(3)}$, σ yields a value of zero. The dashed curve in Fig. 1

is a least-squares fit to Eq. (5) with only real components of $\chi^{(3)}$. The values of the nonlinear coefficients for BaF₂ and other materials are summarized in Table 1, where the absolute errors are $\pm 20\%$.

For z -cut KTP, which has an orthorhombic lattice and belongs to the point group $mm2$, we propagate \mathbf{k} along the crystal's z axis so that the electric-field polarization will be in the xy plane making an angle ϕ with the crystallographic x axis. In this geometry, $d_{\text{eff}} = 0$ for both type I and type II phase matching¹⁵; thus, quasi- $\chi^{(3)}$ effects that are due to cascading of second-order processes¹⁶ are eliminated, and the nonlinearity is purely bound electronic and positive.¹⁶ Applying intrinsic permutation symmetry, we arrive at an effective third-order susceptibility,

$$\chi_{\text{eff}}^{(3)}(\phi) = \chi_{xxxx}^{(3)} \cos^4 \phi + \chi_{yyyy}^{(3)} \sin^4 \phi + B \frac{\sin^2 2\phi}{4}, \quad (7)$$

where B is given by

$$B = 2\chi_{xxyy}^{(3)} + 2\chi_{yyxx}^{(3)} + \chi_{xyyx}^{(3)} + \chi_{yxyx}^{(3)}. \quad (8)$$

Figure 1, curve (b), shows the aperture transmittance versus ϕ at 1064 nm in a 0.76-mm sample of KTP with an irradiance of 46 GW/cm². The least-squares fit to Eq. (7) is shown as the solid curve in Fig. 1.

At 532 nm, KTP exhibits 2PA. The solid curve and dots in Fig. 2 show the transmittance versus ϕ with the aperture removed and the sample at the beam waist for an irradiance of 32 GW/cm². The solid curve in Fig. 2 is a least-squares fit of Eq. (7).

GaAs is a $\bar{4}3m$ cubic material and shows 2PA at 1064 nm. The GaAs sample was oriented so that \mathbf{k} was normal to the [110] plane, and the electric-field polarization was measured relative to the [001] crystallographic axis. The dotted curve and crosses in Fig. 2 show the transmittance versus polarization angle θ in a 0.8-mm sample placed at the beam waist with an irradiance of 180 MW/cm². Following the analysis for cubic BaF₂, we find that

$$\chi_{\text{eff}}^{(3)}(\theta) = \chi_{xxxx}^{(3)} \left[1 + 2\sigma \left(\frac{3}{4} \sin^4 \theta - \sin^2 \theta \right) \right]. \quad (9)$$

In contrast to the case of BaF₂, only the imaginary components of $\chi^{(3)}$ are used in evaluating Eqs. (6) and (9). The least-squares fit to the data is shown as the dashed curve in Fig. 2. The value of the anisotropy of β reported here agrees well with that reported by Bepko,⁹ using nanosecond pulses, where 2PA-generated carrier absorption is large and simply

Table 1. Summary of Nonlinear Coefficients n_2 and β Measured at 532 and 1064 nm

BaF ₂	Re[$\chi_{xxxx}^{(3)}$](m ² /V ²)	σ	n_2 (m ² /W)[100]	n_2 (m ² /W)[010]	n_2 (m ² /W)[110]	
532 nm	1.59×10^{-22}	-1.08 ± 0.10	2.08×10^{-20}	2.08×10^{-20}	3.22×10^{-20}	
GaAs	Im[$\chi_{xxxx}^{(3)}$](m ² /V ²)	σ	β (cm/GW)[100]	β (cm/GW)[110]	β (cm/GW)[111]	
1064 nm	6.35×10^{-19}	-0.74 ± 0.18	18	24	25	
KTP	Re[$\chi_{xxxx}^{(3)}$](m ² /V ²)	Re[$\chi_{xyyy}^{(3)}$](m ² /V ²)	Re(B)(m ² /V ²)	n_2 (m ² /W)[100]	n_2 (m ² /W)[010]	n_2 (m ² /W)[110]
1064 nm	23.2×10^{-22}	19.6×10^{-22}	18.5×10^{-22}	21.4×10^{-20}	18.1×10^{-20}	13.9×10^{-22}
KTP	Im[$\chi_{xxxx}^{(3)}$](m ² /V ²)	Im[$\chi_{xyyy}^{(3)}$](m ² /V ²)	Im(B)(m ² /V ²)	β (cm/GW)[100]	β (cm/GW)[010]	β (cm/GW)[110]
532 nm	11.7×10^{-22}	7.77×10^{-22}	3.96×10^{-22}	0.24	0.16	0.14

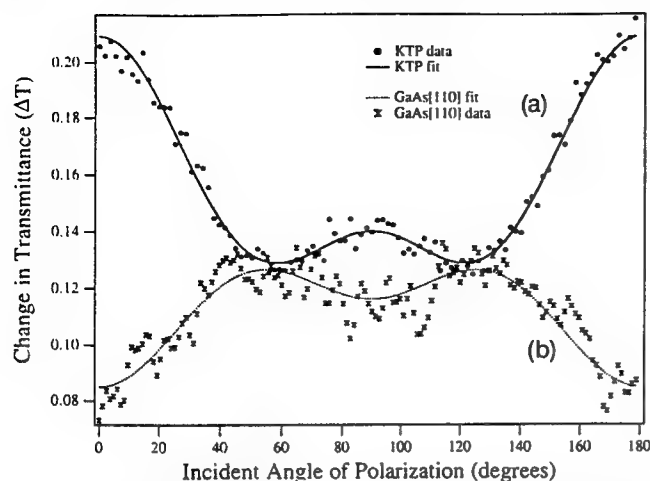


Fig. 2. Curve (a), 532-nm data for KTP showing variation in change in transmittance as a function of incident polarization. Curve (b), 1064-nm trace in [110] GaAs showing variation in transmittance as a function of incident electric-field polarization.

reflects the anisotropic nature of the band structure. The same value of anisotropy has been theoretically predicted¹⁷ and subsequently measured¹⁸ for the real part of $\chi^{(3)}$ at a wavelength of 10.6 μm .

Use of wave-plate rotation rather than repeated Z scans at different electric-field polarization orientations keeps the sample stationary, thus minimizing any beam walk at the aperture, and hence increasing the sensitivity for measuring the anisotropy. By choosing specific crystal orientations and wave-vector propagation directions, different third-order tensor susceptibility elements can be determined.

We gratefully acknowledge the support of the National Science Foundation (Grant ECS-9120590), the Defense Advanced Research Projects Agency/Night Vision and Electro Optics Directorate, and the Florida High Technology and Industrial Council. In addition, we thank Brian Wherrett of Heriot-Watt University for helpful discussions, R. Adair of Lawrence Livermore National Laboratories for supplying the BaF₂ sample, G. Witt of the Massachusetts Institute of Technology for the GaAs sample, and Bruce Chai for determining crystal orientations.

D. J. Hagan is also with the Department of Physics, University of Central Florida.

E. W. Van Stryland is also with the Department of Physics and Electrical Engineering, University of Central Florida.

References

1. E. J. Canto-Said, D. J. Hagan, J. Young, and E. W. Van Stryland, *IEEE J. Quantum Electron.* **27**, 2274 (1991).
2. R. Adair, L. L. Chase, and S. A. Payne, *Phys. Rev. B* **39**, 3337 (1989).
3. A. Owyong, *IEEE J. Quantum Electron.* **QE-11**, 1064 (1973).
4. P. D. Maker and R. W. Terhune, *Phys. Rev.* **137**, A801 (1965).
5. Y. Bae, J. J. Song, and Y. B. Kim, *J. Appl. Phys.* **53**, 615 (1982).
6. A. A. Borshch, M. S. Brodin, and V. N. Semioshko, *Phys. Status Solidi A* **91**, 135 (1985).
7. W. E. Williams, M. J. Soileau, and E. W. Van Stryland, in *Fifteenth Annual Symposium on Optical Materials for High Power Lasers* (National Bureau of Standards, Washington, D.C., 1983).
8. M. Sheik-Bahae, A. A. Said, T. H. Wei, D. J. Hagan, and E. W. Van Stryland, *IEEE J. Quantum Electron.* **26**, 760 (1990).
9. S. J. Bepko, *Phys. Rev. B* **12**, 669 (1975).
10. J. R. DeSalvo, D. J. Hagan, M. Sheik-Bahae, and E. W. Van Stryland, in *Optical Society of America Annual Meeting Technical Digest* (Optical Society of America, Washington, D.C., 1990), paper MTT7.
11. S. I. Shablaev, *Sov. Phys. JETP* **70**, 1105 (1990).
12. A. A. Said, M. Sheik-Bahae, D. J. Hagan, T. H. Wei, J. Wang, J. Young, and E. W. Van Stryland, *J. Opt. Soc. Am. B* **9**, 405 (1992).
13. P. N. Butcher and D. Cotter, *Elements of Nonlinear Optics* (Cambridge U. Press, London, 1990), Chap. 2.
14. D. C. Hutchings, M. Sheik-Bahae, D. J. Hagan, and E. W. Van Stryland, *Opt. Quantum Electron.* **24**, 1 (1992).
15. T. Yee Fan, C. E. Huang, B. Q. Hu, R. C. Echaradt, Y. X. Fan, R. L. Byer, and R. S. Feigelson, *Appl. Opt.* **26**, 2390 (1987).
16. R. DeSalvo, D. J. Hagan, M. Sheik-Bahae, G. I. Stegeman, E. W. Van Stryland, and H. Vanherzeele, *Opt. Lett.* **17**, 28 (1992).
17. C. Flytzanis, *Phys. Lett.* **31A**, 273 (1970).
18. E. Yablonovitch, C. Flytzanis, and N. Bloembergen, *Phys. Rev. Lett.* **29**, 865 (1972).

Direct Measurements of Nonlinear Absorption and Refraction in Solutions of Phthalocyanines

T. H. Wei¹, D. J. Hagan¹, M. J. Sence¹, E. W. Van Stryland¹, J. W. Perry², and D. R. Coulter²

¹ Center for Research in Electro-Optics and Lasers and Department of Physics, University of Central Florida, Orlando, FL 32816, USA

² Jet Propulsion Laboratory, California Institute of Technology, Pasadena, CA 91109, USA

Received 16 June 1991/Accepted 12 September 1991

Abstract. We report direct measurements of the excited singlet state absorption cross section and the associated nonlinear refractive cross section using picosecond pulses at 532 nm in solutions of phthalocyanine and naphthalocyanine dyes. By monitoring the transmittance and far field spatial beam distortion for different pulsewidths in the picosecond regime, we determine that both the nonlinear absorption and refraction are fluence (energy per unit area) rather than irradiance dependent. Thus, excited state absorption (ESA) is the dominant nonlinear absorption process, and the observed nonlinear refraction is also due to real population excitation.

PACS: 33.00, 42.65, 42.80

In recent years, conjugated organic molecules and polymers have come under critical study regarding their potential as nonlinear optical materials [1]. This has led to interest in: 1) developing a fundamental understanding of the mechanisms which contribute to the nonlinear optical response, 2) identifying means of enhancing and maximizing the nonlinear susceptibilities, and 3) obtaining well defined and accurate measurements of the refractive and absorptive contributions to the observed nonlinearities. Here we report on the separation of nonlinear absorption and refraction in phthalocyanine and naphthalocyanine solutions on the picosecond timescale using a combined nonlinear transmittance and beam distortion method which we refer to as the "Z-scan" technique [2, 3]. We find that both the nonlinear absorption and refraction are dominated by creation of a real population of excited states even though the wavelength of observation lies between electronic absorption bands.

Metallophthalocyanines and related conjugated ring molecules have attracted recent interest [4–11] because, as confined, reduced-dimensionality (2D) delocalized electronic systems, large electronic nonlinearities are expected. The rigid structural framework of these molecules leads to a small geometry change on excitation and a concentration of intensity into the $S_1 \leftarrow S_0, 0,0$ vibronic transition, resulting in a strong narrowband absorption ($Q(0)$ band) [12]. Thus, the phthalocyanine dyes can exhibit a low saturation intensity depending on the relevant relaxation rates. For example, chloro-aluminium phthalocyanine (CAP) is well known as a saturable absorber at

694 nm and was used early on as a passive Q -switch for ruby lasers [13–15]. It also exhibits excited triplet state absorption [16] at shorter wavelengths in the range between the Q and B bands [12] where the linear absorption is quite weak. The nonlinear optical response in this spectral region is of interest because it can function as an optical pulse energy limiter [6, 11]. This type of response has been referred to as reverse saturable absorption [17].

As part of our search for dyes which may be useful for optical limiting applications, we have surveyed the nonlinear transmission of a number of metallophthalocyanines and metallo-naphthalocyanines [6, 11]. Here, we present data using picosecond laser pulses on two dyes in solution: CAP in methanol solution and a silicon naphthalocyanine (Nc) derivative [18], $\text{Si}(\text{OSi}(\text{n-hexyl})_3)_2\text{Nc}$, which we will refer to as SINC, in toluene solution. The Q -band absorption peaks of these solutions are at 670 nm and 774 nm respectively, while we are exciting at 532 nm. With picosecond input pulses (shorter than the time required to populate the triplet state), we find that the excited singlet state absorption is quite strong for both dyes [6, 11]. The generic level structure for these molecules is shown in Fig. 1, and consists of five levels showing the possibility of both excited singlet and excited triplet state absorption. The linear absorption at 532 nm is initially low since we are exciting high in the vibrational manifold of S_1 . The fast relaxation to the bottom of this electronic state makes the excited state absorption (ESA) resonant with the 532 nm input light. For longer pulses, intersystem crossing also leads to resonant triplet

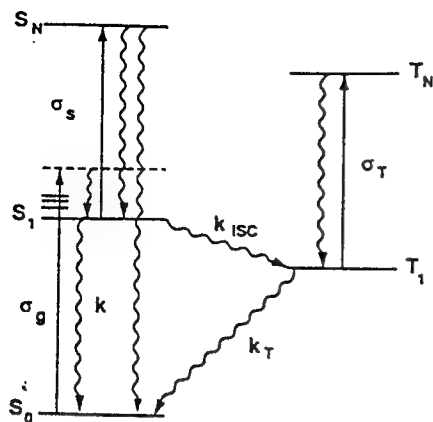


Fig. 1. Generic five-state model for nonlinear behavior of phthalocyanines. S_0 , S_1 , and S_N are singlet states and T_1 and T_N are triplet states. The σ 's are absorption cross sections and the k 's are rate constants. σ_s is represented in the text simply as σ . Wavy lines correspond to spontaneous decay processes. The total decay rate constant for S_1 is $k_s = k + k_{isc}$.

state ESA. This ability to respond on both fast and slow timescales makes these materials particularly attractive for optical limiting. The singlet lifetimes and triplet state formation yields for both CAP and SINC are listed in Table 1.

1 Excited State Absorption

In the following analysis we examine the nonlinear transmittance of a material in which ESA is dominant. In Sect. 3 we show this to be the case for these materials. We solve a rate equation model including excited singlet-singlet state absorption as well as integration over the transverse beam profile. In this model we ignore saturation as discussed in Sect. 4. For pulses short relative to the decay time of the intermediate level the following equations apply:

$$dI/dz' = -\alpha I - \sigma N I \quad (1)$$

and

$$dN/dt = \alpha I / \hbar \omega, \quad (2)$$

where dz' is the differential element of depth in the sample, I the irradiance, α the linear absorption coefficient, σ the excited singlet-singlet absorption cross section, N the density of excited states, and $\hbar\omega$ the photon energy. By temporal integration of (1) and (2) we find

$$dF/dz' = -\alpha F - \alpha \sigma / 2 \hbar \omega F^2, \quad (3)$$

where F is the fluence (i.e. energy per unit area). The solution to this equation, after integrating over the Gaussian spatial distribution of the pulse of on axis fluence F_0 , gives the normalized change in transmittance ΔT of

$$\Delta T = \frac{T}{T_{lin}} - 1 = \frac{\ln(1+q)}{q} - 1 \approx -\frac{q}{2} = -\frac{\alpha \sigma F_0 L_{eff}}{4 \hbar \omega}, \quad (4)$$

where T is the transmittance, T_{lin} the linear transmittance, and $L_{eff} = (1 - e^{-\alpha L})/\alpha$ with L the sample length. Here the last equality defines q and the approximation is valid for small q (i.e. for small ΔT). All energy and fluence levels are quoted as incident in the fluid (i.e. after surface reflections are taken into account).

From (4), the same F for two different pulsewidths is expected to give the same nonlinear absorption for ESA. A similar analysis for two-photon absorption (2PA) gives a result that is I rather than F dependent. Thus, the transmittance change ΔT at a fixed input pulse energy will be independent of pulsewidth for ESA, but will depend on pulsewidth for 2PA. This serves as a simple test to determine the nonlinear mechanism.

2 Z-Scan Techniques

Most of the measurements of the nonlinear properties reported in this paper employed the "Z-scan" technique. This technique, as shown in Fig. 2, involves measurements of the far field sample transmittance of a focused Gaussian beam as a function of the position (Z) of the material relative to the beam waist [2, 3]. Here, we give a brief description of the determination of nonlinear absorption and refraction using this method. First, consider a sample with a negative nonlinear refractive index and an aperture in place in Fig. 2. If we normalize the transmittance T to the linear transmittance of the aperture, and we begin the scan at large negative values of Z in Fig. 2, T is unity. As the sample is moved toward the focus of a

Table 1. Singlet and triplet properties of CAP and SINC

Molecule	τ_s^a	ϕ_T^b	τ_{isc}^c	ϵ_s^d	ϵ_T^e	ϵ_s^f
CAP ^g	7.0 (1)	0.4 ^h	18	580 (40)	19,000	6,000
SINC ⁱ	3.15 (5)	0.2 ^j	16	740 (40)	40,000	10,200

^a S_1 fluorescence lifetime (ns) measured using time-correlated single photon counting

^b Triplet yield

^c Calculated intersystem crossing time constant (ns)

^d Ground state extinction coefficient ($M^{-1} cm^{-1}$) at 532 nm

^e Triplet-triplet extinction coefficient ($M^{-1} cm^{-1}$) at 532 nm estimated from $T-T$ spectra in [16] for CAP and [20] for SINC

^f Excited singlet-singlet extinction coefficient ($M^{-1} cm^{-1}$) calculated from measured σ values, this work

^g In ethanol solution

^h In 1-chloronaphthalene solution, [19]

ⁱ In toluene solution

^j [20]

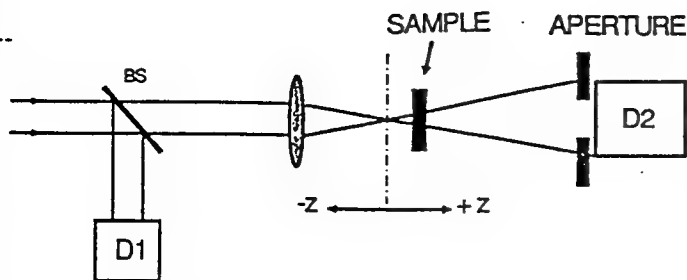


Fig. 2 The Z-scan experimental apparatus in which the ratio $D2/D1$ is recorded as a function of the sample position Z

laser beam the increased irradiance leads to a negative lensing effect which tends to collimate the beam, thus increasing the energy transmitted through the aperture ($T > 1$). With the sample on the $+Z$ side of focus, the negative lensing effect tends to augment beam divergence and the energy transmittance is reduced ($T < 1$). The approximate null at $Z \cong 0$ is analogous to the effect of placing a thin lens at focus which results in a minimal far field pattern change. For still larger $+Z$ values the irradiance is reduced and the transmittance returns to unity. A positive nonlinearity results in the opposite effect, i.e. lowered transmittance for the sample at negative Z and enhanced transmittance for positive Z . The Z-scans are readily analyzed to extract the nonlinear refraction as described in detail in [3].

The induced peak-on-axis phase distortion $\Delta\Phi_0$ is determined by integration of the following equation through the entire length L of the sample:

$$d\Phi_0/dz' = 2\pi\Delta n(z')/\lambda, \quad (5)$$

where Δn is the irradiance or fluence dependent change in refractive index and λ is the wavelength. z' is the distance within the sample, to be distinguished from the sample position, Z . For an instantaneous (irradiance dependent) nonlinearity $\Delta n = n_2|E|^2/2$, where $|E|$ is the electric field amplitude. For an index change due to population of an excited state,

$$\Delta n = \frac{\sigma_r N \lambda}{2\pi}, \quad (6)$$

where σ_r is defined as the nonlinear refractive cross section. Thus, from (2) Δn depends on the temporal integral of the irradiance, or more simply, the fluence.

If the aperture in the Z-scan experiment of Fig. 2 is removed (we term this an "open" aperture Z-scan as opposed to "closed" aperture described above), the Z-scan becomes insensitive to nonlinear refraction and results in a null signal (i.e. flat response with Z) unless nonlinear absorption is present. In this case a symmetrical curve showing a reduced transmittance ($T < 1$) about the focal position is obtained described by (4) where F_0 is a function of Z . If both nonlinear refraction and nonlinear absorption are present simultaneously, an analysis of the open and closed aperture Z-scans can be used to separately determine the nonlinear refraction and nonlinear absorption.

The separation and evaluation process is simple: the closed aperture normalized Z-scan is divided by the one with the aperture open. The result is a new Z-scan showing the sign and magnitude of the refractive nonlinearity. This division process will give a faithful representation of the nonlinear refraction as if nonlinear absorption were absent for relatively small nonlinear absorption. However, in the case of the large ESA shown by these dyes nonlinear absorption dominates, and we fit the data by numerical solution of (2-6) following the analysis given in [3].

3 Experiment and Results

CAP (Eastman Kodak Co.), was extracted from the commercial product with methanol and filtered to remove insoluble material. The methanol was removed by rotary evaporation using a room temperature bath. The resulting solid CAP was used for experiments. SINC was synthesized by the method described in [18]. Solvents used for measurements were absolute methanol for CAP and high purity toluene for SINC.

In our experiments, we use single pulses of picosecond duration at 532 nm with a high quality TEM₀₀ spatial mode obtained from a frequency doubled mode-locked Nd:YAG laser, with a single pulse switch-out apparatus. By selection of various etalons within the laser cavity, the pulsewidth can be varied from 30 to 100 ps full width at half maximum (FWHM). For all of our Z-scan measurements, the beam is focused to a waist of radius $w_0 = 19 \mu\text{m}$ half width at $1/e^2$ maximum (HW1/ e^2 M) and the sample path length is 1 mm.

We performed Z-scan experiments on CAP at a concentration of 1.3×10^{-3} moles per liter. The linear transmittance of 84% gives a linear absorption coefficient of $\alpha = 1.8 \pm 0.1 \text{ cm}^{-1}$, which corresponds to an extinction coefficient of $580 \pm 40 \text{ liters cm}^{-1} \text{ mole}^{-1}$. Here the extinction coefficient is defined as, $\epsilon = -\log_{10} T/CL = 10^{-3}\sigma N_A/\ln(10)$, where C is the concentration in moles per liter. We also give the relation for an absorption cross section σ in cm^2 where N_A is Avogadro's number. In this paper we use σ as the ESA cross section. Similar measurements on SINC give a transmittance of 84% ($\alpha = 1.8 \pm 0.1 \text{ cm}^{-1}$) at a concentration of 1.0×10^{-3} mole per liter, corresponding to an extinction coefficient of $740 \pm 40 \text{ liters cm}^{-1} \text{ mole}^{-1}$.

Figure 3 shows open aperture Z-scans on a CAP solution at 532 nm for two different pulsewidths of 29 ps and 61 ps (FWHM) using the same input energy of $1.17 \mu\text{J}$ and hence, the same on axis fluence at focus of $F_0(Z=0) = 205 \text{ mJ/cm}^2$. Clearly the nonlinear transmittance is independent of pulsewidth and hence we conclude that the mechanism is dominated by ESA.

The solid lines in Fig. 3 are the results of numerically fitting the data to (4) by integrating over space. Here F_0 is a function of Z . This numerical fit gives a value for σ of $\cong 2.3 \times 10^{-17} \text{ cm}^2$ ($\epsilon = 6,020 \text{ liters cm}^{-1} \text{ mole}^{-1}$). Measurements show that σ is the same for concentrations of 5.5×10^{-4} moles per liter and 1.3×10^{-3} moles per liter. A similar measurement on SINC gave σ of $\cong 3.9 \times$

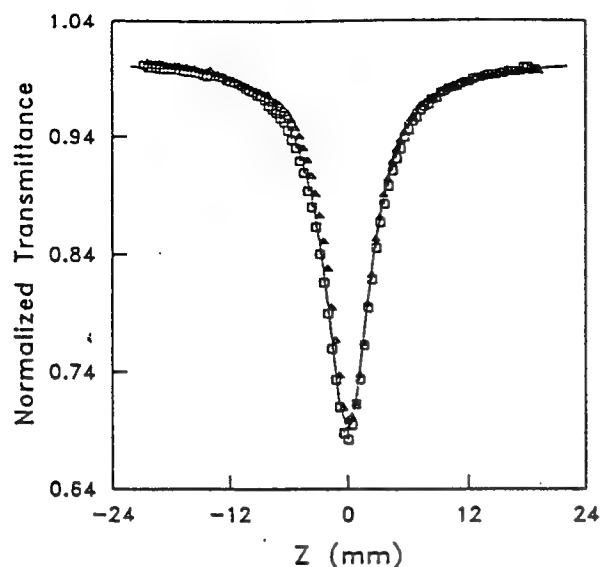


Fig. 3. Open aperture Z-scans for 29 ps (squares) and 61 ps (triangles) pulsewidths at an incident energy of 1.16 μJ in CAP

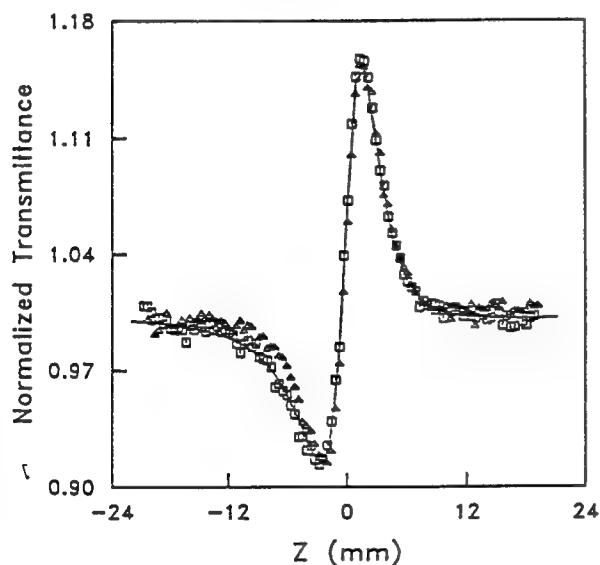


Fig. 4. The results of the division of the closed aperture Z-scan data by the open aperture Z-scan data of Fig. 3 for 29 ps (squares) and 61 ps (triangles) pulsewidths at an incident energy of 1.16 μJ in CAP

10^{-17} cm^2 ($\epsilon = 10,200 \text{ liters cm}^{-1} \text{ mole}^{-1}$). We obtain the same values for σ in CAP at input fluence from 0.4 μJ to 3.6 μJ and for SINC from 0.4 μJ to 1.9 μJ . Absolute errors in the σ values of $\pm 13\%$ were determined from an estimated 7% error in the concentration, 5% fitting error and a 10% possible error in the fluence calculation.

In order to determine the nonlinear refractive coefficients of these dyes, we performed closed aperture Z-scans on CAP for 29 ps and 61 ps (FWHM) pulsewidths. Figure 4 shows the results of dividing these Z-scans by the open-aperture scans of Fig. 3 taken under identical conditions. Clearly we see that the index change is positive and identical for the same fluence. This nonlinear refraction is therefore fluence dependent and as-

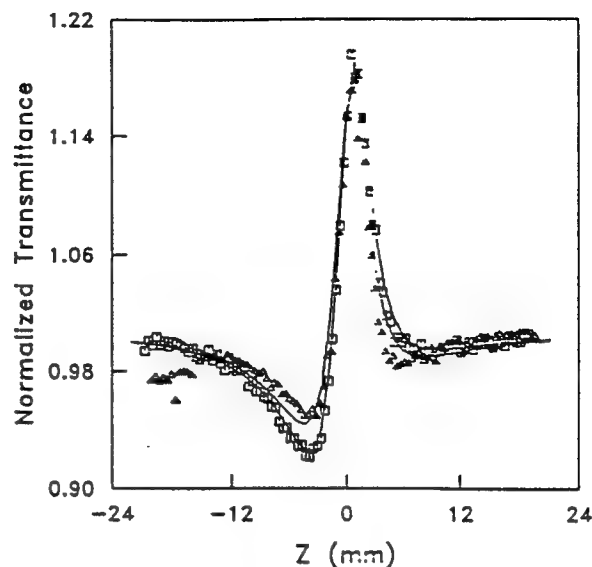


Fig. 5. The results of the division of the closed aperture Z-scan data by the open aperture Z-scan data for 29 ps (squares) and 61 ps (triangles) pulsewidths at an incident energy of 1.89 μJ in SINC

sociated with the real excitation of the singlet state. To determine the contribution of the solvent, Z-scans were performed on the pure methanol and toluene solvents. This yielded an n_2 for methanol of $2.5 \times 10^{-13} \text{ esu}$ and for toluene of $1.9 \times 10^{-12} \text{ esu}$. As expected, no nonlinear absorption was seen in the pure solvents. For the calculation of σ_r , contributions of both solvent (n_2) and dye (σ_r) were included, thus $\Delta n = n_2|E|^2/2 + \sigma_r N \lambda/2\pi$. Substituting this expression into (5) and temporally integrating to numerically fit the data of Fig. 4 then yields $\sigma_r = 1.8 \times 10^{-17} \text{ cm}^2$ for CAP. Measurements at concentrations of $\approx 5.5 \times 10^{-4} \text{ moles/liter}$ and $\approx 1.3 \times 10^{-3} \text{ moles/liter}$ in CAP showed the same σ_r . In Fig. 5, we show divided Z-scans for SINC, again for pulsewidths of 29 ps and 61 ps (FWHM) and with an incident energy of 1.89 μJ . The solid lines show fits obtained in the same way as described above for CAP, giving $\sigma_r = 4.7 \times 10^{-18} \text{ cm}^2$ for SINC. The reason that the two curves in Fig. 5 do not coincide, as do the curves for CAP, is that the instantaneous large nonlinear refraction (n_2) of the toluene solvent plays a significant role. In the case of CAP, the overlap of the Z-scans at different pulsewidths and the independence of our measurements on concentration indicate that the nonlinear refractive contribution of the solvent is negligible. We obtain the same values of σ_r over the input fluence ranges quoted for the determination of σ .

4 Discussion

Our results demonstrate the importance of measuring the nonlinearities at different pulsewidths. Had we looked with only a single pulsewidth, we could equally well have fit the data of Figs. 4 and 5 with simple n_2 values. For example for a pulsewidth of 29 ps for CAP this gives an $n_2 = 4.6 \times 10^{-12} \text{ esu}$ and for SINC this gives

$n_2 = 3.0 \times 10^{-12}$ esu. However, we would obtain a larger n_2 using 61 ps. From these fits and the n_2 's of the solvents, the contribution to the "effective" n_2 's for CAP and SINC at the given concentrations can be obtained by simple subtraction to give $n_2 = 4.4 \times 10^{-12}$ esu for CAP and $n_2 = 1.1 \times 10^{-12}$ esu for SINC. These correspond to effective third order hyperpolarizabilities of 4.5×10^{-31} esu for CAP and 3.3×10^{-32} esu for SINC. The "effective" n_2 is only globally valid if the index change is dependent on the instantaneous irradiance and hence responds on an ultrafast timescale. The most common example of this is the bound electronic Kerr effect. However, if it is due to the population of excited states, it is much more useful to quote the excited state refractive coefficient. Hence what we are observing is not a true $\chi^{(3)}$ effect but is a sequential $\chi^{(1)} : \chi^{(1)}$ process, where $\chi^{(j)}$ refers to the j th order electric susceptibility. Here, the first $\chi^{(1)}$ is associated with the ground state absorption, the second with the resulting excited state refraction.

These refractive changes are a direct result of the changes in the linear absorption, as described by the Kramers-Kronig relations [20]. These relations predict a decrease in index above the induced absorption resonance and an increase below resonance. We can speculate that the cause for the observed positive sign of the nonlinear refraction is the addition of such an absorption centered at a slightly shorter wavelength than our 532 nm light. Measurements of the transient absorption spectrum confirm increasing the absorption centered at a shorter wavelength than 532 nm for CAP [6]. In SINC it is not clear where with respect to 532 nm the increased absorption is centered, and we see a considerably smaller positive nonlinear refraction. In addition we are on the high frequency side of the Q -band absorption which we are saturating. The nonlinear refraction from this saturation is, therefore, also positive in both CAP and SINC.

We have ignored the above mentioned saturation of the Q -band absorption, i.e. depletion of the ground state population, since we experimentally do not see a significant deviation from the fits using (4) and (6) until nearly an order of magnitude higher input fluence. This is our observation even though a simple calculation shows significant ground state depletion at the fluence levels used in these experiments. Allowing for saturation in the rate equations, and numerically integrating, gives excited state cross sections nearly 30% larger than we quote. However, we find a much better fit to the data over the entire range of input fluences used in these experiments with the simple (nonsaturating) model given here. A partial direct repopulation of the ground state from the excited state absorption process may account for the absence of saturation. Time resolved absorption spectra would answer this question. Nevertheless, the main conclusion that excited state absorption and excited state refraction dominate in these experiments remains unchanged.

Garito et al. [9] have recently reported an enhancement of the third order hyperpolarizability using third harmonic generation at 1.54 μ m upon optically inducing a population in the excited singlet state. In our experiments this would appear as a higher order nonlinearity (i.e. a $\chi^{(1)} : \chi^{(3)}$ process, $\chi^{(1)}$ for the initial excitation to the ex-

cited state, and $\chi^{(3)}$ for the subsequent increase in hyperpolarizability). Therefore, the excited state nonlinearities we observe are not directly related to the nonlinearities observed by Garito.

A summary of the results of our measurements along with the singlet and triplet photophysical properties of CAP and SINC are given in Table 1. The excited singlet lifetimes are two orders of magnitude longer than the 30–60 ps pulse durations used in our measurements, so that our results are for excited singlet absorption and we neglect singlet decay in the analysis. While the excited singlet extinction coefficients are roughly an order of magnitude larger than those for the ground states at this wavelength, they are a factor of 3 to 4 smaller than those for the triplet states at 532 nm. The triplet absorption would play a significant role only with much longer pulses.

5 Conclusion

In conclusion we have used a simple sensitive single beam technique (Z -scan) to measure both nonlinear absorption and nonlinear refraction in solutions of phthalocyanine and naphthalocyanine dyes on a picosecond time scale. The nonlinear refraction is determined to be positive and both the nonlinear absorption and refraction are dependent on input pulse fluence (i.e. depend on the excited singlet state population). We give simple relations that allow this excited state absorption cross section and the associated nonlinear refractive cross section to be obtained directly from Z -scan data. For longer nanosecond time scales the triplet excited state absorption becomes significant and will lead to further enhancement of the absorbance. These materials are, therefore, promising materials for optical limiting applications.

Acknowledgements. A portion of this work was performed by the Jet Propulsion Laboratory, California Institute of Technology, as part of its Center for Space Microelectronics Technology. This work was supported in part by the U.S. Army Vulnerability Assessment Laboratory (VAL, LABCOM) through an agreement with the National Aeronautic and Space Administration. The CREOL authors also gratefully acknowledge the support of the U.S. Army Research Office, VAL, LABCOM, the National Science Foundation grant # ECS-8617066, DARPA/CNVEO and the Florida High Technology and Industry Council. The authors also thank Prof. M. E. Kenney of Case Western Reserve University for a sample of $\text{Si}(\text{OSi}(\text{n-hexyl})_3)_2\text{Nc}$ (SINC).

EVS thanks Prof. T. Boggess for helpful discussions.

References

1. See for example, a) D.S. Chemla, J. Zyss (eds.): *Nonlinear Optical Properties of Organic Molecules and Crystals*, Vols. 1 and 2 (Academic, Orlando, 1987) b) R.A. Hann, D. Bloor (eds.): *Organic Materials for Nonlinear Optics* (The Royal Society of Chemistry, London, 1989) c) J. Messier, F. Kajzar, P. Prasad, D. Ulrich (eds.): *Nonlinear Optical Effects in Organic Polymers* (NATO ASI Series E, Vol. 162 (Kluwer, Dordrecht 1989)
2. M. Sheik-bahae, A.A. Said, E.W. Van Stryland: *Opt. Lett.* 14, 955–957 (1989)

3. M. Sheik-bahae, A.A. Said, T.H. Wei, D.J. Hagan, E.W. Van Stryland: IEEE J. QE-26, 760-769 (1990)
4. Z.Z. Ho, C.Y. Ju, W.M. Hetherington III: J. Appl. Phys. 62, 716 (1987)
5. M.K. Casstevens, M. Samoc, J. Pfeiffer, P.N. Prasad: J. Chem. Phys. 92, 2019 (1990)
6. D.R. Coulter, V.M. Miskowski, J.W. Perry, T.H. Wei, E.W. Van Stryland, D.J. Hagan: *Materials for Optical Switches, Isolators and Limiters*, ed. by M.J. Soileau, Proc. SPIE 1105, 42-51 (1989)
7. J.W. Wu, J.R. Heflin, R.A. Norwood, K.Y. Wong, O. Zamani-Khamiri, A.F. Garito, P. Kalyanaraman, J.R. Sounik: J. Opt. Soc. Am. B 6, 707 (1989)
8. J.S. Shirk, J.R. Lindle, F.J. Bartoli, C.A. Hoffman, A.H. Kafafi, A.W. Snow: Appl. Phys. Lett. 55, 1287 (1989)
9. A.F. Garito, J.R. Heflin, N.Q. Wang, Y.M. Cai: Technical digest of the conference on *Nonlinear Optics: Materials, Phenomena and Devices* (IEEE, Washington D.C. 1990) p.73
10. A. Kaltbeitzl, D. Neher, C. Bubeck, T. Sauer, G. Wegner, W. Caseri: In *Electronic properties of Conjugated Polymers III*, Springer Series in Solid State Sci. 91, 220 (1989)
11. J.W. Perry, L.R. Khundkar, D.L. Coulter, D. Alvarez Jr., S.R. Marder, T.H. Wei, M.J. Sence, E.W. Van Stryland, D.J. Hagan: In *Organic Molecules for Nonlinear Optics and Photonics*, ed. by J. Messier, F. Kajzar, P. Prasad, NATO ASI Series E, Vol. 194 (Kluwer, Dordrecht 1991) p. 369
12. M. Gouterman: In *The Porphyrins*, ed. by D. Dolphin (Academic, New York 1978) Vol. III, p. 1
13. F. Gires, F. Combaud: J. de Phys. 26, 325 (1965)
14. J.A. Armstrong: J. Appl. Phys. 36, 471 (1965)
15. M. Hercher, W. Chu, D.L. Stockman: IEEE J. QE-4, 954 (1968)
16. T. Ohno, S. Kato, A. Yamada, T. Tanno: J. Phys. Chem. 87, 775 (1983)
17. W. Blau, H. Byrne, W.M. Dennis, J.M. Kelly: Opt. Commun. 56, 25 (1985)
18. B.L. Wheeler, G. Nagasubramanian, A.J. Bard, L.A. Schectman, D.R. Dininny, M.E. Kenney: J. Am. Chem. Soc. 106, 7404 (1984)
19. J.H. Brannon, D. Magde: J. Am. Chem. Soc. 102, 62 (1980)
20. D.C. Hutchings, M. Sheik-Bahae, D.J. Hagan, E.W. Van Stryland: Opt. Quantum Electron (to be published, 1991)

NONLINEAR OPTICAL CHARACTERIZATION OF ORGANIC MATERIALS

M.J. Soileau, T.H. Wei, M. Sheik-bahae, D.J. Hagan,
Martine Sence, and E.W. Van Stryland

CREOL, Center for Research in Electro-Optics and Lasers
Physics and Electrical Engineering Departments
University of Central Florida, Orlando, Florida 32816

We report a sensitive single beam technique for measuring both the nonlinear refractive index and nonlinear absorption coefficient for a wide variety of materials. We describe the experiment and present a brief analysis including cases where nonlinear refraction is accompanied by nonlinear absorption. In these experiments the transmittance of a sample is measured through a finite aperture in the *far-field* as the sample is moved along the propagation path (z) of a focused Gaussian beam. The sign and magnitude of the nonlinear refraction are easily deduced from such a transmittance curve (Z-scan). Employing this technique a sensitivity of better than $\lambda/300$ wavefront distortion has been achieved using picosecond frequency doubled Nd:YAG laser pulses. In cases where nonlinear refraction is accompanied by nonlinear absorption, it is possible to separately evaluate the nonlinear refraction as well as the nonlinear absorption by performing a second Z-scan with the aperture removed. We demonstrate this method for a solution of chloro-aluminum-phthalocyanine at 532 nm where excited state absorption is present and the nonlinear refraction is positive.

We have recently developed a sensitive single beam technique for measuring both nonlinear refraction and nonlinear absorption.^{1,2} We refer to this technique as a Z-scan. This method is rapidly gaining use for measuring electronic nonlinearities (eg. n_2) and nonlinear absorption (eg. two-photon absorption coefficients β or excited-state cross sections σ) in materials from semiconductors to glasses to organics. We review this technique and the analysis of Z-scan data to show how nonlinear refraction can be separated from nonlinear absorption. We then apply this technique to a solution of chloro-aluminum-phthalocyanine (CAP) dissolved in methanol which we have previously used for passive optical limiting.³

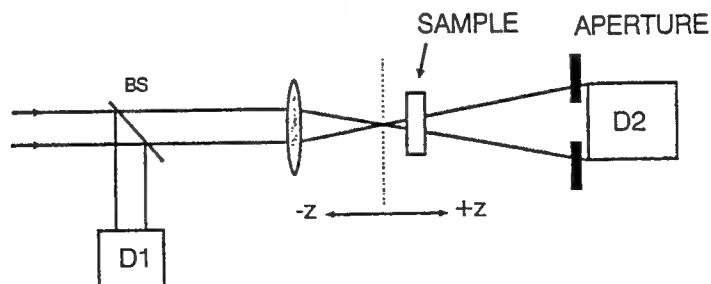


Fig.1 The Z-scan experimental apparatus in which the ratio $D2/D1$ is recorded as a function of the sample position z .

nonlinear refraction and nonlinear absorption are present simultaneously, an analysis of the "open" aperture ($S=1$) and "closed" aperture ($S<1$) experiments can be used to separately determine the nonlinear refraction and nonlinear absorption.

The separation and evaluation process is simple: divide the "closed" aperture normalized Z-scan by the one with open aperture. The result is a new Z-scan where ΔT_{p-v} agrees to within $\pm 10\%$ of that obtained from a purely refractive Z-scan. This division process will give a faithful value for n_2 as long as the nonlinear absorption is not dominant. In practice we have found this method to work quite well provided the curve obtained by division looks like Fig. 2 (ie. appears antisymmetric). We have checked it by numerically calculating the results of Z-scans including both nonlinearities.²

We define β as the two-photon absorption (2PA) coefficient and σ as the excited state absorption (ESA) coefficient. For small nonlinear absorption (ie. $\Delta T_{p-v} < 0.1$) the following approximation can be used to determine β or σ from the open aperture Z-scan;

$$\Delta T_{p-v} \approx -\frac{\beta}{2\sqrt{2}} I_0(1-R)L_{eff}, \text{ for 2PA,} \quad (3a)$$

$$\Delta T_{p-v} \approx -\frac{\sigma\alpha}{4\hbar\omega} F_0(1-R)L_{eff}, \text{ for ESA,} \quad (3b)$$

where $L_{eff} = (1 - e^{-\alpha L})/\alpha$, with α the linear absorption coefficient.^{4,5} Here $I_0(\text{W/cm}^2)$ is the peak on axis irradiance assuming a temporally and spatially Gaussian shaped pulse, and $F_0(\text{J/cm}^2)$ is the on axis fluence assuming a Gaussian spatial beam. In the case of CAP we found that the nonlinear absorption was due to ESA and not 2PA. We determined this by monitoring the nonlinear absorption for different pulsewidths of 29 ps and 61 ps (FWHM). The same fluence for the different pulsewidths gave the same nonlinear absorption as expected from Eq. 3b for excited state absorption. Equation 3a for 2PA predicts that the same irradiance would give the same absorption.

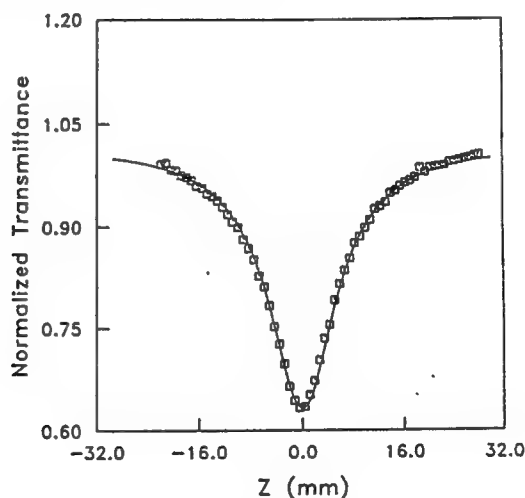


Fig. 3. Open aperture Z-scan on CAP at 3.18 μJ and theoretical fitting (solid line) with $\sigma=1.8 \times 10^{-17} \text{ cm}^2$ at a concentration of 1.0×10^{-3} moles/liter.

The open aperture Z-scan, along with a numerical fit, is shown in Fig. 3 for an input energy of 3.2 μJ at 532 nm using ≈ 27 ps (FWHM) pulses. Note that for Fig. 3 the $\Delta T > 0.1$ and Eq. 3b is not applicable.² The parameters used are $w_0=28 \mu\text{m}$ ($\text{HW1/e}^2\text{M}$), $R=0.05$, $L=0.2 \text{ cm}$, $\alpha=1.42 \text{ cm}^{-1}$ (or 1390 cm^{-1} per mole per liter) as determined from the 68% measured linear transmittance for a concentration of 1.02×10^{-3} moles per liter. This numerical fit gives a value for σ of $\approx 1.8 \times 10^{-17} \text{ cm}^2$.

this technique to several materials displaying a variety of nonlinearities on different time scales. Here we have presented data on chloro-aluminum-phthalocyanine that gives the excited state absorption cross section and the nonlinear refractive index, all for 0.53 μm picosecond pulses. It is expected that this method will be a valuable tool for experimenters searching for highly nonlinear materials.

ACKNOWLEDGEMENT

We gratefully acknowledge the support of the Army Research Office, the National Science Foundation grant #ECS-8617066, the support of DARPA/CNVEO and the Florida High Technology and Industry Council. We also thank Dan Coulter and Joe Perry of the Jet Propulsion Laboratory for providing samples and their expertise on materials.

1. M. Sheik-bahae, A.A. Said, and E.W. Van Stryland, "High Sensitivity, Single Beam n_2 Measurements", Opt. Lett. 14, 955-957 (1989).
2. M. Sheik-bahae, A.A. Said, T.H. Wei, D.J. Hagan, and E.W. Van Stryland, "Sensitive Measurement of Optical Nonlinearities Using a Single Beam", Jour. Quan. Elect., QE 26, 760-769 (1990).
3. D.R. Coulter, V.M. Miskowsky, J.W. Perry, T.H. Wei, E.W. Van Stryland, and D.J. Hagan, Proceedings of SPIE, Materials for Optical Switches, Isolators, and Limiters, 1105, 42-51 (1989).
4. E.W. Van Stryland, H. Vanherzeele, M.A. Woodall, M.J. Soileau, A.L. Smirl, S. Guha, and T.F. Boggess, "Two-Photon Absorption, Nonlinear Refraction, and Optical Limiting in Semiconductors", Opt. Eng. 24, 613-623 (1985).
5. T.F. Boggess, S.C. Moss, I.W. Boyd, and A.L. Smirl, Opt. Lett. 9, 291 (1984).

Measurement of nondegenerate nonlinearities using a two-color Z scan

M. Sheik-Bahae, J. Wang, R. DeSalvo, D. J. Hagan, and E. W. Van Stryland

Center for Research in Electro-Optics and Lasers, University of Central Florida, Orlando, Florida 32816

Received October 9, 1991

A simple dual-wavelength (two-color) Z-scan geometry is demonstrated for measuring nonlinearities at frequency ω_p owing to the presence of light at ω_e . This technique gives the nondegenerate two-photon absorption (2PA) coefficient $\beta(\omega_p; \omega_e)$ and the nondegenerate nonlinear refractive index $n_2(\omega_p; \omega_e)$, i.e., cross-phase modulation. We demonstrate this technique on CS_2 for n_2 and on ZnSe where 2PA and n_2 are present simultaneously.

The newly developed Z-scan technique has been used as an accurate and sensitive tool for determining nonlinear refraction and absorption in a single-beam single-wavelength geometry.¹ Here we introduce a dual-wavelength (two-color) extension of this technique for measuring changes of refraction Δn and absorption $\Delta\alpha$ induced by a strong excitation beam at frequency ω_e on a weak probe beam at a different frequency ω_p ; i.e., $\Delta n(\omega_p; \omega_e)$ and $\Delta\alpha(\omega_p; \omega_e)$, respectively.^{2,3} In the lowest-order nonlinearity such quantities are defined through the third-order susceptibility.

Measurements of these nondegenerate nonlinearities potentially allow determination of material parameters not available from their degenerate counterparts. For example, it has been shown⁴ that the frequency difference ($\omega_p - \omega_e$) can be exploited to obtain information about the dynamics of the nonlinear response with a time resolution much less than the laser pulse width. With ultrashort pulses we can use a time delay between excitation and probing pulses to further give a detailed time-resolved picture of the nonlinear interaction. A recent theory based on the nonlinear Kramers-Kronig transformation predicts dispersion relations between degenerate and nondegenerate nonresonant bound-electronic contributions of Δn and $\Delta\alpha$.⁵ Experiments performed with the single-beam Z scan strongly support the dispersion relations for the degenerate case. The two-color Z scan enables us to investigate the nondegenerate theory experimentally.⁶ From a practical point of view, investigating nondegenerate optical nonlinearities is of interest in the area of dual-wavelength all-optical switching applications in which cross-phase modulation plays an essential role.

The two-color Z-scan experimental arrangement used in these experiments is shown in Fig. 1. Picosecond pulses from a mode-locked Nd:YAG laser ($\lambda = 1.06 \mu\text{m}$) are used as the excitation beam. The copropagating probe is generated by inserting a 3-mm-thick, thin KD*P crystal with a $\approx 1\%$ conversion efficiency in the beam path. The two beams

are then focused with an achromatic lens of focal length $f \approx 15 \text{ cm}$. The transmitted beam is split and sent to two detectors in the far field that each monitor only one wavelength ($\lambda = 0.532$ or $1.06 \mu\text{m}$) as the sample is scanned along the Z direction (propagation path) near the focal plane. Analogous to the usual single-wavelength Z scan, with a fully open aperture (100% transmittance), the measurement is only sensitive to the induced changes in absorption, while a partially closed aperture Z scan displays the induced refractive changes as well. In this geometry, perpendicular polarization results from the type I phase-matched second-harmonic generation. Parallel polarization is obtained by inserting a calcite polarizer before the focusing lens.

In the case of the two-color Z scan, the field consists of a strong excitation beam at frequency ω_e and a weak probe at ω_p . Thus in the weak-probe approximation and for thin samples in the external self-action geometry^{1,4} the propagation of the probe beam within the sample can be fully determined using the following equations:

$$\frac{dI_e}{dz'} = -\alpha_e I_e - \beta_{11}(\omega_e; \omega_e) I_e^2, \quad (1a)$$

$$\frac{dI_p}{dz'} = -2\beta_{12}(\omega_p; \omega_e) I_e I_p, \quad (1b)$$

$$\frac{d\Delta\phi_p}{dz'} = \frac{\omega_p}{c} 2\gamma_{12}(\omega_p; \omega_e) I_e, \quad (1c)$$

where $I_{e,p}$ are the irradiances, which are functions of the depth into the sample z' , the radial coordinate r , the time t , and the sample position Z . The nonlinear phase variation of the probe is given by $\Delta\phi_p$, which is also a function of Z , z' , r , and t . The linear absorption coefficient at the excitation wavelength is α_e , $\beta_{21}(\omega_p; \omega_e)$ and $\beta_{11}(\omega_e; \omega_e)$ denote the nondegenerate and degenerate 2PA coefficients, respectively, and γ_{12} represents the nonlinear refractive coefficient, which can also be given in terms of n_2 (esu).¹ The subscripts 1 and 2 denote the state of polarization of the excitation and probe beams, re-

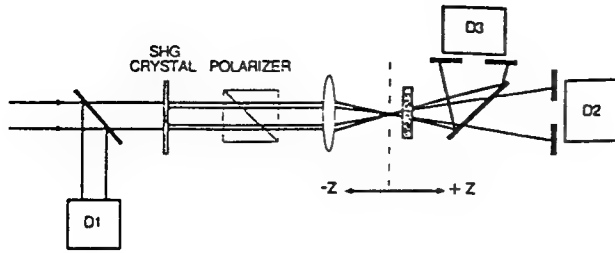


Fig. 1. Two-color Z-scan experimental configuration. The measured signal is the ratio $D2/D1$ as the sample is scanned along the propagation (Z) axis.

spectively, and may correspond to the transverse directions x or y . For example, with the probe and excitation beams perpendicularly polarized, we have $1 = x$ and $2 = y$. Equation (1a) gives the pump depletion caused by 2PA, while Eqs. (1b) and (1c) describe the cross amplitude and the phase modulation of the probe caused by the excitation beam. Note the factor of 2 in front of γ_{12} and β_{12} in Eqs. (1b) and (1c). This factor arises from the interference between excitation and probe fields,^{7,8} and its validity depends on the condition that the response time of the medium τ must be shorter than the beat period; i.e., $\tau|\omega_p - \omega_e| \ll 1$.⁹ This is true for degenerate ($\omega_p = \omega_e$) nonlinearities or nonresonant bound-electronic nonlinearities. For molecular reorientational nonlinearities, such as those in CS_2 ($\tau \approx 2$ ps), this factor of 2 should not be included in the analysis of the nondegenerate case for which $\omega_p - \omega_e = \omega_e$.

The probe is assumed to be sufficiently weak not to induce any self- or cross-modulation effects. The linear absorption, refraction, and surface reflections of the probe beam are immaterial if we normalize the probe transmittance to unity in the absence of any nonlinearity. Equations (1a), (1b), and (1c) can be solved for a sample of length L to give the probe field, which is proportional to $\sqrt{I_p} \exp[-i\Delta\phi(z, r, t, z' = L)]$, at the exit surface of the sample. The far-field electric-field distribution is then calculated from linear-diffraction theory.¹

The measured quantity in a Z-scan experiment is the normalized transmitted power through the far-field aperture that has a radius r_a with a linear transmittance S as given by $1 - \exp(-2r_a^2/w_a^2)$, where w_a is the beam waist of the probe at the aperture when $I_e = 0$. If we assume pulsed radiation, the measured quantity is the transmitted pulse energy. A full analytical expression can be obtained for the Z-scan transmittance by accounting for the differences in beam sizes, pulse widths, and focal lengths (chromatic aberration).²

We first consider liquid CS_2 where only nonlinear refraction is present [i.e., all β 's = 0 in Eqs. (1)]. The measured two-color Z scans for this material at an excitation irradiance of 2.9 GW/cm^2 are shown in Fig. 2 for cases of parallel and perpendicular polarization. The asymmetry in the two-color Z scan (unequal peak and valley magnitudes) results from the small chromatic aberration ($\Delta f/f = 1\%$) of the focusing lens and has been accounted for in the beam propagation analysis. This aberration causes the beam with the shorter wavelength (in this case the

probe) to experience a shorter effective focal length, which leads to unequal peak and valley amplitudes. The peak and valley configuration shows that self-focusing ($\Delta n > 0$) results for parallel polarization and that self-defocusing ($\Delta n < 0$) results for crossed polarizations. Here the excitation beam aligns the cigar-shaped molecules along its polarization (for example, x), which increases the refractive index for light that shares its polarization and reduces the index equally along the other two directions (y and z) for crossed polarization.

Nonlinear refraction in CS_2 arises primarily from the molecular orientation effect (γ_{12}^m) with a ≈ 2 -ps decay time, with small additional contributions from intermolecular, intramolecular, and electronic effects.¹⁰ Here we assume that these latter small contributions, which we denote by γ_{12}^e , are of an electronic type; i.e., they are instantaneous ($|\omega_p - \omega_e|\tau \ll 1$) and isotropic. A simple molecular orientational model predicts that $\gamma_{xx}^m = -2\gamma_{xy}^m$, while symmetry properties for an isotropic electronic nonlinearity dictate that $\gamma_{xx}^e = 3\gamma_{xy}^e$.⁶ Therefore in a two-color Z-scan measurement we can determine each contribution by equating the total index change as the sum of the electronic and the orientational effects $2\gamma_{xx} = \gamma_{xx}^m + 2\gamma_{xx}^e$, $2\gamma_{xy} = -(\gamma_{xx}^m)/2 + (2\gamma_{xy}^e)/3$, respectively. The solid curves in Fig. 3 are the best-fitted results for CS_2 by using $\gamma_{xy} = -0.67 \times 10^{-14} \text{ cm}^2/\text{W}$ and $\gamma_{xx} = 2.13 \times 10^{-14} \text{ cm}^2/\text{W}$, which gives $\gamma_{xx}^m = 3.3 \times 10^{-14} \text{ cm}^2/\text{W}$ and $\gamma_{xx}^e = 0.47 \times 10^{-14} \text{ cm}^2/\text{W}$. These values indicate that the electronic effect contributes $\approx 15\%$ to the total nonlinear refraction.

Although detailed calculations were performed to fit the above results, such a procedure is not always necessary for estimating γ_{12} . As was the case for the degenerate Z scan, for a given aperture transmittance S and input irradiance, it suffices to know

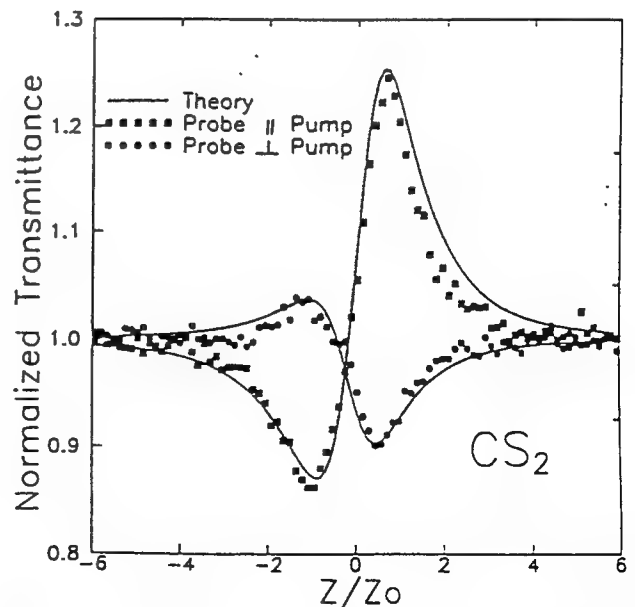


Fig. 2. Measured two-color Z scans ($\lambda = 1.06$ and $0.532 \mu\text{m}$) for liquid CS_2 for parallel (squares) and perpendicular (circles) polarization. The solid curves represent theoretical calculations.

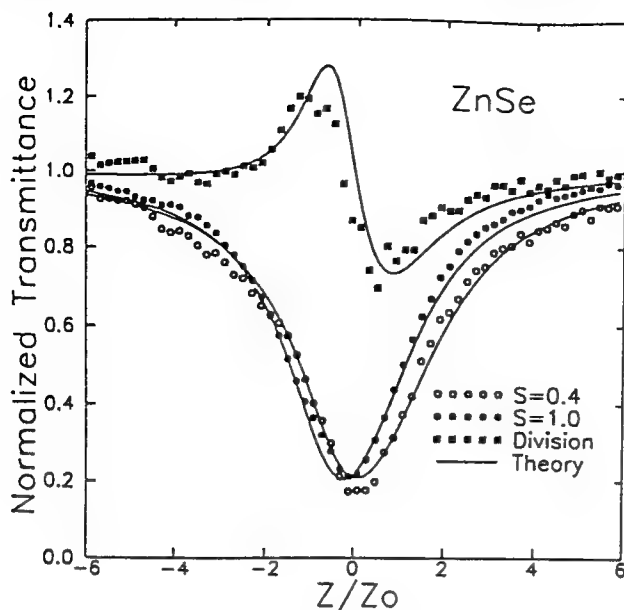


Fig. 3. Normalized transmittance as a function of sample position Z for ZnSe. The solid circles represent the open-aperture Z scan, the open circles represent the closed-aperture Z scan, and the solid squares represent the division of closed by open data values. The lines are from the best-fitted calculations.

only the normalized peak-to-valley transmittance change ΔT_{p-v} , which is defined as the difference between the peak normalized transmittance and the minimum (valley) normalized transmittance. This value is used to extract the peak on-axis phase distortion of the probe ($\Delta\Phi_{12}$) at the exit surface of the sample as derived from Eq. (1c). A useful feature of the Z-scan technique is that for a purely refractive nonlinearity there exists a nearly linear relationship between ΔT_{p-v} and $\Delta\Phi_{12}$ as in the degenerate case,¹

$$\Delta T_{p-v} = p\langle\Delta\Phi_{12}\rangle, \quad (2)$$

where $\Delta\Phi_{12} = \omega_p \gamma_{12} I_{e0}(1 - e^{-\alpha L})/c\alpha_e$, with I_{e0} being the peak on-axis irradiance at the beam waist. Numerical analysis indicates that for very small apertures ($S \approx 0$) and small chromatic aberration, $p = 0.42$ for the two-color case, as compared with $p = 0.406$ for the degenerate case.¹ Chromatic aberration that results in foci separated by one Rayleigh range can actually increase the sensitivity by up to $\approx 20\%$. The dependence of the p coefficient on the aperture transmittance S is numerically evaluated to approximately follow a $(1 - S)^{0.35}$ dependence. Attention should also be given to the time-averaging factor for the pulsed case, where here $\langle\Delta\Phi_{12}\rangle = \Delta\Phi_{12}/\sqrt{1.5}$ as opposed to $\langle\Delta\Phi_{11}\rangle = \Delta\Phi_{11}/\sqrt{2}$ for the single-frequency Z scan.¹

We next consider ZnSe that has a band-gap energy of $E_g = 2.6$ eV for which the degenerate 2PA coefficients are $\beta(1.06 \mu\text{m}) = 0$ and $\beta(0.53 \mu\text{m}) = 5.8 \text{ cm/GW}$.¹ Nondegenerate 2PA with strong $1.06\text{-}\mu\text{m}$ excitation that is probed at $0.53 \mu\text{m}$ is allowed; i.e., $\beta(0.53 \mu\text{m}; 1.06 \mu\text{m}) \neq 0$. Figure 3 shows the two-color Z scan of a 2.7-mm-thick polycrystalline ZnSe sample. These data are obtained by using orthogonal polarization of the

pump and the probe. From the open aperture ($S = 1$), the data β_{12} can be unambiguously determined by using Eqs. (1). The closed-aperture ($S = 0.4$) Z scan, similar to the degenerate measurements, depends on γ_{12} as well as on β_{12} .¹ The effect of this cross-phase modulation can be made more visible by dividing the closed-aperture data by the open-aperture data as was done for the single-wavelength Z scan.¹ The result of this division, shown in Fig. 3, shows a negative (defocusing) effect.¹ The solid curves in Fig. 3 are the results calculated by using Eqs. (1) with $\beta_{12} = 8.8 \text{ cm/GW}$ and $\gamma_{12} = 2.7 \times 10^{-14} \text{ cm}^2/\text{W}$ at a peak pump irradiance of $I_0 = 1.0 \text{ GW/cm}^2$. The irradiances used are low enough that the negative nonlinear refraction from the 2PA ($1.06 \mu\text{m} + 0.53 \mu\text{m}$) generated carriers is negligible. Thus this nonlinear refraction is the third-order nondegenerate bound-electronic Kerr effect.⁵

In summary we have demonstrated an extension of the Z-scan technique to measure nonlinearities at one wavelength caused by a second. This two-color Z scan retains the sensitivity and many of the simple features of the degenerate Z scan and yields the sign and the magnitude of nonlinear refraction even in the presence of nonlinear absorption, where it also yields the nonlinear absorption coefficient.

We gratefully acknowledge the Defense Advanced Research Projects Agency/Center for Night Vision and Electro Optics, the U.S. Army Research Office, the U.S. Army Vulnerability Assessment Laboratory, and the Florida High Technology and Industry Council.

References

1. M. Sheik-Bahae, A. A. Said, T. H. Wei, D. J. Hagan, and E. W. Van Stryland, *IEEE J. Quantum Electron.* **26**, 760 (1990).
2. M. Sheik-Bahae, J. R. De Salvo, J. Wang, D. J. Hagan, and E. W. Van Stryland, in *Conference on Lasers and Electro-Optics*, Vol. 15 of OSA 1991 Technical Digest Series (Optical Society of America, Washington, D.C., 1991), paper CTuW16.
3. H. Ma, A. S. L. Gomes, and C. B. de Araujo, *Appl. Phys. Lett.* **59**, 2666 (1991).
4. R. Adair, L. L. Chase, and S. A. Payne, *J. Opt. Soc. Am. B* **4**, 875 (1987).
5. M. Sheik-Bahae, D. C. Hutchings, D. J. Hagan, and E. W. Van Stryland, *IEEE J. Quantum Electron.* **27**, 1296 (1991).
6. M. Sheik-Bahae, D. C. Hutchings, D. J. Hagan, and E. W. Van Stryland, in *Quantum Electronics Laser Science*, Vol. 11 of 1991 OSA Technical Digest Series (Optical Society of America, Washington, D.C., 1991), paper QTu16.
7. E. W. Van Stryland, A. L. Smirl, T. F. Boggess, M. J. Soileau, B. S. Wherrett, and F. A. Hopf, *Chem. Phys.* **23**, 368 (1982).
8. P. N. Butcher and D. Cotter, *Elements of Nonlinear Optics* (Cambridge U. Press, New York, 1990).
9. N. Bloembergen and P. Lallemand, *Phys. Rev. Lett.* **16**, 81 (1966).
10. D. McMorow, W. T. Lotshaw, and G. A. Kenny-Wallace, *IEEE J. Quantum Electron.* **24**, 443 (1988).

TUTORIAL REVIEW

Kramers-Krönig relations in nonlinear optics

D. C. HUTCHINGS, M. SHEIK-BAHAE, D. J. HAGAN*,
E. W. VAN STRYLAND†

*Center for Research in Electro-Optics and Lasers (CREOL),
University of Central Florida, Orlando, Florida 32826, USA*

Received 17 April; accepted 26 August 1991

We review dispersion relations, which relate the real part of the optical susceptibility (refraction) to the imaginary part (absorption). We derive and discuss these relations as applied to nonlinear optical systems. It is shown that in the nonlinear case, for self-action effects the correct form for such dispersion relations is nondegenerate, i.e. it is necessary to use multiple frequency arguments. Nonlinear dispersion relations have been shown to be very useful as they usually only require integration over a limited frequency range (corresponding to frequencies at which the absorption changes), unlike the conventional linear Kramers-Krönig relation which requires integration over all absorbing frequencies. Furthermore, calculation of refractive index changes using dispersion relations is easier than a direct calculation of the susceptibility, as transition rates (which give absorption coefficients) are, in general, far easier to calculate than the expectation value of the optical polarization. Both resonant (generation of some excitation that is long lived compared with an optical period) and nonresonant 'instantaneous' optical nonlinearities are discussed, and it is shown that the nonlinear dispersion relation has a common form and can be understood in terms of the linear Kramers-Krönig relation applied to a new system consisting of the material plus some 'perturbation'. We present several examples of the form of this external perturbation, which can be viewed as the pump in a pump-probe experiment. We discuss the two-level saturated atom model and bandfilling in semiconductors among others for the resonant case. For the nonresonant case some recent work is included where the electronic nonlinear refractive coefficient, n_2 , is determined from the nonlinear absorption processes of two-photon absorption, Raman transitions and the a.c. Stark effect. We also review how the dispersion relations can be extended to give alternative forms for frequency summation which, for example, allows the real and imaginary parts of $\chi^{(2)}$ to be related.

1. Introduction

In this review we examine the application of causality to obtain dispersion relations for nonlinear optical properties. Linear dispersion relations were first derived for X-rays in the

*Also with the Department of Physics.

†Also with the Departments of Physics and Electrical Engineering.

where \mathcal{P} denotes the Cauchy principal value. It is this relation that is most commonly referred to when one speaks of Kramers-Krönig relations in optics and is the original form of the relation as given in [1, 2] and derived in Section 2.

Although dispersion relations for linear optics are well understood and documented, confusion has existed about applications to nonlinear optics. Clearly causality holds for nonlinear as well as linear systems. The question is, what form do the resulting dispersion relations take? For self-action nonlinear optical effects a nondegenerate form of dispersion relation is appropriate, where, for example, nonlinear refraction of two frequency arguments (the index change at ω due to the presence of a strong perturbing field at Ω) is related to an integral over ω' of the nonlinear absorption at ω' due to the presence of the same perturbing field at Ω . Thus, both the nonlinear absorption and the nonlinear refraction are equivalent to pump-probe spectra with a fixed pump frequency and variable probe frequency.

A first glance at the nonlinear optical susceptibility for a two-level saturated atom [10, 11] could lead one to the result that dispersion relations are not valid for this nonlinear system. However, in the field of solid-state physics, dispersion relations have been used for resonant optical nonlinearities (where some real excitation is created within the material such as free carriers) (see, for example [12]). Furthermore, dispersion relations exist for harmonic generation where the real and imaginary parts of $\chi^{(2)}$ are related (see, for example [13]). It is the aim of this review to show how these different systems are related and to derive more-general dispersion relations. It is also indicated under precisely what conditions these dispersion relations can be used.

The result is that we are able to derive and utilize nonlinear optical Kramers-Krönig relations and apply them to various types of nonlinearities, resonant as well as nonresonant. We present below several extremely useful examples, some of which have only recently been recognized. For example, we show how the electronic Kerr effect and two-photon absorption are related by causality [14, 15].

This review is set out as follows. In Section 2 the linear Kramers-Krönig relations are derived from causality. These are extended to nonlinear optics in Section 3, and the nondegenerate dispersion relation is derived for nonlinear optics. In Section 4 it is shown how dispersion relations can be used in resonant nonlinear optics both for solid-state systems and for atomic systems. In Section 5 we give an example calculation for refractive index changes resulting from the Franz-Keldysh effect (d.c. field) in semiconductors. In Section 6 we consider dispersion relations for nonresonant (a.c. field) optical nonlinearities, and show as an example a calculation of the electronic Kerr effect in solids. We also extend the dispersion relations to derive a degenerate form that is applicable in some special cases such as harmonic generation.

This review uses Gaussian (CGS) units throughout. Appendices are also provided which introduce some of the nonlinear optics terminology, equivalent SI expressions, and some of the more detailed mathematics.

2. Linear Kramers-Krönig relations

In a dielectric medium the optical polarization, $P(t)$ can be obtained from the electric field, $E(t)$, by means of a response function

$$P(t) = \int_{-\infty}^t R(\tau) E(t - \tau) d\tau \quad (2)$$

The response function, $R(\tau)$, is equivalent to a Green's function, as it gives the response

This form of relation is not confined to the field of optics only, but is a general property of Fourier transforms known as Hilbert transforms [8].

It is more usual to write the optical dispersion relations in terms of the more familiar quantities; the refractive index, $n(\omega)$, and absorption coefficient, $\alpha(\omega)$ [5]. In order to derive this, consider the propagation of a monochromatic plane wave through a thin slice of a dielectric medium of (complex) refractive index

$$\eta(\omega) = n(\omega) + i\alpha(\omega)c/2\omega \quad (8)$$

and thickness δz

$$E(z + \delta z, \omega) = \exp\left(\frac{i\eta(\omega)\omega}{c} \delta z\right) E(z, \omega) \quad (9)$$

This is essentially in the same form as Equation 3; that is, a product in frequency space that can be Fourier transformed into a convolution in time

$$E(z + \delta z, t) = \int_{-\infty}^{\infty} g(\delta z, \tau) E(z, t - \tau) d\tau \quad (10)$$

where the response function $g(\delta z, \tau)$ is defined

$$\exp\left(\frac{i\eta(\omega)\omega}{c} \delta z\right) = \int_{-\infty}^{\infty} g(\delta z, \tau) e^{i\omega\tau} d\tau \quad (11)$$

Now relativistic causality states that no signal can propagate faster than c , the speed of light in vacuum. This then requires that $g(\delta z, \tau) = 0$ for $\tau < \delta z/c$. Thus, the lower limit in Equation 11 can be replaced with $\delta z/c$. By substituting $T = \tau - \delta z/c$ we can write

$$\exp\left(\frac{i\omega}{c} [\eta(\omega) - 1] \delta z\right) = \int_0^{\infty} g\left(\delta z, T + \frac{\delta z}{c}\right) e^{i\omega T} dT \quad (12)$$

In a similar manner to the case for the susceptibility, $\chi(\omega)$, the response function, g (time domain), need only be integrated over positive times T in order to calculate its Fourier transform. In terms of complex variables (see Appendix A), this left-hand side of Equation 12 is regular and analytic in the positive imaginary frequency half-plane. This then requires that $\omega[\eta(\omega) - 1]$ can also be defined as an integral over positive times only (i.e. $\omega[\eta(\omega) - 1]$ is also regular and analytic in the upper frequency half-plane) and dispersion relations can be applied. This can be more clearly seen by taking the limit of a thin slice ($\delta z \rightarrow 0$) where the exponential can be expanded to a first-order Maclaurin series and we can write

$$\omega[\eta(\omega) - 1] = \int_0^{\infty} g^*(T) e^{i\omega T} dT \quad (13)$$

where $g^*(T)$ is the Fourier transform of the left-hand side of Equation 13, defined from Equation 12 as

$$g^*(T) = -ic \left(\lim_{\delta z \rightarrow 0} \frac{g(\delta z, T + \delta z/c) - \delta(T)}{\delta z} \right) \quad (14)$$

The delta function is the Fourier transform of the zeroth-order term in the expansion of the exponential. The precise form of $g^*(T)$ is unimportant, and the result we require is that $\omega[\eta(\omega) - 1]$ can be determined by a Fourier transform over positive times only.

We can also obtain Equation 13 by considering the difference in the output field between the cases where the medium is present and absent (vacuum), again in the limit of a

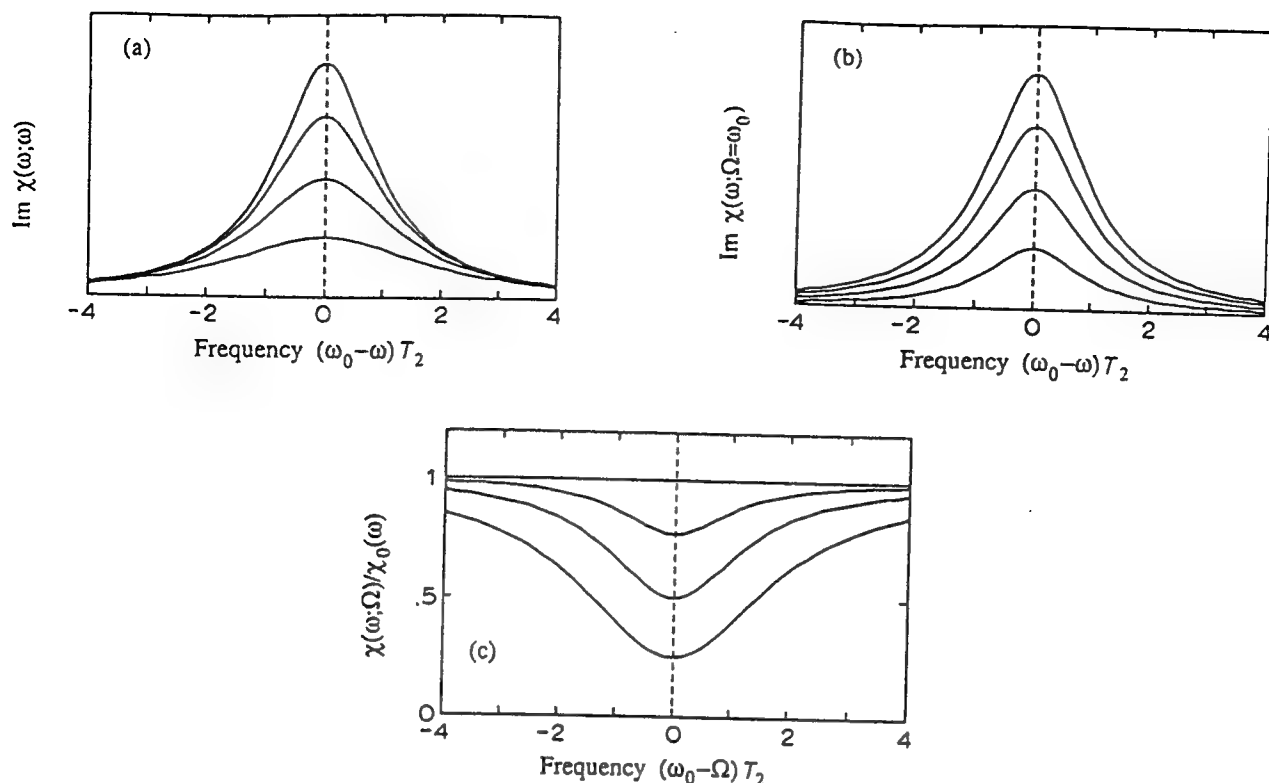


Figure 2 (a) Imaginary part of the degenerate optical susceptibility for a two-level atom versus detuning for various irradiance levels $I/I_s = 0, 0.3, 1$ and 3 . As the irradiance increases, the oscillator strength of the transition is reduced in such a way that the width of the absorption line is broadened, which is often termed a 'power-broadened Lorentzian'. (b) Imaginary part of the nondegenerate optical susceptibility $\chi(\omega; \Omega)$ for a two-level atom versus probe detuning at the same irradiance levels as in (a) for the pump. Note that the Lorentzian lineshape and width is preserved at high pump irradiances and only the overall magnitude decreases, unlike the degenerate form shown in (a). This is also an indication that the Kramers-Krönig relation can be applied in the nondegenerate case. (c) Ratio of the nondegenerate optical susceptibility of a two-level atom (i.e. effect on a weak probe at ω from a strong pump at Ω) to the linear susceptibility as a function of pump detuning for the same irradiance levels as above. This quantity also gives the population difference between the ground and excited states (see text).

calculating the expectation value of the real part of the polarization (see, for example [10]) is that calculating the absorption via transition rates is, in general, far easier. Furthermore, this form of calculation of the refractive index for nonlinear optics is often more useful than for linear optics as absorption changes (which can be either calculated or measured) usually occur only over a limited frequency range and, thus, the integral in Equation 19 need be calculated only over this finite frequency range. In comparison, for the linear Kramers-Krönig calculation, absorption spectra tend to cover a very large frequency range and it is necessary to take account of this full range in order to obtain a quantitative fit for the dispersion, although a qualitative fit to the dispersion can often be obtained using a limited frequency range. Unfortunately, the converse is not true as refractive index changes are usually quite extensive in frequency, so a calculation of absorption changes from refractive index changes is seldom performed.

It is possible to use Equation 19 in nonlinear optics under resonant conditions, where the material is excited into some real state. This excitation can be treated as a perturbation itself. Essentially, the change in refractive index is calculated from the change in absorption.

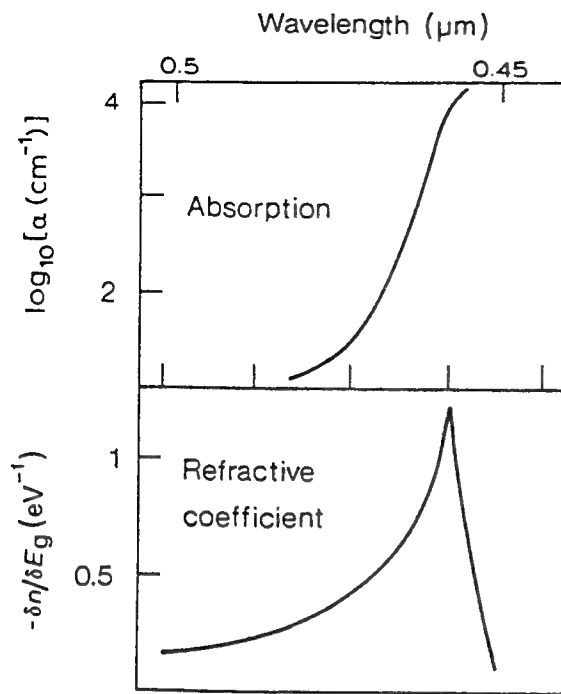


Figure 5 Calculation of the thermo-optic coefficient in a similar manner to Fig. 4, but now using an empirical form of the absorption edge consisting of an exponential tail with a square-root form at higher frequencies. This calculation was performed for thermally deposited ZnSe thin films. (From [38].)

properties; thermally induced nonlinearities, where the absorption of light raises the temperature, which then affects the optical properties; and field-induced nonlinearities, where the creation of carriers causes a change in the d.c. electric field in the material. Note that all three of these mechanisms will take some time to disappear after the excitation, either by carrier recombination or by diffusion, and they cannot be accurately described using a $\chi^{(3)}$ analysis.

The modified relation given by Equation 19 is an extension of the linear relation, and it has not yet been justified for nonresonant nonlinearities where the intermediate (perturbed) state is no longer well defined. Referring to Equation B1 of Appendix B, we now consider causality for the nonlinear contributions to the polarization. The notation used in this section for the nonlinear susceptibility, and its relation to other common descriptions in nonlinear optics, is discussed in Appendix B. Causality requires that no contribution can be made to the n th order polarization, $P^{(n)}(t)$, due to an electric field $E(t - \tau)$ for times $t < (t - \tau)$. This then requires that the response function, $R^{(n)}(\tau_1, \tau_2, \dots, \tau_n)$, must be zero if any one of its arguments $(\tau_1, \tau_2, \dots, \tau_n)$ is less than zero. Hence the n th order

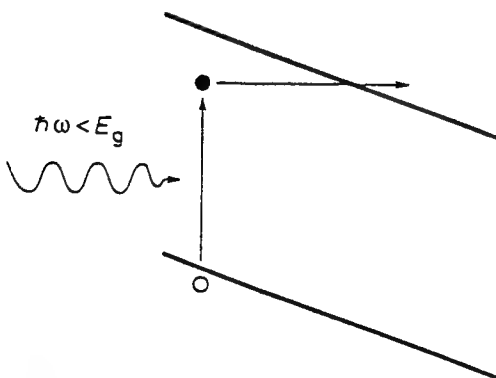


Figure 6 Schematic of the Franz-Keldysh effect where the presence of electric field and tunnelling can permit absorption at frequencies less than the band edge of semiconductors.

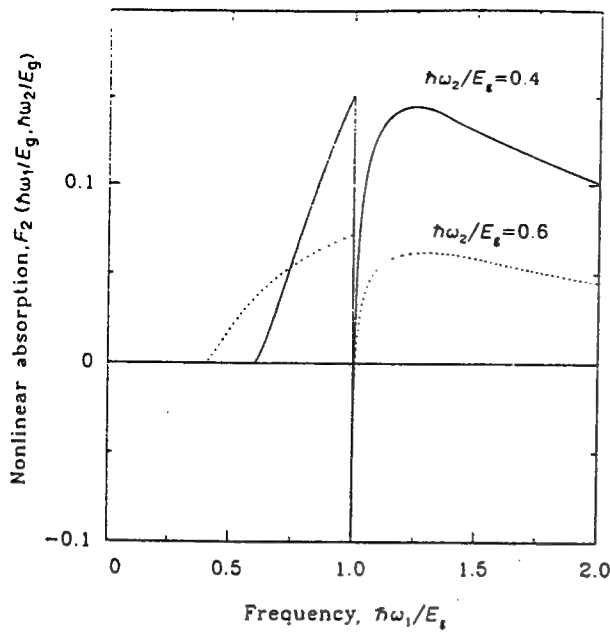


Figure 8 Theoretical frequency dependence of the nondegenerate nonlinear absorption for two different 'pump' frequencies $\hbar\omega_2 = E_g = 0.4$ and 0.6 . Below the fundamental absorption edge $\hbar\omega_1 < E_g$ only two-photon absorption contributes to the nonlinear absorption.

We can thus obtain the generalized nonlinear Kramers-Krönig relation for a nondegenerate nonlinear susceptibility

$$\chi^{(n)}(\omega_1, \omega_2, \dots, \omega_n) = \frac{1}{i\pi} \mathcal{P} \int_{-\infty}^{\infty} \frac{\chi^{(n)}(\omega_1, \omega_2, \dots, \Omega, \dots, \omega_n)}{\Omega - \omega_i} d\Omega \quad (22)$$

Note here that the integral is over only one frequency argument, Ω , and all other frequencies are held constant. Thus, we cannot obtain any relationship between the degenerate Kerr coefficient, $\gamma(\omega)$, and the degenerate two-photon absorption coefficient, $\beta(\omega)$, as defined in Appendix B. If multiple step functions had been used at an earlier stage in Equation 21, a multidimensional integral would have resulted. The derivation of the nonlinear Kramers-Krönig relationship in Equation 22 can also be found in [16-18].

Now consider the case where we have two monochromatic electromagnetic waves incident on a nonlinear material

$$E(t) = \frac{1}{2}(E_a e^{-i\omega_a t} + E_a^* e^{i\omega_a t}) + \frac{1}{2}(E_b e^{-i\omega_b t} + E_b^* e^{i\omega_b t}) \quad (23)$$

On calculating the third-order nonlinear polarization (see Appendix B) and considering

TABLE II Dispersion of the nonlinear refraction $G_2(\hbar\omega/E_g)$ for frequencies below the band edge as defined in Equation 38. $\Theta(x)$ is the Heaviside or step function

Contribution	$G_2(x)$
Two-photon absorption	$[1/(2x)^6][-\frac{3}{8}x^2(1-x)^{-1/2} + 3x(1-x)^{1/2} - 2(1-x)^{3/2} + 2\Theta(1-2x)(1-2x)^{3/2}]$
Raman	$[1/(2x)^6][-\frac{3}{8}x^2(1+x)^{-1/2} - 3x(1+x)^{1/2} - 2(1+x)^{3/2} + 2(1+2x)^{3/2}]$
Linear Stark	$[1/(2x)^6][2 - (1-x)^{3/2} - (1+x)^{3/2}]$
Quadratic Stark	$[1/(2^{10}x^5)][(1-x)^{-1/2} - (1+x)^{-1/2} - \frac{1}{2}x(1-x)^{3/2} - \frac{1}{2}x(1+x)^{3/2}]$
Divergent term	$\frac{1}{(2x)^6} \left(-2 - \frac{35x^2}{8} + \frac{x}{8} (3x-1)(1-x)^{-1/2} - 3x(1-x)^{1/2} + (1-x)^{3/2} \right. \\ \left. + \frac{x}{8} (3x+1)(1+x)^{-1/2} + 3x(1+x)^{1/2} + (1+x)^{3/2} \right)$

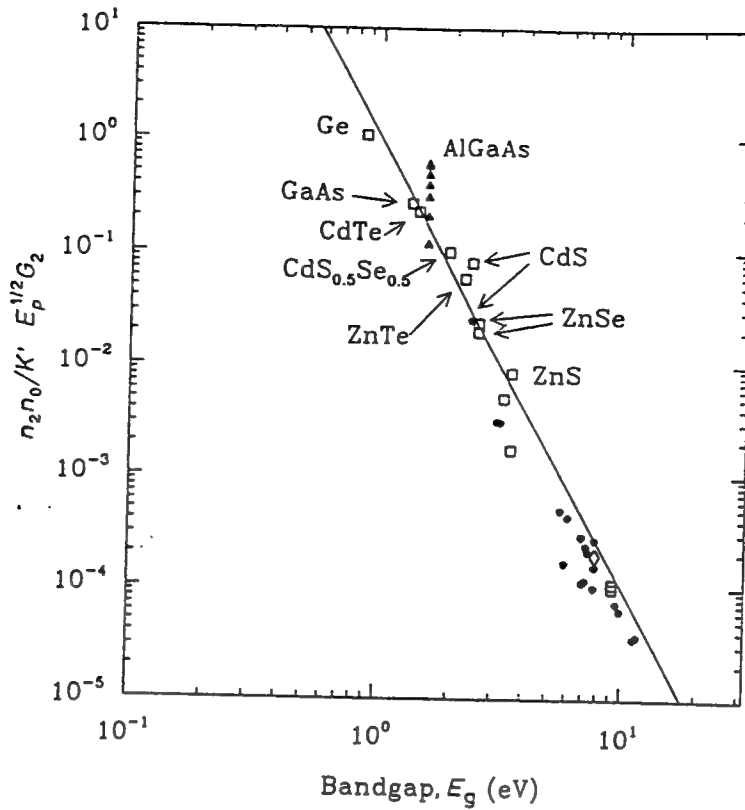


Figure 10 A log-log plot showing the expected E_g^{-4} dependence of n_2 . The data points are identical to those in Fig. 9a and b, but now scaled by the dispersion function $G_2(\hbar\omega/E_g)$. The full line is the function E_g^{-4} that translates into a straight line of slope -4 on a log-log plot.

only the mixed terms that give rise to contributions at frequencies $\pm \omega_a$ (i.e. ignoring all third harmonic and frequency mixing terms, such as $2\omega_b - \omega_a$)

$$P_a^{(3)}(\omega) = \frac{3}{4}|E_b|^2[\chi_{aabb}^{(3)}(\omega_a, \omega_b, -\omega_b)\delta(\omega - \omega_a)E_a + \chi_{aabb}^{(3)*}(\omega_a, \omega_b, -\omega_b)\delta(\omega + \omega_a)E_a^*] \quad (24)$$

These then lead to a change in the refractive index and absorption coefficient at frequency ω_a due to the presence of light at frequency, ω_b

$$\begin{aligned} \Delta n(\omega_a; \omega_b) &= (24\pi^2/n_a n_b c)I_b \text{Re } \chi_{aabb}^{(3)}(\omega_a, \omega_b, -\omega_b) \\ \Delta \alpha(\omega_a; \omega_b) &= (48\pi^2 \omega_a/n_a n_b c^2)I_b \text{Im } \chi_{aabb}^{(3)}(\omega_a, \omega_b, -\omega_b) \end{aligned} \quad (25)$$

where I_b is the irradiance of the light of frequency ω_b , and n_a and n_b are the linear refractive indices at frequencies ω_a and ω_b , respectively, and we have assumed that the linear absorption is sufficiently small that $\alpha(\omega_a)c/\omega_a \ll n_a$. This is not very restrictive, allowing validity even for $\alpha \approx 10^3 \text{ cm}^{-1}$ in the visible, and in most cases is a reasonable approximation. For example, in a semiconductor, changes in the refractive index beneath the bandgap are attributable to absorption changes at frequencies close to the band edge and not the high absorption transitions at higher frequencies. This will be more apparent in later sections. Note that these results in the nondegenerate case are a factor of 2 greater than the corresponding degenerate quantities given in Equation B14 of Appendix B.

Unfortunately, there is no universal convention for the definition of $\chi^{(3)}$, so some of the numerical prefactors may differ from those used in other papers. We discuss other common definitions in Appendix B.

It has been suggested that the contribution of this pole can be included in the contour integral, and one could derive Kramers-Krönig type relations where an additional constant is added to the usual integral [11]. However, since this constant is derived from the residue at the pole of $\chi(\omega)$, it is necessary to know fully the form of $\chi(\omega)$, i.e. both the real and imaginary parts. Since the usefulness of Kramers-Krönig relations is that, given only the imaginary part, the real part of $\chi(\omega)$ can be computed (or vice versa), such a relationship is of little practical use.

In order to apply the modified Kramers-Krönig relations as described in Equation 19 to the two-level atom problem, it is necessary to re-examine the source of the perturbation that causes the optical properties to change. In this instance the perturbation is a change in the excited-state population by optical excitation. Note, however, that if the frequency of the light varies, the excited state population varies also, due to the variation of the linear absorption coefficient with frequency. Thus, it should not be too surprising that the Kramers-Krönig relations do not apply to this form of nonlinear susceptibility, since the perturbation is changing over the frequency integral.

The perturbation (excited-state population) can be forced to be constant, however, by replacing the single pump field by a pump field at a fixed frequency plus a probe field (considered weak) whose frequency can vary. Thus, we require a pump-probe spectrum, where the two frequencies can be different. Returning to the two-level atom calculation [10], if the change in population is calculated solely from a pump field at frequency Ω and then the polarization is calculated at a different probe frequency ω , Equation 27 for the susceptibility now becomes

$$\begin{aligned}\chi(\omega; \Omega) &= \left(\frac{\mu^2 \Delta N_0}{\epsilon_0 \hbar} \right) \left(\frac{(\omega_0 - \omega) + i/T_2}{(\omega_0 - \omega)^2 + 1/T_2^2} \right) \left(\frac{(\omega_0 - \Omega)^2 + 1/T_2^2}{(\omega_0 - \Omega)^2 + (1 + I/I_s)/T_2^2} \right) \\ &= \chi_0(\omega) \frac{(\omega_0 - \Omega)^2 + 1/T_2^2}{(\omega_0 - \Omega)^2 + (1 + I/I_s)/T_2^2}\end{aligned}\quad (29)$$

where I now refers to the pump irradiance. Here population pulsations have been ignored as discussed in the next paragraph. $\chi_0(\omega)$ refers to the susceptibility in the linear (low power, $I \rightarrow 0$) limit. We note that this form of nonlinear susceptibility does satisfy the Kramers-Krönig relations where the integral is over the probe frequency ω only. Figure 2b shows the imaginary part of the nondegenerate susceptibility at a fixed pump frequency ($\Omega = \omega_0$) for several pump irradiances. It is of interest to note that, in the nondegenerate form, the Lorentzian lineshape and width are preserved, which is another indication that dispersion relations can be applied. In fact, this susceptibility can be separated into a product of the linear susceptibility, multiplied by some fraction that depends only on the pump field (Ω), as shown in Equation 29. This fraction is precisely the fraction of atoms that occupy the ground state. Figure 2c demonstrates how this fraction varies with pump irradiance. This two-level description carries over directly to the solid state description of bandfilling, where nonlinear Kramers-Krönig relations have been utilized with great success.

In this example calculation we have neglected any effects of population pulsations (alternate time-ordering) caused by the beating of the two optical frequencies (ω and Ω) in the medium. Strictly, this approximation is valid only when the response of the medium is much slower than the beat frequency. Inclusion of population pulsations will lead to an enhancement in the nondegenerate susceptibility, typically by a factor of 2 for the third-order term $\chi^{(3)}$ in the expansion of the susceptibility. The main point of this example,

This calculation is shown diagrammatically in Fig. 3, in which the reduction in absorption is calculated from the product of the population distribution and the density of states. In other words, the distribution of electrons at the bottom of the conduction band removes the same distribution of states from the potential interband transitions. The modified form of the Kramers-Krönig relation can now be applied to produce the change in refractive index associated with this change in absorption as shown in Fig. 3.

Further examples of this type of calculation have been performed on a theoretical change in absorption due to an excited electron-hole plasma by Bányai and Koch for their plasma model, which includes Coulombic effects for bulk semiconductors [29] and for semiconductor doped glasses [30], and the many-body calculations of Löwenau *et al.* [31].

This form of calculation need not be restricted to theoretical differential spectra. Provided the complete differential absorption spectrum is known (i.e. measured over all frequencies for $\Delta\alpha \neq 0$), the associated refractive index change can be calculated using Equation 19. The converse is also true, but this is unusual as it is far easier to measure absorption spectra (which also tend to be more restricted in frequency) than the dispersion of a material. Examples of this calculation can be found in [32] (bulk GaAs), [33] (saturation of GaAs quantum wells), [34] (quantum-confined Stark effect in GaAs quantum wells) and [35] (semiconductor clusters).

4.3. Thermally induced optical nonlinearities in semiconductors

Changes in the optical properties of a material occur not only for changes in carrier population as described previously, changes of temperature also have an effect. Often this can be a problem for applications involving optical switching; however, thermal effect alone can be used, for example in optical bistability [36, 37].

As an example calculation, consider light incident on a semiconductor. The energy from the illumination usually ends up as heat (for example, light generates carriers which recombine and give up their energy to the lattice). Close to the band edge the optical properties of the semiconductor change, principally through the thermal shift of the bandgap

$$\begin{aligned}\Delta n &= (\partial n / \partial T) \Delta T \\ \frac{\partial n}{\partial T} &= \frac{\partial n}{\partial E_g} \frac{\partial E_g}{\partial T} + \left. \frac{\partial n}{\partial T} \right|_b\end{aligned}\quad (31)$$

where we have also allowed for some background contribution to the thermo-optic coefficient, $\partial n / \partial T$, such as thermal expansion or lattice contributions.

The coefficient $\partial n / \partial E_g$ can be obtained from a Kramers-Krönig transform of the band edge absorption [38]

$$\frac{\partial n}{\partial E_g}(\omega) = \lim_{\delta E_g \rightarrow 0} \frac{c}{\pi} \mathcal{P} \int_0^\infty \frac{\alpha(\omega'; E_g + \delta E_g) - \alpha(\omega'; E_g)}{\omega'^2 - \omega^2} d\omega' \quad (32)$$

Using a square-root absorption edge for a direct-gap material, the dispersion of $\partial n / \partial T$ around the band edge can be determined and is shown plotted in Fig. 4. Note the resonance as the frequency approaches the band edge; in fact, for a sharp square-root absorption this dispersion function is discontinuous at $\hbar\omega = E_g$. Note that since $\partial E_g / \partial T$ is usually negative [39], this means that in most cases $\partial n / \partial T$ is positive beneath the band edge of a semiconductor.

Of course, this form of nonlinear dispersion can be applied to any process that causes a shift in the band edge, e.g. bandgap renormalization. It is also possible to perform the same

transitions and the a.c. stark effect. It is important to emphasize again that in this calculation it is the nondegenerate form of the nonlinear absorption that is required. Existing expressions for nonlinear absorption, e.g. multiphoton absorption [41, 50, 51], are derived only for the degenerate form.

The nondegenerate absorption was derived using tunnelling theory based on an $A \cdot p$ perturbation for a two-band model of a semiconductor. The details of the calculation are not relevant to this paper, but the result can be expressed in the scaling form as [15]

$$\Delta\alpha(\omega_1; \omega_2) = 2K \frac{E_p^{1/2}}{n_1 n_2 E_g^3} F_2 \left(\frac{\hbar\omega_1}{E_g}; \frac{\hbar\omega_2}{E_g} \right) I_2 \quad (34)$$

Here E_g is the energy gap and E_p is related to the momentum matrix element and is nearly constant at $E_p \approx 21$ eV over the vast majority of semiconductors. The refractive indices n_1 and n_2 refer to the frequencies ω_1 and ω_2 , respectively, and I_2 is the irradiance at frequency ω_2 . The constant K is material-independent and was determined from the fit to degenerate two-photon absorption measurements [52] which gives $K = 3100 \text{ cm GW}^{-1} \text{ eV}^{5/2}$. It should be noted, however, that theoretical calculations of this quantity are not too different from this value. The dimensionless spectral function F_2 can be determined for each of the nonlinear optical processes and is the sum of the terms shown in Table I.

The spectrum of the nonlinear absorption $F_2(\hbar\omega_1/E_g; \hbar\omega_2/E_g)$ is shown in Fig. 8 for two different 'pump' frequencies ω_2 . Note that for $\hbar\omega_2 < E_g$ the Raman and Stark terms can contribute only to the nonlinear absorption for $\hbar\omega_1 > E_g$. The negative (i.e. decreasing absorption) divergence at the bandgap results from the quadratic Stark shift causing a blue shift of the band edge.

By using Equation 26 and substituting for the degenerate Δn , the following form for the degenerate Kerr coefficient is obtained [15]:

$$\gamma = K \frac{\hbar c E_p^{1/2}}{2n_0^2 E_g^4} G_2 \left(\frac{\hbar\omega}{E_g} \right) \quad (35)$$

where the dispersion function G_2 is given by

$$G_2(x) = \frac{2}{\pi} \int_0^\infty \frac{F_2(x'; x) dx'}{x'^2 - x^2} \quad (36)$$

We have neglected any dispersion in the linear refractive index n_0 in the integral. The magnitude of the dispersion is typically only 10% of the background refractive index around the band edge of semiconductors, so we do not anticipate any significant error. The factor of 1/2 is introduced when the degenerate coefficient is calculated from the nondegenerate as beating terms (cross-modulation or grating terms), double the magnitude of the nonlinearity in the nondegenerate case when the material can respond to the beat frequency. This is often referred to as weak wave retardation [53]. This factor has also been included in the determination of the nonlinear absorption (Equation 34). The origin of this factor can be seen by comparing the degenerate results in Equation B14 of Appendix B to the nondegenerate results given in Equation 25. Note that this factor of 1/2 was omitted in the nonlinear refractive index calculation in [15]. The individual contributions to G_2 are set out in Table II.

On examining the low frequency limit it is found that these terms diverge as $\omega \rightarrow 0$. In order to investigate such non-physical 'infrared' divergence we go one step back and examine the nondegenerate case. It is found that $\Delta n(\omega; \Omega)$ is not divergent in ω , and

in Equation 20, a change in variables is performed

$$\begin{aligned}\Omega_i &= \sum_j M_{ij} \omega_j \\ T_i &= \sum_j (\tilde{M}^{-1})_{ij} \tau_j\end{aligned}\quad (39)$$

which ensures that $\sum_i \omega_i \tau_i = \sum_j \Omega_j T_j$. This now gives

$$\hat{\chi}^{(n)}(\Omega_1, \Omega_2, \dots, \Omega_n) = \int dT_1 \int dT_2 \cdots \int dT_n \hat{R}^{(n)}(T_1, T_2, \dots, T_n) e^{i(\Omega_1 T_1 + \Omega_2 T_2 + \cdots + \Omega_n T_n)} \quad (40)$$

where the integration region is the equivalent in T -space to the positive quadrant in τ -space. Now consider a special case of the above transform where, for some k , $(\tilde{M}^{-1})_{kj} \geq 0$ for all possible j . Since the response function is integrated over only positive τ_j (as causality demands R be zero for any $\tau_j < 0$), then the transformed variable T_k will be integrated over only positive values. That is, $\hat{R}^{(n)}(T_1, T_2, \dots, T_k, \dots, T_n)$ can be set to zero for $T_k < 0$. Hence, in a similar manner to the linear Kramers-Krönig derivation, by transforming this property to the frequency domain, we obtain the dispersion relation for $\hat{\chi}^{(n)}(\Omega_1, \Omega_2, \dots, \Omega_n)$

$$\hat{\chi}^{(n)}(\Omega_1, \Omega_2, \dots, \Omega_k, \dots, \Omega_n) = \frac{1}{i\pi} \mathcal{P} \int_{-\infty}^{\infty} \frac{\hat{\chi}^{(n)}(\Omega_1, \Omega_2, \dots, \Omega, \dots, \Omega_n)}{\Omega - \Omega_k} d\Omega \quad (41)$$

Note that this is formally identical to the nondegenerate nonlinear Kramers-Krönig relation derived above. On transforming back to real frequencies, we obtain $\omega_i = \sum_j (M^{-1})_{ij} \Omega_j$. Since we have previously required $(\tilde{M}^{-1})_{kj} \geq 0$, the coefficient of Ω_k , $(M^{-1})_{ik}$ is always positive (or zero). This results in a generalized form for the nonlinear Kramers-Krönig transform

$$\begin{aligned}&\chi^{(n)}(\omega_1 + p_1 \omega, \omega_2 + p_2 \omega, \dots, \omega_n + p_n \omega) \\ &= \frac{1}{i\pi} \mathcal{P} \int_{-\infty}^{\infty} \frac{\chi^{(n)}(\omega_1 + p_1 \Omega, \omega_2 + p_2 \Omega, \dots, \omega_n + p_n \Omega)}{\Omega - \omega} d\Omega\end{aligned}\quad (42)$$

where $p_i \geq 0$ for all possible i , provided that at least one $p_i \neq 0$. For the case where only one of the coefficients p_i is nonzero and set equal to unity, we regain the nondegenerate form of the relationship.

We also give here a new, simpler method for obtaining the same relationship in Equation 42 using the Fourier transform as in Equation 7. Starting with the definition of $\chi^{(n)}$ from the response function $R^{(n)}$ in Equation 20, multiplying both sides by $(\Omega - \omega)^{-1}$ and integrating over Ω

$$\begin{aligned}&\mathcal{P} \int_{-\infty}^{\infty} \frac{\chi^{(n)}(\omega_1 + p_1 \Omega, \omega_2 + p_2 \Omega, \dots, \omega_n + p_n \Omega)}{\Omega - \omega} d\Omega \\ &= \int_0^{\infty} d\tau_1 \int_0^{\infty} d\tau_2 \cdots \int_0^{\infty} d\tau_n R^{(n)}(\tau_1, \tau_2, \dots, \tau_n) e^{i(\omega_1 \tau_1 + \omega_2 \tau_2 + \cdots + \omega_n \tau_n)} \\ &\quad \times \mathcal{P} \int_{-\infty}^{\infty} \frac{e^{i\Omega(p_1 \tau_1 + p_2 \tau_2 + \cdots + p_n \tau_n)}}{\Omega - \omega} d\Omega \\ &= i\pi \int_0^{\infty} d\tau_1 \int_0^{\infty} d\tau_2 \cdots \int_0^{\infty} d\tau_n R^{(n)}(\tau_1, \tau_2, \dots, \tau_n) e^{i(\omega_1 \tau_1 + \omega_2 \tau_2 + \cdots + \omega_n \tau_n)} e^{i\omega(p_1 \tau_1 + p_2 \tau_2 + \cdots + p_n \tau_n)} \\ &= i\pi \chi^{(n)}(\omega_1 + p_1 \omega, \omega_2 + p_2 \omega, \dots, \omega_n + p_n \omega)\end{aligned}\quad (43)$$

phase modulator from changes in the absorption spectra of the desired material through a variation in a d.c. electric field.

An important step discussed here is that the perturbation can be another optical field and, thus, extend this relation to nonresonant (fast) optical nonlinearities. This can be obtained from Equation 45, but we also include a derivation based on the causality of the system. However, since the perturbation has to remain constant over the integration, it is necessary to have a nondegenerate form for the change in absorption, i.e. a pump-probe spectrum, with the pump at a fixed frequency. Unfortunately, conventional experiments and theories tend to determine the degenerate (single frequency argument) form only. It is likely that this contributes to the confusion over nonlinear Kramers-Krönig relations, since these conventional results cannot be utilized, leading to the incorrect assumption that nonlinear Kramers-Krönig relations are invalid.

A recent calculation using this dispersion relation is in the calculation of the scaling and dispersion of the electronic nonlinear refractive coefficient n_2 in solids. We reproduce an outline of this calculation in this review. First, all of the relevant nondegenerate nonlinear absorption contributions are determined. This includes terms from two-photon absorption, Raman transitions and the a.c. Stark effect. Then the nonlinear Kramers-Krönig transform is computed and an analytic expression is obtained for the degenerate n_2 . On comparison with experimentally measured values, excellent agreement is obtained, considering the uncertainty in some of the materials parameters and the fact that a simple two-band model was used to calculate the nonlinear absorptive contributions. Note, although we have calculated the degenerate form of the electronic n_2 in order to provide a comparison with experimental data, the nonlinear dispersion relation is much more general. No new information is necessary for the nondegenerate form of n_2 to be calculated.

As a final note, although in general nonlinear dispersion relations must take the nondegenerate form, it can be shown through a change of variables that in the particular case of frequency summation a degenerate form can be used. This has limited applications although as this is not a self-action effect, so one is usually concerned with the magnitude of χ only and not the real and imaginary components.

Acknowledgements

The authors gratefully acknowledge the support of NSF under grant ECS 8617066, DARPA and CNVEO. We also thank A. L. Smirl, A. Miller, A. Yariv and M. Sargent for useful discussions.

References

1. H. A. KRAMERS. *Atti Congr. Int. Fis. Como* 2 (1927) 545.
2. R. DE L. KRÖNIG. *J. Opt. Soc. Am. Rev. Scient. Instrum.* 12 (1926) 547.
3. *Idem*, *Ned. Tijdschr. Natuurk* 9 (1942) 402.
4. H. BODE. 'Network Analysis and Feedback Amplifier Design' (Van Nostrand, New York, 1945).
5. H. M. NUSSENZVEIG. 'Causality and Dispersion Relations' (Academic Press, New York, 1972).
6. W. SCHÜTZER and J. TIOMNO. *Phys. Rev.* 83 (1951) 249.
7. E. P. WIGNER. *Am. J. Phys.* 23 (1955) 371.
8. E. C. TITCHMARSH. 'Introduction to the Theory of Fourier Integrals' (Oxford University Press, Oxford, 1948).
9. J. S. TOLL. *Phys. Rev.* 104 (1956) 1760.
10. A. YARIV. 'Quantum Electronics'. 2nd Edn (Wiley, New York, 1975).
11. K. A. SHORE and D. A. S. CHAN. *Electron. Lett.* 26 (1990) 1206.
12. D. A. B. MILLER, C. T. SEATON, M. E. PRISE and S. D. SMITH. *Phys. Rev. Lett.* 47 (1981) 197.
13. J. F. L. RIDENER and J. R. H. GOOD. *Phys. Rev.* B10 (1974) 4980.

56. M. SHEIK-BAHAE, A. A. SAID, T. H. WEI, D. J. HAGAN and E. W. VAN STRYLAND, *IEEE J. Quantum Electron.* **26** (1990) 760.
57. M. SHEIK-BAHAE, A. A. SAID and E. W. VAN STRYLAND, *Opt. Lett.* **14** (1989) 955.
58. R. ADAIR, L. L. CHASE and S. A. PAYNE, *Phys. Rev.* **B39** (1989) 3337.
59. I. N. ROSS, W. T. TONER, C. J. HOOKER, J. R. M. BARR and I. COFFEY, *J. Modern Opt.* **37** (1990) 555.
60. M. J. LaGASSE, K. K. ANDERSON, C. A. WANG, H. A. HAUS and J. G. FUJIMOTO, *Appl. Phys. Lett.* **56** (1990) 417.
61. J. F. L. RIDENER and J. R. H. GOOD, *Phys. Rev.* **B11** (1975) 2768.
62. F. SMET and A. VAN GROENENDAEL, *ibid.* **A19** (1979) 334.
63. D. J. MOSS, J. E. SIPE and H. M. VAN DRIEL, *ibid.* **B36** (1987) 9708.
64. P. N. BUTCHER and D. COTTER, 'The Elements of Nonlinear Optics' (Cambridge University Press, Cambridge, 1990).
65. F. A. HOPF and G. I. STEGEMAN, 'Applied Classical Electrodynamics', Vol. 2: 'Nonlinear Optics' (Wiley, New York, 1986).
66. S. CHAPMAN, *Am. J. Phys.* **24** (1956) 162.

Appendices

A. Cauchy integral derivation of dispersion relations

The susceptibility $\chi(\omega)$ is derived from the response function by means of the Fourier transform in Equation 4. However, because of causality, the integral need only run over positive times. Generalizing this for complex ω , for the condition $\text{Im } \omega > 0$, the convergence of Equation 4 can only be improved. This can easily be seen by writing $\omega = \omega' + i\omega''$, which leads to a factor $e^{-\omega''T}$ in the integrand. Thus, $\chi(\omega)$ has a regular analytic continuation in the positive imaginary plane of ω .

Consider the Cauchy integral round the contour Γ in the frequency plane as shown in Fig. A1.

$$\int_{\Gamma} \frac{\chi(\omega) d\omega}{\omega - \Omega} = 0 \quad (\text{A1})$$

which is zero since ω is regular and analytic with no poles within the contour. First, consider

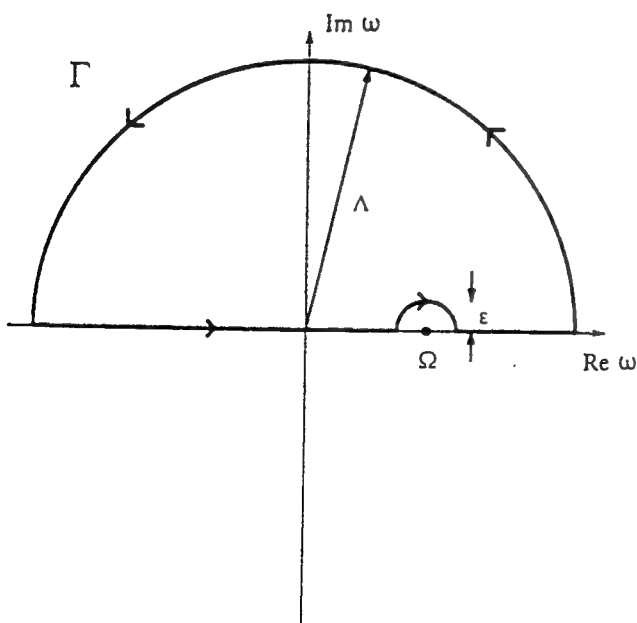


Figure A1 The contour Γ in the complex frequency plane used in the derivation of dispersion relations of the large semicircle of radius Λ , the axis $\text{Im } \omega = 0$ and the small semicircle of radius ϵ centred around the point Ω .

Here the summation over the various directions j, k, l is implied for the various tensor elements of χ . Upon Fourier transformation we obtain the equivalent relations in the frequency domain

$$\begin{aligned}
 P_i^{(1)}(\omega) &= \int_{-\infty}^{\infty} d\omega_1 \chi_{ij}^{(1)}(\omega_1) E_j(\omega_1) \delta(\omega - \omega_1) \\
 P_i^{(2)}(\omega) &= \int_{-\infty}^{\infty} d\omega_1 \int_{-\infty}^{\infty} d\omega_2 \chi_{ijk}^{(2)}(\omega_1, \omega_2) E_j(\omega_1) E_k(\omega_2) \delta(\omega - \omega_1 - \omega_2) \\
 P_i^{(3)}(\omega) &= \int_{-\infty}^{\infty} d\omega_1 \int_{-\infty}^{\infty} d\omega_2 \int_{-\infty}^{\infty} d\omega_3 \chi_{ijkl}^{(3)}(\omega_1, \omega_2, \omega_3) E_j(\omega_1) E_k(\omega_2) \\
 &\quad \times E_l(\omega_3) \delta(\omega - \omega_1 - \omega_2 - \omega_3) \\
 &\vdots \\
 P_i^{(n)}(\omega) &= \int_{-\infty}^{\infty} d\omega_1 \int_{-\infty}^{\infty} d\omega_2 \cdots \int_{-\infty}^{\infty} d\omega_n \chi_{ijk\dots n}^{(n)}(\omega_1, \omega_2, \dots, \omega_n) \\
 &\quad \times E_j(\omega_1) E_k(\omega_2) \dots E_n(\omega_n) \delta(\omega - \omega_1 - \omega_2 - \dots - \omega_n) \quad (B2)
 \end{aligned}$$

where δ is the Dirac delta function. The n th order susceptibility is generally obtained from the Fourier transform of the n th order response function

$$\begin{aligned}
 \chi_{ijk\dots n}^{(n)}(\omega_1, \omega_2, \dots, \omega_n) &= \sum_{-\infty}^{\infty} d\tau_1 \int_{-\infty}^{\infty} d\tau_2 \cdots \\
 &\quad \times \int_{-\infty}^{\infty} d\tau_n R_{ijk\dots n}^{(n)}(\tau_1, \tau_2, \dots, \tau_n) e^{i(\omega_1\tau_1 + \omega_2\tau_2 + \dots + \omega_n\tau_n)} \quad (B3)
 \end{aligned}$$

It can be seen that on evaluating the frequency integral for the linear polarization $P^{(1)}(\omega)$, Equation 3 is again obtained.

In this paper we are mainly concerned with monochromatic electromagnetic fields defined as

$$E(t) = \frac{1}{2}(E_a e^{-i\omega_a t} + E_a^* e^{i\omega_a t}) \quad (B4)$$

whose Fourier transform is

$$E(\omega) = \frac{1}{2}[E_a \delta(\omega - \omega_a) + E_a^* \delta(\omega + \omega_a)] \quad (B5)$$

Throughout much of this paper we are concerned with third-order nonlinearities. The reason for this is that this is the lowest order of nonlinearity that produces a nonlinear polarization at the same frequency as the applied electromagnetic field. This results in self-action effects such as nonlinear absorption and refraction.

Upon inserting the monochromatic field defined in Equation B5 into Equation B2 for the third-order nonlinear polarization and performing the various frequency integrals, one obtains for the component $P^{(3)}(\omega)$ parallel to E

$$\begin{aligned}
 P^{(3)}(\omega) &= \frac{1}{8}[3\chi^{(3)}(\omega_a, \omega_a, -\omega_a) E_a^2 E_a^* \delta(\omega - \omega_a) + 3\chi^{(3)*}(\omega_a, \omega_a, -\omega_a) E_a E_a^{*2} \delta(\omega + \omega_a) \\
 &\quad + \chi^{(3)}(\omega_a, \omega_a, \omega_a) E_a^3 \delta(\omega - 3\omega_a) + \chi^{(3)*}(\omega_a, \omega_a, \omega_a) E_a^{*3} \delta(\omega + 3\omega_a)] \quad (B6)
 \end{aligned}$$

Here we have used permutation symmetry [64] to simplify the above result, where for example

$$\begin{aligned}
 \chi_{ijkl}^{(3)}(\omega_1, \omega_2, \omega_3) &= \chi_{ijk}^{(3)}(\omega_1, \omega_3, \omega_2) \\
 &= \chi_{ilk}^{(3)}(\omega_3, \omega_2, \omega_1) \quad (B7)
 \end{aligned}$$

the relation between these quantities and $\chi^{(3)}$ can be written as

$$\begin{aligned}\beta(\omega) &= (24\pi^2 \omega / n_0^2 c^2) \text{Im} \chi^{(3)}(\omega, \omega, -\omega) \\ \gamma(\omega) &= (12\pi^2 / n_0^2 c) \text{Re} \chi^{(3)}(\omega, \omega, -\omega)\end{aligned}\quad (\text{B14})$$

Note that for the equivalent nondegenerate quantities derived in Equation 25, a factor of 2 appears due to weak wave retardation [53].

C. Conversion from Gaussian to SI units

This review uses Gaussian (CGS) units and in this appendix we indicate the differences that occur when SI (MKS) units are used instead. A good review of the differences in expressions under the systems can be found in [66] for linear quantities. However, in the field of nonlinear optics there are no consistent definitions over all publications, even within one set of units. In this appendix the notation of [64] is used, which is the direct SI equivalent of the notation used throughout here.

In SI units the permittivity of free space, ϵ_0 , appears in the relationship between the polarization and electric field, and hence, for example, for the first-order (linear) polarization we have

$$P_i^{(1)}(t) = \epsilon_0 \int_{-\infty}^{\infty} d\tau_1 R_{ij}^{(1)}(\tau_1) E_j(t - \tau_1) \quad (\text{C1})$$

and in frequency space

$$P_i^{(1)}(\omega) = \epsilon_0 \chi_{ij}^{(1)}(\omega) E_j(\omega) \quad (\text{C2})$$

Furthermore, the relation between electric displacement, polarization and field is now written as

$$D(\omega) = \epsilon_0 [n(\omega) + i\alpha(\omega)c/2\omega]^2 E(\omega) = \epsilon_0 E(\omega) + P(\omega) \quad (\text{C3})$$

Under SI units the irradiance is now given by $I = (\epsilon_0 n_0 c / 2) |E_a|^2$ when the definition $E(t) = (E_a e^{i\omega_a t} + E_a^* e^{-i\omega_a t}) / 2$ is used.

Using the same analysis as previously, which leads to a summation over the three indices for the third-order terms, for a $\chi^{(3)}$ nonlinearity it can be shown that the changes in refractive index and absorption coefficient are now given by

$$\begin{aligned}\Delta n &= \frac{3}{8n_0} \text{Re} \chi^{(3)}(\omega_a, \omega_a, -\omega_a) |E_a|^2 = \frac{3}{4} \frac{I_a}{\epsilon_0 c n_0^2} \text{Re} \chi^{(3)}(\omega_a, \omega_a, -\omega_a) \\ \Delta \alpha &= \frac{3}{4n_0} \text{Im} \chi^{(3)}(\omega_a, \omega_a, -\omega_a) |E_a|^2 = \frac{3}{2} \frac{\omega_a I_a}{\epsilon_0 c^2 n_0^2} \text{Im} \chi^{(3)}(\omega_a, \omega_a, -\omega_a)\end{aligned}\quad (\text{C4})$$

Thus, the definitions for the Kerr and two-photon absorption coefficients will be modified accordingly. It is important to note, however, that the Kramers-Krönig relation between n and α is unaltered in SI units.

Both in the literature and this review, two principal forms have been used for quoting values for nonlinear refraction: n_2 and γ . n_2 is most often quoted in e.s.u. and γ is usually quoted in SI or some derived unit (e.g. $\text{cm}^2 \text{GW}^{-1}$). By comparing Equations B12 and B14 and converting units accordingly, we can write the conversion between these two forms as

$$n_2(\text{e.s.u.}) = (n_0 c / 40\pi) \gamma \quad (\text{SI}) \quad (\text{C5})$$

where all of the quantities on the right-hand side are quoted in SI.

Self-focusing and self-defocusing by cascaded second-order effects in KTP

R. DeSalvo, D. J. Hagan, M. Sheik-Bahae, G. Stegeman, and E. W. Van Stryland

Center for Research in Electro-Optics and Lasers, University of Central Florida, Orlando, Florida 32816

H. Vanherzeele

Department of Central Research and Development, DuPont, Wilmington, Delaware 19898

Received August 9, 1991

We monitor the induced phase change produced by a cascaded $\chi^{(2)}\cdot\chi^{(2)}$ process in KTP near the phase-matching angle on a picosecond 1.06- μm -wavelength beam using the Z-scan technique. This nonlinear refraction is observed to change sign as the crystal is rotated through the phase-match angle in accordance with theory. This theory predicts the maximum small-signal effective nonlinear refractive index of $n_2^{\text{eff}} \approx \pm 2 \times 10^{-14} \text{ cm}^2/\text{W}$ ($\pm 1 \times 10^{-11} \text{ esu}$) for an angle detuning of $\pm 5^\circ$ from phase match for this 1-mm-thick crystal with a measured d_{eff} of 3.1 pm/V. For a fixed phase mismatch, this n_2^{eff} scales linearly with length and as d_{eff}^2 ; however, for the maximum n_2^{eff} the nonlinear phase distortion becomes sublinear with irradiance for phase shifts near $\pi/4$.

The nonlinear phase distortion that arises from second-order processes in noncentrosymmetric crystals has recently received considerable attention.¹⁻⁶ Although the effective $\chi^{(3)}$ that is due to cascading of $\chi^{(2)}(3\omega; 2\omega, \omega) \cdot \chi^{(2)}(2\omega; \omega, \omega)$ has long been used in generating the third harmonic of laser beams using two crystals, its extension to obtain nonlinear refraction through $\chi^{(2)}(\omega; 2\omega, -\omega) \cdot \chi^{(2)}(2\omega; \omega, \omega)$ cascading has not been fully utilized. There are two possible consequences of this nonlinearity for the fundamental beam, loss and phase distortion. The loss is well known and is simply due to conversion of the fundamental to the second harmonic. For low conversion efficiency this loss is nearly indistinguishable from two-photon absorption, thus resulting in an effective $\text{Im}[\chi^{(3)}]$. The refractive effect is less well known and usually ignored, occurring only off phase matching where a portion of the frequency-doubled light is downconverted with a shifted phase. Hence the net phase of the fundamental wave is shifted in proportion to the irradiance of the fundamental, which for low irradiance results in a Kerr-like nonlinearity [an effective $\text{Re}[\chi^{(3)}]$]. Using the Z-scan technique,⁷ we monitor the self-action of 1.06- μm picosecond pulses as they propagate through a KTP crystal close to the phase-matching angle for type II second-harmonic generation⁸ (SHG). It is observed that the sign of the nonlinear phase shift changes from positive (self-focusing) to negative (self-defocusing) on angle tuning the sample from negative to positive phase mismatch. The sign and magnitude of the observed phase change agree with the theoretical results as obtained from the coupled-wave equations. A primary application of a negative, fast (electronic) Kerr-like nonlinearity in the presence of positive group-velocity dispersion is the self-compression of ultrashort pulses that can be achieved during such a cascading process.³ This is

the mechanism responsible for self-compression of the idler pulse during optical parametric oscillation in β -barium borate, described in Ref. 3.

The coupled amplitude equations governing SHG in a noncentrosymmetric crystal as derived from Maxwell's equations in the slowly varying envelope approximation are⁹

$$\frac{dE_2}{dz'} = -i \frac{\omega}{2cn_{2\omega}} \chi^{(2)}(2\omega; \omega, \omega) E_1 E_1 \exp(i\Delta k z'), \quad (1)$$

$$\frac{dE_1}{dz'} = -i \frac{\omega}{4cn_{\omega}} \chi^{(2)}(\omega; 2\omega, -\omega) E_2 E_1^* \exp(-i\Delta k z'), \quad (2)$$

where Eq. (1) describes the growth of $E_2(2\omega)$ with depth z' in the sample, while Eq. (2) gives the evolution (depletion and phase variation) of the fundamental beam $E_1(\omega)$ during the SHG process. The wave-vector mismatch is $\Delta k = k_{2\omega} - 2k_{\omega} = 2\omega(n_{2\omega}^i - n_{\omega}^j)/c$, with i and j denoting the polarization directions at frequencies 2ω and ω , respectively. In the absence of loss, the Manley-Rowe relations apply and $\chi^{(2)}(\omega; 2\omega, -\omega) = 2\chi^{(2)*}(2\omega; \omega, \omega)$. In order to simplify Eqs. (1) and (2), we define the parameter

$$\Gamma = \frac{\omega d_{\text{eff}} |E_0|}{c \sqrt{n_{2\omega} n_{\omega}}}, \quad (3)$$

where $d_{\text{eff}} = |\chi^{(2)}(2\omega; \omega, \omega)|/2$ and E_0 is the incident fundamental field. Solving for the fundamental beam by eliminating E_2 and assuming no initial second-harmonic field, we obtain

$$\frac{d^2 E_1}{dz'^2} + i\Delta k \frac{dE_1}{dz'} - \Gamma^2 (1 - 2|E_1/E_0|^2) E_1 = 0. \quad (4)$$

For perfect phase matching ($\Delta k = 0$), Eq. (4) yields the well-known $E_1 = E_0 \text{sech}(\Gamma L)$ solution. Here we concentrate on the non-phase-matched solu-

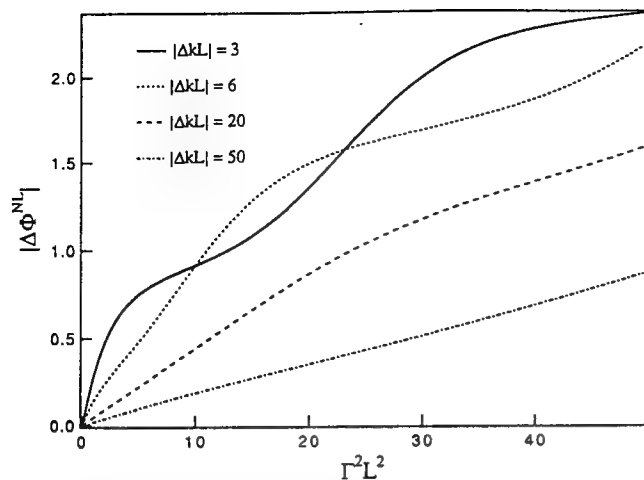


Fig. 1. Induced nonlinear phase shift versus Γ^2L^2 for several values of phase mismatch as calculated by the numerical solution of Eq. (4).

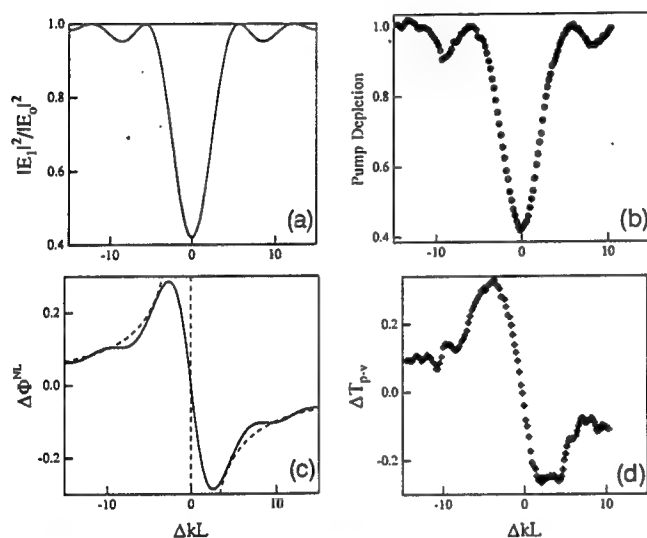


Fig. 2. (a) Calculation of the depletion of the fundamental wave as a function of phase mismatch ΔkL . (b) Experimental measurement of the depletion of the fundamental beam versus ΔkL . (c) Calculation of nonlinear phase shift ($\Delta\Phi^{NL}$) as a function of ΔkL ; the dashed curve is the small conversion efficiency limit, and the solid curve is the exact solution of Eq. (4). (d) Experimental measurement of ΔT_{p-v} as a function of ΔkL as the crystal is rotated through its phase-matching angle.

tion to this equation. In the small conversion efficiency limit, $|E_1| \approx |E_0|$, and hence $E_1(z') = |E_0| \times \exp[-i\Delta\Phi^{NL}(z')]$ for all z' . From Eq. (4), the nonlinear phase change impressed onto the fundamental beam at the exit surface $z' = L$ is given by

$$\Delta\Phi^{NL} \approx \frac{\Delta kL}{2} \{1 - [1 + (2\Gamma/\Delta k)^2]^{1/2}\}. \quad (5)$$

It is clear from relation (5) that there is a nonlinear phase distortion, $\Delta\Phi^{NL}$, on the fundamental beam even though depletion is assumed to be negligible. For large phase mismatch and/or low irradiance (I), $|\Delta k| \gg |\Gamma|$, and this nonlinear phase shift varies linearly with irradiance I , similar to an optical Kerr effect,

$$\Delta\Phi^{NL} \approx -\frac{\Gamma^2L^2}{\Delta kL}, \quad (6)$$

where this phase shift is evaluated at $z' = L$. As the optical Kerr effect is described by $n = n_0 + n_2I$, we can, by analogy, introduce an effective nonlinear index of refraction n_2^{eff} , where $\Delta\Phi^{NL} = (2\pi L/\lambda)n_2^{\text{eff}}I$ and

$$n_2^{\text{eff}} = -\frac{4\pi L}{c\epsilon_0 \lambda} \frac{d_{\text{eff}}^2}{n_{2\omega}n_{\omega}^2} \frac{1}{\Delta kL}. \quad (7)$$

Note that this is proportional to the usual figure of merit for $\chi^{(2)}$ materials, d_{eff}^2/n^3 . For large phase shifts this approximation breaks down, and Eq. (4) must be solved exactly. In Fig. 1 we show the exact dependence of $\Delta\Phi^{NL}$ on Γ^2L^2 as calculated by a numerical solution of Eq. (4) for several values of ΔkL without spatial and temporal averaging. This shows that for large n_2^{eff} the approximation is valid only for small nonlinear phase shifts.

The depletion curve of Fig. 2(a) is a plot of $|E_1(z' = L)|^2/|E_0|^2$ as a function of the phase mismatch with no spatial or temporal integration. The data of Fig. 2(b) are for a 1-mm-thick hydrothermally grown sample of KTP, using 27-ps (FWHM), 1.06- μm pulses, focused to a measured Gaussian waist of 35 μm (half-width at $1/e^2$ of maximum). The result for $I = 9.4 \text{ GW/cm}^2$ at $\Delta kL = 0$, where the spatial and temporal averaging can be readily performed, gives a value of $\Gamma^2L^2 \approx 4.2$, corresponding to $d_{\text{eff}} \approx 3.1 \text{ pm/V}$, which agrees with the results of Ref. 9. Owing to the large depletion observed ($>50\%$), it is important to check that two-photon absorption does not contribute to the depletion. Z-scan measurements of the two-photon absorption coefficient at 532 nm yield a value of 0.1 cm/GW, which gives a depletion much smaller than that due to SHG. In Fig. 2(c), approximate and exact solutions for $\Delta\Phi^{NL}$ are shown as a function of the phase mismatch ΔkL , again with no space-time integration.

In our initial phase-measurement experiments we performed closed-aperture Z scans at $\phi = \pm 10^\circ$

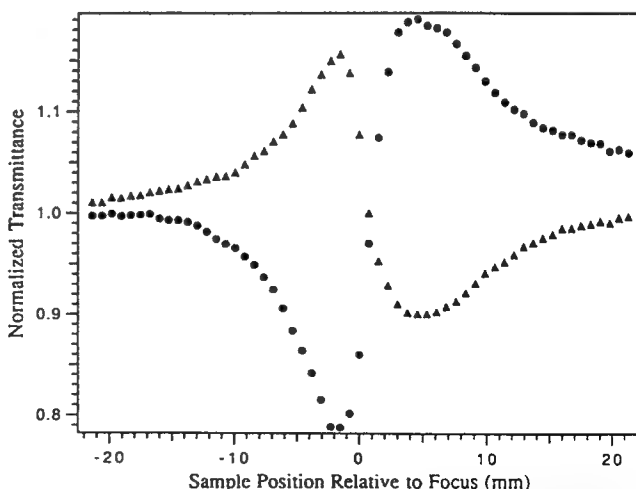


Fig. 3. Z scans showing positive $\Delta\Phi^{NL}$ (circles) performed at $\Delta kL = -6$ and negative $\Delta\Phi^{NL}$ (triangles) performed at $\Delta kL = +6$. The positive $\Delta\Phi^{NL}$ is significantly larger owing to the positive contribution of n_2 (Kerr).

($\Delta kL \approx \pm 2\pi$), which correspond to minima in the SHG signal. These scans,⁷ shown in Fig. 3, show a change in sign of $\Delta\Phi^{NL}$ in accordance with the predictions.⁶ However, an asymmetry is observed, which indicates that there is noticeably more self-focusing than self-defocusing. This is explained by the presence of the bound electronic Kerr effect, n_2 (Kerr), which adds a positive phase distortion irrespective of Δk . We measured this n_2 (Kerr) to be $\approx (2.4 \pm 0.5) \times 10^{-15} \text{ cm}^2/\text{W}$ by Z scanning with the beam propagating along the crystalline z axis, where $d_{\text{eff}} = 0$. This is consistent with n_2 (Kerr) obtained from the asymmetry shown in Fig. 3. We then find that $n_2^{\text{eff}} \approx \pm(1.3 \pm 0.3) \times 10^{-14} \text{ cm}^2/\text{W}$ at $I \approx 26 \text{ GW/cm}^2$ for $\phi = \pm 10^\circ$ ($\Delta kL \approx \pm 2\pi$), where depletion is minimized. Since at this irradiance, the nonlinearity deviates from the n_2^{eff} approximation, this measured value should be somewhat lower than the small-signal value. The maximum n_2^{eff} should occur at $\phi \approx \pm 5^\circ$ ($\Delta kL \approx \pm 3$) and have a value of $\pm 2 \times 10^{-14} \text{ cm}^2/\text{W}$ ($\pm 1 \times 10^{-11} \text{ esu}$).

In order to obtain a plot of $\Delta\Phi^{NL}$ versus phase mismatch we monitored the transmittance through a far-field aperture with $\approx 40\%$ linear transmittance as a function of angle with the sample placed at the position along the beam path that gives minimum transmittance and repeated this with the sample placed at the position of maximum transmittance. As described in Refs. 7 and 10, the difference between the transmittance maximum and minimum is approximately proportional to $\Delta\Phi^{NL}$. The result of this subtraction is shown in Fig. 2(d), where the measured value of n_2 (Kerr) was also subtracted. This curve shows qualitative agreement with the theoretical curve for $\Delta\Phi^{NL}$ shown in Fig. 2(c).

Several conclusions can be drawn from the above observations. While n_2^{eff} for the 1-mm sample of KTP can be approximately as large as that for CS_2 , this n_2^{eff} is linearly dependent on the sample thickness, which permits considerably larger values. The maximum n_2^{eff} occurs for a constant value of $\Delta kL \approx \pm 3$, thus we have the linear dependence on L shown in Eq. (7). Also n_2^{eff} scales as the square of d_{eff} such that larger values will greatly enhance n_2^{eff} . Thus values of $10^{-11} \text{ cm}^2/\text{W}$ ($\approx 10^{-8} \text{ esu}$) can be expected for long, high- $\chi^{(2)}$ materials. Clearly organics are of interest here owing to their large $\chi^{(2)}$ values. Conceivably, organics with a d_{eff} of the order of 100 pm/V can lead to ultrafast all-optical switching with low loss to the fundamental beam by using picosecond pulses over an interaction length of a few hundreds of wavelengths. However, because of the saturable nature of $\Delta\Phi^{NL}$, one must use caution when quoting n_2^{eff} , as Fig. 1 clearly illustrates. In reality, it is the phase $\Delta\Phi^{NL}$ that is the more important parameter, and the advantage of using this method of achieving nonlinear refraction will depend on the particular application and the magnitude of $\Delta\Phi^{NL}$ that it requires.

The availability of an ultrafast nonlinearity that can be tuned in sign opens new device possibilities. For example, the fast electronic negative Kerr-like nonlinearity in a cascading process leads to self-compression of ultrashort pulses in the presence of positive group-velocity dispersion. This mechanism recently has been demonstrated in an optical parametric oscillator.³ Another example of an application of this nonlinearity is mode locking of lasers using the recently reported Kerr mode-locking technique. For example Carruthers and Duling¹¹ report mode locking a cw Nd:YAG laser using KTP in an antiresonant ring cavity, where the mode locking was achieved for an angle tuning slightly off phase match. The induced self-phase modulation from the cascaded process may be the nonlinearity responsible for this mode locking.

In addition the Z-scan technique yields a new and accurate, absolutely calibrated method to measure d_{eff} , which requires only a measurement of the irradiance and either the loss or phase shift on the fundamental beam.

We gratefully acknowledge the support of the National Science Foundation through grant ECS 8617066, the Defense Advanced Research Projects Agency/Center for Night Vision and Electro Optics, and the Florida High Technology and Industrial Council.

D. J. Hagan, G. Stegeman, and E. W. Van Stryland are also with the Departments of Physics and Electrical Engineering, University of Central Florida.

References

1. H. J. Bakker, P. C. M. Planken, L. Kuipers, and A. Lagendijk, *Phys. Rev. A* **42**, 4085 (1990).
2. P. C. M. Planken, H. J. Bakker, L. Kuipers, and A. Lagendijk, *J. Opt. Soc. Am. B* **7**, 2150 (1990).
3. R. Laenen, H. Graener, and A. Laubereau, *J. Opt. Soc. Am. B* **8**, 1085 (1991).
4. G. B. Altshuler and M. V. Inochkin, in *Digest of Conference on Quantum Electronics* (Optical Society of America, Washington, D.C., 1990), paper QWB6.
5. N. R. Belashenkov, S. V. Gagarinskii, and M. V. Inochkin, *Opt. Spectrosc.* **66**, 806 (1989).
6. J. R. Desalvo, D. J. Hagan, M. Sheik-Bahae, and E. W. Van Stryland, in *Digest of Optical Society of America Annual Meeting* (Optical Society of America, Washington, D.C., 1990), paper MTT7.
7. M. Sheik-Bahae, A. A. Said, and E. W. Van Stryland, *Opt. Lett.* **14**, 955 (1989).
8. J. D. Bierlien and H. Vanherzeele, *J. Opt. Soc. Am. B* **6**, 622 (1989).
9. R. C. Eckardt, H. Masuda, Y. X. Fan, and R. L. Byer, *IEEE J. Quantum Electron.* **26**, 922 (1990).
10. M. Sheik-Bahae, A. A. Said, T. H. Wei, D. J. Hagan, and E. W. Van Stryland, *IEEE J. Quantum Electron.* **26**, 760 (1990).
11. T. F. Carruthers and I. L. Duling III, *Opt. Lett.* **15**, 804 (1990).

Nonlinear refraction and optical limiting in thick media

Mansoor Sheik-Bahae

Ali A. Said, MEMBER SPIE

D. J. Hagan, MEMBER SPIE

M. J. Soileau, FELLOW SPIE

Eric W. Van Stryland, MEMBER SPIE

University of Central Florida

Center for Research in Electro-Optics and Lasers

Department of Physics and Electrical Engineering

Orlando, Florida 32816

Abstract. We experimentally and theoretically investigate optical beam propagation in nonlinear refractive materials having a thickness greater than the depth of focus of the input beam (i.e., internal self-action). A simple model based on the "constant shape approximation" is adequate for analyzing the propagation of laser beams within such media under most conditions. In a tight focus geometry, we find that the position of the sample with respect to the focal plane, z , is an important parameter in the fluence limiting characteristics of the output. The behavior with z allows us to perform a "thick sample Z-scan" from which we can determine the sign and magnitude of the nonlinear refraction index. In CS_2 , we have used this method to independently measure the negative thermally induced index change and the positive Kerr nonlinearity with nanosecond and picosecond CO_2 laser pulses, respectively. We have experimentally examined the limiting characteristics of thick CS_2 samples that qualitatively agree with our analysis for both positive and negative nonlinear refraction. This analysis is useful in optimizing the limiting behavior of devices based on self-action.

Subject terms: nonlinear refraction; optical limiting; Z-scan; aberration-free approximation; self-focusing; internal self-action; CS_2 .

Optical Engineering 30(8), 1228-1235 (August 1991).

CONTENTS

1. Introduction
2. Model
3. Z-scan
4. Limiting
5. Experiments
6. Conclusion
7. Appendix
8. Acknowledgments
9. References

1. INTRODUCTION

Passive optical limiters based on nonlinear refraction have been demonstrated and analyzed for a variety of materials and laser wavelengths.¹⁻⁴ A common geometry is illustrated in Fig. 1. The laser beam is focused into a nonlinear refractive material and is then collected through a finite aperture in the far field. At high irradiance the far field beam distortion arising from the self-action of the laser beam inside the medium will result in the limiting of the transmitted light through the aperture. Most of the published analytical work regarding such a device has dealt with thin samples.⁴⁻⁶ Here, "thin" means thinner than the depth of focus. Under this thin sample condition, it has been shown^{7,8} that the position of the sample with respect to the beam waist (z in Fig. 1) is important in determining the output limiting characteristics. We note that for a thin medium, a displacement of the sample in z by a distance of the order of the depth of focus, can result in reversing the operation of the device from limiting to a transmittance enhancement.⁹ We have recently developed a sensitive technique for measuring the sign and magnitude of the nonlinear refractive index n_2 based on the z dependence of the transmitted fluence, which we call a Z-scan.^{9,10}

We observe an analogous, but more complicated z dependence for thick limiters (i.e., nonlinear material thickness greater than the depth of focus).¹¹ It is often desirable to use such thick materials in limiting geometries to either keep the focus away from damage prone surfaces or use in a "self-protecting" geometry.^{3,12} Figure 2 shows the energy transmitted through the aperture of Fig. 1 as a function of input energy of 300-ns (FWHM) 10.6- μm pulses using thermal defocusing in CS_2 as the nonlinear mechanism. Plots are shown for three different sample positions relative to the focal plane, showing the sensitivity to sample placement as described above.

Based on a simple "distributed lens" model, we explain the observed limiting behavior of thick limiters as a function of position z . We find that the lowest threshold for limiting is achieved by focusing the beam at the front surface for negative nonlinearity ($\Delta n < 0$) and rear surface for positive nonlinearity ($\Delta n > 0$).

2. MODEL

The nonlinear wave equation governing the propagation of a laser beam inside a nonlinear refractive medium is expressed as

$$\nabla^2 E - \frac{1}{c^2} \frac{\partial^2}{\partial t^2} [(n_0 + \Delta n)^2 E] = 0, \quad (1)$$

where E is the electric field, n_0 is the linear index of refraction, and the nonlinearity is introduced through Δn , which in general, may include various order contributions such as $\chi^{(3)}$, $\chi^{(5)}$, ..., etc. Here, we consider the lowest order effect, namely a $\chi^{(3)}$ (Kerr-type) nonlinearity, which is commonly expressed in terms of the nonlinear refractive index n_2 (esu) as $\Delta n = n_2 |E|^2/2$. In a thick medium, transverse variations accounted for by the ∇^2 term in Eq. (1) become significant and an exact numerical solution to Eq. (1) can be quite complex. A useful technique to

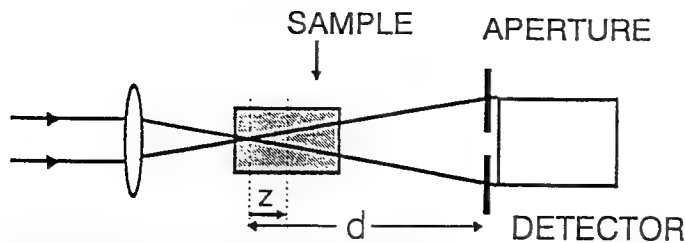


Fig. 1. Schematic of the limiting geometry where z is the distance between the focal plane in free space and the center of the sample, and d is the distance from this plane to the aperture plane.

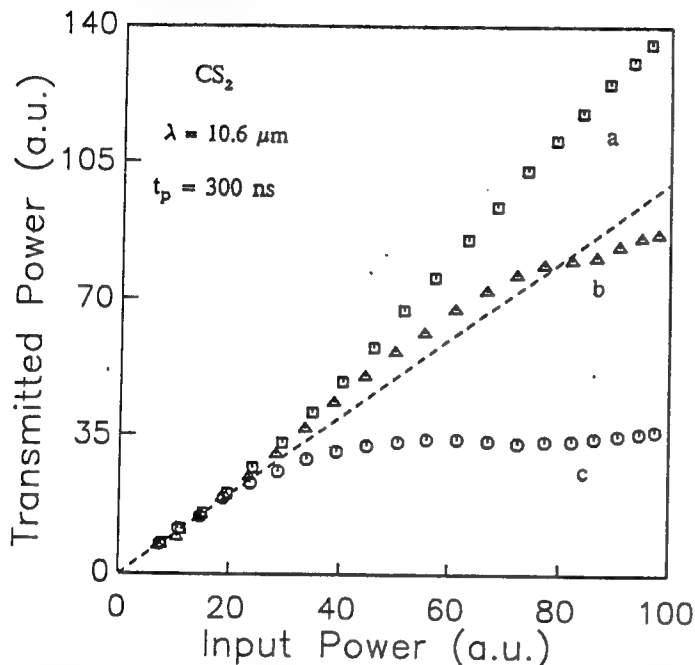


Fig. 2. The limiting characteristics of liquid CS_2 at $10.6 \mu\text{m}$ measured at various z positions indicated by the arrows in Fig. 9, as explained in Secs. 3 and 4.

simplify this problem is known as the "aberration-free" or "constant shape" approximation,^{13,14} in which a Gaussian beam propagating through the thick nonlinear medium is assumed to preserve its Gaussian shape. This requires that the radial variation of the index of refraction be parabolic. For a Gaussian beam and cubic nonlinearity such a requirement is satisfied by using the following approximation:

$$\Delta n(r) = \Delta n(0) \exp(-2r^2/w^2) \approx \Delta n(0)(1 - 2r^2/aw^2), \quad (2)$$

where $\Delta n(0)$ is the on-axis index change, w is the local beam radius ($\text{HW}1/e^2 M$ in irradiance) and we introduce a as a correction factor to account for the higher order terms that have been omitted in the expansion of $\exp(-2r^2/w^2)$. Previous applications of the aberration-free approximation set $a = 1$ (Refs. 13 and 14). Our use of $a \neq 1$ allows for good quantitative agreement in evaluating the nonlinearity or the limiting thresholds. It is expected that the value of a that gives the best fit to the Fresnel wave optics analysis will be geometry and power dependent, and as we will show, a may take on values between 3.77 and 6.4. For a thin medium, the parabolic approximation of Eq. (2) implies that the medium behaves as a thin spherical lens. Therefore, as depicted in Fig. 3, a thick sample can be regarded as a stack of such nonlinear lenses with focal lengths

that depend on the local beam irradiance. The effective focal length of the m 'th element in the stack can be written as

$$f_m = \frac{aw_m^2}{4\Delta n_m \Delta L}, \quad (3)$$

where w_m and Δn_m are the beam radius and on-axis index change at that element, respectively. ΔL denotes the separation between two adjacent lenses and should be chosen to be much smaller than both the diffraction length of the beam and f_m . The latter requirement can be written as

$$\Delta L \ll (aw_m^2/4|\Delta n_m|)^{1/2}. \quad (4)$$

For a given z position of the sample, the input Gaussian beam can be propagated through the nonlinear medium using successive **ABCD** matrices defined for the m 'th element in the stack as

$$\begin{pmatrix} A_m & B_m \\ C_m & D_m \end{pmatrix} = \begin{pmatrix} 1 - \Delta L/n_0 f_m & \Delta L/n_0 \\ -1/f_m & 1 \end{pmatrix}. \quad (5)$$

A final free space propagation **ABCD** matrix is used to obtain the beam radius at the position of the aperture, w_a , which is now a function of the sample position z and the distance to the aperture. The effect of linear absorption in the numerical calculation can be simply included by replacing Δn_m by $\Delta n_m \exp(-\alpha \Delta L)$ in Eq. (3).

In the absence of nonlinearity, the field at any position z' is given by

$$E(r, z', t) = E_0(t) \frac{w_0}{w(z')} \times \exp\left(-\frac{r^2}{w^2(z')} - \frac{ikr^2}{2R(z')}\right) \exp[-i\phi(z', t)], \quad (6)$$

where $w^2(z') = w_0^2(1 + z'^2/z_0^2)$ is the beam radius at z' , $z_0 = kw_0^2/2$ is the depth of focus of the beam, $k = 2\pi/\lambda$ is the wave vector, λ is the laser wavelength, all in air, and $R(z') = z'(1 + z_0^2/z'^2)$ is the radius of curvature of the wavefront. Here, $\phi(z', t)$ contains all the radially uniform phase terms. The term E_0 denotes the electric field at the focus and contains the temporal envelope of the laser pulse.

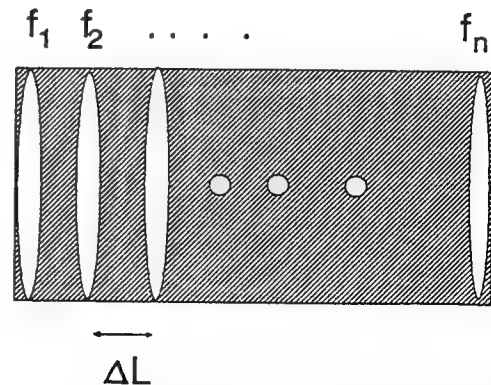


Fig. 3. In the "distributed lens" approximation, the thick nonlinear medium is regarded as a stack of thin nonlinear lenses whose focal lengths depend on the local beam irradiance.

The quantity measured in a limiting experiment or Z-scan experiment is the power P_T (or energy) transmitted through the aperture of radius r_a placed after the sample in the far field. Given the assumption of a Gaussian beam, this quantity, which we write as a function of z , is given by

$$P_T(z) = P_a [1 - \exp(-2r_a^2/w_a^2)] \quad (7)$$

where P_a is the linear power transmitted to the aperture. Accounting for the temporal variation of a pulse, w_a can be considered a function of time t . The normalized transmittance is then given by

$$T(z) = \frac{\int_{-\infty}^{\infty} P_T(z, t) dt}{S \int_{-\infty}^{\infty} P_a(t) dt} \quad (8)$$

where S is the aperture transmittance given by P_T/P_a in the linear (small signal) regime.

We first compare the results for a thin sample using the thin lens approximation to the solution of the wave equation using the Fresnel wave optics approach given in Ref. 10. This allows us to determine the value of the constant a that best approximates the Gaussian beam shape. For the sample at position z with respect to the original focal plane, we can use a single thin lens ABCD matrix. With the aperture placed a distance d behind the original focal plane, this leads to the following expression for the spot size w_a ;

$$\frac{w_a^2}{w_0^2} = D^2 \left(1 - \frac{2\Delta\Phi_0(D-x)x}{aD(1+x^2)^2} \right)^2 + \left(1 - \frac{2\Delta\Phi_0(D-x)}{a(1+x^2)^2} \right)^2 \quad (9)$$

where $D = d/z_0$ and $x = z/z_0$. Here, $\Delta\Phi_0$ is the on-axis nonlinear phase shift at focus ($z = 0$), given in terms of the corresponding index change Δn_0 as

$$\Delta\Phi_0 \approx k\Delta n_0 L \quad (10)$$

where L is the thickness of the sample. In the case where linear absorption (coefficient α) is present L should be replaced by $[1 - \exp(-\alpha L)]/\alpha$.

Ignoring the temporal dependence, as is appropriate for a steady state condition, and using Eqs. 7 and 8 we obtain

$$T(z) = \frac{1 - \exp(-2r_a^2/w_a^2)}{S} \quad (11)$$

For a thin sample in the geometry of Fig. 1, the transmittance calculated using the Fresnel wave optics approach as a function of sample position for a fixed input irradiance is shown in Fig. 4 along with the results obtained from Eq. (11).¹⁰ In these calculations a positive nonlinearity with a $\Delta\Phi_0$ of 0.5 rad was assumed. As shown in Fig. 4, the agreement in the total transmission change (from the valley to the peak) is quite good choosing $a = 5$ for $S = 0.5$. In general, based on a detailed numerical analysis, we find that the peak to valley transmittance change is fit to within $\pm 5\%$ accuracy by choosing a as given by

$$a \approx 6.4(1 - S)^{0.35} \quad \text{for } 0 \leq S \leq 0.7 \text{ and } \Delta\Phi_0 \leq \pi/2 \quad (12)$$

Numerical analyses show that at larger phase distortions a will decrease further. For very large induced phase distortions in thick materials we choose $a = 3.77$ for reasons explained in Sec. 4. The low-field small-aperture ($S \approx 0$) limit of this relation ($a = 6.4$) can be easily derived from Eq. (9) as shown in the Appendix. The deviation of a from Eq. (12) at higher irradiance reflects deviations from the constant shape approximation at large phase distortions.

3. Z-SCAN

Plotting the z dependence of the transmittance as shown in Fig. 4 is a sensitive and useful way to characterize the limiting properties of the nonlinear material. Such pronounced variations of the beam transmittance through the aperture as a function of the sample position z have also provided the basis for an extremely simple and sensitive technique that we call Z-scan and use for accurate measurements of refractive nonlinearities.^{9,10}

The Z-scan technique is based on the transformation of phase distortions to amplitude distortions during beam propagation. The Z-scan experimental apparatus is as shown in Fig. 1, where the sample is moved along the propagation direction z while keeping the input pulse energy fixed. A qualitative physical argument that explains the transmittance variations in the Z-scan experiment¹⁰ can be given as follows: Starting the scan from a distance far away from the focus (negative z), the beam irradiance is low and negligible nonlinear refraction occurs leading to linear transmittance. We normalize the linear transmittance to unity. As the sample is brought closer to the focus, the beam irradiance increases leading to self-lensing in the sample. A negative self-lensing prior to focus tends to collimate the beam and reduce the diffraction leading to a smaller beam at the aperture and an increased transmittance. As the scan continues and the sample crosses the focal plane to the right (positive z),

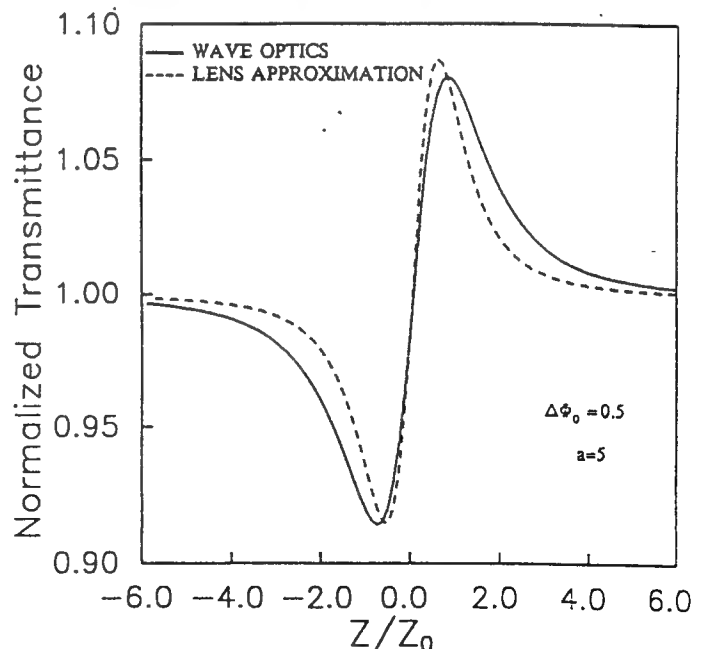


Fig. 4. The Z-scans of a thin nonlinear medium as calculated using the methods of wave optics (solid line) and the thin lens approximation (dashed line). A 50% aperture is assumed ($S = 0.5$).

the same self-defocusing effect will tend to augment diffraction and reduce the aperture transmittance. A prefocal transmittance maximum (peak) and a postfocal transmittance minimum (valley) are, therefore, the Z-scan signature of a negative nonlinearity, while a positive one, following the same analogy, will give rise to an opposite valley-peak configuration. With a small phase shift and a thin sample, the peak and valley are^{9,10} symmetrically positioned about the focal plane and are separated by a distance $\Delta Z_{p-v} \approx 1.7z_0$. This separation is given by the wave optics calculation, while the constant shape approximation gives a somewhat smaller value, as described in the Appendix.

We have used such thin sample Z-scan data to measure n_2 of a large class of materials with a demonstrated sensitivity of $\approx \lambda/300$ wavefront distortion.¹⁰ Here we extend the applicability of the Z-scan method to thick samples. With a limiting device in mind, the obvious optimum sample position to minimize the limiting threshold is the z region where the valley occurs. We will exploit this feature further in optimization of thick limiters.

The calculated Z-scan for a rather extreme case in which $L/(n_0 z_0) = 15$ is shown in Fig. 5. For a thick sample, z is defined as the distance from the center of the sample to the position of the focus in air in the absence of the nonlinear medium. A cubic nonlinearity with either sign and with $\Theta/a = \pm 0.5$ is assumed where $\Theta = kn_0 \Delta n_0 2z_0$. Note that Θ is approximately the induced phase distortion accumulated in the sample between $-z_0$ to $+z_0$. An interesting feature of the thick sample Z-scan is that the separation between peak and valley of these curves is now dominated by the optical length of the sample, L/n_0 . Furthermore, the two extremes correspond to focusing the laser beam on either surface. More generally, we find $\Delta Z_{p-v}(\text{thick}) \approx [(L/n_0)^2 + \Delta Z_{p-v}^2(\text{thin})]^{1/2}$ where $\Delta Z_{p-v}(\text{thin})$ is the thin sample limit of $\approx 1.7z_0$. Also evident from Fig. 5 is the existence of a nearly flat transmittance region where the beam is focused near the middle of the medium. This simply signifies the fact that although the laser beam experiences a large local phase distortion within the medium, the effects of prefocal and postfocal nonlinear refraction are nearly cancelled in the far field. Using the lens analogy, the effect is similar to placing a pair of lenses of

the same sign on both sides of the focal plane such that the far field beam pattern is relatively unaltered.

The observations reported in the "Chinese Tea" paper¹⁵ are easily understood from the above analysis. In that paper, they observed a beam narrowing and expansion depending on the position of the focus within the linearly absorbing sample. This was interpreted as a change in sign of the nonlinearity. Clearly, for a purely defocusing nonlinearity both beam expansion and beam narrowing can be obtained in a thick sample depending on the position of the focus within the sample. We, therefore, explain their results as being due to simple thermal defocusing caused by linear absorptive heating.

The existence of a large internal self-action results in a larger transmittance change for a positive nonlinearity than for a negative one of the same magnitude as seen in Fig. 5. This results from the fact that with a positive nonlinear index the resultant self-focusing is a self-strengthening effect similar to an avalanche process, whereas with a negative nonlinearity we have self-defocusing inside the medium, which leads to a self-weakening of the nonlinear refraction. Nevertheless, at small enough phase distortions where variations of the beam diameter inside the medium due to nonlinear refraction are insignificant, nonlinearities with opposite signs will give rise to the same peak to valley transmittance changes.

It is useful to look at what we call the effective interaction length inside the nonlinear material. Clearly for samples much thicker than z_0 , making the sample thicker will no longer increase the total ΔT_{p-v} . We define L_{eff} as

$$L_{eff} = \frac{\Delta T_{p-v}(\text{thick})}{\Delta T_{p-v}(\text{thin})} L, \quad (13)$$

where $\Delta T_{p-v}(\text{thick})$ is calculated using the distributed lens method and $\Delta T_{p-v}(\text{thin})$ is calculated assuming that the sample is much thinner than the depth of focus. As reported in Ref. 10, $\Delta T_{p-v}(\text{thin})$ is given by

$$\Delta T_{p-v}(\text{thin}) \approx 0.406(1 - S)^{0.25} \Delta \Phi_0 \quad (14)$$

with $\Delta \Phi_0$ defined by Eq.(10).

To graph the results in a way that will be useful in extracting the total phase distortion in the thick sample, we define the dimensionless parameters $l_{eff} = L_{eff}/n_0 z_0$, and $l = L/n_0 z_0$. Figure 6 shows l_{eff} for various values of Θ/a as a function of l . Figure 6 also shows how defocusing ($\Theta < 0$) lowers l_{eff} and self-focusing ($\Theta > 0$) raises l_{eff} as the beam size within the thick ($l > 2$) material is broadened ($\Theta < 0$) and narrowed ($\Theta > 0$), respectively. The curves in Fig. 6 were calculated using $S = 0.5$. Further calculations have shown that l_{eff} is highly insensitive to S .

We see, as expected, that $l \approx l_{eff}$ for small l and that most of the total phase distortion or index change is achieved within a sample of thickness $\approx 2z_0$. Further increases in the sample length lead to only small increases in the Z-scan signal (ΔT_{p-v}) and in the same way will be less effective in lowering a limiting threshold. Applications exist (e.g., when linear absorption is present) where we wish to maximize the phase distortion with a minimum of sample length or linear loss.

As given in Fig. 6, l_{eff} also can be used to obtain an accurate estimate of the induced phase change Θ and, thus, the nonlinear refractive index of the sample. This can be achieved by noting that combining Eqs. (13) and (14) yields

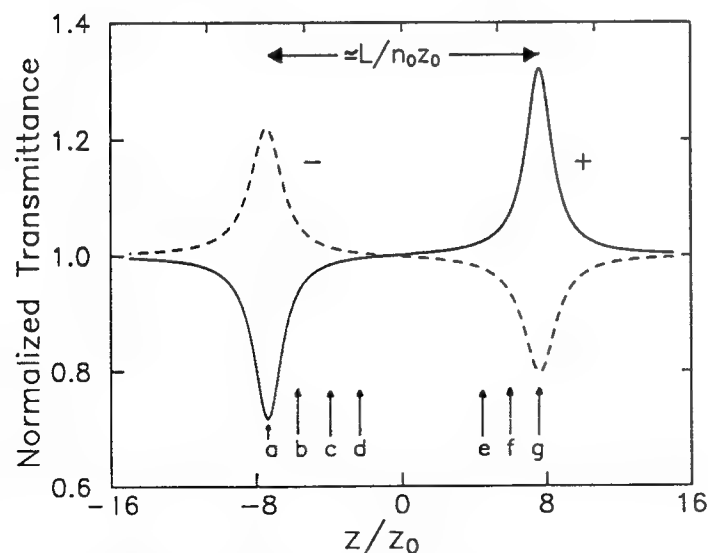


Fig. 5. Calculated Z-scans of a thick medium using the distributed lens method for both positive (solid line) and negative (broken line) nonlinearities ($\Theta/a = \pm 0.5$). The arrows on the z -axis indicate the corresponding positions at which the limiting curves of Figs. 7 and 8 were obtained (see Sec. 4). Here, we chose $n_0 = 1$ and $S = 0.5$.

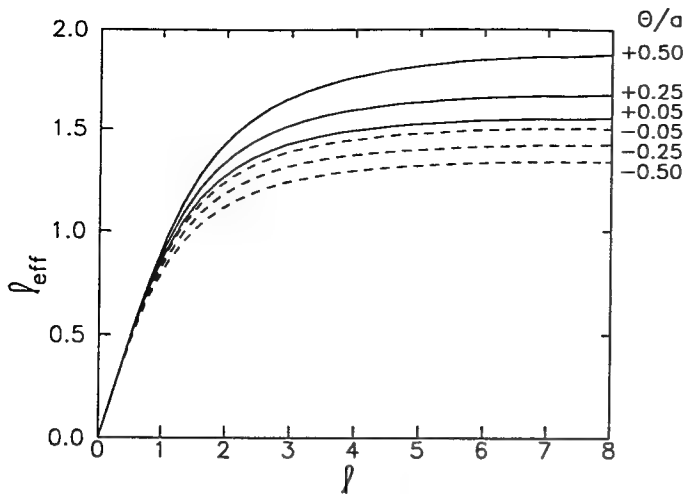


Fig. 6. Calculated effective interaction length as a function of the sample length in units of z_0 for various degrees of nonlinear phase distortion Θ/a .

$$\Delta T_{p-v}(\text{thick}) \approx 0.406(1 - S)^{0.25} \frac{\Theta l_{\text{eff}}}{2} \quad (15)$$

Here $\Theta l_{\text{eff}}/2$ can be interpreted as the effective on-axis nonlinear phase shift when the focus is at the center of the sample. Because, according to Fig. 6, knowing l_{eff} requires knowledge of the value of Θ , an iterative procedure can be used that converges rapidly to give Θ and, thus, Δn_0 . One may start by assuming a small $|\Theta|$ (≤ 0.2). Using Fig. 6, given this Θ and l , we obtain an l_{eff} . Using this l_{eff} , a new Θ can be reevaluated from Eq. (15). Repeating the process quickly converges to the correct Θ . Although the curves in Fig. 6 were obtained assuming a lossless medium ($\alpha = 0$), the same curves can be used if linear absorption is present, provided that the left-hand side of Eq. (15) is multiplied by the absorption factor $[1 - (\exp - \alpha L)]/(\alpha L)$. Numerical calculations show that this procedure works well for $\alpha L < 2$ as long as $|\Theta| < 2$.

4. LIMITING

As for the case of a thin sample, to maximize the limiting effect, we must place the thick sample at a position where the transmittance shows a valley similar to the one in Fig. 5. The theoretical limiting behavior of the thick medium of Fig. 1 is shown in Figs. 7 and 8 for negative and positive nonlinearities, respectively. As the sample is positioned farther from the valley, the limiting threshold increases. We define the limiting threshold as the input at which the transmittance drops by a factor of two. For negative nonlinearity, the lowest limiting threshold is obtained at the valley corresponding to focusing at the front surface. This threshold is given by $\Theta \approx a$. Focusing near the rear surface yields a transmission enhancing behavior that is undesirable for a limiting device. Similarly, for a positive nonlinearity, the lowest limiting threshold occurs at the valley that corresponds to rear surface focusing. However, as seen in Fig. 8, a sudden drop of transmission occurs at $\Theta \approx a$ due to the onset of catastrophic self-focusing. This threshold is seen to be nearly independent of the sample position. The term Θ can also be expressed as a power ratio: P/P_1 , where P denotes the radiation power and P_1 is defined as the first critical power for self-focusing^{16,17}:

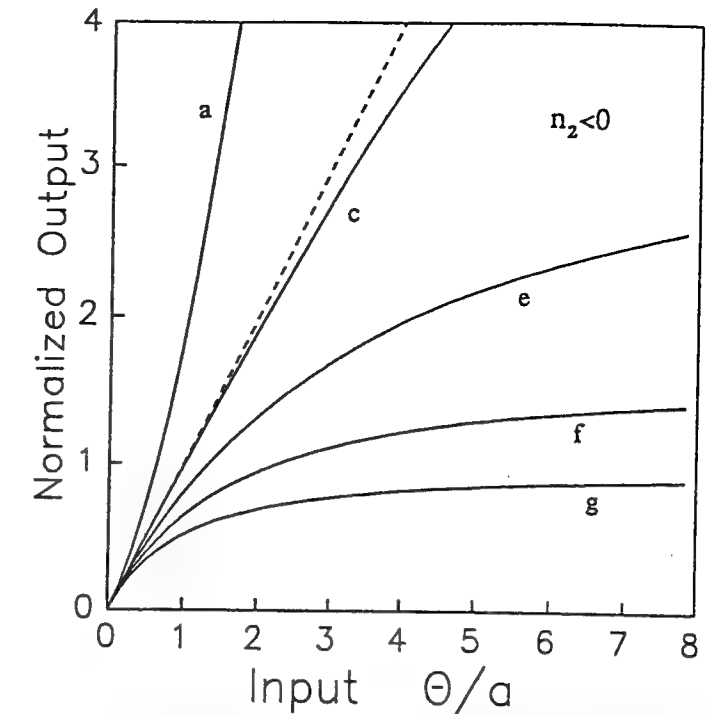


Fig. 7. The normalized limiting curves for a negative nonlinearity ($n_2 < 0$) calculated for various sample positions (z) as indicated by the arrows in Fig. 5. The broken line shows the linear transmittance. ($S = 0.5$ was used in the calculations).

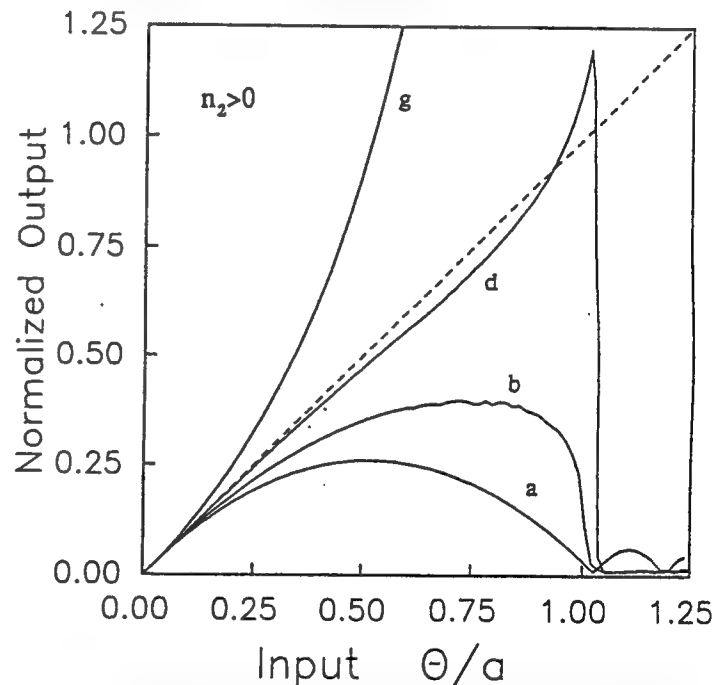


Fig. 8. The normalized limiting curves for a positive nonlinearity ($n_2 > 0$) calculated for various sample positions (z) as indicated by the arrows in Fig. 5. The broken line is the linear transmittance curve. Catastrophic self focusing occurs in all the curves at $\Theta/a = 1$ signified by a sudden drop in the transmitted power. ($S = 0.5$ was used in the calculations).

$$P_1 = \frac{c\lambda^2}{32\pi^2 n_2} \quad (\text{cgs units}) \quad (16)$$

Numerical calculations of the nonlinear wave equation made by Marburger¹⁸ indicate that for focused Gaussian beams in a thick

medium with positive nonlinear index ($n_2 > 0$), a catastrophic self-focus will occur at a critical power of $P_c = 3.77 P_1$ ($\Theta = 3.77$). The distributed lens method, therefore, predicts the correct result, choosing $a = 3.77$, as stated in Sec. 2 for large induced phase distortion.

Referring to Fig. 8, when the self-focusing threshold is reached, the laser beam is predicted to collapse and the local beam irradiance to become infinite. However, the paraxial approximation and, hence, the analysis breaks down as the beam radius becomes¹⁹ comparable to the wavelength λ . In addition, at the high irradiance produced by the self-focusing effect, one must consider higher order nonlinearities as well as plasma production and subsequent optical breakdown of the medium.

5. EXPERIMENTS

Optical limiting in liquid CS₂ was examined using a TEA CO₂ laser with single longitudinal mode pulses of 300-ns duration. The laser beam was focused to $w_0 \approx 60 \mu\text{m}$ ($z_0 \approx 1\text{mm}$) into a 24-mm cell (with NaCl windows) filled with spectrophotometric grade CS₂. With $n_0 = 1.63$, the ratio $L/nz_0 \approx 15$, indicating a thick medium. First, we performed a Z-scan on this sample to verify the locations of the peak and valley of the transmittance. The result for a 1-mJ pulse energy along with the theoretical fit is shown in Fig. 9. The curve exhibits features predicted by the distributed lens method for a negative nonlinearity, namely the peak and valley corresponding to the second and first surface focusing, respectively, and a nearly flat portion corresponding to focusing near the center of the cell. The origin of this negative nonlinearity is believed to be thermal, arising from the finite absorption of 10.6- μm radiation in CS₂ ($\alpha \approx 0.22 \text{ cm}^{-1}$). Thermal lensing in liquids arises from the thermal expansion of the medium and has a rise time given by the "acoustic transit time," which is effectively the time a sound wave takes to traverse the beam radius.²⁰ Knowing the sound velocity in CS₂ ($v_s \approx 1.5 \times 10^5 \text{ cm/s}$) and the focal beam radius ($\approx 60 \mu\text{m}$), a response time of $\approx 40 \text{ ns}$ is obtained, which is almost an order of magnitude smaller than the laser pulsewidth. The decay of the thermal lens, however, is governed by the thermal

diffusion process, which is on the order of 0.1 s, which is orders of magnitude larger than the pulsewidth and can be neglected.²⁰ Under such quasi-steady state conditions, the time averaged nonlinear index change ($\langle \Delta n_0 \rangle$) arising from nonuniform heating can be estimated in terms of the laser pulse fluence (F) at the focus¹⁰

$$\langle \Delta n_0 \rangle \approx \frac{dn}{dT} \frac{\alpha F}{2\rho C_V}, \quad (17)$$

where ρ is the density, C_V is the specific heat and dn/dT is the thermo-optic coefficient of the medium. The factor of 2 comes from the temporal averaging.¹⁰ The coefficient dn/dT has long been investigated for CS₂, and a value of $\approx -8 \times 10^{-4} \text{ }^\circ\text{C}^{-1}$ has been reported in the literature.²¹ With the known value of $\rho C_V \approx 1.3 \text{ J/Kcm}^3$ for CS₂, we obtain $\langle \Delta n_0 \rangle \approx 1.1 \times 10^{-3}$ at a $\approx 17 \text{ J/cm}^2$ fluence. This is in good agreement with the $\langle \Delta n_0 \rangle \approx -1.0 \times 10^{-3}$ used to fit the Z-scan of Fig. 9. Note that in this calculation, a value of ≈ 5 , as obtained for $S \approx 0.5$, was used for the a parameter. Note also that the $z = 0$ point in the Z-scan curve is defined as the position of the focus in air in the absence of the nonlinear medium. After the insertion of a thick sample with $n_0 > 1$, the beam waist inside the sample no longer will coincide with our $z = 0$ point. This is why the $z = 0$ point of the Z-scan in Fig. 9 differs from that of Fig. 4, which was calculated assuming $n_0 = 1$.

The limiting behavior of the same CS₂ cell at 10.6 μm was shown in Fig. 2, where the normalized transmitted power was plotted versus the input power as measured for the various sample positions indicated in Fig. 9. They exhibit the predicted features given in Fig. 7. It is evident from Eq. (17) that thermal self-action can be enhanced by increasing the absorption coefficient of the medium. We obtained a limiting threshold of $\approx 0.5 \text{ kW}$ (150 μJ) in CS₂ at 10.6 μm by desolving impurities (e.g., sulfur) to increase the absorption coefficient to $\approx 2 \text{ cm}^{-1}$. This is shown in Fig. 10 where the results for two samples of pure and modified

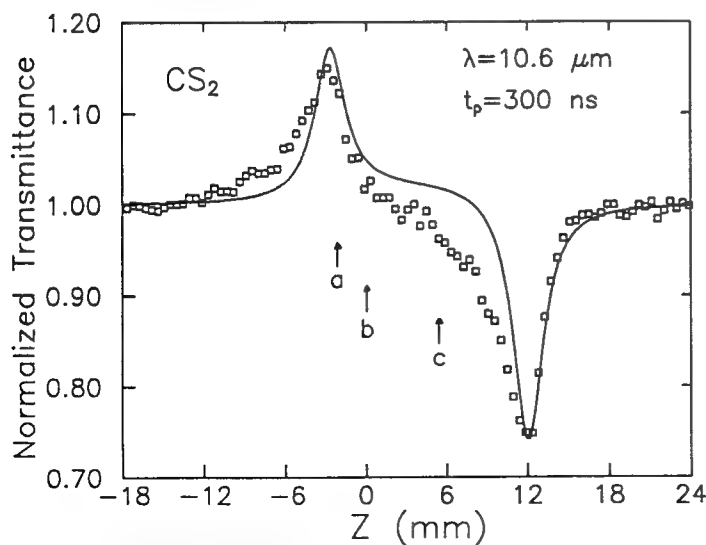


Fig. 9. The measured Z-scan of a 24-mm thick CS₂ sample using 300-ns TEA CO₂ laser pulses at 10.6 μm . The theoretical fit (solid curve) is obtained based on thermal self-defocusing in CS₂. The arrows on the z -axis indicate the positions at which the limiting data of Fig. 2 were obtained. Because $n_0 \neq 1$, the curve is no longer symmetric about $z = 0$.

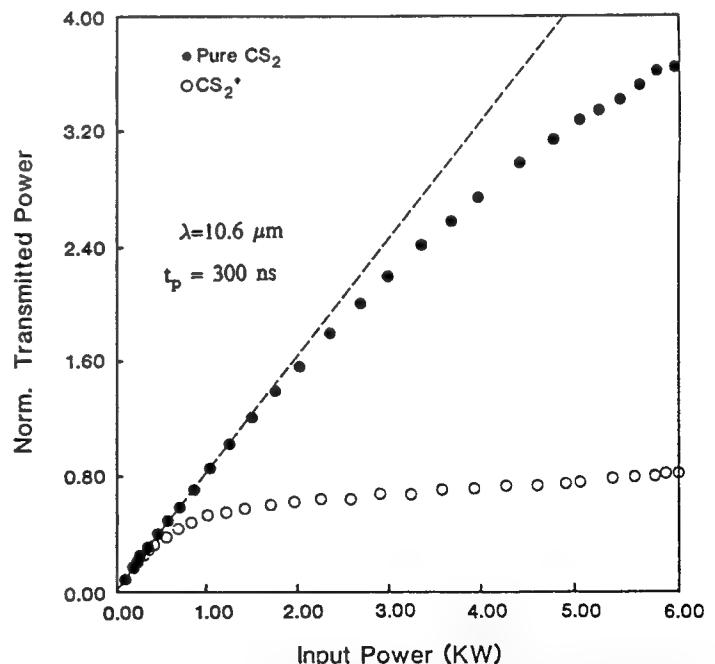


Fig. 10. A low-threshold fluence limiter at 10.6 μm using modified CS₂ ($\alpha \approx 2 \text{ cm}^{-1}$) as compared to pure CS₂ ($\alpha \approx 0.22 \text{ cm}^{-1}$). The measurements were obtained using a 3-mm cell placed at the transmittance valley.

CS₂ are compared for a 3-mm cell positioned in the transmittance valley.

Liquid CS₂ is also well known for its strong optical Kerr effect with a relatively dispersionless nonlinear index $\gamma \approx +3 \cdot 4 \times 10^{-14} \text{ cm}^2/\text{W}$ ($n_2 \approx 1.3 \times 10^{-11} \text{ esu}$).²²⁻²⁴ This effect was ignored when the thermal nonlinearity was dominant as was the case with 30-ns pulses. With picosecond pulses, however, $t_p \ll t_{ac}$ and nonlocal nonlinearities such as thermal or electrostriction no longer dominate. Thus, the reorientational Kerr effect with ≈ 2 picosecond decay time²² becomes the dominant mechanism for nonlinear refraction. Using 130-ps "optical free-induction decay" pulses at 10.6 μm (Ref. 25) and a peak power of 350 kW, we performed Z-scans with the 24-mm CS₂ cell. The result as shown in Fig. 11 exhibits a valley-peak configuration showing self-focusing indicative of the positive sign of the Kerr coefficient. The theoretical fit in Fig. 11 with $S = 0.4$ is obtained using $n_2 = 1.5 \times 10^{-11} \text{ esu}$, which is in close agreement with previously reported values of n_2 in CS₂ measured in the visible and near IR regions.^{23,24} Note that use of gentler focusing gives a larger diffractive length ($z_0 = 4 \text{ mm}$ or $l = 3.7$), resulting in the disappearance of the rather flat portion of the Z-scan that was more visible in Fig. 9.

A quick estimate of the nonlinear phase shifts can be evaluated from Eq. (15) and L_{eff} as obtained from Fig. 6 for both nanosecond and picosecond Z-scan experiments.

6. CONCLUSION

We have shown that limiting in thick Kerr-like media may be simply modeled using a modification of the aberration-free approximation. For small nonlinear phase shifts ($\Theta < 2$), this model shows excellent agreement with our Z-scan and limiting experiments. Therefore, we conclude that the method is of considerable use both in experimental measurement of n_2 in thick media and in designing optimized limiting devices.

This extension of our ability to measure n_2 in media thicker than the depth of focus may find application for media where the nonlinearity is small and the laser beam must be focused very tightly to see a measurable effect. This is exemplified by our picosecond 10.6- μm measurement of n_2 in CS₂, shown in Fig. 11. Here, $l = 3.7$ so that $l_{eff} \approx 1.5$, whereas if a truly

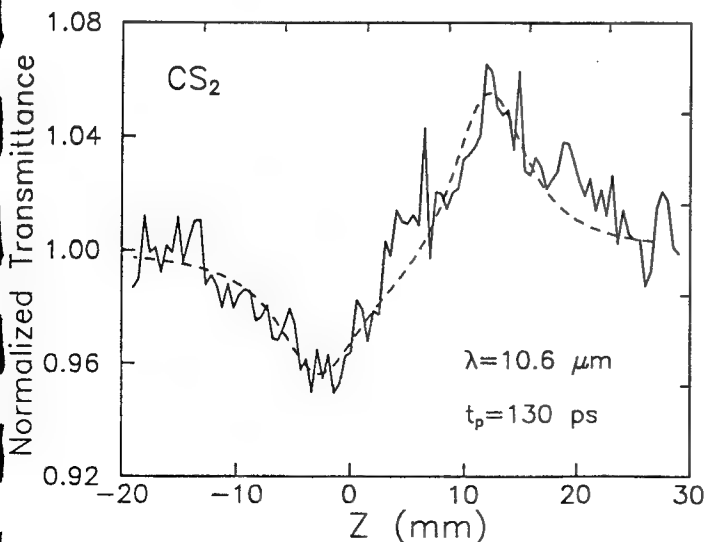


Fig. 11. The measured Z-scan of the 24-mm CS₂ sample using 130-ps CO₂ laser pulses. The broken line is the calculated result using $n_2 = 1.5 \times 10^{-11} \text{ esu}$. Here $S = 0.4$ giving $a = 5.4$.

thin sample were used, $l_{eff} \ll 1$. Given that the result shown in Fig. 11 was obtained with the maximum energy available from our picosecond source, a measurement of n_2 would not have been possible with a thin sample. Furthermore, we have shown that a quick estimate of the nonlinear coefficient can be deduced from the Z-scan transmittance curve of a thick media by using the calculated effective interaction length l_{eff} , introduced in Sec. 3.

The results of this modeling as applied to limiting indicate that the minimum limiting threshold is obtained by positioning the focus at the front (or rear) surface of the sample for a negative (or positive) nonlinearity, respectively. In both cases this corresponds to the Z-scan valley. Such a conclusion might lead one to believe that such limiters are inherently prone to damage, because a positive n_2 with a long propagation path leads to catastrophic beam collapse. Similarly, for a negative n_2 , the beam must be focused on the damage-prone front surface. However, other geometries for limiting may be envisioned that do not have this problem. For example, the simple addition of a second lens behind the sample will reverse the order of peak and valley in some plane after the lens. Thus, for a negative n_2 , the limiting is optimized with the focus at the rear surface.²⁶ Although to consider the optimization of other possible geometries is beyond the scope of this paper, the method of analysis introduced here should be adequate for such a task. However, the model has been applied to a purely refractive third-order nonlinearity in the presence of linear absorption. Nonlinear absorption, such as occurs in semiconductor limiters, has not yet been included.³

In light of the conclusions made here, the observations reported in the "Chinese Tea" paper¹⁵ are easily understood as being due to simple thermal defocusing. The reported sign change of the nonlinearity was not in fact a sign change, but simply the consecutive observation of the transmission "valley" to "peak" as the sample position was changed with respect to focus.

7. APPENDIX

To examine the validity and limitations of the "constant shape" approximation, we compare Eq. (9) in the limit of the small phase distortion with that of Ref. 10, which was obtained using the Fresnel wave optics approach.

The far field condition imposed by having $D \gg 1$ (see Fig. 1) along with the small phase distortion assumption ($|\Delta\Phi_0| < 1$) will reduce Eq. 9 to

$$\frac{w_a^2}{w_0^2} = D^2 \left(1 - \frac{4x\Delta\Phi_0/a}{(1+x^2)^2} \right). \quad (18)$$

The on-axis ($S \approx 0$) irradiance is then inversely proportional to the beam area ($\pi w_a^2/2$). Therefore, the normalized on-axis transmittance is simply obtained as

$$T(\Delta\Phi_0, x) \approx 1 + \frac{\Delta\Phi_0}{a} \frac{4x}{(1+x^2)^2}. \quad (19)$$

The extrema (peak and valley) of the transmittance can be obtained from $dT/dx = 0$. This gives $x_{p,v} = \pm 1/\sqrt{3}$ as compared to the more rigorous result of ± 0.858 as given in Ref. 10. The peak-valley transmittance difference can, therefore, be deduced as

$$\Delta T_{p-v} = T(\Delta\Phi_0, x_p) - T(\Delta\Phi_0, x_v) = p|\Delta\Phi_0|, \quad (20)$$

where $p = 3\sqrt{3}/(2a)$. Equating this value for p with the value of $p \approx 0.406$ (Ref. 10) yields $a \approx 6.4$, indicating the significance of introducing this correction factor into the aberration-free approximation theory.

3. ACKNOWLEDGMENTS

We gratefully acknowledge the support of the National Science Foundation grant ECS #8617066, DARPA/CNVEO, ARO, and the Florida High Technology and Industrial Council.

9. REFERENCES

1. R. C. C. Leite, S. P. Porto, and T. C. Damen, "The thermal lens effect as a power-limiting device," *Appl. Phys. Lett.* 10, 100-101 (1967).
2. W. E. Williams, M. J. Soileau, and E. W. Van Stryland, "Optical switching and n_2 measurements in CS_2 ," *Opt. Commun.* 50, 256-260 (1984).
3. E. W. Van Stryland, Y. Y. Wu, D. J. Hagan, M. J. Soileau, and K. Mansour, "Optical limiting with semiconductors," *J. Opt. Soc. Am.* 5, 1980-1989 (1988).
4. J. H. Hermann, "Simple model for a passive optical power limiter," *Opt. Acta* 32, 541-547 (1985).
5. A. E. Kaplan, "External self-focusing of light by a nonlinear layer," *Radiophys. Quantum Electron.* 12, 692-696 (1969).
6. E. W. Van Stryland, H. Vanherzeele, M. A. Woodall, M. J. Soileau, A. L. Smirl, S. Guha, T. G. Boggess, "Two-photon absorption, nonlinear refraction, and optical limiting in semiconductors," *Opt. Eng.* 25, 613-623 (1985).
7. J. R. Hill, G. Parry, and A. Miller, "Nonlinear refraction index changes in CdHgTe at 175 K with 1.06 μm radiation," *Opt. Commun.* 43, 151-156 (1982).
8. T. F. Boggess, S. C. Moss, I. W. Boyd, and A. L. Smirl, "Picosecond nonlinear-optical limiting in silicon," in *Ultrafast Phenomena IV*, D. H. Huston and K. B. Eisenthal, eds., Springer-Verlag, New York, pp. 202 (1984).
9. M. Sheik-Bahae, A. A. Said, and E. W. Van Stryland, "High sensitivity, single beam n_2 measurements," *Opt. Lett.* 14, 955-957 (1989).
10. M. Sheik-Bahae, A. A. Said, T. H. Wei, D. J. Hagan, and E. W. Van Stryland, "Sensitive measurement of optical nonlinearities using a single beam," *IEEE J. Quantum Electron.* 26, 760-769 (1990).

11. M. Sheik-Bahae, A. A. Said, D. J. Hagan, M. J. Soileau, and E. W. Van Stryland, "Simple analysis and geometric optimization of passive optical limiters based on internal self-action," in *Materials for Optical Switches and Limiters*, Proc. SPIE 1105, 146-153 (1989).
12. D. J. Hagan, E. W. Van Stryland, M. J. Soileau, Y. Y. Wu, and S. Guha, "Self-protecting semiconductor optical limiters," *Opt. Lett.* 13, 315-317 (1988).
13. S. A. Akhmanov, A. D. Sukhorokov, and R. V. Khokhlov, "Self-focusing and diffraction of light in a nonlinear medium," *Sov. Phys. Usp.* 10, 609 (1968).
14. A. Yariv and P. Yeh, "The application of Gaussian beam formalism to optical propagation in nonlinear media," *Opt. Commun.* 27, 295-298 (1978).
15. H. J. Zhang, J. H. Dai, P. Y. Wang, and L. A. Wu, "Self-focusing and self-trapping in new types of Kerr media with large nonlinearities," *Opt. Lett.* 14, 695-696 (1989).
16. G. M. Zverev and V. A. Pashkov, "Self-focusing and laser radiation in solid dielectrics," *Sov. Phys. JETP* 30, 616 (1970).
17. M. J. Soileau, W. E. Williams, N. Mansour, and E. W. Van Stryland, "Laser-induced damage and the role of self-focusing," *Opt. Eng.* 28, 1133-1144 (1990).
18. J. H. Marburger, "Progress in quantum electronics," J. H. Sanders and S. Stenholm, eds., Pergamon, New York, p. 35 (1977).
19. M. D. Feit and J. A. Fleck, Jr., "Beam nonparaxiality, filament formation, and beam breakup in the self-focusing of optical beams," *J. Opt. Soc. Am. B* 5, 633-640 (1988).
20. J. N. Hayes, "Thermal blooming of laser beams in fluids," *Appl. Opt.* 2, 455-461 (1972).
21. V. Raman and K. S. Venkataraman, "Determination of the adiabatic piezooptic coefficient of liquids," *Proc. R. Soc. London A* 171, 137 (1939).
22. P. P. Ho and R. R. Alfano, "Optical Kerr effects in liquids," *Phys. Rev. A* 20, 2170-2187 (1979).
23. I. Golub, Y. Beaudoin, and S. L. Chin, "Nonlinear refractions in CS_2 at 10.6 μm ," *Opt. Lett.* 13, 488-491 (1988).
24. P. Thomas, A. Jares, and B. P. Stoicheff, "Nonlinear refractive index and "DC" Kerr constant of liquid CS_2 at 10.6 μm ," *IEEE J. Quantum Electron.* QE-10, 493-494 (1974).
25. M. Sheik-Bahae and H. S. Kwok, "Characterizations of a picosecond CO_2 laser system," *Appl. Opt.* 24, 666-670 (1985).
26. J. A. Hermann and P. B. Chapple, "External self-focusing and in a two-lens system: shift and compression of the focal profile," Submitted to *J. Mod. Opt.*

Biographies and photographs not available.

MEASUREMENTS OF THIRD ORDER OPTICAL NONLINEARITIES OF NEMATIC LIQUID CRYSTALS

P. Palffy-Muhoray, H.J. Yuan, L. Li and Michael A. Lee
Liquid Crystal Institute
Kent State University
Kent, OH 44242, USA

and

J.R. DeSalvo, T.H. Wei, M. Sheik-Bahae, D.J. Hagan, and E.W. Van Stryland
CREOL
University of Central Florida
Orlando, FL 32826, USA

ABSTRACT

In order to better understand the physical mechanisms responsible for the large observed optical nonlinearities of nematic liquid crystals, we have carried out nonlinear absorption and nonlinear refraction measurements on the pure liquid crystals 5CB and 8CB, and the liquid crystal mixture E7 using picosecond, nanosecond and millisecond pulses. We have used the recently developed Z-scan method¹⁻², a sensitive single-beam technique which allows the determination of the sign and magnitude of the nonlinear refraction and the magnitude of the nonlinear absorption for aligned samples³. We have performed these measurements on aligned samples at wavelengths of 514nm and 532nm. In addition, we have studied the temperature dependence of the nonlinear refractive indices. Possible mechanisms responsible for the observed nonlinearities are discussed.

2. Z-SCAN TECHNIQUE

The schematic of the setup for the Z-scan experiment is shown in Fig. 1. A Gaussian laser beam is focused at $z=0$ plane, and the transmittance of a nonlinear medium through a finite aperture at $z=+d_0$ (where d_0 is the distance from focus to aperture) is measured in the far field as a function of the sample position z .

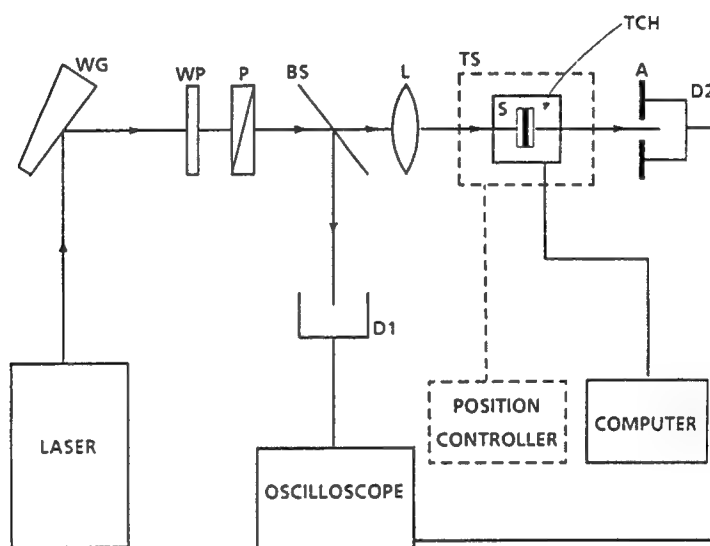


Fig. 1. Schematic of experimental setup for Z-scan measurements. The abbreviations are: WG, wedged glass; WP, wave plate; P, polarizer; BS, beam splitter; L, lens; TS, translation stage; S, liquid crystal sample; TCH, temperature controlled housing; A, aperture; D1 and D2, photodiode detectors.

The following example illustrates the Z-scan method. A thin sample, with thickness smaller than the diffraction length of the focused beam, with a positive nonlinear refractive index n_2 can be regarded as a thin converging lens,

$$\Delta T_{p-v} \simeq 0.406(1-A)^{0.25} < \Delta \Phi_o > \quad (2)$$

where A is the linear transmittance of the aperture, and the phase distortion $< \Phi_o >$ is

$$< \Phi_o > = \frac{2\pi}{\lambda} < \Delta n_o > L_{eff}. \quad (3)$$

The on axis index change at focus is related to the nonlinear refractive index n_2 and γ by

$$< \Delta n_o > = < \frac{n_2}{2} |E_o|^2 > = < \gamma I_o > \quad (4)$$

where E_o is the peak electric field on axis at focus.

In the case where nonlinear absorption is taking place simultaneously with nonlinear refraction, the nonlinear absorption coefficient β can be determined from an open aperture Z-scan. With β known, a finite aperture ($A < 1$) Z-scan can be performed to determine the nonlinear refractive index γ or n_2 . Detailed calculations show¹ that for a material with $\beta/2k|\gamma| \leq 1$, there exists a simple procedure to calculate γ with less than 10% error. The process is simply to divide the normalized finite aperture ($A < 1$) transmittance by the normalized open aperture one ($A = 1$); the new transmittance curve thus obtained can then be used to calculate n_2 as if $\beta = 0$.

3. EXPERIMENTAL RESULTS

The pure liquid crystals 5CB and 8CB, and the mixture E7 obtained from EMI Chemicals were used without further purification. The nematic-isotropic transition temperatures of 5CB, 8CB and E7 are 35.3°C, 40.5°C and 60°C,

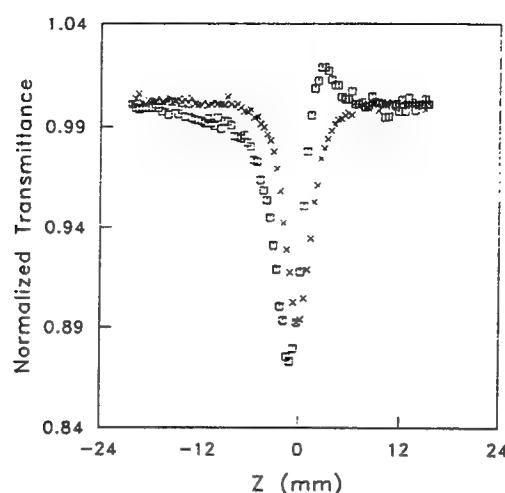


Fig. 2. Transmittance of a planar aligned $120\mu\text{m}$ thick 5CB sample in $\hat{n} \perp \mathbf{E}$ geometry using 33 ps laser pulses from a frequency doubled Nd:YAG laser. \square represents transmittance with 40% aperture; \times represents transmittance with open aperture. The peak on-axis laser intensity was $I_0 = 23.3 \text{ GW}/\text{cm}^2$.

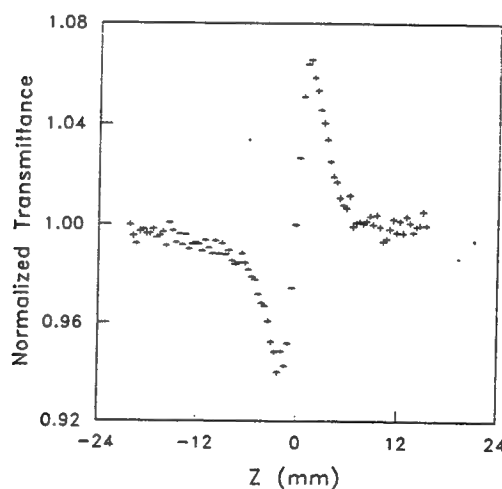


Fig. 3. Transmittance obtained by dividing the small aperture transmittance data by the open aperture transmittance of Fig. 2.

Fig.4 shows measurements for the same planar sample but with the $E \parallel \hat{n}$ geometry. The pulse duration $T_{FWHM} = 33\text{ps}$ is the same, but here the peak on-axis laser intensity is $I_0 = 8.33 \text{ GW/cm}^2$. The symbols used are the same as in Fig. 2, with \square for the 40% aperture measurements and \times for the open aperture measurements. From the open aperture measurements we obtain $\beta_{\parallel}(\text{HGA}) = 2.27 \text{ cm/GW}$. The data, after removing the nonlinear absorption effects, is shown in Fig.5 and the nonlinear refractive index in this geometry is $n_{2\parallel}(\text{HGA}) = 1.04 \times 10^{-11} \text{ esu}$.

Fig. 6 shows the results of measurements on a $120\mu\text{m}$ thick homeotropically aligned 5CB sample with $T_{FWHM} = 33\text{ps}$ pulses from the frequency doubled Nd:YAG laser with peak on-axis laser intensity $I_0 = 23.3 \text{ GW/cm}^2$. In this case, the electric field E of the laser beam is perpendicular to the nematic director \hat{n} . The open aperture measurements are shown with the symbol \times , and the 40% aperture measurements are shown in with the symbol \square . The nonlinear absorption coefficient is $\beta_{\perp}(\text{HTA}) = 0.81 \text{ cm/GW}$.

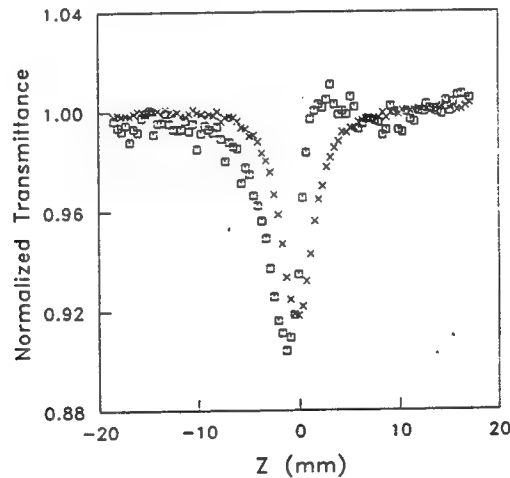


Fig. 6. Transmittance of a homeotropically aligned $120\mu\text{m}$ thick 5CB sample ($\hat{n} \perp E$) using 33 ps laser pulses from a frequency doubled Nd:YAG laser. \square represents transmittance with 40% aperture; and \times represents transmittance with open aperture. The peak on-axis laser intensity was $I_0 = 23.3 \text{ GW/cm}^2$.

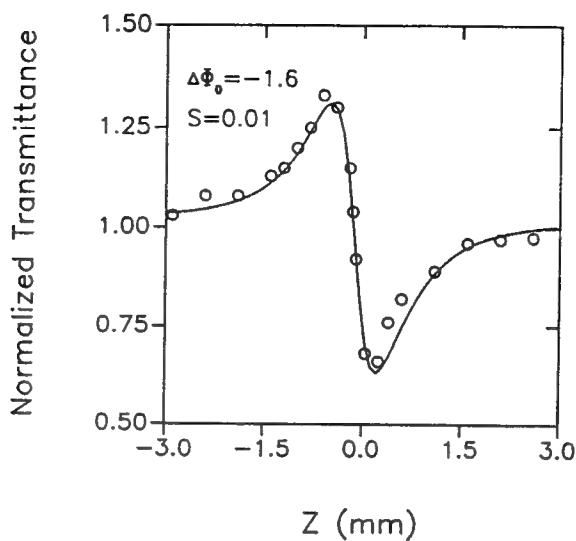


Fig. 8. Transmittance obtained by dividing the small aperture transmittance data by those obtained with open aperture. 7 ns pulses were used from a frequency doubled Nd:YAG laser. Open circles are results of division, and the solid line is the theoretical fit.

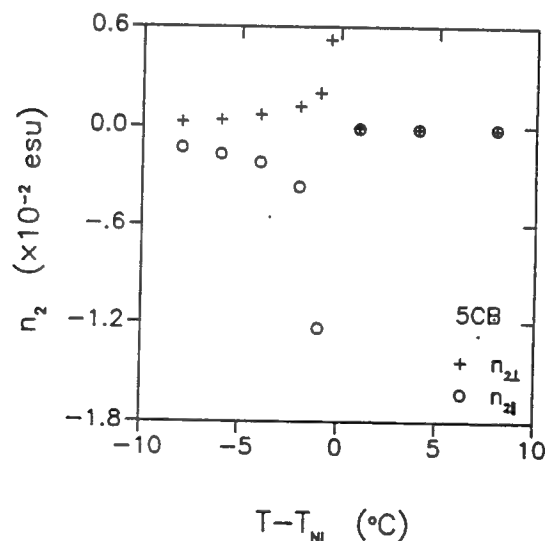


Fig. 9. The temperature dependence of $n_{2||}$ and $n_{2\perp}$ for the nematic liquid crystal 5CB using 10ms Ar^+ laser pulses at $\lambda=514$ nm. The nonlinear birefringence diverges as $(T_{NI}-T)^{-1}$.

Table II. Nonlinear refractive indices and nonlinear absorption coefficients for homogeneously aligned 5CB at 24°C.

T_{FWHM} (s)	10×10^{-2}	6.5×10^{-9}	33×10^{-12}
λ (nm)	514	532	532
$n_{2 }$ (esu)	-1.30×10^{-3}	-1.75×10^{-9}	$+1.04 \times 10^{-11}$
$n_{2\perp}$ (esu)	$+0.26 \times 10^{-3}$	$+0.25 \times 10^{-9}$	$+0.69 \times 10^{-11}$
$\beta_{ }$ (cm/GW)		265	2.27
β_{\perp} (cm/GW)		36	0.78

4. DISCUSSION AND CONCLUSIONS

All measurements reported in this paper were carried out using a single laser pulse at each sample position. Using 33 ps pulses at $\lambda=532$ nm, we measured both nonlinear refractive indices and absorption coefficients for nematic liquid crystal 5CB in both $\hat{n} \perp E$ and $\hat{n} \parallel E$ geometries using the Z-scan technique. For both polarizations we observed self-focusing. Electronic effects likely dominate in these picosecond measurements, although optical field induced changes in the orientational order could also contribute. Calculations to estimate the extent of this contribution are currently under way. The population of excited states may also contribute to the nonlinear response. If fast electronic effects dominate, then it may be possible to relate the measured anisotropies of both n_2 and β to the results of molecular hyperpolarizability calculations.

In the 10 ms pulse measurements at $\lambda=514$ nm we have observed strong nonlinear refraction and nonlinear birefringence. Self defocusing occurs in the $E \parallel \hat{n}$ geometry where the polarization is parallel to the director, and self focusing in the $E \perp \hat{n}$ geometry. The nonlinear birefringence is strongly temperature dependent with $\Delta n_2 = n_{2\perp} - n_{2||} \approx 1.4 \times 10^{-2} (T_{NI} - T)^{-1}$ esu·K. In our geometry, director reorientation is not expected to occur because there is no

REFERENCES

1. M. Sheik-Bahae, A.A. Said and E.W. Van Stryland, *Opt. Lett.* 14, 955 (1989).
2. M. Sheik-Bahae, A.A. Said, T.H. Wei, D.J. Hagan, E.W. Van Stryland, *IEEE J. Quantum Electron.* QE-26, 760 (1990).
3. H.J. Yuan, L. Li and P. Palffy-Muhoray, *SPIE Proc.* 1307 (1990).
4. N.V. Tabiryan, A.V. Sukhov and B.Ya. Zel'dovich, *Mol. Cryst. Liq. Cryst.* Special Topics XIX, 136, 1,(1986).
5. I.C. Khoo, in '*Progress in Optics, XXVI*', ed. E. Wolf (North Holland, New York, 1988).
6. I. Janossy, in '*Perspectives in Condensed Matter Physics*', ed. L. Miglio, (Kluwer Academic Publisher, 1990).
7. P. Palffy-Muhoray, in '*Liquid Crystals - Applications and Uses*', ed. B. Bahadur, (World Scientific, Singapore, 1990).
8. M.J. Weber, D. Milam, and W.L. Smith, *Opt. Eng.* 17, 463 (1978).
9. S.R. Friberg and P.W. Smith, *IEEE J. Quantum Electron.* QE-23, 2089 (1987).
10. P.A. Madden, F.C. Saunders and A.M. Scott, *IEEE J. Quantum Electron.* QE-22, 1287 (1986).
11. W.E. Williams, M.J. Soileau, and E.W. Van Stryland, *Opt. comm.* 50, 256 (1984).
12. E. Santamato, G. Abbate and P. Maddalena, *Phys. Rev. A* 36, 2389 (1987).

Degenerate Four-Wave Mixing Measurements of High Order Nonlinearities in Semiconductors

**E. J. Canto-Said
D. J. Hagan
J. Young
Eric W. Van Stryland**

**Reprinted from
IEEE JOURNAL OF QUANTUM ELECTRONICS
Vol. 27, No. 10, October 1991**

Degenerate Four-Wave Mixing Measurements of High Order Nonlinearities in Semiconductors

E. J. Canto-Said, D. J. Hagan, *Member, IEEE*, J. Young, and Eric W. Van Stryland, *Senior Member, IEEE*

Abstract—We describe degenerate four-wave mixing experiments on ZnSe and CdTe semiconductor samples with picosecond laser pulses at wavelengths below the bandgap. Nonlinearities of third, fifth, and seventh order are observed and the mechanisms for each are identified. In all of our measurements, we observe a fast third order nonlinearity. For two-photon absorbers, this is attributed to contributions from both the real (refractive) and imaginary (absorptive) parts of the third-order susceptibility. Below the two-photon absorption edge, the nonlinearity is purely refractive. The higher order effects are due to carriers generated by multiphoton excitation. In ZnSe at 0.532 μm , carriers are generated by two-photon absorption such that a fifth order nonlinearity arises from the change in index due to these carriers, a sequential $\chi^{(3)}:\chi^{(1)}$ nonlinearity. From such measurements we determine the refractive index change per photoexcited carrier pair and the density dependence of the carrier diffusion coefficient. Analogous signals are observed in CdTe at 1.064 μm . The seventh order nonlinearity observed in ZnSe at 1.064 μm results from the refractive index contribution of carriers generated by three-photon absorption.

I. INTRODUCTION

WE report a series of picosecond degenerate four-wave mixing (DFWM) studies conducted in ZnSe and CdTe at wavelengths of 0.532 and 1.064 μm . The DFWM signal shows a fast third order nonlinearity, as well as higher order slowly decaying nonlinearities due to multiphoton absorption generated carriers. We attribute this signal to the combined effects of the real and imaginary parts of the third order susceptibility $\chi^{(3)}$. The imaginary part corresponds to two-photon absorption (2PA), while the real part is due to bound-electronic nonlinear refraction (index n_2), as opposed to a free-carrier effect [1]. From our measurements, we obtain the absolute value of the third order nonlinear susceptibility for both ZnSe and CdTe. This, combined with independent 2PA mea-

surements, allows us to extract the real part of the susceptibility which corresponds to the nonlinear refraction.

We also observe a rapid third order nonlinear effect which is dominant at low incident irradiances in both semiconductors when all three beams are temporally coincident (zero delay). Fifth and seventh order nonlinear effects are evident, depending on wavelength, when the gratings are probed at time delays greater than the pulse-width to eliminate the signal from the fast third order effect. These higher order refractive nonlinearities are attributed to the refractive effect of carriers generated by 2PA (fifth order) and 3PA (seventh order). Most of the experiments discussed here consist of the generation of a modulated carrier density or carrier grating created by interfering two of the three beams made coincident in the semiconductor sample. Diffraction of a third beam from this grating produces a DFWM signal yielding information on the nonlinearities resulting from the photogenerated carriers and their decay mechanisms [2], [3]. Decay of this signal, which is the phase conjugate of one of the two interfering beams, takes place due to carrier diffusion and recombination. An expression for the diffraction efficiency at long temporal delays is obtained from coupled-wave theory [4]. This expression leads to a calculation of the index of refraction change per carrier pair per unit volume generated via 2PA in ZnSe at 0.532 μm . Measurements of the grating decay for several pump-probe angles gives values for the carrier diffusion and recombination lifetimes in ZnSe at 0.532 μm .

After describing the experimental techniques in Section II, we identify in Section III-A the dominant nonlinearities in the two materials ZnSe and CdTe. We determine these to be fast third order nonlinearities, due to the same processes which give rise to the effects of bound-electronic refraction and two-photon absorption, while higher order effects are due to free-carrier refraction. In Section III-B we describe our measurements of the absolute magnitude of the combined third order susceptibilities. Studies of higher order effects due to free-carrier gratings are discussed in Section III-C. In order to obtain a quantitative measurement of the carrier induced nonlinearities, in Section III-D we develop an expression for the diffraction efficiency of these carrier gratings and hence find a value for the free-carrier refractive index coefficient in ZnSe. By measuring the angular dependence of the grating decay, we determine the carrier diffusion coefficient as a function of carrier density.

Manuscript received December 28, 1990; revised May 1, 1991. This work was supported in part by the National Science Foundation by Grant ECS#8617066, DARPA/CNVEO, and the Florida High Technology and Industry Council.

E. J. Canto-Said is with McLennan Physical Laboratories, The University of Toronto, Toronto, Ont., Canada M5S 1A7.

D. J. Hagan is with the Department of Physics, Center for Research in Electro-Optics and Lasers (CREOL), University of Central Florida, Orlando, FL 32816.

J. Young is with the Department of Physics, Heriot Watt University, Edinburgh EH14 4AS, Scotland.

E. W. Van Stryland is with the Departments of Physics and Electrical Engineering, Center for Research in Electro-Optics and Lasers (CREOL), University of Central Florida, Orlando, FL 32816.

IEEE Log Number 9101808.

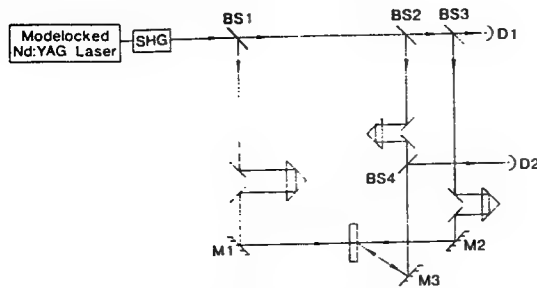


Fig. 1. Schematic of experimental DFWM apparatus. D_1 is the input pulse energy monitor, while D_2 monitors the phase-conjugate signal pulse energy.

II. EXPERIMENTAL TECHNIQUE

In our experiments the “backward” DFWM geometry is used. A schematic of the experimental geometry using single 43 ps (FWHM) $1.064\ \mu\text{m}$ pulses, or 30 ps (FWHM) $0.532\ \mu\text{m}$ pulses is shown in Fig. 1. The picosecond, Gaussian spatial profile pulses are derived from a Q -switched mode-locked Nd:YAG laser system operating at $1.064\ \mu\text{m}$. An electrooptic switch between the oscillator and amplifier ensures single pulse performance. A second-harmonic crystal (KDP) produces the $0.532\ \mu\text{m}$ pulses. This single pulse is divided into three pulses which, after passing through variable time delays, are incident on the semiconductor samples. The three pulses can be independently adjusted in amplitude and polarization using half-wave plate and polarizer combinations. Two strong beams, forward (E_f) and backward (E_b) pumps, of approximately equal irradiance are incident on the semiconductor from counterpropagating directions. A weaker beam, the probe (E_p), is incident on the sample at an angle θ with respect to E_f . The grating spacing determined from the angle θ can be varied from 1.2 to $8\ \mu\text{m}$ for the experiments at $0.532\ \mu\text{m}$. At $1.064\ \mu\text{m}$ the grating spacing is fixed at $8\ \mu\text{m}$. The conjugate wave E_c , which retraces the path of E_p , is detected by a large area integrating photodiode as are various reference beams. These detectors are calibrated against pyroelectric energy monitors. All pulsewidths quoted are measured by autocorrelation using a second-harmonic generator, while all quoted spot sizes were measured in both horizontal and vertical directions at the sample position by the method of scanning pinholes.

The samples used in this series of experiments consist of zincblende, chemical-vapor-deposition-grown polycrystalline samples of ZnSe and CdTe [5]. The ZnSe sample was 3 mm thick and the CdTe was 2 mm thick.

III. RESULTS AND DISCUSSION

A. Identification of the Nonlinear Processes

Using pulses at $0.532\ \mu\text{m}$, the DFWM signal in ZnSe was monitored as a function of input energy and pulse delay for different combinations of the polarization of the three input beams. Fig. 2 shows a plot of the signal versus the delay τ_b of E_b , with E_b polarized perpendicular to both E_f and E_p . The angle θ between the forward pump and

probe, measured outside the sample, was 13° and the peak input irradiance of each pump was $I_b = 34\ \text{MW}/\text{cm}^2$ and $I_f = 22\ \text{MW}/\text{cm}^2$. Clearly, two very distinct nonlinearities are evident from Fig. 2. Near zero delay, a large rapidly decaying signal is seen, while at longer delays, we observe a more slowly decaying signal. To better understand the two nonlinear regimes, irradiance dependence experiments were performed at different delays. Fig. 3 shows a log-log plot of the DFWM signal versus the total input irradiance, (all three input beams were varied simultaneously) at two different delay times. Fig. 3(a) shows the irradiance dependence at zero delay. The least-squares fit gives a power dependence of $I^{3.2 \pm 0.2}$, indicative of a third order nonlinearity dominant at the zero delay peak. Fig. 3(b) shows the dependence at a delay of 240 ps, with a best fit giving a power dependence of $I^{5.0 \pm 0.2}$. The fifth order dependence of the DFWM signal on the input beams can be explained by 2PA induced carrier refraction. This mechanism can be viewed as a two step process. First, a modulated carrier density is generated via 2PA; this is an $\text{Im}\{\chi^{(3)}\}$ effect. Second, a third beam diffracts off the carrier modulation; this is a $\text{Re}\{\chi^{(1)}\}$ effect. Hence, the mechanism is a sequential $\chi^{(3)}:\chi^{(1)}$ process that appears as an overall fifth order nonlinearity [6]. Studies in CdTe at $1.06\ \mu\text{m}$, where this material exhibits 2PA, reveal the same basic behavior, i.e., a fast third order signal followed by a slowly decaying fifth order signal.

B. Fast Third Order Nonlinearity

The third order effect observed near zero delay, as can be seen from Fig. 2, decays within the 30 ps pulsewidth, and appears unchanged when the pump-probe angle is varied. As DFWM is sensitive only to the absolute value of $\chi^{(3)}$, this third order signal may arise from both the real and imaginary parts of the susceptibility, $\chi_R^{(3)}$ and $\chi_I^{(3)}$, where $\chi^{(3)} = \chi_R^{(3)} + i\chi_I^{(3)}$. We define $\chi^{(3)}$ in terms of the nonlinear polarization in c.g.s.-Gaussian units by: $P = \chi^{(1)}E + \chi^{(3)}|E|^2E/2$. For all beams linearly polarized parallel to each other, $\chi^{(3)} = 6\chi_{1111}^{(3)}[11]$, as we are dealing with polycrystalline (grain size $\approx 1\ \mu\text{m}$) and hence effectively isotropic media. The source of $\chi_I^{(3)}$ in the range $E_g/2 \leq \hbar\omega \leq E_g$, is 2PA (coefficient β_2). The real part of $\chi^{(3)}$ corresponds to nonlinear refraction. Usually, this nonlinear refraction is expressed in terms of n_2 , where $n_2 = n_0 + n_2|E|^2/2$. n_2 and β_2 are related to $\chi^{(3)}$ by

$$n_2 = \frac{2\pi}{n_0} \chi_R^{(3)} \quad (1)$$

and

$$\beta_2 = \frac{4\pi\omega}{9 \times 10^8 \epsilon_0 n_0^2 c^2} \chi_I^{(3)} \quad (2)$$

where ϵ_0 is the permittivity of free space, n_0 is the linear refractive index, and c is the speed of light in vacuum. Here n_2 and $\chi^{(3)}$ are expressed in esu, and all other parameters are in MKS units. We can estimate the magnitude of n_2 from measurements of the DFWM reflectivity ϵ_c/ϵ_p .

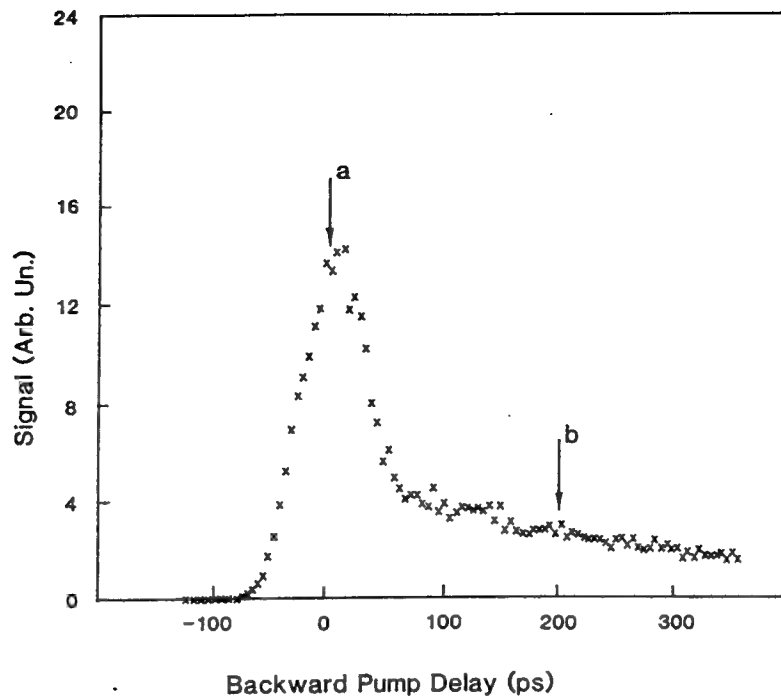


Fig. 2. Phase-conjugate signal versus backward pump delay for a 13° pump-probe angle and with the backward pump polarized perpendicular to the other two waves. The peak pump irradiances are $I_f = 22 \text{ MW/cm}^2$ and $I_b = 34 \text{ MW/cm}^2$.

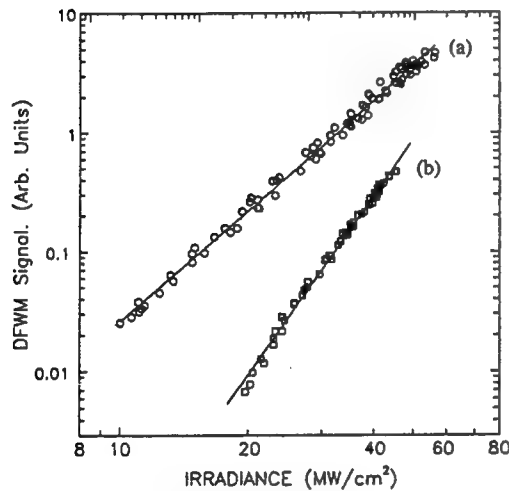


Fig. 3. Log-log plots of the phase conjugate signal versus the total input irradiance ($I_f + I_b + I_p$) as all three beams were varied together, for (a) zero delay and (b) 240 ps delay. The solid lines are best fits to the data giving power dependencies of $I^{3.1 \pm 0.2}$ and $I^{5.0 \pm 0.2}$, respectively. The other experimental parameters are as in Fig. 2.

where ϵ_c and ϵ_p are the energies of the conjugate and probe pulses, respectively. In the degenerate case for small reflectivity and in the "undepleted" pumps approximation the third order susceptibility is given by [7]

$$|\chi^{(3)}|^2 = \frac{n^4 c^4 \epsilon_0^2}{\omega^2 L^2 I_f I_b} \frac{I_c}{I_p} \quad (3)$$

where I is the peak irradiance for each beam, n is the linear refractive index, and L is the sample thickness. In (3), the ratio of irradiances is given by

$$I_c/I_p = \frac{\epsilon_c t_p}{\epsilon_p t_c} \left(\frac{w_p}{w_c} \right)^2 \quad (4)$$

For ZnSe $n = 2.7$ [9], $L = 0.3 \text{ cm}$, and the measured probe and calculated conjugate spot radii are $w_p = 1.41 \text{ mm}$ (HW1/ $e^2 M$) and $w_c = 0.99 \text{ mm}$, respectively. t_p/t_c is the ratio of the probe to conjugate beam pulsewidth which for a third order effect should equal $\sqrt{3}$, giving $I_c/I_p = 0.069$. At zero delay and $0.532 \mu\text{m}$ the DFWM energy reflectivity of ZnSe was measured to be 1.6% for $I_f = 46 \text{ MW/cm}^2$, $I_b = 65 \text{ MW/cm}^2$, and $I_p \approx I_f/10$. The 2PA coefficient for ZnSe at this wavelength is $\beta_2 \approx 5.5 \text{ cm/GW}$, [10] hence at these irradiance levels losses due to 2PA are less than 6%, so that the undepleted pumps approximation is valid. This gives for ZnSe:

$$|\chi^{(3)}| = 2.6 \times 10^{-19} \text{ m}^2/\text{V}^2 = 1.9 \times 10^{-12} \text{ esu}$$

where the estimated total absolute error in our measurement is estimated to be $\pm 30\%$. Substituting β_2 in (2) gives $\chi_f^{(3)} = 6.4 \times 10^{-12} \text{ esu}$. As this is much smaller than our measured value, this indicates that there must also be a significant real component to $\chi^{(3)}$. Using

$$|\chi^{(3)}| = \sqrt{\left(\chi_R^{(3)}\right)^2 + \left(\chi_I^{(3)}\right)^2}$$

we obtain $|\chi_R^{(3)}| = 1.8 \times 10^{-12} \text{ esu}$. Thus, the effect of the 2PA contribution to the DFWM signal is negligibly small, given our estimated errors of $\pm 30\%$. Expressing the measured $|\chi_R^{(3)}|$ in terms of n_2 as $|n_2| = 4.2 \times 10^{-11} \text{ esu}$, we find this is in close agreement with the results of

references [1], [8] who measured $n_2 = -4.4 \times 10^{-11}$ esu. using the Z-scan technique.

In order to further investigate the nature of this fast third order susceptibility, we also performed DFWM experiments in polycrystalline CdTe at $1.064 \mu\text{m}$. CdTe exhibits 2PA at this wavelength. By measuring the conjugate signal in CdTe versus the delay of the backward pump, using the same configuration as for ZnSe except using $1.064 \mu\text{m}$, we see results similar to those shown in Figs. 2 and 3 for ZnSe. At zero delay we find that the signal varies as $I^{3.1 \pm 0.3}$ while at long delays the signal varies as $I^{4.5 \pm 0.4}$. For CdTe $\beta \approx 22 \text{ cm/GW}$ [10] and thus beam depletion due to 2PA is no longer negligible for irradiance levels above $\approx 50 \text{ MW/cm}^2$. The somewhat reduced slope observed at long delays can be accounted for by beam depletion at higher irradiances. At an irradiance of $\approx 35 \text{ MW/cm}^2$ per pump, the DFWM reflectivity for CdTe is 14.8% at zero delay. This yields a third order susceptibility of $|\chi^{(3)}| = 1.1 \times 10^{-11}$ esu. The 2PA coefficient in CdTe at $1.06 \mu\text{m}$ has been measured as $\beta_2 = 22 \text{ cm/GW}$. [10] Hence, $\chi^{(3)} = 5.6 \times 10^{-11}$ esu, giving $|\chi_R^{(3)}| = 9.5 \times 10^{-11}$ esu, and $|n_2| = 2.1 \times 10^{-10}$ esu. Once again, this is in remarkably close agreement with Z-scan results, which gave -2×10^{-10} esu [8].

DFWM experiments were also performed in ZnSe at $1.064 \mu\text{m}$ where it exhibits three-photon absorption. At irradiance levels below 1 GW/cm^2 per pump only a zero delay peak was observed that varied as $I^{2.8 \pm 0.3}$, indicating the dominance, once again, of a third order nonlinearity. The DFWM signal as a function of delay of the backward pump is shown in Fig. 4, while in Fig. 5 we show a log-log plot of the irradiance dependence of the signal at zero delay. As the phase-conjugate reflectance measured at this wavelength was very much smaller than 4%, the comparative method used previously for determining $\chi^{(3)}$ could not be used in this case. Therefore, $\chi^{(3)}$ was determined by comparison with the known CS_2 value of $n_2 = 1.3 \times 10^{-11}$ esu, and hence $|\chi_{\text{eff}}^{(3)}| = 5.6 \times 10^{-12}$ esu. [12] In order to make such a comparative measurement, we must account for differences in refractive index, surface reflectance and lengths of the two samples by using the following relationship [13]

$$\frac{|\chi_{\text{eff}}^{(3)}(\text{ZnSe})|^2}{|\chi_{\text{eff}}^{(3)}(\text{CS}_2)|^2} = \left[\frac{n_{\text{ZnSe}}}{n_{\text{CS}_2}} \right]^4 \times \text{signal ratio} \times \frac{L_{\text{CS}_2}^2 (1-R)_{\text{CS}_2}^4}{L_{\text{ZnSe}}^2 (1-R)_{\text{ZnSe}}^4} \quad (5)$$

where R is the surface reflectance and the signal ratio is the ratio of observed conjugate signal energies for ZnSe and CS_2 , respectively. Comparison of the signals from the two materials under identical experimental conditions gives a value of $|\chi^{(3)}| \approx 1.2 \pm 0.35 \times 10^{-11}$ esu for ZnSe at $1.064 \mu\text{m}$. As there is no 2PA in this wavelength region for ZnSe, the imaginary part of $\chi^{(3)}$ is zero. Thus, we can rewrite our result as $|n_2| = 2.7 \pm 0.9 \times 10^{-11}$

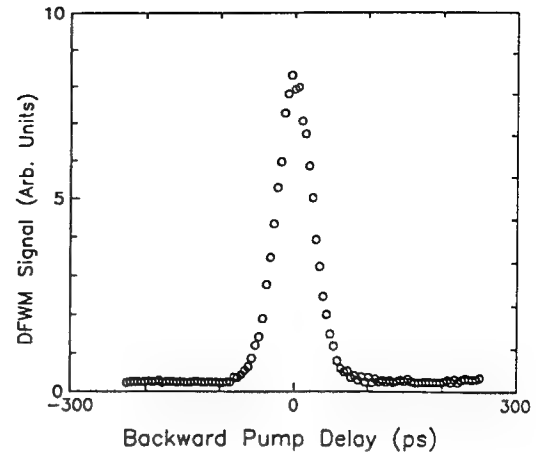


Fig. 4. DFWM signal in ZnSe at $1.064 \mu\text{m}$ versus backward pump delay with all beams parallel and both pump irradiances $\approx 600 \text{ MW/cm}^2$.

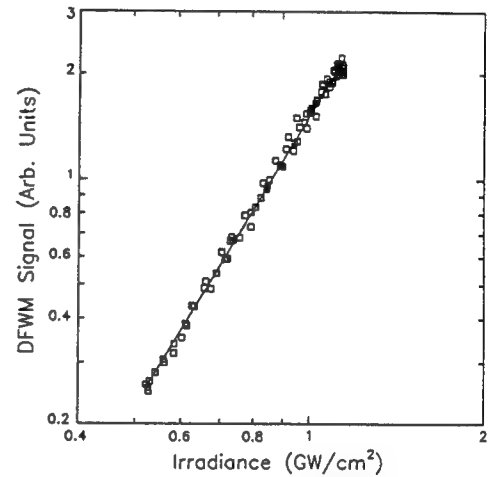


Fig. 5. Logarithmic plot of the DFWM signal in ZnSe at $1.064 \mu\text{m}$ versus the total incident irradiance, at zero delay. The solid line is a best fit to the data, giving an $I^{2.8 \pm 0.3}$ dependence.

esu. This also agrees within errors with Z-scan results, which gave $n_2 = +1.7 \times 10^{-11}$ esu [8].

C. Studies of the Carrier Nonlinearities in ZnSe and CdTe

Neglecting diffusion and recombination within the picosecond pulses, [14] the growth of the carrier density N generated in a 2PA semiconductor is governed by

$$\frac{dN}{dt} = \frac{\beta_2 I^2}{2\hbar\omega} \quad (6)$$

where β_2 is the 2PA coefficient. Here we have ignored the z dependence of N which is valid for our experiments in ZnSe at $0.532 \mu\text{m}$ where the irradiance is low and, therefore, the 2PA is small ($\leq 6\%$ loss). In the DFWM geometry $I^2 = (E_f + E_b + E_p)^4$. We concentrate only on those terms which contain $E_f E_p^*$ (for the large period grating) and neglect terms in $|E_p|^2 E_p^*$ since $|E_p| \ll |E_f|, |E_b|$. Then the component of I^2 effective in producing a grating leading to the DFWM signal is $I_{\text{eff}}^2 = (n_0 c \epsilon_0 / 2)^2 (|E_f|^2 +$

$2|E_b|^2[2E_fE_p^* + \text{c.c.}]$. Note that while I_{eff}^2 is real, it has been broken down into the sum of two complex conjugate terms. The first gives rise to the conjugate signal, the second to a term which radiates with a wave vector of $k_p - 2k_f$, and hence is not phasematched. As both terms are required to form the sinusoidal grating, we must retain both of them to calculate the solution of the diffusion equation; however, the effective contribution to the signal is $I_{\text{eff}}^2/2$. Thus, the effective carrier density is given by

$$N_{\text{eff}}(t) = \frac{1}{2} \left(\frac{\beta_2}{2\hbar\omega} \right) \int_{-\infty}^t I_{\text{eff}}^2 dt'.$$

The resulting nonlinear polarization source term P_{NL} is proportional to $E_b N_{\text{eff}}$. In the case where E_b is not temporally overlapped with E_p or E_f , I_{eff}^2 becomes $2(E_f E_p^* + \text{c.c.})|E_f|^2$ (effects of grating decay will be treated in the next section). Assuming phase distortions on E_p to be small, $E_p^* = E_{p0} \exp \{ik_p(z \cos \theta + x \sin \theta)\}$ and $E_f = E_{f0} \exp \{-ik_f z\}$, so that N_{eff} can be written as

$$N_{\text{eff}}(t) = \left(\frac{\beta_2}{2\hbar\omega} \right) \left(\frac{nc\epsilon_0}{2} \right)^2 \cdot 2 \cos [K_g x] \int_{-\infty}^t |E_f(t')|^3 |E_p(t')| dt'. \quad (7)$$

where $K_g = k_f - k_p$ is the grating wave vector. In the limit of small θ , $K_g = 2\pi\theta/\lambda$, where λ is the free-space wavelength. Since $E_c \propto P_{\text{NL}}$, the total irradiance dependence of the DFWM signal is

$$I_c \propto I_b I_p I_f^3. \quad (8)$$

In order to verify this, we measured the DFWM signal in CdTe at 1.064 μm as a function of I_f , only with the backward pump delayed by 240 ps. The signal was plotted logarithmically against I_f and the slope of the resulting straight line was found to be 2.8 ± 0.3 in accordance with (8).

A similar expression can be obtained when the carriers are generated via a three-photon absorption process. Following an analogous procedure, the end result is a seventh order dependence of the DFWM signal on the input beams as three-photon absorption is an $\text{Im } \chi^{(5)}$ process. In our experiments in ZnSe at 1.064 μm , we find that at higher input irradiances, on the order of 1.2 GW/cm^2 per strong pump, a free-carrier tail became evident. Fig. 6 shows a log-log plot of the irradiance dependence for $\tau_b = 240$ ps. A best fit gives a dependence of $I^{6.9 \pm 0.2}$, agreeing closely with the power of 7 expected for 3PA induced carrier refraction. Under our experimental conditions with the backward pump delayed, the DFWM signal dependence is

$$I_c \propto I_b I_p I_f^5. \quad (9)$$

Fig. 7 shows a similar plot to Fig. 6, except that in this case only I_f is varied resulting in a power dependence of $I^{5.1 \pm 0.3}$, close to the power of 5 predicted in (9).

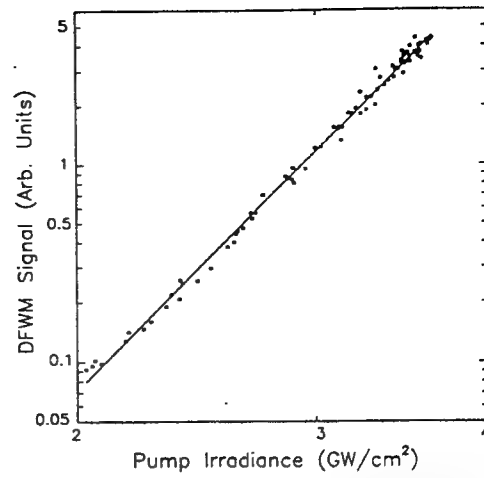


Fig. 6. Logarithmic plot of the DFWM signal resulting from the three-photon absorption generated carrier grating in ZnSe at 1.064 μm versus the total input irradiance. The measurement was performed with the backward pump delayed by 240 ps. The solid line is a best fit to the data, indicating an $I^{6.9 \pm 0.2}$ dependence.

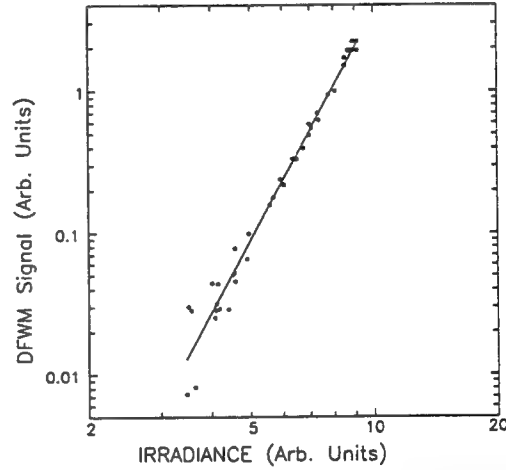


Fig. 7. As Fig. 6, but with only the forward pump varied and the backward pump and probe held at constant irradiance. The forward pump energy was not calibrated for this experiment. The solid line is the best fit, giving an $I^{5.1 \pm 0.3}$ dependence for the DFWM signal in this case.

D. Temporal Evolution of Diffraction Efficiency in ZnSe

In order to determine the refractive index change per excited carrier pair per unit volume, σ_n (units of cm^3), we need to measure the diffraction efficiency of the carrier grating in the absence of the third order signal. This necessitates measurement of the DFWM signal at a delay long compared to the pulsewidth. σ_n is thus obtained by fitting the theoretical diffraction efficiency to the measured value. However, to calculate this diffraction efficiency we require a knowledge of the temporal dependence of the density of 2PA-generated carriers $N(x, t)$. This is governed by [15]

$$\frac{dN_{\text{eff}}(x, t)}{dt} + \frac{N_{\text{eff}}(x, t)}{\tau} - D \frac{d^2 N_{\text{eff}}(x, t)}{dx^2} = \frac{\beta I_{\text{eff}}^2(x, t)}{2\hbar\omega} \quad (10)$$

where τ is the carrier decay time and D is the carrier diffusion coefficient. We use a constant carrier lifetime as the carrier densities in our experiments are several orders of magnitude too low to have significant bimolecular or Auger recombination. This is verified by the I^5 power dependence in our experiments. Since the beam radius is much larger than the grating period we assume the diffusion occurs only in the direction x between grating maxima and minima. Further, we have assumed low excitation such that the spatial amplitude of I^2 does not vary in the propagation direction z , i.e., $\beta IL \ll 1$ which was true for the irradiance levels used. The solution to the diffusion equation is then

$$N_{\text{eff}}(x, t) = \frac{\beta_2}{2\hbar\omega} \exp(-t/\tau_g) \cdot \int_{-\infty}^t \exp(t'/\tau_g) I_{\text{eff}}^2(x, y, t') dt' \quad (11)$$

where τ_g is the total decay time of the grating, given by $\tau_g = \tau_D \tau_R / (\tau_D + \tau_R)$. Here τ_D is the grating diffusion lifetime and τ_R is the carrier recombination lifetime [14]. We have again assumed that E_b is time delayed. Note that the product $E_f E_p^*$ in I_{eff}^2 has a term $2|E_f||E_p| \exp(iK_g x)$, where $K_g = 2\pi/\Lambda$, and $\Lambda = \lambda/[2n \sin(\theta/2)]$ is the grating spacing. Hence $1/\tau_g = (4\pi^2 D)/\Lambda^2 + 1/\tau$ [16]. For the sample thickness and grating spacings used, we were always in the thick grating limit. The diffraction efficiency for weak excitation of a thick lossless phase grating was derived by Kogelnik [4], [17] to be

$$\eta = \sin^2 \left(\frac{\Delta n \pi L}{\lambda \cos \theta} \right) \approx \left(\frac{\Delta n \pi L}{\lambda \cos \theta} \right)^2 \quad (12)$$

where $\Delta n = \sigma_n N_{\text{eff}}$. The energy diffracted into the conjugate beam ϵ_c is then given by temporally and spatially integrating the product of the diffraction efficiency η and the beam irradiance incident on the grating giving

$$\epsilon_c(\tau_b) = \int_{-\infty}^{\infty} \eta(x', y', t') I_b(x', y', t' - \tau_b) dx' dy' dt' \quad (13)$$

where $I_b(x, y, t) = I_{b0} \exp[-(x^2 + y^2)/w^2 - (t^2/t_p^2)]$. Here τ_b accounts for the time delay of the backward pump with respect to the interfering beams. Note for $\eta = 1$, (13) gives the energy in the backward pump ϵ_b . Defining η_c as the energy diffraction efficiency, we find

$$\eta_c = \epsilon_c/\epsilon_b = \xi(1 + \xi)^2 \frac{2\sqrt{2}\beta_2^2 \sigma_n^2 I_f^4 \sqrt{\pi} t_p L^2}{80 (\hbar\omega)^2 \lambda^2 \cos^2 \theta} \exp(t_p^2/4\tau_g^2) \cdot \int_{-\infty}^{\infty} \exp(-(t' - \tau_b)^2/t_p^2) \exp(-2t'/\tau_g) \cdot \{1 + \text{erf}[\sqrt{2}/t_p(t' - t_p^2/4\tau_g)]\}^2 dt' \quad (14)$$

where ξ is the ratio of I_p to I_f . Note that this derivation is valid only when the beam widths are large compared to the grating period, when the length of interaction of the interfering beams is much larger than the sample thick-

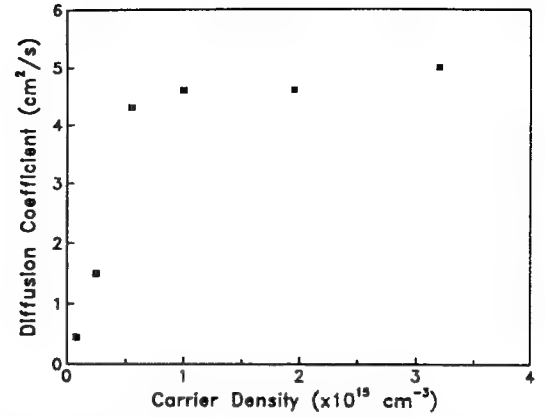


Fig. 8. Plot of measured diffusion coefficient versus peak carrier density.

ness, and when absorption of the interacting beams is small. Given $\beta_2 = 5.5 \text{ cm/GW}$ [10] at 532 nm for ZnSe, a numerical fit of (14) yields σ_n and τ_g .

The experimentally measured value for the diffraction efficiency for ZnSe at 0.532 μm at $\tau = 240 \text{ ps}$ is $\eta = 6.8 \times 10^{-5}$ for a pump-probe angle θ of 13° . The grating decay rate τ_g was determined from the best fit exponential decay to the data at long delays for several input irradiances. Using $t_p = 18 \text{ ps}$ (HW1/eM in irradiance), and $\tau_g = 247 \text{ ps}$, and numerically integrating (14), we obtain $|\sigma_n| = 5.1 \pm 2.5 \times 10^{-21} \text{ cm}^3$. This is considerably larger than the result of another recent measurement of σ_n that obtained $\sigma_n = -0.8 \pm 0.2 \times 10^{-21}$ [18] and probably indicates the difficulty of obtaining accurate absolute values of nonlinearities from multiple beam diffraction efficiency measurements. Note that the measurement in [18] showed the sign of σ_n to be negative [3]. The uncertainties stated are relative fitting errors. The absolute error bars on σ_n are estimated to be $\approx 50\%$.

We were also able to extract the density dependence of the carrier diffusion coefficient by measuring the angular dependence of the grating decay time for a number of different pump irradiances and therefore different carrier densities [19]. This dependence is plotted in Fig. 8. We find that for irradiances above 40 MW/cm^2 , corresponding to carrier densities $> 5 \times 10^{14} \text{ cm}^{-3}$, D maintains a constant value of $4.5 \pm 0.5 \text{ cm}^2/\text{s}$, while below $5 \times 10^{14} \text{ cm}^{-3}$, the diffusion coefficient decreases rapidly. For these densities we do not expect to have any density dependence of either the mobility or the recombination lifetime. We therefore propose that the small diffusion coefficient at low density may be due to trapping of the 2PA excited carriers. As the carrier density is increased, these traps become filled and the diffusion is dominated by the ambipolar mobility. This high density result is comparable to the result of $2.5 \pm 0.5 \text{ cm}^2/\text{s}$ obtained by Jarasiunas and Gerritsen, but their carrier density is not given [3]. Using data from Hall mobility measurements in ZnSe, [20] we calculate an ambipolar mobility of $26 \text{ cm}^2 \text{ V}^{-1} \text{ s}^{-1}$, corresponding to a diffusion coefficient of $0.7 \text{ cm}^2/\text{s}$ at 300°K . This is in good agreement with our low density measurements, since the Hall mobility measurements are

performed with low dopant densities. It should be noted that over the entire range of carrier densities measured, the carrier nonlinearity is fifth order. This rules out the possibility that the traps are filled by linear absorption. These measurements also gave an estimate for the recombination lifetime of $\tau_R = 725 \pm 275$ ps.

IV. CONCLUSION

We have presented a series of picosecond transient DFWM measurements performed in two direct-gap II-VI semiconductors. For ZnSe, large third order nonlinear mechanisms were observed both at 0.532 and 1.064 μm . The origin of these fast third order nonlinearities is believed to be due to both two-photon absorption and the bound electronic Kerr effect [8]. The magnitude of the nonlinear susceptibilities found were $|\chi^{(3)}| \approx 1.9 \pm 0.57 \times 10^{-11}$ esu and $1.2 \pm 0.35 \times 10^{-11}$ esu at 0.532 μm and 1.064 μm , respectively. Similarly, for CdTe a third order effect yielded a $|\chi^{(3)}| \approx 7.2 \pm 2.1 \times 10^{-10}$ esu at 1.064 μm . Combined with independent measurements [10] of the two-photon absorption coefficients in these materials, this indicates that the measured susceptibility in ZnSe at 532 nm and CdTe at 1.06 μm is dominated by nonlinear refraction. As there is no 2PA in ZnSe at 1.06 μm , we conclude that this susceptibility is entirely refractive. Other data [8] indicates that in ZnSe n_2 is negative at 0.532 μm and positive at 1.064 μm , while in CdTe at 1.064 μm , n_2 is negative. Higher order nonlinearities (higher than third order) were also observed in both semiconductors. These nonlinearities are attributed to nonlinear absorption induced carrier refraction.

When carriers are excited via the absorption of two photons, we have seen a fifth order dependence of the conjugate field on the input fields as expected. In the same manner, for carrier excitation achieved via the absorption of three photons, an effective seventh order nonlinearity was found.

For ZnSe at 0.532 μm and for low excitation, a value for the index of refraction per carrier pair generated of $\sigma_n \approx 5.1 \pm 2.5 \times 10^{-21} \text{ cm}^3$ was estimated. By monitoring the grating decay times for different grating spacings, the density dependence of the diffusion coefficient was extracted.

ACKNOWLEDGMENT

We wish to thank B. S. Wherrett for his critical review of this paper, G. M. Moharam for useful discussions on the diffraction efficiency calculations, and E. Miesak for help in taking data.

REFERENCES

- [1] M. Sheik-Bahae, A. A. Said, T. H. Wei, D. J. Hagan, and E. W. Van Stryland, "Sensitive measurement of optical nonlinearities using a single beam," *IEEE J. Quantum Electron.*, vol. 26, pp. 760-769, 1990.
- [2] R. K. Jain and M. B. Klein, "Degenerate four-wave mixing in semiconductors," in *Optical Phase Conjugation*, R. A. Fisher, Ed. New York: Academic, 1983, pp. 307-415.
- [3] K. Jarasiunas and H. J. Gerritsen, "Ambipolar diffusion measurements in semiconductors using nonlinear transient gratings," *Appl. Phys. Lett.*, vol. 33, pp. 190-193, 1978.
- [4] H. Kogelnik, "Coupled wave theory for thick hologram gratings," *Bell Syst. Tech. J.*, vol. 48, pp. 2909-2947, 1969.
- [5] Sample obtained from II-VI, Inc., Saxonburg, PA.
- [6] E. W. Van Stryland, Y. Y. Wu, D. J. Hagan, M. J. Soileau, and K. Mansour, "Optical limiting with semiconductors," *J. Opt. Soc. Amer. B.*, vol. 5, pp. 1980-1989, 1988.
- [7] J. J. Wynne, "Optical third-order mixing in GaAs, Ge, Si, and InAs," *Phys. Rev.*, vol. 178, pp. 1295-1303, 1969.
- [8] M. Sheik-Bahae, D. J. Hagan, and E. W. Van Stryland, "Dispersion and band-gap scaling of the electronic Kerr effect in solids associated with two-photon absorption," *Phys. Rev. Lett.*, vol. 65, pp. 96-99, 1989.
- [9] Landolt-Börnstein, *Numerical Data and Functional Relationships in Science and Technology*, Volume 17, Semiconductors, K.-H. Hellwege, Ed. New York: Springer-Verlag, 1982.
- [10] E. W. Van Stryland, H. Vanherzeele, M. A. Woodall, M. J. Soileau, A. L. Smirl, S. Guha, T. F. Boggess, "Two-photon absorption, nonlinear refraction and optical limiting in semiconductors," *Opt. Eng.*, vol. 24, pp. 613-623, 1985.
- [11] P. N. Butcher, "Nonlinear optical phenomena," *Bulletin 200*, Ohio State Univ., Columbus, OH, 1965.
- [12] M. J. Soileau, W. E. Williams, and E. W. Van Stryland, "Optical power limiter with picosecond response time," *IEEE J. Quantum Electron.*, vol. QE-19, p. 731, 1983.
- [13] R. Adair, L. L. Chase, and S. A. Payne, "Nonlinear refractive index of optical crystals," *Phys. Rev. B*, vol. 39, pp. 3377-3350, 1987.
- [14] J. H. Bechtel and W. L. Smith, "Two-photon absorption in semiconductors with picosecond laser pulses," *Phys. Rev. B*, vol. 13, pp. 3515-3522, 1976.
- [15] W. Van Roosbroeck, "The transport of added current carriers in a homogeneous semiconductor," *Phys. Rev.*, vol. 91, pp. 282-289, 1953.
- [16] J. R. Salcedo, A. E. Siegman, D. D. Diott, and M. D. Fayer, "Dynamics of energy transport in molecular crystals: the picosecond transient grating method," *Phys. Rev. Lett.*, vol. 41, p. 131, 1978.
- [17] H. J. Eichler, P. Gunter, and D. W. Pohl, *Laser-Induced Dynamic Gratings*, Springer Series in Optical Sciences, J. M. Enoch, D. L. MacAdam, A. L. Schawlow, K. Shimoda, and T. Tamir, Eds. New York: Springer-Verlag, 1988.
- [18] A. A. Said, M. Sheik-Bahae, D. J. Hagan, E. J. Canto-Said, Y. Y. Wu, J. Young, T. H. Wei, and E. W. Van Stryland, "Nonlinearities in semiconductors for optical limiting," in *Proc. SPIE, Electro-Optical Materials for Switches, Coatings, Sensor Optics, and Detectors*, Orlando, 1990, conf. 1370.
- [19] D. J. Hagan, H. A. MacKenzie, H. A. Al Attar, and W. J. Firth, "Carrier diffusion measurements in InSb by the angular dependence of degenerate four-wave mixing," *Opt. Lett.*, vol. 10, p. 187, 1985.
- [20] B. Ray, *II-VI compounds*. Edinburgh: Pergamon, 1969, ch. 6.

E. J. Canto-Said, photograph and biography not available at the time of publication.

D. J. Hagan (M'87), for a photograph and biography, see p. 1309 of the June 1991 issue of this JOURNAL.

J. Young, photograph and biography not available at the time of publication.

Eric W. Van Stryland (M'84-SM'90), for a photograph and biography, see p. 1309 of the June 1991 issue of this JOURNAL.

MEASUREMENTS OF THIRD ORDER OPTICAL NONLINEARITIES OF NEMATIC LIQUID CRYSTALS

P. Palffy-Muhoray, H.J. Yuan, L. Li and Michael A. Lee

Liquid Crystal Institute

Kent State University

Kent, OH 44242, USA

and

J.R. DeSalvo, T.H. Wei, M. Sheik-Bahae, D.J. Hagan, and E.W. Van Stryland

CREOL

University of Central Florida

Orlando, FL 32826, USA

ABSTRACT

In order to better understand the physical mechanisms responsible for the large observed optical nonlinearities of nematic liquid crystals, we have carried out nonlinear absorption and nonlinear refraction measurements on the pure liquid crystals 5CB and 8CB, and the liquid crystal mixture E7 using picosecond, nanosecond and millisecond pulses. We have used the recently developed Z-scan method¹⁻², a sensitive single-beam technique which allows the determination of the sign and magnitude of the nonlinear refraction and the magnitude of the nonlinear absorption for aligned samples³. We have performed these measurements on aligned samples at wavelengths of 514nm and 532nm. In addition, we have studied the temperature dependence of the nonlinear refractive indices. Possible mechanisms responsible for the observed nonlinearities are discussed.

1. INTRODUCTION

The nonlinear optical response of liquid crystals has become the subject of increased study in recent years⁴⁻⁷. A large variety of mechanisms ranging from collective reorientation to electronic hyperpolarizability can contribute to the optical nonlinearities in these materials. We have carried out measurements of third order responses of the liquid crystals 5CB (4-cyano-4'-*n*-pentybiphenyl), 8CB (4-cyano-4'-*n*-octylbiphenyl) and E7 (a commercial mixture of biphenyls and terphenyls). In order to better understand the mechanisms contributing to the observed nonlinearities, we used geometries where director reorientation is not expected to occur, and we measured the nonlinearities on timescales ranging from milliseconds to picoseconds.

Several techniques have been developed in the past to measure the nonlinear refractive index n_2 , or, equivalently, the real part of the third order susceptibility $\chi^{(3)}$. These include nonlinear interferometry⁸, wave mixing^{9,10}, and beam-distortion measurements¹¹. Interferometry and wave mixing are potentially sensitive techniques, but require relatively complex experimental arrangements. Beam-distortion measurements, on the other hand, require precise beam scans followed by complex wave-propagation analyses. We find that the single-beam Z-scan technique^{1,2} is attractive because of its simplicity and sensitivity in measuring both the nonlinear refraction and nonlinear absorption. This technique is based on the transformation of phase distortion induced by the nonlinear medium to amplitude distortion during beam propagation.

In this paper, we report our measurements using the Z-scan technique of the intensity dependent third order nonlinearities of the pure liquid crystals 5CB and 8CB and the mixture E7 using nanosecond and picosecond pulses from frequency doubled Nd:YAG lasers and millisecond pulses from a CW Ar⁺ laser. Both the nonlinear refractive indices and nonlinear absorption coefficients for light polarized parallel (denoted by the subscript \parallel) and perpendicular (denoted by \perp) to the director have been measured.

2. Z-SCAN TECHNIQUE

The schematic of the setup for the Z-scan experiment is shown in Fig. 1. A Gaussian laser beam is focused at $z=0$ plane, and the transmittance of a nonlinear medium through a finite aperture at $z=+d_0$ (where d_0 is the distance from focus to aperture) is measured in the far field as a function of the sample position z .

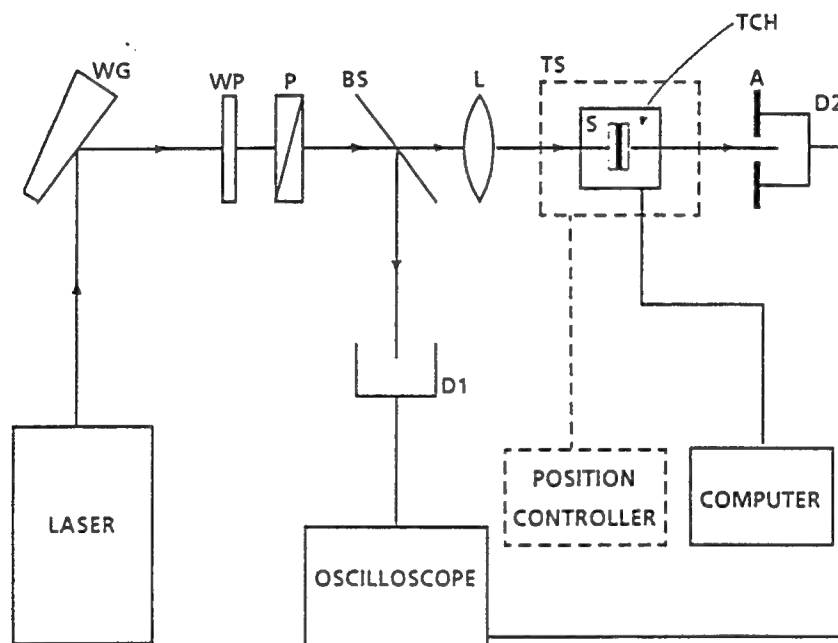


Fig. 1. Schematic of experimental setup for Z-scan measurements.

The abbreviations are: WG, wedged glass; WP, wave plate; P, polarizer; BS, beam splitter; L, lens; TS, translation stage; S, liquid crystal sample; TCH, temperature controlled housing; A, aperture; D1 and D2, photodiode detectors.

The following example illustrates the Z-scan method. A thin sample, with thickness smaller than the diffraction length of the focused beam, with a positive nonlinear refractive index n_2 can be regarded as a thin converging lens,

whose focal length varies with intensity; that is, with sample position along the z -axis. Starting the scan far from the focal point at large negative values of z , the beam intensity is low and nonlinear effects are negligible. Initially, therefore, the transmittance remains essentially constant. As the sample is moved closer to the focus, the beam intensity increases significantly, leading to a self-focusing in the sample. This self-focusing with the sample positioned at small negative values of z will cause the beam to broaden at the aperture, decreasing the measured transmittance. As the sample is moved through the focus to a post-focal position, the same self-focusing causes the beam to narrow at the aperture, increasing the transmittance. Consequently a pre-focal minimum (valley) followed by a post-focal maximum (peak) in the transmittance versus sample position curve corresponds to a positive n_2 ; and conversely a peak followed by a valley is a signature of a negative n_2 . The magnitude of n_2 can be evaluated using the analysis presented in Refs. 1 and 2.

In addition, the nonlinear absorption can be determined by performing a Z-scan with the aperture removed (open aperture Z-scan). The transmittance in this case is independent of the effects of nonlinear refraction, so that the change in transmittance gives a measure of the nonlinear absorption.

While a complete analysis is given in Refs. 1 and 2, an estimate of both the nonlinear absorption coefficient β and the nonlinear refractive index n_2 can be made as follows. For an open aperture Z-scan, the total change in transmittance ΔT_{abs} in moving the sample from a position far from focus ($z >$ diffraction length) to focus ($z=0$) is

$$\Delta T_{\text{abs}} \simeq -\frac{\beta}{2\sqrt{2}} I_0(1-R) L_{\text{eff}} \quad (1)$$

where $L_{\text{eff}} = (1 - e^{-\alpha L})/\alpha$ and α is the linear absorption coefficient, L is the sample thickness, I_0 is the on axis intensity at focus, and R is the surface reflectivity.

For a purely refractive nonlinearity, as shown in Ref. 2, the change in transmittance from peak to valley $\Delta T_{\text{p-v}}$ is linear in the (time averaged) phase distortion on axis at focus. For a finite aperture, this is given by

$$\Delta T_{p-v} \simeq 0.406(1-A)^{0.25} \langle \Delta \Phi_o \rangle \quad (2)$$

where A is the linear transmittance of the aperture, and the phase distortion $\langle \Phi_o \rangle$ is

$$\langle \Phi_o \rangle = \frac{2\pi}{\lambda} \langle \Delta n_o \rangle L_{\text{eff}}. \quad (3)$$

The on axis index change at focus is related to the nonlinear refractive index n_2 and γ by

$$\langle \Delta n_o \rangle = \langle \frac{n_2}{2} |E_o|^2 \rangle = \langle \gamma I_o \rangle \quad (4)$$

where E_o is the peak electric field on axis at focus.

In the case where nonlinear absorption is taking place simultaneously with nonlinear refraction, the nonlinear absorption coefficient β can be determined from an open aperture Z-scan. With β known, a finite aperture ($A < 1$) Z-scan can be performed to determine the nonlinear refractive index γ or n_2 . Detailed calculations show¹ that for a material with $\beta/2k|\gamma| \leq 1$, there exists a simple procedure to calculate γ with less than 10% error. The process is simply to divide the normalized finite aperture ($A < 1$) transmittance by the normalized open aperture one ($A = 1$); the new transmittance curve thus obtained can then be used to calculate n_2 as if $\beta = 0$.

3. EXPERIMENTAL RESULTS

The pure liquid crystals 5CB and 8CB, and the mixture E7 obtained from EMI Chemicals were used without further purification. The nematic-isotropic transition temperatures of 5CB, 8CB and E7 are 35.3°C, 40.5°C and 60°C,

respectively, and 8CB also exhibits a nematic - smectic A transition at 33.5°C. The liquid crystal samples were sandwiched between two 25mm x 38mm x 0.9mm glass plates. The plates were either coated with PVF (polyvinyl formal) and then buffed to achieve homogeneous (planar) alignment (HGA), or coated with silane for homeotropic alignment (HTA). The glass plates were separated by 25 μ m and 120 μ m mylar spacers. The experimental setup is shown in Fig. 1. We used frequency doubled Nd:YAG lasers, one with $T_{FWHM} = 33$ ps and the other with $T_{FWHM} = 7$ ns Gaussian pulses, and a CW Ar⁺ laser with a shutter providing 10ms square pulses for our measurements. A wave plate and polarizer combination was used to control the pulse energy, which was selected to optimize the Z-scan measurements. In the millisecond and nanosecond measurements, the temporal pulse profile was monitored using a fast photodiode D1, and the transmittance after the aperture was measured by detector D2. A converging lens ($f=125$ mm) was used to focus the Gaussian beam to a beam waist ($HWe^{-2}M$) of $w_0=14.5\mu$ m in the millisecond case, $w_0=7.5\mu$ m in the nanosecond case, and of $w_0=18.9\mu$ m in the picosecond case. The liquid crystal samples were mounted in an Instec temperature controlled housing (TCH) whose temperature was computer controlled. A Daedal translation stage (TS) was used to position the sample with $\pm 1\mu$ m resolution.

Fig. 2 shows the Z-scans (normalized transmittance as function of sample position z) of an 120 μ m thick homogeneously aligned 5CB sample for the $E \perp \hat{n}$ geometry. $T_{FWHM} = 33$ ps pulses from a frequency doubled Nd:YAG laser with peak on-axis laser intensity $I_0 = 23.3$ GW/cm² were used in this measurement. The symbols \square show the normalized transmittance with a 40% aperture before detector D2. The valley-peak configuration indicates self-focusing, while the strongly suppressed peak indicates strong nonlinear absorption occurring simultaneously with the nonlinear refraction. Measured transmittances from an open aperture Z-scan are shown with the symbol \times in Fig. 2. From this data we obtain the nonlinear absorption coefficient $\beta_{\perp}(HGA) = 0.78$ cm/GW. After removing the contribution of nonlinear absorption by dividing the finite (40% in this case) aperture transmittance by the open aperture transmittance, the antisymmetric shape of the curve is recovered. The results of the division are shown in Fig.3 with the symbol $+$. The nonlinear refractive index obtained by analysing the results of these measurements is $n_{2\perp}(HGA) = +6.9 \times 10^{-12}$ esu.

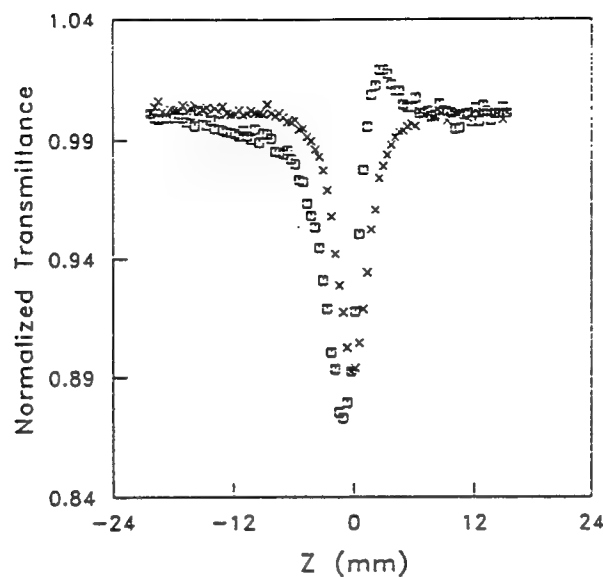


Fig. 2. Transmittance of a planar aligned $120\mu\text{m}$ thick 5CB sample in $\hat{n} \perp E$ geometry using 33 ps laser pulses from a frequency doubled Nd:YAG laser. \square represents transmittance with 40% aperture; \times represents transmittance with open aperture. The peak on-axis laser intensity was $I_0 = 23.3 \text{ GW/cm}^2$.

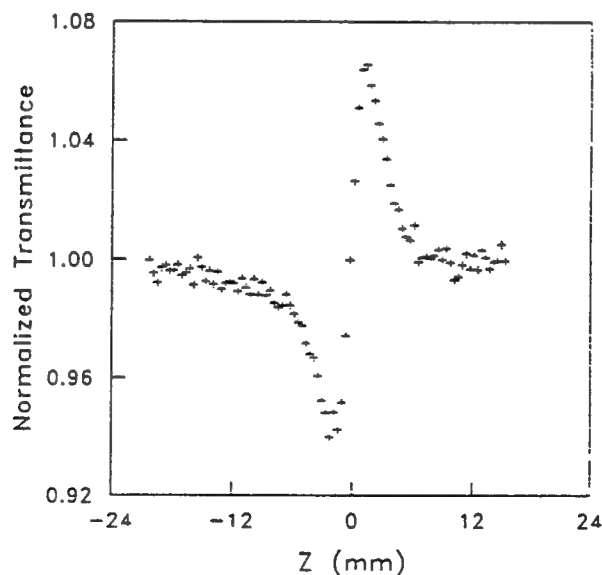


Fig. 3. Transmittance obtained by dividing the small aperture transmittance data by the open aperture transmittance of Fig.2.

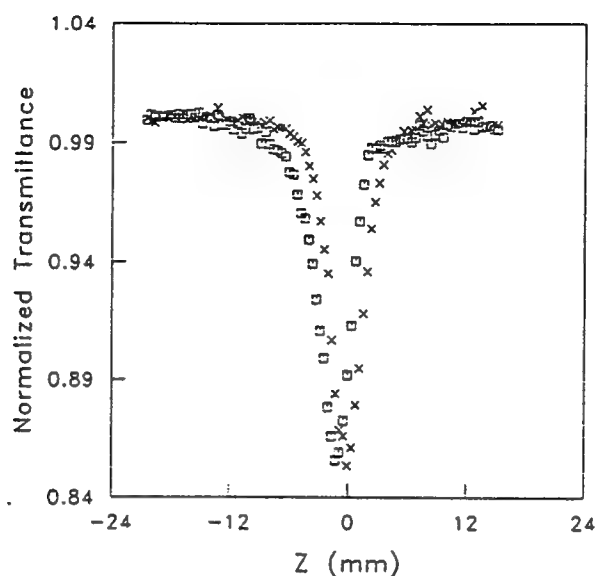


Fig. 4. Transmittance of a planar aligned 120 μm thick 5CB sample in $\hat{n}||E$ geometry using 33 ps laser pulses from a freefrequency doubled Nd:YAG laser. \square represents transmittance with 40% aperture; \times represents transmittance with open aperture. The peak on-axis laser intensity was $I_0 = 8.33 \text{ GW/cm}^2$.

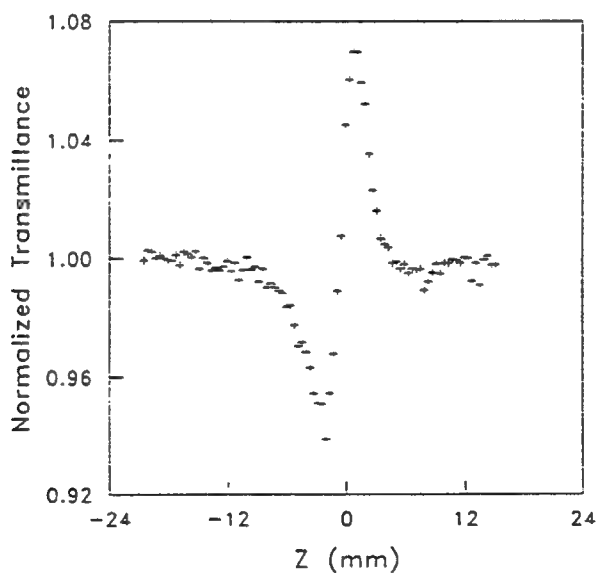


Fig. 5. Transmittance obtained by dividing the small aperture transmittance data by the open aperture transmittance of Fig.4.

Fig.4 shows measurements for the same planar sample but with the $E||\hat{n}$ geometry. The pulse duration $T_{FWHM} = 33\text{ps}$ is the same, but here the peak on-axis laser intensity is $I_0 = 8.33\text{ GW/cm}^2$. The symbols used are the same as in Fig. 2, with \square for the 40% aperture measurements and \times for the open aperture measurements. From the open aperture measurements we obtain $\beta_{||}(\text{HGA}) = 2.27\text{ cm/GW}$. The data, after removing the nonlinear absorption effects, is shown in Fig.5 and the nonlinear refractive index in this geometry is $n_{2||}(\text{HGA}) = 1.04 \times 10^{-11}\text{ esu}$.

Fig. 6 shows the results of measurements on a $120\mu\text{m}$ thick homeotropically aligned 5CB sample with $T_{FWHM} = 33\text{ps}$ pulses from the frequency doubled Nd:YAG laser with peak on-axis laser intensity $I_0 = 23.3\text{ GW/cm}^2$. In this case, the electric field E of the laser beam is perpendicular to the nematic director \hat{n} . The open aperture measurements are shown with the symbol \times , and the 40% aperture measurements are shown in with the symbol \square . The nonlinear absorption coefficient is $\beta_{\perp}(\text{HTA}) = 0.81\text{ cm/GW}$.

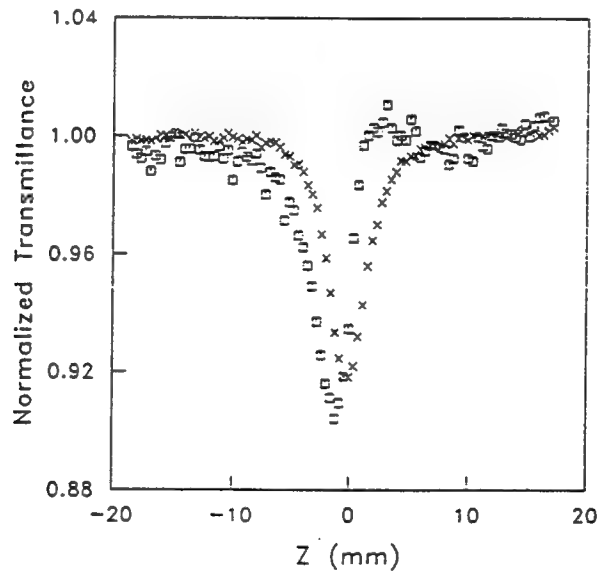


Fig. 6. Transmittance of a homoeotropically aligned $120\mu\text{m}$ thick 5CB sample ($\hat{n} \perp E$) using 33 ps laser pulses from a frequency doubled Nd:YAG laser. \square represents transmittance with 40% aperture; and \times represents transmittance with open aperture. The peak on-axis laser intensity was $I_0 = 23.3\text{ GW/cm}^2$.

The results after division are shown in Fig.7, and the nonlinear refractive index is $n_{2\perp}(\text{HTA}) = 5.7 \times 10^{-12}$ esu.

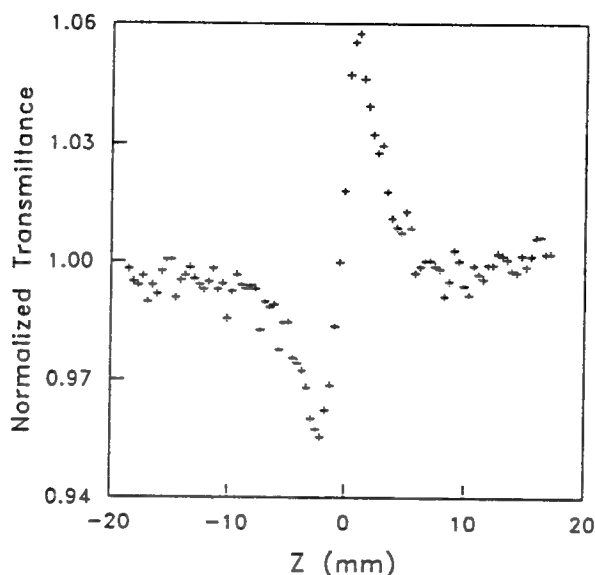


Fig. 7. Transmittance obtained by dividing the small aperture transmittance data by the open aperture transmittance of Fig.6.

We have also carried out measurements on the $25\mu\text{m}$ thick planar aligned 5CB sample in both $\hat{n} \perp E$ and $\hat{n} \parallel E$ geometries with $T_{\text{FWHM}} = 6.5\text{ns}$ Gaussian pulses from a frequency-doubled Nd:YAG laser and 10 ms square pulses from a CW Ar^+ laser. Fig.8 shows the nanosecond results measured at $T=25.0^\circ\text{C}$ in the $\hat{n} \parallel E$ geometry for a 1% aperture after division by nonlinear absorption (open aperture) data. The peak-valley configuration of the data shows a strong self-defocusing process and the nonlinear coefficients are $\beta_{\parallel}(\text{HGA}) = 265 \text{ cm/GW}$ and $n_{2\parallel}(\text{HGA}) = -1.75 \times 10^{-9}$ esu. The measurements for the same sample for $\hat{n} \perp E$ geometry give $\beta_{\perp}(\text{HGA}) = 36 \text{ cm/GW}$ and $n_{2\perp}(\text{HGA}) = +0.25 \times 10^{-9}$ esu.

In the 10 ms measurements, the nonlinear refractive indices obtained at $T=24^\circ\text{C}$ are $n_{2\parallel}(\text{HGA}) = -1.30 \times 10^{-3}$ esu and $n_{2\perp}(\text{HGA}) = +0.26 \times 10^{-3}$ esu. Fig.9 shows the temperature dependence of the measured nonlinear refractive indices for both parallel and perpendicular geometries. These results are qualitatively consistent with laser heating of the sample and the consequent reduction of orientational order.

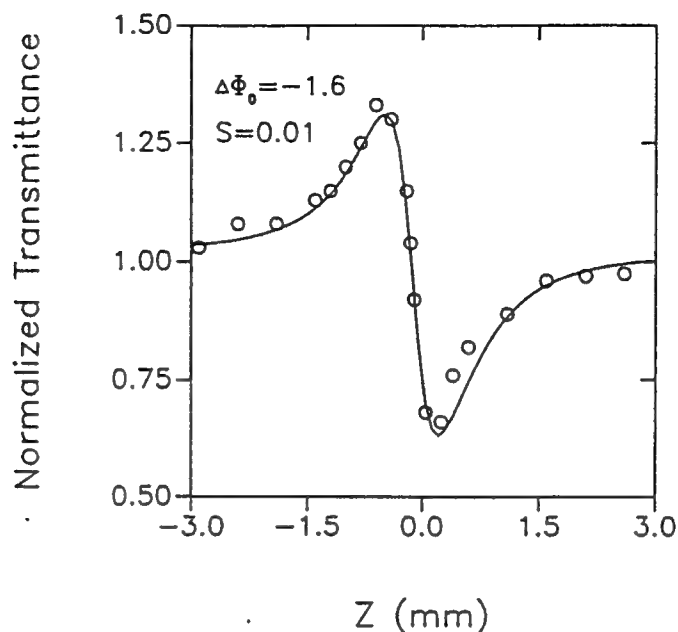


Fig. 8. Transmittance obtained by dividing the small aperture transmittance data by those obtained with open aperture. 7 ns pulses were used from a frequency doubled Nd:YAG laser. Open circles are results of division, and the solid line is the theoretical fit.

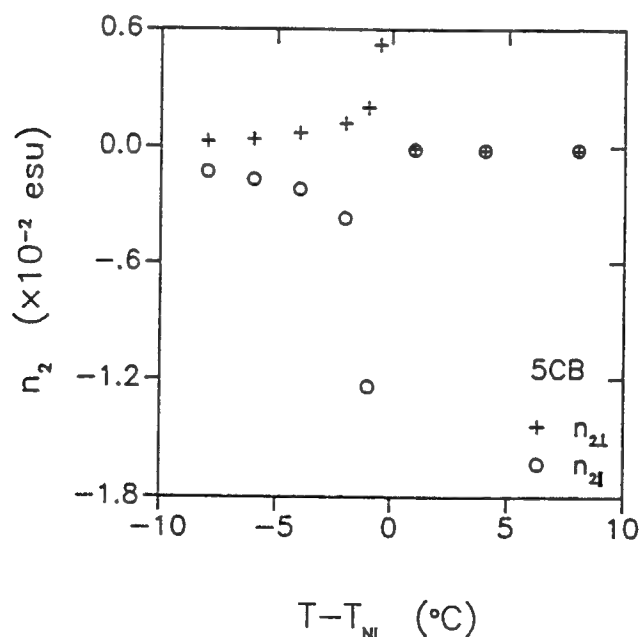


Fig. 9. The temperature dependence of $n_{2||}$ and $n_{2\perp}$ for the nematic liquid crystal 5CB using 10ms Ar^+ laser pulses at $\lambda = 514$ nm. The nonlinear birefringence diverges as $(T_{NI} - T)^{-1}$.

The nonlinear birefringence approximately follows the power law $(n_{2\perp} - n_{2\parallel}) \propto (T_{NI} - T)^{-1}$ for temperatures below the nematic to isotropic transition temperature T_{NI} . If the linear absorption and laser heating of the sample are independent of polarization, then one would expect the relation $n_{2\parallel} \simeq -2 n_{2\perp}$ to hold⁷. Deviations from this relation in our results are likely due to dichroism of our sample. In this regime (10ms Ar^+ pulses) we did not observe nonlinear absorption within the sensitivity of our experiment.

The measured nonlinear refractive indices and nonlinear absorption coefficients for the liquid crystals 5CB, 8CB and E7 at $T=24^\circ\text{C}$ and $\lambda=532\text{ nm}$ with $T_{FWHM}=6.5\text{ ns}$ pulses from a Q-switched Nd:YAG laser are summarized in Table I. The results are compared with the nonlinear refractive indices of CS_2 . For polarization parallel to the nematic director, the nonlinearities of these liquid crystals are two orders of magnitude larger than that of CS_2 . For polarization perpendicular to the nematic director, the nonlinearities are one order of magnitude larger than that of CS_2 .

Table I. Nonlinear refractive indices and nonlinear absorption coefficients for sample materials* at 24°C . $T_{FWHM} = 6.5\text{ns}$, $\lambda = 532\text{nm}$.

material	CS_2	5CB	8CB	E7
$n_{2\parallel} (\times 10^{-11}\text{esu})$	+1.2	-175	- 77	-115
$n_{2\perp} (\times 10^{-11}\text{esu})$	+1.2	+ 25	+ 11	+ 10
$\beta_{\parallel} (\text{cm/GW})$		265	246	284
$\beta_{\perp} (\text{cm/GW})$		36	20	40

*homogeneously aligned liquid crystal samples

The nonlinear refractive indices and absorption coefficients measured for liquid crystal 5CB at $T=24^\circ\text{C}$ with different pulse durations are summarized in Table II. It is interesting to note that $n_{2\parallel}$ changes sign from negative to positive as the pulse duration is changed from nano- to picoseconds indicating a change in the physical response.

Table II. Nonlinear refractive indices and nonlinear absorption coefficients for homogeneously aligned 5CB at 24°C.

T_{FWHM} (s)	10×10^{-2}	6.5×10^{-9}	33×10^{-12}
λ (nm)	514	532	532
$n_{2 }$ (esu)	-1.30×10^{-3}	-1.75×10^{-9}	$+1.04 \times 10^{-11}$
$n_{2\perp}$ (esu)	$+0.26 \times 10^{-3}$	$+0.25 \times 10^{-9}$	$+0.69 \times 10^{-11}$
$\beta_{ }$ (cm/GW)		265	2.27
β_{\perp} (cm/GW)		36	0.78

4. DISCUSSION AND CONCLUSIONS

Using 33 ps pulses at $\lambda=532$ nm, we measured both nonlinear refractive indices and absorption coefficients for nematic liquid crystal 5CB in both $\hat{n} \perp E$ and $\hat{n} || E$ geometries using the Z-scan technique. For both polarizations we observed self-focusing. Electronic effects likely dominate in these picosecond measurements, although optical field induced changes in the orientational order could also contribute. Calculations to estimate the extent of this contribution are currently under way. The population of excited states may also contribute to the nonlinear response. If fast electronic effects dominate, then it may be possible to relate the measured anisotropies of both n_2 and β to the results of molecular hyperpolarizability calculations.

In the 10 ms pulse measurements at $\lambda=514$ nm we have observed strong nonlinear refraction and nonlinear birefringence. Self defocusing occurs in the $E || \hat{n}$ geometry where the polarization is parallel to the director, and self focusing in the $E \perp \hat{n}$ geometry. The nonlinear birefringence is strongly temperature dependent with $\Delta n_2 = n_{2\perp} - n_{2||} \approx 1.4 \times 10^{-2} (T_{NI} - T)^{-1}$ esu.K. In our

geometry, director reorientation is not expected to occur because there is no torque exerted on the director by the optical field with $E \parallel \hat{n}$; and because the threshold for optical twist transition¹¹ in the $E \perp \hat{n}$ configuration is well above the intensities used in this experiment. We expect therefore that the observed nonlinearity is mainly due to laser heating of the sample. Such heating would result in changes in the orientational order parameter, the density, and consequently the refractive indices. A crude estimate of the magnitude of the thermally induced nonlinearity⁷ is consistent with our measured values. However, preliminary measurements of the temporal profile of the outgoing pulse suggest that the response time of the process is longer than the estimated thermal diffusion time. The reason for this discrepancy is not understood at this time.

In the measurements using 7 ns pulses at $\lambda = 532$ nm, we observed strong nonlinear refraction, birefringence and nonlinear absorption. The mechanisms which give rise to these large nonlinearities and large anisotropy are not well understood. It might be expected that one important contribution is again laser heating of the sample. The measured values are six orders of magnitude smaller than the millisecond results, which is comparable to the expected contribution⁷ from thermal effects with millisecond response times. However, preliminary pulse profile measurements indicate that this is a fast process, on the nanosecond scale. In addition, the large nonlinear absorption observed here, but not in the millisecond regime, suggest that excited state absorption rather than laser heating may be the responsible mechanism.

The third order nonlinearities in the liquid crystals studied with nanosecond pulses are two orders of magnitude larger than that of CS_2 . The large nonlinear refractive index and nonlinear birefringence of these materials may be useful for device applications.

5. ACKNOWLEDGEMENTS

This work was supported by DARPA through US Army CECOM Center for Night Vision and Electro-Optics. We acknowledge useful discussions with J. Kelly of the Liquid Crystal Institute at Kent State University and M. J. Soileau of CREOL at the University of Central Florida.

REFERENCES

1. M. Sheik-Bahae, A.A. Said and E.W. Van Stryland, *Opt. Lett.* 14, 955 (1989).
2. M. Sheik-Bahae, A.A. Said, T.H. Wei, D.J. Hagan, E.W. Van Stryland, *IEEE J. Quantum Electron.* QE-26, 760 (1990).
3. H.J. Yuan, L. Li and P. Palffy-Muhoray, *SPIE Proc.* 1307 (1990).
4. N.V. Tabiryan, A.V. Sukhov and B.Ya. Zel'dovich, *Mol. Cryst. Liq. Cryst.* Special Topics XIX, 136, 1, (1986).
5. I.C. Khoo, in '*Progress in Optics, XXVI*', ed. E. Wolf (North Holland, New York, 1988).
6. I. Janossy, in '*Perspectives in Condensed Matter Physics*', ed. L. Miglio, (Kluwer Academic Publisher, 1990).
7. P. Palffy-Muhoray, in '*Liquid Crystals - Applications and Uses*', ed. B. Bahadur, (World Scientific, Singapore, 1990).
8. M.J. Weber, D. Milam, and W.L. Smith, *Opt. Eng.* 17, 463 (1978).
9. S.R. Friberg and P.W. Smith, *IEEE J. Quantum Electron.* QE-23, 2089 (1987).
10. P.A. Madden, F.C. Saunders and A.M. Scott, *IEEE J. Quantum Electron.* QE-22, 1287 (1986).
11. W.E. Williams, M.J. Soileau, and E.W. Van Stryland, *Opt. comm.* 50, 256 (1984).
12. E. Santamato, G. Abbate and P. Maddalena, *Phys. Rev. A* 36, 2389 (1987).

NEW MEASUREMENT METHOD FOR NONLINEARITIES IN SEMICONDUCTORS

E.W. Van Stryland*, A.A. Said, M. Sheik-Bahae, D.J. Hagan*, E.J. Canto-Said,
Y.Y. Wu and T.H. Wei

CREOL Center for Research in Electro-Optics and Lasers University of Central Florida, Orlando, FL 32816

**also with the Department of Physics*

We describe the use of a novel method for the characterization of the nonlinear optical properties of materials which we refer to as a Z-scan. We utilize this technique along with other methods to determine the nonlinearities occurring in semiconductors when irradiated with picosecond pulses within the spectral region where two-photon absorption (2PA) is large. For example, we determine that nonlinear refraction at 532 nm in ZnSe is caused by a negative third order electronic Kerr effect in addition to the 2PA induced free-carrier refraction. We used beam distortion, and picosecond time-resolved degenerate four-wave mixing in addition to the Z-scan technique. Using these complementary characterization methods we determine the 2PA coefficient, the sign and magnitude of the bound electronic nonlinearity, n_2 and the negative refractive index change per free carrier.

1. Introduction

In this paper, we present the results of a comprehensive study of the nonlinear processes involved in semiconductors when exposed to picosecond pulses in a spectral range where two-photon absorption (2PA) is allowed, but so close to the energy band gap that direct band blocking from linear absorption or excitonic nonlinearities are present. This is spectral region of linear transparency where nonlinearities are useful for applications including passive optical limiting (OL). OL utilizes the combined effects of nonlinear absorption and nonlinear refraction in semiconductors [1-3]. An ideal passive optical limiter may be described as the optical analogue of a Zener diode circuit. It has a high linear transmission up to a certain input threshold after which the output becomes clamped to a constant value.

The nonlinearities present in this spectral range are 2PA, refraction arising from the 2PA generated free carriers and nonlinear refraction due to the electronic Kerr effect. We conducted picosecond degenerate four-wave mixing (DFWM) studies to examine the temporal response as well as the order of the refractive nonlinearities. The Z-scan technique [4] was employed to accurately de-

termine the sign and magnitude of the different refractive nonlinearities as well as the 2PA coefficient of the semiconductors. Finally beam distortion was used to verify the dominance of the nonlinearities for OL applications.

We briefly describe the theory for the irradiance and phase changes on a beam induced by these nonlinearities in section 2, and in section 3 the DFWM results are presented. In section 4 the Z-scan technique is briefly described and the results of the Z-scan measurements are presented. In section 5 we show the beam distortion measurements. Finally, in section 6 the experimental results are compared to theoretical models.

2. Theory

In all the experiments Gaussian spatial mode beams were used incident on samples thinner than the diffraction length of the beam. In this geometry the thin sample approximation can be used to describe the beam propagation inside the sample. This allows separation of the wave equation into one equation for the irradiance I and one for the phase Φ . Also with 30 ps (FWHM) pulses and at low irradiance levels we can ignore the absorption

due to the 2PA generated carriers but not carrier induced refraction [5]. This leaves the nonlinear differential equations,

$$\frac{dI}{dz} = -\alpha I - \beta I^2, \quad (1)$$

and

$$\frac{d\Delta\Phi}{dz} = k\gamma I - k\sigma N, \quad (2)$$

where α is the linear absorption coefficient, β is the 2PA coefficient, $k = 2\pi/\lambda$, λ is the wavelength of incident radiation, γ is the refractive index change due to the electronic Kerr effect, N is the density of free carriers and σ is the change in the index of refraction per free carrier pair density generated [6]. Since the free carriers are created by 2PA, the generation rate is given by

$$\frac{dN}{dt} = \frac{\beta I^2}{2\hbar\omega}. \quad (3)$$

When N is substituted in eq. (2), it becomes clear that the phase change due to the carriers depends on the square of the irradiance. Hence, the free carrier refraction appears as an effective fifth order nonlinearity [7, 8].

3. Degenerate four-wave mixing experiments

DFWM with picosecond pulses is a sensitive technique that gives information about the temporal evolution of nonlinear process in semiconductors and other materials. Two counter-propagating strong beams, forward pump E_f and backward pump E_b , are incident on the sample with a third weaker probe beam, E_p , incident at an angle θ with respect to the forward pump. Two of these beams interfere inside the sample to form a grating from which the third beam diffracts to form a conjugate signal E_c that retraces the probe path. The pulses used in these experiments are 30 ps (FWHM) pulses at 532 nm. Various combinations of polarizers and half-wave plates were placed in the path of each beam to independently change their polarization and irradiance. Figure 1 shows a plot of the conjugate signal versus the delay τ_{D} of E_b which was polarized perpendicular to E_f and E_p . Two distinct regions are present,

a fast decaying signal near zero delay and a slow decaying signal at long delays. To better understand the two nonlinear regimes, irradiance dependence experiments were performed at different delays. A log-log plot of the DFWM signal versus input irradiance (all three inputs varied) gives two different slopes as shown in the inset of Fig. 1. At zero delay a slope of 2.8 was measured indicating a third order nonlinearity and at long delays a slope of 4.9 was found. The fifth order dependence can be explained by the 2PA induced carrier refraction as mentioned in the previous section. A modulated carrier density is created via 2PA; this is an imaginary $\chi^{(3)}$ effect. Then a third beam diffracts off the carrier modulation; this is a real $\chi^{(1)}$ effect. Hence, the mechanism is a sequential $\chi^{(3)}:\chi^{(1)}$ process that appears as a fifth order nonlinearity. As to the third order effect decays within the 30 ps pulse width which is consistent with a bound electronic nonlinearity. This fast decaying effect can either be of refractive or absorptive nature as far as DFWM is concerned, Assuming that it is a refractive effect a value of $|n_2| = 4.4 \cdot 10^{-11}$ esu was extracted where n_2 is related to γ by n_2 (esu) = $n_0 c / (40\pi) \gamma$ (MKS) [7, 8]. Note that the sign of n_2 is not given by DFWM.

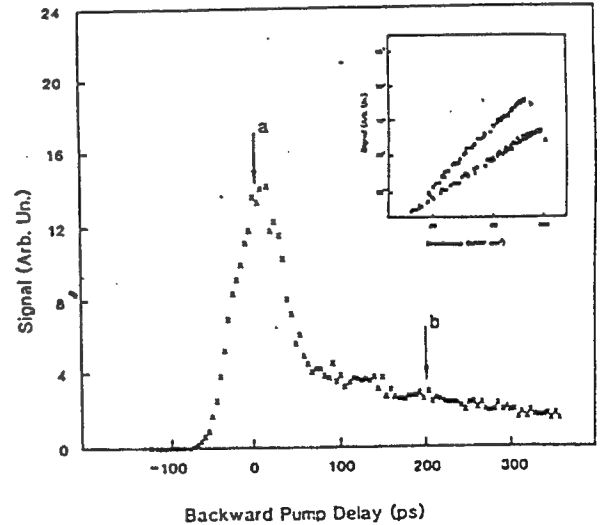


Fig. 1. The DFWM signal vs backward pump delay for 30 ps pulses at $0.53 \mu\text{m}$ in ZnSe. The inset shows a log-log plot of the conjugate signal as a function of the input irradiance at 0 ps (a) and 200 ps (b).

4. Z-scan measurements

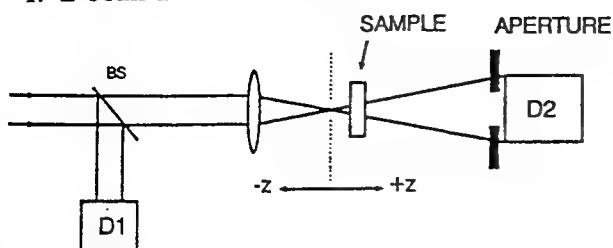


Fig. 2. The Z-scan experimental setup in which the normalized transmittance is measured as a function of the sample position z .

The Z-scan technique, which was recently developed at our laboratories, is a simple single measurement experiment technique that readily gives the sign and magnitude of nonlinear refraction as well as nonlinear absorption [9]. It is also an excellent guide for geometrical optimization of optical limiting [10]. Figure 2 shows the Z-scan experimental setup. A focused Gaussian beam is incident on the sample and transmitted beam is collected through a finite aperture in the far field into detector D_2 . D_1 monitors the input energy. Keeping the input energy fixed, the transmittance is measured as a function of the sample position relative to the focal plane. Since nonlinear refraction causes a lensing effect in the incident beam, the sample behaves as a negative or positive lens depending on the sign of the nonlinearity. As explained in reference [4] a valley-peak configuration in the Z-scan signal is a signature of a positive refractive nonlinearity and peak-valley pattern denotes a negative nonlinearity. When the aperture is removed, i.e. all the transmitted light is collected, the Z-scan is only sensitive to nonlinear absorption. For semiconductors with 2PA present, the Z-scan experiment was simulated by solving eqs. (1-3). Three parameters are to be determined β , n_2 and σ . Using 27 ps pulses (FWHM) at 532 nm Z-scan measurements were performed on a 2.7 mm thick

ZnSe sample at different input energies. With the aperture removed a Z-scan was performed at $I_0 = 0.1 \text{ GW/cm}^2$ where I_0 is the on axis peak irradiance at the focus. In this case the measurement is insensitive to nonlinear refraction and thus independently gives the nonlinear absorption coefficient. The best fit to the data shown in Fig. 3a gave $\beta = 5.8 \text{ cm/GW}$, in good agreement with the value of 5.5 cm/GW obtained in reference [6]. Our experimental errors were $\pm 30\%$ mostly arising from uncertainties in the irradiance values. Figure 3a shows the data and fit of the Z-scan signal at the same irradiance with the 40% transmitting aperture in place. At this low irradiance we expect the nonlinear refraction to be mostly due to the 3rd order nonlinearity as can be deduced from eqs. 2 and 3. Hence, the carrier term in eq. 2 was dropped and an $n_2 = -4 \cdot 10^{-11}$ was extracted.

The negative sign of n_2 is evident from the peak-valley pattern in the data. Moreover, this n_2 value is within 10% of the value obtained by our DFWM measurement. For a 3rd order nonlinearity, the change in the index or refraction, Δn , is a linear function of the irradiance, I . Figure 4 shows that this is not the case at higher irradiance values meaning that the refraction due to the 2PA generated carriers becomes more significant at these levels. At $I_0 = 2.4 \text{ GW/cm}^2$ (Fig. 5), and with β and n_2 known, the experimental data was fit with $\sigma = 0.8 \cdot 10^{-21} \text{ cm}^3$. The above measured values for n_2 , β and σ were used at other irradiance values and gave good fits to the experimental data. The Z-scan was also used to determine the above parameters for other semiconductors at different wavelengths. For example at $1.06 \mu\text{m}$, we measured $\beta = 26 \text{ cm/GW}$, $n_2 = -2 \cdot 10^{-10} \text{ esu}$, $\sigma = 5 \cdot 10^{-21} \text{ cm}^3$ for CdTe and $\beta = 26 \text{ cm/GW}$, $n_2 = -2.7 \cdot 10^{-10} \text{ esu}$, $\sigma = 8 \cdot 10^{-21} \text{ cm}^3$ for GaAs. The experimental errors were $\pm 30\%$.

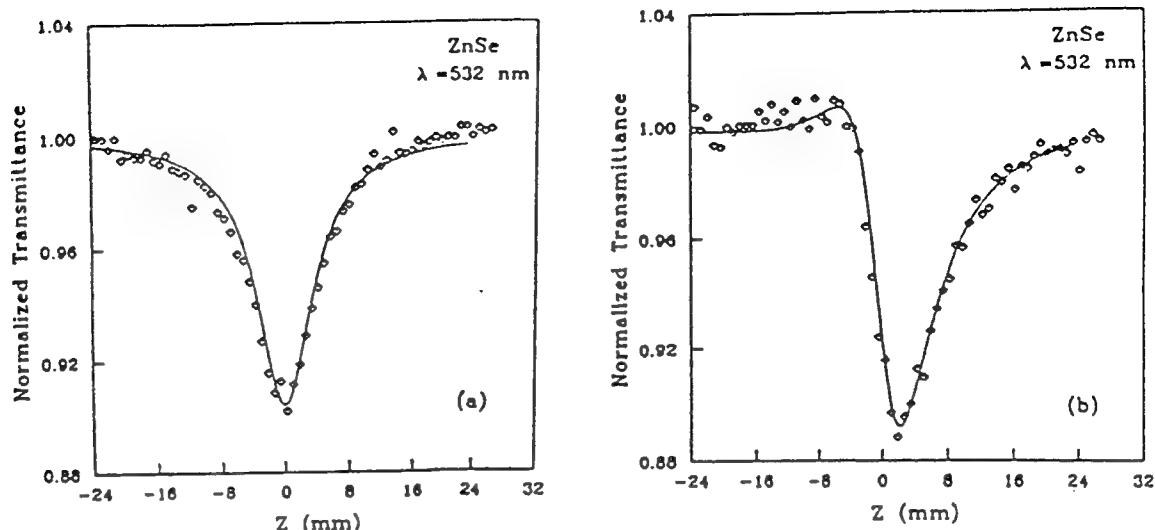


Fig. 3. Normalized Z-scan signal of a 2.7 mm thick ZnSe sample using 27 ps $0.53 \mu\text{m}$ pulses at $0.21 \text{ GW}/\text{cm}^2$ input irradiance. The solid lines are the theoretical results. (a) No aperture data and fit using $\beta = 5.8 \text{ cm}/\text{GW}$. (b) 40% aperture data fitted with $\beta = 5.8 \text{ cm}/\text{GW}$ and $n_2 = -4 \cdot 10^{-11}$ esu.

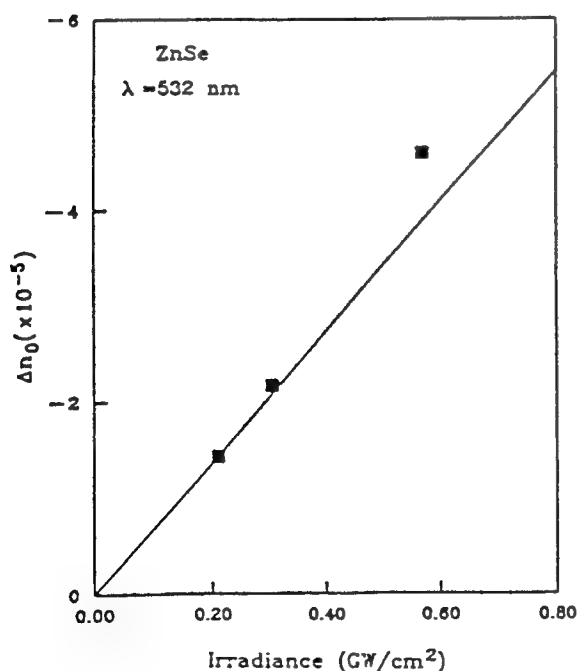


Fig. 4. The refractive index change in ZnSe as a function of input irradiance as measured from the Z-scan experiments. The line represents a 3rd order nonlinearity.

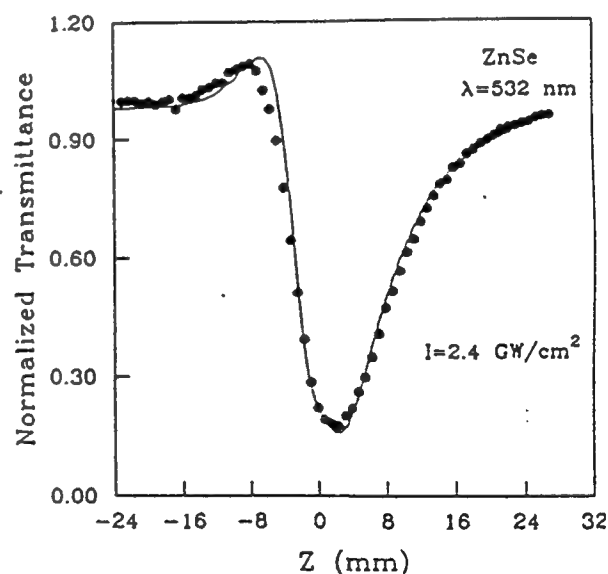


Fig. 5. Normalized Z-scan signal for ZnSe at input peak irradiance of $2.4 \text{ GW}/\text{cm}^2$ with a 40% aperture. The solid line is the theoretical fit with $\beta = 5.8 \text{ cm}/\text{GW}$, $n_2 = -4 \cdot 10^{-11}$ esu and $\sigma = 0.8 \cdot 10^{-21} \text{ cm}^3$.

5. Beam distortion measurements

A collimated beam 0.57 mm in radius ($\text{HW}_{\frac{1}{2}}\text{M}$) at 532 nm was incident on a 3 mm polycrystalline ZnSe sample and the transmitted beam fluence was monitored with a vidicon in the near field. These data are shown in Fig. 6. The solution to eqs. (1-3) gives the electric field at the exit surface of the sample, which we then propagate in free space to the vidicon using a Hygens-Fresnel integral. We proceeded to fit the experimental data with the nonlinear coefficients obtained from the Z-scan and DFWM results. The result is the fit to the experimental data shown in Fig. 6 using $\beta = 5.5 \text{ cm/GW}$, $n_2 = -4 \cdot 10^{-11} \text{ esu}$ and $\sigma = 0.8 \cdot 10^{-21} \text{ cm}^3$.

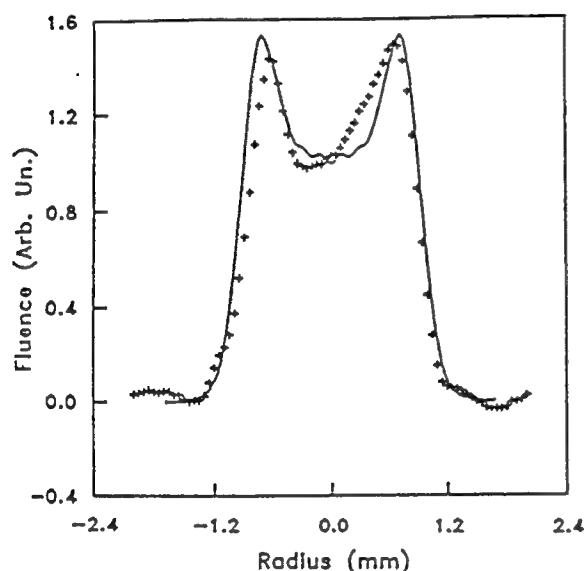


Fig. 6. (a) Transmitted spatial energy distribution of a 30 ps $0.53 \mu\text{m}$ pulse after propagation through ZnSe at 2.7 GW/cm^2 as viewed on a vidicon. The theoretical fit (solid line) is obtained with $\sigma = 0.8 \cdot 10^{-21} \text{ cm}^3$, $n_2 = -4 \cdot 10^{-11} \text{ esu}$ and $\beta = 5.5 \text{ cm/GW}$.

6. Conclusion

As a result of conducting thorough studies of the nonlinearities in ZnSe at 532 nm using different experimental techniques, we conclude that the bound electronic nonlinearity is negative and is a significant contribution to the overall nonlin-

ear refraction. There is a great deal of experimental evidence that the bound electronic refraction index change in solids is a positive effect, i.e. $n_2 > 0$. This is seen for wide band-gap materials, since self-focusing plays a significant role in the laser induced damage of these solids [11]. However, we find that for wavelengths significantly above the 2PA edge that the sign on n_2 becomes negative. We now understand this dispersion and sign change of n_2 . As discussed in reference [12], n_2 , the real part of $\chi^{(3)}$, and 2PA, the imaginary part of $\chi^{(3)}$, are related by causality (a relation similar to the Kramers-Kronig connection between linear absorption and the linear index of refraction) [12]. The value obtained for the refraction index change per free carrier pair agrees with the band-blocking model suggested by Auston et al. [13]. The σ calculated from the above model is $1.1 \cdot 10^{-21} \text{ cm}^3$ compared to our experimental value of $0.8 \cdot 10^{-21} \text{ cm}^3$. In conclusion, we have identified the different nonlinearities that occur in semiconductors when two-photon absorption is present.

Acknowledgements

We gratefully acknowledge the support of the National Science Foundation grant #ECS-8617066, DARPA/CNVEO and the Florida High Technology and Industry Council.

References

- [1] E.W. Van Stryland, Y.Y. Wu, D.J. Hagan, M.J. Soileau and K. Mansour, *J. Opt. Soc. Am.* B5 (1980) No.9. Also see, D.J. Hagan, E.W. Van Stryland, Y.Y. Wu, T.H. Wei, M. Sheik-Bahae, A.A. Said, K. Mansour, J. Young and M.J. Soileau, *SPIE Proc.* 1105 (1989) 103.
- [2] T.F. Boggess, S.C. Moss, I.W. Boyd and A.L. Smirl, *Opt. Lett.* 9 (1984) 219.
- [3] J.M. Ralston and K.R. Chang, *Appl. Phys. Lett.* 15 (1969) 164.
- [4] M. Sheik-Bahae, A.A. Said and E.W. Van Stryland, *Opt. Lett.* 14(1989) 955.

- [5] E.W. Van Stryland, M.A. Woodall, H. Vanherzeele and M.J. Soileau, *Opt. Lett.* 10 (1985) 490.
- [6] E.W. Van Stryland, H. Vanherzeele, M.A. Woodall, M.J. Soileau, A.L. Smirl, S. Guha and T.F. Boggess, *Opt. Eng.* 24 (1985) 613.
- [7] E. Canto, Ph.D. Dissertation (University of North Texas, 1990).
- [8] E.J. Canto, D.J. Hagan, J. Young and E.W. Van Stryland, to be published.
- [9] M. Sheik-Bahae, A.A. Said, T.H. Wei, D.J. Hagan and E.W. Van Stryland, *IEEE J. Quantum Electron.* April (1990).
- [10] M. Sheik-Bahae, A.A. Said, D.J. Hagan, M.J. Soileau and E.W. Van Stryland, *SPIE Proc.* 1105 (1989) 146.
- [11] D.H. Auston, S. McAfee, C.V. Shank, E.P. Ippen and O. Teschke, *Solid State Electron.* 21 (1978) 147.
- [12] M.J. Soileau, W.E. Williams, N. Mansour and E.W. Van Stryland, *Opt. Eng.* 28 (1989) 1133.
- [13] M. Sheik-Bahae, D.J. Hagan, A.A. Said, J. Young, T.H. Wei and E.W. Van Stryland, *SPIE Proc.* 1307 (1990).

NEW MEASUREMENT METHOD FOR NONLINEARITIES IN SEMICONDUCTORS

E.W. Van Stryland*, A.A. Said, M. Sheik-Bahae, D.J. Hagan*, E.J. Canto-Said,
Y.Y. Wu and T.H. Wei

CREOL Center for Research in Electro-Optics and Lasers University of Central Florida, Orlando, FL 32816

**also with the Department of Physics*

We describe the use of a novel method for the characterization of the nonlinear optical properties of materials which we refer to as a Z-scan. We utilize this technique along with other methods to determine the nonlinearities occurring in semiconductors when irradiated with picosecond pulses within the spectral region where two-photon absorption (2PA) is large. For example, we determine that nonlinear refraction at 532 nm in ZnSe is caused by a negative third order electronic Kerr effect in addition to the 2PA induced free-carrier refraction. We used beam distortion, and picosecond time-resolved degenerate four-wave mixing in addition to the Z-scan technique. Using these complementary characterization methods we determine the 2PA coefficient, the sign and magnitude of the bound electronic nonlinearity, n_2 and the negative refractive index change per free carrier.

1. Introduction

In this paper, we present the results of a comprehensive study of the nonlinear processes involved in semiconductors when exposed to picosecond pulses in a spectral range where two-photon absorption (2PA) is allowed, but so close to the energy band gap that direct band blocking from linear absorption or excitonic nonlinearities are present. This is spectral region of linear transparency where nonlinearities are useful for applications including passive optical limiting (OL). OL utilizes the combined effects of nonlinear absorption and nonlinear refraction in semiconductors [1-3]. An ideal passive optical limiter may be described as the optical analogue of a Zener diode circuit. It has a high linear transmission up to a certain input threshold after which the output becomes clamped to a constant value.

The nonlinearities present in this spectral range are 2PA, refraction arising from the 2PA generated free carriers and nonlinear refraction due to the electronic Kerr effect. We conducted picosecond degenerate four-wave mixing (DFWM) studies to examine the temporal response as well as the order of the refractive nonlinearities. The Z-scan technique [4] was employed to accurately de-

termine the sign and magnitude of the different refractive nonlinearities as well as the 2PA coefficient of the semiconductors. Finally beam distortion was used to verify the dominance of the nonlinearities for OL applications.

We briefly describe the theory for the irradiance and phase changes on a beam induced by these nonlinearities in section 2, and in section 3 the DFWM results are presented. In section 4 the Z-scan technique is briefly described and the results of the Z-scan measurements are presented. In section 5 we show the beam distortion measurements. Finally, in section 6 the experimental results are compared to theoretical models.

2. Theory

In all the experiments Gaussian spatial mode beams were used incident on samples thinner than the diffraction length of the beam. In this geometry the thin sample approximation can be used to describe the beam propagation inside the sample. This allows separation of the wave equation into one equation for the irradiance I and one for the phase Φ . Also with 30 ps (FWHM) pulses and at low irradiance levels we can ignore the absorption

due to the 2PA generated carriers but not carrier induced refraction [5]. This leaves the nonlinear differential equations,

$$\frac{dI}{dz} = -\alpha I - \beta I^2, \quad (1)$$

and

$$\frac{d\Delta\Phi}{dZ} = k\gamma I - k\sigma N, \quad (2)$$

where α is the linear absorption coefficient, β is the 2PA coefficient, $k = 2\pi/\lambda$, λ is the wavelength of incident radiation, γ is the refractive index change due to the electronic Kerr effect, N is the density of free carriers and σ is the change in the index of refraction per free carrier pair density generated [6]. Since the free carriers are created by 2PA, the generation rate is given by

$$\frac{dN}{dt} = \frac{\beta I^2}{2\hbar\omega}. \quad (3)$$

When N is substituted in eq. (2), it becomes clear that the phase change due to the carriers depends on the square of the irradiance. Hence, the free carrier refraction appears as an effective fifth order nonlinearity [7, 8].

3. Degenerate four-wave mixing experiments

DFWM with picosecond pulses is a sensitive technique that gives information about the temporal evolution of nonlinear process in semiconductors and other materials. Two counter-propagating strong beams, forward pump E_f and backward pump E_b , are incident on the sample with a third weaker probe beam, E_p incident at an angle θ with respect to the forward pump. Two of these beams interfere inside the sample to form a grating from which the third beam diffracts to form a conjugate signal E_c that retraces the probe path. The pulses used in these experiments are 30 ps (FWHM) pulses at 532 nm. Various combinations of polarizers and half-wave plates were placed in the path of each beam to independently change their polarization and irradiance. Figure 1 shows a plot of the conjugate signal versus the delay $\tau_{zs}D$ of E_b which was polarized perpendicular to E_f and E_p . Two distinct regions are present,

a fast decaying signal near zero delay and a slow decaying signal at long delays. To better understand the two nonlinear regimes, irradiance dependence experiments were performed at different delays. A log-log plot of the DFWM signal versus input irradiance (all three inputs varied) gives two different slopes as shown in the inset of Fig. 1. At zero delay a slope of 2.8 was measured indicating a third order nonlinearity and at long delays a slope of 4.9 was found. The fifth order dependence can be explained by the 2PA induced carrier refraction as mentioned in the previous section. A modulated carrier density is created via 2PA; this is an imaginary $\chi^{(3)}$ effect. Then a third beam diffracts off the carrier modulation; this is a real $\chi^{(1)}$ effect. Hence, the mechanism is a sequential $\chi^{(3)}\chi^{(1)}$ process that appears as a fifth order nonlinearity. As to the third order effect decays within the 30 ps pulse width which is consistent with a bound electronic nonlinearity. This fast decaying effect can either be of refractive or absorptive nature as far as DFWM is concerned, Assuming that it is a refractive effect a value of $|n_2| = 4.4 \cdot 10^{-11}$ esu was extracted where n_2 is related to γ by n_2 (esu) = $n_0 c / (40\pi) \gamma$ (MKS) [7, 8]. Note that the sign of n_2 is not given by DFWM.

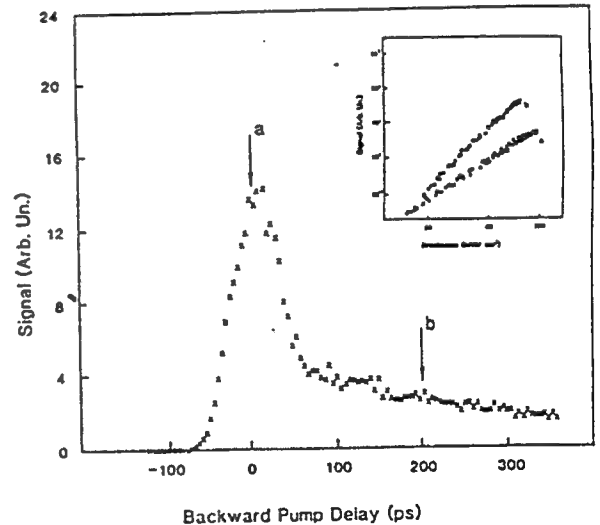


Fig. 1. The DFWM signal vs backward pump delay for 30 ps pulses at $0.53 \mu\text{m}$ in ZnSe. The inset shows a log-log plot of the conjugate signal as a function of the input irradiance at 0 ps (a) and 200 ps (b).

4. Z-scan measurements

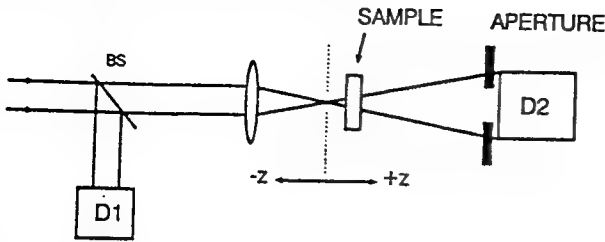


Fig. 2. The Z-scan experimental setup in which the normalized transmittance is measured as a function of the sample position z .

The Z-scan technique, which was recently developed at our laboratories, is a simple single measurement experiment technique that readily gives the sign and magnitude of nonlinear refraction as well as nonlinear absorption [9]. It is also an excellent guide for geometrical optimization of optical limiting [10]. Figure 2 shows the Z-scan experimental setup. A focused Gaussian beam is incident on the sample and transmitted beam is collected through a finite aperture in the far field into detector D_2 . D_1 monitors the input energy. Keeping the input energy fixed, the transmittance is measured as a function of the sample position relative to the focal plane. Since nonlinear refraction causes a lensing effect in the incident beam, the sample behaves as a negative or positive lens depending on the sign of the nonlinearity. As explained in reference [4] a valley-peak configuration in the Z-scan signal is a signature of a positive refractive nonlinearity and peak-valley pattern denotes a negative nonlinearity. When the aperture is removed, i.e. all the transmitted light is collected, the Z-scan is only sensitive to nonlinear absorption. For semiconductors with 2PA present, the Z-scan experiment was simulated by solving eqs. (1-3). Three parameters are to be determined β , n_2 and σ . Using 27 ps pulses (FWHM) at 532 nm Z-scan measurements were performed on a 2.7 mm thick

ZnSe sample at different input energies. With the aperture removed a Z-scan was performed at $I_0 = 0.1 \text{ GW/cm}^2$ where I_0 is the on axis peak irradiance at the focus. In this case the measurement is insensitive to nonlinear refraction and thus independently gives the nonlinear absorption coefficient. The best fit to the data shown in Fig. 3a gave $\beta = 5.8 \text{ cm/GW}$, in good agreement with the value of 5.5 cm/GW obtained in reference [6]. Our experimental errors were $\pm 30\%$ mostly arising from uncertainties in the irradiance values. Figure 3a shows the data and fit of the Z-scan signal at the same irradiance with the 40% transmitting aperture in place. At this low irradiance we expect the nonlinear refraction to be mostly due to the 3rd order nonlinearity as can be deduced from eqs. 2 and 3. Hence, the carrier term in eq. 2 was dropped and an $n_2 = -4 \cdot 10^{-11}$ was extracted.

The negative sign of n_2 is evident from the peak-valley pattern in the data. Moreover, this n_2 value is within 10% of the value obtained by our DFWM measurement. For a 3rd order nonlinearity, the change in the index of refraction, Δn , is a linear function of the irradiance, I . Figure 4 shows that this is not the case at higher irradiance values meaning that the refraction due to the 2PA generated carriers becomes more significant at these levels. At $I_0 = 2.4 \text{ GW/cm}^2$ (Fig. 5), and with β and n_2 known, the experimental data was fit with $\sigma = 0.8 \cdot 10^{-21} \text{ cm}^3$. The above measured values for n_2 , β and σ were used at other irradiance values and gave good fits to the experimental data. The Z-scan was also used to determine the above parameters for other semiconductors at different wavelengths. For example at $1.06 \mu\text{m}$, we measured $\beta = 26 \text{ cm/GW}$, $n_2 = -2 \cdot 10^{-10} \text{ esu}$, $\sigma = 5 \cdot 10^{-21} \text{ cm}^3$ for CdTe and $\beta = 26 \text{ cm/GW}$, $n_2 = -2.7 \cdot 10^{-10} \text{ esu}$, $\sigma = 8 \cdot 10^{-21} \text{ cm}^3$ for GaAs. The experimental errors were $\pm 30\%$.

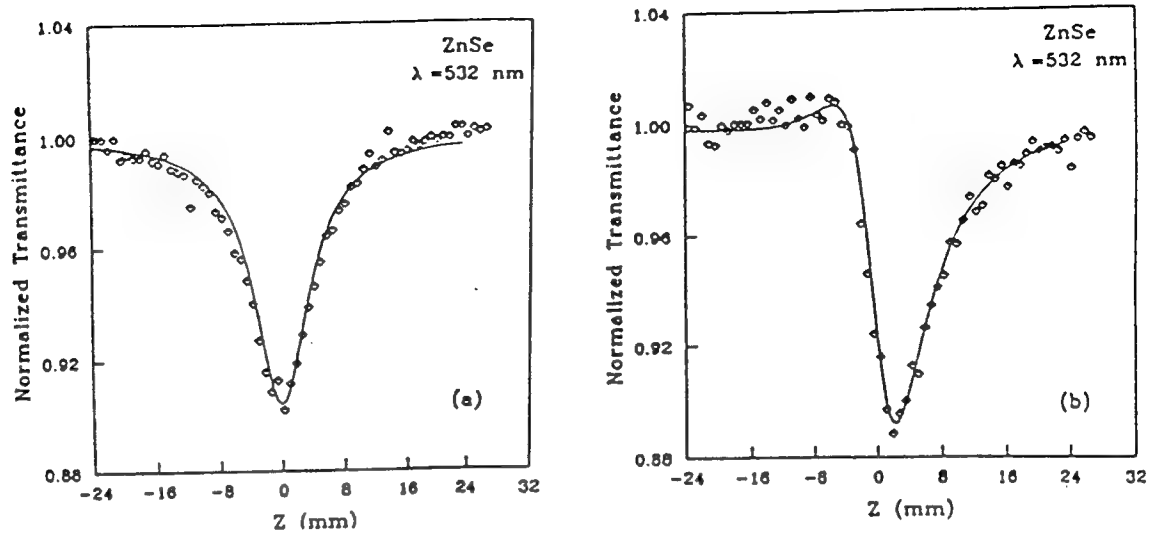


Fig. 3. Normalized Z-scan signal of a 2.7 mm thick ZnSe sample using 27 ps $0.53 \mu\text{m}$ pulses at 0.21 GW/cm^2 input irradiance. The solid lines are the theoretical results. (a) No aperture data and fit using $\beta = 5.8 \text{ cm/GW}$. (b) 40% aperture data fitted with $\beta = 5.8 \text{ cm/GW}$ and $n_2 = -4 \cdot 10^{-11} \text{ esu}$.

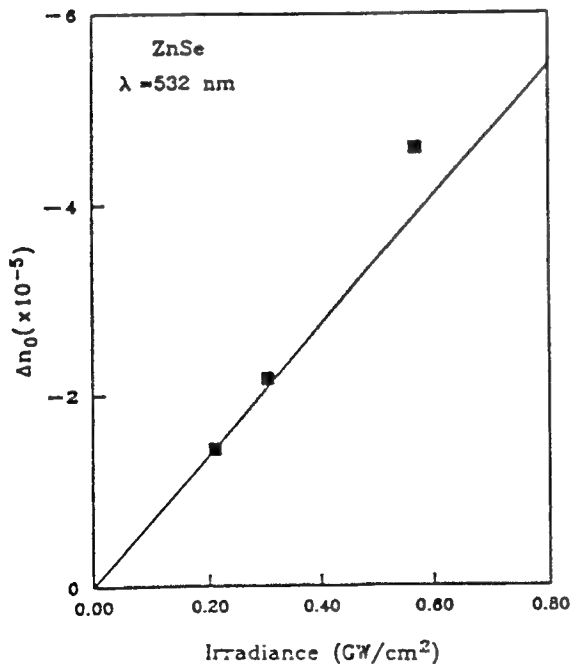


Fig. 4. The refractive index change in ZnSe as a function of input irradiance as measured from the Z-scan experiments. The line represents a 3rd order nonlinearity.

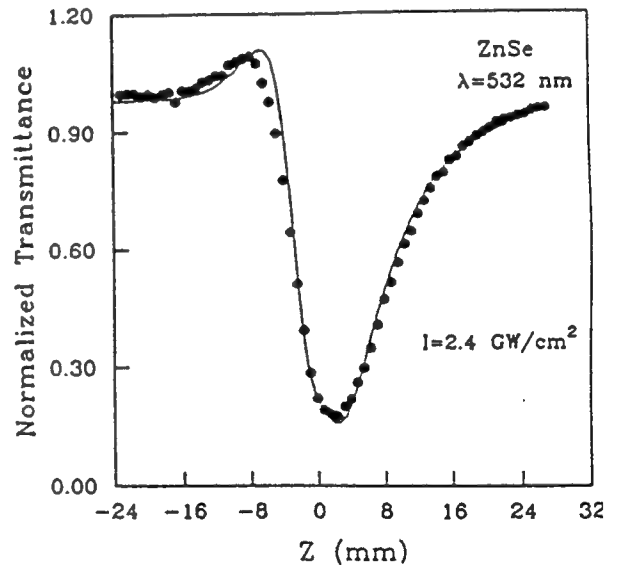


Fig. 5. Normalized Z-scan signal for ZnSe at input peak irradiance of 2.4 GW/cm^2 with a 40% aperture. The solid line is the theoretical fit with $\beta = 5.8 \text{ cm/GW}$, $n_2 = -4 \cdot 10^{-11} \text{ esu}$ and $\sigma = 0.8 \cdot 10^{-21} \text{ cm}^3$.

5. Beam distortion measurements

A collimated beam 0.57 mm in radius ($HW_{\frac{1}{2}}M$) at 532 nm was incident on a 3 mm polycrystalline ZnSe sample and the transmitted beam fluence was monitored with a vidicon in the near field. These data are shown in Fig. 6. The solution to eqs. (1-3) gives the electric field at the exit surface of the sample, which we then propagate in free space to the vidicon using a Hygens-Fresnel integral. We proceeded to fit the experimental data with the nonlinear coefficients obtained from the Z-scan and DFWM results. The result is the fit to the experimental data shown in Fig. 6 using $\beta = 5.5 \text{ cm/GW}$, $n_2 = -4 \cdot 10^{-11} \text{ esu}$ and $\sigma = 0.8 \cdot 10^{-21} \text{ cm}^3$.

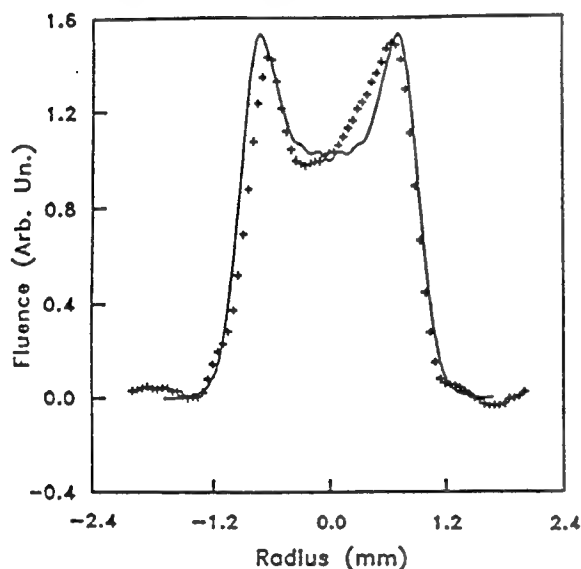


Fig. 6. (a) Transmitted spatial energy distribution of a 30 ps $0.53 \mu\text{m}$ pulse after propagation through ZnSe at 2.7 GW/cm^2 as viewed on a vidicon. The theoretical fit (solid line) is obtained with $\sigma = 0.8 \cdot 10^{-21} \text{ cm}^3$, $n_2 = -4 \cdot 10^{-11} \text{ esu}$ and $\beta = 5.5 \text{ cm/GW}$.

6. Conclusion

As a result of conducting thorough studies of the nonlinearities in ZnSe at 532 nm using different experimental techniques, we conclude that the bound electronic nonlinearity is negative and is a significant contribution to the overall nonlin-

ear refraction. There is a great deal of experimental evidence that the bound electronic refraction index change in solids is a positive effect, i.e. $n_2 > 0$. This is seen for wide band-gap materials, since self-focusing plays a significant role in the laser induced damage of these solids [11]. However, we find that for wavelengths significantly above the 2PA edge that the sign on n_2 becomes negative. We now understand this dispersion and sign change of n_2 . As discussed in reference [12], n_2 , the real part of $\chi^{(3)}$, and 2PA, the imaginary part of $\chi^{(3)}$, are related by causality (a relation similar to the Kramers-Kronig connection between linear absorption and the linear index of refraction) [12]. The value obtained for the refraction index change per free carrier pair agrees with the band-blocking model suggested by Auston et al. [13]. The σ calculated from the above model is $1.1 \cdot 10^{-21} \text{ cm}^3$ compared to our experimental value of $0.8 \cdot 10^{-21} \text{ cm}^3$. In conclusion, we have identified the different nonlinearities that occur in semiconductors when two-photon absorption is present.

Acknowledgements

We gratefully acknowledge the support of the National Science Foundation grant #ECS-8617066, DARPA/CNVEO and the Florida High Technology and Industry Council.

References

- [1] E.W. Van Stryland, Y.Y. Wu, D.J. Hagan, M.J. Soileau and K. Mansour, *J. Opt. Soc. Am.* B5 (1980) No.9. Also see, D.J. Hagan, E.W. Van Stryland, Y.Y. Wu, T.H. Wei, M. Sheik-Bahae, A.A. Said, K. Mansour, J. Young and M.J. Soileau, *SPIE Proc.* 1105 (1989) 103.
- [2] T.F. Boggess, S.C. Moss, I.W. Boyd and A.L. Smirl, *Opt. Lett.* 9 (1984) 219.
- [3] J.M. Ralston and K.R. Chang, *Appl. Phys. Lett.* 15 (1969) 164.
- [4] M. Sheik-Bahae, A.A. Said and E.W. Van Stryland, *Opt. Lett.* 14(1989) 955.

- [5] E.W. Van Stryland, M.A. Woodall, H. Vanherzeele and M.J. Soileau, *Opt. Lett.* 10 (1985) 490.
- [6] E.W. Van Stryland, H. Vanherzeele, M.A. Woodall, M.J. Soileau, A.L. Smirl, S. Guha and T.F. Boggess, *Opt. Eng.* 24 (1985) 613.
- [7] E. Canto, Ph.D. Dissertation (University of North Texas, 1990).
- [8] E.J. Canto, D.J. Hagan, J. Young and E.W. Van Stryland, to be published.
- [9] M. Sheik-Bahae, A.A. Said, T.H. Wei, D.J. Hagan and E.W. Van Stryland, *IEEE J. Quantum Electron.* April (1990).
- [10] M. Sheik-Bahae, A.A. Said, D.J. Hagan, M.J. Soileau and E.W. Van Stryland, *SPIE Proc.* 1105 (1989) 146.
- [11] D.H. Auston, S. McAfee, C.V. Shank, E.P. Ippen and O. Teschke, *Solid State Electron.* 21 (1978) 147.
- [12] M.J. Soileau, W.E. Williams, N. Mansour and E.W. Van Stryland, *Opt. Eng.* 28 (1989) 1133.
- [13] M. Sheik-Bahae, D.J. Hagan, A.A. Said, J. Young, T.H. Wei and E.W. Van Stryland, *SPIE Proc.* 1307 (1990).

Dispersion of Bound Electronic Nonlinear Refraction in Solids

Mansoor Sheik-Bahae, *Member, IEEE*, David Crichton Hutchings, David J. Hagan, *Member, IEEE*, and Eric W. Van Stryland, *Senior Member, IEEE*

Abstract—A two-band model is used to calculate the scaling and spectrum of the nondegenerate nonlinear absorption $\Delta\alpha(\omega_1; \omega_2)$. From this, the bound electronic nonlinear refractive index n_2 is obtained using a Kramers–Krönig transformation. We include the effects of two-photon and Raman transitions and the ac Stark shift (virtual band blocking). The theoretical calculation for n_2 shows excellent agreement with measured values for a five order of magnitude variation in the modulus of n_2 in semiconductors and wide-gap optical solids. We also present new measurements of n_2 in semiconductors using the Z-scan method. The observed change of sign of n_2 midway between the two-photon absorption edge and the fundamental absorption edge is also predicted. Thus, we now have a comprehensive theory that allows a determination of n_2 at wavelengths beneath the band edge, given only the bandgap energy and the linear index of refraction. Such information is useful for a variety of applications including optical limiting, laser-induced damage, and all-optical switching. Some consequences for all-optical switching are discussed, and a wavelength criterion for the observation of switching is derived.

I. INTRODUCTION

RECENTLY we reported measurements of the nonlinear refractive index n_2 of a variety of solids using beam distortion methods (Z-scan technique) [1], [2] and four-wave mixing [3]. These data show a strong systematic dispersion of the bound electronic nonlinearity (electronic Kerr effect n_2) near the two-photon absorption (2PA) edge. This eventually turns from positive to negative at higher frequencies. We found that by using a Kramers–Krönig (KK) integral based on the degenerate 2PA spectrum as predicted by a two-parabolic band model, we could predict the observed universal dispersion, scaling, and values of n_2 that range over four orders of magnitude and change sign [2]. This KK analysis relates the real and imaginary parts of the third-order susceptibility. The re-

sulting scaling rule correctly predicted the value of n_2 for the 26 different materials we had examined at that time, except very near the gap where there was a systematic departure of the data from the theory towards larger negative n_2 values. More recent data taken at wavelengths closer to the gap show an even larger departure from the predictions of the 2PA model. We had speculated in [2] that the bandgap resonant ac Stark effect might make $|n_2|$ larger near the gap. Here, we present a model that includes the ac Stark effect and the electronic Raman effect, as well as 2PA. Indeed, the inclusion of these new effects does explain the large negative increase in n_2 near the gap.

There are two distinct frequency regimes for nonlinear optics in semiconductors which correspond to real and virtual excitation. Most studies have primarily concentrated on bandgap resonant effects which result in real excitation [4], [5]. The very large nonlinear effects observed are the saturation of interband and excitonic absorption due to photoexcited free carriers and excitons. Real excitations usually result in a reduction of the refractive index at frequencies of interest. In contrast, by exciting optical solids at frequencies much less than the gap, a considerably smaller, but faster, positive nonlinear refractive index n_2 due to bound electronic effects is observed [6]. This n_2 arises from the real part of the third-order susceptibility $\chi^{(3)}$, and is defined through the refractive index change Δn where

$$\Delta n(\omega) = \gamma(\omega) I_\omega = n_2(\omega) \frac{|E_\omega|^2}{2} \quad (1)$$

with I_ω and E_ω being the irradiance and electric field at frequency ω , respectively, and $n_2 \propto \text{Re } \chi^{(3)}/n_0$. The linear refractive index is n_0 , and γ and n_2 are related by n_2 (esu) = $cn_0\gamma/40\pi$ (SI) where c is the speed of light. The magnitude and dispersion of n_2 is of interest because of its importance in applications such as nonlinear propagation in fibers, fast optical switching, self-focusing and damage in optical materials, and optical limiting in semiconductors [7]–[9].

Measurements of wide bandgap dielectrics show that $n_2 > 0$, which explains catastrophic self-focusing damage in such materials as NaCl and SiO₂ [8]. Our measurements in semiconductors below or near the 2PA edge ($\hbar\omega = E_g/2$) also show positive n_2 . However, we found recently that for wavelengths substantially above the 2PA edge, n_2 is negative [1]. We performed measurements on

Manuscript received October 19, 1990; revised February 7, 1991. This work was supported by the National Science Foundation under Grant ECS 8617066, by DARPA/CNVEO, and by the Florida High Technology and Industry Council.

M. Sheik-Bahae and D. C. Hutchings are with the Center for Research in Electro-Optics and Lasers (CREOL), University of Central Florida, Orlando, FL 32826.

D. J. Hagan is with the Center for Research in Electro-Optics and Lasers (CREOL) and the Department of Physics, University of Central Florida, Orlando, FL 32826.

E. W. Van Stryland is with the Center for Research in Electro-Optics and Lasers (CREOL) and the Departments of Physics and Electrical Engineering, University of Central Florida, Orlando, FL 32826.

IEEE Log Number 9144871.

a large number of other materials, including semiconductors and dielectrics, above and below the 2PA edge. As a result, we have been able to clearly demonstrate the dispersion of n_2 .

Our measurements utilized a newly developed sensitive technique (Z scan) [1], [10] that accurately determines the magnitude and sign of n_2 , even in the presence of 2PA where it also gives the 2PA coefficient β . For example we found a negative n_2 in materials such as ZnSe at $0.523 \mu\text{m}$ where 2PA is present, and a positive n_2 at $1.064 \mu\text{m}$ where 2PA is absent. The values obtained for β were in excellent agreement with our earlier measurements using standard transmission experiments [11]. We also performed picosecond degenerate four-wave mixing (DFWM) measurements which showed this third-order response to be fast (time resolution limited by the 30 ps pulsewidth). At wavelengths where 2PA was present, this fast third-order nonlinearity was dominant at low irradiance (e.g., up to $0.5 \text{ GW}/\text{cm}^2$ in ZnSe at 532 nm), while at higher irradiance, the slowly decaying 2PA-generated free-carrier refraction (self-defocusing) became important [3]. DFWM studies in other semiconductors and other wavelengths showed this to be a universal phenomenon [12].

It has previously been predicted that $\chi^{(3)}$ should vary as E_g^{-4} [13]. Using this scaling and the relation between n_2 and $\chi^{(3)}$ that includes the linear index n_0 , we can remove the E_g and n_0 dependencies from the experimental values of n_2 by multiplying them by $n_0 E_g^4$. In Fig. 1, a plot of our experimentally determined scaled values of n_2 as a function of $\hbar\omega/E_g$ is shown. We also divide the data by a constant K' which we explain in what follows. We show, on the same plot, several data for large-gap optical crystals obtained from recent measurements by Adair *et al.* using a "nearly degenerate three-wave mixing" scheme [6]. Our own measurements of several of the same materials studied in [6] show excellent absolute agreement. Assuming that there are no other relevant parameters unique to each material other than bandgap and index, this plot should be general to all optical solids. Upon examination of Fig. 1, we immediately see a trend giving small positive values for low ratios of photon energy to bandgap energy which slowly rises to a broad resonance peak at the 2PA edge and then decreases, eventually turning negative between the two-photon and single-photon absorption edges. We should note that the scaling with E_g hides a variation in magnitude of n_2 of four orders of magnitude so that the observation of a universal dispersion curve as in Fig. 1 is quite remarkable. This dispersion curve is qualitatively similar to the dispersion of the linear index around the single-photon absorption edge [14]. As these linear quantities are related by causality via a KK relation, it seems logical to investigate whether the observed dispersion of n_2 can be calculated using a nonlinear KK relation between the real and imaginary parts of $\chi^{(3)}$. Indeed, as we showed in [2], making some reasonable assumptions, the observed tendencies as well as the absolute magnitudes of this dispersion are well predicted by such a calculation. The solid line in Fig. 1 as reproduced

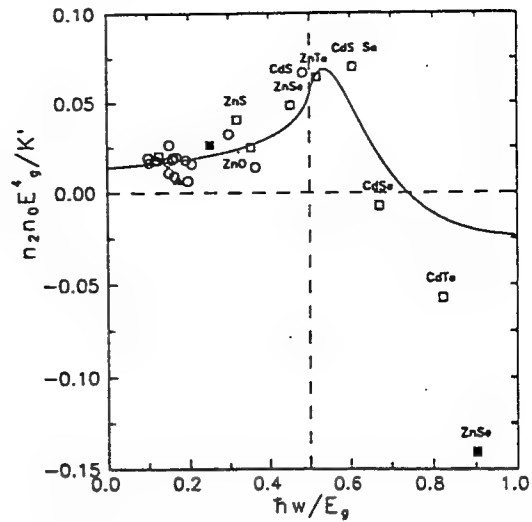


Fig. 1. Data of n_2 scaled as $n_2 n_0 E_g^4 / K'$ versus $\hbar\omega/E_g$ from [2]. Note that the definition of the constant K' in this reference differs slightly from that used in this paper. These data include measurements of n_2 at $1.06 \mu\text{m}$ in [6], as well as our own measurements at 1.06 and $0.53 \mu\text{m}$. Recent measurements have revised some of the semiconductor n_2 values shown in this figure (see Fig. 5). The solid line demonstrates the fit obtained in [2] using a quasi-degenerate 2PA.

from [2] is the direct result of such a calculation, including only the degenerate 2PA contribution to the imaginary part of $\chi^{(3)}$. It should be noted that since the 2PA spectrum was previously determined [11], [13], [15], no additional fitting parameter was used in this calculation.

II. KRAMERS-KRÖNIG (KK) RELATION

Most theoretical calculations of n_2 have been confined to the zero-frequency limit [16]–[20]. Of these, semi-empirical formulations have been the most successful in predicting the magnitude of n_2 [19], [20]. For example, the formula obtained by Boling, Glass, and Owyong (BGO) in relating n_2 to the linear index (n_0) and the dispersion of n_0 in terms of the Abbe number has been successfully applied to a large class of transparent materials [6], [20]. Their theory predicts the low-frequency magnitude of n_2 , but does not give the dispersion. The KK method predicts the dispersion as well as the magnitude of n_2 . While the calculation presented in [2] only included 2PA in the imaginary part of $\chi^{(3)}$, the present calculation includes all other relevant contributions, that is, from electronic Raman and the ac Stark effect ("virtual band blocking"). We, however, do not include possible effects from excitonic enhancement [21].

Based on the principle of causality, KK relates the refractive index and the absorption coefficient for any linear material [22]:

$$n(\omega) - 1 = \frac{c}{\pi} \int_0^\infty \frac{\alpha(\omega')}{\omega'^2 - \omega^2} d\omega'. \quad (2)$$

We now introduce some perturbation ξ into the system, and consider the change in the refractive index resulting from the effect of ξ . The KK transformation states that a

change in the refractive index (Δn) at ω is associated with changes in the absorption coefficient ($\Delta\alpha$) throughout the spectrum (ω') and vice versa. We write this as

$$\Delta n(\omega; \xi) = \frac{c}{\pi} \int_0^\infty \frac{\Delta\alpha(\omega'; \xi)}{\omega'^2 - \omega^2} d\omega' \quad (3)$$

where ξ is a parameter (or parameters) denoting the "cause" of change in the absorption.

The cause need not be of optical origin, but of any external perturbation. For example, this method has been used to calculate the refractive index change resulting from an excited electron-hole plasma [23] and a thermal shift of the band edge [24]. For cases where an electron-hole plasma is injected, the consequent change of absorption gives the plasma contribution to the refractive index. In this case, the ξ parameter is taken as the change in plasma density (ΔN) regardless of the mechanism of generation of the plasma or the pump frequency. In the case of 2PA, the change is due to the presence of a pump field of frequency Ω (i.e., $\xi = \Omega$). The corresponding nonlinear refraction is $\Delta n(\omega; \Omega)$, which gives the index change at ω due to the presence of light at Ω . Although the calculation as illustrated above gives the nondegenerate nonlinear refraction, in most cases we would set $\Omega = \omega$ and consider self-refraction. This gives what is commonly referred to as n_2 . Van Vechten and Aspnes [18] obtained the low-frequency limit of n_2 from a similar KK transformation of the Franz-Keldysh electroabsorption effect where, in this case, ξ is the dc field. It is important to note that we must set $\Omega = \omega$ and not $\Omega = \omega'$, otherwise nonlinear KK relations do not apply as shown, for example, for the two-level atom [25]. The bound electronic contribution to $\chi^{(3)}$ can originate from various absorptive counterparts that are quadratic functions of the pump field. Effects of this order are 2PA, the electronic Raman effect, and the optical Stark effect.

An alternative way of considering the nonlinear Kramers-Krönig calculation is to examine the causality of the system. By treating the system as consisting of the material plus light, causality relations between the nonlinear polarization and an additional light field give rise to relations between the real and imaginary parts of $\chi^{(3)}$ [26], [27] in an analogous way to the usual "linear" Kramers-Krönig relations. These resulting relations can be reexpressed in the form given above. One can therefore think of the nonlinear KK relations as being not on a bare material, but on a system consisting of the material and an optical pump.

In order to perform the KK calculation, it is necessary to know the nondegenerate absorption $\Delta\alpha(\omega, \Omega)$, which is the absorption of light at frequency ω when a light field of frequency Ω is applied to the material. This is necessary even if only self-refraction is desired. In what follows, we calculate the nondegenerate absorption originating from $\chi^{(3)}$, including the 2PA, ac Stark, and Raman contributions. The degenerate 2PA result, found by setting $\omega = \Omega$, will serve as a check against previous theoretical and experimental results.

Although nondegenerate nonlinear absorption is required for the correct calculation of n_2 , an estimate can be obtained by substituting the degenerate 2PA at the mean frequency for the nondegenerate absorption:

$$\Delta\alpha(\omega; \omega') \rightarrow \beta \left(\frac{\omega + \omega'}{2} \right) I_{\omega'} \quad (4)$$

This calculation was presented in [2]. We note that (4) provides a good estimate of n_2 , except close to the band edge where the ac Stark contribution becomes large. This agreement reflects the fact that the denominator in the KK integrand (3) has the effect of strongly weighting frequencies close to ω' , so for self-refraction, $\Delta\alpha(\omega; \omega')$ needs to be known accurately only for ω in the vicinity of ω' . This approximation breaks down, however, when it is necessary to include divergent terms such as the ac Stark effect.

III. NONLINEAR ABSORPTION CALCULATION

Two-photon absorption processes require that perturbation theory be taken to second order. A variation of this is to use first-order perturbation theory on "dressed" states for the conduction and valence bands where the effect of the acceleration (tunneling) of the electrons due to the oscillating electric field is already taken into account [28], [29]. In all of the following, we shall use the dipole approximation for the radiation interaction Hamiltonian:

$$\mathcal{H}_{\text{int}} = -\frac{e}{m_0 c} \mathbf{A} \cdot \mathbf{p} \quad (5)$$

where \mathbf{A} is the magnetic vector potential, \mathbf{p} is the electron momentum operator, $-e$ is the electron charge, and m_0 is the free electron mass. We assume a two-beam interaction with both beams linearly polarized in the same direction, giving

$$\mathbf{A} = \hat{\mathbf{a}} [A_{01} \cos(\omega_1 t) + A_{02} \cos(\omega_2 t + \phi)] \quad (6)$$

where $\hat{\mathbf{a}}$ is the unit vector in the direction of the optical polarization. Following Keldysh [28], in the same manner as [29], [30], such a dressed state can be approximated by a Volkov-type wavefunction [31]:

$$\psi_i(\mathbf{k}, \mathbf{r}, t) = u_i(\mathbf{k}, \mathbf{r}) \exp \left[i\mathbf{k} \cdot \mathbf{r} - \frac{i}{\hbar} \int_0^t E_i(\tau) d\tau \right] \quad (7)$$

where i refers to either the conduction or valence band. $u_i(\mathbf{k}, \mathbf{r})$ are the usual Bloch wavefunctions which have the same periodicity as the lattice. The effect of the optical field is to alter the energy of the electrons and holes in the final and initial states, respectively. Only the first- and second-order ac Stark shifting of the bands give rise to a $\chi^{(3)}$ effect:

$$E_c(\tau) = E_{c0} + \Delta E_{cc}(\tau) + \Delta E_{cv} \quad (8)$$

$$E_v(\tau) = E_{v0} + \Delta E_{vv}(\tau) + \Delta E_{vc} \quad (9)$$

where, within the effective mass approximation,

$$E_{c0} = E_g + \frac{\hbar^2 k^2}{2m_c} \quad (10)$$

$$E_{v0} = \frac{\hbar^2 k^2}{2m_v} \quad (11)$$

$$\Delta E_{ii}(\tau) = \frac{-e\hbar}{m_i c} k \cdot A(\tau) \quad (12)$$

where we have defined the hole mass m_v as being negative. ΔE_{cv} and ΔE_{vc} are the time-independent quadratic ac Stark shifts of the bands, which are proportional to $|A_0|^2$ and will be discussed in Section III-C. The transition rates will be calculated using an S -matrix formalism [32], with

$$S = -\frac{i}{\hbar} \int_{-\infty}^{\infty} dt \int d^3 r \psi_c^*(k, r, t) \mathcal{H}_{int} \psi_v(k', r, t). \quad (13)$$

The resulting S matrix for these processes is

$$S = \frac{i}{\hbar} \frac{e\hat{a} \cdot p_{vc}}{m_0 c} \delta_{kk'} \int_{-\infty}^{\infty} dt \cdot e^{i\omega_{vc}t} [A_{01} \cos(\omega_1 t) + A_{02} \cos(\omega_2 t + \phi)] \cdot \exp[i\eta_1 \sin(\omega_1 t) + i\eta_2 \sin(\omega_2 t + \phi)] \quad (14)$$

where p_{vc} is the interband momentum matrix element given by

$$p_{vc} = \frac{i}{\hbar} \int d^3 r u_c^*(k, r) \nabla u_v(k, r). \quad (15)$$

We define

$$\hbar\omega_{vc} = E_g - \Delta E_{vc} + \Delta E_{cv} + \frac{\hbar^2 k^2}{2m_{vc}} \quad (16)$$

the reduced mass, by

$$\frac{1}{m_{vc}} = \frac{1}{m_c} - \frac{1}{m_v}, \quad (17)$$

and

$$\eta_j = \frac{eA_{0j} k \cdot \hat{a}}{m_{vc} c \omega_j}. \quad (18)$$

In order to perform the time integral, we make use of the identity

$$\exp[i\eta \sin(\omega t)] = \sum_{n=-\infty}^{\infty} J_n(\eta) e^{in\omega t}. \quad (19)$$

On substitution and performing the time integral, the S

matrix becomes

$$S = \frac{i\pi}{\hbar} \frac{e\hat{a} \cdot p_{vc}}{m_0 c} \sum_{m,n=-\infty}^{\infty} J_m(\eta_1) J_n(\eta_2) \cdot \{A_{01}[\delta((m+1)\omega_1 + n\omega_2 + \omega_{vc}) + \delta((m-1)\omega_1 + n\omega_2 + \omega_{vc})] + A_{02}[\delta(m\omega_1 + (n+1)\omega_2 + \omega_{vc}) + \delta(m\omega_1 + (n-1)\omega_2 + \omega_{vc})]\}. \quad (20)$$

A. Degenerate 2PA Calculation

The delta function terms in the above expression indicate various combinations of multiphoton absorption processes. From the S -matrix description, transition rates can be determined [32] which lead to absorption coefficients. We first consider 2PA at frequency ω_1 in order to determine the scaling. Therefore, consider the terms arising from $A_{02} = 0$, $m = -1$, $n = 0$. Using the lowest order MacLaurin expansion term for the Bessel function $J_n(x) \approx x^n/2^n n!$, and ignoring the quadratic Stark shift terms for now, the resulting change in the transition rate due to 2PA is

$$\Delta W = \sum_{\text{spin}} \int \frac{d^3 k}{(2\pi)^3} \left[\frac{\pi e^2 A_{01}^2}{2m_0 m_{vc} c^2 \omega_1} \right]^2 |\hat{a} \cdot p_{vc}|^2 \cdot |k \cdot \hat{a}|^2 \frac{1}{2\pi\hbar} \delta\left(E_g + \frac{\hbar^2 k^2}{2m_{vc}} - 2\hbar\omega_1\right). \quad (21)$$

A two-band model will be used in this paper for the calculation of transition rates, consisting of a conduction band and a valence band of opposite curvature ($m_v = -m_c$), each of which is doubly degenerate in spin. We will consider parabolic bands only. There is an angular dependence in k space for the $|\hat{a} \cdot p_{vc}|^2$ and $|k \cdot \hat{a}|^2$ terms, which results in a factor of $1/5$ when the angular integral is performed, assuming that p_{vc} is parallel to k . For other cases, the resulting transition rate will have the same functional form and only differ by a numeric factor. For instance, in the Kane four-band model for the heavy-hole band, p_{vc} is perpendicular to k [33] and the numeric factor is $2/15$.

Using the fact that $A_{0j}^2 = 8\pi c I_j / n_j \omega_j^2$ where I_j is the irradiance (cgs) and n_j is the linear index, the result for the change in transition rate is

$$\Delta W = \frac{2^4 \pi}{5} \frac{e^4}{n_1^2 c^2} \frac{m_c^{1/2} |p_{vc}|^2}{m_0^2} \frac{I_1^2}{(\hbar\omega_1)^6} (2\hbar\omega_1 - E_g)^{3/2} \quad (22)$$

from which the two-photon absorption rate can be determined; $\beta(\omega) = 2\hbar\omega \Delta W I_1^{-2}$. In order to obtain a universal scaling law, we make use of the identity

$$\frac{|p_{vc}|^2}{m_0^2} \approx \frac{E_g}{2m_c}, \quad (23)$$

which is obtained using $k \cdot p$ theory [33]. The resulting expression for the 2PA has exactly the same scaling and frequency dependence as that calculated in [13], [15] using the second-order perturbation approach, namely,

$$\beta(\omega) = K \frac{\sqrt{E_p}}{n_0^2 E_g^3} F_2\left(\frac{\hbar\omega}{E_g}\right) \quad (24)$$

where $E_p = 2|p_{vc}|^2/m_0$ and

$$F_2(x) = \frac{(2x-1)^{3/2}}{(2x)^5}. \quad (25)$$

Note that $\beta \propto \omega \text{Im} \chi^{(3)}/n_0$. The function F_2 is only a function of the ratio of the photon energy $\hbar\omega$ to E_g (i.e., denoting the optically coupled states). The functional form of F_2 reflects the assumed band structure and the intermediate states considered in calculating the 2PA transition rate. E_p is nearly material independent and possesses a value $E_p \approx 21$ eV for most direct gap semiconductors, and K is a material-independent constant:

$$K = \frac{2^9 \pi}{5} \frac{e^4}{\sqrt{m_0} c^2} \quad (26)$$

which has a value of $K = 1940$ in units such that β is in cm/GW and E_g and E_p are in eV. A wealth of experimental and theoretical work regarding 2PA in semiconductors and crystalline materials exists. The best fit to the data of [11] using (24) and (25) gave $K = 3100$ in the same units as above, while Weiher's second-order perturbation calculation for a four-band model gave $K = 5200$ for parabolic bands neglecting any coulomb interaction [15]. When nonparabolicity was included, the predicted values of β were on average only 26% higher than experiment; however, the frequency dependence of β changed very little. Interestingly, (24) and (25) also give a fair estimate of β for a number of transparent materials measured using the third and fourth harmonics of picosecond Nd:YAG laser pulses [34], [9]. In Fig. 2, β scaled by $n_0^2/(K\sqrt{E_p}F_2)$ versus E_g on a log-log plot is shown. The slope of the straight line is -3 , and it shows good agreement with the data for semiconductors and is within a factor of ≈ 5 , even for wide-gap dielectrics [9].

B. Nondegenerate 2PA and Raman Transitions

We now consider the case where one photon from each of (ω_1, ω_2) is absorbed, i.e., terms which contain $\delta(\omega_{vc} - \omega_1 - \omega_2)$, $\delta(\omega_{vc} - \omega_1 + \omega_2)$, and $\delta(\omega_{vc} + \omega_1 - \omega_2)$ in (20). The first term corresponds to nondegenerate 2PA, whereas the second and third terms correspond to Raman transitions. On performing the integral over k space, it can be shown that for 2PA, the change in the transition

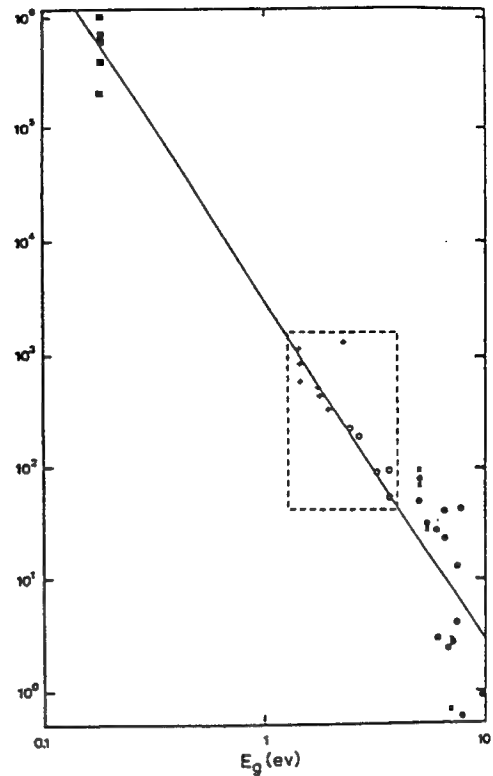


Fig. 2. A log-log plot of the scaled two-photon absorption coefficient $\beta n_0^2 / K \sqrt{E_p} F_2$ versus energy gap from [9]. The solid line is a least squares fit of the semiconductor data enclosed by the dashed box to a line of slope -3 . The fit also gives a good estimate of 2PA in wide-gap optical solids (lower right) [34] and InSb (upper left) [35].

rate is given as

$$\begin{aligned} \Delta W = & \sum_{\text{spin}} \int \frac{d^3 k}{(2\pi)^3} \left[\frac{\pi e^2 A_{01} A_{02}}{2m_0 m_{vc} c^2} \right]^2 |\hat{a} \cdot p_{vc}|^2 |k \cdot \hat{a}|^2 \\ & \cdot \left(\frac{1}{\omega_1} + \frac{1}{\omega_2} \right)^2 \frac{1}{2\pi\hbar} \delta \left(E_g + \frac{\hbar^2 k^2}{2m_{vc}} - \hbar\omega_1 - \hbar\omega_2 \right) \\ = & \frac{2^4 \pi}{5} \frac{e^4}{n_1 n_2 c^2} \frac{m_c^{1/2} |p_{vc}|^2}{m_0^2} \frac{I_1 I_2}{(\hbar\omega_1)^2 (\hbar\omega_2)^2} \\ & \cdot \left(\frac{1}{\hbar\omega_1} + \frac{1}{\hbar\omega_2} \right)^2 (\hbar\omega_1 + \hbar\omega_2 - E_g)^{3/2}. \end{aligned} \quad (27)$$

Using this expression for the transition rate, a change in absorption of the ω_1 beam due to the presence of ω_2 is calculated to have the general form

$$\Delta\alpha(\omega_1; \omega_2) = 2K \frac{\sqrt{E_p}}{n_1 n_2 E_g^3} F_2\left(\frac{\hbar\omega_1}{E_g}; \frac{\hbar\omega_2}{E_g}\right) I_2 \quad (28)$$

where for nondegenerate 2PA, the F_2 function as obtained from (27) is given by

$$F_2^{2PA}(x_1; x_2) = \frac{(x_1 + x_2 - 1)^{3/2}}{2^7 x_1 x_2^2} \left(\frac{1}{x_1} + \frac{1}{x_2} \right)^2. \quad (29)$$

Needless to say, F_2^{2PA} , and hence 2PA, is zero when $(x_1 + x_2 - 1) < 0$.

In a similar manner, the Raman terms can be calculated to give a change in absorption as in (28) with

$$F_2^{\text{RAM}}(x_1; x_2) = \frac{(x_1 - x_2 - 1)^{3/2} - (-x_1 + x_2 - 1)^{3/2}}{2^7 x_1 x_2^2} \cdot \left(\frac{1}{x_1} - \frac{1}{x_2} \right)^2. \quad (30)$$

The above expression contains the Raman transitions in which an electron is excited from the valence band into the conduction band via absorption of a photon at $\hbar\omega_1$ and emission of a photon at $\hbar\omega_2$ and vice versa. Therefore, the energy conservation terms corresponding to these transitions denoted by the $(\dots)^{3/2}$ terms in (30) are zero when their argument is negative.

The total $\Delta\alpha(\omega_1; \omega_2)$ from these multiphoton processes is the sum of the 2PA and Raman terms. Note that 2PA turns on when the sum of the frequencies is equal to the bandgap, but the Raman term turns on when the difference of the frequencies is equal to the bandgap so that one frequency must exceed the bandgap.

C. Linear and Quadratic Stark Effects

In addition to multiphoton absorption processes which involve the absorption or emission of a photon from both light fields, there can be a change in the absorption coefficient due to a shift in bandgap as a result of the ac Stark effect. For example, a change in the linear absorption of ω_1 occurs when the bands are shifted due to the ac Stark effect caused by ω_2 . Two terms arise out of this as the $A \cdot p$ radiation perturbation term couples 1) the conduction (or valence) band to itself, which we will term the linear Stark effect (LSE), and 2) the conduction band to the valence band, which we will term the quadratic Stark effect (QSE). In a physical sense, the effect of the LSE on the linear absorption is essentially a reduction of the oscillator strength by renormalizing the interband coupling due to the acceleration of the electrons (or holes) in their final dressed state. The QSE, on the other hand, alters the linear absorption through blue shifting the bandgap.

The linear Stark shift (self-coupling) can be obtained from the previous calculation by expanding the zero-order Bessel function to the next higher order term in (20), $J_0(x) \approx 1 - x^2/4$. This results in a modification to the S -matrix term which describes the one-photon absorption. The transition rate for the single-photon absorption of ω_1 is then modified as

$$W = \sum_{\text{spin}} \int \frac{d^3k}{(2\pi)^3} \left[\frac{\pi e A_{01}}{m_0 c} \right]^2 |\hat{a} \cdot p_{vc}|^2 \cdot \left[1 - \left(\frac{e A_{02}}{2m_{vc} c \omega_2} \right)^2 |k \cdot \hat{a}|^2 \right] \cdot \frac{1}{2\pi\hbar} \delta \left(E_g + \frac{\hbar^2 k^2}{2m_{vc}} - \hbar\omega_1 \right). \quad (31)$$

On performing this integral over k space and considering the term proportional to $I_1 I_2$, the following is obtained for the change in the transition rate:

$$\Delta W = -\frac{2^5 \pi}{5} \frac{e^4}{n_1 n_2 c^2} \frac{m_c^{1/2} |p_{vc}|^2}{m_0^2} \frac{I_1 I_2}{(\hbar\omega_1)^2 (\hbar\omega_2)^4} \cdot (\hbar\omega_1 - E_g)^{3/2}. \quad (32)$$

The resultant change of absorption $\Delta\alpha$ can be given in terms of (28) with F_2 given by

$$F_2^{\text{LSE}}(x_1; x_2) = -\frac{(x_1 - 1)^{3/2}}{2^6 x_1 x_2^4} \quad (33)$$

where the scaling is the same as in (28).

The quadratic Stark shift resulting from the coupling between the conduction and valence bands due to ω_2 is given by

$$\begin{aligned} \Delta E_{cv} &= -\Delta E_{vc} \\ &= \left(\frac{e A_{02}}{2m_0 c} \right)^2 |\hat{a} \cdot p_{vc}|^2 \left[\left(E_g + \frac{\hbar^2 k^2}{2m_{vc}} - \hbar\omega_2 \right)^{-1} \right. \\ &\quad \left. + \left(E_g + \frac{\hbar^2 k^2}{2m_{vc}} + \hbar\omega_2 \right)^{-1} \right]. \end{aligned} \quad (34)$$

It should be expected that in the low-frequency limit $\hbar\omega_2 \ll E_g$, the energy shift due to the QSE as given by the above equations would approach the classical pondermotive energy of the electron/hole in an oscillating electromagnetic field. This equivalence can indeed be simply verified by substituting $|p_{vc}|$ from (23) into (34), which would yield

$$\Delta E_e = -\Delta E_h = \frac{e^2 A_{02}^2}{4m_c c^2}. \quad (35)$$

This classical energy shift, which is also referred to as the "mass energy shift," has been used in previous "dressed state" (tunneling) calculations of the interband transition rate [28], [30].

Returning to the QSE energy shift, we note that this energy term is time independent (i.e., nonoscillating). Therefore, it only appears in the δ -function energy conservation terms. Thus, the one-photon transition rate is modified to give

$$W = \sum_{\text{spin}} \int \frac{d^3k}{(2\pi)^3} \left[\frac{\pi e A_{01}}{m_0 c} \right]^2 |\hat{a} \cdot p_{vc}|^2 \frac{1}{2\pi\hbar} \cdot \delta \left(E_g + \frac{\hbar^2 k^2}{2m_{vc}} + \Delta E_{cv} - \Delta E_{vc} - \hbar\omega_1 \right). \quad (36)$$

On performing the integration and expanding to obtain the term proportional to $I_1 I_2$, the change in the transition rate is given as

$$\begin{aligned} \Delta W &= -\frac{4\pi}{5} \frac{e^4}{n_1 n_2 c^2} \frac{m_c^{3/2} |p_{vc}|^4}{m_0^4} \frac{I_1 I_2}{(\hbar\omega_1)^2 (\hbar\omega_2)^2} \\ &\quad \cdot (\hbar\omega_1 - E_g)^{-1/2} \left[\frac{1}{\hbar\omega_1 - \hbar\omega_2} + \frac{1}{\hbar\omega_1 + \hbar\omega_2} \right]. \end{aligned} \quad (37)$$

TABLE I
FREQUENCY DEPENDENCE OF THE NONDEGENERATE ABSORPTION $F_2(\hbar\omega_1/E_g; \hbar\omega_2/E_g)$ AS
DEFINED IN (28)

Contribution	$F_2(x_1; x_2)$
Two-Photon Absorption	$\frac{(x_1 + x_2 - 1)^{3/2}}{2^7 x_1 x_2^2} \left(\frac{1}{x_1} + \frac{1}{x_2} \right)^2$
Raman	$\frac{(x_1 - x_2 - 1)^{3/2}}{2^7 x_1 x_2^2} \left(\frac{1}{x_1} - \frac{1}{x_2} \right)^2$
Linear Stark	$-\frac{(x_1 - 1)^{3/2}}{2^6 x_1 x_2^2} \frac{1}{x_2^2}$
Quadratic Stark	$-\frac{1}{2^{10} x_1 x_2^2 (x_1 - 1)^{1/2}} \left[\frac{1}{x_1 - x_2} + \frac{1}{x_1 + x_2} \right]$

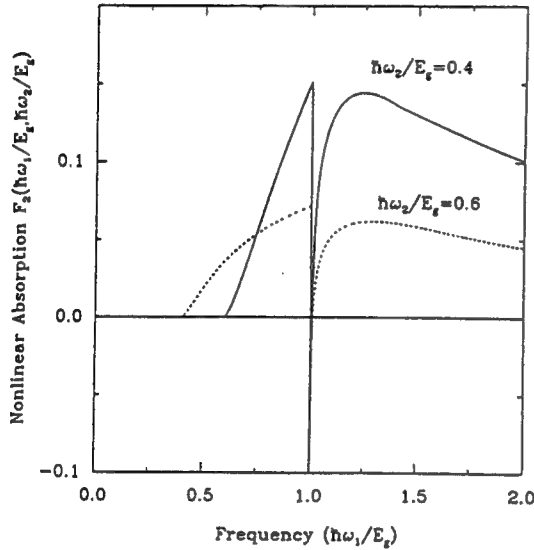


Fig. 3. Theoretical frequency dependence of the nondegenerate nonlinear absorption for two different "pump" frequencies $\hbar\omega_2/E_g = 0.4, 0.6$. Below the fundamental absorption edge $\hbar\omega_1 < E_g$, only 2PA contributes to the nonlinear absorption.

The resulting change in absorption coefficient is given by (28) with

$$F_2^{QSE}(x_1; x_2) = -\frac{1}{2^{10} x_1 x_2^2 (x_1 - 1)^{1/2}} \left[\frac{1}{x_1 - x_2} + \frac{1}{x_1 + x_2} \right] \quad (38)$$

Again, the total $\Delta\alpha(\omega_1; \omega_2)$ is given by (28) and using the sum of all the F_2 terms for multiphoton and Stark shift terms. These results for the spectrum of the nondegenerate absorption change for the two-band model with parallel optical polarization vectors and $\hbar\omega_2 < E_g$ are summarized in Table I.

The spectrum of the nonlinear absorption $F_2(\hbar\omega_1/E_g; \hbar\omega_2/E_g)$ is shown in Fig. 3 for two different "pump" frequencies ω_2 . Note that for $\hbar\omega_2 < E_g$, the Raman and Stark terms can only contribute to the nonlinear absorption for $\hbar\omega_1 > E_g$. The negative (i.e., decreasing absorption) divergence at the bandgap results from the quadratic Stark shift causing a blue shift of the band edge. The spectrum in Fig. 3 resembles that obtained by Yacoby [36], who calculated the interband transition rate when the modulating source (ω_2) is of very low frequency (i.e.,

RF excitation) and the resonant ac Stark effect is neglected.

IV. NONLINEAR REFRACTION

In general, we can evaluate the nondegenerate refractive index change $\Delta n(\omega; \Omega)$ as given by the Kramers-Krönig dispersion relation:

$$\Delta n(\omega; \Omega) = \frac{c}{\pi} \int_0^\infty \frac{\Delta\alpha(\omega'; \Omega)}{\omega'^2 - \omega^2} d\omega'. \quad (39)$$

However, there are few experiments which measure this quantity other than at $\Omega = \omega$. We therefore present in this paper only the calculated results for the degenerate $\Delta n(\omega; \omega)$ which, in turn, will lead to the Kerr coefficients n_2 or γ as defined by (1):

$$\gamma = K \frac{\hbar c \sqrt{E_g}}{n_0^2 E_g^4} G_2 \left(\frac{\hbar\omega}{E_g} \right) \quad (40)$$

where the dispersion function G_2 is given by

$$G_2(x_2) = \frac{2}{\pi} \int_0^\infty \frac{F_2(x_1; x_2) dx_1}{x_1^2 - x_2^2}. \quad (41)$$

We have neglected any dispersion in the linear refractive index n_0 in the integral. The magnitude of the dispersion is typically only 10% of the background refractive index around the band edge of semiconductors, so we do not anticipate any significant error. All that remains is for the above integral to be evaluated for the various contributions to the nondegenerate absorption $F_2(x_1; x_2)$. All of the integrals are performed in a similar manner and make use of the identity

$$\int_0^\infty \frac{x^{\mu-1} dx}{(a+x)^n} = a^{\mu-n} \frac{\Gamma(\mu)\Gamma(n-\mu)}{\Gamma(n)} \quad (42)$$

for $n > \mu$. The individual contributions are given in Table II.

On examining the low-frequency limit, it is found that these terms diverge as $\omega \rightarrow 0$. In order to investigate such unphysical "infrared" divergences, we go one step back and examine the nondegenerate case as given by (39). This equation indicates that, in general, $\Delta n(\omega; \Omega)$ is not divergent in ω , and therefore any zero-frequency divergence must be in the pump frequency Ω as it appears in $\Delta\alpha$. To

TABLE II
DISPERSION OF THE NONLINEAR REFRACTION $G_2(\hbar\omega/E_g)$ FOR FREQUENCIES BELOW THE BAND
EDGE AS DEFINED IN (44). $\Theta(x)$ IS THE HEAVISIDE OR STEP FUNCTION.

Contribution	$G_2(x)$
Two-Photon Absorption	$\frac{1}{(2x)^6} \left[-\frac{3}{8} x^2(1-x)^{-1/2} + 3x(1-x)^{1/2} - 2(1-x)^{3/2} + 2\Theta(1-2x)(1-2x)^{3/2} \right]$
Raman	$\frac{1}{(2x)^6} \left[-\frac{3}{8} x^2(1+x)^{-1/2} - 3x(1+x)^{1/2} - 2(1+x)^{3/2} + 2(1+2x)^{3/2} \right]$
Linear Stark	$\frac{1}{(2x)^6} [2 - (1-x)^{3/2} - (1+x)^{3/2}]$
Quadratic Stark	$\frac{1}{2^{10} x^5} \left[(1-x)^{-1/2} - (1+x)^{-1/2} - \frac{x}{2} (1-x)^{-3/2} - \frac{x}{2} (1+x)^{-3/2} \right]$
Divergent Term	$\frac{1}{(2x)^6} \left[-2 - \frac{35x^2}{8} + \frac{x}{8} (3x-1)(1-x)^{-1/2} - 3x(1-x)^{1/2} + (1-x)^{3/2} + \frac{x}{8} (3x+1)(1+x)^{-1/2} + 3x(1+x)^{1/2} + (1+x)^{3/2} \right]$

further identify these divergences, $\Delta n(\omega; \Omega)$ can be expanded as a Laurent series around $\Omega = 0$. We find that there exist terms which diverge as Ω^{-4} , Ω^{-3} , Ω^{-2} , and Ω^{-1} . On summing these terms, however, all the divergences vanish apart from a term proportional to Ω^{-2} , leaving the divergent term as

$$G_2^{\text{div}} = \frac{g(\omega)}{\Omega^2} \quad (43)$$

where $g(\omega)$ has no divergence at $\omega = 0$. Now, by setting $\Omega = \omega$, one arrives at the degenerate divergence function as shown in Table II. This diverging term is expected as $A \cdot p$ perturbation theory has been used in the transition rate calculations, and it is well known that divergences of this order can be introduced [37], whereas the comparable $E \cdot r$ perturbation theory avoids such divergences. The latter perturbation technique, however, is not suitable for solids with extended wavefunctions, and simple scaling rules cannot be easily derived. In a similar manner to Moss *et al.* [38], we treat such a divergence as unphysical and subtract it from the result for the nonlinear refraction.

The individual contributions to the nonlinear refraction are shown in Fig. 4 as a function of frequency. The divergence in each physically identifiable process has been subtracted for clarity. It can be seen that the most significant contribution to the spectral dependence of G_2 arises from the 2PA term, except close to the band edge where the quadratic Stark term becomes dominant. The linear Stark term arising from the self-coupling of the bands is insignificant compared to the quadratic term. In terms of second-order perturbation theory, this is a result of the momentum matrix element being much larger when taken between conduction and valence bands than between the

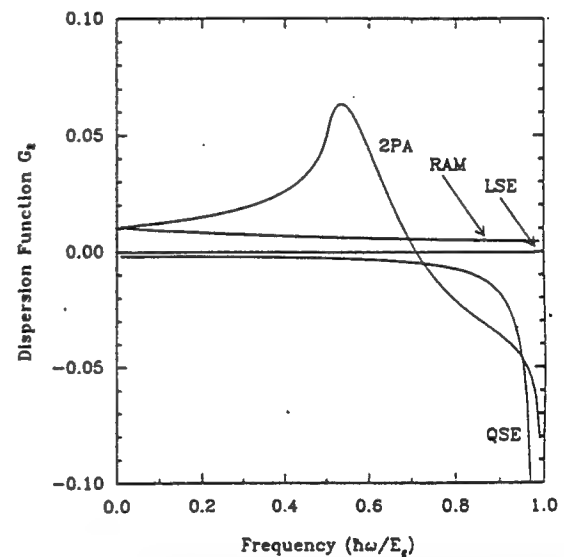


Fig. 4. Frequency dependence of the various contributions to the nonlinear refractive index n_2 . Each contribution is derived from a Kramers-Kronig transform of the various nonlinear absorption processes: two-photon absorption, Raman transitions, and linear and quadratic Stark shifts of the band edge. The divergence of each term as $\omega \rightarrow 0$ has been removed for clarity.

same bands [13]. The only significance of the linear Stark term in the present calculation is that it cancels terms which diverge as ω^{-4} arising from the 2PA and Raman contributions.

The general scaled form for n_2 is given by

$$n_2(\text{esu}) = K' \frac{\sqrt{E_p}}{n_0 E_g^4} G_2(\hbar\omega/E_g) \quad (44)$$

where, using the value of K obtained from the fit to 2PA in semiconductors (3100), the constant $K' = 1.50 \times 10^{-8}$ when E_g and E_p are defined in eV. Using the value of K predicted by theory (no fitting) gives $K' = 0.94 \times 10^{-8}$. We note the E_g^{-4} dependence for the magnitude of n_2 , corresponding to the scaling predicted by Wherrett [13].

A graphical comparison of the dispersion function $G_2(\hbar\omega/E_g)$ with measured values of n_2 is shown in Fig. 5(a). The values for semiconductors (squares) were obtained from Z-scan measurements at 1.06 and 0.53 μm [1], [10] (as previously plotted in Fig. 1). Included in these data are some new measurements. We also show "nearly degenerate three-wave mixing" n_2 measurements of large-gap optical materials [6] (solid circles) and a measurement of n_2 in silica at 249 nm [39] (diamond).

Fig. 5(b) shows the extension to Fig. 5(a) for frequencies close to the band edge where the bound electronic refractive nonlinearity shows a resonance due to the quadratic ac Stark effect. This graph also includes recent measurements of n_2 in AlGaAs by LaGasse *et al.* [40] using femtosecond time-division interferometry techniques (solid triangles). Table III shows the measured values for n_2 for the various semiconductors and wide-gap optical solids which are plotted in Fig. 5. The data for the semiconductor bandgaps and linear refractive index were obtained from [41], [42]. From the theory presented here, we also give the predicted values for n_2 . For the semiconductor measurements at 1.06 and 0.53 μm (excluding CdSe at 1.06 μm whose n_2 could not be measured with any degree of accuracy because of the 2PA-induced band-filling refractive nonlinearity), we find an average difference of less than 30% between the measured and predicted values. Including the measurements for dielectrics, the average difference was less than a factor of 2. We note, however, that the measured n_2 for these wide-gap solids are consistently smaller than the predicted values. One possible reason for this is that the absorption edge has been used to determine the bandgap. The band structure for these materials is not well known, and the direct gap may well be larger than this. We find, however, for these wide-gap materials, that a good fit to the n_2 data can be obtained by using a smaller value for the constant $K' = 0.86 \times 10^{-8}$, as shown by the dashed line in Fig. 5(a).

For frequencies close to the band edge, the Stark effect results in a divergence in the nonlinear refractive index of $-(E_g - \hbar\omega)^{-3/2}$. This region can be examined in more detail by replotting data and theory in a log-log plot as shown in Fig. 6. Note the straight line dependence for small detunings, with a slope of $-3/2$ corresponding to the above asymptotic relationship. From Figs. 5(b) and 6, one notices an increasing deviation of the AlGaAs data from the theory as the photon energy is approaching the energy gap. One possible cause for this deviation is the excitonic enhancement which becomes significant near the band edge.

The Stark effect can also be described as virtual band blocking since a blue shift of the band edge is equivalent

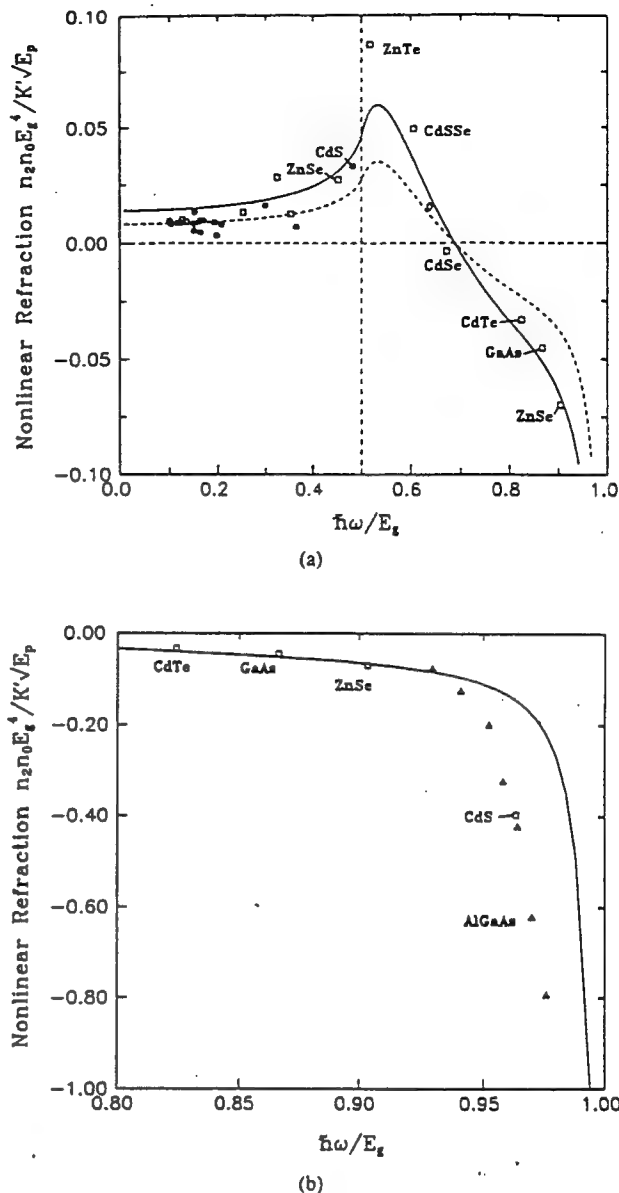


Fig. 5. (a) Dispersion of the nonlinear refractive index n_2 . Data for n_2 are scaled as $n_2 n_0 E_g^4 / K' \sqrt{E_p}$. The circles are measurements in [6], the diamond is from [39], and the squares are our own Z-scan measurements. We have labeled the semiconductor data. The solid line is the $G_2(\hbar\omega/E_g)$ function derived here for a two-band model of a semiconductor using the 2PA data for the fit to the constant K' . The dashed line corresponds to a fit to n_2 for the wide-gap solids ($K' = 0.86 \times 10^{-8}$). (b) Extension of (a) to frequencies close to the band edge. The triangles are n_2 measurements of AlGaAs in [40].

to a reduction of optically coupled states at photon energies corresponding to the bottom of the band (in a similar manner to the dynamic Burstein-Moss shift [43]). Indeed, the direct saturation model [44] predicts exactly the same frequency and material dependence of the nonlinear refractive index just beneath the band edge. This allows a conceptual link between below-gap (virtual carriers) and bandgap resonant (real carriers) nonlinear optical effects [45].

Hidden in Figs. 5 and 6 is the E_g^{-4} scaling of n_2 that gives a variation of n_2 from 2.5×10^{-14} esu for a material

TABLE III

LIST OF n_2 DATA SHOWING PARAMETERS USED IN THE CALCULATION (FROM [41], [42]) ALONG WITH THE EXPERIMENTALLY MEASURED AND THEORETICALLY PREDICTED VALUES OF n_2 . THESE n_2 DATA INCLUDE MEASUREMENTS IN [6], [39], [40].
 † INDICATES WHERE WE HAVE USED THE DIRECT GAP RATHER THAN THE FUNDAMENTAL ABSORPTION EDGE. THE COLUMN INDICATED BY * USES A FIT TO THE CONSTANT K' FOR WIDE-GAP MATERIALS RATHER THAN THE FIT TO 2PA IN SEMICONDUCTORS [SEE FIG. 5(a)]

Material	Wavelength (μm)	Bandgap (eV)	Refr. Index	n_2 (Exp.) $\times 10^{-13}$ (esu)	n_2 (Pred.) $\times 10^{-13}$ (esu)	n_2 (Pred.)* $\times 10^{-13}$ (esu)
Ge	10.6	0.87†	4.00	2700	4400	
GaAs	1.06	1.35	3.47	-2700	-3100	
CdTe	1.06	1.44	2.84	-2000	-2100	
CdSe	1.06	1.74	2.56	-90	180	
CdS _{0.5} Se _{0.5}	1.06	1.93	2.45	1000	720	
ZnTe	1.06	2.26	2.79	830	540	
CdS	0.53	2.42	2.34	-3400	-1200	
ZnSe	1.06	2.58	2.48	170	190	
ZnSe	0.53	2.58	2.70	-400	-380	
SBN	1.06	3.3	2.4	30	51	29
ZnS	1.06	3.54	2.40	48	36	
KTP	1.06	3.54	1.78	13	49	28
BaF ₂	1.06	9.21	1.47	0.67	0.95	0.54
BaF ₂	0.53	9.21	1.47	0.85	1.10	0.63
AlGaAs	0.850	1.57	3.30	-2000	-2800	
AlGaAs	0.840	1.57	3.30	-4000	-3300	
AlGaAs	0.830	1.57	3.30	-7000	-3900	
AlGaAs	0.825	1.57	3.30	-10000	-4300	
AlGaAs	0.820	1.57	3.30	-14000	-4900	
AlGaAs	0.815	1.57	3.30	-20000	-5900	
AlGaAs	0.810	1.57	3.30	-26000	-7300	
CdS	1.06	2.42	2.34	280	330	
AgCl	1.06	3.10	2.07	23	81	46
ZnO	1.06	3.20	1.96	23	73	41
NaBr	1.06	5.63	1.64	3.3	6.6	3.8
CaCO ₃	1.06	5.88	1.60	1.1	5.6	3.2
KBr	1.06	6.04	1.56	2.9	5.1	2.9
KCl	1.06	6.89	1.49	2.0	3.1	1.8
KDP	1.06	6.95	1.60	0.7	2.8	1.6
KH ₂ PO ₄	1.06	7.12	1.50	0.8	2.7	1.5
NaCl	1.06	7.21	1.53	1.6	2.5	1.4
Al ₂ O ₃	1.06	7.30	1.75	1.2	2.1	1.2
KF	1.06	7.75	1.36	0.75	2.1	1.2
MgO	1.06	7.77	1.70	1.6	1.6	0.94
SiO ₂	1.06	7.80	1.40	1.1	2.0	1.1
SrF ₂	1.06	9.54	1.44	0.50	0.84	0.48
CaF ₂	1.06	9.92	1.43	0.43	0.72	0.41
MgF ₂	1.06	11.27	1.38	0.25	0.44	0.25
LiF	1.06	11.60	1.39	0.26	0.39	0.22
SiO ₂	0.249	7.80	1.60	1.7	2.4	1.4

such as MgF₂ at 1.06 μm to -2.6×10^{-9} esu for AlGaAs at 810 nm [40] and 2.7×10^{-10} esu for Ge at 10.6 μm , which we measured with a picosecond CO₂ laser. This five orders of magnitude variation of n_2 is better displayed by plotting n_2 scaled by n_0 and G_2 as a function of E_g on a log-log plot, as shown in Fig. 7. In spite of this very large variation in the magnitude of n_2 (and the change in sign), this extremely simple model gives good agreement with the data for materials including both semiconductors and insulators. It is found that the E_g^{-4} scaling law holds true over the five orders of magnitude variation in the modulus of n_2 for the data presented here. Additionally note that although the measured values of n_2 for ZnSe at 1.06 and 0.53 μm have different signs, both measurements are consistent with the scaling law.

V. IMPLICATIONS FOR ALL-OPTICAL SWITCHING

One of the applications of the nonlinear refractive index n_2 is in the role of all-optical switching. Some examples are a nonlinear Fabry-Perot filter for image processing, or parallel optical computing [46], [47], or coupled waveguides for communication switching networks [48], [7]. When it comes to optimizing devices for optical switching, it is important that optical losses in the system are not too large. For instance, if optical absorption is too large, then the change in refractive index will fall off rapidly as the optical beam propagates.

It can be shown that for any optical switching system, one must achieve a refractive index change Δn such that

$$|\Delta n| > c_{\text{sw}} \alpha \lambda \quad (45)$$

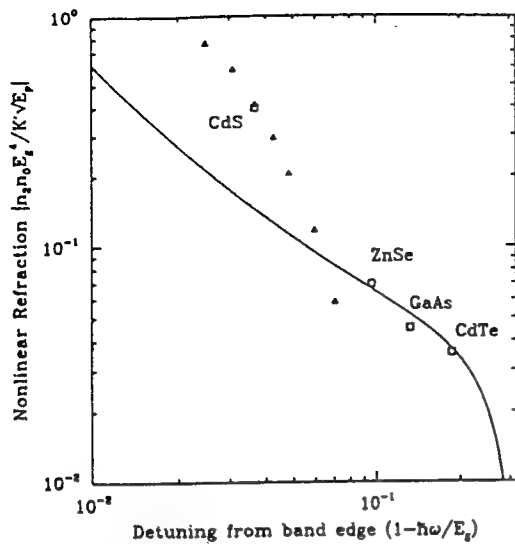


Fig. 6. Same as n_2 data close to the band edge as plotted in Fig. 5(b), but now plotted on a log-log scale to emphasize the asymptotic form $n_2 \propto -(1 - \hbar\omega/E_g)^{-3/2}$ as the frequency approaches the band edge. Again, the solid line shows the predicted form.

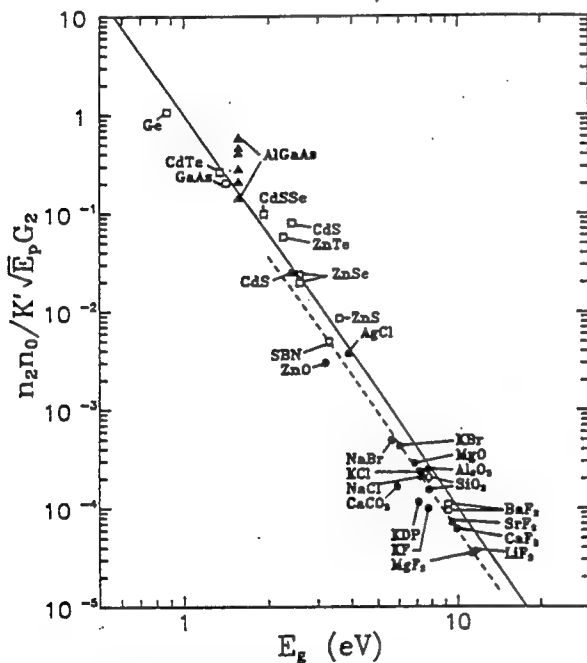


Fig. 7. A log-log plot showing the expected E_g^{-4} dependence of n_2 . The data points are identical to those in Figs. 5 and 6, but now are scaled by the dispersion function $G_2(\hbar\omega/E_g)$. The solid line is the function E_g^{-4} which translates into a straight line of slope -4 on a log-log plot. The dashed line indicates the fit to the wide-gap solids which also have the E_g^{-4} dependence.

where c_{sw} is a numeric constant of the order of unity whose precise value depends on the exact switching scheme. For example, using a Fabry-Perot filter, $c_{sw} = (2\sqrt{3}\pi)^{-1}$ [49], whereas a nonlinear coupled waveguide gives $c_{sw} = 2$ [50], [51].

Below the band edge, the principal contribution to the absorption at irradiance levels of interest is two-photon absorption, $\alpha \approx \beta I$. In addition, the electronic Kerr effect gives the change in refractive index $\Delta n = \gamma I$. Hence, in

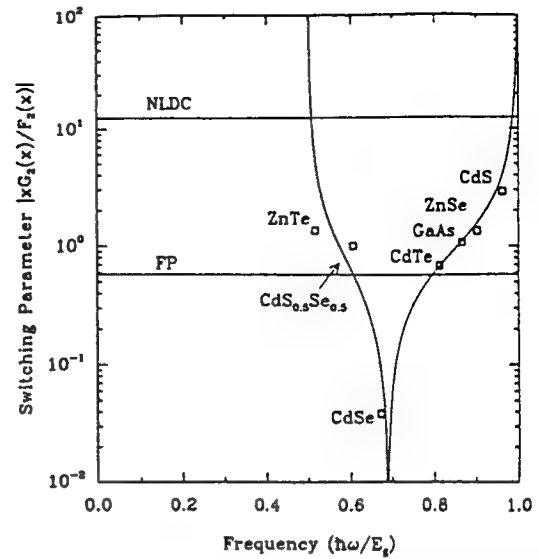


Fig. 8. Material-independent switching parameter as a function of frequency. Also shown are the minimum limits for all-optical switching in two different geometries: nonlinear directional coupler (NLDC) and Fabry-Perot (FP) filter. For switching to be possible, the switching parameter must exceed the relevant limit. The experimentally determined values of this parameter are based on the semiconductor n_2 measurements here and our β measurements in [11].

this regime, the requirement for all-optical switching is [50]

$$\left| \frac{\gamma}{\beta \lambda} \right| > c_{sw}. \quad (46)$$

The theory presented in this paper gives the scaling and dispersion for both β and γ , which are related through nonlinear Kramers-Krönig relations. Inserting the functional forms of β and γ given here gives the frequency dependence for the all-optical switching requirement:

$$\frac{\hbar\omega}{E_g} \left| \frac{G_2(\hbar\omega/E_g)}{F_2(\hbar\omega/E_g)} \right| > 2\pi c_{sw}. \quad (47)$$

Note that (47) has no explicit material dependence since it is only a function of the ratio $\hbar\omega/E_g$. Thus, although n_2 can be enhanced by using smaller gap materials, this does not necessarily improve the conditions for switching. The left-hand side of (47) is plotted in Fig. 8. In the same figure, we also show the experimentally measured values for this parameter $|2\pi\gamma/\beta\lambda|$ for some semiconductors using the n_2 values measured here and our 2PA coefficients from [11]. We note that there is a range of optical frequencies where this quantity becomes too small for optical switching, which is given approximately by $0.6 < \hbar\omega/E_g < 0.9$. This region is centered around the point where there is a change of sign in n_2 , covering most of the range of frequencies where 2PA is observed. Therefore, given a certain wavelength of operation, this immediately excludes certain materials from consideration for all-optical switching. This was first noted by Stegeman *et al.* [50]. DeLong and Stegeman [52] recently used the results of [2], which only included the 2PA contribution to γ , to give a similar requirement for all-optical

switching. Our result ignores free-carrier absorption and refraction, exciton effects, and linear absorption which may further restrict or enhance the choice of material.

This result can also be extended to other applications for nonlinear optics. For instance, 2PA has been a problem in the observation of spatial optical solitons based on the electronic Kerr effect [53]. We can use the above result as a rule of thumb in determining for what material/frequency combination 2PA would cause problems for nonlinear refractive applications.

VI. CONCLUSIONS

We have presented a simple two-band model calculation that gives a universal bandgap scaling and dispersion of the electronic Kerr effect in solids. This simple model, for the first time, draws a direct relationship between the nonlinear refractive index n_2 and its nonlinear absorptive counterparts, namely, two-photon absorption, Raman transitions, and the ac Stark effect. We have also presented measurements of the bound electronic nonlinear refractive index for various materials beneath the band edge. Several new data, along with previously published data, are compared to this theory, and remarkable agreement is observed.

A wide range of theoretical papers exists where nonlinear absorption is calculated by means of transition rates. We used a nonlinear Kramers-Krönig transformation approach to obtain the nonlinear refraction in terms of this electronic nonlinear absorption because this method circumvents a direct calculation of the complex nonlinear susceptibility. However, it is necessary to know the nondegenerate absorption in order to perform the calculation (or refraction in the equivalent converse expression). That is, we need expressions for the nonlinear absorption at all frequencies ω_1 when an optical field ω_2 is applied. This can be thought of as a pump-probe spectrum where, in the present convention, ω_2 would be the pump frequency and ω_1 the variable probe frequency. We calculated this nondegenerate nonlinear absorption using a simple two-band model for a direct gap semiconductor. The next stage of complexity would be to do the same calculation for the Kane four-band model of a semiconductor. It was necessary to include transitions over all frequencies so that the Raman and Stark shift terms are included, as well as two-photon absorption.

We performed the Kramers-Krönig integral on the nondegenerate nonlinear absorption to obtain analytic expressions for the nonlinear self-refraction. In this calculation, we set the two frequencies in the nonlinear refraction equal to determine self-refraction, but in general the nondegenerate refraction can also be obtained, i.e., the change in refractive index seen by the light of frequency ω when the light of frequency Ω is present.

Comparing the experimentally measured values of n_2 to the theoretical dispersion presented here, we find that good agreement is obtained over a wide range of frequencies and materials, with only one fitting parameter K' obtained

from 2PA measurements in semiconductors. We note, however, that the theoretical value for this parameter is only about 40% smaller than this fitted value for K' . This is quite remarkable, and to some extent surprising as a simple two-band model has been used to calculate the nonlinear refraction with no account for the full-band structure or excitonic effects. However, as has been shown by earlier calculations of the 2PA coefficients in semiconductors [15], the effect of nonparabolicity of the bands becomes important only for small-gap semiconductors such as InSb. Also ignored in this model is the contribution of higher bands (conduction or split-off valence bands), and hence the effect of their specific structure. This can be justified by noticing the strong inverse photon energy dependence of the nonlinear transition rate as shown in Table I. This is better illustrated in Fig. 3 where the change in absorption becomes progressively smaller at higher frequencies ($\hbar\omega/E_g > 1.5$), and hence the near-gap transitions will dominate. Including the effect of higher bands in calculating the transition rate will contain terms involving high-energy photons, and therefore, it should have a negligible effect.

The other important simplification in our model has been the exclusion of the coulomb interaction or excitonic enhancement. Earlier calculations of the excitonic effects on two-photon transition rates had indicated a significant enhancement near the two-photon resonance $\hbar\omega \approx E_g/2$ [15], [21]. For example, the underestimation of both n_2 and the 2PA coefficient β of ZnTe at $\lambda = 1.06 \mu\text{m}$ may well be due to this two-photon exciton resonance [11]. Similarly, for photon energies approaching the energy gap, an excitonic enhancement of the quadratic Stark effect is expected. For example, nonlinear refraction can occur due to the ac Stark shift of an exciton resonance [54]. We also expect the contribution from the quadratic Stark effect to be relatively larger when a four-band model for a semiconductor is used since the density of the valence band states is larger, which also may lead to a better fit. Therefore, the deviation of the measured n_2 data on CdS (at 532 nm) and AlGaAs (at ~ 800 nm) from the predicted values may be due to these other near-bandgap effects.

It is also remarkable that the theory gives a reasonable fit to the data for large-gap optical materials, as well as conventional semiconductors. However, it can be seen that the predicted value for n_2 is consistently on the large side for these materials. This may be due to the fact that the absorption edge has been used to determine the direct bandgap. We find that for Ge, as expected, it is necessary to use the direct bandgap rather than the smaller indirect gap in order to obtain a satisfactory fit, and the same should be true for wide-gap solids. This is because the transitions involving the lower indirect gaps require phonon scattering, and thus they should have a smaller oscillator strength than direct interband transitions. Unfortunately, the band structure of these materials is not well known. We have also used the mean value of E_p for

semiconductors in order to predict n_2 , and this parameter may also be quite different in other materials. We find that for the wide-gap solid data presented here, a better estimate for n_2 is obtained by replacing the K' from the fit to the semiconductor 2PA data with a smaller value, which may be more appropriate for these wide-gap materials, as indicated in Fig. 5(a) and Table III.

The change in sign of n_2 at about $\hbar\omega/E_g \approx 0.7$ is predicted and observed. It is also demonstrated that the expected E_g^{-4} bandgap dependence holds true for a five order of magnitude variation in the modulus of n_2 .

It is noted that the main contribution to the dispersion of n_2 below the bandgap arises from the two-photon transition term, with the Stark shift term becoming dominant close to the band edge. This partly explains the good fit obtained by using the quasi-nondegenerate two-photon absorption alone, as shown in a previous letter by the authors [2].

ACKNOWLEDGMENT

The authors thank A. Miller, O. Heinonen, S. Epifanov, and B. S. Wherrett for useful discussions, and A. Said, T. Wei, E. Canto, and J. Young for taking and analyzing portions of the n_2 data.

REFERENCES

- [1] M. Sheik-Bahae, A. A. Said, T. H. Wei, D. J. Hagan, and E. W. Van Stryland, "Sensitive measurements of optical nonlinearities using a single beam," *IEEE J. Quantum Electron.*, vol. 26, pp. 760-769, 1990.
- [2] M. Sheik-Bahae, D. J. Hagan, and E. W. Van Stryland, "Dispersion and band-gap scaling of the electronic Kerr effect in solids associated with two-photon absorption," *Phys. Rev. Lett.*, vol. 65, pp. 96-99, 1990.
- [3] D. J. Hagan, E. Canto, E. Meisak, M. J. Soileau, and E. W. Van Stryland, "Picosecond degenerate four-wave mixing studies in ZnSe," in *Tech. Dig. Conf. Lasers Electro-Opt.*, Anaheim, CA, 1988, vol. 7, p. 160.
- [4] D. H. Auston *et al.*, "Research on nonlinear optical materials: An assessment," *Appl. Opt.*, vol. 26, pp. 211-234, 1987.
- [5] D. A. B. Miller, M. H. Mozolowski, A. Miller, and S. D. Smith, "Nonlinear optical effects in InSb with a c.w. CO laser," *Opt. Commun.*, vol. 27, pp. 133-136, 1978.
- [6] R. Adair, L. L. Chase, and S. A. Payne, "Nonlinear refractive index of optical crystals," *Phys. Rev. B*, vol. 39, pp. 3337-3349, 1989.
- [7] S. R. Friberg, A. M. Weiner, Y. Silberberg, B. G. Sfez, and P. S. Smith, "Femtosecond switching in a dual-core fibre nonlinear coupler," *Opt. Lett.*, vol. 13, pp. 904-906, 1988.
- [8] M. J. Soileau, W. E. Williams, N. Mansour, and E. W. Van Stryland, "Laser-induced damage and the role of self-focusing," *Opt. Eng.*, vol. 28, pp. 1133-1144, 1989.
- [9] E. W. Van Stryland, Y. Y. Wu, D. J. Hagan, M. J. Soileau, and K. Mansour, "Optical limiting with semiconductors," *J. Opt. Soc. Amer. B*, vol. 5, pp. 1980-1989, 1988.
- [10] M. Sheik-Bahae, A. A. Said, and E. W. Van Stryland, "High sensitivity, single beam n_2 measurements," *Opt. Lett.*, vol. 14, pp. 955-957, 1989.
- [11] E. W. Van Stryland, H. Vanherzeele, M. A. Woodall, M. J. Soileau, A. L. Smirl, S. Guha, and T. F. Boggess, "Two photon absorption, nonlinear refraction, and optical limiting in semiconductors," *Opt. Eng.*, vol. 24, pp. 613-623, 1985.
- [12] E. J. Canto-Said, D. J. Hagan, J. Young, and E. W. Van Stryland, "Degenerate four-wave mixing measurements of high order nonlinearities in semiconductors," *IEEE J. Quantum Electron.*, to be published.
- [13] B. S. Wherrett, "Scaling rules for multiphoton interband absorption in semiconductors," *J. Opt. Soc. Amer. B*, vol. 1, pp. 67-72, 1984.
- [14] J. Callaway, *Quantum Theory of the Solid State*. New York: Academic, 1974, p. 540.
- [15] M. H. Weiler, "Nonparabolicity and exciton effects in two-photon absorption in zincblende semiconductors," *Solid State Commun.*, vol. 39, pp. 937-940, 1981.
- [16] S. S. Jha and N. Bloembergen, "Nonlinear optical susceptibilities in group-IV and III-V semiconductors," *Phys. Rev.*, vol. 171, pp. 891-898, 1968.
- [17] C. Flytzanis, "Third-order optical susceptibilities in IV-IV and III-V semiconductors," *Phys. Lett.*, vol. 31A, pp. 273-274, 1970.
- [18] J. A. Van Vechten and D. E. Aspnes, "Franz-Keldysh contributions to third-order optical susceptibilities," *Phys. Lett.*, vol. 30A, pp. 346-347, 1969.
- [19] C. C. Wang, "Empirical relation between the linear and third-order nonlinear optical susceptibilities," *Phys. Rev. B*, vol. 2, pp. 2045-2048, 1970.
- [20] N. L. Boling, A. J. Glass, and A. Owyong, "Empirical relationships for predicting nonlinear refractive index changes in optical solids," *IEEE J. Quantum Electron.*, vol. QE-14, pp. 601-608, 1978.
- [21] C. C. Lee and H. Y. Fan, "Two-photon absorption with exciton effect for degenerate bands," *Phys. Rev. B*, vol. 9, pp. 3502-3516, 1974.
- [22] H. M. Nussenzveig, *Causality and Dispersion Relations*. New York: Academic, 1972.
- [23] D. A. B. Miller, C. T. Seaton, M. E. Prise, and S. D. Smith, "Band-gap-resonant nonlinear refraction in III-V semiconductors," *Phys. Rev. Lett.*, vol. 47, pp. 197-200, 1981.
- [24] B. S. Wherrett, D. Hutchings, and D. Russell, "Optically bistable interference filters: Optimization considerations," *J. Opt. Soc. Amer. B*, vol. 3, pp. 351-362, 1986.
- [25] A. Yariv, *Quantum Electronics*, 2nd ed. New York: Wiley, 1975.
- [26] S. M. Kogan, "On the electrodynamics of weakly nonlinear media," *Sov. Phys. JETP*, vol. 16, pp. 217-219, 1963.
- [27] P. J. Price, "Theory of quadratic response functions," *Phys. Rev.*, vol. 130, pp. 1792-1797, 1963.
- [28] L. V. Keldysh, "Ionization in the field of a strong electromagnetic wave," *Sov. Phys. JETP*, vol. 20, pp. 1307-1314, 1965.
- [29] H. S. Brandi and C. B. de Araújo, "Multiphoton absorption coefficients in solids: A universal curve," *J. Phys. C: Solid State Phys.*, vol. 16, pp. 5929-5936, 1983.
- [30] H. D. Jones and H. R. Reiss, "Intense-field effects in solids," *Phys. Rev. B*, vol. 16, pp. 2466-2473, 1977.
- [31] D. M. Volkov, "Concerning a class of solutions of the Dirac equation," *Z. Phys.*, vol. 94, pp. 250-260, 1935.
- [32] T.-Y. Wu and T. Ohmura, *Quantum Theory of Scattering*. Englewood Cliffs, NJ: Prentice-Hall, 1962.
- [33] E. O. Kane, "Band structure of indium antimonide," *J. Phys. Chem. Solids*, vol. 1, pp. 249-261, 1957.
- [34] P. Liu, W. L. Smith, H. Lotem, J. H. Bechtel, N. Bloembergen, and R. S. Adhav, "Absolute two-photon absorption coefficients at 355 and 266 nm," *Phys. Rev. B*, vol. 17, pp. 4620-4632, 1978.
- [35] A. M. Johnson, C. R. Pidgeon, and J. Dempsey, "Frequency dependence of two-photon absorption in InSb and HgCdTe," *Phys. Rev. B*, vol. 22, pp. 825-831, 1980.
- [36] Y. Yacoby, "High-frequency Franz-Keldysh effect," *Phys. Rev.*, vol. 169, pp. 610-619, 1968.
- [37] J. M. Worlock, "Two-photon spectroscopy," in F. T. Aracchi and E. D. Schulz-DuBois, Eds., *Laser Handbook*. Amsterdam: North-Holland, 1972, pp. 1323-1369.
- [38] D. J. Moss, E. Ghahramani, J. E. Sipe, and H. M. van Driel, "Band-structure calculation of dispersion and anisotropy in $\chi^{(3)}$ for third-harmonic generation in Si, Ge, and GaAs," *Phys. Rev. B*, vol. 41, pp. 1542-1560, 1990.
- [39] I. N. Ross, W. T. Toner, C. J. Hooker, J. R. M. Barr, and I. Coffey, "Nonlinear properties of silica and air for picosecond ultraviolet pulses," *J. Modern Opt.*, vol. 37, pp. 555-573, 1990.
- [40] M. J. LaGasse, K. K. Anderson, C. A. Wang, H. A. Haus, and J. G. Fujimoto, "Femtosecond measurements of the nonresonant nonlinear index in AlGaAs," *Appl. Phys. Lett.*, vol. 56, pp. 417-419, 1990.
- [41] R. C. Weast, Ed., *CRC Handbook of Chemistry and Physics*, 65th ed. Boca Raton, FL: CRC Press, 1984.
- [42] E. D. Palik, Ed., *Handbook of Optical Constants of Solids*. Orlando, FL: Academic, 1985.
- [43] T. S. Moss, "Theory of intensity dependence of refractive index," *Phys. Status Solidi(b)*, vol. 101, pp. 555-561, 1980.

- [44] B. S. Wherrett and N. A. Higgins, "Theory of nonlinear refraction near the band edge of a semiconductor," *Proc. Roy. Soc. London A*, vol. 379, pp. 67-90, 1982.
- [45] B. S. Wherrett, "A comparison of theories of resonant nonlinear refraction in semiconductors," *Proc. Roy. Soc. London A*, vol. 390, pp. 373-396, 1983.
- [46] B. S. Wherrett and S. D. Smith, "Bistable semiconductor elements for optical data processing and photonic logic," *Physica Scripta*, vol. T13, pp. 189-194, 1986.
- [47] S. D. Smith, A. C. Walker, F. A. P. Tooley, and B. S. Wherrett, "The demonstration of restoring digital optical logic," *Nature*, vol. 325, pp. 27-31, 1987.
- [48] P. LiKamWa, J. E. Stich, N. J. Mason, J. S. Roberts, and P. N. Robson, "All optical multiple-quantum-well waveguide switch," *Electron. Lett.*, vol. 21, pp. 26-27, 1985.
- [49] D. C. Hutchings, C. H. Wang, and B. S. Wherrett, "Optically bistable interference filters: Self-consistent modeling of nonlinear optical characteristics and optimization," *J. Opt. Soc. Amer. B*, vol. 8, pp. 618-631, 1991.
- [50] V. Mizrahi, K. W. DeLong, G. I. Stegeman, M. A. Saifi, and M. J. Andrejco, "Two-photon absorption as a limitation to all-optical switching," *Opt. Lett.*, vol. 14, pp. 1140-1142, 1989.
- [51] K. W. DeLong, K. B. Rochford, and G. I. Stegeman, "Effect of two-photon absorption on all-optical guided-wave devices," *Appl. Phys. Lett.*, vol. 55, pp. 1823-1825, 1989.
- [52] K. W. DeLong and G. I. Stegeman, "Two-photon absorption as a limitation to all-optical waveguide switching in semiconductors," *Appl. Phys. Lett.*, vol. 57, pp. 2063-2064, 1990.
- [53] J. S. Aitchison, A. M. Weiner, Y. Silberberg, M. K. Oliver, J. L. Jackel, D. E. Leaird, E. M. Vogel, and P. W. E. Smith, "Observation of the fundamental spatial optical soliton in a glass waveguide," in *Proc. Opt. Soc. Amer. Annu. Meet.*, Orlando, FL, 1989, p. PD20.
- [54] M. Lindberg and S. W. Koch, "Theory of the optical Stark effect in semiconductors under ultrashort-pulse excitation," *Phys. Status Solidi (b)*, vol. 150, pp. 379-385, 1988.



Mansoor Sheik-Bahae (M'87) was born in Isfahan, Iran, in 1956. He received the B.S. and M.S. degrees in electrical engineering from the Catholic University of America, Washington DC, in 1980 and 1982, respectively, and the Ph.D. degree in electrophysics from the State University of New York (SUNY) at Buffalo, in 1987.

He then joined the Center for Research in Electro-Optics and Lasers (CREOL) at the University of Central Florida, Orlando, where he is now an Assistant Research Professor in the area of nonlinear optics and ultrafast phenomena. His research activities have been concentrated on both the experimental and theoretical study of nonlinear optical processes in various materials, particularly in bulk semiconductors. He has also been involved in the development and characterization of the ultrafast (picosecond) CO₂ laser systems. He is currently investigating the ultrafast optical Kerr nonlinearities in semiconductors and organic materials with an emphasis on their applications to optical power limiting and all optical switching devices.

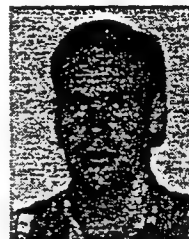
Dr. Sheik-Bahae is a member of the Optical Society of America.



David Crichton Hutchings was born in Edinburgh, Scotland, on November 29, 1963. He received the B.Sc. degree and the Ph.D. degree on nonlinear refraction and optical bistability in semiconductors, from Heriot-Watt University, Edinburgh, in 1984 and 1988, respectively.

He was employed as a Research Associate at Heriot-Watt University from 1987 to 1990. He is currently employed as a Research Associate at the Center for Research in Electro-Optics and Lasers (CREOL), University of Central Florida, Orlando.

His current research interests include nonlinear optics in semiconductors and carrier dynamics in quantum wells.



David J. Hagan (M'87) received the B.Sc. and Ph.D. degrees in physics in 1982 and 1985, respectively, from Heriot-Watt University, Edinburgh, Scotland. His Ph.D. dissertation was on the effects of carrier diffusion on resonant semiconductor nonlinear effects, such as phase conjugation, Sagnac-effect enhancement, and arrays of optically bistable switches. In 1982 and 1985, he worked as a student engineer in the Precision Instruments Group at Ferranti, plc. on reduction of scatter in ring laser gyroscopes.

From 1985 to 1987, he was a Research Scientist in the Center for Applied Quantum Electronics, North Texas State University, Denton, where he worked on optical nonlinearities and limiting in II-VI semiconductors. Currently, he is an Assistant Professor with the Department of Physics and the Center for Research in Electro-Optics and Lasers (CREOL) at the University of Central Florida, Orlando, where his current research interests are superconductive detectors and the fundamental mechanisms and applications of nonlinear optical processes in organic molecules, microcrystallites, and bulk semiconductors.



Eric W. Van Stryland (M'84-SM'90) was born in 1947. He received the Ph.D. degree in physics in 1976 from the University of Arizona, Tucson, where he worked at the Optical Sciences Center on optical coherent transients.

He worked in the areas of femtosecond pulse production, multiphoton absorption in solids, and laser-induced damage at the Center for Laser Studies at the University of Southern California, Los Angeles. He joined the Department of Physics at North Texas State University, Denton, in

1978 and was instrumental in forming the Center for Applied Quantum Electronics there. In 1987 he joined the newly formed Center for Research in Electro-Optics and Lasers (CREOL) at the University of Central Florida, Orlando, where he is a Professor with the Departments of Physics and Electrical Engineering, working in the area of nonlinear optics.

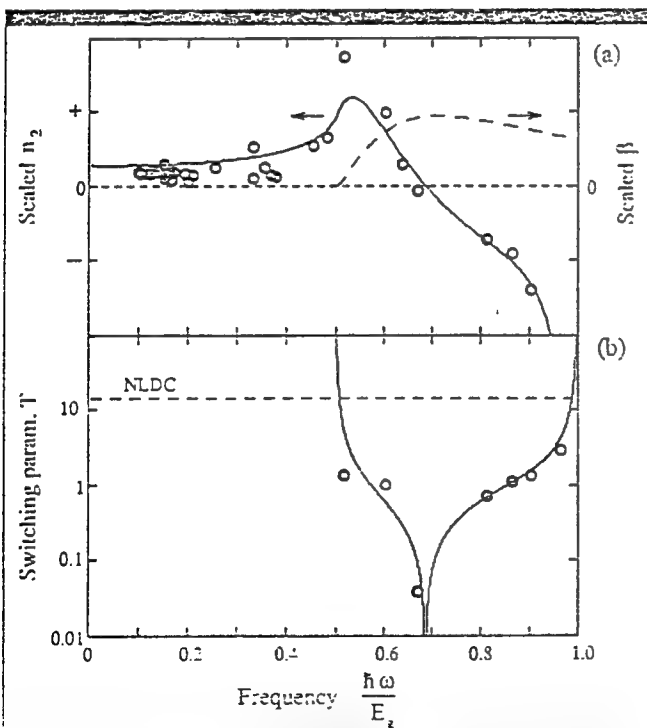
NONLINEAR OPTICS



UNIVERSAL DISPERSION AND BAND-GAP SCALING OF n_2 IN SOLIDS

BY M. SHEIK-BAHAE, D.C. HUTCHINGS, D.J. HAGAN, AND E.W. VAN STRYLAND, CREOL, UNIVERSITY OF CENTRAL FLORIDA

Using the "Z-scan" technique,¹ which can separately and accurately measure nonlinear absorption (NLA) and nonlinear refraction (NLR), two-photon absorption (2PA) and the bound electronic Kerr effect (n_2) have been measured in a large number of inorganic solids.² As a result of this large database and detailed characterization, a universal, predictive capability for both the NLA and NLR of solids has been developed over a range of band-gaps from 0.2 to 10 eV. It is found that n_2 displays strong dispersion and sign reversal as $\hbar\omega$ approaches the band-gap energy E_g .



(a) UPPER TRACE: DISPERSION OF THE NONLINEAR REFRACTION WITH APPROPRIATELY SCALED DATA (RE-MULTIPLIED BY E_g^{-4}) INCLUDING DATA FROM REF. 3 (LEFT SCALE) AND THE 2PA SPECTRUM $\beta/(\hbar\omega E_g)$ SCALED BY E_g^{-4} (RIGHT SCALE). (b) LOWER TRACE: FIGURE OF MERIT T VERSUS $\hbar\omega/E_g$. THE DASHED LINE INDICATES THE MINIMUM VALUE OF T NECESSARY IN A NONLINEAR DIRECTIONAL COUPLER (NLDC).

This universal dispersion and band-gap scaling law for n_2 were calculated using a Kramers-Kronig (KK) transformation of the NLA spectrum.³ The KK transformation relates nondegenerate NLR to the nondegenerate NLA (e.g., a change in absorption at ω_1 due to the presence of ω_2). To third order, 2PA, AC-Stark, and electronic Raman effects contribute to this NLA and were calculated using a "dressed" state Keldysh formalism from a two parabolic band model. The resulting n_2 varies as $G_2 n_0^2 E_g^{-4}$, where n_0 is the linear index and G_2 is a dimensionless dispersion function that is an analytical expression, depending only on the ratio $\hbar\omega/E_g$.

The significant features of this theory are depicted in the top part of the figure, where our Z-scan experimental data, scaled by the predicted E_g^{-4} dependence, are compared with theory. Also included are measurements of Ref. 3 for large gap dielectrics. As evident from the dispersion curve, n_2 is positive and nondispersive at long wavelengths (small $\hbar\omega/E_g$). A resonant enhancement due to 2PA is exhibited at half the band-gap energy where n_2 reaches its positive maximum value and then exhibits anomalous dispersion, becoming negative near the band edge due primarily to the band-gap resonance of the AC-Stark effect.

The remarkable agreement between this simple theory and the vast amount of experimental data that spans over four orders of magnitude in n_2 , points out the simple and fundamental physics underlying the fast electronic nonlinear processes in bulk semiconductors and large gap dielectrics. In addition, the KK transformation of the NLA spectrum yields, for the first time, a unified relationship between n_2 and 2PA, AC-Stark, and electronic Raman effects.² Such a relationship is crucial in evaluating a generalized figure of merit for all-optical switching applications where 2PA imposes serious limitations.⁴

Given both the 2PA coefficient β that scales as $n_0^2 E_g^{-3}$ and n_2 , one can calculate the all-optical switching figure of merit $T = \omega_1 n_2 / \beta c$.⁴ The theory shows that T is material independent, being only a function of $\hbar\omega/E_g$ as shown in the lower part of the figure. Also shown are data obtained through a combination of β and n_2 measurements, verifying this material independence. For efficient switching, T must exceed some value (typically of the order of unity) that weakly depends on the particular switching scheme. As seen in the lower part of the figure, for most applications, switching must be performed at frequencies below the 2PA edge.

REFERENCES

1. M. Sheik-Bahae *et al.*, "Sensitive measurements of optical nonlinearities using a single beam," IEEE J. Quantum Electron. QE-26, 1990, 760-769.
2. M. Sheik-Bahae *et al.*, "Dispersion of bound electronic nonlinear refraction in solids," IEEE J. Quantum Electron. QE-27, 1991, 1296-1309.
3. R. Adair *et al.*, "Nonlinear refractive index of optical crystals," Phys. Rev. B 39, 1989, 3337-3349.
4. V. Mizrahi *et al.*, "Two-photon absorption as a limitation to all-optical switching," Opt. Lett. 14, 1989, 1140-1142.

Sensitive Measurement of Optical Nonlinearities Using a Single Beam

MANSOOR SHEIK-BAHAE, MEMBER, IEEE, ALI A. SAID, TAI-HUEI WEI,
DAVID J. HAGAN, MEMBER, IEEE AND E. W. VAN STRYLAND, SENIOR MEMBER, IEEE

Abstract—We report a sensitive single-beam technique for measuring both the nonlinear refractive index and nonlinear absorption coefficient for a wide variety of materials. We describe the experimental details and present a comprehensive theoretical analysis including cases where nonlinear refraction is accompanied by nonlinear absorption. In these experiments, the transmittance of a sample is measured through a finite aperture in the *far field* as the sample is moved along the propagation path (z) of a focused Gaussian beam. The sign and magnitude of the nonlinear refraction are easily deduced from such a transmittance curve (Z-scan). Employing this technique, a sensitivity of better than $\lambda/300$ wavefront distortion is achieved in n_2 measurements of BaF₂ using picosecond frequency-doubled Nd:YAG laser pulses. In cases where nonlinear refraction is accompanied by nonlinear absorption, it is possible to separately evaluate the nonlinear refraction as well as the nonlinear absorption by performing a second Z scan with the aperture removed. We demonstrate this method for ZnSe at 532 nm where two-photon absorption is present and n_2 is negative.

I. INTRODUCTION

RECENTLY we reported a single-beam method for measuring the sign and magnitude of n_2 that has a sensitivity comparable to interferometric methods [1]. Here, we describe this method in detail and demonstrate how it can be applied and analyzed for a variety of materials. We also extend this method to the measurement of nonlinear refraction in the presence of nonlinear absorption. Thus, this method allows a direct measurement of the nonlinear absorption coefficient. In addition, we present a simple method to minimize parasitic effects due to the presence of linear sample inhomogeneities.

Previous measurements of nonlinear refraction have used a variety of techniques including nonlinear interferometry [2], [3], degenerate four-wave mixing [4], nearly degenerate three-wave mixing [5], ellipse rotation [6], and beam distortion measurements [7], [8]. The first three methods, namely, nonlinear interferometry and wave mixing, are potentially sensitive techniques, but all require relatively complex experimental apparatus. Beam distortion measurements, on the other hand, are relatively insensitive and require detailed wave propagation analysis. The technique reported here is based on the principles of spatial beam distortion, but offers simplicity as well as very high sensitivity.

Manuscript received November 6, 1989. This work was supported by the National Science Foundation under Grant ECS-8617066, the DARPA/CNVEO, and the Florida High Technology and Industry Council.

The authors are with the Center for Research in Electro-Optics and Lasers (CREOL), University of Central Florida, Orlando, FL 32826.

IEEE Log Number 8933825.

We will describe this simple technique, referred to as a "Z-scan," in Section II. Theoretical analyses of Z-scan measurements are given in Section III for a "thin" nonlinear medium. It will be shown that for many practical cases, nonlinear refraction and its sign can be obtained from a simple linear relationship between the observed transmittance changes and the induced phase distortion without the need for performing detailed calculations. In Section IV, we present measurements of nonlinear refraction in a number of materials such as CS₂ and transparent dielectrics at wavelengths of 532 nm, 1.06 μ m, and 10.6 μ m. In CS₂ at 10 μ m, for example, both thermo-optical and reorientational Kerr effects were identified using nanosecond and picosecond pulses, respectively. Furthermore, in Section V, we will consider the case of samples having a significant absorptive nonlinearity as well as a refractive one. This occurs in, for example, two-photon absorbing semiconductors. It will be shown that both effects can easily be separated and measured in the Z-scan scheme. We also show how effects of linear sample inhomogeneities (e.g., bulk index variations) can be effectively removed from the experimental data.

II. THE Z-SCAN TECHNIQUE

Using a single Gaussian laser beam in a tight focus geometry, as depicted in Fig. 1, we measure the transmittance of a nonlinear medium through a finite aperture in the *far field* as a function of the sample position z measured with respect to the focal plane. The following example will qualitatively elucidate how such a trace (Z-scan) is related to the nonlinear refraction of the sample. Assume, for instance, a material with a negative nonlinear refractive index and a thickness smaller than the diffraction length of the focused beam (a thin medium). This can be regarded as a thin lens of variable focal length. Starting the scan from a distance far away from the focus (negative z), the beam irradiance is low and negligible nonlinear refraction occurs; hence, the transmittance (D_2/D_1 in Fig. 1) remains relatively constant. As the sample is brought closer to focus, the beam irradiance increases, leading to self-lensing in the sample. A negative self-lensing prior to focus will tend to collimate the beam, causing a beam narrowing at the aperture which results in an increase in the measured transmittance. As the scan in z continues and the sample passes the focal plane to the right (positive z), the same self-defocusing increases the

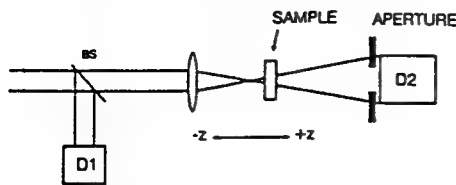


Fig. 1. The Z-scan experimental apparatus in which the ratio $D2/D1$ is recorded as a function of the sample position z .

beam divergence, leading to beam broadening at the aperture, and thus a decrease in transmittance. This suggests that there is a null as the sample crosses the focal plane. This is analogous to placing a thin lens at or near the focus, resulting in a minimal change of the far-field pattern of the beam. The Z-scan is completed as the sample is moved away from focus (positive z) such that the transmittance becomes linear since the irradiance is again low. Induced beam broadening and narrowing of this type have been previously observed and explained during nonlinear refraction measurements of some semiconductors [9], [10]. A similar technique was also previously used to measure thermally induced beam distortion by chemicals in solvents [11].

A prefocal transmittance maximum (peak) followed by a postfocal transmittance minimum (valley) is, therefore, the Z-scan signature of a negative refractive nonlinearity. Positive nonlinear refraction, following the same analogy, gives rise to an opposite valley-peak configuration. It is an extremely useful feature of the Z-scan method that the sign of the nonlinear index is immediately obvious from the data, and as we will show in the following section, the magnitude can also be easily estimated using a simple analysis for a thin medium.

In the above picture describing the Z-scan, one must bear in mind that a purely refractive nonlinearity was considered assuming that no absorptive nonlinearities (such as multiphoton or saturation of absorption) are present. Qualitatively, multiphoton absorption suppresses the peak and enhances the valley, while saturation produces the opposite effect. The sensitivity to nonlinear refraction is entirely due to the aperture, and removal of the aperture completely eliminates the effect. However, in this case, the Z-scan will still be sensitive to nonlinear absorption. Nonlinear absorption coefficients can be extracted from such "open" aperture experiments. We will show in Section V how the data from the two Z-scans, with and without the aperture, can be used to separately determine both the nonlinear absorption and the nonlinear refraction. We will demonstrate this data analysis on semiconductors where two-photon absorption and self-refraction are simultaneously present.

III. THEORY

Much work has been done in investigating the propagation of intense laser beams inside a nonlinear material and the ensuing self-refraction [12], [13]. Considering the geometry given in Fig. 1, we will formulate and discuss a simple method for analyzing the Z-scan data based on modifications of existing theories.

In general, nonlinearities of any order can be considered; however, for simplicity, we first examine only a cubic nonlinearity where the index of refraction n is expressed in terms of nonlinear indexes n_2 (esu) or γ (m^2/W) through

$$n = n_0 + \frac{n_2}{2} |E|^2 = n_0 + \gamma I \quad (1)$$

where n_0 is the linear index of refraction, E is the peak electric field (cgs), and I denotes the irradiance (MKS) of the laser beam within the sample. (n_2 and γ are related through the conversion formula $n_2(\text{esu}) = (cn_0/40\pi)\gamma(m^2/W)$ where c (m/s) is the speed of light in vacuum.) Assuming a TEM₀₀ Gaussian beam of beam waist radius w_0 traveling in the $+z$ direction, we can write E as

$$E(z, r, t) = E_0(t) \frac{w_0}{w(z)} \cdot \exp\left(-\frac{r^2}{w^2(z)} - \frac{ikr^2}{2R(z)}\right) e^{-i\phi(z,t)} \quad (2)$$

where $w^2(z) = w_0^2(1 + z^2/z_0^2)$ is the beam radius, $R(z) = z(1 + z_0^2/z^2)$ is the radius of curvature of the wavefront at z , $z_0 = kw_0^2/2$ is the diffraction length of the beam, $k = 2\pi/\lambda$ is the wave vector, and λ is the laser wavelength, all in free space. $E_0(t)$ denotes the radiation electric field at the focus and contains the temporal envelope of the laser pulse. The $e^{-i\phi(z,t)}$ term contains all the radially uniform phase variations. As we are only concerned with calculating the radial phase variations $\Delta\phi(r)$, the slowly varying envelope approximation (SVEA) applies, and all other phase changes that are uniform in r are ignored.

If the sample length is small enough that changes in the beam diameter within the sample due to either diffraction or nonlinear refraction can be neglected, the medium is regarded as "thin," in which case the self-refraction process is referred to as "external self-action" [14]. For linear diffraction, this implies that $L \ll z_0$, while for nonlinear refraction, $L \ll z_0/\Delta\phi(0)$. In most experiments using the Z-scan technique, we find that the second criterion is automatically met since $\Delta\phi$ is small. Additionally, we have found that the first criterion for linear diffraction is more restrictive than it need be, and it is sufficient to replace it with $L < z_0$. We have determined this empirically by measuring n_2 in the same material using various z_0 's and the same analysis and have obtained the same value for n_2 . Such an assumption simplifies the problem considerably, and the amplitude \sqrt{I} and phase ϕ of the electric field as a function of z' are now governed in the SVEA by a pair of simple equations:

$$\frac{d\Delta\phi}{dz'} = \Delta n(I) k \quad (3)$$

and

$$\frac{dI}{dz'} = -\alpha(I) I \quad (4)$$

where z' is the propagation depth in the sample and $\alpha(l)$, in general, includes linear and nonlinear absorption terms. Note that z' should not be confused with the sample position z . In the case of a cubic nonlinearity and negligible nonlinear absorption, (3) and (4) are solved to give the phase shift $\Delta\phi$ at the exit surface of the sample which simply follows the radial variation of the incident irradiance at a given position of the sample z . Thus,

$$\Delta\phi(z, r, t) = \Delta\phi_0(z, t) \exp\left(-\frac{2r^2}{w^2(z)}\right) \quad (5a)$$

with

$$\Delta\phi_0(z, t) = \frac{\Delta\Phi_0(t)}{1 + z^2/z_0^2} \quad (5b)$$

$\Delta\Phi_0(t)$, the on-axis phase shift at the focus, is defined as

$$\Delta\Phi_0(t) = k\Delta n_0(t) L_{\text{eff}} \quad (6)$$

where $L_{\text{eff}} = (1 - e^{-\alpha L})/\alpha$, with L the sample length and α the linear absorption coefficient. Here, $\Delta n_0 = \gamma I_0(t)$ with $I_0(t)$ being the on-axis irradiance at focus (i.e., $z = 0$). We ignore Fresnel reflection losses such that, for example, $I_0(t)$ is the irradiance within the sample.

The complex electric field exiting the sample E_e now contains the nonlinear phase distortion

$$E_e(r, z, t) = E(z, r, t) e^{-\alpha L/2} e^{i\Delta\phi(z, r, t)} \quad (7)$$

By virtue of Huygen's principle, one can obtain the far-field pattern of the beam at the aperture plane through a zeroth-order Hankel transformation of E_e [15]. We will follow a more convenient treatment applicable to Gaussian input beams which we refer to as the "Gaussian decomposition" (GD) method given by Weaire *et al.* [14], in which they decompose the complex electric field at the exit plane of the sample into a summation of Gaussian beams through a Taylor series expansion of the nonlinear phase term $e^{i\Delta\phi(z, r, t)}$ in (7). That is,

$$e^{i\Delta\phi(z, r, t)} = \sum_{m=0}^{\infty} \frac{[i\Delta\phi_0(z, t)]^m}{m!} e^{-2mr^2/w^2(z)} \quad (8)$$

Each Gaussian beam can now be simply propagated to the aperture plane where they will be resummed to reconstruct the beam. When including the initial beam curvature for the focused beam, we derive the resultant electric field pattern at the aperture as

$$E_a(r, t) = E(z, r=0, t) e^{-\alpha L/2} \sum_{m=0}^{\infty} \frac{[i\Delta\phi_0(z, t)]^m}{m!} \frac{w_{m0}}{w_m} \cdot \exp\left(-\frac{r^2}{w_m^2} - \frac{ikr^2}{2R_m} + i\theta_m\right) \quad (9)$$

Defining d as the propagation distance in free space from the sample to the aperture plane and $g = 1 + d/R(z)$, the remaining parameters in (9) are expressed as

$$w_{m0}^2 = \frac{w^2(z)}{2m+1}$$

$$d_m = \frac{kw_{m0}^2}{2}$$

$$w_m^2 = w_{m0}^2 \left[g^2 + \frac{d^2}{d_m^2} \right]$$

$$R_m = d \left[1 - \frac{g}{g^2 + d^2/d_m^2} \right]^{-1}$$

and

$$\theta_m = \tan^{-1} \left[\frac{d/d_m}{g} \right].$$

The expression given by (9) is a general case of that derived by Weaire *et al.* [15] where they considered a collimated beam ($R = \infty$) for which $g = 1$. We find that this GD method is very useful for the small phase distortions detected with the Z-scan method since only a few terms of the sum in (9) are needed. The method is also easily extended to higher order nonlinearities.

The transmitted power through the aperture is obtained by spatially integrating $E_a(r, t)$ up to the aperture radius r_a , giving

$$P_T(\Delta\Phi_0(t)) = c\epsilon_0 n_0 \pi \int_0^{r_a} |E_a(r, t)|^2 r dr \quad (10)$$

where ϵ_0 is the permittivity of vacuum. Including the pulse temporal variation, the normalized Z-scan transmittance $T(z)$ can be calculated as

$$T(z) = \frac{\int_{-\infty}^{\infty} P_T(\Delta\Phi_0(t)) dt}{S \int_{-\infty}^{\infty} P_i(t) dt} \quad (11)$$

where $P_i(t) = \pi w_0^2 I_0(t)/2$ is the instantaneous input power (within the sample) and $S = 1 - \exp(-2r_a^2/w_a^2)$ is the aperture linear transmittance, with w_a denoting the beam radius at the aperture in the linear regime.

We first consider an instantaneous nonlinearity and a temporally square pulse to illustrate the general features of the Z-scan. This is equivalent to assuming CW radiation and the nonlinearity has reached the steady state. The normalized transmittance $T(z)$ in the far field is shown in Fig. 2 for $\Delta\Phi_0 = \pm 0.25$ and a small aperture ($S = 0.01$). They exhibit the expected features, namely, a valley-peak ($v-p$) for the positive nonlinearity and a peak-valley ($p-v$) for the negative one. For a given $\Delta\Phi_0$, the magnitude and shape of $T(z)$ do not depend on the wavelength or geometry as long as the far-field condition for the aperture plane ($d \gg z_0$) is satisfied. The aperture size S , however, is an important parameter since a large aperture reduces the variations in $T(z)$. This reduction is more prominent in the peak where beam narrowing occurs and can result in a peak transmittance which cannot exceed $(1 - S)$. Needless to say, for very large aperture or no aperture ($S = 1$), the effect vanishes and $T(z) = 1$ for all z and $\Delta\Phi_0$. For small $|\Delta\Phi_0|$, the peak and valley occur

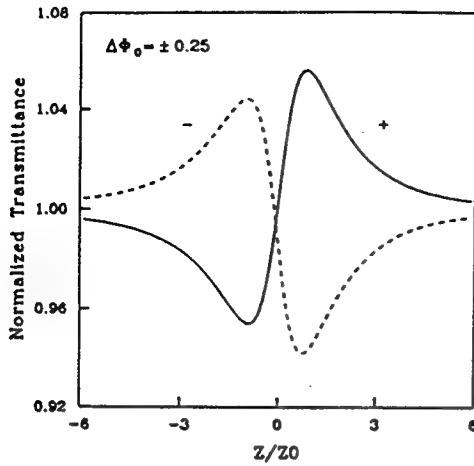


Fig. 2. Calculated Z-scan transmittance curves for a cubic nonlinearity with either polarity and a small aperture ($S = 0.01$).

at the same distance with respect to focus, and for a cubic nonlinearity, this distance is found to be $\approx 0.86 z_0$ as shown in the Appendix. With larger phase distortions ($|\Delta\Phi_0| > 1$), numerical evaluation of (9)–(11) shows that this symmetry no longer holds and peak and valley both move toward $\pm z$ for the corresponding sign of nonlinearity ($\pm\Delta\Phi_0$) such that their separation remains nearly constant, given by

$$\Delta Z_{p-v} \approx 1.7 z_0. \quad (12)$$

We can define an easily measurable quantity ΔT_{p-v} as the difference between the normalized peak and valley transmittance: $T_p - T_v$. The variation of this quantity as a function of $|\Delta\Phi_0|$, as calculated for various aperture sizes, is illustrated in Fig. 3. These curves exhibit some useful features. First, for a given order of nonlinearity, they can be considered universal. In other words, they are independent of the laser wavelength, geometry (as long as the far-field condition is met), and the sign of nonlinearity. Second, for all aperture sizes, the variation of ΔT_{p-v} is found to be almost linearly dependent on $|\Delta\Phi_0|$. As shown in the Appendix for small phase distortion and small aperture ($S \approx 0$),

$$\Delta T_{p-v} \approx 0.406 |\Delta\Phi_0|. \quad (13a)$$

Numerical calculations show that this relation is accurate to within 0.5 percent for $|\Delta\Phi_0| \leq \pi$. As shown in Fig. 3, for larger apertures, the linear coefficient 0.406 decreases such that with $S = 0.5$, it becomes ≈ 0.34 , and at $S = 0.7$, it reduces to ≈ 0.29 . Based on a numerical fitting, the following relationship can be used to include such variations within a $\pm 2\%$ accuracy:

$$\Delta T_{p-v} = 0.406(1 - S)^{0.25} |\Delta\Phi_0| \quad \text{for } |\Delta\Phi_0| \leq \pi. \quad (13b)$$

The implications of (13a) and (13b) are quite promising in that they can be used to readily estimate the nonlinear index (n_2) with good accuracy after a Z-scan is performed. What is most intriguing about these expressions is that they reveal the highly sensitive nature of the Z-scan

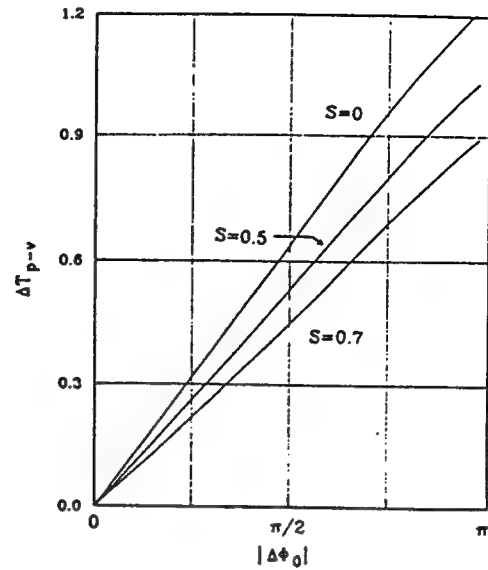


Fig. 3. Calculated ΔT_{p-v} as a function of the phase shift at the focus ($\Delta\Phi_0$). The sensitivity, as indicated by the slope of the curves, decreases slowly for larger aperture sizes ($S > 0$).

technique. For example, if our experimental apparatus and data acquisition systems are capable of resolving transmittance changes ΔT_{p-v} of $\approx 1\%$, we will be able to measure phase changes corresponding to less than $\lambda/250$ wavefront distortion. Achieving such sensitivity, however, requires relatively good optical quality of the sample under study. We describe in the experimental Section IV a means to minimize problems arising from poor optical quality samples.

We can now easily extend the steady-state results to include transient effects induced by pulsed radiation by using the time-averaged index change $\langle \Delta n_0(t) \rangle$ where

$$\langle \Delta n_0(t) \rangle = \frac{\int_{-\infty}^{\infty} \Delta n_0(t) I_0(t) dt}{\int_{-\infty}^{\infty} I_0(t) dt}. \quad (14)$$

The time-averaged $\langle \Delta\Phi_0(t) \rangle$ is related to $\langle \Delta n_0(t) \rangle$ through (6). With a nonlinearity having instantaneous response and decay times relative to the pulsewidth of the laser, one obtains for a temporally Gaussian pulse

$$\langle \Delta n_0(t) \rangle = \Delta n_0 / \sqrt{2} \quad (15)$$

where Δn_0 now represents the peak-on-axis index change at the focus. For a cumulative nonlinearity having a decay time much longer than the pulsewidth (e.g., thermal), the instantaneous index change is given by the following integral:

$$\Delta n_0(t) = A \int_{-\infty}^t I_0(t') dt' \quad (16)$$

where A is a constant which depends on the nature of the nonlinearity. If we substitute (16) into (14), we obtain a fluence averaging factor of $1/2$. That is,

$$\langle \Delta n_0(t) \rangle = \frac{1}{2} AF \quad (17)$$

where F is the pulse fluence at focus within the sample. Interestingly, the factor of $1/2$ is independent of the temporal pulse shape.

These equations were obtained based on a cubic nonlinearity (i.e., a $\chi^{(3)}$ effect). A similar analysis can be performed for higher order nonlinearities. Regardless of the order of the nonlinearity, the same qualitative features are to be expected from the Z-scan analysis. In particular, to quantify such features, we examined the effects of a $\chi^{(5)}$ nonlinearity which can be represented by a nonlinear index change given as $\Delta n = \eta I^2$. Nonlinearities encountered in semiconductors where the index of refraction is altered through charge carriers generated by two-photon absorption (i.e., a sequential $\chi^{(3)}:\chi^{(1)}$ effect) appear as such a fifth-order nonlinearity [20].

For a fifth-order effect, assuming a thin sample and using the GD approach, we find that the peak and valley are separated by $\approx 1.2 z_0$ as compared to $1.7 z_0$ obtained for the third-order effect. Furthermore, the calculations also show that for a small aperture ($S \approx 0$),

$$\Delta T_{p-v} \approx 0.21 |\Delta \Phi_0| \quad (18)$$

where, in this case, the phase distortion is given by

$$\Delta \Phi_0 = k\eta I^2 \left(\frac{1 - e^{-2\alpha L}}{2\alpha} \right). \quad (19)$$

Calculations also indicate that the aperture size dependence of (18) can be approximated by multiplying the right-hand term by $(1 - S)^{0.25}$, as was the case for a third-order nonlinearity.

As will be shown in Section V, we can also determine the nonlinear refraction in the presence of nonlinear absorption by separately measuring the nonlinear absorption in a Z-scan performed with the aperture removed. Within approximations elaborated in Section V, a simple division of the curves obtained from the two Z-scans will give the nonlinear refraction.

IV. EXPERIMENTAL RESULTS

We examined the nonlinear refraction of a number of materials using the Z-scan technique. Fig. 4 shows a Z-scan of a 1 mm thick cuvette with NaCl windows filled with CS_2 using 300 ns TEA CO_2 laser pulses having an energy of 0.85 mJ. The peak-valley configuration of this Z-scan is indicative of a negative (self-defocusing) nonlinearity. The solid line in Fig. 4 is the calculated result using $\langle \Delta \Phi_0 \rangle = -0.6$, which gives an index change of $\langle \Delta n_0 \rangle = -1 \times 10^{-3}$. As mentioned earlier, such detailed theoretical fitting is not necessary for obtaining $\langle \Delta n_0 \rangle$ (only ΔT_{p-v} is needed). The defocusing effect shown in Fig. 4 is attributed to a thermal nonlinearity resulting from linear absorption of CS_2 ($\alpha \approx 0.22 \text{ cm}^{-1}$ at $10.6 \mu\text{m}$). The rise time of a thermal lens in a liquid is determined by the acoustic transit time $\tau \approx w_0/v_s$, where v_s is the velocity of sound in the liquid [17]. For CS_2 with $v_s = 1.5 \times 10^5 \text{ cm/s}$ and having $w_0 = 60 \mu\text{m}$, we obtain a rise time of $\approx 40 \text{ ns}$, which is almost an order of magnitude smaller than the TEA laser pulsewidth. Furthermore, the relaxation of the thermal lens, governed by

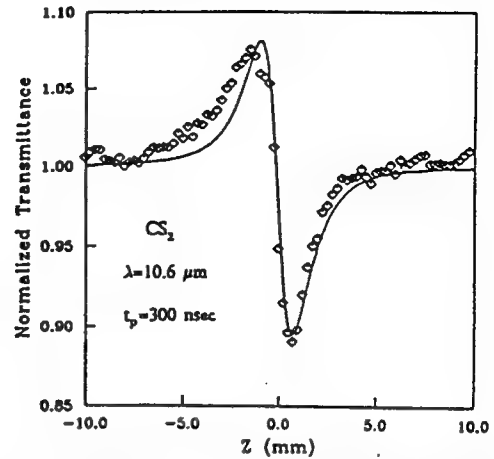


Fig. 4. Measured Z-scan of a 1 mm thick CS_2 cell using 300 ns pulses at $\lambda = 10.6 \mu\text{m}$ indicating thermal self-defocusing. The solid line is the calculated result with $\langle \Delta \Phi_0 \rangle = -0.6$ and 60% aperture ($S = 0.6$).

thermal diffusion, is on the order of 100 ms [17]. Therefore, we regard the nonuniform heating caused by the 300 ns pulses as quasi-steady state, in which case, from (17), the average on-axis nonlinear index change at focus can be determined in terms of the thermo-optic coefficient dn/dT as

$$\langle \Delta n_0 \rangle = \frac{dn}{dT} \frac{F_0 \alpha}{2\rho C_p} \quad (20)$$

where F_0 is the fluence, ρ is the density, C_p is the specific heat, and $1/2$ denotes the fluence averaging factor. With the known value of $\rho C_p \approx 1.3 \text{ J/K} \cdot \text{cm}^3$ for CS_2 , we deduce $dn/dT \approx -(8.3 \pm 1.0) \times 10^{-4} \text{ }^\circ\text{C}^{-1}$, which is in good agreement with the reported value of $-8 \times 10^{-4} \text{ }^\circ\text{C}^{-1}$ [16].

With ultrashort pulses, nonlocal nonlinearities such as thermal or electrostriction are no longer significant. Particularly, in CS_2 , the molecular reorientational Kerr effect becomes the dominant mechanism for nonlinear refraction. CS_2 is frequently used as a standard reference nonlinear material [18], [19]. We have used picosecond pulses at 10.6, 1.06, and $0.53 \mu\text{m}$ to measure n_2 in CS_2 . We obtain the same value of n_2 , within errors, at all three wavelengths, $(1.5 \pm 0.6) \times 10^{-11} \text{ esu}$ at $10.6 \mu\text{m}$, $(1.3 \pm 0.3) \times 10^{-11} \text{ esu}$ at $1.06 \mu\text{m}$, and $(1.2 \pm 0.2) \times 10^{-11} \text{ esu}$ at $0.53 \mu\text{m}$. The external self-focusing arising from the Kerr effect in CS_2 is shown in Fig. 5 where a Z-scan of a 1 mm cell using 27 ps (FWHM) pulses focused to a beam waist w_0 of $25 \mu\text{m}$ from a frequency-doubled Nd:YAG laser is illustrated. Its valley-peak configuration indicates the positive sign of n_2 . With $\Delta T_{p-v} = 0.24$, and using (13b) with a 40% aperture ($S = 0.4$), one readily obtains a $\langle \Delta n_0 \rangle = 5.6 \times 10^{-5}$. Using the peak irradiance of 2.6 GW/cm^2 , this value of $\langle \Delta n_0 \rangle$ corresponds to an $n_2 = (1.2 \pm 0.2) \times 10^{-11} \text{ esu}$. The main source of uncertainty in the value of n_2 is the absolute measurement of the irradiance. In this paper, all irradiance values quoted are values within the sample, i.e., including front surface reflection losses. A plot of ΔT_{p-v} versus peak laser irradiance as measured from various Z-scans on the same CS_2 cell is shown in Fig. 6. The linear behavior of this plot follows (13) as derived for a cubic nonlinearity.

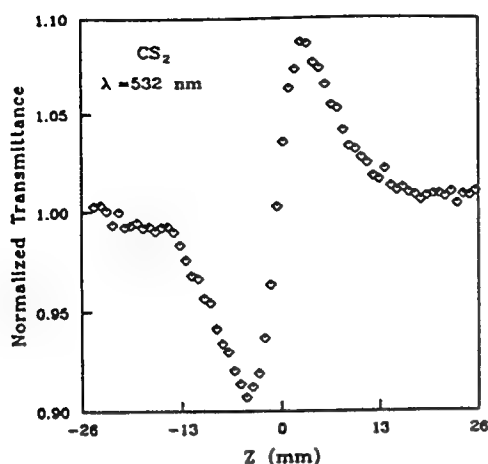


Fig. 5. Measured Z-scan of a 1 mm thick CS_2 cell using 27 ps pulses at $\lambda = 532$ nm. It depicts the self focusing effect due to the reorientational Kerr effect.

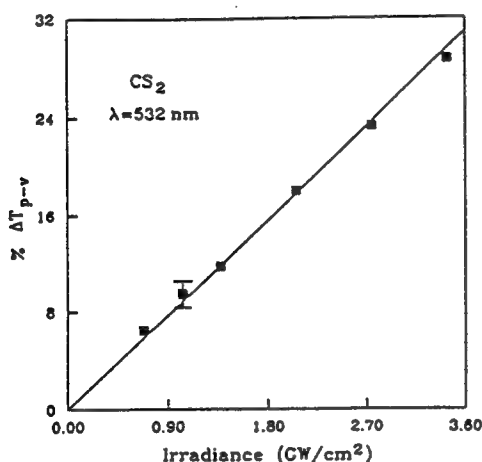


Fig. 6. ΔT_{p-r} in percent as a function of the peak irradiance from the Z-scan data of CS_2 at 532 nm, indicative of the reorientational Kerr effect.

Transparent dielectric window materials have relatively small nonlinear indexes. Recently, Adair *et al.* [21] have performed a careful study of the nonlinear index of refraction of a large number of such materials in a nearly degenerate three-wave mixing scheme at $\lambda = 1.06 \mu\text{m}$. Using the Z-scan technique, we examined some of these materials at 532 nm. For example, the result for a randomly oriented sample of BaF_2 (2.4 mm thick) is shown in Fig. 7, using the same beam parameters as for CS_2 . This Z-scan was obtained with a 50% aperture and at a pulse energy of $\approx 28 \mu\text{J}$ corresponding to a peak irradiance (I_0) of $\approx 100 \text{ GW}/\text{cm}^2$. A low irradiance ($4 \mu\text{J}$) Z-scan of the same sample was shown in [1] to have a phase distortion resolution of better than $\lambda/300$. (The pulse energy for this Z-scan was misquoted as $2 \mu\text{J}$ in [1].) Such a resolution is also shown in Fig. 7 by the arrows indicating the corresponding transmittance variation equal to the maximum scatter in the Z-scan data. For laser systems having better amplitude and pulsewidth stability, the sensitivity will be correspondingly improved.

Aside from the statistical fluctuations of the laser irradiance, surface imperfections or wedge in the sample may lead to systematic transmittance changes with z that could mask the effect of nonlinear refraction. We found, how-

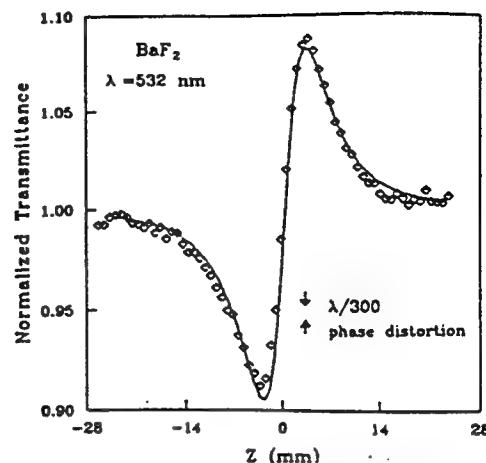


Fig. 7. Measured Z-scan of a 2.4 mm thick BaF_2 sample using 27 ps pulses at $\lambda = 532$ nm, indicating the self-focusing due to the electronic Kerr effect. The solid line is the calculated result with a peak $\Delta\Phi_0 = 0.73$. The separation of the arrows corresponds to an induced phase distortion of $\lambda/300$.

ever, that such "parasitic" effects may be substantially reduced by subtracting a low irradiance background Z-scan from the high irradiance scan, after normalizing each scan. Fig. 8 shows Z-scan data before and after subtraction in a particularly poor 1 mm thick sample of ZnSe . A simple computer simulation of this process, assuming that the surface imperfections do not disturb the circular symmetry of the beam or cause any beam steering, indicated that background subtraction indeed recovers the original ΔT_{p-r} arising from the nonlinear refraction effect, even for quite large surface disturbances, that is, $\Delta\phi_s$ of up to π .

Returning to the Z-scan of Fig. 7, we obtain $n_2 = (0.9 \pm 0.15) \times 10^{-13} \text{ esu}$ for BaF_2 at 532 nm, which is in close agreement with our low irradiance measurement of $\approx (0.8 \pm 0.15) \times 10^{-13} \text{ esu}$ as reported in [1]. This compares well with other reported values of $0.7 \times 10^{-13} \text{ esu}$ [21] and $1.0 \times 10^{-13} \text{ esu}$ [3] as measured at $1.06 \mu\text{m}$ using more complex techniques of nearly degenerate three-wave mixing and time-resolved nonlinear interferometry, respectively. Similarly for MgF_2 , we measure $n_2 = 0.25 \times 10^{-13} \text{ esu}$ at 532 nm as compared to the reported value of $0.32 \times 10^{-13} \text{ esu}$ at $1.06 \mu\text{m}$ for this material as given in [21]. Since the transparency region of these materials extends from mid-IR to UV, the dispersion in n_2 between 1 and $0.5 \mu\text{m}$ is expected to be negligible. It should be noted that the n_2 values extracted from the Z-scans are absolute rather than relative measurements. If the beam parameters are not accurately known, however, it should be possible to calibrate the system by using a standard nonlinear material such as CS_2 .

V. EFFECTS OF NONLINEAR ABSORPTION

We now describe a method by which the Z-scan technique can be used to determine both the nonlinear refractive index and the nonlinear absorption coefficient for materials that show such nonlinearities simultaneously. Large refractive nonlinearities in materials are commonly associated with a resonant transition which may be of single or multiphoton nature. The nonlinear absorption in such

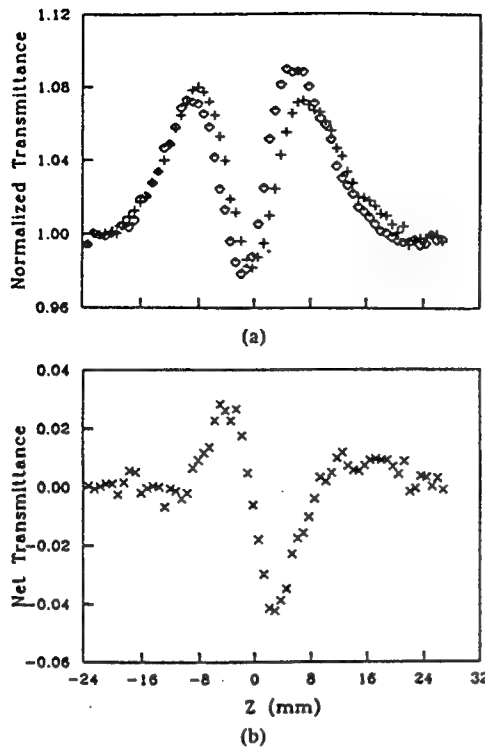


Fig. 8. (a) Measured Z-scans of a 1 mm thick ZnSe sample with poor surface quality for low irradiance (diamonds) showing the background and high irradiance (+). (b) Net transmittance change versus z after the background subtraction of the data in (a).

materials arising from either direct multiphoton absorption, saturation of the single photon absorption, or dynamic free-carrier absorption have strong effects on the measurements of nonlinear refraction using the Z-scan technique. Clearly, even with nonlinear absorption, a Z-scan with a fully open aperture ($S = 1$) is insensitive to nonlinear refraction (thin sample approximation). Such Z-scan traces with no aperture are expected to be symmetric with respect to the focus ($z = 0$) where they have a minimum transmittance (e.g., multiphoton absorption) or maximum transmittance (e.g., saturation of absorption). In fact, the coefficients of nonlinear absorption can be easily calculated from such transmittance curves.

Here, we analyze two-photon absorption (2PA), which we have studied in semiconductors with $E_g < 2\hbar\omega < 2E_g$ where E_g is the bandgap energy and ω is the optical frequency [22]. The third-order nonlinear susceptibility is now considered to be a complex quantity:

$$\chi^{(3)} = \chi_R^{(3)} + i\chi_I^{(3)} \quad (21)$$

where the imaginary part is related to the 2PA coefficient β through

$$\chi_I^{(3)} = \frac{n_0^2 \epsilon_0 c^2}{\omega} \beta \quad (22a)$$

and the real part is related to γ through

$$\chi_R^{(3)} = 2n_0^2 \epsilon_0 c \gamma. \quad (22b)$$

Here, we are concerned with the low excitation regimes where the free-carrier effects (refractive and absorptive) can be neglected. In view of this approximation, (3) and

(4) will be reexamined after the following substitution:

$$\alpha(I) = \alpha + \beta I. \quad (23)$$

This yields the irradiance distribution and phase shift of the beam at the exit surface of the sample as

$$I_e(z, r, t) = \frac{I(z, r, t) e^{-\alpha L}}{1 + q(z, r, t)} \quad (24)$$

and

$$\Delta\phi(z, r, t) = \frac{k\gamma}{\beta} \ln [1 + q(z, r, t)] \quad (25)$$

where $q(z, r, t) = \beta I(z, r, t) L_{\text{eff}}$ (again, z is the sample position). Combining (24) and (25), we obtain the complex field at the exit surface of the sample to be [23]

$$E_e = E(z, r, t) e^{-\alpha L/2} (1 + q)^{(ik\gamma/\beta - 1/2)}. \quad (26)$$

Equation (26) reduces to (7) in the limit of no two-photon absorption. In general, a zeroth-order Hankel transform of (26) will give the field distribution at the aperture which can then be used in (10) and (11) to yield the transmittance. For $|q| < 1$, following a binomial series expansion in powers of q , (26) can be expressed as an infinite sum of Gaussian beams similar to the purely refractive case described in Section III as follows:

$$E_e = E(z, r, t) e^{-\alpha L/2} \sum_{m=0}^{\infty} \frac{q(z, r, t)^m}{m!} \cdot \left[\prod_{n=0}^{m-1} (ik\gamma/\beta - 1/2 - n) \right] \quad (27)$$

where the Gaussian spatial profiles are implicit in $q(z, r, t)$ and $E(z, r, t)$. The complex field pattern at the aperture plane can be obtained in the same manner as before. The result can again be represented by (9) if we substitute the $(i\Delta\phi_0(z, t))^m/m!$ terms in the sum by

$$f_m = \frac{(i\Delta\phi_0(z, t))^m}{m!} \prod_{n=0}^{m-1} \left(1 + i(2n-1) \frac{\beta}{2k\gamma} \right) \quad (28)$$

with $f_0 = 1$. Note that the coupling factor $\beta/2k\gamma$ is the ratio of the imaginary to real parts of the third-order nonlinear susceptibility $\chi^{(3)}$.

The Z-scan transmittance variations can be calculated following the same procedure as described previously. As is evident from (28), the absorptive and refractive contributions to the far-field beam profile and hence to the Z-scan transmittance are coupled. When the aperture is removed, however, the Z-scan transmittance is insensitive to beam distortion and is only a function of the nonlinear absorption. The total transmitted fluence in that case ($S = 1$) can be obtained by spatially integrating (24) without having to include the free-space propagation process. Integrating (24) at z over r , we obtain the transmitted power $P(z, t)$ as follows:

$$P(z, t) = P_i(t) e^{-\alpha L} \frac{\ln [1 + q_0(z, t)]}{q_0(z, t)} \quad (29)$$

where $q_0(z, t) = \beta I_0(t) L_{\text{eff}} / (1 + z^2/z_0^2)$ and $P_i(t)$ was

defined in (11). For a temporally Gaussian pulse, (29) can be time integrated to give the normalized energy transmittance

$$T(z, S = 1) = \frac{1}{\sqrt{\pi} q_0(z, 0)} \cdot \int_{-\infty}^{\infty} \ln[1 + q_0(z, 0) e^{-\tau^2}] d\tau. \quad (30)$$

For $|q_0| < 1$, this transmittance can be expressed in terms of the peak irradiance in a summation form more suitable for numerical evaluation:

$$T(z, S = 1) = \sum_{m=0}^{\infty} \frac{[-q_0(z, 0)]^m}{(m+1)^{3/2}}. \quad (31)$$

Thus, once an open aperture ($S = 1$) Z-scan is performed, the nonlinear absorption coefficient β can be unambiguously deduced. With β known, the Z-scan with aperture in place ($S < 1$) can be used to extract the remaining unknown, namely, the coefficient γ .

An experimental example of this procedure is shown in Fig. 9 where a 2.7 mm thick ZnSe sample is examined using 27 ps (FWHM) pulses at 532 nm. ZnSe with a band-gap energy of 2.67 eV is a two-photon absorber at this wavelength. With a linear index of 2.7, the diffraction length inside the sample ($n_0 z_0$) was approximately four times the sample thickness. This allows us to safely apply the thin sample analysis developed in this paper. Fig. 9(a) depicts the open aperture data at a peak irradiance I_0 of 0.21 GW/cm². Also plotted is the theoretical result using (28) in (9) with $\beta = 5.8$ cm/GW. This is in excellent agreement with the previously measured value of 5.5 cm/GW [22]. Under the same conditions, the Z-scan with a 40% aperture, as shown in Fig. 9(b), exhibits a self-defocusing effect. These data have had a low irradiance background Z-scan subtracted to reduce the effects of linear sample inhomogeneities. Note the significant difference between this Z-scan and that of a purely refractive case. Here, the nonlinear absorption (2PA) has greatly suppressed the peak and enhanced the valley of the transmittance. The theoretical fit in Fig. 9(b) is obtained by setting $\beta = 5.8$ cm/GW and adjusting γ to be 6.8×10^{-14} cm²/W ($n_2 = 4.4 \times 10^{-11}$ esu) with an uncertainty of $\pm 25\%$ arising predominantly from the irradiance calibration.

An irradiance-dependent Z-scan study of the ZnSe indicates that for an irradiance $I_0 < 0.5$ GW/cm², the nonlinear refraction is dominated by a third-order effect. This is depicted in Fig. 10 where the measured nonlinear index change Δn_0 varies linearly with the irradiance. At higher irradiance levels, however, the nonlinear refraction caused by 2PA generated charge carriers, an effective fifth-order nonlinearity, becomes important. This is indicated in Fig. 10 by the small deviation of Δn_0 at $I_0 = 0.57$ GW/cm² from the line representing the cubic nonlinearity. An earlier investigation of ZnSe using picosecond time-resolved degenerate four-wave mixing (DFWM) at 532 nm had indicated that a fast $\chi^{(3)}$ effect followed by a slowly decay-

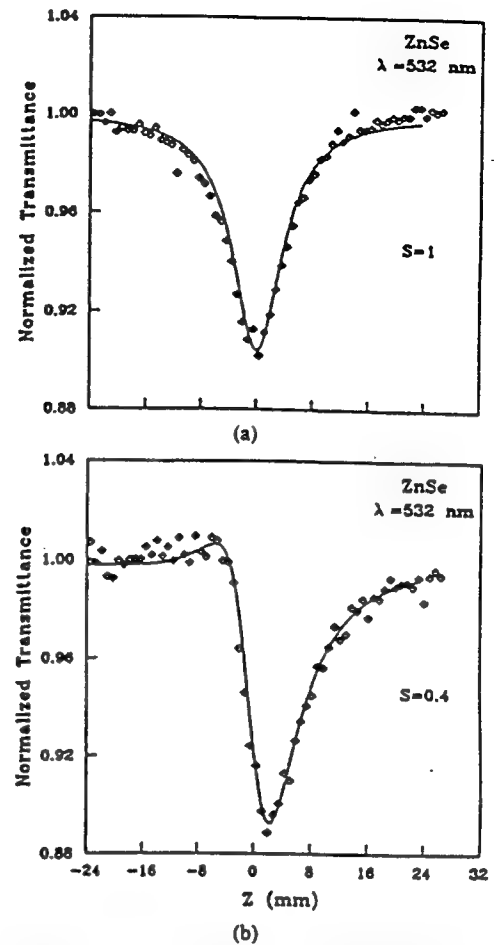


Fig. 9. Normalized Z-scan transmittance of ZnSe measured using picosecond pulses at $\lambda = 532$ nm with $I_0 = 0.21$ GW/cm². The solid lines are the theoretical results. (a) No aperture ($S = 1$) data and fit using 5.8 cm/GW. (b) 40% aperture data fitted with $\beta = 5.8$ cm/GW and $\gamma = 6.8 \times 10^{-14}$ cm²/GW.

ing $\chi_{eff}^{(5)}$ resulting from two-photon generated charge carriers was responsible for the DFWM signal [24]. Z-scan experiments reported here verify those results, and in addition, can accurately determine the sign and magnitude of these nonlinearities.

As was done for the case of a purely refractive effect, it is desirable to be able to estimate γ and β without having to perform a detailed fitting of the experimental data. A thorough numerical evaluation of the theoretical results derived in this section indicated that within less than 10% uncertainty, such a procedure is possible provided that $q_0(0, 0) \leq 1$ and $\beta/2k\gamma \leq 1$. The first condition can be met by adjusting the irradiance. The second condition is an intrinsic property of the material implying that the $\text{Im}(\chi^{(3)})$ should not be larger than the $\text{Re}(\chi^{(3)})$. This is the case for the semiconductors studied as well as for a wide variety of other materials. The separation and evaluation process is simple: divide the closed aperture ($S < 1$) normalized Z-scan (with background subtracted) by the one with open aperture ($S = 1$). The result is a new Z-scan where ΔT_{p-n} agrees to within $\pm 10\%$ of that obtained from a purely refractive Z-scan. The result of this procedure for the Z-scans of Fig. 9 is illustrated in Fig. 11 where the division of the two Z-scans of both experiment and theory are compared to the calculated Z-scan with β

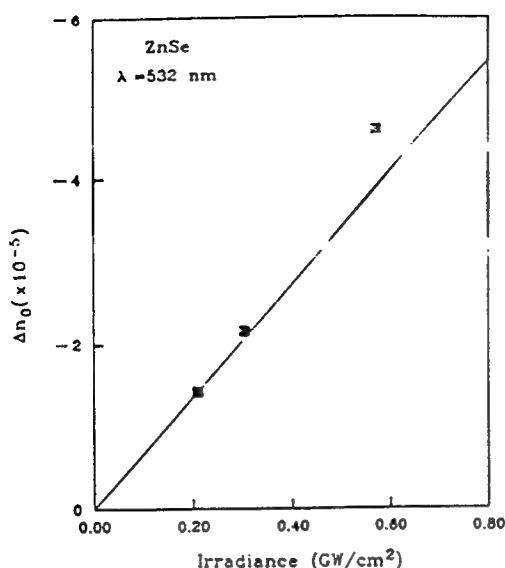


Fig. 10. The change of index in ZnSe versus the peak irradiance I_0 as measured from the Z-scan experiments. The line represents a cubic (n_2 type) nonlinearity. The deviation from the line is indicative of higher order refractive effects arising from two-photon generated charge carriers. The negative sign of the index change is apparent from the peak-valley configuration of Fig. 9(b).

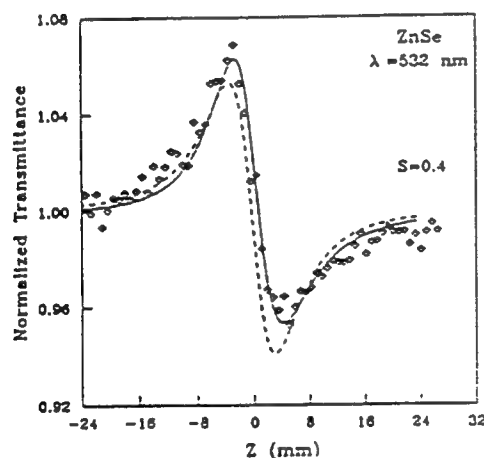


Fig. 11. The result of the division of the Z-scans of Fig. 9 (b)/(a): experimental (diamonds) and theoretical (solid line). The broken line shows the calculated result assuming $\beta = 0$. The ΔT_{p-v} of the latter agrees with that of the solid line fit to within 3%, making it possible to quickly estimate γ .

$= 0$. A simple measurement of ΔT_{p-v} and using (13) readily gives a value of $\gamma = 6.7 \times 10^{-14} \text{ cm}^2/\text{W}$, which is in excellent agreement with the value $6.8 \times 10^{-14} \text{ cm}^2/\text{W}$ obtained earlier.

VI. CONCLUSION

We have demonstrated a simple single-beam technique that is sensitive to less than $\lambda/300$ nonlinearly induced phase distortion. Using the Z-scan data, the magnitude of the nonlinear absorption and the magnitude and sign of the nonlinear refraction can be separately determined. We have derived simple relations that allow the refractive index to be obtained directly from the Z-scan data without resorting to computer fits. We have applied this technique to several materials displaying a variety of nonlinearities on different time scales. It is expected that this method

will be a valuable tool for experiments searching for highly nonlinear materials.

Here, we derive a relation between the n_2 and n_3 cubic nonlinearity and a small phase change. The on-axis electric field at the aperture plane can be obtained by letting $\Delta\Phi = 0$. The n_2 and n_3 nonlinearities are assumed to be small, and the nonlinear phase change $\Delta\Phi$ is assumed to be small. In the sum in (9), neglecting the n_3 term and making simplifications, the normalized transmittance can be written as

$$T(z, \Delta\Phi_0) = \frac{|E_1(z, r=0, \Delta\Phi_0)|^2}{|E_1(z, r=0, \Delta\Phi_0=0)|^2} = \frac{|(g + id/d_0)^{-1} + i\Delta\Phi_0(g - id/d_1)^{-1}|^2}{|(g - id/d_1)^{-1}|^2} \quad (\text{A1})$$

The far-field condition $d \gg z_0$ can be used to further simplify (A1) to give a geometry-independent normalized transmittance as

$$T(z, \Delta\Phi_0) = 1 - \frac{4\Delta\Phi_0 x}{(x^2 - 9)(x^2 + 1)} \quad (\text{A2})$$

where $x = z/z_0$.

The extrema (peak and valley) of the Z-scan transmittance can be calculated by solving the equation $dT(z, \Delta\Phi_0)/dz = 0$. Solutions to this equation yield

$$x_{p,v} = \pm \frac{\sqrt{52 - 5}}{2} = \pm 5.111 \quad (\text{A3})$$

Therefore, we can write the peak-valley separation as

$$\Delta z_{p-v} = 10.2 z_0 \quad (\text{A4})$$

Also, inserting the x value from (A3) into (A2), the peak-valley transmittance change is

$$\Delta T_{p-v} = \frac{S \Delta\Phi_0}{(x^2 - 9)(x^2 + 1)} = 0.406 \Delta\Phi_0 \quad (\text{A5})$$

ACKNOWLEDGMENT

We wish to thank A. Miller and M. J. Solleau for helpful discussions.

REFERENCES

- [1] S. R. Friberg, "Nonlinear optical materials for ultrafast optical switching," *IEEE J. Quantum Electron.*, vol. QE-16, pp. 955-967, 1980.
- [2] M. J. Weber, "Nonlinear optical materials for ultrafast optical switching," *IEEE J. Quantum Electron.*, vol. QE-16, pp. 968-978, 1980.
- [3] M. J. Moran, "Nonlinear optical materials for ultrafast optical switching," *IEEE J. Quantum Electron.*, vol. QE-16, pp. 979-989, 1980.
- [4] S. R. Friberg and P. A. Smith, "Nonlinear optical glasses for ultrafast optical switching," *IEEE J. Quantum Electron.*, vol. QE-23, pp. 2089-2094, 1987.



Reprinted from

Electro-Optical Materials for Switches, Coatings, Sensor Optics, and Detectors

16-20 April 1990
Orlando, Florida



Volume 1307

NONLINEARITIES IN SEMICONDUCTORS FOR OPTICAL LIMITING

A. A. Said, M. Sheik-bahae, D. J. Hagan, E. J. Canto-Said
Y. Y. Wu, J. Young, T. H. Wei and E. W. Van Stryland

CREOL

Center for Research in Electro-Optics and lasers
University of Central Florida, Orlando, FL 32816

ABSTRACT

We present measurements of nonlinear absorption and refraction in semiconductors used in the realization of optical limiters. We show that nonlinear refraction at 532 nm in ZnSe is caused by a negative third order electronic Kerr effect in addition to the two-photon-absorption (2PA) induced carrier refraction. We have used time-resolved beam distortion, picosecond time-resolved degenerate four-wave mixing and our recently developed Z-scan technique to determine the sign and magnitude of the 2PA coefficient, the bound electronic nonlinearity, n_2 , and the refractive index change per free carrier.

1. INTRODUCTION

Passive optical limiting utilizing the combined effects of nonlinear absorption and nonlinear refraction in semiconductors has been demonstrated previously.[1,2,3] An ideal passive optical limiter may be described as the optical analogue of a Zener diode circuit. It has a high linear transmission up to a certain input threshold after which the output becomes clamped to a constant value. In reference [1] we described the development and characterization of broad-band self-protecting ZnSe limiters. In this paper, we present the results of a comprehensive study of the nonlinear processes involved in such devices using various experimental techniques. These nonlinearities are two photon absorption (2PA), refraction arising from the 2PA generated free carriers and nonlinear refraction due to the electronic Kerr effect. Picosecond degenerate four wave mixing (DFWM) studies were conducted to examine the temporal response as well as the order of the refractive nonlinearities. Also, our newly developed Z-scan technique [4] was employed to accurately determine the sign and magnitude of the different refractive nonlinearities as well as the 2PA coefficient of the semiconductors.

In section 2 we describe the time-resolved beam distortion measurements and the equations for nonlinear propagation of light inside the semiconductors. In section 3 the DFWM results are presented. In section 4 the Z-scan technique is briefly described and the results of the Z-scan measurements are presented. Finally, in section 5 the experimental results are compared to theoretical models.

2. BEAM DISTORTION MEASUREMENTS

A collimated beam 0.57 mm in radius ($HW1/e^2M$) at 532 nm was incident on a 3 mm polycrystalline ZnSe sample and the transmitted beam fluence was monitored with a vidicon in the near field. In this geometry the thin sample approximation (the sample length is smaller than the diffraction length of the beam) can be used to describe the beam propagation inside the sample. This allows us to separate the wave equation into two equations, one for the irradiance I and one for the phase Φ . Also with 30 ps (FWHM) pulses and at low irradiance levels we can ignore the absorption due to the 2PA generated carriers but not carrier induced refraction [5]. This leaves the nonlinear differential equations,

$$\frac{dI}{dz} = -\alpha I - \beta I^2, \quad (1)$$

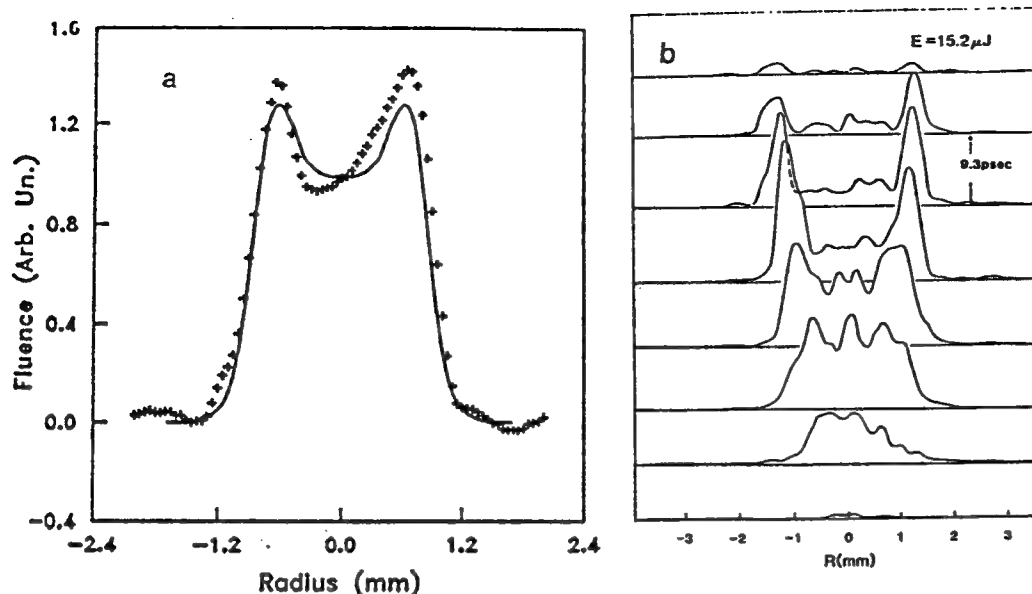


Fig.1. (a) Transmitted spatial energy distribution of a 30 ps $0.53 \mu\text{m}$ pulse after propagation through ZnSe at 2.7 GW/cm^2 as viewed on a vidicon. The solid line is the theoretical fit to the experiment with $\sigma=1.6 \times 10^{-21}$, $n_2=0$, and $\beta=5.5 \text{ cm/GW}$. In (b) the temporal evolution of the spatial profile shows the defocusing increases with time.

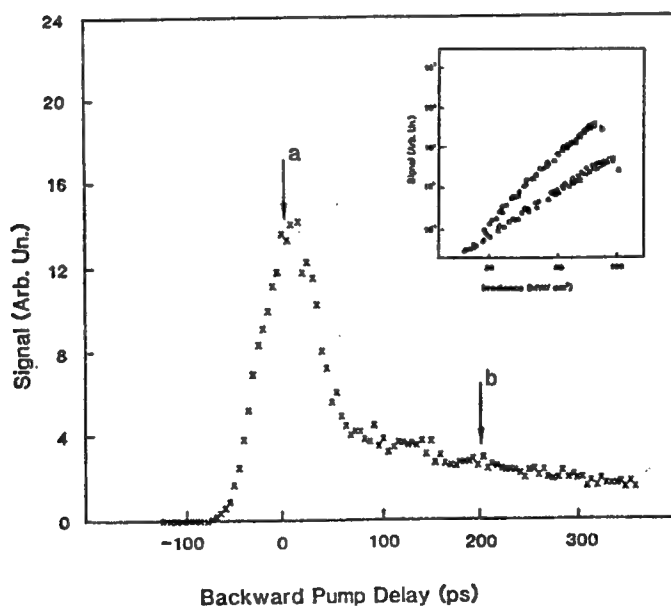


Fig.2. The DFWM signal vs backward pump delay for 30 ps pulses at $0.53 \mu\text{m}$ in ZnSe. The inset shows a log-log plot of the conjugate signal as a function of the input irradiance at 0 ps (a) and 200 ps (b).

and

$$\frac{d\Delta\Phi}{dz} = k\gamma I - k\sigma N, \quad (2)$$

where α is the linear absorption coefficient, β is the 2PA coefficient, $k=2\pi/\lambda$, λ is the wavelength of the incident radiation, γ is the refractive index change due to the electronic Kerr effect, N is the density of free carriers and σ is the change in the index of refraction per free carrier pair density generated. Since the free carriers are created by 2PA, the generation rate is given by

$$\frac{dN}{dt} = \frac{\beta I^2}{2\hbar\omega} \quad (3)$$

When N is substituted in equation (2), it becomes clear that the phase change due to the carriers depends on the square of the irradiance. Hence, the free carrier refraction appears as an effective fifth order nonlinearity.[7,8]

The solution to equations (1-3) gives the electric field at the exit surface of the sample, which we then propagate in free space to the vidicon using a Hygens-Fresnel integral. Using $\beta=5.5$ cm/GW for the 2PA coefficient from reference [6] we proceeded to fit the experimental data considering only free carrier refraction. The best fit was obtained with $\sigma=1.6 \times 10^{-21}$ cm³ as shown in figure 1(a). Using a streak camera in front of the vidicon, the time evolution of the spatial irradiance profile of the beam could be monitored as shown in figure 1(b). Here the beam is continuously broadened as the pulse temporally evolves, further indicating that the defocusing mechanism is a time integrating effect which is true for free carrier refraction. Therefore, our preliminary conclusion was that the self-defocusing observed in ZnSe is entirely caused by the carriers generated via 2PA.

There is a great deal of experimental evidence that the bound electronic refractive index change in solids is a positive effect, i.e. $n_2 > 0$. This is seen for wide band-gap materials, since self-focusing plays a significant role in the laser induced damage of these solids.[13] Based on this, and since all beam distortion experiments showed a self-defocusing effect, we at first attributed nonlinear refraction to 2PA generated free carriers alone.[1] However, as shown below we find n_2 is negative for semiconductors at energies well above the 2PA edge.

3. DEGENERATE FOUR WAVE MIXING EXPERIMENTS

DFWM with picosecond pulses is a sensitive technique that gives information about the temporal evolution of nonlinear processes in semiconductors and other materials. Two counter-propagating strong beams, forward pump E_f and backward pump E_b , are incident on the sample with a third weaker probe beam, E_p incident at an angle θ with respect to the forward pump. Two of these beams interfere inside the sample to form a grating from which the third beam diffracts to form a conjugate signal E_c that retraces the probe path. The pulses used in these experiments are the second harmonic of a Q-switched Nd:YAG laser output with a 30 ps (FWHM) pulse width and a Gaussian spatial profile. Various combinations of polarizers and half-wave plates were placed in the path of each beam to independently change their polarization and irradiance. Figure 2 shows a plot of the conjugate signal versus the delay τ_D of E_b which was polarized perpendicular to E_f and E_p . Two distinct regions are present, a fast decaying signal near zero delay and a slowly decaying signal at long delays. To better understand the two nonlinear regimes, irradiance dependence experiments were performed at different delays. A log-log plot of the DFWM signal versus input irradiance (all three inputs varied) gives two different slopes as shown in the inset of figure 2. At zero delay a slope of 2.8 was measured indicating a third order nonlinearity and at long delays a slope of 4.9 was found. The fifth order dependence can be explained by the 2PA induced carrier refraction as mentioned in the previous section. A modulated carrier density is created via 2PA; this is an imaginary $\chi^{(3)}$

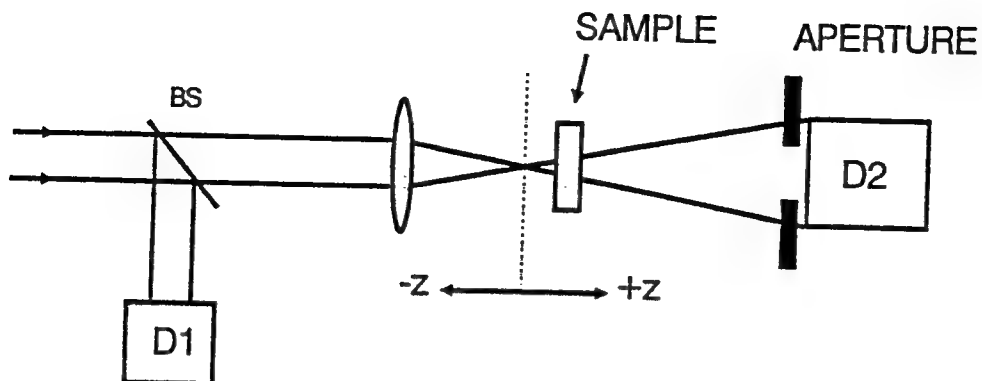


Fig.3. The Z-scan experimental setup in which the normalized transmittance is measured as a function of the sample position z .

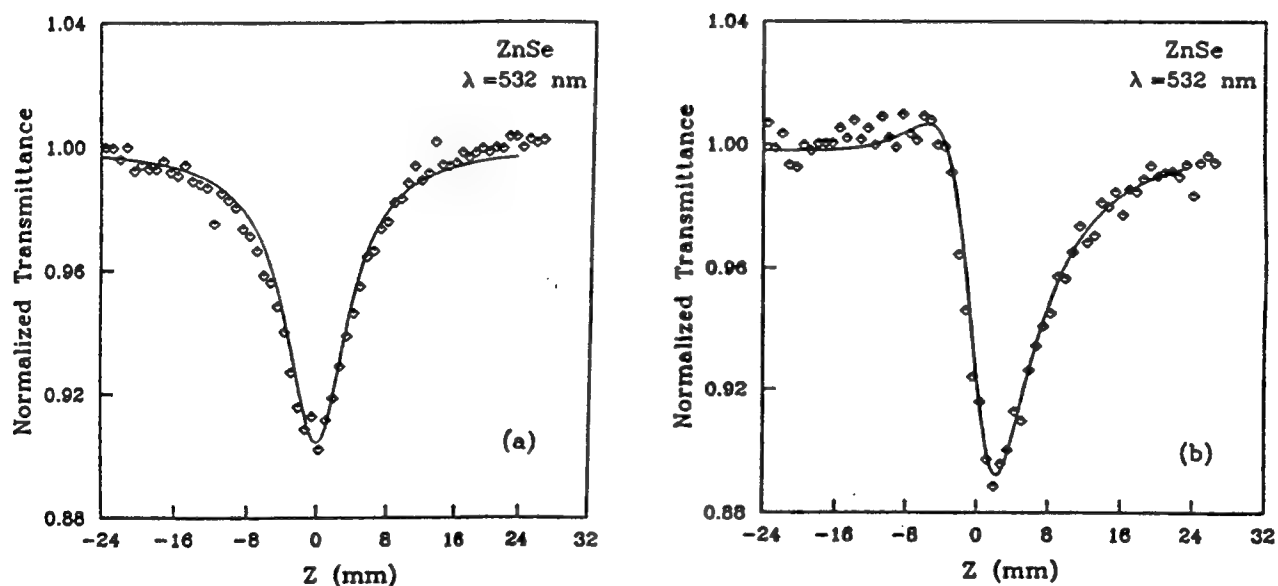


Fig.4. Normalized Z-scan signal of a 2.7 mm thick ZnSe sample using 27 ps $0.53\mu\text{m}$ pulses at 0.21 GW/cm^2 input irradiance. The solid lines are the theoretical results. (a) No aperture data and fit using $\beta=5.8\text{ cm/GW}$. (b) 40% aperture data fitted with $\beta=5.8\text{ cm/GW}$ and $n_2=-4 \times 10^{-11}\text{ esu}$.

effect. Then a third beam diffracts off the carrier modulation; this is a real $\chi^{(1)}$ effect. Hence, the mechanism is a sequential $\chi^{(3)} : \chi^{(1)}$ process that appears as a fifth order nonlinearity. As to the third order effect the signal decays within the 30 ps pulse width which is consistent with a bound electronic nonlinearity. This fast decaying effect can either be of refractive or absorptive nature as far as DFWM is concerned. Assuming that it is a refractive effect a value of $|n_2| = 4.4 \times 10^{-11}$ esu was extracted where n_2 is related to γ by $n_2 \text{ (esu)} = n_0 c / (40\pi) \gamma \text{ (MKS)}$. [7,8] Note that the sign of n_2 is not given by DFWM. This third order effect was not expected from the fits of the beam distortion experiments.

4. Z-SCAN MEASUREMENTS

The Z-scan technique, which was recently developed at our laboratories, is a simple single beam experimental technique that readily gives the sign and magnitude of nonlinear refraction as well as nonlinear absorption.[9] It is also an excellent guide for geometrical optimization of optical limiting.[10] Figure 3 shows the Z-scan experimental setup. A focused Gaussian beam is incident on the sample and the transmitted beam is collected through a finite aperture in the far field into detector D_2 . D_1 monitors the input energy. Keeping the input energy fixed, the transmittance is measured as a function of the sample position relative to the focal plane. Since nonlinear refraction causes a lensing effect in the incident beam, the sample behaves as a negative or positive lens depending on the sign of the nonlinearity. As explained in reference [4] a valley-peak configuration in the Z-scan signal is a signature of a positive refractive nonlinearity and a peak-valley pattern denotes a negative nonlinearity. When the aperture is removed, i.e. all the transmitted light is collected, the Z-scan is only sensitive to nonlinear absorption. For semiconductors with 2PA present, the Z-scan experiment was simulated by solving equations (1-3). Three parameters are to be determined β , n_2 and σ . Using 27 ps pulses (FWHM) at 532 nm Z-scan measurements were performed on a 2.7 mm thick ZnSe sample at different input energies. With the aperture removed a Z-scan was performed at $I_0 = 0.1 \text{ GW/cm}^2$ where I_0 is the on axis peak irradiance at the focus. In this case the measurement is insensitive to nonlinear refraction and thus independently gives the nonlinear absorption coefficient. The best fit to the data shown in figure 4(a) gave a $\beta = 5.8 \text{ cm/GW}$, in good agreement with the value of 5.5 cm/GW obtained in reference [6]. Our experimental errors were $\pm 30\%$ mostly arising from uncertainties in the irradiance values. Figure 4(b) shows the data and fit of the Z-scan signal at the same irradiance with the 40% transmitting aperture in place. At this low irradiance we expect the nonlinear refraction to be mostly due to the 3rd order nonlinearity as can be deduced from equations (2) and (3). Hence, the carrier term in equation (2) was dropped and an $n_2 = -4 \times 10^{-11}$ was extracted. The negative sign of n_2 is evident from the peak-valley pattern in the data. Moreover, this n_2 value is within 10% of the value obtained by our DFWM measurement. For a 3rd order nonlinearity, the change in the index of refraction, Δn , is a linear function of the irradiance, I . Figure 5 shows that this is not the case at higher irradiance values meaning that the refraction due to the 2PA generated carriers becomes more significant at these levels. At $I_0 = 2.4 \text{ GW/cm}^2$ (fig. 6), and with β and n_2 known, the experimental data was fit with $\sigma = 0.8 \times 10^{-21} \text{ cm}^3$. The above measured values for n_2 , β and σ were used at other irradiance values and gave good fits to the experimental data. The Z-scan was also used to determine the above parameters for other semiconductors at different wavelengths. For example at $1.06 \mu\text{m}$, we measured $\beta = 26 \text{ cm/GW}$, $n_2 = -2 \times 10^{-10} \text{ esu}$, $\sigma = 5 \times 10^{-21} \text{ cm}^3$ for CdTe and $\beta = 26 \text{ cm/GW}$, $n_2 = -2.7 \times 10^{-10} \text{ esu}$, $\sigma = 8 \times 10^{-21} \text{ cm}^3$ for GaAs. The experimental errors were $\pm 30\%$.

Based on the results obtained from both the DFWM and the Z-scan measurements we reexamined our beam distortion conclusion. The same data shown in figure 1(a) was fitted again with the 3rd order refraction included in the propagation equations. The result is a much better fit to the experimental data shown in figure 7 using $\beta = 5.5 \text{ cm/GW}$, $n_2 = -4 \times 10^{-11} \text{ esu}$ and $\sigma = 0.8 \times 10^{-21} \text{ cm}^3$.

5. CONCLUSION

As a result of conducting thorough studies of the nonlinearities in ZnSe at 532 nm using different experimental techniques, we conclude that the bound electronic nonlinearity is negative and is a significant contribution to the overall nonlinear refraction. We now understand the negative sign of n_2 . As discussed

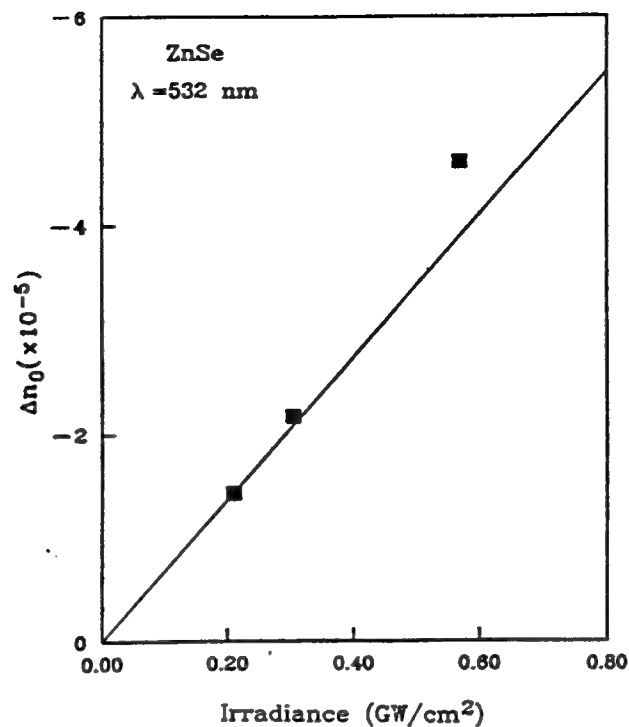


Fig.5. The refractive index change in ZnSe as a function of input irradiance as measured from the Z-scan experiments. The line represents a 3rd order nonlinearity. The deviation from the line indicates the higher order refraction arising from the 2PA generated free carriers.

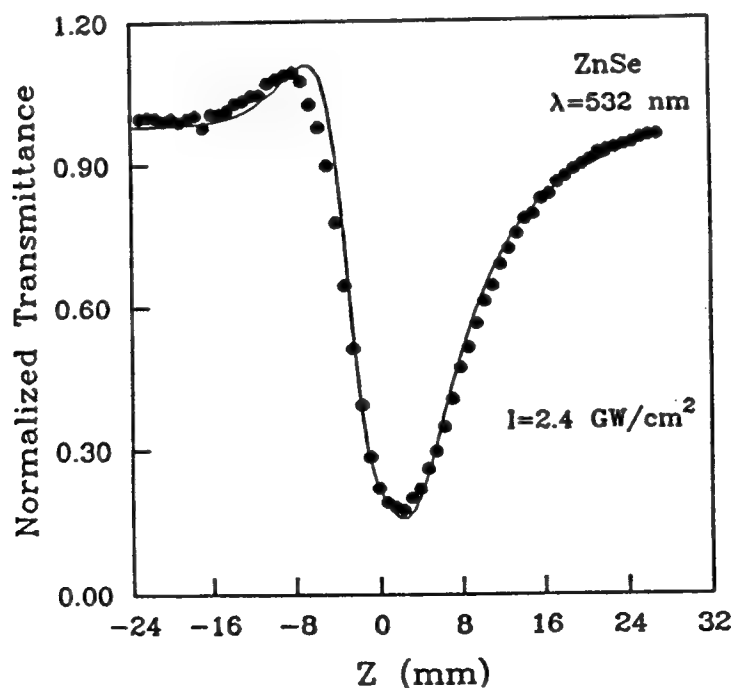


Fig.6. Normalized Z-scan signal for ZnSe at input peak irradiance of $2.4 \text{ GW}/\text{cm}^2$ with a 40% aperture. The solid line is the theoretical fit with $\beta = 5.8 \text{ cm}/\text{GW}$, $n_2 = -4 \times 10^{-11} \text{ esu}$ and $\sigma = 0.8 \times 10^{-21} \text{ cm}^3$.

in reference [11], n_2 , the real part of $\chi^{(3)}$, and 2PA, the imaginary part of $\chi^{(3)}$, are related by causality and a relation similar to the Kramers-Kronig connection between linear absorption and the linear index of refraction.[11] The value obtained for the refractive index change per free carrier pair agrees with the band-blocking model suggested by Auston et al.[12]. The σ calculated from the above model is $1.1 \times 10^{-21} \text{ cm}^3$ compared to our experimental value of $0.8 \times 10^{-21} \text{ cm}^3$. In conclusion, we have identified the different nonlinearities that make semiconductors good optical limiters.

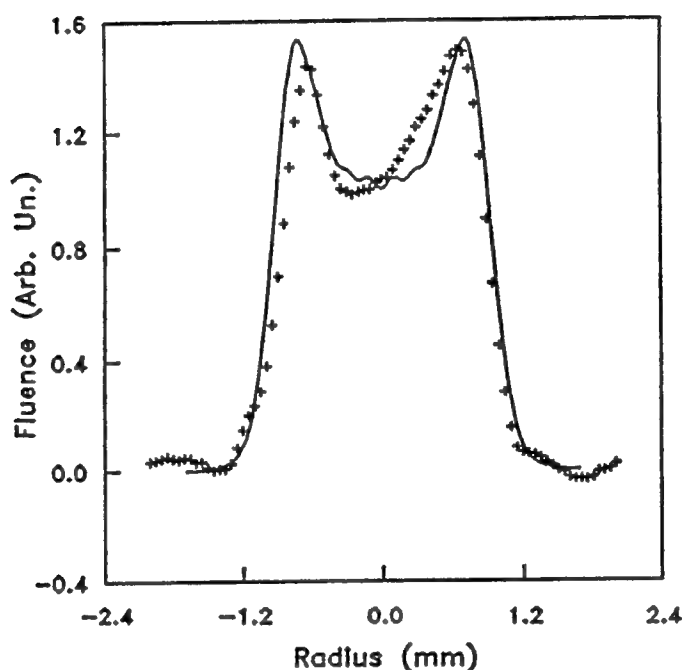


Fig.7. Same experimental data as in fig.1(a). The theoretical fit (solid line) is obtained with $\sigma=0.8 \times 10^{-21} \text{ cm}^3$, $n_2=-4 \times 10^{-11} \text{ esu}$ and $\beta=5.5 \text{ cm/GW}$. It is clear that this is a better fit than the one in figure 1(a) where the electronic Kerr refraction was neglected.

6. ACKNOWLEDGEMENTS

We gratefully acknowledge the support of the National Science Foundation grant #ECS-8617066, DARPA/CNVEO and the Florida High Technology and Industry Council.

7. REFERENCES

1. E. W. Van Stryland, Y. Y. Wu, D. J. Hagan, M. J. Soileau and K. Mansour, "Optical limiting with semiconductors", J. Opt. Soc. Am. B, Vol. 5, NO.9, 1980, September 1988. Also see, D. J. Hagan, E. W. Van Stryland, Y. Y. Wu, T. H. Wei, M. Sheik-Bahae, A. A. Said, K. Mansour, J. Young and M. J. Soileau, "Passive broadband high dynamic range semiconductor limiters," SPIE Proc. Vol.1105, 103 (1989).
2. T. F. Boggess, S. C. Moss, I. W. Boyd and A. L. Smirl, "Nonlinear- optical energy regulation by nonlinear refraction and absorption in silicon", Opt. Lett. 9, 291(1984).

3. J. M. Ralston and K. R. Chang, "Optical limiting in semiconductors," Appl. Phys. Lett. 15,164 (1969).
4. M. Sheik-Bahae, A. A. Said and E. W. Van Stryland, "High Sensitivity, Single Beam n_2 Measurements," Opt. Lett. Vol. 14, NO. 17, 955, (1989).
5. E. W. Van Stryland, M. A. Woodall, H. Vanherzeele, and M. J. Soileau, "Energy band-gap dependence of two-photon absorption," Opt. Lett. 10,490 (1985).
6. E. W. Van Stryland, H. Vanherzeele, M. A. Woodall, M. J. Soileau, A. L. Smirl, S. Guha, and T. F. Boggess, Opt. Eng. Vol 24, 613 (1985).
7. Edesly Canto, Ph.D. Dissertation, University of North Texas, May (1990).
8. E. J. Canto, D. J. Hagan, J. Young, and E. W. Van Stryland, "Degenerate four-wave mixing measurements of high order nonlinearities in semiconductors," To be published.
9. M. Sheik-Bahae, A. A. Said, T. H. Wei, D. J. Hagan, and E. W. Van Stryland, "Sensitive measurements of optical Nonlinearities using a single beam," IEEE J. Quantum Electron. April (1990).
10. Mansoor Sheik-Bahae, Ali A. Said, D. J. Hagan, M. J. Soileau and Eric W. Van Stryland, SPIE Proc. Vol. 1105, 146 (1989).
11. M. Sheik-Bahae, D. J. Hagan, A. A. Said, J. Young, T. H. Wei and E. W. Van Stryland, "Kramers-Kronig relation between n_2 and two-photon absorption," SPIE Proc. Vol 1307,(1990).
12. D. H. Auston, S. McAfee, C. V. Shank, E. P. Ippen, and O. Teschke, Solid State Electron. Vol 21, 147 (1978).
13. M. J. Soileau, William. E. Williams, Nastaran Mansour and E. W. Van Stryland, "Laser-Induced Damage and the Role of Self-Focusing," Opt. Eng. Vol. 28, 1133-1144 (1989).

Dispersion and Band-Gap Scaling of the Electronic Kerr Effect in Solids Associated with Two-Photon Absorption

M. Sheik-Bahae, D. J. Hagan,^(a) and E. W. Van Stryland^(b)

Center for Research in Electro-Optics and Lasers (CREOL), University of Central Florida, Orlando, Florida 32816

(Received 1 December 1989)

Measurements of the nonlinear refractive index using beam-distortion methods and four-wave mixing show a strong systematic dispersion in the bound-electronic nonlinearity (electronic Kerr effect n_2) near the two-photon-absorption edge. We find that with the two-photon-absorption spectrum predicted by a two-parabolic-band model, we can predict the observed universal dispersion, scaling, and values of n_2 that range over 4 orders of magnitude and change sign, using a simple Kramers-Kronig analysis. The resulting scaling rule correctly predicts the value of n_2 for 26 different materials, including wide-gap dielectrics and semiconductors.

PACS numbers: 78.20.Wc, 42.65.Bp, 42.65.Jx

The study of nonlinear optics in semiconductors has primarily concentrated on band-gap-resonant effects. The very large nonlinear effects observed in this case are the saturation of interband and excitonic absorption due to photoexcited free carriers and excitons, and the associated negative change in the refractive index. In contrast, by exciting optical solids at frequencies much less than the gap, a considerably smaller and faster, positive nonlinear refractive index (n_2) due to bound-electronic effects is observed. This n_2 arises from the real part of the third-order susceptibility $\chi^{(3)}$ and is defined through the refractive index change Δn , where

$$\Delta n(\omega) = \gamma(\omega) I_\omega = \frac{1}{2} n_2(\omega) |E_\omega|^2, \quad (1)$$

with I_ω and E_ω being the irradiance and electric field at frequency ω , respectively, and $n_2 = (2\pi/n_0) \text{Re}\{\chi^{(3)}\}$. The linear refractive index is n_0 , and γ and n_2 are related by $n_2(\text{esu}) = (cn_0\gamma/40\pi)(\text{mks})$, where c is the speed of light. The magnitude and dispersion of n_2 is of interest because of its importance in applications such as nonlinear propagation in fibers, fast optical switching, self-focusing and damage in optical materials, and optical limiting in semiconductors.

Most studies of n_2 in optical solids usually concentrate on wavelengths far below the energy gap (E_g). However, recently we found that measurements in semiconductors substantially above the two-photon-absorption (2PA) edge ($E_g/2$) yield negative values for n_2 .¹ We have extended these measurements to a large number of other materials including semiconductors and dielectrics above and below the 2PA edge. As a result, we have been able to clearly demonstrate the behavior of the dispersion of n_2 .

Utilizing a newly developed technique (Z scan) for n_2 measurements^{1,2} that can determine its magnitude and sign, we have measured n_2 for several semiconductors and wide-gap dielectrics at 1.064 and 0.532 μm . This simple technique has been shown to be an accurate and sensitive tool for measuring n_2 even in the presence of

nonlinear absorption. For example, we find a negative n_2 in materials such as ZnSe at 0.532 μm where 2PA is present, but find that the sign changes at 1.064 μm . We have also performed picosecond, degenerate, four-wave-mixing (DFWM) measurements which show this third-order response to be fast (time-resolution limited by the 30-ps pulse width) and dominant at irradiances up to $\approx 0.5 \text{ GW/cm}^2$, while at higher irradiances the slowly decaying 2PA-generated free-carrier refraction becomes important.³ DFWM studies in other semiconductors and other wavelengths show this to be a universal phenomenon.

It has previously been predicted that $\chi^{(3)}$ should vary as E_g^{-4} .^{4,5} Using this scaling and the relation between n_2 and $\chi^{(3)}$ that includes the linear index n_0 , we can remove the E_g and n_0 dependences from the experimental values of n_2 by multiplying them by $n_0 E_g^4$. Figure 1 shows a plot of our experimentally determined scaled values of n_2 as a function of $\hbar\omega/E_g$. We also divide the data by a constant K' which we explain in what follows. We show on the same plot several data for large-gap optical crystals obtained from recent measurements by Adair, Chase, and Payne using a "nearly degenerate three-wave-mixing" scheme.⁶ Our own measurements of several of the same materials studied in Ref. 6 show excellent absolute agreement. Assuming that there are no other relevant parameters unique to each material other than band gap and index, this plot should be general to all optical solids. Upon examination of Fig. 1 we immediately see a trend giving small positive values for low ratios of photon energy to band-gap energy which slowly rises to a broad resonance peak at the 2PA edge and then decreases, eventually turning negative between the two-photon- and single-photon-absorption edges. We should note that the scaling with E_g hides a variation in magnitude of n_2 of 4 orders of magnitude so that the observed universal dispersion curve is quite remarkable. This dispersion curve is qualitatively similar to the dispersion of the linear index around the single-photon-

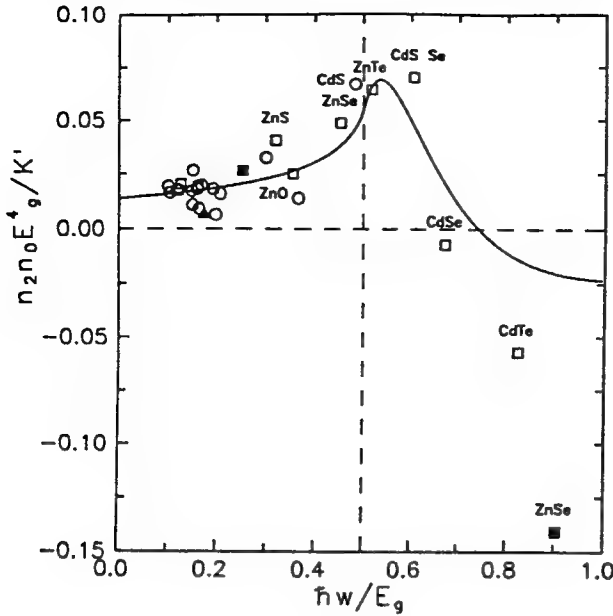


FIG. 1. Data of n_2 scaled as $n_2 n_0 E_g^4 / K'$ vs $\hbar \omega / E_g$. The open circles represent the data from Ref. 6 all obtained at $\lambda = 1.06 \mu\text{m}$. The remaining data are our measurements using the Z-scan technique taken at $\lambda = 1.06 \mu\text{m}$ (open squares), at $\lambda = 0.532 \mu\text{m}$ (solid squares), and at $\lambda = 10.6 \mu\text{m}$ (solid triangle). Only the semiconductor data within the highly dispersive region are labeled for comparison. The solid line is the calculated dispersion function G_2 with no adjustable parameters.

absorption edge.⁷ As these linear quantities are related by causality via a Kramers-Kronig (KK) relation, it seems logical to investigate whether the observed dispersion of n_2 can be calculated using a nonlinear Kramers-Kronig relation between the real and imaginary parts of $\chi^{(3)}$. Indeed, as we will show, making some reasonable assumptions, the observed tendencies as well as the absolute magnitudes of this dispersion are well predicted by such a calculation. Figure 1 is the direct result of such a calculation including only the 2PA contribution to the imaginary part of $\chi^{(3)}$. The 2PA spectral dependence is well established both experimentally and theoretically.⁸⁻¹¹ It should be noted that no fitting parameter is used in this calculation, which is presented below.

Most theoretical calculations of n_2 have been confined to the zero-frequency limit.¹²⁻¹⁶ Of these, semiempirical formulations have been most successful in predicting the magnitude of n_2 .^{15,16} For example, the formula obtained by Boling, Glass, and Owyong in relating n_2 to the linear index (n_0) and the dispersion of n_0 in terms of the Abbe number has been successfully applied to a large class of transparent materials.^{6,16} Their theory predicts the low-frequency magnitude of n_2 , but does not give the dispersion. The KK method described here predicts the dispersion as well as the magnitude of n_2 . This calculation assumes that 2PA gives the dominant contribution to n_2 and that other contributions from electronic Raman and the ac Stark effect ("virtual band blocking")

are ignored. We will return to this assumption later.

Based on the principle of causality, the KK transformation states that a change in the refractive index (Δn) at ω is associated with changes in the absorption coefficient ($\Delta \alpha$) throughout the spectrum (ω') and vice versa. We write this as

$$\Delta n(\omega; \xi) = \frac{c}{\pi} \int_0^\infty \frac{\Delta \alpha(\omega'; \xi)}{\omega^2 - \omega'^2} d\omega', \quad (2)$$

where c is the velocity of light in vacuum and ξ is a parameter (or parameters) denoting the "cause" of change in the absorption. The cause need not be of optical origin but could be any external perturbation, such as thermal excitation, etc. For cases where an electron-hole plasma is injected, the consequent change of absorption has been used to obtain the plasma contribution to the refractive index. In this case, the ξ parameter is taken as the change in plasma density (ΔN) regardless of the mechanism of generation of the plasma or the pump frequency.¹⁷ In the case of 2PA the change is due to the presence of a pump field at Ω (i.e., $\xi = \Omega$). The corresponding nonlinear refraction is $\Delta n(\omega, \Omega)$, which gives the dispersion of the index change with ω . For the case of self-refraction, $\omega = \Omega$, and this gives what is commonly referred to as n_2 . Van Vechten and Aspnes¹⁴ obtained the low-frequency limit of n_2 from a similar KK transformation of the Franz-Keldysh electroabsorption effect where, in this case ξ is the dc field. The bound-electronic contribution to $\chi^{(3)}$ can originate from various absorptive counterparts that are quadratic functions of the pump field. Effects of this order may include 2PA, the electronic Raman effect, and the optical Stark effect. Here we consider only 2PA.

A wealth of experimental and theoretical work regarding 2PA in semiconductors and crystalline materials exists. In accordance with the predictions derived from either a second-order perturbation calculation of the transition rate^{5,8} or a Keldysh-type formalism,⁹ the 2PA coefficients of the semiconductors studied in Ref. 10 were found to be in good agreement with the theoretical expression given as

$$\beta(2\omega') = K \frac{\sqrt{E_p}}{n_0^2 E_g^3} F_2 \left(\frac{2\hbar\omega'}{E_g} \right), \quad (3)$$

where K is a material-independent constant and E_p (related to the Kane momentum parameter, a momentum matrix element) is nearly material independent and possesses a value of ≈ 21 eV for most direct-gap semiconductors. Note that $\beta = (4\pi\omega/n_0) \text{Im}\{\chi^{(3)}\}$. The function F_2 is only a function of the ratio of the photon energy $\hbar\omega'$ to E_g (i.e., the optically coupled states). The functional form of F_2 reflects the assumed band structure and the intermediate states considered in calculating the 2PA transition rate. The simplest model assumes a pair of isotropic and parabolic bands and intermediate states that are degenerate to initial (valence) or final (conduc-

tion) states. Neglecting the Coulomb interaction, this simple formalism yields⁵

$$F_2(2x) = \frac{(2x-1)^{3/2}}{(2x)^5} \text{ for } 2x > 1. \quad (4)$$

The best fit to the data of Ref. 10 using Eqs. (3) and (4) gave $K = 3.1 \times 10^3$ in units such that E_p and E_g were in eV and β was in cm/GW, while theory gave 5.2×10^3 .⁸ When nonparabolicity was included the average β was 26% lower than theory; however, the frequency dependence of β changed very little. Interestingly, Eqs. (3) and (4) also give a fair estimate of β for a number of transparent materials measured using the third and fourth harmonics of picosecond Nd-doped yttrium-aluminum-garnet laser pulses.^{11,18}

Equations (3) and (4) pertain to a degenerate case where the two photons involved are of the same frequency and source. For a KK transformation the nondegenerate 2PA coefficient for two distinct frequencies is needed [i.e., Ω the "cause" and ω' the integration variable in Eq. (2)]. Extending the same simple model to obtain the nondegenerate 2PA coefficient has led to dispersion functions that are afflicted with "infrared divergences."^{19,20} This has been a common problem originating from the use of the $\mathbf{A} \cdot \mathbf{p}$ perturbation to calculate the bound-electronic nonlinear susceptibilities in solids.¹⁹ Although

special cases have been considered,²¹ a general theory that would rigorously address the proper scaling and spectrum of the nondegenerate 2PA is yet to be developed. For this reason we assume that the spectral function F_2 for the nondegenerate 2PA coefficient $\beta(\omega', \Omega)$ can be given by Eq. (4) modified with the substitution of $2\hbar\omega'$ by $\hbar\omega' + \hbar\Omega$; thus, $F_2(2x)$ is replaced by $F_2(x' + X)$, where $x' = \hbar\omega'/E_g$, $X = \hbar\Omega/E_g$, and $x' + X > 1$. This substitution is strictly valid only for $x' = X$; however, the predictions resulting from this substitution show remarkable agreement with the data, as will be shown.

The change of the absorption spectrum (at ω') induced by the presence of a strong pump at Ω can be written for 2PA as $\Delta\alpha(\omega'; \Omega) = \beta(\omega'; \Omega)I_\Omega$, where I_Ω denotes the irradiance of the pump field. Similarly, the change in refractive index at ω induced by the presence of a strong pump at Ω can be written as $\Delta n(\omega; \Omega) = \gamma(\omega; \Omega)I_\Omega$. Applying the KK transformation Eq. (2) at this point yields a relation between $\gamma(\omega; \Omega)$ and $\beta(\omega'; \Omega)$. Using Eq. (3) with $F_2(x' + X)$ in Eq. (2) we obtain for the degenerate case ($\omega = \Omega$),

$$\gamma = K \frac{\hbar c \sqrt{E_p}}{2n_0^2 E_g^4} G_2 \left(\frac{\hbar\omega}{E_g} \right), \quad (5)$$

where the dispersion function $G_2(x)$ is given by

$$G_2(x) = \frac{-2 + 6x - 3x^2 - x^3 - \frac{1}{4}x^4 - \frac{1}{4}x^5 + 2(1-2x)^{3/2}\Theta(1-2x)}{64x^6}, \quad (6)$$

with $\Theta(x)$ being the unit step function.

Using the value of K obtained from the 2PA measurements, $E_p = 21$ eV, and converting from γ to n_2 , we obtain the final expression for n_2 as

$$n_2(\text{esu}) = K' \frac{G_2(\hbar\omega/E_g)}{n_0 E_g^4} \quad (7)$$

where $K' = 3.4 \times 10^{-8}$ and E_g is in eV. Equation (7) explicitly shows an E_g^{-4} band-gap dependence for the magnitude of n_2 as predicted in Refs. 4 and 5, and the sign and the frequency dispersion of this quantity are given by the simple closed-form function G_2 . G_2 is the function plotted as the solid line in Fig. 1. It is important to note that no fitting parameter was used in plotting the theoretical curve and that the agreement between data and the calculation is extremely good for this wide variety of materials and large disparity in magnitudes of n_2 . A noticeable difference between the magnitude of the measured and calculated values is seen near the one-photon-absorption edge in Fig. 1. Considering the simplicity of the model in deriving Eq. (7), such deviations are not expected. The measured large negative values of n_2 as compared to the calculated values near the functional absorption edge may be attributed to the refraction due to the optical Stark effect which has been ignored in our calculations. The contribution of this mech-

anism to the electronic nonlinear susceptibility has been shown to have a strong band-gap resonance and follows the same scaling as given in Eq. (7).⁴ This effect, which is negative for all frequencies below the band gap, vanishes quickly for longer wavelengths ($\hbar\omega < E_g/2$) and gives a negligible contribution in the transparency region of the material.

The E_g^{-4} dependence of n_2 gives a variation of n_2 from 2.5×10^{-14} esu for a material such as MgF_2 at 1.06 μm to 3×10^{-10} esu for germanium at 10.6 μm , which we measured using a picosecond CO_2 laser. This large variation of n_2 is better displayed by plotting n_2 scaled by n_0 and G_2 as a function of E_g on a log-log plot as shown in Fig. 2. In spite of this very large variation in magnitude of n_2 (and change in sign), this extremely simple model gives good agreement with the data for materials including both semiconductors and insulators, except very near the absorption edge. However, we must emphasize that the justification for splitting 2ω into $\omega' + \Omega$ in Eq. (4) is empirical.

In conclusion, the measured n_2 data follow a universal dispersion curve (see Fig. 1) from which values of n_2 for other materials at other wavelengths can be calculated. We have also experimentally verified the predicted band-gap scaling of n_2 . From the excellent overall agreement

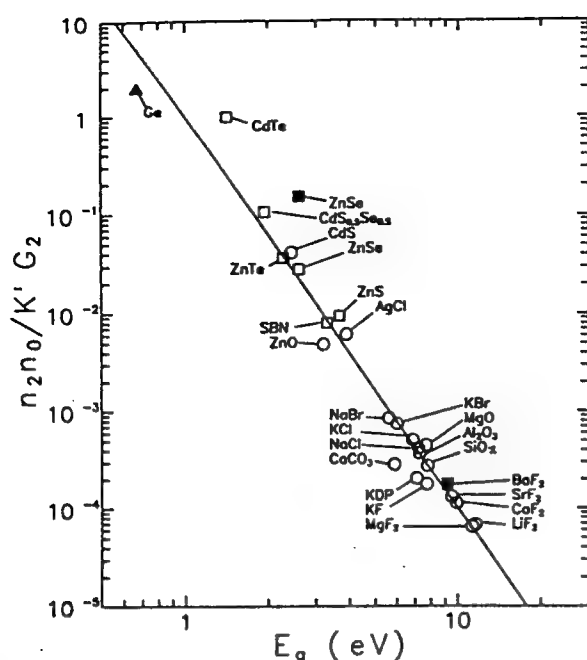


FIG. 2. A log-log plot of the data of Fig. 1 vs energy gap (E_g). Here the data are scaled by $n_0(K'G_2)^{-1}$. The solid line represents the theoretical result as obtained from Eq. (7) with no adjustable parameters and has a slope of -4 . The open circles represent the data from Ref. 6 all obtained at $\lambda = 1.06 \mu\text{m}$. The remaining data are our measurements using the Z-scan technique taken at $\lambda = 1.06 \mu\text{m}$ (open squares), at $\lambda = 0.532 \mu\text{m}$ (solid squares), and at $\lambda = 10.6 \mu\text{m}$ (solid triangle).

of the predicted magnitude and dispersion of n_2 , as calculated via the KK method, with the large number of experimental data, we conclude that the process responsible for 2PA also gives a significant if not dominant contribution to n_2 . This in turn implies that the bound-electronic nonlinear refractive index is predominantly a causal consequence of two-photon absorption just as the linear index is a causal consequence of linear absorption. This calculational approach takes advantage of the historical fact that, for the solid state, the 2PA coefficient has been calculated from a transition-rate approach.²² Thus, we have circumvented problems associated with performing a direct calculation of the third-order susceptibility.

We gratefully acknowledge the support of the National Science Foundation Grant No. ECS 8617066, U.S. Defense Advanced Research Projects Agency-Center for Night Vision and Electro-Optics, and the Florida High Technology and Industry Council. In addition, we thank

A. Miller, B. S. Wherrett, and S. Koch for useful discussions and J. Young, T. Wei, A. Said, and E. Canto for taking and analyzing portions of the n_2 data.

(a) Also with the Department of Physics.

(b) Also with the Departments of Physics and Electrical Engineering.

¹M. Sheik-Bahae, A. A. Said, T. H. Wei, D. J. Hagan, and E. W. Van Stryland, IEEE J. Quantum Electron. (to be published).

²M. Sheik-Bahae, A. A. Said, and E. W. Van Stryland, Opt. Lett. 14, 955-957 (1989).

³D. J. Hagan, E. Canto, E. Miesak, M. J. Soileau, and E. W. Van Stryland, in *Technical Digest of the Conference on Lasers and Electro-Optics, Anaheim, CA*, Technical Digest Series Vol. 7 (Optical Society of America, Washington, DC, 1988), p. 160.

⁴B. S. Wherrett, A. C. Walker, and F. A. P. Tooley, in *Optical Nonlinearities and Instabilities in Semiconductors*, edited by H. Haug (Academic, New York, 1988), pp. 239-272.

⁵B. S. Wherrett, J. Opt. Soc. Am. B 1, 67-72 (1984).

⁶R. Adair, L. L. Chase, and S. A. Payne, Phys. Rev. B 39, 3337-3349 (1989).

⁷J. Callaway, *Quantum Theory of the Solid State* (Academic, New York, 1974), p. 540.

⁸M. H. Weiler, Solid State Commun. 39, 937-940 (1981).

⁹H. S. Brandi and C. B. de Araujo, J. Phys. C 16, 5929-5936 (1983).

¹⁰E. W. Van Stryland, M. A. Woodall, H. Vanherzeele, and M. J. Soileau, Opt. Lett. 10, 490-492 (1985).

¹¹P. Liu, W. L. Smith, H. Lotem, J. H. Bechtel, N. Bloembergen, and R. S. Adhav, Phys. Rev. B 17, 4620-4632 (1978).

¹²S. S. Jha and N. Bloembergen, Phys. Rev. 171, 891-898 (1968).

¹³C. Flytzanis, Phys. Lett. 31A, 273-274 (1970).

¹⁴J. A. Van Vechten and D. E. Aspnes, Phys. Lett. 30A, 346-347 (1969).

¹⁵C. C. Wang, Phys. Rev. B 2, 2045-2048 (1970).

¹⁶N. L. Boling, A. J. Glass, and A. Owyong, IEEE J. Quantum Electron. 14, 601-608 (1978).

¹⁷D. A. B. Miller, C. T. Seaton, M. E. Prise, and S. D. Smith, Phys. Rev. Lett. 47, 197-200 (1981).

¹⁸E. W. Van Stryland, Y. Y. Wu, D. J. Hagan, M. J. Soileau, and K. Mansour, J. Opt. Soc. Am. B 5, 1980-1989 (1988).

¹⁹J. M. Worlock, in *Laser Handbook*, edited by F. T. Arecchi and E. D. Schulz-DuBois (North-Holland, Amsterdam, 1972), pp. 1323-1369.

²⁰G. D. Mahan, Phys. Rev. 170, 825-838 (1968).

²¹F. V. Bunkin, Zh. Eksp. Teor. Fiz. 50, 1685 (1966) [Sov. Phys. JETP 23, 1121 (1966)].

²²M. Göppert-Mayer, Ann. Phys. (N.Y.) 9, 273 (1931).

PROCEEDINGS REPRINT



SPIE—The International Society for Optical Engineering

Reprinted from

Electro-Optical Materials for Switches, Coatings, Sensor Optics, and Detectors

16-20 April 1990
Orlando, Florida



Volume 1307

©1990 by the Society of Photo-Optical Instrumentation Engineers
Box 10, Bellingham, Washington 98227 USA. Telephone 206/676-3290.

OPTICAL NONLINEARITIES IN CARBON BLACK PARTICLES

Kamjou Mansour, E. W. Van Stryland, M. J. Soileau

CREOL

Center for Research in Electro-Optics and Lasers
University of Central Florida, Orlando, FL 32826

ABSTRACT

We have characterized the nonlinear optical properties of carbon black particles in liquids and layers deposited on glass. We find that the limiting is dependent on the energy density (fluence) and that the material changes from a linear absorber to a nonlinear scatterer for fluence levels $\approx 0.2 \text{ J/cm}^2$ and $\approx 0.38 \text{ J/cm}^2$ for $0.532 \text{ }\mu\text{m}$, 14 ns and $1.064 \text{ }\mu\text{m}$, 20 ns laser pulses respectively. In this paper, we will discuss the possible mechanisms that have been proposed to explain the nonlinear scattering. These mechanisms are plasma formation, micro-bubble formation and change in index of refraction of the liquid surrounding the particles. We will show through a series of experiments that plasma formation is consistent with all of the experimental results while bubble formation may influence the limiting behavior at fluence levels substantially above the limiting threshold. In this model, the microscopic carbon particles are heated by linear absorption to a temperature at which a plasma can be created by the optical field. These microplasmas rapidly expand, thus scattering the incident light and limiting the transmittance.

1. INTRODUCTION

A wide variety of optical materials have been investigated for applications in optical limiting. An optical limiter utilizes the nonlinear properties of materials to limit the transmitted energy, power, fluence, or irradiance. One of the promising materials for constructing such a limiter is absorbing carbon black micro-particles suspended in a liquid. We show here that a layer of carbon black deposited on a glass substrate also limits the transmission.

In this paper, we review measurements in which we apply a wide variety of techniques to characterize the nonlinear optical processes that occur in carbon black suspension in liquids (CBS) and carbon black particles deposited as layers on a glass substrate (CBG). As it will be shown, the results of these experiments indicate that nonlinear scattering is the dominant optical nonlinearity in both CBS and CBG. The possible mechanisms that have been proposed to explain the observed nonlinear scattering are micro-bubble formation, the change in the refractive index of the liquid surrounding the particles and plasma formation. The micro-bubble formation model is based on degassing and vaporization of the liquid around the particles. The second model is based on the change in index of refraction of the surrounding liquid due to thermal heating and shock waves. The plasma formation model is based on formation and rapid growth of micro-plasmas created by the optical field. After considering each mechanism we have found that only the plasma formation model is consistent with all the experimental results while the other models fail to explain one or more of the experimental results.

We begin by reviewing some of the experimental results of optical limiting in CBS and CBG using ns and ps laser pulses at $0.532 \text{ }\mu\text{m}$ and $1.064 \text{ }\mu\text{m}$, and we discuss experiments showing that nonlinear scattering is the dominant limiting mechanism in CBS and CBG. In order to understand the nature of the scattering mechanism, we present an experiment in which we measure scattered light as a function of angle for different incident fluences for ns laser pulses. The measured angular scattering profile indicates an increase of the scattered light in the forward direction as a function of incident fluence of the laser pulses. The dependence of scattered intensity as a function of laser pulse fluence is similar to numerical calculations of the angular scattering profile as a function of particle size derived from Mie's scattering theory.[1] To investigate whether micro-plasmas are created by thermo-ionization of carbon particles, we measure the

emission spectrum of the particles using ns pulses for fluences where limiting is observed. In addition, we measure the emission decay rate at 800 nm. This result enables us to understand the decay of the scatterers with time which is important for understanding the switching recovery. To understand how the excited volume relaxes we have performed excitation and probe measurements. Specifically, we measured the switching recovery time of CBS and CBG, using a 20 ns, 1.064 μm excitation pulse and a continuous-wave (cw) HeNe as a probe beam.

2. OPTICAL LIMITING

Last year [2] we presented a detailed characterization of passive optical limiting in carbon black particles suspended in a mixture of water and ethylene glycol using nanosecond and picosecond laser pulses at 0.532 μm and 1.064 μm . We showed that the optical limiting threshold for such optical limiters is ≈ 80 watts peak power for 15 ns, 0.532 μm pulses and ≈ 160 watts peak power for 20 ns, 1.064 μm laser pulses. We also showed that the limiting in this material is fluence dependent rather than intensity or power dependent. This effect was observed by performing transmission measurements for collimated beams for different beam radii for 20 ns, 1.064 μm and 14 ns, 0.532 μm laser pulses. In addition, the onset of limiting was measured for both 14 ns and 30 ps, 0.532 μm laser pulses. The limiting occurred for approximately the same incident fluence for both ns and ps laser pulses. However, the input peak power was larger by a factor of 400 for ps pulses than for ns pulses.

In this paper, we reexamine the optical limiting threshold of CBS as a function of incident fluence for 20 ns, 1.064 μm laser pulse for beam radii from 14 μm up 460 μm (HW1/e² M). The experimental setup is a simple transmission measurement. We used a 100 μm thick flowing jet of CBS for tightly focused beams and a 1 cm thick cuvette of CBS for larger spot sizes. The result of this measurement is shown in Figure 1.

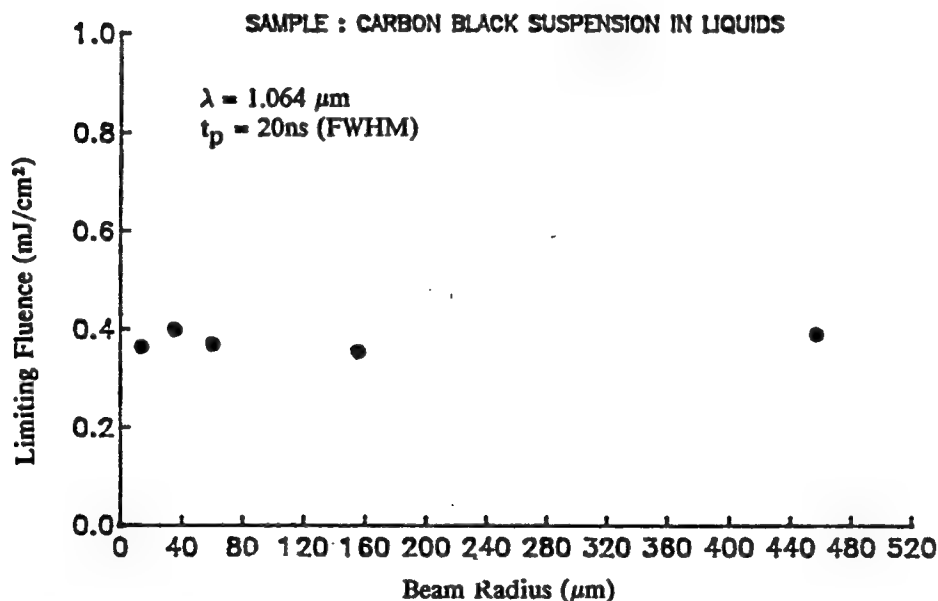


Figure 1. Plot of transmitted fluence (J/cm^2) as a function of beam radius (HW1/e² M) for 20 ns (FWHM), 1.064 μm laser pulses.

This result along with previous picosecond measurements illustrates that limiting in CBS is fluence dependent and the limiting fluence is on the order of 380 mJ/cm^2 for 1.064 μm laser pulses.

We also investigated the passive optical limiting for the CBG using 20 ns, 1.064 μm laser pulses. The motivation for this measurement was to determine how the liquid affected the limiting. These samples were prepared from carbon black particles which are commercially in use as toners in photocopying machine. These particles were uniformly deposited on a glass substrate. The sample linear transmission for 1.064 μm light was 30 percent. Using an optical limiting geometry discussed in detail in reference 2 we measured the limiting threshold for this material to be ≈ 600 watts. This is shown in Figure 2. The relatively large scatter in the data compared to that for CBS is due to the fact that the coated glass had to be moved after each firing and each data point is a single laser firing.

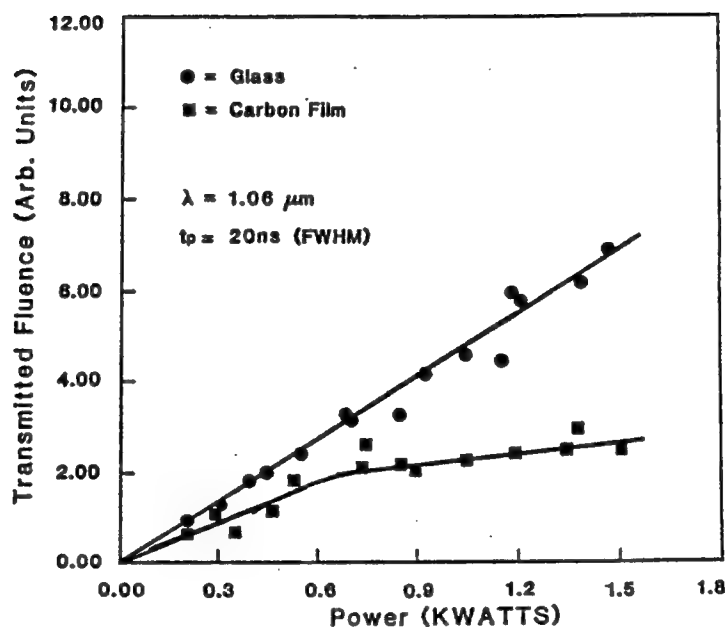


Figure 2. The limiting response of CBG (squares) and uncoated glass (circles) as a function of incident power for 20 ns (FWHM), 1.064 laser pulses. The limiting of CBG occurs at ≈ 600 watts.

3. OPTICAL NONLINEARITIES

The transmission experiments using both CBS and CBG showed limiting thresholds of the same order (within a factor of three) for carbon particles in liquid or in air. The factor of three difference may be attributed to the different carbon particle sizes. While the CBS has an average particle size of $\approx .1 \mu\text{m}$ with agglomerates up to $0.5 \mu\text{m}$. The toner particles used for the CBG has an average particle size of $\approx 5 \mu\text{m}$. The results of this experiment indicate that bubble formation is not a necessary occurrence for limiting with carbon black.

To understand the nature of optical nonlinearities leading to limiting in a liquid containing carbon black particles, we performed an experiment in which we monitored the change of transmittance, absorbance and fraction of side scattered light as a function of fluence for ns laser pulses at $0.532 \mu\text{m}$ and $1.064 \mu\text{m}$. The detailed description of this experiment is reported in reference 2. The experimental results for 20 ns, $1.064 \mu\text{m}$ in CBS is shown in figure 3.

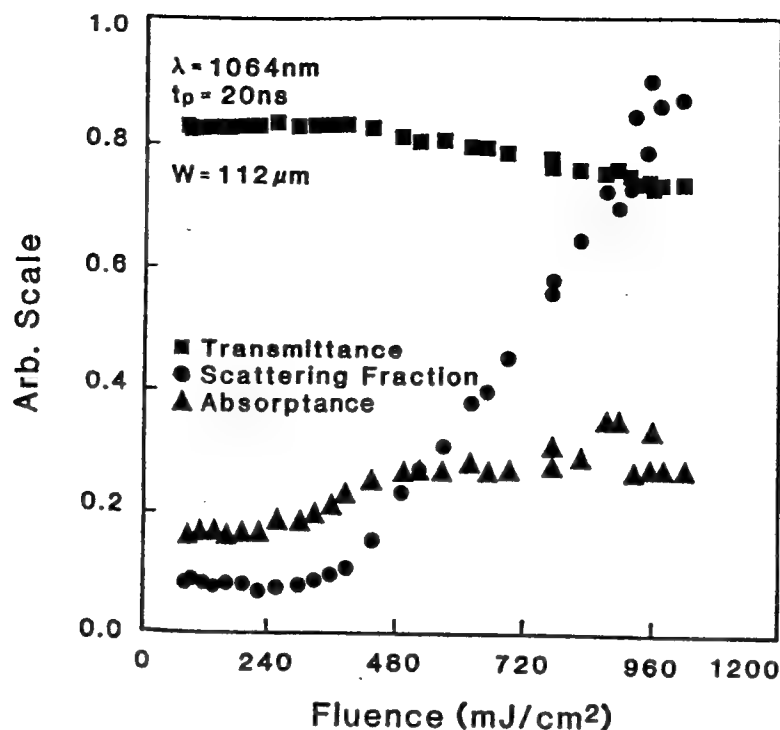


Figure 3. Plot of change of transmittance (squares), absorptance (triangles) and scattering fraction (circles) as a function of incident fluence (mJ/cm^2) for $1.06\text{ }\mu\text{m}$, 20 ns (FWHM) laser pulses.

As shown in Figure 3, for incident fluences close to $0.36\text{ J}/\text{cm}^2$ at $1.064\text{ }\mu\text{m}$, the transmittance begins to decrease nonlinearly, the absorptance increases nonlinearly for incident fluences close to threshold value (i.e., onset of change of transmittance) and levels off at a higher input and the scattered fraction (side scattered light / input light) increases nonlinearly as the transmittance decreases. This trend continues for input fluences even two order of magnitude above threshold. Similar results are observed for 14 ns, $0.532\text{ }\mu\text{m}$ laser pulses at incident fluences of $0.20\text{ J}/\text{cm}^2$. These results indicate that the observed nonlinear transmission is dominated by nonlinear scattering.

We have repeated these measurements using CBG to monitor the transmittance and the fraction of side scattered light as a function of input fluence using the geometry of Figure 4. The laser light was focused by a 15 cm focal length "best form" lens and collected by a Si: PIN photodiode energy monitor (D2). Identical detectors (D2) and (D3) were used to monitor the input energy and side scattered light respectively. The input was varied using a rotating $\lambda/2$ wave plate/polarizer combination. The polarization of the light was made perpendicular with respect to the line connecting the sample and D3. This polarization gave the maximum scattered signal at D3 for all input fluences as is expected from scattering theory. Figure 5 shows results for this experiment. The plain glass substrate showing no nonlinearity and was used as a reference. Again each data point is a single laser firing and the linear transmission of the CBG was 30 percent.

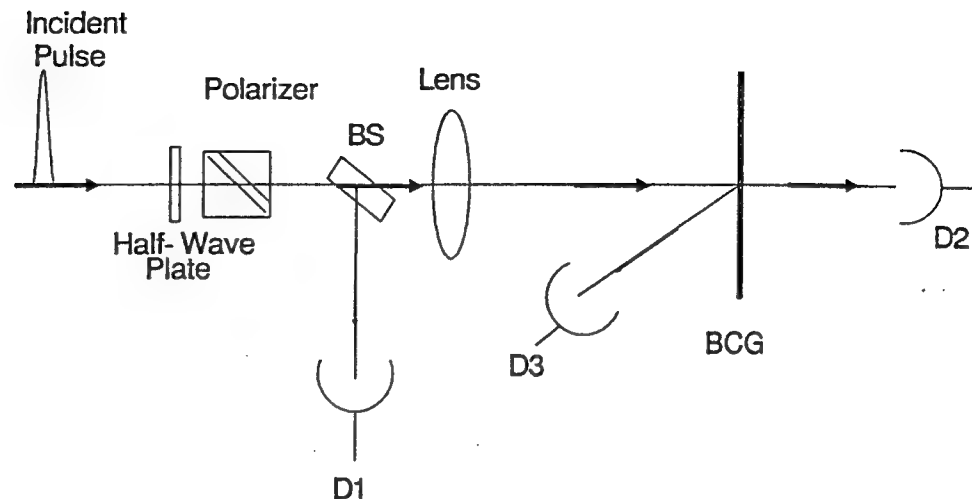


Figure 4. Experimental setup for simultaneous measurement of transmitted fluence and scattered light fraction as a function of incident fluence for ns, 1.064 μm laser pulses

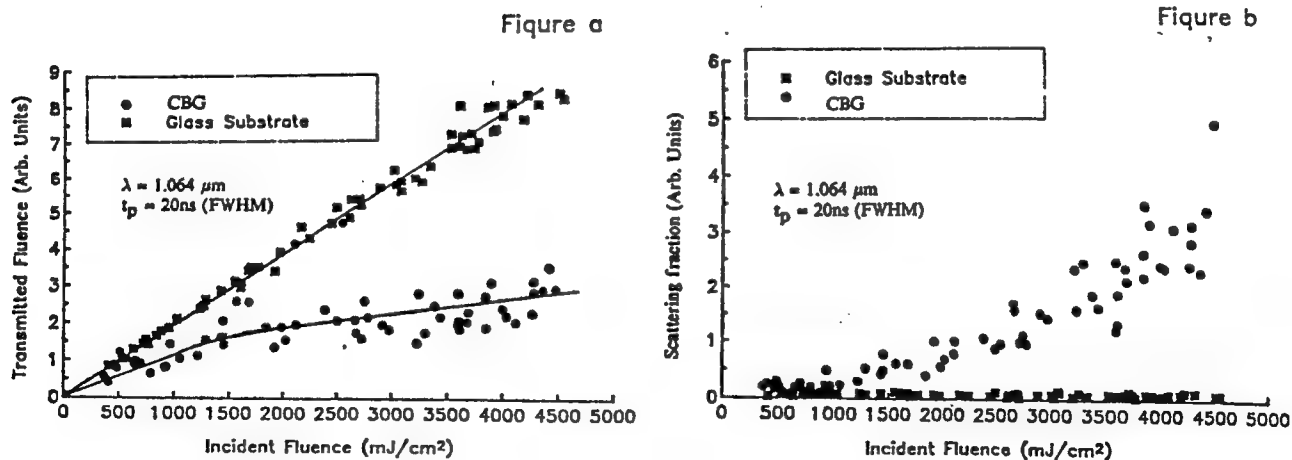


Figure 5. The experimental results for transmitted fluence and fraction of side scattered light for samples of CBG and plain glass used as a reference. Graph (a) shows the response of CBG shown as circles and glass substrate shown as squares. Graph (b) shows the side scattered light fraction using the same symbols as for (a).

As is shown in Figure 5, for incident fluences above $\approx 1 \text{ J/cm}^2$ the transmittance decreased and the side scattered light fraction increased nonlinearly. This behavior is similar to that of CBS.

The experimental techniques that we have used so far, allow us only to study the contribution of nonlinear scattering and nonlinear absorption in these samples. In order to investigate the contributions of phase distortion due to a thermo-optic effect, electrostriction, or other nonlinear refractive mechanism, we have performed a series of measurements. First, we monitored the far field spatial transmitted beam profile of the TEM₀₀ Gaussian input pulses at $0.532 \mu\text{m}$ using a vidicon tube interfaced to an optical multichannel analyzer. The spatial profile of the transmitted pulse was undistorted for incident fluences below and up to an order of magnitude higher than the limiting threshold. Second, we performed Z-scan measurements which are very sensitive to the self-focusing and self-defocusing nonlinearities. Details of the Z-scan technique are discussed in reference 3. The results of Z-scan measurements for 14 ns, $0.532 \mu\text{m}$ and 20 ns, $1.064 \mu\text{m}$ laser pulses with incident fluences below and above threshold indicate that nonlinear refraction is negligible in this material and has no influence on the limiting characteristic. In order to further validate this point we performed limiting experiments with and without an aperture in front of the transmitted detector and observed no change in limiting threshold.

From our experimental results we conclude that the dominant nonlinearity for limiting in carbon black particles in liquids or as layers deposited on glass substrate, is nonlinear scattering. There are three models that have been proposed to explain the mechanism of nonlinear scattering for these samples. The first model is based on the formation of micro-bubbles in the host media (i.e., water and ethylene glycol). The formation of these bubbles is based on degassing and vaporizing of the liquid around the absorbing particles, therefore, the dynamics of formation and growth of these micro-bubbles is a function of the properties of the absorbing particles and the properties of the liquid surrounding these particles. Hence, one would expect that the limiting threshold must be drastically decreased or increased as the properties of the host medium are changed. This has not been observed from our experimental results. Another model possible to explain the nonlinear scattering is due to a change in index by diffusion of heat or shock wave in the liquid (or gas) surrounding the carbon micro-particles. The size of these scattering centers (thermally induced index change) could be substantially larger than the carbon particles themselves yet smaller than the separation between particles thus, possibly leading to larger scattering according to Mie's theory. These effects are very small for 20 ns laser pulses since the heated liquid layers surrounding the particles are on the order of 100 \AA calculated from $\approx \sqrt{Dt_p}$ where t_p is the laser pulse width and D is the diffusion constant for liquid. This is clearly insufficient to give the observed nonlinear scattering. In the case of propagation of shock wave, a shock wave travels $\approx 70 \mu\text{m}$ during the 20 ns pulse. The average separation between particles for the densities used ($\approx 10^{11} \text{ 1/cm}^3$) is $\approx 9 \mu\text{m}$. Thus, the index of the entire liquid must be considered to change. We have observed no net linear refraction with a sensitivity of $\approx \lambda/100$ induced phase distortion. These leaves us with the micro-plasma model. As it will be shown this model is consistent with all of the experimental results.

4. ANGULAR SCATTERING MEASUREMENT

In all of these models the mechanism for nonlinear scattering is due to growth and expansion of "particles" (eg, air bubbles, micro-plasmas). To examine the validity of this volumetric expansion experimentally and also have an estimate for the size of these "particles" we have constructed a light-scattering apparatus. The basic components of this apparatus are shown in Figure 6. This experiment was conducted using 20 ns, $1.064 \mu\text{m}$ and 14 ns, $0.532 \mu\text{m}$ laser pulses. The laser light was focused by a 50 cm focal length "best form" lens into a $100 \mu\text{m}$ thick, 3mm wide flowing jet of carbon black suspension in a 50/50 mixture of water and ethylene glycol. The measured beam radius at focus was $93 \mu\text{m}$ ($\text{HW}1/e^2 \text{ M}$) for $0.532 \mu\text{m}$ and $96 \mu\text{m}$ ($\text{HW}1/e^2 \text{ M}$) for $1.064 \mu\text{m}$ laser pulses. The flow rate was set such that a laminar flow was achieved. The transmitted light was detected using a Si photodetector placed 60 cm from the sample. The detector used to monitor the scattered light could rotate in a plane which was perpendicular to the flow direction and parallel to the propagation direction. This plane defines the plane of observation and the polarization of the

incident light was set parallel to this plane. A 0.5 mm aperture was placed in front of the scattering detector to increase the angular resolution. The rotating platform and detectors were interfaced to an IBM computer. Scattering profiles for 20ns, 1.064 μm laser pulses at two different fluences are plotted in polar graphs in Figure 7. The size of the detector limited the angles to be between 20° and 160°.

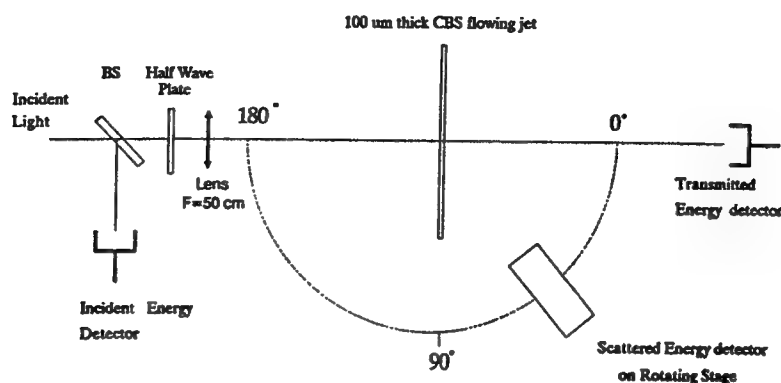


Figure 6. Schematic for angular scattering measurement

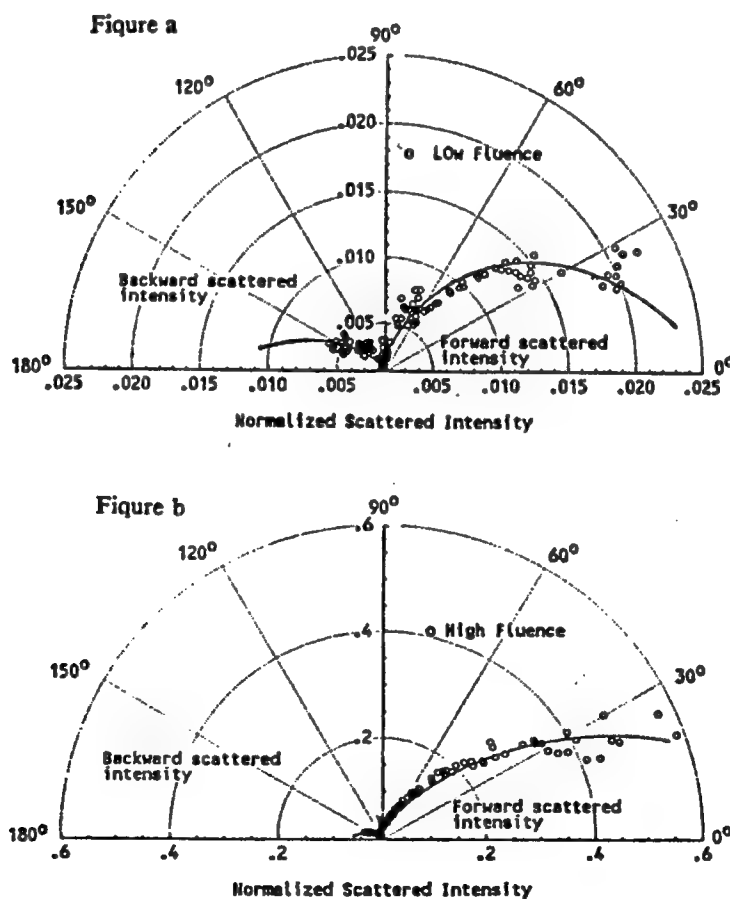


Figure 7. A polar plot of the fraction of scattered light for CBS using 20 ns (FWHM), 1.064 μm laser pulses. The solid lines are a guide to the eye and an extrapolation to smaller and larger angles. a) low fluences b) 5 times above the limiting threshold.

Figure 7a is for input fluences where the sample behaves linearly. The asymmetry observed is due to agglomerates which are smaller than the wavelength of light but are larger than particles where one would see isotropic Rayleigh scattering. Figure 7b presents scattering data for incident fluences where limiting is observed. In this profile the scattered light is highly asymmetric and all of the scattered light is in the forward direction. This asymmetry is due to larger scattering "particles". This increase of scattered light in the forward direction as a function "particle" radius can be modeled using Mie's scattering theory. Calculated scattering profiles as a function of size parameter x where $x=2\pi a/\lambda$ and a is the radius of the particles are shown in Figure 8.

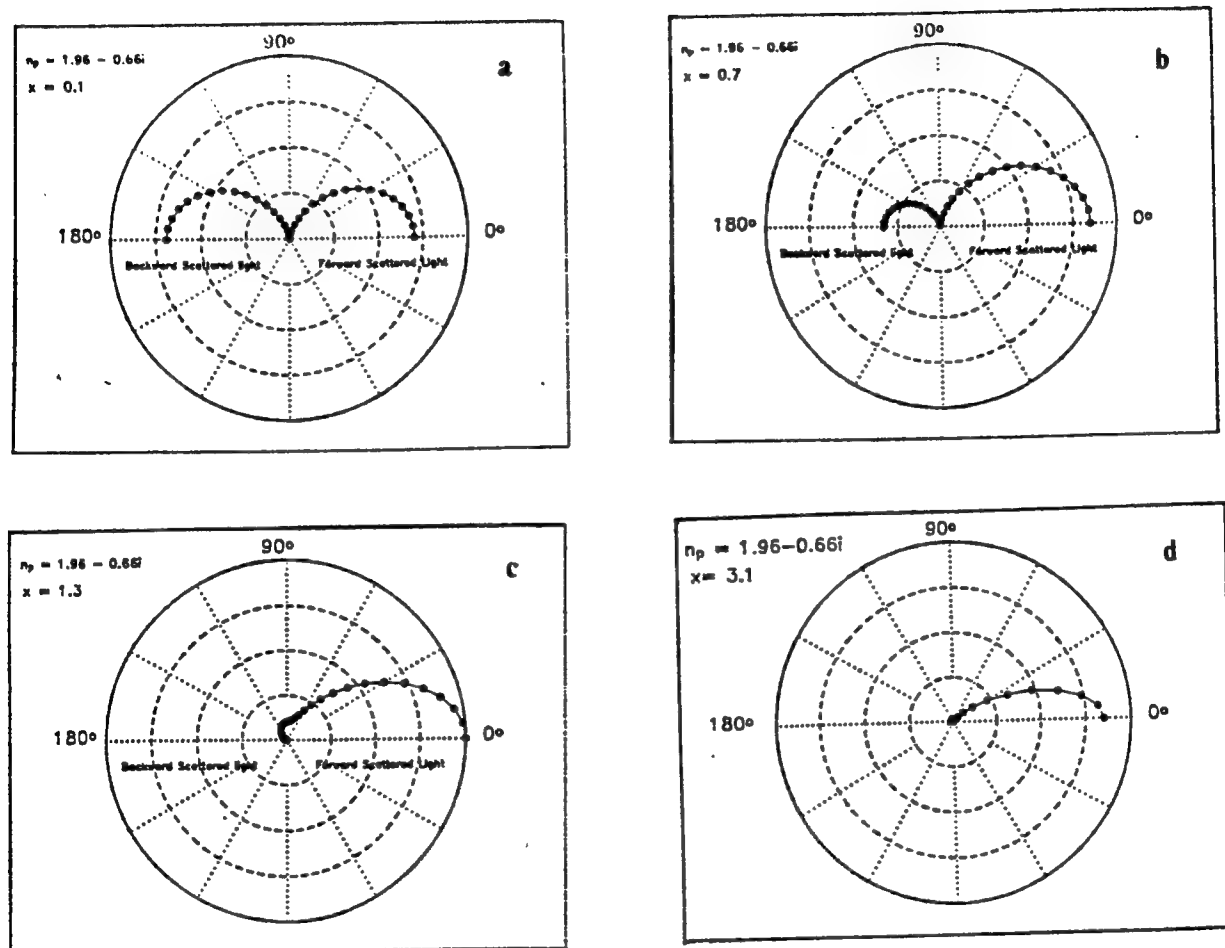


Figure 8. The numerical simulation of the 0° to 180° scattering profile for different size parameters (x). Plot a,b,c and d are for $x=0.1$, $x=0.7$, $x=1.3$ and 3.1 respectively.

Figure 8a shows the scattering profile for particle sizes which are very small compared to the wavelength of light. The scattering profile is symmetric and appears as a simple dipole radiation pattern. As the size parameter increases (i.e., particle radius increases) the scattered light in the forward direction increases relative to the backward scattered light. These results are shown in plots b,c and d. In plot d all the scattering is in the forward direction and the profile is highly asymmetric. This is similar to our experimental scattering profiles as the incident fluence increases. Therefore, results of angular scattering measurements indicate that nonlinear scattering observed is due to expansion of the "particles". Since, the observed scattering profile can be explained qualitatively by Mie's scattering theory we have used this theory

to calculate the scattering cross section and absorption cross section as a function of "particle" size. This numerical calculation was performed for two different types of "particles". First, we assume micro-bubbles growing with a purely real index of refraction. Second, we assume the expanding "particles" are micro-plasmas with complex index of refraction. We took the complex index to be $n = 1.96 - 0.66i$ which is the reported index of carbon black [4] and is consistent with what can be expected for a plasma. Our preliminary results for absorption cross section and scattering cross section indicate that both quantities are in a good agreement with experimental results if the expanding "particles" are assumed to be micro-plasmas.

5. FLUORESCENCE MEASUREMENT

If micro-plasmas are initiated by thermionic emission from carbon black particles we should expect to see an emission spectrum of ionized carbons. In order to investigate this, we have set up an experiment which enables us to monitor emission spectra resulting from irradiation using 40 ns, 1.064 μm laser pulses. In this measurement, the laser light is focused by a 15 cm "best form" lens into a 1 cm thick cuvette cell of CBS or onto samples of carbon particles deposited on glass substrates. The sample was placed about 1 cm from the entrance slit of a 1/4 meter monochromator. An SI fast response photomultiplier was connected to the exit port of the monochromator. The output signal from the photomultiplier was recorded and analyzed on a Tektronics digital oscilloscope and Tektronics computer. A tungsten calibrated blackbody source at 3250 $^{\circ}\text{K}$ was used to determine the instrument spectral response. The schematic for the experiment is shown in Figure 9.

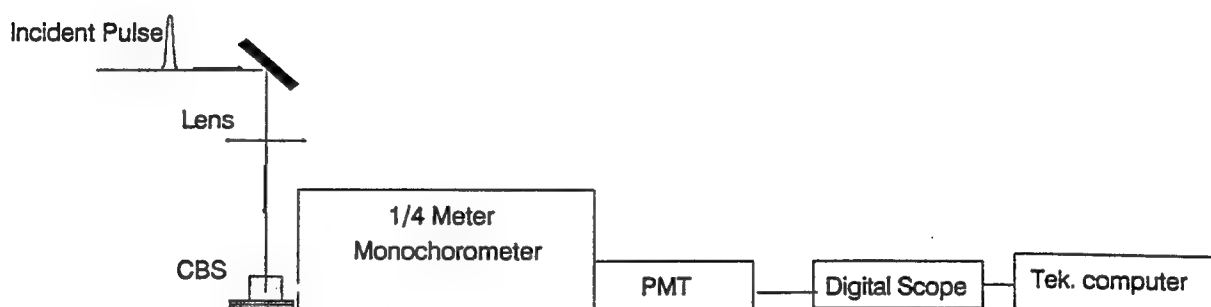


Figure 9. Experimental set-up for fluorescence measurement.

Using the experimental set-up shown in Figure 9, we measured the emission spectrum from carbon black particles from 400 nm to 900 nm. The spectrum is shown in Figure 10. The strongest singly ionized lines tabulated in reference [5] are indicated by small connected triangles. These lines are consistent with peaks in the measured spectrum. Furthermore, we have calculated the radiation spectrum for a black body source at 4250 $^{\circ}\text{K}$ using Planck's equation. The calculated blackbody spectrum from 200 nm to 1200 nm is also shown in Figure 10 and is consistent with the experimental background emission.

In order to determine the emission lifetime of the ionized particles we measured the emission intensity as a function of time at the emission line near 800 nm. We observed that the emitted light decays very rapidly to 50 percent of the peak intensity in the first 150 ns and decays much slower for later times. This is shown in Figure 11. In addition, we have plotted the incident pulse to show the time response of the detection system. These results are consistent with the decay of a plasma (150 ns) followed by the slow cooling of the thermal background emission. The results of these measurements are important for understanding the limiting and switching recovery time of CBS as discussed in the next section.

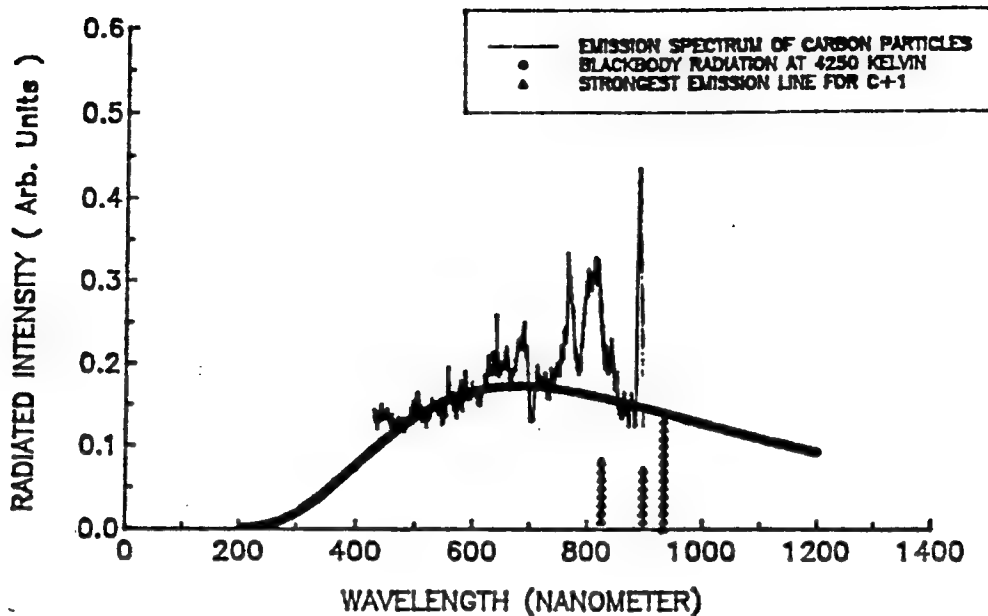


Figure 10. Plot of the spectral emission from carbon particles using 40 ns, 1.064 μm laser pulses. The solid line present experimental results. The triangles show tabulated results for singly ionized line. The connected circles show the calculated emission for a blackbody source at 4250 °K.

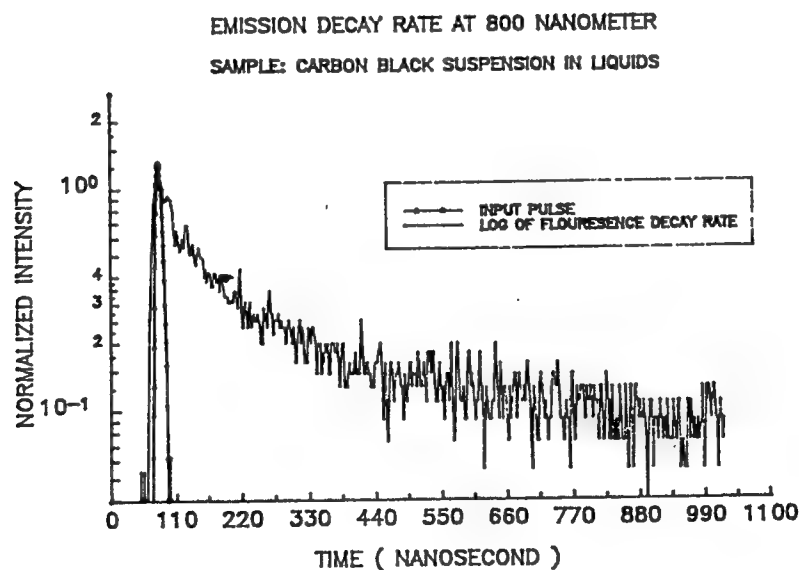


Figure 11. A semilogarithmic plot of the emission decay rate at 800 nm as a function of time.

6. EXCITATION AND PROBE MEASUREMENT

The dynamics of the attenuation of Q-switched, 20 ns laser pulses in carbon black suspensions in liquid was investigated by time resolved transmission measurements.[2] We observed that the transmitted pulse had a sharp cutoff and was strongly attenuated during later portions of the pulse. To investigate the dynamics of limiting for times longer than the duration of the incident pulse we have set up an excitation and probe measurement. In this experiment the interaction of 20 ns, 1.064 μm laser pulses with carbon particles was monitored using a low power cw, 0.6328 μm laser beam. The excitation and probe beam were focused using a 75 mm focal length "best form" lens into the samples of 1 cm thick cuvette of CBS and CBG. All the transmitted HeNe beam was collected by a 2 inch diameter, 150 mm focal length "best form" lens and was monitored with a fast photomultiplier tube connected to preamplifiers and a 1 GHz bandwidth oscilloscope and transient digitizer. The response time of the system was ≈ 20 ns. A 633 nm bandpass filter and 1.064 μm attenuating filters were used to block the 1.064 μm radiation. The experimental setup is shown in Figure 12.

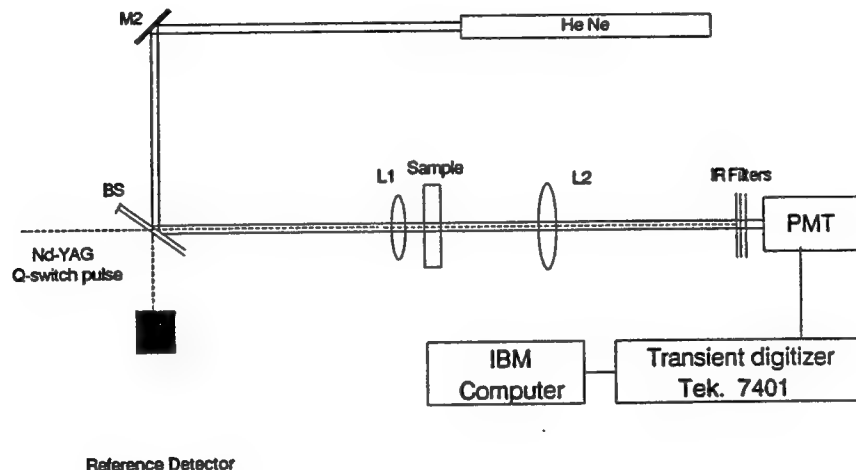


Figure 12. The experimental setup for 20 ns, 1.064 μm excitation pulse and cw HeNe probe beam. To measure the temporal response.

Using this optical geometry, we monitored the change of transmission of the HeNe probe beam as a function of time for different incident fluences of the excitation pulse. The probe transmission of the sample in the absence of any excitation pulse was 70 percent. For excitation pulses with peak powers close to the onset of limiting (i.e., ≈ 300 watts) we observed that the probe beam transmission decreases within the duration of the excitation pulse and recovers back to the 70 percent transmission level within 200 ns. This is consistent with the emission decay time of the ionized carbon particles discussed in the previous section. However, as the energy of the excitation pulse increased we observed that not only was the probe transmission attenuated more strongly but it remained partially attenuated for long periods of time. These results are shown in Figure 13.

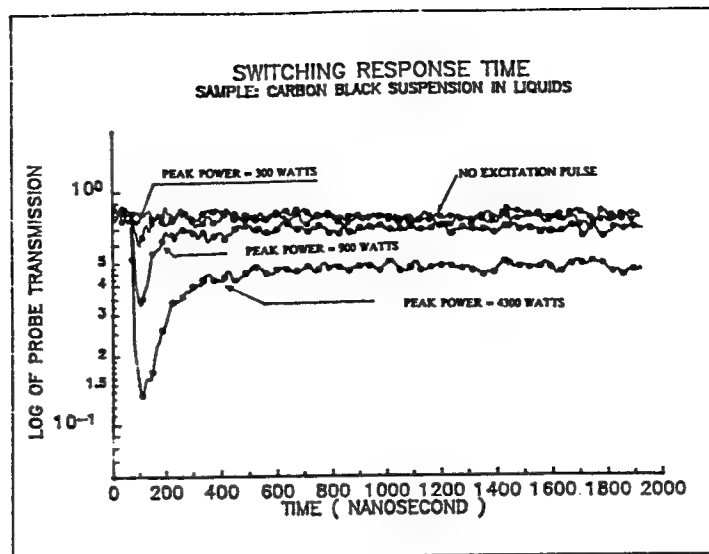


Figure 13. A semilogarithmic plot of the HeNe probe transmission as a function of time for powers for 20 ns (FWHM), 1.064 μm excitation pulse from 300 to 4200 watts.

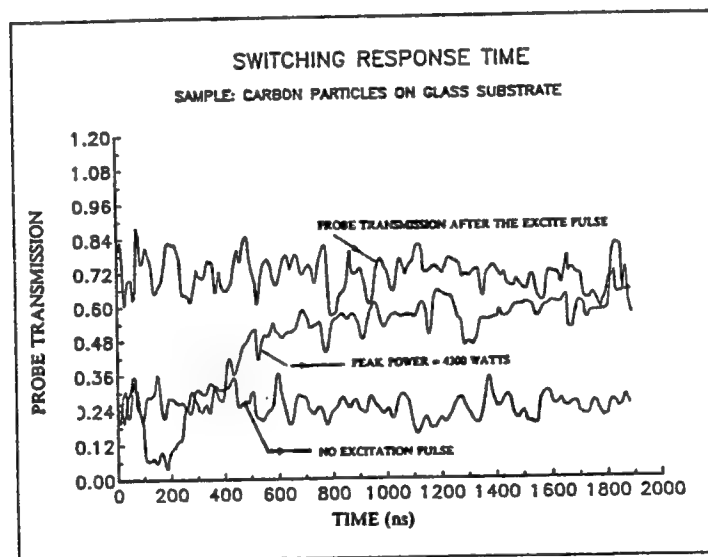


Figure 14. Plot of HeNe probe beam transmission of CBG as a function of time for 4.2 KW, 20 ns, 1.064 μm laser excitation.

As is shown in Figure 13, for high input powers the HeNe transmission decreases within the the duration of the excitation pulse and recovers to the original level in two distinct time periods. In the first time period, the probe transmission recovers back to 50 percent of the total attenuation within 200 to 400 ns after the excitation pulse which is consistent with the emission decay rate measured using the fluorescence measurement. The recovery of the probe beam in the second time period is much slower and depends on

the excitation energy. The long time recovery for light input (4.3 KW) of $\approx 100 \mu\text{sec}$ appears to be either diffusion or convection dominated. Since all the transmitted light was collected we can rule out the contribution of thermal self-refraction. It may be that at input fluences well above threshold and after the plasma decays, bubbles are formed which can scatter ≈ 50 percent of the HeNe beam. If bubbles are formed we should see a different response with CBG. This data is shown in Figure 14 using the same experimental apparatus of Figure 12. The linear transmission at $0.6328 \mu\text{m}$ was 28 percent as seen in Figure 14. Upon irradiation with $\approx 4.4 \text{ KW}$ at $1.064 \mu\text{m}$ the transmittance decreases rapidly and recovers to the original transmittance level of 28 percent within 200 ns. However, the transmittance continues to increase to ≈ 72 percent within $2 \mu\text{sec}$. Indeed this high transmittance is permanent. Microscopic examination reveals that the carbon coating is nearly completely removed by the excitation pulse. These experiments show that this removal occurs within $2 \mu\text{sec}$. These data are consistent with plasma induced scattering and recovery, however, the recovery time can also be explained by simple thermally induced ejection of the particles out of the beam. Clearly bubbles play no role in this experiment on CBG.

7. CONCLUSION

The experimental results indicate that nonlinear scattering is the dominant mechanism for limiting in CBS and CBG. Results of angular scattering measurements clearly show that the nonlinear scattering is due to the increase in size of the scatterers (i.e., micro-plasmas or micro-bubbles) as a function of incident fluence for ns laser pulses. The results of transmission measurements in CBG indicate that bubble formation is not a necessary occurrence for limiting with carbon black particles. In addition, from excitation and probe measurements in CBS and CBG we observed that the probe beam transmission decreases within the duration of the pulse for both samples and recovers back to 50 percent of the total attenuation within 150 ns. This is consistent with the measured emission life time from ionized carbon atoms. All of our experimental results are consistent with the plasma formation model while the other proposed models such as bubble formation fail to explain one or more of the experimental results.

8. ACKNOWLEDGMENTS

We wish to express our thanks to Martin Stalder and Mike Bass of CREOL, for allowing us to carry out the fluorescence measurement in their laboratory. This research was supported with funds from the National Science Foundation grant ECS # 8617066, DARPA/CNVEO, and the Florida High Technology and Industrial Council.

9. REFERENCES

1. H. C. Van de Hulst, *Light Scattering by Small Particles*, Dover publication, New York, 1981.
2. Kamjou Mansour, E. W. Vanstryland, M. J. Soileau, "Optical limiting in a Media with Absorbing Microparticles," SPIE Proc. Vol. 1105, 91, (1989).
3. M. Sheik-Bahae, A. A. Said and E. W. Vanstryland, "High Sensitivity, Single Beam n_2 Measurements," Opt. Lett. Vol. 14, No. 17, 955, (1989)
4. Jean-Baptiste Donnet, Andries Voet, *Carbon Black Physics, Chemistry, and Elastomer Reinforcement*, Marcel Dekker, New York, 1976.
5. Robert C. Weast, *Handbook of Chemistry and Physics*, 65th edition, CRC Press, 1984.

Bound Electron Nonlinearities and Their Application to Optical Switching

D. J. Hagan*, M. Sheik-Bahae, D. C. Hutchings,
A.A. Said, T.H. Wei and E. W. Van Stryland
Center for Research in Electro-Optics and Lasers (CREOL)
University of Central Florida, Orlando, Florida 32826

Abstract

We have performed an extensive series of measurements of the bound electronic nonlinear refractive index n_2 of a variety of solids at several wavelengths. We find that as the photon energy approaches E_g (the band-gap energy), that n_2 changes from positive to negative. This observed wavelength dispersion of n_2 can be well explained for wavelengths well below the fundamental absorption edge using a Kramers-Kronig transformation on two-photon absorption, AC Stark (virtual band-blocking), and electronic Raman contributions to the imaginary part of the third order susceptibility. The fit thus obtained for n_2 is amazingly good for more than four orders of magnitude change of n_2 including a change in sign. The change in sign from positive to negative with increasing frequency occurs roughly midway between the two-photon absorption edge and the fundamental absorption edge. Thus, we now have a comprehensive theory that allows prediction of n_2 at any wavelength below the band edge given only E_g and the linear index of refraction. Such information is useful for a variety of applications including optical limiting, laser-induced damage, and all-optical switching. We use our theory to estimate the minimum obtainable ultrafast switching powers for various wavelengths of practical interest.

* also with the Departments of Physics and Electrical Engineering

2. Introduction

Recent measurements of the bound electronic nonlinear refractive index n_2 of several semiconductors and dielectric materials show that there is a strong systematic dispersion of n_2 above the two-photon absorption (2PA) edge.[1] These data were taken using the newly developed Z-scan technique [2,3](a beam distortion method), and degenerate four-wave mixing,[4] and show that n_2 turns negative between the 2PA edge and the fundamental absorption edge. We found that by using a Kramers-Kronig (KK) integral of the 2PA spectrum as given by a two-parabolic band model, we could predict the observed universal dispersion, scaling, and values of n_2 that range more than four orders of magnitude and change sign.[1] This KK analysis relates the real and imaginary parts of the third order susceptibility. The resulting scaling rule correctly predicts the value of n_2 for the 26 different materials we had examined at that time, except very near the gap where there was a systematic departure of the data from the theory toward larger negative n_2 values. More recent data taken at wavelengths nearer the gap show an even larger departure from the predictions of the 2PA model. We had speculated in Ref. [1] that the band-gap resonant AC Stark effect might make $|n_2|$ larger near the gap. Here we present a model that includes 2PA the AC Stark effect and the electronic Raman effect. Indeed the inclusion of these effects does explain the large negative increase in n_2 near the gap.

There are two distinct frequency regimes for nonlinear optics in semiconductors which correspond to real and virtual excitation. The study of nonlinear optics in semiconductors has primarily concentrated on bandgap-resonant effects which result in a real excitation. The very large nonlinear effects observed in this case are the saturation of interband and excitonic absorption due to photoexcited free carriers and excitons. Real excitations usually result in a reduction of the refractive index at frequencies of interest. In contrast, by exciting optical solids at frequencies much less than the gap, a considerably smaller but faster, positive nonlinear refractive index, n_2 , due to bound electronic effects is observed. This n_2 arises from the real part of the third-order susceptibility, $\chi^{(3)}$, and is defined through the refractive index change Δn , where

$$\Delta n(\omega) = \gamma(\omega) I_\omega = \frac{n_2(\omega)}{2} |E_\omega|^2, \quad (1)$$

with I_ω and E_ω being the irradiance and electric field at frequency ω respectively and $n_2 = (2\pi/n_0)\text{Re}\{\chi^{(3)}\}$. The linear refractive index is n_0 , and γ and n_2 are related by $n_2(\text{esu}) = (cn_0\gamma/40\pi)(\text{MKS})$ where c is the speed of light. The magnitude and dispersion of n_2 is of interest because of its importance in applications such as nonlinear propagation in fibers, fast optical switching, self-focusing and damage in optical materials, and optical limiting in semiconductors.

Our measurements utilize a newly developed technique (Z-scan) [2,3] that determines the magnitude and sign of n_2 even in the presence of 2PA where it also gives the 2PA coefficient β . This simple technique has been shown to be an accurate and sensitive tool for measuring n_2 and β . Measurements of wide band-gap dielectrics show $n_2 > 0$ which explains catastrophic self-focusing damage in such materials as NaCl and SiO_2 . Our measurements in semiconductors below or near the 2PA edge ($\hbar\omega \approx E_g/2$) also show positive n_2 . However, we found a negative n_2 in materials such as ZnSe at $0.532 \mu\text{m}$ where 2PA is present, but a positive n_2 at $1.064 \mu\text{m}$ where 2PA is absent. The values obtained for β are in excellent agreement with our earlier measurements using standard transmission.[5] We also performed picosecond degenerate-four-wave mixing (DFWM) measurements which showed this third order response to be fast (time resolution limited by the 30 ps pulsewidth).[6] At wavelengths where 2PA was present this fast third order nonlinearity was dominant at low irradiance (eg. up to $\approx 0.5 \text{ GW/cm}^2$ in ZnSe at 532nm), while at higher irradiances the slowly decaying 2PA generated free-carrier refraction (self-defocusing) became important. DFWM studies in other semiconductors and other wavelengths showed this to be a universal phenomenon.[6] We have also included in our analysis n_2 data taken on a series of wide gap materials by "nearly degenerate three wave mixing" by Adair et. al. [7], and data taken by LaGasse et. al. [8] on AlGaAs using interferometry. As a result, we have been able to clearly demonstrate the behavior of the E_g^{-4} band gap scaling[9,10] and dispersion of n_2 . It should be noted that since the 2PA spectrum was previously determined [11], no fitting parameter was used in the calculation of Ref. [1].

3. Kramers-Kronig (KK) Relation

Most theoretical calculations of n_2 have been confined to the zero frequency limit.[12-16] Of these, semi-empirical formulations have been most successful in predicting the magnitude of n_2 . [15,16] For example, the formula obtained by Boling, Glass and Owyong (BGO) in relating n_2 to the linear index (n_0) and the dispersion of n_0 in terms of the Abbe number has been successfully applied to a large class of transparent materials.[7,16] Their theory predicts the low frequency magnitude of n_2 , but does not give the dispersion. The KK method predicts the dispersion as well as the magnitude of n_2 . While the calculation presented in Ref. [1] only included 2PA in the imaginary part of $\chi^{(3)}$, this calculation includes all other relevant contributions, that is, from electronic Raman and the AC Stark effect ("virtual band-blocking").

Based on the principle of causality, the KK relates the refractive index and absorption coefficient for any linear material.

$$n(\omega) - 1 = \frac{c}{\pi} \int_0^\infty \frac{\alpha(\omega')}{\omega'^2 - \omega^2} d\omega' \quad (2)$$

Now introduce some causal source of change ξ into the system and consider the change in the refractive index resulting from the effect of ξ . The KK transformation states that a change in the refractive index (Δn) at ω is associated with changes in the absorption coefficient ($\Delta\alpha$) throughout the spectrum (ω') and vice versa. We write this as:

$$\Delta n(\omega, \xi) = \frac{c}{\pi} \int_0^\infty \frac{\Delta\alpha(\omega'; \xi)}{\omega'^2 - \omega^2} d\omega'. \quad (3)$$

where c is the velocity of light in vacuum and ξ is a parameter (or parameters) denoting the "cause" of change in

the absorption.

The cause need not be of optical origin but of any external perturbation. For example this method has been used to calculate the refractive index change resulting from an excited electron-hole plasma [17] and a thermal shift of the band edge [9]. For cases where an electron-hole plasma is injected, the consequent change of absorption gives the plasma contribution to the refractive index. In this case, the ξ parameter is taken as the change in plasma density (ΔN) regardless of the mechanism of generation of the plasma or the pump frequency.[17] In the case of 2PA the change is due to the presence of a pump field at Ω (ie. $\xi=\Omega$). The corresponding nonlinear refraction is $\Delta n(\omega;\Omega)$, which gives the dispersion of the index change with ω . Although the calculation as illustrated above gives the nondegenerate nonlinear refraction, in most cases we would set $\Omega=\omega$ and consider self-refraction. This gives what is commonly referred to as n_2 . Van Vechten and Aspnes [14] obtained the low frequency limit of n_2 from a similar KK transformation of the Franz-Keldysh electro-absorption effect where, in this case, ξ is the DC field. The bound electronic contribution to $\chi^{(3)}$ can originate from various absorptive counterparts that are quadratic functions of the pump field. Effects of this order are 2PA, the electronic Raman effect, and the optical Stark effect.

An alternative way of considering the KK calculation is to do the calculation not for the basic material but on a system which consists of the material plus a light field. Thus, it is necessary to know the nondegenerate absorption change $\Delta\alpha(\omega;\Omega)$, which is the absorption of light at ω when a light-field of Ω is applied to the material. Degenerate 2PA can be related to the case where the two frequencies are set equal.

Two-photon absorption processes require that perturbation theory be taken to second order. A variation of this is to use first order perturbation theory on a "dressed" final state where the effect of the acceleration of the electrons due to the oscillating electric field is already taken into account. We assume a two beam A-P interaction with both beams linearly polarized in the same direction [18-20]. Using this approach the degenerate 2PA coefficient can be determined; $\beta(\omega)=2\hbar\omega W I^{-2}$ where W is the two-photon transition rate. The resulting expression for the 2PA has exactly the same scaling and frequency dependence form as that calculated in references [10], namely,

$$\beta(\omega)=K \frac{\sqrt{E_p}}{n_0^2 E_g^3} F_2(\hbar\omega/E_g), \quad (4)$$

where $F_2(x)=(2x-1)^{3/2}(2x)^5$. Here K is a material independent constant and E_p (related to the Kane momentum parameter) is nearly material independent and possesses a value $E_p \approx 21$ eV for most direct gap semiconductors. The best fit to the data of reference [21] gives $K=3100 \text{ cm(eV)}^{-5/2}/\text{GW}$, whereas theory [22] gives $K=5200 \text{ cm(eV)}^{-5/2}/\text{GW}$. This difference can largely be explained by the effects of nonparabolicity which has the effect of reducing β slightly without significantly changing the frequency dependence [22]. Using the same method the nondegenerate 2PA is found to be,

$$\frac{\Delta\alpha(\omega_1;\omega_2)}{I_2} = \frac{2K\sqrt{E_p}}{n_0^2 E_g^3} F_2(\hbar\omega_1/E_g; \hbar\omega_2/E_g), \quad (5)$$

where the 2PA frequency dependence is given by,

$$F_2^{2PA}(x_1;x_2) = \frac{(x_1+x_2-1)^{3/2}}{2^7 x_1 x_2^2} \left(\frac{1}{x_1} + \frac{1}{x_2} \right)^2. \quad (6)$$

However, we now have an additional term attributed to Raman terms giving a change in absorption of,

$$F_2^{\text{RAM}} = \frac{(x_1 - x_2 - 1)^{3/2} - (-x_1 + x_2 - 1)^{3/2}}{2^7 x_1 x_2^2} \left(\frac{1}{x_1} - \frac{1}{x_2} \right)^2, \quad (7)$$

where the scaling is the same as in Eq. 5. The total F_2 due to two photon processes is just the sum of $F_2^{2\text{PA}}$ and F_2^{RAM} .

Another effect which must be taken account of in these calculations is the change in linear absorption at ω_1 due to the presence of the field at ω_2 shifting the bands by the AC Stark effect. Two terms arise out of this as the radiation perturbation term couples the conduction band to itself and to the valence band. It can be shown that linear AC Stark effect produces a change in absorption $\Delta\alpha$ with a spectral dependence given by F_2^{S1} , where,

$$F_2^{\text{S1}}(x_1; x_2) = - \frac{2(x_1 - 1)^{3/2}}{2^7 x_1 x_2^4}. \quad (8)$$

The quadratic Stark shift resulting from the coupling between the conduction and valence band leads to a $\Delta\alpha$ given by,

$$F_2^{\text{S2}}(x_1; x_2) = - \frac{1}{2^{10} x_1 x_2^2 (x_1 - 1)^{1/2}} \left[\frac{1}{x_1 - x_2} + \frac{1}{x_1 + x_2} \right]. \quad (9)$$

4. Nonlinear Refraction

In principle we can evaluate $\Delta n(\omega_1; \omega_2)$ as defined in Eq. 2, however, there are few experiments of this quantity other than at $\omega_1 = \omega_2$, which is the case of self refraction. Using the KK relations discussed earlier, the change in refractive index $\Delta n(\omega; \omega) = \gamma I$ can be calculated to give,

$$\gamma = \frac{K \hbar c \sqrt{E_p}}{n_0^2 E_g^4} G_2(\hbar\omega/E_g), \quad (11)$$

where the dispersion function $G_2(x)$ is given by,

$$G_2(x) = \frac{2}{\pi} \int_0^\infty \frac{F_2(x'; x)}{x'^2 - x^2} dx'. \quad (12)$$

All that remains is for the above integral to be evaluated for the various contributions to the nondegenerate absorption, $F_2(x_1; x_2)$.

When these integrals are performed and the results summed a single divergent term proportional to ω^{-2} is left. This diverging term is not unexpected as A-p perturbation theory has been used in the transition rate calculations and it is well known that divergences of this order can be introduced whereas the comparable E-r perturbation theory avoids such divergences. In a similar manner to Moss et al. [23] we treat such a divergence as unphysical and subtract it from the result for the nonlinear refraction. Using the value of K obtained from 2PA measurements and using $E_p \approx 21$ eV, which is true for the majority of semiconductors, we obtain,

$$n_2(\text{esu}) = \frac{K' \sqrt{E_p}}{n_0 E_g^4} G_2(\hbar\omega/E_g), \quad (13)$$

where the constant $K'=1.5 \times 10^{-8}$ when E_g is defined in eV. We note the E_g^{-4} bandgap dependence for the magnitude of n_2 .

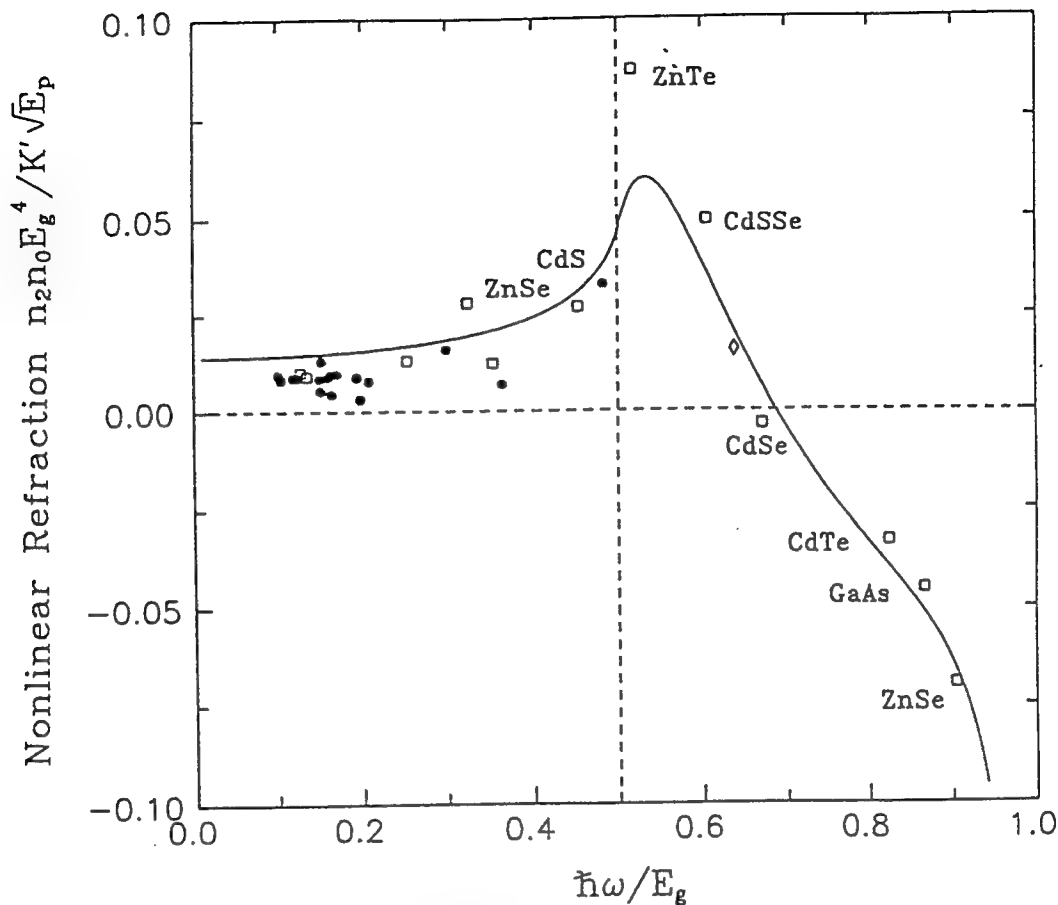


Fig. 1. A plot of n_2 dispersion function $G_2(\hbar\omega/E_g)$ containing contribution from 2PA, Raman and AC Stark effect. Data are scaled by $n_0 E_g^4 / K' \sqrt{E_p}$.

A graphical comparison of the dispersion function $G_2(\hbar\omega/E_g)$ with measured values of n_2 obtained from Z-scan measurements at $1.06 \mu\text{m}$ and $0.53 \mu\text{m}$ [2, 3] and nearly degenerate three-wave mixing measurements of large gap optical materials [7] is shown in Fig. 1. Note we have agreement within a factor of 2 for a wide range of semiconductors and large gap optical materials.

The scaling of n_2 with bandgap is demonstrated in Fig. 2. Here we plot the ratio of n_2 to the dispersion function $G_2(\hbar\omega/E_g)$. The straight line indicated shows the expected E_g^{-4} dependence. It is found that the scaling law holds true over more than orders of magnitude variation in the modulus of n_2 .

The E_g^{-4} dependence of n_2 gives a variation of n_2 from 2.5×10^{-14} esu for a material such as MgF_2 at $1.06 \mu\text{m}$ to 3×10^{-10} esu for Germanium at $10.6 \mu\text{m}$, which we measured using a picosecond CO_2 laser. This large variation of n_2 is better displayed by plotting n_2 scaled by n_0 and G_2 as a function of E_g on a log-log plot as shown in Fig. 2. In spite of this very large variation in magnitude of n_2 (and change in sign), this extremely simple model gives good agreement with the data for materials including both semiconductors and insulators.

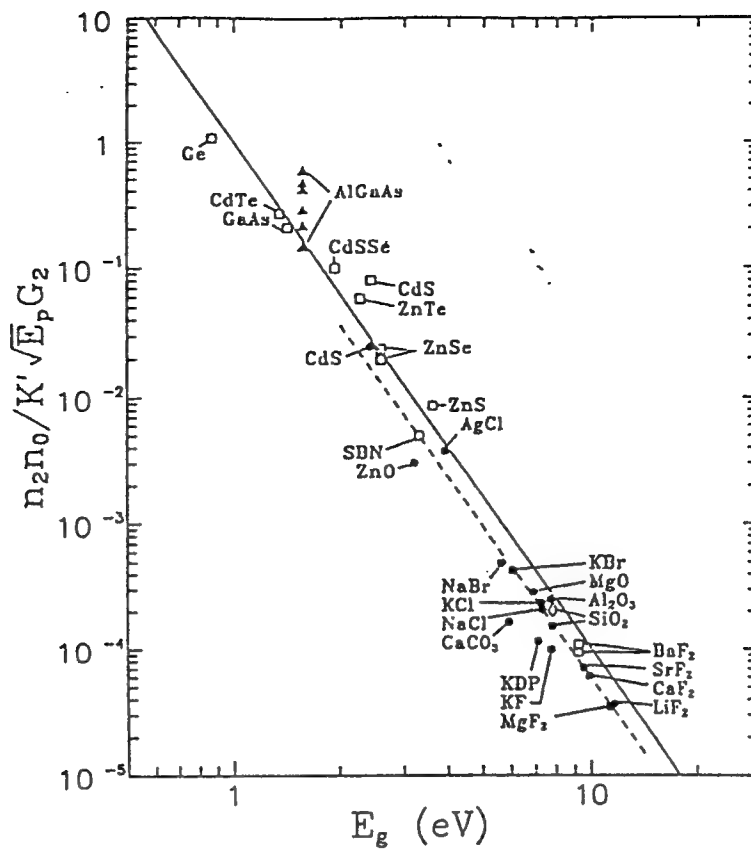


Fig. 2. A log-log plot showing the expected E_g^{-4} dependence of n_2 . The data points are identical to those in Fig. 2 but now scaled by the dispersion function $G_2(\hbar\omega/E_g)$. The solid line is the function E_g^{-4} which translates into a straight line of slope -4 on the log-log scale.

5. Application to All-Optical Switching

One of the applications of n_2 is in the role of all-optical switching. Some examples are the nonlinear Fabry-Perot for image processing or parallel optical computing [24,25] or coupled waveguides for communications switching networks [26,27]. When it comes to optimizing devices for optical switching it is important that optical losses in the system are not too large. If optical absorption is large, then the change in refractive index will fall off rapidly as the optical wave propagates.

It can be shown that for any optical switching system, one must achieve a refractive index change Δn such that,

$$|\Delta n| > c_{sw} \alpha \lambda, \quad (14)$$

where c_{sw} is a numeric constant of the order of unity whose precise value depends on the particular switching scheme. For example, for a Fabry-Perot, $c_{sw} = (2\sqrt{3}\pi)^{-1}$ [28], and for a nonlinear coupled waveguide, $c_{sw} = 2$ [29,30].

Below the band edge, the principal contribution to the absorption is $2PA$, $\propto \beta I$ at irradiance levels of interest. As the electronic Kerr effect gives an index change of $\Delta n = \gamma I$, the requirement for all-optical switching is [29],

$$\left| \frac{\gamma}{\beta \lambda} \right| > c_{sw}. \quad (15)$$

Using our relationship between γ and β through the KK relations, we obtain the frequency dependence for the all-optical switching requirement,

$$\frac{\hbar\omega}{E_g} \frac{|G_2(\hbar\omega/E_g)|}{F_2(\hbar\omega/E_g)} > 2\pi c_{sw} \quad (16)$$

Note that equation 16 has no explicit material dependence as it is only a function of the ratio $\hbar\omega/E_g$. Thus although n_2 can be enhanced by using smaller gap materials, this does not necessarily improve conditions for switching. The left hand side of (16) is plotted in Fig. 3. In the same figure we also show the experimentally determined values for this parameter $|2\pi\gamma/\beta\lambda|$ for some semiconductors using the n_2 values reported here and 2PA coefficients from [5]. We see that there is a range of optical frequencies where this quantity becomes too small for optical switching which is given approximately by $0.6 < \hbar\omega/E_g < 0.9$, covering most of the region where 2PA is observed. This was first noted by Mizrahi et al [29].

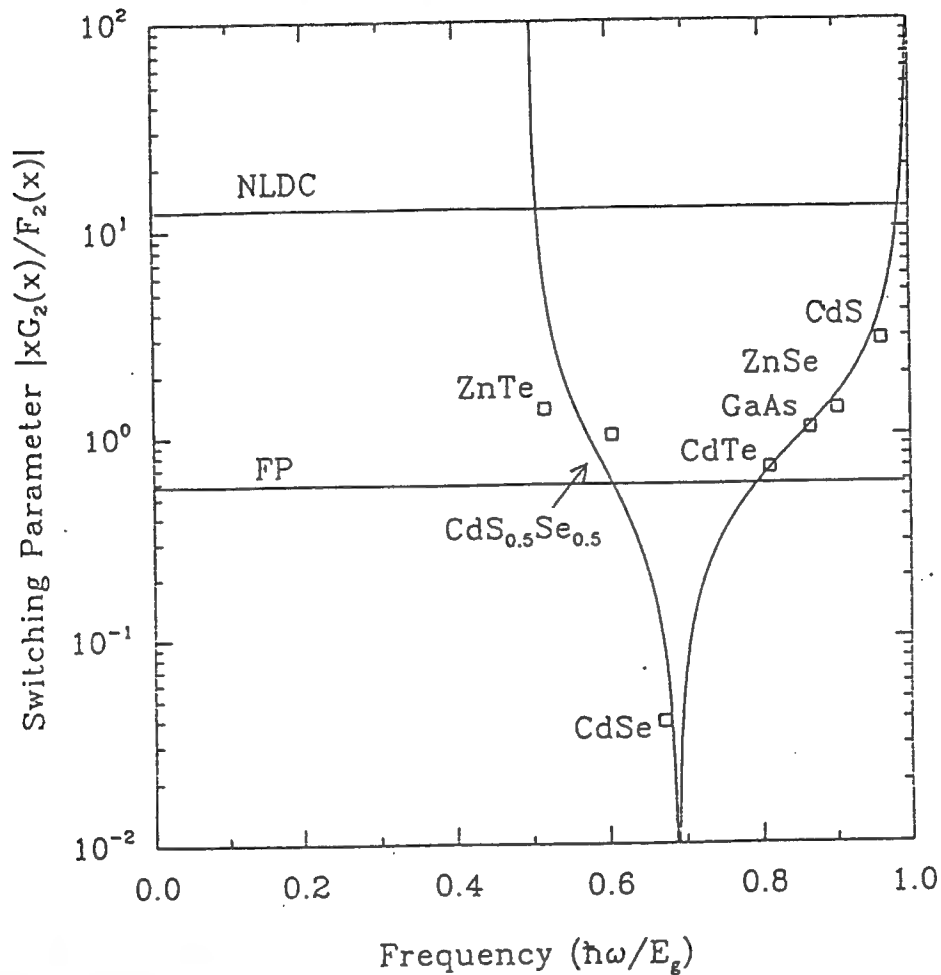


Fig. 3. Material independent switching parameter as a function of frequency. Also shown are the minimum limits for all-optical switching for the nonlinear directional coupler and the nonlinear Fabry-Perot. For switching to be possible the switching parameter must exceed the relevant limit. The data points are based on our semiconductor n_2 and β measurements.

We can use our results to predict switching powers in the nonlinear directional coupler ($c_{sw}=2$) for the technologically important wavelengths $0.85\mu\text{m}$, $1.55\mu\text{m}$ and $10.6\mu\text{m}$. We choose suitable materials based on the criterion that the photon energy must be just below the two photon absorption edge, i.e. $\hbar\omega/E_g \approx 0.45$, or as close to this as available materials will allow. Under this criterion, some of the best available materials are ZnS for $0.83\mu\text{m}$, CdSe or the appropriate alloy concentration of AlGaAs (such that $\hbar L/E_g \approx 0.45$) for $1.55\mu\text{m}$ and the corresponding alloy concentration of InAsSb for $10.6\mu\text{m}$. Following reference [29] we calculate the switching power as,

$$P_{sw} = \frac{2\lambda^3}{\gamma L},$$

(17)

where we assume that the beam area is the minimized and hence $\propto \lambda^2$. L is the interaction length in the directional coupler. The resulting switching powers are shown below in Table 1. This shows that while switching powers decrease for longer wavelengths with correspondingly smaller bandgaps, the power does not decrease according to the E_g^{-4} dependence of n_2 . This is due to the fact that longer wavelengths require proportionately larger index changes to produce a given phase shift and that the minimum cross-sectional area of a waveguide mode is $\propto \lambda^2$. Also, even in the best case of $P_{sw}=80$ Watts, this compares poorly with alternative technologies, such as excited carrier induced nonlinear refraction [29]. However, if longer interaction lengths can be tolerated, the lack of 2PA may make such devices useful in certain interactions [27]. In fact our studies indicate how the switching powers reported in reference [27] on switching in glass fibers may be considerably reduced by choosing more appropriate materials to optimize $\hbar\omega/E_g$.

Wavelength	Material	Switching Power
0.85 μm	ZnS	1500W
1.55 μm	CdSe	410W
	AlGaAs	340W
10.6 μm	InAsSb	80W

Table 1. Calculated switching powers for the nonlinear directional coupler utilizing the bound electronic Kerr effect.

6. Conclusion

In conclusion, the measured n_2 data follow a universal dispersion curve from which values of n_2 for other materials at other wavelengths can be calculated. We have also experimentally verified the predicted band-gap scaling of n_2 . From the excellent overall agreement with the predicted magnitude and dispersion of n_2 , as calculated via Kramers-Kronig, to the large number of experimental data, we conclude that the processes responsible for 2PA and the AC Stark effect also determine n_2 . This in turn implies that the bound electronic nonlinear refractive index is predominantly a causal consequence of these nonlinear absorptive processes just as the linear index is a causal consequence of linear absorption. This calculational approach takes advantage of the historical fact that, for the solid state, the 2PA coefficient has been calculated from a transition rate approach.[24] Thus, we have circumvented problems associated with performing a direct calculation of the third order susceptibility.

7. Acknowledgement

We gratefully acknowledge the support of the National Science Foundation grant ECS#8617066, DARPA/CNVEO and the Florida High Technology and Industry Council. In addition we thank O. Heinonen, A. Miller and S. Epifanov for useful discussions and J. Young and E. Canto for taking and analyzing portions of the n_2 data.

8. References

- [1] M. Sheik-Bahae, D.J. Hagan, and E.W. Van Stryland, Phys. Rev. Lett. 65, 96-99(1990).
- [2] M. Sheik-Bahae, A.A. Said, T.H. Wei, D.J. Hagan, and E.W. Van Stryland, IEEE J. Quantum Electron. QE-26, 760-769(1990).
- [3] M. Sheik-Bahae, A.A. Said, and E.W. Van Stryland, Opt. Lett. 14, 955-957(1989).
- [4] D.J. Hagan, E. Canto, E. Miesak, M.J. Soileau, and E.W. Van Stryland, pp.160, Technical Digest of the Conference on Lasers and Electro-Optics, Anaheim, CA, OSA Technical Digest Series, No. 7, 1988.
- [5] E.W. Van Stryland, H. Vanherzeele, M.A. Woodall, M.J. Soileau, A.L. Smirl, S.Guha, and T.F. Boggess, Opt. Eng. 24, 613-623(1985).
- [6] E. Canto-Said, D.J. Hagan, J. Young, and E.W. Van Stryland, to be published
- [7] R. Adair, L.L. Chase, and S.A. Payne, Phys. Rev. B 39, 3337-3349(1989).
- [8] M.J. LaGasse, K.K. Anderson, C.A. Wang, H.A. Haus, and J.G. Fujimoto, Appl. Phys. Lett. 56, 417-419(1990).
- [9] B.S. Wherrett, A.C. Walker, and F.A.P. Tooley, in Optical Nonlinearities and Instabilities in Semiconductors, H. Haug, eds. (Academic Press, Inc. 1988.) pp.239-272.
- [10] B.S. Wherrett, J. Opt. Soc. Am. B 1, 67-72(1984).
- [11] E.W. Van Stryland, M.A. Woodall, H. Vanherzeele, and M.J. Soileau, Opt. Lett. 10, 490-492(1985).
- [12] S.S. Jha and N. Bloembergen, Phys. Rev. 171, 891-898(1968).
- [13] C. Flytzanis, Phys. Lett. 31A, 273-274(1970).
- [14] J.A. Van Vechten and D.E. Aspnes, Phys. Lett. 30A, 346-347(1969).
- [15] C.C. Wang, Phys. Rev. B, 2, 2045-2048(1970).
- [16] N.L. Boling, A.J. Glass, and A. Owyong, IEEE J. Quantum Electron. QE-14, 601-608(1978).
- [17] D.A.B. Miller, C.T. Seaton, M.E. Prise, and S.D. Smith, Phys. Rev. Lett. 47, 197-200(1981).
- [18] L.V. Keldysh, Sov. Phys. JETP, 20, 1307-1314(1965)
- [19] H.D. Jones and H.R. Reiss, Phys. Rev. B 16, 2466-2473(1977).
- [20] H.S. Brandi and C.B. de Araujo, J. Phys. C 16, 5929-5936(1983).
- [21] E.W. Van Stryland, Y.Y. Wu, D.J. Hagan, M.J. Soileau, and K. Mansour, J. Opt. Soc. Am. B, 5, 1980-1989(1988).
- [22] M.H. Weiler, Solid State Commun. 39, 937-940(1981).
- [23] D.J. Moss, E. Ghahramani, J.E. Sipe, and H.M. van Driel, Phys. Rev. B 41, 1542-1560(1990).
- [23] M. Göppert-Mayer, Ann. Physik 9, 273(1931).
- [24] B.S. Wherrett and S.D. Smith, Physica Scripta, T13, 189-194 (1986)
- [25] S.D. Smith, A.C. Walker, F.A.P. Tooley and B.S. Wherrett, Nature, 325, 27-31 (1987)
- [26] P. LiKamWa, J.E. Stich, N.J. Mason, J.S. Roberts and P.N. Robson, Electron. Lett. 21, 26-27 (1985)
- [27] S.R. Friberg, A.M. Weiner, Y. Siberberg, B.G.Sfez and P.W. Smith, Opt. Lett., 13, 904-906 (1988)
- [28] D.C. Hutchings, C.H. Wang and B.S. Wherrett, J. Opt. Soc. Am. (Accepted for Publication)
- [29] V. Mizrahi, K. W. DeLong, G.I. Stegeman, M.A. Saifi and M.J. Andrejco, Opt. Lett., 14, 1140-1142 (1989)
- [30] K.W. DeLong, K.B. Rochford and G.I. Stegeman, Appl. Phys. Lett., 55, 1823-1825 (1989)

Proceedings SPIE Boulder 40

Boulder Damage Conf.
1996

Dispersion of n_2 in Solids

M. Sheik-Bahae, D. C. Hutchings, D. J. Hagan*,

M.J. Soileau*, and E. W. Van Stryland*

Center for Research in Electro-Optics and Lasers (CREOL)

University of Central Florida, Orlando, Florida 32826

ABSTRACT

We recently performed an extensive series of measurements of the bound electronic nonlinear refractive index n_2 of a variety of solids at several wavelengths. We found that as the photon energy approached E_g (the band-gap energy), that n_2 changed from positive to negative. This observed wavelength dispersion of n_2 can be well explained for wavelengths well below the fundamental absorption edge using a Kramers-Kronig transformation on the two-photon absorption coefficient β which we had previously studied. While this theory fit the data well for $0.1E_g < \hbar\omega < 0.8E_g$ (E_g is the band-gap energy), there was a significant deviation toward larger negative values of n_2 near the fundamental absorption edge. We speculated that the AC Stark effect could account for this deviation. Here we extend the data to photon energies nearer the gap and redo the Kramers-Kronig calculation to include the AC Stark (virtual band-blocking), and electronic Raman contributions to the imaginary part of the third order susceptibility. Indeed the fit obtained for n_2 as calculated by Kramers-Kronig is amazingly good for a five orders of magnitude change of n_2 including a change in sign. The change in sign from positive to negative with increasing frequency occurs midway between the two-photon absorption edge and the fundamental absorption edge. Thus, we now have a comprehensive theory that allows prediction of n_2 at any wavelength below the band edge given only E_g and the linear index of refraction. Such information is useful for a variety of applications including optical limiting, laser-induced damage, and all-optical switching.

* also with the Department of Physics and Electrical Engineering

2. INTRODUCTION

Recent measurements of the bound electronic nonlinear refractive index n_2 of several semiconductors and dielectric materials show that there is a strong systematic dispersion of n_2 above the two-photon absorption (2PA) edge.[1] These data were taken using the newly developed Z-scan technique [2,3](a beam distortion method), and degenerate four-wave mixing,[4] and show that n_2 turns negative between the 2PA edge and the fundamental absorption edge. We found that by using a Kramers-Kronig (KK) integral of the 2PA spectrum as predicted by a two-parabolic band model, we could predict the observed universal dispersion, scaling, and values of n_2 that range over four orders of magnitude and change sign.[1] This KK analysis relates the real and imaginary parts of the third order susceptibility. The resulting scaling rule correctly predicted the value of n_2 for the 26 different materials we had examined at that time, except very near the gap where there was a systematic departure of the data from the theory toward larger negative n_2 values. More recent data taken at wavelengths nearer the gap show an even larger departure from the predictions of the 2PA model. We had speculated in Ref. [1] that the band-gap resonant AC Stark effect might make $|n_2|$ larger near the gap. Here we present a model that includes 2PA the AC Stark effect and the electronic Raman effect. Indeed the inclusion of these effects does explain the large negative increase in n_2 near the gap.

There are two distinct frequency regimes for nonlinear optics in semiconductors which correspond to real and virtual excitation. The study of nonlinear optics in semiconductors has primarily concentrated on bandgap-resonant effects which result in a real excitation. The very large nonlinear effects observed in this case are the saturation of interband and excitonic absorption due to photoexcited free carriers and excitons. Real excitations usually result in a reduction of the refractive index at frequencies of interest. In contrast, by exciting optical solids at frequencies much less than the gap, a considerably smaller but faster, positive nonlinear refractive index, n_2 , due to bound electronic effects is observed. This n_2 arises from the real part of the third-order susceptibility, $\chi^{(3)}$, and is defined through the refractive index change Δn , where

$$\Delta n(\omega) = \gamma(\omega) I_\omega = \frac{n_2(\omega)}{2} |E_\omega|^2, \quad (1)$$

with I_ω and E_ω being the irradiance and electric field at frequency ω respectively and $n_2 = (2\pi/n_0) \text{Re}\{\chi^{(3)}\}$. The linear refractive index is n_0 , and γ and n_2 are related by $n_2(\text{esu}) = (cn_0\gamma/40\pi)(\text{MKS})$ where c is the speed of light. The magnitude and dispersion of n_2 is of interest because of its importance in applications such as nonlinear propagation in fibers, fast optical switching, self-focusing and damage in optical materials, and optical limiting in semiconductors.

Our measurements utilized a newly developed technique (Z-scan) [2,3] that determines the magnitude and sign of n_2 even in the presence of 2PA where it also gives the 2PA coefficient β . This simple technique has been shown to be an accurate and sensitive tool for measuring n_2 and β . Measurements of wide band-gap dielectrics show $n_2 > 0$ which explains catastrophic self-focusing damage in such materials as NaCl and SiO₂. Our measurements in semiconductors below or near the 2PA edge ($\hbar\omega \approx E_g/2$) also show positive n_2 . However, we found a negative n_2 in materials such as ZnSe at 0.532 μm where 2PA is present, but a positive n_2 at 1.064 μm where 2PA is absent. The values obtained for β are in excellent agreement with our earlier measurements using standard transmission.[5] We also performed picosecond degenerate-four-wave mixing (DFWM) measurements which showed this third order response to be fast (time resolution limited by the 30 ps pulsewidth).[6] At wavelengths where 2PA was present this fast third order nonlinearity was dominant at low irradiance (eg. up to $\approx 0.5 \text{ GW/cm}^2$ in ZnSe at 532nm), while at higher irradiances the slowly decaying 2PA generated free-carrier refraction (self-defocusing) became important. DFWM studies in other semiconductors and other wavelengths showed this to be a universal phenomenon.[6] We have also included in our analysis n_2 data taken on a series of wide gap materials by "nearly degenerate three wave mixing" by Adair et. al. [7], and data taken by LaGasse et. al. [8] on AlGaAs using interferometry. As a result, we have been able to clearly demonstrate the behavior of the dispersion of n_2 .

It has previously been predicted that $\chi^{(3)}$ should vary as E_g^{-4} .[9,10] Using this scaling and the relation between n_2 and $\chi^{(3)}$ that includes the linear index n_0 , we can remove the E_g and n_0 dependencies from the experimental values of n_2 by multiplying them by $n_0 E_g^4$. Figure 1 shows a plot of our experimentally determined scaled values of n_2 as a function of $\hbar\omega/E_g$. We also divide the data by a constant K' which we explain in what follows. We show on the same plot several data for large gap optical crystals obtained from recent measurements by Adair et.al. using a "nearly degenerate-three-wave-mixing" scheme.[7] Our own measurements of several of the same materials studied in [7] show excellent absolute agreement. Assuming that there are no other relevant parameters unique to each material other than bandgap and index, this plot should be general to all optical solids. Upon examination of Fig. 1 we immediately see a trend giving small positive values for low ratios of photon energy to band-gap energy which slowly rises to a broad resonance peak at the 2PA edge and then decreases, eventually turning negative between the two-photon and single-photon absorption edges. We should note that the scaling with E_g hides a variation in magnitude of n_2 of four orders of magnitude so that the observed universal dispersion curve is quite remarkable. This dispersion curve is qualitatively similar to the dispersion of the linear index around the single photon absorption edge. As these linear quantities are related by causality via a KK relation, it seems logical to investigate whether the observed dispersion of n_2 can be calculated using a nonlinear KK relation between the real and imaginary parts of $\chi^{(3)}$. Indeed, as we showed in Ref. [1], making some reasonable assumptions, the observed tendencies as well as the absolute magnitudes of this dispersion are well predicted by such a calculation. In

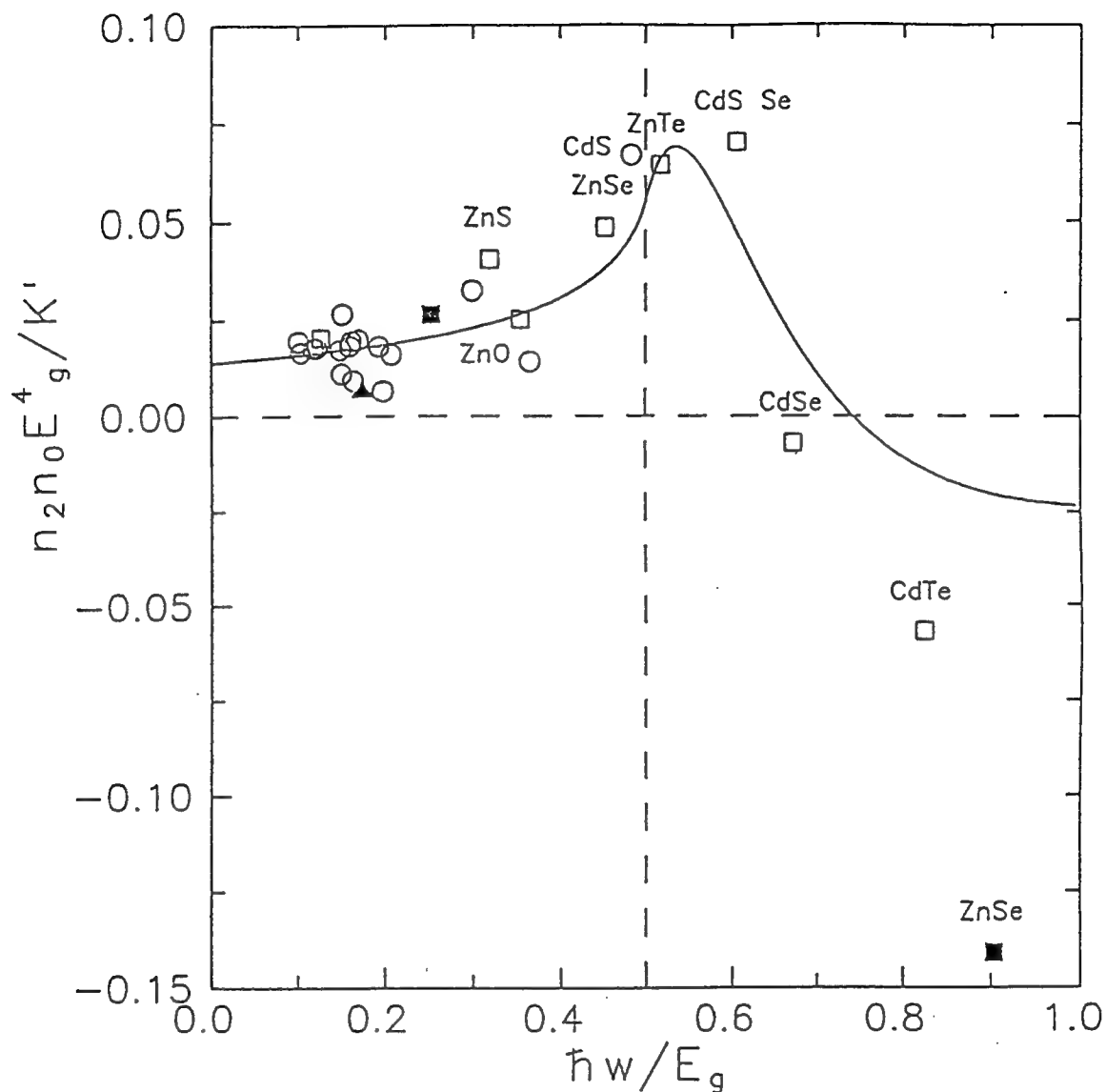


Fig. 1. Data of n_2 scaled as $n_2 n_0 E_g^4 / K'$ from reference [1]. Note that the definition of the constant K' in this reference differs slightly from that used in this paper. These data include measurements of n_2 at $1.06 \mu\text{m}$ in Ref.[7] as well as our own measurement at $1.06 \mu\text{m}$ and $0.532 \mu\text{m}$. Recent measurements have revised some of the semiconductor data shown in this figure (see figure 2). The solid line demonstrates the fit obtained in reference [1] using a quasi-degenerate 2PA.

Ref. [1] a calculation of n_2 including only the 2PA contribution to the imaginary part of $\chi^{(3)}$ was presented. The solid line in Fig. 1 as reproduced from Ref. [1] is the direct result of such calculation. It is seen that the calculated result is in good agreement with most experimental data measured at $\hbar\omega/E_g < 0.8$. It should be noted that since the 2PA spectrum was previously determined [11], no fitting parameter was used in the calculation of Ref. [1].

3. KRAMERS-KRONIG (KK) RELATION

Most theoretical calculations of n_2 have been confined to the zero frequency limit.[12-16] Of these, semi-empirical formulations have been most successful in predicting the magnitude of n_2 . [15,16] For example, the formula obtained by Boling, Glass and Owyong (BGO) in relating n_2 to the linear index (n_0) and the dispersion of n_0 in terms of the Abbe number has been successfully applied to a large class of transparent materials.[7,16] Their theory predicts the low frequency magnitude of n_2 , but does not give the dispersion. The KK method predicts the dispersion as well as the magnitude of n_2 . While the calculation presented in Ref. [1] only included 2PA in the imaginary part of $\chi^{(3)}$, this calculation includes all other relevant contributions, that is, from electronic Raman and the AC Stark effect ("virtual band-blocking").

Based on the principle of causality, the KK relates the refractive index and absorption coefficient for any linear material.

$$n(\omega) - 1 = \frac{c}{\pi} \int_0^{\infty} \frac{\alpha(\omega')}{\omega'^2 - \omega^2} d\omega' \quad (2)$$

Now introduce some causal source of change ξ into the system and consider the change in the refractive index resulting from the effect of ξ . The KK transformation states that a change in the refractive index (Δn) at ω is associated with changes in the absorption coefficient ($\Delta\alpha$) throughout the spectrum (ω') and vice versa. We write this as:

$$\Delta n(\omega; \xi) = \frac{c}{\pi} \int_0^{\infty} \frac{\Delta\alpha(\omega'; \xi)}{\omega^2 - \omega'^2} d\omega'. \quad (3)$$

where c is the velocity of light in vacuum and ξ is a parameter (or parameters) denoting the "cause" of change in the absorption.

The cause need not be of optical origin but of any external perturbation. For example this method has been used to calculate the refractive index change resulting from an excited electron-hole plasma [17] and a thermal shift of the band edge [9]. For cases where an electron-hole plasma is injected, the consequent change of absorption gives the plasma contribution to the refractive index. In this case, the ξ parameter is taken as the change in plasma density (ΔN) regardless of the mechanism of generation of the plasma or the pump frequency.[17] In the case of 2PA the change is due to the presence of a pump field at Ω (ie. $\xi=\Omega$). The corresponding nonlinear refraction is $\Delta n(\omega;\Omega)$, which gives the dispersion of the index change with ω . Although the calculation as illustrated above gives the nondegenerate nonlinear refraction, in most cases we would set $\Omega=\omega$ and consider self-refraction. This gives what is commonly referred to as n_2 . It is important to note that we must first perform the integral before setting $\Omega=\omega$. Van Vechten and Aspnes [14] obtained the low frequency limit of n_2 from a similar KK transformation of the Franz-Keldysh electro-absorption effect where, in this case, ξ is the DC field. The bound electronic contribution to $\chi^{(3)}$ can originate from various absorptive counterparts that are quadratic functions of the pump field. Effects of this order are 2PA, the electronic Raman effect, and the optical Stark effect.

An alternative way of considering the KK calculation is to do the calculation not for the basic material but on a system which consists of the material plus a light field. Thus, it is necessary to know the nondegenerate absorption change $\Delta\alpha(\omega;\Omega)$, which is the absorption of light at ω when a light-field of Ω is applied to the material. Degenerate 2PA can be related to the case where the two frequencies are set equal.

Two-photon absorption processes require that perturbation theory be taken to second order. A variation of this is to use first order perturbation theory on a "dressed" final state where the effect of the acceleration of the electrons due to the oscillating electric field is already taken into account. We assume a two beam A-P interaction with both beams linearly polarized in the same direction. Following Keldysh [18] and Jones and Reiss [19] such a final state can be approximated by a Volkov-type wavefunction. The transition rates are calculated using an S matrix formalism.[19,20] Using this approach the degenerate 2PA coefficient can be determined; $\beta(\omega)=2\hbar\omega WI^{-2}$ where W is the two-photon transition rate. The resulting expression for the 2PA has exactly the same scaling and frequency dependence form as that calculated in references [10], namely,

$$\beta(\omega)=K \frac{\sqrt{E_p}}{n_0^2 E_g^3} F_2(\hbar\omega/E_g) \quad (4)$$

with

$$F_2(x) = \frac{(2x-1)^{3/2}}{(2x)^5}.$$

Here K is a material independent constant and E_p (related to the Kane momentum parameter) is nearly material independent and possesses a value $E_p \approx 21$ eV for most direct gap semiconductors. The best fit to the data of reference [21] gives $K = 3100 \text{ cm(eV)}^{-5/2}/\text{GW}$, whereas theory [22] gives $K = 5200 \text{ cm(eV)}^{-5/2}/\text{GW}$. This difference can largely be explained by the effects of nonparabolicity which has the effect of reducing β slightly without significantly changing the frequency dependence [22].

Using the same method the nondegenerate 2PA is found to be,

$$\frac{\Delta\alpha(\omega_1; \omega_2)}{I_2} = \frac{2K\sqrt{E_p}}{n_0^2 E_g^3} F_2(\hbar\omega_1/E_g; \hbar\omega_2/E_g), \quad (5)$$

where the 2PA frequency dependence is given by,

$$F_2^{2PA}(x_1; x_2) = \frac{(x_1 + x_2 - 1)^{3/2}}{27x_1x_2^2} \left(\frac{1}{x_1} + \frac{1}{x_2} \right)^2. \quad (6)$$

However, we now have an additional term attributed to Raman terms giving a change in absorption of,

$$F_2^{RAM} = \frac{(x_1 - x_2 - 1)^{3/2} - (-x_1 + x_2 - 1)^{3/2}}{27x_1x_2^2} \left(\frac{1}{x_1} - \frac{1}{x_2} \right)^2, \quad (7)$$

where the scaling is the same as in Eq. 5.

The total F_2 due to two photon processes is just the sum of F_2^{2PA} and F_2^{RAM} .

Another effect which must be taken account of in these calculations is the change in linear absorption at ω_1 due to the presence of the field at ω_2 shifting the bands by the AC Stark effect. Two terms arise out of this as the radiation perturbation term couples the conduction band to itself and to the valence band.

It can be shown that linear AC Stark effect produces a change in absorption $\Delta\alpha$ with a spectral dependence given by F_2^{S1} , where,

$$F_2^{S1}(x_1; x_2) = - \frac{2(x_1-1)^{3/2}}{2^7 x_1 x_2^4} . \quad (8)$$

The quadratic Stark shift resulting from the coupling between the conduction and valence band leads to a $\Delta\alpha$ given by,

$$F_2^{S2}(x_1; x_2) = - \frac{1}{2^{10} x_1 x_2^2 (x_1-1)^{1/2}} \left[\frac{1}{x_1-x_2} + \frac{1}{x_1+x_1} \right] . \quad (9)$$

4. NONLINEAR REFRACTION

In principle we can evaluate $\Delta n(\omega_1; \omega_2)$ as defined in Eq. 2, however, there are few experiments of this quantity other than at $\omega_1 = \omega_2$. Additionally, we have found an analytical expression for self refraction. Using the KK relations discussed earlier, the change in refractive index $\Delta n(\omega; \omega) = \gamma I$ can be calculated to give,

$$\gamma = \frac{K \hbar c \sqrt{E_p}}{n_0^2 E_g^4} G_2(\hbar\omega/E_g) , \quad (11)$$

where the dispersion function $G_2(x)$ is given by,

$$G_2(x) = \frac{2}{\pi} \int_0^\infty \frac{F_2(x'; x)}{x'^2 - x^2} dx' . \quad (12)$$

All that remains is for the above integral to be evaluated for the various contributions to the nondegenerate absorption, $F_2(x_1; x_2)$.

When these integrals are performed and the results summed a single divergent term proportional to ω^{-2} is left given by,

$$G_2^{\text{div}}(x) = \frac{5}{2^9 x^2} . \quad (13)$$

This diverging term is not unexpected as A-p perturbation theory has been used in the transition rate calculations and it is well known that divergences of this order can be introduced whereas the comparable E-r

perturbation theory avoids such divergences. In a similar manner to Moss et al. [23] we treat such a divergence as unphysical and subtract it from the result for the nonlinear refraction.

Using the value of K obtained from 2PA measurements and using $E_p \approx 21$ eV, which is true for the majority of semiconductors, we obtain,

$$n_2(\text{esu}) = \frac{K' \sqrt{E_p}}{n_0 E_g^4} G_2(\hbar\omega/E_g), \quad (14)$$

where the constant $K' = 1.5 \times 10^{-8}$ when E_g is defined in eV. We note the E_g^{-4} bandgap dependence for the magnitude of n_2 .

A graphical comparison of the dispersion function $G_2(\hbar\omega/E_g)$ with measured values of n_2 obtained from Z-scan measurements at $1.06 \mu\text{m}$ and $0.53 \mu\text{m}$ [2,3] and nearly degenerate three-wave mixing measurements of large gap optical materials [7] is shown in Fig. 2. Note we have agreement within a factor of 2 for a wide range of semiconductors and large gap optical materials.

The scaling of n_2 with bandgap is demonstrated in Fig. 3. Here we plot the ratio of n_2 to the dispersion function $G_2(\hbar\omega/E_g)$. The straight line indicated shows the expected E_g^{-4} dependence. It is found that the scaling law holds true over 5 orders of magnitude variation in the modulus of n_2 .

5. CONCLUSION

It has been established that the Kramers-Kronig relations not only hold true for linear optical properties but can be extended to nonlinear effects also. We derive a Kramers-Kronig relation between nonlinear refraction and nonlinear absorption. However, it is necessary to know the nondegenerate absorption (or refraction in the equivalent converse expression) i.e. the nonlinear absorption over all frequencies ω_1 when a constant optical field ω_2 is applied. This can be thought of as a pump-probe spectrum.

We calculate the nondegenerate nonlinear absorption using a simple two-band model for a direct semiconductor. It is necessary to include transitions over all frequencies so Raman and Stark shift terms are included as well as two-photon absorption. In order to obtain the scaling of the absorption terms a comparison is made to the previously measured degenerate 2PA.

The Kramers-Kronig integral can be performed analytically to give the nonlinear refraction. In this

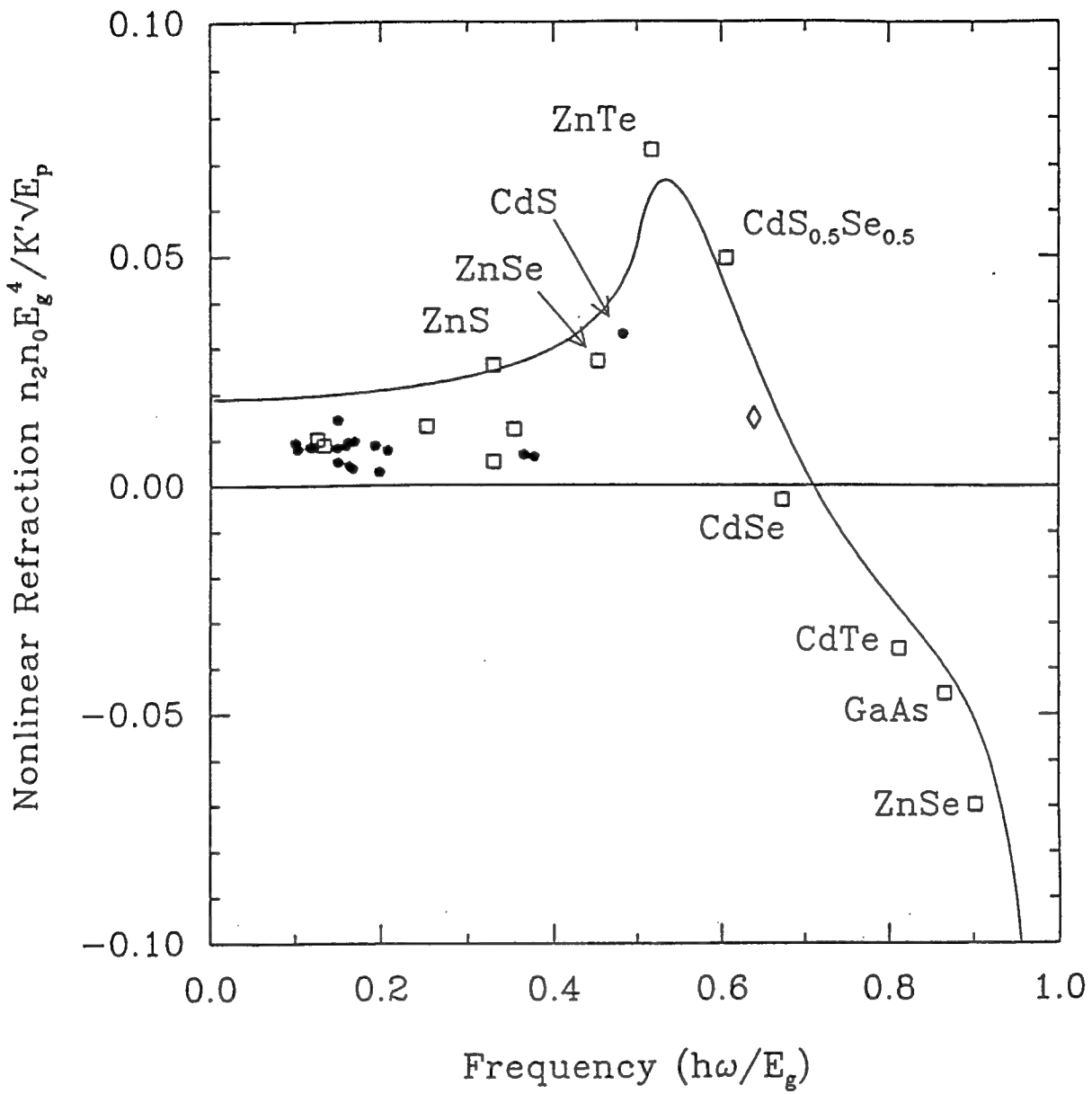


Fig. 2. A plot of n_2 dispersion function $G_2(\hbar\omega/E_g)$ containing contribution from 2PA, Raman and AC Stark effect. Data are scaled by $n_0 E_g^4 / K' \sqrt{E_p}$ as in Fig. 1.

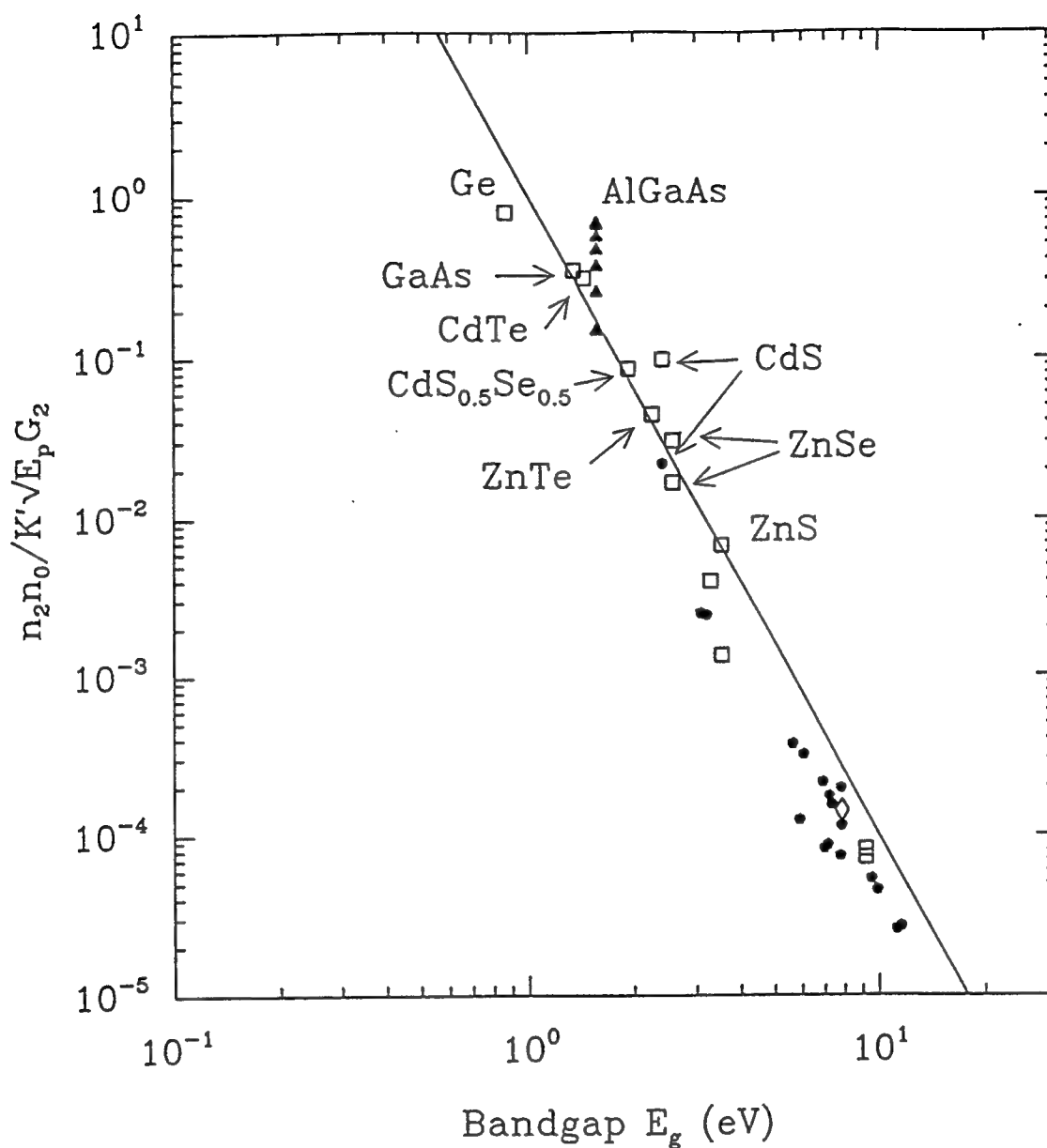


Fig. 3. A log-log plot showing the expected E_g^{-4} dependence of n_2 . The data points are identical to those in Fig. 2 but now scaled by the dispersion function $G_2(\hbar\omega/E_g)$. The solid line is the function E_g^{-4} which translates into a straight line of slope -4 on the log-log scale.

calculation we set the two frequencies in the nonlinear refraction equal as we wish to determine self-refraction, but in general the nondegenerate refraction can be obtained, i.e. the change in refractive index seen by light of frequency ω when light of frequency Ω is present.

A comparison is made between experimentally measured values of n_2 and the theoretical dispersion presented here. It is found that agreement is obtained over a wide range of materials (within a factor of ≈ 2). We also note that no fitting parameter is used since the 2PA coefficients were previously determined. Factors of two variation are quite reasonable as a very simple model has been used to calculate the nonlinear refraction with no account for the correct band structure or excitonic effects. Indeed the theory appears to apply to optical materials other than semiconductors as well. The change in sign of n_2 at about $\hbar\omega/E_g \approx 3/4$ (ie. halfway between the 1PA edge and 2PA edge) is predicted and observed. It is also demonstrated that the expected E_g^{-4} bandgap dependence holds true for over four orders of magnitude variation in the modulus of n_2 .

It is noted that the main contribution to the dispersion of n_2 below the bandgap arises from the two-photon transition term with the Stark shift term becoming dominant close to the band edge. This partly explains the good fit obtained by using the quasi-nondegenerate 2PA alone in a previous letter by the authors [1].

The E_g^{-4} dependence of n_2 gives a variation of n_2 from 2.5×10^{-14} esu for a material such as MgF_2 at $1.06 \mu\text{m}$ to 3×10^{-10} esu for Germanium at $10.6 \mu\text{m}$, which we measured using a picosecond CO_2 laser. This large variation of n_2 is better displayed by plotting n_2 scaled by n_0 and G_2 as a function of E_g on a log-log plot as shown in Fig. 3. In spite of this very large variation in magnitude of n_2 (and change in sign), this extremely simple model gives good agreement with the data for materials including both semiconductors and insulators.

In conclusion, the measured n_2 data follow a universal dispersion curve (see Fig. 3) from which values of n_2 for other materials at other wavelengths can be calculated. We have also experimentally verified the predicted band-gap scaling of n_2 . From the excellent overall agreement with the predicted magnitude and dispersion of n_2 , as calculated via Kramers-Kronig, to the large number of experimental data, we conclude that the processes responsible for 2PA and the AC Stark effect also determine n_2 . This in turn implies that the bound electronic nonlinear refractive index is predominantly a causal consequence of these nonlinear absorptive processes just as the linear index is a causal consequence of linear absorption. This calculational approach takes advantage of the historical fact that, for the solid state, the 2PA coefficient has been calculated from a transition rate approach.[24] Thus, we have circumvented problems associated with performing a direct calculation of the third order susceptibility.

6. ACKNOWLEDGEMENT

We gratefully acknowledge the support of the National Science Foundation grant ECS#8617066, DARPA/CNVEO and the Florida High Technology and Industry Council. In addition we thank O. Heinonen, A. Miller and S. Epifanov for useful discussions and A. Said, T. Wei, and E. Canto for taking and analyzing portions of the n_2 data.

7. REFERENCES

- [1] M. Sheik-Bahae, D.J. Hagan, and E.W. Van Stryland, Phys. Rev. Lett. 65, 96-99(1990).
- [2] M. Sheik-Bahae, A.A. Said, T.H. Wei, D.J. Hagan, and E.W. Van Stryland, IEEE J. Quantum Electron. QE-26, 760-769(1990).
- [3] M. Sheik-Bahae, A.A. Said, and E.W. Van Stryland, Opt. Lett. 14, 955-957(1989).
- [4] D.J. Hagan, E. Canto, E. Miesak, M.J. Soileau, and E.W. Van Stryland, pp.160, Technical Digest of the Conference on Lasers and Electro-Optics, Anaheim, CA, OSA Technical Digest Series, No. 7, 1988.
- [5] E.W. Van Stryland, H. Vanherzeele, M.A. Woodall, M.J. Soileau, A.L. Smirl, S.Guha, and T.F. Boggess, Opt. Eng. 24, 613-623(1985).
- [6] E. Canto-Said, D.J. Hagan, J. Young, and E.W. Van Stryland, *to be published*
- [7] R. Adair, L.L. Chase, and S.A. Payne, Phys. Rev. B 39, 3337-3349(1989).
- [8] M.J. LaGasse, K.K. Anderson, C.A. Wang, H.A. Haus, and J.G. Fujimoto, Appl. Phys. Lett. 56,417-419(1990).
- [9] B.S. Wherrett, A.C. Walker, and F.A.P. Tooley, in *Optical Nonlinearities and Instabilities in Semiconductors*, H. Haug, eds. (Academic Press, Inc. 1988.) pp.239-272.
- [10] B.S. Wherrett, J. Opt. Soc. Am. B 1, 67-72(1984).
- [11] E.W. Van Stryland, M.A. Woodall, H. Vanherzeele, and M.J. Soileau, Opt. Lett. 10, 490-492(1985).
- [12] S.S. Jha and N. Bloembergen, Phys. Rev. 171, 891-898(1968).
- [13] C. Flytzanis, Phys. Lett. 31A, 273-274(1970).
- [14] J.A. Van Vechten and D.E. Aspnes, Phys. Lett. 30A, 346-347(1969).
- [15] C.C. Wang, Phys. Rev. B, 2, 2045-2048(1970).
- [16] N.L. Boling, A.J. Glass, and A. Owyong, IEEE J. Quantum Electron. QE-14, 601-608(1978).
- [17] D.A.B. Miller, C.T. Seaton, M.E. Prise, and S.D. Smith, Phys. Rev. Lett. 47, 197-200(1981).
- [18] L.V. Keldysh, Sov. Phys. JETP, 20, 1307-1314(1965)
- [19] H.D. Jones and H.R. Reiss, Phys. Rev. B 16, 2466-2473(1977).
- [20] H.S. Brandi and C.B. de Araujo, J. Phys. C 16, 5929-5936(1983).
- [21] E.W. Van Stryland, Y.Y. Wu, D.J. Hagan, M.J. Soileau, and K. Mansour, J. Opt. Soc. Am. B, 5,

1980-1989(1988).

[22] M.H. Weiler, Solid State Commun. 39, 937-940(1981).

[23] D.J. Moss, E. Ghahramani, J.E. Sipe, and H.M. van Driel, Phys. Rev. B 41, 1542-1560(1990).

[23] M. Göppert-Mayer, Ann. Physik 9, 273(1931).

NONLINEARITIES IN SEMICONDUCTORS FOR OPTICAL LIMITING

A. A. Said, M. Sheik-bahae, D. J. Hagan, E. J. Canto-Said
Y. Y. Wu, J. Young, T. H. Wei and E. W. Van Stryland

CREOL
Center for Research in Electro-Optics and lasers
University of Central Florida, Orlando, FL 32816

ABSTRACT

We present measurements of nonlinear absorption and refraction in semiconductors used in the realization of optical limiters. We show that nonlinear refraction at 532 nm in ZnSe is caused by a negative third order electronic Kerr effect in addition to the two-photon-absorption (2PA) induced carrier refraction. We have used time-resolved beam distortion, picosecond time-resolved degenerate four-wave mixing and our recently developed Z-scan technique to determine the sign and magnitude of the 2PA coefficient, the bound electronic nonlinearity, n_2 and the refractive index change per free carrier.

1. INTRODUCTION

Passive optical limiting utilizing the combined effects of nonlinear absorption and nonlinear refraction in semiconductors has been demonstrated previously.[1,2,3] An ideal passive optical limiter may be described as the optical analogue of a Zener diode circuit. It has a high linear transmission up to a certain input threshold after which the output becomes clamped to a constant value. In reference [1] we described the development and characterization of broad-band self-protecting ZnSe limiters. In this paper, we present the results of a comprehensive study of the nonlinear processes involved in such devices using various experimental techniques. These nonlinearities are two photon absorption (2PA), refraction arising from the 2PA generated free carriers and nonlinear refraction due to the electronic Kerr effect. Picosecond degenerate four wave mixing (DFWM) studies were conducted to examine the temporal response as well as the order of the refractive nonlinearities. Also, our newly developed Z-scan technique [4] was employed to accurately determine the sign and magnitude of the different refractive nonlinearities as well as the 2PA coefficient of the semiconductors.

In section 2 we describe the time-resolved beam distortion measurements and the equations for nonlinear propagation of light inside the semiconductors. In section 3 the DFWM results are presented. In section 4 the Z-scan technique is briefly described and the results of the Z-scan measurements are presented. Finally, in section 5 the experimental results are compared to theoretical models.

2. BEAM DISTORTION MEASUREMENTS

A collimated beam 0.57 mm in radius ($HW1/e^2M$) at 532 nm was incident on a 3 mm polycrystalline ZnSe sample and the transmitted beam fluence was monitored with a vidicon in the near field. In this geometry the thin sample approximation (the sample length is smaller than the diffraction length of the beam) can be used to describe the beam propagation inside the sample. This allows us to separate the wave equation into two equations, one for the irradiance I and one for the phase Φ . Also with 30 ps (FWHM) pulses and at low irradiance levels we can ignore the absorption due to the 2PA generated carriers but not carrier induced refraction [5]. This leaves the nonlinear differential equations,

$$\frac{dI}{dz} = -\alpha I - \beta I^2,$$

(1)

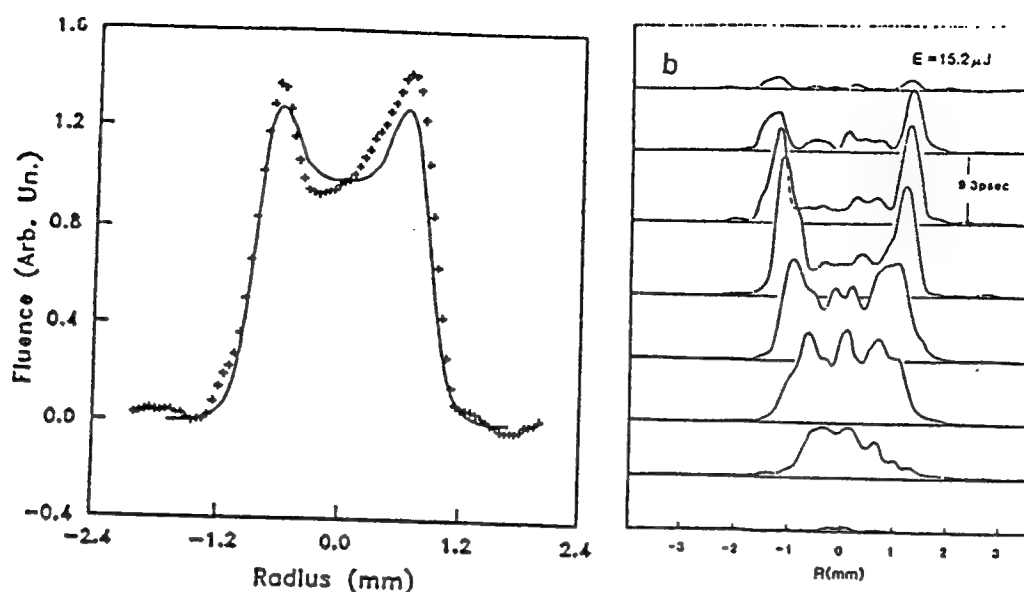


Fig.1. (a) Transmitted spatial energy distribution of a 30 ps $0.53 \mu\text{m}$ pulse after propagation through ZnSe at 2.7 GW/cm^2 as viewed on a vidicon. The solid line is the theoretical fit to the experiment with $\sigma = 1.6 \times 10^{-21}$, $n_2 = 0$, and $\beta = 5.5 \text{ cm/GW}$. In (b) the temporal evolution of the spatial profile shows the defocusing increases with time.

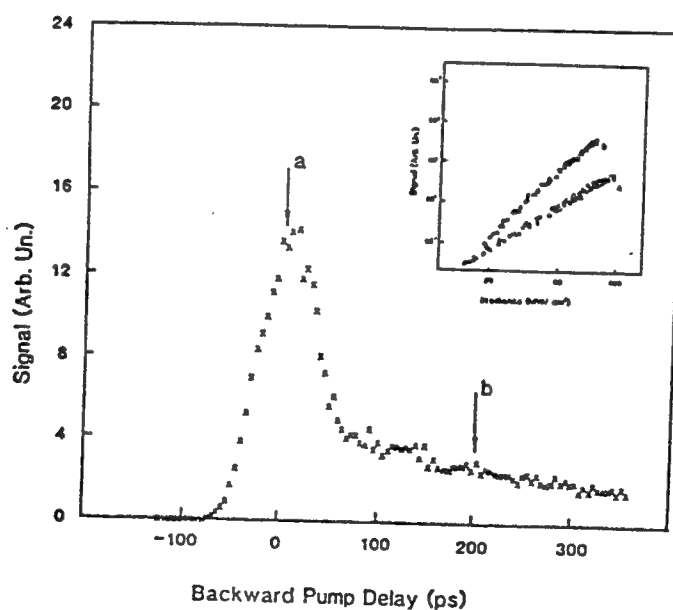


Fig.2. The DFWM signal vs backward pump delay for 30 ps pulses at $0.53 \mu\text{m}$ in ZnSe. The inset shows a log-log plot of the conjugate signal as a function of the input irradiance at 0 ps (a) and 200 ps (b).

and

$$\frac{d\Delta\Phi}{dz} = k\gamma I - k\sigma N, \quad (2)$$

where α is the linear absorption coefficient, β is the 2PA coefficient, $k=2\pi/\lambda$, λ is the wavelength of the incident radiation, γ is the refractive index change due to the electronic Kerr effect, N is the density of free carriers and σ is the change in the index of refraction per free carrier pair density generated. Since the free carriers are created by 2PA, the generation rate is given by

$$\frac{dN}{dt} = \frac{\beta I^2}{2\hbar\omega} \quad (3)$$

When N is substituted in equation (2), it becomes clear that the phase change due to the carriers depends on the square of the irradiance. Hence, the free carrier refraction appears as an effective fifth order nonlinearity.[7,8]

The solution to equations (1-3) gives the electric field at the exit surface of the sample, which we then propagate in free space to the vidicon using a Hygens-Fresnel integral. Using $\beta=5.5$ cm/GW for the 2PA coefficient from reference [6] we proceeded to fit the experimental data considering only free carrier refraction. The best fit was obtained with $\sigma=1.6 \times 10^{-21}$ cm³ as shown in figure 1(a). Using a streak camera in front of the vidicon, the time evolution of the spatial irradiance profile of the beam could be monitored as shown in figure 1(b). Here the beam is continuously broadened as the pulse temporally evolves, further indicating that the defocusing mechanism is a time integrating effect which is true for free carrier refraction. Therefore, our preliminary conclusion was that the self-defocusing observed in ZnSe is entirely caused by the carriers generated via 2PA.

There is a great deal of experimental evidence that the bound electronic refractive index change in solids is a positive effect, i.e. $n_2 > 0$. This is seen for wide band-gap materials, since self-focusing plays a significant role in the laser induced damage of these solids.[13] Based on this, and since all beam distortion experiments showed a self-defocusing effect, we at first attributed nonlinear refraction to 2PA generated free carriers alone.[1] However, as shown below we find n_2 is negative for semiconductors at energies well above the 2PA edge.

3. DEGENERATE FOUR WAVE MIXING EXPERIMENTS

DFWM with picosecond pulses is a sensitive technique that gives information about the temporal evolution of nonlinear processes in semiconductors and other materials. Two counter-propagating strong beams, forward pump E_f and backward pump E_b , are incident on the sample with a third weaker probe beam, E_p incident at an angle θ with respect to the forward pump. Two of these beams interfere inside the sample to form a grating from which the third beam diffracts to form a conjugate signal E_c that retraces the probe path. The pulses used in these experiments are the second harmonic of a Q-switched Nd:YAG laser output with a 30 ps (FWHM) pulse width and a Gaussian spatial profile. Various combinations of polarizers and half-wave plates were placed in the path of each beam to independently change their polarization and irradiance. Figure 2 shows a plot of the conjugate signal versus the delay τ_D of E_b which was polarized perpendicular to E_f and E_p . Two distinct regions are present, a fast decaying signal near zero delay and a slowly decaying signal at long delays. To better understand the two nonlinear regimes, irradiance dependence experiments were performed at different delays. A log-log plot of the DFWM signal versus input irradiance (all three inputs varied) gives two different slopes as shown in the inset of figure 2. At zero delay a slope of 2.8 was measured indicating a third order nonlinearity and at long delays a slope of 4.9 was found. The fifth order dependence can be explained by the 2PA induced carrier refraction as mentioned in the previous section. A modulated carrier density is created via 2PA; this is an imaginary $\chi^{(3)}$ effect. Then a third beam diffracts off

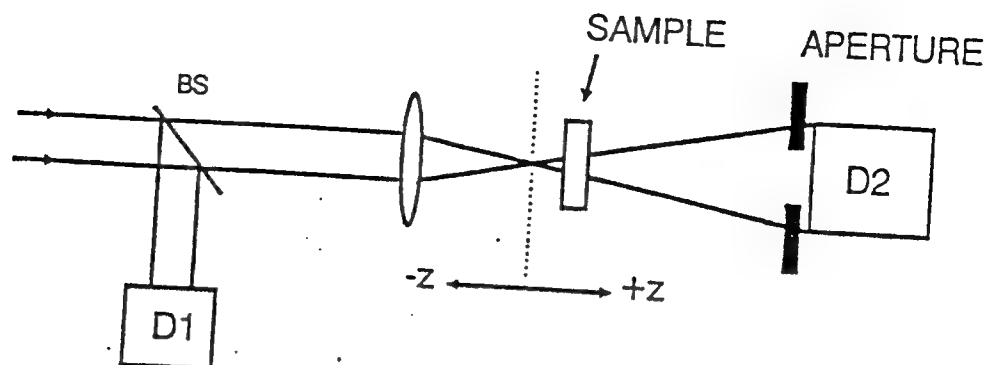


Fig.3. The Z-scan experimental setup in which the normalized transmittance is measured as a function of the sample position z .

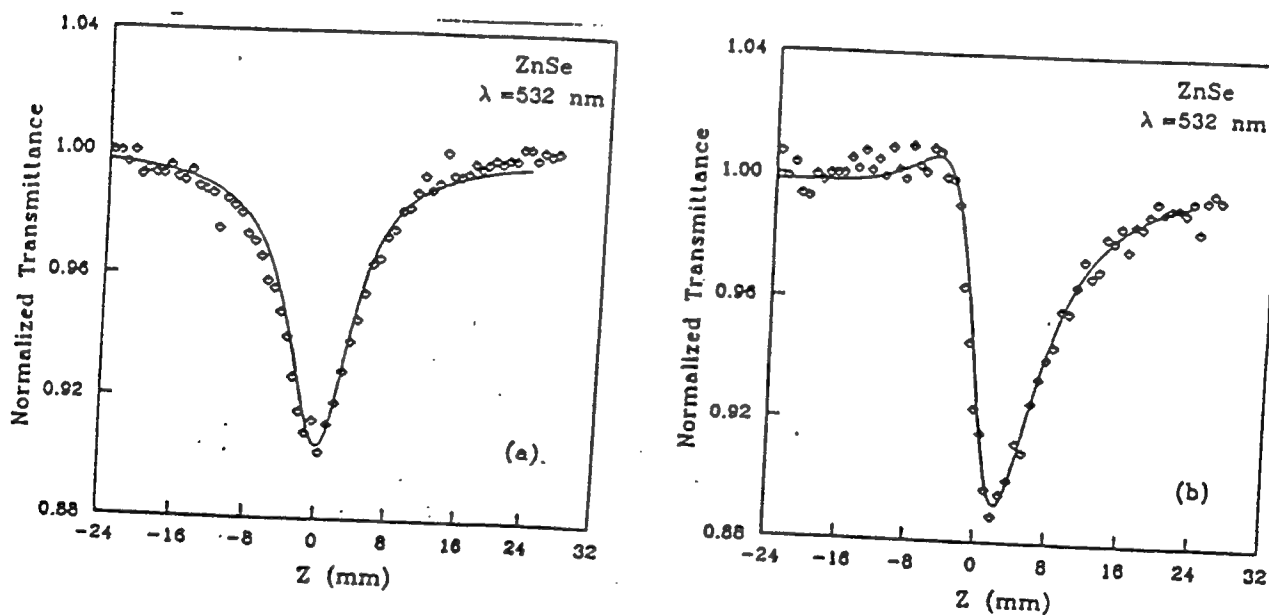


Fig.4. Normalized Z-scan signal of a 2.7 mm thick ZnSe sample using 27 ps $0.53 \mu\text{m}$ pulses at 0.21 GW/cm^2 input irradiance. The solid lines are the theoretical results. (a) No aperture data and fit using $\beta = 5.8 \text{ cm/GW}$. (b) 40% aperture data fitted with $\beta = 5.8 \text{ cm/GW}$ and $n_2 = -4 \times 10^{-11} \text{ esu}$.

the carrier modulation; this is a real $\chi^{(1)}$ effect. Hence, the mechanism is a sequential $\chi^{(3)} : \chi^{(1)}$ process that appears as a fifth order nonlinearity. As to the third order effect the signal decays within the 30 ps pulse width which is consistent with a bound electronic nonlinearity. This fast decaying effect can either be of refractive or absorptive nature as far as DFWM is concerned. Assuming that it is a refractive effect a value of $|n_2| = 4.4 \times 10^{-11}$ esu was extracted where n_2 is related to γ by $n_2 (\text{esu}) = n_0 c / (40\pi) \gamma (\text{MKS})$. [7,8] Note that the sign of n_2 is not given by DFWM. This third order effect was not expected from the fits of the beam distortion experiments.

4. Z-SCAN MEASUREMENTS

The Z-scan technique, which was recently developed at our laboratories, is a simple single beam experimental technique that readily gives the sign and magnitude of nonlinear refraction as well as nonlinear absorption.[9] It is also an excellent guide for geometrical optimization of optical limiting.[10] Figure 3 shows the Z-scan experimental setup. A focused Gaussian beam is incident on the sample and the transmitted beam is collected through a finite aperture in the far field into detector D_2 . D_1 monitors the input energy. Keeping the input energy fixed, the transmittance is measured as a function of the sample position relative to the focal plane. Since nonlinear refraction causes a lensing effect in the incident beam, the sample behaves as a negative or positive lens depending on the sign of the nonlinearity. As explained in reference [4] a valley-peak configuration in the Z-scan signal is a signature of a positive refractive nonlinearity and a peak-valley pattern denotes a negative nonlinearity. When the aperture is removed, i.e. all the transmitted light is collected, the Z-scan is only sensitive to nonlinear absorption. For semiconductors with 2PA present, the Z-scan experiment was simulated by solving equations (1-3). Three parameters are to be determined β , n_2 and σ . Using 27 ps pulses (FWHM) at 532 nm Z-scan measurements were performed on a 2.7 mm thick ZnSe sample at different input energies. With the aperture removed a Z-scan was performed at $I_0 = 0.1 \text{ GW/cm}^2$ where I_0 is the on axis peak irradiance at the focus. In this case the measurement is insensitive to nonlinear refraction and thus independently gives the nonlinear absorption coefficient. The best fit to the data shown in figure 4(a) gave a $\beta = 5.8 \text{ cm/GW}$, in good agreement with the value of 5.5 cm/GW obtained in reference [6]. Our experimental errors were $\pm 30\%$ mostly arising from uncertainties in the irradiance values. Figure 4(b) shows the data and fit of the Z-scan signal at the same irradiance with the 40% transmitting aperture in place. At this low irradiance we expect the nonlinear refraction to be mostly due to the 3rd order nonlinearity as can be deduced from equations (2) and (3). Hence, the carrier term in equation (2) was dropped and an $n_2 = -4 \times 10^{-11}$ was extracted. The negative sign of n_2 is evident from the peak-valley pattern in the data. Moreover, this n_2 value is within 10% of the value obtained by our DFWM measurement. For a 3rd order nonlinearity, the change in the index of refraction, Δn , is a linear function of the irradiance, I . Figure 5 shows that this is not the case at higher irradiance values meaning that the refraction due to the 2PA generated carriers becomes more significant at these levels. At $I_0 = 2.4 \text{ GW/cm}^2$ (fig. 6), and with β and n_2 known, the experimental data was fit with $\sigma = 0.8 \times 10^{-21} \text{ cm}^3$. The above measured values for n_2 , β and σ were used at other irradiance values and gave good fits to the experimental data. The Z-scan was also used to determine the above parameters for other semiconductors at different wavelengths. For example at $1.06 \mu\text{m}$, we measured $\beta = 26 \text{ cm/GW}$, $n_2 = -2 \times 10^{-10} \text{ esu}$, $\sigma = 5 \times 10^{-21} \text{ cm}^3$ for CdTe and $\beta = 26 \text{ cm/GW}$, $n_2 = -2.7 \times 10^{-10} \text{ esu}$, $\sigma = 8 \times 10^{-21} \text{ cm}^3$ for GaAs. The experimental errors were $\pm 30\%$.

Based on the results obtained from both the DFWM and the Z-scan measurements we reexamined our beam distortion conclusion. The same data shown in figure 1(a) was fitted again with the 3rd order refraction included in the propagation equations. The result is a much better fit to the experimental data shown in figure 7 using $\beta = 5.5 \text{ cm/GW}$, $n_2 = -4 \times 10^{-11} \text{ esu}$ and $\sigma = 0.8 \times 10^{-21} \text{ cm}^3$.

5. CONCLUSION

As a result of conducting thorough studies of the nonlinearities in ZnSe at 532 nm using different experimental techniques, we conclude that the bound electronic nonlinearity is negative and is a significant contribution to the overall nonlinear refraction. We now understand the negative sign of n_2 . As discussed in

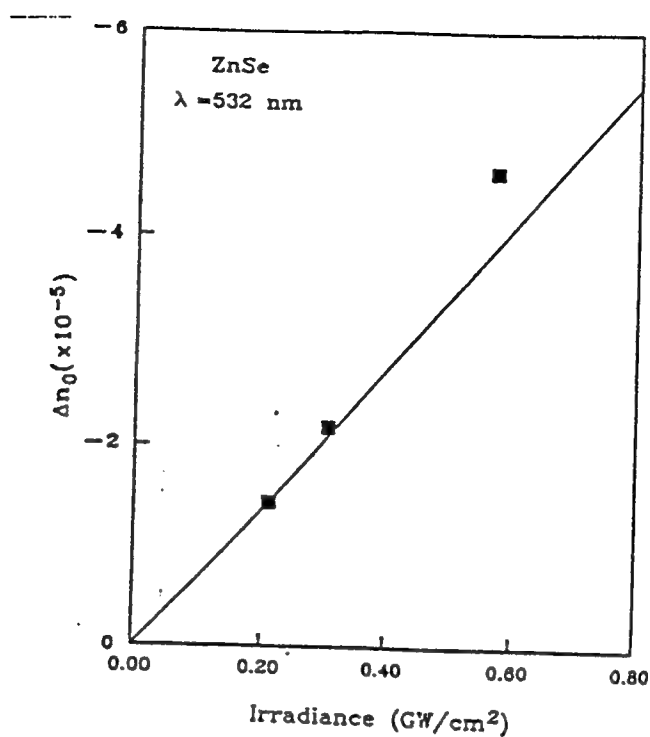


Fig.5. The refractive index change in ZnSe as a function of input irradiance as measured from the Z-scan experiments. The line represents a 3rd order nonlinearity. The deviation from the line indicates the higher order refraction arising from the 2PA generated free carriers.

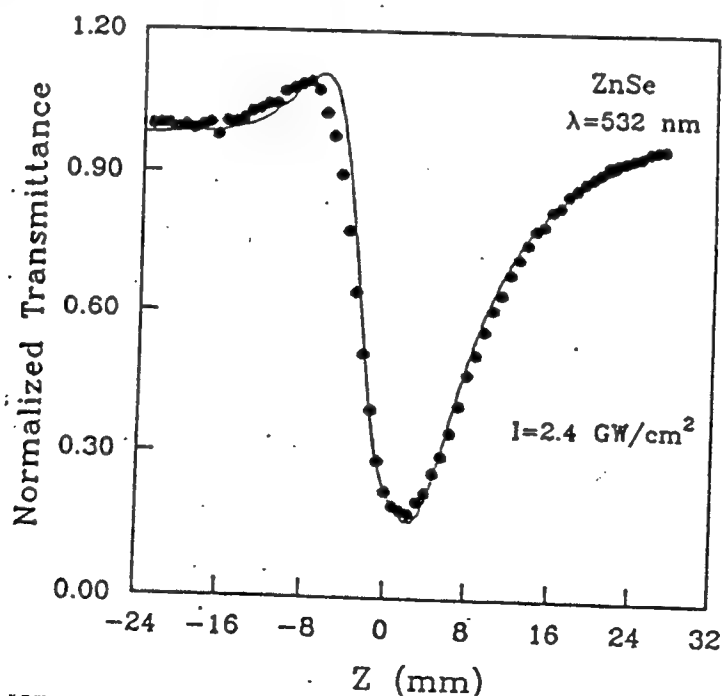


Fig.6. Normalized Z-scan signal for ZnSe at input peak irradiance of $2.4 \text{ GW}/\text{cm}^2$ with a 40% aperture. The solid line is the theoretical fit with $\beta = 5.8 \text{ cm}/\text{GW}$, $n_2 = -4 \times 10^{-11} \text{ esu}$ and $\sigma = 0.8 \times 10^{-21} \text{ cm}^3$.

reference [11], n_2 , the real part of $\chi^{(3)}$, and 2PA , the imaginary part of $\chi^{(3)}$, are related by causality and a relation similar to the Kramers-Kronig connection between linear absorption and the linear index of refraction.[11] The value obtained for the refractive index change per free carrier pair agrees with the band-blocking model suggested by Auston et al.[12]. The σ calculated from the above model is $1.1 \times 10^{-21} \text{ cm}^3$ compared to our experimental value of $0.8 \times 10^{-21} \text{ cm}^3$. In conclusion, we have identified the different nonlinearities that make semiconductors good optical limiters.

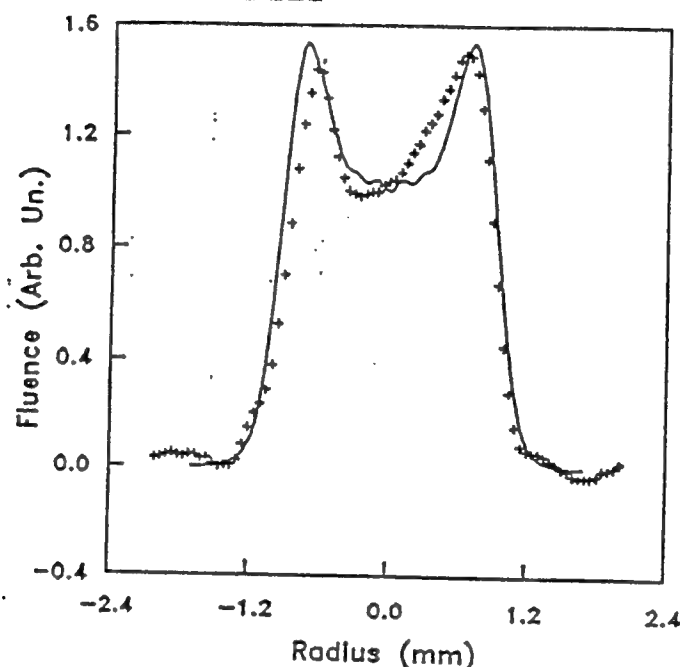


Fig.7. Same experimental data as in fig.1(a). The theoretical fit (solid line) is obtained with $\sigma=0.8 \times 10^{-21} \text{ cm}^3$, $n_2=-4 \times 10^{-11} \text{ esu}$ and $\beta=5.5 \text{ cm/GW}$. It is clear that this is a better fit than the one in figure 1(a) where the electronic Kerr refraction was neglected.

6. ACKNOWLEDGEMENTS

We gratefully acknowledge the support of the National Science Foundation grant #ECS-8617066, DARPA/CNVEO and the Florida High Technology and Industry Council.

7. REFERENCES

1. E. W. Van Stryland, Y. Y. Wu, D. J. Hagan, M. J. Soileau and K. Mansour, "Optical limiting with semiconductors", J. Opt. Soc. Am. B, Vol. 5, NO.9, 1980, September 1988. Also see, D. J. Hagan, E. W. Van Stryland, Y. Y. Wu, T. H. Wei, M. Sheik-Bahae, A. A. Said, K. Mansour, J. Young and M. J. Soileau, "Passive broadband high dynamic range semiconductor limiters," SPIE Proc. Vol.1105, 103 (1989).
2. T. F. Boggess, S. C. Moss, I. W. Boyd and A. L. Smirl, "Nonlinear- optical energy regulation by nonlinear refraction and absorption in silicon", Opt. Lett. 9, 291(1984).
3. J. M. Ralston and K. R. Chang, "Optical limiting in semiconductors," Appl. Phys. Lett. 15,164 (1969).

4. M. Sheik-Bahae, A. A. Said and E. W. Van Stryland, "High Sensitivity, Single Beam n_2 Measurements," Opt. Lett. Vol. 14, NO. 17, 955, (1989).
5. E. W. Van Stryland, M. A. Woodall, H. Vanherzeele, and M. J. Soileau, "Energy band-gap dependence of two-photon absorption," Opt. Lett. 10, 490 (1985).
6. E. W. Van Stryland, H. Vanherzeele, M. A. Woodall, M. J. Soileau, A. L. Smirl, S. Guha, and T. F. Boggess, Opt. Eng. Vol 24, 613 (1985).
7. Edesly Canto, Ph.D. Dissertation, University of North Texas, May (1990).
8. E. J. Canto, D. J. Hagan, J. Young, and E. W. Van Stryland, "Degenerate four-wave mixing measurements of high order nonlinearities in semiconductors," To be published.
9. M. Sheik-Bahae, A. A. Said, T. H. Wei, D. J. Hagan, and E. W. Van Stryland, "Sensitive measurements of optical Nonlinearities using a single beam," IEEE J. Quantum Electron. April (1990).
10. Mansoor Sheik-Bahae, Ali A. Said, D. J. Hagan, M. J. Soileau and Eric W. Van Stryland, SPIE Proc. Vol. 1105, 146 (1989).
11. M. Sheik-Bahae, D. J. Hagan, A. A. Said, J. Young, T. H. Wei and E. W. Van Stryland, "Kramers-Kronig relation between n_2 and two-photon absorption," SPIE Proc. Vol 1307, (1990).
12. D. H. Auston, S. McAfee, C. V. Shank, E. P. Ippen, and O. Teschke, Solid State Electron. Vol 21, 147 (1978).
13. M. J. Soileau, William. E. Williams, Nastaran Mansour and E. W. Van Stryland, "Laser-Induced Damage and the Role of Self-Focusing," Opt. Eng. Vol. 28, 1133-1144 (1989).

Kramers-Kronig relation between n_2 and two-photon absorption

M. Sheik-Bahae, D.J. Hagan, A.A. Said, J. Young, T.H. Wei, and
E.W. Van Stryland

CREOL
Center for Research in Electro-Optics and Lasers
University of Central Florida
Orlando, FL 32816

ABSTRACT

Nonlinear refractive index and two-photon absorption measurements on semiconductors show that the bound electronic nonlinearity can be calculated from two-photon absorption dispersion via a simple Kramers-Kronig analysis. This analysis shows n_2 changing from positive to negative as the photon energy approaches the band-gap energy, consistent with observations. Additionally, this simple calculation, which assumes two parabolic bands, gives good agreement with measured values of n_2 in wide-gap dielectrics that are 2 to 3 orders of magnitude smaller than in semiconductors.

2. INTRODUCTION

The study of nonlinear optics in semiconductors has concentrated on bandgap-resonant effects. The very large nonlinear effects observed in this case are the saturation of interband and excitonic absorption due to photoexcited free carriers and excitons, and the associated negative change in the refractive index. In contrast, by exciting optical solids at frequencies much less than the gap, a considerably smaller, and faster, positive nonlinear refractive index (n_2) due to bound electronic effects is observed. However, recently we found that measurements in semiconductors substantially above the two-photon-absorption (2PA) edge yield negative values for n_2 . [1] This dramatic dispersion of n_2 can be partially explained using a nonlinear Kramers-Kronig (KK) relation between n_2 and the 2PA coefficient β , or between the real and imaginary parts of the third order nonlinear susceptibility $\chi^{(3)}$. The magnitude and dispersion of n_2 is of interest because of its importance in nonlinear propagation in fibers, fast optical switching, self-focusing and damage in optical materials, and optical limiting in semiconductors. In this letter, we describe our calculation of the bound electronic Kerr effect, n_2 , and compare our results with data for a large number of materials, including semiconductors and dielectrics.

This n_2 arises from the real part of $\chi^{(3)}$, and is defined through the refractive index change Δn , where

$$\Delta n(\omega) = \gamma(\omega) I_\omega = \frac{n_2(\omega)}{2} |E_\omega|^2, \quad (1)$$

with I_ω and E_ω being the irradiance and electric field at frequency ω respectively and $n_2 = (2\pi/n_0) \text{Re}(\chi^{(3)})$. The linear refractive index is n_0 , and γ and n_2 are related by $n_2(\text{esu}) = (cn_0\gamma/40\pi)(\text{MKS})$ with c the speed of light.

Most theoretical calculations of n_2 have been confined to the zero frequency limit. [2-6] Semi-empirical formulations have been most successful in predicting the magnitude of n_2 . [5,6] For example, the formula obtained by Boling, Glass and Owyong (BGO) in relating n_2 to the linear index (n_0) and the dispersion of n_0 in terms of the Abbe number has been successfully applied to a large class of transparent materials. [6,7] Their theory predicts the low frequency magnitude of n_2 . We describe a KK method of calculation of n_2 that predicts the dispersion as well as the magnitude of n_2 . This calculation assumes that 2PA gives the dominant contribution to n_2 and that other contributions from Raman and the AC Stark effect or virtual band-blocking are ignored. We will return to this assumption later.

3. CAUSALITY AND KRAMERS-KRONIG TRANSFORMATION

Based on the principle of causality, the KK transformation states that a change in the refractive index (Δn) at ω is associated with changes in the absorption coefficient ($\Delta\alpha$) throughout the spectrum (ω') and vice versa. We write this as:

$$\Delta n(\omega, \xi) = \frac{c}{\pi} \int_0^{\infty} \frac{\Delta\alpha(\omega', \xi)}{\omega^2 - \omega'^2} d\omega', \quad (2)$$

where c is the velocity of light in vacuum and ξ is a parameter (or parameters) denoting the "cause" of change in the absorption. The cause need not be of optical origin but of any external perturbation such as thermal excitation, etc. For cases where an electron-hole plasma is injected, the consequent change of absorption has been used to obtain the plasma contribution to the refractive index. In this case, the ξ parameter is taken as the change in plasma density (Δn) regardless of the mechanism of generation of the plasma or the pump frequency.[8] In the case of 2PA the change is due to the presence of a pump field at Ω (ie. $\xi=\Omega$). The corresponding nonlinear refraction is $\Delta n(\omega, \Omega)$, which gives the dispersion of the index change with ω . For the case of self-refraction, $\omega=\Omega$, and this gives what is commonly referred to as n_2 . Van Vechten and Aspnes [4] obtained the low frequency limit of n_2 from a similar KK transformation of the Franz-Keldysh electro-absorption effect where, in this case, ξ is the DC field. The bound electronic contribution to $\chi^{(3)}$ can originate from various absorptive counterparts that are quadratic functions of the pump field. Effects of this order may include 2PA, the electronic Raman effect, and the optical Stark effect. Here we consider only 2PA.

A wealth of experimental and theoretical work regarding 2PA in semiconductors and crystalline materials exists. In accordance with the predictions derived from either second order perturbation theory [9,10] or a Keldysh-type formalism [11], the 2PA coefficients of the semiconductors studied in Ref. [12] were found to be in good agreement with the theoretical expression given as:

$$\beta(2\omega) = K \frac{\sqrt{E_p}}{n_0^2 E_g} F_2(2\hbar\omega'/E_g), \quad (3)$$

where K is a material independent constant and E_p (related to the Kane momentum parameter, a momentum matrix element) is nearly material independent and possesses a value of ≈ 21 eV for most direct gap semiconductors. Note $\beta = (4\pi\omega/n_0)\text{Im}(\chi^{(3)})$. The function F_2 is only a function of the ratio of the photon energy $\hbar\omega'$ to E_g (ie. the optically coupled states). The functional form of F_2 reflects the assumed band structure and the intermediate states considered in calculating the 2PA transition rate. The simplest model assumes a pair of isotropic and parabolic bands and intermediate states that are degenerate to initial (valence) or final (conduction) states. Neglecting the Coulomb interaction, this simple formalism yields:[10]

$$F_2(2x) = \frac{(2x-1)^{3/2}}{(2x)^6} \quad \text{for } 2x > 1. \quad (4)$$

The best fit to the data of Ref. 12 using Eqs. 3 and 4 gave $K=3.1 \times 10^3$ in units such that E_p and E_g were in eV and β was in cm/GW, while theory gave 5.2×10^3 [9]. When nonparabolicity was included the average β was 26% lower than theory; however, the frequency dependence of β changed very little. Interestingly, Eqs. 3 and 4 also give a fair estimate of β for a number of transparent materials measured using the 3rd and 4th harmonics of picosecond Nd:YAG laser pulses.[13,14]

Equations 3 and 4 pertain to a degenerate case where the two photons involved are of the same frequency and

source. For a KK transformation the nondegenerate 2PA coefficient for two distinct frequencies is needed (ie. Ω the "cause" and ω' the integration variable in Eq. 2). Extending the same simple model to obtain the non-degenerate 2PA coefficient has led to dispersion functions that are afflicted with "infrared divergences". [15, 16] This has been a common problem originating from the use of the A-p perturbation to calculate the bound electronic nonlinear susceptibilities in solids. [15] Although special cases have been considered [17], a general theory that would rigorously address the proper scaling and dispersion of the non-degenerate 2PA is yet to be developed. For this reason we assume that the dispersion function F_2 for the nondegenerate 2PA coefficient, $\beta(\omega', \Omega)$, can be given by Eqn. 4 modified with the substitution of $2\hbar\omega'$ by $\hbar\omega' + \hbar\Omega$; thus, $F_2(2x)$ is replaced by $F_2(x' + X)$, where $x' = \hbar\omega'/E_g$ and $X = \hbar\Omega/E_g$, and $x' + X > 1$. This substitution is strictly valid only for $x' = X$, however, the predictions resulting from this substitution show remarkable agreement with the data, as will be shown.

The change of the absorption spectrum (at ω') induced by the presence of a strong pump at Ω can be written for 2PA as $\Delta\alpha(\omega'; \Omega) = \beta(\omega'; \Omega)I_\Omega$, where I_Ω denotes the irradiance of the pump field. Similarly the change in refractive index at ω induced by the presence of a strong pump at Ω can be written as $\Delta n(\omega; \Omega) = \gamma(\omega; \Omega)I_\Omega$. Applying the KK transformation Eq. 2 at this point yields a relation between $\gamma(\omega; \Omega)$ and $\beta(\omega', \Omega)$. Using Eq. 3 with $F_2(x' + X)$ in Eq. 2 we obtain for the degenerate case ($\omega = \Omega$):

$$\gamma = K \frac{\hbar c \sqrt{E_p}}{2n_0^2 E_g^4} G_2(\hbar\omega/E_g), \quad (5)$$

where the dispersion function $G_2(x)$ is given by,

$$G_2(x) = \frac{-2+6x-3x^2-x^3-3/4x^4-3/4x^5+2(1-2x)^{3/2}\Theta(1-2x)}{64x^6}, \quad (6)$$

with $\Theta(x)$ being the unit step function.

Using the value of K obtained from the 2PA measurements, $E_p = 21$ eV, and converting from γ to n_2 , we obtain the final expression for n_2 as:

$$n_2(\text{esu}) = K' \frac{G_2(\hbar\omega/E_g)}{n_0 E_g^4}, \quad (7)$$

where $K' = 3.4 \times 10^{-8}$ and E_g is in eV. Equation 7 explicitly shows an E_g^{-4} band-gap dependence for the magnitude of n_2 , and the sign and the frequency dispersion of this quantity are given by the simple closed form function G_2 . We can now readily compare the predictions of this theory with experiment.

4. COMPARISON WITH EXPERIMENTAL RESULTS

Utilizing a newly developed technique (Z-scan) for n_2 measurements [1, 18] that can determine its magnitude and sign, we have measured n_2 for several materials at 1.06 and 0.53 μm . This simple technique has been shown to be an accurate and sensitive tool for measuring n_2 even in the presence of nonlinear absorption. We find, for example, in materials such as ZnSe at 0.53 μm , where 2PA is present, n_2 is negative, but that the sign changes at 1.06 μm . Picosecond degenerate-four-wave-mixing measurements show this third order response (time resolution limited by the 30 ps pulsewidth), while at higher irradiances the slowly decaying 2PA generated free-carrier refraction is seen. [19] We have also measured n_2 in a number of wide-gap dielectrics using the Z-scan method.

A graphical comparison of the data is given in Fig. 1 which shows the band-gap scaling law and in Fig. 2

where the dispersion and sign of n_2 are explicitly compared to the G_2 of Eq. 7. Many of the experimental values for large gap optical crystals are obtained from recent measurements by Adair et.al. using a "nearly degenerate-three-wave-mixing" scheme.[7]

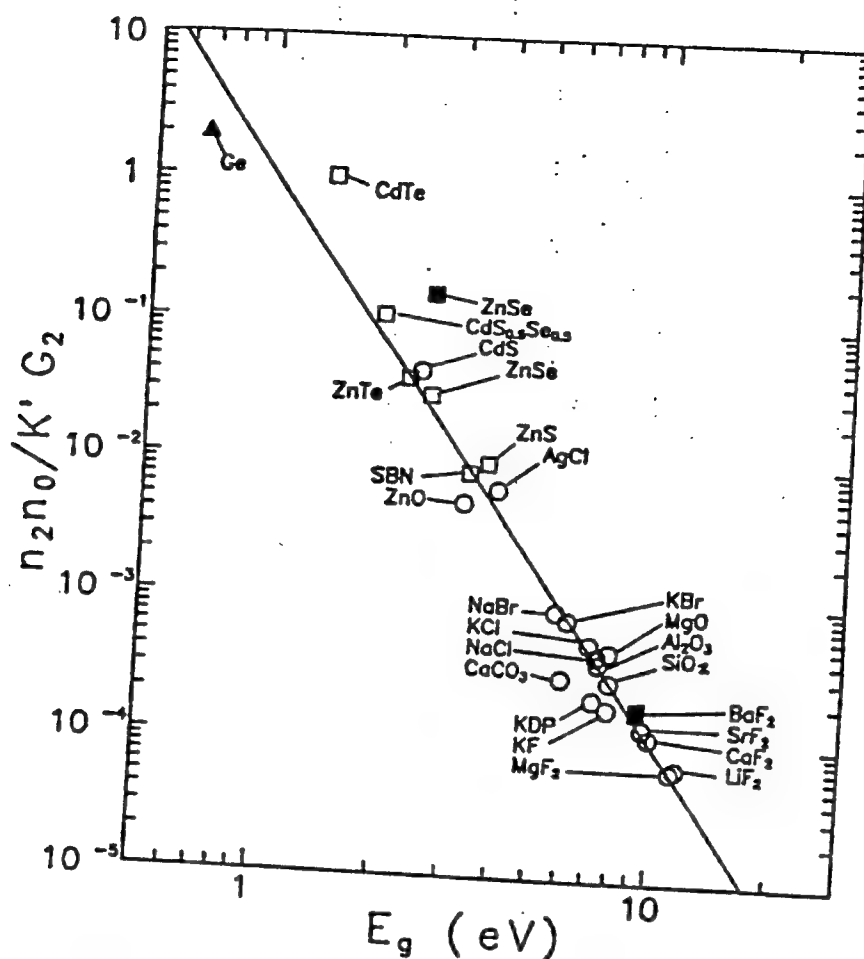


Fig. 1 A log-log plot of the scaled n_2 versus energy gap (E_g) for a large class of optical materials. The solid line represents the theoretical result as obtained from Eq.(7) with no adjustable parameters and has a slope of -4. The open circles represent the data from ref.[7] all obtained at $\lambda=1.06 \mu\text{m}$. The remaining data are our measurements using the Z-scan technique taken at $\lambda=1.06 \mu\text{m}$ (open squares), at $\lambda=.532 \mu\text{m}$ (solid squares) and at $\lambda=10.6 \mu\text{m}$ (solid triangle).

The dispersive behavior of n_2 in Fig. 2 is seen to be most significant within the range $E_g/2 < \hbar\omega < E_g$ where 2PA is present and relatively small in the low frequency limit $\hbar\omega \ll E_g$. A noticeable difference between the magnitude of the measured and calculated values is seen near the one photon absorption edge. Considering the simplicity of the model in deriving Eq. 7, such deviations are not unexpected. The measured large negative values of n_2 as compared to the calculated values near the fundamental absorption edge may be attributed to the refraction due to the "optical Stark effect" which is also referred to as "virtual band-blocking" and has been ignored in our calculations. The contribution of this mechanism to the electronic nonlinear susceptibility has been shown to have a strong band-gap resonance and follows the same scaling as given in Eq. 7.[20] This effect, which is negative for all frequencies below the band-gap, vanishes quickly for longer wavelengths ($\hbar\omega < E_g/2$) and has negligible contribution in the transparency region of the material. The E_g^{-4} dependence of n_2 gives a variation of n_2 from $n_2=7 \times 10^{-14}$ esu for a material such as BaF_2 to

$n_2 = 1.5 \times 10^{-11}$ esu for ZnSe at $1.06 \mu\text{m}$ which turns negative at $0.53 \mu\text{m}$ to $n_2 = -4 \times 10^{-11}$ esu. In spite of this very large variation in magnitude of n_2 (and change in sign), this extremely simple model gives good agreement with the data for materials including both semiconductors and insulators, except very near the absorption edge. However, we must emphasize that the justification for splitting 2ω into $\omega' + \Omega$ in Eq. 4 is empirical.

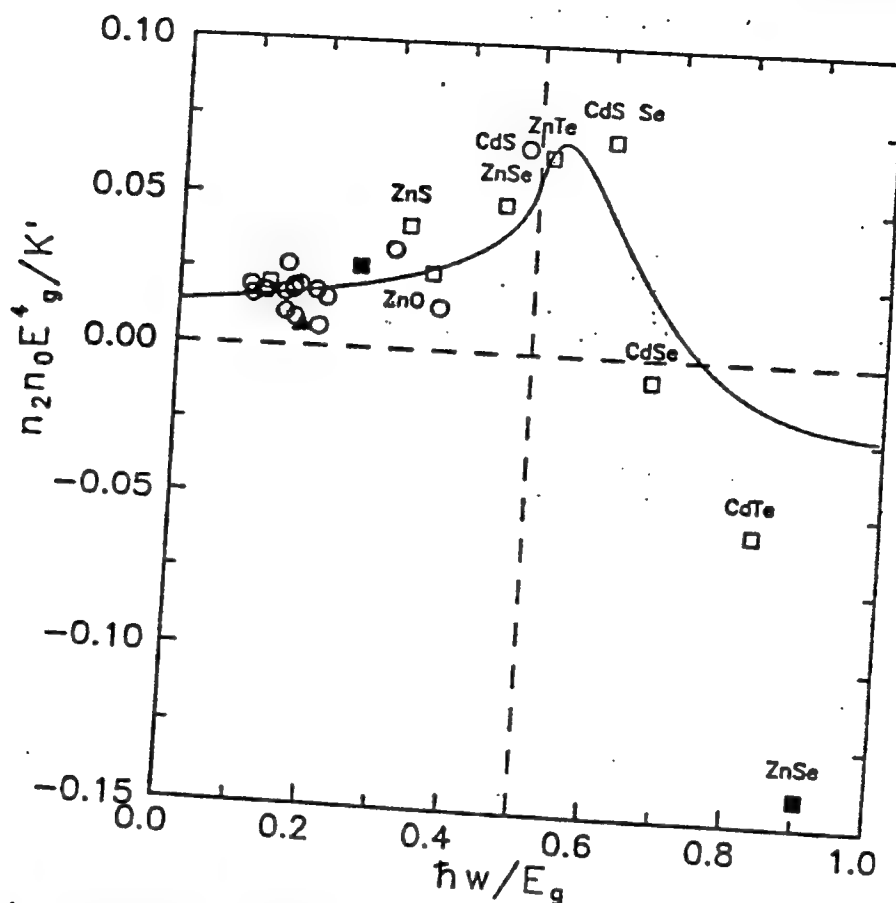


Fig. 2 The calculated dispersion function G_2 versus $\hbar\omega/E_g$. The same n_2 data as in Fig. 1, here scaled as $n_2 n_0 E_g^4 / K'$, are compared with the theory. Only the semiconductor data within the highly dispersive region are labeled for comparison.

5. CONCLUSION

We conclude from the excellent overall agreement with the predicted magnitude and dispersion of n_2 to the large number of experimental data, that the KK model presented gives a significant if not dominant contribution to n_2 . This in turn implies that the bound electronic nonlinear refractive index is predominantly a causal consequence of two-photon absorption just as the linear index is a causal consequence of linear absorption.

6. ACKNOWLEDGEMENT

We gratefully acknowledge the support of the National Science Foundation grant ECS#8617066, DARPA/CNVEO and the Florida High Technology and Industry Council. In addition we thank A. Miller, B.S. Wherrett, and S. Koch for useful discussions.

7. REFERENCES

1. M. Sheik-bahae, A.A. Said, T.H. Wei, D.J. Hagan, and E.W. Van Stryland, "Sensitive Measurements of Optical Nonlinearities Using a Single Beam," to be published in IEEE J. Quantum Electron.
2. S.S. Jha and N. Bloembergen, "Nonlinear Optical Susceptibility in Group-IV and III-V Semiconductors," Phys. Rev. **171**, 891-898(1968).
3. C. Flytzanis, "Third Order Optical Susceptibilities in IV-IV and III-V Semiconductors," Phys. Lett. **31A**, 273-274(1970).
4. J.A. Van Vechten and D.E. Aspnes, "Franz-Keldysh contributions to Third-Order Optical Susceptibilities," Phys. Lett. **30A**, 346-347(1969).
5. C.C. Wang, "Empirical Relation between the Linear and the Third-Order Nonlinear Optical Susceptibilities," Phys. Rev. B, **2**, 2045-2048(1970).
6. N.L. Boling, A.J. Glass, and A. Owyong, "Empirical Relationships for Predicting Nonlinear Refractive Index Changes in Optical Solids," IEEE J. Quantum Electron. **QE-14**, 601-608(1978).
7. R. Adair, L.L. Chase, and S.A. Payne, "Nonlinear Refractive Index of Optical Crystals," Phys. Rev. B **39**, 3337-3349(1989).
8. D.A.B. Miller, C.T. Seaton, M.E. Prise, and S.D. Smith, "Band-gap Resonant Nonlinear Refraction in III-V Semiconductors," Phys. Rev. Lett. **47**, 197-200(1981).
9. M.H. Weiler, "Nonparabolicity and Exciton Effects in Two-Photon Absorption in Zincblende Semiconductors," Solid State Commun. **39**, 937-940(1981).
10. B.S. Wherrett, "Scaling Rules for Multiphoton Interband Absorption in Semiconductors," J. Opt. Soc. Am. B **1**, 67-72(1984).
11. H.S. Brandi and C.B. de Araujo, "Multiphoton Absorption Coefficients in Solids: a Universal Curve," J. Phys. C **16**, 5929-5936(1983).
12. E.W. Van Stryland, M.A. Woodall, H. Vanherzeele, and M.J. Soileau, "Energy Band-gap Dependence of Two-Photon Absorption," Opt. Lett. **10**, 490-492(1985).
13. P. Liu, W.L. Smith, H. Lotem, J.H. Bechtel, N. Bloembergen, and R.S. Adhav, "Absolute Two-Photon Absorption Coefficients at 355 and 266 nm," Phys. Rev. B **17**, 4620-4632(1978).
14. E.W. Van Stryland, Y.Y. Wu, D.J. Hagan, M.J. Soileau, and K. Mansour, "Optical Limiting with Semiconductors," J. Opt. Soc. Am. B, **5**, 1980-1989(1988).
15. J.M. Worlock, "Two-Photon Spectroscopy", in Laser Handbook, F.T. Arecchi and E.O. Schulz-DuBois, eds. (North-Holland Publ. Co., 1972) pp.1323-1369.
16. G.D. Mahan, "Theory of Two-Photon Spectroscopy in Solids," Phys. Rev. **170**, 825-838(1968).
17. F.V. Bunkin, "Two Quantum Transitions in Optics," Sov. Phys. JETP, **23**, 1121-1123(1966).
18. M. Sheik-bahae, A.A. Said, and E.W. Van Stryland, "High Sensitivity, Single Beam n_2 Measurements," Opt. Lett. **14**, 955-957(1989).
19. D.J. Hagan, E. Canto, E. Miesak, M.J. Soileau, and E.W. Van Stryland, "Picosecond Degenerate Four Wave Mixing Studies in ZnSe," paper, TUX, pp.160, Technical Digest of the Conference on Lasers and Electro-Optics, Anaheim, CA, OSA Technical Digest Series, No. 7, 1988.
20. B.S. Wherrett, A.C. Walker, and F.A.P. Tooley, "Nonlinear Refraction for CW Optical Bistability," in Optical Nonlinearities and Instabilities in Semiconductors, H. Haug, eds. (Academic Press, Inc. 1988.) pp.239-272.

SENSITIVE n_2 MEASUREMENTS USING A SINGLE BEAM

M. Sheik-Bahae, A.A. Said, T.H. Wei,
D.J. Hagan, E.W. Van Stryland and M.J. Soileau

CREOL
Center for Research in Electro Optics and Lasers
University of Central Florida, Orlando, FL 32826

We present a sensitive single beam technique for measuring nonlinear refraction in a variety of materials that offers simplicity, sensitivity and speed. The transmittance of a sample is measured through a finite aperture in the far-field as the sample is moved along the propagation path (z) of a focused Gaussian beam. The sign and magnitude of the nonlinearity is easily deduced from such a transmittance curve (Z-scan). Employing this technique a sensitivity of better than $\lambda/300$ wavefront distortion is achieved in n_2 measurements of BaF_2 using picosecond visible laser pulses.

Key words: BaF_2 ; CS_2 ; experimental technique; Kerr effect; nonlinear refraction; Z-scan

1. INTRODUCTION

We have recently reported a single beam method, which we refer to as a Z-scan, for measuring the sign and magnitude of the nonlinear refractive index n_2 . [1] In practice we have found that this method has a sensitivity comparable to interferometric methods. Here we describe this method in detail and demonstrate how it can be applied and analyzed for a variety of materials. We also present a simple method to minimize parasitic effects due to the presence of linear sample inhomogeneities.

Previous measurements of nonlinear refraction have used a variety of techniques including nonlinear interferometry [2], [3], degenerate four-wave mixing [4], nearly-degenerate three-wave mixing [5], ellipse rotation [6], beam distortion measurements [7], [8], and our recently reported Z-scan technique. The first three methods, namely nonlinear interferometry and wave mixing are potentially sensitive techniques but require a relatively complex experimental apparatus. Beam distortion measurements, on the other hand, are relatively insensitive and require detailed wave propagation analysis. The Z-scan technique is based on the principles of spatial beam distortion but offers simplicity as well as very high sensitivity.

We will describe this simple technique in Section II. Theoretical analyses of Z-scan measurements are given in Section III for a "thin" nonlinear medium. It will be shown that for many practical cases, nonlinear refraction and its sign can be obtained from a simple linear relationship between the observed transmittance changes and the induced phase distortion without the need for performing detailed calculations. In Section IV we present measurements of nonlinear refraction in a number of materials such as CS_2 , and transparent dielectrics at wavelengths of 532 nm, 1.06 μm and 10.6 μm . In CS_2 at 10 μm , for example, both thermo-optical and reorientational Kerr effects were identified using nanosecond and picosecond pulses respectively. We also describe how effects of linear sample inhomogeneities (eg. bulk index variations) can be effectively removed from the experimental data.

2. THE Z-SCAN TECHNIQUE

Using a single Gaussian laser beam in a tight focus geometry, as depicted in Fig. 1, we measure the transmittance of a nonlinear medium through a finite aperture in the far field as a function of the sample position z measured with respect to the focal plane. The following example will qualitatively elucidate how such a trace (Z-scan) is related to the nonlinear refraction of the sample. Assume, for instance, a material with a negative nonlinear refractive index and a thickness smaller than the diffraction length of the focused beam (a thin medium). This can be regarded as a thin lens of variable focal length. Starting the scan from a distance far away from the focus (negative z) the beam irradiance is low and negligible nonlinear refraction occurs; hence, the transmittance (D_2/D_1 in Fig. 1) remains relatively constant. As the sample is brought closer to focus, the beam irradiance increases leading to self-lensing in the sample. A negative self-lensing prior to focus will tend to collimate the beam, causing a beam narrowing at the aperture which results in an increase in the measured transmittance. As the scan in z continues and the sample passes the focal plane to the right

(positive z), the same self-defocusing increases the beam divergence leading to beam broadening at the aperture and, thus, a decrease in transmittance. This suggests that there is a null as the sample crosses the focal plane. This is analogous to placing a thin lens at or near the focus, resulting in a minimal change of the far field pattern of the beam. The Z-scan is completed as the sample is moved away from focus (positive z) such that the transmittance becomes linear since the irradiance is again low. Induced beam broadening and narrowing of this type have been previously observed and explained during nonlinear refraction measurements of some semiconductors.[9],[10] A similar technique was also previously used to measure thermally induced beam distortion of chemicals in solvents.[11]

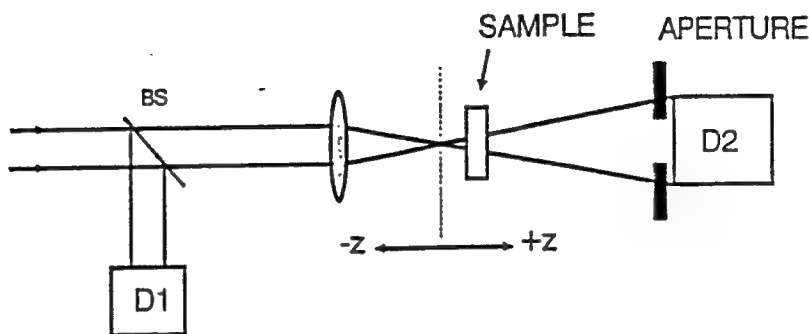


Fig.1 The Z-scan experimental apparatus in which the ratio $D2/D1$ is recorded as a function of the sample position z .

A pre-focal transmittance maximum (peak) followed by a post-focal transmittance minimum (valley) is, therefore, the Z-scan signature of a negative refractive nonlinearity. Positive nonlinear refraction, following the same analogy, gives rise to an opposite valley-peak configuration. It is an extremely useful feature of the Z-scan method that the sign of the nonlinear index is immediately obvious from the data, and as we will show in the following section the magnitude can also be easily estimated using a simple analysis for a thin medium.

In the above picture describing the Z-scan, one must bear in mind that a purely refractive nonlinearity was considered assuming that no absorptive nonlinearities (such as multiphoton or saturation of absorption) are present. Qualitatively, multiphoton absorption suppresses the peak and enhances the valley, while saturation produces the opposite effect. The sensitivity to nonlinear refraction is entirely due to the aperture, and removal of the aperture completely eliminates the effect. However, in this case the Z-scan will still be sensitive to nonlinear absorption. Nonlinear absorption coefficients could be extracted from such "open" aperture experiments.

3. THEORY

Much work has been done in investigating the propagation of intense laser beams inside a nonlinear material and the ensuing self-refraction [12], [13]. Considering the geometry given in Fig. 1, we will formulate and discuss a simple method for analyzing the Z-scan data based on modifications of existing theories.

In general, various order nonlinearities can be considered; however, for simplicity, we first examine only a cubic nonlinearity where the index of refraction n is expressed in terms of nonlinear indices n_2 (esu) or γ (m²/W) through:

$$n = n_0 + \frac{n_2}{2} |E|^2 = n_0 + \gamma I \quad (1)$$

where n_0 is the linear index of refraction, E is the peak electric field (cgs), and I denotes the irradiance (MKS) of the laser beam within the sample. [n_2 and γ are related through the conversion formula, n_2 (esu) = $(cn_0/40\pi)\gamma$ (m²/W), where c (m/sec) is the speed of light in vacuum]. Assuming a TEM₀₀ Gaussian beam of beam waist radius w_0 traveling in the + z direction, we can write E as:

$$E(z, r, t) = E_0(t) \frac{w_0}{w(z)} \exp \left[-\frac{r^2}{w^2(z)} - \frac{ikr^2}{2R(z)} \right] e^{-i\phi(z, t)}, \quad (2)$$

where $w^2(z) = w_0^2(1 + z^2/z_0^2)$ is the beam radius, $R(z) = z(1 + z_0^2/z^2)$ is the radius of curvature of the wavefront at z , $z_0 = kw_0^2/2$ is the diffraction length of the beam, $k = 2\pi/\lambda$ is the wave vector and λ is the laser wavelength, all in free space. $E_0(t)$ denotes the radiation electric field at the focus and contains the temporal envelope of the laser pulse. The $\phi(z, t)$ term contains all the radially uniform phase variations. As we are only concerned with calculating the radial phase variations $\Delta\phi(r)$, the slowly varying envelope approximation (SVEA) applies, and all other phase changes that are uniform in r are ignored.

If the sample length is small enough that changes in the beam diameter within the sample due to either diffraction or nonlinear refraction can be neglected, the medium is regarded as "thin", in which case the self-refraction process is referred to as "external self-action". Such an assumption simplifies the problem considerably, and the amplitude \sqrt{I} and phase ϕ of the electric field as a function of z' are now governed in the SVEA by a pair of simple equations:

$$\frac{d\Delta\phi}{dz'} = \Delta n(I) k, \quad (3)$$

$$\frac{dI}{dz'} = -\alpha I, \quad (4)$$

where z' is the propagation depth in the sample and α is the linear absorption coefficient. Note that z' should not be confused with the sample position z . In the case of a cubic nonlinearity, Eqns. 3 and 4 are solved to give the phase shift at the exit surface of the sample, which simply follows the radial variation of the incident irradiance at a given position of the sample z . Thus,

$$\Delta\phi(z, r, t) = \Delta\phi_0(z, t) \exp \left[-\frac{2r^2}{w^2(z)} \right]. \quad (5-a)$$

$$\Delta\phi_0(z, t) = \frac{\Delta\Phi_0(t)}{1 + z^2/z_0^2}. \quad (5-b)$$

$\Phi_0(t)$, the on-axis phase shift at the focus, is defined as,

$$\Delta\Phi_0(t) = k\Delta n_0(t) \frac{1 - e^{-\alpha L}}{\alpha}, \quad (6)$$

where L is the sample length, and $\Delta n_0 = \gamma I_0(t)$ with $I_0(t)$ being the on-axis irradiance at focus (ie. $z=0$). Again we take $I_0(t)$ as the irradiance within the sample to account for Fresnel reflection losses.

The complex electric field after the sample, E' , now contains the nonlinear phase distortion,

$$E' = E(z, r, t) e^{-\alpha L/2} e^{i\Delta\phi(z, r, t)}. \quad (7)$$

By virtue of Huygen's principle one can obtain the far field pattern of the beam at the aperture plane through a zeroth order Hankel transformation of E' . [14] We will follow a more convenient treatment applicable to Gaussian input beams which we refer to as the "Gaussian Decomposition" (GD) method given by Weaire et. al. [15], in which they decompose the complex electric field at the exit plane of the sample into a summation of Gaussian beams through a Taylor series expansion of the nonlinear phase term $e^{i\Delta\phi(z, r, t)}$ in Eq. 7. That is,

$$e^{i\Delta\phi(z, r, t)} = \sum_{m=0}^{\infty} \frac{[i\Delta\phi_0(z, t)]^m}{m!} e^{-2mr^2/w^2(z)}. \quad (8)$$

Each Gaussian beam can now be simply propagated to the aperture plane where they will be resummed to reconstruct

the beam. When including the initial beam curvature for the focused beam, we derive the resultant electric field pattern at the aperture as:

$$E_a(r, t) = E(z, r=0, t) e^{-\alpha L/2} \sum_{m=0}^{\infty} \frac{(i\Delta\phi_0(t))^m}{m!} \left(g^2 + \frac{d^2}{d_m^2} \right)^{-\frac{1}{2}} \exp \left[-\frac{r^2}{w_m^2} - \frac{ikr^2}{2R_m} + i\theta_m \right], \quad (9)$$

where d is the propagation distance in free space from the sample to the aperture plane, and $g=1+d/R$, $R=R(z)$ being the beam radius of curvature at the sample. As long as the far field condition is met, d can be considered independent of the sample position z resulting in symmetric Z-scans. The remaining parameters in Eq. 9 are expressed as:

$$w_{m0}^2 = \frac{w^2(z)}{2m+1}, \quad d_m = \frac{kw_{m0}^2}{2}, \quad w_m^2 = w_{m0}^2 \left[g^2 + \frac{d^2}{d_m^2} \right],$$

$$R_m = d \left[1 - \frac{g}{g^2 + d^2/d_m^2} \right]^{-1}, \quad \text{and } \theta_m = \tan^{-1} \left[\frac{d/d_m}{g} \right].$$

The expression given by Eq. 9 is a general case of that derived in Ref. [15] where they considered a collimated beam ($R=\infty$) for which $g=1$. We find that this GD method is very useful for the small phase distortions detected with the Z-scan method since only a few terms of the sum in Eq. 9 are needed. The method is also easily extended to higher order nonlinearities.

The transmitted power through the aperture is obtained by spatially integrating $E_a(r, t)$ up to the aperture radius r_a , giving,

$$P_T(\Delta\Phi_0(t)) = \frac{c\epsilon_0 n_0}{2} \int_0^{r_a} |E_a(r, t)|^2 r dr. \quad (10)$$

Including the pulse temporal variation, the normalized Z-scan transmittance $T(z)$ can be calculated as:

$$T(z) = \frac{\int_{-\infty}^{\infty} P_T(\Delta\Phi_0(t)) dt}{S \int_{-\infty}^{\infty} P_i(t) dt}, \quad (11)$$

where $P_i(t) = \pi w_0^2 I_0(t)/2$ is the instantaneous input power (within the sample) and S is the aperture transmittance in the linear regime.

We first consider an instantaneous nonlinearity and a temporally square pulse to illustrate the general features of the Z-scan. This is equivalent to assuming cw radiation and the nonlinearity has reached the steady state. The normalized transmittance, $T(z)$, in the far field, is shown in Fig. 2 for $\Delta\Phi_0 = \pm 0.1$ and a small aperture ($S=0.01$). They exhibit the expected features, namely a valley-peak (v-p) for the positive nonlinearity and a peak-valley (p-v) for the negative one. For a given $\Delta\Phi_0$, the magnitude and shape of $T(z)$ do not depend on the wavelength or geometry as long as the far field condition for the aperture plane is satisfied. The aperture size S , however, is an important parameter since a large aperture reduces the variations in $T(z)$. This reduction is more prominent in the peak where beam narrowing occurs and can result in a peak transmittance which cannot exceed $(1-S)$. Needless to say, for very large aperture or no aperture ($S=1$), the effect vanishes and $T(z) = 1$ for all z and $\Delta\Phi_0$. For small $|\Delta\Phi_0|$, the peak and valley occur at the same distance with respect to focus, and for a cubic nonlinearity this distance is found to be $\approx 0.85z_0$. With larger phase distortions ($|\Delta\Phi_0| > 1$) this symmetry no longer holds and both peak and valley move toward $\pm z$ for the corresponding sign of nonlinearity ($\pm\Delta\Phi_0$) such that their separation remains relatively constant given by,

$$\Delta Z_{p-v} \approx 1.7z_0. \quad (12)$$

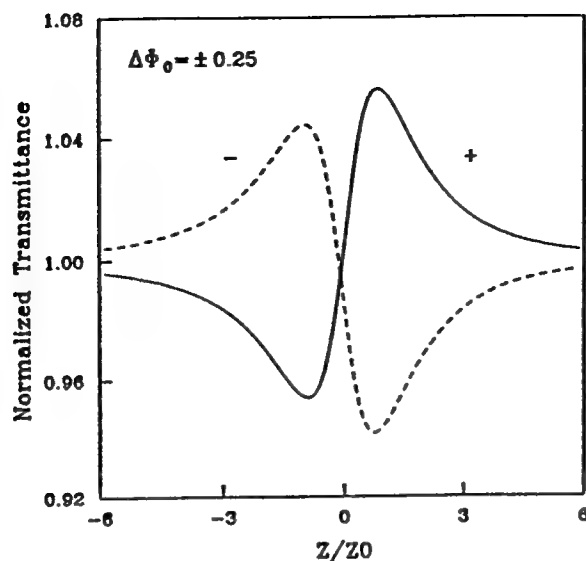


Fig. 2 Calculated Z-scan transmittance curves for a cubic nonlinearity with either polarity and a small aperture ($S=0.01$).

We can define an easily measurable quantity ΔT_{p-v} as the difference between the normalized peak and valley transmittance: $T_p - T_v$. The variation of this quantity as a function of $|\Delta\Phi_0|$, as calculated for various aperture sizes is illustrated in Fig. 3. These curves exhibit some useful features. First, for a given order of nonlinearity, they can be considered universal. In other words, they are independent of the laser wavelength, geometry (as long as the far field condition is met) and the sign of nonlinearity. Second, for all aperture sizes, the variation of ΔT_{p-v} is found to be nearly dependent on $|\Delta\Phi_0|$. Particularly for on axis ($S=0$) we find,

$$\Delta T_{p-v} \approx 0.406 |\Delta\Phi_0| \quad \text{for} \quad |\Delta\Phi_0| \leq \pi, \quad (13-a)$$

be accurate to within 0.5 percent. As shown in Fig. 3, for larger apertures, the linear coefficient 0.405 decreases such that with $S=0.5$ it becomes 0.34 and at $S=0.7$ it reduces to 0.29. Based on a numerical fitting, the following relationship can be used to include such variations within a $\pm 2\%$ accuracy;

$$\Delta T_{p-v} \approx 0.406(1-S)^{0.25} |\Delta\Phi_0| \quad \text{for} \quad |\Delta\Phi_0| \leq \pi. \quad (13-b)$$

The implications of Eqns. 13-a and 13-b are quite promising in that they can be used to readily estimate the nonlinear index (n_2) with good accuracy after a Z-scan is performed. What is most intriguing about these expressions is that they reveal the highly sensitive nature of the Z-scan technique. For example, if our experimental apparatus and data acquisition systems are capable of resolving transmission changes ΔT_{p-v} of $\approx 1\%$, we will be able to measure phase changes corresponding to less than $\lambda/250$ wavefront distortion. Achieving such sensitivity, however, requires relatively good optical quality of the sample under study. We describe in the experimental section IV a means to minimize problems arising from poor optical quality samples.

We can now easily extend the steady state cw results to include transient effects along with pulsed radiation by using the time averaged index change $\langle \Delta n_0(t) \rangle$ where,

$$\langle \Delta n_0(t) \rangle = \frac{\int_{-\infty}^{\infty} \Delta n_0(t) I_0(t) dt}{\int_{-\infty}^{\infty} I_0(t) dt}, \quad (14)$$

The time averaged $\langle \Delta\Phi_0(t) \rangle$ is related to $\langle \Delta n_0(t) \rangle$ through Eq. 6. With a nonlinearity having instantaneous response and decay times relative to the pulsewidth of the laser, one obtains for a temporally Gaussian pulse:

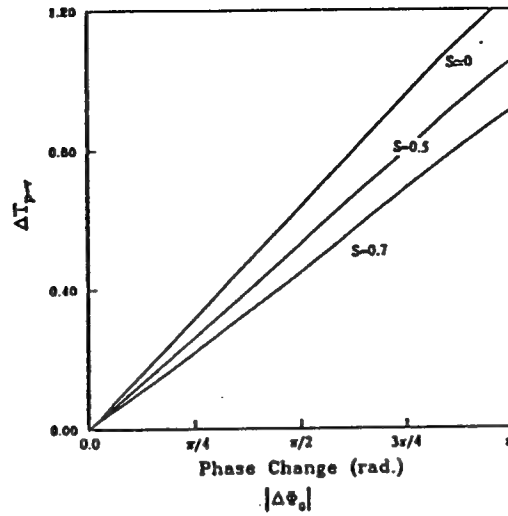


Fig.3 Calculated ΔT_{p-v} as a function of the phase shift at the focus ($\Delta\Phi_0$). The sensitivity, as indicated by the slope of the curves, decreases slowly for larger aperture sizes ($S>0$).

$$\langle \Delta n_0(t) \rangle = \Delta n_0 / \sqrt{2}, \quad (15)$$

where Δn_0 now represents the peak-on-axis index change at the focus. For a cumulative nonlinearity having a decay time much longer than the pulsewidth (eg. thermal), the instantaneous index change is given by the following integral:

$$\Delta n_0(t) = A \int_{-\infty}^t I_0(t') dt', \quad (16)$$

where A a constant which depends on the nature of the nonlinearity. If we substitute Eq. 16 into Eq. 14 we obtain a fluence averaging factor of 1/2. That is,

$$\langle \Delta n_0(t) \rangle = \frac{1}{2} A F, \quad (17)$$

where F is the pulse fluence at focus within the sample. Interestingly, the factor of 1/2 is independent of the temporal pulse shape.

4. EXPERIMENTAL RESULTS

We examined the nonlinear refraction of a number of materials using the Z-scan technique. Fig. 4 shows a Z-scan of a 1 mm thick cuvette with NaCl windows filled with CS_2 using 300 ns TEA CO_2 laser pulses having an energy of 0.85 mJ. The peak-valley configuration of this Z-scan is indicative of a negative (self-defocusing) nonlinearity. The solid line in Fig. 4 is the calculated result using $\langle \Delta\Phi_0 \rangle = -0.6$ which gives an index change of $\langle \Delta n_0 \rangle \approx -1 \times 10^{-3}$. As mentioned earlier such detailed theoretical fitting is not necessary for obtaining $\langle \Delta n_0 \rangle$ (only ΔT_{p-v} is needed). The defocusing effect shown in Fig. 4 is attributed to a thermal nonlinearity resulting from linear absorption of CS_2 ($\alpha \approx 0.22 \text{ cm}^{-1}$ at 10.6 μm). The risetime of a thermal lens in a liquid is determined by the acoustic transit time, $\tau = w_0/v_s$, where v_s is the velocity of sound in the liquid [17]. For CS_2 with $v_s \approx 1.5 \times 10^5 \text{ cm/sec}$ and having $w_0 \approx 60 \mu\text{m}$, we obtain a risetime of $\approx 40 \text{ ns}$ which is almost an order of magnitude smaller than the TEA laser pulsewidth. Furthermore, the relaxation of the thermal lens, governed by thermal diffusion, is of the order of 100 ms.[17] Therefore, we regard the nonuniform heating caused by the 300 ns pulses as quasi-steady state, in which case, from Eq. 17, the average on-axis nonlinear index change at focus can be determined in terms of the thermo-optic coefficient, dn/dT , as:

$$\langle \Delta n_0 \rangle \approx \frac{dn}{dT} \frac{F_0 \alpha}{2\rho C_v}, \quad (18)$$

where F_0 is the fluence, ρ is the density, C_v is the specific heat and $1/2$ denotes the fluence averaging factor. With the known value of $\rho C_v \approx 1.3 \text{ J/}^\circ\text{Kcm}^3$ for CS_2 , we deduce $dn/dT \approx -(8.3 \pm 1.0) \times 10^{-4} \text{ }^\circ\text{C}^{-1}$ which is in good agreement with the reported value of $-8 \times 10^{-4} \text{ }^\circ\text{C}^{-1}$ [16]

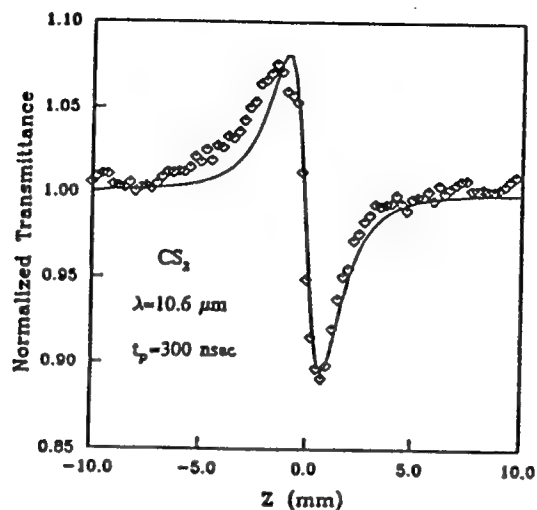


Fig.4 Measured Z-scan of a 1mm thick CS_2 cell using 300 ns pulses at $\lambda=10.6 \mu\text{m}$ indicating thermal self-defocusing. The solid line is the calculated result with $\Delta\Phi_0=-0.6$ and 60% aperture ($S=0.6$).

With ultrashort pulses, nonlocal nonlinearities such as thermal or electrostriction are no longer significant. Particularly, in CS_2 , the molecular reorientational Kerr effect becomes the dominant mechanism for nonlinear refraction. CS_2 is frequently used as a standard reference nonlinear material.[18,19] We have used picosecond pulses at $10.6 \mu\text{m}$, $1.06 \mu\text{m}$ and at $0.53 \mu\text{m}$ to measure n_2 in CS_2 . We obtain the same value of n_2 , within errors, at all three wavelengths, $(1.5 \pm 0.6) \times 10^{-11}$ esu at $10.6 \mu\text{m}$, $(1.3 \pm 0.3) \times 10^{-11}$ esu at $1.06 \mu\text{m}$ and $(1.2 \pm 0.2) \times 10^{-11}$ esu at $0.53 \mu\text{m}$. The external self-focusing arising from the Kerr effect in CS_2 is shown in Fig. 5, where a Z-scan of a 1mm cell using 27 ps (FWHM) pulses focused to a beam waist w_0 of $26 \mu\text{m}$ from a frequency doubled Nd:YAG laser is illustrated. Its valley-peak configuration indicates the positive sign of n_2 . With $\Delta T_{p-v} = 0.24$, and using Eq. 13-b with a 40 percent aperture ($S = 0.4$), one readily obtains a $\langle \Delta n_0 \rangle = 5.6 \times 10^{-5}$. Using the peak irradiance of 2.6 GW/cm^2 , this value of $\langle \Delta n_0 \rangle$ corresponds to an $n_2 \approx (1.2 \pm 0.2) \times 10^{-11}$ esu.

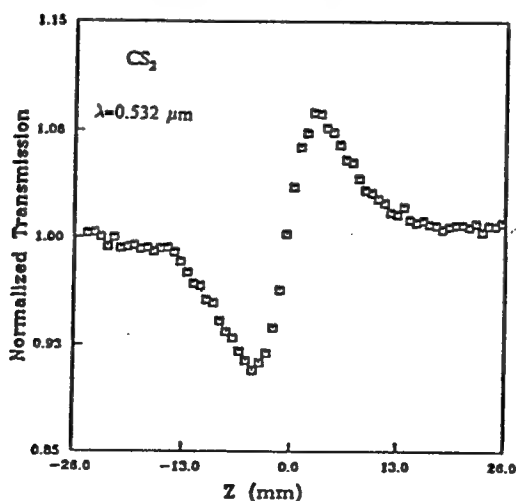


Fig.5 Measured Z-scan of a 1mm thick CS_2 cell using 27 ps pulses at $\lambda=532 \text{ nm}$. It depicts the self-focusing effect due to the reorientational Kerr effect.

The main source of uncertainty in the value of n_2 is the absolute measurement of the irradiance. A plot of ΔT_{p-v} versus peak laser irradiance as measured from various Z-scans on the same CS_2 cell is shown in Fig. 6. The linear behavior of this plot follows Eq. 13 as derived for a cubic nonlinearity.

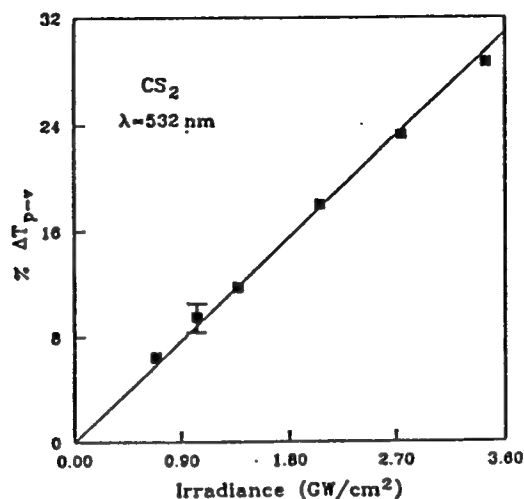


Fig.6 T_{p-v} in percent as a function of the peak irradiance from the Z-scan data of CS_2 at 532 nm, indicative of the reorientational Kerr effect.

Transparent dielectric window materials have relatively small nonlinear indices. Recently, Adair et. al. [20] have performed a careful study of the nonlinear index of refraction of a large number of such materials in a nearly degenerate-three-wave-mixing scheme at $\lambda \approx 1.06 \mu m$. Using the Z-scan technique, we examined some of these materials at 532 nm. For example, the result for BaF_2 (2.4mm thick) is shown in Fig.7, using the same beam parameters as for CS_2 . This Z-scan was obtained by purposely lowering the pulse energy to $2 \mu J$ in order to observe the resolution and the sensitivity of this measurement. With a $\Delta T_{p-v} \approx 0.035$, this Z-scan corresponds to a $\lambda/75$ induced phase distortion. For a unity signal-to-noise-ratio for our particular laser system, it is seen from Fig. 7 that the sensitivity to phase distortion is better than $\lambda/300$. For laser systems having better amplitude and pulsewidth stability, the sensitivity should be correspondingly increased.

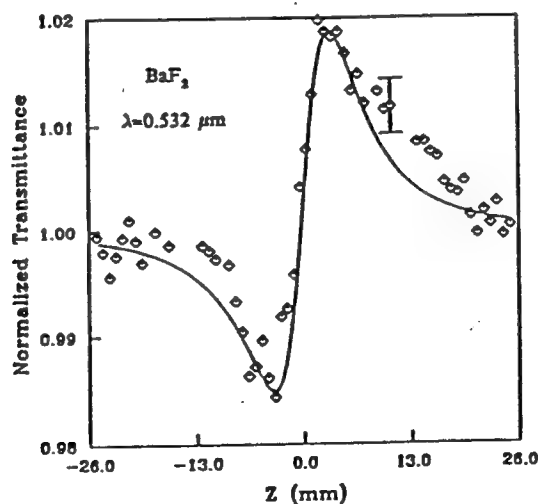


Fig.7 Measured Z-scan of a 2.4 mm thick BaF_2 sample using 20 ps pulses at $\lambda=532$ nm indicating the self-focusing due to the electronic Kerr effect. The solid line is the calculated result with $\Delta\Phi_0=0.085$ corresponding to $\approx\lambda/75$ total phase distortion. The error bar shown corresponds to approximately $\lambda/480$ induced phase distortion.

Aside from the statistical fluctuations of the laser irradiance, surface imperfections or wedge in the sample may lead to systematic transmittance changes with z that could mask the effect of nonlinear refraction. We found, however, that such "parasitic" effects may be substantially reduced by subtracting a low irradiance background Z-scan from the high irradiance scan. A simple computer simulation of this process assuming that the surface imperfections do not disturb the circular symmetry of the beam or cause any beam steering, indicated that background subtraction indeed recovers the original ΔT_{p-v} arising from the nonlinear refraction effect even for quite large surface disturbances $\Delta\phi_s$ of up to π .

Returning to the Z-scan of Fig. 7, we obtain $n_2 \approx (0.8 \pm 0.15) \times 10^{-13}$ esu for BaF_2 at 532 nm, which is in close agreement with the reported values of 0.7×10^{-13} esu [20] and 1.0×10^{-13} esu [3] as measured at $1.06 \mu\text{m}$ using more complex techniques of nearly degenerate-three-wave-mixing and time-resolved-nonlinear-interferometry, respectively. Similarly for MgF_2 , we measure $n_2 \approx 0.25 \times 10^{-13}$ esu at 532 nm as compared to the reported value of 0.32×10^{-13} esu at $1.06 \mu\text{m}$ for this material as given in [20]. Dispersion in n_2 for these materials between 1 and $0.5 \mu\text{m}$ is expected to be minimal. It should be noted that the n_2 values extracted from the Z-scans are absolute rather than relative measurements. If the beam parameters are not accurately known, however, it should be possible to calibrate the system by using a standard nonlinear material such as CS_2 .

5. CONCLUSION

We have demonstrated a simple single beam technique that is sensitive to less than $\lambda/300$ nonlinearly induced phase distortion. Using the Z-scan data the magnitude and sign of the nonlinear refraction can be simply determined. We have derived relations that allow the refractive index to be obtained directly from the Z-scan data without resorting to computer fits. We have applied this technique to several materials displaying a variety of nonlinearities on different time scales. It is expected that this method will be a valuable tool for experimenters searching for highly nonlinear materials.

6. ACKNOWLEDGEMENT

We gratefully acknowledge the support of the National Science Foundation grant #ECS-8617066, and the support of DARPA/CNVEO and the Florida High Technology and Industry Council. We also wish to thank Alan Miller for helpful discussions.

7. REFERENCES

1. Sheik-Bahae, M.; Said, A.A.; Van Stryland, E. W. "High Sensitivity Single Beam n_2 Measurement," *Opt. Lett.* **14**, 955-957 (1989).
2. Weber, M.J.; Milam, D.; Smith, W.L. "Nonlinear Refractive Index of Glasses and Crystals," *Optical Engineering*, **17**, 463-469 (1978).
3. Moran, M.J.; She, C.Y.; Carman, R.L. "Interferometric Measurements of Nonlinear Refractive-Index Coefficient Relative to CS_2 in Laser-System-Related Materials," *IEEE J. Quantum Electron.* **QE-11**, 259-263 (1975).
4. Friberg, S.R.; Smith, P.W. "Nonlinear Optical Glasses for Ultrafast Optical Switches," *IEEE J. Quantum Electron.* **QE-23**, 2089-2094 (1987).
5. Adair, R.; Chase, L.L.; Payne, S.A. "Nonlinear refractive index measurement of glasses using three-wave frequency mixing," *J. Opt. Soc. Am. B* **4**, 875-881 (1987).
6. Owyong, A. "Ellipse Rotations Studies in Laser Host Materials," *IEEE J. Quantum Electron.* **QE-9**, 1064-1069 (1973).
7. Williams, W.E.; Soileau, M.J.; Van Stryland, E.W. "Optical Switching and n_2 Measurements in CS_2 ," *Opt. Comm.* **50**, 256-260 (1984).
8. Williams, W.E.; Soileau, M.J.; Van Stryland, E.W. "Simple direct measurements of n_2 ," *Proc. 15th Annual Symp. on Optical Materials for High Power Lasers*, Boulder, CO (1983).
9. Hill, J.R.; Parry, G.; Miller, A. "Non-linear Refraction Index Changes in CdHgTe at 175K with $1.06 \mu\text{m}$ Radiation," *Opt. Commun.*, **43**, 151-156 (1982).
10. Boggess, T.F.; Moss, S.C.; Boyd, I.W.; Smirl, A.L. "Picosecond Nonlinear-Optical Limiting in Silicon," in *Ultrafast Phenomena IV*, edited by D.H. Huston and K.B. Eisenthal (Springer-Verlag), (New York, 1984). pp. 202.
11. Harris, J.M.; Dovichi, N.J. "Thermal Lens Calorimetry," *Analytical Chem.* **52**, 695-700 (1980).
12. Akhmanov, S.A.; Sukhorokov, A.D.; Khokhlov, R.V. "Self-focusing and Diffraction of Light in a Nonlinear Medium," *Sov. Phys. Vspkhi*; English Translation, **10**, 609 (1968).
13. Smith, W.L.; Bechtel, J.H.; Bloembergen, N. "Dielectric-Breakdown Threshold and Nonlinear-refractive Index Measurements with Picosecond Laser Pulses," *Phys. Rev. B* **12**, 706-714 (1975).
14. Gaskill, J.D. *Linear Systems, Fourier Transforms, and Optics*, John Wiley & Sons, New York, 1978.

15. Weaire, D.; Wherrett, B.S.; Miller, D.A.B.; Smith, S.D. "Effect of Low-Power Nonlinear refraction on laser beam propagation in InSb," Opt. Lett., 4, 331-333 (1974).
16. Raman, V.; Venkataraman, K.S. "Determination of the adiabatic piezo-optic coefficient of liquids." Proc. Roy. Soc. A, 171, 137 (1939).
17. Hayes, J.N. "Thermal Blooming of Laser Beams in Fluids," Appl. Opt. 2, 455-461 (1972).
18. Ho, P.P.; Alfano, R.R. "Optical Kerr effects in Liquids," Phys. Rev. A, 20, 2070-2087 (1979).
19. Thomas, P.; Jares, A.; Stoicheff, B.P. "Nonlinear Refractive Index and "DC" Kerr Constant of Liquid CS₂," IEEE J. Quantum Electron. QE-10, 493-494(1974).
20. Adair, R.; Chase, L.L.; Payne, A. "Nonlinear Refractive Index of Optical Crystals," Phys. Rev. B, 39, 3337-3350(1989).

COMMENTS

Question: Are your results affected by surface nonuniformity?

Answer: If the scatter is homogeneous then it's no problem. If it's grossly inhomogeneous or if the surface is corrugated or something, then it really effects the technique quite a bit. In fact, you can use it to measure surface quality as well if you turn the radiance down to very low values. We have done experiments where we had rough surfaces and just took data from lower radiance values. Then we took the data from higher radiance values and just divided it up. We still get good signal, but it does degrade as the quality of the optics degrade.

RELATION BETWEEN n_2 AND TWO-PHOTON ABSORPTION

M. Sheik-Bahae, D.J. Hagan, E.W. Van Stryland,
T.H. Wei, A.A. Said, E. Canto, and A. Miller

Center for Research in Electro-Optics and Lasers
and the Department of Physics
University of Central Florida
Orlando, FL 32816

We present evidence from nonlinear refractive index measurements, two-photon absorption measurements, and four-wave mixing measurements on semiconductors showing that the bound electronic nonlinearity can be calculated from two-photon absorption dispersion via a simple Kramers-Kronig analysis. This analysis shows n_2 changing from positive to negative as the photon energy approaches the band-gap energy, consistent with observations. Additionally, this simple calculation, which assumes two parabolic bands, gives good agreement with measured values of n_2 in wide-gap dielectrics that are 2 to 3 orders of magnitude smaller than in semiconductors.

Key words: nonlinear refraction, two-photon absorption, Kramers-Kronig, four-wave mixing, semiconductors

Optical nonlinearities in semiconductors and transparent materials have been the subject of extensive studies during the past two decades. Of particular interest have been the third order effects in semiconductors. This interest has primarily dealt with the production of a real carrier plasma and the associated negative change in the refractive index. In this letter we will discuss the smaller and "faster" nonlinearities due to bound electrons which is positive for photon energies much less than the bandgap energy. The analogy in wide-gap dielectric materials is to self-focusing from the positive nonlinear refractive index n_2 (eg. self-focusing in glasses). Recently we found that measurements in semiconductors substantially above the two-photon-absorption (2PA) edge yield negative values for n_2 . [1] This dramatic dispersion of n_2 can be partially explained using a nonlinear Kramers-Kronig (KK) relation between n_2 and the 2PA coefficient β , or between the real and imaginary parts of the third order nonlinear susceptibility $\chi^{(3)}$. The magnitude and dispersion of n_2 is of interest because of its importance in nonlinear propagation in fibers, fast optical switching, self-focusing and damage in optical materials, and optical limiting in semiconductors. Below, we describe our calculation of the bound electronic Kerr effect, n_2 , and compare our results with data for a large number of materials, including semiconductors and dielectrics.

This n_2 arises from the real part of $\chi^{(3)}$, and is defined through the refractive index change Δn , where

$$\Delta n(\omega) = \gamma(\omega) I_\omega = \frac{n_2(\omega)}{2} |E_\omega|^2, \quad (1)$$

with I_ω and E_ω being the irradiance and electric field at frequency ω respectively and $n_2 = (2\pi/n_0) \text{Re}\{\chi^{(3)}\}$. The linear refractive index is n_0 , and γ and n_2 are related by $n_2(\text{esu}) = (cn_0\gamma/40\pi)(\text{MKS})$ with c the speed of light.

Most theoretical calculations of n_2 have been confined to the zero frequency limit. [2-6] Semi-empirical formulations have been most successful in predicting the magnitude of n_2 . [5, 6] For example, the formula obtained by Boling, Glass and Owyong (BGO) in relating n_2 to the linear index (n_0) and the dispersion of n_0 in terms of the Abbe number has been successfully applied to a large class of transparent materials. [6, 7] Their theory predicts the low frequency magnitude of n_2 . We describe a KK method of calculation of n_2 that predicts the dispersion as well as the magnitude of n_2 . This calculation assumes that 2PA gives the dominant contribution to n_2 and that other contributions from Raman and the AC Stark effect or virtual band-blocking are ignored. We will return to this assumption later.

Based on the principle of causality, the KK transformation states that a change in the refractive index (Δn) at ω is associated with changes in the absorption coefficient ($\Delta\alpha$) throughout the spectrum (ω') and vice versa. We write this as:

$$\Delta n(\omega, \xi) = \frac{c}{\pi} \int_0^{\infty} \frac{\Delta\alpha(\omega', \xi)}{\omega^2 - \omega'^2} d\omega', \quad (2)$$

where c is the velocity of light in vacuum and ξ is a parameter (or parameters) denoting the "cause" of change in the absorption. The cause need not be of optical origin but of any external perturbation such as thermal excitation, etc. For cases where an electron-hole plasma is injected, the consequent change of absorption has been used to obtain the plasma contribution to the refractive index. In this case, the ξ parameter is taken as the change in plasma density (ΔN) regardless of the mechanism of generation of the plasma or the pump frequency.[8] In the case of 2PA the change is due to the presence of a pump field at Ω (ie. $\xi=\Omega$). The corresponding nonlinear refraction is $\Delta n(\omega, \Omega)$, which gives the dispersion of the index change with ω . For the case of self-refraction, $\omega=\Omega$, and this gives what is commonly referred to as n_2 . Van Vechten and Aspnes [4] obtained the low frequency limit of n_2 from a similar KK transformation of the Franz-Keldysh electro-absorption effect where, in this case, ξ is the DC field. The bound electronic contribution to $\chi^{(3)}$ can originate from various absorptive counterparts that are quadratic functions of the pump field. Effects of this order may include 2PA, the electronic Raman effect, and the optical Stark effect. Here we consider only 2PA.

A wealth of experimental and theoretical work regarding 2PA in semiconductors and crystalline materials exists. In accordance with the predictions derived from either second order perturbation theory [9,10] or a Keldysh-type formalism [11], the 2PA coefficients of the semiconductors studied in Ref. [12] were found to be in good agreement with the theoretical expression given as:

$$\beta(2\omega') = K \frac{\sqrt{E_p}}{n_0^2 E_g} F_2(2\hbar\omega'/E_g), \quad (3)$$

where K is a material independent constant and E_p (related to the Kane momentum parameter, a momentum matrix element) is nearly material independent and possesses a value of ≈ 21 eV for most direct gap semiconductors. These data are shown in Fig. 1. Note $\beta = (4\pi\omega/n_0) \text{Im}\{\chi^{(3)}\}$. The function F_2 is only a function of the ratio of the photon energy $\hbar\omega'$ to E_g (ie. the optically coupled states). The functional form of F_2 reflects the assumed band structure and the intermediate states considered in calculating the 2PA transition rate. The simplest model assumes a pair of isotropic and parabolic bands and intermediate states that are degenerate to initial (valence) or final (conduction) states. Neglecting the Coulomb interaction, this simple formalism yields:[10]

$$F_2(2x) = \frac{(2x-1)^{3/2}}{(2x)^5} \quad \text{for } 2x > 1. \quad (4)$$

Figure 2 shows the dispersion of β as given by Eq. 4.

The best fit to the data of Ref. 12 using Eqs. 3 and 4 gave $K=3.1 \times 10^3$ (see the line in Fig. 1) in units such that E_p and E_g were in eV and β was in cm/GW, while theory gave 5.2×10^3 [9]. When nonparabolicity was included the average β was 26% lower than theory; however, the frequency dependence of β changed very little. Interestingly, Eqs. 3 and 4 also give a fair estimate of β for a number of transparent materials measured using the 3rd and 4th harmonics of picosecond Nd:YAG laser pulses.[13,14]

Equations 3 and 4 pertain to a degenerate case where the two photons involved are of the same frequency and source. For a KK transformation the nondegenerate 2PA coefficient for two distinct frequencies is needed (ie. Ω the "cause" and ω' the integration variable in Eq. 2). Extending the same simple model to obtain the non-degenerate 2PA coefficient has led to dispersion functions that are afflicted with "infrared divergences" [15,16]. This has been a common problem originating from the use of the A-p perturbation to calculate the bound electronic nonlinear susceptibilities in solids.[15]

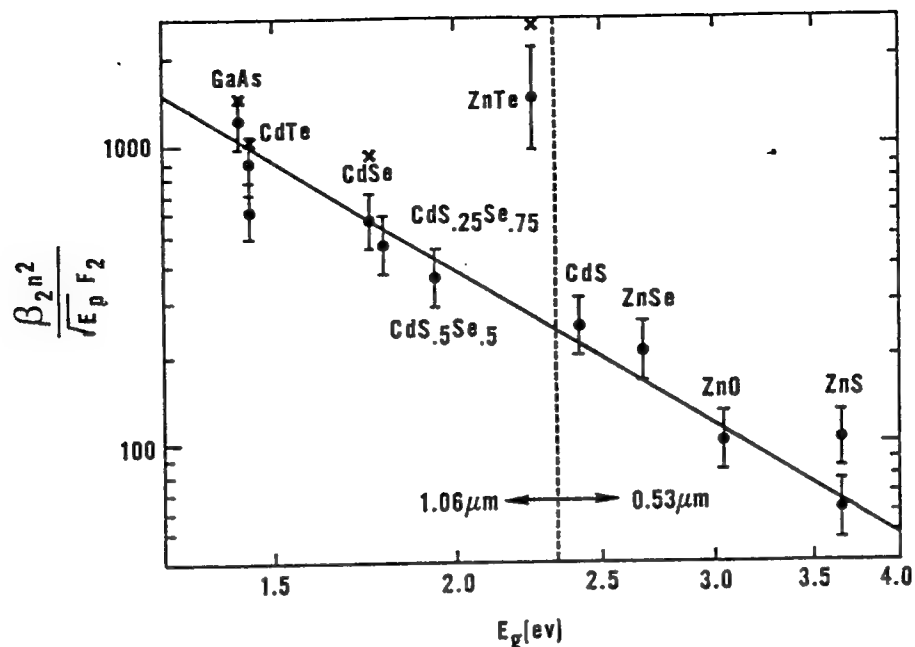


Figure 1. A log-log plot of the scaled value of β as a function of E_g to show the E_g^3 dependence. The line is a fit to the data using the F_2 of Eq. 4.

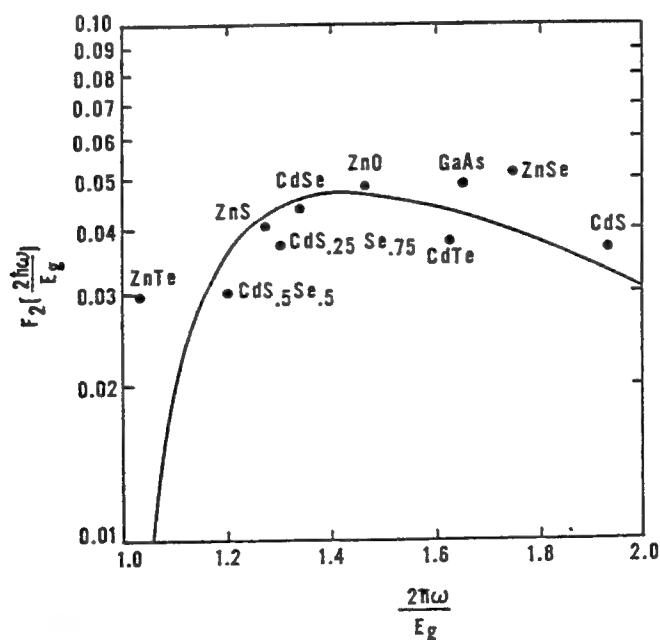


Figure 2. A semilogarithmic plot of F_2 as a function of $2\hbar\omega/E_g$ with the data of Fig. 1 superimposed.

Although special cases have been considered [17], a general theory that would rigorously address the proper scaling and dispersion of the non-degenerate 2PA is yet to be developed. For this reason we assume that the dispersion function F_2 for the nondegenerate 2PA coefficient, $\beta(\omega, \Omega)$, can be given by Eqn. 4 modified with the substitution of $2\hbar\omega'$ by $\hbar\omega' + \hbar\Omega$; thus, $F_2(2x)$ is replaced by $F_2(x' + X)$, where $x' = \hbar\omega'/E_g$ and $X = \hbar\Omega/E_g$, and $x' + X > 1$. This substitution is strictly valid only for $x' = X$, however, the predictions resulting from this substitution show remarkable agreement with the data, as will be shown.

The change of the absorption spectrum (at ω') induced by the presence of a strong pump at Ω can be written for 2PA as $\Delta\alpha(\omega';\Omega) = \beta(\omega';\Omega)I_\Omega$, where I_Ω denotes the irradiance of the pump field. Similarly the change in refractive index at ω induced by the presence of a strong pump at Ω can be written as $\Delta n(\omega;\Omega) = \gamma(\omega;\Omega)I_\Omega$. Applying the KK transformation Eq. 2 at this point yields a relation between $\gamma(\omega;\Omega)$ and $\beta(\omega';\Omega)$. Using Eq. 3 with $F_2(x'+X)$ in Eq.2 we obtain for the degenerate case ($\omega=\Omega$):

$$\gamma = K \frac{\hbar c \sqrt{E_p}}{2n_0^2 E_g^4} G_2(\hbar\omega/E_g), \quad (5)$$

where the dispersion function $G_2(x)$ is given by,

$$G_2(x) = \frac{-2+6x-3x^2-x^3-3/4x^4-3/4x^5+2(1-2x)^{3/2}\Theta(1-2x)}{64x^6}, \quad (6)$$

with $\Theta(x)$ being the unit step function.

Using the value of K obtained from the 2PA measurements, $E_p=21$ eV, and converting from γ to n_2 , we obtain the final expression for n_2 as:

$$n_2(\text{esu}) = K' \frac{G_2(\hbar\omega/E_g)}{n_0 E_g^4}, \quad (7)$$

where $K'=3.4 \times 10^{-8}$ and E_g is in eV. Equation 7 explicitly shows an E_g^{-4} band-gap dependence for the magnitude of n_2 , and the sign and the frequency dispersion of this quantity are given by the simple closed form function G_2 . We can now readily compare the predictions of this theory with experiment.

Utilizing a newly developed technique (Z-scan) for n_2 measurements [1,18] that can determine its magnitude and sign, we have measured n_2 for several materials at 1.06 and 0.53 μm . This simple technique has been shown to be an accurate and sensitive tool for measuring n_2 even in the presence of nonlinear absorption. We find, for example, in materials such as ZnSe at 0.53 μm , where 2PA is present, n_2 is negative, but that the sign changes at 1.06 μm .

Picosecond degenerate-four-wave-mixing (DFWM) measurements show this third order response (time resolution limited by the 30 ps pulsewidth), while at higher irradiances the slowly decaying 2PA generated free-carrier refraction is seen.[19] Figure 3 shows the DFWM experimental geometry. The DFWM signal as a function of backward pump delay is shown in Figure 4. This signal shows a "fast" third order nonlinearity followed by a slowly decaying "fifth" order nonlinearity.

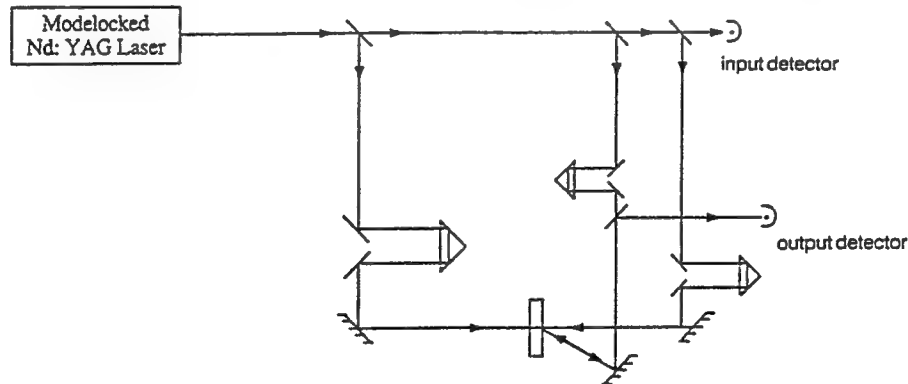


Figure 3. A schematic of the experimental geometry of the degenerate-four-wave-mixing experiment.

The order of the nonlinearity was determined by fixing the temporal delay at a) zero delay, or at b) long delay, and simultaneously varying the input energy of all three input beams. A log-log plot of the DFWM signal versus input energy (or irradiance) shows straight lines having slopes of three at zero delay (a) and five at long delay (b) as shown in Figure 5. The fast response of the third order nonlinearity at zero delay (time response limited by the 30 picosecond laser pulsewidth) indicate its bound electronic origin. The higher order nonlinearity observed at long delays is the

plasma nonlinearity due to carriers produced by 2PA, a sequential $\text{Im}\{\chi^{(3)}\}:\text{RE}\{\chi^{(1)}\}$ effect. This appears as an effective fifth order nonlinearity.

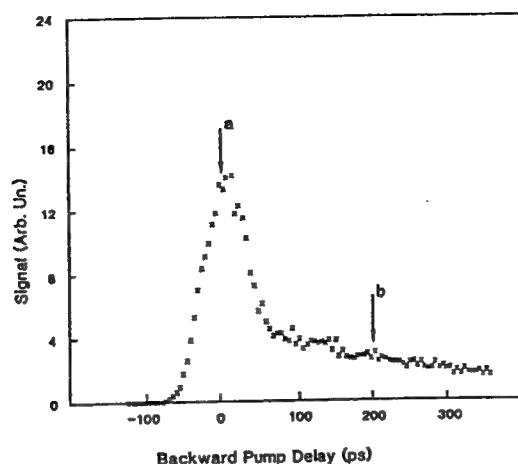


Figure 4. A plot of degenerate-four-wave-mixing signal as a function of backward pump beam temporal delay using the geometry of Figure 3.

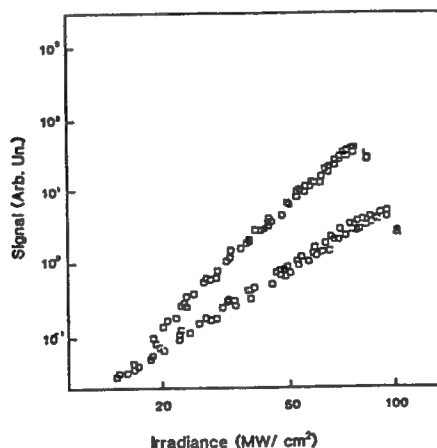


Figure 5. A log-log plot of the DFWM signal at delays a) and b) of Fig. 4 as a function of input with the energy of all three input beams varied simultaneously.

A graphical comparison of the data for n_2 is given in Figure 6 which shows the band-gap scaling law and in Figure 7 where the dispersion and sign of n_2 are explicitly compared to the G_2 of Eq. 7. Many of the experimental values for large gap optical crystals are obtained from recent measurements by Adair et.al. using a "nearly degenerate-three-wave-mixing" scheme.[7] We have also measured n_2 in a number of these wide-gap dielectrics using the Z-scan method and have obtained comparable results. The dispersive behavior of n_2 in Figure 6 is seen to be most significant within the range $E_g/2 < \hbar\omega < E_g$ where 2PA is present and relatively small in the low frequency limit $\hbar\omega \ll E_g$.

A noticeable difference between the magnitude of the measured and calculated values is seen near the one photon absorption edge. Considering the simplicity of the model in deriving Eq. 7, such deviations are not unexpected. The measured large negative values of n_2 as compared to the calculated values near the fundamental absorption edge may be attributed to the refraction due to the "optical Stark effect" which is also referred to as "virtual band-blocking" and has been ignored in our calculations. The contribution of this mechanism to the electronic nonlinear susceptibility has been shown to have a strong band-gap resonance and follows the same scaling as given in Eq. 7.[20] This effect, which is negative for all frequencies below the band-gap, vanishes quickly for longer wavelengths ($\hbar\omega < E_g/2$) and has negligible contribution in the transparency region of the material.

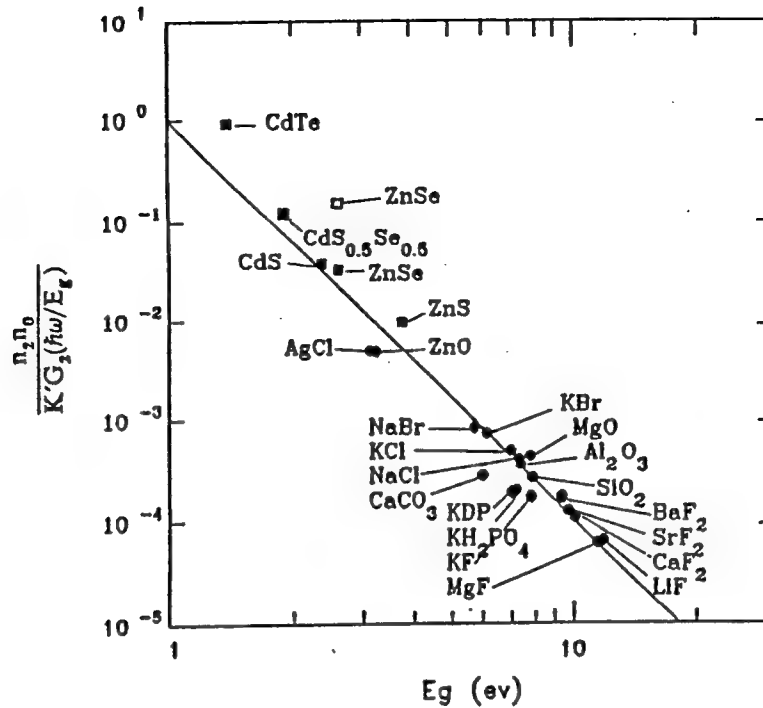


Figure 6. A log-log plot of the scaled n_2 versus energy gap (E_g) for a large class of optical materials. The solid line represents the theoretical result as obtained from Eq.(7) with no adjustable parameters and has a slope of -4 . The solid circles represent the data from ref.[7] all obtained at $\lambda=1.06 \mu\text{m}$. The remaining data are our measurements using the Z-scan technique taken at $\lambda=1.06 \mu\text{m}$ (solid squares) and at $\lambda=.532 \mu\text{m}$ (open squares).

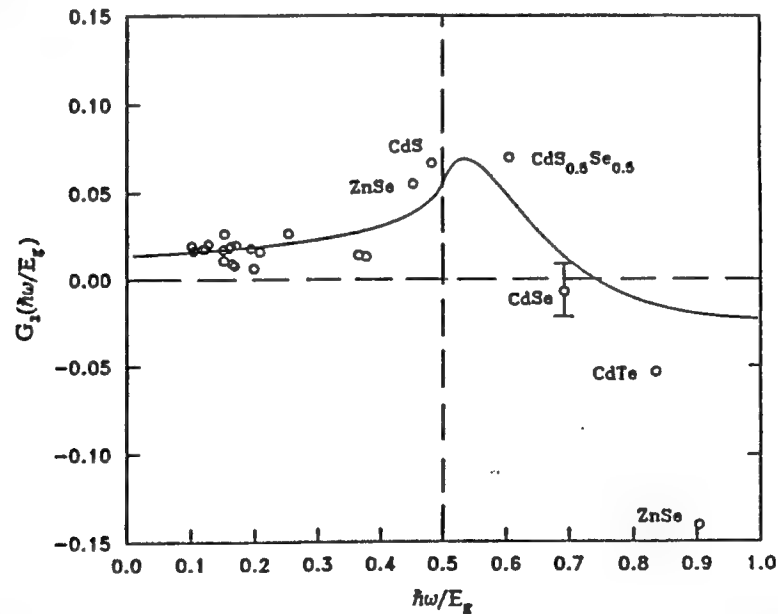


Figure 7. The calculated dispersion function G_2 versus $\hbar\omega/E_g$. The same n_2 data as in Figure 6, here scaled as $n_2 n_0 E_g^4 / K'$, are compared with the theory. Only the semiconductor data within the highly dispersive region are labeled for comparison.

- [16] G.D. Mahan, "Theory of Two-Photon Spectroscopy in Solids," Phys. Rev. 170, 825-838(1968).
- [17] F.V. Bunkin, "Two Quantum Transitions in Optics," Sov. Phys. JETP, 23, 1121-1123(1966).
- [18] M. Sheik-bahae, A.A. Said, and E.W. Van Stryland, "High Sensitivity, Single Beam n_2 Measurements," Opt. Lett. 14, 955-957(1989).
- [19] D.J. Hagan, E. Canto, E. Miesak, M.J. Soileau, and E.W. Van Stryland, "Picosecond Degenerate Four Wave Mixing Studies in ZnSe," paper, TUX, pp.160, Technical Digest of the Conference on Lasers and Electro-Optics, Anaheim, CA, OSA Technical Digest Series, No. 7, 1988.
- [20] B.S. Wherrett, A.C. Walker, and F.A.P. Tooley, "Nonlinear Refraction for CW Optical Bistability," in Optical Nonlinearities and Instabilities in Semiconductors, H. Haug, eds. (Academic Press, Inc. 1988.) pp.239-272.

Manuscript received
3-8-90

**Laser Induced Damage
to Thallium Arsenic Selenide (TAS)**

A. A. Said, M. Sheik-Bahae, M. J. Soileau, E. W. Van Stryland
Center for Research in Electro-Optics and Lasers (CREOL)
University of Central Florida
12424 Research Parkway, Orlando, FL 32826

and

N. B. Singh, T. Henningsen
Crystal and Device Research and Development Center
Westinghouse Electric Corp.
Pittsburgh, PA 15235

We present results of a study of the laser induced damage thresholds of Ti_3AsSe_3 at $10\text{ }\mu\text{m}$ using nanosecond and picosecond pulses. The damage threshold was found to be $\approx 10\text{ J/cm}^2$ with 130 ns (FWHM) and no damage was observed using 60 ps pulses.

Key words: damage threshold; CO_2 laser; nonlinear crystals; TAS; SHG.

Introduction:

Thallium Arsenic Selenide, Ti_3AsSe_3 , or TAS is an important optical material for frequency conversion in the infrared region. It is an efficient material for harmonic generation and optical parametric oscillation. TAS possesses second order optical susceptibilities that are nearly three times larger than those of Ag_3AsS_2 (Proustite) and a transparency range from 1.26 to $18\text{ }\mu\text{m}$. [1] This material has a low absorption coefficient of 8.2 m^{-1} which was determined by Barnes *et al* [2] by using a calorimetric technique.

In this paper, we present the results of a study of laser induced damage thresholds of two samples of Thallium Arsenic Selenide grown at Westinghouse.

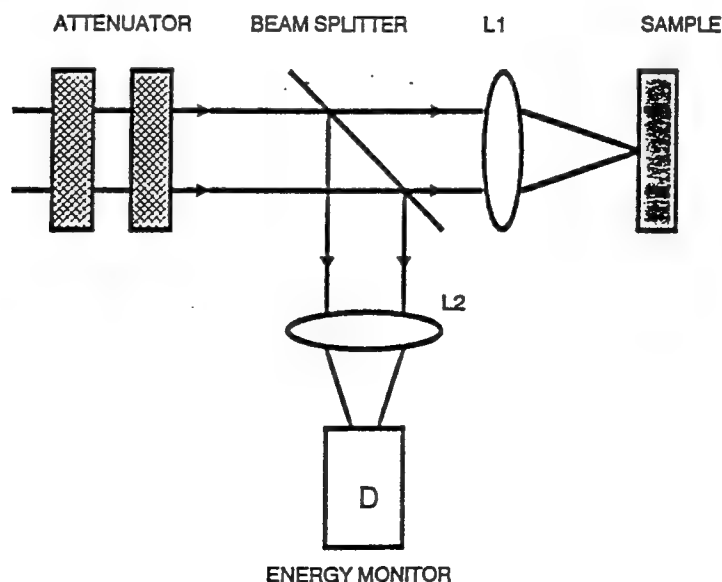


Fig.1. The experimental set-up. The $10.6\text{ }\mu\text{m}$ pulse was tightly focused on the front surface of the sample.

Experiment and Results:

Of the two samples one was doped with silver. It was cylindrical with a 2.5 cm diameter and 1.5 cm length. Only one surface was polished on which the damage measurements were taken. The other sample was undoped with a cone shape. The polished surface had a 2 cm diameter. The measurements were performed using linearly polarized, normally incident pulses from a TEA CO₂ laser system equipped with an optical free-induction decay system that can produce pulses from 30 ps to 300 ns. The laser beam was focused on the first surface of the sample by lens L₁ as depicted in Figure 1. The continuously variable attenuator consisted of two wire grid polarizers. Rotation of the first polarizer varied the input energy keeping the polarization at the sample constant. Detector D, which monitored the input energy, was calibrated using various Gentec energy detectors. The laser was operated in the TEM₀₀ mode and single longitudinal mode with pulsewidths of 130 ns (FWHM) and 60 ps (FWHM). Figure 2 shows the temporal shape of the nanosecond pulse and the second order autocorrelation function of the picosecond pulse. This autocorrelation function was obtained using a pump-probe method in another TAS crystal to produce 5 μm light dependent on the temporal overlap of the pump and probe.

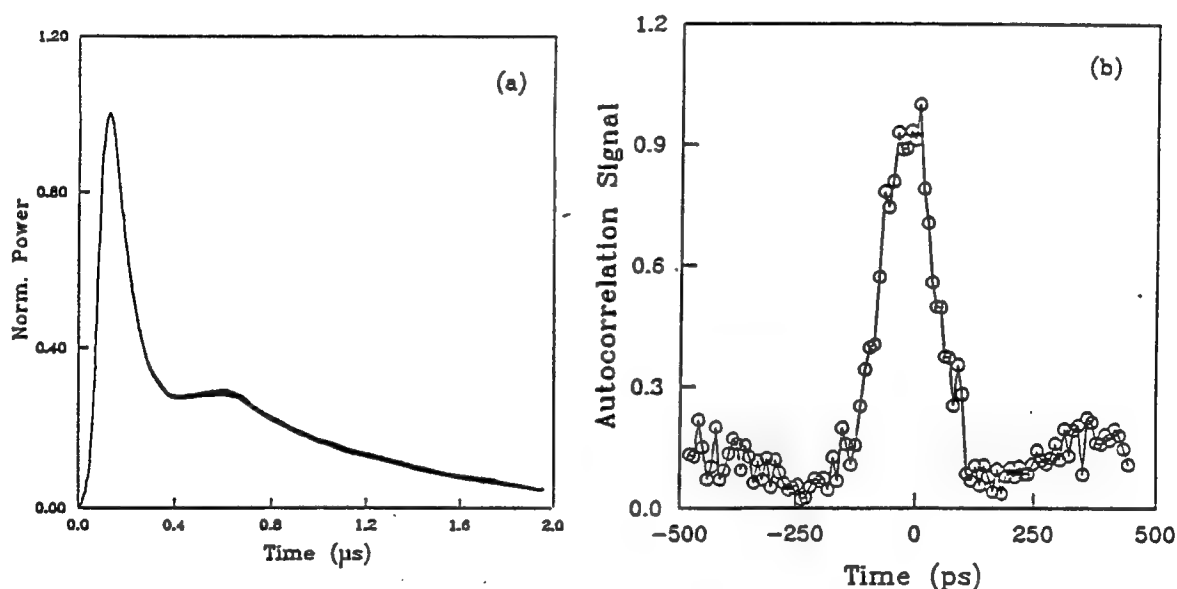


Fig.2. The temporal shape of the nanosecond (130 ns FWHM) 10.6 μm pulse (a) and autocorrelation scan of the OFID picosecond pulse (b). A pulsewidth of 60 ps (FWHM) was measured.

Pinhole size spatial beam scans were taken for each pulsewidth at the focal position of a 6.35 cm focal length lens L₁. These are shown in Figure 3 for nanosecond and picosecond pulses respectively. The beam spot size ω_0 measured was 57 μm (HW1/e²M in the irradiance). This value agrees to within 5% with the calculated ω_0 using the diffraction equation $\omega_0 = \lambda f / \pi \omega$, where ω and ω_0 are the beam spot size before and after focusing respectively, λ is the wavelength and f is the focal length of the focusing lens. Each site was irradiated only once. The damage was visually detected through a long working distance microscope. With the nanosecond pulses, a damage threshold of 9.2 J/cm² (30 MW/cm²) was measured for the doped sample when the beam waist was 57 μm and 11 J/cm² (37 MW/cm²) with a calculated beam waist of 114 μm which was obtained by scaling the previously measured ω_0 to a 12.7 cm focal length lens. These thresholds do not show a significant difference. The damage thresholds for the undoped sample were 8.8 J/cm² (29 MW/cm²) and 12 J/cm² (41 MW/cm²) respectively. Figures 4 and 5 show the data from which the above damage thresholds were extracted. With 60 ps pulses, no damage was observed on either sample. The maximum fluence that could be reached was approximately 1.56 J/cm² (19 GW/cm²). Note that this maximum irradiance is \approx 500 times higher than the nanosecond threshold. At this maximum fluence, one site of each sample was irradiated for 5 minutes at 2 pulses per second without any damage observed.

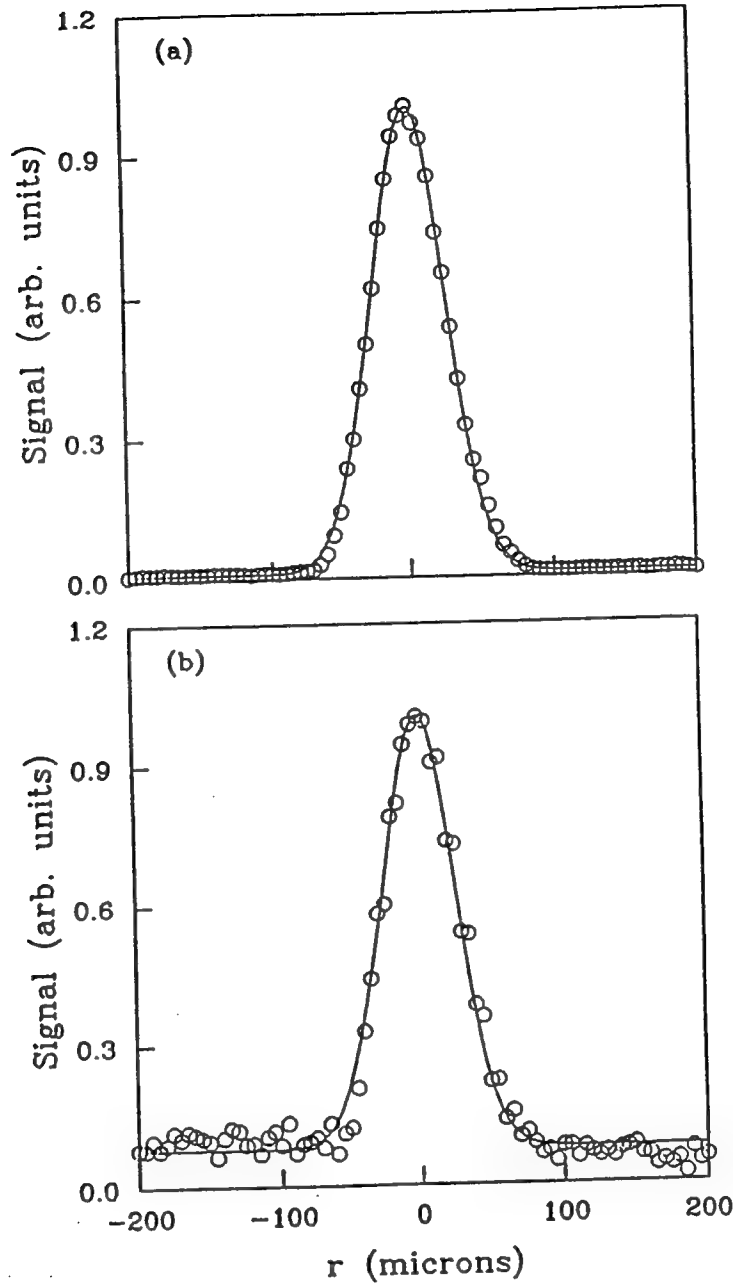


Fig.3. Beam scan of the nanosecond pulse.(a) A spot size of $57 \mu\text{m}$ ($\text{HW1/e}^2\text{M}$) in the irradiance was measured. Beam scan of the picosecond pulse.(b) The high background is due to the EMI noise arising from the 40 KV discharge of the laser amplifier.

Conclusion:

The damage threshold of TAS as obtained from the above measurements is deduced to be $\approx 10 \text{ J/cm}^2$. This value is comparable to the damage thresholds of GaSe and ZnGeP_2 [3]. The damage threshold did not change upon doping TAS with silver. Moreover, changing the spot size by a factor of two did not make a significant change on the damage threshold value. While frequency doubling the $10.6 \mu\text{m}$ radiation an energy efficiency of 7% was obtained from a 3.8 cm long TAS crystal using 60 ps pulses with an input irradiance of 150 MW/cm^2 and a beam radius of .22 mm ($1/\text{e}^2\text{M}$ in the irradiance).

References:

- [1] J. D. Feichtner and G. W. Roland, Optical properties of a nonlinear optical material: Ti_3AsSe_3 , Appl. Opt., vol. 11, 993-998, 1972.
- [2] N. P. Barnes, Roger C. Eckhardt, D. J. Gettemy and L. B. Edgett, IEEE JQE, vol. QE-15, NO. 10, 1979.
- [3] G. B. Abdullaev, K. R. Allakhverdiev, M. E. Karasev, V. I. Konov, L. A. Kulevskii, N. B. Mustafaev, P. P. Pashinin, A. M. Prokhorov, Yu. M. Starodumov and N. I. Chapleiv, Sov. J. Quantum Electron. 19 (4), 1989.

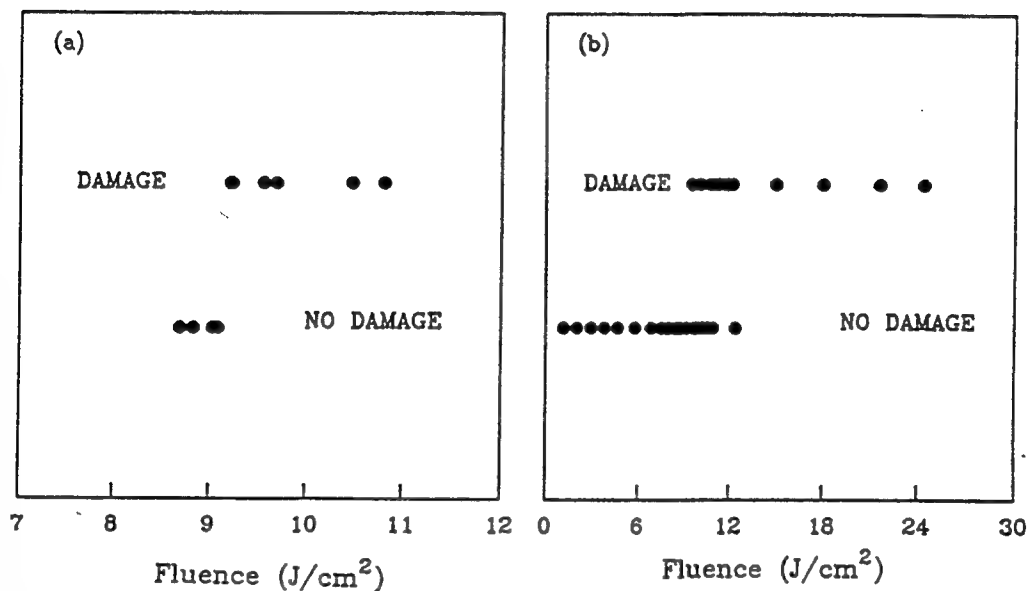


Fig.4. Damage data on doped sample using 130 ns (FWHM) pulses with 57 μm (a) and 114 μm (b) incident spot size at 10.6 μm .

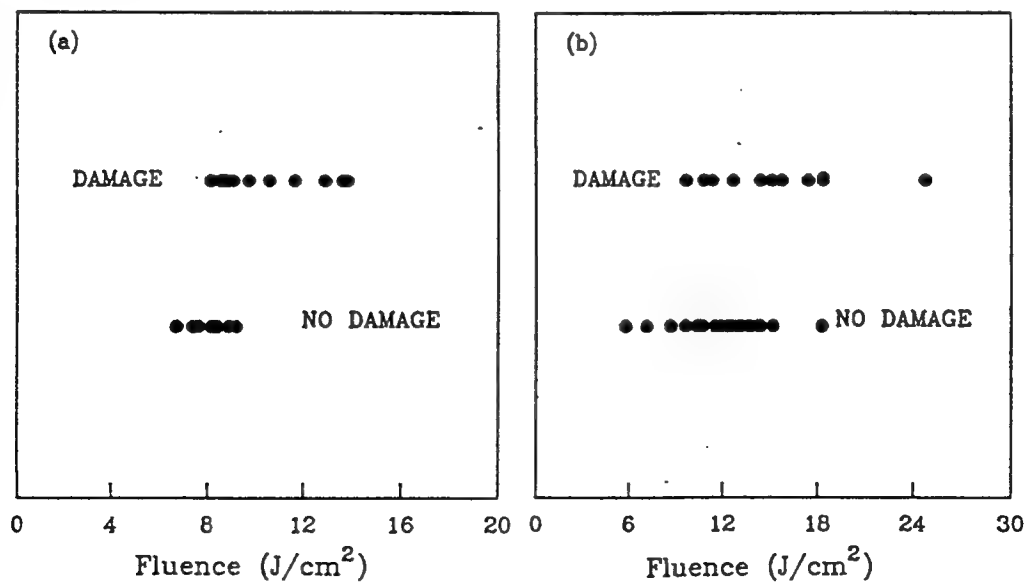


Fig.5. Damage data on undoped sample using 130 ns pulses with 57 μm (a) and 114 μm (b) incident spot size at 10.6 μm .

Bound Electron Nonlinearities and Their Application to Optical Switching

D. J. Hagan*, M. Sheik-Bahae, D. C. Hutchings,
A.A. Said, T.H. Wei and E. W. Van Stryland
Center for Research in Electro-Optics and Lasers (CREOL)
University of Central Florida, Orlando, Florida 32826

Abstract

We have performed an extensive series of measurements of the bound electronic nonlinear refractive index n_2 of a variety of solids at several wavelengths. We find that as the photon energy approaches E_g (the band-gap energy), that n_2 changes from positive to negative. This observed wavelength dispersion of n_2 can be well explained for wavelengths well below the fundamental absorption edge using a Kramers-Kronig transformation on two-photon absorption, AC Stark (virtual band-blocking), and electronic Raman contributions to the imaginary part of the third order susceptibility. The fit thus obtained for n_2 is amazingly good for more than four orders of magnitude change of n_2 including a change in sign. The change in sign from positive to negative with increasing frequency occurs roughly midway between the two-photon absorption edge and the fundamental absorption edge. Thus, we now have a comprehensive theory that allows prediction of n_2 at any wavelength below the band edge given only E_g and the linear index of refraction. Such information is useful for a variety of applications including optical limiting, laser-induced damage, and all-optical switching. We use our theory to estimate the minimum obtainable ultrafast switching powers for various wavelengths of practical interest.

* also with the Departments of Physics and Electrical Engineering

2. Introduction

Recent measurements of the bound electronic nonlinear refractive index n_2 of several semiconductors and dielectric materials show that there is a strong systematic dispersion of n_2 above the two-photon absorption (2PA) edge.[1] These data were taken using the newly developed Z-scan technique [2,3] (a beam distortion method), and degenerate four-wave mixing,[4] and show that n_2 turns negative between the 2PA edge and the fundamental absorption edge. We found that by using a Kramers-Kronig (KK) integral of the 2PA spectrum as given by a two-parabolic band model, we could predict the observed universal dispersion, scaling, and values of n_2 that range more than four orders of magnitude and change sign.[1] This KK analysis relates the real and imaginary parts of the third order susceptibility. The resulting scaling rule correctly predicts the value of n_2 for the 26 different materials we had examined at that time, except very near the gap where there was a systematic departure of the data from the theory toward larger negative n_2 values. More recent data taken at wavelengths nearer the gap show an even larger departure from the predictions of the 2PA model. We had speculated in Ref. [1] that the band-gap resonant AC Stark effect might make $|n_2|$ larger near the gap. Here we present a model that includes 2PA the AC Stark effect and the electronic Raman effect. Indeed the inclusion of these effects does explain the large negative increase in n_2 near the gap.

There are two distinct frequency regimes for nonlinear optics in semiconductors which correspond to real and virtual excitation. The study of nonlinear optics in semiconductors has primarily concentrated on bandgap-resonant effects which result in a real excitation. The very large nonlinear effects observed in this case are the saturation of interband and excitonic absorption due to photoexcited free carriers and excitons. Real excitations usually result in a reduction of the refractive index at frequencies of interest. In contrast, by exciting optical solids at frequencies much less than the gap, a considerably smaller but faster, positive nonlinear refractive index, n_2 , due to bound electronic effects is observed. This n_2 arises from the real part of the third-order susceptibility, $\chi^{(3)}$, and is defined through the refractive index change Δn , where

$$\Delta n(\omega) = \gamma(\omega) I_\omega = \frac{n_2(\omega)}{2} |E_\omega|^2, \quad (1)$$

with I_ω and E_ω being the irradiance and electric field at frequency ω respectively and $n_2 = (2\pi/n_0) \text{Re}(\chi^{(3)})$. The linear refractive index is n_0 , and γ and n_2 are related by $n_2(\text{esu}) = (cn_0\gamma/40\pi)(\text{MKS})$ where c is the speed of light. The magnitude and dispersion of n_2 is of interest because of its importance in applications such as nonlinear propagation in fibers, fast optical switching, self-focusing and damage in optical materials, and optical limiting in semiconductors.

Our measurements utilize a newly developed technique (Z-scan) [2, 3] that determines the magnitude and sign of n_2 even in the presence of 2PA where it also gives the 2PA coefficient β . This simple technique has been shown to be an accurate and sensitive tool for measuring n_2 and β . Measurements of wide band-gap dielectrics show $n_2 > 0$ which explains catastrophic self-focusing damage in such materials as NaCl and SiO₂. Our measurements in semiconductors below or near the 2PA edge ($\hbar\omega \approx E_g/2$) also show positive n_2 . However, we found a negative n_2 in materials such as ZnSe at 0.532 μm where 2PA is present, but a positive n_2 at 1.064 μm where 2PA is absent. The values obtained for β are in excellent agreement with our earlier measurements using standard transmission.[5] We also performed picosecond degenerate-four-wave mixing (DFWM) measurements which showed this third order response to be fast (time resolution limited by the 30 ps pulsewidth).[6] At wavelengths where 2PA was present this fast third order nonlinearity was dominant at low irradiance (eg. up to $\approx 0.5 \text{ GW/cm}^2$ in ZnSe at 532nm), while at higher irradiances the slowly decaying 2PA generated free-carrier refraction (self-defocusing) became important. DFWM studies in other semiconductors and other wavelengths showed this to be a universal phenomenon.[6] We have also included in our analysis n_2 data taken on a series of wide gap materials by "nearly degenerate three wave mixing" by Adair et. al. [7], and data taken by LaGasse et. al. [8] on AlGaAs using interferometry. As a result, we have been able to clearly demonstrate the behavior of the E_g^{-4} band gap scaling[9,10] and dispersion of n_2 . It should be noted that since the 2PA spectrum was previously determined [11], no fitting parameter was used in the calculation of Ref. [1].

3. Kramers-Kronig (KK) Relation

Most theoretical calculations of n_2 have been confined to the zero frequency limit.[12-16] Of these, semi-empirical formulations have been most successful in predicting the magnitude of n_2 . [15,16] For example, the formula obtained by Boling, Glass and Owyong (BGO) in relating n_2 to the linear index (n_0) and the dispersion of n_0 in terms of the Abbe number has been successfully applied to a large class of transparent materials.[7,16] Their theory predicts the low frequency magnitude of n_2 , but does not give the dispersion. The KK method predicts the dispersion as well as the magnitude of n_2 . While the calculation presented in Ref. [1] only included 2PA in the imaginary part of $\chi^{(3)}$, this calculation includes all other relevant contributions, that is, from electronic Raman and the AC Stark effect ("virtual band-blocking").

Based on the principle of causality, the KK relates the refractive index and absorption coefficient for any linear material.

$$n(\omega) - 1 = \frac{c}{\pi} \int_0^\infty \frac{\alpha(\omega')}{\omega'^2 - \omega^2} d\omega' \quad (2)$$

Now introduce some causal source of change ξ into the system and consider the change in the refractive index resulting from the effect of ξ . The KK transformation states that a change in the refractive index (Δn) at ω is associated with changes in the absorption coefficient ($\Delta\alpha$) throughout the spectrum (ω') and vice versa. We write this as:

$$\Delta n(\omega; \xi) = \frac{c}{\pi} \int_0^\infty \frac{\Delta\alpha(\omega'; \xi)}{\omega'^2 - \omega^2} d\omega'. \quad (3)$$

where c is the velocity of light in vacuum and ξ is a parameter (or parameters) denoting the "cause" of change in

the absorption.

The cause need not be of optical origin but of any external perturbation. For example this method has been used to calculate the refractive index change resulting from an excited electron-hole plasma [17] and a thermal shift of the band edge [9]. For cases where an electron-hole plasma is injected, the consequent change of absorption gives the plasma contribution to the refractive index. In this case, the ξ parameter is taken as the change in plasma density (ΔN) regardless of the mechanism of generation of the plasma or the pump frequency [17]. In the case of 2PA the change is due to the presence of a pump field at Ω (ie. $\xi = \Omega$). The corresponding nonlinear refraction is $\Delta n(\omega; \Omega)$, which gives the dispersion of the index change with ω . Although the calculation as illustrated above gives the nondegenerate nonlinear refraction, in most cases we would set $\Omega = \omega$ and consider self-refraction. This gives what is commonly referred to as n_2 . Van Vechten and Aspnes [14] obtained the low frequency limit of n_2 from a similar KK transformation of the Franz-Keldysh electro-absorption effect where, in this case, ξ is the DC field. The bound electronic contribution to $\chi^{(3)}$ can originate from various absorptive counterparts that are quadratic functions of the pump field. Effects of this order are 2PA, the electronic Raman effect, and the optical Stark effect.

An alternative way of considering the KK calculation is to do the calculation not for the basic material but on a system which consists of the material plus a light field. Thus, it is necessary to know the nondegenerate absorption change $\Delta\alpha(\omega; \Omega)$, which is the absorption of light at ω when a light-field of Ω is applied to the material. Degenerate 2PA can be related to the case where the two frequencies are set equal.

Two-photon absorption processes require that perturbation theory be taken to second order. A variation of this is to use first order perturbation theory on a "dressed" final state where the effect of the acceleration of the electrons due to the oscillating electric field is already taken into account. We assume a two beam A-P interaction with both beams linearly polarized in the same direction [18-20]. Using this approach the degenerate 2PA coefficient can be determined; $\beta(\omega) = 2\hbar\omega W I^{-2}$ where W is the two-photon transition rate. The resulting expression for the 2PA has exactly the same scaling and frequency dependence form as that calculated in references [10], namely,

$$\beta(\omega) = K \frac{\sqrt{E_p}}{n_0^2 E_g^3} F_2(\hbar\omega/E_g), \quad (4)$$

where $F_2(x) = ((2x-1)^{3/2})(2x)^5$. Here K is a material independent constant and E_p (related to the Kane momentum parameter) is nearly material independent and possesses a value $E_p \approx 21$ eV for most direct gap semiconductors. The best fit to the data of reference [21] gives $K = 3100 \text{ cm}(\text{eV})^{-5/2}/\text{GW}$, whereas theory [22] gives $K = 5200 \text{ cm}(\text{eV})^{-5/2}/\text{GW}$. This difference can largely be explained by the effects of nonparabolicity which has the effect of reducing β slightly without significantly changing the frequency dependence [22]. Using the same method the nondegenerate 2PA is found to be,

$$\frac{\Delta\alpha(\omega_1; \omega_2)}{I_2} = \frac{2K\sqrt{E_p}}{n_0^2 E_g^3} F_2(\hbar\omega_1/E_g; \hbar\omega_2/E_g), \quad (5)$$

where the 2PA frequency dependence is given by,

$$F_2^{2PA}(x_1; x_2) = \frac{(x_1 + x_2 - 1)^{3/2}}{27x_1x_2^2} \left(\frac{1}{x_1} + \frac{1}{x_2} \right)^2. \quad (6)$$

However, we now have an additional term attributed to Raman terms giving a change in absorption of,

$$F_2^{\text{RAM}} = \frac{(x_1 - x_2 - 1)^{3/2} - (-x_1 + x_2 - 1)^{3/2}}{2^7 x_1 x_2^2} \left(\frac{1}{x_1} - \frac{1}{x_2} \right)^2, \quad (7)$$

where the scaling is the same as in Eq. 5. The total F_2 due to two photon processes is just the sum of $F_2^{2\text{PA}}$ and F_2^{RAM} .

Another effect which must be taken account of in these calculations is the change in linear absorption at ω_1 due to the presence of the field at ω_2 shifting the bands by the AC Stark effect. Two terms arise out of this as the radiation perturbation term couples the conduction band to itself and to the valence band. It can be shown that linear AC Stark effect produces a change in absorption $\Delta\alpha$ with a spectral dependence given by F_2^{S1} , where,

$$F_2^{\text{S1}}(x_1; x_2) = -\frac{2(x_1 - 1)^{3/2}}{2^7 x_1 x_2^4}. \quad (8)$$

The quadratic Stark shift resulting from the coupling between the conduction and valence band leads to a $\Delta\alpha$ given by,

$$F_2^{\text{S2}}(x_1; x_2) = -\frac{1}{2^{10} x_1 x_2^2 (x_1 - 1)^{1/2}} \left[\frac{1}{x_1 - x_2} + \frac{1}{x_1 + x_2} \right]. \quad (9)$$

4. Nonlinear Refraction

In principle we can evaluate $\Delta n(\omega_1; \omega_2)$ as defined in Eq. 2, however, there are few experiments of this quantity other than at $\omega_1 = \omega_2$, which is the case of self refraction. Using the KK relations discussed earlier, the change in refractive index $\Delta n(\omega; \omega) = \gamma I$ can be calculated to give,

$$\gamma = \frac{K \hbar c \sqrt{E_p}}{n_0^2 E_g^4} G_2(\hbar\omega/E_g), \quad (11)$$

where the dispersion function $G_2(x)$ is given by,

$$G_2(x) = \frac{2}{\pi} \int_0^\infty \frac{F_2(x'; x)}{x'^2 - x^2} dx'. \quad (12)$$

All that remains is for the above integral to be evaluated for the various contributions to the nondegenerate absorption, $F_2(x_1; x_2)$.

When these integrals are performed and the results summed a single divergent term proportional to ω^{-2} is left. This diverging term is not unexpected as A·p perturbation theory has been used in the transition rate calculations and it is well known that divergences of this order can be introduced whereas the comparable E·r perturbation theory avoids such divergences. In a similar manner to Moss et al. [23] we treat such a divergence as unphysical and subtract it from the result for the nonlinear refraction. Using the value of K obtained from 2PA measurements and using $E_p \simeq 21$ eV, which is true for the majority of semiconductors, we obtain,

$$n_2(\text{esu}) = \frac{K' \sqrt{E_p}}{n_0 E_g^4} G_2(\hbar\omega/E_g), \quad (13)$$

where the constant $K'=1.5 \times 10^{-8}$ when E_g is defined in eV. We note the E_g^{-4} bandgap dependence for the magnitude of n_2 .

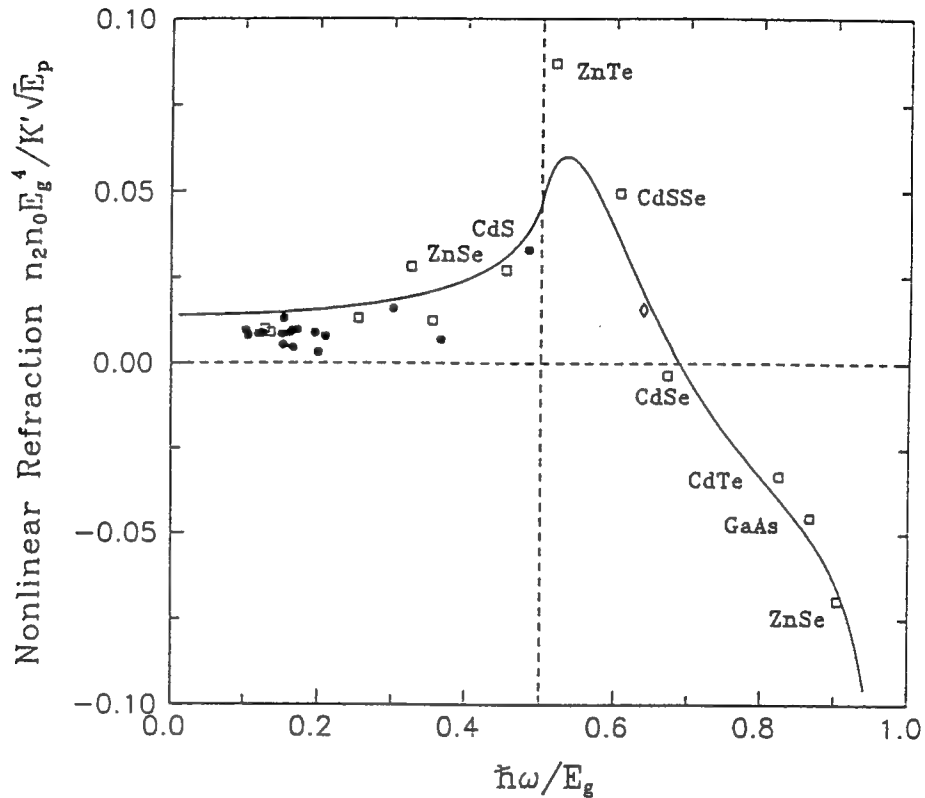


Fig. 1. A plot of n_2 dispersion function $G_2(\hbar\omega/E_g)$ containing contribution from 2PA, Raman and AC Stark effect. Data are scaled by $n_0 E_g^4 / K' \sqrt{E_p}$.

A graphical comparison of the dispersion function $G_2(\hbar\omega/E_g)$ with measured values of n_2 obtained from Z-scan measurements at $1.06 \mu\text{m}$ and $0.53 \mu\text{m}$ [2,3] and nearly degenerate three-wave mixing measurements of large gap optical materials [7] is shown in Fig. 1. Note we have agreement within a factor of 2 for a wide range of semiconductors and large gap optical materials.

The scaling of n_2 with bandgap is demonstrated in Fig. 2. Here we plot the ratio of n_2 to the dispersion function $G_2(\hbar\omega/E_g)$. The straight line indicated shows the expected E_g^{-4} dependence. It is found that the scaling law holds true over more than orders of magnitude variation in the modulus of n_2 .

The E_g^{-4} dependence of n_2 gives a variation of n_2 from 2.5×10^{-14} esu for a material such as MgF_2 at $1.06 \mu\text{m}$ to 3×10^{-10} esu for Germanium at $10.6 \mu\text{m}$, which we measured using a picosecond CO_2 laser. This large variation of n_2 is better displayed by plotting n_2 scaled by n_0 and G_2 as a function of E_g on a log-log plot as shown in Fig. 2. In spite of this very large variation in magnitude of n_2 (and change in sign), this extremely simple model gives good agreement with the data for materials including both semiconductors and insulators.

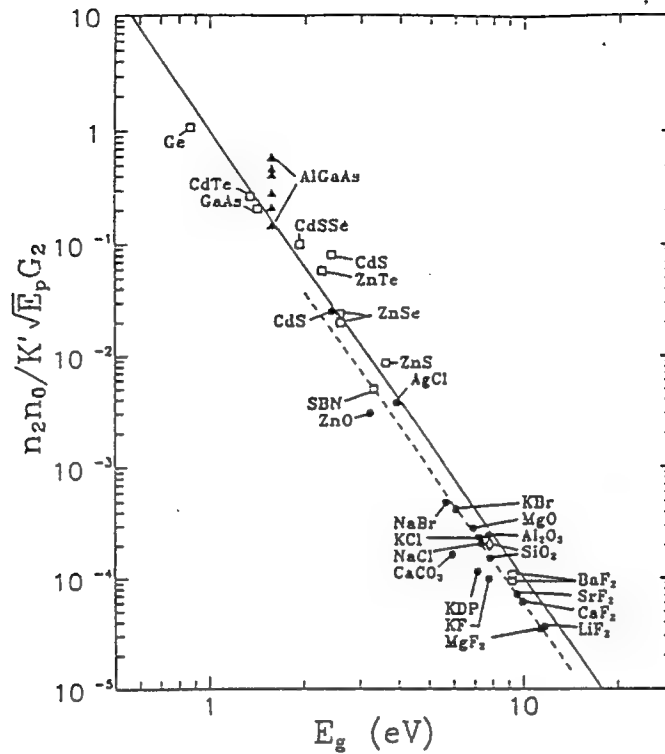


Fig. 2. A log-log plot showing the expected E_g^{-4} dependence of n_2 . The data points are identical to those in Fig. 2 but now scaled by the dispersion function $G_2(\hbar\omega/E_g)$. The solid line is the function E_g^{-4} which translates into a straight line of slope -4 on the log-log scale.

5. Application to All-Optical Switching

One of the applications of n_2 is in the role of all-optical switching. Some examples are the nonlinear Fabry-Perot for image processing or parallel optical computing [24,25] or coupled waveguides for communications switching networks [26,27]. When it comes to optimizing devices for optical switching it is important that optical losses in the system are not too large. If optical absorption is large, then the change in refractive index will fall off rapidly as the optical wave propagates.

It can be shown that for any optical switching system, one must achieve a refractive index change Δn such that,

$$|\Delta n| > c_{sw} \alpha \lambda, \quad (14)$$

where c_{sw} is a numeric constant of the order of unity whose precise value depends on the particular switching scheme. For example, for a Fabry-Perot, $c_{sw} = (2\sqrt{3}\pi)^{-1}$ [28], and for a nonlinear coupled waveguide, $c_{sw} = 2$ [29,30].

Below the band edge, the principal contribution to the absorption is 2PA, $\alpha \propto \beta I$ at irradiance levels of interest. As the electronic Kerr effect gives an index change of $\Delta n = \gamma I$, the requirement for all-optical switching is [29],

$$\left| \frac{\gamma}{\beta \lambda} \right| > c_{sw}. \quad (15)$$

Using our relationship between γ and β through the KK relations, we obtain the frequency dependence for the all-optical switching requirement,

$$\frac{\hbar\omega}{E_g} \frac{|G_2(\hbar\omega/E_g)|}{F_2(\hbar\omega/E_g)} > 2\pi c_{sw} . \quad (16)$$

Note that equation 16 has no explicit material dependence as it is only a function of the ratio $\hbar\omega/E_g$. Thus although n_2 can be enhanced by using smaller gap materials, this does not necessarily improve conditions for switching. The left hand side of (16) is plotted in Fig. 3. In the same figure we also show the experimentally determined values for this parameter $|2\pi\gamma/\beta\lambda|$ for some semiconductors using the n_2 values reported here and 2PA coefficients from [5]. We see that there is a range of optical frequencies where this quantity becomes too small for optical switching which is given approximately by $0.6 < \hbar\omega/E_g < 0.9$, covering most of the region where 2PA is observed. This was first noted by Mizrahi et al [29].

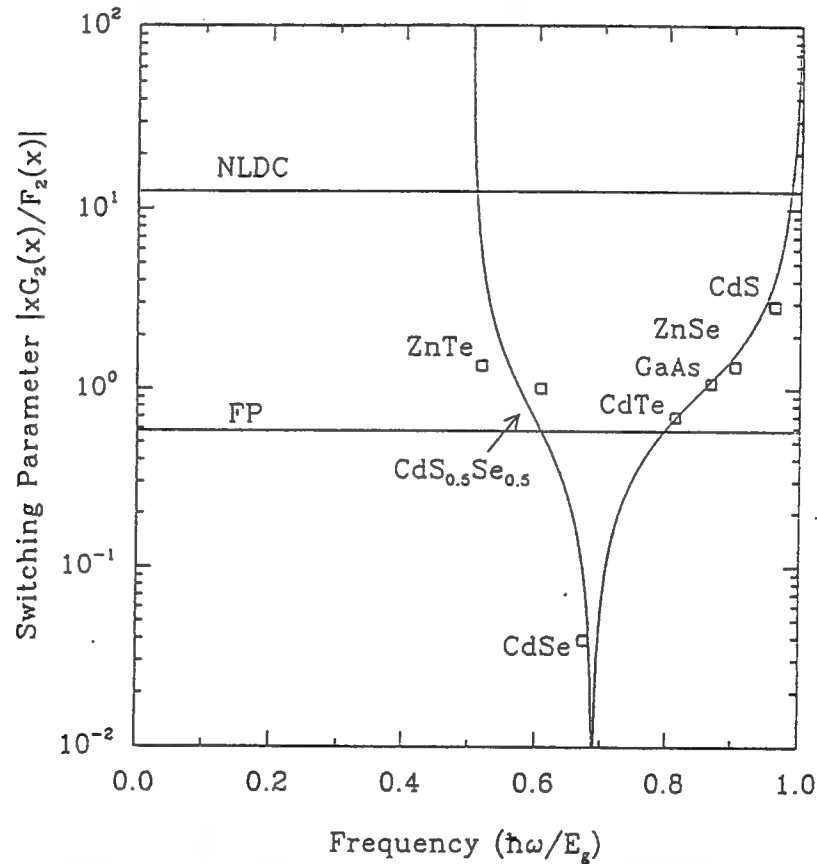


Fig. 3. Material independent switching parameter as a function of frequency. Also shown are the minimum limits for all-optical switching for the nonlinear directional coupler and the nonlinear Fabry-Perot. For switching to be possible the switching parameter must exceed the relevant limit. The data points are based on our semiconductor n_2 and β measurements.

We can use our results to predict switching powers in the nonlinear directional coupler ($c_{sw}=2$) for the technologically important wavelengths $0.85\mu\text{m}$, $1.55\mu\text{m}$ and $10.6\mu\text{m}$. We choose suitable materials based on the criterion that the photon energy must be just below the two photon absorption edge, i.e. $\hbar\omega/E_g \approx 0.45$, or as close to this as available materials will allow. Under this criterion, the some of the best available materials are ZnS for $0.83\mu\text{m}$, CdSe or the appropriate alloy concentration of AlGaAs (such that $\hbar L/E_g \approx 0.45$) for $1.55\mu\text{m}$ and the corresponding alloy concentration of InAsSb for $10.6\mu\text{m}$. Following reference [29] we calculate the switching power as,

$$P_{sw} = \frac{2\lambda^3}{\gamma L}, \quad (17)$$

where we assume that the beam area is the minimized and hence $\propto \lambda^2$. L is the interaction length in the directional coupler. The resulting switching powers are shown below in Table 1. This shows that while switching powers decrease for longer wavelengths with correspondingly smaller bandgaps, the power does not decrease according to the E_g^{-4} dependence of n_2 . This is due to the fact that longer wavelengths require proportionately larger index changes to produce a given phase shift and that the minimum cross-sectional area of a waveguide mode is $\approx \lambda^2$. Also, even in the best case of $P_{sw}=80$ Watts, this compares poorly with alternative technologies, such as excited carrier induced nonlinear refraction [29]. However, if longer interaction lengths can be tolerated, the lack of 2PA may make such devices useful in certain interactions [27]. In fact our studies indicate how the switching powers reported in reference [27] on switching in glass fibers may be considerably reduced by choosing more appropriate materials to optimize $\hbar\omega/E_g$.

Wavelength	Material	Switching Power
0.85 μm	ZnS	1500W
1.55 μm	CdSe	410W
	AlGaAs	340W
10.6 μm	InAsSb	80W

Table 1. Calculated switching powers for the nonlinear directional coupler utilizing the bound electronic Kerr effect.

6. Conclusion

In conclusion, the measured n_2 data follow a universal dispersion curve from which values of n_2 for other materials at other wavelengths can be calculated. We have also experimentally verified the predicted band-gap scaling of n_2 . From the excellent overall agreement with the predicted magnitude and dispersion of n_2 , as calculated via Kramers-Kronig, to the large number of experimental data, we conclude that the processes responsible for 2PA and the AC Stark effect also determine n_2 . This in turn implies that the bound electronic nonlinear refractive index is predominantly a causal consequence of these nonlinear absorptive processes just as the linear index is a causal consequence of linear absorption. This calculational approach takes advantage of the historical fact that, for the solid state, the 2PA coefficient has been calculated from a transition rate approach.[24] Thus, we have circumvented problems associated with performing a direct calculation of the third order susceptibility.

7. Acknowledgement

We gratefully acknowledge the support of the National Science Foundation grant ECS#8617066, DARPA/CNVEO and the Florida High Technology and Industry Council. In addition we thank O. Heinonen, A. Miller and S. Epifanov for useful discussions and J. Young and E. Canto for taking and analyzing portions of the n_2 data.

8. References

- [1] M. Sheik-Bahae, D.J. Hagan, and E.W. Van Stryland, Phys. Rev. Lett. 65, 96-99(1990).
- [2] M. Sheik-Bahae, A.A. Said, T.H. Wei, D.J. Hagan, and E.W. Van Stryland, IEEE J. Quantum Electron. QE-26, 760-769(1990).
- [3] M. Sheik-Bahae, A.A. Said, and E.W. Van Stryland, Opt. Lett. 14, 955-957(1989).
- [4] D.J. Hagan, E. Canto, E. Miesak, M.J. Soileau, and E.W. Van Stryland, pp.160, Technical Digest of the Conference on Lasers and Electro-Optics, Anaheim, CA, OSA Technical Digest Series, No. 7, 1988.
- [5] E.W. Van Stryland, H. Vanherzeele, M.A. Woodall, M.J. Soileau, A.L. Smirl, S.Guha, and T.F. Boggess, Opt. Eng. 24, 613-623(1985).
- [6] E. Canto-Said, D.J. Hagan, J. Young, and E.W. Van Stryland, to be published
- [7] R. Adair, L.L. Chase, and S.A. Payne, Phys. Rev. B 39, 3337-3349(1989).
- [8] M.J. LaGasse, K.K. Anderson, C.A. Wang, H.A. Haus, and J.G. Fujimoto, Appl. Phys. Lett. 56, 417-419(1990).
- [9] B.S. Wherrett, A.C. Walker, and F.A.P. Tooley, in Optical Nonlinearities and Instabilities in Semiconductors, H. Haug, eds. (Academic Press, Inc. 1988.) pp.239-272.
- [10] B.S. Wherrett, J. Opt. Soc. Am. B 1, 67-72(1984).
- [11] E.W. Van Stryland, M.A. Woodall, H. Vanherzeele, and M.J. Soileau, Opt. Lett. 10, 490-492(1985).
- [12] S.S. Jha and N. Bloembergen, Phys. Rev. 171, 891-898(1968).
- [13] C. Flytzanis, Phys. Lett. 31A, 273-274(1970).
- [14] J.A. Van Vechten and D.E. Aspnes, Phys. Lett. 30A, 346-347(1969).
- [15] C.C. Wang, Phys. Rev. B, 2, 2045-2048(1970).
- [16] N.L. Boling, A.J. Glass, and A. Owyong, IEEE J. Quantum Electron. QE-14, 601-608(1978).
- [17] D.A.B. Miller, C.T. Seaton, M.E. Prise, and S.D. Smith, Phys. Rev. Lett. 47, 197-200(1981).
- [18] L.V. Keldysh, Sov. Phys. JETP, 20, 1307-1314(1965)
- [19] H.D. Jones and H.R. Reiss, Phys. Rev. B 16, 2466-2473(1977).
- [20] H.S. Brandi and C.B. de Araujo, J. Phys. C 16, 5929-5936(1983).
- [21] E.W. Van Stryland, Y.Y. Wu, D.J. Hagan, M.J. Soileau, and K. Mansour, J. Opt. Soc. Am. B, 5, 1980-1989(1988).
- [22] M.H. Weiler, Solid State Commun. 39, 937-940(1981).
- [23] D.J. Moss, E. Ghahramani, J.E. Sipe, and H.M. van Driel, Phys. Rev. B 41, 1542-1560(1990).
- [23] M. Göppert-Mayer, Ann. Physik 9, 273(1931).
- [24] B.S. Wherrett and S.D. Smith, Physica Scripta, T13, 189-194 (1986)
- [25] S.D. Smith, A.C. Walker, F.A.P. Tooley and B.S. Wherrett, Nature, 325, 27-31 (1987)
- [26] P. LiKamWa, J.E. Stich, N.J. Mason, J.S. Roberts and P.N. Robson, Electron. Lett. 21, 26-27 (1985)
- [27] S.R. Friberg, A.M. Weiner, Y. Siberberg, B.G.Sfez and P.W. Smith, Opt. Lett., 13, 904-906 (1988)
- [28] D.C. Hutchings, C.H. Wang and B.S. Wherrett, J. Opt. Soc. Am. (Accepted for Publication)
- [29] V. Mizrahi, K. W. DeLong, G.I. Stegeman, M.A. Saifi and M.J. Andrejco, Opt. Lett., 14, 1140-1142 (1989)
- [30] K.W. DeLong, K.B. Rochford and G.I. Stegeman, Appl. Phys. Lett., 55, 1823-1825 (1989)

Anomalous Dispersion of the Electronic Kerr Effect n_2

D.J. Hagan, Y.Y. Wu, E. Canto, M. Sheik-bahae, A.A. Said, J. Young, T.H. Wei,
M. Junnarkar, and E.W. Van Stryland

Center for Research in Electro-Optics and Lasers,
University of Central Florida, Orlando, FL 32816, USA

Measurements of the bound electronic nonlinear refractive index n_2 , using picosecond DFWM and beam distortion, show a region of anomalous dispersion where n_2 eventually turns negative between the two-photon absorption edge and the fundamental edge.

We have performed picosecond Degenerate Four-Wave Mixing (DFWM) experiments and beam distortion experiments, including using the newly developed Z-scan technique,[1] to accurately measure the bound electronic nonlinear refractive index n_2 in a variety of materials at 1.06 and 0.53 μm . In semiconductors where two-photon absorption (2PA) is allowed, we find that n_2 decreases from its maximum value near the 2PA ($2\hbar\omega \approx E_g$) edge to zero as the wavelength is increased, changing to negative nearer the fundamental absorption edge. In order to measure n_2 , we experimentally separated the effects of 2PA excited carrier refraction (coefficient σ) from the electronic Kerr effect induced refraction. Using DFWM this is accomplished by observing that the carrier effects last for hundreds of picoseconds and vary as the fifth power of the incident irradiance I , while the $\chi^{(3)}$ effect follows the temporal variation of the pulse and varies as I^2 . Such a signal is shown in Fig. 1.

The inset shows the order of the nonlinearity (all beam irradiances varied simultaneously) at zero delay and at long delays where only the free-carrier refraction remains. DFWM studies in CdTe at 1.06 μm showed similar fast $\chi^{(3)}$ and slow fifth order signals.

To determine the nature of these unexpectedly large and fast $\chi^{(3)}$ s, beam distortion measurements were made at various irradiance levels and fitted numerically to a nonlinear beam

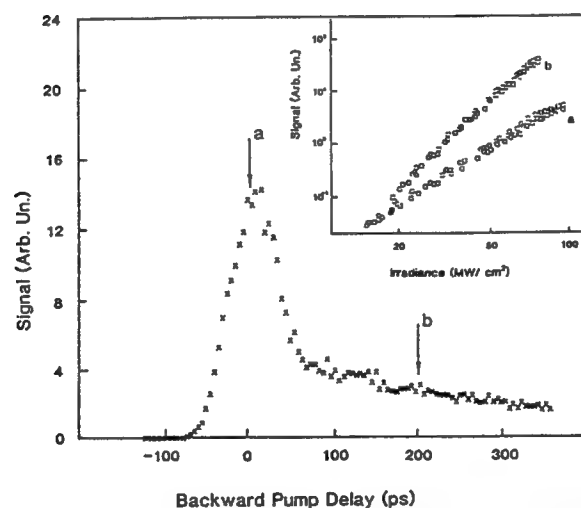


Fig. 1. The DFWM signal as a function of the temporal delay of the backward propagating pump beam (forward pump and probe temporally overlapped) for 30 ps, 0.53 μm pulses in ZnSe. The inset shows a log-log plot of the irradiance dependence at temporal delays of a) 0 ps and b) 200ps respectively (all three input beams varied simultaneously).

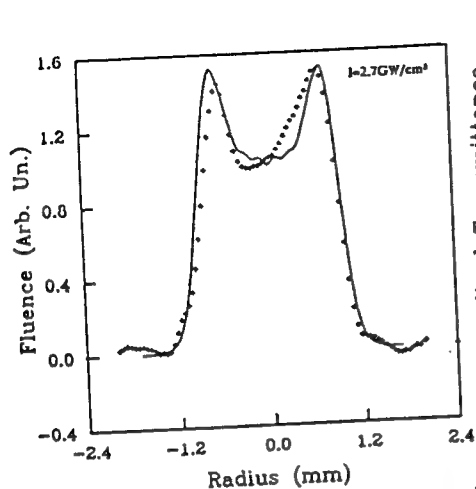


Fig. 2. The transmitted spatial energy distribution of a 30 ps 0.53 μm pulse after transmission and propagation through ZnSe as viewed on a vidicon. The solid line is the theoretical fit to the defocusing.

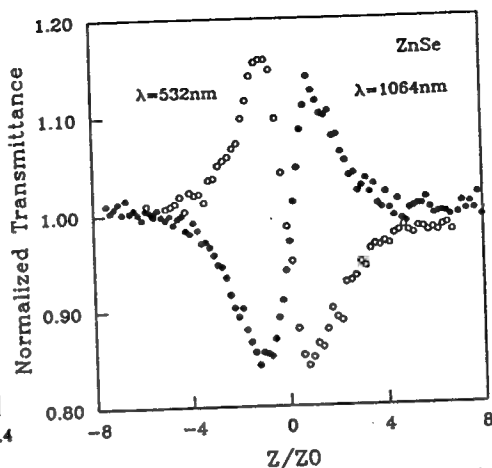


Fig. 3. Normalized transmittance versus sample position in units of $Z_0 = \pi \omega^2 / \lambda$ in a Z-scan experiment showing the sign change of n_2 from + at 1.06 μm to - at 0.53 μm .

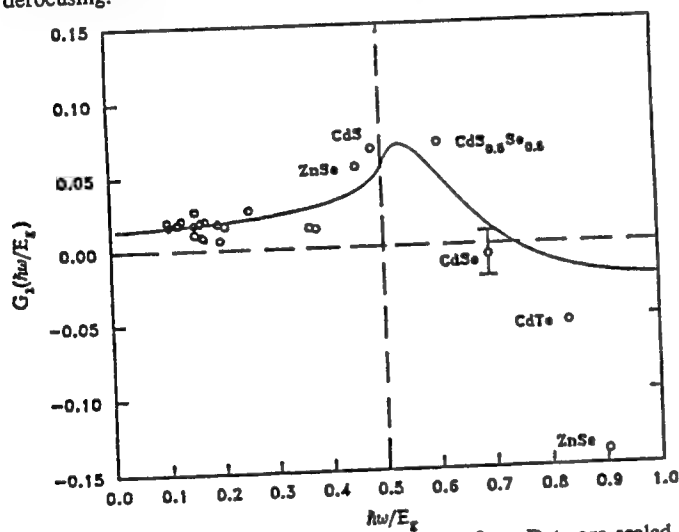


Fig. 4. A plot of $G_2(\hbar\omega/E_g)$, the dispersion of n_2 . Data are scaled by $n_0 E_g^4 / K$, where n_0 is the linear index and K is a numerical constant.

propagation code. Figure 2 shows the spatial energy distribution of a 0.53 μm pulse ≈ 10 cm after transmission through a 3 mm thick polycrystalline sample of ZnSe. The solid line fit to the data using $\beta = 5.5 \text{ cm/GW}$ [2] and $\sigma = 0.8 \times 10^{-21} \text{ cm}^3$ [1] gives $n_2 \approx -4 \times 10^{-11} \text{ esu}$.

These numbers agree with those determined from Z-scan measurements where the transmittance of an aperture placed in the far field is monitored as a function of the sample position with respect to the linear optics focal position.[1] Z-scans, as shown in Fig. 3, give the position with respect to the linear optics focal position. Z-scans, as shown in Fig. 3, give the sign of n_2 and show that for ZnSe the nonlinear refraction changes from positive at 1.06 μm to negative at 0.53 μm . We have performed similar experiments on CdTe and many other materials and they show similar behavior. The data for n_2 obtained by these methods along with the data from Ref. 3 for n_2 in wide gap dielectric materials fits a universal dispersion curve for n_2 as

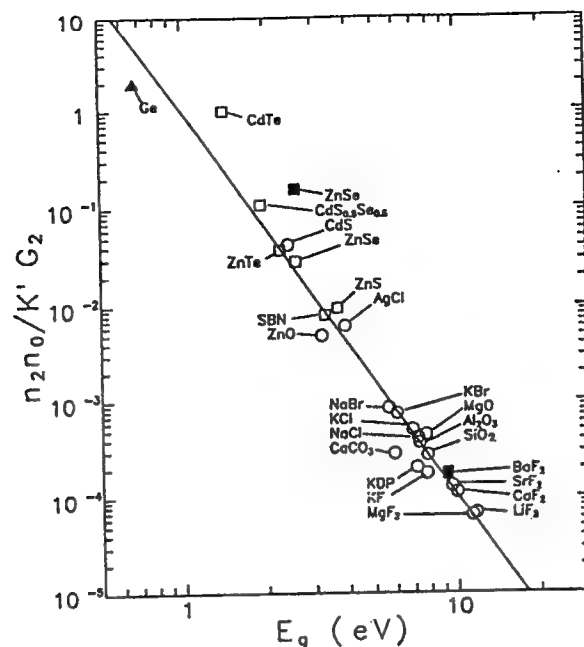


Fig. 5. Log-log plot of the scaled n_2 versus E_g showing the E_g^{-4} dependence of the straight line.

shown in Fig. 4. The solid curve in Fig. 4 was obtained from a nonlinear Kramers-Kronig transformation of the 2PA dispersion as given in Ref. 2. This theory, as well as the data, show a region of anomalous dispersion in n_2 between the 2PA edge and the fundamental edge.

1. M. Sheik-bahae, A.A. Said, T.H. Wei, D.J. Hagan, and E.W. Van Stryland, Jour. Quan. Elect., QE XX, April(1990).
2. M. Sheik-bahae, D.J. Hagan, and E.W. Van Stryland, submitted to Phys. Rev. Lett., (1990).
3. R. Addair, L.L. Chase, and S.A. Payne, Phys. Rev B39, 3337-3349 (1989).

Diffusion of color centers generated by two-photon absorption at 532 nm in cubic zirconia

Nastaran Mansour, Kamjou Mansour, E. W. Van Stryland, and M. J. Soileau
Center for Research in Electro-Optics and Lasers (CREOL), University of Central Florida,
Research Pavilion, Suite 400, 12424 Research Parkway, Orlando, Florida 32826

(Received 6 March 1989; accepted for publication 11 October 1989)

We have recently reported the formation of color centers in stabilized cubic zirconia (ZrO_2 , 18% Y_2O_3) by two-photon absorption at 532 nm. Here we present the results of measurements of the transmission of the colored samples as a function of time at room temperature. The results are found to be in good agreement with theory that assumes the color centers diffuse out of the irradiated region. The initial distribution of centers is assumed to have a Gaussian profile. For this model, the diffusion equation was solved exactly and the diffusion constant obtained ($\sim 3.4 \times 10^{-8} \text{ cm}^2/\text{s}$).

We have reported¹⁻³ that the transmission of stabilized cubic zirconia (ZrO_2 , 18% Y_2O_3) is decreased (about 15%) by exposing the samples to high-irradiance nanosecond and picosecond, 532-nm pulses. The mechanism was found to be due to formation of color centers by two-photon absorption.^{2,3} The induced color centers can be removed by repeated irradiation with relatively low irradiance at the same wavelength (532 nm) as shown in Fig. 1. These processes (coloring and discoloring) have potential application in making erasable optical memory devices.

In the present experiment, the transmission of colored samples (i.e., the density of color centers) was measured as a function of time at room temperature and was found to decrease due to diffusion to the surrounding medium. The measurement of the diffusion constant is presented.

The laser used in this study was a Nd:YAG oscillator-amplifier system, which has been described elsewhere.³ The laser was actively Q switched, operating at 1064 nm. Single pulses of measured Gaussian spatial profile were produced by the oscillator and amplified by a single pass through the amplifier. A KD*P crystal was used to produce pulses at 532 nm. Residual 1064-nm radiation was eliminated by reflecting off three dichroic mirrors. The temporal pulse width was approximately 15 ns (FWHM) at 532 nm. The temporal width of each pulse was monitored by a *p-i-n* photodiode detector and fast storage oscilloscope.

The laser beam was focused into the sample using a single element "best-form" lens designed for minimum spherical aberrations. The lens was a $f = 999 \text{ mm}$, which provided a nominal focal spot size of $155 \mu\text{m}$ (HW $1/e^2$ M in irradiance). For this measurement the actual focused spot sizes were obtained by scanning the spatial profile in both the horizontal and vertical dimensions with a $5\text{-}\mu\text{m}$ -diam pin-hole placed in the plane of the sample. By using a rotating half-wave plate/polarizer combination to vary the irradiance on the sample, the beam profile for high and low irradiance was held constant. The incident energy was continuously monitored by a sensitive photodiode where the output was digitized and calibrated with respect to pyroelectric energy meters.

We measured the transmission of the colored samples as a function of time in the following sequence. First, the stabi-

lized cubic zirconia (ZrO_2 , 18% Y_2O_3) sample was colored by exposing it to high-irradiance laser pulses at 532 nm. Second, after different time delays, the transmission of the sample was monitored by low-irradiance laser pulses at the same wavelength (532 nm) as shown in Fig. 2. As clearly indicated in the graph, when the sample was irradiated with high irradiance ($\sim 300 \text{ MW}/\text{cm}^2$), the transmission started to decrease, which indicated that color centers were generated in this material. After some number of shots, the transmission remained constant with further irradiation showing the saturation effects of the formation of these induced centers.

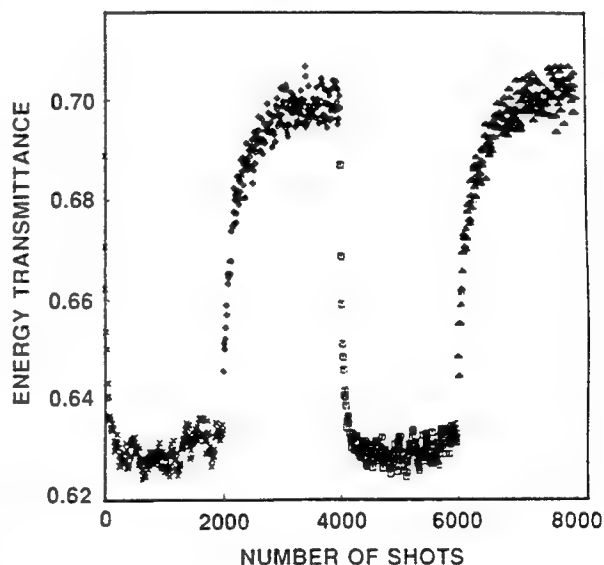


FIG. 1. Formation and bleaching of color centers in the stabilized cubic zirconia (ZrO_2 , 18% Y_2O_3) sample. The change of transmission is shown as a function of number of laser shots at various input irradiance levels in the ZrO_2 sample with 15-ns, 532-nm pulses. Note that in the first set of data (shown by \times 's) the transmission decreases with successive high-irradiance pulses of $300 \text{ MW}/\text{cm}^2$ until the effect (formation of color centers) saturates. The second set of data (shown by diamonds) was taken immediately after the first one by irradiating the sample at the same position with low-irradiance pulses of $20 \text{ MW}/\text{cm}^2$. As indicated in the figure, the transmission increased, and after some number of shots the transmission remained constant and equal to its value prior to the high-irradiance laser radiation. The other two sets of data show that the processes of generating and bleaching of the color centers are repeatable.

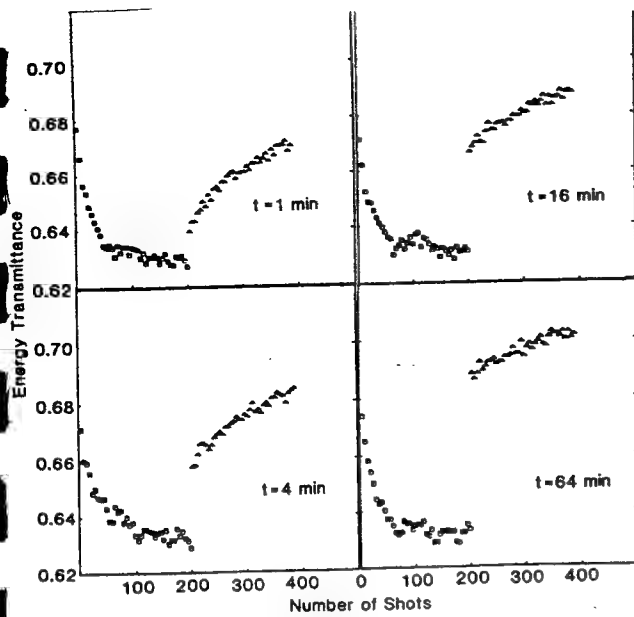


FIG. 2. The transmission of the irradiated region in stabilized cubic zirconia (ZrO_2 , 18% Y_2O_3) for 15-ns, 532-nm laser pulses. The jump shown after 200 laser firings appears after shutting off the laser for times of $t = 1, 4, 16$, and 64 min.

This allowed us to probe the transmission of the colored region of the sample for different time lapses before low-irradiance exposure ($\sim 20 \text{ MW/cm}^2$). As clearly indicated in Fig. 2, the transmission of the colored specimen increases with time (i.e., the density of color centers decreases) at room temperature. In the paragraphs to follow, it will be shown that this is due to diffusion of the color centers to the surrounding medium.

The general diffusion equation for the density $N(\mathbf{r}, t)$ of the color centers is given by

$$\frac{\partial}{\partial t} N(\mathbf{r}, t) = D \nabla^2 N(\mathbf{r}, t), \quad (1)$$

where D is the diffusion coefficient and has units of cm^2/s . Since the color centers are induced by irradiating the stabilized cubic zirconia (ZrO_2 , 18% Y_2O_3) samples with well-collimated laser pulses, the initial distribution of these centers was modeled as cylinders of Gaussian profile extending in the radial direction. For cylindrical symmetry, the diffusion equation [Eq. (1)] is simplified to

$$\frac{\partial}{\partial t} N(r, t) = D \frac{1}{r} \frac{\partial}{\partial r} \left(r \frac{\partial}{\partial r} N(r, t) \right), \quad (2)$$

subject to the initial condition ($t = 0$) of

$$N(r, 0) = N_0 \exp\left(-\frac{r^2}{(\Delta w)^2}\right), \quad (3)$$

where Δw is the $1/e$ radius of the spatial irradiance profile of the laser pulses. The contribution of diffusion of the color centers in the z direction is neglected, since in the case of a thick sample ($\sim 1 \text{ cm}$) the net flux is very small. Also, as discussed in the previous paragraph, the transmission change saturates after a number of high-irradiance pulses giving rise to constant color center density in the z direction.

To solve this problem, we introduce the Fourier transform pair for N :

$$N(\mathbf{k}, t) = \frac{1}{(2\pi)^n} \int_{-\infty}^{\infty} N(\mathbf{r}, t) \exp(i\mathbf{k} \cdot \mathbf{r}) d^n \mathbf{r}, \quad (4)$$

and

$$N(\mathbf{r}, t) = \int_{-\infty}^{\infty} N(\mathbf{k}, t) \exp(-i\mathbf{k} \cdot \mathbf{r}) d^n \mathbf{k}, \quad (5)$$

where n determines the dimension of the problem. We substitute (5) into (1) and perform the ∇^2 operation. Then Eq. (2) reduces to

$$\frac{\partial}{\partial t} N(\mathbf{k}, t) + D k^2 N(\mathbf{k}, t) = 0, \quad (6)$$

where $k^2 = \mathbf{k} \cdot \mathbf{k}$. The general solution of this ordinary differential equation is

$$N(\mathbf{k}, t) = C(\mathbf{k}) \exp(-D k^2 t), \quad (7)$$

where $C(\mathbf{k})$ is the Fourier transform of the initial distribution of color centers $N(\mathbf{r}, 0)$:

$$C(\mathbf{k}) = \frac{1}{(2\pi)^n} \int_{-\infty}^{\infty} N(\mathbf{r}, 0) \exp(i\mathbf{k} \cdot \mathbf{r}) d^n \mathbf{r}. \quad (8)$$

Performing the inverse Fourier transform of $N(\mathbf{k}, t)$, we obtain

$$N(\mathbf{r}, t) = \int_{-\infty}^{\infty} \left(\frac{1}{(2\pi)^n} \int_{-\infty}^{\infty} N(\mathbf{r}', 0) \exp(i\mathbf{k} \cdot \mathbf{r}') d^n \mathbf{r}' \right) \times \exp(-D k^2 t) \exp(-i\mathbf{k} \cdot \mathbf{r}) d^n \mathbf{k}. \quad (9)$$

Rearranging the order of integration,

$$N(\mathbf{r}, t) = \frac{1}{(2\pi)^n} \int_{-\infty}^{\infty} N(\mathbf{r}', 0) \left(\int_{-\infty}^{\infty} \exp(-D k^2 t) \times \exp[-i\mathbf{k} \cdot (\mathbf{r} - \mathbf{r}')] d^n \mathbf{k} \right) d^n \mathbf{r}'. \quad (10)$$

The Fourier transform of $\exp(-D k^2 t)$ is given in Ref. 4 as

$$\frac{1}{(2\pi)^n} \int_{-\infty}^{\infty} \exp(-D k^2 t) \exp[-i\mathbf{k} \cdot (\mathbf{r} - \mathbf{r}')] d^n \mathbf{k} = \frac{1}{(2\pi)^n} \left(\frac{\pi}{Dt} \right)^{n/2} \exp\left(-\frac{(\mathbf{r} - \mathbf{r}')^2}{4Dt}\right).$$

Hence

$$N(\mathbf{r}, t) = \left(\frac{1}{4\pi Dt} \right)^{n/2} \int_{-\infty}^{\infty} \exp\left(-\frac{(\mathbf{r} - \mathbf{r}')^2}{4Dt}\right) N(\mathbf{r}', 0) d^n \mathbf{r}'. \quad (11)$$

Since we have cylindrical symmetry and the diffusion occurs in the radial direction, $n = 2$ and Eq. (11) can be reduced using Eq. (3) to

$$N(r, t) = \frac{1}{4\pi Dt} \int_0^{2\pi} d\theta \int_0^{\infty} r' dr' \exp\left(-\frac{(r - r')^2}{4Dt}\right) \times N_0 \exp\left(-\frac{r'^2}{(\Delta w)^2}\right). \quad (12)$$

Performing the integration over θ and r , we obtain

$$N(r, t) = \frac{N_0}{1 + [4D/(\Delta w)^2]} \exp\left(\frac{-r^2}{(\Delta w)^2 + 4Dt}\right). \quad (13)$$

Note that the solution has a Gaussian profile which broadens in time.

The total number of carriers in an element of sample length dz is given by $\eta(t)dz$ where

$$\eta(t) = \int_0^{2\pi} d\theta \int_0^\infty r dr N(r,t).$$

If we weight this function with the Gaussian irradiance distribution, we obtain the effective number of color centers per unit length encountered by the beam in the irradiated region $M(t)$:

$$M(t) = \int_0^{2\pi} d\theta \int_0^\infty r dr N(r,t) \exp\left(\frac{-r^2}{(\Delta w)^2}\right). \quad (14)$$

Substituting for $N(r,t)$ from Eq. (13) and performing the integration, the expression for $M(t)$ can be found as

$$M(t) = \frac{\pi}{2} N_0 \frac{(\Delta w)^4}{(\Delta w)^2 + 2Dt}. \quad (15)$$

The number of carriers at $t = 0$ is

$$M(0) = \frac{\pi}{2} N_0 \pi (\Delta w)^2. \quad (16)$$

Rewriting Eq. (15) in terms of the initial carrier density ($t = 0$), we have

$$\frac{M(0)}{M(t)} = 1 + \frac{2D}{(\Delta w)^2} t, \quad (17)$$

which indicates that the ratio of the initial number of color centers per unit length $M(0)$ to $M(t)$ is a linear function of t with slope $2D/(\Delta w)^2$.

This ratio can be determined by monitoring the transmission of the sample as a function of time, given the transmission $T(t)$ of the sample:

$$T(t) = T' \exp[-\alpha M(t)L], \quad (18)$$

where α is the linear absorption coefficient, T' shows the linear transmission of the unirradiated sample, and L is the thickness of the sample. Thus $M(t)$ can be found from

$$\alpha M(t) = -\frac{1}{L} \ln\left(\frac{T(t)}{T'}\right), \quad (19)$$

where $M(t)$ denotes the number of color centers encountered by the beam at time t (i.e., for a given pulse at time t).

In the process of coloring the sample as is presented in Fig. 2, the saturation effect on the formation of the color centers was observed and the transmission remained constant at $T(0)$. Thus the initial number density of centers can be found from

$$\alpha M(0) = -\frac{1}{L} \ln\left(\frac{T(0)}{T'}\right). \quad (20)$$

Using Eqs. (23) and (24), $M(0)/M(t)$ can be written as

$$\frac{M(0)}{M(t)} = \ln\left(\frac{T(0)}{T'}\right) / \ln\left(\frac{T(t)}{T'}\right) = 1 + \frac{2D}{(\Delta w)^2} t. \quad (21)$$

The experimental results of $M(0)/M(t)$ as a function of t are presented in Fig. 3. The solid line presents the theoretical fit [Eq. (25)] with the extracted diffusion constant ($D = 3.4 \times 10^{-8} \text{ cm}^2/\text{s}$).

In order for a color center to diffuse at room tempera-

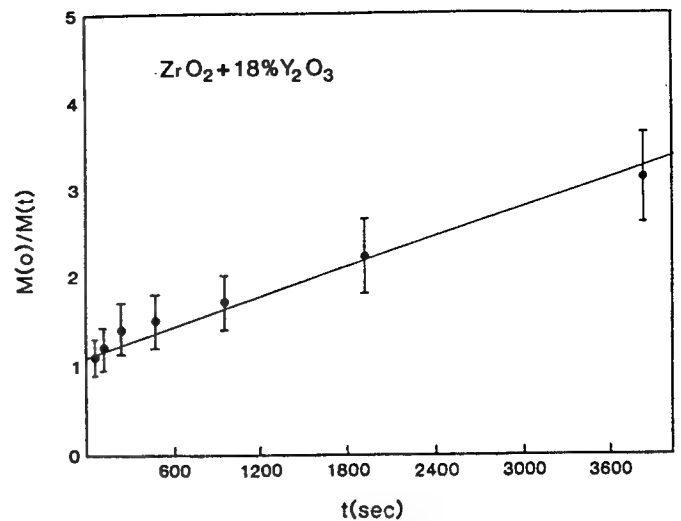


FIG. 3. The ratio of induced color center density at time $t = 0$ to the density at time t as a function of t .

ture, it must have sufficient thermal energy to overcome the potential energy barrier presented by its neighbors. This activation energy E is related to the diffusion coefficient D which is generally described by⁵

$$D = D_0 \exp\left(-\frac{E}{kT}\right), \quad (22)$$

where D_0 is a temperature independent factor. Using the values of $D_0 = 1.3 \text{ cm}^2/\text{s}$ (Ref. 6) and $T = 300 \text{ K}$, one can obtain the activation energy of approximately 0.5 eV given the diffusion coefficient obtained by our model. This activation energy is the right order of magnitude for migration of anion vacancies as obtained in Ref. 7 for cubic zirconia.

To conclude, we have shown that the density of color centers generated by two-photon absorption at 532 nm in stabilized cubic zirconia (ZrO_2 , 18% Y_2O_3) decreases due to slow diffusion to the surrounding medium with a diffusion coefficient of $D = 3.4 \times 10^{-8} \text{ cm}^2/\text{s}$ at room temperature. This can be seen by the fit of experimental results with the diffusion model in Fig. 3.

ACKNOWLEDGMENTS

We gratefully acknowledge the support of the Florida High Technology and Industry Council and The Defense Advanced Research Projects Agency.

¹ N. Mansour, E. Canto, M. J. Soileau, and E. W. VanStryland, in *Laser Induced Damage in Optical Materials*, Natl. Bur. Stand. (U.S.) Spec. Pub. (1986).

² N. Mansour, K. Mansour, M. J. Soileau, and E. W. VanStryland, in *Laser Induced Damage in Optical Materials*, Natl. Bur. Stand. (U.S.) Spec. Pub. (1987).

³ N. Mansour, Ph.D. dissertation, University of North Texas (1988).

⁴ J. D. Gaskill, *Linear System, Fourier Transforms, and Optics* (Wiley, New York, 1978), p. 201.

⁵ P. G. Shewmon, *Diffusion in Solids* (McGraw-Hill, New York, 1963), Chaps. 2-5.

⁶ A. Nakamura and J. B. Wagner, Jr., *J. Electrochem. Soc.* 133, 1542 (1986).

⁷ W. C. Mackrodt and P. M. Woodrow, *J. Am. Ceram. Soc.* 69, 277 (1986).

Laser-induced damage and the role of self-focusing

J. J. Soileau, FELLOW SPIE
University of Central Florida
Center for Research in Electro-Optics
and Lasers
Orlando, Florida 32816

William E. Williams, MEMBER SPIE
Photon Laser Systems
787 S. Orange Blossom Trail
Opoka, Florida 32703

Mustafar Mansour
Eric W. Van Stryland, MEMBER SPIE
University of Central Florida
Center for Research in Electro-Optics
and Lasers
Orlando, Florida 32816

Abstract. We review the influence of self-focusing on the measurement of bulk laser-induced-damage (LID) thresholds in normally transparent optical materials. This role is experimentally determined by measuring the spot size and polarization dependence of LID and by observing beam distortion in the far field. Utilizing these techniques, we find that by using a tight focusing geometry in which the breakdown power is below P_2 , the effects of self-focusing can be practically eliminated in an LID experiment. P_2 is the so-called second critical power for self-focusing, and $P_2 = 3.77P_1$, where $P_1 = c\lambda^2/32\pi^2n_2$, where c is the speed of light in vacuum, λ is the laser wavelength and n_2 is the nonlinear index of refraction. This is in accordance with numerical calculations by J. H. Marburger [in *Progress in Quantum Electronics*, J. H. Sanders and S. Stenholm, eds., Vol. 4, Part 1, pp. 35-110, Pergamon, Oxford (1975)]. With this knowledge we determine that damage is only partially explained by avalanche ionization and that the initiation of damage is strongly influenced by extrinsic processes. We therefore conclude that we are measuring extrinsic LID.

Subject terms: laser-induced material modification; laser-induced damage; laser-induced breakdown; avalanche ionization; dielectric breakdown; multiphoton absorption; self-focusing.

Optical Engineering 28(10), 1133-1144 (October 1989).

CONTENTS

Introduction
Historical review
Theory
3.1. Self-focusing
3.2. Polarization dependence of self-focusing
Experiment
4.1. Experimental verification of Marburger's theory
4.2. Polarization dependence
Conclusions from the role of self-focusing in laser-induced damage
5.1. Re-evaluation of extrinsic laser-induced damage data
5.2. Wavelength, temporal, and spot size dependence
Controlled defect studies
Conclusion
Acknowledgments
References

1. INTRODUCTION

In this paper we discuss bulk (as opposed to surface) laser-induced-damage (LID) in transparent optical materials, i.e., materials whose linear absorption at the input laser wavelength is the order of 10^{-3} or less.¹⁻³ In anticipation of our conclusion that, with few possible exceptions, LID is influenced by extrinsic processes, we refer to the damage as extrinsic laser-induced-damage (ELID) in what follows. However, it is important to realize that how self-focusing affects damage threshold data is independent of the damage mechanism (i.e., intrinsic or extrinsic). By intrinsic we mean that the threshold is not increased by reducing the defect or impurity density. We investigate the role of self-focusing in LID and how the experimental geometry can alter this role. Misunderstandings concerning self-focusing effects have led researchers to incorrect conclusions concerning the observed parametric dependences of ELID, which in turn affect conclusions of the importance of extrinsic effects in LID. A clear understanding of the role of self-focusing in LID allows us to design experimental geometries in which such effects can be practically eliminated.

Invited Paper LI-112 received March 24, 1989; revised manuscript received May 5, 1989; accepted for publication June 26, 1989.
© 1989 Society of Photo-Optical Instrumentation Engineers.

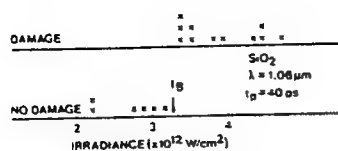


Fig. 1. Method of LID threshold determination. Damage (X on upper line) or no damage (X on lower line) for SiO_2 .

Parametric dependencies of ELID thresholds can then be unambiguously compared with predictions of theory. The overwhelming evidence from such studies points to the conclusion that damage in these transparent materials is not completely explained by avalanche ionization theory^{4,5} but is heavily influenced by extrinsic effects. We give evidence supporting this conclusion by presenting ELID data for doped glasses and gamma-irradiated SiO_2 .

ELID is a threshold-like phenomenon. The threshold behavior is illustrated in Fig. 1, which shows a set of ELID data taken on a fused silica sample using 40 ps, linearly polarized, 1.06 μm pulses focused to a Gaussian spot size of approximately 6.8 μm . Throughout this paper pulsewidths are quoted as FWHM, and spot sizes are the HW $1/e^2$ M in irradiance. The data are plotted as a function of internal irradiance with an X on the lower line if no damage occurred and on the upper line if damage did occur. The threshold is defined as the peak-on-axis fluence (J/cm^2), irradiance (W/cm^2), or rms electric field (V/cm), which results in an irreversible change in the specimen as determined by one or more of the following: an increase in scattering of a HeNe probe beam (either by visual observation or photometric detection), a change in morphology as seen in a microscope, or a permanent change in the transmittance of the sample. In most cases this type of damage is obvious and all of the symptoms are observed. In addition, ELID in these materials is usually accompanied by a visual flash associated with the onset of dielectric breakdown (i.e., avalanche ionization). These data as well as other data discussed in this paper are one-on-one measurements in which each site is irradiated only once even if the site did not incur damage. It is observed in some materials that preirradiation with pulses below the damage threshold as defined can alter the ELID threshold, the so-called N-on-one effect. Note the very sharp threshold shown in Fig. 1, which is indicative of damage in transparent dielectrics. The threshold shown of approximately $3.3 \times 10^{12} \text{ W}/\text{cm}^2$ is about two orders of magnitude larger than could be expected from the same sample used as an optical component in a system. This is the case since the failure mode for large illuminated areas used in practice is more likely surface damage where other extrinsic effects cause damage. In the experiments relevant to this paper, surface damage is avoided by focusing into the bulk of the material, keeping the irradiance at the damage-prone surfaces low.

The threshold-like behavior illustrated in Fig. 1 is indicative of an extremely nonlinear process. Considerable effort has been spent to monitor subthreshold changes in the optical properties of these materials with little success. A notable exception is the recent work of Bräunlich and coworkers at Washington State University.⁶⁻⁸ They report the observation of multiphoton absorption of 532 nm light in carefully selected alkali halide samples of as high an order as four prior to damage using luminescence and the photoacoustic tech-

nique. We comment on the possible implications of their results in Sec. 5. No connection between the linear optical properties and the ELID thresholds has been found. Experiments have also shown that the transmittance of a laser pulse is cut off within a few picoseconds of the initiation of damage with no pulse distortion prior to damage.⁹ This highly nonlinear behavior of ELID makes precise determination of the damage mechanism(s) difficult. In fact, we must infer the mechanism(s) of failure from parametric dependences (e.g., pulsewidth and wavelength dependence). This has resulted in slow progress in developing a complete understanding of the physical processes involved in ELID. On the other hand, as we shall see later in this paper, the first qualitative description of ELID was essentially correct.^{10,11}

2. HISTORICAL REVIEW

The first reports of bulk ELID were by Bruma¹⁰ and Hercher¹¹ in papers at the 1964 spring meeting of the Optical Society of America. The principal conclusions of these initial reports are as follows: (1) Linear absorption plays no major role in this type of failure. (2) The damage process is highly nonlinear. (3) Electron avalanche breakdown may be initiated by defects and/or impurities. (4) The ELID threshold and morphology depend on spot size. While there has been some controversy regarding the third statement, data now tends to confirm all of the statements made 25 years ago. Excellent sources for data on ELID in many materials are the proceedings of the annual Boulder Damage Conference starting in 1970 and the references therein.¹²

One can divide much of the past results in ELID experiments into two distinct categories. Category A consists largely of work conducted at Harvard University by Bloembergen¹ and his students Yablonovitch,¹³⁻¹⁵ Fradin,¹⁶⁻²⁰ and Smith^{2,21-23} and by their coworkers. The Category A experiments represent a systematic investigation of the breakdown thresholds of several alkali halides and fused quartz over wavelengths ranging from 10.6 μm to 0.355 μm and for pulse durations ranging from nanoseconds to tens of picoseconds. The results were interpreted in terms of an intrinsic model of electron avalanche breakdown.² The breakdown thresholds were found to vary little from sample to sample for a given material even if the samples were supplied by different crystal growers. The breakdown thresholds were found to agree within $\pm 15\%$ over wavelengths ranging from 10.6 μm to 1.06 μm . It is important to note that this agreement in damage threshold for the alkali halides was obtained by comparing damage thresholds for different focusing conditions at the different wavelengths over a wide range of pulse durations and focusing conditions. In addition, the Category A workers found that the frequency dependence of the breakdown thresholds agreed with the theory of intrinsic avalanche ionization over the full wavelength range, although some evidence of multiphoton ionization was observed at 0.355 μm .²²

In part, the agreement of the results of the Category A workers with the predicted frequency dependence of intrinsic electron avalanche breakdown arose from attempts to correct the data at 1.064 μm , 0.694 μm , 0.532 μm , and 0.355 μm for the presumed effects of self-focusing. For example, Smith et al.^{21,22} scaled the results of their picosecond breakdown work under the assumption that P_1 (discussed in the next section) was the critical power of importance for focused Gaussian beams. They observed a slow increase in the scaled

thresholds with increasing frequency, consistent with the predictions of intrinsic avalanche theory. We now know P_1 is not the critical power of importance in those experiments and the data should not have been scaled, thus invalidating the conclusions. The unscaled thresholds *decrease* with increasing frequency, opposite to the prediction of the intrinsic avalanche ionization theory.

On the other hand, the results of Category B workers were often found to be inconsistent with those of the Harvard group. Category B workers include Olness,^{24,25} Yasojima and coworkers in Japan,^{26,27} Bass and Barrett²⁸ and coworkers at the University of Southern California, Manenkov²⁹ and coworkers in the Soviet Union, Soileau,^{30,31} Van Stryland,³² and Sparks.⁴ One of the main conclusions to be drawn from the Category B experiments is that laser-induced breakdown is caused by extrinsic properties of the material. In a study reported by Manenkov²⁹ in 1977, the breakdown irradiance at 1.06 μm measured for 100 NaCl samples varied from sample to sample by a factor of 50. The highest thresholds reported in Manenkov's work were higher than previously reported "intrinsic" thresholds (e.g., three times those reported in Ref. 13). Similar results have been seen by Soileau^{30,31} and in earlier studies by Olness²⁵ and Yasojima.²⁷ In addition, no systematic variation in the breakdown thresholds as a function of material bandgap was observed in the results of Olness^{24,25} and Yasojima^{26,27} in contrast to the Category A measurements. A decrease in the breakdown threshold with decreasing laser wavelength was seen by Soileau et al.^{30,31} in the alkali halides over wavelengths ranging from 10.6 μm to 1.06 μm , as was observed for the unscaled thresholds of Smith et al.^{21,22} Again, this is opposite to the trend predicted by intrinsic avalanche ionization theory. Finally, results in Category B experiments indicate the presence of a strong spot size dependence for the breakdown field in the alkali halides and fused quartz as well as other materials that could not be explained by self-focusing and is inconsistent with intrinsic avalanche breakdown theory. Also, the measured damage thresholds differed from sample to sample even in materials from the same manufacturer.

Much of the controversy found in the literature is due to the differences in the ways in which various authors account for, or attempt to account for, self-focusing. Early in the history of studies of ELID, self-focusing was recognized as one of the major contributors to catastrophic, irreversible changes in material properties.¹² Over the years many studies, both theoretical and experimental, have been conducted in attempts to account for self-focusing effects in bulk damage experiments. However, due to the complexity of the problem, agreement between theory and experiment has been mixed. While accurate, direct measurements of the nonlinear index of refraction, n_2 , have been made using various techniques (e.g., interferometry^{33,34}), the power for which significant changes occur in the linear propagation of focused Gaussian beams through nonlinear materials has only recently been established experimentally.^{35,36} We present some of that work in what follows.

3. THEORY

3.1. Self-focusing

Nonlinear refraction in a highly transparent dielectric results from a change in the index of refraction given by

$$\Delta n = n_2 \langle E^2 \rangle . \quad (1)$$

where $\langle E^2 \rangle$ is the time-averaged square of the electric field and n_2 is the nonlinear index of refraction. Here, we assume that the nonlinearity has a response time much less than the pulse duration. An alternative way of expressing the index change that has come into common use recently is $\Delta n = \gamma I$, where I is the irradiance and γ is a nonlinear index coefficient. These coefficients are related by a constant with³³ n_2 (esu) = $cn/40\pi \gamma$ (m²/W), where c is the speed of light in vacuum (m/s) and n is the linear index of refraction. Many mechanisms can give rise to self-focusing effects in solids. For tight focusing geometries using nanosecond and longer pulse durations, electrostriction, thermal self-focusing, and the electronic Kerr effect can all contribute to a catastrophic self-focus. For picosecond pulse durations the dominant mechanism in transparent solids is believed to be the electronic Kerr effect.

A large volume of work has been devoted to the study of self-focusing effects in solids.¹² The theories developed to describe the process indicate that self-focusing is dependent on the power of the laser beam in the material. Two critical powers of importance are often cited in the literature for Gaussian beams. The first of these, P_1 , is given by³⁷

$$P_1 = \frac{c\lambda^2}{32\pi^2 n_2} , \quad (2)$$

where λ is the laser wavelength. Many theories based on the constant shape approximation have assumed that a catastrophic collapse of the beam will occur in the material when the beam power approaches P_1 . This idea was first introduced by Zverev and Pashkov,³⁸ who suggested the following equation for the irradiance enhancement due to self-focusing:

$$I_{\text{SF}} \approx \frac{I_0}{1 - P/P_1} , \quad (3)$$

where I_{SF} is the peak irradiance in the presence of self-focusing and I_0 is the peak irradiance in the absence of self-focusing. This equation was subsequently used by researchers to "scale" damage data and "correct" for the effects of self-focusing.^{16,21,22} Equation (3) can be rearranged to give the following equation:

$$\frac{1}{P} = \frac{1}{I_D} \left(\frac{1}{A} \right) + \frac{1}{P_1} , \quad (4)$$

where A is the focal beam area in the absence of self-focusing. Thus, a plot of inverse power for damage, versus inverse area, or spot size squared, was expected to yield both the critical power for self-focusing P_1 as the intercept and the damage irradiance I_D from the slope. A critical assumption made in using this equation is that the damage irradiance is independent of focal area in the absence of self-focusing. We find this assumption invalid as discussed in Sec. 5.2.

In contrast to the earlier self-focusing studies, exact solutions of the nonlinear wave equation made by Marburger³⁷ have shown that even for focused geometries, significant deviations from normal linear propagation do not occur until the beam power exceeds P_1 and a catastrophic collapse of the beam within the depth of focus does not occur until the beam

TABLE I. Comparison of the constant shape approximation (CSA) to numerical solutions³⁷ (NS) for focused Gaussian beams.

P/P_2	I/I_0 CSA	I/I_0 NS
0.27	1.37	1.30
0.60	2.50	2.08
0.80	5.00	3.94
0.90	10.00	7.15
0.95	20.00	16.45
0.96	25.00	28.60
0.97	33.30	63.40
0.98	50.00	100.00
0.99	100.00	192.00

power exceeds the second critical power P_2 . P_2 is defined as (for Gaussian beams)

$$P_2 = 3.77 P_1. \quad (5)$$

The factor of 3.77 in Eq. (5) comes from numerical solutions of the nonlinear wave equation for an input beam with a Gaussian spatial profile. The power P_2 is the least power for a singular self-focus to occur within the Rayleigh range, i.e., the beam confocal parameter, for both prefocused and unfocused geometries. This means that for samples thicker than the Rayleigh range (as is the case for most bulk laser-induced damage experiments) a singular self-focus will occur *within* the sample, and LID will occur for an input power equal to P_2 . Note that for tightly focused beams, i.e., very small spot sizes, the breakdown field will be reached before P approaches P_2 . If that is the case, then LID results can be nearly independent of self-focusing effects. The small focal spot size needed will depend on the material, P_2 , and the material breakdown threshold.

Marburger³⁷ found that the irradiance enhancement within the nonlinear material was given approximately by

$$I_{SF} = \frac{I_0}{1 - P/P_2}, \quad (6)$$

which is only valid for $P \leq P_2/4$. Note that this is identical to Eq. (3) with P_1 replaced by P_2 . When the input power is significantly greater than $P_2/4$ one must use the more complete numerical solution to compute the enhanced irradiance due to self-focusing. Table I is a comparison of the approximation given by Eq. (6) and the exact numerical solution given by Marburger (see Ref. 37, p. 66). Note that while the enhancement cannot be calculated accurately by Eq. (6) for $P > P_2/4$, it still correctly predicts breakdown at a power of P_2 .

In 1977 Smith et al.²² also found some problem in using P_1 for correcting their 532 nm and 355 nm picosecond damage thresholds for self-focusing. In most cases, their 355 nm thresholds were higher than P_1 . A scaling factor was proposed such that the critical power varied between P_1 and P_2 depending on the value of P at damage. However, since the exact functional dependence for the intensification was unknown at the time, the thresholds reported in Ref. 22 included the breakdown power and the uncorrected focal area so that future workers could re-examine the data in the light of new measurements. We re-examine that data in Sec. 5.1.

We previously presented experimental evidence showing that, as predicted by Marburger, the important power for focused geometries is the second critical power, P_2 .^{35,37}

Indeed, Eq. (5) can be "verified" (i.e., we show that P_2 is the critical power of importance) as shown in Sec. 4. Additional evidence for high P_2 materials is given by measurements of the polarization dependence of the breakdown powers and measurements of beam distortions in the transmitted, time-integrated spatial beam profile discussed in Sec. 4.

3.2. Polarization dependence of self-focusing

The use of short pulses presents us with the advantage that we need only consider the fast electronic Kerr nonlinearity in data analysis. This nonlinearity is polarization dependent, and this polarization dependence presents us with a simple way of determining whether or not self-focusing effects are present in LID measurements.

Early papers in the literature have shown that the nonlinear refractive index for isotropic materials (such as fused quartz) is given by³⁹⁻⁴¹

$$n_2(\text{L.P.}) = \frac{12\pi}{n} \chi_{1111}^{(3)}, \quad (7)$$

$$n_2(\text{C.P.}) = \frac{24\pi}{n} \chi_{1122}^{(3)},$$

for linearly polarized and circularly polarized light, respectively, where the $\chi_{ijkl}^{(3)}$ are third-order nonlinear susceptibility tensor elements. A symmetry relation exists for isotropic materials such that

$$\chi_{1111}^{(3)} = 2\chi_{1122}^{(3)} + \chi_{1221}^{(3)}. \quad (8)$$

Measured values for these tensor elements indicate that for fused quartz $\chi_{1122}^{(3)}$ is approximately equal to $\chi_{1221}^{(3)}$.⁴¹ Thus, we can express $n_2(\text{C.P.})$ in terms of the same $\chi^{(3)}$ tensor element as $n_2(\text{L.P.})$, giving

$$n_2(\text{C.P.}) = \frac{8\pi}{n_0} \chi_{1111}^{(3)}. \quad (9)$$

We see that the ratio of n_2 for circular polarization to n_2 for linear polarization is 2/3. This implies that the ratio of the critical powers for self-focusing for the two cases is 1.5.

A similar but slightly more complicated analysis for NaCl gives a ratio for the critical powers that varies between 1.37 and 1.46 depending on the propagation direction in the cubic crystal. We do not know the orientation of the large grain size crystalline samples and, therefore, expect a ratio between the above values near 1.4.

If we extend this concept to measurements of bulk optical breakdown and if self-focusing dominates the breakdown process, then, in both the isotropic and cubic cases, the ratios of the breakdown powers for the two polarization states should be equal to the ratio of the critical powers (i.e., 1.5 for SiO_2 and ≈ 1.4 for NaCl).

The polarization dependence of self-focusing has already been well established experimentally. For example, Moran et al.³⁴ measured n_2 for various laser glasses (isotropic materials) using time-resolved interferometry and found that $n_2(\text{L.P.}) = 1.5 n_2(\text{C.P.})$. Feldman et al.⁴² measured the breakdown powers as a function of polarization for fused quartz and other glasses using nanosecond pulse durations at 1.06 μm . He used the observed polarization dependence in an attempt to sepa-

TABLE II: The nonlinear refractive index n_2 as measured using beam distortion⁴³ compared with other methods.

MATERIAL	WAVELENGTH μm	n_2 ($\times 10^{13}$ esu)	n_2 (Others) ($\times 10^{13}$ esu)
CS ₂	1.06	128 \pm 30	125 \pm 30 ⁴⁵
	0.53	123 \pm 30	
NaCl	1.06	1.37 \pm 0.30	1.22 \pm 0.21 ³³ 1.59 ⁵⁷
	0.53	1.38 \pm 0.30	
SiO ₂	1.06	0.62 \pm 0.15	0.95 \pm 0.10 ³³ 0.85 ⁴⁷
	0.53	0.60 \pm 0.15	
BK-7	1.06	1.45 \pm 0.30	1.46 \pm 0.10 ⁴⁶ 1.30 ⁴⁷
	0.53	1.01 \pm 0.25	

rate the various contributions to n_2 and was the first to point out that the presence or absence of self-focusing in breakdown measurements could be determined by measuring the breakdown threshold power as a function of polarization. We use this concept in our own measurements to determine the contribution of self-focusing. The data presented in Sec. 4.2 on fused quartz and NaCl clearly show the transition from an experimental geometry in which self-focusing dominates the damage process to a geometry in which self-focusing can be neglected. In the next section we first verify Marburger's theory by monitoring breakdown in CS₂ at 1.06 μm and 0.53 μm .

4. EXPERIMENT

4.1. Experimental verification of Marburger's theory

Marburger's prediction³⁷ that breakdown will occur at an input power P_2 given by Eq. (5) in a tight focusing geometry can be verified by arranging an experiment in which the breakdown threshold is very high and P_2 is very low. A classic example of such a material is the liquid CS₂. This material is an excellent choice for model system studies since its nonlinear behavior has been studied for years and is relatively well understood. The nonlinearity is due to nonresonant reorientation of the CS₂ molecules, which relaxes with a time constant of approximately 2 ps. The first step is to measure n_2 in a manner independent of the laser-induced breakdown measurements. Table II is a summary of such measurements for CS₂ and other materials of interest using the beam distortion technique described in Ref. 43. Values obtained by other workers using various techniques are listed for comparison.^{33,44-47} With the possible exception of SiO₂ (a 30% difference) the agreement with other methods is excellent. It is important to note that the observation of beam distortion in the far field as reported in Ref. 43 is performed at irradiance levels not far below damage, and the agreement with other data confirms the propagation analysis for high input powers.

We next set up a bulk breakdown experiment in CS₂, i.e., arranged the sample length to be much longer than the confocal beam parameter, and measured the breakdown power.⁴⁸ We then used Eq. (5) to calculate n_2 at both 1.06 μm and 0.53 μm and compared this with values obtained by beam distortion measurements⁴⁴ and time-integrated interferometry.⁴⁵ The results of this comparison are shown in Table III. In this experiment laser-induced breakdown is totally dominated by self-focusing and the breakdown power was experimentally determined to be independent of the focusing conditions. Note the excellent agreement between the n_2 determined from the breakdown measurements using Eq. (5), which assumes

TABLE III. Comparison of the LID method using P_2 with other methods of measuring n_2 in CS₂.

METHOD	$\lambda(\mu\text{m})$	n_2 ($\times 10^{11}$ esu)
Equation 5	1.06	1.3 \pm 0.3 ⁴⁸
Equation 5	0.53	1.2 \pm 0.3 ⁴⁸
Beam Distortion	1.06	1.5 \pm 0.3 ⁴³
Beam Distortion	0.53	1.5 \pm 0.3 ⁴³
Interferometry	1.32	1.3 \pm 0.3 ⁴⁵

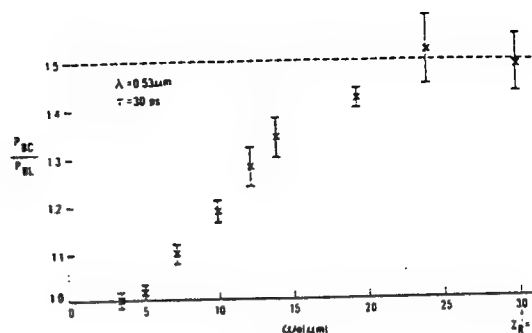


Fig. 2. A plot of the ratio of P_B for circularly polarized light to P_B for linearly polarized light as a function of spot size in SiO₂ (sample 79-FQ-7940-1). The dashed line represents the expected ratio when self-focusing dominates.

that P_2 is the critical power, and those determined by beam distortion measurements. This verifies that the factor of 3.77 predicted by the theory in Ref. 37 is correct to within the error bars shown.

We have also experimentally determined when self-focusing is present in bulk breakdown experiments by observing the polarization dependence of damage as discussed in the following section.

4.2. Polarization dependence

Figure 2 is a plot of the ratio of the breakdown power for circular polarization to the breakdown power for linear polarization as a function of the focal spot radius measured in air.^{35,36} The material is fused quartz, the laser wavelength is 0.53 μm , and the pulse duration is 30 ps. Three regions of interest are clearly evident. For small focal radii and small breakdown powers the ratio $P_{Bcircular}/P_{Blinear}$ is approximately unity, indicating the lack of electronic self-focusing as discussed in Sec. 3.2. For focal radii greater than 23 μm and large breakdown powers the ratio levels off to near the theoretical value of 1.5 indicating the dominance of self-focusing. The transition regime shows the data increasing from unity to the theoretical maximum, clearly showing the onset of electronic self-focusing in fused quartz.

Now, rather than looking at the ratio of the critical powers we examine the behavior of the breakdown powers directly in Fig. 3. Here, the breakdown power in megawatts is plotted as a function of the focal spot radius in air. The triangles represent the breakdown powers for linear polarization, and the circles are the breakdown powers for circular polarization. The horizontal dashed line represents the critical power P_2 for linear polarization calculated from our measured n_2 values for this sample.⁴³ As can be seen, the breakdown power for linear polarization increases with increasing focal radius and then reaches P_2 for larger focal radii. In the region where the

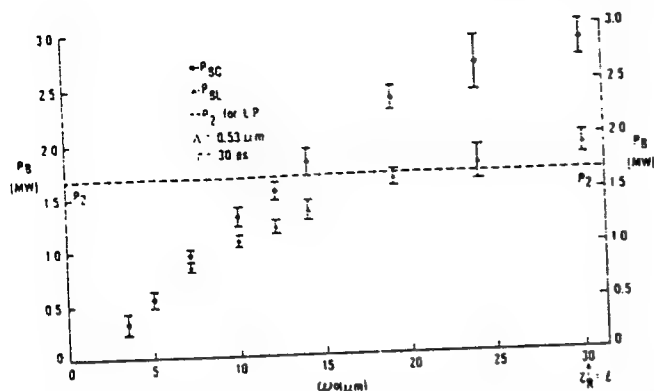


Fig. 3. A plot of the breakdown power versus spot size for the sample of Fig. 2 (triangles—linear polarization, circles—circular polarization). The dashed line gives P_2 as calculated from the measured value of n_2 .⁴³

breakdown power becomes constant, the polarization ratio is approximately 1.5. Similar results are seen for fused quartz at $1.06 \mu\text{m}$. Both of these trends indicate that self-focusing dominates the breakdown process when the breakdown power approaches P_2 .

Results similar to those seen for SiO_2 are observed for NaCl. At $0.53 \mu\text{m}$ for 30 ps pulses and small focal radii and therefore, small breakdown powers, the ratio is approximately unity. This indicates the lack of electronic self-focusing, whereas for large focal radii and large breakdown powers the ratio levels off near the mean theoretical value of approximately 1.4. In this region self-focusing dominates the breakdown process. Again, in the region where the breakdown powers remain constant with increasing spot size, the ratio of the breakdown powers reaches approximately 1.4. Similar results are also seen for this sample at $1.06 \mu\text{m}$. We discuss some of those measurements and their significance below.

At this point we remind the reader of the definition of the critical power for self-focusing and discuss more of Marburger's results.³⁷ P_2 is the least power for which a catastrophic collapse will occur for both focused and unfocused geometries. The point of maximum on-axis irradiance does not occur at the beam waist; it occurs "downstream" of the beam waist at a distance comparable to the Rayleigh range in the material for $P = P_2$. If the sample thickness is thinner than the Rayleigh range, insufficient nonlinear material exists for self-focusing to cause a catastrophic collapse of the beam to occur in the material at P_2 . For damage dominated by self-focusing, this means that the material will not fail until the beam power exceeds P_2 . This type of behavior can be seen in the data presented in Fig. 4. Here we have plotted the breakdown power in megawatts as a function of the focal spot radius in air for the NaCl sample. The laser wavelength is $1.06 \mu\text{m}$, and the pulsewidth is 42 ps. The horizontal dashed line represents the critical power P_2 calculated from measured n_2 values of this sample (see Table II).⁴³ The vertical dotted line divides the data for which the sample thickness is less than the Rayleigh range (region to the right) from that in which the sample is thicker than the Rayleigh range (region to the left). Let us first examine only the triangular data points that are for a NaCl sample thickness of 2 in. If we examine the data for the region to the left, we see that the breakdown power increases with increasing focal radius to approximately P_2 . However, when the sample becomes shorter than the depth of focus (region to the right), the breakdown power continues to

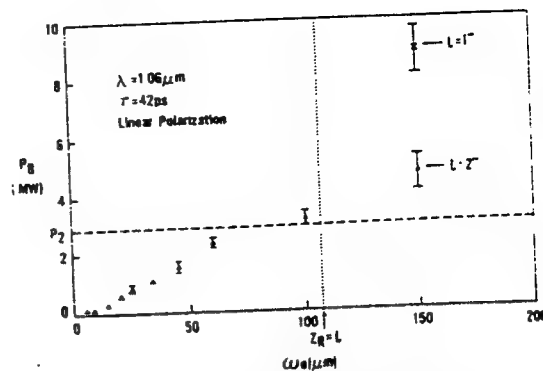


Fig. 4. Breakdown power as a function of spot size in NaCl for a 2 in. thick sample (triangles) and a 1 in. thick sample (X). The horizontal dashed line gives P_2 as calculated from n_2 ,⁴³ and the vertical dotted line gives the spot size at which the Rayleigh range of the focused beam equals the sample thickness for the 2 in. sample.

increase. If we now rotate the sample so that the beam propagates through 1 in. of material instead of 2 in., a dramatic increase in the breakdown power is observed. This is seen by examining the data points for the $150 \mu\text{m}$ spot size. The triangular point is for a sample thickness of 2 in., and the point represented by the X is for 1 in. of material. No other parameters have been changed. To show that the change in the breakdown power was not due to an orientation effect a similar test was performed for a case in which the sample was thick compared with the Rayleigh range for 1 in. of material. No change in the breakdown power was observed when the sample was rotated. This simple test clearly shows the effects of self-focusing in breakdown measurements.

5. CONCLUSIONS FROM THE ROLE OF SELF-FOCUSING IN LID

5.1. Re-evaluation of ELID data

The significance of this work should be emphasized. Much of the early experimental work on self-focusing used the scaling law proposed by Zverev et al.³⁸ to correct the data for self-focusing. In that work the critical power of importance was assumed to be P_1 . Spot size dependencies of the laser-induced damage thresholds were assumed to be merely a reflection of the effect of self-focusing since the breakdown powers were in most cases a fair fraction of P_1 . However, since the self-focusing theory predicts and this work confirms that the critical power is in fact P_2 and not P_1 , the spot size dependencies are in most cases due to other mechanisms in the material, possibly the contribution of defects to the LID thresholds. Work that used the method of Zverev et al. needs to be re-examined.

Unfortunately, much of the work using the Zverev and Pashkov³⁸ scaling is not recoverable from the literature since the uncorrected thresholds are not reported and cannot be extracted due to insufficient information. However, Fradin et al.¹⁹ in anticipation of some problem with the Zverev and Pashkov method did not scale the data reported in 1973 for self-focusing, and in retrospect they were correct in not scaling the data. They observed that the damaging power in NaCl scaled as the square of the focal length of the lenses used for the picosecond pulsewidths. As noted earlier, in 1977 Smith et al.²² also found some problem in using P_1 to correct their 532 nm and 355 nm picosecond damage thresholds for self-focusing. They included the breakdown power and the uncorrected focal area in their report so that future workers could re-

TABLE IV. Breakdown thresholds at 0.53 μm of Ref. 22 scaled for self-focusing using P_1 (column 7) and P_2 (column 8). P stands for the breakdown power P_B , E_0 is the breakdown field, and A is the focal area calculated using linear optics.

Material	P_B (KW)	A (μm^2) (unscathed)	P/P_1	P/P_2	E_0 (MV/cm) (unscathed)	E_{P_1} (scaled)	E_{P_2} (scaled)
KH_2PO_4	151.0	16.0	0.57	0.15	15.3	23.4 (53%)	16.6 (8%)
SiO_2	129.0	15.9	0.46	0.12	14.5	19.0 (31%)	15.4 (6%)
NaCl	38.4	15.1	0.60	0.05	7.9	12.4 (57%)	8.1 (3%)
CaF_2	146.0	15.9	0.62	0.09	15.5	25.2 (63%)	16.3 (5%)
NaF	126.0	15.8	0.45	0.05	15.0	19.4 (30%)	15.4 (3%)
LiF	171.0	16.1	0.59	0.06	16.9	26.5 (57%)	17.5 (4%)

examine the data in the light of new measurements.

We can now use Eq. (5) to re-examine the 532 nm breakdown data of Smith et al.²² In that work, the breakdown powers are all below P_1 , so the irradiance increase predicted by Eq. (5) should be valid. Six materials were studied, including fused quartz and NaCl, as shown in Table IV. In examining the data we find that the breakdown threshold fields increased as much as 50% to 60% using P_1 . These increased thresholds were reported. However, when the thresholds are properly corrected using the second critical power P_2 we find on the average only a 5% increase. This is well within the $\pm 15\%$ absolute uncertainty in the measurements.

Smith et al.²² also reported breakdown thresholds at 355 nm for three of the materials listed in Table IV. The results for this near-UV study indicate that, in most cases, the breakdown threshold powers for these materials were substantially higher than the P_1 critical powers at this wavelength. The only exception was CaF_2 where P_B was found to be $0.7P_1$. In an attempt to correct their data for the presence of self-focusing they scaled their breakdown threshold irradiance levels in KH_2PO_4 , LiF , and SiO_2 using Eq. (5) but with a critical power somewhere between P_1 and P_2 .

While they were on the right track, meaningful comparison of the 355 nm data with results at other wavelengths is difficult due to the reported poor spatial quality of the 355 nm beam used in the measurements. The uncertainty in the energy distribution within the focal area lead Smith et al.²² to assign a factor of two range for the scaled breakdown threshold fields at this wavelength. The actual breakdown thresholds may or may not be within this range. A further complicating factor for interpreting the 355 nm work is the recent result that the effective n_2 for a material may not be constant as a function of wavelength for photon energies approaching a substantial fraction of the band-gap energy. Based on our measurements using the technique of Ref. 43 in BK-7 (see Table II comparing n_2 at 1 μm and 0.5 μm) and those of White et al.⁴⁹ in BK-10 at 355 nm, the n_2 values for the three materials studied at the third harmonic wavelength may well be substantially lower than the values at 1064 nm. This points to the need for accurate measurements of n_2 in these materials in the regime where multiphoton effects may be coming into play. It may also be necessary to measure nonlinear refraction at near-damaging irradiance levels as is done in the beam distortion method.⁴³ This being the case, we will not attempt at this time to reexamine the 355 nm thresholds.

In our re-evaluation of the breakdown results of other workers, we have concentrated on the work of Ref. 22 for two reasons. The first reason is that the breakdown measurements in that work were conducted for pulse durations comparable to our own. Therefore, the self-focusing mechanisms in the test materials will be the same. The second reason is that, of the experimenters who scaled their breakdown thresholds for the presumed presence of self-focusing, Smith et al.²² compose one of few groups whose work contains sufficient information and experimental parameters to determine the true breakdown thresholds. Other workers merely reported the scaled breakdown threshold irradiance levels without including the focal spot radii used in the measurements. This makes it impossible to recalculate the breakdown thresholds. In addition, the incorrectly scaled data of Smith et al.²² was used in support of the intrinsic avalanche ionization model.

Several other breakdown studies have been conducted in these materials in which no self-focusing corrections were made. For example, Manenkov²⁹ reported breakdown measurements in the alkali halides (including NaCl) for nanosecond pulse durations at 10.6, 1.06, 0.69, and 0.53 μm laser wavelengths. There is some uncertainty in the focal spot radius used in the measurements since two values are reported without specifying which correspond to the breakdown irradiance levels listed in Manenkov's work.²⁹ Feldman et al.⁴² estimate that electrostriction is of relatively minor importance for the nanosecond pulses used in these experiments. However, we will use the larger value of $n_2 = 4 \times 10^{-13}$ esu calculated from nanosecond three-wave mixing experiments.⁵⁰ With this in mind we find that P_B in NaCl is $0.5P_2$ at 532 nm and P_B is $0.14P_2$ at 1064 nm if we use the larger of the two focal radii cited in Ref. 29. If we use the small focal radius we find that P_B for NaCl is $0.07P_2$ at 532 nm and $0.02P_2$ for 1064 nm. Thus, self-focusing effects in Manenkov's²⁹ work for NaCl are negligible except perhaps for the combination of the largest spot size and shortest wavelength and, therefore, should not be scaled. The wavelength dependence reported by Manenkov from 10.6 μm to 0.69 μm was an increase in threshold much stronger than that reported by Fradin¹⁷ (a factor of three). However, the threshold dropped at 0.53 μm for a net drop going from 1 μm to 0.5 μm consistent with our measurements.

In a similar nanosecond study, Merkle et al.⁵¹⁻⁵³ reported single shot damage thresholds for Corning 7940 fused quartz for laser wavelengths ranging from 1064 nm to 355 nm. In fused quartz as well as in NaCl, for the tight focusing geometry used, electrostriction has been shown to play a small role in self-focusing effects for pulse durations around 30 ns.⁴² We use the n_2 value of 0.95×10^{-13} esu reported by Feldman et al.⁴² for nanosecond pulse durations in SiO_2 . We find that the breakdown powers reported by Merkle et al.⁵¹ for Corning 7940 were less than $0.08P_2$ at 1064 nm and equal to $0.07P_2$ at 532 nm. Therefore, self-focusing effects in the work of Merkle et al.⁵¹ are negligible. They report a decrease by a factor of two in threshold in going from 1.06 μm to 0.53 μm .⁵¹

We have also re-examined our own results published in Refs. 3 and 32. In Ref. 3 we used beam distortion and polarization dependence to verify that self-focusing was not the dominant breakdown effect. However, these tests (i.e., polarization dependence and beam distortion) were not conducted for each experimental condition used. For the most part, little (a few percent) or no adjustment of the originally published numbers is needed. For the ultra-short pulse data (pulsewidth

less than 5 ps) and largest spot size of $14\text{ }\mu\text{m}$ for SiO_2 at 1054 nm , adjustments as high as a factor of two were needed. These corrections do not change any of the trends observed or conclusions drawn from that data as discussed in the next section.^{3,22} In addition, we should note that we have studied many samples of these materials grown by various techniques over the past 15 years. While the thresholds vary from sample to sample, from boule to boule, and even from different samples taken from the same boule, the data presented here is consistent with data obtained from similar "good" optical quality material. We have not found an exceptional sample that behaved differently from the behavior of the samples reported here.

5.2. Wavelength, temporal, and spot size dependence

Given that we now can account for the effects of self-focusing in an LID experiment, we can unambiguously determine the dependence of the threshold on various parameters such as pulsewidth, spot size, and wavelength. The conclusion reported by Smith et al.²² that the observed wavelength dependence agreed with the predictions of avalanche ionization theory depended on the scaling using Eq. (3) with P_1 as the critical power. Using P_2 , the data of Ref. 22 shows a decrease in threshold with decreasing wavelength, which is not consistent with intrinsic avalanche breakdown. We find similar results for the wavelength dependence. While this wavelength dependence is in the direction predicted by intrinsic multiphoton-induced damage,⁵⁴ the dependence is much too weak.

As the order m of the multiphoton absorption process is increased, the irradiance needed to obtain the same absorptance increases approximately as the inverse ratio of the nonlinear absorption coefficients.⁵⁵ This ratio is estimated by Wherrett⁵⁵ to be $\approx 10^{-4}I$, where I is the irradiance. Experiments indicate that this ratio is $\approx 10^{-3}I$ (Refs. 56 and 58). For example, the two-photon absorption coefficient of CdS at $0.53\text{ }\mu\text{m}$ is reported⁵⁶ as 5.5 cm/GW , and its three-photon absorption coefficient at $1.06\text{ }\mu\text{m}$ is reported⁵⁸ as $0.01\text{ cm}^3/\text{GW}^2$. Thus, to obtain the same absorptance at the two different wavelengths would require an irradiance of $\approx 550\text{ GW/cm}^2$ (or more, theoretically). Four-photon absorption would require a correspondingly higher irradiance. From $10\text{ }\mu\text{m}$ to $0.5\text{ }\mu\text{m}$ the experimentally measured irradiance thresholds change but only by factors of two to four. The reported observation of four-photon absorption at 532 nm prior to damage by the group at Washington State University is interesting and may indicate that intrinsic multiphoton absorption is responsible or partially responsible for damage in the selected samples of NaCl studied by that group. We note, however, that the high irradiance used by the WSU group of 550 GW/cm^2 for picosecond pulses is ≈ 5.5 times the damage threshold observed for the "best" samples reported by Manenkov using nanosecond pulses.²⁹ The absorptance due to direct four-photon absorption would then be of the order of 5.5^{-3} , which is $\approx 6 \times 10^{-3}$, lower for the nanosecond pulses. It seems unlikely that if damage for picosecond pulses is caused by intrinsic multiphoton absorption that the same mechanism is responsible for the nanosecond data of Manenkov.²⁹ Gorshkov et al.⁵⁹ also found inconsistencies with the avalanche model in the temperature dependence of damage of the alkali halides at $0.53\text{ }\mu\text{m}$. We agree with the authors of Ref. 8 that "insufficient and contradictory data exist for $m = 4$ in NaCl ($E_g = 8.6\text{ eV}$, $h\nu = 2.33\text{ eV}$) to unequivocally assign

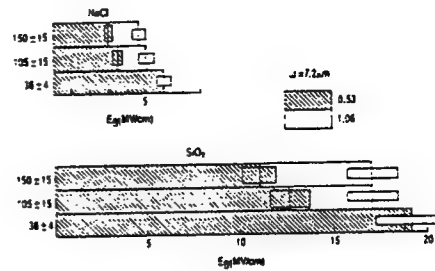


Fig. 5. Wavelength dependence of E_B for NaCl and SiO_2 for several pulsewidths at 1.06 and $0.53\text{ }\mu\text{m}$. These thresholds have been scaled by a few percent for self-focusing using P_2 and measured values of n_2 .⁴³

damage to the avalanche mechanism." However, since the damage threshold varies considerably from sample to sample, we must still conclude that extrinsic effects are present and dominant for the lower threshold samples. Additionally, intrinsic multiphoton absorption may contribute carriers for an eventual avalanche, although no evidence for this was observed in the photoacoustic data of Ref. 8. At $0.5\text{ }\mu\text{m}$ in these wide-gap materials the question of the role of intrinsic multiphoton absorption in LID remains. However, it is unlikely that for the wavelengths of $1\text{ }\mu\text{m}$ and longer intrinsic multiphoton absorption is playing a role.

We reported damage on 13 samples of NaCl at $1\text{ }\mu\text{m}$ and $0.5\text{ }\mu\text{m}$ in Ref. 3. While the field thresholds varied from sample to sample by as much as a factor of four, we saw no systematic differences in the parametric dependencies of the ELID thresholds, although not all experiments were performed for all samples. Figure 5 shows a bar graph of damage in NaCl (upper) and SiO_2 (lower) for a focal spot size in air of $7.2\text{ }\mu\text{m}$ for various pulsewidths as indicated, for both $1.06\text{ }\mu\text{m}$ (unshaded) and $0.53\text{ }\mu\text{m}$ (shaded). The small corrections for self-focusing have been included in this figure. Except for the shortest pulses in both NaCl and SiO_2 samples, the ELID threshold is reduced in going from a wavelength of $1\text{ }\mu\text{m}$ to $0.5\text{ }\mu\text{m}$, which is inconsistent with an intrinsic avalanche model.

In the avalanche breakdown model of Refs. 4 and 5 the ionization rate is proportional to E^2 in the high field limit (i.e., short pulse limit). Then, the buildup of carriers is given by

$$N = N_0 \exp(aE^2 t) \quad (10)$$

where N is the carrier density, N_0 is the initial carrier density, and a is a material dependent constant. This limit corresponds to the situation in which the increase in energy of the electrons in the conduction band is simply proportional to the input irradiance and that all losses are negligible. This says that the ionization rate is limited by the rate at which the input light beam can supply energy to the conduction band electrons. It is commonly assumed that damage occurs when the carrier density reaches a critical value N_c . Thus, Eq. (10) can be solved for the breakdown field showing a $t_p^{-0.5}$ dependence:

$$E_B = \frac{1}{\sqrt{at_p}} \ln^{1/2} \left(\frac{N_c}{N_0} \right) \quad (11)$$

We find that for very short pulses for NaCl this pulsewidth dependence is valid and the breakdown fluence is constant, while for SiO_2 we see a somewhat weaker $t_p^{-0.3}$ dependence.

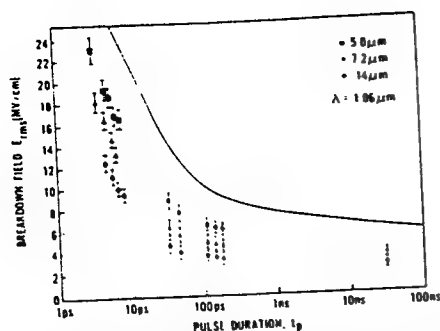


Fig. 6. Pulsewidth dependence of the rms breakdown field E_B for NaCl at $1.06 \mu\text{m}$ for three different spot sizes. Data are scaled for self-focusing using P_2 .⁴³ The solid line was obtained from the electron avalanche ionization theory of Sparks et al.⁴

For the low field limit, i.e., longer pulses, the ionization rate is exponentially dependent on E and the resulting pulsewidth dependence is relatively weak.⁴ In Fig. 6, we reproduced the theoretical curves derived by Sparks et al.⁴ showing the predicted dependence of the breakdown field E_B on pulsewidth and have extended the pulsewidth scale to longer and shorter pulses. The overall dependence of the data for a given spot size is in remarkably good agreement with this theory using no adjustable parameters. However, intrinsic avalanche ionization does not predict a spot size dependence, which is clearly seen in the data. This relatively large spot size dependence may well be due to extrinsic materials parameters such as multiphoton ionization of impurities or defects that provide the starter electrons for the avalanche N_0 .^{3,32}

While the observed temporal dependence is consistent with an intrinsic avalanche, the wavelength and spot size dependence strongly indicate that the phenomena is an *extrinsic* property of materials. In addition, the strong sample-to-sample variations in thresholds support this conclusion.^{12,29} The extrinsic nature of bulk damage makes quantitative, first principle descriptions of the damage process very difficult. One problem is that the good optical materials of interest have very low levels of defects and impurities. One solution to this problem is to do experiments with samples prepared with known type and densities of defects and impurities. This is the approach we take below.

6. CONTROLLED DEFECT STUDIES

The effects of γ irradiation (which produces, among other defects, E' centers)⁶⁰ on the ELID thresholds of fused silica, were investigated. Samples were sliced into four quadrants. One quadrant was kept as a control (i.e., no irradiation), and the remaining three quadrants were subjected to 10^6 , 10^7 , and 10^8 rad of cobalt γ irradiation from the Naval Research Laboratory cobalt source. Unfortunately, the density of defects cannot be determined,⁶⁰ although their effects on linear absorption and ELID can be measured. Single specimens of three types of fused silica were tested: Spectrasil A, B, and WF (water free). Damage was performed with 18 ns (FWHM) pulses at $1.06 \mu\text{m}$ and $0.53 \mu\text{m}$ focused into the bulk of three 3 mm thick samples using a 40 mm focal length lens. Each site was irradiated only once. The ELID thresholds were found to be independent of γ irradiation at the $1.06 \mu\text{m}$ wavelength. However, significant reduction in damage thresholds (up to 40%) was measured for the irradiated samples at $0.53 \mu\text{m}$.^{61,62} Again, the effects of self-focusing were determined to be negligible by performing polarization dependent damage mea-

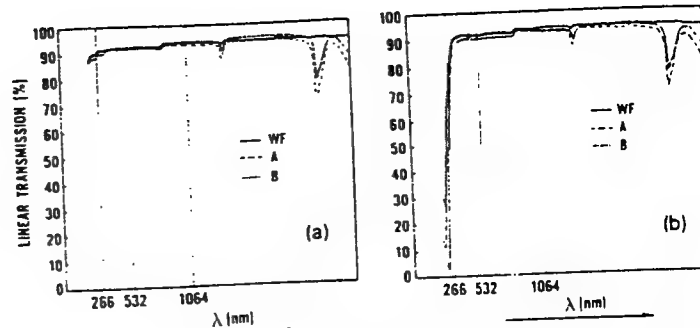


Fig. 7. Transmission as a function of wavelength λ for the three samples of SiO_2 (a) unirradiated and (b) γ irradiated with 10^8 rad.

TABLE V. Composition of the various fluorozirconate glasses studied.

Sample	Color	ZrF ₄ (mol%)	BaF ₂ (mol%)	LaF ₃ (mol%)	AlF ₃ (mol%)	CrF ₃ (mol%)	MnF ₂ (mol%)	NiF ₂ (mol%)	NdF ₃ (mol%)
A	Clear	57	34.5	4.5	4				
B	Green	56.75	34.25	4.5	4	0.5			
C	Green	56.5	34	4.5	4	0.5	0.5		
D	Green	56.5	34	4.5	4	0.5			0.5
E	Violet	55.75	33.75	4.5	4		1		1
F	Yellow	56.75	34.25	4.5	4			0.5	

surements. The ELID thresholds at $0.53 \mu\text{m}$ are substantially lower than those at $1.06 \mu\text{m}$ even for the unirradiated witness samples. Avalanche ionization predicts an increase in threshold for reduced wavelength. Thus, the ELID process is not simply avalanche breakdown even for the witness sample.

Figure 7 shows the linear transmission spectra of the unirradiated and irradiated (10^8 rad) samples.^{61,62} Note that this figure shows no observable change in transmission at either $1.06 \mu\text{m}$ or $0.53 \mu\text{m}$ but does show a substantial change at $0.266 \mu\text{m}$ for the irradiated samples. This suggests that the decrease in ELID threshold at $0.53 \mu\text{m}$ may be associated with the change in transmission at the harmonic $0.266 \mu\text{m}$. We will examine this relation after presenting data that shows a similar dependence of ELID on linear absorption at a harmonic.

We also performed a series of LID experiments on fluorozirconate (FZ) glasses, undoped and doped with Cr, Mn, Ni, and Nd.⁶³ Table V shows the glass compositions. The linear absorption spectra are given in Ref. 63. The doped and undoped FZ glasses were studied at $1.06 \mu\text{m}$ using 45 ps and 18 ns pulses and a calculated $5.3 \mu\text{m}$ focused spot size. Measurements at $0.53 \mu\text{m}$ were performed using 18 ns pulses and a calculated focused spot size, assuming negligible aberrations, equal to $2.7 \mu\text{m}$.⁶³ Polarization dependent studies confirmed the absence of self-focusing effects. The breakdown fields decreased significantly at both wavelengths for all of the doped FZ glasses when compared with the undoped sample A.

We present below a two-photon assisted electron avalanche breakdown model as given in Refs. 62 and 63 that we justify primarily on the basis of its surprisingly good fit of the data. Our experimental results for both the irradiated silica and FZ glass materials were found to be in good agreement with this very simplified model in which two-photon absorption by impurities or defects provides the starter electrons for an avalanche. In this model we assume that laser-induced breakdown occurs when the density of free carriers generated by a combination of two-photon and avalanche processes

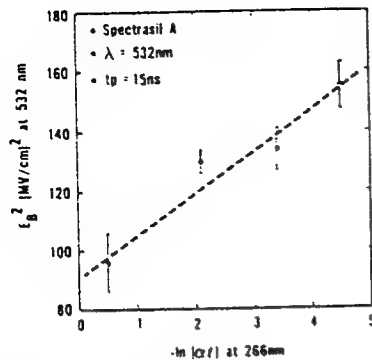


Fig. 8. Square of the damaging electric field at 532 nm versus the negative natural logarithm of the linear absorption at 266 nm for the irradiated and unirradiated Spectrasil A SiO_2 samples.

reaches some critical value N_c . In the avalanche process the buildup of free carrier density is given by Eq. (10), where we assumed the high field limit with an ionization rate proportional to E_B^2 . The model assumes that the initial free carriers are generated by two-photon absorption from impurity states within the bandgap. Therefore, N_0 can be written as $N_0 \propto n$, where n is the density of two-photon allowed impurity or defect states. Taking the natural logarithm of Eq. (10) yields

$$aE_B^2 = -\ln(n) + \text{constant} \quad (12)$$

The final assumption is that the density of two-photon allowed states at the fundamental wavelength (λ) is proportional to the linear absorption at the second harmonic ($\lambda/2$). For that assumption Eq. (12) gives

$$E_B^2|_{\lambda} \propto -\ln(\alpha l)|_{\lambda/2} \quad (13)$$

where α is the linear absorption coefficient at the second harmonic wavelength and l is the sample length.

Figure 8 is a plot of the square of the breakdown field at 532 nm as a function of $-\ln(\alpha l)$ at 266 nm for the Spectrasil A sample. Note that increasing irradiation dosage goes from right to left in this figure. A linear relation is also seen for the other samples (B and WF), although sample B shows a significant increase in absorption for only the highest γ irradiation level. Figure 9 is a plot of the square of the breakdown field at 1.06 μm versus $-\ln(\alpha l)$ at 0.53 μm using picosecond pulses for the undoped and doped FZ glasses. A similar plot for nanosecond pulses also yields a linear relation. Plotting the breakdown field squared at 0.532 μm versus the $-\ln(\alpha l)$ at 0.266 μm using nanosecond pulses again gives a linear relation. Similar plots of damage versus linear losses at the damaging wavelength show no systematic trends. The agreement with the prediction of Eq. (13) is quite good considering the extreme simplicity of the model and the assumptions made. Note that even in cases in which nanosecond pulses were used where the ionization rate is expected to depart from the E_B^2 dependence good fits are obtained. At what pulsewidth or irradiance the deviation from an E_B^2 dependence becomes large is not well established. However, we found that for all of the FZ glasses where both nanosecond and picosecond data were taken, the reduction in ELID threshold for the doped samples was nearly a factor of two larger for the picosecond irradiation. This trend is expected in this model where the starter electrons for an avalanche are created by nonlinear

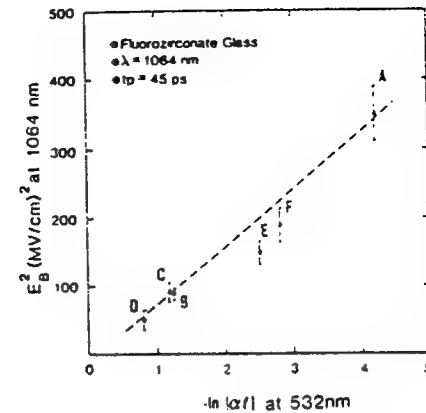


Fig. 9. Square of the damaging electric field at 1064 nm versus the negative natural logarithm of the linear absorption at 532 nm for the Fluorozirconate glass samples listed in Table V.

absorption since the breakdown field is substantially larger for picosecond pulses.

In spite of the complexity associated with laser-induced damage mechanisms for dielectric materials, our experimental results are consistent with a two-photon-assisted electron avalanche process. We should note that if this model is correct, the implication is that the witness samples at 0.53 μm , in the case of the fused silica samples, and the undoped glass (sample A) in the case of the fluoro-zirconate glass samples are also dominated by extrinsic defect (or impurity) initiated ELID. This conclusion comes from the fact that these samples are included in the curves of ELID versus $-\ln$ absorption, and they fit. Just how far we can take this simple model is not clear. The primary justification in presenting it is that the data fits the prediction. One conclusion, however, is certainly true; the damage in these materials is dependent on defects and impurities.

7. CONCLUSION

We have clarified the role of self-focusing in laser-induced damage experiments and can readily account for its effects on measured thresholds. With this knowledge we have carefully examined both our data and the data of others to determine that intrinsic avalanche ionization theory cannot account for the parametric dependencies observed. Sample-to-sample variations, wavelength dependence, and spot size dependence of damage thresholds strongly suggest that damage to transparent dielectric materials is an extrinsic process. In a sense, this is good news in that the implication is that ELID thresholds can be increased as progress is made in the materials growth and preparation areas.

8. ACKNOWLEDGMENTS

We gratefully acknowledge the support of the Office of Naval Research, the Florida High Technology and Industry Council, and the Defense Advanced Research Projects Agency, and we wish to thank D. Griscom of the Naval Research Laboratory for irradiating samples.

9. REFERENCES

1. N. Boembergen, "Laser induced electric breakdown in solids," IEEE J. Quantum Electron. QE-10, 375 (1974).
2. W. L. Smith, "Laser induced breakdown in optical materials," Opt. Eng. 17(5), 489-503 (1978).

3. M. J. Soileau, W. E. Williams, E. W. Van Stryland, T. F. Boggess, and A. L. Smirl, "Picosecond damage studies at 0.5 and 1 micrometer," *Opt. Eng.* 22(4), 424-430 (1983).
4. M. Sparks, D. L. Mills, R. Warren, T. Holstein, A. A. Maradudin, L. J. Sham, E. Loh, Jr., and D. F. King, "Theory of electron-avalanche breakdown in solids," *Phys. Rev. B* 24, 3519 (1981).
5. A. S. Epifanov, A. A. Manenkov, and A. M. Prokhorov, *Sov. Phys. JETP* 43, 377 (1976).
6. S. C. Jones, X. A. Shen, P. F. Bräunlich, P. Kelly, and A. S. Epifanov, "Mechanism of prebreakdown nonlinear energy deposition from intense photon fields at 532 nm in NaCl," *Phys. Rev. B* 35, 894-987 (1987).
7. X. A. Shen, S. C. Jones, P. F. Bräunlich, and P. Kelly, "Four photon absorption cross section in potassium bromide at 532 nm," *Phys. Rev. B* 36, 2831-2843 (1987).
8. S. C. Jones, A. H. Fischer, P. F. Bräunlich, and P. Kelly, "Prebreakdown energy absorption from intense laser pulses at 532 nm in NaCl," *Phys. Rev. B* 37, 755-770 (1988).
9. J. P. Anthes and M. Bass, "Direct observation of the dynamics of picosecond-pulse optical breakdown," *Appl. Phys. Lett.* 31, 412 (1977).
10. M. S. Bruma, "Mechanism for energy transfer between a focused laser beam and a transparent medium involving electromagnetic-field gradients," *J. Opt. Soc. Am.* 54, 563 (1964).
11. M. Hercher, "Laser-induced damage in transparent media," *J. Opt. Soc. Am.* 54, 563 (1964).
12. See *Proc. Symposium on Laser-Induced Damage in Optical Materials*, Nat'l. Bureau of Standards Special Pubs. 341 (1970), 356 (1971), 372 (1972), 387 (1973), 414 (1974), 435 (1975), 462 (1976), 509 (1977), 541 (1978), 568 (1979), 620 (1980), 638 (1981), 669 (1982), 688 (1983), 727 (1984), 746 (1985), 752 (1986), 756 (1987), U.S. Government Printing Office, Washington, DC.
13. E. Yablonovitch and N. Bloembergen, "Avalanche ionization and the limiting diameter of filaments induced by light pulses in transparent media," *Phys. Rev. Lett.* 29, 907-910 (1972).
14. E. Yablonovitch, "Nonlinear optics with the carbon dioxide laser," Ph.D. thesis, Harvard Univ. (1972) (unpublished).
15. E. Yablonovitch, "Optical dielectric strength of alkali-halide crystals obtained by laser-induced breakdown," *Appl. Phys. Lett.* 19, 495 (1971).
16. D. W. Fradin, "The measurement of self-focusing parameters using intrinsic optical damage," *IEEE J. Quantum Electron.* QE-9, 954 (1973).
17. D. W. Fradin, "Laser induced damage in solids," Ph.D. thesis, Harvard Univ. (1973) (unpublished).
18. D. W. Fradin and D. P. Bua, "Laser induced damage in ZnSe," *Appl. Phys. Lett.* 24, 555 (1974).
19. D. W. Fradin, N. Bloembergen, and J. P. Letellier, "Dependence of laser-induced breakdown field strength on pulse duration," *Appl. Phys. Lett.* 22, 635 (1973).
20. D. W. Fradin, E. Yablonovitch, and M. Bass, "Confirmation of an electron avalanche causing laser-induced bulk damage at 1.06 μm ," *Appl. Opt.* 12, 700 (1973).
21. W. L. Smith, J. H. Bechtel, and N. Bloembergen, "Dielectric breakdown threshold and nonlinear refractive index measurements with picosecond laser pulses," *Phys. Rev. B* 12, 706 (1975).
22. W. L. Smith, J. H. Bechtel, and N. Bloembergen, "Picosecond laser-induced breakdown at 532 and 355 nm: observation of frequency dependent behavior," *Phys. Rev. B* 15, 4039 (1977).
23. W. L. Smith, J. H. Bechtel, and N. Bloembergen, "Picosecond laser-induced-damage morphology: spatially resolved microscopic plasma sites," *Opt. Commun.* 18, 592 (1976).
24. D. Olness, "Laser-induced breakdown in transparent dielectric," *J. Appl. Phys.* 39, 6-8 (1968).
25. D. Olness, "Laser damage threshold in NaCl crystals," *Appl. Phys. Lett.* 8, 283-285 (1966).
26. Y. Yasojima, Y. Ohmari, N. Okumura, and Y. Inuishi, *Jpn. J. Appl. Phys.* 14, 815 (1975).
27. Y. Yasojima, M. Takeda, and Y. Onnishi, "Laser-induced breakdown in ionic crystals and a polymer," *Jpn. J. Appl. Phys.* 7, 552 (1968).
28. M. Bass and H. J. Barrett, "Avalanche breakdown and the probabilistic nature of laser-induced damage," *IEEE J. Quantum Electron.* QE-8, 338 (1971).
29. A. A. Manenkov, "New results on avalanche ionization as a laser damage mechanism in transparent solids," Nat'l. Bureau of Standards Special Publ. 509, p. 455, U.S. Government Printing Office, Washington, D.C. (1977).
30. M. J. Soileau, M. Bass, and E. W. Van Stryland, "Frequency dependence of breakdown fields in single-crystal NaCl and KCl," Nat'l. Bureau of Standards Special Pub. 541, p. 309, U.S. Government Printing Office, Washington, D.C. (1978).
31. M. J. Soileau, "Frequency and focal volume dependence of laser-induced breakdown in wide band gap insulators," Ph.D. thesis, Univ. of Southern California (1979) (unpublished).
32. E. W. Van Stryland, M. J. Soileau, A. L. Smirl, and W. E. Williams, "Pulsewidth and focal volume dependence of laser-induced breakdown," *Phys. Rev. B* 23, 2144 (1981).
33. M. J. Weber, D. Milam, and W. L. Smith, "Nonlinear refractive index of glasses and crystals," *Opt. Eng.* 17(5), 463-469 (1978).
34. M. J. Moran, C.-Y. She, and R. L. Carmen, "Interferometric measurements of the nonlinear refractive index coefficient relative to CS_2 in laser-system-related materials," *IEEE J. Quantum Electron.* QE-11, 259 (1975).
35. W. E. Williams, M. J. Soileau, and E. W. Van Stryland, "The effects of self-focusing on laser-induced breakdown," Nat'l. Bureau of Standards Special Pub. 688, p. 513, U.S. Government Printing Office, Washington, D.C. (1983).
36. M. J. Soileau, W. E. Williams, and E. W. Van Stryland, "Self-focusing in damage experiments revisited," Nat'l. Bureau of Standards Special Pub. 727, pp. 394-403, U.S. Government Printing Office, Washington, D.C. (1984).
37. J. H. Marburger, "Self-focusing theory," in *Progress in Quantum Electronics*, J. H. Sanders and S. Stenholm, eds., Vol. 4, Part 1, pp. 35-110, Pergamon, Oxford (1975).
38. G. M. Zverev and V. A. Pashkov, "Self-focusing of laser radiation in solid dielectrics," *Sov. Phys. JETP* 30, 616 (1970).
39. P. D. Maker and R. W. Terhune, "Study of optical effects due to an induced polarization third order in the electric field strength," *Phys. Rev.* 137, 801-818 (1965).
40. R. W. Hellwarth, "Third order optical susceptibilities of liquids and solids," in *Progress in Quantum Electronics*, J. H. Sanders and S. Stenholm, eds., Vol. 5, pp. 1-68, Pergamon, N.Y. (1977).
41. A. Owyong, "Elipse rotation in laser host materials," *IEEE J. Quantum Electron.* QE-9, 1064 (1973).
42. A. Feldman, D. Horowitz, and R. M. Waxler, "Mechanisms for self-focusing in optical glasses," *IEEE J. Quantum Electron.* QE-9, 1054 (1973).
43. W. E. Williams, M. J. Soileau, and E. W. Van Stryland, "Simple direct measurements of n_2 ," Nat'l. Bureau of Standards Special Pub. 688, p. 522, U.S. Government Printing Office, Washington, D.C. (1983).
44. W. E. Williams, M. J. Soileau, and E. W. Van Stryland, "Optical switching and n_2 measurements in CS_2 ," *Opt. Commun.* 50, 256 (1984).
45. K. J. Witte, M. Galanti, and R. Volk, " n_2 measurements at 1.32 μm of some organic compounds usable as solvents in a saturable absorber for an atomic iodine laser," *Opt. Commun.* 34, 278 (1980).
46. A. Owyong, R. W. Hellwarth, and N. George, "Intensity-induced changes in optical polarization in glasses," *Phys. Rev. B* 5, 628 (1972).
47. R. Adair, L. L. Chase, and S. A. Payne, "Nonlinear refractive-index measurements of glasses using three-wave mixing," *JOSA B* 4, 875-881 (1987).
48. M. J. Soileau, W. E. Williams, and E. W. Van Stryland, "Optical power limiter with picosecond response time," *IEEE J. Quantum Electron.* QE-19, 731 (1983).
49. W. T. White, W. L. Smith, and D. Milam, "Direct measurement of the nonlinear refractive index coefficient at 355 nm in fused silica and BK-10 glass," *Opt. Lett.* 9, 10-12 (1984).
50. M. D. Levinson and N. Bloembergen, "Dispersion of the nonlinear optical susceptibility tensor in centrosymmetric media," *Phys. Rev. B* 10, 4447 (1974).
51. L. D. Merkle, N. Koumvakalis, and M. Bass, "Laser-induced bulk damage in SiO_2 at 1.064, 0.532, and 0.355 μm ," *J. Appl. Phys.* 55, 772-775 (1984).
52. L. D. Merkle, M. Bass, and R. T. Swimm, "Multiple pulse laser-induced bulk damage in crystalline and fused quartz at 1.064 and 0.532 micrometers," Nat'l. Bureau of Standards Special Pub. 669, 50-59, U.S. Government Printing Office, Washington D.C. (1982).
53. L. D. Merkle, M. Bass, and R. T. Swimm, "Multiple pulse laser-induced bulk damage in crystalline and fused quartz at 1.064 and 0.532 micrometers," *Opt. Eng.* 22(4), 405-410 (1983).
54. P. Bräunlich, A. Schmid, and P. Kelly, "Contributions of multiphoton absorption to laser-induced intrinsic damage in NaCl," *Appl. Phys. Lett.* 26, 150-153 (1975).
55. B. S. Wherrett, "Scaling rules for multiphoton interband absorption in semiconductors," *JOSA B* 1, 67-72 (1984).
56. E. W. Van Stryland, M. A. Woodall, H. Vanhezele, and M. J. Soileau, "Energy band-gap dependence of two-photon absorption," *Opt. Lett.* 10, 490-492 (1985).
57. R. Adair, L. L. Chase, and S. A. Payne, "Nonlinear refractive index of optical crystals," *Phys. Rev. B* 39, 3337-3350 (1989).
58. A. Penzkofer and W. Falkenstein, "Three-photon absorption and subsequent excited-state absorption in CdS ," *Opt. Commun.* 16, 247-250 (1976).
59. B. G. Gorshkov, Yu. K. Danileiko, V. A. Lobachev, and A. A. Manenkov, "Laser induced breakdown of alkali-halide crystals," *Sov. Phys. JETP* 45, 612-618 (1978).
60. E. J. Friebele and D. L. Griscom, "Radiation effects in glass," in *Glass II*, Vol. 17, p. 257, Academic Press, New York (1979).
61. M. J. Soileau, N. Mansour, E. Canto, and D. L. Griscom, "Effects of ionizing radiation on laser-induced damage in SiO_2 ," *Nucl. Instrum. Methods Phys. Res. B* 32, 311-314 (1988).
62. M. J. Soileau, N. Mansour, E. Canto, and D. L. Griscom, "Effects of radiation induced defects on laser-induced breakdown in SiO_2 ," Nat'l. Bureau of Standards Special Pub. 746, 486-496, U.S. Government Printing Office, Washington, D.C. (1985).

63. N. Mansour, S. Guha, M. J. Soileau, B. Bendow, and D. Martin, "Laser-induced damage in doped and undoped fluorozirconate glass," Natl. Bureau of Standards Special Pub. 746, 108-119, U.S. Government Printing Office, Washington, D.C. (1985).



M. J. Soileau was born in 1944. He received the Ph.D. degree in quantum electronics in 1979 from the University of Southern California, Los Angeles, where he worked at the Center for Laser Studies on laser-induced damage to wide-bandgap optical materials. He spent six years in the U.S. Air Force and worked for seven years at the Navy Michelson Laboratory. Dr. Soileau joined the faculty of the Department of Physics of North Texas State University in 1980 and was a founding member

of the Center for Applied Quantum Electronics. In 1987 he became the first director of the newly formed Center for Research in Electro-Optics and Lasers at the University of Central Florida, where he is a professor of electrical engineering and physics. Dr. Soileau's research interests include laser-induced damage to optical materials, nonlinear absorption and refraction, and optical limiting.



William E. Williams received his BS degree from Lamar University, Beaumont, Texas, in 1978. He then attended graduate school at North Texas State University, Denton, where he received his MS degree in 1981 and his Ph.D. degree in 1984, both in physics. His dissertation, "Parametric studies of picosecond laser-induced breakdown in fused quartz and NaCl," dealt with the influence of self-focusing on optical damage in solids and liquids. In 1984 Dr. Williams joined the technical staff of

Texas Instruments, Inc. (TI), Defense Systems and Electronics Group. While at TI he evaluated a number of optical limiting technologies for system level applications and was cofounder of a dedicated laboratory at TI for development of optical limiters. Since 1987 he has been at Litton Laser Systems, Orlando, as a member of the research staff. His research interests include laser-induced damage, optical limiters, optical phase conjugation, and frequency conversion by nonlinear optical processes. Dr. Williams is currently a member of the OSA, the IEEE Laser and Electro-Optics Society, SPIE, and the Association of Old Crows.

Nastaran Mansour received a BS (first class honors) in physics from the National University, Tehran, Iran, an MS (honors) in physics from Southern Methodist University, Dallas, Texas, and a Ph.D. in physics (quantum electronics) in 1988 from the University of North Texas, Denton. She then worked as a research scientist at the Center for Research in Electro-Optics and Lasers at the University of Central Florida, Orlando. Dr. Mansour is currently assistant professor of physics at the National University (Shahid Baheshti), Tehran. She is also on the research staff of the Organization of Atomic Energy, Laser Division, in Tehran. Her research interests include optical nonlinearities in dielectric and semiconductor materials, laser-induced damage to optical materials, optical limiting, and laser physics. Dr. Mansour is a member of the OSA, IEEE, and APS.



E. W. Van Stryland was born in 1947. He received the Ph.D. degree in physics in 1976 from the University of Arizona, Tucson, where he worked at the Optical Sciences Center on optical coherent transients. He worked in the areas of femtosecond pulse production, multiphoton absorption in solids, and laser-induced damage at the Center for Laser Studies at the University of Southern California, Los Angeles. Dr. Van Stryland joined the physics department at North Texas State University in 1978

and was instrumental in forming the Center for Applied Quantum Electronics there. In 1987 he joined the newly formed Center for Research in Electro-Optics and Lasers at the University of Central Florida, Orlando, where he is a professor of physics and electrical engineering, working in the area of nonlinear optics.

Optical limiting in solutions of metallo-phthalocyanines and naphthalocyanines

Daniel R. Coulter, Vincent M. Miskowski and Joseph W. Perry

Jet Propulsion Laboratory
California Institute of Technology
4800 Oak Grove Dr.
Pasadena, California
91109

and

Tai-Huei Wei, Eric W. Van Stryland and D. J. Hagan

Center for Research in Electro-Optics and Lasers
University of Central Florida
Orlando, Florida
32826

ABSTRACT

Optical limiting measurements have been made on solutions of several metal containing phthalocyanines and naphthalocyanines. Measurements at 532nm using nanosecond pulses from a Q-switched Nd:YAG laser show limiting throughputs of 1-10 millijoules with mild focussing in alcohol solutions with nominal transmissions of 30-70%. Measurements on chloro-aluminum-phthalocyanine solutions utilizing individual 30 psec pulses or trains (spanning about 100nsec) of modelocked pulses have shown even lower limiting throughputs. Thus, the dynamic range of the limiting behavior has been shown to cover at least three orders of magnitude. Prompt limiting is attributed to strong singlet-singlet (S_1-S_n) absorption, whereas the longer time limiting behavior is postulated to result from strong triplet-triplet (T_1-T_n) absorption. In addition to these studies, efforts have been underway to identify materials with reduced limiting throughput and improved optical transmission characteristics.

1. INTRODUCTION

Transmission of light through an absorbing medium can usually be described by Beer's Law. The ratio of the transmitted to the incident intensity, $I(\text{out})/I(\text{in})$, is a constant which depends only on the absorption coefficient and pathlength of the medium and is independent of the magnitude of $I(\text{in})$. In certain cases, however, when $I(\text{in})$ becomes large, as from a focussed laser beam, the transmitted intensity decreases relative to simple linear behavior and ultimately become fixed at a constant value independent of $I(\text{in})$. This phenomenon is known as optical limiting.

Such behavior can result from a number of processes which fall generally into two classes: nonlinear absorption and nonlinear refraction processes. Nonlinear absorption can occur when incident

radiation is resonant or nearly resonant with an allowed transition in a medium and generates a population of excited metastable species which exhibit strong absorption at the incident wavelength, thus resulting in greatly enhanced extinction at that wavelength. Nonlinear refraction occurs when the local index of refraction of a medium changes in response to intense (resonant or nonresonant) incident radiation, resulting in the formation of an index gradient or "lens". This lens either focusses or defocusses the propagating light beam resulting in divergence in the far field and thus altering the transmission through an aperture located further along the optical path.

Optical limiting devices based on nonlinear materials are envisioned to have applicability in a number of areas including optical communications, optical processing and laser hardening. Clearly, the detailed requirements placed on the limiter are dependant on the application. Properties such as nominal transparency, bandwidth, switching threshold, temporal dynamic range and damage threshold are all relevant.

Several years ago, optical limiting, or "reverse saturable absorption", was reported in some tetraphenylporphyrins¹. It occurred to us that this phenomenon might be exhibited by other highly conjugated macrocyclic dyes. Recent experiments on optical limiting in solutions and suspensions of several metallophthalocyanine (M-Pc) and metallonaphthalocyanine (M-NPc) dyes have shown that some of these materials may indeed have application as passive optical limiters. For passive limiters, no external impulses (e.g. electric fields) are required to initiate the limiting, rather, the materials are "self-acting". Examples of M-Pc and M-NPc structures are shown in Figure 1. The best studied compound to date in our laboratories is chloro-aluminum-phthalocyanine (CAP). In this paper, we report linear, nonlinear and transient transmission measurements on solutions of CAP for a wide range of input powers and pulse durations. Preliminary limiting measurements on several related compounds are also reported.

2. EXPERIMENTAL

CAP was purchased from Eastman Kodak Co. Other M-Pc and M-NPc dyes were prepared by standard procedures². Solutions and/or suspensions for analysis were prepared by heating and stirring small quantities of dye in spectrophotometric grade methanol or ethanol. True solutions were filtered to remove any undissolved matter. Transmission spectra were recorded on a dual beam spectrometer (Perkin-Elmer Lambda-9) before and after limiting experiments to detect any degradation of the samples.

Nanosecond nonlinear transmission measurements were performed utilizing the standard geometry³. Excitation was with 5 nsec pulses at 532nm from a frequency doubled, Q-switched Nd:YAG laser (Quanta Ray, DCR-2A). Detection was with an integrating calorimeter. Experiments were performed in a single shot mode to avoid cumulative thermal effects in the solution. Many single shot measurements were averaged to obtain the incident and transmitted intensities. Picosecond optical limiting measurements were also performed in the standard geometry⁴ utilizing 30 psec pulses at 532nm from a frequency doubled, modelocked Nd:YAG laser. In some experiments, trains of eight to ten 30 psec pulses separated from each other by 10 nsec were utilized.

Fluorescence lifetime measurements were performed by utilizing time-correlated single photon counting with 5 psec pulses at 600nm from a CW-modelocked Nd:YAG/synchronously pumped dye laser combination. Emission was detected with a red sensitive multichannel plate photomultiplier tube. The response function of this system is typically 75 psec FWHM. Transient absorption spectra were

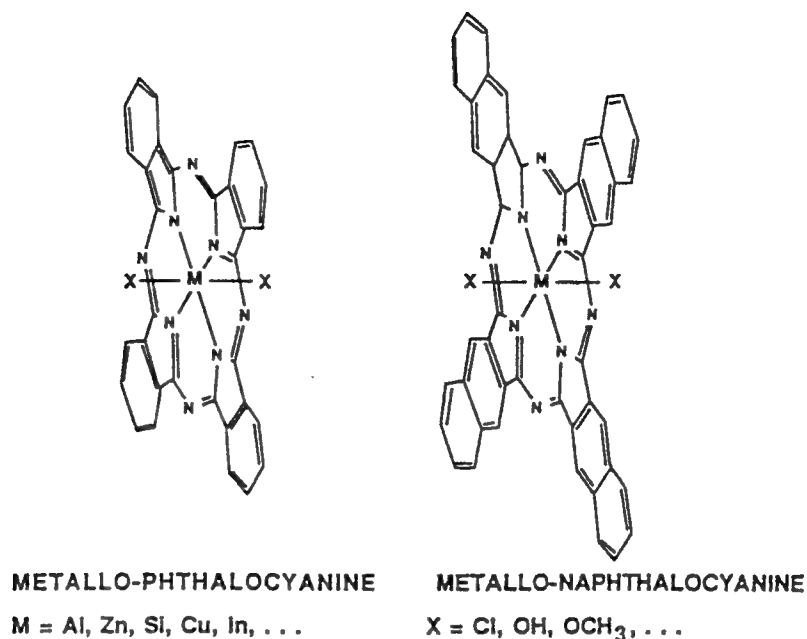


Figure 1. Structures of metallophthalocyanine and metallonaphthalocyanine dyes.

recorded by exciting with 3 nsec pulses at 355nm from a frequency tripled, Q-switched Nd:YAG laser and probing with white light from a pulsed Xe lamp. Detection was with a gated optical multichannel analyzer which allowed for recording of entire spectra on each shot at a predetermined delay relative to the exciting pulses.

3. RESULTS

3.1 Absorption Spectra

The absorption spectrum of CAP in ethanol solution between 200 and 800nm is shown in Figure 2. It is seen that this material (as is common to most phthalocyanines) shows two sets of absorption bands in this region associated with $\pi\text{-}\pi^*$ transitions in the macrocyclic ring system. The lower energy bands, commonly referred to as the Q-bands, are associated with transitions between the ground state (S_0) and the first strongly dipole coupled excited singlet state (S_1), and show a maximum absorption at 670nm with an extinction coefficient of $\epsilon=2.5 \times 10^5 \text{ L/mol-cm}$ in this solvent. The bands in the near UV, commonly referred to as the Soret bands, show a maximum at 355nm with an extinction coefficient of $\epsilon=6.0 \times 10^4 \text{ L/mol-cm}$. Close examination of the spectra between 400 and 600nm reveals a broad weak absorption ($\epsilon=900 \text{ L/mol-cm}$ @ 532nm) which is presumably associated with transitions to high vibronic levels of S_1 or the low energy tail of the Soret band.

3.2 Emission Spectra

Excitation throughout the visible and near UV results in a deep red emission with a maximum near 680 nm. The very small stokes shift and the mirror image character of this emission relative to the Q-

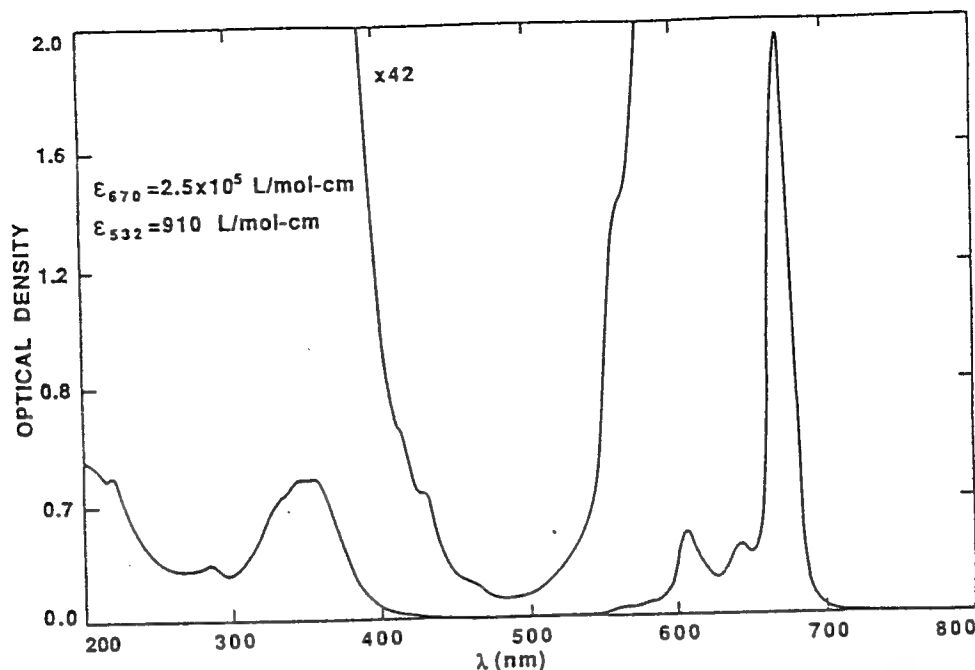


Figure 2. Absorption spectrum of chloro-aluminum-phthalocyanine in ethanol solution.

bands indicates that it is a fluorescence from S1. The measured fluorescence lifetime in ethanol is 7.0 nsec which is in good agreement with the value of 6.8 nsec measured in 1-chloronaphthalene⁵. The photophysics of CAP and several related compounds has been studied in some detail in 1-chloronaphthalene and the fluorescence and triplet yields for CAP were reported to be 0.58 and 0.4 respectively⁵ in that solvent. Given the similar fluorescence lifetimes and radiative lifetimes these quantities are not expected to differ drastically in alcohols.

3.3 Transient Absorption Spectra

It is known that the excited state absorption in certain conjugated macrocyclic compounds is strong ($\epsilon > 60000$ L/mol-cm) and broadband⁶. Transient absorption spectra recorded at 5 nsec and 40 nsec delays after the excitation pulse are shown in Figure 3. The spectra at short times are dominated by S1-Sn absorption and at long times by T1-Tn absorption. It is seen that indeed, the excited state spectral bands are much broader than the ground state bands, covering the entire visible region of the spectrum. Although excited state extinction coefficients (ϵ) have not been measured accurately, it has been estimated based on ground state bleaching considerations, that ϵ s are in the range of 10^4 - 10^5 . Thus, with these materials there exists the possibility of the situation described in Section 1 for nonlinear absorption where, throughout most of the visible region of the spectrum, the ground state is weakly optically coupled to strongly absorbing long lived excited states (both S1 and T1).

3.4 Nonlinear Absorption and Optical Limiting Measurements

The first limiting experiments performed on CAP in our laboratory were nanosecond nonlinear transmission measurements carried out as a function of dye concentration in methanol solutions. The 5 nsec, 532nm pulses were focussed into 1 cm pathlength cells containing the dye. The focussing

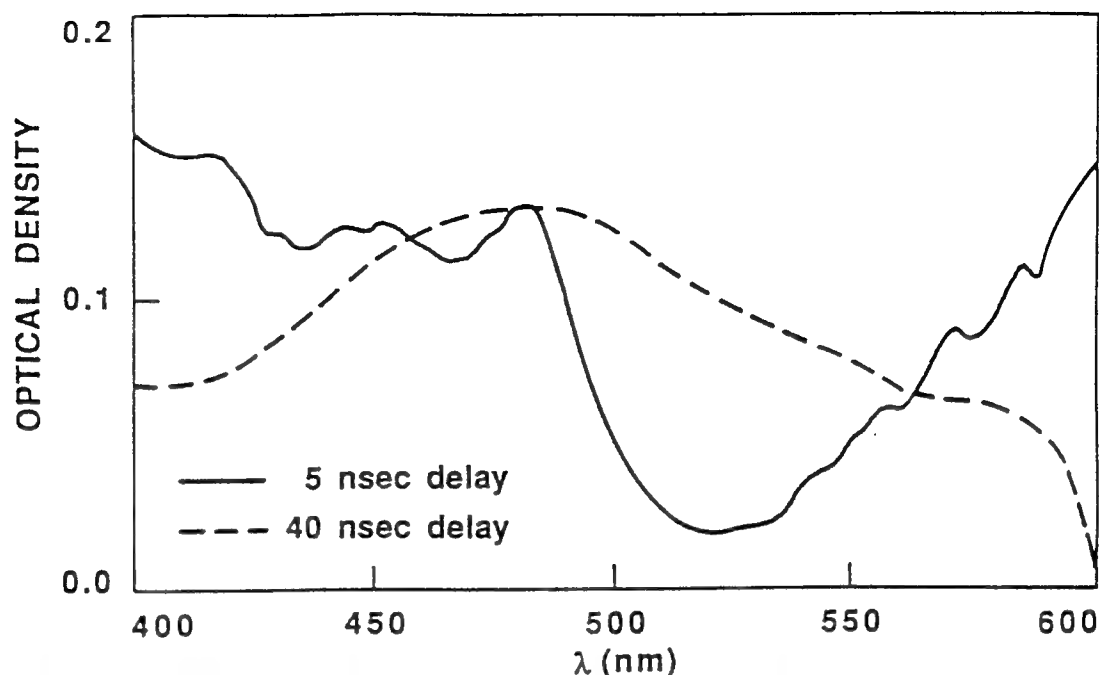


Figure 3. Transient absorption spectra of chloro-aluminum-phthalocyanine in methanol solution. The solid line represents the spectrum recorded with a 5 nsec delay relative to the exciting pulse. The dashed line represents the spectrum recorded 40 nsec after the exciting pulse.

conditions were very mild with a minimum spot diameter of only approximately 2.5 mm. The data from these measurements are shown in Figure 4. The thresholds for nonlinear response are in the range of a few millijoules and limiting throughputs of 5-13 millijoules have been achieved with solutions of 32-75% nominal transmission. Maximum input pulse energies have been in excess of 120 millijoules/pulse. After many thousands of pulses, no degradation of the dye solution was observed. Qualitative observations made during the limiting experiments suggest that there is at least a partial nonlinear refraction component to the limiting in the nanosecond time regime. A refractive component is indicated by the occurrence of "blooming" of the fluorescent trace through the cell at high input energies. No information is available as to the relative contributions of nonlinear absorption and nonlinear refraction in the nanosecond measurements. It is believed that with nanosecond pulses, the limiting throughput could possibly be pushed lower by increasing the fluence. However, attempts to focus more tightly have resulted in damage to the optical cell. Improved limiting might be achieved by altering the cell geometry to reduce intensity at the cell window and thus alleviate the damage.

Since fast response is of interest in many applications, studies were undertaken to characterize optical limiting effects in CAP solutions on a picosecond timescale. Utilizing 30 psec pulses with energies of up to 0.5 millijoules and focussing to a 75 μ m spot size, a limiting throughput of approximately 60 μ joules has been achieved in solutions with nominal transmission of 58%. These data are shown in Figure 5. Complete flattening of the response has not been achieved because the maximum input energy was limited by the output capability of the laser system. Studies of the relative contributions of nonlinear absorption and refraction⁷ have shown that the limiting in this case is largely independent of whether the transmitted beam is apertured or not and thus is predominantly due to nonlinear absorption.

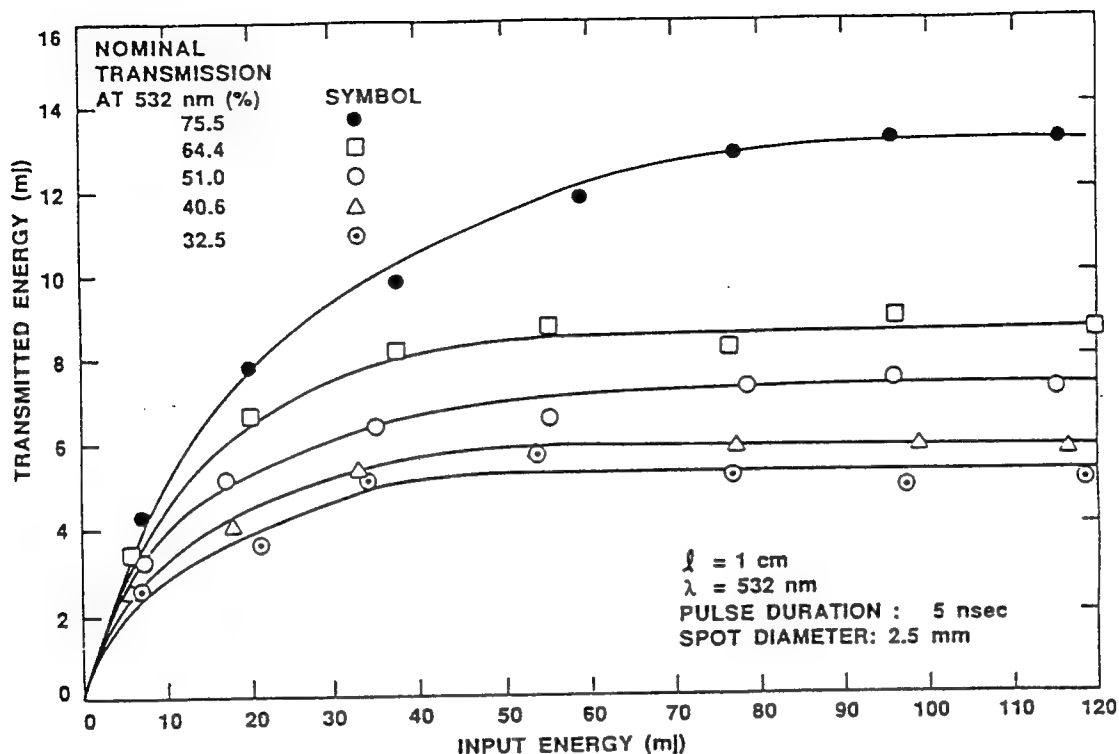


Figure 4. Nanosecond nonlinear transmission data for methanol solutions of chloro-aluminum-phthalocyanine.

Observation of optical limiting in solutions of CAP on the picosecond and nanosecond timescales along with the knowledge that there is likely a large triplet yield led us attempt to characterize the limiting behavior on longer timescales. In order to do this, picosecond pulse trains of eight to ten 30 psec pulses separated by 10 nsec were used in limiting experiments. The total input energy in the train was up to 1 millijoule, however, individual pulses typically contained 0.05-0.2 millijoules each. The intensity distribution in the train had the usual symmetric character with pulse energies increasing to a maximum and then falling off. The data from these measurements are shown in Figure 6. Limiting throughput of approximately 100 microjoules has been achieved under the same nominal transmission and focussing conditions described previously for the single picosecond pulse studies. It must be understood that the energies of the individual pulses in the train are much lower than was the case in the single pulse experiments. Prediction of the transmitted intensity based on summing the effects of single weak pulses (determined in the single pulse experiments) gives a transmitted intensity much higher than that observed. Consequently, it is apparent that on the timescale of up to roughly 100 nsec, there is some cumulative effect occurring which increases the extinction of the pulses in the train beyond what would be predicted on the basis of the single pulse experiments. Indications are that for the pulse train there is a slight nonlinear refraction (self-defocussing) component to the limiting, similar to that observed qualitatively in the nanosecond experiments, but that the dominant process is still nonlinear absorption.

A preliminary survey of several other M-Pc and M-NPc dyes has been carried out using 5 nsec, 532-nm excitation. In addition to CAP, chloro-indium-phthalocyanine (CIP), chloro-aluminum-t-butyl-naphthalocyanine (CA-t-Bu-NPc) and zinc-t-butyl-naphthalocyanine (Zn-t-Bu-NPc) have been

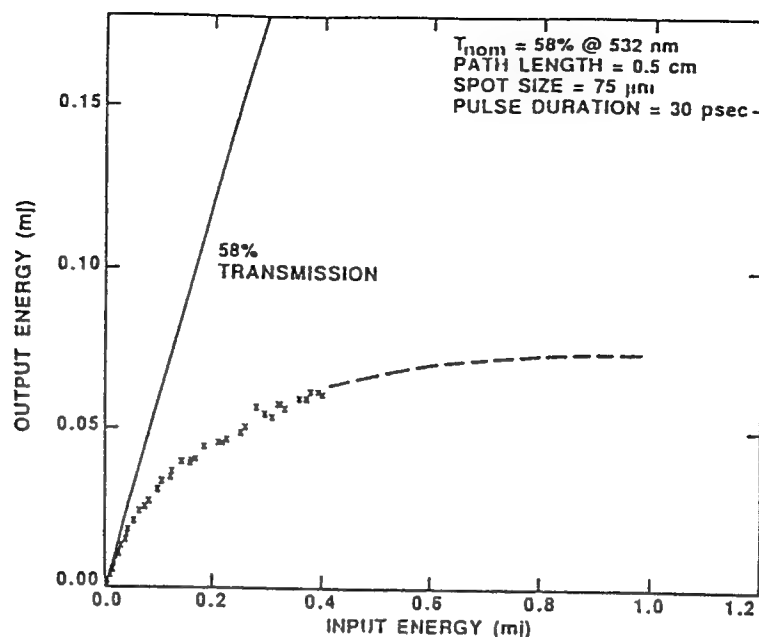


Figure 5. Single picosecond pulse optical limiting data on chloro-aluminum-phthalocyanine in methanol solution.

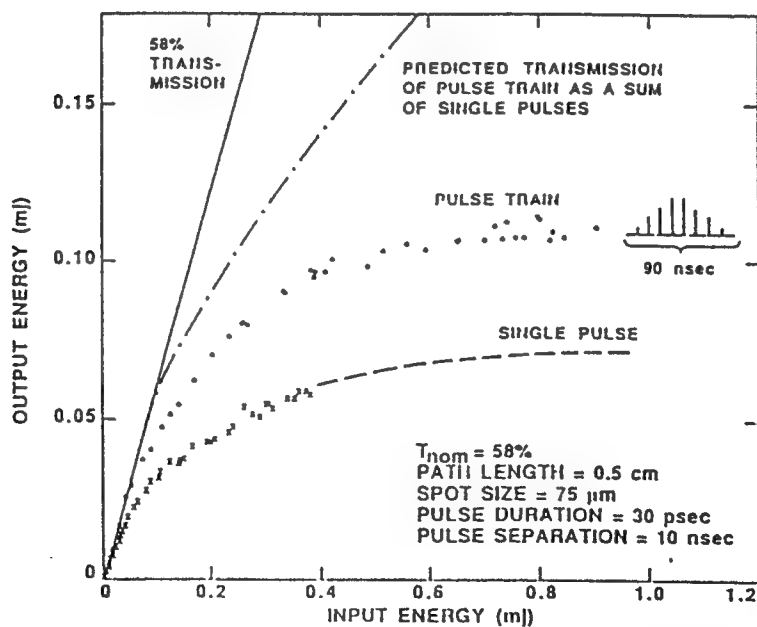


Figure 6. Picosecond optical limiting data on chloro-aluminum-phthalocyanine in methanol solution. The incident radiation was a train of eight 30 picosecond pulses separated by 10 nanoseconds shown schematically in the figure. The abscissa represents the total energy of the train. Also shown is the nominal transmission curve and a prediction of the transmission based on summing the expected transmitted intensities of the individual pulses.

investigated. Under conditions similar to those described above for the nanosecond experiments and nominal transmission of 50%, solutions of the latter three materials show limiting throughput values of approximately 2.5 and 1 millijoules respectively. The CIP material does not form a true solution but rather a suspension in methanol which must be agitated periodically to maintain activity. The two naphthalocyanines are interesting because the Q-bands in these materials are shifted to longer wavelengths thus improving the transmission in the visible. Unfortunately, these materials appear to degrade somewhat with exposure to air and light.

4. Discussion

The observation of nonlinear absorption in solutions of CAP on timescales from tens of picoseconds to hundreds of nanoseconds can be understood in terms of a relatively simple five state model shown in Figure 7. The leading edge of a visible laser pulse incident on the medium is weakly absorbed. The transition is from S_0 to some weak vibronic levels of the S_1 state (or some other electronic state) which rapidly relaxes to the S_1 state. Once a significant population is built up in S_1 , the remainder of the pulse is strongly absorbed via S_1 - S_n absorption which facilitates the limiting. The magnitude of the nonlinear absorption is related to the ratio of the excited state to ground state extinction coefficients at the exciting wavelength, ϵ_s/ϵ_0 . The larger this ratio, the better the limiting. In the case of CAP at 532nm this ratio is estimated to be between 10 and 50, based on transient absorption measurements. Since the single picosecond pulses used in this study are so much shorter than the S_1 lifetime of 7 nsec, this picture completely describes the limiting for that time regime.

When excitation of longer duration is used, then the decay of the singlet state should have a mitigating effect on the limiting behavior. However, in the case of CAP, significant limiting behavior extends for one hundred nanoseconds. The limiting throughput for the pulse train is less than a factor of two greater than for a single pulse of equivalent energy and is much less than that predicted by summing the effects of individual pulses. While the limiting throughput for 5 nsec pulses is much greater than for picosecond pulses, it must be remembered that in the case of the nanosecond pulses, the incident power density is approximately three orders of magnitude lower.

The question thus arises: What is the nature of the nonlinear response of the system at long times? One obvious possibility is that the triplet state, T_1 , produced via intersystem crossing from S_1 with a quantum yield of 0.4 shows strong T_1 - T_n absorption. Indeed, the transient absorption studies at long delay times support this concept showing significant absorption near 532nm thus indicating that the ratio of excited triplet state to ground state extinction coefficients, ϵ_t/ϵ_0 , is large. For long times, temporal properties of the nonlinear absorption will be limited by the lifetime of the triplet state which is likely to be on the order of 1 millisecond or longer.

It has been suggested earlier in this paper that there is some indication of nonlinear refractive effects on nanosecond and longer timescales. These effects may be due to inherent electronic nonlinearities in the dyes or dye/solvent combinations or they may be due to "thermal" nonlinearities resulting from energy dissipation in the medium. In any case, these effects appear to be weak relative to the nonlinear absorption effects.

5. Conclusions

Optical limiting measurements have been reported on CAP and several related compounds. Thresholds of limiting as low as tens of microjoules and limiting throughputs as low as 60 microjoules

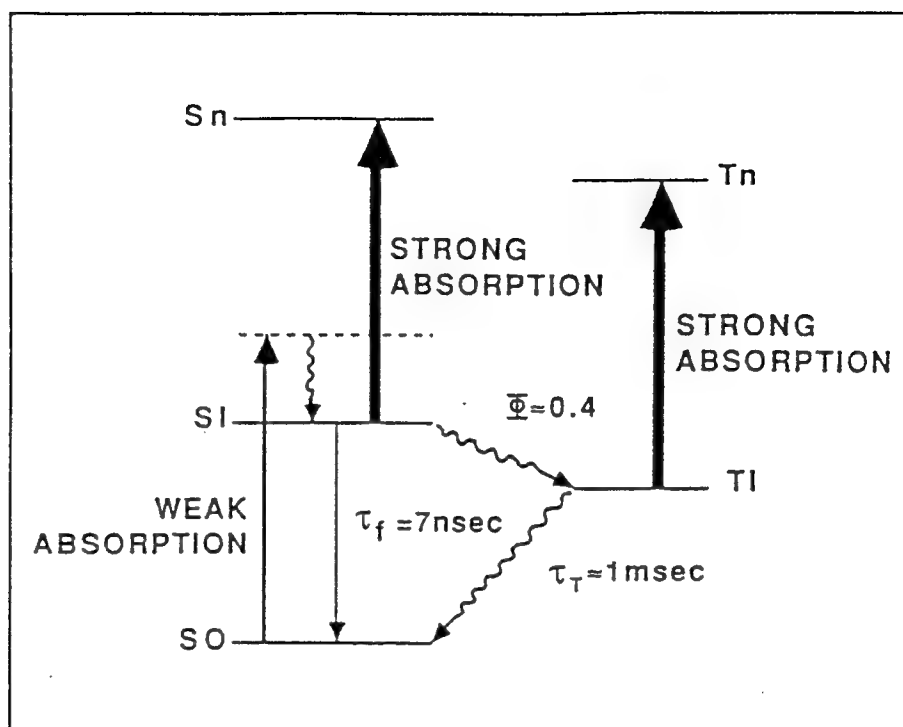


Figure 7. Simple five state model for optical limiting in chloro-aluminum-phthalocyanine.

have been observed for media with nominal transparency of close to 60%. The "switching" or response times for limiting are on the order of a few picoseconds or less while the temporal dynamic range is at least 3000 (30 psec-100 nsec) and may be as high as 10^8 .

While the experiments reported in this paper were all performed at 532 nm it is expected that the nonlinear behavior will be observed throughout most of the visible region of the spectrum. There is "continuous" weak absorption in S0 between 400 and 600 nm and there appears to be "continuous" strong absorption in S1 and T1 over the same region. In fact, the limiting behavior may well be better at other wavelengths since, at least for the S1 state, there appears to be a minimum in the absorption near 525nm.

While the results to date on CAP are interesting and indicate the viability of this approach to optical limiting, there is still interest in improving the linear and nonlinear response of the materials. Specifically, it would be desirable to improve the nominal transparency and reduce the threshold for limiting. Both of these things could be accomplished if the ratio of the excited state to ground state extinction coefficients could be increased. In CAP, this ratio is believed to be relatively low (10-50) at 532nm in both S1 and T1. It would be desirable to achieve a value in excess of 100. There are two ways of doing this. First, it is possible to alter the chemical structure of the macrocyclic ring to achieve less ground state absorption in the visible. Secondly, it may be possible to find materials with stronger excited state absorption bands. We have begun to explore the first option. Several M-NPc dyes have been synthesized in our laboratory. In these materials, as stated previously, the absorption bands are shifted thus resulting in better transmission in the visible. Further exploration of the

plethora of possible related compounds is called for to build up a photophysical data base from which structure-property relationships can be identified. Once these relationships are clearly understood, it will be possible to identify the most promising synthetic targets.

6. Acknowledgements

The authors wish to acknowledge Dr. L. Khundhar, JPL, for performing the fluorescence lifetime measurements and Dr. R. Goldbeck, Chemistry Department, University of California, Santa Cruz for performing the transient absorption measurements reported in this paper. Part of the research described in this paper was carried out at the Jet Propulsion Laboratory, California Institute of Technology and was sponsored by the U.S. Army through an agreement with the National Aeronautics and Space Administration. The authors from the University of Central Florida also gratefully acknowledge support from the National Science Foundation Grant ECS # 8617066 and the Florida High Technology and Industry Council

7. References

1. W. Blau, H. Byrne, W.M. Dennis and J.M. Kelly, Opt. Comm., 56, 25 (1985)
2. A.H. Jackson, "Azaporphyrins", in The Porphyrins, Vol1. Structure and Synthesis, Part A, ed. by David Dolphin, Academic Press, New York (1978), p. 365 and references therein.
3. C.C. Frazier, S. Guha, W.P. Chen, M.P. Cockerham, P.L. Porter, E.A. Chauchard and Chi H. Lee, Polymer, 24, 553 (1987)
4. W.E. Williams, M.J. Soileau and E.W. Van Stryland, Opt. Comm., 50, 256 (1984).
5. James H. Brannon and Douglas Magde, J. Am. Chem. Soc., 102, 62 (1980)
6. Patricia A. Firey, William E. Ford, James R. Sounik, Malcolm E. Kenny and Michael A. J. Rogers, J. Am. Chem. Soc., 110, 7626 (1988)
7. M. Sheik-bahae, A. A. Said and E. W. Van Stryland, to be published, Opt. Lett.

SIMPLE ANALYSIS AND GEOMETRIC OPTIMIZATION OF A PASSIVE OPTICAL LIMITER BASED ON INTERNAL SELF-ACTION

Mansoor Sheik-bahae, Ali A. Said, D.J. Hagan, M.J. Soileau and Eric W. VanStryland

CREOL

Center for Research in Electro-Optics and Lasers
University of Central Florida, Orlando, FL 32816

ABSTRACT

Passive optical limiting based on nonlinear refraction in a "thick" medium is analyzed using a simple model. In a tight focus geometry we found that the position of the sample with respect to the focal plane is an important parameter in the limiting characteristics of the device. In particular we have examined such characteristics in liquid CS₂ using 300 ns pulses at 10.6 μm.

1. INTRODUCTION

Passive optical limiters based on nonlinear refraction have been extensively demonstrated and analyzed for a variety of materials and laser wavelengths. [1-4] A general (and most common) geometry is illustrated in Figure 1. The laser beam is focused into a nonlinear index material and is then collected through a finite aperture in the far field. At a high enough irradiance the far field beam broadening arising from the self-action of the laser beam inside the medium will result in the limiting of the transmitted light through the aperture. Most of the published experimental and analytical work regarding such a device has dealt with an "on focus" geometry in which the laser beam is focused at the middle of the sample indicated by having $z=0$ in Figure 1. Based on a simple "distributed lens" model, we show that depending on the nature of the refractive nonlinearity, this distance (z) is an important parameter in such a geometry. In fact, for a thin medium, a displacement of the sample by a distance of the order of a diffraction length (z_0) would result in reversing the operation of the device from limiting to a saturating type behavior. Similar characteristics are also found for "thick" limiters where the thickness of the sample is larger than the diffraction length of the focused beam. In this case, the lowest threshold for limiting is achieved by focusing the beam at the front surface for negative nonlinearity ($\Delta n < 0$) and rear surface for a positive nonlinearity ($\Delta n > 0$).

Such pronounced variations of the beam transmittance through the aperture as a function of the sample position (z) have also provided the basis for an extremely simple and sensitive technique called "Z-scan" which we developed and currently use for accurate measurements of refractive nonlinearities in a large class of materials with a demonstrated resolution of $\approx \lambda/200$ wave front distortion.[5]

2. FORMALISM

The nonlinear wave equation governing the propagation of the laser beam inside a nonlinear medium is expressed as:

$$\nabla^2 E - \frac{1}{c^2} \frac{\partial^2}{\partial t^2} [(n_0 + \Delta n)^2 E] = 0 \quad (1)$$

where E is the electric field, n_0 is the linear index of refraction and the nonlinearity is introduced through Δn which in general, may include various order contributions such as $\chi^{(3)}$, $\chi^{(5)}$, ... etc. Here we consider the lowest order effect, namely a $\chi^{(3)}$ (Kerr type) nonlinearity which is commonly expressed in terms of the nonlinear coefficient n_2 (esu) as: $\Delta n = n_2 |E|^2/2$. In a thick medium, transverse variations accounted for by the ∇^2 term in Eq.1 become significant and an exact numerical solution to Eq.1 is extremely complex. A common technique to simplify this problem is known as the "aberration-free" approximation [6,7], in which

a Gaussian beam propagating through the thick nonlinear medium is assumed to preserve its Gaussian shape. This requires that the radial variation of the index of refraction be parabolic. For a Gaussian beam and cubic nonlinearity such a requirement is satisfied by using the following approximation:

$$\Delta n(r) = \Delta n_0 e^{-2r^2/w^2} \simeq \Delta n_0 (1 - 2r^2/aw^2), \quad (2)$$

where Δn_0 is the on-axis index change, w is the local beam radius ($HW1/e^2M$ in irradiance) and a is a correction factor introduced to account for the higher order terms that have been omitted in the actual expansion of e^{-2r^2/w^2} and its value is only of quantitative significance in evaluating the nonlinearity or the limiting thresholds. For a thin medium, the parabolic approximation of Eq.(2) implies that the medium behaves like a thin spherical lens. Therefore, as depicted in Figure 2, a thick sample can be regarded as a stack of such nonlinear lenses with focal lengths that depend on the local beam irradiance. The effective focal length of the i -th element in the stack can be written as:

$$f_i = \frac{aw_i^2}{4\Delta n_i \Delta L}, \quad (3)$$

where w_i and Δn_i are the beam radius and on-axis index change at that element respectively. ΔL denotes the separation between two adjacent lenses and should be chosen to be much smaller than both the diffraction length of the beam and f_i . The latter requirement can be written as:

$$\Delta L \ll (aw_i^2 / 4\Delta n_i)^{1/2}. \quad (4)$$

For a given position of the sample (z) the input Gaussian beam can be propagated through the nonlinear medium using successive ABCD matrices defined for the i -th element in the stack as:

$$\begin{pmatrix} A_i & B_i \\ C_i & D_i \end{pmatrix} = \begin{pmatrix} 1 - \Delta L/n_0 f_i & \Delta L/n_0 \\ -1/f_i & 1 \end{pmatrix}. \quad (5)$$

Having calculated the beam size at the aperture (w_a) we can obtain the normalized transmittance through the aperture with radius r_a as

$$T(z) = \frac{1 - \exp(-2r_a^2/w_a^2)}{S}, \quad (6)$$

where S is the aperture transmission in the (small signal) linear regime and r_a is the aperture radius. For simplicity we have assumed only cw radiation and a steady state nonlinearity. Temporal variations and transient effects, however, can be included with ease if pulsed laser radiation is to be assumed.

3. DISCUSSION

First, let's consider only a single thin sample in the geometry of Figure 1. In this case the transverse effect inside the sample is negligible and the propagation process can be analyzed using an exact wave optics approach and has been given by us in reference [5]. Here we compare those results with that of the "thin lens" approximation. The calculated transmittance as a function of sample position for a fixed input irradiance is shown in Figure 3 using both techniques. In this calculation a positive nonlinearity with an on-focus ($z=0$) on-axis ($r=0$) phase change ($\Delta\Phi_0$) of 0.5 radian was assumed. $\Delta\Phi_0$ can be given in terms of the corresponding index change (Δn_0) as,

$$\Delta\Phi_0 \simeq \frac{2\pi}{\lambda} \Delta n_0 L, \quad (7)$$

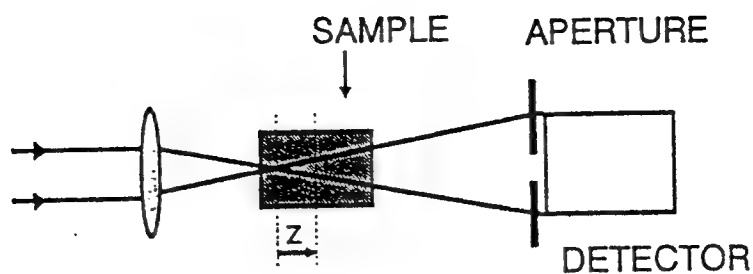


Fig.1 The passive limiting geometry based on nonlinear self-action. Limiting occurs due to a significant beam broadening at the far-field aperture in the nonlinear regime. The important parameter, z , is taken as the distance between the focal plane and the center of the sample.

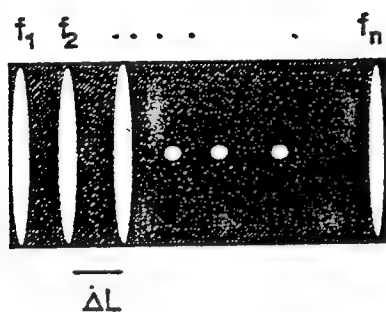


Fig.2 In the "distributed lens" approximation, the thick nonlinear medium is regarded as a stack of thin nonlinear lenses whose focal lengths depend on the local beam irradiance.

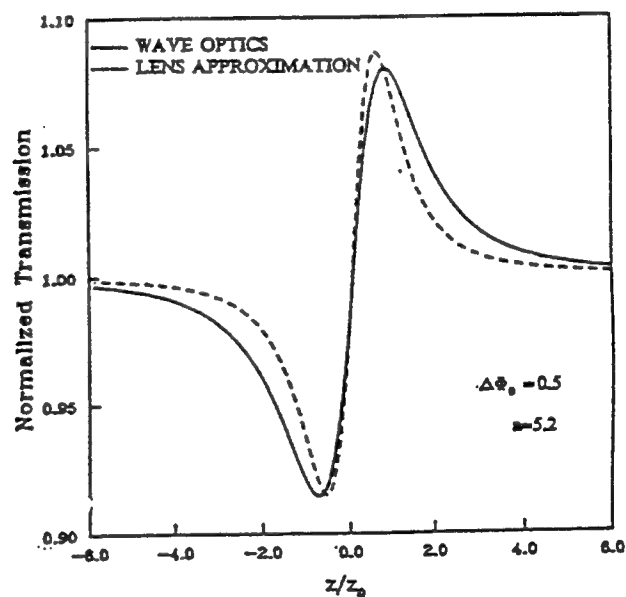


Fig.3 The Z-scans of a thin nonlinear medium as calculated using the methods of wave optics (ref.[5]) and thin lens approximation. A 50% aperture is assumed ($S=0.5$).

where λ is the laser wavelength and L is the thickness of the sample. A qualitative physical argument that explains the transmittance variations in such an experiment, which we refer to as a Z-scan [5], can be given as follows. Starting the scan from a distance far away from the focus (negative z), the beam irradiance is low and negligible nonlinear refraction occurs leading to linear transmittance. As the sample is brought closer to the focus, the beam irradiance increases leading to formation of a self-lensing in the sample. A positive self-lensing prior to the focus will enhance the diffraction leading to a beam broadening at the aperture which decreases the transmittance. As the scan continues and sample crosses the focal plane to the right (positive z), the same self-lensing effect will tend to recollimate the beam, causing a beam narrowing at the aperture which results in an increase in the transmittance. A pre-focal transmittance minimum (valley) and a post-focal transmittance maximum (peak) are, therefore, the Z-scan signature of a positive nonlinearity while a negative one, following the same analogy, will give rise to an opposite (peak-valley) configuration. With a small phase shift, the peak and valley occur at a distance of $\approx 0.85z_0$ from the focal plane where $z_0 = \pi w_0^2 / \lambda$ with w_0 being the beam waist. With a limiting device in mind, one readily realizes that the optimum sample position to minimize the limiting threshold is the z region where the valley occurs. We will exploit this feature further in optimization of a thick limiter.

Returning to Figure 3, we notice good agreement between the results of the lens approximation and the wave optics approach is obtained by adjusting the correction factor a , to be 5.2 at an aperture size such that $S=0.5$. In general we numerically found that for $|\Delta\Phi_0| < \pi/2$ the value of a decreases with larger apertures but is nearly independent of $\Delta\Phi_0$. At larger phase distortions a will further decrease. Since the limiting thresholds occur at a relatively large phase shift, we will assume $a=4$ in obtaining the limiting curves. We can now proceed to analyze the limiting characteristics of a thick medium using the method of a distributed lens. The calculated Z-scan for a rather extreme case for which $L/n_0z_0=15$ are shown in Figure 4. A cubic nonlinearity with either polarity and with $N=\pm 1.4$ is assumed where $N=(2\pi/\lambda)n_0\Delta n_0z_0$ is defined as the phase distortion number. An interesting feature of the thick sample Z-scan is that the separation between peak and valley of these curves is now dominated by the optical length of the sample; L/n_0 . Furthermore, the two extremes correspond to focusing the laser beam on either surface. Evident from Figure 4 is also the existence of a nearly flat transmittance region where the beam is focused near the middle of the medium. This simply signifies the fact that although the laser beam experiences a large local phase distortion within the medium, the pre-focal and post-focal nonlinear refractions cancel each other's effect in the far field. In the lens analogy it is similar to placing pairs of lenses of the same sign on both sides of the focal plane such that the far field beam pattern is relatively unaltered.

It is also noted (Figure 4) that the existence of a large internal self-action results in a larger transmittance change for a positive nonlinearity than for a negative one of the same magnitude. This results from the fact that with a positive nonlinear index the resultant self-focusing is a self-strengthening effect similar to an avalanche process whereas with a negative nonlinearity we have self-defocusing inside the medium which leads to a self-weakening of the nonlinear refraction. Nevertheless, at small enough phase distortions where variations of the beam diameter inside the medium due to nonlinear refraction is insignificant, nonlinearities with opposite polarities will give rise to the same transmittance changes.

From a limiting point of view, as pointed out in the case of a thin sample, we must place the sample in a valley position to minimize the threshold. The limiting behavior of the thick medium of Figure 4 are explicitly shown in Figures 5 and 6 for negative and positive nonlinearities, respectively. It is seen that as the sample is positioned farther from the valley the limiting threshold increases. For negative nonlinearity, as shown in Figure 5, the lowest limiting threshold is obtained at the valley corresponding to focusing at the front surface. This threshold is given by $N \approx 2$. Focusing near the rear surface yields a bleaching type behavior which is undesirable for a limiting device. Similarly, for a positive nonlinearity, the lowest limiting threshold occurs at the valley which corresponds to rear surface focusing. However, as seen in Figure 6, there is a sudden drop of transmission at $N \approx 2$ (for $a=4$) due to the onset of catastrophic self-focusing. This threshold is seen to be nearly independent of the sample position. The phase distortion number, N , can also be expressed as a power ratio: $P/2P_1$ where P denotes the radiation power and P_1 is defined as:

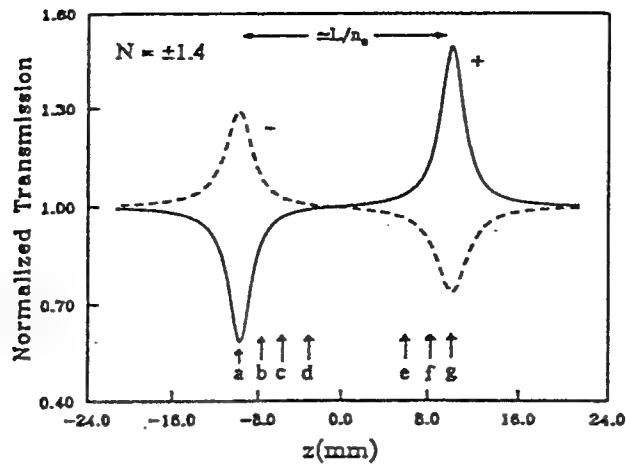


Fig.4 Calculated Z-scans of a "thick" medium using the method of distributed lens for both positive (solid line) and negative (broken line) nonlinearities. The arrows on the z axis indicate the corresponding positions at which the limiting curves of figs. 5 and 6 were obtained.

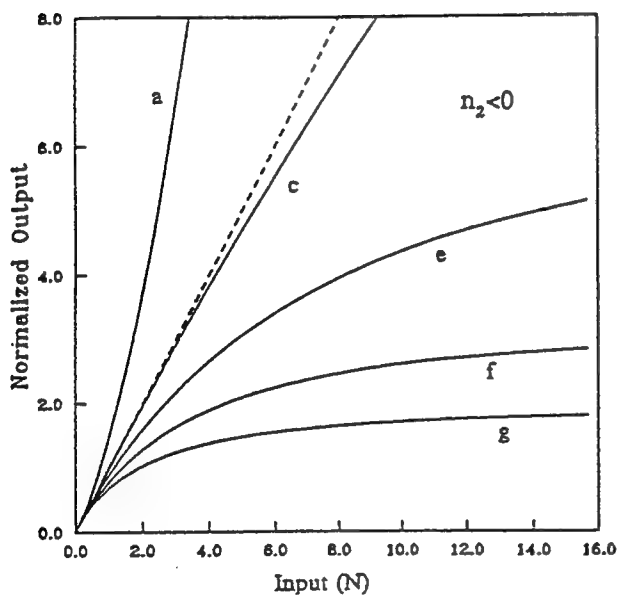


Fig.5 The normalized power transfer curves for a negative nonlinearity ($n_2 < 0$) calculated for various sample positions (z) as indicated by the arrows in Fig.4. The broken line shows the linear transmittance. ($a=4$ and $S=0.5$ were used in the calculations).

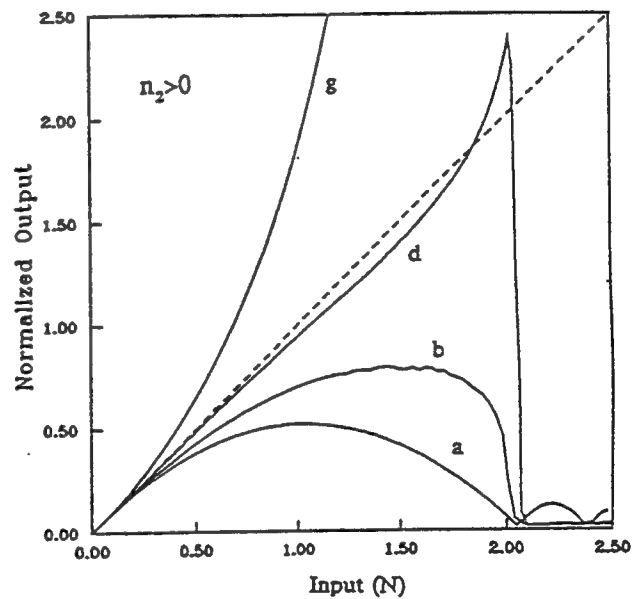


Fig.6 The normalized power transfer curves for a positive nonlinearity ($n_2 > 0$) calculated for various sample positions (z) as indicated by the arrows in Fig.4. The broken line is the linear transmittance curve. The catastrophic self-focusing occurs in all the curves at $N \approx 2$ signified by a sudden drop in the transmitted power. ($a=4$ and $S=0.5$ were used in the calculations).

$$P_1 = \frac{c\lambda^2}{32\pi^2 n_2} \quad (\text{cgs units}).$$

(8)

Numerical calculations of the nonlinear wave equation made by Marburger [8] indicate that for focused Gaussian beams in a thick medium with positive nonlinear index ($n_2 > 0$) a catastrophic self-focus will occur at a critical power of $P_c = 3.77 P_1$ ($N_c = 1.88$). The method of distributed lens, however, predicts a well defined threshold for the beam collapse at a critical power of $P_c \approx a P_1$, ($N_c \approx a/2$) which agrees with the Marburger's result if we choose $a \approx 3.77$. According to our earlier discussion regarding the a parameter, this value is nearly within the evaluated range for a large phase distortion and presents a plausible argument for the introduction of this correction factor.

When the self-focusing threshold is reached, the laser beam collapses abruptly and the local beam irradiance becomes infinite. However, the paraxial approximation on which the method of a nonlinear distributed lens is based breaks down as the beam radius becomes comparable to the wavelength of the laser. [9] In addition, at the high irradiance produced by the self-focusing effect one must consider saturation of the nonlinear index, plasma production and subsequent optical breakdown of the medium.

4. EXPERIMENTS

Optical limiting in liquid CS_2 was examined using a TEA CO_2 laser with single longitudinal mode pulses of 300 ns duration. The laser beam was focused to $w_0 \approx 60 \mu\text{m}$ ($z_0 \approx 1\text{mm}$) into a 24mm cell (with NaCl windows) filled with spectrophotometric CS_2 . With $n_0 = 1.63$ the ratio $L/nz_0 \approx 15$, indicating a "thick" medium. First we performed a Z-scan on this sample to verify the locations of the peak and valley of the transmittance. The result for a 1 mJ pulse energy along with the theoretical fit is shown in Figure 7. The curve exhibits features predicted by the distributed lens method for a negative nonlinearity, namely the peak and valley corresponding to the second and first surface focusing respectively and a nearly flat portion corresponding to focusing near the center of the cell. The origin of this negative nonlinearity is believed to be thermal, arising from the finite absorption of $10.6 \mu\text{m}$ radiation in CS_2 ($\alpha \approx 0.22 \text{ cm}^{-1}$). Thermal lensing in liquids arises from the thermal expansion of the medium and has a rise time given by the "acoustic transit time" which is effectively the time it takes for a sound wave to traverse the beam radius [10]. Knowing the sound velocity in CS_2 ($v_s \approx 1.5 \times 10^5 \text{ cm/sec}$) and the focal beam radius ($\approx 60 \mu\text{m}$) a response time of $\approx 40 \text{ ns}$ is obtained which is almost an order of magnitude smaller than the laser pulsewidth. The decay of the thermal lens, however, is governed by the thermal diffusion process which is of the order of 0.1 second which is orders of magnitude larger than the pulsewidth and its effect can be neglected [10]. Under such quasi-steady state conditions the nonlinear index change arising from nonuniform heating can be estimated in terms of the laser pulse fluence (F) at the focus:

$$\Delta n_0 \approx 0.5 \frac{dn}{dT} \frac{\alpha F}{\rho C_v}, \quad (9)$$

where ρ is the density, C_v is the specific heat and dn/dT is the thermo-optic coefficient of the medium. The latter coefficient (dn/dT) has long been investigated for CS_2 and a value of $\approx -8 \times 10^{-4} \text{ } ^\circ\text{C}^{-1}$ has been reported in the literature [11]. With the known value of $\rho C_v \approx 1.3 \text{ J/}^\circ\text{Kcm}^3$ for CS_2 we obtain $\Delta n_0 \approx -2.3 \times 10^{-3}$ at a $\approx 17 \text{ J/cm}^2$ fluence. This is in good agreement with the $\Delta n_0 \approx -2.1 \times 10^{-3}$ used to fit the Z-scan of Figure 7. It should be noted that in this calculation, a value of 5.2, as obtained for $S=0.5$ (see Fig.3), was used for the a parameter. Note also that the $z=0$ point in the Z-scan curve is defined as the position of the focus in air in the absence of the nonlinear medium. After the insertion of a "thick" sample with $n_0 > 1$, the beam waist inside the sample no longer will coincide with our $z=0$ point. This is why the $z=0$ point of the Z-scan in Figure 7 differs from that of Figure 4 which was calculated assuming $n_0=1$.

The limiting behavior of the same CS_2 cell at $10.6 \mu\text{m}$ is shown in Figure 8 where the normalized transmitted power is plotted versus the input power as measured for various sample positions. They exhibit the predicted features given in Figure 5. It is evident from eq.(9) that thermal self-action can be enhanced

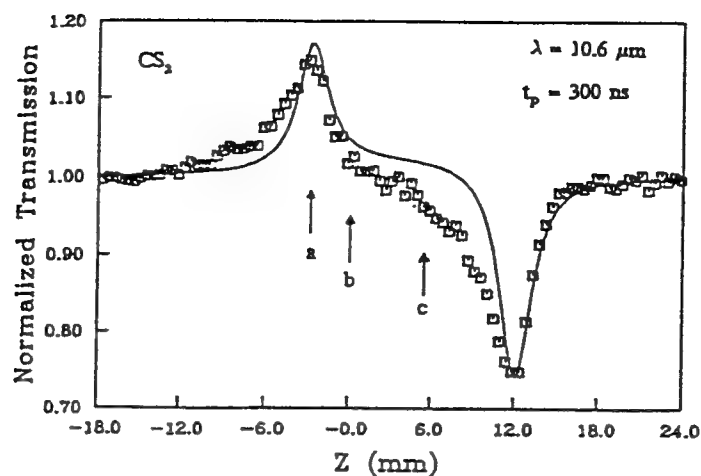


Fig.7 The measured Z-scan of a thick liquid CS_2 cell using 300 ns TEA CO_2 laser pulses at $10.6 \mu\text{m}$. The theoretical fit (solid curve) is obtained based on the thermal self-defocusing in CS_2 . The arrows on the z axis indicate the positions at which the limiting data of Fig.8 were obtained.

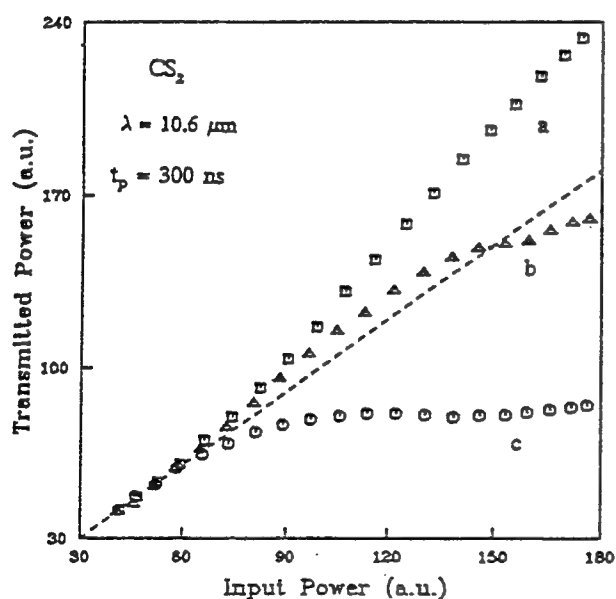


Fig.8 The limiting characteristics of liquid CS_2 at $10.6 \mu\text{m}$ measured at various z positions indicated by the arrows in Fig.7.

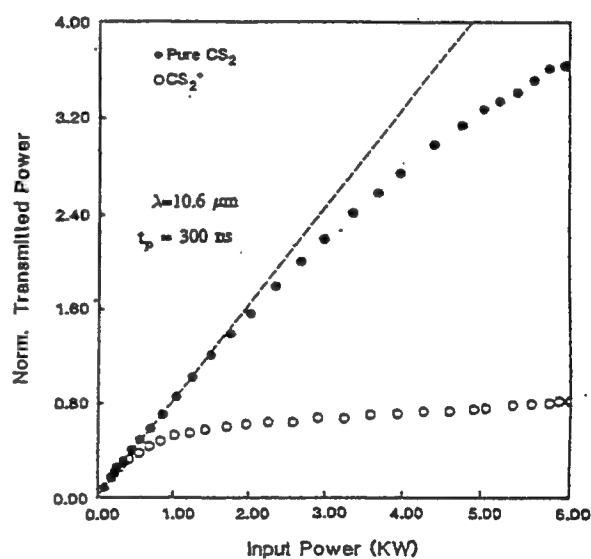


Fig.9 A low threshold fluence limiter at $10.6 \mu\text{m}$ using modified CS_2 ($\alpha \approx 2 \text{ cm}^{-1}$) as compared to pure CS_2 ($\alpha \approx 0.22 \text{ cm}^{-1}$). The measurements were obtained using a 3mm cell placed at the transmittance valley.

by increasing the absorption coefficient of the medium. We obtained a limiting threshold of ≈ 0.5 kW (150 μ J) in CS₂ at 10.6 μ m by desolving impurities (eg. sulfur) to increase the absorption coefficient to ≈ 2 cm⁻¹. This is shown in Figure 9 where the results for two samples of pure and modified CS₂ are compared for a 3mm cell positioned in the transmittance valley.

It must be remembered that though surface focusing renders a low threshold for limiting, it may also cause damage to the window or surface of the sample. For a given specific application and type of nonlinear material, an optimum self-protecting geometry may be achieved using the simple model presented in this paper.

ACKNOWLEDGEMENT

We gratefully acknowledge the support of the National Science Foundation grant ECS #8617066, DARPA/CNVEO and the Florida High Technology and Industrial Council.

REFERENCES

1. R.C.C. Leite, S.P. Porto, and T.C. Damen, "The Thermal Lens Effect as a Power-Limiting Device," *Apl. Phys. Lett.*, **10**, 100-101(1967).
2. W.E. Williams, M.J. Soileau, and E.W. Van Stryland, "Optical Switching and n₂ Measurements in CS₂," *Opt. Lett.*, **50**, 256-260(1984).
3. E.W. Van Stryland, Y.Y. Wu, D.J. Hagan, M.J. Soileau, and K. Mansour, "Optical Limiting with Semiconductors," *J. Opt. Soc. Am.*, **5**, 1980-1989(1988).
4. J.H. Hermann, "Simple Model for a Passive Optical Power Limiter," *Optica Acta*, **32**, 541-547(1985).
5. M. Sheik-bahae, A.A. Said, and E.W. Van Stryland, "High Sensitivity, Single Beam n₂ Measurements," Submitted to *Opt. Lett.*
6. S.A. Akhmanov, A.D. Sukhorokov, and R.V. Khokhlov, "Self-focusing and Diffraction of Light in a Nonlinear Medium," *Sov. Phys. Vspeski; English Translation*, **10**, 609(1968).
7. A. Yariv and P. Yeh, "The Application of Gaussian Beam Formalism to Optical Propagation in Nonlinear Media," *Opt. Commun.*, **27**, 295-298(1978).
8. J.H. Marburger, "Progress in Quantum Electronics," eds. J.H. Sanders and S. Stenholm (Pergamon, New York, 1977) p. 35.
9. M.D. Feit, and J.A. Fleck, Jr., "Beam Nonparaxiality, Filament Formation, and Beam Breakup in the Self-Focusing of Optical Beams," *J. Opt. Soc. Am. B*, **5**, 633-640(1988).
10. J.N. Hayes, "Thermal Blooming of Laser Beams in Fluids," *Appl. Opt.*, **2**, 455-461(1972).
11. V. Raman, F.R.S., and K.S. Venkataraman, "Determination of the Adiabatic Piezo-Optic Coefficient of Liquids," *Proc. Roy. Soc. A*, **171**, 137(1939).

PASSIVE BROADBAND HIGH DYNAMIC RANGE SEMICONDUCTOR LIMITERS

D.J. Hagan, E.W. Van Stryland, Y.Y. Wu, T.H. Wei, M. Sheik-Bahae,
A. Said, Kamjou Mansour, J. Young and M.J. Soileau.

Center for Research in Electro-Optics and Lasers
University of Central Florida, Orlando, FL 32826

ABSTRACT

The principles of operation of semiconductor optical limiters which utilize two-photon absorption and free-carrier induced defocusing are described. We present a review of early work using psec pulses at 532 nm in ZnSe, in which the problem of damage in solid state limiters is overcome by optimizing the focusing geometry. Limiting energies as low as 10 nJ are seen, and a dynamic range (damage energy divided by limiting energy) in excess of 10^4 is demonstrated. The somewhat complicated propagation theory is simplified into a set of scaling rules which are used to predict operating characteristics of semiconductor limiters at longer wavelengths and for shorter pulses. We present new limiting data obtained with longer pulses in ZnSe, in CdTe at 1.06 μm and InSb at 10.6 μm , and we compare these results with the scaling rules.

1. INTRODUCTION

Passive optical limiting results from irradiance-dependent nonlinear-optical processes in materials. [1,2] The ideal optical limiter has the characteristics shown in Figure 1. It has a high linear transmittance for low input (e.g., energy E or power P), a variable limiting input E or P , and a large dynamic range, defined as the ratio of E or P at which the device damages (irreversibly) to the limiting input. Since a primary application of the optical limiter is for protection of sensitive optical components such as detectors, and damage to detectors is normally determined by fluence, this is the quantity of interest for the output of the limiter. Getting the response of Figure 1 turns out to be possible by using a wide variety of materials; however, it is difficult to get the limiting threshold as low as is often required and at the same time to have a large dynamic range.

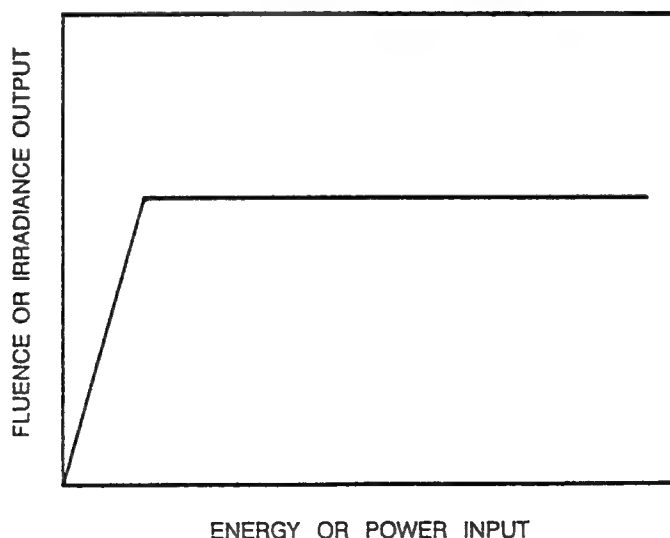


Fig. 1. Fluence output of an ideal optical limiter as a function of the input power or energy.

Because high transmittance for low inputs is desired, we must have low linear absorption. These criteria lead to the use of two-photon absorption (2PA) and nonlinear refraction. In this paper we present the detailed operational characteristics and a theoretical description of optical limiting devices based on 2PA and the subsequent photogenerated free-carrier defocusing in semiconductors.

2. HISTORICAL BACKGROUND

Semiconductors have exhibited some of the largest optical nonlinearities of all materials. [3] Unfortunately, from the standpoint of optical limiting, these extremely large nonlinearities are associated with near bandgap resonance and thus are in a region of relatively high linear absorption. In addition, solids undergo irreversible optical damage. Even so, effective limiting has been demonstrated by using other mechanisms. In 1969, Geusic *et al.* reported limiting behavior in Si attributed to stepwise nonlinear absorption at 1.06 μm . [4] Later, Boggess *et al.* showed fluence limiting in Si that was due to a combination of nonlinear absorption with a refractive contribution induced by the photoexcitation of free carriers. [5] Power-limiting experiments were conducted by Ralston and Chang in a series of semiconductors such as CdS, GaAs, and CdSe. [6] This was the first report to our knowledge of the use of 2PA for optical limiting. In those studies nanosecond pulses were used where absorption by the 2PA-generated free carriers was significant. In addition, although this was not noted at the time, the refractive index change caused by photo-generated carriers is strong and also useful in the limiting process. In particular, this defocusing limits the transmitted fluence. Another type of limiter, which uses a combination of 2PA and nonlinear refraction in the narrow gap semiconductor InSb at 10 μm , was developed by Walker *et al.* [7] This device relies on the etalon properties of the nonlinear sample, and the device exhibits regions of bistability, but the range of input energies over which limiting is obtained is small. Boggess *et al.* were the first to use the combined effects of 2PA and carrier defocusing to obtain optical fluence limiting. [8] The geometry used was to focus picosecond 1.06 μm pulses onto the surface of a thin sample of GaAs, refocus the beam, and monitor the transmittance of an aperture. Since the damage-prone surfaces are subjected to the maximum fluence of the input pulses, the range over which these devices function without incurring damage is low. What we have found is that if thick samples are used, the large nonlinearities of the semiconductor can actually be used to prevent damage. [9] The trick is simply to focus the light tightly into the bulk of the material. Nonlinear absorption combined with nonlinear refraction keeps the irradiance within the semiconductor below the damage threshold, and the device is self-protecting. One problem now is that the wave equation can no longer be separated into two propagation equations, one for the irradiance and one for the phase. This makes even numerical solutions difficult. However, we find that the analysis of thin limiters qualitatively describes the operation of thick limiters.

3. CHARACTERISTICS OF SELF-PROTECTING LIMITERS

Our initial experiments on thick limiters were performed in ZnSe using 30 ps (FWHM) pulses of 532 nm wavelength light obtained from a frequency-doubled mode-locked and Q-switched Nd:YAG laser with a single pulse switched out. The experimental arrangement is depicted in Figure 2.

The second lens was used to refocus the transmitted beam through a pinhole, such that the low-energy pinhole transmittance was approximately 90 percent. The energy transmitted through the pinhole was measured on a large-area Si photodiode placed immediately behind the pinhole. The input energy and pulsewidth were simultaneously monitored for each pulse. [10] The incident energy was continuously variable without beam distortion or deviation by using a half-wave plate and polarizer. As the laser repetition rate was 0.5 Hz, the experiments were effectively single shot. The total energy transmittance could be measured by removing the pinhole, thus showing the contribution of nonlinear absorption to the limiting. At high input levels, this was found to be less significant than the fluence limiting caused by self-defocusing. the device showed a linear transmittance for input energies much less than the limiting energy

(E_L) and a constant transmitted fluence for input energies much greater than (E_L). E_L is defined as the input energy at which the transmittance falls to one half of the low-energy transmittance. It should be noted that E_L was not particularly sensitive to the choice or position either of the pinhole or of the refocusing lens. We note that the aperture is used only as a convenient means for monitoring the on axis fluence.

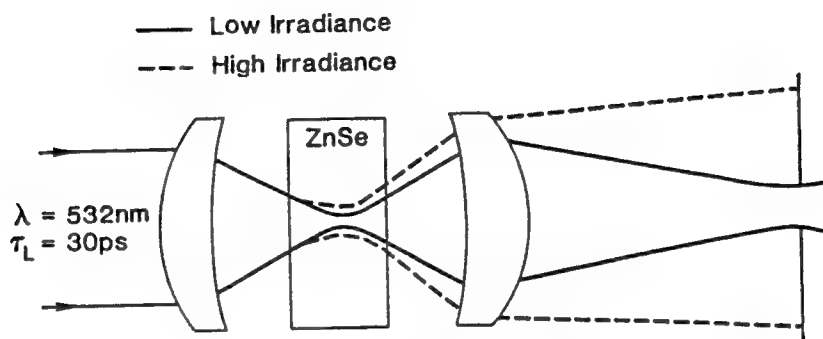


Fig. 2. Configuration for a Self-Protecting Optical Limiter.

The limiting energy and the damage energy, E_D , were measured for various distances ΔZ between the sample front surface and the beam waist. This was done for two sample thicknesses L ($L = 10$ and 3 mm) and two focusing lenses ($f = 37$ and 75 mm, producing measured focused spot radii in air of 8 and $14 \mu\text{m}$ half-width $1/e^2$ maximum, respectively). Figure 3(a) shows the limiting energy as a function of ΔZ for both samples with the $f = 37$ mm lens. A minimum limiting energy of 14 nJ was observed for the 10 -mm sample, and 32 nJ for the 3 -mm sample. The limiting energies when focused on the rear surface are similar for both samples. The data for the $f = 75$ mm lens showed a similar response but with limiting energies between 3 and 5 times greater. For each position ΔZ , the device transmittance was measured for increasing energy until the front surface was damaged.

It is useful to define the dynamic range (DR) of the limiter as the ratio of E_D to E_L . Single-shot damage occurred at a wide range of fluences attributed to variations in surface quality, as the general condition of the surfaces was poor. Assuming that a well prepared surface would give a constant damage fluence (or irradiance), we can show the variation of the DR with ΔZ by using the fact that E_D is directly proportional to the beam area on the front surface of the sample. In Figure 3(b) we show this version of the dynamic range plotted versus ΔZ for the 10 -mm-thick sample and 37 -mm focal-length lens. This shows that the optimum condition for a large DR is when the focus is as far into the sample as possible (i.e., in this case on the rear face of the sample). Using a previously measured damage threshold, we estimate that with carefully prepared surfaces the maximum dynamic range would be $>10^4$. The dynamic range was also measured for the 3 -mm-thick sample with the same lens and the 10 -mm-thick sample with a 75 -mm focal-length lens. The behavior was similar for all configurations. However, the absolute value of the DR was found to be strongly dependent on the configuration. The 3 -mm sample gave a maximum DR that was a factor of 20 smaller than for the 10 -mm sample with the same lens. The f -number used is an even more important factor in determining the DR. The maximum DR for the 10 -mm sample with a 75 -mm focusing lens was almost 10^2 smaller than for the 37 -mm lens with the same sample.

These results allowed us to conclude that tight focusing and longer sample lengths are clearly advantageous in a low-energy, large-dynamic-range limiter. On the basis of this, we have designed and constructed a monolithic optical power limiter (MONOPOL). This device was fabricated from a single piece of semiconductor with spherically polished ends, so that a collimated input beam focuses inside the medium and is recollimated on leaving it for low input. In choosing this design, we have optimized the dynamic range of the device for the given f -number, in that the front surface is as far from the beam waist as is possible.

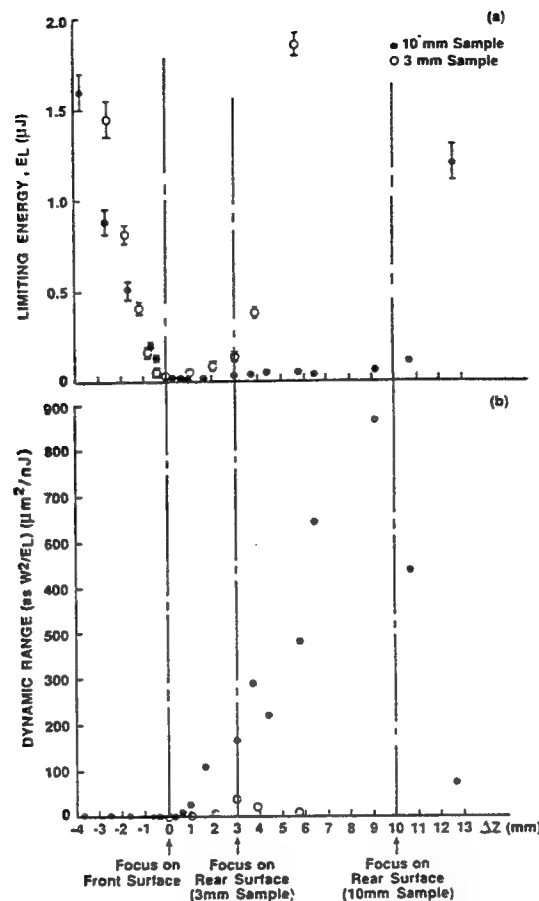


Fig. 3(a). Plot of limiting energy versus position of beam waist relative to the front surface of the sample ΔZ . (b) Dynamic range, plotted as w^2/E_L , where w is the spot size on the front surface of the sample. The true dynamic range (E_D/E_L) is approximately 1.3 times this number.

The MONOPOL was fabricated from chemical-vapor-deposition-grown polycrystalline ZnSe. The ZnSe device had a length of 32 mm and diameter of 12 mm. The performance was determined by placing it in the path of the beam. A further 100-mm focal-length lens was placed at the output of the limiter to focus the output onto a pinhole detector arrangement as in the previous experiments. In this case, the low-energy (1-nJ) pinhole transmittance was ≈ 65 percent. Thus we are monitoring primarily the output fluence. The limiting input energy, E_L , is 10 nJ, which is within a factor of 2 of the predicted scaling. We have calculated the DR of the ZnSe MONOPOL to be $\approx 5 \times 10^5$, using a conservative estimate for the surface-damage threshold of $\approx 10 \text{ GW/cm}^2$. The device was not tested to destruction, but it was successfully tested up to input energies of 100 μJ , so that a minimum DR of $>10^4$ may be confidently stated for 20-psec pulses. From the input energy where the input-output curve first becomes horizontal, up to the maximum

tested energy, the transmitted on-axis fluence changed by only a factor of 3. This corresponds to an average slope $dE_T/dE_{in} \approx 3 \times 10^{-4}$. The maximum energy transmitted was 3 nJ, while the low energy transmittance was 10 percent.

4. SPATIAL AND TEMPORAL RESPONSE

The spatial distribution of the transmitted fluence was measured for a number of different input energies using a vidicon. The vidicon was placed ≈ 2.8 m behind the ZnSe device (toward the far field) we see the fluence-limiting characteristics of Figure 4(b). Here the temporally integrated spatial energy distribution is shown as a function of position for input energies from 13 nJ to 61 μ J. For the data shown, no filters were changed in front of the vidicon. As the input energy is increased, the energy simply gets spread out in space, limiting the fluence and thus protecting the sensitive vidicon photocathode. If we look just at the on-axis portion of this light through a 0.4 mm aperture, we get the input-output characteristics shown in Figure 4 (a).

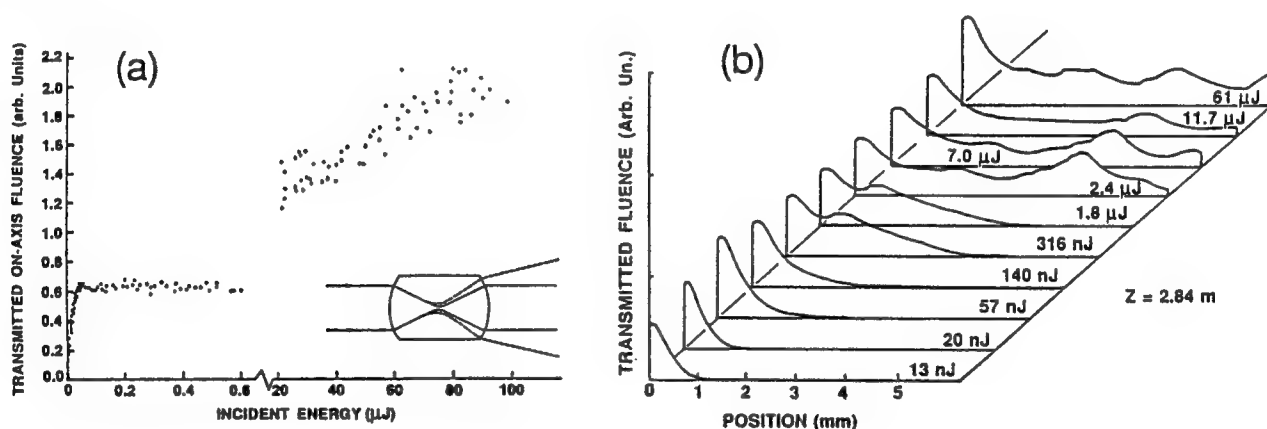


Fig. 4. (a) Input-output characteristic for the ZnSe MONOPOL (note change of scale). The transmittance changes by a factor of 3 between the turnover energy and the maximum tested energy. Inset: Schematic of the MONOPOL. The beam focuses in the center. (b) Transmitted fluence at 2.8m behind the ZnSe monolithic limiter as detected by a vidicon as a function of position at various input energies.

Sending the pulse through the limiter onto the entrance slit of a 2-psec-resolution streak camera allows us to look at the spatial and temporal energy distribution simultaneously on the vidicon screen. What we see at low inputs, shown in Figure 5 (a), is the Gaussian spatial distribution and a nearly Gaussian distribution in time. At higher input, Figure 5(b), as the pulse develops, the energy spreads out in space into two wings. This is clearly advantageous from the standpoint of protecting optical components.

5. SCALING RULES

The effect of nonlinear beam distortion inside the nonlinear medium itself makes a detailed theoretical analysis of self-protecting thick limiters difficult. No analytical solution of the nonlinear wave equation is known for this problem, and a numerical solution is extremely complicated. For these reasons, we have made some relatively simple approximations which allow us to predict how thick limiters will behave for longer pulsewidths, how will they work at other wavelengths, and how well other direct-gap semiconductors with smaller bandgaps will work as limiters in the infrared.

In what follows, we assume that at the limiting threshold, the beam is not strongly distorted by nonlinear effects, and that the beam is therefore still essentially a Gaussian in the region of the focus. The limiting in the far field is thus caused by only a nonlinear phase distortion $\Delta\phi$, in this focal region. We assume that at the limiting threshold, the nonlinearly induced phase change Δn_L caused by a refractive index change Δn is $\Delta\phi \simeq 2\pi$. Since $\Delta\phi = 2\pi \Delta n L_{\text{eff}} / \lambda$, this gives $\Delta n_L \simeq \lambda / L_{\text{eff}}$. Now for a thick limiter, the effective interaction length, L_{eff} , is that length over which the beam remains intense. Thus, $L_{\text{eff}} \propto z_0$, where z_0 is the confocal beam parameter, $\pi w_0^2 / \lambda$, where w_0 is the $1/e^2$ beam radius at the beam waist, this leads to $\Delta n_L \propto \lambda^2 / w_0^2$.

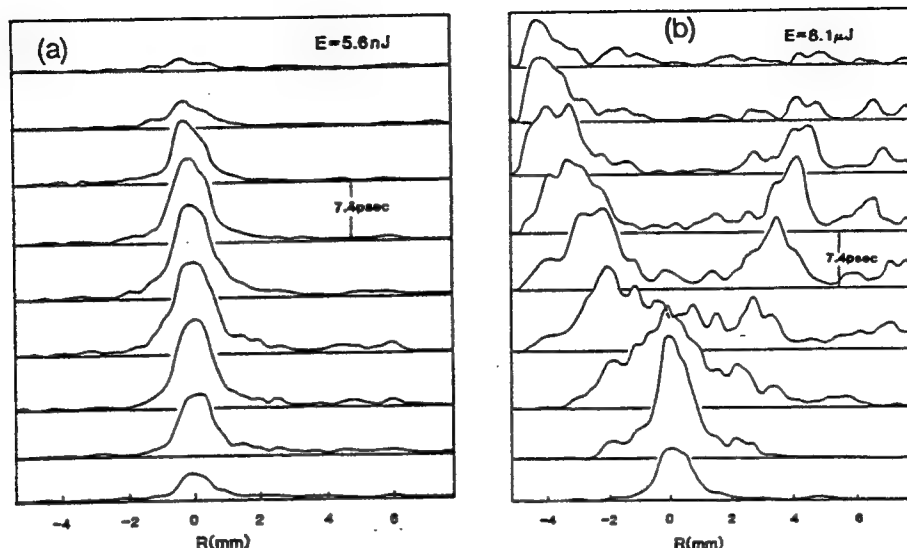


Fig. 5. (a) Spatial energy distribution at 2.8m behind the ZnSe monolithic limiter at various times as detected by a streak-camera-vidicon system for an input energy of 5.6 nJ. (b) Same as (a) for an input energy of 8.1 μ J.

The refractive index change, Δn , is in proportion to the number of photo-generated carriers, N . This has been shown to be true [3] at least in the case of low to moderate carrier densities, which is appropriate for the modelling of the onset of limiting. We have used two models for this nonlinear refraction, the "plasma generation" model of Auston et al. [11] and a slightly more sophisticated band filling or "Moss-Burstein shift" first proposed by Moss [12] and later developed by Miller et al [3]. Both give remarkably similar results so we shall concentrate on Auston's model for the purpose of demonstration. This yields

$$\Delta n \propto N \frac{E_g}{(\hbar\omega)^2} \frac{1}{1 - (\hbar\omega/E_g)^2} \quad (1)$$

where E_g is the semiconductor energy gap, and material independent and frequency independent constants have been incorporated into the constant of proportionality for simplicity. The carrier density is given by

$$N(t) = \frac{\beta_2}{2\hbar\omega} \exp(-t/\tau_R) \int_{-\infty}^t I^2(t') \exp(t'/\tau_R) dt' = \frac{\beta_2}{\hbar\omega} G(I, \tau_R) \quad (2)$$

where we have used $G(I, \tau_R)$ to represent a (frequency independent) carrier generation function, τ_R is the carrier recombination time and β_2 is the two photon absorption coefficient, $\beta_2 \propto F_2(2\hbar\omega/E_g)/E_g^3$ and $F_2(x) = (x-1)^{3/2}/x^5$. These two-photon absorption relationships have previously been experimentally verified. [2]

Combining the above relations gives:

$$\Delta n(t) \propto G(I, \tau_R) \frac{E_g}{(\hbar\omega)^8} \frac{(2\hbar\omega/E_g - 1)^{3/2}}{1 - (\hbar\omega/E_g)^2} \quad (3)$$

This is shown as a function of photon energy for the semiconductor ZnSe ($E_g = 2.67$ eV) in Figure 6 below.

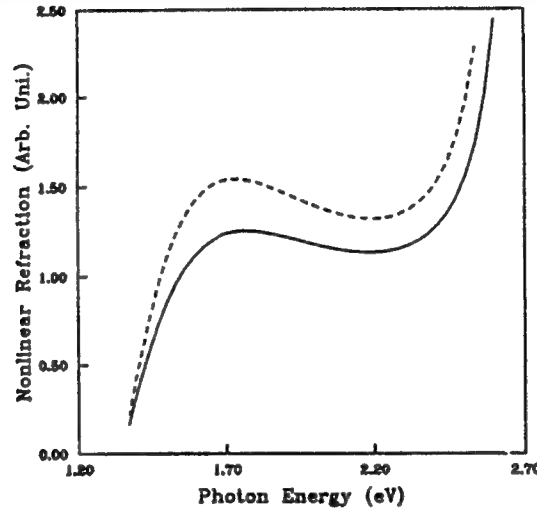


Fig. 6. Nonlinear refraction by two-photon excited carriers, calculated by Auston model (dotted line) and by Moss-Burstein shift (solid line).

Remarkably, this somewhat complicated function gives an extremely flat response in the region of 2PA ($E_g < 2\hbar\omega < 2E_g$). This is as expected, since above the two-photon resonance the efficiency of 2PA starts to decrease, while the excited carrier refractive index increases with frequency. The result is a flat response and Δn varies by less than $\pm 25\%$ in the range $0.57 < (\hbar\omega/E_g) < 0.94$, corresponding to $500 < \lambda < 810$ nm for ZnSe. For shorter wavelengths, Δn becomes very large as the bandgap resonance is approached, but here the linear absorption is also large, so that there is no application for power limiting in that wavelength region.

We may use the above result to simplify our scaling to other semiconductor/wavelength combinations. If we make the reasonable assumption that the limiter will be operated in the "flat" region defined above, then we can remove all terms in $(\hbar\omega/E_g)$ from the formula for Δn given in equation 3. Thus,

$$\Delta n(t) \propto G(I, \tau_R) \frac{1}{(\hbar\omega)^7} \propto G(I, \tau_R) E_g^{-7}, \quad (4)$$

since we always choose a suitable semiconductor bandgap for the particular optical frequency, ω , and within the operating range $\hbar\omega/E_g$ acts as a constant. Now $\Delta n_L \propto \lambda^2/w_0^2$ so that $G_L(I, \tau_R) \propto E_g^{-7} \lambda^2/w_0^2$, where G_L is the value of the carrier generation function at limiting. However, $\lambda \propto (\hbar\omega)^{-1} \propto E_g^{-1}$ in our case, giving, $G_L \propto E_g^{-5} w_0^{-2}$. The calculation of the carrier generation function is simplified in two limits. (i) $\tau_R \gg \tau_p$, where τ_p is the pulsewidth, i.e., the short pulse limit, and (ii) $\tau_R \ll \tau_p$, the long pulse limit. For the short pulse limit, we can ignore recombination, and $G_L(t \rightarrow \infty) \propto I_L^2 \tau_p$, where I_L is the peak limiting irradiance which can now be given by

$$I_L \propto \frac{(E_g)^{5/2}}{w_0 \sqrt{\tau_p}}, \quad (5a)$$

and thus, the limiting energy is determined by

$$E_L \propto (E_g)^{5/2} w_0 \sqrt{\tau_p} . \quad (5b)$$

Note that for longer pulses, carrier generation is more efficient and I_L decreases, however, E_L increases as the square root of the pulsewidth. In the long pulse limit, the performance is expected to be degraded by the effects of carrier recombination. In this case, $G(t) \propto I^2(t)\tau_R$, so that the peak limiting irradiance and energy are

$$I_L \propto \frac{(E_g)^{5/2}}{w_0 \sqrt{\tau_R}} , \quad (6a)$$

and

$$E_L \propto (E_g)^{5/2} w_0 \frac{\tau_p}{\sqrt{\tau_R}} . \quad (6b)$$

Note that performance is reduced from the short pulse limit by a factor of $(\tau_p / \tau_R)^{1/2}$. Otherwise, the scaling is identical.

Clearly then, narrow-gap semiconductor limiters should work in the infrared much better than the ZnSe visible limiter we tested. There is, however, one further restriction in that the focused spot size for any given f -number optics is proportional to λ , i.e., $w_0 \propto E_g^{-1}$. Thus, in the case of diffraction-limited focusing we have

$$E_L \propto (E_g)^{3/2} \sqrt{\tau_p} \quad (\text{short pulse limit}) , \quad (7)$$

and

$$E_L \propto (E_g)^{3/2} \frac{\tau_p}{\sqrt{\tau_R}} \quad (\text{long pulse limit}) . \quad (8)$$

6. COMPARISON OF SCALING RULES WITH NANOSECOND AND INFRARED DATA

In addition to ZnSe with 532 nm picosecond pulses, a number of other limiting experiments have been performed. In this section, we will compare our results of limiting in ZnSe with longer pulses, and with other materials at appropriately longer wavelengths.

First, the ZnS monolithic limiter was tested using 532 nm picosecond pulses. Applying equation (4), our scaling rules indicate that the limiting energy should be a factor of $[E_g(\text{ZnS})/E_g(\text{ZnSe})]^7$ larger than E_L for ZnSe, as in this case the wavelengths are the same. This gives a factor of 9.1, indicating an E_L of 91 nJ. In fact, the measured limiting energy for the ZnS monolithic limiter was 120 nJ, in reasonable agreement with the calculation.

Limiting experiments were also performed in a 10mm thick sample of ZnSe with nanosecond pulses of 532 nm light. The limiting energy is shown in Figure 7 as a function of position of the beam waist along z .

Comparing with the psec results when the waist is in the middle of the sample, we see that the nanosecond pulses produce a limiting energy of $2 \mu\text{J}$, as opposed to 40 nJ for psec pulses. The appropriate equation for the picosecond data is (5b), whereas for the nanosecond data the long pulse approximation, equation (6b), is more appropriate. Substituting for τ_p , w_0 in each of these equations, and assuming a 1 ns recombination time, we estimate $E_L (\text{nsec}) \approx 40E_L (\text{psec}) \approx 1.6 \mu\text{J}$, again in good agreement. We estimate the 1 nsec recombination time from our degenerate four wave mixing experiment.

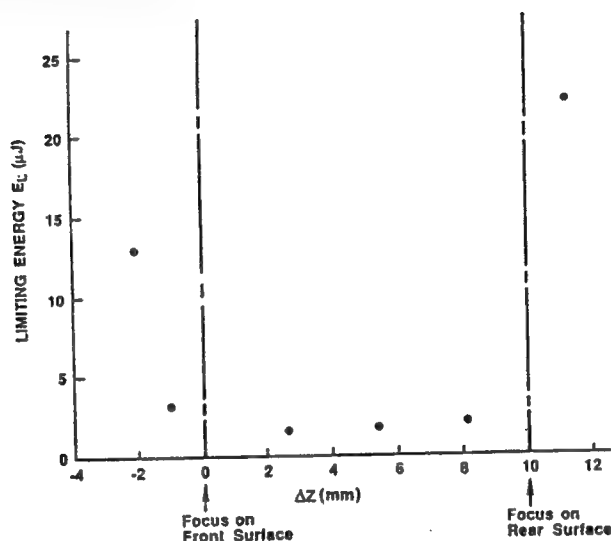


Fig. 7. Limiting energy as a function of waist position inside a 10 mm thick ZnSe polycrystalline sample. $\lambda = 532 \text{ nm}$, $\tau_p = 20 \text{ ns}$ (FWHM) and $w_0 = 3.2 \mu\text{m}$.

Limiting at $1.06 \mu\text{m}$ with picosecond pulses was also observed in CdTe (see Figure 8). This sample was 3 mm thick, so we compare our data with the data obtained in thick ZnSe . To make this comparison, we apply equation (5b) as the short pulse limit is valid for both cases. Accounting for the different spot sizes, pulsewidths and energy gaps, the predicted limiting energy in CdTe is 27 nJ , whereas we measured $E_L \approx 35 \text{ nJ}$, again in very close agreement.

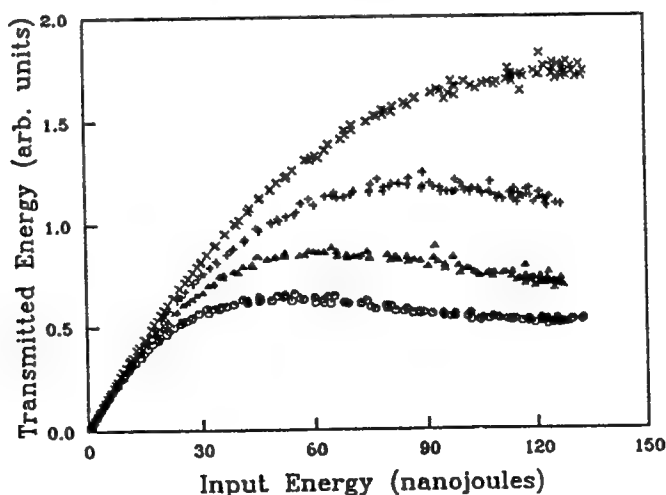


Fig. 8. Limiting curves for CdTe with 45 ps (FWHM) pulses of $1.06 \mu\text{m}$ light and a spot size $w_0 \approx 11 \mu\text{m}$. $\circ - \Delta Z = 0$; $\Delta - \Delta Z = 0.73 \text{ mm}$; $+- \Delta Z = 1.27 \text{ mm}$; $\times - \Delta Z = 1.82 \text{ mm}$.

In Figure 9, we show limiting curves for InSb with 10.6 μm wavelength light from a CO_2 laser. This experiment involved a rather different experimental configuration than the previous data. The spot size was 60 μm and the sample length was 1mm, so that the limiter was not truly "thick". The observed limiting energy, using an aperture in the beam to detect on axis fluence, was 4 μJ with a 170 ns (HW1/eM) pulsewidth. It was decided to compare this with the nanosecond ZnSe data, as both results are in the same long pulse limit, and equation (6b) applies to both cases. However, scaling was difficult to do in this case, as the limiter was not thick, and there were difficulties in predicting the recombination time, which is almost certainly carrier-density dependent. Using a best-guess of ≈ 5 ns for the recombination time, and $L/L_{\text{eff}} \approx 4$, we obtain a scaled E_L of 0.6 μJ , considerably smaller than the 4 μJ observed. Although this result is probably good to within one order of magnitude, the uncertainties make the scaling unreliable in this case. It is worth noting that we are extrapolating both the 2PA coefficient and the nonlinear refraction over three orders of magnitude, while assuming that there is no excited state absorption, to obtain this result.

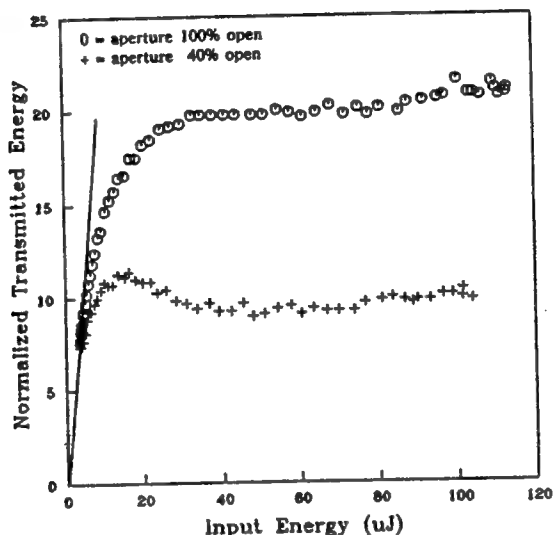


Fig. 9. Input-Output curves for 1mm thick InSb at room temperature, with 10.6 μm radiation.

7. CONCLUSION

We have built and characterized limiters for the visible which exhibit very low limiting energies. Limiting energies (powers) as low as 10 nJ (300 Watts) for picosecond pulses and 2 μJ (80 Watts) for nanosecond pulses have been measured. We have shown how theory predicts that these limiters should be very broad band, and should work better (i.e. lower threshold) using narrow gap semiconductors in the infrared. We have developed simple scaling rules to predict performance at longer wavelengths in appropriate narrow gap semiconductors, and for longer pulses. Initial experiments have verified these scaling rules.

8. ACKNOWLEDGEMENTS

The authors wish to acknowledge the support of DARPA/CNVEO, the Florida High Technology and Industrial Council and the National Science Foundation grant ECS #8617066.

9. REFERENCES

1. S.A. Akhmanov, R.V. Khokholov and A.P. Sukhorukov, "Self-focusing, self-defocusing, and self-modulation of laser beams" in *laser Handbook*, F.T. Arecchi and E.O. Schulz-Dubois eds. (North-Holland, Amsterdam, 1972) Vol. 2, pp. 1151-1228.

2. E.W. Van Stryland, H. Vanherzeele, M.A. Woodall, M.J. Soileau, A.L. Smirl, S. Guha and T. F. Boggess, *Opt. Eng.* **24**, 613 (1985).
3. D.A.B. Miller, C.T. Seaton, M.E. Prise and S.D. Smith, *Phys. Rev. Lett.* **47**, 197 (1981)
4. J.E. Geusic, S. Singh, D.W. Tipping, and T.C. Rich, *Phys. Rev. Lett.* **19**, 1126 (1969)
5. T.F. Boggess, S.C. Moss, I.W. Boyd, and A.L. Smirl, *Opt. Lett.* **9**, 291 (1984)
6. J.M. Ralston and K.R. Chang, *Appl. Phys. Lett.* **15**, 164 (1969).
7. A.C. Walker, A.K. Kar, Wei Ji, U. Keller, and S.D. Smith, *Appl. Phys. Lett.* **48**, 683 (1986).
8. T.F. Boggess, A.L. Smirl, S.C. Moss, I.W. Boyd, and E.W. Van Stryland, *IEEE J. Quantum Electron.* **QE-21**, 488 (1985).
9. D.J. Hagan, E.W. Van Stryland, M.J. Soileau, and Y.Y. Wu, *Opt. Lett.* **13**, 315 (1988).
10. E.W. Van Stryland, *Opt. Commun.* **31**, 93 (1979).
11. D.H. Auston, S. McAfee, C.V. Shank, E.P. Ippen, and O. Teschke, *Solid State Electron.* **21**, 147 (1978).
12. T.S. Moss, *Phys. Stat. Sol. B* **101**, 555 (1980).

OPTICAL LIMITING IN MEDIA WITH ABSORBING MICROPARTICLES

Kamjou Mansour, E.W. Van Stryland and M.J. Soileau

Center for Research in Electro-Optics & Lasers (CREOL)
University of Central Florida
12424 Research Parkway, Orlando, FL 32826

ABSTRACT

We have characterized the nonlinearities observed in suspensions of carbon black particles in liquids (CBS). We have developed a preliminary explanation of the optical limiting characteristic of the CBS that qualitatively explains the low thresholds, broad-band response and other limiting characteristics. In this model, the microscopic carbon particles are heated by linear absorption to a temperature at which a plasma can be created by the optical field. These microplasmas rapidly expand, thus scattering the incident light and limiting the transmittance. This model is consistent with our observations that nonlinear scattering dominates transmission losses. We find that limiting depends on the input fluence (J/cm^2) rather than irradiance (W/cm^2). Therefore, limiting works well (i.e., low limiting energy) for long pulses (≥ 10 nsec) but is less effective for short pulses (\approx psec). In addition, the CBS rapidly degrades with repetitive laser firings, thus, flowing or moving the liquid between firings is necessary.

1. INTRODUCTION

Recently there has been a growing interest in the use of microparticle suspensions as nonlinear media. Most of the reported literature on microparticle suspensions, artificial Kerr medium and micro-emulsions which are formed from nonabsorbing microparticles, is on nonlinear refraction.[1,2,3] Here, we demonstrate and review the dynamics of limiting in a suspension of absorbing microparticles that exhibit primarily nonlinear scattering and nonlinear absorption. The absorbing microparticles of interest are carbon black particles which are ≈ 35 nm in diameter with agglomerates up to 500 nm in diameter. We demonstrate an optical limiting threshold as low as 80 watts peak power for $0.532 \mu\text{m}$ and 160 Watts for $1.06 \mu\text{m}$ using pulses of 14 nsec and 20 nsec (FWHM), respectively.

Limiting is effective for five orders of magnitude above the threshold value. This large dynamic range is defined by the eventual damage of the glass cell containing the CBS. Because of the structure of these dispersions, different mechanisms including nonlinear absorption, nonlinear refraction (self-focusing, self-defocusing), nonlinear scattering and combinations of these mechanisms could be the source of the optical nonlinearity leading to such a low optical limiting threshold. In order to investigate the relative contributions of these mechanisms we perform a series of experiments. We first perform optical limiting experiments in the CBS at $0.532 \mu\text{m}$ and $1.06 \mu\text{m}$ for nanosecond pulses. We present transmission measurements which directly show the fluence dependence of limiting in CBS. We also perform a measurement that monitors the absorbance, transmittance and fraction of side scattered light simultaneously. In essence, as will be demonstrated, we are performing a laser-induced-damage experiment on a material with an extremely low damage threshold. This leads us to discuss and show the repetition rate dependence of the CBS. We then examine the contribution of nonlinear refraction to limiting in CBS. At the end we present a simple model that qualitatively explains all of our experimental results.

2. OPTICAL LIMITING

Passive optical limiting utilizing nonlinearities in a variety of materials including gases, liquids, semiconductors and liquid crystals has been demonstrated.[4,5,6,7] However, in any of these materials, all

of the criteria needed for a good optical limiter have not been satisfied. These criteria are high transmittance for low inputs, broad-band frequency response, fast switching time (ns or shorter), and low input requirements for the onset of switching. The device should also be resistant to optical damage (i.e., self-protecting). Here we show that a suspension of carbon black particles (CBS) meet the above criteria. We also present a model which qualitatively explains all the data taken on CBS.

The optical geometry often used as a screening test, as it is sensitive to both nonlinear absorption and nonlinear refraction, is shown in Figure 1. We used this arrangement with pulses from an Nd:YAG laser operated in the TEM₀₀ mode of 14 ns (FWHM) duration at 0.532 μm and 20 ns at 1.064 μm . These pulses were focused by either a 40mm (532nm) or 50mm (1064nm) "best form" lens, shown as L₁. This results in calculated beam radii of 3.5 μm at a wavelength of 532 nm and 7 μm at 1064 nm inside the 1 cm cuvette. The spot radii quoted in this paper are half-widths at the 1/e² maximum in irradiance. The transmitted pulse was then collected by a 102 mm focal length "best form" lens L₂ placed behind the sample. The laser beam then passed through a 400 μm aperture placed in front of a silicon photodiode. This system had an overall low input transmittance of 70 percent for both wavelengths.

Using this optical geometry we have looked at optical limiting in various concentrations of CBS and a known standard sample CS₂, which has been previously used as an optical limiting material [5]. Optical limiting in CS₂ is primarily due to molecular reorientation of the molecules although a small contribution from electrostriction may be present for nanosecond pulses and tight focusing geometries. The optical limiting of CBS and CS₂ in a 1 cm thick cuvette is shown in Figure 2, for nanosecond laser pulses at 0.532 μm . In order to resolve the onset of limiting, the measurement was performed for lower input powers as shown in Figure 3. The CBS begins clamping the transmitted fluence above approximately 80 watts input power and continues clamping for ≈ 5 orders of magnitude of increased input power. The limiting of the CBS at 1.064 μm is shown in Figure 4 and Figure 5. As is shown, the onset of limiting for 1.064 μm laser pulses is approximately 160 watts.

The onset of limiting occurs approximately two orders of magnitude before that of CS₂ for ns pulses. However, for 0.532 μm laser pulses with a pulse duration of 30 ps (FWHM), the CS₂ limiting occurs for input powers lower than that of CBS. This is shown in Figure 6. The laser used is a passively mode-locked Nd:YAG laser with a single pulse switched out. The CBS limits the input light for ps laser pulses at a peak power in excess of 30 kw at 0.532 μm as shown in Figure 7. The limiting energy of 1.1 μJ obtained with picosecond pulses is approximately the same as the 1.2 μJ limiting energy for nanosecond pulses using the same focusing geometry. It has been demonstrated earlier that the optical limiting for picosecond laser pulses in CS₂ is due to molecular reorientation (Kerr effect) and is a power dependent phenomenon. However, as we see here and will further demonstrate, the limiting in CBS is fluence dependent, i.e. the onset of limiting for both nanosecond and picosecond measurements occurs approximately at the same fluence.

The observed optical limiting using the geometry shown in Figure 1, could be due to several mechanisms including nonlinear absorption, nonlinear refraction and nonlinear scattering. Below we describe a series of experiments performed to determine the dominant nonlinearity.

3. NONLINEAR TRANSMITTANCE MEASUREMENT

We have studied the fluence dependence of the transmittance of CBS at 0.532 μm and 1.064 μm . The optical geometry used is shown in Figure 8. Both a one meter and 50 centimeter "best form" lens were used to focus the nsec pulsed input beams at the two wavelengths. This resulted in spot sizes of 158 μm and 460 μm for 1.064 μm , and 108 μm and 254 μm for 0.532 μm . The transmitted signal was collected by a large area uniform response Si photodiode located very close to the cell. The diameter of the detector is 1 centimeter and the beam radius at the detector is approximately 1mm in diameter. The difference between this geometry and the optical limiting geometry of Figure 1 is that we are not using tight focusing and the aperture has been removed so that this experiment is insensitive to nonlinear refraction. The results of the

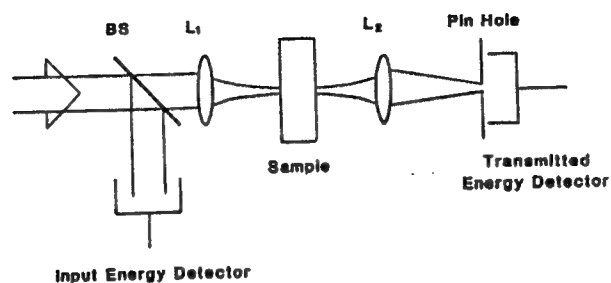


Figure 1. Optical limiting geometry.

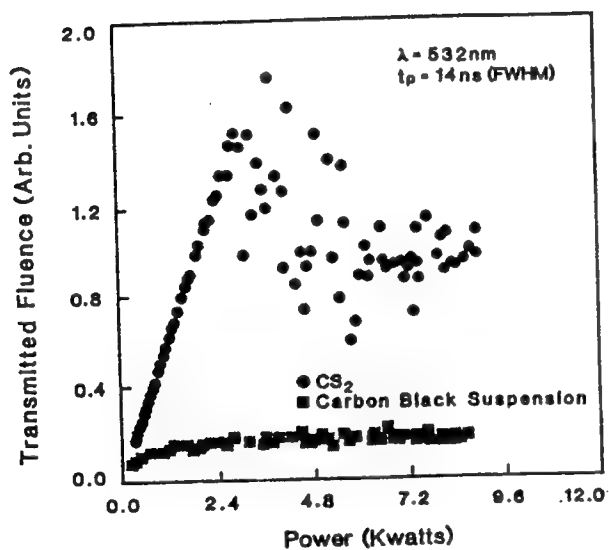


Figure 2. Plot of the limiting of CS_2 (circles) and CBS (squares) as a function of input power for 14 ns (FWHM), $0.532\text{ }\mu\text{m}$ pulses.

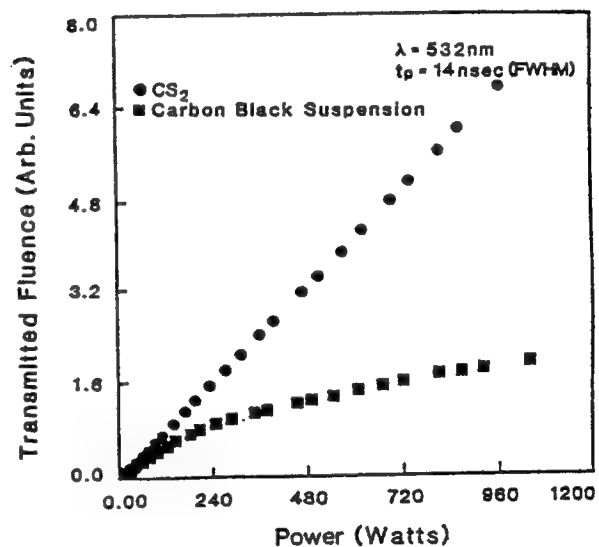


Figure 3. Plot of onset of limiting of CS_2 (circles) and CBS (squares) as a function of input power for 14 ns (FWHM), $0.53\text{ }\mu\text{m}$ pulses.

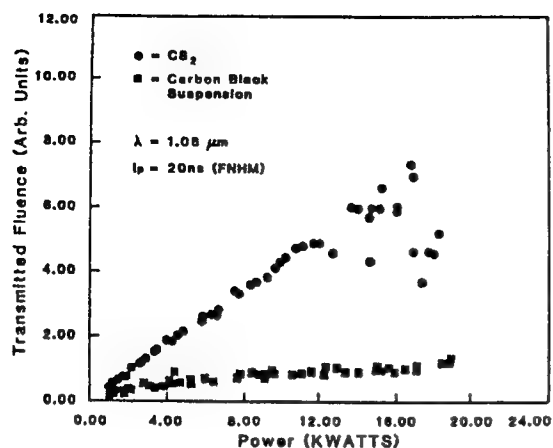


Figure 4. Plot of limiting of CS_2 (circles) and CBS (squares) as a function of input power for 20 ns (FWHM), $1.06 \mu\text{m}$ pulses.

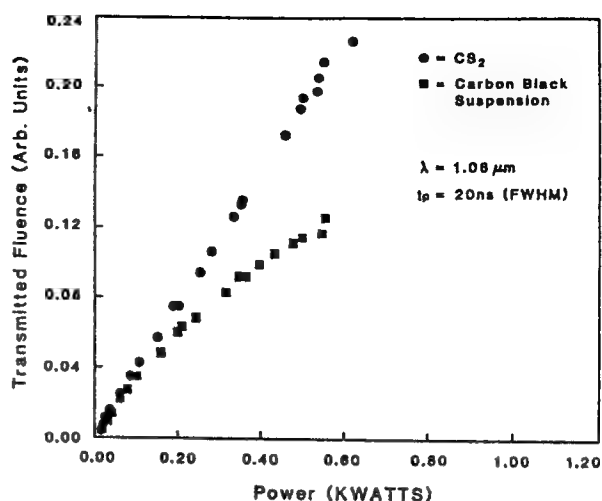


Figure 5. Plot of on set of limiting of CS_2 (circles) and CBS (squares) as a function of input power for 20 ns (FWHM), $1.06 \mu\text{m}$ pulses.

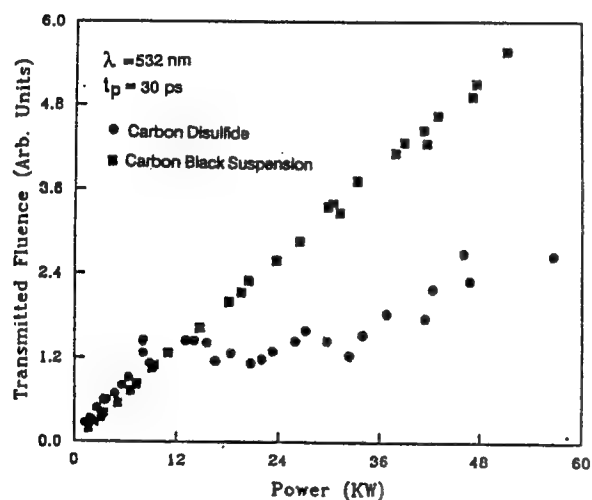


Figure 6. Plot of limiting of CS_2 (circles) and CBS (squares) as a function of input power for 30 psec (FWHM), $0.532 \mu\text{m}$.

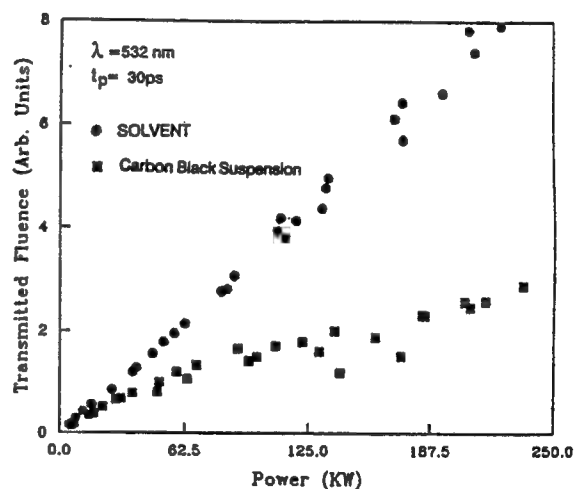


Figure 7. Plot of limiting of solvent (circles) and CBS (squares) as a function of input power for 30 psec (FWHM), $0.532 \mu\text{m}$ pulses.

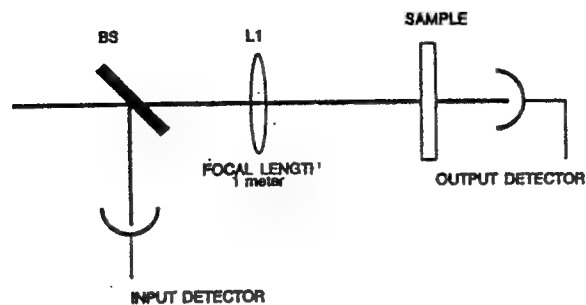


Figure 8. Optical geometry for transmission measurement.

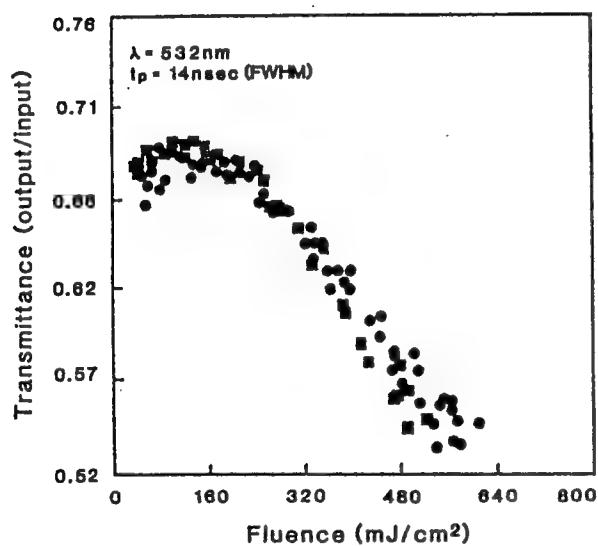


Figure 9. Measured CBS transmittance as a function of incident fluence (mJ/cm^2) for $108\text{ }\mu\text{m}$ (circles) and $254\text{ }\mu\text{m}$ (squares) spot sizes at $0.532\text{ }\mu\text{m}$.

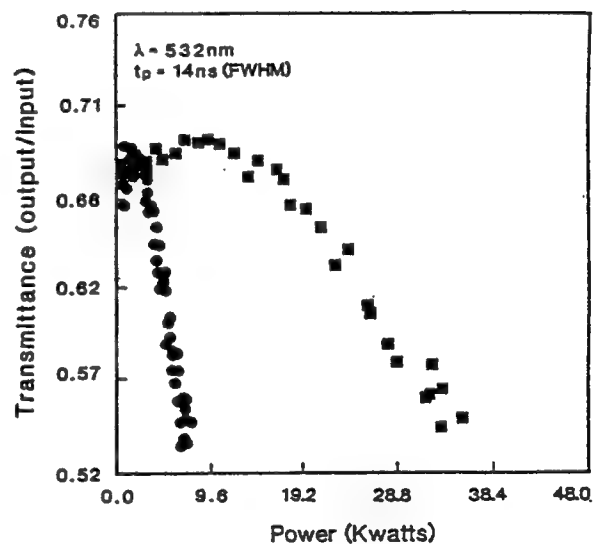


Figure 10. Measured CBS transmittance as a function of incident power (KW) for $108\text{ }\mu\text{m}$ (circles) and $254\text{ }\mu\text{m}$ (squares) spot sizes at $0.532\text{ }\mu\text{m}$.

transmittance measurements are plotted as a function of incident fluence and incident power in Figures 9, 10, 11 and 12 for 0.532 μm and 1.064 μm laser pulses. For incident fluences above 200 mj/cm^2 for 0.532 μm and 350 mj/cm^2 for 1.06 μm , the transmission becomes increasingly nonlinear and is essentially identical for both beam radii at a given wavelength as shown in Figures 9 and 11, respectively. However, the onset of a change in transmittance appears at two different incident power levels for these beam radii as shown in Figure 10 and Figure 12. This again clearly indicates that the nonlinear transmittance observed is fluence dependent.

4. MEASUREMENT OF TRANSMITTANCE, SCATTERING AND ABSORBTANCE

In order to understand the nature of this fluence dependent nonlinear transmittance, we have set up an experiment which enables us to monitor for a single pulse, the absorptance and the fraction of side scattered light simultaneously with the transmittance measurement. This simultaneous measurement was conducted using the Q-switched Nd:YAG laser. The laser light was focused by a 1 meter focal length "best form" lens L_1 into a one centimeter cuvette cell. (See Figure 13) The transmitted light was monitored as previously described. The absorption of the incident light was directly monitored by a sensitive piezoelectric transducer which was placed in contact with the bottom of the cuvette with silicone grease. Photoacoustic measurements have been used to directly detect very small changes in absorption.[8] The side scattered light was collected by a two-inch diameter, 98 mm focal length lens and detected by a Si photodiode. The optical geometry for this measurement is shown in Figure 13.

The results of the simultaneous measurement of absorptance, transmittance, and the fraction of side scattered light (side scattering light divided by incident light) are plotted as a function of incident fluence for 0.532 μm and 1.064 μm laser pulses in Figure 14 and Figure 15, respectively. For very low input fluences the CBS is linear and there is no change in the three quantities monitored. However, for input fluences close to 200 mj/cm^2 for 0.532 μm light and 360 mj/cm^2 for 1.064 μm light, the transmittance begins to decrease nonlinearly as is shown by squares in Figures 12 and 14. The absorptance increases nonlinearly for incident fluence close to this threshold value (i.e., onset of change of transmittance) and levels off at higher values even for input fluences two orders of magnitude above threshold. The scattered fraction increases nonlinearly as the transmittance decreases as shown by circles in Figures 14 and 15. This trend continues for two orders of magnitude above threshold. From these results we see that blocking of the light by the CBS above threshold is primarily due to nonlinear scattering.

5. NONLINEAR SCATTERING

The blocking of the transmission of incident light by scattering can readily be photographed as shown in Figure 16. These pictures were taken by looking at the side window of the cuvette perpendicular to the direction of incident light. For low input fluences, top picture, the bright region in the photograph represents the input pulse which is linearly scattered (Mie scattering) by carbon black particles. However, for incident fluences above 200 mj/cm^2 , the light is nonlinearly scattered to the sides and thus blocks the incident light from being transmitted. This is shown in the lower picture.

The dynamics of the transmittance loss is studied by time resolved transmission measurements conducted using nanosecond pulses. The geometry used is shown in Figure 17. Here, by delaying the transmitted pulse with respect to the input pulse we are able to monitor both the incident and transmitted pulses. This is shown in Figure 18 for below and above threshold. Graph A shows the transmitted signal below threshold. For an incident fluence above 200 mj/cm^2 , there is a sharp cut off in the transmitted pulse as shown in Figure 18, Graph B. Note that the input pulse was attenuated by a factor of 10 using neutral density filters. The transmitted laser pulse is most strongly attenuated during the later portions of the pulse, thus, the pulse appears advanced in time because if no attenuation had occurred the peak would have extended far off scale. This experiment again suggests that the attenuation of the laser beam is produced by a laser-induced-breakdown plasma.

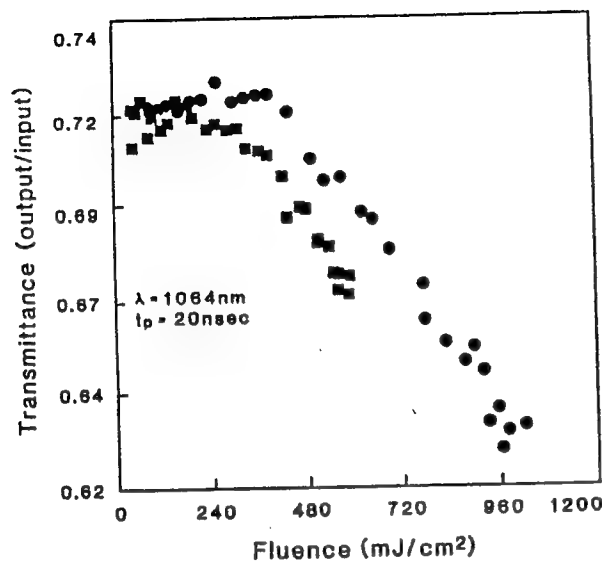


Figure 11. Measured CBS transmittance as a function of incident fluence (mJ/cm^2) for $158 \mu\text{m}$ (circles) and $460 \mu\text{m}$ (squares) spot sizes at $1.06 \mu\text{m}$.

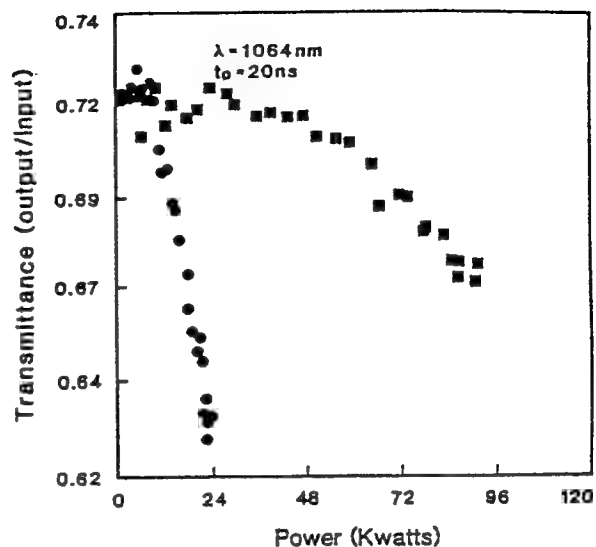


Figure 12. Measured CBS transmittance as a function of incident power (kW) for $158 \mu\text{m}$ (circles) and $460 \mu\text{m}$ (squares) at $1.06 \mu\text{m}$.

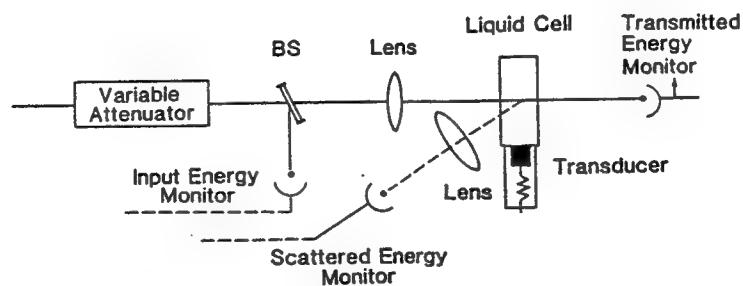


Figure 13. Optical geometry used to monitor the transmittance, absorptance and side scattered light.

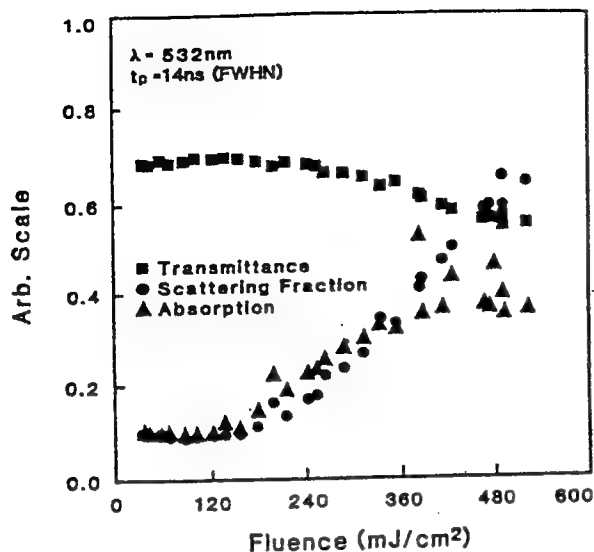


Figure 14. Plot of change of transmittance (squares), absorptance (triangle) and scattering fraction (circles) as a function of incident fluence (mj/cm²) for 0.532 μm, 14 ns pulses.

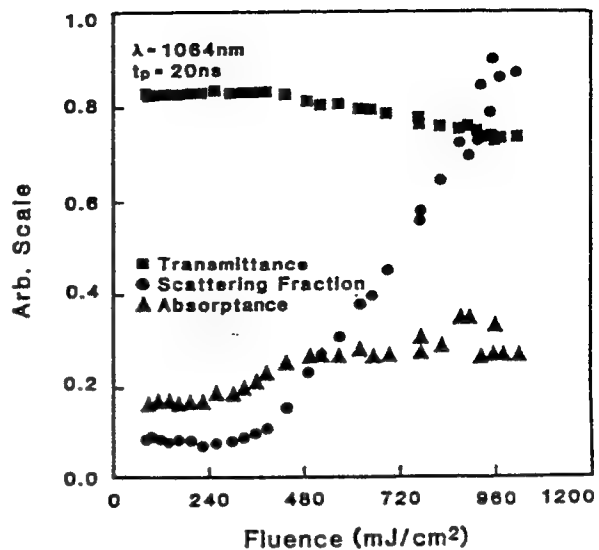
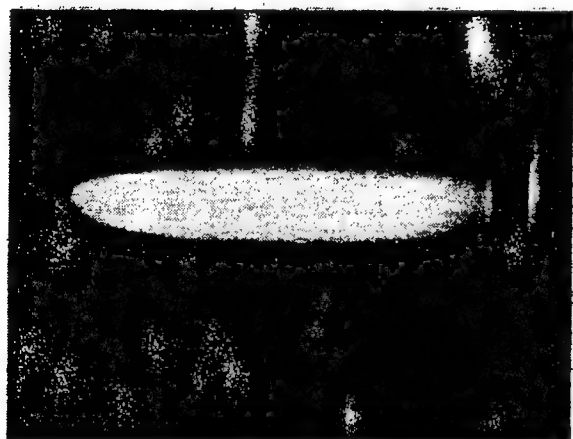


Figure 15. Plot of change of transmittance (squares), absorptance (triangle) and scattering fraction (circles) as a function of incident fluence (mj/cm²) for 1.06 μm, 20 ns pulses.



(A)



(B)

Figure 16. Photographs A and B represent the input pulse which is scattered by CBS for low and high incident fluences respectively.

Under this assumption, the attenuation is dominated by scattering losses of the laser light by the plasma as seen in Figures 14 and 15. Thus, we are performing a laser-induced-damage experiment, and we have prepared a material with an extremely low damage threshold. This is consistent with having high linear absorption by the very small carbon particles (≈ 35 nm), and is also consistent with the disappearance of the nonlinearities after repeated laser irradiation as discussed in the next section.

6. REPETITION RATE DEPENDENCE

Recently, we reported the repetition rate dependence of the CBS.[9] In that report we indicated that the onset of the limiting threshold for 1 and 10 Hz repetition rate laser pulses is considerably different and is higher for the 10 Hz repetition rate. This repetition rate dependence was removed by flowing the material at such a rate that virgin material was exposed to each laser pulse.

This bleaching or reduction of limiting of the laser light in the nonflowing liquid after repeated irradiation on the same region of the sample can be observed by monitoring the transmitted signal and scattered signal at a fixed fluence above the single shot threshold for limiting. Using the geometry shown in Figure 13 and setting the incident fluence at 350 mJ/cm^2 for $0.532 \text{ }\mu\text{m}$ laser pulses and a 1 Hz repetition rate, we can observe that the transmitted signal increases as the number of the incident pulses irradiating the sample increases. Note that using a tight focusing geometry and a 1 Hz repetition rate that we do not see these cumulative effects. The transmittance levels off to a value that is less than the linear transmittance of the solvent as shown in Figure 19. The scattered signal reduces and levels off after repeated laser firings. This is shown as circles in Figure 19. For flowing liquid, stirred liquid or a long elapse time between the laser pulses irradiating the liquid, we have observed that the transmitted signal and scattered signal remain fixed as shown in Figure 20. The maximum limiting capability is for the first laser firing and recovery of the irradiated region of the sample is due to convection in the liquid at room temperature which for the spot size used is a slow process in comparison with the repetition rate of 1 Hz. We also observed that this recovery time is proportional to the radius of the laser beam in the cell, consistent with convection.

The bleaching of CBS also can be monitored as shown in Figure 21 where we have used a very large spot size of more than $254 \text{ }\mu\text{m}$. Here, we have used a HeNe laser beam expanded to illuminate the region close to the front surface of the cell. The scattering of the HeNe beam by the suspended microparticles is readily observable. We irradiated the CBS using an incident fluence of 350 mJ/cm^2 and photographed the scattered light after 10 seconds. This is shown in Figure 22a. The dark spot appearing in the middle of the bright screen is the irradiated region showing that the scattering centers have been "removed" by the laser pulse. Figure 21b shows how this excited volume is slowly replaced by fresh CBS after two minutes due to convection. The conjecture is that the microparticles have been considerably reduced in size or "atomized" so that they no longer efficiently scatter the HeNe light.

7. NONLINEAR REFRACTION

In order to investigate contributions of phase distortion due to a thermo-optic effect, electrostriction, or other nonlinear refractive mechanism, we monitored the far field profile of the transmitted beam using a vidicon tube with an optical multichannel analyzer. For incident fluences below threshold and up to an order of magnitude higher than threshold, we have not observed any broadening of the spatial profile of the transmitted beam. Therefore, the change in index of refraction of the CBS is very small and the phase distortion due to this index change is less than 0.2λ which is the sensitivity of our detection system. From this measurement we conclude that the contribution of nonlinear refraction is small in comparison with the nonlinear scattering observed. In order to further validate this point we removed the aperture in the original limiting geometry shown in Figure 1 and observed no change in limiting threshold.

8. MODEL

It appears from our experimental results that the dominant mechanism in the CBS is nonlinear scattering.

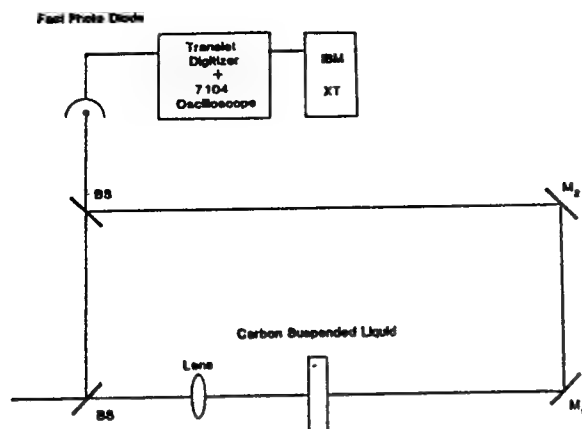


Figure 17. Optical geometry for time resolved transmission measurement for ns pulses.

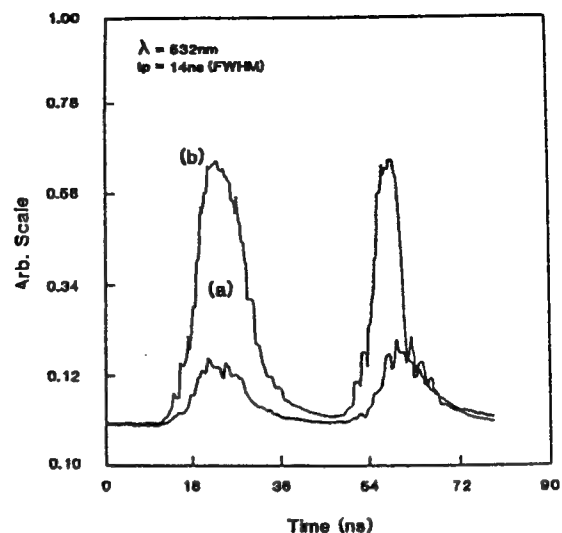


Figure 18. Photographs A and B represent the incident and transmitted pulse for fluence levels below and above the threshold.

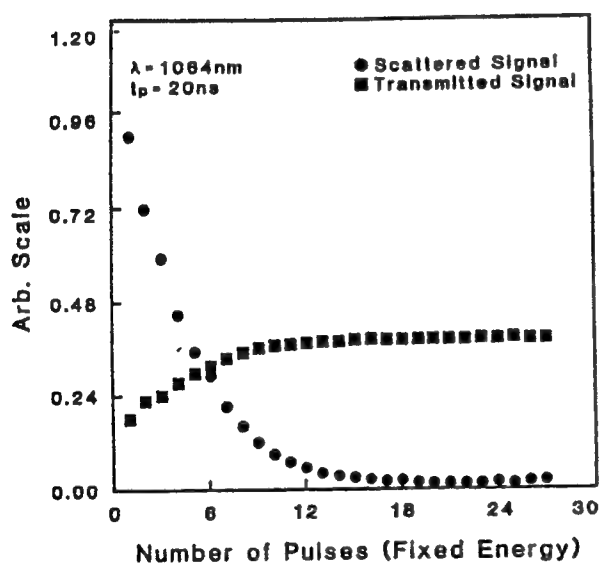


Figure 19. Plot of fraction of scattered light (circles) and transmittance (squares) as a function of the number consecutive laser pulses for 1.06 μm , 20 ns pulses at a fluence of 450 mJ/cm^2 .

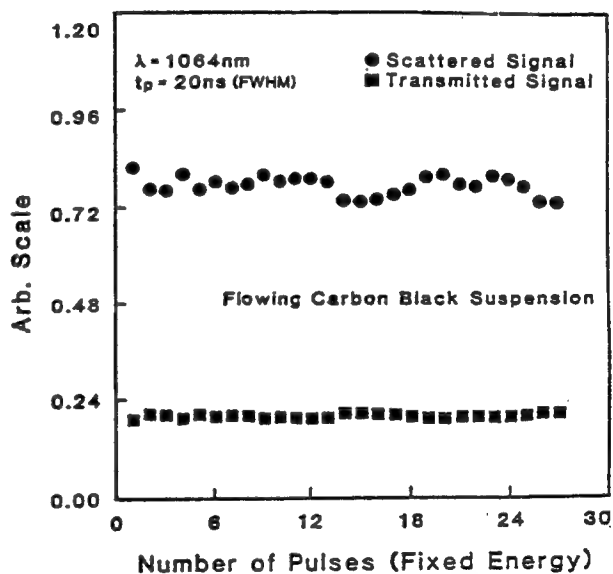


Figure 20. Plot of fraction of scattered light (circles) and transmittance (squares) in flowing CBS as a function of the number of consecutive laser pulses for 1.06 μm , 20 ns pulses at a fluence of 450 mJ/cm^2 .

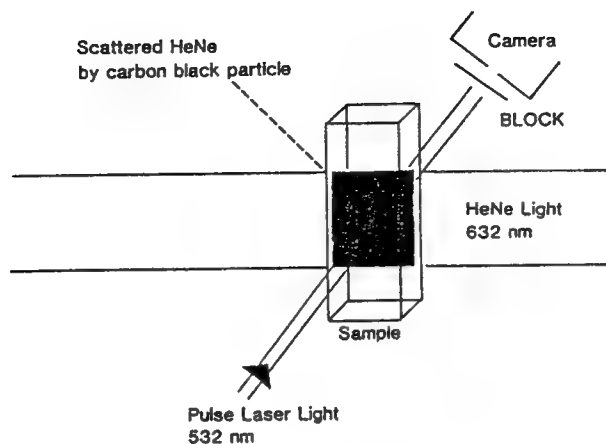
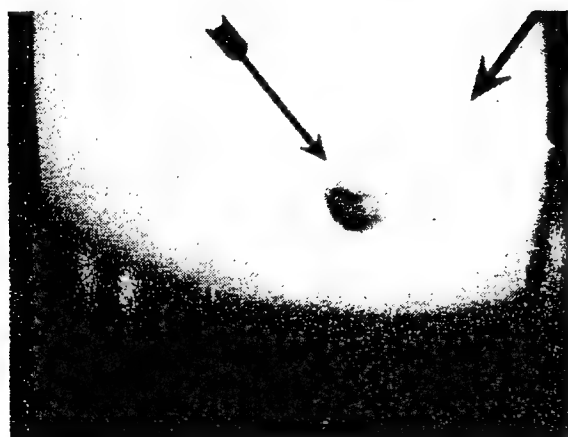


Figure 21. Optical geometry to monitor "bleaching" of carbon particles in CBS.



(A)



(B)

Figure 22. Photographs A and B represent the "bleaching" of carbon particles within the irradiated region and replacement of the irradiated region with fresh liquid, respectively.

The nature of this nonlinear scattering is consistent with the formation of microplasmas by laser-induced-breakdown of the carbon particles. Therefore, the dynamics of limiting in CBS can be described by a simple model. The carbon linearly absorbs the incident light very efficiently. The carbon is rapidly heated to several thousand degrees Celcius. A simple calculation of the particle temperature at threshold gives a few thousand degrees Celcius. The carbon then vaporizes and ionizes to form a rapidly expanding microplasma which absorbs and scatters later portions of the laser light and blocks the transmission. This model is also consistent with the disappearance of the nonlinearities after repeated laser firings as the carbon particles will have undergone vaporization.

9. CONCLUSION

We have characterized the nonlinearities observed in a suspension of carbon black particles (CBS) in liquids. We have developed a qualitative model based on laser-induced breakdown to explain the low limiting threshold of the CBS. From our results, we conclude that nonlinear scattering due to rapidly expanding microplasmas is the dominate mechanism leading to limiting. The broad-band nature of the nonlinearity is primarily due to the fact that carbon is black and heavily absorbing over a broad range of frequencies. We have demonstrated this limiting at 1 and 0.5 μm .

10. ACKNOWLEDGEMENTS

This research was supported with funds from the DARPA/CNVEO and the Florida High Technology and Industry Council.

11. REFERENCES

1. A. Jay Palmer, Optics Letters, Vol. 5, No. 2, 54, February 1980.
2. E. Freyez, M. Afifi, A. Ducasse, B. Pouligny and J.R. Lalanne, J. Physique Letters, Vol. 46, March 1985.
3. A. Ashkin, J.M. Dziedzic, P.W. Smith, Optics Letters, Vol. 7, 284, 1982.
4. R.C.C. Leite, S.P.S. Porto, and J.C. Damen, Appl. Phys. Lett. 10, 100, 1967.
5. M.J. Soileau, William E. Williams, and Eric W. VanStryland, IEEE J. Quantum Electronics, QE. 19, No. 4, 731, April 1983.
6. J.E. Bjorkholm, P.W. Smith, W.J. Tomlinson, and A.E. Kaplan, Opt. Lett. 6, 345, 1981.
7. Shekhar Guha, M.J. Soileau, G.L. Wood, E.J. Sharp, and J.L.W. Pohlman, MRS, Extended Abstracts, Nonlinear Optical Material, 1985.
8. A.C. Tam and C.K.N. Patel, Appl. Opt. 18 (19), 3348-1979, 3348.
9. M.J. Soileau, Kamjou Mansour, E.W. VanStryland, E. Canto, and David Hagan, Joint U.S. - U.K. Conference on Sensor Protection, Malvern England, 1987.

Proceedings

Boulder Damage

Conf. 1988

Power Co

OPTICAL BREAKDOWN IN PARTICLE SUSPENSION

Kamjou Mansour, M.J. Soileau and E.W. Van Stryland

Center for Research in Electro-Optics & Lasers (CREOL)
University of Central Florida
12424 Research Parkway, Orlando, FL 32826

We have characterized the nonlinearities observed in suspensions of carbon black particles in liquids (CBS). We have developed a preliminary explanation of the optical limiting characteristic of the CBS that qualitatively explains the low limiting thresholds. We have found that the limiting depends primarily on the input optical fluence (J/cm^2) rather than irradiance (W/cm^2). We have monitored transmission, side scattered light, and the photoacoustic response of the CBS simultaneously. The nonlinear scattered light appears to be the dominant nonlinearity. Additionally, we have observed that the nonlinearities disappear after repeated laser firings. Thus, in essence, we are performing a laser induced damage experiment, and we have prepared a material with a low damage threshold. These data have led us to the following model. The carbon first linearly absorbs the input light efficiently. The carbon is rapidly heated, vaporizes and ionizes to form a rapidly expanding microplasma. This plasma absorbs and scatters subsequent light, thus limiting the transmittance.

Key words: carbon black suspension; nonlinear absorption; nonlinear scattering; nonlinear transmission; nsec pulses; optical limiting; psec pulses; $.53 \mu m$, $1.06 \mu m$.

1. INTRODUCTION

Recently there has been a growing interest in the use of microparticle suspensions as nonlinear media. Here, we demonstrate and review the dynamics of limiting in a suspension of absorbing microparticles that exhibit primarily nonlinear scattering and nonlinear absorption. The absorbing microparticles of interest are carbon black particles which are ≈ 35 nm in diameter with agglomerates up to 500 nm in diameter. We demonstrate an optical limiting threshold as low as 80 watts peak power for $0.532 \mu m$ and 160 Watts for $1.06 \mu m$ using pulses of 14 nsec and 20 nsec (FWHM), respectively.

Because of the structure of these dispersions, different mechanisms including nonlinear absorption, nonlinear refraction (self-focusing, self-defocusing), nonlinear scattering and combinations of these mechanisms could be the source of the optical nonlinearity leading to such a low optical limiting threshold.[1] In order to investigate the relative contributions of these mechanisms we perform a series of experiments. We first perform optical limiting experiments in the CBS and in the carbon black particles which are deposited on the surface of a glass substrate at $0.532 \mu m$ and $1.06 \mu m$ for nanosecond pulses. We present transmission measurements which directly show the fluence dependence of limiting in CBS. We also perform a measurement that monitors the absorbance, transmittance and fraction of side scattered light simultaneously. As will be demonstrated, we are performing a laser-induced-damage experiment on a material with an extremely low damage threshold. This leads us to discuss and show the repetition rate dependence of the CBS, and carbon black particles deposited on the glass substrate.

2. OPTICAL LIMITING

The optical geometry often used as a screening test, as it is sensitive to both nonlinear absorption and nonlinear refraction, is shown in Figure 1.[1] We used this arrangement with pulses from an Nd:YAG laser operated in the TEM₀₀ mode of 14 ns (FWHM) duration at $0.532 \mu m$ and 20 ns at $1.064 \mu m$. These pulses were focused by either a 40mm ($.532 \mu m$) or 50mm ($1.064 \mu m$) "best form" lens, shown as L₁. This results in calculated beam radii of $3.5 \mu m$ at a wavelength of $.532 \mu m$ and $7 \mu m$ at $1.064 \mu m$ inside the 1 cm cuvette. The spot radii quoted in this paper are half-widths at the $1/e^2$ maximum in irradiance. The transmitted pulse was then collected by a 102 mm focal length "best form" lens L₂ placed behind the sample. The laser beam then passed through a $400 \mu m$ aperture placed in front of a silicon photodiode. This system had an overall low input transmittance of 70 percent for both wavelengths.

Using this optical geometry we have looked at optical limiting in various concentrations of CBS and a known standard sample, CS₂, which has been previously used as an optical limiting material [2]. Optical limiting in CS₂ is primarily due to molecular reorientation of the molecules although a small contribution from electrostriction may be

present for nanosecond pulses and tight focusing geometries. The optical limiting of CBS and CS₂ in a 1 cm thick cuvette is shown in Figure 2 for nanosecond laser pulses at 0.532 μm . In order to resolve the onset of limiting, the measurement was performed for lower input powers as shown in Figure 3. The CBS begins clamping the transmitted fluence above approximately 80 watts input power and continues clamping for ≈ 5 orders of magnitude of increased input power. It is important to note that each laser firing irradiates "new" material as discussed in Section 5. The limiting of the CBS at 1.064 μm is shown in Figures 4 and 5. As is shown, the onset of limiting for 1.064 μm laser pulses is approximately 160 watts. The optical limiting in a film of carbon black particles deposited on a glass substrate at 1.06 μm is shown in Figure 6. The sample was moved to a new site for each laser firing. As is shown, the onset of limiting for 1.064 μm laser pulses is approximately 600 watts.

The observed optical limiting using the geometry shown in Figure 1, could be due to several mechanisms including nonlinear absorption, nonlinear refraction and nonlinear scattering. Below we describe a series of experiments performed to determine the dominant nonlinearity.

3. NONLINEAR TRANSMITTANCE MEASUREMENT

We have studied the fluence dependence of the transmittance of CBS at 0.532 μm and 1.064 μm . The optical geometry used is shown in Figure 7. Both a one meter and 50 centimeter "best form" lens were used to focus the nsec pulsed input beams at the two wavelengths. This resulted in measured spot sizes of 108 μm and 254 μm for 0.532 μm light. The transmitted signal was collected by a large area uniform response Si photodiode located very close to the cell. The diameter of the detector is 1 centimeter and the beam radius at the detector is approximately 1mm in diameter. The difference between this geometry and the optical limiting geometry of Figure 1 is that we are not using tight focusing and the aperture has been removed so that this experiment is insensitive to nonlinear refraction. The results of the transmittance measurements are plotted as a function of incident fluence and incident power in Figures 8, and 9 for 0.532 μm . For incident fluences above 200 mJ/cm² for 0.532 μm , the transmission becomes increasingly nonlinear and is essentially identical for both beam radii at a given wavelength as shown in Figure 8. However, the onset of a change in transmittance appears at two different incident power levels for these beam radii as shown in Figure 9. Similar results are observed for 1.06 μm laser pulses. We also observed that the onset of limiting for both nanosecond and picosecond measurements occurs approximately at the same fluence. The experiments indicate that the nonlinear transmittance observed is fluence dependent.

4. MEASUREMENT OF TRANSMITTANCE, SCATTERING AND ABSORPTANCE

In order to understand the nature of this fluence dependent nonlinear transmittance, we have set up an experiment which enables us to monitor for a single pulse, the absorptance and the fraction of side scattered light simultaneously with the transmittance measurement. This simultaneous measurement was conducted using the Q-switched Nd:YAG laser. The laser light was focused by a 1 meter focal length "best form" lens L₁ into a one centimeter cuvette cell. (See Figure 7) The transmitted light was monitored as previously described. The absorption of the incident light was directly monitored by a sensitive piezoelectric transducer which was placed in contact with the bottom of the cuvette with silicone grease. Photoacoustic measurements have been used to directly detect very small changes in absorption.[3] The side scattered light was collected by a two-inch diameter, 98 mm focal length lens and detected by a Si photodiode. The optical geometry for this measurement is shown in Figure 11.

The results of the simultaneous measurement of absorptance, transmittance, and the fraction of side scattered light (side scattering light divided by incident light) are plotted as a function of incident fluence for 1.064 μm laser pulses in Figure 11. For very low input fluences the CBS behaves linearly and there is no change in the three quantities monitored. However, for input fluences close to 360 mJ/cm² for 1.064 μm light, the transmittance begins to decrease nonlinearly as is shown by squares in Figure 11. The absorptance increases nonlinearly for incident fluence close to this threshold value (i.e., onset of change of transmittance) and levels off at a higher value even for input fluences two orders of magnitude above threshold. The scattered fraction increases nonlinearly as the transmittance decreases as shown by circles in Figure 11. This trend continues for at least two orders of magnitude above threshold. Similar results observed for .532 μm light. From these results we see that blocking of the light by the CBS above threshold is primarily due to nonlinear scattering.

5. NONLINEAR SCATTERING

The blocking of the incident light by scattering can readily be photographed as shown in Figure 12. These pictures were taken by looking at the side window of the cuvette perpendicular to the direction of the incident light. For low input fluences, top picture, the bright region in the photograph represents the input pulse which is linearly scattered (Mie scattering) by carbon black particles. However, for incident fluences above 200 mJ/cm², the light is nonlinearly scattered to the sides and thus, blocks the incident light from being transmitted. This is shown in the lower picture.

The dynamics of the transmittance loss is studied by time resolved transmission measurements conducted using nanosecond pulses. By delaying the transmitted pulse with respect to the input pulse we are able to monitor both the incident and transmitted pulses shown in Figure 13. For an incident fluence above 200 mJ/cm², there is a sharp cut off in time of the transmitted pulse (shown in graph b). The transmitted laser pulse is most strongly attenuated during the

later portions of the pulse, thus, the pulse appears advanced in time. This experiment again suggests that the attenuation of the laser beam is produced by a laser-induced-breakdown plasma.

Under this assumption, the attenuation is dominated by scattering losses of the laser light by the plasma as seen in Figures 11. Thus, we are performing a laser-induced-damage experiment, and we have prepared a material with an extremely low damage threshold. This is consistent with having high linear absorption, and is also consistent with the disappearance of the nonlinearities after repeated laser irradiation as discussed in the next section.

6. REPETITION RATE DEPENDENCE

Recently, we reported the repetition rate dependence of the CBS.[4] In that report we indicated that the onset of the limiting threshold for 1 and 10 Hz repetition rate laser pulses is considerably different and is higher for the 10 Hz repetition rate. This repetition rate dependence was removed by flowing the material at such a rate that virgin material was exposed to each laser pulse.

This bleaching or reduction of limiting of the laser light in the nonflowing liquid after repeated irradiation on the same region of the sample can be observed by monitoring the transmitted signal and scattered signal at a fixed fluence above the single shot threshold for limiting. Using the geometry shown in Figure 11 and setting the incident fluence at 350 mJ/cm^2 for $0.532 \text{ }\mu\text{m}$ laser pulses and a 1 Hz repetition rate, we can observe that the transmitted signal increases as the number of the incident pulses irradiating the sample increases. The transmittance levels off to a value that is less than the linear transmittance of the solvent as shown in Figure 14. The scattered signal reduces and levels off after repeated laser firings. This is shown as circles in Figure 14. For flowing liquid, stirred liquid or a long elapse time between the laser pulses irradiating the liquid, we have observed that the transmitted signal and scattered signal remain fixed as shown in Figure 15. The maximum limiting capability is for the first laser firing and recovery of the irradiated region of the sample is due to convection in the liquid at room temperature which for the spot size used is a slow process in comparison with the repetition rate of 1 Hz. Note that using a tight focusing geometry and a 1 Hz repetition rate that we do not see these cumulative effects. We observed that this recovery time is proportional to the radius of the laser beam in the cell, consistent with convection.

The bleaching of CBS can also be monitored as shown in Figure 16 where we have used a very large spot size of more than $254 \text{ }\mu\text{m}$. Here, we have used a HeNe laser beam expanded to illuminate the region close to the front surface of the cell. The scattering of the HeNe beam by the suspended microparticles is readily observable. We irradiated the CBS using an incident fluence of 350 mJ/cm^2 and photographed the scattered light after 10 seconds. This is shown in Figure 17. The dark spot appearing in the middle of the bright screen is the irradiated region showing that the scattering centers have been "removed" by the laser pulse. We find that this excited volume is slowly replaced by fresh CBS after approximately two minutes due to convection. The conjecture is that the microparticles have been considerably reduced in size or "atomized" so that they no longer efficiently scatter the HeNe light. The carbon particles deposited on glass are blown off the surface with repetitive firings and therefore, limiting also disappears.

7. NONLINEAR REFRACTION

In order to investigate contributions of phase distortion due to a thermooptic effect, electrostriction, or other nonlinear refractive mechanism, we monitored the far field profile of the transmitted beam using a vidicon tube with an optical multichannel analyzer. For incident fluences below threshold and up to an order of magnitude higher than threshold, we have not observed any broadening of the spatial profile of the transmitted beam. Therefore, the change in index of refraction of the CBS is very small and the phase distortion due to this index change is less than 0.2λ which is the sensitivity of our detection system. From this measurement we conclude that the contribution of nonlinear refraction is small in comparison with the nonlinear scattering observed. In order to further validate this point we removed the aperture in the original limiting geometry shown in Figure 1 and observed no change in limiting threshold.

8. MODEL

It appears from our experimental results that the dominant mechanism in the CBS is nonlinear scattering. The nature of this nonlinear scattering is consistent with the formation of microplasmas by laser-induced-breakdown of the carbon particles. Therefore, the dynamics of limiting in CBS can be described by a simple model. The carbon linearly absorbs the incident light very efficiently. The carbon is rapidly heated to several thousand degrees Celsius. A simple calculation of the particle temperature at threshold gives a few thousand degrees Celsius. The carbon then vaporizes and ionizes to form a rapidly expanding microplasma which absorbs and scatters later portions of the laser light and blocks the transmission. This model is also consistent with the disappearance of the nonlinearities after repeated laser firings as the carbon particles will have undergone vaporization.

9. CONCLUSION

We have characterized the nonlinearities observed in a suspension of carbon black particles (CBS) in liquid. We have developed a qualitative model based on laser-induced breakdown to explain the low limiting threshold of the CBS. From our results, we conclude that nonlinear scattering due to rapidly expanding microplasmas is the dominant mechanism leading to limiting. While the evidence obtained is insufficient to give details of this damage process, the

mechanism leading to limiting. While the evidence obtained is insufficient to give details of this damage process, the predictions closely match our observations. We note that the broad-band nature of the nonlinearity is primarily due to the fact that carbon is black, i.e., it absorbs all wavelengths.

10. ACKNOWLEDGEMENTS

This research was supported with funds from the DARPA/CNVEO and the Florida High Technology and Industry Council.

11. REFERENCES

1. E.W. Van Stryland, Y.Y. Wu, D.J. Hagan, M.J. Soileau, and K. Mansour, JOSAB, Vol. 5, 1980, September 1988.
2. M.J. Soileau, Williams E. Williams, and Eric W. Van Stryland, IEEE J. Quantum Electronics, QE 19, No. 4, 731, April 1983.
3. A.C. Tam and C.K.N. Patel, Appl. Opt. 18(19), 3348, 1979.
4. M.J. Soileau, Kamjou Mansour, E.W. Van Stryland, E. Canto, and David J. Hagan, Joint U.S. - U.K. Conference on Sensor Protection, Malvern, England, 1987.

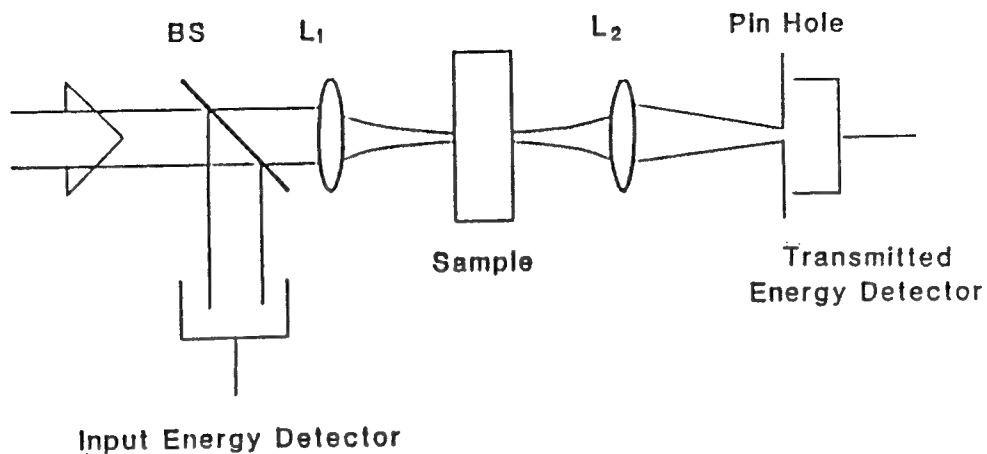


Figure 1. Optical limiting geometry.

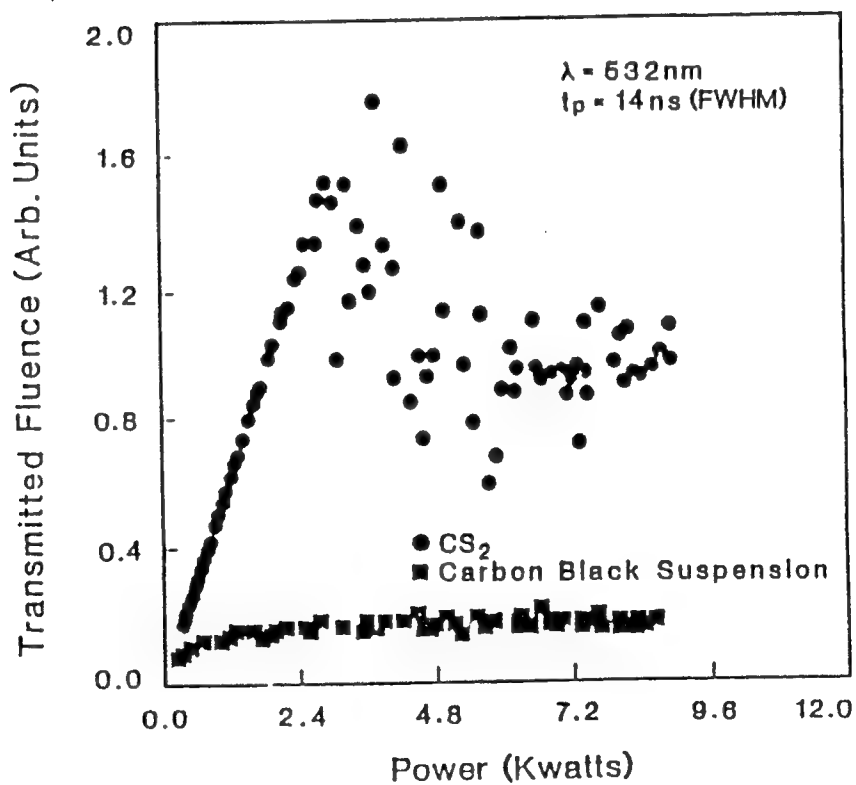


Figure 2. Plot of the limiting of CS₂ (circles) and CBS (squares) as a function of input power for 14 ns (FWHM), 0.532 μm pulses.

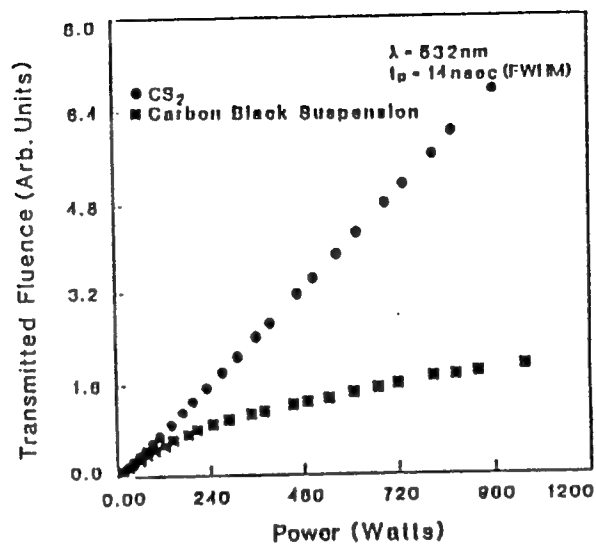


Figure 3. Plot of onset of limiting of CS₂ (circles) and CBS (squares) as a function of input power for 14 ns (FWHM), 0.53 μm pulses.

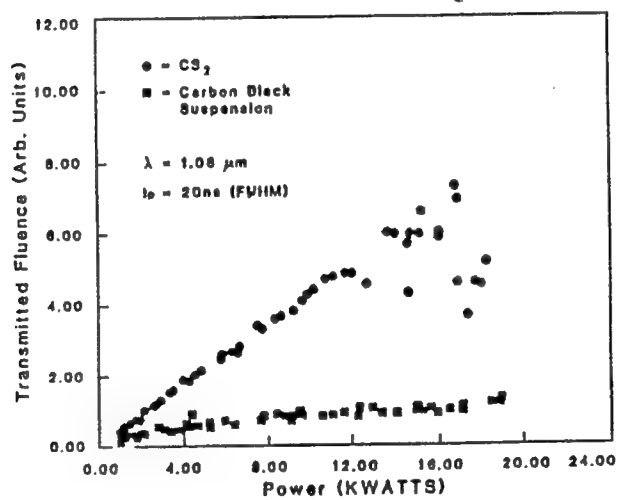


Figure 4. Plot of limiting of CS₂ (circles) and CBS (squares) as a function of input power for 20 ns (FWHM), 1.06 μm pulses.

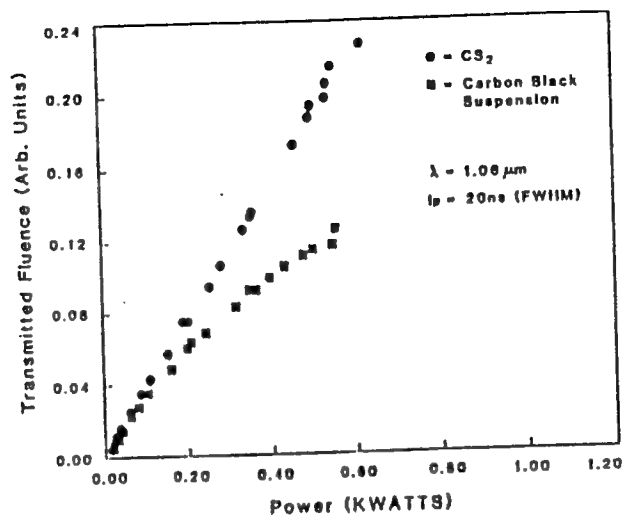


Figure 5. Plot of on set of limiting of CS₂ (circles) and CBS (squares) as a function of input power for 20 ns (FWHM), 1.06 μm pulses.

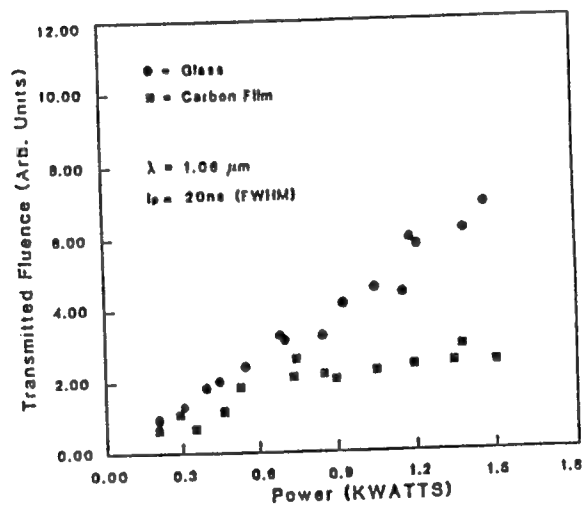


Figure 6. Plot of limiting of Carbon Particle on glass (squares) and glass as a function of input power for 20 ns (FWHM), 1.06 μm pulses.

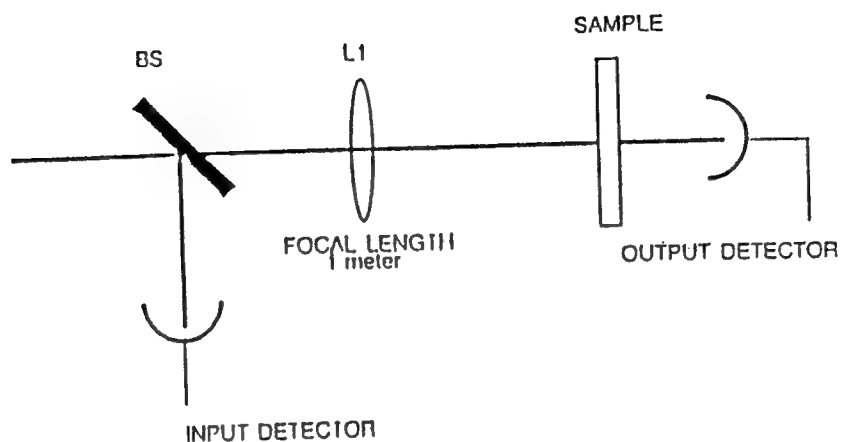


Figure 7. Optical geometry for transmission measurement.

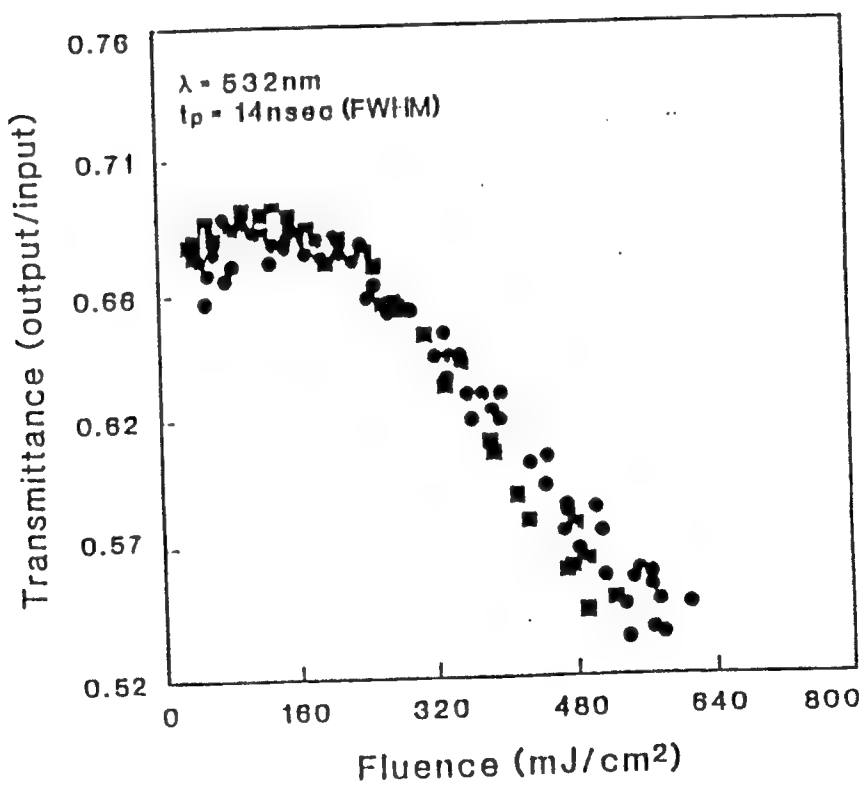


Figure 8. Measured CDS transmittance as a function of incident fluence (mJ/cm^2) for $108 \mu\text{m}$ (circles) and $254 \mu\text{m}$ (squares) spot sizes at $0.532 \mu\text{m}$.

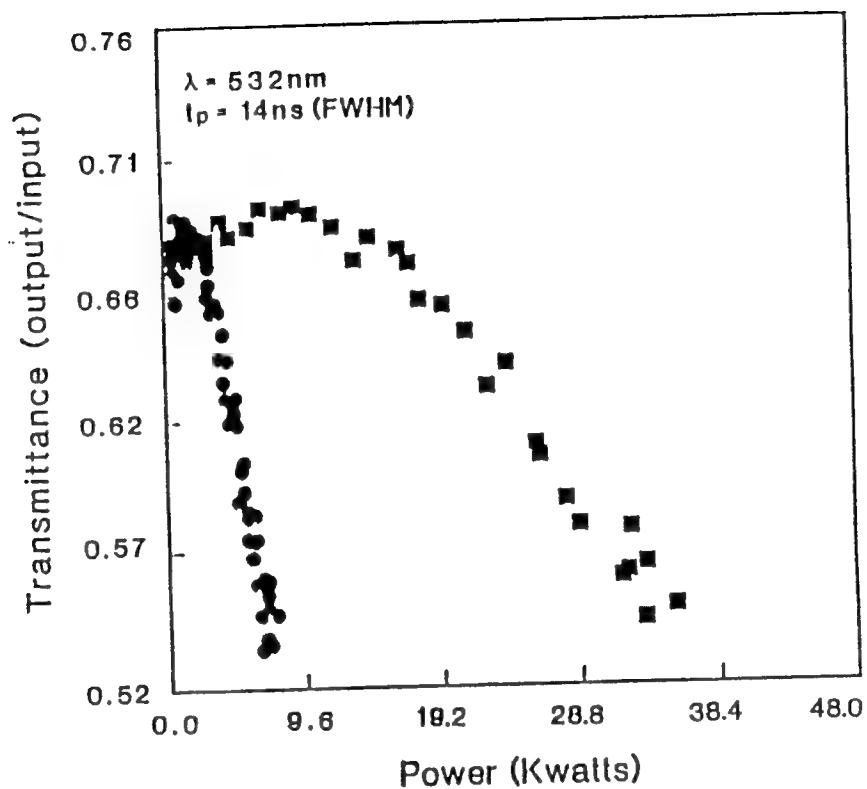


Figure 9. Measured CBS transmittance as a function of incident power (K.W) for 108 μm (circles) and 254 μm (squares) spot sizes at 0.532 μm .

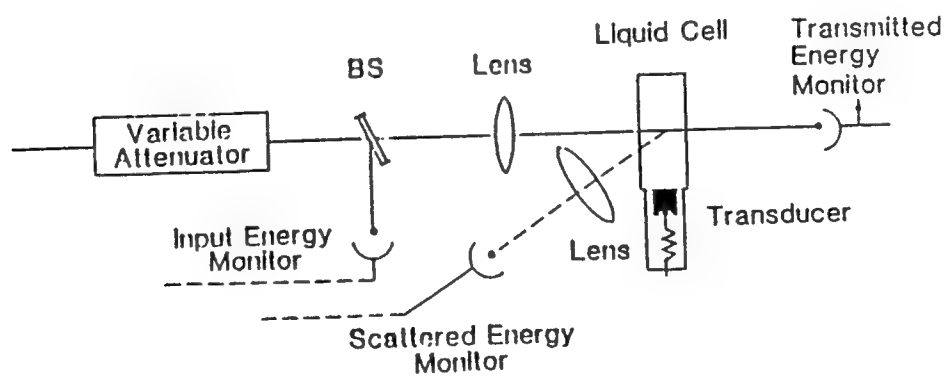


Figure 10. Optical geometry used to monitor the transmittance, absorbance and side scattered light.

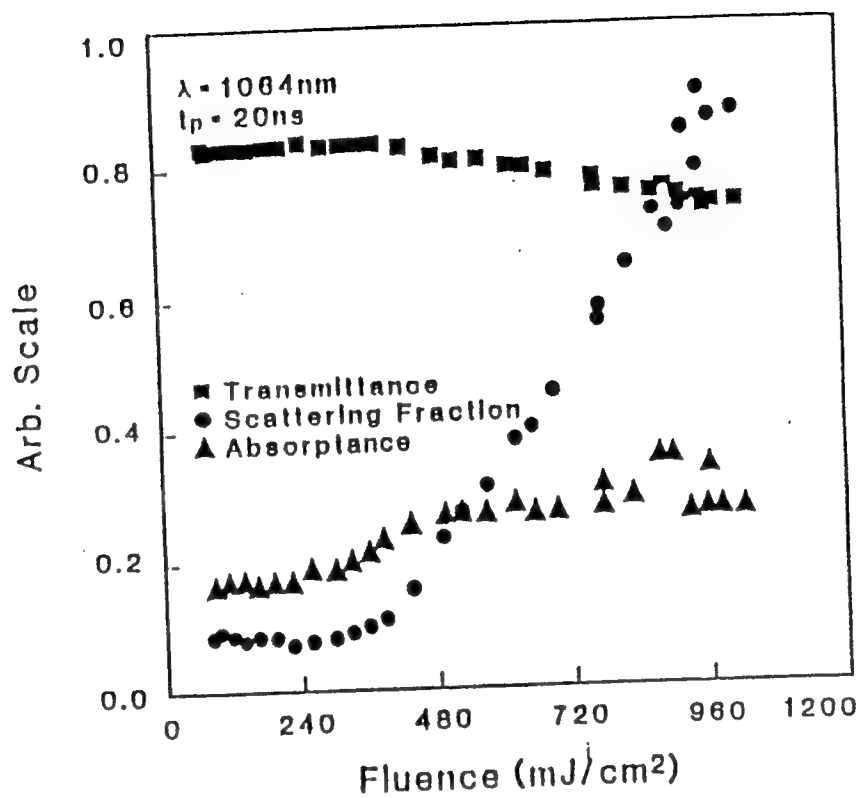
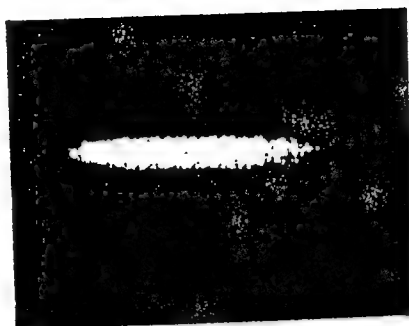


Figure 11. Plot of change of transmittance (squares), absorbance (triangle) and scattering fraction (circles) as a function of incident fluence (mJ/cm²) for 1.06 μm , 20 ns pulses.

$\lambda = 532 \text{ nm}$
 $t_p = 14 \text{ nsec}$

Low Intensity



(a)

Front of the Cell ←

1 CM

→ Back of the Cell

High Intensity



(b)

Figure 12. Photographs A and B represent the input pulse which is scattered by CBS for low and high incident fluences respectively.

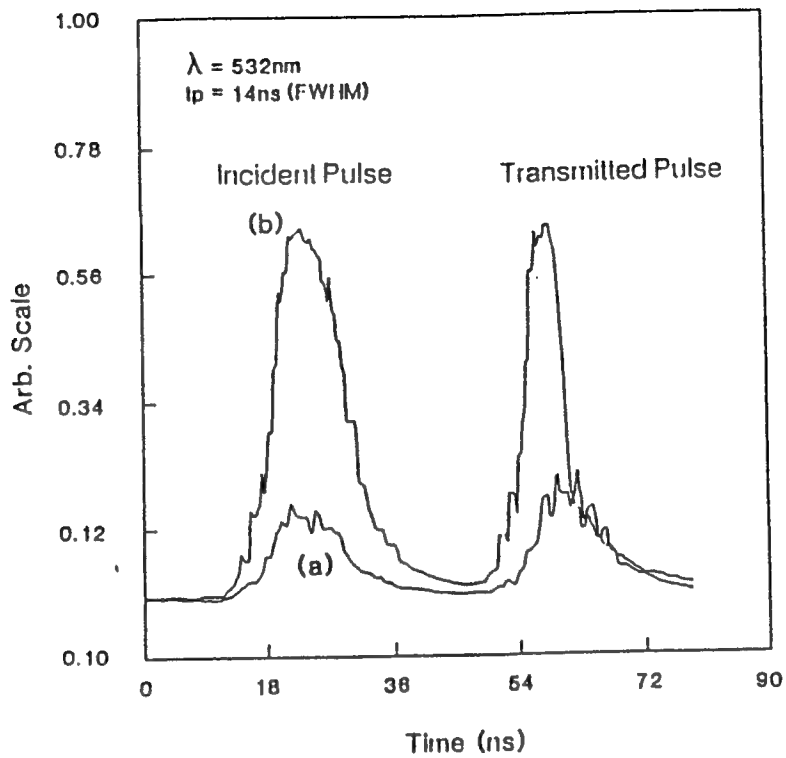


Figure 13. Graphs A and B represent the incident and transmitted pulse for fluence levels below and above the threshold. Incident pulse in graph B has been attenuated by a factor of 10 in respect to the transmitted pulse.

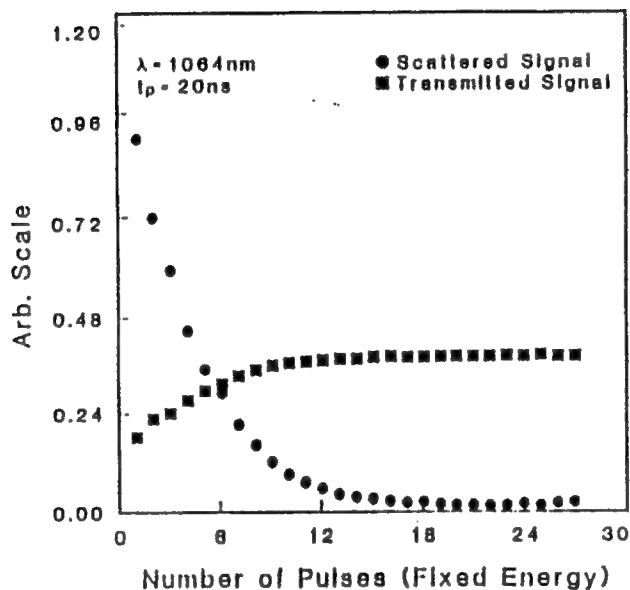


Figure 14. Plot of fraction of scattered light (circles) and transmittance (squares) as a function of the number consecutive laser pulses for $1.06 \mu\text{m}$, 20 ns pulses at a fluence of 450 mJ/cm^2 .

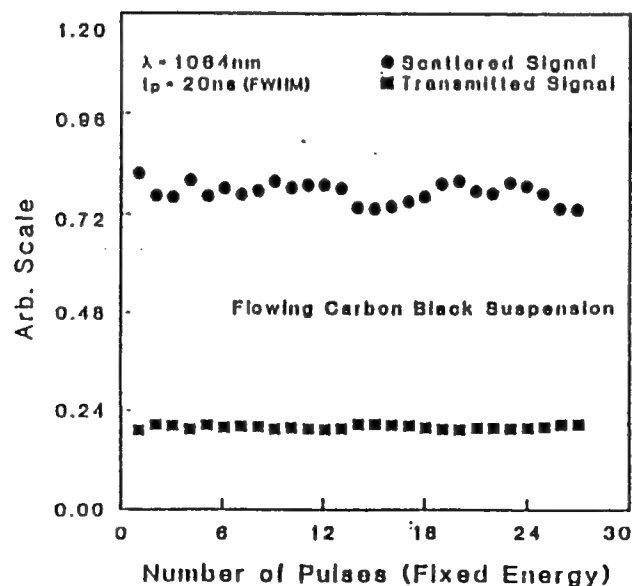


Figure 15. Plot of fraction of scattered light (circles) and transmittance (squares) in flowing CBS as a function of the number of consecutive laser pulses for $1.06 \mu\text{m}$, 20 ns pulses at a fluence of 450 mJ/cm^2 .

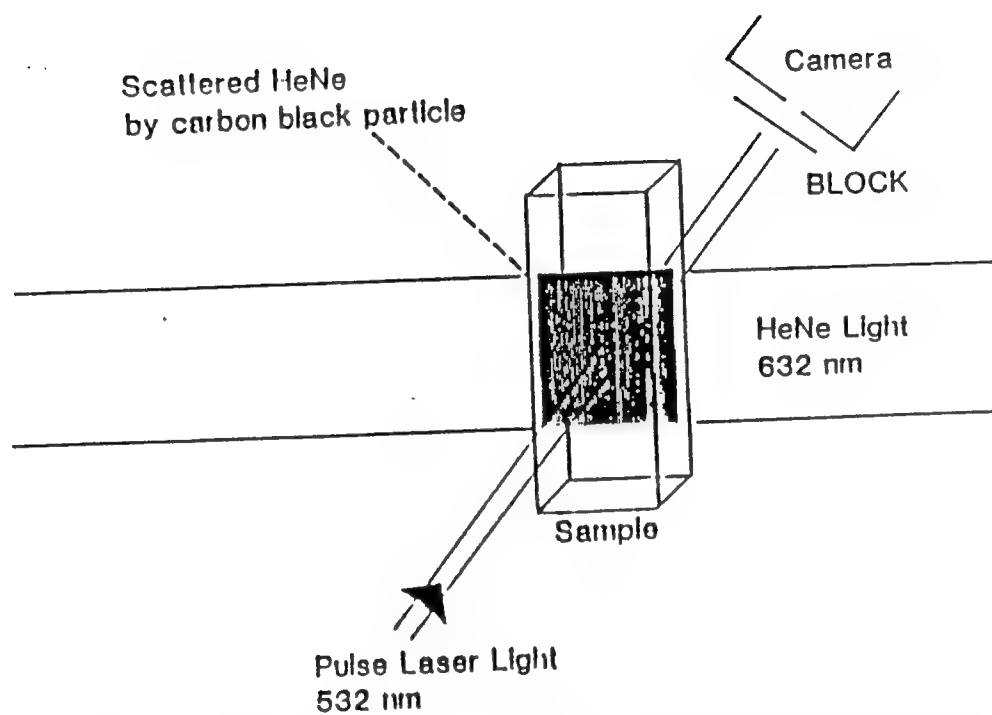
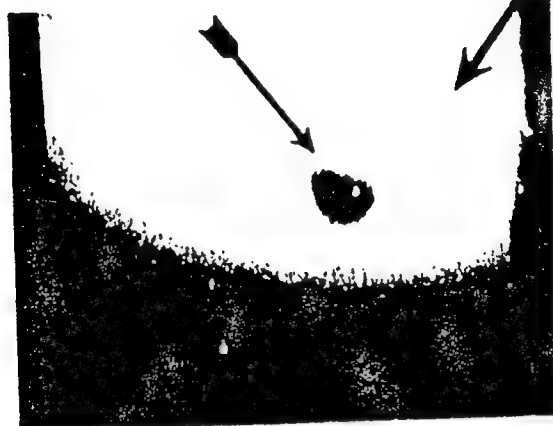


Figure 16. Optical geometry to monitor "bleaching" of carbon particles in CBS.

Exposed Area
to the Laser Light

Scattered HeNe Light
by Carbon Particles



(a)

Film Exposure after 10 Seconds



(b)

Film Exposure after 2 Minutes

Figure 17. Photographs A and B represent the "bleaching" of carbon particles within the irradiated region and replacement of the irradiated region with fresh liquid, respectively.

J. Opt. Soc. Am. 1988

Z-SCAN: A SIMPLE AND SENSITIVE TECHNIQUE FOR NONLINEAR REFRACTION MEASUREMENTS

M. Sheik-bahae, A.A. Said, T.H. Wei, Y.Y. Wu,
D.J. Hagan, M.J. Soileau, and E.W. Van Stryland

CREOL

Center for Research in Electro Optics and Lasers
University of Central Florida, Orlando, FL 32826

ABSTRACT

We describe a sensitive technique for measuring nonlinear refraction in a variety of materials that offers simplicity, sensitivity and speed. The transmittance of a sample is measured through a finite aperture in the *far-field* as the sample is moved along the propagation path (z) of a focused Gaussian beam. The sign and magnitude of the nonlinearity is easily deduced from such a transmittance curve (Z-scan). Employing this technique a sensitivity of better than $\lambda/300$ wavefront distortion is achieved in n_2 measurements of BaF_2 using picosecond frequency doubled Nd:YAG laser pulses.

1. INTRODUCTION

We are currently developing a single beam method, which we refer to as a Z-scan, for measuring the sign and magnitude of the nonlinear refractive index n_2 . [1] In practice we have found that this method has a sensitivity comparable to interferometric methods. Here we describe this method in detail and demonstrate how it can be applied and analyzed for a variety of materials. We also present a simple method to minimize parasitic effects due to the presence of linear sample inhomogeneities.

Previous measurements of nonlinear refraction have used a variety of techniques including nonlinear interferometry [2], [3], degenerate four-wave mixing [4], nearly-degenerate three-wave mixing [5], ellipse rotation [6], beam distortion measurements [7], [8], and our recently reported Z-scan technique. The first three methods, namely nonlinear interferometry and wave mixing are potentially sensitive techniques but require a relatively complex experimental apparatus. Beam distortion measurements, on the other hand, are relatively insensitive and require detailed wave propagation analysis. The Z-scan technique is based on the principles of spatial beam distortion but offers simplicity as well as very high sensitivity.

We will describe this simple technique in Section II. Theoretical analyses of Z-scan measurements are given in Section III for a "thin" nonlinear medium. It will be shown that for many practical cases, nonlinear refraction and its sign can be obtained from a simple linear relationship between the observed transmittance changes and the induced phase distortion without the need for performing detailed calculations. In Section IV we present measurements of nonlinear refraction in a number of materials such as CS_2 , and transparent dielectrics at wavelengths of 532 nm, 1.06 μm and 10.6 μm . In CS_2 at 10 μm , for example, both thermo-optical and reorientational Kerr effects were identified using nanosecond and picosecond pulses respectively. We also describe how effects of linear sample inhomogeneities (eg. bulk index variations) can be effectively removed from the experimental data.

2. THE Z-SCAN TECHNIQUE

Using a single Gaussian laser beam in a tight focus geometry, as depicted in Fig. 1, we measure the transmittance of a nonlinear medium through a finite aperture *in the far field* as a function of the sample position z measured with respect to the focal plane. The following example will qualitatively elucidate how such a trace (Z-scan) is related to the nonlinear refraction of the sample. Assume, for instance, a material

with a negative nonlinear refractive index and a thickness smaller than the diffraction length of the focused beam (a thin medium). This can be regarded as a thin lens of variable focal length. Starting the scan from a distance far away from the focus (negative z) the beam irradiance is low and negligible nonlinear refraction occurs; hence, the transmittance (D_2/D_1 in Fig. 1) remains relatively constant. As the sample is brought closer to focus, the beam irradiance increases leading to self-lensing in the sample. A negative self-lensing prior to focus will tend to collimate the beam, causing a beam narrowing at the aperture which results in an increase in the measured transmittance. As the scan in z continues and the sample passes the focal plane to the right (positive z), the same self-defocusing increases the beam divergence leading to beam broadening at the aperture and, thus, a decrease in transmittance. This suggests that there is a null as the sample crosses the focal plane. This is analogous to placing a thin lens at or near the focus, resulting in a minimal change of the far field pattern of the beam. The Z-scan is completed as the sample is moved away from focus (positive z) such that the transmittance becomes linear since the irradiance is again low. Induced beam broadening and narrowing of this type have been previously observed and explained during nonlinear refraction measurements of some semiconductors.[9],[10] A similar technique was also previously used to measure thermally induced beam distortion of chemicals in solvents.[11]

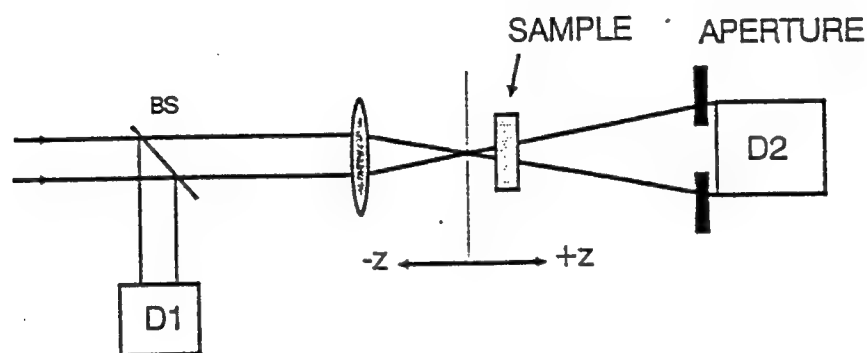


Fig.1 The Z-scan experimental apparatus in which the ratio D_2/D_1 is recorded as a function of the sample position z .

A pre-focal transmittance maximum (peak) followed by a post-focal transmittance minimum (valley) is, therefore, the Z-scan signature of a negative refractive nonlinearity. Positive nonlinear refraction, following the same analogy, gives rise to an opposite valley-peak configuration. It is an extremely useful feature of the Z-scan method that the sign of the nonlinear index is immediately obvious from the data, and as we will show in the following section the magnitude can also be easily estimated using a simple analysis for a thin medium.

In the above picture describing the Z-scan, one must bear in mind that a purely refractive nonlinearity was considered assuming that no absorptive nonlinearities (such as multiphoton or saturation of absorption) are present. Qualitatively, multiphoton absorption suppresses the peak and enhances the valley, while saturation produces the opposite effect. The sensitivity to nonlinear refraction is entirely due to the aperture, and removal of the aperture completely eliminates the effect. However, in this case the Z-scan will still be sensitive to nonlinear absorption. Nonlinear absorption coefficients could be extracted from such "open" aperture experiments.

3. THEORY

Much work has been done in investigating the propagation of intense laser beams inside a nonlinear material and the ensuing self-refraction [12], [13]. Considering the geometry given in Fig. 1, we will formulate and discuss a simple method for analyzing the Z-scan data based on modifications of existing theories.

In general, various order nonlinearities can be considered; however, for simplicity, we first examine only a cubic nonlinearity where the index of refraction n is expressed in terms of nonlinear indices $n_2(\text{esu})$ or $\gamma(\text{m}^2/\text{W})$ through:

$$n = n_0 + \frac{n_2}{2} |E|^2 = n_0 + \gamma I \quad (1)$$

where n_0 is the linear index of refraction, E is the peak electric field (cgs), and I denotes the irradiance (MKS) of the laser beam within the sample. [n_2 and γ are related through the conversion formula, $n_2(\text{esu}) = (cn_0/40\pi)\gamma(\text{m}^2/\text{W})$, where c (m/sec) is the speed of light in vacuum]. Assuming a TEM₀₀ Gaussian beam of beam waist radius w_0 traveling in the $+z$ direction, we can write E as:

$$E(z, r, t) = E_0(t) \frac{w_0}{w(z)} \exp\left[-\frac{r^2}{w^2(z)} - \frac{ikr^2}{2R(z)}\right] e^{-i\phi(z, t)}, \quad (2)$$

where $w^2(z) = w_0^2(1 + z^2/z_0^2)$ is the beam radius, $R(z) = z(1 + z_0^2/z^2)$ is the radius of curvature of the wavefront at z , $z_0 = kw_0^2/2$ is the diffraction length of the beam, $k = 2\pi/\lambda$ is the wave vector and λ is the laser wavelength, all in free space. $E_0(t)$ denotes the radiation electric field at the focus and contains the temporal envelope of the laser pulse. The $e^{-i\phi(z, t)}$ term contains all the radially uniform phase variations. As we are only concerned with calculating the radial phase variations $\Delta\phi(r)$, the slowly varying envelope approximation (SVEA) applies, and all other phase changes that are uniform in r are ignored.

If the sample length is small enough that changes in the beam diameter within the sample due to either diffraction or nonlinear refraction can be neglected, the medium is regarded as "thin", in which case the self-refraction process is referred to as "external self-action". Such an assumption simplifies the problem considerably, and the amplitude \sqrt{I} and phase ϕ of the electric field as a function of z' are now governed in the SVEA by a pair of simple equations:

$$\frac{d\Delta\phi}{dz'} = \Delta n(I) k, \quad (3)$$

and

$$\frac{dI}{dz'} = -\alpha I, \quad (4)$$

where z' is the propagation depth in the sample and α is the linear absorption coefficient. Note that z' should not be confused with the sample position z . In the case of a cubic nonlinearity, Eqns. 3 and 4 are solved to give the phase shift $\Delta\phi$ at the exit surface of the sample, which simply follows the radial variation of the incident irradiance at a given position of the sample z . Thus,

$$\Delta\phi(z, r, t) = \Delta\phi_0(z, t) \exp\left[-\frac{2r^2}{w^2(z)}\right], \quad (5-a)$$

with

$$\Delta\phi_0(z,t) = \frac{\Delta\Phi_0(t)}{1+z^2/z_0^2} \quad (5-b)$$

$\Delta\Phi_0(t)$, the on-axis phase shift at the focus, is defined as,

$$\Delta\Phi_0(t) = k\Delta n_0(t) \frac{1-e^{-\alpha L}}{\alpha}, \quad (6)$$

where L is the sample length, and $\Delta n_0 = \gamma I_0(t)$ with $I_0(t)$ being the on-axis irradiance at focus (ie. $z=0$). Again we take $I_0(t)$ as the irradiance within the sample to account for Fresnel reflection losses.

The complex electric field after the sample, E' , now contains the nonlinear phase distortion,

$$E' = E(z,r,t) e^{-\alpha L/2} e^{i\Delta\phi(z,r,t)} \quad (7)$$

By virtue of Huygen's principle one can obtain the far field pattern of the beam at the aperture plane through a zeroth order Hankel transformation of E' . [14] We will follow a more convenient treatment applicable to Gaussian input beams which we refer to as the "Gaussian Decomposition" (GD) method given by Weaire et. al. [15], in which they decompose the complex electric field at the exit plane of the sample into a summation of Gaussian beams through a Taylor series expansion of the nonlinear phase term $e^{i\Delta\phi(z,r,t)}$ in Eq. 7. That is,

$$e^{i\Delta\phi(z,r,t)} = \sum_{m=0}^{\infty} \frac{[i\Delta\phi_0(z,t)]^m}{m!} e^{-2mr^2/w^2(z)} \quad (8)$$

Each Gaussian beam can now be simply propagated to the aperture plane where they will be resummed to reconstruct the beam. When including the initial beam curvature for the focused beam, we derive the resultant electric field pattern at the aperture as:

$$E_a(r,t) = E(z,r=0,t) e^{-\alpha L/2} \sum_{m=0}^{\infty} \frac{(i\Delta\phi_0(t))^m}{m!} \left(g^2 + \frac{d^2}{d_m^2} \right)^{-\frac{1}{2}} \exp \left[-\frac{r^2}{w_m^2} - \frac{ikr^2}{2R_m} + i\theta_m \right], \quad (9)$$

where d is the propagation distance in free space from the sample to the aperture plane, and $g=1+d/R$, $R=R(z)$ being the beam radius of curvature at the sample. As long as the far field condition is met, d can be considered independent of the sample position z resulting in symmetric Z-scans. The remaining parameters in Eq. 9 are expressed as:

$$w_{mo}^2 = \frac{w^2(z)}{2m+1}, \quad d_m = \frac{kw_{mo}^2}{2}, \quad w_m^2 = w_{m0}^2 \left[g^2 + \frac{d^2}{d_m^2} \right],$$

$$R_m = d \left[1 - \frac{g}{g^2 + d^2/d_m^2} \right]^{-1}, \quad \text{and } \theta_m = \tan^{-1} \left[\frac{d/d_m}{g} \right].$$

small aperture ($S=0.01$). They exhibit the expected features, namely a valley-peak (v-p) for the positive nonlinearity and a peak-valley (p-v) for the negative one. For a given $\Delta\Phi_0$, the magnitude and shape of $T(z)$ do not depend on the wavelength or geometry as long as the far field condition for the aperture plane is satisfied. The aperture size S , however, is an important parameter since a large aperture reduces the variations in $T(z)$. This reduction is more prominent in the peak where beam narrowing occurs and can result in a peak transmittance which cannot exceed $(1-S)$. Needless to say, for very large aperture or no aperture ($S=1$), the effect vanishes and $T(z) = 1$ for all z and $\Delta\Phi_0$. For small $|\Delta\Phi_0|$, the peak and valley occur at the same distance with respect to focus, and for a cubic nonlinearity this distance is found to be $\approx 0.85z_0$. With larger phase distortions ($|\Delta\Phi_0| > 1$) this symmetry no longer holds and both peak and valley move toward $\pm z$ for the corresponding sign of nonlinearity ($\pm\Delta\Phi_0$) such that their separation remains relatively constant given by,

$$\Delta Z_{p-v} \approx 1.7z_0. \quad (12)$$

We can define an easily measurable quantity ΔT_{p-v} as the difference between the normalized peak and valley transmittance: $T_p - T_v$. The variation of this quantity as a function of $|\Delta\Phi_0|$, as calculated for various aperture sizes is illustrated in Fig. 3. These curves exhibit some useful features. First, for a given order of nonlinearity, they can be considered universal. In other words, they are independent of the laser wavelength, geometry (as long as the far field condition is met) and the sign of nonlinearity. Second, for all aperture sizes, the variation of ΔT_{p-v} is found to be linearly dependent on $|\Delta\Phi_0|$. Particularly for on axis ($S \approx 0$) we find,

$$\Delta T_{p-v} \approx 0.405 |\Delta\Phi_0| \quad \text{for} \quad |\Delta\Phi_0| \leq \pi, \quad (13-a)$$

to be accurate to within 0.5 percent. As shown in Fig. 3, for larger apertures, the linear coefficient 0.405 decreases such that with $S=0.5$ it becomes 0.34 and at $S=0.7$ it reduces to 0.29. Based on a numerical fitting, the following relationship can be used to include such variations within a $\pm 2\%$ accuracy;

$$\Delta T_{p-v} \approx 0.405(1-S)^{0.25} |\Delta\Phi_0| \quad \text{for} \quad |\Delta\Phi_0| \leq \pi. \quad (13-b)$$

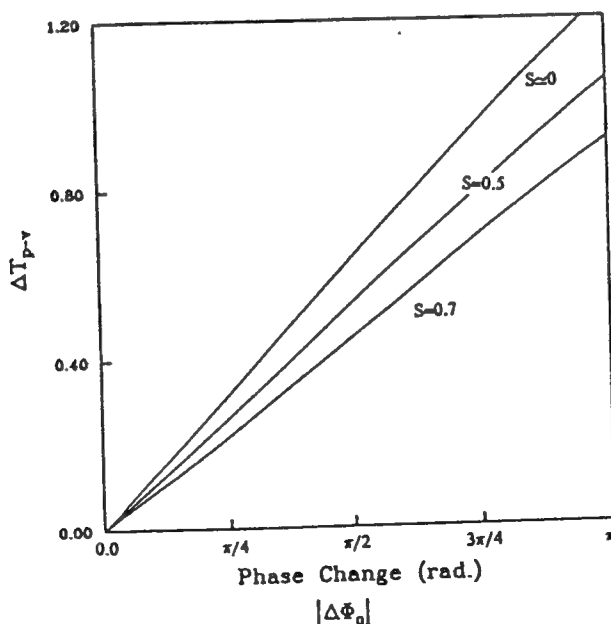


Fig.3 Calculated ΔT_{p-v} as a function of the phase shift at the focus ($\Delta\Phi_0$). The sensitivity, as indicated by the slope of the curves, decreases slowly for larger aperture sizes ($S > 0$).

The implications of Eqns. 13-a and 13-b are quite promising in that they can be used to readily estimate the nonlinear index (n_2) with good accuracy after a Z-scan is performed. What is most intriguing about these expressions is that they reveal the highly sensitive nature of the Z-scan technique. For example, if our experimental apparatus and data acquisition systems are capable of resolving transmission changes ΔT_{p-v} of $\approx 1\%$, we will be able to measure phase changes corresponding to less than $\lambda/250$ wavefront distortion. Achieving such sensitivity, however, requires relatively good optical quality of the sample under study. We describe in the experimental section IV a means to minimize problems arising from poor optical quality samples.

We can now easily extend the steady state cw results to include transient effects along with pulsed radiation by using the time averaged index change $\langle \Delta n_0(t) \rangle$ where,

$$\langle \Delta n_0(t) \rangle = \frac{\int_{-\infty}^{\infty} \Delta n_0(t) I_0(t) dt}{\int_{-\infty}^{\infty} I_0(t) dt}, \quad (14)$$

The time averaged $\langle \Delta \Phi_0(t) \rangle$ is related to $\langle \Delta n_0(t) \rangle$ through Eq. 6. With a nonlinearity having instantaneous response and decay times relative to the pulsewidth of the laser, one obtains for a temporally Gaussian pulse:

$$\langle \Delta n_0(t) \rangle = \Delta n_0 / \sqrt{2}, \quad (15)$$

where Δn_0 now represents the peak-on-axis index change at the focus. For a cumulative nonlinearity having a decay time much longer than the pulsewidth (eg. thermal), the instantaneous index change is given by the following integral:

$$\Delta n_0(t) = A \int_{-\infty}^t I_0(t') dt', \quad (16)$$

where A a constant which depends on the nature of the nonlinearity. If we substitute Eq. 16 into Eq. 14 we obtain a fluence averaging factor of 1/2. That is,

$$\langle \Delta n_0(t) \rangle = \frac{1}{2} A F, \quad (17)$$

where F is the pulse fluence at focus within the sample. Interestingly, the factor of 1/2 is independent of the temporal pulse shape.

4. EXPERIMENTAL RESULTS

We examined the nonlinear refraction of a number of materials using the Z-scan technique. Fig. 4 shows a Z-scan of a 1 mm thick cuvette with NaCl windows filled with CS_2 using 300 ns TEA CO_2 laser pulses having an energy of 0.85 mJ. The peak-valley configuration of this Z-scan is indicative of a negative (self-defocusing) nonlinearity. The solid line in Fig. 4 is the calculated result using $\langle \Delta \Phi_0 \rangle = -0.6$ which gives an index change of $\langle \Delta n_0 \rangle \approx -1 \times 10^{-3}$. As mentioned earlier such detailed theoretical fitting is not necessary

for obtaining $\langle \Delta n_0 \rangle$ (only ΔT_{p-v} is needed). The defocusing effect shown in Fig. 4 is attributed to a thermal nonlinearity resulting from linear absorption of CS_2 ($\alpha \approx 0.22 \text{ cm}^{-1}$ at $10.6 \mu\text{m}$). The risetime of a thermal lens in a liquid is determined by the acoustic transit time, $\tau = w_0/v_s$, where v_s is the velocity of sound in the liquid [17]. For CS_2 with $v_s \approx 1.5 \times 10^5 \text{ cm/sec}$ and having $w_0 \approx 60 \mu\text{m}$, we obtain a risetime of $\approx 40 \text{ ns}$ which is almost an order of magnitude smaller than the TEA laser pulsewidth. Furthermore, the relaxation of the thermal lens, governed by thermal diffusion, is of the order of 100 ms . [17] Therefore, we regard the nonuniform heating caused by the 300 ns pulses as quasi-steady state, in which case, from Eq. 17, the average on-axis nonlinear index change at focus can be determined in terms of the thermo-optic coefficient, dn/dT , as:

$$\langle \Delta n_0 \rangle \approx \frac{dn}{dT} \frac{F_0 \alpha}{2\rho C_v}, \quad (18)$$

where F_0 is the fluence, ρ is the density, C_v is the specific heat and $1/2$ denotes the fluence averaging factor. With the known value of $\rho C_v \approx 1.3 \text{ J/}^\circ\text{Kcm}^3$ for CS_2 , we deduce $dn/dT \approx -(8.3 \pm 1.0) \times 10^{-4} \text{ }^\circ\text{C}^{-1}$ which is in good agreement with the reported value of $-8 \times 10^{-4} \text{ }^\circ\text{C}^{-1}$. [16]

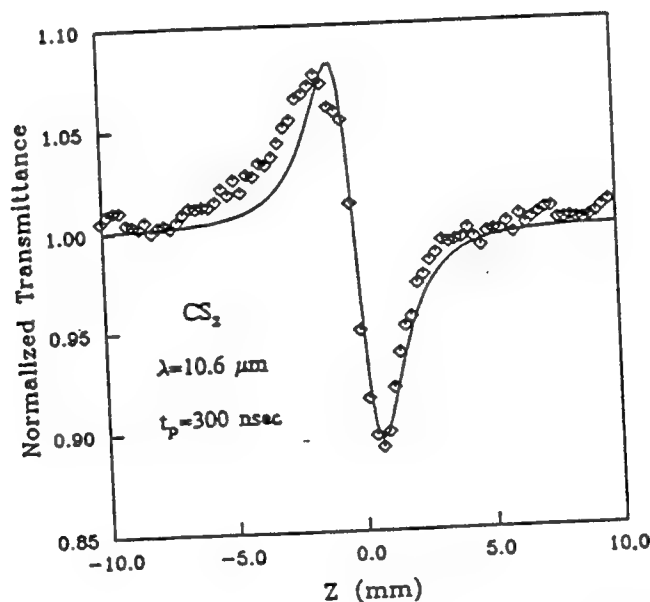


Fig.4 Measured Z-scan of a 1mm thick CS_2 cell using 300 ns pulses at $\lambda=10.6 \mu\text{m}$ indicating thermal self-defocusing. The solid line is the calculated result with $\Delta\Phi_0=-0.6$ and 60% aperture ($S=0.6$).

With ultrashort pulses, nonlocal nonlinearities such as thermal or electrostriction are no longer significant. Particularly, in CS_2 , the molecular reorientational Kerr effect becomes the dominant mechanism for nonlinear refraction. CS_2 is frequently used as a standard reference nonlinear material. [18,19] We have used picosecond pulses at $10.6 \mu\text{m}$, $1.06 \mu\text{m}$ and at $0.53 \mu\text{m}$ to measure n_2 in CS_2 . We obtain the same value of n_2 , within errors, at all three wavelengths, $(1.5 \pm 0.6) \times 10^{-11} \text{ esu}$ at $10.6 \mu\text{m}$, $(1.3 \pm 0.3) \times 10^{-11} \text{ esu}$ at $1.06 \mu\text{m}$ and $(1.2 \pm 0.2) \times 10^{-11} \text{ esu}$ at $0.53 \mu\text{m}$. The external self-focusing arising from the Kerr effect in CS_2 is shown in Fig. 5, where a Z-scan of a 1mm cell using 27 ps (FWHM) pulses focused to a beam waist w_0 of $26 \mu\text{m}$ from a frequency doubled Nd:YAG laser is illustrated. Its valley-peak configuration indicates the positive sign of n_2 . With $\Delta T_{p-v} = 0.24$, and using Eq. 13-b with a 40% aperture ($S = 0.4$), one readily obtains a $\langle \Delta n_0 \rangle = 5.6 \times 10^{-5}$. Using the peak irradiance of 2.6 GW/cm^2 , this value of $\langle \Delta n_0 \rangle$ corresponds to an $n_2 \approx (1.2 \pm 0.2) \times 10^{-11} \text{ esu}$. The main source of uncertainty in the value of n_2 is the absolute measurement of the irradiance. A plot of ΔT_{p-v} versus peak laser irradiance as measured from

various Z-scans on the same CS_2 cell is shown in Fig. 6. The linear behavior of this plot follows Eq. 13 as derived for a cubic nonlinearity.

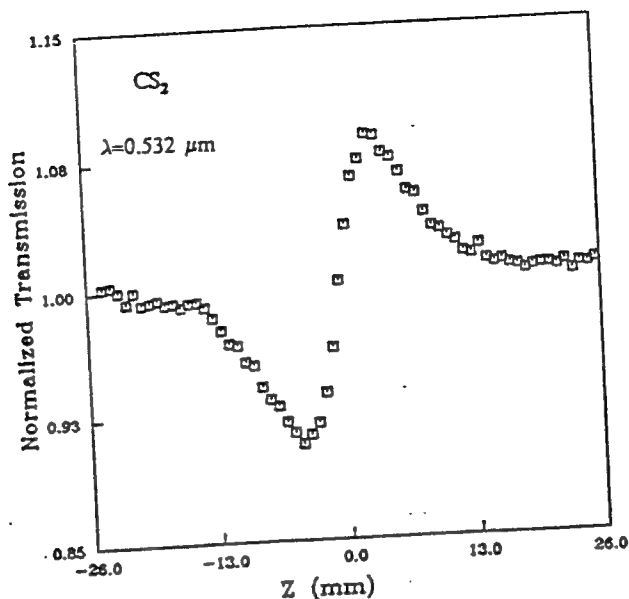


Fig.5 Measured Z-scan of a 1mm thick CS_2 cell using 27 ps pulses at $\lambda=532$ nm. It depicts the self-focusing effect due to the reorientational Kerr effect.

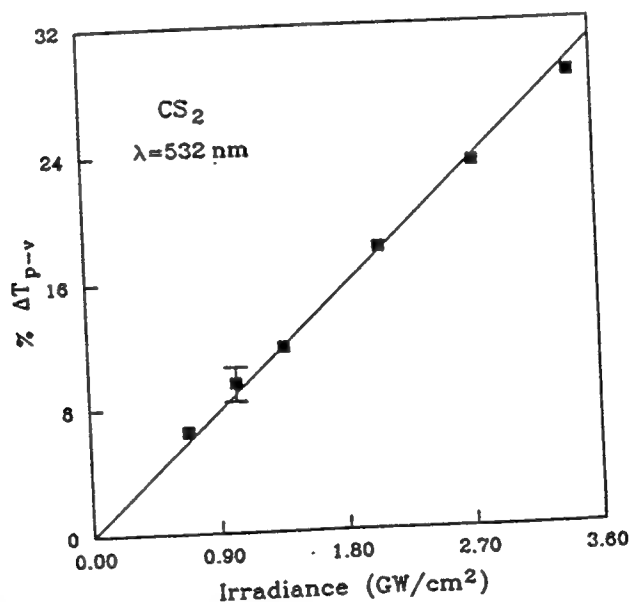


Fig.6 T_{p-v} in percent as a function of the peak irradiance from the Z-scan data of CS_2 at 532 nm, indicative of the reorientational Kerr effect.

Transparent dielectric window materials have relatively small nonlinear indices. Recently, Adair et. al. [21] have performed a careful study of the nonlinear index of refraction of a large number of such materials in a nearly degenerate-three-wave-mixing scheme at $\lambda \approx 1.06$ μm . Using the Z-scan technique, we examined some of these materials at 532 nm. For example, the result for BaF_2 (2.4mm thick) is shown in Fig.7, using the same beam parameters as for CS_2 . This Z-scan was obtained by purposely lowering the pulse energy to

2 μJ in order to observe the resolution and the sensitivity of this measurement. With a $\Delta T_{p-v} \approx 0.035$, this Z-scan corresponds to a $\lambda/75$ induced phase distortion. For a unity signal-to-noise-ratio for our particular laser system, it is seen from Fig. 7 that the sensitivity to phase distortion is better than $\lambda/300$. For laser systems having better amplitude and pulsewidth stability, the sensitivity should be correspondingly increased.

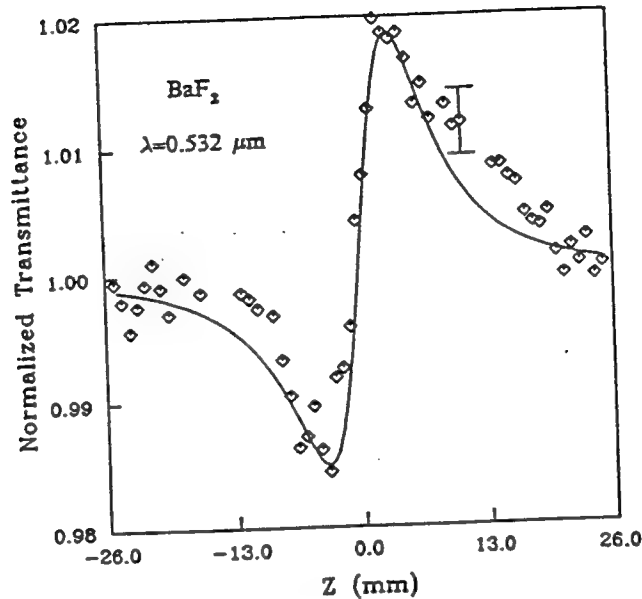


Fig.7 Measured Z-scan of a 2.4 mm thick BaF_2 sample using 20 ps pulses at $\lambda=532$ nm indicating the self-focusing due to the electronic Kerr effect. The solid line is the calculated result with $\Delta\Phi_0=0.085$ corresponding to $\approx\lambda/75$ total phase distortion. The error bar shown corresponds to approximately $\lambda/480$ induced phase distortion.

Aside from the statistical fluctuations of the laser irradiance, surface imperfections or wedge in the sample may lead to systematic transmittance changes with z that could mask the effect of nonlinear refraction. We found, however, that such "parasitic" effects may be substantially reduced by subtracting a low irradiance background Z-scan from the high irradiance scan. A simple computer simulation of this process assuming that the surface imperfections do not disturb the circular symmetry of the beam or cause any beam steering, indicated that background subtraction indeed recovers the original ΔT_{p-v} arising from the nonlinear refraction effect even for quite large surface disturbances $\Delta\phi_s$ of up to π .

Returning to the Z-scan of Fig.7, we obtain $n_2 \approx (0.8 \pm 1.5) \times 10^{-13}$ esu for BaF_2 at 532 nm, which is in close agreement with the reported values of 0.7×10^{-13} esu [21] and 1.0×10^{-13} esu [3] as measured at $1.06 \mu\text{m}$ using more complex techniques of nearly degenerate-three-wave-mixing and time-resolved-nonlinear-interferometry, respectively. Similarly for MgF_2 , we measure $n_2 \approx 0.25 \times 10^{-13}$ esu at 532 nm as compared to the reported value of 0.32×10^{-13} esu at $1.06 \mu\text{m}$ for this material as given in [21]. Dispersion in n_2 for these materials between 1 and $0.5 \mu\text{m}$ is expected to be minimal. It should be noted that the n_2 values extracted from the Z-scans are absolute rather than relative measurements. If the beam parameters are not accurately known, however, it should be possible to calibrate the system by using a standard nonlinear material such as CS_2 .

5. CONCLUSION

We have demonstrated a simple single beam technique that is sensitive to less than $\lambda/300$ nonlinearly induced phase distortion. Using the Z-scan data the magnitude and sign of the nonlinear refraction can be simply determined. We have derived relations that allow the refractive index to be obtained directly from

the Z-scan data without resorting to computer fits. We have applied this technique to several materials displaying a variety of nonlinearities on different time scales. It is expected that this method will be a valuable tool for experimenters searching for highly nonlinear materials.

6. ACKNOWLEDGEMENT

We gratefully acknowledge the support of the National Science Foundation grant #ECS-8617066, and the support of DARPA/CNVEO and the Florida High Technology and Industry Council. We also wish to thank Alan Miller for helpful discussions.

7. REFERENCES

1. M. Sheik-Bahae, A.A. Said, and E.W. Van Stryland, "High Sensitivity Single Beam n_2 Measurement," Opt. Lett. to be published in Sept. 1989.
2. M.J. Weber, D. Milam, and W.L. Smith, "Nonlinear Refractive Index of Glasses and Crystals," Optical Engineering, 17, 463-469 (1978).
3. M.J. Moran, C.Y. She, R.L. Carman, "Interferometric Measurements of Nonlinear Refractive-Index Coefficient Relative to CS_2 in Laser-System-Related Materials," IEEE J. Quantum Electron. QE-11, 259-263 (1975).
4. S.R. Friberg and P.W. Smith, "Nonlinear Optical Glasses for Ultrafast Optical Switches," IEEE J. Quantum Electron. QE-23, 2089-2094 (1987).
5. R. Adair, L.L. Chase, and S.A. Payne, "Nonlinear refractive index measurement of glasses using three-wave frequency mixing," J. Opt. Soc. Am. B 4, 875-881 (1987).
6. A. Owyong, "Ellipse Rotations Studies in Laser Host Materials," IEEE J. Quantum Electron. QE-9, 1064-1069 (1973).
7. W.E. Williams, M.J. Soileau, and E.W. Van Stryland, "Optical Switching and n_2 Measurements in CS_2 ," Opt. Comm. 50, 256-260 (1984).
8. W.E. Williams, M.J. Soileau, and E.W. Van Stryland, "Simple direct measurements of n_2 ," Proc. 15th Annual Symp. on Optical Materials for High Power Lasers, Boulder, CO (1983).
9. J.R. Hill, G. Parry and A. Miller, "Non-linear Refraction Index Changes in CdHgTe at 175K with 1.06 μm Radiation," Opt. Commun., 43, 151-156 (1982).
10. T.F. Boggess, S.C. Moss, I.W. Boyd, and A.L. Smirl, "Picosecond Nonlinear-Optical Limiting in Silicon," in Ultrafast Phenomena IV, edited by D.H. Huston and K.B. Eisenthal (Springer-Verlag), (New York, 1984). pp. 202.
11. J.M. Harris and N.J. Dovichi, "Thermal Lens Calorimetry," Analytical Chem. 52, 695-700(1980).
12. S.A. Akhmanov, A.D. Sukhorokov, and R.V. Khokhlov, "Self-focusing and Diffraction of Light in a Nonlinear Medium," Sov. Phys. Vspokhi; English Translation, 10, 609 (1968).
13. W.L. Smith, J.H. Bechtel and N. Bloembergen, "Dielectric-Breakdown Threshold and Nonlinear-refractive Index Measurements with Picosecond Laser Pulses, Phys. Rev. B 12, 706-714 (1975).
14. J.D. Gaskill, *Linear Systems, Fourier Transforms, and Optics*, John Wiley & Sons, New York, 1978.
15. D. Weaire, B.S. Wherrett, D.A.B. Miller, and S.D. Smith, "Effect of Low-Power Nonlinear refraction on laser beam propagation in InSb," Opt. Lett., 4, 331-333 (1974).
16. V. Raman, F.R.S., and K.S. Venkataraman, "Determination of the adiabatic piezo-optic coefficient of liquids," Proc. Roy. Soc. A, 171, 137 (1939).
17. J.N. Hayes, "Thermal Blooming of Laser Beams in Fluids," Appl. Opt. 2, 455-461 (1972).
18. P.P. Ho and R.R. Alfano, "Optical Kerr effects in Liquids," Phys. Rev. A, 20, 2170-2187 (1979).
19. P. Thomas, A. Jares, and B.P. Stoicheff, "Nonlinear Refractive Index and "DC" Kerr Constant of Liquid CS_2 ," IEEE J. Quantum Electron. QE-10, 493-494(1974).
20. E.W. Van Stryland, H. Vanherzeele, M.A. Woodall, M.J. Soileau, A.L. Smirl, S. Guha, T.G. Boggess, "Two-Photon Absorption, Nonlinear Refraction, and Optical Limiting in Semiconductors," Opt. Eng., 25, 613-623 (1985).
21. R. Adair, L.L. Chase, and A. Payne, "Nonlinear Refractive Index of Optical Crystals," Phys. Rev. B, 39, 3337-3350(1989).

Manuscript received
8-20-89

OPTICAL BREAKDOWN IN PARTICLE SUSPENSION

Kamjou Mansour, M.J. Soileau and E.W. Van Stryland

Center for Research in Electro-Optics & Lasers (CREOL)
University of Central Florida
12424 Research Parkway, Orlando, FL 32826

We have characterized the nonlinearities observed in suspensions of carbon black particles in liquids (CBS). We have developed a preliminary explanation of the optical limiting characteristic of the CBS that qualitatively explains the low limiting thresholds. We have found that the limiting depends primarily on the input optical fluence (J/cm^2) rather than irradiance (W/cm^2). We have monitored transmission, side scattered light, and the photoacoustic response of the CBS simultaneously. The nonlinear scattered light appears to be the dominant nonlinearity. Additionally, we have observed that the nonlinearities disappear after repeated laser firings. Thus, in essence, we are performing a laser induced damage experiment, and we have prepared a material with a low damage threshold. These data have led us to the following model. The carbon first linearly absorbs the input light efficiently. The carbon is rapidly heated, vaporizes and ionizes to form a rapidly expanding microplasma. This plasma absorbs and scatters subsequent light, thus limiting the transmittance.

Key words: carbon black suspension; nonlinear absorption; nonlinear scattering; nonlinear transmission; nsec pulses; optical limiting; psec pulses; .53 μm , 1.06 μm .

1. INTRODUCTION

Recently there has been a growing interest in the use of microparticle suspensions as nonlinear media. Here, we demonstrate and review the dynamics of limiting in a suspension of absorbing microparticles that exhibit primarily nonlinear scattering and nonlinear absorption. The absorbing microparticles of interest are carbon black particles which are ≈ 35 nm in diameter with agglomerates up to 500 nm in diameter. We demonstrate an optical limiting threshold as low as 80 watts peak power for 0.532 μm and 160 Watts for 1.06 μm using pulses of 14 nsec and 20 nsec (FWHM), respectively.

Because of the structure of these dispersions, different mechanisms including nonlinear absorption, nonlinear refraction (self-focusing, self-defocusing), nonlinear scattering and combinations of these mechanisms could be the source of the optical nonlinearity leading to such a low optical limiting threshold.[1] In order to investigate the relative contributions of these mechanisms we perform a series of experiments. We first perform optical limiting experiments in the CBS and in the carbon black particles which are deposited on the surface of a glass substrate at 0.532 μm and 1.06 μm for nanosecond pulses. We present transmission measurements which directly show the fluence dependence of limiting in CBS. We also perform a measurement that monitors the absorptance, transmittance and fraction of side scattered light simultaneously. As will be demonstrated, we are performing a laser-induced-damage experiment on a material with an extremely low damage threshold. This leads us to discuss and show the repetition rate dependence of the CBS, and carbon black particles deposited on the glass substrate.

2. OPTICAL LIMITING

The optical geometry often used as a screening test, as it is sensitive to both nonlinear absorption and nonlinear refraction, is shown in Figure 1.[1] We used this arrangement with pulses from an Nd:YAG laser operated in the TEM₀₀ mode of 14 ns (FWHM) duration at 0.532 μm and 20 ns at 1.064 μm . These pulses were focused by either a 40mm (.532 μm) or 50mm (1.064 μm) "best form" lens, shown as L₁. This results in calculated beam radii of 3.5 μm at a wavelength of .532 μm and 7 μm at 1.064 μm inside the 1 cm cuvette. The spot radii quoted in this paper are half-widths at the 1/e² maximum in irradiance. The transmitted pulse was then collected by a 102 mm focal length "best form" lens L₂ placed behind the sample. The laser beam then passed through a 400 μm aperture placed in front of a silicon photodiode. This system had an overall low input transmittance of 70 percent for both wavelengths.

Using this optical geometry we have looked at optical limiting in various concentrations of CBS and a known standard sample, CS₂, which has been previously used as an optical limiting material [2]. Optical limiting in CS₂ is primarily due to molecular reorientation of the molecules although a small contribution from electrostriction may be

present for nanosecond pulses and tight focusing geometries. The optical limiting of CBS and CS_2 in a 1 cm thick cuvette is shown in Figure 2 for nanosecond laser pulses at $0.532 \mu\text{m}$. In order to resolve the onset of limiting, the measurement was performed for lower input powers as shown in Figure 3. The CBS begins clamping the transmitted fluence above approximately 80 watts input power and continues clamping for ≈ 5 orders of magnitude of increased input power. It is important to note that each laser firing irradiates "new" material as discussed in Section 5. The limiting of the CBS at $1.064 \mu\text{m}$ is shown in Figures 4 and 5. As is shown, the onset of limiting for $1.064 \mu\text{m}$ laser pulses is approximately 160 watts. The optical limiting in a film of carbon black particles deposited on a glass substrate at $1.06 \mu\text{m}$ is shown in Figure 6. The sample was moved to a new site for each laser firing. As is shown, the onset of limiting for $1.064 \mu\text{m}$ laser pulses is approximately 600 watts.

The observed optical limiting using the geometry shown in Figure 1, could be due to several mechanisms including nonlinear absorption, nonlinear refraction and nonlinear scattering. Below we describe a series of experiments performed to determine the dominant nonlinearity.

3. NONLINEAR TRANSMITTANCE MEASUREMENT

We have studied the fluence dependence of the transmittance of CBS at $0.532 \mu\text{m}$ and $1.064 \mu\text{m}$. The optical geometry used is shown in Figure 7. Both a one meter and 50 centimeter "best form" lens were used to focus the nsec pulsed input beams at the two wavelengths. This resulted in measured spot sizes of $108 \mu\text{m}$ and $254 \mu\text{m}$ for $0.532 \mu\text{m}$ light. The transmitted signal was collected by a large area uniform response Si photodiode located very close to the cell. The diameter of the detector is 1 centimeter and the beam radius at the detector is approximately 1mm in diameter. The difference between this geometry and the optical limiting geometry of Figure 1 is that we are not using tight focusing and the aperture has been removed so that this experiment is insensitive to nonlinear refraction. The results of the transmittance measurements are plotted as a function of incident fluence and incident power in Figures 8, and 9 for $0.532 \mu\text{m}$. For incident fluences above $200 \text{ mJ}/\text{cm}^2$ for $0.532 \mu\text{m}$, the transmission becomes increasingly nonlinear and is essentially identical for both beam radii at a given wavelength as shown in Figure 8. However, the onset of a change in transmittance appears at two different incident power levels for these beam radii as shown in Figure 9. Similar results are observed for $1.06 \mu\text{m}$ laser pulses. We also observed that the onset of limiting for both nanosecond and picosecond measurements occurs approximately at the same fluence. The experiments indicate that the nonlinear transmittance observed is fluence dependent.

4. MEASUREMENT OF TRANSMITTANCE, SCATTERING AND ABSORBTANCE

In order to understand the nature of this fluence dependent nonlinear transmittance, we have set up an experiment which enables us to monitor for a single pulse, the absorptance and the fraction of side scattered light simultaneously with the transmittance measurement. This simultaneous measurement was conducted using the Q-switched Nd:YAG laser. The laser light was focused by a 1 meter focal length "best form" lens L_1 into a one centimeter cuvette cell. (See Figure 7) The transmitted light was monitored as previously described. The absorption of the incident light was directly monitored by a sensitive piezoelectric transducer which was placed in contact with the bottom of the cuvette with silicone grease. Photoacoustic measurements have been used to directly detect very small changes in absorption.[3] The side scattered light was collected by a two-inch diameter, 98 mm focal length lens and detected by a Si photodiode. The optical geometry for this measurement is shown in Figure 11.

The results of the simultaneous measurement of absorptance, transmittance, and the fraction of side scattered light (side scattering light divided by incident light) are plotted as a function of incident fluence for $1.064 \mu\text{m}$ laser pulses in Figure 11. For very low input fluences the CBS behaves linearly and there is no change in the three quantities monitored. However, for input fluences close to $360 \text{ mJ}/\text{cm}^2$ for $1.064 \mu\text{m}$ light, the transmittance begins to decrease nonlinearly as is shown by squares in Figure 11. The absorptance increases nonlinearly for incident fluence close to this threshold value (i.e., onset of change of transmittance) and levels off at a higher value even for input fluences two orders of magnitude above threshold. The scattered fraction increases nonlinearly as the transmittance decreases as shown by circles in Figure 11. This trend continues for at least two orders of magnitude above threshold. Similar results observed for $.532 \mu\text{m}$ light. From these results we see that blocking of the light by the CBS above threshold is primarily due to nonlinear scattering.

5. NONLINEAR SCATTERING

The blocking of the incident light by scattering can readily be photographed as shown in Figure 12. These pictures were taken by looking at the side window of the cuvette perpendicular to the direction of the incident light. For low input fluences, top picture, the bright region in the photograph represents the input pulse which is linearly scattered (Mie scattering) by carbon black particles. However, for incident fluences above $200 \text{ mJ}/\text{cm}^2$, the light is nonlinearly scattered to the sides and thus, blocks the incident light from being transmitted. This is shown in the lower picture.

The dynamics of the transmittance loss is studied by time resolved transmission measurements conducted using nanosecond pulses. By delaying the transmitted pulse with respect to the input pulse we are able to monitor both the incident and transmitted pulses shown in Figure 13. For an incident fluence above $200 \text{ mJ}/\text{cm}^2$, there is a sharp cut off in time of the transmitted pulse (shown in graph b). The transmitted laser pulse is most strongly attenuated during the

later portions of the pulse, thus, the pulse appears advanced in time. This experiment again suggests that the attenuation of the laser beam is produced by a laser-induced-breakdown plasma.

Under this assumption, the attenuation is dominated by scattering losses of the laser light by the plasma as seen in Figures 11. Thus, we are performing a laser-induced-damage experiment, and we have prepared a material with an extremely low damage threshold. This is consistent with having high linear absorption, and is also consistent with the disappearance of the nonlinearities after repeated laser irradiation as discussed in the next section.

6. REPETITION RATE DEPENDENCE

Recently, we reported the repetition rate dependence of the CBS.[4] In that report we indicated that the onset of the limiting threshold for 1 and 10 Hz repetition rate laser pulses is considerably different and is higher for the 10 Hz repetition rate. This repetition rate dependence was removed by flowing the material at such a rate that virgin material was exposed to each laser pulse.

This bleaching or reduction of limiting of the laser light in the nonflowing liquid after repeated irradiation on the same region of the sample can be observed by monitoring the transmitted signal and scattered signal at a fixed fluence above the single shot threshold for limiting. Using the geometry shown in Figure 11 and setting the incident fluence at 350 mJ/cm^2 for $0.532 \text{ }\mu\text{m}$ laser pulses and a 1 Hz repetition rate, we can observe that the transmitted signal increases as the number of the incident pulses irradiating the sample increases. The transmittance levels off to a value that is less than the linear transmittance of the solvent as shown in Figure 14. The scattered signal reduces and levels off after repeated laser firings. This is shown as circles in Figure 14. For flowing liquid, stirred liquid or a long elapse time between the laser pulses irradiating the liquid, we have observed that the transmitted signal and scattered signal remain fixed as shown in Figure 15. The maximum limiting capability is for the first laser firing and recovery of the irradiated region of the sample is due to convection in the liquid at room temperature which for the spot size used is a slow process in comparison with the repetition rate of 1 Hz. Note that using a tight focusing geometry and a 1 Hz repetition rate that we do not see these cumulative effects. We observed that this recovery time is proportional to the radius of the laser beam in the cell, consistent with convection.

The bleaching of CBS can also be monitored as shown in Figure 16 where we have used a very large spot size of more than $254 \text{ }\mu\text{m}$. Here, we have used a HeNe laser beam expanded to illuminate the region close to the front surface of the cell. The scattering of the HeNe beam by the suspended microparticles is readily observable. We irradiated the CBS using an incident fluence of 350 mJ/cm^2 and photographed the scattered light after 10 seconds. This is shown in Figure 17. The dark spot appearing in the middle of the bright screen is the irradiated region showing that the scattering centers have been "removed" by the laser pulse. We find that this excited volume is slowly replaced by fresh CBS after approximately two minutes due to convection. The conjecture is that the microparticles have been considerably reduced in size or "atomized" so that they no longer efficiently scatter the HeNe light. The carbon particles deposited on glass are blown off the surface with repetitive firings and therefore, limiting also disappears.

7. NONLINEAR REFRACTION

In order to investigate contributions of phase distortion due to a thermo-optic effect, electrostriction, or other nonlinear refractive mechanism, we monitored the far field profile of the transmitted beam using a vidicon tube with an optical multichannel analyzer. For incident fluences below threshold and up to an order of magnitude higher than threshold, we have not observed any broadening of the spatial profile of the transmitted beam. Therefore, the change in index of refraction of the CBS is very small and the phase distortion due to this index change is less than 0.2λ which is the sensitivity of our detection system. From this measurement we conclude that the contribution of nonlinear refraction is small in comparison with the nonlinear scattering observed. In order to further validate this point we removed the aperture in the original limiting geometry shown in Figure 1 and observed no change in limiting threshold.

8. MODEL

It appears from our experimental results that the dominant mechanism in the CBS is nonlinear scattering. The nature of this nonlinear scattering is consistent with the formation of microplasmas by laser-induced-breakdown of the carbon particles. Therefore, the dynamics of limiting in CBS can be described by a simple model. The carbon linearly absorbs the incident light very efficiently. The carbon is rapidly heated to several thousand degrees Celsius. A simple calculation of the particle temperature at threshold gives a few thousand degrees Celsius. The carbon then vaporizes and ionizes to form a rapidly expanding microplasma which absorbs and scatters later portions of the laser light and blocks the transmission. This model is also consistent with the disappearance of the nonlinearities after repeated laser firings as the carbon particles will have undergone vaporization.

9. CONCLUSION

We have characterized the nonlinearities observed in a suspension of carbon black particles (CBS) in liquid. We have developed a qualitative model based on laser-induced breakdown to explain the low limiting threshold of the CBS. From our results, we conclude that nonlinear scattering due to rapidly expanding microplasmas is the dominant mechanism leading to limiting. While the evidence obtained is insufficient to give details of this damage process, the

mechanism leading to limiting. While the evidence obtained is insufficient to give details of this damage process, the predictions closely match our observations. We note that the broad-band nature of the nonlinearity is primarily due to the fact that carbon is black, i.e., it absorbs all wavelengths.

10. ACKNOWLEDGEMENTS

This research was supported with funds from the DARPA/CNVEO and the Florida High Technology and Industry Council.

11. REFERENCES

1. E.W. Van Stryland, Y.Y. Wu, D.J. Hagan, M.J. Soileau, and K. Mansour, JOSAB, Vol. 5, 1980, September 1988.
2. M.J. Soileau, Williams E. Williams, and Eric W. Van Stryland, IEEE J. Quantum Electronics, QE 19, No. 4, 731, April 1983.
3. A.C. Tam and C.K.N. Patel, Appl. Opt. 18(19), 3348, 1979.
4. M.J. Soileau, Kamjou Mansour, E.W. Van Stryland, E. Canto, and David J. Hagan, Joint U.S. - U.K. Conference on Sensor Protection, Malvern, England, 1987.

High-sensitivity, single-beam n_2 measurements

M. Sheik-bahae, A. A. Said, and E. W. Van Stryland

Center for Research in Electro-Optics and Lasers, University of Central Florida, Orlando, Florida 32816

Received February 24, 1989; accepted June 11, 1989

We present a simple yet highly sensitive single-beam experimental technique for the determination of both the sign and magnitude of n_2 . The sample is moved along the z direction of a focused Gaussian beam while the repetitively pulsed laser energy is held fixed. The resultant plot of transmittance through an aperture in the far field yields a dispersion-shaped curve from which n_2 is easily calculated. A transmittance change of 1% corresponds to a phase distortion of $\approx \lambda/250$. We demonstrate this method on several materials using both CO_2 and Nd:YAG laser pulses.

Numerous techniques are known for the measurement of nonlinear refraction in materials. Nonlinear interferometry,^{1,2} degenerate four-wave mixing,³ nearly degenerate three-wave mixing,⁴ ellipse rotation,⁵ and beam-distortion measurements^{6,7} are among the techniques frequently reported. The first three methods, interferometry and wave mixing, are potentially sensitive techniques but require a complex experimental apparatus. Beam-distortion measurements, on the other hand, require precise beam scans followed by detailed wave-propagation analysis. Based on the principles of spatial beam distortion, however, we present a single-beam technique for measuring the sign and magnitude of refractive nonlinearities that offers simplicity as well as high sensitivity. The technique is based on the transformation of phase distortion to amplitude distortion during beam propagation. We demonstrate this technique, which we refer to as a Z scan, on several materials in the IR and the visible, with nanosecond and picosecond pulses, for thermal and electronic Kerr nonlinearities. The demonstrated sensitivity to nonlinearly induced phase changes is better than $\lambda/100$.

The Z-scan experimental apparatus is shown in Fig. 1. Using a Gaussian laser beam in a tight-focus limiting geometry, we measure the transmittance of a nonlinear medium through a finite aperture placed in the far field as a function of the sample position (z) measured with respect to the focal plane. The following example qualitatively explains how such a trace (Z scan) is related to the nonlinear refraction of the sample. We place a thin material (i.e., with a thickness much less than the beam depth of focus) having $n_2 < 0$ well in front of the focus ($-z$ in Fig. 1). As the sample is moved toward the focus the increased irradiance leads to a negative lensing effect that tends to collimate the beam, thus increasing the aperture transmittance. With the sample on the $+z$ side of the focus, the negative lensing effect tends to augment diffraction, and the aperture transmittance is reduced. The approximate null at $z = 0$ is analogous to placing a thin lens at the focus that results in a minimal far-field pattern change. For still larger $+z$ the irradiance is reduced and the transmittance returns to the original linear value. We normalize this value to unity. A

positive nonlinearity results in the opposite effect, i.e., lowered transmittance for the sample at negative z and enhanced transmittance at positive z . Induced beam broadening and narrowing of this type have been previously observed and explained for the case of band filling and plasma nonlinearities⁸ and in the presence of nonlinear absorption in semiconductors.⁹

Not only is the sign of n_2 apparent from a Z scan, but the magnitude of n_2 can also be easily calculated using a simple analysis for a thin medium. Considering the geometry given in Fig. 1, we formulate and discuss a simple method of analyzing the Z scan. For a fast cubic nonlinearity the index of refraction is expressed in terms of nonlinear indices n_2 (esu) through

$$n = n_0 + \frac{n_2}{2} |E|^2 = n_0 + \Delta n, \quad (1)$$

where n_0 is the linear index of refraction and E is the electric field. Assuming a Gaussian beam traveling in the $+z$ direction, we can write the magnitude of E as

$$|E(r, z, t)| = |E_0(t)| \frac{w_0}{w(z)} \exp\left[-\frac{r^2}{w^2(z)}\right], \quad (2)$$

where $w^2(z) = w_0^2(1 + z^2/z_0^2)$ is the beam radius at z , $z_0 = k w_0^2/2$ is the diffraction length of the beam, $k = 2\pi/\lambda$ is the wave vector, and λ is the laser wavelength, all in air. E_0 denotes the radiation electric field at the focus and contains the temporal envelope of the laser pulse.

If the sample length is small enough such that changes in the beam diameter within the sample due to either diffraction or nonlinear refraction can be

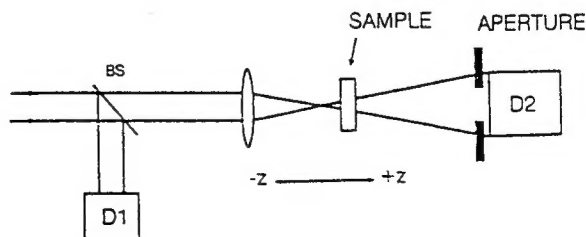


Fig. 1. Simple Z-scan experimental apparatus in which the transmittance ratio D_2/D_1 is recorded as a function of the sample position z . BS, Beam splitter.

neglected, the medium is regarded as thin. Such an assumption simplifies the problem considerably, and the amplitude and nonlinear phase change $\Delta\phi$ of the electric field within the sample are now governed by

$$\frac{d\Delta\phi}{dz} = 2\pi/\lambda \Delta n \text{ and } \frac{d|E|}{dz} = -\alpha/2 |E|, \quad (3)$$

where α is the linear absorption coefficient. Equations (3) are solved to give the phase shift $\Delta\phi$ at the exit surface of the sample, which simply follows the radial variation of the incident irradiance at a given position of the sample z :

$$\Delta\phi(r, z, t) = \frac{\Delta\Phi_0}{1 + z^2/z_0^2} \exp\left[-\frac{2r^2}{w^2(z)}\right], \quad (4a)$$

with

$$\Delta\Phi_0(t) = \frac{2\pi}{\lambda} \Delta n_0(t) \frac{1 - e^{-\alpha L}}{\alpha}, \quad (4b)$$

where L is the sample length and $\Delta n_0(t)$ is the instantaneous on-axis index change at the focus ($z = 0$). The electric field E' at the exit surface of the sample z_1 now contains the nonlinear phase distortion,

$$E'(r, z_1, t) = E(r, z_1, t) \exp(-\alpha L/2) \exp[i\Delta\phi(r, z_1, t)]. \quad (5)$$

By virtue of Huygens's principle one can obtain the far-field pattern of the beam at the aperture plane through a zeroth-order Hankel transformation of E' .¹⁰ We use a numerically simpler Gaussian decomposition method given by Weaire *et al.*¹¹

Having calculated the electric-field profile, E_a , at the aperture, we obtain the normalized instantaneous Z-scan power transmittance as

$$T(z, t) = \frac{\int_0^{r_0} |E_a(\Delta\Phi_0, r, z, t)|^2 r dr}{S \int_0^\infty |E_a(0, r, z, t)|^2 r dr}, \quad (6)$$

where r_0 is the aperture radius and S is the aperture transmittance in the linear regime. The laser temporal pulse shape can be taken into account by simply performing a separate time integration on both the upper and lower terms in Eq. (6). This gives the Z-scan fluence transmittance $T(z)$. We first discuss the general features of the Z scan using a constant input field such that $T(z, t) = T(z)$.

For a given $\Delta\Phi_0$, the magnitude and shape of $T(z)$ do not depend on the wavelength or geometry as long as the far-field condition for the aperture plane is satisfied. The aperture size S is, however, an important parameter in that a larger aperture reduces the variations in $T(z)$, i.e., the sensitivity. This reduction is more prominent in the peak, where beam narrowing occurs, and results in a peak transmittance that cannot exceed $(1 - S)$. The effect vanishes for a large aperture or no aperture, where $S = 1$, and $T(z) = 1$ for all z and $\Delta\Phi_0$ (assuming no nonlinear absorption). For small $|\Delta\Phi|$, the peak and valley occur at the same distance with respect to the focus, and for a cubic nonlinearity their separation is found to be $\approx 1.7z_0$.

This distance may be used to determine the order of the nonlinearity.

We can define an easily measurable quantity ΔT_{p-v} as the difference between the normalized peak (maximum) and valley (minimum) transmittances, $T_p - T_v$. The variation of this quantity as a function of $\Delta\Phi_0$ as calculated for various aperture sizes is found to be almost linearly dependent on $\Delta\Phi_0$. Within $\pm 3\%$ accuracy the following relationship holds:

$$\Delta T_{p-v} \approx p |\Delta\Phi_0| \text{ for } |\Delta\Phi_0| \leq \pi, \quad (7a)$$

with $p = 0.405(1 - S)^{0.25}$. Particularly, for on-axis transmission ($S \approx 0$) we find that

$$\Delta T_{p-v} \approx 0.405 |\Delta\Phi_0| \text{ for } |\Delta\Phi_0| \leq \pi. \quad (7b)$$

The linear nature of relations (7) makes it convenient to account for the temporal and transient effects in Eq. (6) by simply averaging the instantaneous phase distortion $\Delta\Phi_0(t)$ over the laser pulse shape. An average phase distortion $\Delta\Phi_0$ can be obtained as the product of the peak phase shift $\Delta\Phi_0(0)$ and an averaging factor that is a constant of the pulse shape for a given type of nonlinearity. For example, for a Gaussian pulse shape and a fast cubic nonlinearity, this factor is $1/\sqrt{2}$. For a cumulative nonlinearity having a decay time much longer than the pulse width (e.g., thermal) a fluence averaging factor of 0.5 is to be used regardless of the shape of the pulse. Relations (7) can thus be used to calculate the nonlinear index n_2 to within $\pm 3\%$. This equation also reveals the highly sensitive nature of the Z-scan technique. For example, if the experimental apparatus is capable of resolving transmittance changes (ΔT_{p-v}) of $\approx 1\%$, phase changes corresponding to $\lambda/250$ wave-front distortion are detectable.

Figure 2 shows a Z scan of a 1-mm-thick CS_2 cell using 300-nsec pulses from a single-longitudinal-mode

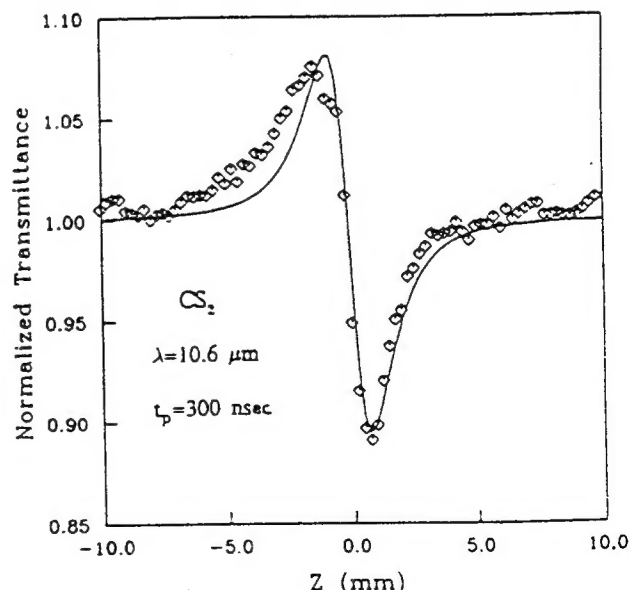


Fig. 2. Measured Z scan of a 1-mm-thick CS_2 cell using 300-nsec pulses at $\lambda = 10.6 \mu\text{m}$ indicating thermal self-defocusing. The solid curve is the calculated result with $\Delta\Phi_0 = -0.6$.

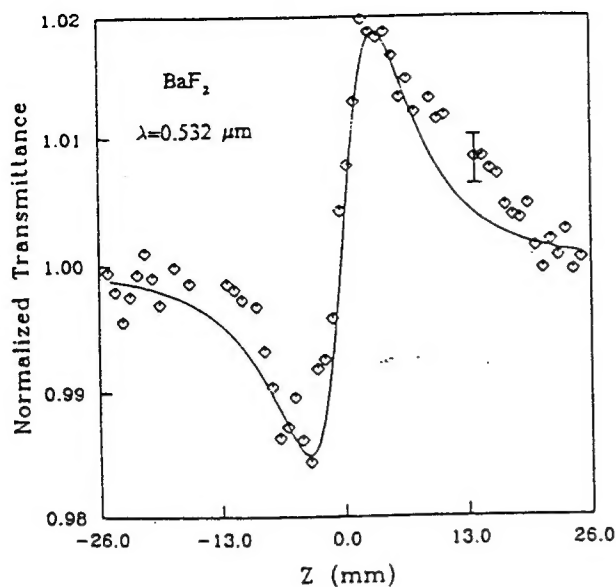


Fig. 3. Measured Z scan of a 2.5-mm-thick BaF_2 sample using 27-psec (FWHM) pulses at $\lambda = 0.532 \mu\text{m}$ indicating the self-focusing due to the electronic Kerr effect. The solid curve is the theoretical fit with $\Delta\Phi_0 = 0.085$ corresponding to $\approx \lambda/75$ phase distortion.

TEA CO_2 laser having an energy of 0.85 mJ. The peak-to-valley configuration of this Z scan is indicative of a negative (self-defocusing) nonlinearity. The solid curve in Fig. 2 is the calculated result using $\Delta\Phi_0 = -0.6$, which gives an index change of $\Delta n_0 = -1 \times 10^{-3}$. This is attributed to a thermal nonlinearity resulting from linear absorption of CS_2 ($\alpha \approx 0.22 \text{ cm}^{-1}$) at $10.6 \mu\text{m}$. The rise time of a thermal lens in a liquid is determined by the acoustic transit time, $\tau = w_0/v_s$, where v_s is the velocity of sound in the liquid. For CS_2 with $v_s \approx 1.5 \times 10^5 \text{ cm/sec}$ and $w_0 \approx 60 \mu\text{m}$, we obtain a rise time of $\approx 40 \text{ nsec}$, which is almost an order of magnitude smaller than the transversely excited atmosphere laser pulse width. Furthermore, the relaxation of the thermal lens, governed by thermal diffusion, is of the order of 100 msec.¹² Therefore we regard the nonuniform heating caused by the 300-nsec pulses as quasi-steady state, in which case the average on-axis nonlinear index change at focus can be determined in terms of the thermo-optic coefficient, dn/dT , as

$$\Delta n_0 \approx \frac{dn}{dT} \frac{0.5 F_0 \alpha}{\rho C_v}, \quad (8)$$

where F_0 is the fluence, ρ is the density, C_v is the specific heat, and 0.5 denotes the fluence averaging factor. With the known value of $\rho C_v \approx 1.3 \text{ J/K cm}^3$ for CS_2 , we calculate that $dn/dT \approx -(8.3 \pm 1.0) \times 10^{-4} \text{ }^\circ\text{C}^{-1}$, which is in good agreement with the reported value of $-8 \times 10^{-4} \text{ }^\circ\text{C}^{-1}$.¹³

Using 27-psec (FWHM), 2.0- μJ pulses from a frequency-doubled Nd:YAG laser focused to a spot size w_0 of $18 \mu\text{m}$, we performed a Z scan on a 2.5-mm-thick BaF_2 crystal. The result (Fig. 3) indicates a positive (self-focusing) nonlinearity. The theoretical fit assuming Gaussian-shaped pulses was obtained for $\Delta\Phi_0 = 0.085$, from which an n_2 value of $\approx (0.8 \pm 0.15) \times 10^{-13} \text{ esu}$ is calculated. This value is in agreement with the reported values of $\approx 0.7 \times 10^{-13}$ and $\approx 1.0 \times 10^{-13} \text{ esu}$ as measured using nearly degenerate three-wave mixing⁴ and time-resolved interferometry,² respectively. BaF_2 has a particularly small value of n_2 . In addition, the laser input energy was purposely lowered to 2.0 μJ to illustrate the sensitivity of this technique to small induced phase changes. The peak wave-front distortion shown in Fig. 3 corresponds to $\lambda/75$.

The simplicity and sensitivity of the technique described here make it attractive as a screening test to give the sign, magnitude, and order of the nonlinear response of new nonlinear-optical materials.

We gratefully acknowledge the support of the National Science Foundation through grant ECS 8617066 and funding from the Defense Advanced Research Projects Agency/CNVEO and the Florida High Technology and Industrial Council. We also thank T. H. Wei and Y. Y. Wu for performing several Z-scan measurements and D. J. Hagan, A. Miller, and M. J. Soileau for helpful discussions.

References

1. M. J. Weber, D. Milam, and W. L. Smith, *Opt. Eng.* 17, 463 (1978).
2. M. J. Moran, C. Y. She, and R. L. Carman, *IEEE J. Quantum Electron.* QE-11, 259 (1975).
3. S. R. Friberg and P. W. Smith, *IEEE J. Quantum Electron.* QE-23, 2089 (1987).
4. R. Adair, L. L. Chase, and S. A. Payne, *J. Opt. Soc. Am.* B 4, 875 (1987).
5. A. Owyong, *IEEE J. Quantum Electron.* QE-9, 1064 (1973).
6. W. E. Williams, M. J. Soileau, and E. W. Van Stryland, *Opt. Commun.* 50, 256 (1984).
7. W. E. Williams, M. J. Soileau, and E. W. Van Stryland, presented at the Fifteenth Annual Symposium on Optical Materials for High Power Lasers, Boulder, Colo., 1983.
8. J. R. Hill, G. Parry, and A. Miller, *Opt. Commun.* 43, 151 (1982).
9. T. F. Boggess, S. C. Moss, I. W. Boyd, and A. L. Smirl, in *Ultrafast Phenomena IV*, D. H. Huston and K. B. Eisenthal, eds. (Springer-Verlag, New York, 1984), p. 202.
10. J. D. Gaskill, *Linear Systems, Fourier Transforms, and Optics* (Wiley, New York, 1978).
11. D. Weaire, B. S. Wherrett, D. A. B. Miller, and S. D. Smith, *Opt. Lett.* 4, 331 (1979).
12. J. N. Hayes, *Appl. Opt.* 11, 455 (1972).
13. V. Raman and K. S. Venkataraman, *Proc. R. Soc. London Ser. A* 171, 137 (1939).